

UNCLASSIFIED

| |
|--|
| |
| |
| |
| AD NUMBER |
| AD876608 |
| NEW LIMITATION CHANGE |
| TO Approved for public release, distribution unlimited |
| FROM Distribution authorized to U.S. Gov't. agencies and their contractors; Administrative/Operational use; Jun 1970. Other requests shall be referred to Air Force Aero Propulsion Laboratory, Air Force Systems Command, Wright-Patterson Air Force Base, Ohio 45433. |
| AUTHORITY |
| AFRPL ltr, 30 Jun 1975 |

THIS PAGE IS UNCLASSIFIED

AFAPL-TR-69-103

AD 876608

12

**PROCEEDINGS OF THE AIR FORCE
AIRFRAME-PROPULSION
COMPATIBILITY SYMPOSIUM**

24-26 June 1969

COSPONSORED BY

*AIR FORCE AERO PROPULSION LABORATORY
AIR FORCE FLIGHT DYNAMICS LABORATORY*

AD 12
DDG FILE COPY

TECHNICAL REPORT AFAPL-TR-69-103

JUNE 1970

DDC
NOV 17 1970
REGISTRATION
B

This document is subject to special export controls and each transmittal to foreign governments or foreign nationals may be made only with prior approval of the Air Force Aero Propulsion Laboratory (APL), Wright-Patterson Air Force Base, Ohio.

**AIR FORCE AERO PROPULSION LABORATORY
AIR FORCE SYSTEMS COMMAND
WRIGHT-PATTERSON AIR FORCE BASE, OHIO**

NOTICE

When Government drawings, specifications, or other data are used for any purpose other than in connection with a definitely related Government procurement operation, the United States Government thereby incurs no responsibility nor any obligation whatsoever; and the fact that the government may have formulated, furnished, or in any way supplied the said drawings, specifications, or other data, is not to be regarded by implication or otherwise as in any manner licensing the holder or any other person or corporation, or conveying any rights or permission to manufacture, use, or sell any patented invention that may in any way be related thereto.

This document is subject to special export controls and each transmittal to foreign governments or foreign nationals may be made only with prior approval of the Air Force Aero Propulsion Laboratory (APLA), Wright-Patterson Air Force Base, Ohio.

The distribution of this report is limited for the protection of technical know-how pertaining to the design and production of military aircraft systems.

A rectangular stamp or routing slip with a vertical border. It contains several lines of text, some of which are partially obscured or faded. There are three checkboxes on the right side. The middle checkbox is checked with a black dot. A handwritten mark, possibly '2', is written to the left of the stamp. A diagonal line is drawn across the top right corner of the stamp.

Copies of this report should not be returned unless return is required by security considerations, contractual obligations, or notice on a specific document.

AFAPL-TR-69-103

**PROCEEDINGS OF THE AIR FORCE
AIRFRAME-PROPULSION
COMPATIBILITY SYMPOSIUM**

24-26 June 1969

COSPONSORED BY

*AIR FORCE AERO PROPULSION LABORATORY
AIR FORCE FLIGHT DYNAMICS LABORATORY*

This document is subject to special export controls and each transmittal to foreign governments or foreign nationals may be made only with prior approval of the Air Force Aero Propulsion Laboratory (APTA), Wright-Patterson Air Force Base, Ohio.

FOREWORD

The first National Airframe-Propulsion Compatibility Symposium, sponsored by the Air Force Aero Propulsion Laboratory (AFAPL) and the Air Force Flight Dynamics Laboratory (AFFDL) of Wright-Patterson Air Force Base, Ohio, was held in Miami Beach, Florida, on 24, 25, and 26 June 1969. The six technical sessions were held in the Carillon Hotel. In addition, 10 company-sponsored exhibits were displayed for the public. Twenty-seven technical papers were presented with an additional five papers accepted for publication. The 31 Unclassified papers are published as AFAPL-TR-69-103 with the one Confidential paper being published as Supplement 1 to AFAPL-TR-69-103. This report was submitted 29 October 1969.

The papers were submitted in reproducible form and are published substantially as received, accounting for certain variation in styling and treatment.

The symposium committee was composed of the following members:

Chairmen: Col H. A. Lyon, AFAPL
Col J. R. Myers, AFFDL

Deputy Chairmen: M. Dunnam, AFAPL
W. Lamar, AFFDL

Symposium Directors: C. Simpson, AFAPL
P. Antonatos, AFFDL

Executive Director: H. J. Gratz

Arrangements Committee: H. J. Gratz, AFAPL
1st Lt D. Engwall, AFFDL
A. J. Cannon, ASD - Assistant to Committee

Exhibit Chairman: R. Martin, AFAPL

Symposium Secretary: L. Limberg, AFAPL

FAA, Army, Navy, NASA Coordination: AFFDL

Technical Chairman: H. Schumacher, AFAPL

Propulsion System Integrated Performance Chairman: H. I. Bush, AFAPL

Session I Cochairman: G. K. Rickey, AFFDL

Session II Cochairman: Sq Ldr Brian Brimelow, RAF, AFAPL

Propulsion System Stability Chairman: Major G. E. Strand, USAF, AFAPL

Session III Cochairman: L. E. Surber, AFFDL

Session IV Cochairman: L. D. McKenny, AFAPL

**Inlet-Engine Controls and Airframe Propulsion Compatibility Management
Chairman: Major J. R. Nelson, USAF, AFAPL**

Session V Cochairman: C. E. Bentz, AFAPL

Session VI Cochairman: R. H. Klepinger, ASD

During the dinner, held the night of 25 June 1969, Mr. George S. Schairer, Vice President, Research and Development, The Boeing Company, spoke on Systems Engineering. The Toastmaster was Mr. E. C. Simpson, Director, Turbine Engine Division, Air Force Aero Propulsion Laboratory.

Publication of this report does not constitute Air Force approval of the report's findings or conclusions. It is published only for the exchange and stimulation of ideas.



**HOWARD E. SCHUMACHER, Chief
Performance Branch
Turbine Engine Division
Air Force Aero Propulsion Laboratory
Technical Chairman**

ABSTRACT

This report presents the proceedings of the Air Force Airframe-Propulsion Compatibility Symposium, held at the Carillon Hotel, Miami Beach, Florida, on 24-26 June 1969. Three topics were discussed during the symposium: (1) Propulsion System Integrated Performance, (2) Propulsion System Stability, and (3) Inlet-Engine Controls and Airframe Propulsion Compatibility Management. The first topic covered a session on Aircraft and Engine System Installations and another on Exhaust System Considerations. The two sessions under topic two concerned Inlet Distortion Investigations and Engine Stability Investigations. Last, the third topic also covered two sessions: one dealt with Control Aspects for Propulsion Installation and the other dealt with Management and Systems Data for Engine Inlet Compatibility.

(The distribution of this abstract is unlimited.)

TABLE OF CONTENTS

| | PAGE |
|--|------|
| INTRODUCTION | 1 |
| WELCOMING ADDRESS | 3 |
| Colonel Herbert A. Lyon Commander, Air Force Aero Propulsion Laboratory | |
| KEYNOTE ADDRESS | 5 |
| Mr. Joe C. Jones Deputy Assistant Secretary of the Air Force for Research and Development | |
| PROPULSION SYSTEM INTEGRATED PERFORMANCE (24 June 1969) | 11 |
| Chairman: Mr. H. Ivan Bush, Air Force Aero Propulsion Laboratory | |
| SESSION I - AIRCRAFT AND ENGINE SYSTEM INSTALLATION | 11 |
| Cochairman: Mr. G. K. Richey, Air Force Flight Dynamics Laboratory | |
| AIRFRAME PROPULSION INTEGRATION EFFECTS ON VEHICLE DESIGN | 13 |
| Philip Antonatos, George K. Richey, Air Force Flight Dynamics Laboratory and Richard H. Klepinger, Aeronautical Systems Division | |
| PROPULSION SYSTEM INTEGRATION AND TEST PROGRAM | 49 |
| W. H. Hand and R. H. Johnson, North American Rockwell Corporation, Los Angeles Division | |
| EXPERIMENTAL INVESTIGATION OF TRANSONIC INLET DRAG | 93 |
| F. D. McVey, E. J. Phillips, and J. V. Rejeske, McDonnell Aircraft Company, St Louis MO | |

| | PAGE |
|--|------|
| A PLAN FOR BOOKKEEPING ON THE PROPULSION AND AERO-DYNAMIC ELEMENTS OF AIRPLANE PERFORMANCE | 133 |
| Leonard H. Schreiber, General Dynamics, Fort Worth Division | |
| FIGHTER EXHAUST SYSTEM BLENDING | 159 |
| D. Migdal and W. K. Greathouse, Grumman Aircraft Engineering Corp. | |
| ANALYSIS AND DEMONSTRATION TECHNIQUES FOR INSTALLATION AERODYNAMICS EFFECTS ON HIGH BYPASS TURBOFANS | 161 |
| James S. Holdhusen, Fluidyne Engineering Corporation | |
| SESSION II - EXHAUST SYSTEM CONSIDERATION | 187 |
| Cochairman: Sqn Ldr Brian Brimelow, RAF Air Force Aero Propulsion Laboratory | |
| FORCE MEASUREMENT OF AFTERBODY INTERACTION DRAG AT TRANSONIC AND SUPERSONIC MACH NUMBERS WITH PROPULSION EXIT PARAMETERS SIMULATED | 189 |
| P. L. Lemoine, North American Rockwell Corporation, Los Angeles Division | |
| TWIN-JET AIRCRAFT AFT-FUSELAGE PERFORMANCE PREDICTION | 229 |
| Craig E. Swavely, Pratt & Whitney Aircraft, Florida Research and Development Center | |
| EXHAUST NOZZLE-AFTERBODY INTEGRATION ON TACTICAL FIGHTER TYPE AIRCRAFT | 251 |
| John L. Benson and Edsel R. Glasgow, Lockheed-California Company | |
| WIND TUNNEL INVESTIGATION OF INSTALLATION EFFECTS ON UNDERWING SUPERSONIC CRUISE EXHAUST NOZZLES AT TRANSONIC SPEEDS | 281 |
| Bernard J. Blaha, Daniel C. Mikkelson, and Douglas E. Harrington, Lewis Research Center, NASA | |

| | PAGE |
|---|------|
| CALCULATION OF SUBSONIC INLET DRAG | 297 |
| T. C. Rockow, G. M. Sharp, and E. D. Spong McDonnell Aircraft Company, St Louis MO | |
| INVESTIGATION OF INTEGRATED BOOSTER-SUSTAINER- AFTERBODY DESIGN ON OVERALL VEHICLE PERFORMANCE | 333 |
| H. H. Korst and J. S. Divita, North American Rockwell Corporation, Rocketdyne Division Los Angeles CA | |
| PROPULSION SYSTEM STABILITY (25 June 1969) | 369 |
| Chairman: Major G. E. Strand, USAF Air Force Aero Propulsion Laboratory | |
| SESSION III - INLET DISTORTION INVESTIGATIONS | 369 |
| Cochairman: Mr. L. E. Surber Air Force Flight Dynamics Laboratory | |
| LARGE SCALE INLET COMPATIBILITY TEST RESULTS | |
| Paul H. Kutchenreuter, Jr. (CLASSIFIED PAPER) General Electric Company | |
| PARADOX IN INTERPRETING INLET-ENGINE COMPATIBILITY WITH HIGH RESPONSE INLET INSTRUMENTATION | 371 |
| C. E. Porcher, General Dynamics, Fort Worth Division | |
| EXPERIMENTAL STUDY OF INLET-GENERATED PRESSURE FLUCTUATIONS | 427 |
| Dale A. Sherman and David C. Motycka, Pratt & Whitney Aircraft Division of United Aircraft Corporation and Gordon C. Oates, Professor of Aeronautics and Astronautics, University of Washington, Seattle Wash | |
| A POSSIBLE MECHANISM FOR INLET/ENGINE INTERACTIONS DUE TO INLET FLOW FLUCTUATIONS | 459 |
| M. B. Sussman and G. W. N. Lampard The Boeing Company | |

| | PAGE |
|--|------|
| UPSTREAM INFLUENCE OF AN AXIAL COMPRESSOR ON CIRCUMFERENTIALLY DISTORTED FLOW | 475 |
| Alan H. Spring, General Dynamics, Fort Worth Division | |
| SESSION IV - ENGINE STABILITY INVESTIGATIONS | 489 |
| Cochairman: Mr. L. D. McKenny Air Force Aero Propulsion Laboratory | |
| PROPULSION SYSTEM FLOW STABILITY | 491 |
| Arnold W. Martin, North American Rockwell Los Angeles Division | |
| DEVELOPMENT OF A PROTOTYPE DISCRETE-FREQUENCY, TOTAL PRESSURE FLUCTUATION GENERATOR FOR JET ENGINE-INLET COMPATIBILITY INVESTIGATIONS | 517 |
| G. R. Lazaller and J. T. Tate, ARO Inc. AEDC | |
| COMPUTER CONTROLLED PHOTOGRAPHY FOR REDUCTION OF DYNAMIC DISTORTION DATA | 551 |
| W. J. Elliott and A. Medlock, and R. C. Hood Allison Division, General Motors Corporation | |
| PRESSURE FLUCTUATIONS CAUSE COMPRESSOR INSTABILITY | 567 |
| G. A. Plourde, Pratt & Whitney Aircraft, Division of United Aircraft, East Hartford CT Sqd Ldr Brian Brimiow Air Force Aero Propulsion Laboratory | |
| STALL AND DISTORTION INVESTIGATION OF A YTF30-P-1 TURBOFAN ENGINE | 605 |
| John H. Povolny Lewis Research Center, NASA | |
| THE PERFORMANCE PREDICTION OF MULTISTAGE AXIAL COM- PRESSORS OF ARBITRARY GEOMETRY OPERATING WITH COMBINED RADIAL AND CIRCUMFERENTIAL DISTORTION | 627 |
| R. A. Novak and R. M. Hearsey, Northern Research and Engineering Corp. Cambridge MA | |

| | PAGE |
|---|------|
| INLET-ENGINE CONTROLS AND AIRFRAME PROPULSION COMPATIBILITY MANAGEMENT (26 June 1969) | 673 |
| <p style="margin-left: 40px;">Chairman: Major J. R. Nelson, USAF Air Force Aero Propulsion Laboratory</p> | |
| SESSION V - CONTROL ASPECTS FOR PROPULSION INSTALLATION | 673 |
| <p style="margin-left: 40px;">Cochairman: Mr. C. E. Bentz Air Force Aero Propulsion Laboratory</p> | |
| CRITERIA FOR A TURBINE ENGINE CONTROL SYSTEM DEVELOP- MENT MODEL | 675 |
| <p style="margin-left: 40px;">Stephan J. Przybylko, Air Force Aero Propulsion Laboratory</p> | |
| ANALYSIS FOR SPECIAL ENGINE CONTROLS REQUIREMENTS FOR UNSTART/RESTART OF MIXED COMPRESSION INLETS | 689 |
| <p style="margin-left: 40px;">I. E. Marvin and T. L. Schilling General Electric Company</p> | |
| IMPACT OF MULTIPLEXING ENGINE/AIRCRAFT INSTRUMENTATION AND CONTROL SIGNALS | 713 |
| <p style="margin-left: 40px;">Henry R. Ask, John Games, and Daniel Stone Hamilton Standard-Electronics Dept Division of United Aircraft</p> | |
| RESPONSIBLE THRUST CONTROL-ADAPTABILITY TO ADVANCED TACTICAL AIRCRAFT DESIGN | 761 |
| <p style="margin-left: 40px;">Sandro Westermayer, The Boeing Company</p> | |
| PROPULSION CONTROL PROBLEMS GENERATED BY ENERGY MANAGEMENT CONTROL REQUIREMENTS | 783 |
| <p style="margin-left: 40px;">Ross D. Schmidt Honeywell, Inc. Minneapolis MN</p> | |
| SESSION VI - MANAGEMENT AND SYSTEM DATA FOR ENGINE INLET COMPATIBILITY | 799 |
| <p style="margin-left: 40px;">Cochairman: Mr. R. H. Klepinger, Aeronautical Systems Division</p> | |

| | PAGE |
|--|-------------|
| ENGINEERING MANAGEMENT PHILOSOPHY ON AIRFRAME PROPULSION COMPATIBILITY | 801 |
| <p style="margin-left: 40px;">K. Kanouse, G. K. Richey, G. Strand and D. A. Watne, Airframe-Propulsion Compatibility Committee Wright-Patterson AFB OH</p> | |
| MANAGEMENT OF AIRFRAME-PROPULSION COMPATIBILITY | 877 |
| <p style="margin-left: 40px;">Leonard H. Schrieber, General Dynamics, Fort Worth Division</p> | |
| PROPULSION COMPATIBILITY CONSIDERATIONS FOR ENGINE TRANSIENTS DURING EXTREME MANEUVERS | 891 |
| <p style="margin-left: 40px;">R. A. Herzmark, McDonnell Aircraft Company and I. W. Victor, General Electric Company</p> | |
| ICE CRYSTAL INDUCED COMPRESSOR STALL IN THE F-102 | 931 |
| <p style="margin-left: 40px;">D. S. Oesterle, General Dynamics/Convair Division and J. L. Tubbs, Hq SAAMA, Kelly AFB TX</p> | |
| CLOSING REMARKS | 945 |
| <p style="margin-left: 40px;">H. E. Schumacher Air Force Aero Propulsion Laboratory Wright-Patterson AFB OH</p> | |
| EXHIBITORS | 947 |

INTRODUCTION

The Airframe-Propulsion Compatibility Symposium provided a medium for the exchange of ideas concerning the problems associated with the performance and stability of integrated propulsion systems.

The specific objectives were:

1. To provide an awareness of the magnitude of potential problems associated with airframe-engine integration
2. To stimulate thought and ideas which will provide solutions to compatibility problems as they arise during all phases of system development
3. To focus more attention upon the management and engineering techniques which might be employed to bring about closer working relationship among all agencies

Papers presented at the Symposium treated the propulsion system performance, stability, and integration of tactical and strategic airbreathing systems. A variety of topics such as inlets, engines, exhaust nozzles, controls, data processing, instrumentation and test techniques emphasized the importance of compatibility to all research and development activities.

WELCOMING ADDRESS

Colonel Herbert A. Lyon

Commander, Air Force Aero Propulsion Laboratory

Good morning -- on behalf of the Air Force Flight Dynamics Laboratory and the Air Force Aero Propulsion Laboratory, it is my pleasure to welcome you to this symposium on Airframe Propulsion Compatibility. It is gratifying to see such a good turnout -- over 500 -- for this important meeting. Before introducing our keynote speaker, I want to say a few words about why the Aero Propulsion and Flight Dynamics Laboratories have cosponsored this meeting and why we consider it important.

It is no news to anyone here that the Air Force has experienced serious difficulties in achieving the specified range on some of its latest aircraft. Also, we have had a hard time trying to get stable engine operation throughout the desired operating envelope of the airplane. Both of these problems are intimately involved with the integration of the engine and the airframe. It is essential that we learn how to integrate engine and airframe if we are to have effective aircraft systems in the future.

Looking to past painful experience, it is evident that we must reach a position where it can be shown with a measured level of confidence before first flight that the integration of propulsion system and airframe will, in fact, result in total system compatibility. That measured level can only be achieved through a timely, coordinated set of valid testing efforts which isolate the required data in such a manner that there is no question among engine, airframe or Air Force people as to which numbers apply to design or off-design operation in all regions of the operating envelope.

The papers of this symposium will show there has been a great deal of progress in the effort to develop methods of integrating the work of airframe and propulsion system manufacturers. We are far from a complete solution to the problem, however. By continuing to concentrate our efforts in this area, we expect to reach the point where inlet, exhaust nozzle, and engine design and testing are accomplished in such a way that performance goals realistically include all items which affect not only installed thrust, but propulsion system stability.

In the last two years, much progress has been made in injecting some science into the heretofore black art of compatibility. Research into the nature of the inlet flow maldistribution phenomena led to the requirement for high response instrumentation. Data gained from this instrumentation when analyzed has resulted in a much more fundamental understanding of the engine environment and the engine's response.

These lessons from recent history deserve our serious attention today, if we are to avoid similar pitfalls in our upcoming developments. For, the demanding performance of the new Air Force and Navy aircraft developments represents significant challenges, not only to the airframe and propulsion system design teams, but to all of us. The F-15 air-superiority fighter, in particular, couples imposing inlet/engine stability criteria with stringent thrust/drag installation demands in order to achieve the superior energy maneuverability required throughout its flight envelope. And, meeting the demanded performance will entail numerous design trades between stability margin and both engine and airframe performance parameters in arriving at the finally balanced design.

Looking back, we can see that the late 1950's and the early 1960's witnessed a great flurry in missile developments and space activities which attracted the attention and absorbed the talents of a great many scientists and engineers in the military and NASA laboratories and in the aerospace industry who, otherwise, might have concerned themselves with research in aircraft/propulsion installation problems. And, while military aircraft developments in general were waning, this period did see the development of the subsonic turbofan engine for extending the legs of our long-range subsonic bomber, the B-52. The significant reduction in specific fuel consumption (SFC) made these engines natural candidates for the already expanding commercial airliner industry and also made them of extreme importance for military transports. While these subsonic installations were not completely immuned to performance problems, the general success had been striking.

Yet, on the first attempt to exploit the potentials of the turbofan engine in an afterburning configuration for the supersonic multi-mission F-111 fighter aircraft, severe stability and installation difficulties were encountered that had not been anticipated. Possibly the general success in adapting the turbofan to the relatively simple pod-mounted installations on subsonic transport-type aircraft had tended to mask certain of the problem potentials of the more sophisticated supersonic installation. The significant engineering challenges in the missile and space programs and the general success being achieved may also have in itself contributed a lulling effect. Additionally, the Government and industry engineering management environment of that period, coupled with the new fixed-price incentive contractual relationships, created an additional obstacle to a broad scale and rapid attack on the fundamental engineering problems at the outset. Internally, within the Air Force, the technical laboratories had become sufficiently separated from the SPO organizations that they lacked a proper understanding or sense of responsibility for the technical problems being encountered. Finally, the engine and airframe contractors, operating under the terms and conditions of their individual contracts with their own specifications, performance guarantees, correction of deficiency clauses, and schedule problems, were not prone to become involved in each others efforts anymore

than was absolutely necessary. As a result of this general environment, when confronted with serious inlet/engine stability and nozzle/airframe backend problems in the F-111, we found ourselves with too little fundamental knowledge and with the various engineering groups constrained by an awkward management and contractual relationship. Even more recently, many of the same constraints were initially prevalent in developing a solution for the F-4E/J-79 installation problems. Fortunately, the system did finally awaken and reveal its resiliency. Once the seriousness of these problems was recognized and appreciated, ad hoc arrangements were made and the military laboratories, SPO technical personnel, NASA, and airframe and engine contractor teams rose to the challenge and initiated the necessary collaborative effort to effect solutions. But, the time lag had been costly.

The focus of attention, brought about by these experiences, was sufficient to stimulate the initiation of an Aircraft-Propulsion Subsystem Integration Program as a joint venture between the Air Force Aero Propulsion and Flight Dynamics Laboratories. This program, which has been developed in close collaboration with the NASA laboratories, has had the basic objective of providing that fundamental understanding of the dynamics of the engine/airframe compatibility problems which had been missing. Largely, as a result of the F-111 and F-4E problems, the early concentration of effort has been on developing an understanding of the dynamics of engine stall as an evolving technique for analyzing and properly categorizing transient inlet and duct pressure distortion effects. Recent results from testing with high response instrumentation has added considerably to the understanding of the stall mechanism within turbo machinery as it is effected by transient pressure fluctuations. Interface criteria can now be more meaningfully applied. A visual appreciation has even been developed. Recently, during a review of the status of this work, I had an opportunity to view a movie that displayed the results of a computer-plotted sequence of compressor face flow distortion patterns. It was extremely revealing to get a visual appreciation of the dynamic nature of the pressure patterns that an engine encounters during transient conditions. This technique should provide a convenient and significant tool for analyzing and studying pressure distortion characteristics from inlet and turbo machinery perturbations. From these and other efforts, it is apparent that we have come a long way during the last few years in increasing our knowledge and understanding of the fundamental elements involved in the complex dynamic problems associated with today's sophisticated inlet/engine stability matching.

While there appears to have been less fundamental analysis and experimentation involving inlet and integrated nozzle airframe configuration effects under way during the same period, the recent design and development activities on the Navy F-14 and the Air Force F-15 fighters have certainly stimulated increased activity in this area. The papers to be presented in this area during the Symposium will further add to

our base of knowledge. And, it appears evident, from the broad range of subjects to be covered in the various sessions, that we have overcome a major part of our past lethargy. There is now in evidence an awareness, among the engineering groups of both Government and industry in the managerial as well as the technical aspects, of the overall airframe/propulsion compatibility problem. But, I caution against deriving too much comfort from the activity thus far displayed; for, we are just now reaching that crucial point where we must translate the results of that activity into positive technical accomplishments in our forthcoming aircraft developments. This is now the challenge--our ability to translate the results of individual efforts into a complete integrated design.

In approaching these new undertakings, a look at our past developments reveals that one of the most serious deficiencies has been the lack of a sufficiently broad analytical ability to treat the total airframe/engine installation on an integrated basis--i.e., the inlet, duct, engine, integrated nozzle, and configuration effects. And this, of course, is aggravated by the, thus far, impossible task of properly simulating, through scale model wind tunnel testing, the inlet and exhaust flow conditions at the same time we are attempting to obtain force measurements. As a consequence, our first truly integrated tests do not occur until we fly. And, by that time, of course, there has already been a major commitment to the design of aircraft and engine hardware. Since we still find ourselves forced to rely on separate inlet/engine and nozzle/backend tests in the early design and development phase, our ability to analyze and understand these individual test results and properly relate them to the integrated design analysis remains critically important.

As a forcing function, the Air Force has established an approach of requiring detailed design analyses, fortified by specific testing criteria, to begin the matching of the engine stability with potential aircraft inlets at as early a point in the engine development cycle as possible. In this regard, tests involving the candidate F-15 inlets and the candidate engines are being carried out during the current Contract Definition and Initial Engine Development phase. Additionally, in keeping with the new Demonstrated Milestone Development approach, which will be established in the new system development programs, an attempt will be made to identify specific airframe/engine compatibility and installed performance test points in the system development schedule where successful results must be demonstrated before major hardware commitments can be undertaken. The success of this approach will again be critically dependent upon our ability to analyze and understand the integrated system design at the outset and to establish meaningful performance demonstration criteria. The principal difference in the current approach and development and production efforts will now be

contractually tied to the successful accomplishment of the established milestone demonstrations. The criticality of the management decisions thus established will place added demands upon both the Government and industry's engineering talents in providing sound technical criteria as a baseline for correlating the test results to overall system performance. So much so that it may be that our past practices in relation to specifications and interface documents between the propulsion and airframe system contractors may no longer prove to be adequate. Nor is it entirely clear that the total system performance responsibility techniques, as recently employed, will completely suffice without some modification in approach. We must therefore innovate effective changes to engineering management approaches and attitudes.

As a result of the experimental efforts that have been under way, there is a noticeable difference today in the awareness among the airframe and propulsion technical community relative to the major part that each must play in the integration task. However, I do not personally believe that we are yet practicing or, for that matter, have we yet found the essential administrative, engineering management and contractual mechanisms to insure that we practice an approach that combines the best talents of both groups in a collaborative effort to provide the initial integrated design and to solve propulsion system integration problems throughout the course of the airframe and engine technical development programs. Therefore, I would submit, for your consideration during the course of the discussions and deliberations at this Symposium, that additional attention must be given to the following three areas, if we are to avoid the pitfalls of the past:

1. Some means must be found to insure an integrated design team approach at the outset, which will include both the airframe and engine contractors' technical personnel, and this integrated approach must be continued throughout the development and test programs that follow.
2. The technical criteria, definitions, and technical book-keeping must be simply defined and clearly understood and agreed upon from the outset such that the contractors, SPO engineering, Air Force laboratories, and NASA are all using the same guide and talking the same language. This will become of critical importance in relating the milestone demonstration results to baseline design performance.
3. The Government technical laboratory personnel, both Air Force and NASA, must continue to maintain an awareness and assume a sense of responsibility for the technical success of the system design in support of the contractor design teams and the SPO engineering, and must remain active participants during the course of design and development testing.

For, if the course of our recent experiences has revealed to us any singular lesson, it would appear to be that the dynamic inter-relationship of the airframe/propulsion installation task requires an integrated design and engineering approach from beginning to end--both in a physical installation and a development cycle sense. And, further, that such integration does not only relate to the efforts of the airframe and propulsion engineers but to the integrated efforts of the Government and industry engineers as well.

PROPULSION SYSTEM INTEGRATED PERFORMANCE

(24 June 1969)

**H. I. Bush, Chairman
Air Force Aero Propulsion Laboratory**

SESSION I. AIRCRAFT AND ENGINE SYSTEM INSTALLATION

**G. K. Richey, Cochairman
Air Force Flight Dynamics Laboratory**

AIRFRAME PROPULSION INTEGRATION EFFECTS ON VEHICLE DESIGN

Philip P. Antonatos, Air Force Flight Dynamics Laboratory

George K. Richey, Air Force Flight Dynamics Laboratory

Richard H. Klepinger, Aeronautical Systems Division

INTRODUCTION

With the trend of closely coupled propulsion airframe designs, the proper integration of both the airframe and propulsion subsystems must be recognized in the early conceptual phases. Individually it is possible to develop component performance such as inlet pressure, acceptable distortion levels, recovery, nozzle efficiency, aerodynamic lift-to-drag ratio, maneuvering envelope, maximum lift coefficient, structural weight, volume and volume distribution that can meet the desired mission goals, but the integration of components and their related effects can and will dictate the overall performance characteristics of the flight vehicle. The complication of mixed missions, subsonic and supersonic, low altitude and high altitude impose a serious burden on developing optimum configurations whose design parameters require close scrutiny to assess the sensitivity of trade-off to assure maximum efficiency. The vehicle drag and lifting characteristics coupled with its stability and control must be matched with the large variations of engine airflow demand, inlet and nozzle drag, and weight. The off design conditions become critical for inlet-engine stability and performance.

The mix of mission requirements in terms of speed and altitude clearly emphasize the sensitivity of design parameters to properly integrate the propulsion system with the airframe to provide an optimum configuration.

A representative air superiority mission as shown in Figure 1 depicts the basic mission in terms of best cruise altitude and best cruise Mach



REPRESENTATIVE AIR SUPERIORITY MISSION

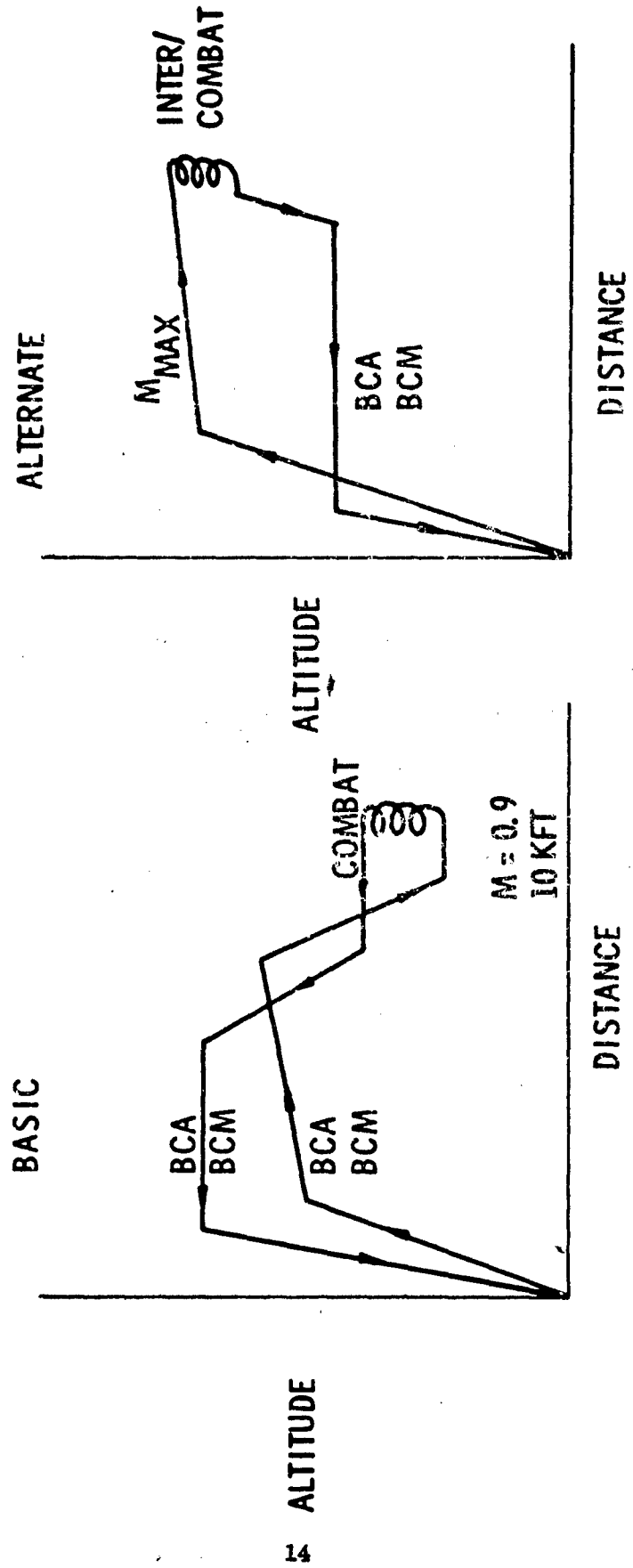


FIGURE 1

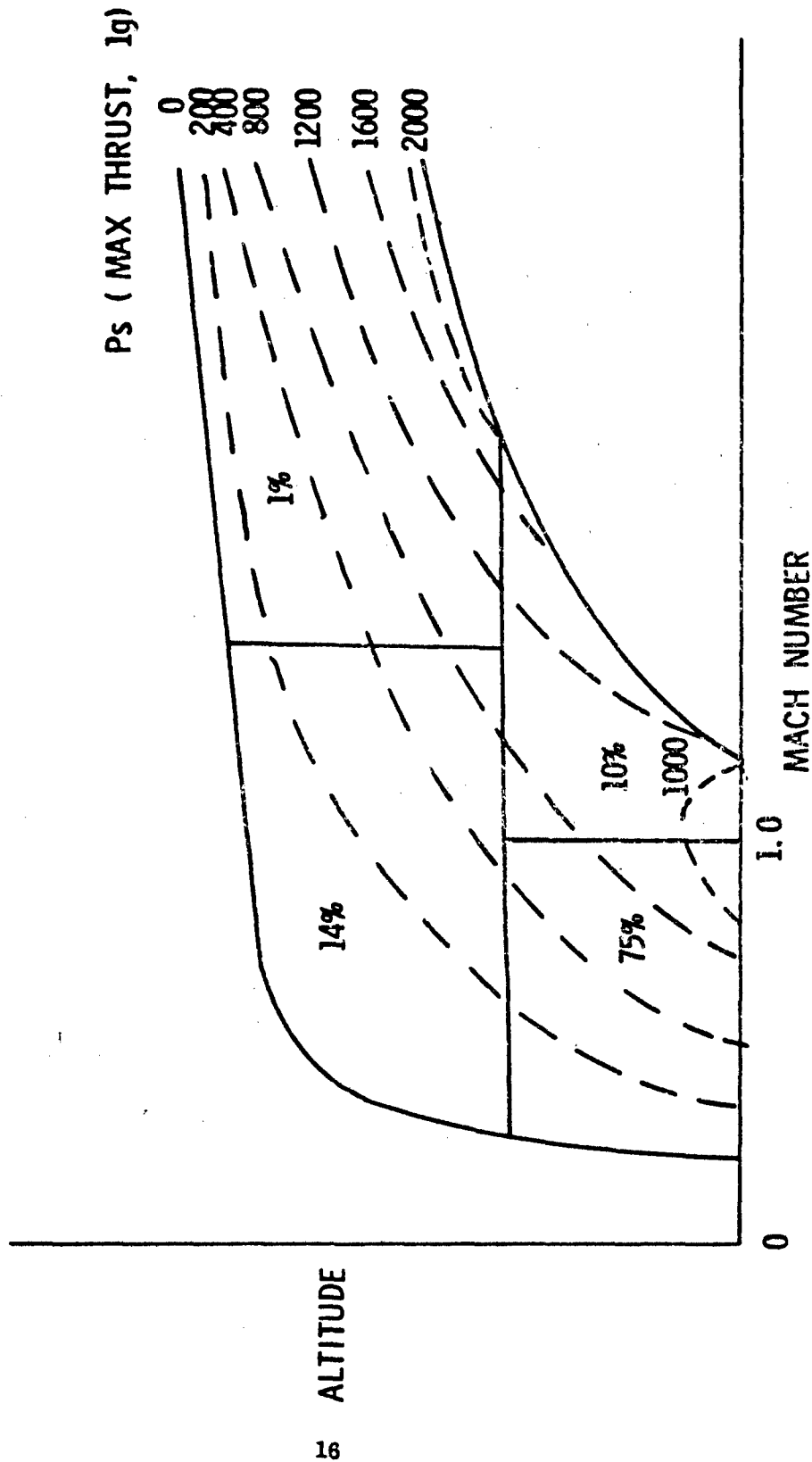
number at high subsonic speeds with effective combat in the lower transonic region of $M = .9$. The alternate mission includes a supersonic interception leg with combat again taking place in the transonic area. The requirements of inlet propulsion matching coupled with fuel requirements and efficient aerodynamic parameters require careful trade-offs to insure maximum effectiveness.

For a typical specific design of air superiority fighter, Figure 2 depicts the percentage of time spent at various speed regimes. The supersonic dash and intercept, because of excessive fuel requirements, are usually limited to about 1% of total time and usually not greater than 2%. In the future expansion to 5% may be possible with improvements in fuel consumption. Use of the afterburner degrades the propulsion efficiency, increases the specific fuel consumption and therefore to increase the supersonic time of flight appreciably would increase gross weight of air superiority fighter excessively. Upon completing interception and the beginning of effective combat, power and altitude are bled off such that the transonic and high subsonic regions become the speed areas of interest.

Representative strategic aircraft missions again have a mix of both the basic subsonic and alternative supersonic capability as shown on Figure 3. The mission requires long ranges of cruise in either mode with delivery capability at either a subsonic or supersonic dash mode. The design trade-offs are not hampered or limited with the maneuverability requirements of a superiority fighter; therefore, we require trade-off analysis to provide more efficient cruise capability.



REPRESENTATIVE COMBAT ZONE MODEL
AIR SUPERIORITY AIRCRAFT



REPRESENTATIVE STRATEGIC AIRCRAFT MISSIONS

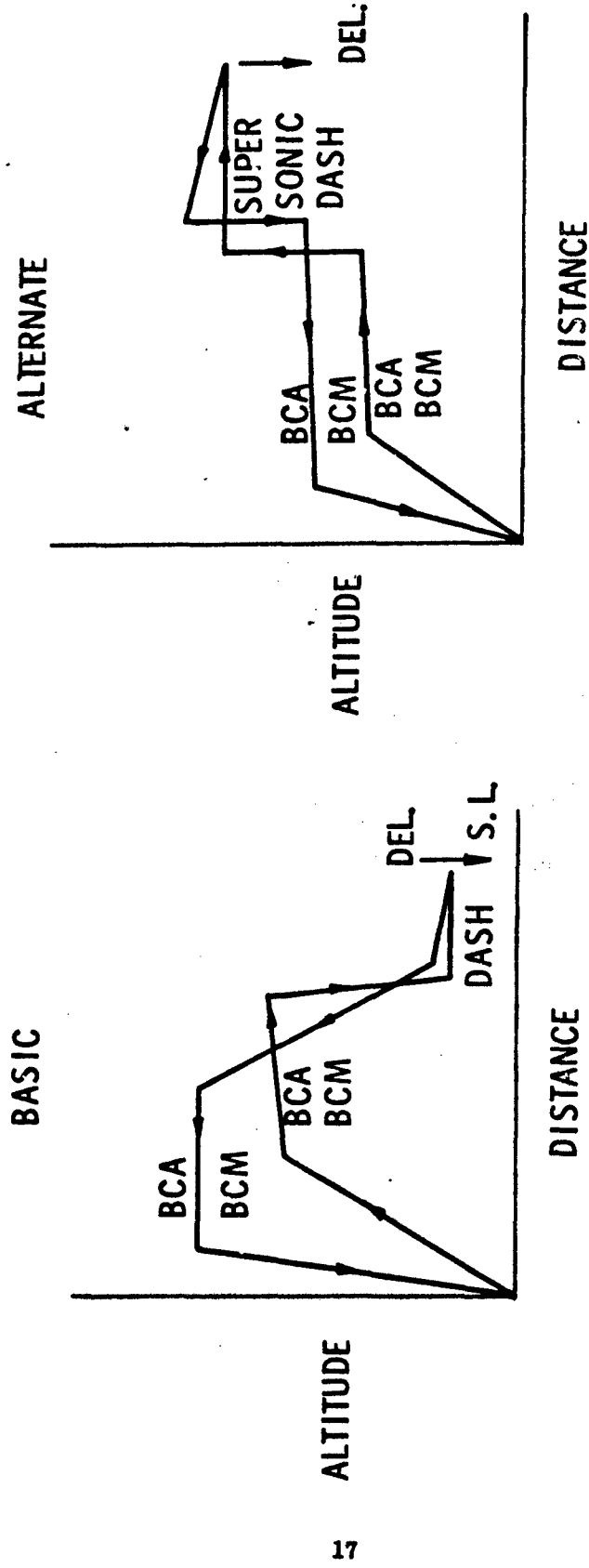


FIGURE 3

PROPULSION CYCLE SELECTION

A critical part of the design integration of a strategic or tactical vehicle is the selection of the proper propulsion system. In a preliminary design phase, the propulsion system is characterized by the propulsion cycle parameters of by-pass ratio, cycle pressure ratio, and turbine inlet temperature. Consideration must be given in the design of the vehicle to make sure that the proper balance of these parameters is chosen in order to maximize the mission capability of the selected aircraft.

If one looks at the optimum engine cycle for a point design at each of three operating conditions of subsonic high altitude, transonic sea level, and supersonic high altitude, the best engine will have the by-pass ratio and cycle pressure ratio values as shown in Figure 4. For high altitude subsonic flight the best by-pass ratio will likely be in the 7 to 10 level. If one only considers the sea level dash at subsonic speeds, by-pass ratio near 4 may tend to be more optimum. For supersonic high altitude flight, a low by-pass ratio or perhaps even a turbo-jet will tend to be the optimum engine cycle. It becomes clear from the diverse optimum cycles at different flight conditions that an aircraft which is designed to operate over a range of conditions will require a by-pass ratio and engine cycle pressure ratio which will be a compromise. The best compromise engine cycle must be determined on the basis of aircraft and mission performance.

For tactical aircraft, a high level of thrust is required to make rapid changes in altitude, rapid acceleration to higher Mach number, and to allow high "G" maneuvers to be performed. These maneuvers must be available over the complete flight profile of the aircraft. The extra thrust required during these short periods of time can only be achieved by use of an



POINT DESIGN ENGINES - CYCLE TRENDS

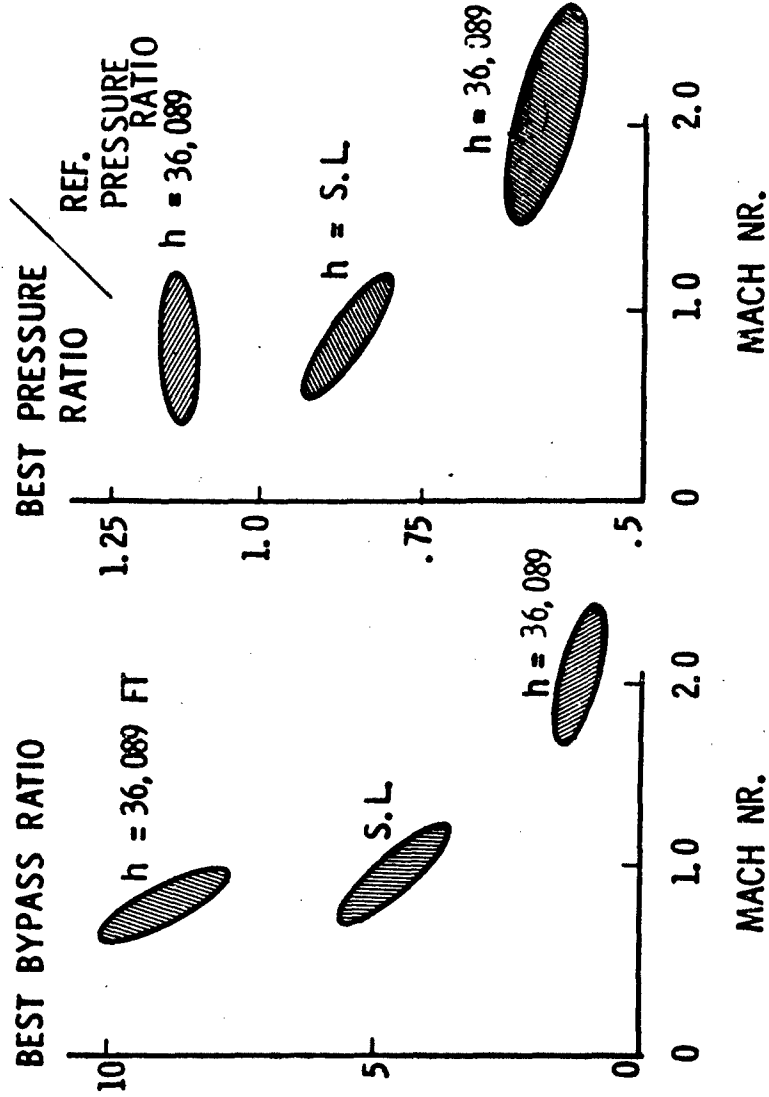


FIGURE 4

afterburning engine, since the extra thrust is not required during the normal cruise or low energy parts of the mission. For advanced tactical aircraft, the extra thrust requirement can and will influence the choice of engine by-pass ratio. Figure 5 compares the thrust level in afterburner versus by-pass ratio at supersonic conditions and the military thrust (without afterburner) versus by-pass ratio at transonic conditions. For high by-pass ratio engines, a very high level of thrust is available in afterburner (since more air can be burned) at the required maneuvering points of the aircraft. In order to increase the combat time and the combat radius of the aircraft, however, it is desirable to perform the high thrust maneuvers in military power as much as possible since less fuel is consumed. Unfortunately, the thrust in military power tends to decrease (as shown in Figure 5) as the by-pass ratio increases for the same total airflow. Although an afterburning turbo-fan engine can satisfy the requirements of fuel economy and efficiency with by-pass ratio in dry power and high levels of thrust with afterburning power, the fuel consumption as a function of net thrust produced in afterburner must also be examined to determine the allowable combat time and to show the effects on aircraft radius. Figure 5 shows that in non-afterburning operation, a turbo-fan with by-pass ratio of 1 has a lower fuel consumption than a turbo-jet. However, when the afterburner is turned on, the turbo-fan engine has a significantly higher fuel consumption than a turbo-jet. Therefore, although the thrust is higher with a by-pass engine, the penalty is paid in fuel consumption which decreases combat time and decreases allowable aircraft mission radius.

For a given tactical aircraft combat model as was shown in Figure 2, this trade-off between thrust available and fuel consumption in afterburning



EFFECTS OF BYPASS ON ENGINE THRUST AND FUEL CONSUMPTION

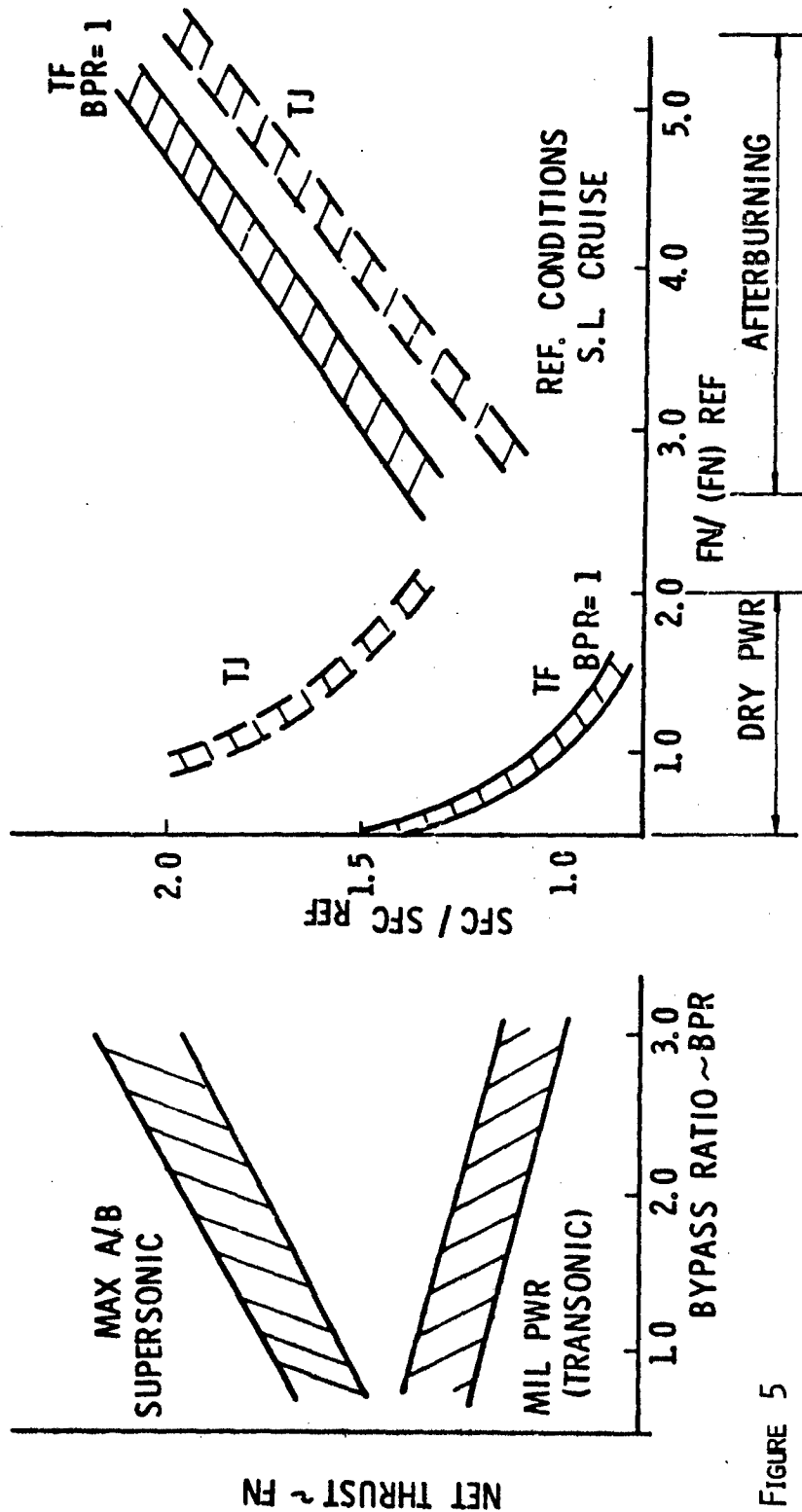


FIGURE 5

operation will tend to optimize the by-pass ratio for a tactical aircraft at a by-pass ratio approximately equal to 1. This result is shown in Figure 6 by the amount of combat fuel excess as a function of by-pass ratio. The "combat fuel excess" is that which is left over after a given tactical mission (such as shown in Figure 1) is performed. The combat fuel excess associated with a particular design could then be used for additional combat time or for additional mission radius. It is therefore an index used in preliminary design which is a measure of the efficiency of the propulsion system as it is integrated with the aircraft. Figure 6 indicates that the fuel excess index is maximized at a by-pass ratio near 1 and that increases of by-pass ratio over approximately 1.5 tend to decrease the combat fuel excess due to the high fuel consumption in afterburner operation, which is required during combat. For a selected by-pass ratio, the engine cycle pressure ratio and turbine temperature will then be varied to select the optimum cycle for the aircraft in the given mission.

For strategic aircraft, the proper choice of engine cycle parameters is equally critical and can have significant effects on the gross weight of the aircraft designed to meet a particular mission. If a strategic aircraft is considered to have a mixed subsonic and supersonic mission as was shown in Figure 3, the effects of engine cycle variations for the basic and alternate missions are shown in Figure 7. For the supersonic mission, although a low by-pass ratio is more efficient in the supersonic portion of flight, which requires afterburner, the subsonic cruise portion of the mission requires a somewhat higher by-pass ratio to achieve the desired efficiency (SFC). This has a more significant effect on the gross



BASIC TACTICAL AIRCRAFT MISSION



BYPASS RATIO EFFECTS

CPR = CONST.
TOGW = CONST.
ENGINE CYCLE VARIABLE

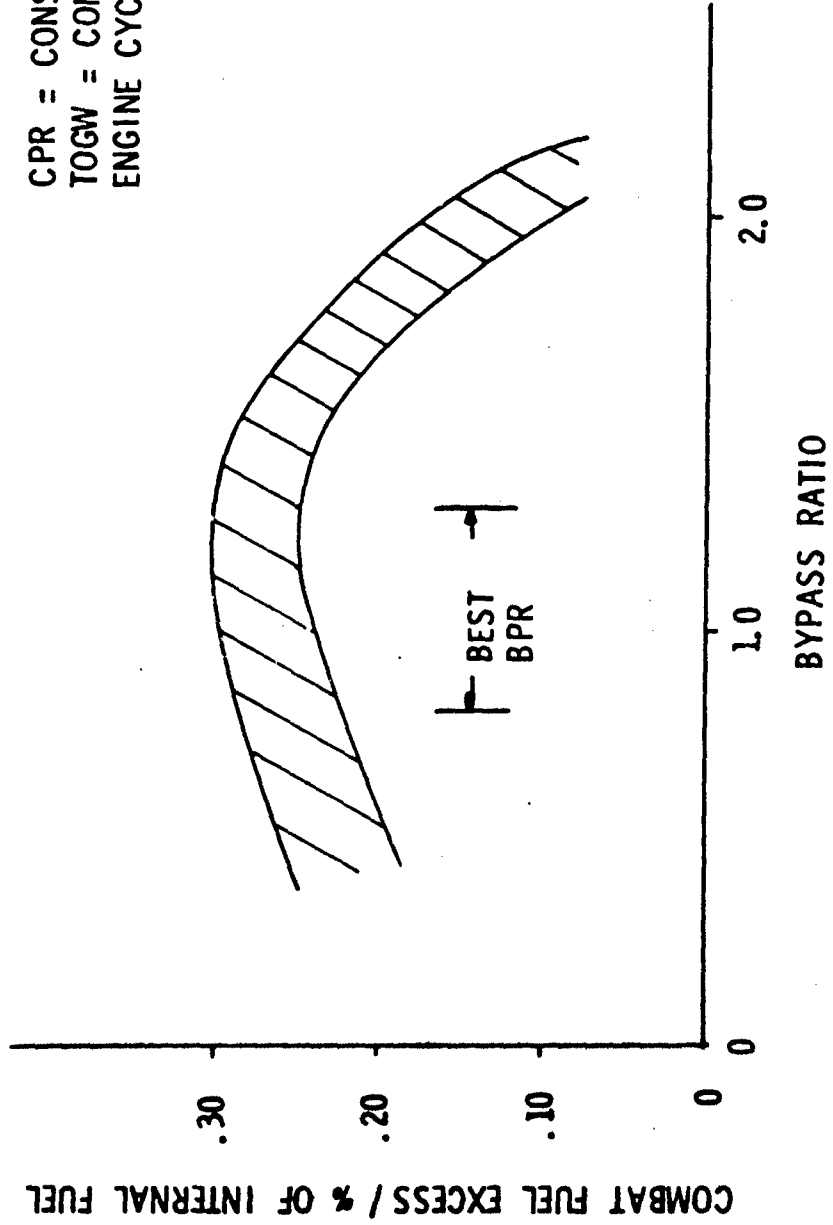


FIGURE 6

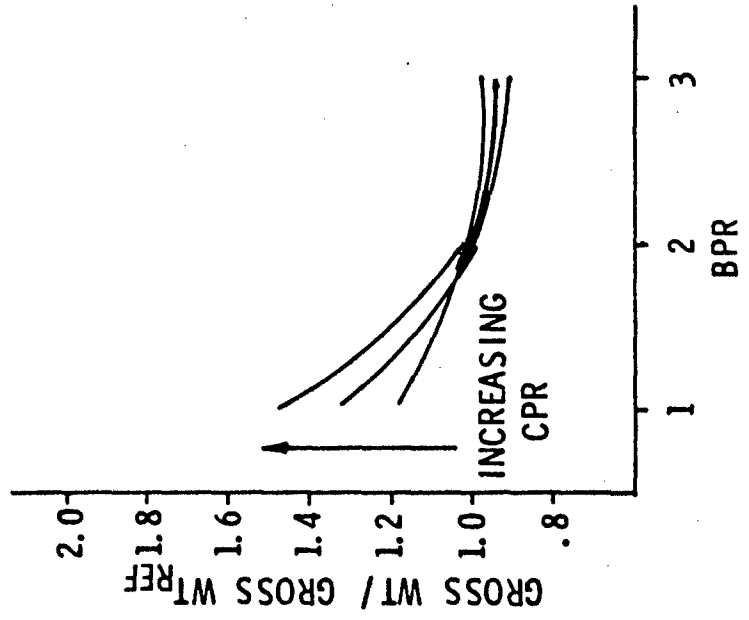


ENGINE CYCLE EFFECTS ON AIRCRAFT WEIGHT

TURBINE TEMP - CONST.



SUPERSONIC MISSION DESIGN



SUBSONIC MISSION DESIGN

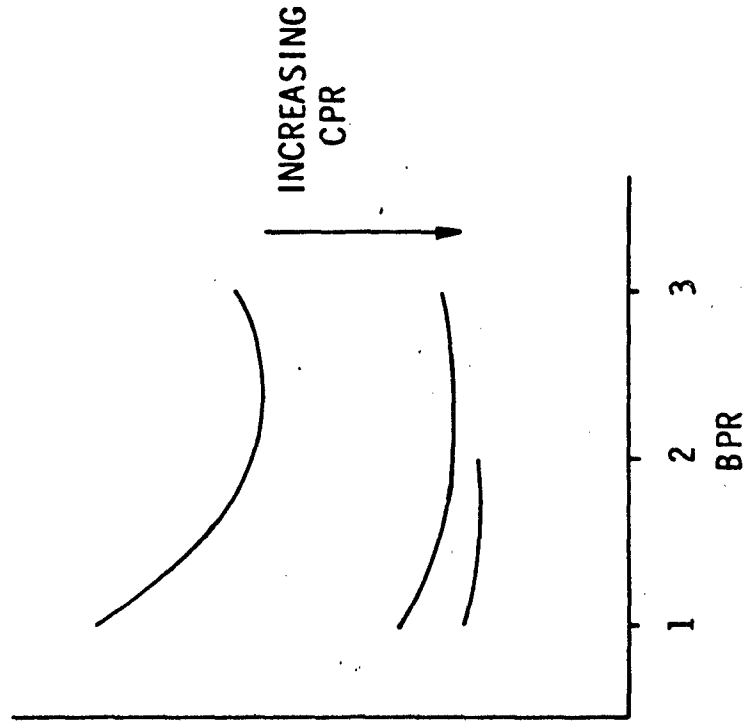
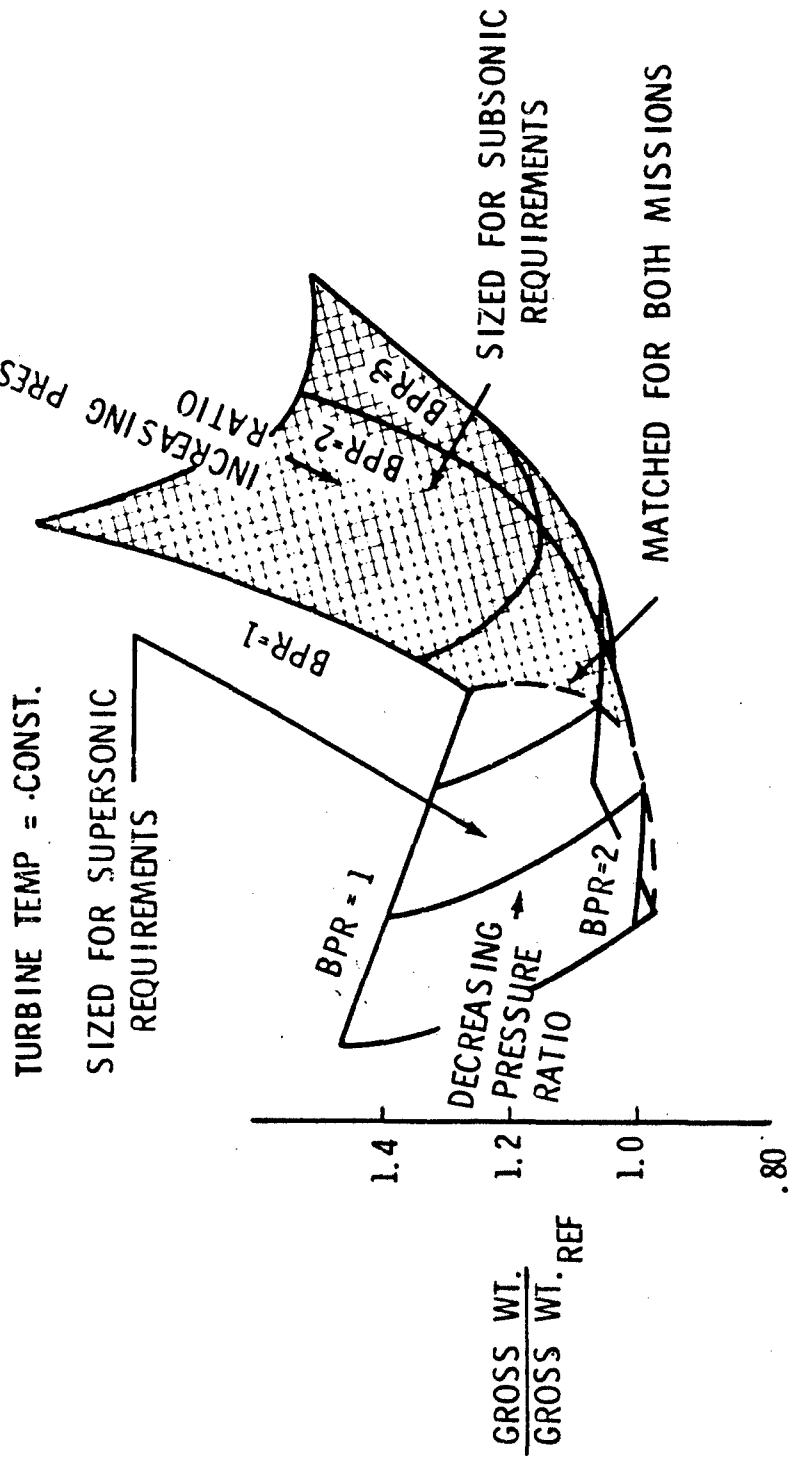


FIGURE 7

weight of the vehicle than the supersonic design point and results in a minimum gross weight aircraft with a by-pass ratio near 2.0. For the all subsonic mission of a strategic aircraft, the variation in cycle pressure ratio may be significant as well as the variation in engine by-pass ratio. During the sea level dash in this mission, which is made in dry power if possible, increasing cycle pressure ratio increases efficiency and lowers SFC. With increasing by-pass ratio, the engine must be made larger to match thrust at sea level. As engine size increases, the frontal area and weight increase so that there is a diminishing return at BPR over about 3. As for the tactical aircraft, the proper choice of engine cycle in a strategic aircraft must be determined by the overall efficiency of the aircraft in terms of one of the basic design parameters such as the gross weight of the aircraft, for a specified mission and vehicle design constraints. The engine cycle variations for subsonic and supersonic mission capabilities shown in Figure 7 can be combined to gain insight into the engine requirements desired for an aircraft designed to perform both the subsonic and supersonic missions. Overlapping the subsonic mission engine requirements and the supersonic mission engine requirements results in a single line (or family of engine types) as shown in Figure 8 which will allow satisfaction of both missions for a specified range requirement in each case. An engine which is not on the intersection will result in a reduced range or payload for one mission or the other. From this type of carpet the engine cycle for both missions which results in a minimum gross weight of the aircraft can be selected.



VEHICLE SIZING FOR SUBSONIC & SUPERSONIC
STRATEGIC MISSION PROFILES





For the strategic aircraft mission, the influence of exhaust nozzle internal thrust coefficient, and inlet total pressure recovery are also important design parameters. Figure 9 shows a typical sensitivity of aircraft range and gross weight to 4% variations in either nozzle thrust coefficient or inlet total pressure recovery if the penalty in these parameters is assumed to exist over the entire mission of the aircraft. The typical results, which are dependent on configuration design, but can be expected to follow the trends shown, indicate a strong sensitivity of range and gross weight with changes in inlet or nozzle component efficiency. For increases in nozzle thrust coefficient or inlet pressure recovery, the range is increased by as much as 10% for a 1% improvement in η_R or 3% improvement in nozzle component performance, conversely, a substantial reduction in gross weight is shown to be possible with improvements in component performance for the given range desired. This variation does not assume any changes in exhaust nozzle or inlet weight to achieve the increased performance, and this would have to be considered in a particular installation to determine the real benefit. The point to be made is that inlet and nozzle efficiency is an important design parameter.

The propulsion system selection curves discussed above are merely shown as examples and illustrate the effect of engine cycle variations and propulsion system integration on mission capability of tactical and strategic aircraft. Since each aircraft design may be somewhat different, the type of cycle analysis shown here must be done for each aircraft baseline design and the proper cycle picked which maximizes aircraft performance.

WEIGHT AND PERFORMANCE SENSITIVITIES

To show the sensitivity of the various weight parameters in the design of a tactical aircraft their order of magnitude are listed in Figure 10. The


**AIRPLANE SENSITIVITY TO NOZZLE THRUST COEFFICIENT
AND INLET PRESSURE RECOVERY
STRATEGIC MISSION**


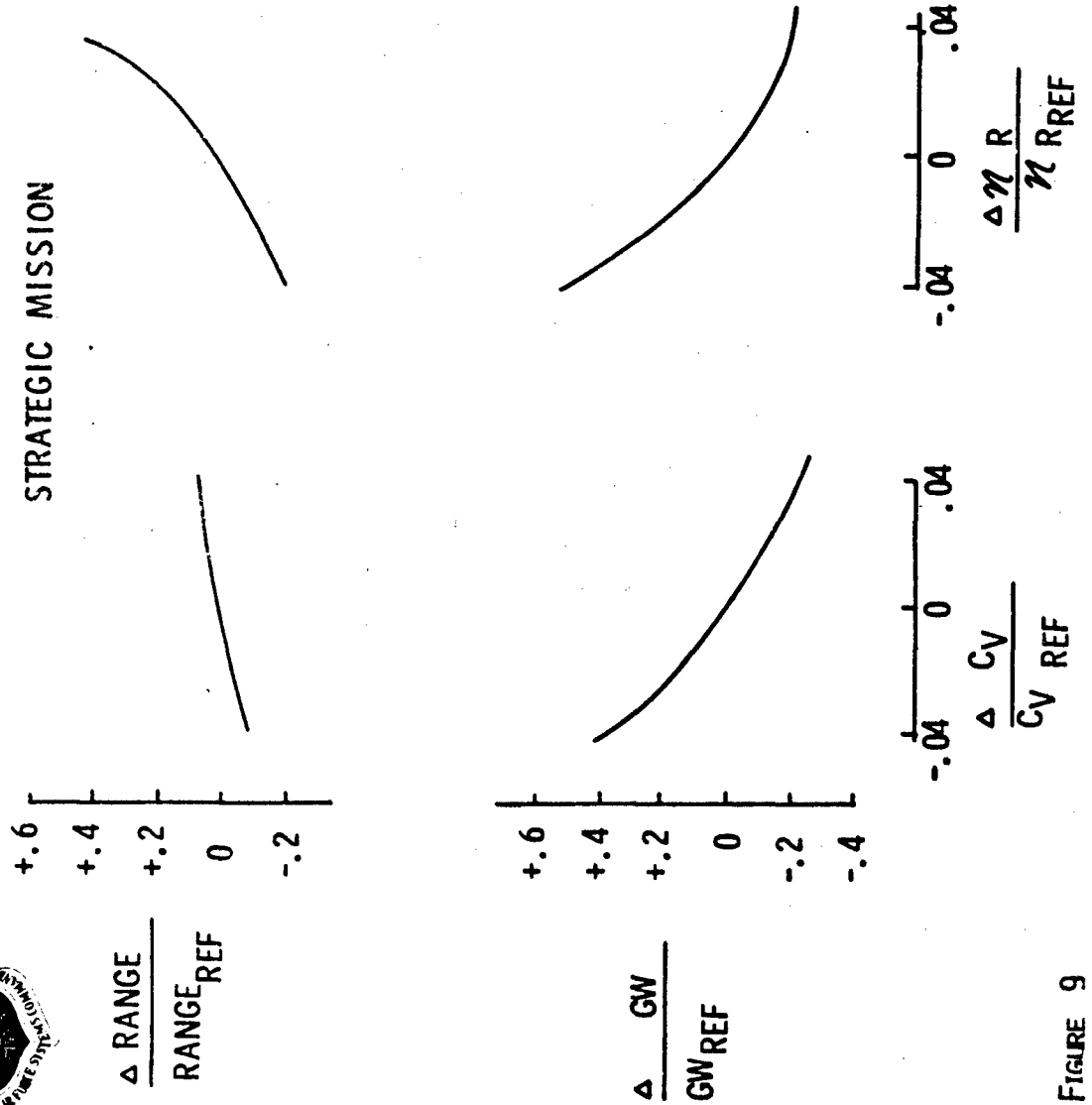


FIGURE 9



TYPICAL TACTICAL AIRCRAFT
WEIGHT BREAKDOWN



$$\frac{W_{PROP}}{W_0} = .22$$

$$\frac{W_{STRUCT}}{W_0} = .32$$

$$\frac{W_{EQUIP, AVIONICS}}{W_0} \approx .14$$

$$\frac{W_{FUEL}}{W_0} = .26$$

$$\frac{W_{PAYLOAD}}{W_0} = .06$$

FIGURE 10

propulsion, structural and equipment ratio vary from 14% to 32%. The fuel ratio is in the order of 26% while the payload is in the order of 6%. The importance of these ratios lies in the designer's ability to contain small changes in the weight fractions under the rules that if we keep the payload ratio constant, the fuel ratio then becomes the variable. This has a critical effect on the range and or combat time of the aircraft. Conversely keeping the fuel ratio constant, small errors in the other ratios can cause the effective payload to disappear thereby eliminating the capability of the vehicle to carry its design weapons. To provide a high level of credibility the design trades have to be carried out to high levels of accuracy. The relatively small differences of large numbers as for example between thrust and drag or take-off gross weight and empty weight can result in large errors. Growth factor is important since adding incremental weight causes the gross weight to increase by multiple factors as high as 10 times the incremental addition. The complexity of today's vehicle requires a high degree of sensitivity of design synthesis due to the multiplicity of disciplines involved from technology oriented efforts, through configuration development and finally the requirements and mission analysis. Computerized programs have been developed to assist in the integration of a design to provide detail parametric analyses and trade-off data to develop optimum configurations. However a sufficiently detailed and accurate description must be provided the computer, e.g., drag estimates and weight breakdowns to assure no major discrepancies exist in the final answer.

Given a specific mission, the parametric analysis of take-off gross weight and thrust loading can be developed with the necessary limitations imposed by maximum Mach number, design aerodynamic acceleration, specific power, take-off requirements and the characteristics of the lift and drag curves. This then develops into the final design stages to optimize the configuration to keep the gross weight at a minimum keeping in mind structural reliability and load factor. From such parametric analysis plots it is then possible to develop individual sensitivity parameters. An example of such trade-offs are shown in Figure 11 where although the plots are based on absolute values of wing area and engine size they in actuality refer to two of the most critical design parameters, that is, wing loading and thrust loading. For a given aerodynamic acceleration a design wing loading is obtained as a baseline configuration. For a constant take-off gross weight and constant engine size, the sensitivity of fuel loading, air to air combat radius and interception time is shown as the wing area is allowed to vary. Figure 11 shows that a 10% change in aerodynamic g's causes changes in the order of 10% in fuel loading and change in radius of mission. The increased g-maneuvers are accomplished by increasing wing area. This in turn reduces the fuel fraction and combat radius if we hold gross weight constant. For the example shown in the top part of Figure 11, however, one of the desired specific excess power (P_S) design points was not quite met. This could not be appreciably helped by changes in wing area, and it was thus necessary to consider engine size scaling. A 1% increase in engine size results in a 10% increase in P_S , and has a negligible effect on wing area. However increasing engine size again degrades



PROPULSION / AERODYNAMIC TRADE OFF STUDIES
CONSTANT TOGW

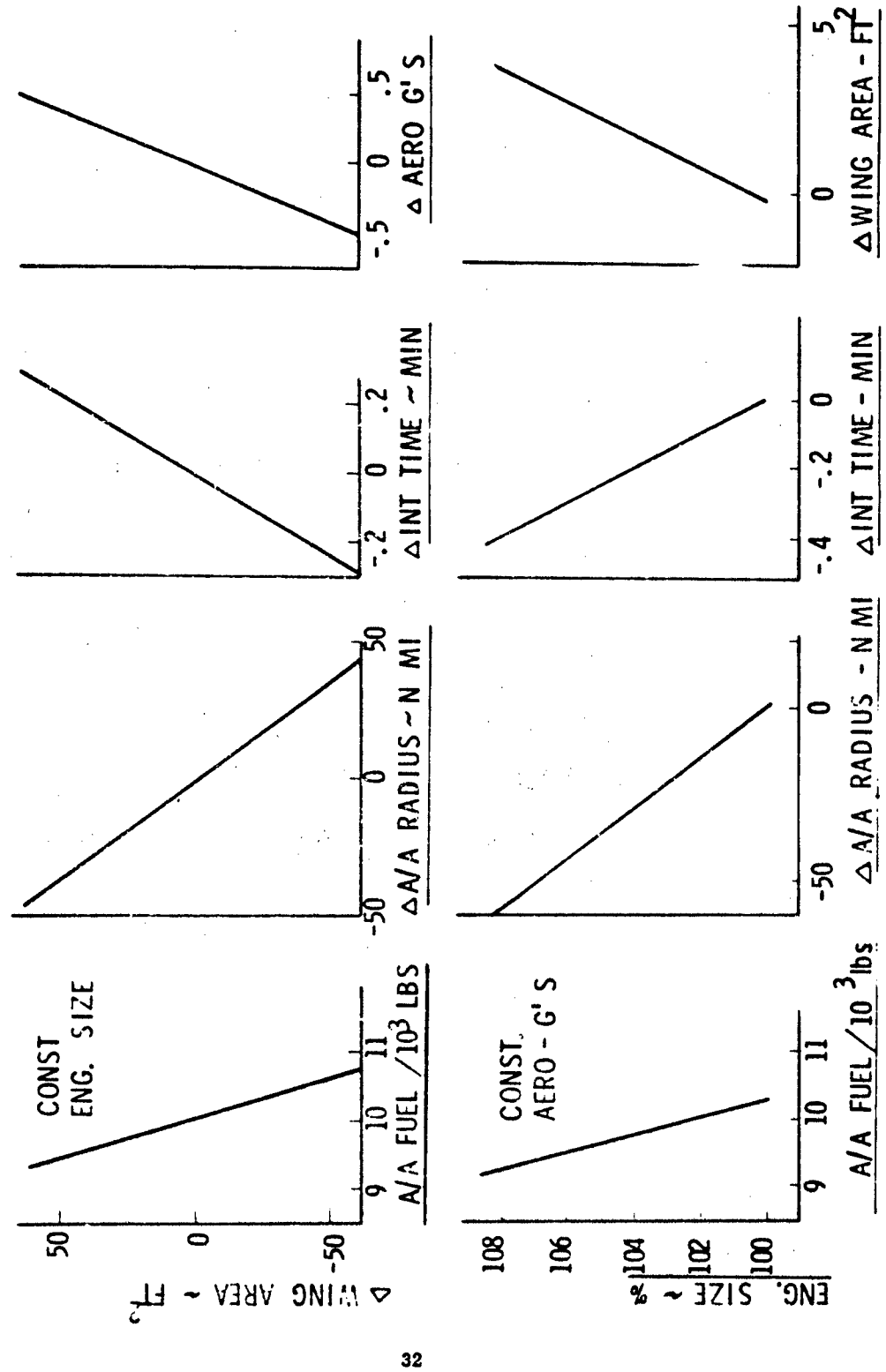


FIGURE 11

range capability and combat time. Intercept time is reduced due to a higher thrust engine. This type of interaction among the various factors must be clearly understood in preliminary design.

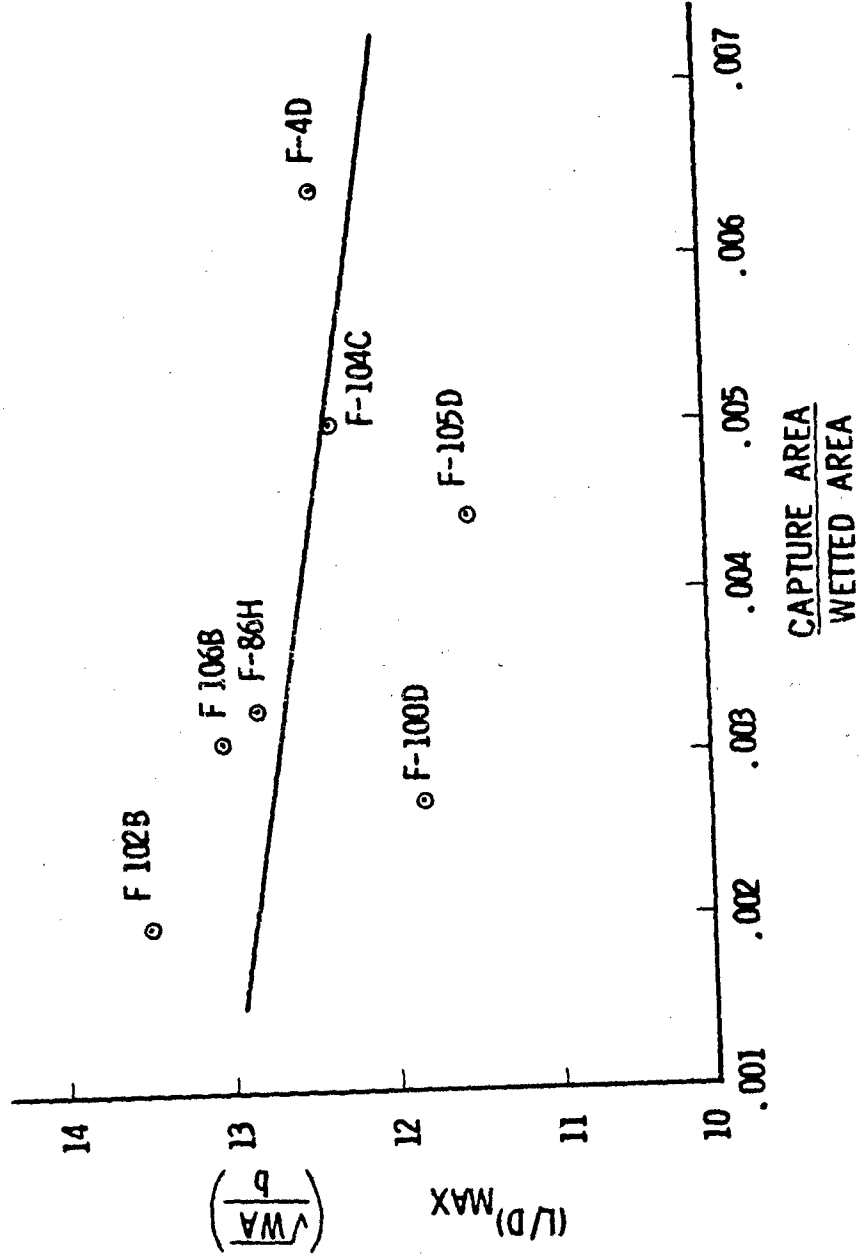
AIRFRAME-PROPULSION INTEGRATION

Figure 12 indicates the reduced aerodynamic efficiency which may be attendant with increased capture area of the inlet in advanced types of aircraft. This trend indicates that as the capture area of the inlet increases, due to higher thrust and higher airflow engines, it becomes more difficult to integrate the inlet and the propulsion system with the vehicle to achieve the desired efficiency. This trend can be expected to continue with more advanced aircraft, since the primary reason for the decrease in aerodynamic efficiency is the larger drag of the inlet system for increased capture areas characteristic of modern turbo-jet and turbo-fan engines. One possible way of reducing the inlet drag and thereby increase the aircraft aerodynamic efficiency is to properly integrate the inlet with the aircraft flow field.

Two examples of flow field integration of a propulsion system are shown in Figure 13, which compares the drag of an inlet system mounted in the wing flow field as compared to an inlet system mounted on the top of an aircraft in the aft position. The wing flow field installation for the inlet tends to reduce the required capture area of the inlet, thereby allowing a better match with the engine airflow which decreases spillage and by-pass drag, and also provides a reduced wetted area contribution to the vehicle. For the inlet in the top/aft mounted position, the aircraft flow field tends to produce a local Mach number which is higher than the



EFFECT OF INCREASED PROPULSION INTEGRATION
ON AERODYNAMIC PERFORMANCE





AIRFRAME INLET INTERACTION EFFECTS ON INLET DRAG

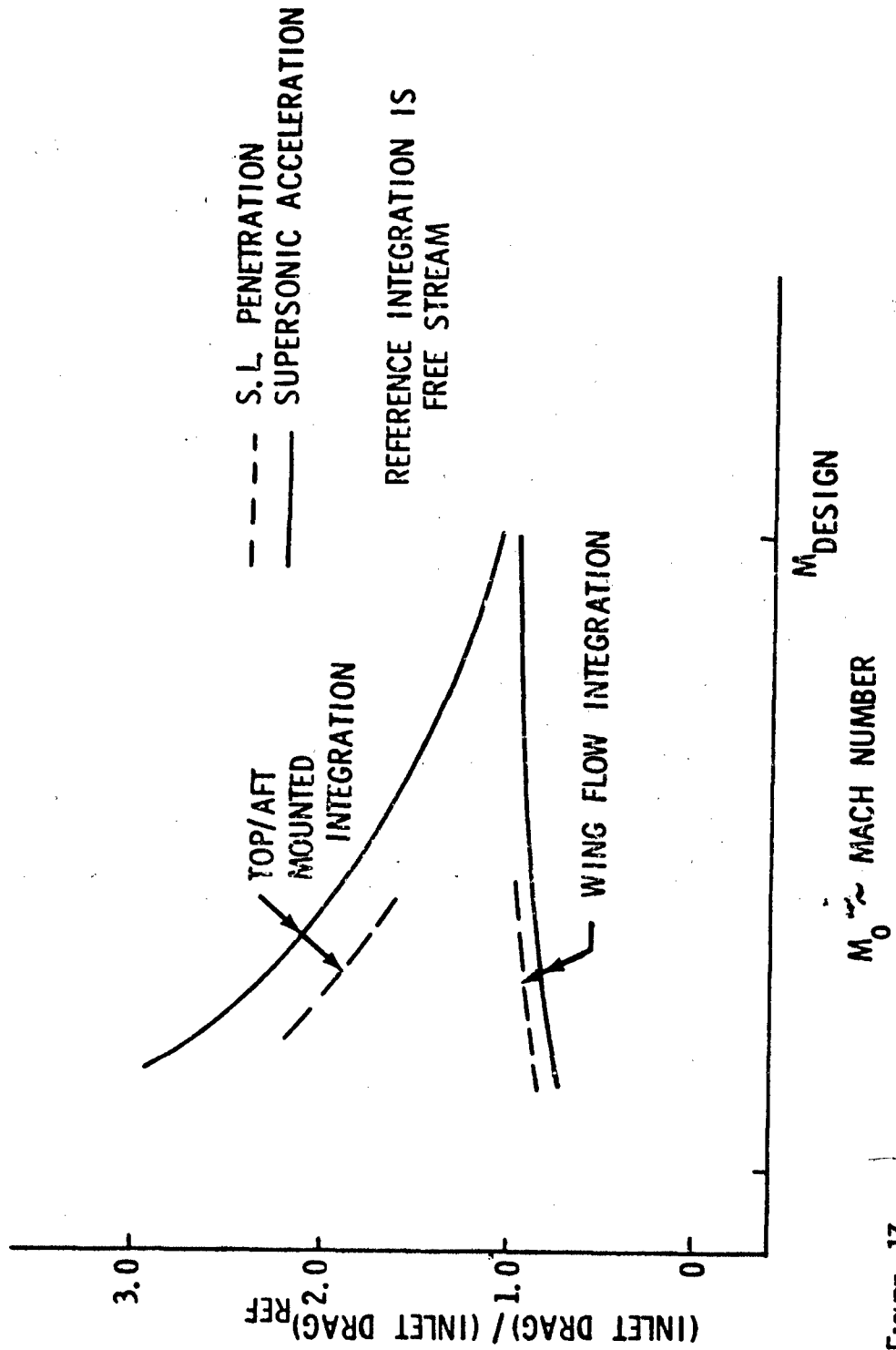


FIGURE 13

free stream Mach number to the inlet system, causing an increase in inlet capture area and increased drag. Figure 13 indicates a substantial increase in inlet drag which includes spillage, by-pass, bleed and cowl drag, for the top aft mounted inlet during both supersonic acceleration to the design Mach number and during transonic sea level acceleration. The difference in drag decreases as the design Mach number of the aircraft is approached, since both inlets are assumed to be matched with the engine, resulting in minimal spillage or by-pass drag. However, there is still some benefit for the wing flow integration scheme due to the smaller size inlet and nacelle required.

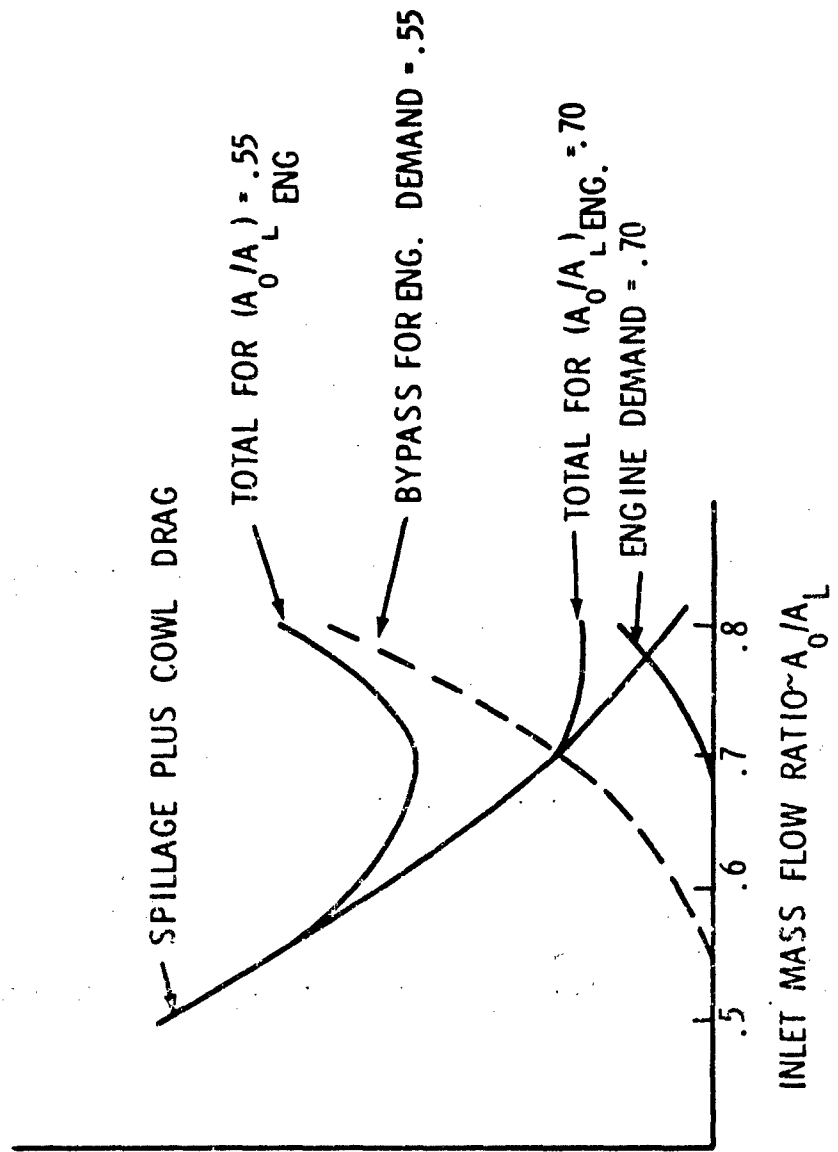
In order to realize the maximum performance from an advanced strategic or tactical aircraft, the placement of the inlet on the vehicle must be carefully considered and must account for the overall drag and performance of the aircraft in its intended mission. The integration must also consider the stability of the propulsion system in terms of the flow distortion in the inlet. Unfortunately, more experimental and analytical work is required before these considerations can be effectively used in a trade-off study. Candidate inlet locations must be examined for stability and wind tunnel tests conducted to validate the chosen location.

At Mach numbers less than the design point of the inlet, the inlet delivers considerably more airflow than required by the engine. This excess airflow delivered by the inlet must either be spilled around the inlet or taken aboard and by-passed before it gets to the engine. At subsonic cruise conditions, this mismatch of inlet airflow supply and engine airflow demand is particularly important because the spillage drag is a significant contribution to the overall vehicle drag, and will have

the strongest influence on aircraft performance in the long subsonic cruise portions of the aircraft mission. Reductions in inlet drag at these flight conditions can therefore have large payoffs in mission range and aircraft capability. Therefore, for use in preliminary design and for accurate aircraft performance estimates, combinations of engine airflow changes and inlet matching schemes must be investigated to determine the minimum drag configurations. Figure 14 shows a typical trade-off between spillage flow drag and by-pass flow drag for a representative turbo-fan engine requirement. For an engine mass flow ratio demand of 55%, this trade-off indicates that by-passing approximately 15% of the inlet airflow and spilling the remaining 30% of the maximum captured inlet airflow results in a minimum total drag penalty for the inlet-airflow mismatch. Other schemes for by-passing the inlet air to match engine demands on recent aircraft have included ducting some of the extra air to the exhaust nozzle and pumping it over the aircraft boattail to reduce aft end drag, but the amount of air which can be efficiently used in this manner is limited, and experience has shown that the bulk of the excess airflow must still be spilled around the inlet. As the flow spills around the inlet, it will produce a negative pressure differential on forward facing surfaces of the engine nacelle near the cowl lip. This lip suction is in such a direction so as to cancel a portion of the spillage drag, but it is effective only for a blunt cowl with substantial forward area for this force to act upon. Design requirements for high supersonic speeds, particularly for mixed compression inlets, tend to dictate relatively sharp lips on the inlet cowl which produce a small lip suction cancellation of the spillage drag. Further research is needed to investigate various lip shapes for mixed compression and external compression



INLET DRAG TRADE-OFF SUBSONIC CRUISE



INLET DRAG
COEFFICIENT $\sim C_{D_i}$

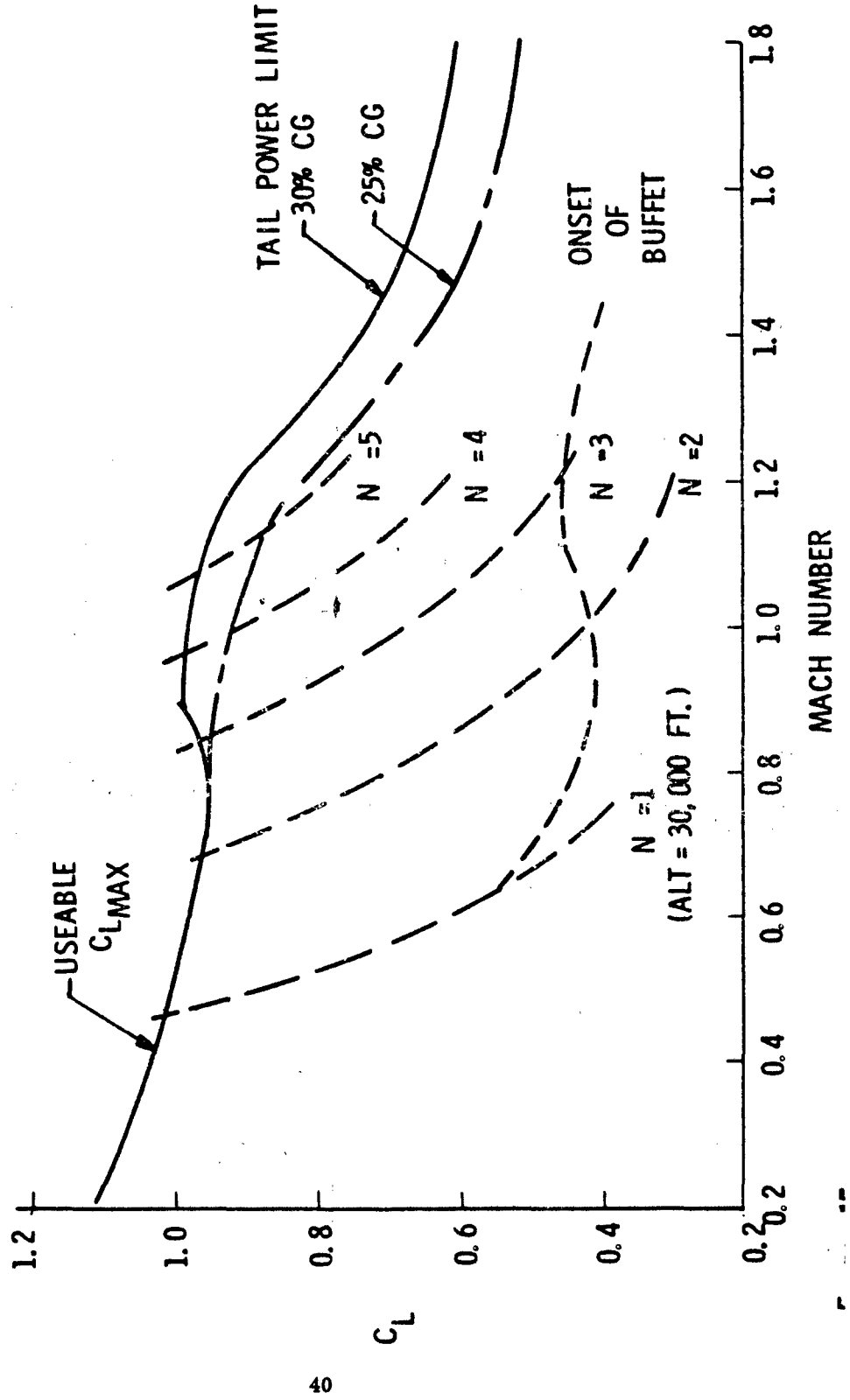
inlets in order to reduce the high level of transonic spillage drag, particularly for sea level penetration portions of a desired mission.

For highly maneuverable tactical aircraft the proper integration of the airframe and propulsion system must be accomplished to realize the maximum benefit of the aircraft's "designed-in" maneuverability which is generally limited by allowable g-forces. The main contributor to maneuverability is the wing and the important parameter to examine is the useable maximum lift coefficient ($C_{L_{max}}$). Figure 15 depicts C_L versus Mach number for a given aircraft which has an onset of buffet. In the transonic arena where maneuvering for today's aircraft is important, this onset occurs at about one half of the useable C_L . Depending on the aircraft characteristics, entrance into the buffet area can become increasingly severe to a point where first the vehicle loses its capability as a stable weapons platform. Farther entry into the buffet region can cause loss of aircraft control leading to catastrophic failure. The lines of constant load factor (N) on Figure 15 depict the levels that become necessary for maneuvering in advanced aircraft. Therefore the aerodynamic parameters governing wing, tail, and auxiliary surface design must be more accurately controlled to alleviate the buffet phenomena. This, in turn, requires close attention to dynamic structural criteria to assure safety and reliability of operation.

A given aircraft design may have several limits to its maneuverability. If problems of buffet, as described above, or propulsion system incompatibilities are at lower g's than the basic structural strength of the aircraft, then we are not realizing the maximum benefit of the design. This type of limiting process is shown on Figure 16. It is therefore the purpose of



TYPICAL MAXIMUM MANEUVERING LIFT CAPABILITY



TYPICAL TACTICAL AIRCRAFT TRANSONIC
MANEUVERABILITY LIMITS

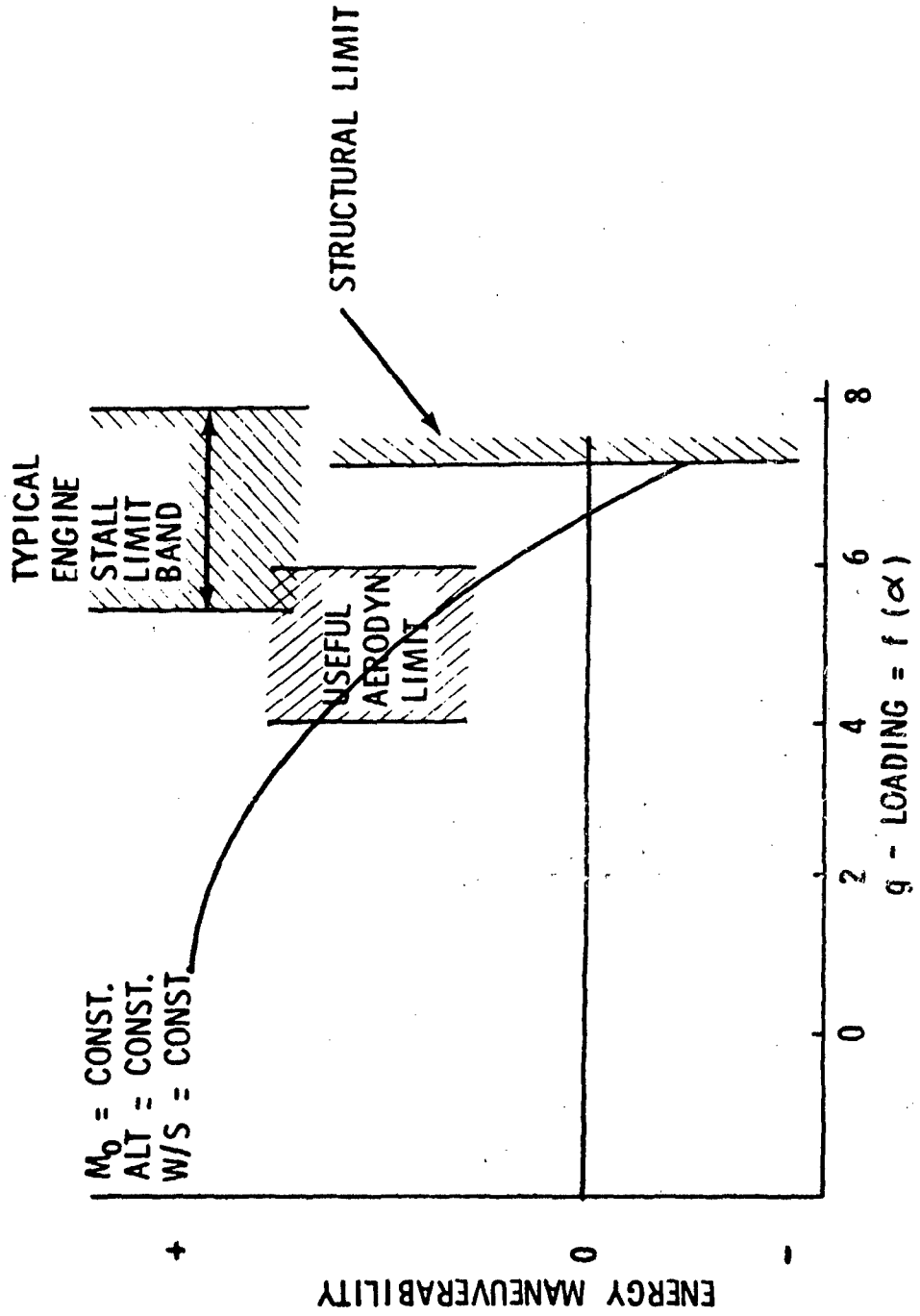


FIGURE 16

proper airframe and propulsion integration to eliminate these limits which are lower in g's than the aircraft structural limit. To provide some alleviation of the inlet-airframe interaction problems, we can consider various locations of the engine installation, for example, the location on the wing span. Such locations also provide easier access to the engine for maintenance in addition to reducing the possibility of high distortion levels during maneuvering flight due to inlet flow fuselage boundary layer ingestion. A final advantage is that of permitting growth potential of the aircraft by installing improved engines at much less expense than if the power plant was integrated with the fuselage. However, close attention must be paid to the engine out performance. Shown in Figure 17 are the deflections of the rudder required during engine out operation for various locations of the engine on the wing span. Plotted on Figure 17 are the requirements for both military power and afterburner power. Rudder deflections at low altitude are quickly reached at some span locations that would be beyond the control power and structural capability of the tail.

For both tactical and strategic aircraft, the exhaust nozzle of the engine is a critical propulsion component in determining aircraft performance and its operation in the desired mission. Many types of exhaust nozzles may be considered for installation in these types of aircraft which are compatible with advanced turbo-jet and turbo-fan engines. With our present capability, based on test data, there is a generally good understanding of idealized internal nozzle flow behavior, and of the isolated exhaust nozzle performance where it is not strongly influenced



ENGINE OUT EFFECTS ON AERODYNAMIC STABILITY

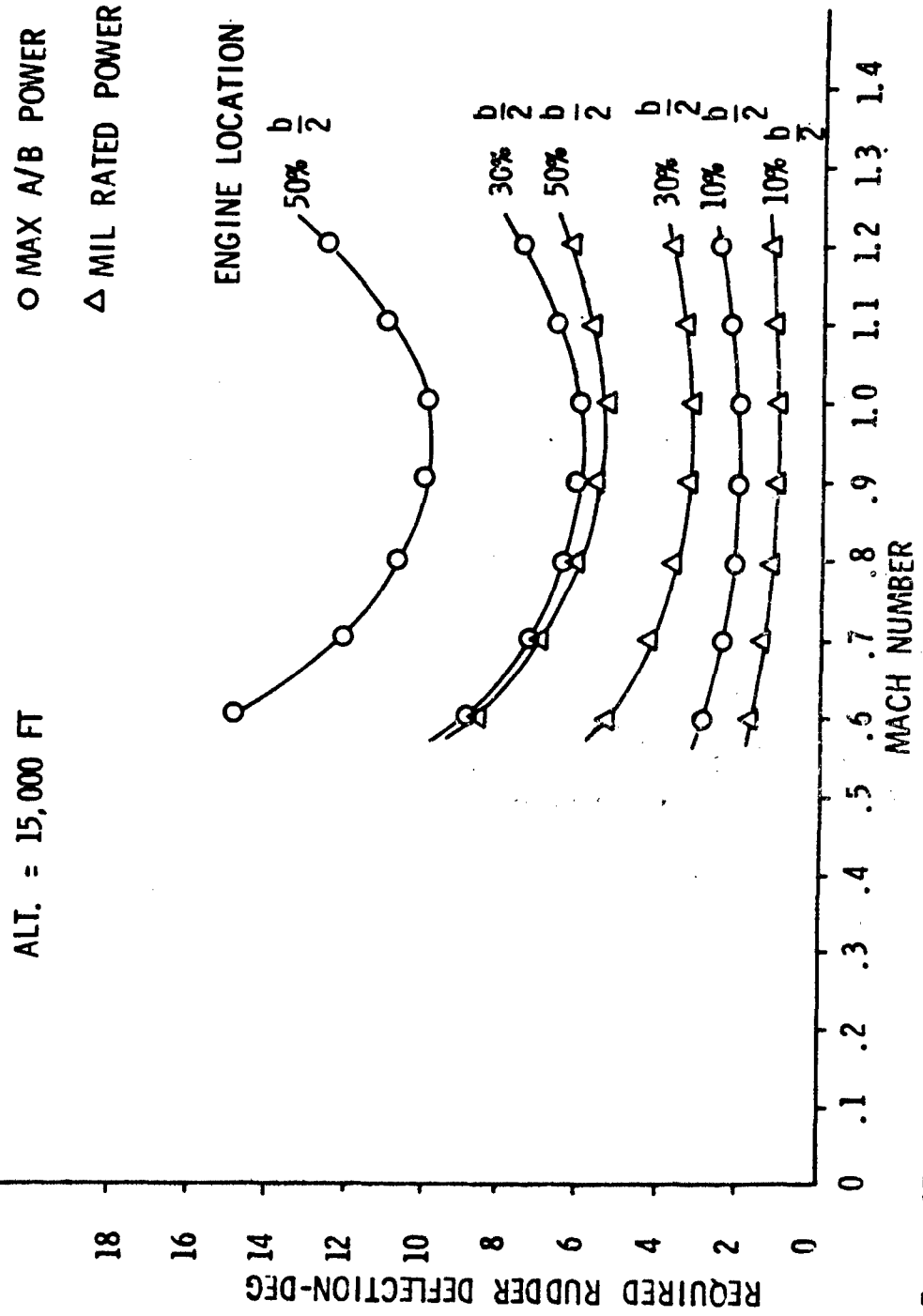


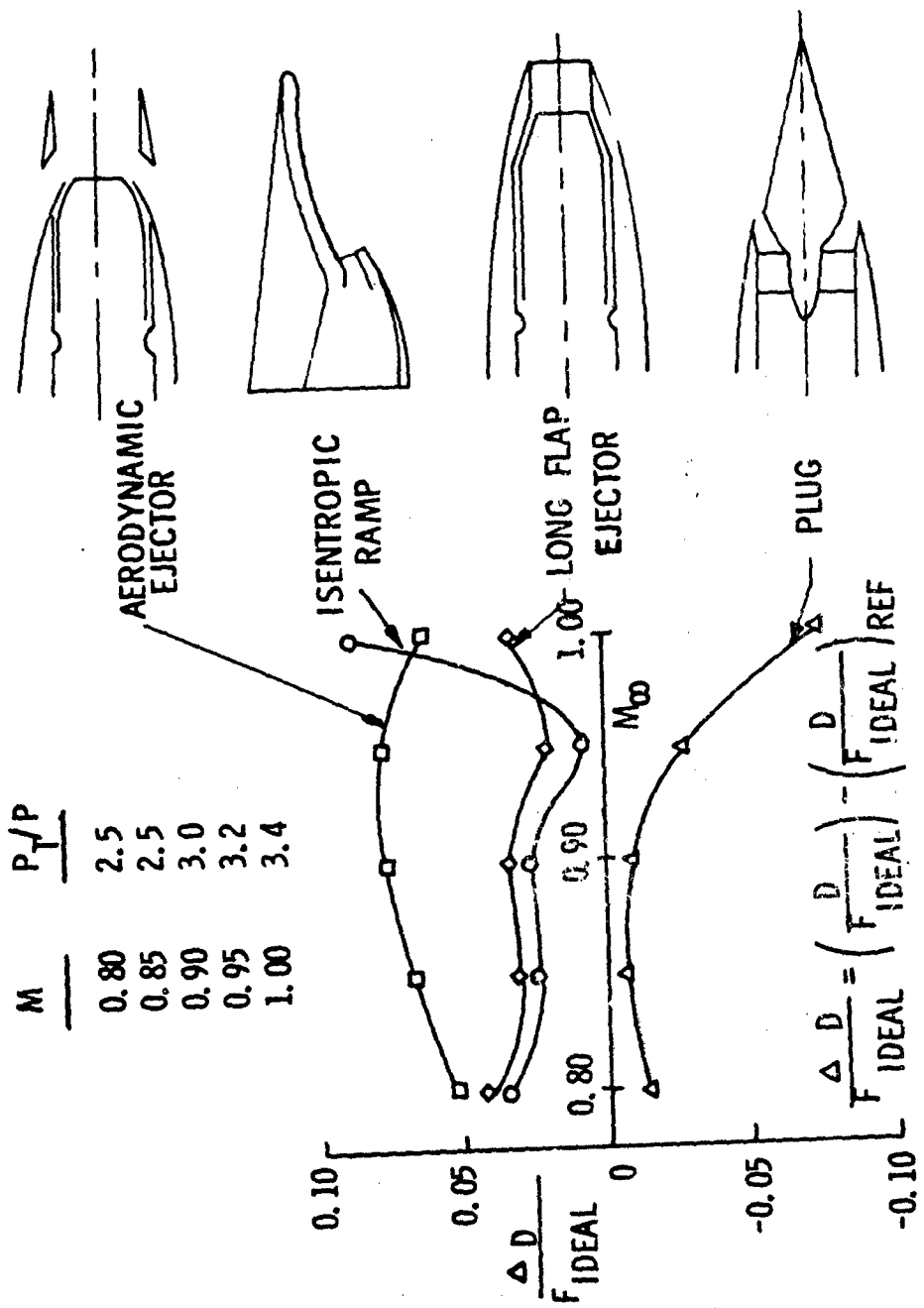
FIGURE 17

by its installation in the aircraft. Some examples of the various types of nozzles which can be considered by the designer and their associated drags for an essentially isolated installation are shown in Figure 18. Since exhaust nozzle drag is most important in the transonic speed regime where the flow over the aircraft will tend to produce high boattail and base drag contributions, the various nozzles are compared on the basis of an installed drag penalty (relative to a reference nozzle) divided by the ideal thrust of the nozzle for the pressure ratios shown. This particular experimental data, which was generated by the Boeing Aircraft Co. indicates that for an isolated installation, the plug nozzle may be a lower drag installation than the aerodynamic ejector, isentropic ramp, or long flap ejector type nozzles. However, the plug nozzle may have a lower performance at supersonic speeds if the plug shape assumes an off-design geometry. Other problems with the plug nozzle include cooling and weight considerations which must be resolved before it can be considered by the designer for use in an aircraft installation with an afterburning engine.

The main problem in exhaust nozzle integration is with closely integrated dual engine aircraft such as twin engine tactical aircraft or multi-engine strategic aircraft. If the nozzles are closely spaced, as they often are in these types of designs, they may interfere with each other and the aircraft surface adjacent to the nozzles, and thus result in extremely high interference drags which cannot be accurately predicted by available theory. Extreme care must be taken in the integration of the



DRAG PENALTIES FOR TYPICAL NOZZLES



exhaust nozzle with the back end of an aircraft to minimize the installation effect. Figure 19 shows a summary of data from a Grumman - NASA test program which compares various types of nozzles such as the variable flap ejector, blow-in-door ejector (bide), iris type translating shroud nozzle, and a convergent-divergent iris nozzle designed for high supersonic speeds. The penalty in exhaust nozzle/back end performance at subsonic dry power conditions, where nozzle drag is the highest, is expressed as a percent of ideal net thrust of the engine and is seen to be a strong function of the installation scheme and, to a lesser extent, on the exhaust nozzle type. For close spaced nozzles, as in an F-4 type or F-111 type, the blow-in-door ejector nozzle is susceptible to external flow effects and suffers from a combined external and internal flow interaction. The other types of nozzles, which do not "communicate" as well with the external stream, have less severe penalties in close spaced installations, but still contribute substantially to increases in aircraft drag. Recent test data generated by NASA indicate that even the blow-in-door ejector nozzle can be properly integrated with the back end of an aircraft, if care is taken to reduce the interference with adjacent horizontal and vertical tail/control surfaces or aft end fairings which may be present on the aircraft. As indicated in Figure 19, a clean close coupled installation can have comparable drag levels to the wide spaced low interference type of installation. The proper choice of close spaced or wide spaced exhaust nozzles must not only consider their performance characteristics, but their weight, complexity and the effect on aircraft operation during engine-out or maneuvering flight. If a close spaced installation is chosen, extreme care must be taken in the testing of the nozzle to assure that a minimum exhaust nozzle-aircraft back end drag is achieved.



AIRFRAME / NOZZLE INTERACTIONS

SUBSONIC NON-A/B

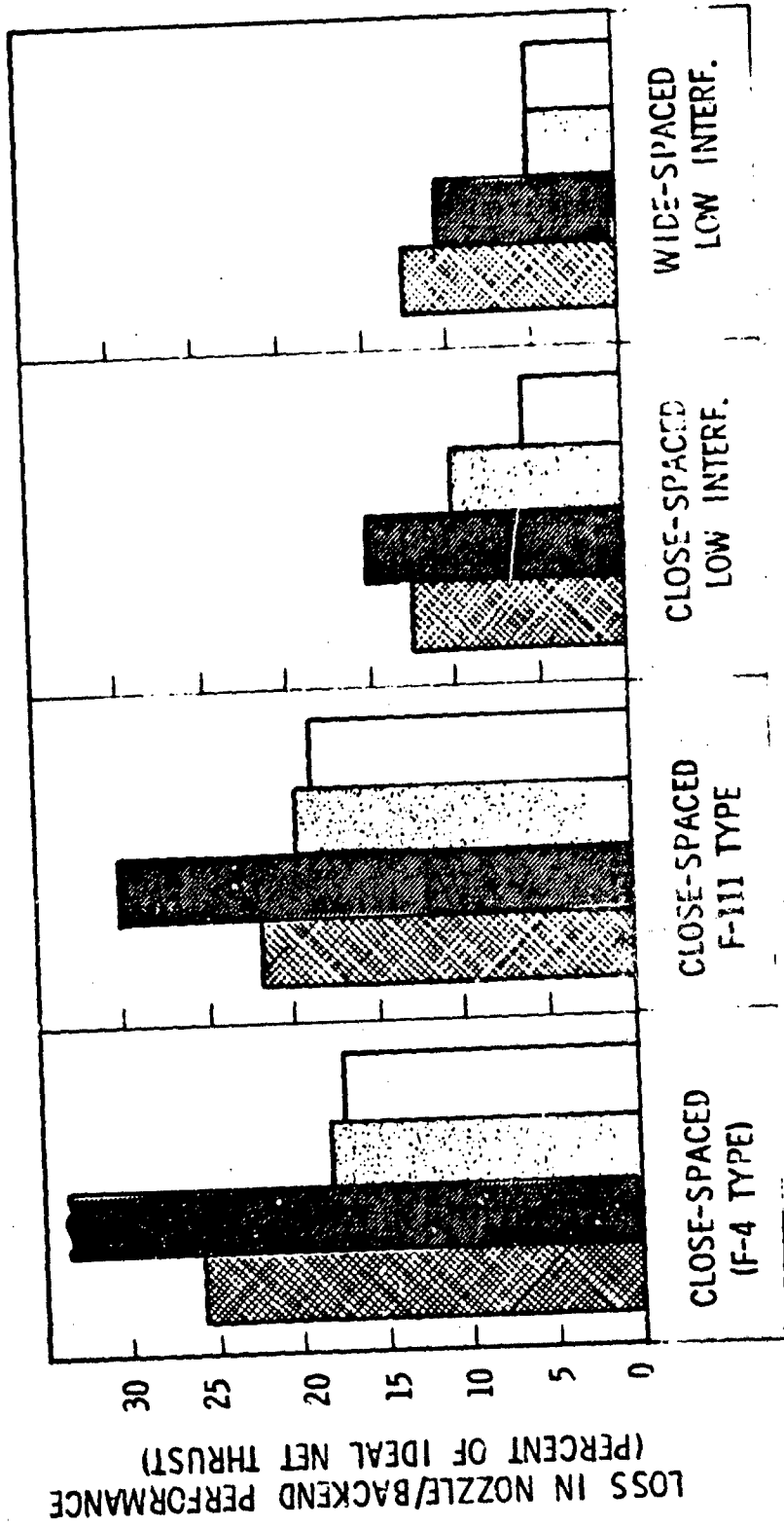


FIGURE 19

SUMMARY

Airframe and propulsion integration is strongly dependent on the aircraft mission ground rules, depending on its requirements, from either fighter or strategic mission models. The wide range of speed capability coupled with effective weapon delivery dictate stringent performance requirements. Cruising conditions must be efficient to obtain maximum range, yet maneuvering capability coupled with dash effectiveness are critical in the combat strike zone. To achieve all this, preliminary design considerations must effectively consider the sensitivity of each of many parameters singly and in consonance as it interacts with other design parameters. Multiple trade-offs are needed to a high degree of accuracy to assure a combat effective weapon system at minimum cost. The advancing technologies give rise to consideration of improved effectiveness but only through careful assessment of their risk, reliability and cost can they be integrated successfully for development of future flight vehicles.

PROPULSION SYSTEM INTEGRATION AND TEST PROGRAM

W. H. Hand and R. H. Johnson

North American Rockwell Corporation, Los Angeles Division

ABSTRACT

The major components of a propulsion system are the inlet, the engine, and the exhaust nozzle. Experience with current multi-mode aircraft suggests that a relatively independent assessment of these components, so often used in the past, is no longer a satisfactory base from which to predict overall weapon system performance. Two objectives of the program described in this paper were to establish a numerical procedure for defining the overall performance of integrated propulsion systems, and to provide reliable data and test techniques to enable accurate performance predictions. One of the unique items described is the reference inlet, used in inlet tests along with the actual inlet shape to obtain forces chargeable to the inlet. Another somewhat different approach described is the use of a reference shape for the aft end of the vehicle. A major conclusion was that the techniques developed for evaluating the integration aspects of multi-mission mode propulsion/airframe systems appear to have the necessary resolution and flexibility to evaluate a wide range of changes to a basic propulsion system. The inlet tests showed that methods used to estimate recovery and drag generally resulted in good agreement with the data. This was also true for the internal nozzle performance. Agreement between the estimated and measured external forces on the nozzles was not as good.

Introduction

The effort, which I will briefly summarize today, was an extensive program of analysis and tests funded by the Air Force Aero Propulsion Laboratory addressed to the integration problem. (Contract F33615-67-C-1829) The program is complete, except for updating some of the test reports. Final reports on the program have been published, and I will refer you to them in a moment. The present discussion deals with the steady state aspects of the integration problem. Another program, also sponsored by the AFAPL, is currently being conducted at North American Rockwell Corporation on the dynamic aspects of the problem. Mr. Arnold Martin will discuss this program tomorrow.

The scope of the steady state program is shown in the first slide.

IPS Program Scope

The reports noted in parentheses are the program final reports which are addressed to the major program objectives listed.

The third objective will not be discussed today, since many of the results are classified secret, and some are proprietary.

I can say that the final objective listed was attained.

A summary of what will be discussed today is shown on the next slide.

Discussion Scope

First I'll cover the approach used in the integration procedure, explain the reference models, how they are used, how the bookkeeping is done, and how the data are presented. Then, I will describe the inlet and the nozzle interaction tests and the test results.

Please remember that time permits discussion of only a portion of the work done on the program. I hope that this talk will encourage you to look at the reports on the program.

Also, I don't intend to lead you to any conclusions, such as "This is how its done, there is nothing left to do,". There is a lot more work to be done in this area of propulsion system integration.

Outline of Propulsion System Integration Technique

To provide an orderly approach to perform an integration study, it is necessary to set up a framework to link the various major component design disciplines. An outline of such a framework is shown in this slide. Although there are a variety of ways to set up an outline for such a study, and under different situations it might be desirable to change it, some consistent interface system is necessary to assure that all losses are accounted for in a consistent manner. The first step in the use of the technique is to establish a basepoint vehicle and mission. Vehicle characteristics such as shape, volume, and aerodynamic characteristics and detailed ground rules for the mission are defined. The reference models to be used are also defined at this time. Next, the

various groups involved perform analyses on the inlet, engine, nozzle, weight items, and vehicle aero characteristics. Propulsion system data are fed to a Propulsion System Analysis where the installed performance is determined. This data, along with weight breakdowns and aero characteristics go to a Mission Analysis activity where the range on various mission legs, energy maneuverability values, and propulsion system and vehicle sizes and weights are determined.

This is obviously an outline of the general approach followed in a typical air vehicle preliminary design study, and in fact the same design analysis techniques are used. Optimization is accomplished by repeating the process, varying design parameters in an orderly manner to drive the design toward a superior performance level.

An essential requirement of the integration technique is to carry out all of the steps shown in this slide. It is not sufficient, for example, to proceed through only the Propulsion System Analysis block and look at net thrust and specific fuel consumption to select an optimum propulsion system. It may be that a weight increase would cancel out the apparent benefits.

Some of the various analysis blocks and the input/output data shown in this slide will be discussed in more detail later. First, the use of reference models and how they are used to obtain forces on the airplane will be discussed.

Reference Model Integration (1)

The information on the next five slides is more easily grasped when seen on one piece of paper, but one slide would be way too crowded. Therefore, I'm going to have to ask you to remember some things from each slide as we go along.

We are seeking the forces on the actual airplane. In general, we must use several models to get these forces. First, let us look at some simple arithmetic to see what these are.

A sketch of an airplane in flight, omitting minor items such as wings and tails for clarity, is shown at the top of the slide. To keep things simple and still illustrate the important points, the airplane is shown at zero angle of attack, and we will only concern ourselves with forces in the horizontal direction for this example.

The various chord forces, or drag, indicated on the sketch are as follows:

- F_4 - chord force of the external air on the inlet cowl
- F_5 - chord force of the external air on the afterbody
- F_a - chord force of the external air on the remainder of the airplane
- F_2 - chord force of the internal air on the inlet duct to the approximate engine face location

F_3 - chord force of the internal air on the remainder of the duct, to the nozzle exit

F_1 - additive drag force on the external streamtube

The net force on the airplane in the flight direction is shown by the first equation. Performing a momentum balance on the streamtube passing through the engine gives the second equation. By combining the two equations we get the third equation. Here, the terms in the brackets represent the net thrust which may also be represented by

$$F_N = C_V F_{IDEAL} - \rho_0 V_0^2 A_0$$

The net thrust is determined by analysis or internal nozzle tests to obtain C_V .

The terms in parenthesis are determined from other model data to obtain the last equation. Here the terms in parenthesis are

C' - corrected chord force on aero model

ΔC_I - corrected chord force chargeable to the inlet

ΔC_{AB} - corrected external chord force chargeable to the nozzle

The last two are, of course, the propulsion system drag forces.

Now let us look at the other models to see how we link the terms in parenthesis in the third and fourth equations. Remember, we want to find F_a , F_1 , F_4 , and F_5 in terms of C' , ΔC_I , and ΔC_{AB} .

Reference Model Integration (2)

A reference aerodynamic (aero) model is one whose external shape represents the air vehicle. The model is used to determine the forces and moments on the airplane, exclusive of those forces and moments due to bringing air on board or discharging air overboard. By doing this, the forces and moments on the inlet and nozzle systems may be determined independently in other tests or analysis and combined with the reference aero model forces and moments to obtain those on the complete vehicle. Ideally, the reference aero model has a flow-through inlet. The inlet has a collapsed ramp system, and the internal cross-sectional area increases in the downstream direction sufficient to permit the free-stream streamtube to flow directly into the inlet capture area. The inlet cowl represents the actual cowl. The aft end of the reference aero model is shaped to correspond to one of the expected nozzle configurations, if practical. Thus, the inlet portion of the reference aero model determines the reference inlet shape, and the aft end portion, the reference nozzle configuration. The inlet configuration results in zero additive drag if a collapsed ramp system, as shown here, is used.

On this, and the other reference models, the forces and quantities that are different from those on the actual airplane are indicated with

primed. The forces on the reference aero model are:

- F_4' - chord force of the external air on the reference inlet cowl
- F_5' - chord force of the external air on the reference nozzle afterbody
- F_a - chord force of the external air on the remainder of the model
- F_2' - chord force of the internal air on the inlet duct to the approximate engine face location
- F_3' - chord force of the internal air on the remainder of the duct, to the exit nozzle

The chord force measured by the balance is shown by the first equation. Again, a momentum balance on the streamtube gives the second equation. The measured chord force is corrected as shown by the third equation. This removes the internal forces which will be accounted for in the propulsion system. Combining the three equations we get the fourth equation which gives the corrected aero model chord force.

Note that we have found F_a but have introduced two new terms to find, F_4' and F_5' .

Reference Model Integration (3)

This slide shows the reference nozzle model and the actual nozzle model.

The reference nozzle model is identical to the aft end of the reference aero model. Since one is also interested in nozzle jet effects on afterbody forces, the flow coming from the nozzle exit on the reference nozzle model should be the same as on the reference aero model. Also, since afterbody forces may be sensitive to the oncoming flow field, it is advisable to simulate as much of the rest of the airplane model as practical. Flow-through inlets are not used, however, since the nozzle flow is controlled by other means to obtain a wide range of nozzle operating conditions to simulate the actual nozzle operation. It may be convenient and/or more accurate to split the model near the aft end and measure only the aft end forces. The actual nozzle is tested at various boattail angles, expansion ratios, and ratios of total pressure to freestream static pressure. In this way, the effects of both configuration changes and plume shapes on afterbody forces are determined. The nozzle exit station and the flow properties indicated on the sketch correspond to those of the reference aero model and vehicle configuration. The primed quantities again refer to flow property values for the reference configuration.

The first equation shows the measured chord force on the reference model. The second equation shows the measured chord force on the actual model. The difference between these two is the chord force chargeable

to the nozzle, as shown by the last equation.

Now we have found an expression for F_5 and the value F_5' introduced by the aero model.

Reference Model Integration (4)

The reference inlet model simulates the forward portion of the reference aero model. Unless shown otherwise, it is most desirable to include the vehicle forebody, mounted separate from the inlet. As on the reference aero model, the reference inlet has a collapsed ramp system and is operated at a mass flow ratio of unity so that the additive drag is zero. The external inlet lines are identical to those in the reference aero model. The reference inlet model extends to the approximate location of the engine face.

The chord force measured by the balance is shown by the first equation. Performing a momentum balance on the streamtube between stations 0 and e gives the second equation.

The corrected chord force is shown by the third equation. It is worth noting here that the corrections to the measured value are large and must be determined accurately.

Combining the above equations gives the last equation. For now, just remember this equation.

Reference Model Integration (5)

The operational inlet, with ramps, boundary layer bleed, bypass doors, etc. is depicted here. This model is operated at various mass flow ratios to obtain the inlet forces.

The first equation shows the measured chord force. The second equation results from a conservation of momentum on the streamtube.

The third equation is the corrected chord force of the actual inlet. By combining the above equations we get the fourth equation. Here, F_1 is the additive drag term.

Finally, the chord force chargeable to the inlet is obtained by subtracting the corrected reference model value from the actual inlet value, as shown by the last equation.

In our inlet tests, which I will describe in a moment, we also measured the forebody forces.

We have now expressed all the forces in the parenthesis on the first of these slides in terms of the corrected and chargeable model forces.

Our bookkeeping system is shown to be consistent and to give the answer we seek; the forces on the airplane.

Now, let us briefly review how some of the model data are presented and used in the propulsion system analysis.

Propulsion System Analysis Input/Output

This slide depicts how the data, obtained from tests just described, is presented to a propulsion system analysis. The chargeable inlet drag versus mass flow ratio is given for various mach numbers. Although not mentioned before, the chargeable inlet lift and recovery are also used.

The nozzle thrust coefficient, obtained in other tests, is given versus pressure ratio for various nozzle settings and primary to secondary weight flows. The external nozzle chargeable chord force and normal force are given versus nozzle exit area ratio, or its equivalent, boattail angle.

Engine component maps are also presented but have been left off this slide.

The propulsion system analysis then uses these data to calculate the data shown at the bottom of the slide. For low angles of attack, the net propulsive effort is the net thrust minus the propulsion system drag. Values of chargeable inlet and nozzle lift and drag are also passed through the propulsion system analysis to the mission analysis, along with the other data.

Now let us review two of the tests performed as a part of the program.

Inlet Model Installed In Tunnel

During the program, a number of vehicle configurations were determined and analyzed. One of the configurations was selected for inlet tests and nozzle interaction tests. No tests were performed to obtain the aerodynamic forces on the configuration, i.e., there was no aero model.

This slide is a photograph of a 0.135 scale model of the inlet and forebody installed in the North American Rockwell Corporation Transonic Wind Tunnel. The forebody and inlet were mounted on separate balances to obtain the forces on each. The model is mounted upside-down in the tunnel. Only one inlet, the righthand inlet, was tested.

Basic Inlet Configuration

A closeup photograph of the basic inlet is shown in this slide. The boundary layer bleed air openings are visible near the rear of the model. Two fixed ramps, and one moveable ramp were employed.

Reference Inlet Configuration

The external lines of the reference inlet are identical to those of the basic inlet. The reference inlet has a collapsed ramp system, however, to permit operation at zero spillage drag.

Remember, the reference aero model, as was explained before, was equipped with a reference inlet shape.

Effect of Forebody on Drag

The circle symbols represent the corrected drag values of the basic inlet. The square symbols represent the chargeable inlet drag and are the basic inlet values minus the reference inlet values. The flagged symbols indicate the forebody is off. We found that for this mach number, $M = 1.2$, and for the other mach numbers tested using the reference inlet ($M = .6, .85$ and 1.3) that the chargeable inlet drag was the same with the forebody on or off.

The drag coefficient is for one inlet and referenced to the capture area. (Note: $2A_c/S = .0327$)

Effect of Forebody on Lift

This slide is similar to the previous slide except we are now looking at lift. In this case, and at the other mach numbers, the chargeable inlet lift was higher with the forebody on. This would indicate that inlet tests should be performed with the forebody simulated.

Comparison between Theoretical and Test Inlet Chargeable Drags (3 slides)

This and the next two, show comparisons between measured and estimated chargeable drags. The estimates using K_{ADD} values referenced in the program are quite close to the measurements. Note that it is important to include the lip suction in the estimates. Also note that the critical mass flow and drag levels are estimated quite well.

Chargeable Inlet Drag Summary

This slide shows a carpet plot summarizing the chargeable inlet drag values throughout the mach number range. Beyond $M = 1.3$, the reference inlet values used to obtain the chargeable drags were estimated since, through an oversight, we did not test the reference inlet past $M = 1.3$.

Chargeable Inlet Lift

The inlet chargeable lift is summarized on this slide. The values are quite sizeable and should not be ignored in accounting for propulsion system forces.

Although I don't have a slide showing this, the changes in the forces on the forebody, when the reference and the actual inlets were installed, were negligible.

Comparison Between Estimated and Measured Total Pressure Recovery

This slide shows measured and estimated inlet pressure recovery versus mach number. The measured values are based on the knee-points of the various recovery curves.

Sketch of Nozzle Interaction Model Installation

A 0.09 scale model of the same vehicle configuration used for the

inlet tests was used for nozzle interaction testing. The forward portion of the vehicle, including wings, horizontal tail, and a no-flow inlet were simulated. Only the forces on the aft portion of the model, the metric section, were measured, however.

High pressure cold air was routed through the strut and exhausted at controlled pressures through two sets of nozzles.

An internal balance was mounted inside the model to measure forces on the aft end.

Pressure Instrumentation on Metric Section

An enlarged sketch of the metric section is shown on this slide. By using four nozzles, one pair of plug nozzles, and one pair of C-D nozzles, we were able to obtain both near wake (C-D) and far wake (plug) effects on one model.

Nozzle thrust forces were not measured and were isolated from the external aft end model shell. The isolation was not as complete as we had hoped, however, and the internal balance chord force readings were sometimes subjected to rather large tare forces. The normal force data were not affected.

The aft end of the model had fairly dense static pressure instrumentation, as seen here, and by integrating the pressures over appropriate areas, we obtained what appear to be reliable chord force data. The chord force data I will show in a moment are based on integrated pressures.

Please fix in your mind what I mean by plug nozzle and C-D nozzle because I will use these terms later.

Reference Cone Configurations

Afterbody configuration changes were accomplished by using a series of nozzle shrouds and liners to vary the C-D nozzle exit area (A_0/A_M) and internal area ratio. The plug nozzle configuration was the same for all tests.

Since we did not test an aero model the choice of a reference nozzle model was arbitrary. We choose to use the configuration of $A_0/A_M = .5$ as the common, or baseline, configuration. The main purpose of the cones was to provide a simple axisymmetric shape that could be easily tested and that was amenable to our available subsonic analysis tool. The cones are attached to the non-metric portion of the model and forces on them are not measured.

In the following slides, incremental values of chord force or normal force mean differences between the configuration being shown and the baseline configuration.

As a matter of interest, the drag of the metric reference afterbody was about 40 percent of the estimated vehicle drag throughout the mach number range.

Afterbody Configuration Effects on Chord Force Increments

This slide shows comparisons between measured and estimated chord force with the nozzle jets off. These are just changes in drag caused by changing boattail angle (A_0/A_M) and mach number. The best agreement appears to be at the subsonic mach numbers and at $M = 2.0$. The general agreement is quite good considering the rather complicated shape of the aft end of the model.

The chord force coefficient is referenced to the wing area.

Afterbody Configuration Effects on Normal Force Increment

This slide shows normal force changes due to boattail angle changes. No estimates were made of normal force. As in the use of the inlet, these values should not be ignored.

Now let us look at some jet effects.

C-D Nozzle Static Pressure Ratio Effect in Chord Force Increment - $M = .614$

The data at the top show near wake effects. The C-D nozzle is operating and the plug nozzle is off and has the cone installed. The C-D nozzle exit static to freestream static pressure ratio (P_0/P_∞) is used to show power effects. The estimated near wake effects are in fair agreement with the data. Also note the drag changes very little with change in C-D pressure ratio.

The bottom curve shows the same as the above but with the plug nozzle operating at a total to freestream static pressure ratio of 5. The far wake effects were not accounted for in the analysis and are seen to be unfavorable.

C-D Nozzle Static Pressure Ratio Effect on Chord Force Increment - $M = 1.27$

The axes are the same as on the previous slide. For the supersonic mach numbers, the estimates include both near wake (C-D) and far wake (plug) effects. The near wake effects were estimated to be zero. Some small effects are seen in the data, however. The far wake effects are not predicted too well at this mach number.

C-D Nozzle Static Pressure Ratio Effects on Chord Force Increment - $M = 2.0$

The best agreement between estimated and measured combinations of configuration and jet effects was obtained at $M = 2.0$.

Summary of Configuration and Jet Effects on Chord Force Increment - $M = .6, 1.27$

Integration of the internal and external nozzle data can be a problem. Not only power settings, but both internal and external nozzle

geometry must be considered. It turned out, in the case of the data we obtained, that the exit static pressure ratio effects, which may be thought of as exhaust plume effects, were quite small for the C-D nozzles. Because of this, the C-D nozzle chord force increments, at a pressure ratio of about unity, may be taken to represent the correct value for a range of pressure ratios between about .6 and 1.2. The error in doing this amounts to only a few drag counts. If this is accepted, the data may be plotted versus exit area ratio.

This slide summarizes the $M = .6$ and $M = 1.27$ data plotted in this fashion. The solid lines represent measured data with the jets on. The dashed lines represent the measured data with jets off.

At $M = .6$ both configuration and jet effects are small. At $M = 1.27$ the configuration effects are dominant, and the jet effects are favorable.

Summary of Configuration and Jet Effects in Chord Force Increment -
 $M = 1.7, 2.0$

This slide summarizes the $M = 1.7$ and $M = 2.0$ data. Again, the jet effects are favorable, but small, and the boattail angle changes dominate.

Conclusions and Recommendations

1. The integration technique described is workable and provides the required degree of flexibility.
2. It is desirable to proceed through the entire integration procedure to determine the effect of a propulsion system parameter change. If not, an important effect, such as the effect of a weight change on vehicle range, would not be known.
3. The proper use of reference models is essential to a meaningful integration procedure. Reference models should be used for vehicle evaluations involving just analysis, tests, or a combination of both.
4. Satisfactory testing techniques to obtain data required for vehicle/propulsion system integration were demonstrated.

IPS PROGRAM SCOPE STEADY STATE

- **ESTABLISH NUMERICAL PROCEDURE TO DEFINE OVERALL VEHICLE PERFORMANCE, INCLUDING PROPULSION SYSTEM (AFAPL-TR-69-36, PART I)**
- **PROVIDE RELIABLE DATA AND DEMONSTRATE TEST TECHNIQUES (AFAPL-TR-69-36, PART I)**
- **DEMONSTRATE INCREASED PROPULSION SYSTEM PERFORMANCE THROUGH IMPROVED TECHNIQUES, BACKED BY TEST DATA (AFAPL-TR-69-36, PART II)**

2

DISCUSSION SCOPE

- **INTEGRATION PROCEDURE**

 - APPROACH**

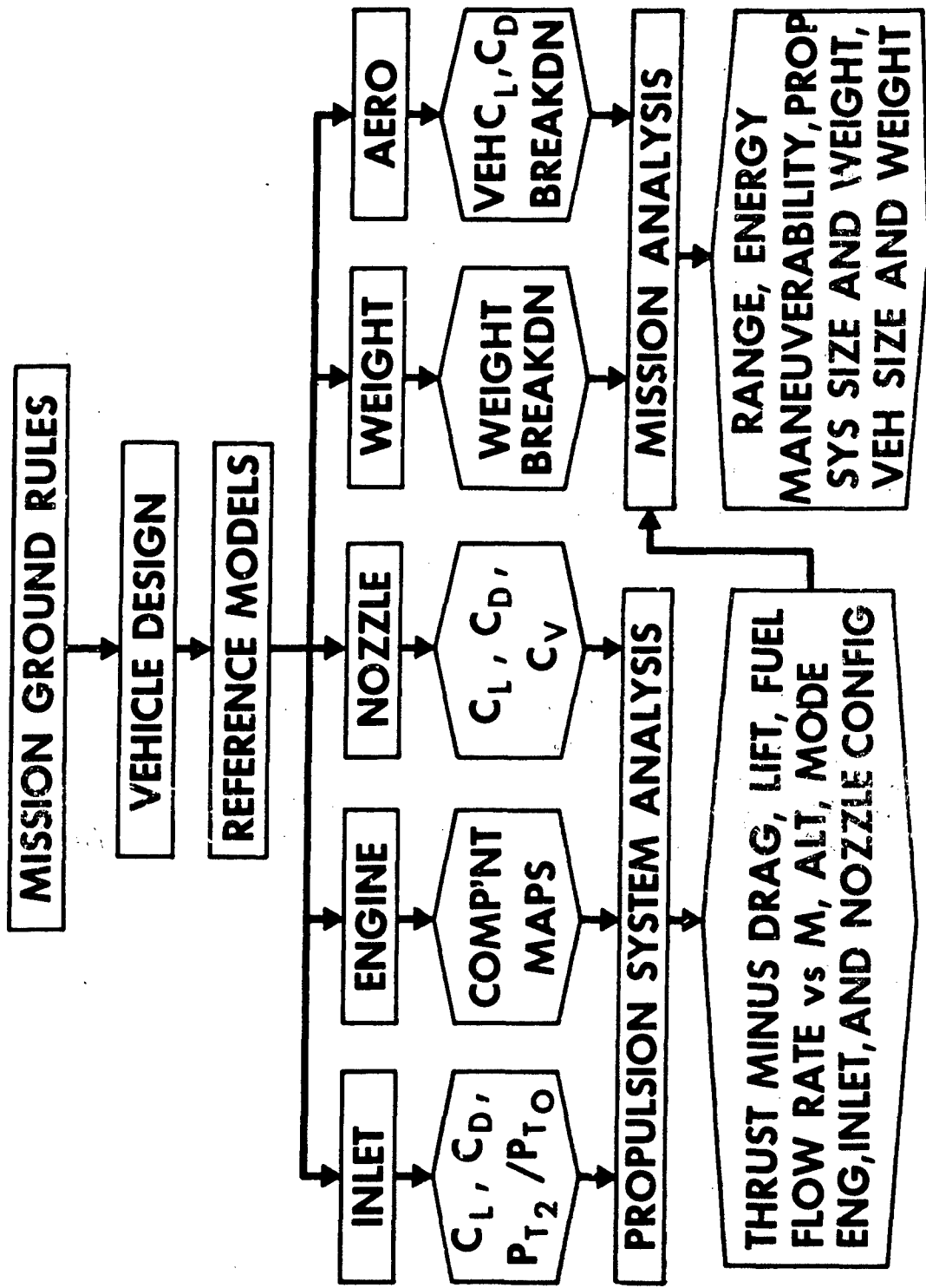
 - REFERENCE MODELS AND
DATA INTEGRATION**

- **TEST PROGRAM**

 - INLET TESTS**

 - NOZZLE INTERACTION TESTS**

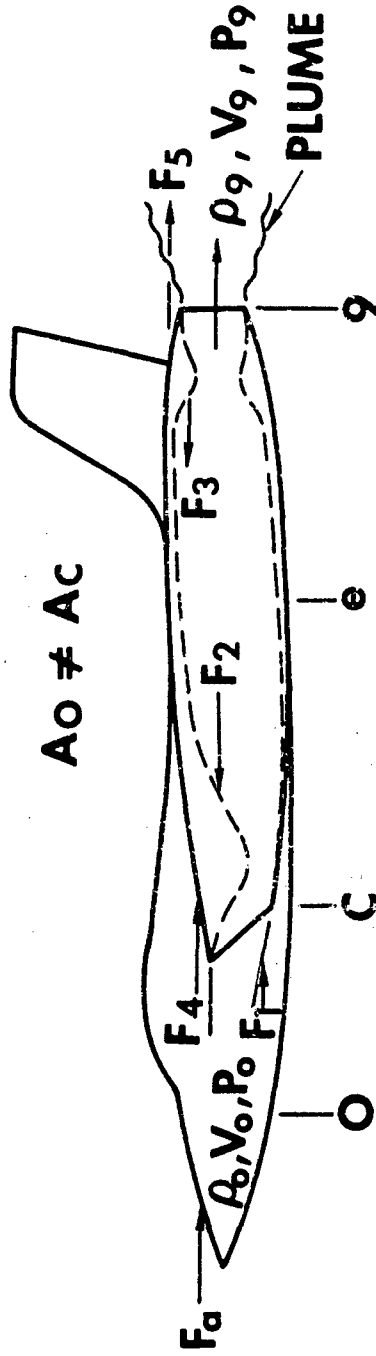
OUTLINE OF PROP SYS INTEG TECHNIQUE



REFERENCE MODEL INTEGRATION (I)

AIRPLANE

$A_0 \neq A_C$



64

NET FORCE IN FLIGHT DIRECTION

$$F = F_2 + F_3 - (F_a + F_4 + F_5)$$

CONSERVATION OF MOMENTUM

$$(P_0 - P_9)A_0 + F_1 + F_2 + F_3 - (P_9 - P_0)A_9 = \rho_9 V_9^2 A_9 - \rho_0 V_0^2 A_0$$

COMBINE TO GET

$$F = \underbrace{[\rho_9 V_9^2 A_9 - \rho_0 V_0^2 A_0 + (P_9 - P_0)A_9]}_{\text{NET THRUST}} - \underbrace{(F_a + F_1 + F_4 + F_5)}_{\text{FROM MODEL DATA}}$$

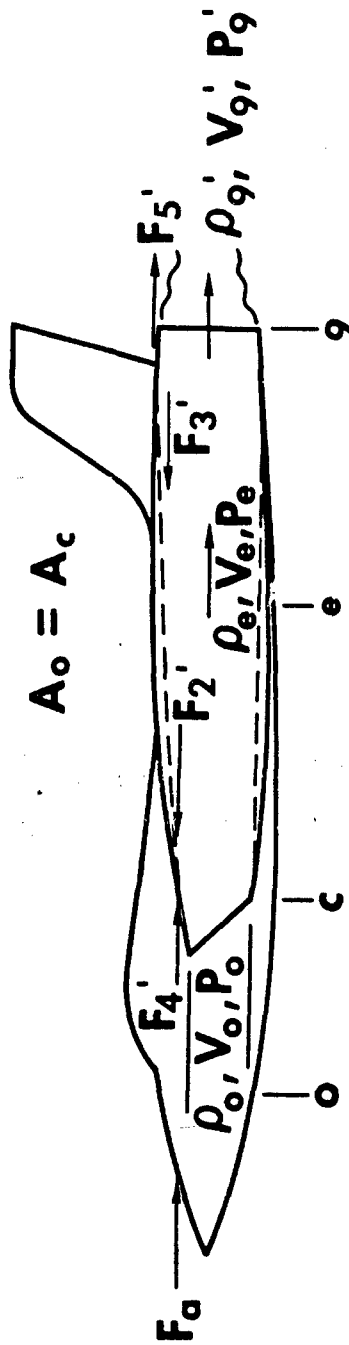
NET THRUST

FROM MODEL DATA

$$F = F_N - (C'_1 + \Delta C_{AB})$$

REFERENCE MODEL INTEGRATION (2)

REFERENCE AERO MODEL



MEASURED CHORD FORCE

$$C_M' = F_a + F_4 + F_5 - (F_2' + F_3')$$

CONSERVATION OF MOMENTUM

$$(P_0 - P_9)A_c + F_2' + F_3' - (P_9' - P_0)A_9 = \rho_9' V_9'^2 A_9 - \rho_0 V_0^2 A_c$$

CORRECTED CHORD FORCE

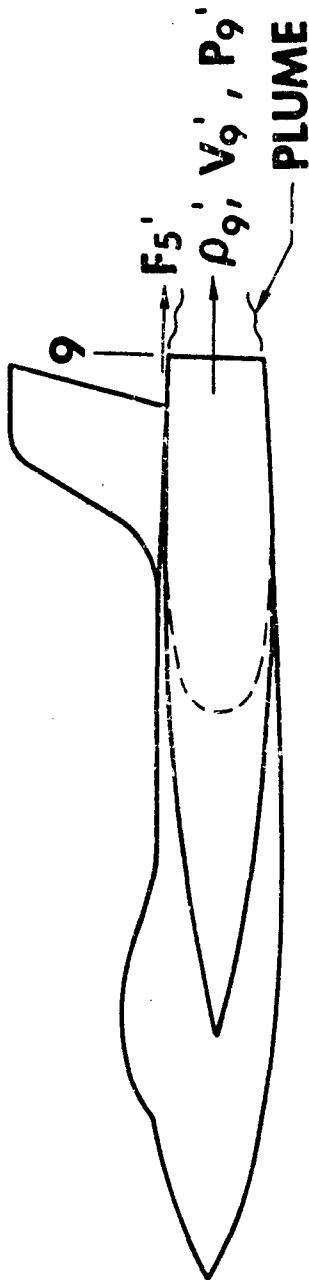
$$C' = C_M' - \rho_0 V_0^2 A_c - (P_0 - P_9)A_c + \rho_9' V_9'^2 A_9 + (P_9' - P_0)A_9$$

COMBINE TO GET

$$C' = F_a + F_4 + F_5$$

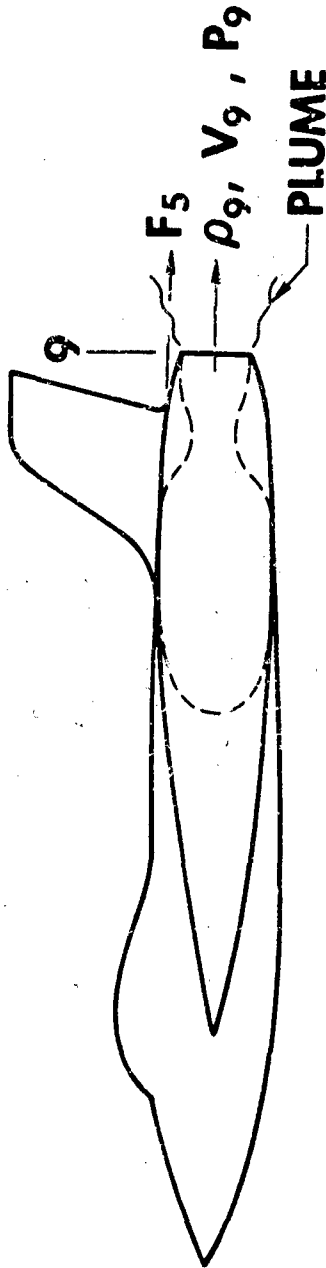
REFERENCE MODEL INTEGRATION (3)

REFERENCE NOZZLE MODEL



MEASURED REF NOZZLE MODEL CHORD FORCE WITH EXIT FLOW
 EQUAL TO THAT OF THE REF AERO MODEL IS $C_{AB} = F_5'$

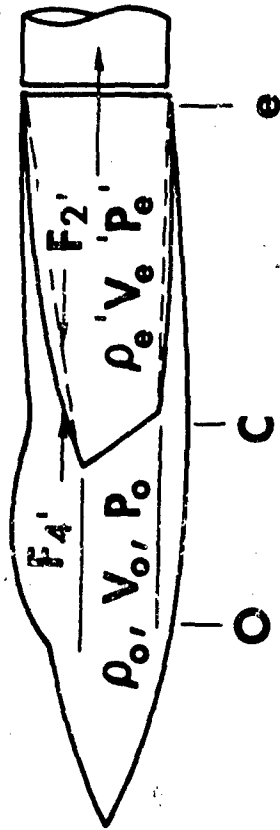
ACTUAL NOZZLE CONFIGURATIONS



MEASURED ACTUAL NOZZLE CHORD FORCE $C_{AB} = F_5$
 CHORD FORCE CHARGEABLE TO THE NOZZLE
 $\Delta C_{AB} = C_{AB} - C_{AB}' = F_5 - F_5'$

REFERENCE MODEL INTEGRATION (4)

REFERENCE INLET MODEL $A_o = A_c$



MEASURED CHORD FORCE

$$C'_{M1} = F_4 - F_2$$

CONSERVATION OF MOMENTUM

$$(P_o - P_e)A_c + F_2 - (P_e - P_o)A_e = \rho_e V_e^2 A_e - \rho_o V_o^2 A_c$$

CORRECTED CHORD FORCE

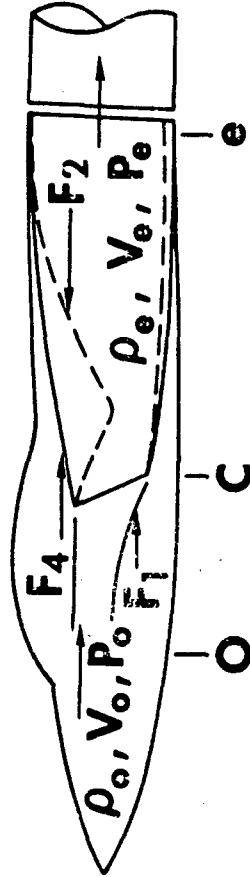
$$C_i = C'_{M1} - \rho_o V_o^2 A_c + \rho_e V_e^2 A_e + (P_e - P_o)A_e$$

COMBINE TO GET

$$C_i = F_4$$

REFERENCE MODEL INTEGRATION (5)

ACTUAL INLET MODEL $A_o \neq A_c$



MEASURED CHORD FORCE $C_{M1} = F_4 - F_2$

CONSERVATION OF MOMENTUM

$$(P_o - P_e)A_o + F_1 + F_2 - (P_e - P_o)A_e = \rho_e V_e^2 A_e - \rho_o V_o^2 A_o$$

CORRECTED CHORD FORCE

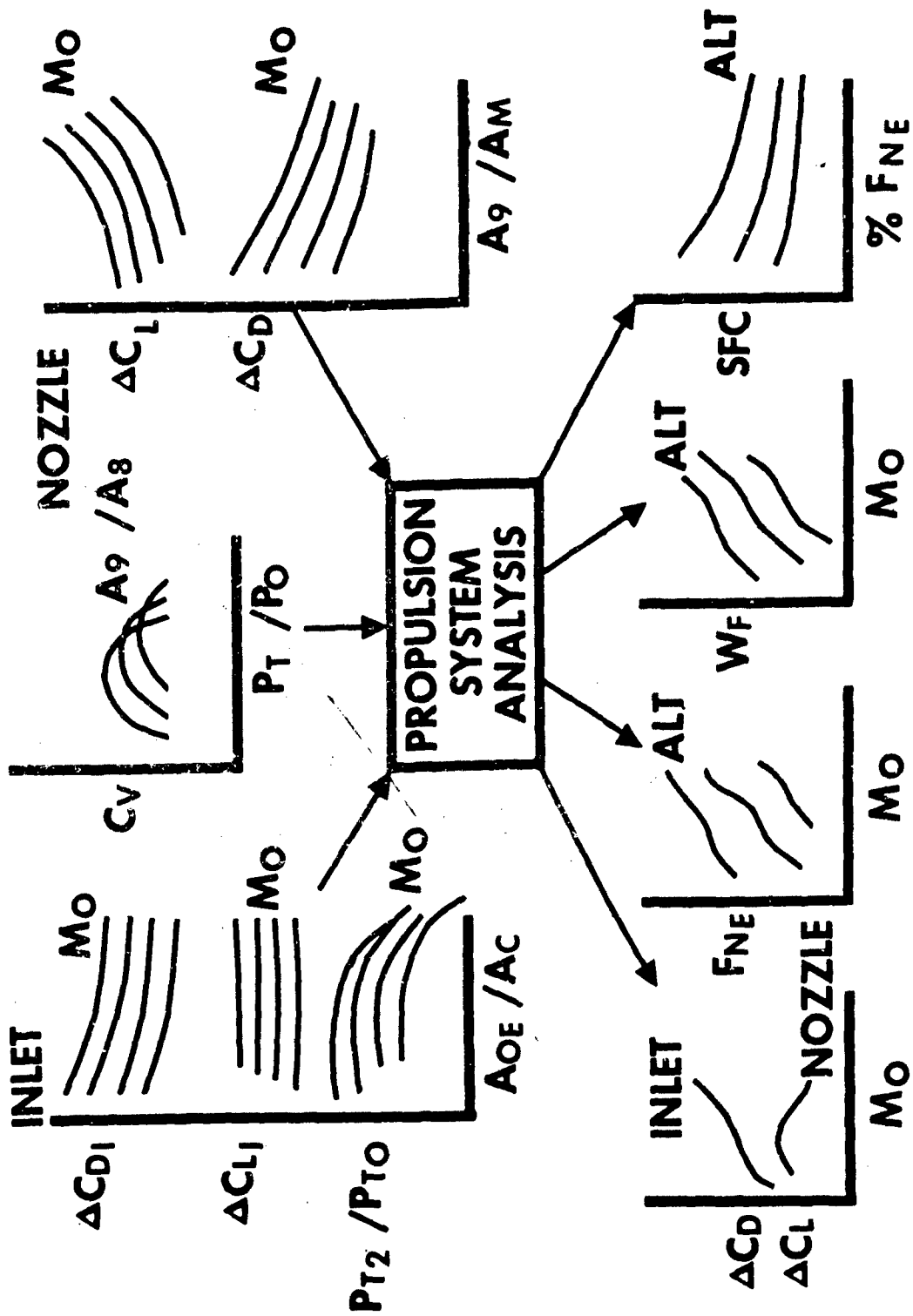
$$C_1 = C_{M1} - \rho_o V_o^2 A_o + \rho_e V_e^2 A_e + (P_e - P_o)A_e$$

COMBINE TO GET $C_1 = F_4 + F_1$

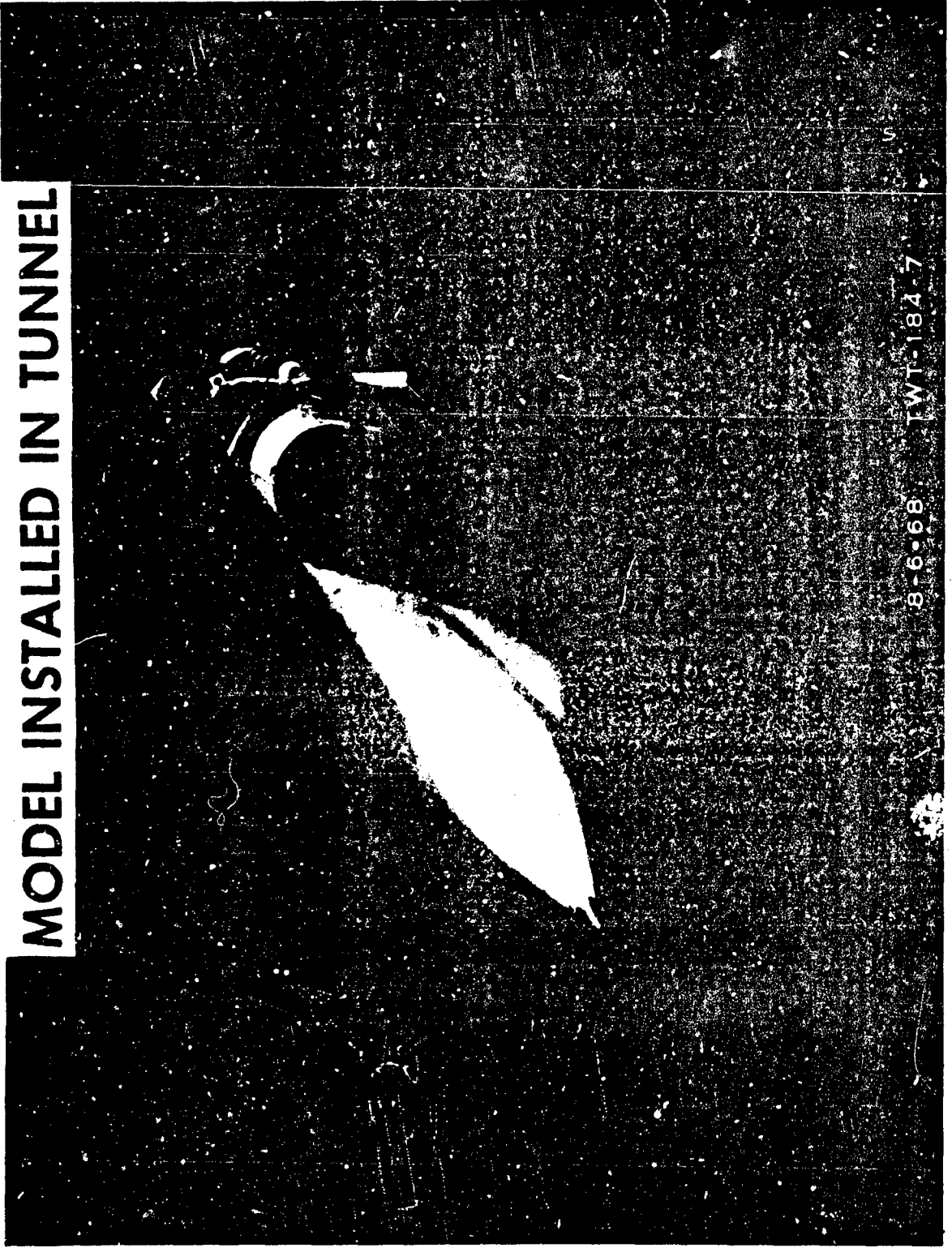
CHORD FORCE CHARGEABLE TO THE INLET

$$\Delta C_1 = C_1 - C_1' = F_4 + F_1 - F_4'$$

PROPULSION SYSTEM ANALYSIS INPUT/OUTPUT

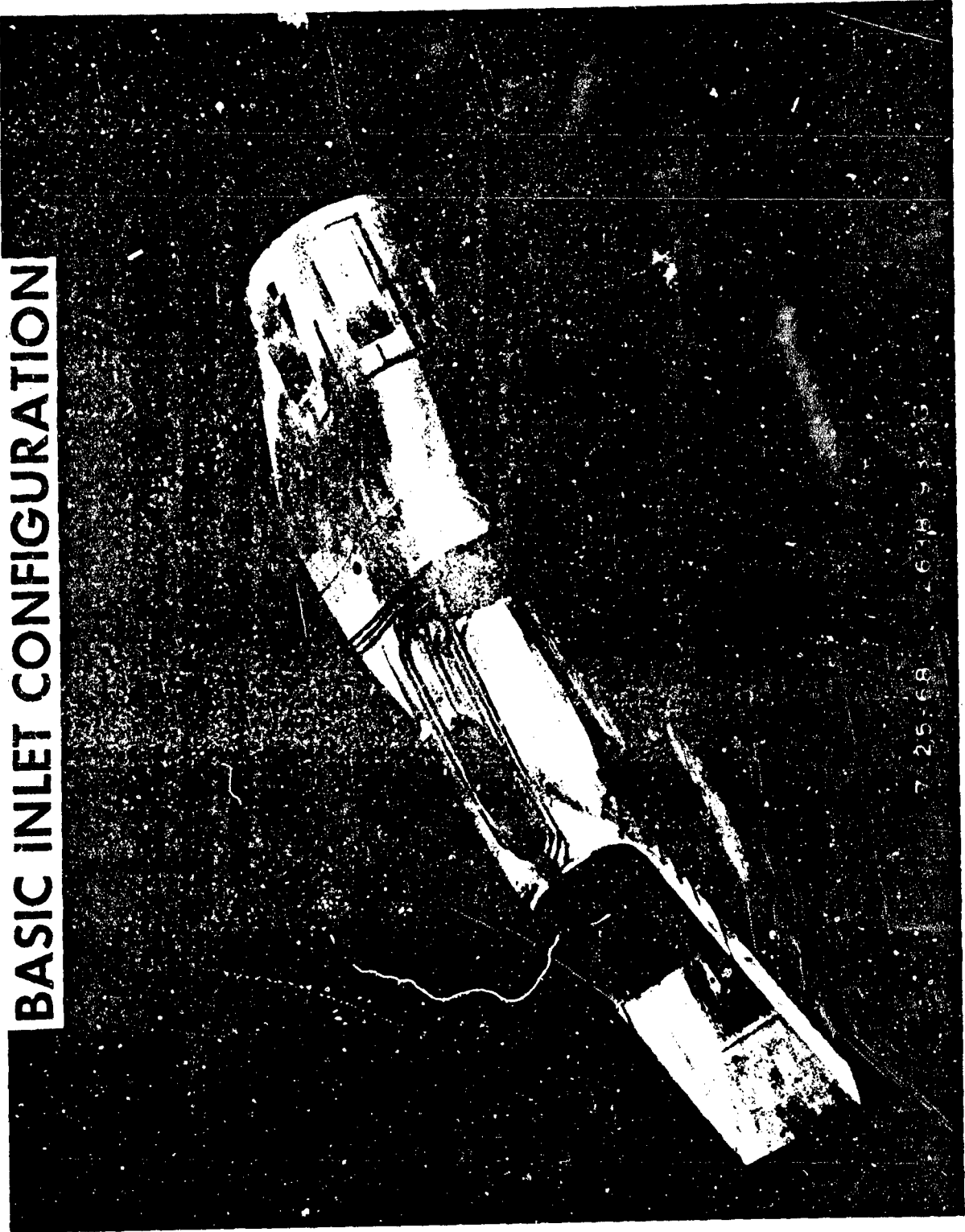


MODEL INSTALLED IN TUNNEL



8-6-68 FWT-184-7

BASIC INLET CONFIGURATION

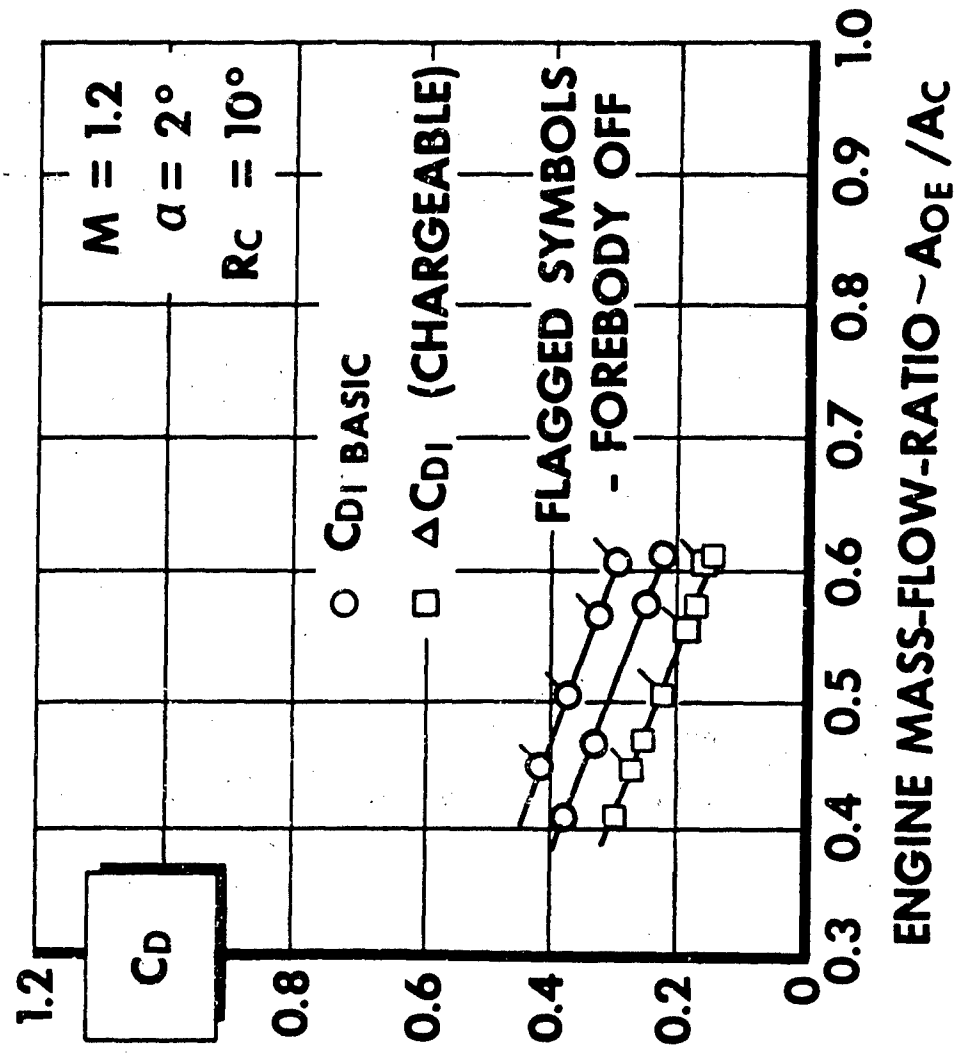


REFERENCE INLET CONFIGURATION

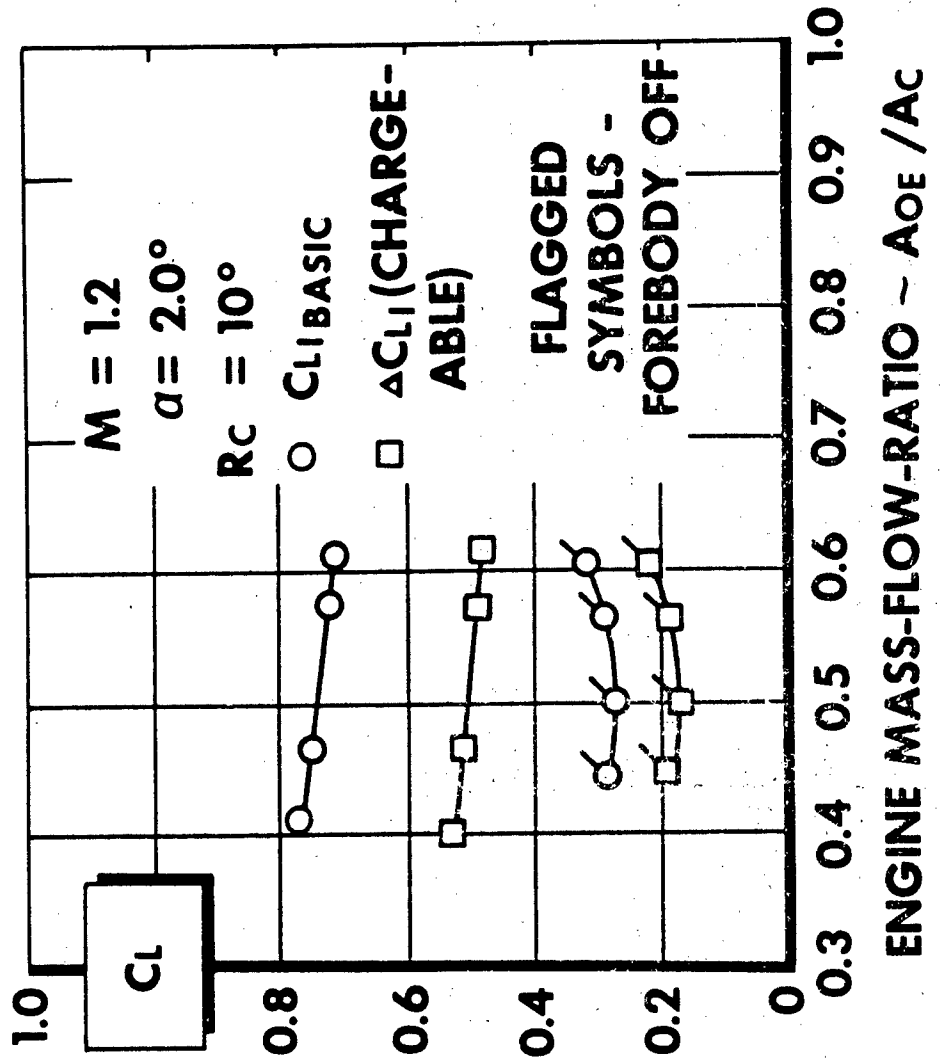


7-25-68 2638-93-1E

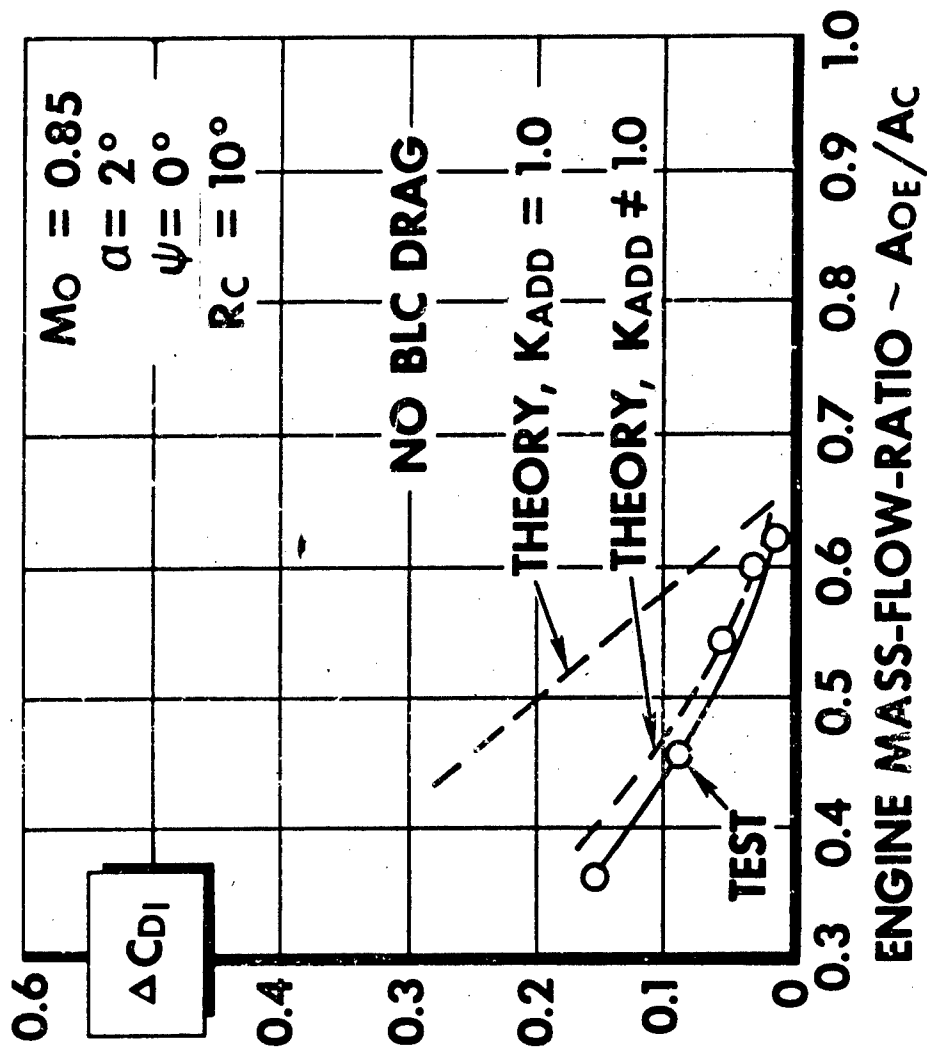
EFFECT OF FOREBODY ON INLET DRAG



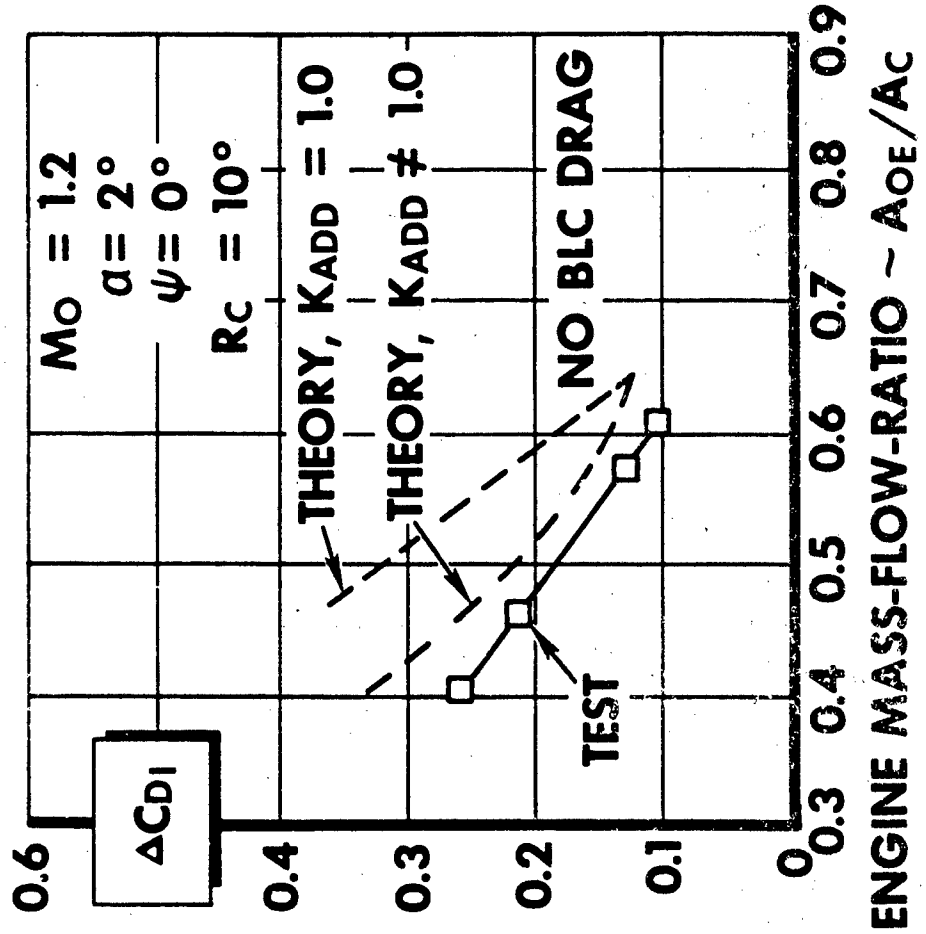
EFFECT OF FOREBODY ON INLET LIFT



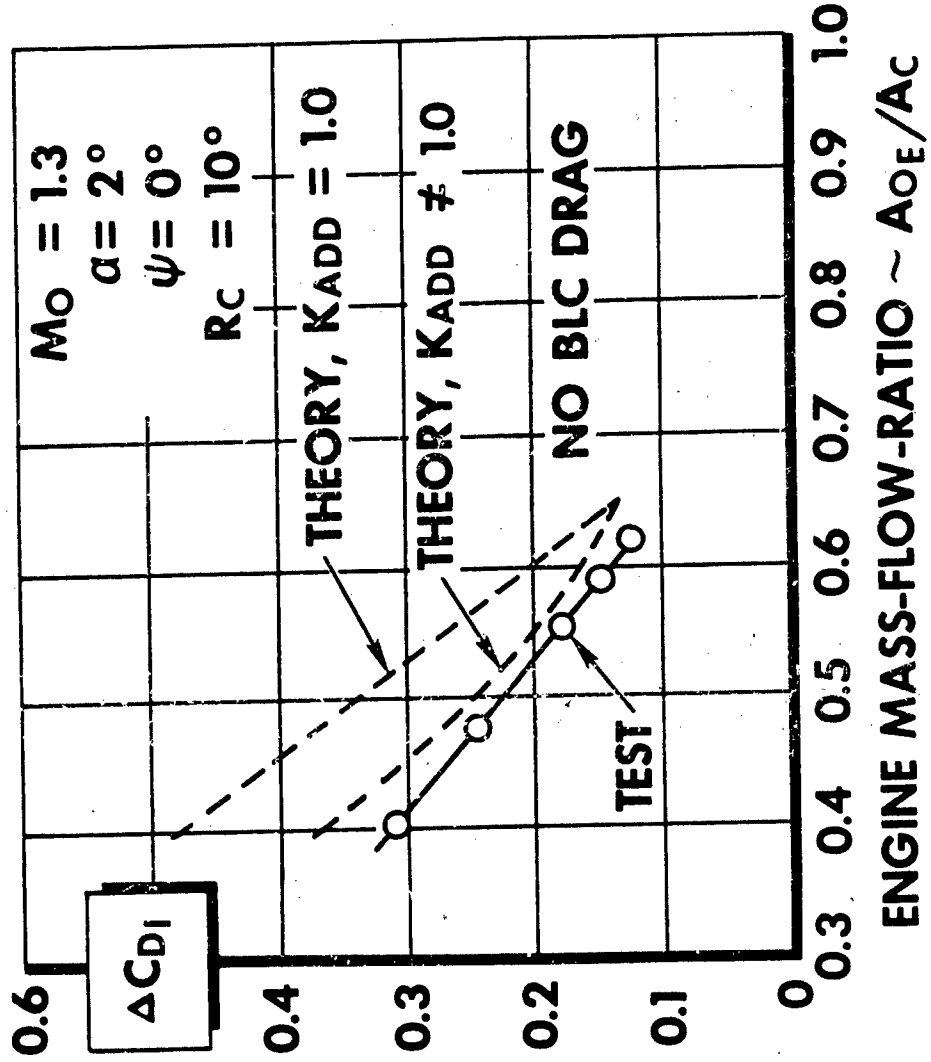
COMPARISON BETWEEN THEORETICAL AND TEST INLET CHARGEABLE DRAGS, $M_0 = 0.85$



COMPARISON BETWEEN THEORETICAL AND TEST INLET CHARGEABLE DRAGS, $M_0 = 1.2$



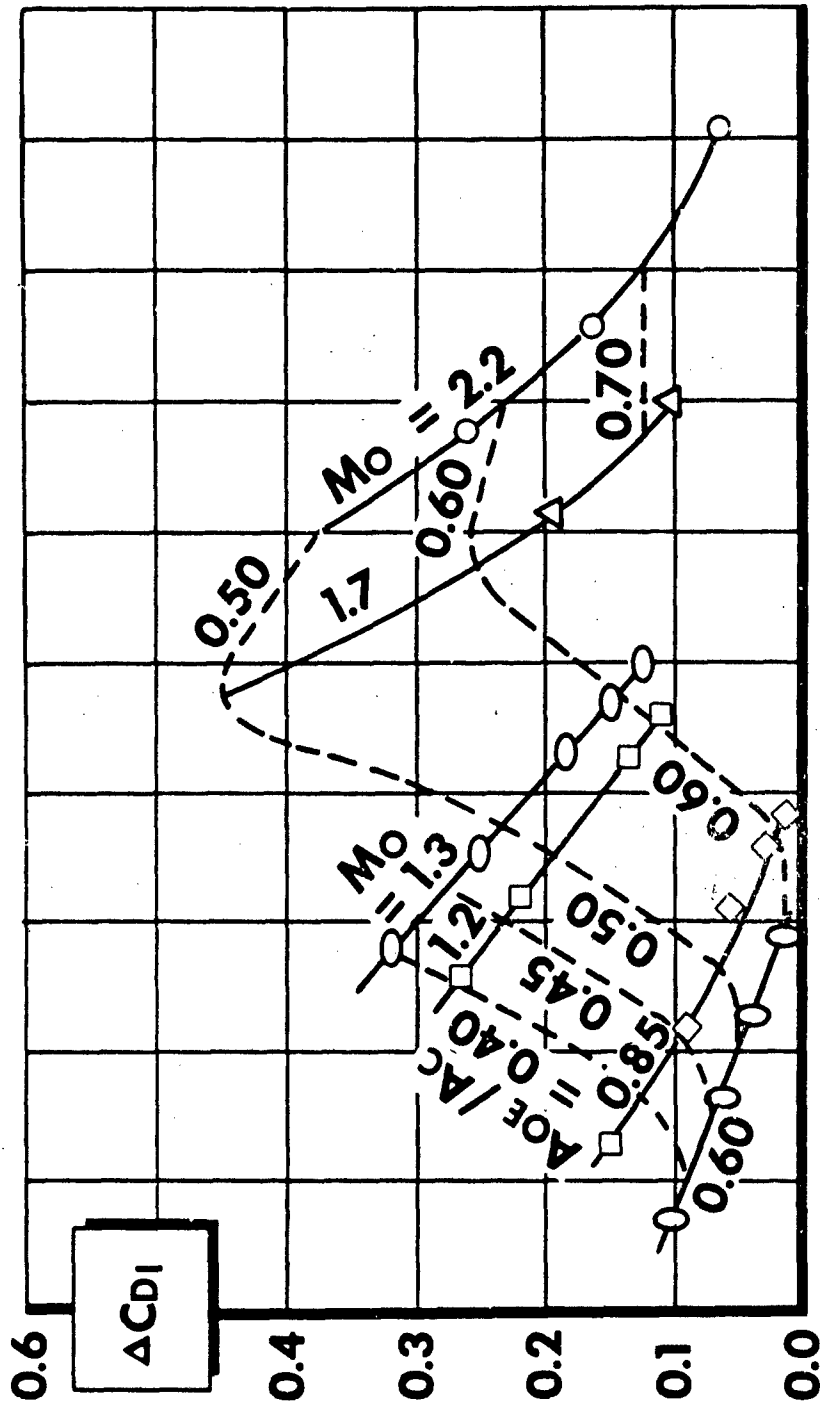
COMPARISON BETWEEN THEORETICAL AND TEST INLET CHARGEABLE DRAGS, $M_0 = 1.3$



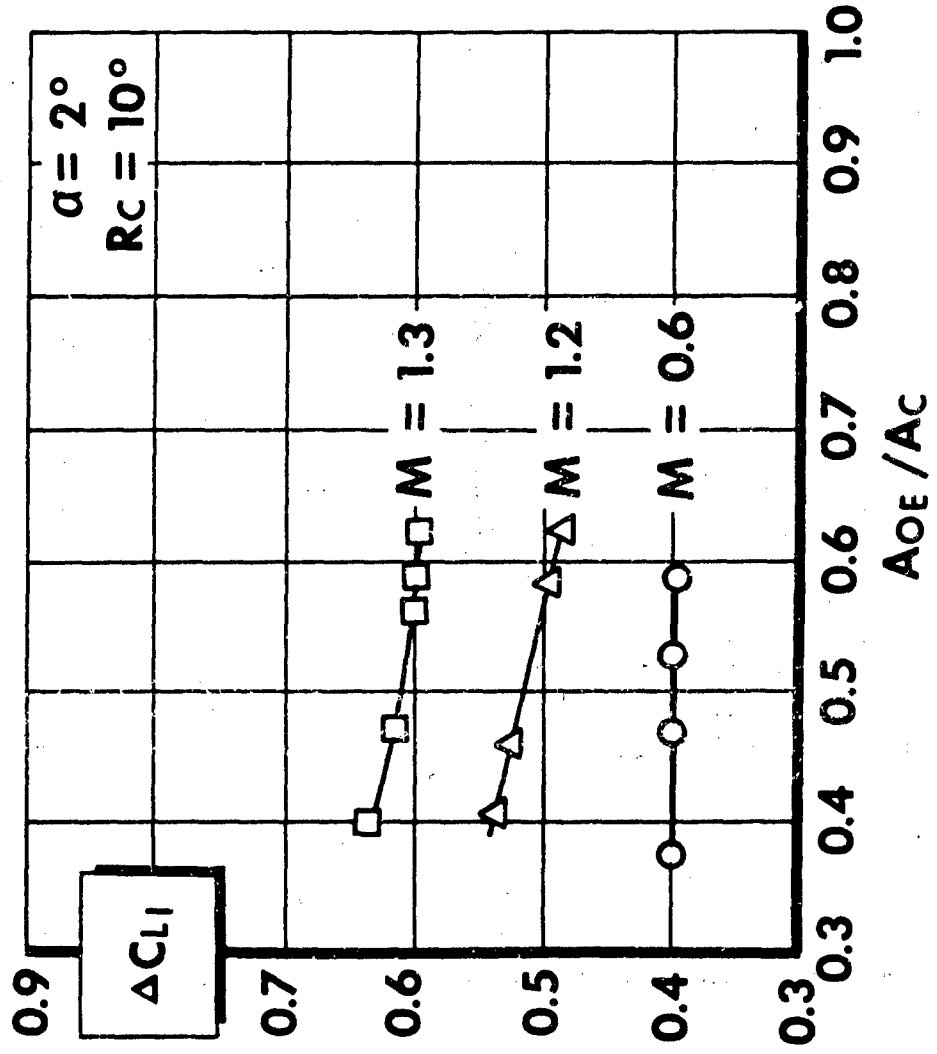
TSP69 - 9358

TFD-69-992

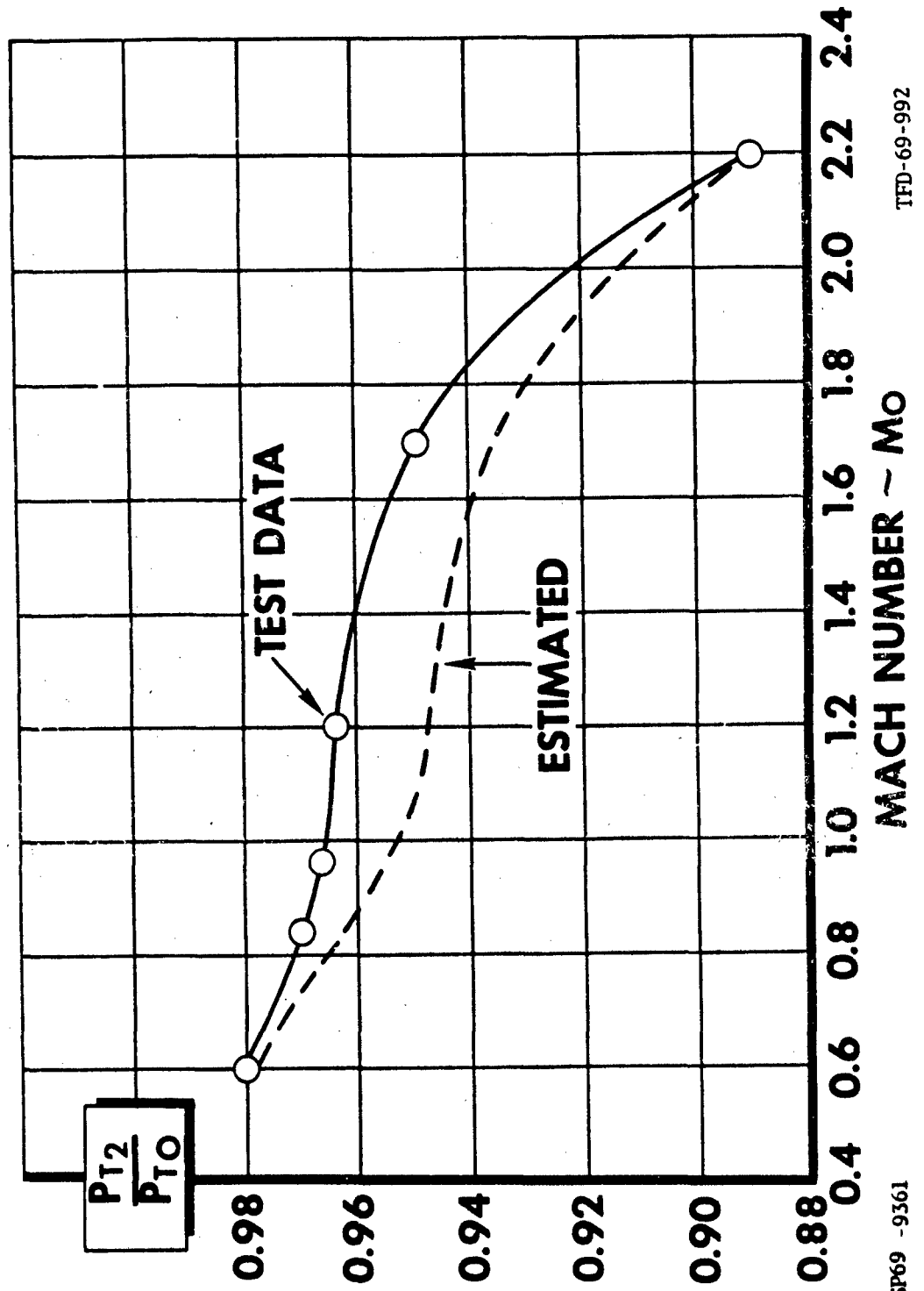
CHARGEABLE INLET DRAG SUMMARY



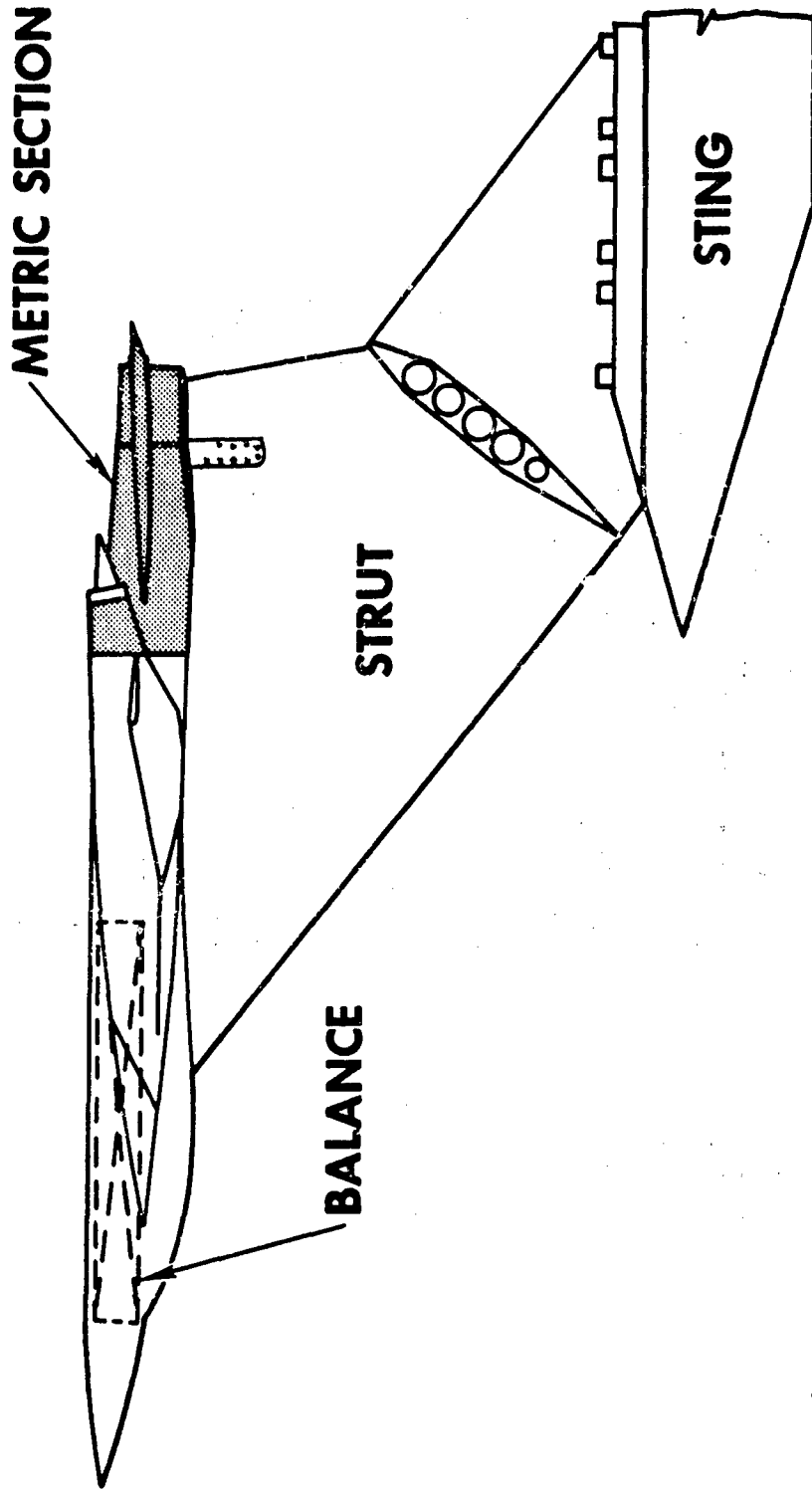
CHARGEABLE INLET LIFT SUMMARY



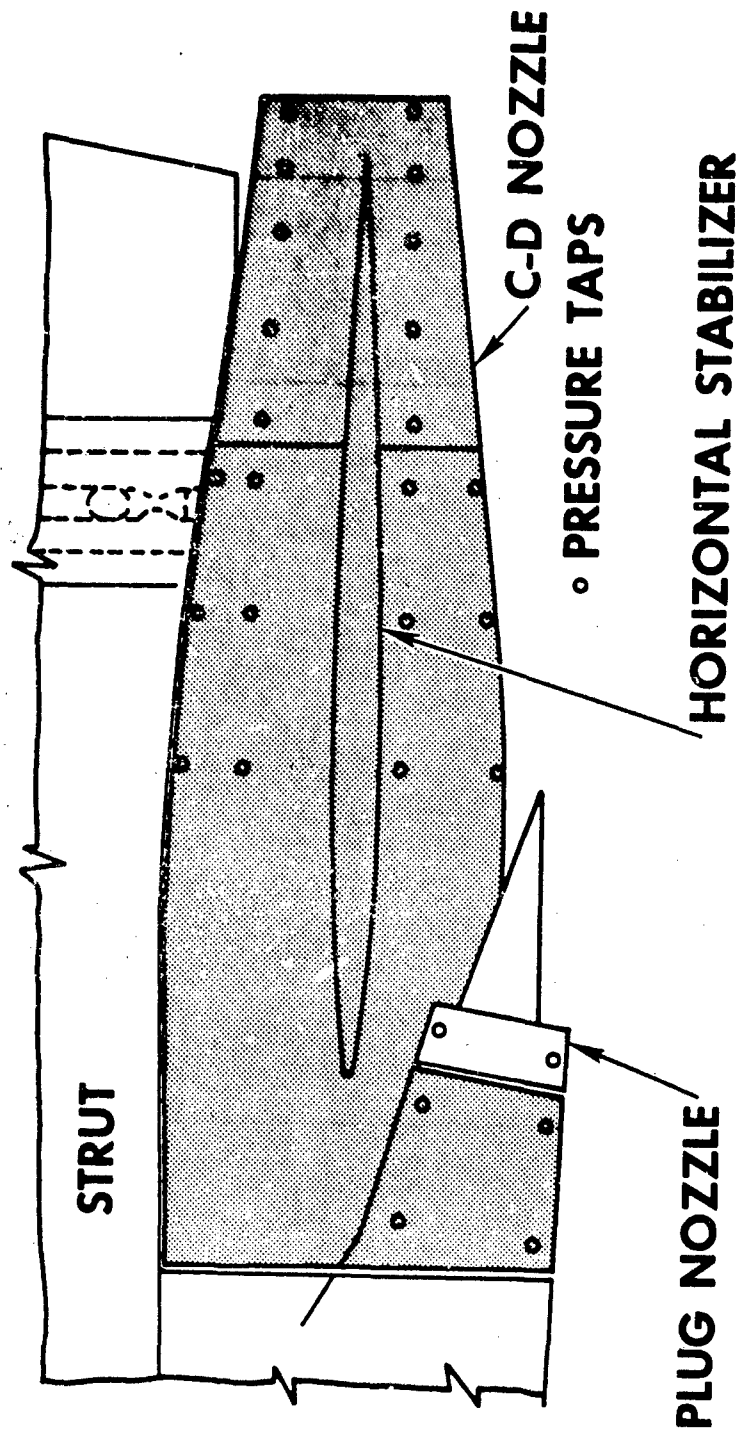
COMPARISON BETWEEN ESTIMATED AND MEASURED TOTAL PRESSURE RECOVERY



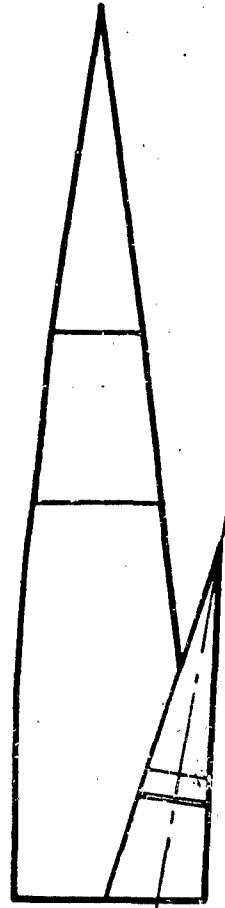
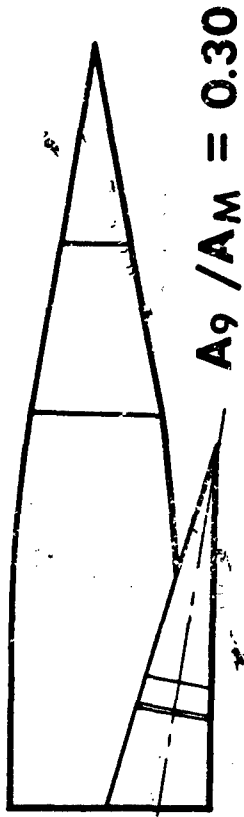
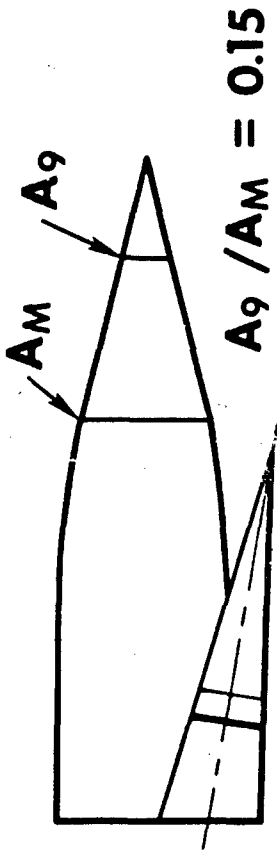
SKETCH OF NOZZLE INTERACTION MODEL INSTALLATION



PRESSURE INSTRUMENTATION ON METRIC SECTION



REFERENCE CONE CONFIGURATIONS

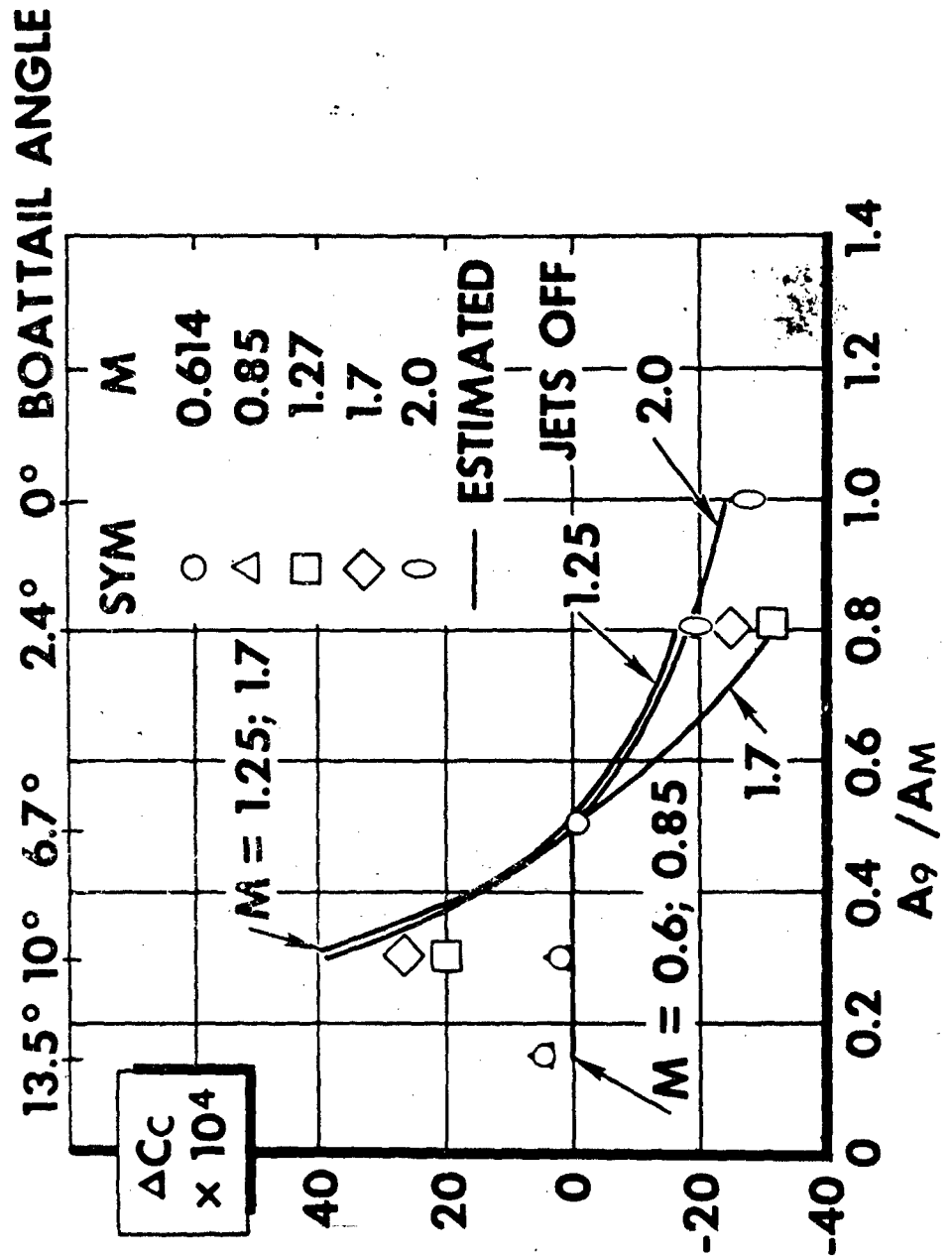


$A_9 / A_M = 0.50$ BASE LINE CONFIGURATION

TSP69 - 9364

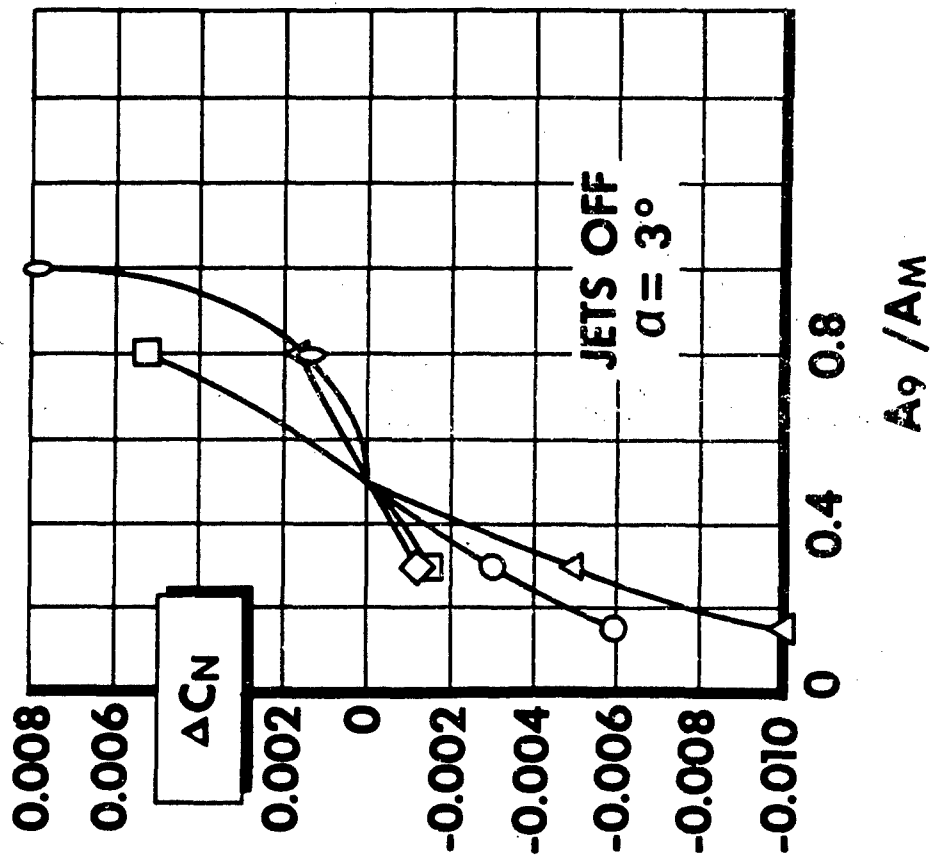
TFD-69-992

AFTERBODY CONFIGURATION EFFECTS ON CHORD FORCE INCREMENTS - COMPARISON WITH ESTIMATES



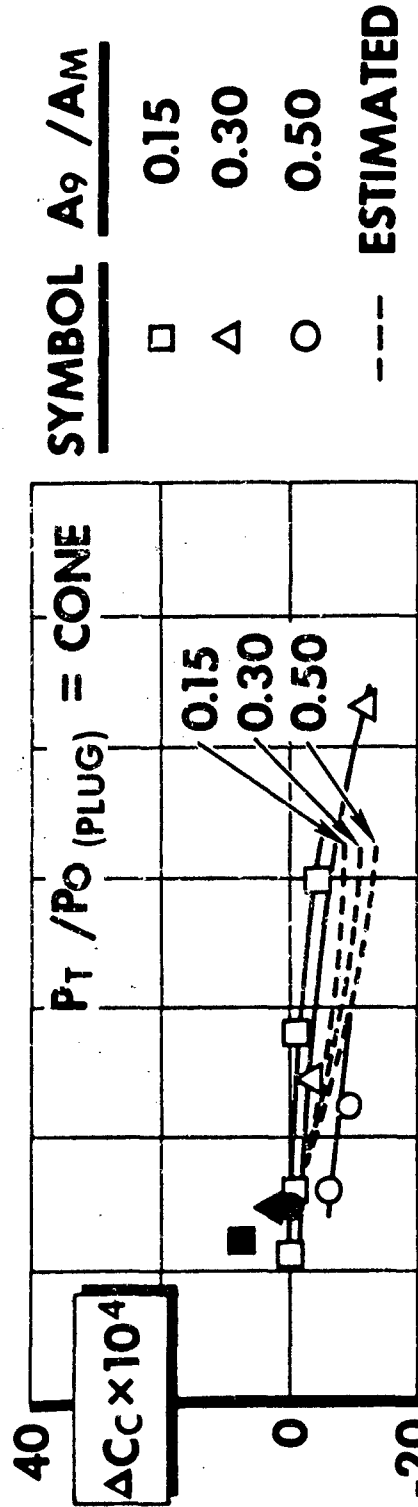
ΔCC
x 10⁴

AFTERBODY CONFIGURATION EFFECTS ON NORMAL FORCE INCREMENT - SUMMARY



| <u>SYMBOL</u> | <u>M</u> |
|---------------|----------|
| ○ | 0.614 |
| △ | 0.85 |
| □ | 1.27 |
| ◇ | 1.7 |
| ○ | 2.0 |

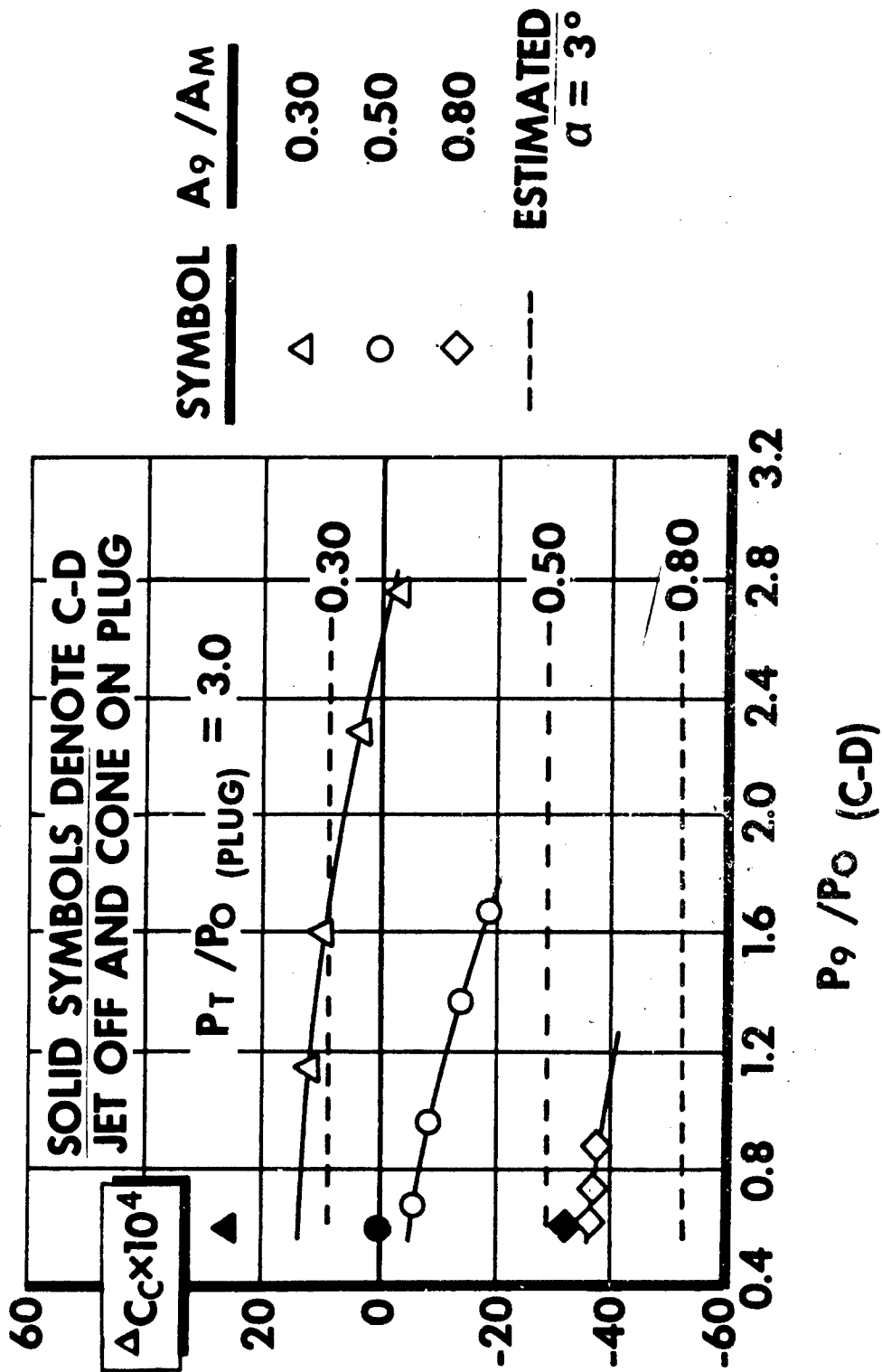
C-D NOZZLE STATIC PRESSURE RATIO EFFECT ON CHORD FORCE INCREMENT - $M = 0.614$



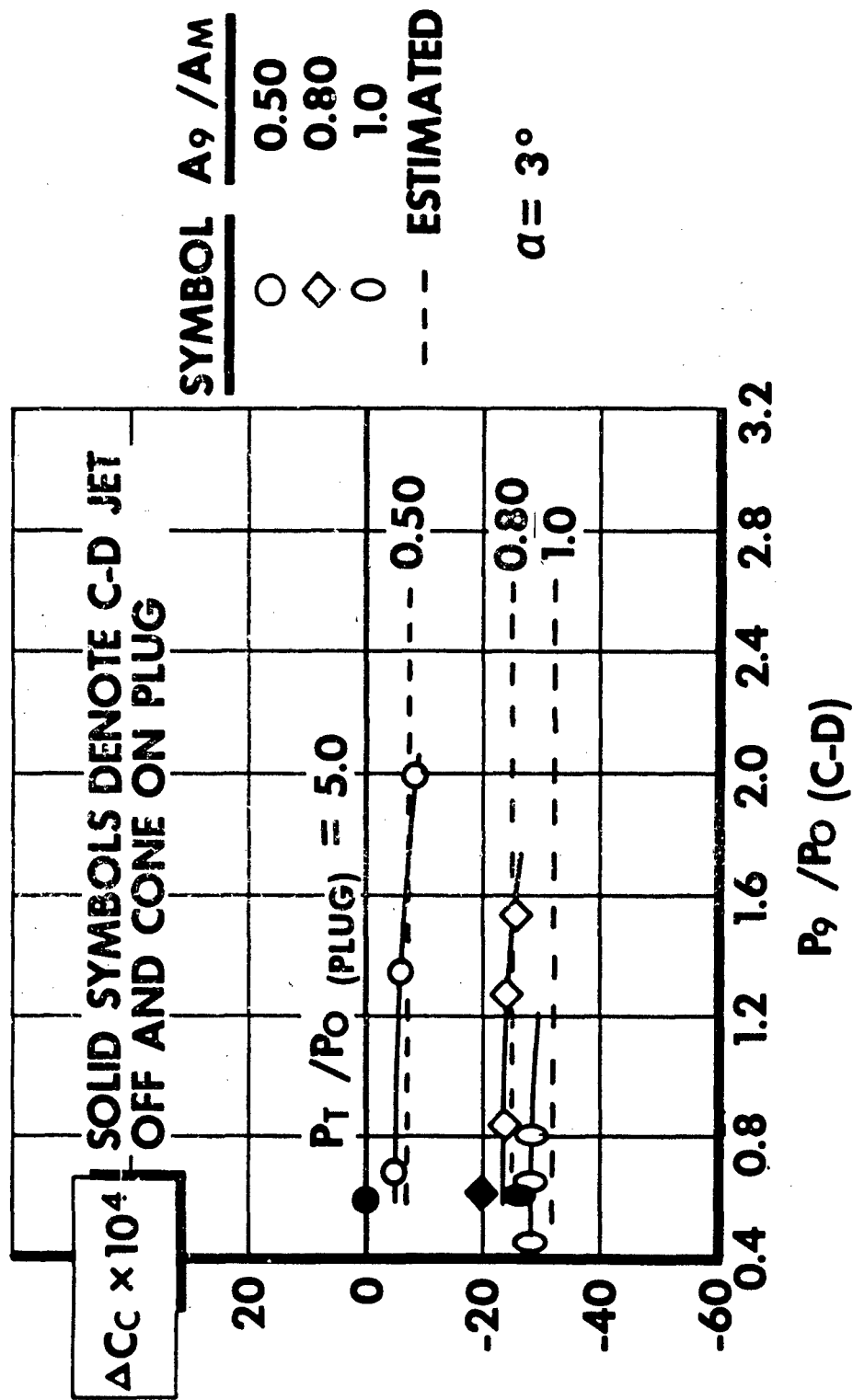
$\alpha = 3^\circ$

SOLID SYMBOLS
DENOTE CONE
ON C-D

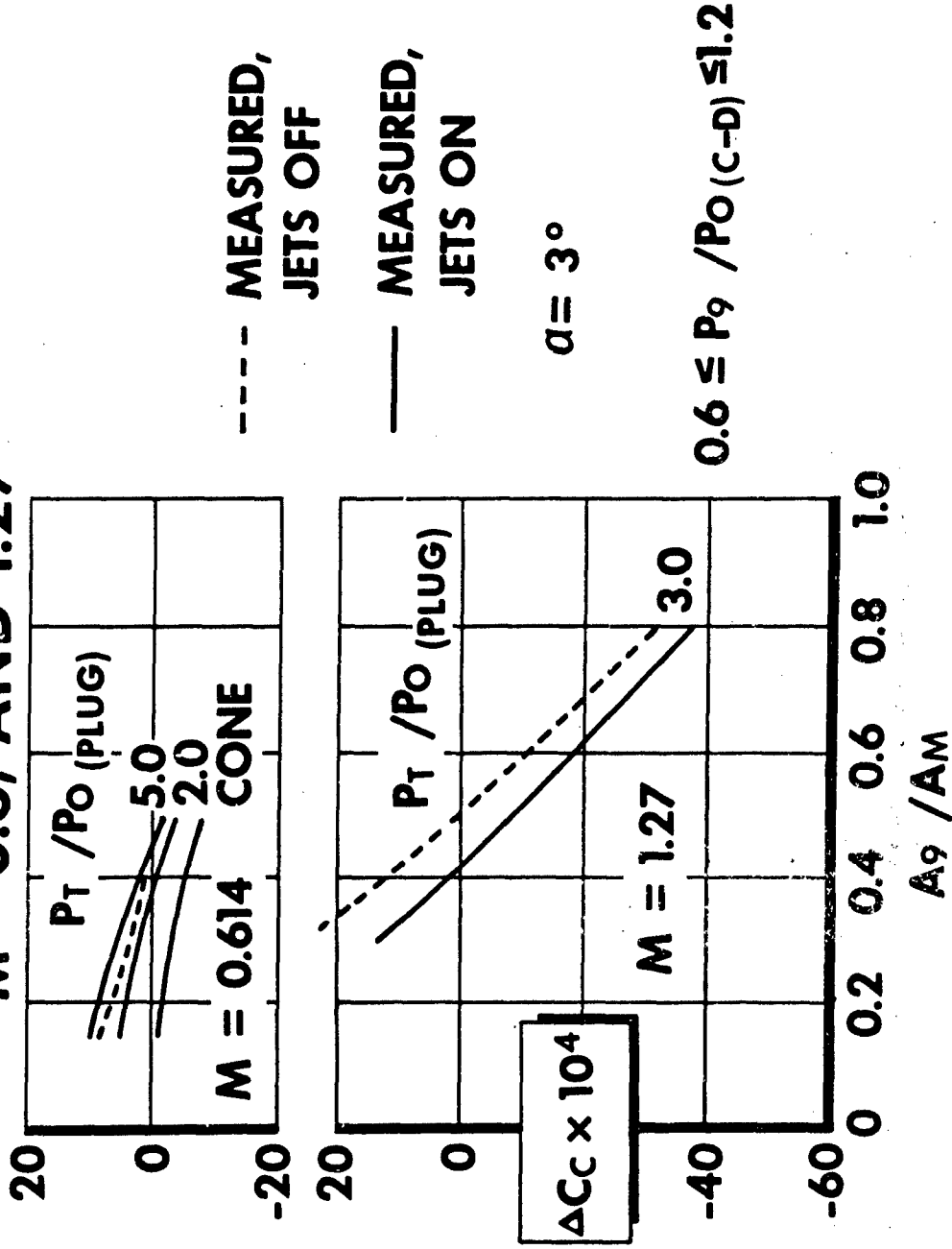
C-D NOZZLE STATIC PRESSURE RATIO EFFECT ON CHORD FORCE INCREMENT $M=1.27$



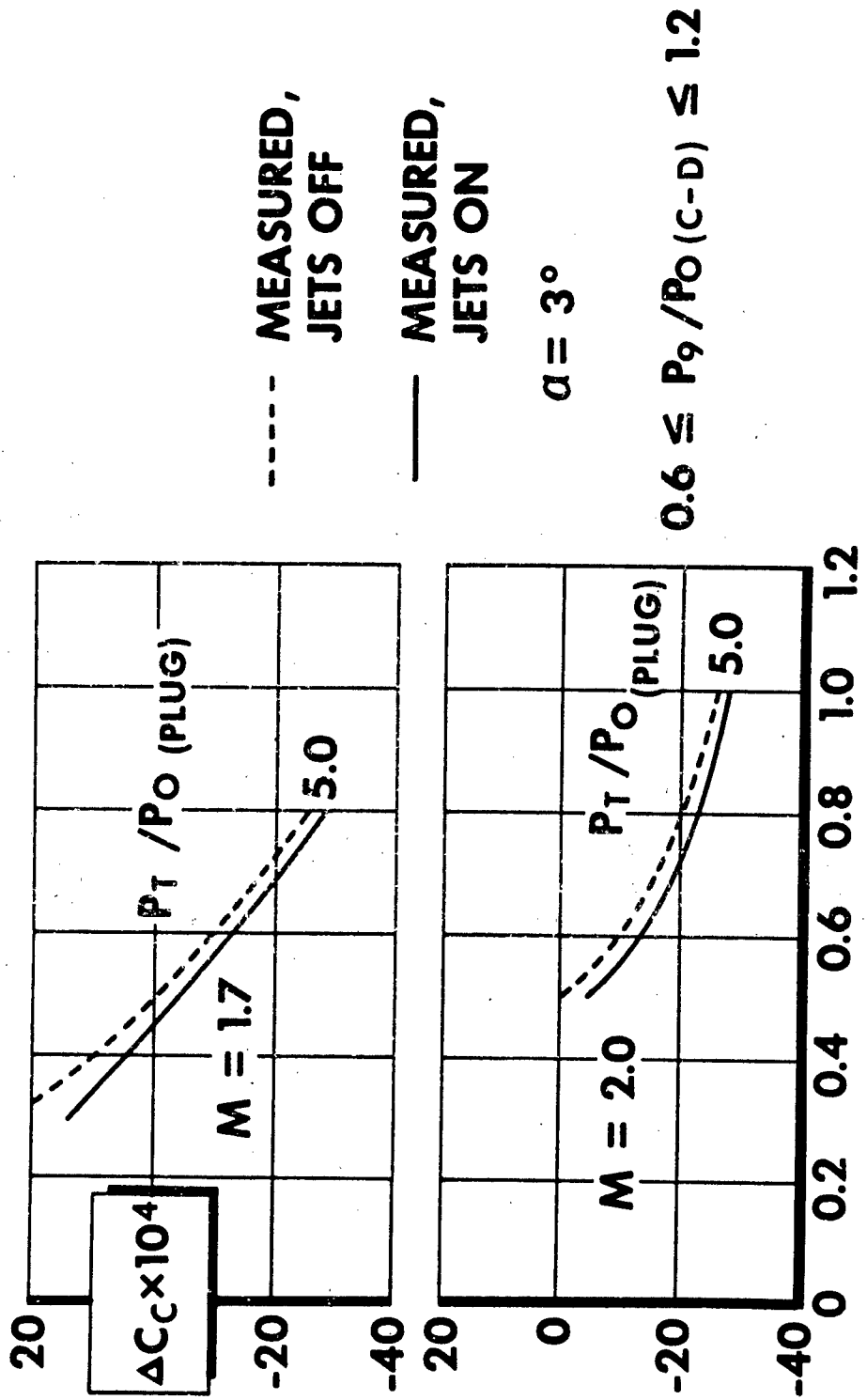
C-D NOZZLE STATIC PRESSURE RATIO EFFECT ON CHORD FORCE INCREMENT - $M = 2.0$



SUMMARY OF CONFIGURATION AND JET EFFECTS ON CHORD FORCE INCREMENT - M = 0.6, AND 1.27



SUMMARY OF CONFIGURATION AND JET EFFECTS ON CHORD FORCE INCREMENT - M = 1.7 AND 2.0



A_9 / A_M

CONCLUSIONS

1. INTEGRATION TECHNIQUE IS
WORKABLE AND FLEXIBLE
2. PROCEED THROUGH ENTIRE
INTEGRATION PROCEDURE
3. USE REFERENCE MODELS
4. SATISFACTORY TESTING TECHNIQUES
WERE DEMONSTRATED

EXPERIMENTAL INVESTIGATION OF TRANSONIC INLET DRAG

F. D. McVey, E. J. Phillips, and J. V. Rejeske

McDonnell Aircraft Company

ABSTRACT

The off-design inlet drag of supersonic fighter aircraft contributes a significant portion of the total drag of the aircraft making it necessary that thorough experimental and analytical studies are performed to establish techniques for assessing the drag of the inlet. Past experimental programs produced only a limited amount of inlet drag data in the transonic regime because most drag measurements were made with models which integrate the inlet with the full airframe. The most useful experimental programs prior to this effort dealt only with the measurement of additive drag or the variations in drag with mass flow using an isolated inlet model. This paper deals with an experimental program to accomplish the following objectives:

- (a) Provide measurement of absolute inlet drag.
- (b) Assemble parametric data defining the drag as a function of flight speed, mass flow ratio, and geometric parameters of inlets.
- (c) Establish criteria for the design of supersonic inlets to operate with low drag in the transonic regime.
- (d) Develop techniques to predict the transonic drag of inlets.
- (e) Demonstrate forebody effects on inlet drag.

It includes measurement of isolated inlet drag on a family of axisymmetric configurations, on a variable geometry opposed ramp two-dimensional inlet, and on an F-4 inlet. The paper presents a thorough discussion of the testing technique, the choice of instrumentation, design of models and the application of an inlet drag balance. Significant conclusions drawn from the experimental program are discussed in the paper.

SYMBOLS AND NOMENCLATURE

| | |
|-------------------|--|
| A_B | Axisymmetric inlet body area. |
| A_c | Inlet capture area (projected area of cowl normal to C). |
| A_e | Exit area of model (internal duct area of balance). |
| A_{LIP} | Flow area at the inlet lip station. |
| A_o | Captured freestream tube area. |
| A_{THROAT} | The minimum flow area of the internally contracted inlets. |
| A_c/A_B | Ratio of inlet capture area to model body area. |
| A_{LIP}/A_c | Inlet lip to inlet capture area ratio. |
| A_o/A_c | Mass flow ratio (capture area ratio). |
| $(A_o/A_c)_{max}$ | Maximum theoretical inlet mass flow ratio (capture area ratio). |
| A_o/A_{THROAT} | Mass flow area ratio based on A_{THROAT} (internally contracted inlets). |
| A_{THROAT}/A_c | Inlet throat to inlet capture area ratio. |
| C_{ADD} | Additive drag coefficient based on inlet capture area - $F_{ADD}/q_o A_c$. |
| C_c | Cowl drag coefficient based on inlet capture area - $F_c/q_o A_c$. |
| C_I | Inlet drag coefficient ($C_{ADD} + C_c$) based on inlet capture area - $F_I/q_o A_c$. |
| C_I' | Inlet drag coefficient based on minimum inlet flow area - either A_{LIP} or A_{THROAT} . |
| F_A | Adapter force on the F-4 or Opposed Ramp model. |
| F_{AC} | Axisymmetric aft cowl force. |
| F_{ADD} | Inlet additive drag force. |
| F_b | Balance base force. |
| F_{BAL} | The measured balance force. |
| F_c | Cowl drag force. |

| | |
|----------------|--|
| F_{Df} | Skin friction drag force. |
| F_e | Model exit stream thrust (at rake). |
| F_I | Inlet drag force [$F_{ADD} + F_c$]. |
| F_{IB} | Innerbody or ramp drag force. |
| F_{LIP} | Stream thrust at the inlet lip station. |
| F_o | Stream thrust of the captured streamtube. |
| F_p | Balance plenum force. |
| F_s | Aft seal force on the F-4 or Opposed Ramp model. |
| M_D | Inlet design Mach number. |
| M_e | Model exit Mach number (at rake). |
| M_{LIP} | Mach number at the inlet lip station. |
| M_o | Freestream Mach number. |
| P | Model or balance static pressure. |
| P_o | Freestream static pressure. |
| P_{T_o} | Freestream total pressure. |
| q_c | Freestream dynamic pressure $\frac{P_o \gamma M_o^2}{2}$ |
| R_{LIP} | Axisymmetric cowl lip leading edge radius. |
| α | Angle of attack. |
| γ | Ratio of specific heats. |
| δ_1 | F-4 fixed leading ramp angle. |
| δ_2 | F-4 variable second ramp angle. |
| θ_c | Axisymmetric cowl angle. |
| θ_{IB} | Axisymmetric innerbody half-angle. |
| θ_{IR} | Opposed Ramp inner ramp angle |
| θ_{LIP} | Flow angle at the inlet lip station. |
| θ_{OR} | Opposed Ramp outer ramp angle. |

INTRODUCTION

The design and integration of the propulsion system for high performance fighter aircraft requires evaluation of the performance of the inlet from several aspects - pressure recovery, distortion, and drag. The drag of the inlet, and its effect on the selection of the optimum configuration, has not been adequately investigated in previous programs due to the difficulty of its measurement. In most of the programs to date, the inlet drag was measured with models of the full vehicle. The effects of detailed variations in design such as changes in lip geometry, design Mach number or compression contours could not be isolated from the measurements of the total aircraft drag. As a result, estimates of inlet drag have been made by analytical procedures and by empiricisms from the available literature including small quantities of data.

This program was conducted to produce accurate experimental data defining the drag of inlets in the transonic Mach number regime. A family of axisymmetric inlets was designed for this test program to produce data useful in assessing the drag of any single cone supersonic inlet. Each parameter of the inlet design, cone angle, design Mach number, lip angle, etc., was varied systematically. These data were also intended for the verification of analytical methods which were being developed to predict inlet drag. As a reference configuration and a geometry typical of two-dimensional inlets, the F-4 inlet was tested in an isolated mode and with the F-4 forebody. Variations in ramp geometry were evaluated at both subsonic and supersonic test conditions.

A third configuration was included in the test program to investigate more complex two-dimensional configurations with variable geometry designed to reduce the drag at subsonic speeds. The three inlet configurations tested in this program are illustrated in Figure 1.

The importance of the proper evaluation of inlet drag is clear for the case where cruise range is involved. The fraction of the total aircraft drag which is generated by the inlet is significant at the reduced airflow conditions corresponding to cruise. Figure 2 illustrates estimates of the level of inlet drag relative to the vehicle drag for the F-4 and F-101 aircraft.

This program is different from previous studies in that the measured inlet drag is the total drag contributed by the pressure on the captured streamtube and on the inlet cowl, as illustrated in Figure 3. In previous programs the experiments have determined the variations in inlet drag with mass flow, or only the additive drag component (References 1 and 2). This measurement of total drag is important if the inlet designed is to be optimum. For example, shaping of the cowl can reduce the drag at subsonic speeds and at supersonic Mach numbers the same geometry may increase drag. Variations in the cowl drag have not been measured independently in transonic tests prior to this program.

The data presented in this paper is assembled in a complete form in Reference 3. That report is an interim report on a test program sponsored by the Aero Propulsion Laboratory, Wright-Patterson Air Force Base. The models used were supplied by McDonnell Aircraft Company. The testing and reporting was sponsored by the Air Force and supported by the Airbreathing Propulsion Branch, NASA-Ames. Special recognition is due to Mr. Harlan Gratz, Air Force Project Officer, and Messrs. Warren Anderson and Edward Perkins of NASA-Ames for their support, recommendations and review.

INLET MODELS AND DRAG BALANCE

Axisymmetric Inlet Models

All models were designed to adapt to an existing inlet drag balance. The axisymmetric configurations consisted of a set of normal shock inlets and a series of conical inlets applicable to supersonic flight. These conical configurations were designed to investigate the effects of modifications of five primary geometric parameters:

Ratio of capture area to body area, A_c/A_b : .53, .62, .71
Cowl angle, θ_c : 15°, 20°, 25°
Cowl lip radius, R_{LIP} : .008", .016", .024"
Innerbody half-angle, θ_{IB} : 20°, 25°, 30°
Inlet design Mach number, M_D : 2.3, 2.7, 3.1.

The design Mach number is defined here to be the Mach number at which the conical shock wave intercepts the cowl lip. The variables of the design are defined in Figure 4. For each design parameter three models were constructed in which a single parameter was modified. Eleven models are represented.

Only two parameters are necessary to define the normal shock configurations. Three values of each parameter were again incorporated in the family of normal shock inlets resulting in a total of five models:

Cowl angle, θ_c : 15°, 20°, 25°
Cowl lip radius, R_{LIP} : .008", .016", .024"

In addition, a variation in cowl configuration potentially offering a reduced subsonic drag was incorporated in the study. The cowl shape differed from that shown in Figure 4 in cross section. For this configuration the leading edge was formed by an ellipse with a section essentially that of an NACA 10-10 two-percent thick airfoil shape. The major to minor axes of the ellipse were in the ratio of 10:1. This airfoil contour is a low drag shape with acceptable characteristics in the transonic Mach number range (Reference 4). This cowl shape was incorporated on one normal shock and one single cone configuration. The ellipse was faired on the cowl contours of configurations A5 and A9 to replace the conical leading edge shown in Figure 4.

Table I defines the geometry of eighteen axisymmetric inlet configurations in terms of the parameters discussed above. The nomenclature is that shown in Figure 4. The majority of the configurations were

instrumented with static pressures on the centerbody and cowls. Two of the configurations included inlet lip rakes used to assess the drag from pressure integrations as well as force measurements.

TABLE I
AXISYMMETRIC INLET GEOMETRY

| Conf. | Type | Cowl | Inner- body | A_c/A_B | θ_c ($^\circ$) | RLIP (in.) | θ_{IB} ($^\circ$) | M_D | ALIP/ A_c |
|-------|--------|------|----------------|-----------|----------------------------|---------------|-------------------------------|-------|-------------|
| A1 | Normal | C3 | - | .40 | 20 | .024 | - | - | 1.0 |
| A2 | Shock | C4 | - | .40 | 25 | .024 | - | - | |
| A3 | | C5 | - | .40 | 15 | .024 | - | - | |
| A4 | | C6 | - | .40 | 15 | .016 | - | - | |
| A5 | | C7 | - | .40 | 15 | .008 | - | - | |
| A6 | | C7A | - | .40 | NACA | .008 | - | - | |
| A7 | Single | C8 | IBL | .62 | 15 | .024 | 2C | 2.7 | .619 |
| A8 | Cone | C9 | IB1 | .62 | 15 | .016 | 20 | 2.7 | .619 |
| A9 | | C10 | IB1 | .62 | 15 | .008 | 20 | 2.7 | .619 |
| A10 | | C11 | IB2 | .62 | 20 | .008 | 20 | 2.7 | .619 |
| A11 | | C12 | IB3 | .62 | 25 | .008 | 20 | 2.7 | .619 |
| A12 | | C11 | IB4 | .62 | 20 | .008 | 20 | 2.3 | .697 |
| A13 | | C11 | IB5 | .62 | 20 | .008 | 20 | 3.1 | .551 |
| A14 | | C13 | IB6 | .62 | 20 | .008 | 25 | 2.7 | .557 |
| A15 | | C13 | IB7 | .62 | 20 | .008 | 30 | 2.7 | .519 |
| A16 | | C14 | IB8 | .53 | 25 | .008 | 20 | 2.7 | .619 |
| A17 | | C15 | IB9 | .71 | 25 | .008 | 20 | 2.7 | .619 |
| A18 | | C7B | IB10 | .62 | NACA | .008 | 20 | 2.7 | .619 |

F-4 Inlet Models

The F-4 inlet was tested in this program to produce drag data representative of present day fighter configurations. The model was designed to adapt to the balance by incorporating a windshield and a large splitter plate. Figure 5 illustrates the assembly of the model on the balance extension. The splitter plate and windshield were connected to the non-metric element of the balance. The cylindrical section which supports the transition between the inlet and the duct exit connects directly to the metric element of the balance. The boundary layer diverter was rigidly installed on the splitter plate and formed the fairing shown in the phantom view of Figure 5. The cowl and ramps are the elements on which the drag forces were measured. The inlet cowl and the first ramp were fixed. The second ramp could be modified by replacing the ramp portion of the model. Three configurations representing alternate second ramp angles were tested in the program. These geometries represent the variable features of the F-4 inlet applicable to the range of test Mach numbers. The parameters of the model are illustrated in Table II. The nomenclature defining the F-4 inlet is presented in Figure 6.

The splitter plate of Figure 5 could be removed and replaced by the forebody so that the proper flow field representing the effect of

the forebody could be duplicated. This alternate configuration was tested in the program to illustrate the effect of integration of the inlet and forebody and proves the applicability of isolated inlet drag data to integrated configurations. This test model is illustrated in Figure 7.

TABLE II

F-4 INLET MODEL GEOMETRY

| Configuration | Leading Ramp Angle (δ_1) | Second Ramp Angle (δ_2) | $\frac{A_{LIP}}{A_c}$ | $\frac{A_{THROAT}}{A_c}$ |
|---------------|--------------------------------------|-------------------------------------|-----------------------|--------------------------|
| F1 | 10° | 0° | .649 | .609 |
| F3 | 10° | 8° | .541 | .487 |
| F4 | 10° | 12° | .486 | .428 |

The cowl and ramp surfaces on the F-4 model were instrumented with static pressures. A set of throat boundary layer rakes were installed on the model during the pressure tests. The model was designed to remove pressure instrumentation during runs in which the drag force was measured.

Opposed Ramp Inlet Models

Since the drag of a fixed capture area inlet like the F-4 is representative of designs developed during the past decade, an alternate configuration was included in the program to investigate the prospect of drag reduction through the use of variable geometry on the outer cowl. The model schematically shown in Figure 6 is defined as an Opposed Ramp inlet. It is designed to produce the supersonic compression through a system of shock waves generated on the ramp and the inboard surface of the cowl. This configuration had been previously tested showing high pressure recovery at moderate supersonic speeds. The variable cowl is included to allow reduction of the drag at the cruise Mach number by adjusting the cowl position, affecting a reduced drag through a decrease in pressure on all external surfaces of the cowl. The model incorporated alternate elements of the opposed ramps. Tests were conducted with various combinations of ramp angles to produce data defining the appropriate ramp configurations for reduced drag at transonic and supersonic flight conditions. A sideplate was employed with one configuration to demonstrate its effect on drag. The ramp geometries for this model are given in Table III.

The elements of these models were also instrumented with pressures to identify the contributions of additive and cowl drag to the total inlet drag.

TABLE III

OPPOSED RAMP INLET MODEL GEOMETRY

| Configuration | Ramp Angle (θ_{IR}) | Ramp Angle (θ_{OR}) | $\frac{A_{LIP}}{A_c}$ | $\frac{A_{THROAT}}{A_c}$ |
|---------------|------------------------------|------------------------------|-----------------------|--------------------------|
| | | | | |
| B1 | 4.75° | -4.75° | .701 | .701 |
| B2 | 4.75° | -3.25° | .709 | .701 |
| B3 | 4.75° | +0.50° | .749 | .701 |
| B4 | 4.75° | +2.00° | .796 | .701 |
| B5 | 9.10° | -4.75° | .557 | .557 |
| B6 | 9.10° | +2.00° | .650 | .557 |
| B7(Sideplate) | 4.75° | -4.75° | .701 | .701 |

Inlet Drag Balance

The inlet model support and drag balance includes provisions to (a) measure diffuser pressure recovery, (b) determine steady state velocity distribution (distortion) at the model exit, (c) measure mass flow through the inlet model, (d) vary inlet mass flow ratio, (e) measure the axial force (drag) applied to the inlet model, and (f) support the entire test assembly. This apparatus has been used extensively to measure the drag of axisymmetric inlets at supersonic speeds. This "flow-through" balance was designed to measure the axial force on an inlet suspended with a strain gage system. Measurement of the difference in the stream thrust between the freestream and the instrumentation station in the duct along with base pressure measurements form an accurate means of deducing inlet drag.

The support consists of three concentric shells, illustrated in Figures 8 and 9. The inner shell is non-metric and is an extension of the duct contour and supports the model exit rake. The middle shell is metric and is attached to the diffuser duct section of the inlet model to be tested and acts on instrumented cantilever beams when an axial force is applied. The outer shell provides support for the internal mechanism and also acts as a windshield. The inner and outer shells are rigidly fastened together. The middle shell is supported between the inner and outer shells by means of eight support bearings which allow it to move fore and aft as axial loads are applied. Strain gages are mounted on two cantilever beams which restrain the motion of the middle shell. The strain gages on the two beams are connected electrically in parallel and temperature compensated at the test operating conditions. A throttle located behind the rake is moved axially to vary the exit area and pressure and thereby the mass flow through the balance. The balance incorporates a windshield which forms a smooth external contour downstream of the metric element of the inlet model. For the F-4 and Opposed Ramp models the windshield was extended to insure a smooth external contour at the end of the metric element of the inlet, as shown in Figures 3, 5, and 7. For all models a technique of sealing the gap between the metric and non-metric elements, at the inlet-windshield interface, was developed. A dental dam seal was installed to prevent flow circulation associated with non-uniform cross

sections of the F-4 and Opposed Ramp models. The windshield cavities were vented to the tunnel static pressure to guarantee the uniformity of the pressure level on the nonsymmetric adapter, and also to guarantee that the force applied to the external contours of the adapter at all test conditions would remain constant with respect to the tunnel conditions.

INSTRUMENTATION AND TEST TECHNIQUES

Determination of Inlet Drag

Figure 10 illustrates the forces which are applied to the inlet model and balance assembly, and provides an indication of the calculations required to determine the inlet drag from the measured data. The terms of Equations (1) and (2) of Figure 10 involve the measurement of: (a) pressures within the cavities of the balance, (b) pressures on the forward facing surface of the model adapter (two-dimensional models), (c) static and total pressures in the rake located in the duct at the break between the metric and non-metric elements, (d) the force indicated by the strain gage element, and (e) the throttle position.

The mass flow control is accomplished on the balance with a remotely operated throttle which has been carefully calibrated using measurements of the rake total pressure, plug position, and exit static pressures. The use of a well calibrated mass flow measuring system is imperative if the inlet drag is to be measured accurately.

The balance strain gage force measurement included the external skin friction drag. This force is not included in the total inlet drag and is removed from the gage measurement by calculations assuming a turbulent boundary layer over the complete cowl surface (Reference 5).

To separate the additive drag and cowl drag, separate pressure tests were accomplished where pressure distributions on the compression surfaces and the external surfaces of the cowls were measured. These tests duplicated the force tests. The additive drag was calculated using the innerbody or ramp pressure data and assuming a uniform velocity profile and total pressure recovery at the lip plane of the inlet. The cowl drag was calculated by integration of the external pressures over the cowl area. The additive drag calculation procedure is illustrated in Figure 11.

The elements of inlet drag (additive and cowl) were deduced from both pressure tests and force tests. For the axisymmetric configurations the additive drag was deduced by subtracting the cowl drag measured from the pressure tests. For the two-dimensional configurations the cowl drag was deduced by subtracting the additive drag measured during pressure tests. It was thought that the pressure integrated additive drag was more accurate than pressure integrated cowl drags because of the complicated geometry of the two-dimensional inlet cowls.

Requirements on Instrumentation

A systematic examination of the data reduction represented by the force components in Equations (1) and (2) was performed to specify

the instrumentation. Sensitivity calculations were made which indicated the required accuracy of the drag balance and adapter cavity pressures. From this study it was apparent that accurate instrumentation was required for the measurements of base, adapter, plenum and rake static pressures. Slack diaphragm gages were used to insure an accuracy of ± 0.10 pound in any measured force component. Accurate measurement of the rake total pressures at the model exit was accomplished by employing a scanivalve system using a low range differential pressure transducer and a wind tunnel reference pressure.

TEST PROGRAM

The program was accomplished in two phases. The first consisted of isolated inlet tests of the Axisymmetric, F-4, and Opposed Ramp models. In the second phase the effects of the forebody on the F-4 inlet were measured. The F-4 and Opposed Ramp configurations were run at several angles of attack. The Axisymmetric inlets were all tested at zero angle of attack only. The test Mach numbers were between 0.6 and 1.05 for the majority of the runs, however, several tests were conducted at supersonic conditions.

RESULTS

Axisymmetric Inlet Drag Data

The drag coefficients presented in this section are defined in terms of two reference areas. The coefficient C_D is referenced to the projected frontal area of the inlet at the lip. The second coefficient, C_D' , is formed by referencing the drag to the throat area of the inlet. This technique allows a drag comparison of inlets with differing throat area. Since the model configurations could not be made to pass the same flow rate at each test Mach number, comparisons based on the throat area coefficient C_D' show the drag of configurations with equal flow capacity. The results of the tests at Mach 0.9 on the family of axisymmetric inlets are summarized in Figures 12 through 16. These curves illustrate the drag of configurations with various cowl angles, cone angles, lip radii, design Mach numbers and the ratio of capture to body areas. The results show a surprising insensitivity of the drag to variations in the design parameters of the inlets. The data is parametric with respect to the mass flow ratio which again shows a small variation in drag with spill. Figures 17 and 18 compare the total inlet drag and additive drag, respectively, measured for configuration A10. Data for Mach numbers from 0.7 to 1.05 are presented. These results show that the cowl forces are in the thrust direction and that this force essentially cancels the additive drag. The drag reduction due to the cowl pressures rapidly disappears for test Mach numbers above 1.0. Comparison of the additive drag curves for Mach number 1.05 and 0.9 of Figure 18 illustrate this point. This behavior is expected, since the cowl pressures will ultimately be well above freestream static as the flight Mach number increases.

The most significant parameter affecting the drag of axisymmetric configurations was the contour of the cowl leading edge. The effects of lip radius are eliminated from the comparison by the technique used to incorporate the elliptical cowl leading edge. Figure 19 shows a

comparison of the inlet drag coefficient determined on two configurations differing only in cowl shape. The effect of mass flow ratio and Mach number are illustrated. For the high mass flow ratios where the streamline is inclined slightly with respect to the body axis, both configurations exhibit equivalent drag. As the mass flow ratio is decreased, the local flow angle approaching the cowl leading edges increases and the superior characteristics of the elliptical cowl shape are evident. The elliptical leading edge contour is thought to maintain an attached flow while the blunted conical leading edge is thought to experience separation. The data of Reference 4 suggests this advantage. Further tests of alternate cowl configurations appear to be a fruitful area for research.

Comparisons of Force and Pressure Determinations of Inlet Drag

The axisymmetric data allows the most direct comparisons to be made between the inlet drag deduced from pressure distributions and that obtained from force measurements. The pressure distributions were integrated to predict the cowl drag and the drag on the innerbody. To determine the total inlet drag the stream thrust at the lip and in the captured streamtube were calculated assuming one-dimensional flow. The total pressure loss between the inlet lip and freestream was assumed to be negligible at transonic conditions. Figure 20 compares the drag measured with the force balance with that determined as described above for two test Mach numbers. These data agree well at high mass flow ratios where the pressure distribution on the lip may be integrated with good accuracy.

The cowl pressure distribution is extremely steep near the lip. All cowl pressure data indicates the existence of a slight rise in pressure forward of the first tap at high mass flow ratios, but extremely low pressure levels in this region at low mass flow ratios. These trends were indicated in the Schlieren photographs of Reference 3, which show the existence of a low pressure or separated region on the cowl lip at reduced mass flow conditions.

Comparison of Predicted and Measured Inlet Drag

An analysis of the flow field generated by axisymmetric inlets at high subsonic speeds was accomplished in a parallel study described in Reference 6. The method is a solution of the compressible flow equation using a finite difference procedure based upon the construction of a network or grid which surrounds the inlet. The boundaries of the network are formed by the inlet contour, a plane across the flow within the duct, an undisturbed streamline parallel to the axis of symmetry, and planes defining uniform flow conditions upstream and downstream of the inlet. The method produces a prediction of the inlet drag as well as a definition of local flow conditions at all points in the flow field network. This method was used to calculate the inlet drag for axisymmetric configurations as a function of mass flow ratio and Mach number. Comparison of the predictions with the data at a mass flow condition which produces a choked inlet yield a predicted drag higher than the data. Since a one-dimensional flow assumption at the choked inlet plane will produce the highest additive drag, an empirical adjustment of the theoretical model was applied at the maximum mass flow ratio.

Figure 21 shows a comparison of drag data determined by force measurements with the modified analytical method. With choked flow conditions at the inlet, the inlet stream thrust is calculated assuming a one-dimensional flow and the centerbody and cowl drags are determined from predicted pressure distributions. The variation in drag with mass flow ratio is determined directly from the analysis.

F-4 Inlet Drag Data

Selected results from the F-4 inlet drag tests are presented here to illustrate the effects of the forebody and changes in second ramp angle on the drag characteristics of the inlet. The inlet drag (C_I) is determined from the force data and the additive drag (C_{ADD}) is determined from pressure data. Figures 22 and 23 present the inlet drag (C_I) and Figures 24 and 25 present the additive drag for the $10^\circ-0^\circ$ ramp configuration operating at transonic speeds. This inlet configuration was tested with and without the splitter plate and with the F-4B aircraft forebody mounted on the non-metric element of the balance. The inlet alone tests showed the highest drag, both inlet and additive drag. With the F-4B forebody configuration installed, it exhibited the least drag.

The changes in drag which occurred with the introduction of the splitter plate and the aircraft forebody on the isolated model are expected. The splitter plate eliminates any spill across the leading edge of the first ramp insuring that all spill takes place in a region where the deflected stream can produce a reduced cowl force. With the F-4B forebody the drag reduction may be due to several effects; flow angularity at the inlet plane, the development of additive drag on the forebody, or finally by a change in local Mach number at the inlet plane.

It should be noted that only the drag levels are different between isolated and integrated configurations, and that the drag variation with mass flow is constant for all configurations.

Figure 26 presents the inlet drag data for the $10^\circ-8^\circ$ ramp configuration tested at supersonic conditions with both the splitter plate and the aircraft forebody. The results show the same characteristics as discussed above for the $10^\circ-0^\circ$ ramp configuration.

The effect of varying the second ramp angle on F-4 inlet drag is illustrated in Figure 27 at a Mach number of 0.90. At subsonic conditions, increasing the second ramp angle decreases the drag at a given capture ratio. This characteristic is important since a significant reduction in inlet drag may be realized at low mass flow ratio by changing the ramp and increasing the inlet Mach number. The effect of the ramp angle change on pressure recovery must be considered.

Opposed Ramp Inlet Drag Data

Selected results showing the drag of the Opposed Ramp configurations are presented in Figures 28 and 29. Figure 28 shows the effect of varying the outboard ramp angle at cruise conditions. The effect of two extreme positions of this second ramp is shown in the figure to identify that the low cowl angle reduces the drag significantly.

As expected, an increase in inlet drag at cruise conditions is indicated by the addition of the single sideplate. This is illustrated in Figure 29. This increase in drag can be attributed to increased streamline turning that results when all of the side spill is deflected in one direction.

Figure 30 presents a comparison of the Opposed Ramp and F-4 inlet drag at cruise conditions. The drag coefficient and mass flow ratios in this figure are referenced to the inlet throat area rather than the inlet capture area in order to compare models with equal air-flow capacity. As intended with this design, the Opposed Ramp inlet provides a drag reduction at cruise conditions.

Comparison of Drag Data for Axisymmetric and Two-Dimensional Inlets

The drag data from each of the tests was summarized to construct the boundaries of the drag data with mass flow ratio for each inlet type. The reference area for the drag coefficients of Figures 31 and 32 is the inlet throat area.

The difference in drag characteristics between axisymmetric configurations and the two-dimensional models is expected, and may be explained on the basis of the geometry of the captured streamtube. If one considers the streamtube geometry for an axisymmetric inlet compared to two-dimensional inlets at the same mass flow ratio, it is clear that the pressure on the axisymmetric streamtube is lower since the deflection is less than that of the two-dimensional configuration, therefore its drag is smaller. The drag of the two-dimensional models is dependent on the aspect ratio, since the amount of deflection of the captured streamtube and the extent of the cowl area are directly related.

It appears for this data that changes in aspect ratio and sideplate geometry for two-dimensional inlets are important variables controlling the variation in inlet drag with mass flow ratio.

Figures 31 and 32 show that the drag of two-dimensional configurations may be controlled by the use of variable geometry features when the inlet operates at a high mass flow ratio.

CONCLUSIONS

The program has provided a compilation of data on the drag of different inlet types - a fraction of which are presented in this paper. However, the important results of the program are:

1. Accurate measurements of the isolated and integrated inlet drag may be made on both axisymmetric and two-dimensional inlets using a properly designed drag balance.
2. The presence of an aircraft forebody does not alter the slope of the inlet drag variation with mass flow ratio.
3. The determination of total inlet drag from integrated pressure data is unreliable due to uncertainties in flow conditions at the inlet

lip plane and pressure variations near the lip of the cowl.

4. As a result of the symmetry of the flow field and the large cowl area, variations in the design variables and mass flow ratios produce relatively small changes in inlet drag on the axisymmetric inlets at subsonic speeds.
5. The data illustrates that low drag characteristics may be maintained for two-dimensional inlets by appropriate control of the inlet geometry.
6. The additive and cowl drag predicted by analytical methods agrees well with experimental data.

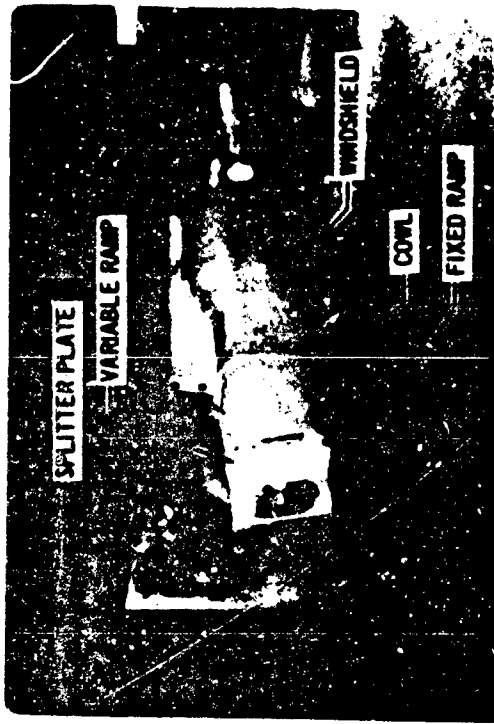
REFERENCES

1. Muller, George L. and Gasko, William F., "Subsonic-Transonic Drag of Supersonic Inlets," Report TDM-1973, Pratt & Whitney Aircraft, May 1966.
2. Petersen, Martine W. and Tamplin, Gordon C., "Experimental Review of Transonic Spillage Drag of Rectangular Inlets," Report AFAPL-TR-66-30, May 1966.
3. McVey, Francis D., Rejeske, John V., Phillips, Edward J., "Experimental Evaluation of Inlet Drag Characteristics in the Transonic Mach Number Regime," Report AFAPL-TR-68-119, November 1968.
4. Lindsey, Walter F. and Landrum, Emma J., "Flow and Force Characteristics of 2-Percent-Thick Airfoils at Transonic Speeds," Report RM L54I30, NACA, January 1955.
5. Schlichting, Hermann, "Boundary Layer Theory," McGraw-Hill Book Company, Inc., New York, 1968.
6. Sharp, Brooks M. and Rochow, Thomas C., "Compressible Subsonic Flow Analysis of Axisymmetric Inlets," Report EN 685, McDonnell Douglas Corporation, March 1969.

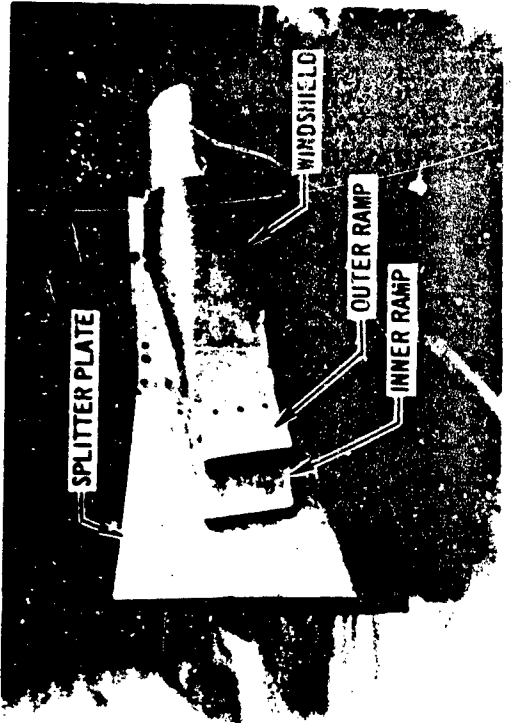
FIGURE 1
INLET DRAG TEST MODELS



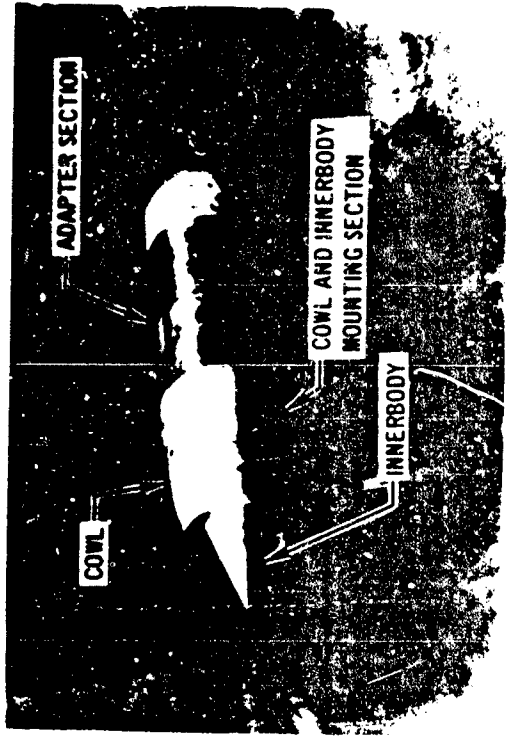
F-4 AIRCRAFT



F-4 INLET MODEL



ADAPTER SECTION



COWL AND INNERBODY MOUNTING SECTION

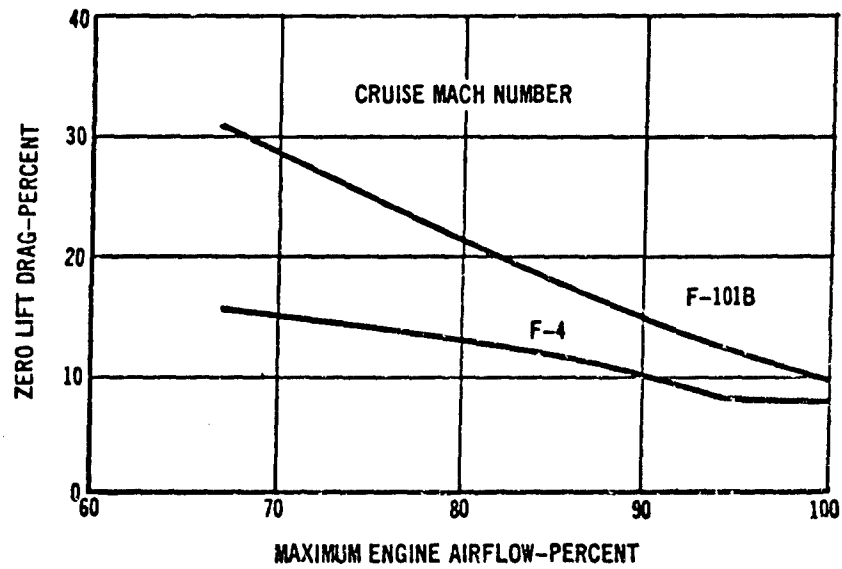


FIGURE 2
INLET DRAG CONTRIBUTION TO AIRPLANE ZERO LIFT DRAG

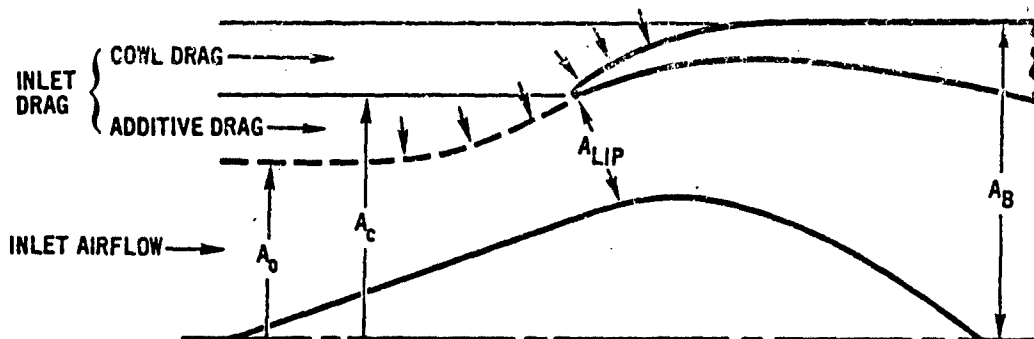


FIGURE 3
INLET DRAG COMPONENTS

FIGURE 4
AXISYMMETRIC INLET DESIGN PARAMETERS

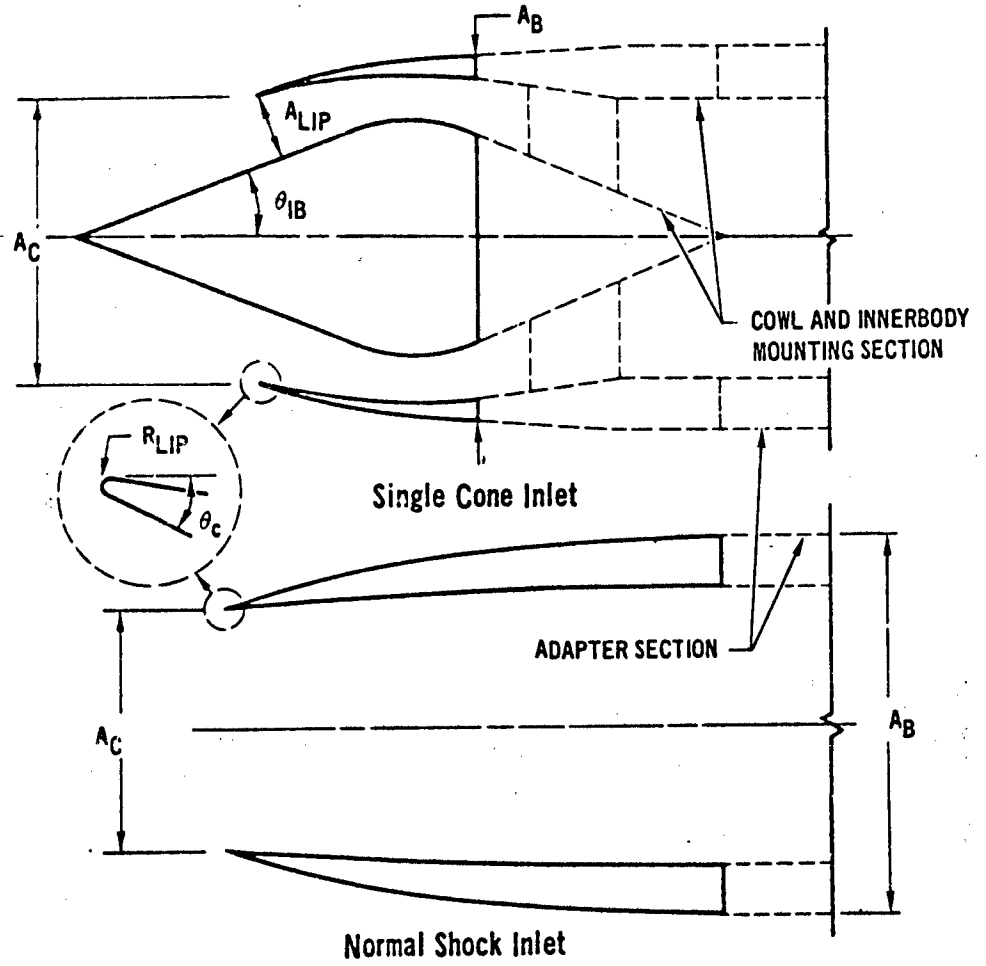


FIGURE 5

F-4 INLET MODEL AND SPLITTER PLATE TEST ASSEMBLY

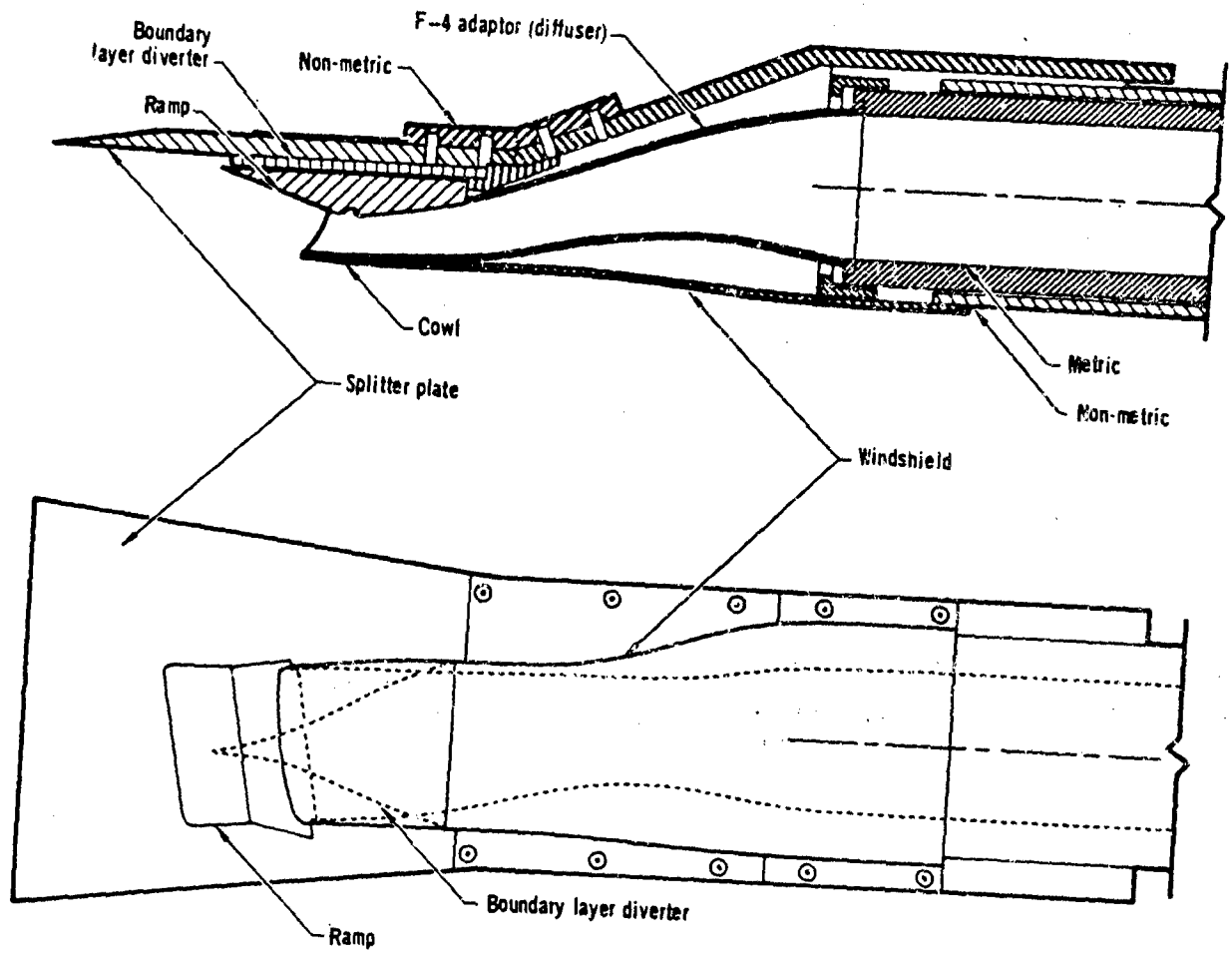


FIGURE 6
F-4 AND OPPOSED RAMP INLET GEOMETRY

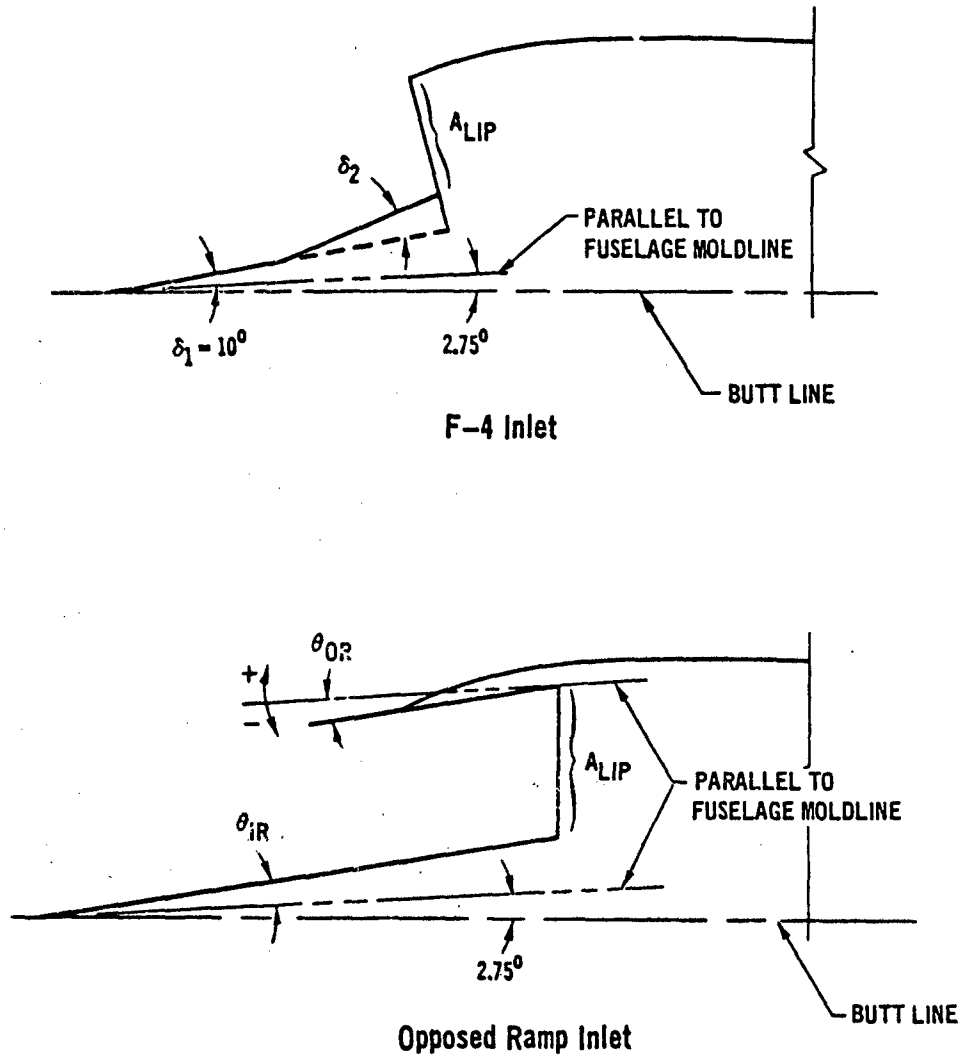


FIGURE 7
F-4 INLET MODEL AND FOREBODY TEST ASSEMBLY

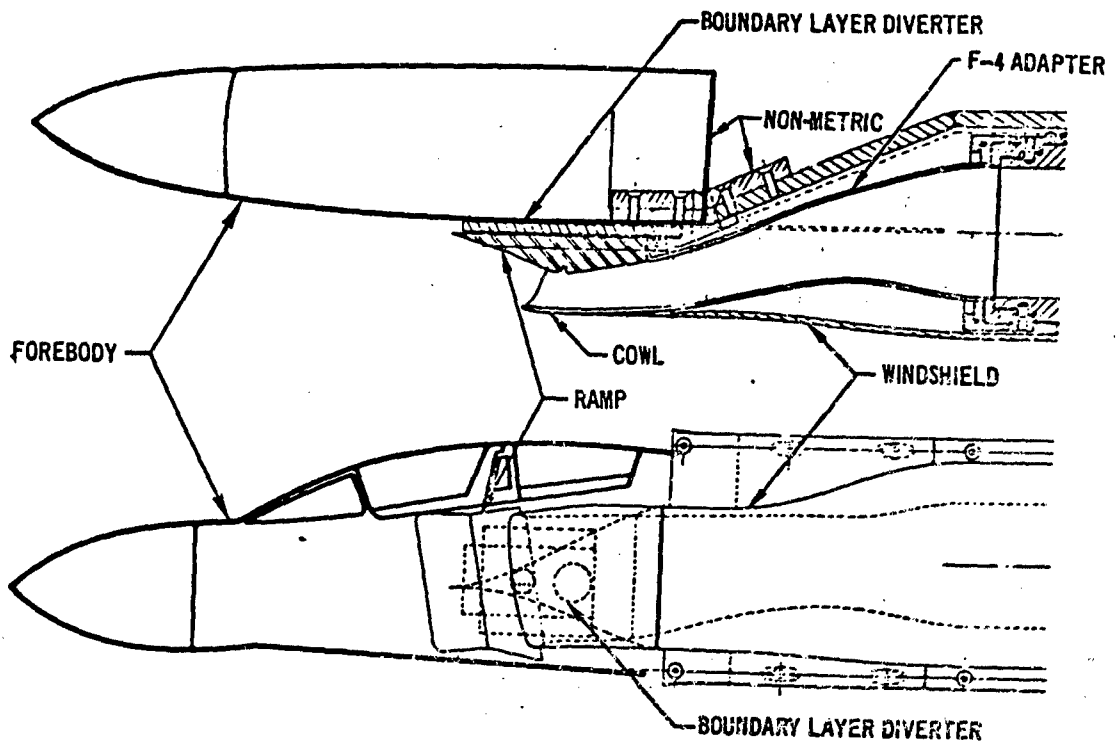


FIGURE 8
MODEL SUPPORT AND DRAG BALANCE SCHEMATIC

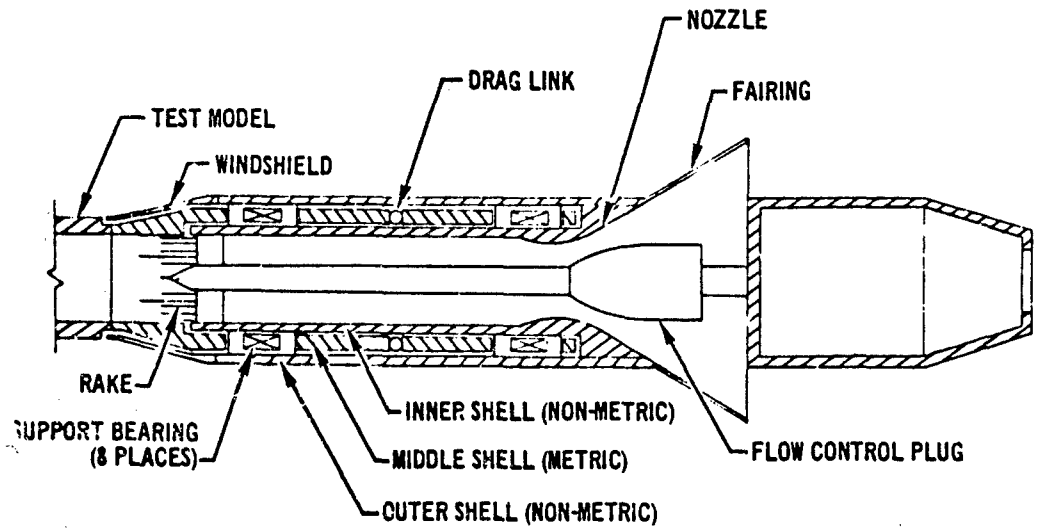


FIGURE 9
DRAG BALANCE COMPONENTS

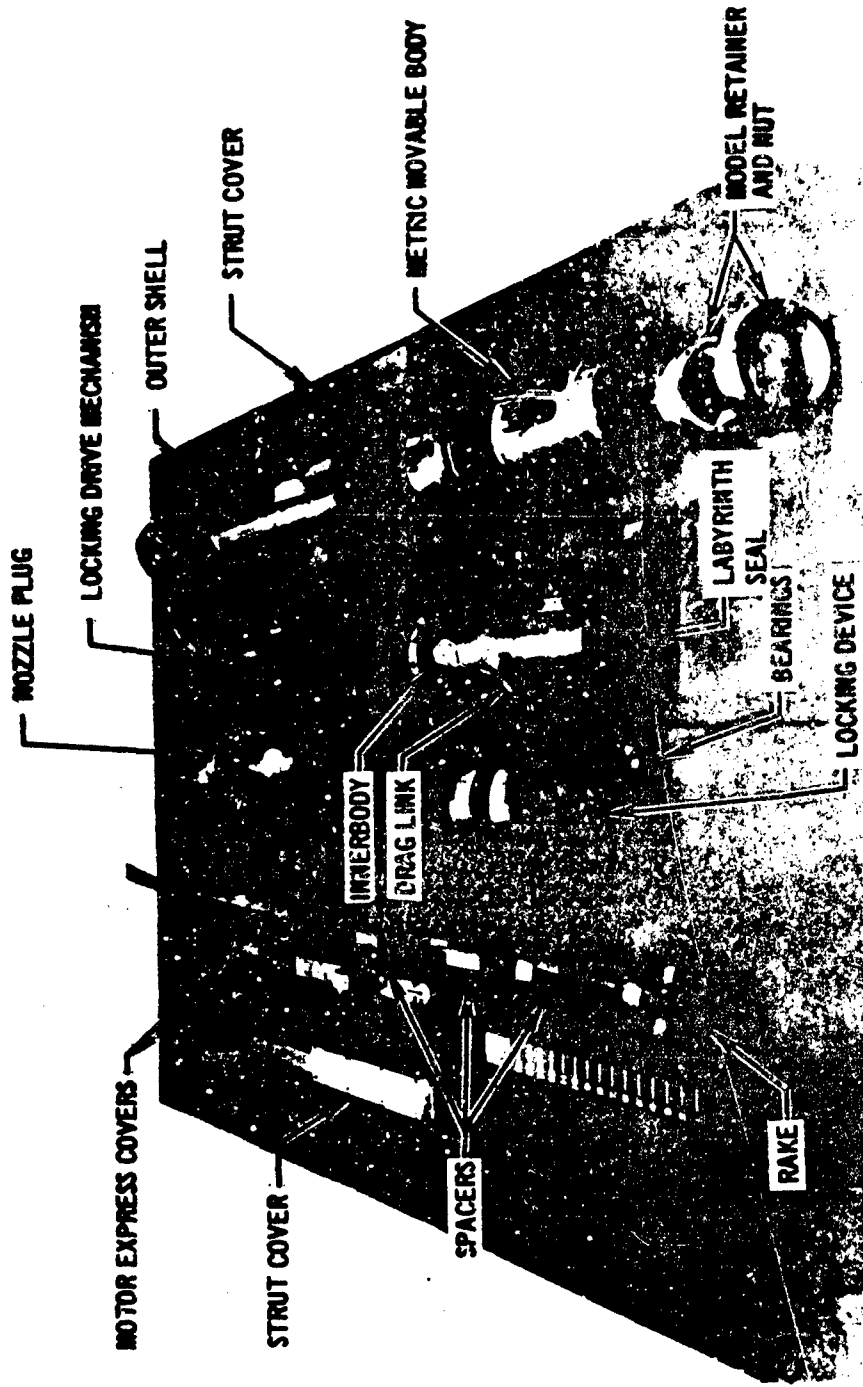
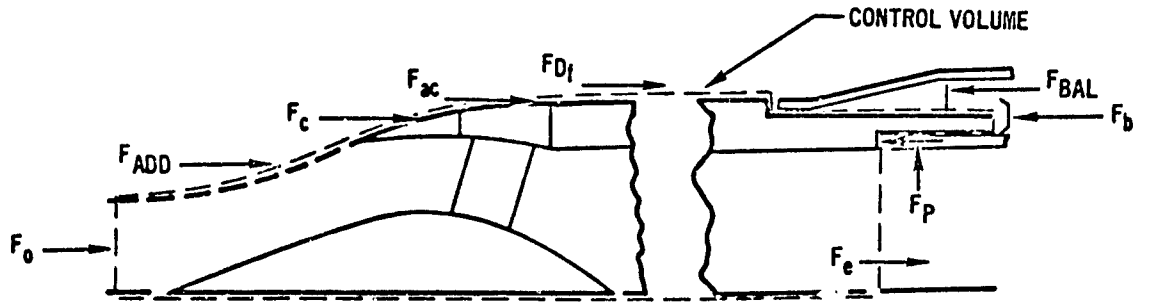
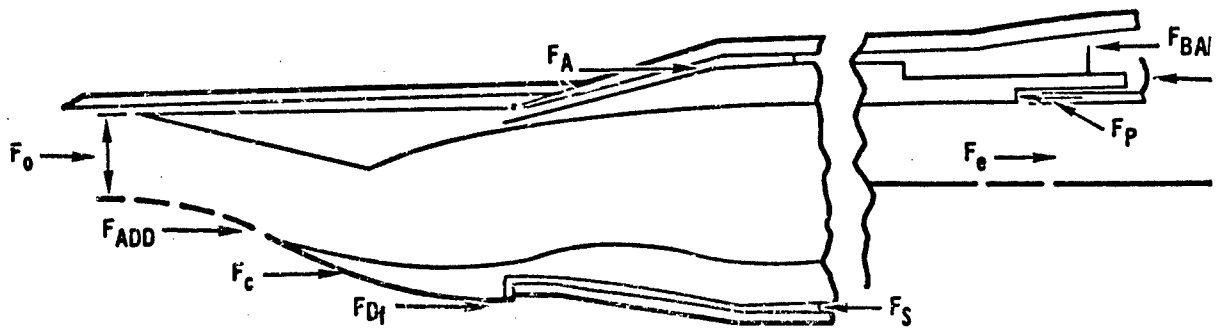


FIGURE 10
BALANCE LOAD DIAGRAMS



$$F_l + F_c + F_{ADD} = F_{BAL} + F_e + F_b + F_p - (F_0 + F_{Df} + F_{AC}) \quad (1)$$

Axisymmetric Inlet



$$F_l = F_c + F_{ADD} = F_{BAL} + F_e + F_b + F_p - (F_0 + F_A + F_s + F_{Df}) \quad (2)$$

F-4 Inlet and Opposed Ramp Inlet

FIGURE 11
CONTROL VOLUME APPLICABLE TO THE DATA REDUCTION AND THE
COMPRESSIBLE FLOW THEORY

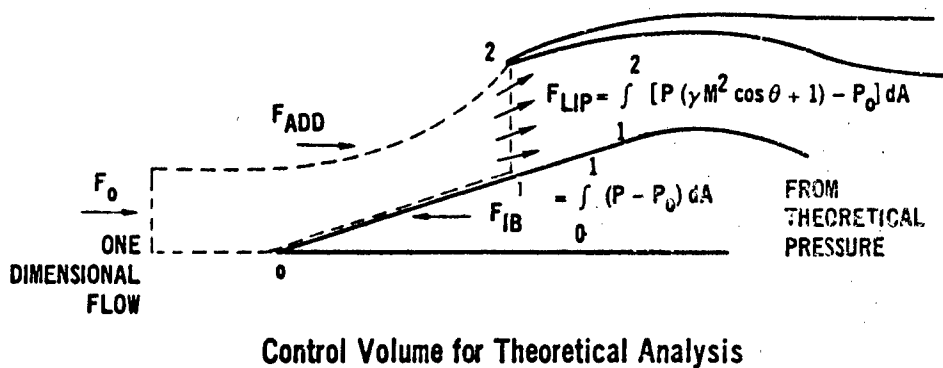
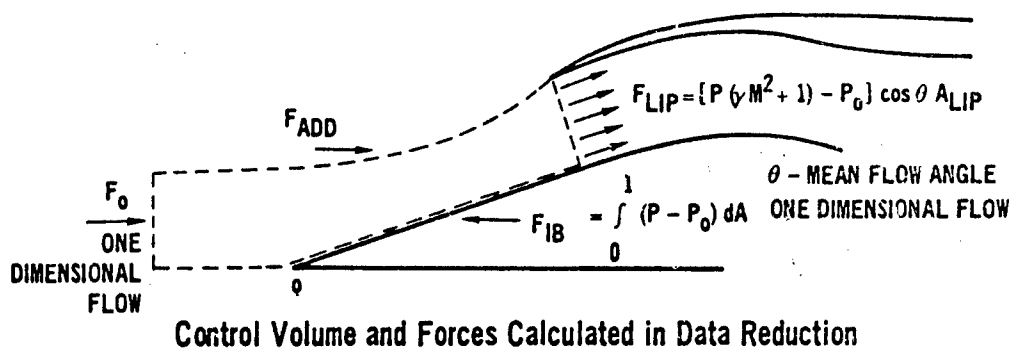


FIGURE 12
EFFECT OF COWL ANGLE ON INLET DRAG

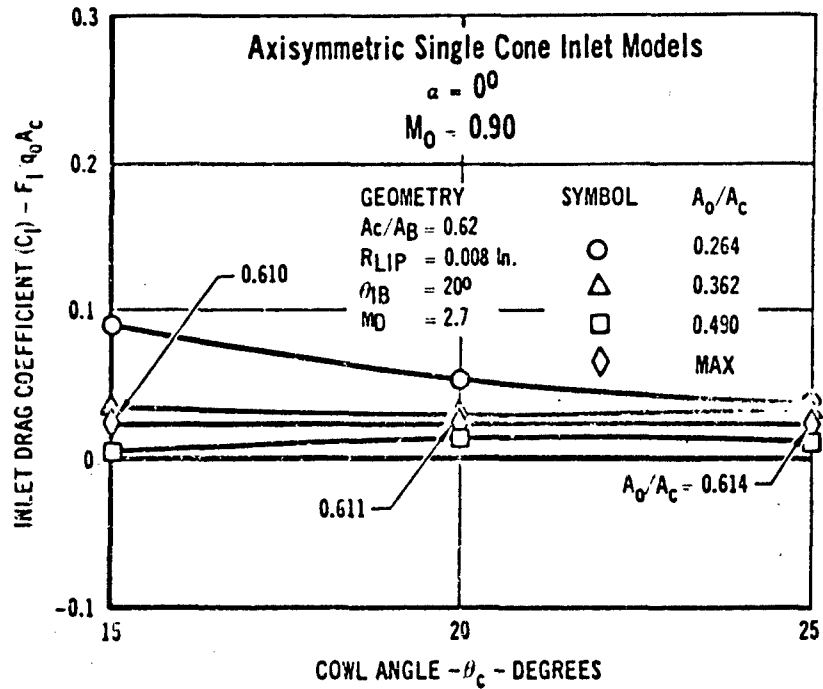
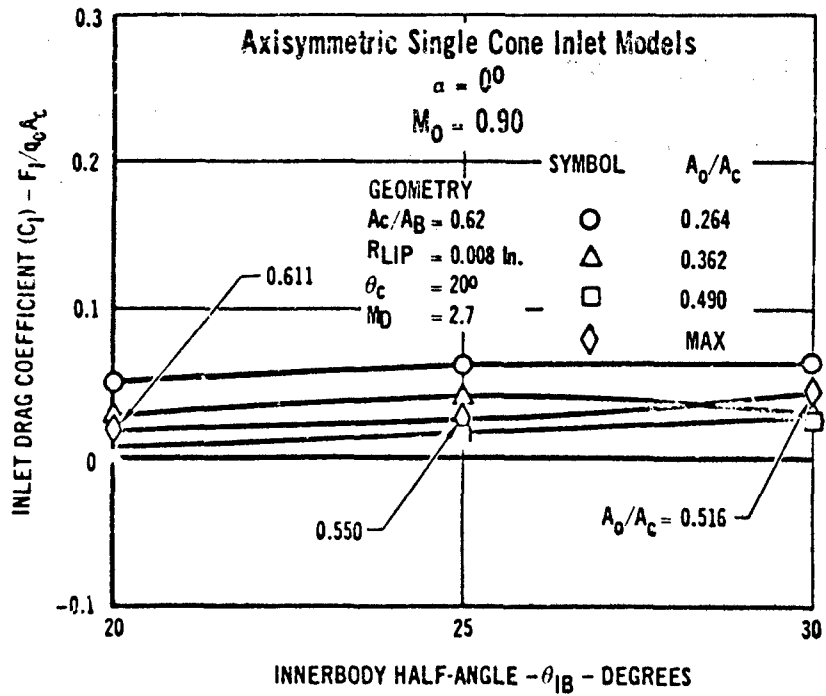


FIGURE 13
EFFECT OF INNERBODY HALF-ANGLE ON INLET DRAG



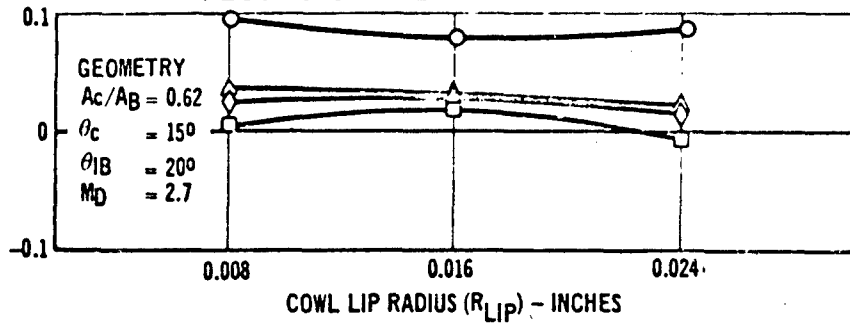
Axisymmetric Single Cone Inlet Models

$$\alpha = 0^\circ$$

$$M_0 = 0.90$$

FIGURE 14

EFFECT OF COWL LIP RADIUS ON INLET DRAG



| Symbol | A_o/A_B |
|--------|-----------|
| ○ | 0.264 |
| △ | 0.362 |
| □ | 0.490 |
| ◇ | MAX |

FIGURE 15

EFFECT OF DESIGN MACH NUMBER ON INLET DRAG

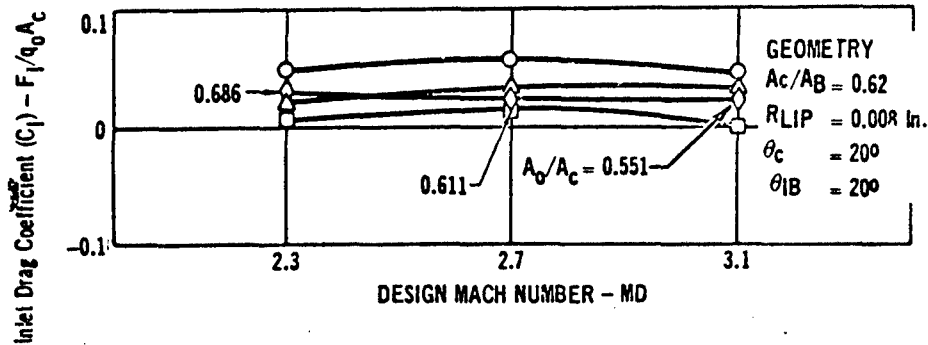


FIGURE 16

EFFECT OF CAPTURE AREA ON INLET DRAG

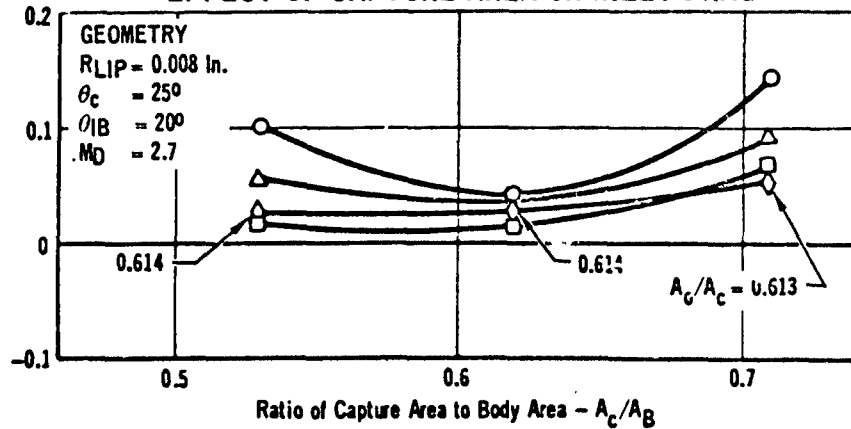


FIGURE 17
AXISYMMETRIC INLET DRAG COEFFICIENT
 Axisymmetric Single Cone Inlet Model
 Configuration A10
 $\alpha = 0^\circ$

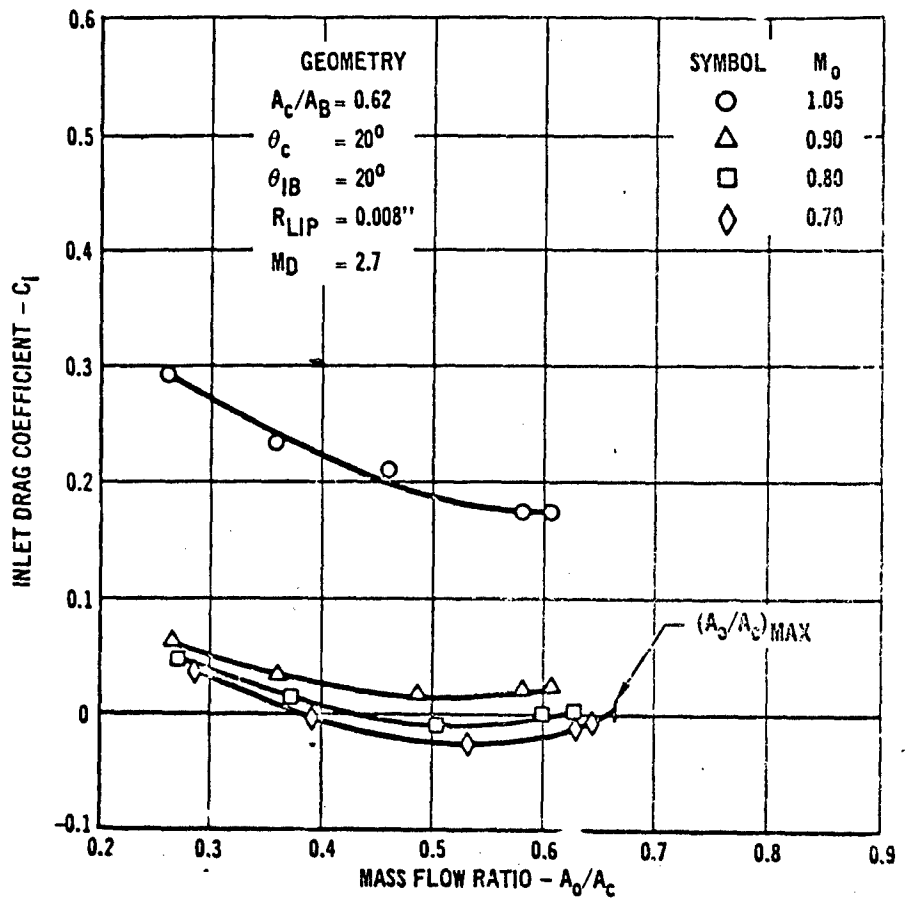


FIGURE 18
AXISYMMETRIC ADDITIVE DRAG COEFFICIENT
 Axisymmetric Single Cone Inlet Model
 Configuration A10
 $\alpha = 0^\circ$

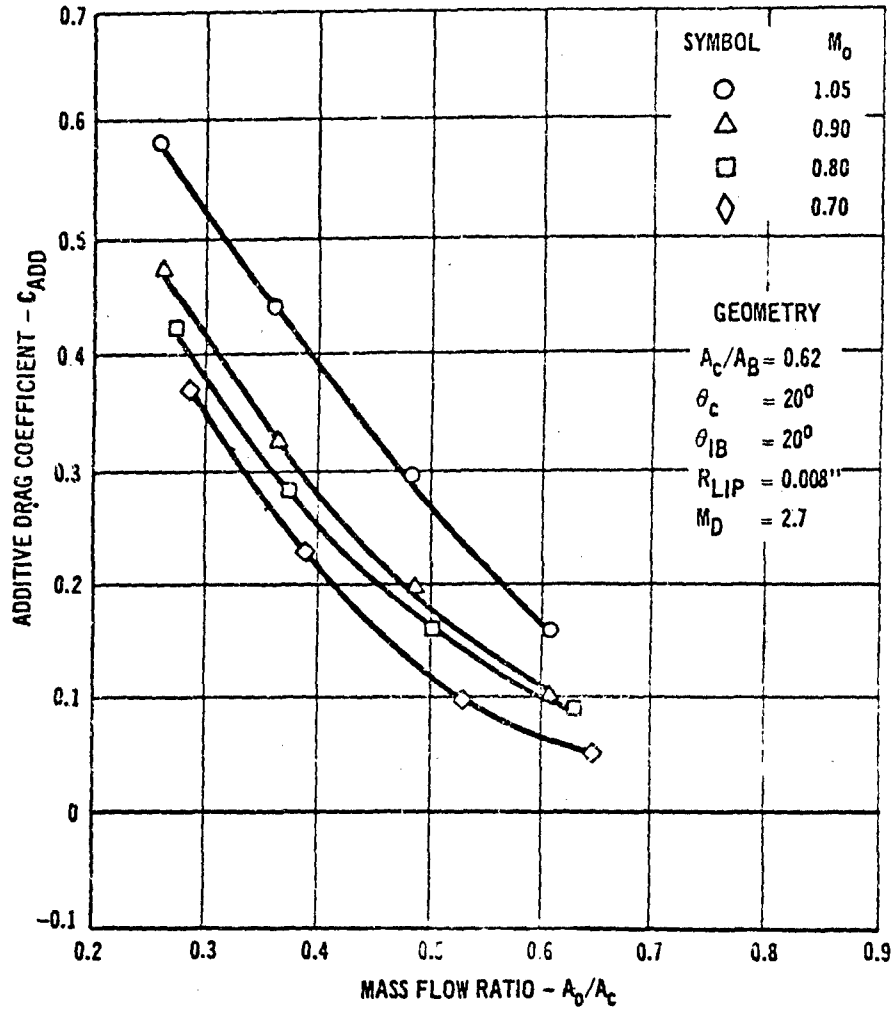


FIGURE 19
COMPARISON OF THE CONICAL AND ELLIPTICAL LIP INLET DRAG
Axisymmetric Single Cone Inlet Models
Configurations A9 and A18
 $\alpha = 0^\circ$

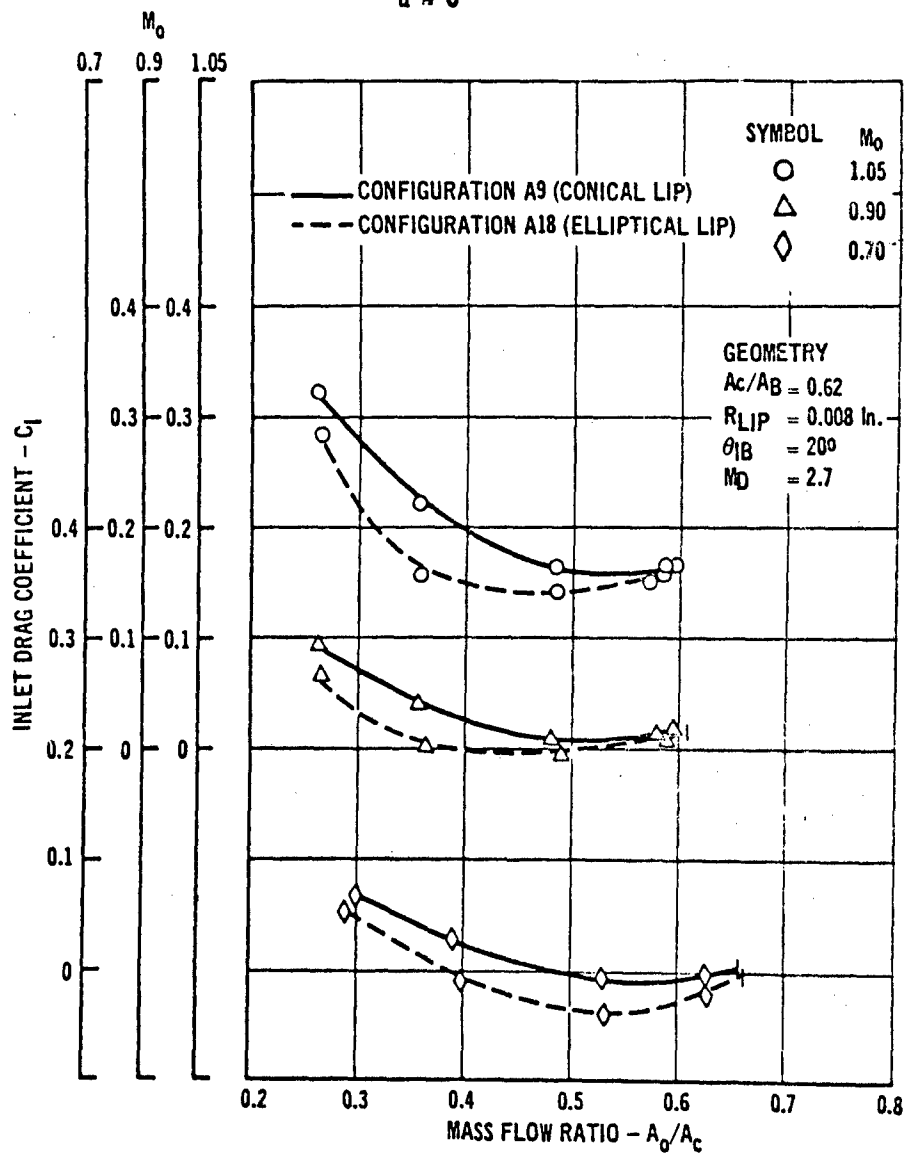


FIGURE 20
COMPARISON OF PRESSURE AND FORCE DATA
FOR AN AXISYMMETRIC INLET

Axisymmetric Single Cone Inlet Model
Configuration A10

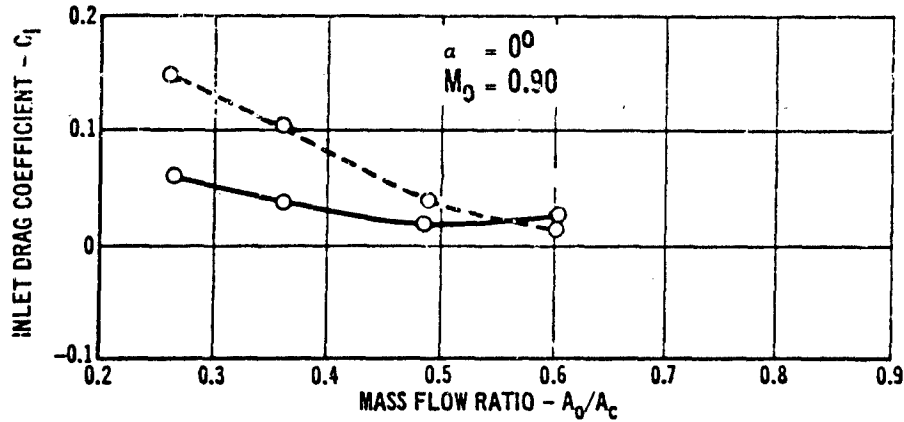
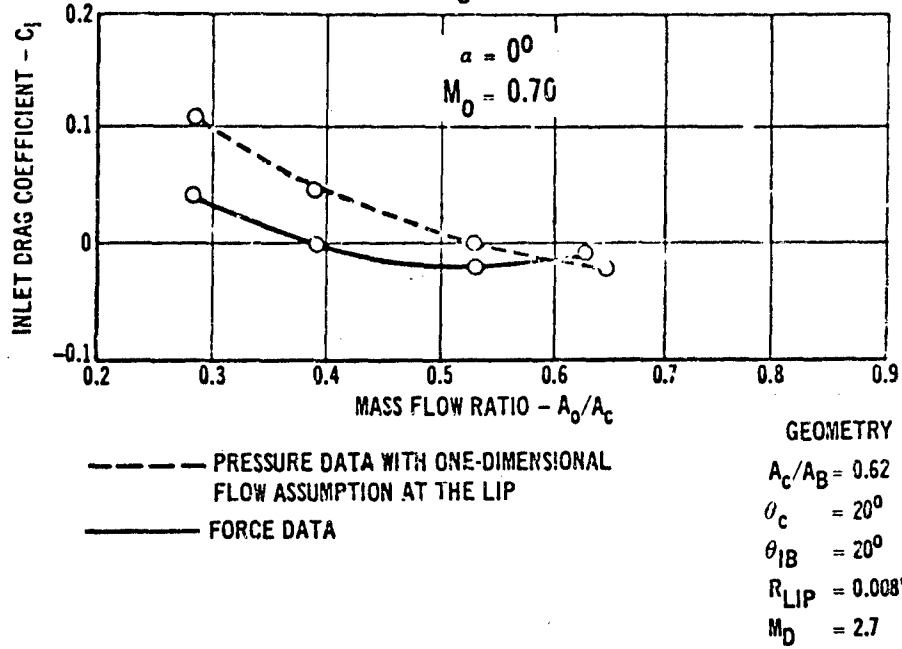


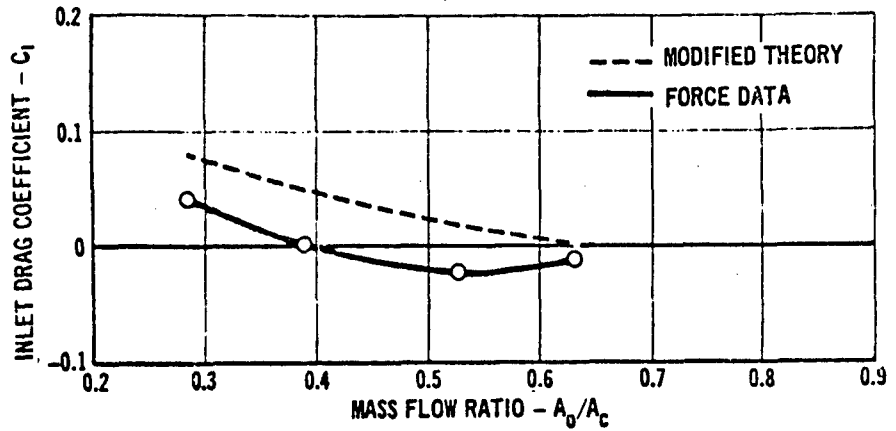
FIGURE 21
COMPARISON BETWEEN MODIFIED THEORY AND TEST DATA

Axisymmetric Single Cone Inlet Model

Configuration A10

$\alpha = 0^\circ$

$M_0 = 0.70$



Axisymmetric Single Cone Inlet Model

Configuration A10

$\alpha = 0^\circ$

$M_0 = 0.90$

GEOMETRY

$A_c/A_B = 0.62$

$\theta_c = 20^\circ$

$\theta_{1B} = 20^\circ$

RLIP = 0.008 in.

$M_D = 2.7$

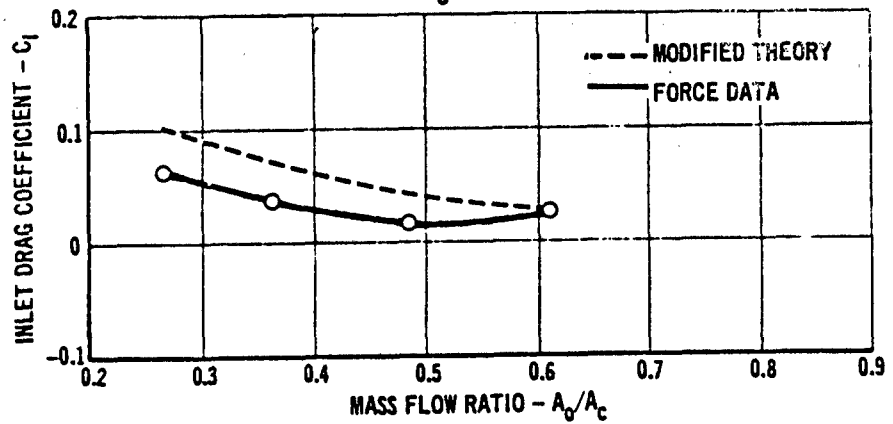


FIGURE 22
FOREBODY EFFECTS ON THE F-4 INLET DRAG

F-4 INLET MODEL

RAMP CONFIGURATION ($10^{\circ}-0^{\circ}$)

$M_0 = 0.7$

$\alpha = 0^{\circ}$

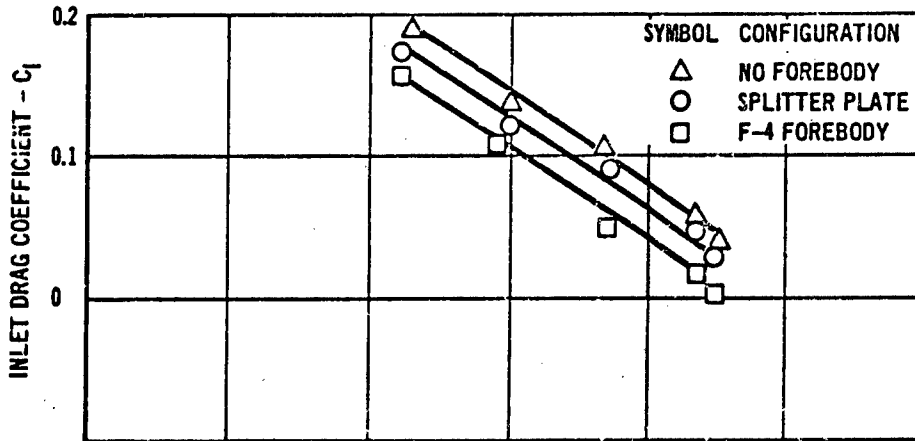
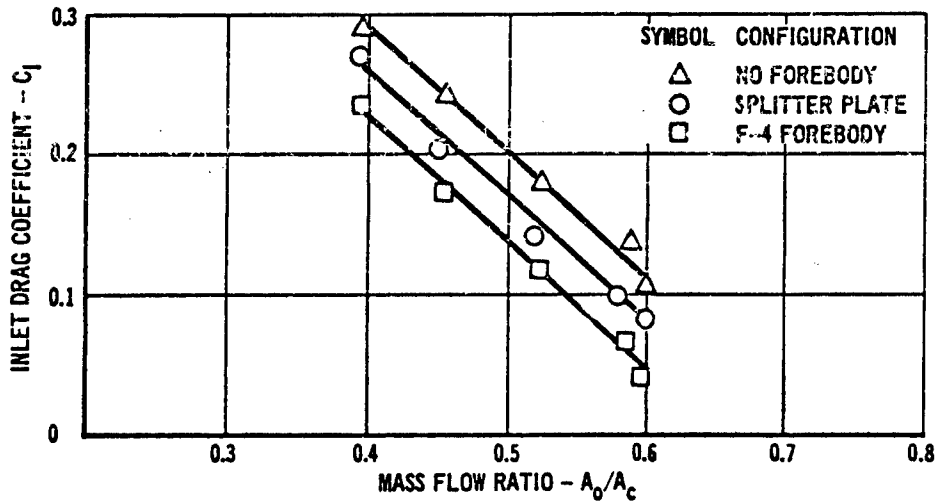


FIGURE 23

$M_0 = 0.9$

$\alpha = 0^{\circ}$



FOREBODY EFFECTS ON THE F-4 ADDITIVE DRAG

FIGURE 24

F-4 INLET MODEL

RAMP CONFIGURATION ($10^\circ-0^\circ$)

$M_0 = 0.70$ $\alpha = 0^\circ$

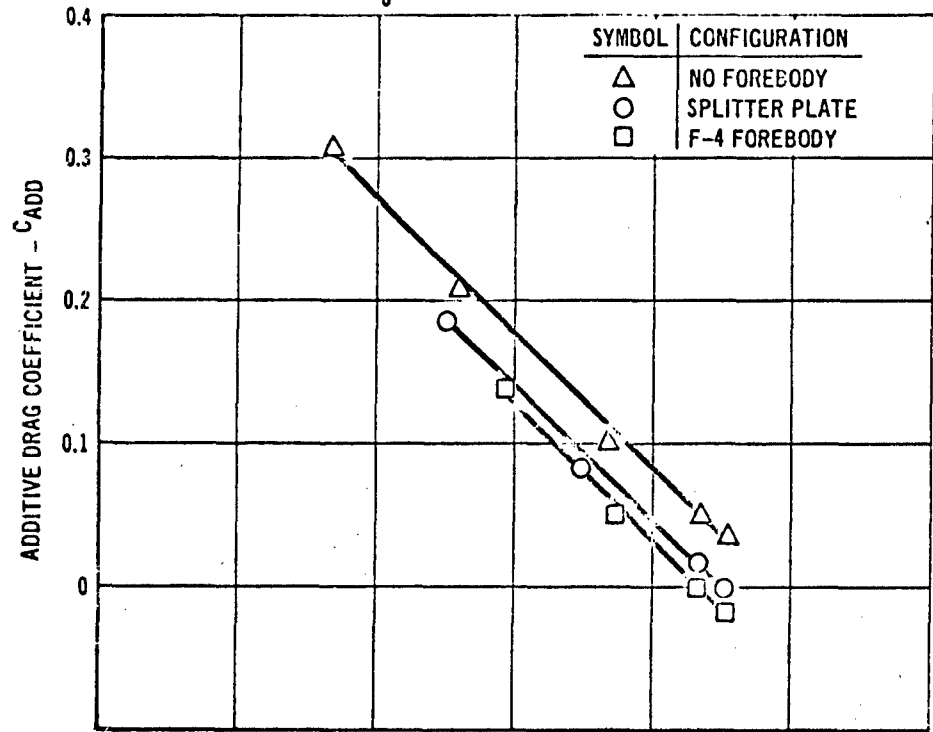
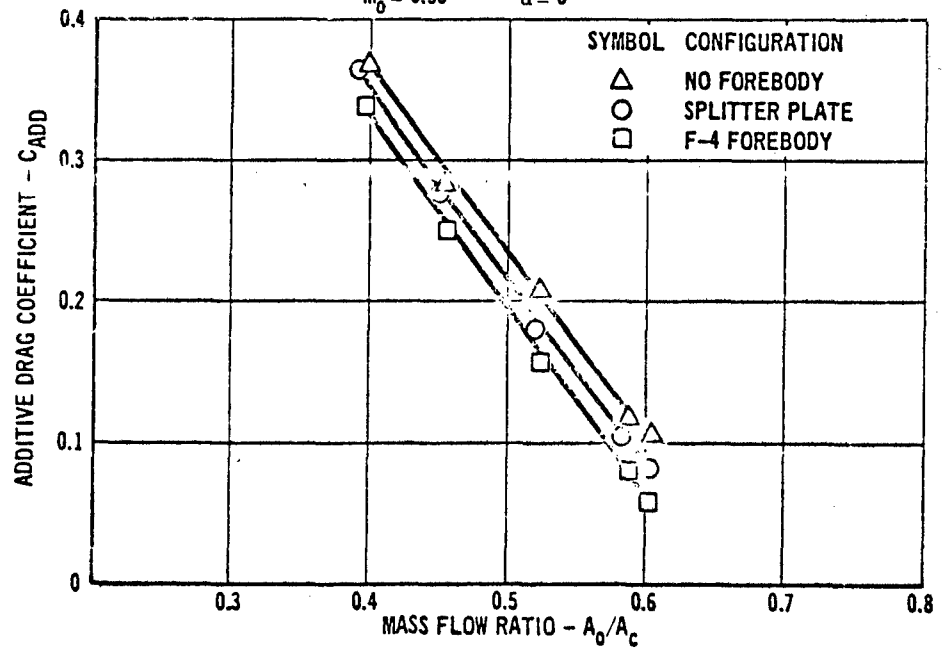


FIGURE 25

$M_0 = 0.90$ $\alpha = 0^\circ$



FOREBODY EFFECTS ON THE F-4 INLET DRAG

FIGURE 26

F-4 INLET MODEL
 RAMP CONFIGURATION (10^0-8^0)
 $M_0 = 2.0$
 $\alpha = 0^0$

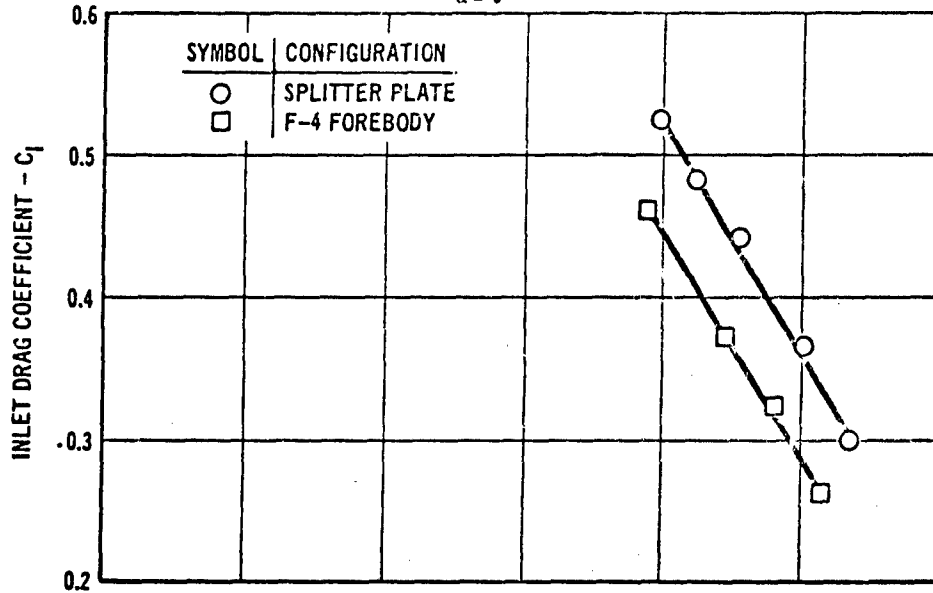


FIGURE 27

EFFECT OF RAMP ANGLE ON THE F-4 INLET DRAG

$M_0 = 0.90$
 $\alpha = 0^0$

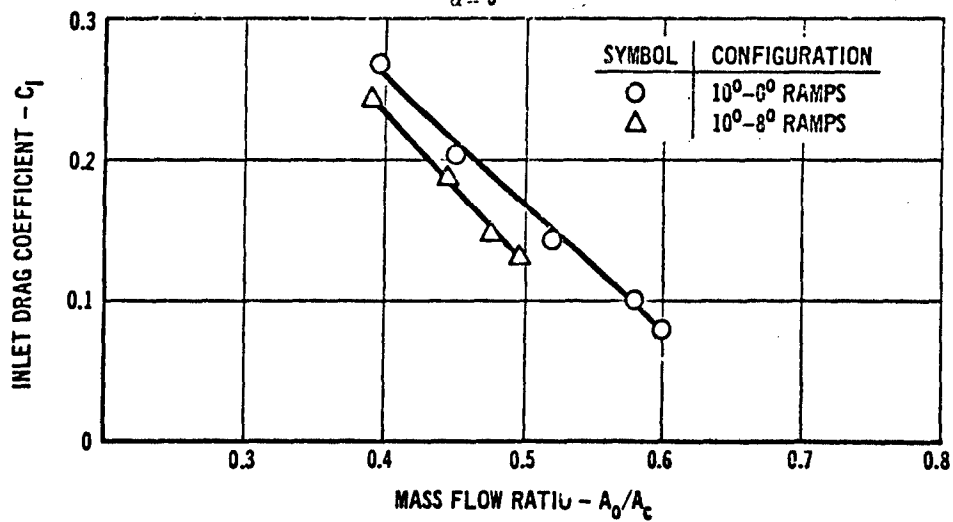


FIGURE 28
EFFECT OF RAMP ANGLE ON THE OPPOSED RAMP INLET DRAG

Opposed-Ramp Inlet Model

$$\alpha = 0^\circ$$

$$M_0 = 0.90$$

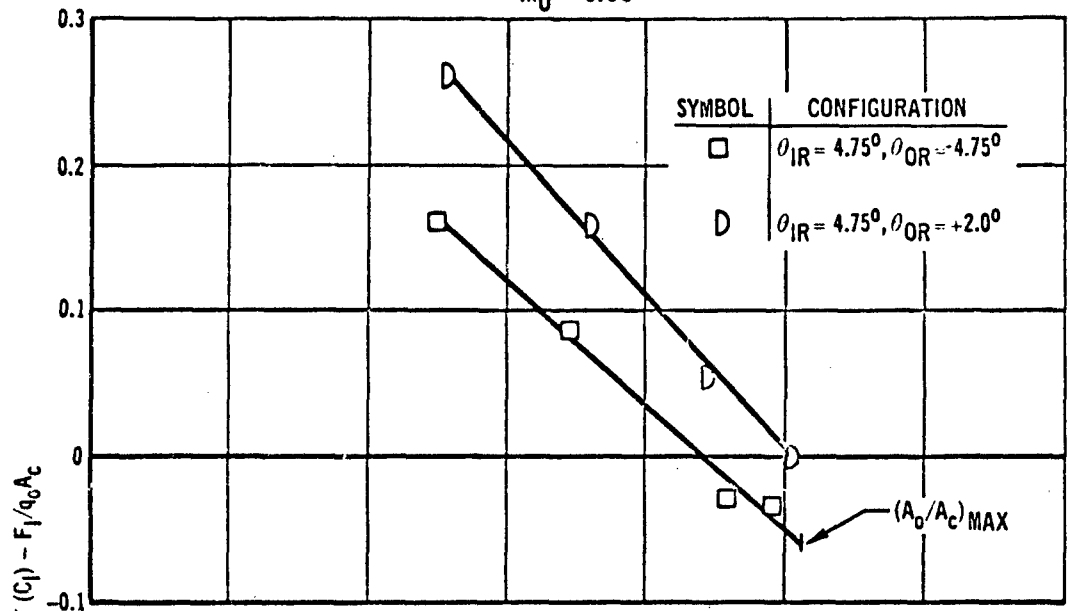


FIGURE 29
EFFECT OF SIDEPLATE ON THE OPPOSED RAMP INLET DRAG

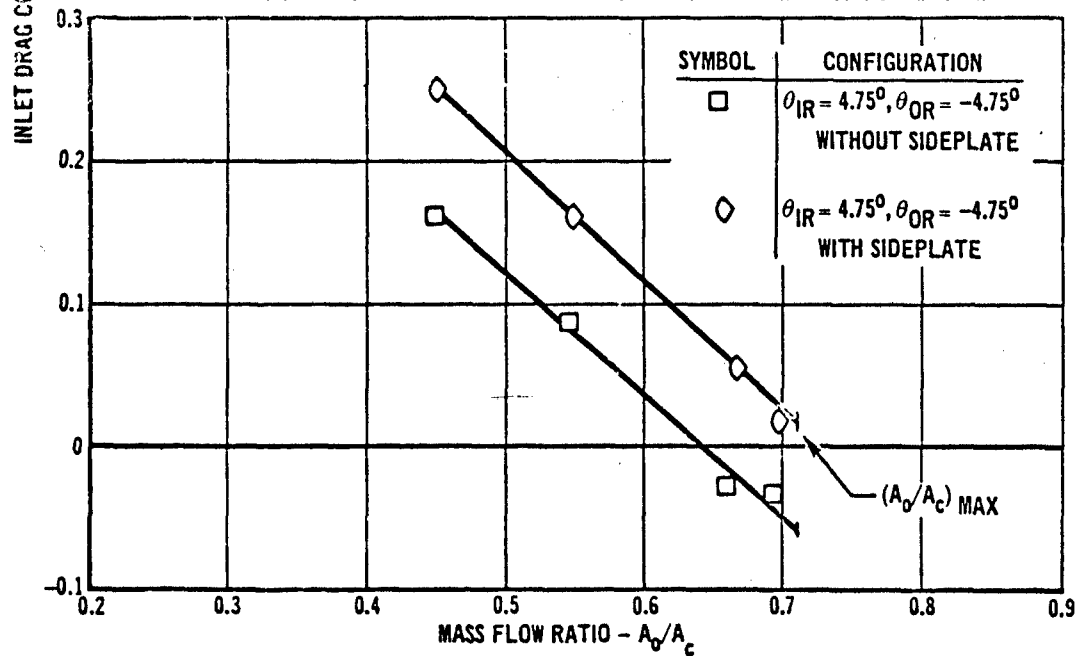


FIGURE 30
 COMPARISON OF THE F-4 AND OPPOSED RAMP INLET DRAG
 $\alpha = 0^\circ$
 $M_0 = 0.90$

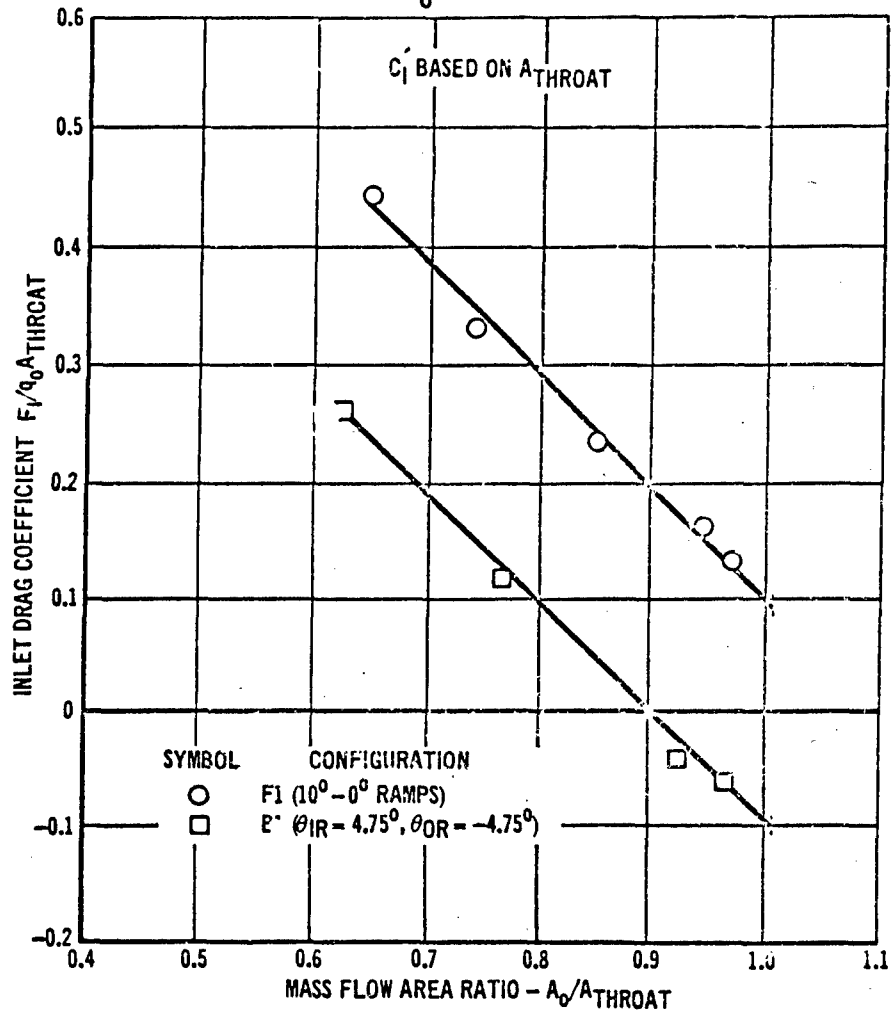


FIGURE 31
 ENVELOPE OF THE DRAG DATA FOR EACH FAMILY OF INLET CONFIGURATIONS

$\alpha = 0^\circ$
 $M_0 = 0.70$

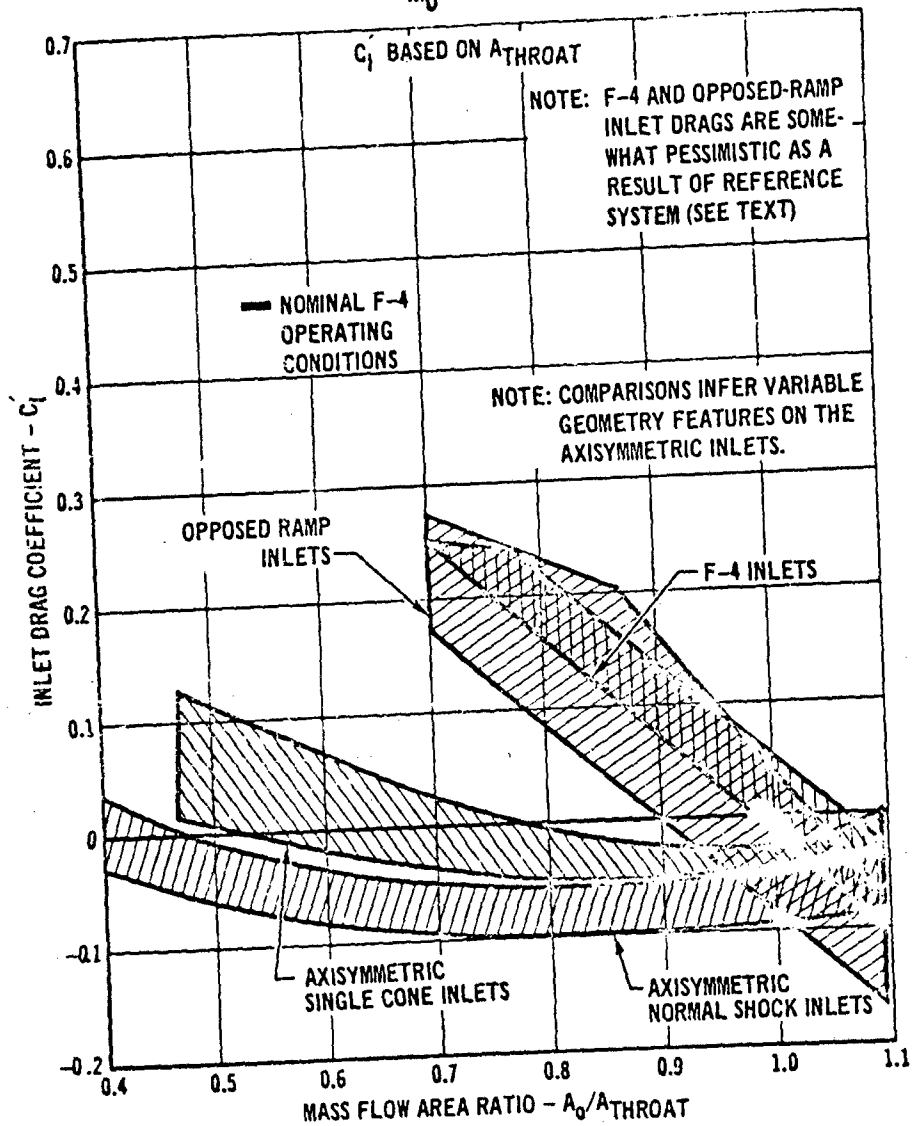
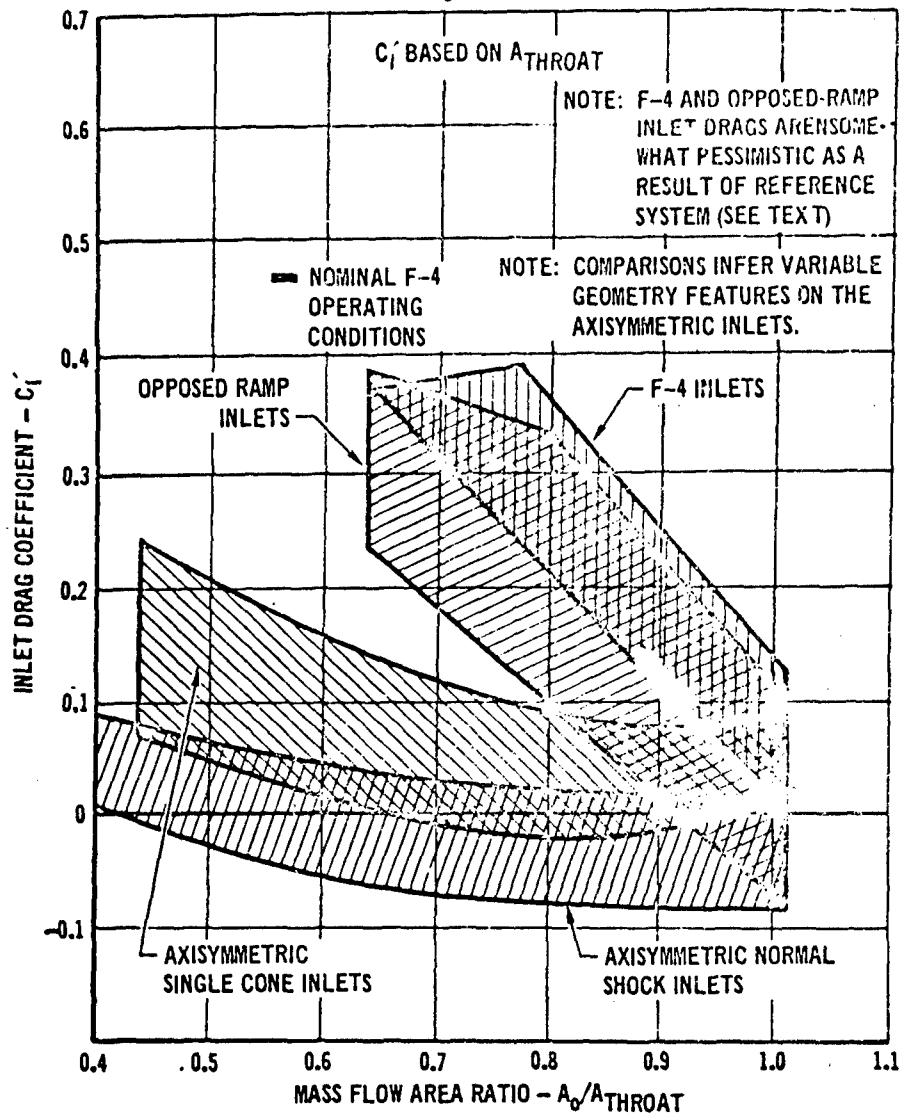


FIGURE 32
 ENVELOPE OF THE DRAG DATA FOR EACH FAMILY OF INLET CONFIGURATIONS

$\alpha = 0^\circ$
 $M_0 = 0.90$



A PLAN FOR BOOKKEEPING OF THE PROPULSION AND
AERODYNAMIC ELEMENTS OF AIRPLANE PERFORMANCE

Leonard H. Schreiber

Manager of Propulsion
The Fort Worth Division of General Dynamics

ABSTRACT

One of the difficulties in calculating airplane performance is in defining a consistent methodology for correctly including all elements of the propulsion and aerodynamic forces. The difficulties arise with respect to the propulsion/aerodynamic interfaces, i.e. the inlet and the nozzle, and they basically exist because the aerodynamic configurations of these propulsion system components are not fixed, but rather vary with the engine operating conditions. Further, multiple models are required when wind tunnel test data are used to predict the propulsion and/or aerodynamic characteristics. Unfortunately, a universal bookkeeping system does not exist. The purpose of this paper is to present a specific bookkeeping system to exhibit one method for ensuring that all propulsion and aerodynamic forces are properly accounted for and that the airframe and engine companies' data are compatible. A proposed methodology is presented for an arbitrary airframe configuration. The propulsion system includes a variable-geometry inlet and a plug-type exhaust nozzle. The forces acting on the real airplane (as opposed to wind tunnel models) which must be accounted for are identified, as well as the parameters which cause them to vary. The typical force model used in wind tunnel testing to obtain aerodynamic data is considered, including its simulation limitations. Further, the propulsion wind tunnel test models, which more closely simulate the true propulsion system configuration(s) and operating conditions, are considered so as to explain how additional aerodynamic and propulsion data may be obtained from these models.

LIST OF SYMBOLS

| | |
|---|---|
| A_e | nozzle exit area |
| A_i | inlet capture area |
| A_o | area of freestream tube which enters the inlet |
| A_p | plug projected area |
| A_{REF} | reference area for calculating drag |
| A_t | nozzle throat area |
| C_D | drag coefficient |
| C_{DA} | additive drag coefficient |
| $C_{DA/P}$ | airplane drag coefficient |
| C_{DFM} | drag coefficient from force model |
| C_{DI} | inlet interference drag |
| C_{DIN} | installed-inlet drag |
| C_{DLS} | change in cowl drag due to lip suction |
| C_{DN} | nozzle cowl drag |
| C_{DS} | inlet spillage drag ($C_{DA} - C_{DLS}$) |
| $\left[\Delta C_{DA/P} \right]_{NM}$ | airplane drag increment obtained from nozzle model test (see Figure 8) |
| $\left[\Delta_1 C_{DA/P} \right]_{NM}$ | part of $\left[\Delta C_{DA/P} \right]_{NM}$ |
| $\left[\Delta_2 C_{DA/P} \right]_{NM}$ | part of $\left[\Delta C_{DA/P} \right]_{NM}$ |
| $\left[\Delta_2^1 C_{DA/P} \right]_{NM}$ | same as $\left[\Delta_2 C_{DA/P} \right]_{NM}$, but referenced to ideal gross thrust rather than $q_o \times A_{REF}$ |

LIST OF SYMBOLS (Continued)

| | |
|---------------|---|
| C_v | nozzle velocity coefficient |
| $C_{v_{in}}$ | installed-nozzle velocity coefficient |
| C_{v_s} | nozzle velocity coefficient at static conditions |
| ΔC_v | change in nozzle velocity coefficient due to external flow and installation effects |
| $F_{G_{id.}}$ | ideal gross thrust |
| L | nozzle plug length |
| m_e | nozzle exhaust flow |
| m_I | inlet flow |
| M_o | freestream Mach number |
| NPR | nozzle pressure ratio |
| P_e | static pressure at nozzle exit plane |
| P_o | freestream static pressure |
| P_x | nozzle plug static pressure |
| q_o | freestream dynamic pressure |
| Re | Reynolds number |
| T_o | freestream total temperature |
| V_e | exhaust gas velocity at nozzle exit |
| V_o | freestream velocity |
| x | distance along nozzle plug |
| α | airplane angle-of-attack |

1. INTRODUCTION

That there is considerable uncertainty in the calculation of airplane performance prior to the availability of flight test data is a point that I believe is not controversial. There are many technical difficulties involved in making these predictions, such as the inability to completely simulate the true configuration on a scale model and the extrapolation of wind tunnel data to full-scale conditions. But there is also the problem of defining a consistent methodology for correctly including all elements of the propulsion and aerodynamic forces. It is this latter problem that I would like to discuss in this paper.

If a consistent methodology is not defined, the extrapolation of the scale model wind tunnel data, in conjunction with the other analyses leading to the prediction of airplane performance, will prove to be a futile effort. Here again, I do not believe that it is too argumentative to conclude that some of the past differences between predicted and actual airplane performance can be traced to the lack of a consistent methodology. For, if the methodology is not clear, we can expect to have difficulties in communication among the technical specialists within a given organization - and probably even more so when this involves interagency activities.

The correct bookkeeping of all propulsion and aerodynamic forces is complicated by (1) the existence of propulsion/aerodynamic interfaces, i.e. the inlet and the nozzle, for which the aerodynamic configurations are not fixed but, rather, vary with the engine operating conditions; and (2) the need for multiple scale models for wind tunnel tests, none of which fully simulate the desired configuration and/or operating conditions, therefore requiring integration of these various sets of data in order to interpret the test results correctly.

Unfortunately, a universal bookkeeping system neither exists nor is feasible, at least in the ultimate sense. Thus, the purpose of this paper is to present a specific system to exhibit one method that will ensure (1) that all propulsion and aerodynamic forces are accounted for, and (2) that the airframe and engine companies' data are compatible. No attempt will be made to discuss the theoretical

methods for predicting these forces; however, the significant wind tunnel tests will be described briefly.

For the purpose of this discussion, the airframe/propulsion system (Figure 1) is assumed to have an inlet with variable-geometry compression surface but with fixed inlet capture area. A plug-type exhaust nozzle, with movable nozzle cowl and collapsible plug, is included to illustrate the effects of the internal/external aerodynamic interactions of this nozzle type.

The proposed methodology will be defined by considering the forces acting on the full-scale airplane. The identification and accounting of the aerodynamic and propulsion forces have been established with the following objectives in mind:

1. The forces should be identified in a manner that will permit the engineer to predict them with a reasonable effort (either theoretically or from empirical correlations).
2. All of these forces should be measurable on the scale wind tunnel models tested during the configuration development/evaluation test program.
3. A meaningful evaluation of the engine thrust should be feasible.

However, we must not be misled into optimizing each element of the bookkeeping system. Rather, the summation of these forces, the airplane thrust minus drag, should be optimized. The sole purpose of the bookkeeping system is to organize the thrust-minus-drag data into manageable and, hopefully, understandable elements.

Therefore, let us review the inlet and nozzle operations as they affect the external aerodynamics of the airplane. Throughout the discussion, the airplane flight condition will be considered to be constant, unless noted otherwise, but engine operation will be allowed to vary in order to illustrate the airframe/engine interactions.

2. INLET

At a typical supersonic flight condition, the inlet capture area ratio will be less than the maximum value of 1.0, and some inlet spillage will exist, as depicted in Figure 2. As a result of this spillage, the inlet additive drag must be included in the airplane drag. For a particular operating inlet capture area ratio, a given cowl drag will exist. As the inlet capture area ratio is varied, the additive drag and cowl drag will vary in a manner such as shown in Figure 2.

It is convenient to consider inlet operation at a capture area ratio of 1.0 as a reference condition, since, by definition, the additive drag is zero at $A_0/A_1 = 1.0$. Thus, at reduced capture area ratios, the total inlet drag (spillage drag) is equal to the additive drag less the decrease in cowl drag (lip suction), as shown in Figure 2. Similar drag relationships exist at subsonic conditions, although the magnitude of the inlet drag is lower.

In the above discussion no consideration was given to any potential interaction between the inlet flow and the total airplane flow field. In the real situation, the inlet flow may interact with the airplane (in addition to the cowl, which has already been accounted for by the lip-suction effect). For example, as shown in Figure 3, these interactions may affect the inviscid flow field, or there may be an effect on the airplane boundary layer, or the installed local flow may differ from the isolated case. In any case, the existence of inlet spillage may result in a larger drag increase for the composite configuration than it would for the case of an isolated inlet, as discussed above. We can consider this excess drag to be an "inlet interference drag". In Figure 4 the inlet interference drag is shown added to the additive, lip-suction, and spillage drags of Figure 2.

From the above description, the total effect of airframe/inlet interactions has been provided for, and this has resulted in the definition of an installed-inlet drag (Figure 4) as being comprised of three components--additive drag, lip suction, and inlet interference drag. The installed-inlet drag is the parameter of real interest.

Now, it is appropriate to consider the criteria previously defined, i.e. that the propulsion/aerodynamic forces

should be predictable and measurable. With regard to predicting the installed-inlet drag, it is clear that the approach should be to predict each of the three components. The additive drag and lip suction parameters should "present no problem" since we have been calculating them for some time now. However, while it is not the intent of this paper to discuss the appropriate technical methods, but rather only the bookkeeping system, it is noteworthy that the available additive drag and lip-suction prediction techniques are not adequate to permit these predictions to be made with real confidence. And even less work has been done in the area of inlet interference drag, as evidenced by the lack of data comparing measured inlet drag as a function of A_0/A_1 for an isolated inlet with similar measured data for an installed inlet. This limitation of the prediction techniques, and the fact that the installed-inlet drag is sensitive to the airframe configuration and the inlet installation details, suggests that the installed-inlet drag must be measured if we are to avoid excessive drag. However, this measurement task is not a simple one for speeds in excess of approximately Mach 2.0 to 2.2.

The normal approach to measuring the installed-inlet drag is to utilize an airplane force model (Figure 5) which is the basic tool for investigating airplane drag. However, because of the requirements for large angle-of-attack variation, this model is usually of fairly small scale. Thus, it is not practical to simulate various geometric features of the full-scale inlet, including such detail characteristics as the cowl lip shape and the inlet compression-surface boundary-layer bleed that is needed above Mach 2.0 to 2.2. Therefore, we can expect that boundary-layer separation will occur on the force model inlet compression surfaces. For sub-critical inlet airflows, this will result in an inlet shock system that differs from the full-scale pattern and, therefore, an incorrect measurement of installed-inlet drag. We can overcome this deficiency by using a larger scale model in which the inlet compression-surface bleed can be installed. Because of the large model size, it would be limited to low angle-of-attack tests. The larger model would also permit a better simulation of the cowl lip details, which are important to the generation of lip suction.

3. EXHAUST NOZZLE

The plug nozzle shown in Figure 6 is an excellent example of the bookkeeping system complications that can be introduced by the engine exhaust system. This results from the aerodynamic interactions of the exhaust stream with the external flow and with the aircraft components downstream of the nozzle, as well as from the variable cowl. These interactions affect the nozzle thrust, nozzle drag, and aerodynamic characteristics of the affected airframe components.

Let us first consider the full-scale nozzle in an isolated configuration. As the engine power setting is varied, the jet pressure ratio will vary and the cowl and collapsible plug will move to change the nozzle throat area and nozzle expansion ratio. As a result, the nozzle drag will vary because of the change in cowl external lines and because of the jet effects on boattail pressures. Also, for each nozzle geometry, the nozzle gross thrust is determined by the nozzle internal geometry, nozzle pressure ratio and exhaust gas temperature, and the plug pressures affected by the aerodynamic interactions between the exhaust stream and the external flow. (See Figure 6 for the definition of gross thrust.) Thus, we can properly account for the isolated nozzle forces if we account for the nozzle drag, C_{DN} , and the nozzle thrust, C_T , as functions of M_0 , NPR, A_e , and A_t .

When we consider the nozzle in its installed configuration, the nozzle drag can still be accounted for as a function of M_0 , NPR, A_e , and A_t , although its level will be different than in the isolated configuration. However, the drag of the airplane surfaces in the vicinity of the nozzle cowl and plug will also vary with these same parameters because of aerodynamic interactions. Further, the drag of the airplane components downstream of the nozzle will be affected by jet effects. Therefore, the total airplane drag (including the nozzle drag) is a function of M_0 , NPR, A_e , and A_t . The nozzle thrust coefficient, C_T , will vary with these same parameters, as in the isolated case, although the absolute level will differ because of the change in plug pressures with the external flow field of the real airplane as compared to the isolated case.

Thus, we have defined airplane drag and nozzle thrust in a compatible manner, and we now need to consider the

previously stated criteria of predictability and measurability. We are all aware that methods are available for predicting airplane drag, but with various limitations. We cannot account for the true exhaust jet with current prediction techniques, i.e., we assume that the jet is cylindrical out to infinity. Also, while data are available to predict the jet effects on nozzle boattail drag, for isolated-type configurations and very specific installed configurations, we find it difficult to estimate (1) the jet effects on the airplane surfaces in the immediate vicinity of the nozzle, and (2) the effect of the installation on nozzle drag and nozzle thrust coefficient.

Thus, although we have established a rational book-keeping system, we find that we must depend to a great extent on wind tunnel data to obtain the total effect of the exhaust jet on the drag of a specific airplane configuration. Here again, however, we find that the problem is complicated by the limitations of the wind tunnel models.

If we could measure the total airplane drag on a model in which the nozzle geometry and the exhaust jet are simulated, and which operated with the desired inlet flow, we would have a fairly direct measurement of total airplane drag (at tunnel Reynolds number). However, we are not yet able to accomplish this degree of simulation on the normal force model (Figure 5) since the jet requires pressurized air. Studies of scale-engine simulators are in work and may provide such a capability in the future. The present force models provide airplane drag data for a value of NPR that is less than ram pressure ratio (due to non-isentropic inlet pressure recovery and internal losses). The effect of nozzle cowl geometry variations can be determined, but only for the excessively low NPR values.

Thus, we find that airplane drag must be measured on a force model which does not simulate the exhaust jet, and that jet effects must be obtained as incremental effects on a separate model (Figure 7) on which the nozzle and exhaust jet are properly simulated. In view of the need for the separate nozzle model, we find it expedient to not even simulate the true nozzle plug on the force model. The effect of the true plug can be obtained on the nozzle model in conjunction with the other incremental drag effects.

The nozzle model is used to determine the effect on aft airplane drag of changing from the force model nozzle configuration to the true nozzle configurations (various cowl

and plug settings), including the effects of NPR variations. This is accomplished by attaching the aft portion of the airplane and part of the nacelle/nozzle to a force balance. The resulting airplane drag increments, depicted in Figure 8 are then added to the force model airplane drag data to arrive at the total airplane drag, $C_{DA/P}$, as a function of M_0 , NPR, A_e , and A_t . Since the nozzle model correctly simulates the airplane in the vicinity of the nozzle and downstream of it, and since the jet is simulated fairly well, the change in airplane drag due to the real jet as compared to the force model jet is available (at test Reynolds number). Thus,

$$C_{DA/P} = C_{DFM} + \left[\Delta C_{DA/P} \right]_{NM}$$

where

$$C_{DA/P} = f(M_0, NPR, A_e, A_t)$$

$$C_{DFM} = f(M_0) \text{ for a constant } \alpha \text{ and Reynolds number}$$

$$\left[\Delta C_{DA/P} \right]_{NM} = f(M_0, NPR, A_e, A_t)$$

By combining the data from the force and nozzle models, we are able to determine the total airplane drag. However, whereas the force model is deficient in not simulating the nozzle and exhaust jet, the nozzle model is also limited in that the inlet is not simulated. The inlet is faired over, as shown in Figure 7, resulting in some change in the upstream external flow at the nozzle.

We previously defined the performance for the installed nozzle as $C_V = f(M_0, NPR, A_e, A_t)$. This quantity is predictable to the extent that it is a meaningful term. In actuality, we have data from nozzle tests and from theoretical calculations with which we can attempt to predict installed nozzle performance, but we must recognize that these methods leave much to be desired. Therefore, the nozzle model used to obtain the drag increments due to jet effects (Figure 7) is also used to measure nozzle performance in the installed configuration. Nozzle thrust (as defined in Figure 6) is measured by the force balance and corrected by adding the nozzle cowl drag from cowl pressure measurements.

If we were willing to use these scale model nozzle data in conjunction with measurements of engine gas generator characteristics (i.e., tailpipe pressures and temperatures, gas flows) to imply the thrust of the engine and nozzle (during either ground facility tests or in-flight), then the absolute level of installed nozzle thrust coefficients from the nozzle model would have real meaning. However, since the engine contractor has the responsibility to develop the engine and nozzle hardware, it is extremely desirable to have the performance of his full-scale hardware demonstrated. But, it is not possible to do this in the installed condition. Therefore, we have elected to consider the installed nozzle performance to be made up of two parts. These parts, as shown in Figure 9, are (1) the static nozzle performance, and (2) the combined effects of external flow and nozzle installation.

This approach permits the engine contractor to predict the static nozzle performance as part of his presentation of the total engine plus nozzle performance for static conditions (i.e., no external flow over the nozzle, but with the appropriate freestream conditions corresponding to the Mach/altitude envelope at the engine inlet). Subsequently, the engine contractor can demonstrate full-scale engine plus nozzle performance at static conditions. These demonstration tests are not limited to sea-level static conditions, but can simulate flight operating conditions by varying the total pressure and temperature at the engine compressor face, with the nozzle exhausting to an altitude facility to produce the desired pressure ratio. The change in nozzle performance, ΔC_V , due to the external flow of the real airplane is obtained by subtracting static nozzle performance from the installed performance, both obtained on the same nozzle model. Thus,

$$C_{V_{in}} = C_{V_S} + \Delta C_V$$

where

$$C_{V_{in}} = f(M_0, NPR, A_e, A_t)$$

$$C_{V_S} = f(NPR, A_e, A_t) \text{ for } M_0 = 0 \text{ (from model and full-scale tests)}$$

$$\Delta C_V = f(M_0, NPR, A_e, A_t) \text{ (from the nozzle model)}$$

If, in lieu of the above approach, the engine contractor quotes of engine plus nozzle performance were to consider the effects of external flow, the effects would have to apply to a configuration in which the full-scale hardware could subsequently be tested to demonstrate its performance. This configuration would likely be defined as having the nozzle installed on an isolated cylindrical forebody (large enough to house the engine in the full-scale configuration). But this approach would complicate the engine testing significantly by requiring external flow over the nozzle. And it would only result in the definition of an alternate reference condition (as compared to the previously selected static condition) for which the incremental effect of the installation would still have to be determined. By selecting static conditions as the reference level, as stated previously, the engine plus nozzle performance demonstration tests in a ground test facility are comparable to similar tests for an engine with either convergent or convergent-divergent nozzle.

As stated previously, the increment in nozzle performance from static to installed conditions includes both the effect of external flow and the effects of the specific installation. No attempt is made to isolate these effects since the individual components are not significant.

4. AIRPLANE

The discussion thus far has been concerned mainly with the incremental change in airplane drag due to the inlet and nozzle as measured on the force and nozzle models, respectively. With the reference systems selected for defining these effects, it follows that the basic airplane drag is measured on the force model, with the inlet operating at $A_0/A_i = 1.0$ and with a specific nozzle cowl geometry operating at the NPR resulting from the use of a ducted inlet. The total airplane drag at given inlet and nozzle conditions is as shown in Figure 10 in accordance with the bookkeeping system described thus far. The installed-nozzle thrust coefficient is also shown as the sum of the static value plus the external flow/installation effect.

There is still one difficulty with the system presented in Figure 10: the drag and gross-thrust coefficients both vary with engine operating conditions (A_0/A_i , NPR, A_e , A_t). For convenience of calculating airplane performance, it is

desirable to define the airplane drag so that it is invariant with engine power and is a function of only the normal parameters (M_0 , α , Re , airplane trim). This can be accomplished by including part of the drag in the installed-engine performance (i.e., the inlet drag, CD_I) and by dividing the term $[\Delta C_{DA/P}]_{NM}$ into two parts, as follows:

$$[C_{DA/P}]_{NM} = [\Delta_1 C_{DA/P}]_{NM} + [\Delta_2 C_{DA/P}]_{NM}$$

where the first term corrects the force model data to a set of reference values of NPR, A_e , and A_t (these are unique values which vary with M_0 and are selected to be representative of the most important engine operating conditions), and the second term corrects from these reference conditions to any other engine operating condition. The first term is then included in the airplane drag, while the second term is included in the installed-engine performance. This only requires that the available data be interpreted in the manner described above, as opposed to including the total nozzle drag correction, $[\Delta C_{DA/P}]_{NM}$, in the airplane drag.

This final bookkeeping system is presented in Figure 11. As seen, all terms which vary with engine power setting are included in the installed net thrust. Further, the portion of the net thrust which is quoted by the engine company is

$$\left\{ [CV_S (FG_{id.})] - m_I V_0 \right\}$$

5. SUMMARY

A bookkeeping system has been defined which clearly identifies the responsibilities of the various technical specialists and should facilitate communication among them. It has the desired feature that the airplane drag does not vary with engine power setting and, conversely, that the installed net thrust includes all forces which do vary with engine power. This facilitates the calculation of airplane performance. Further, it permits the engine contractor to quote the engine and nozzle performance in a manner that permits it to be verified by tests that are meaningful in the context of the total bookkeeping system.

However, the basic problems inherent with wind tunnel testing still remain. Simulation of both the inlet and exhaust flows in a given model is lacking, and the extrapolation from test to full-scale Reynolds numbers is not always understood because of flow phenomena which are unique to the specific airplane configuration.

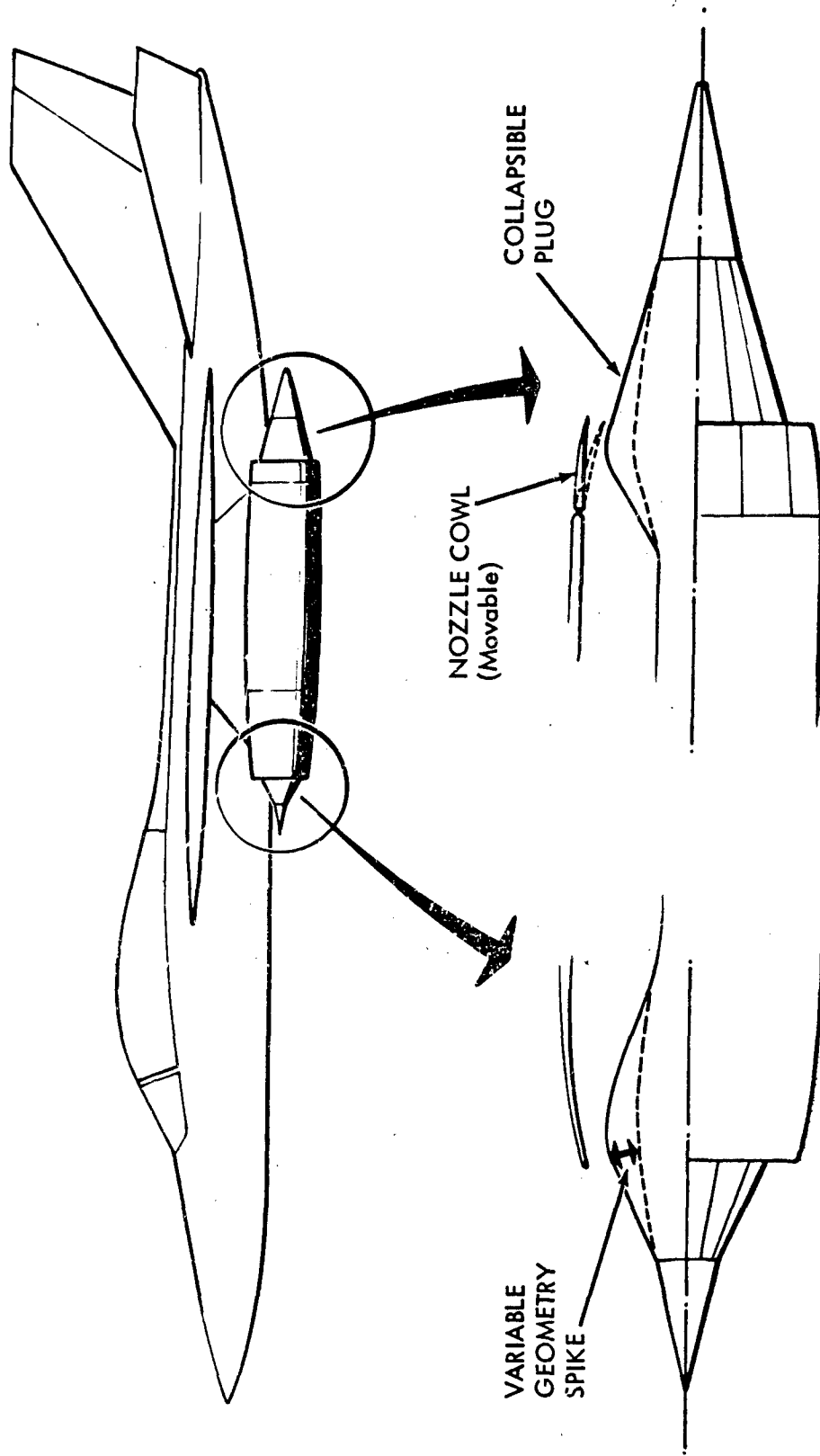
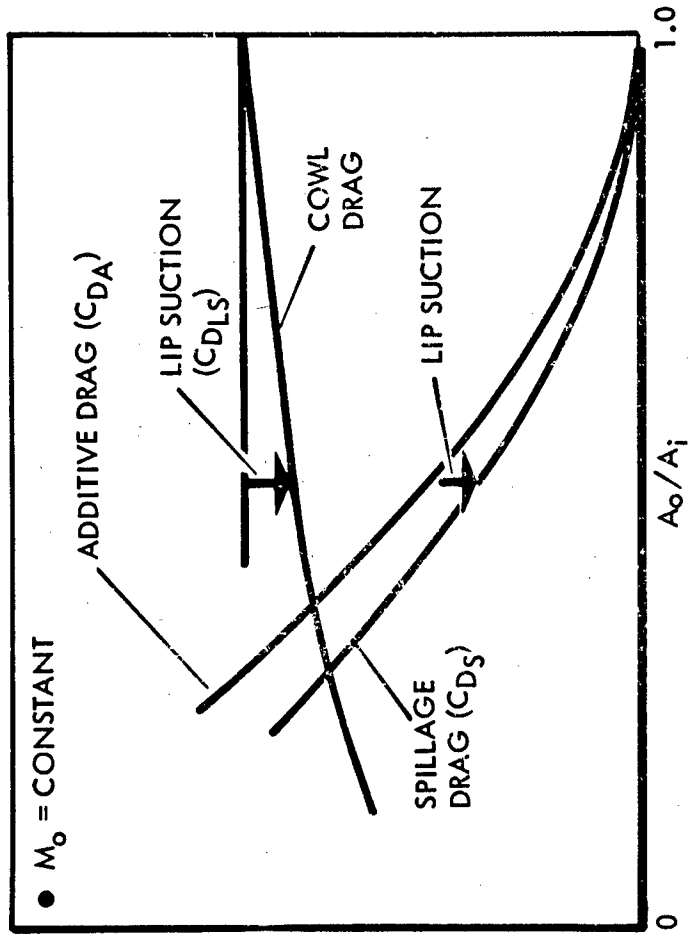
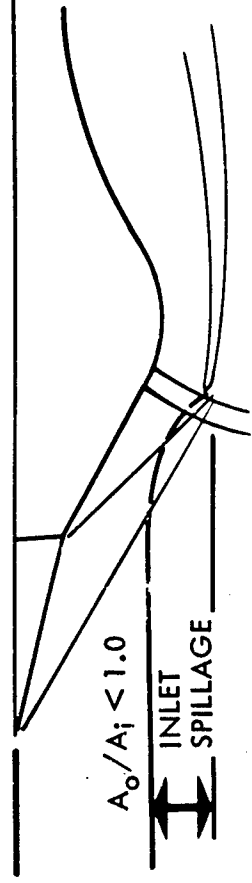
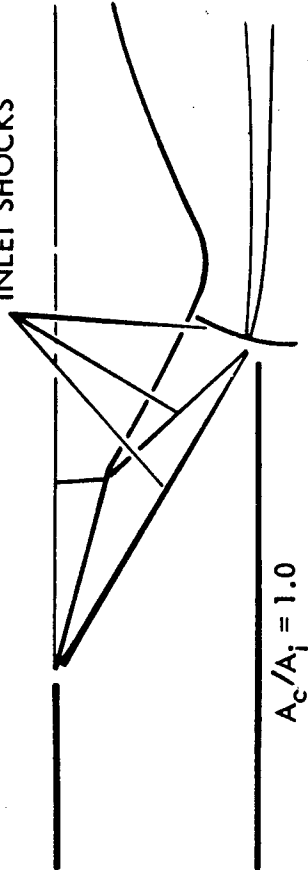


Figure 1 AIRFRAME/PROPULSION CONFIGURATION

INLET SHOCKS



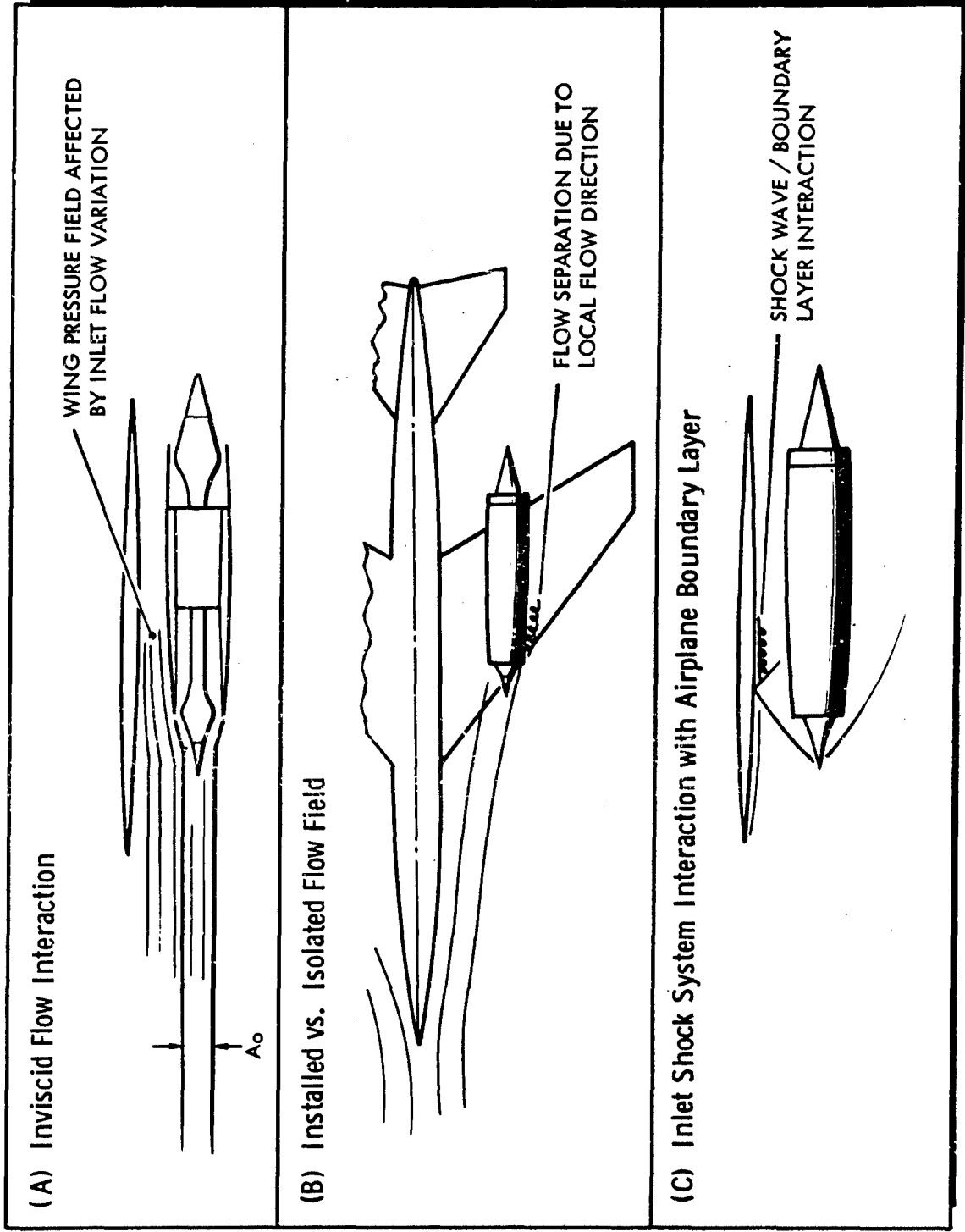


Figure 3 INLET/AIRFRAME AERODYNAMIC INTERACTIONS DUE TO SPILLAGE

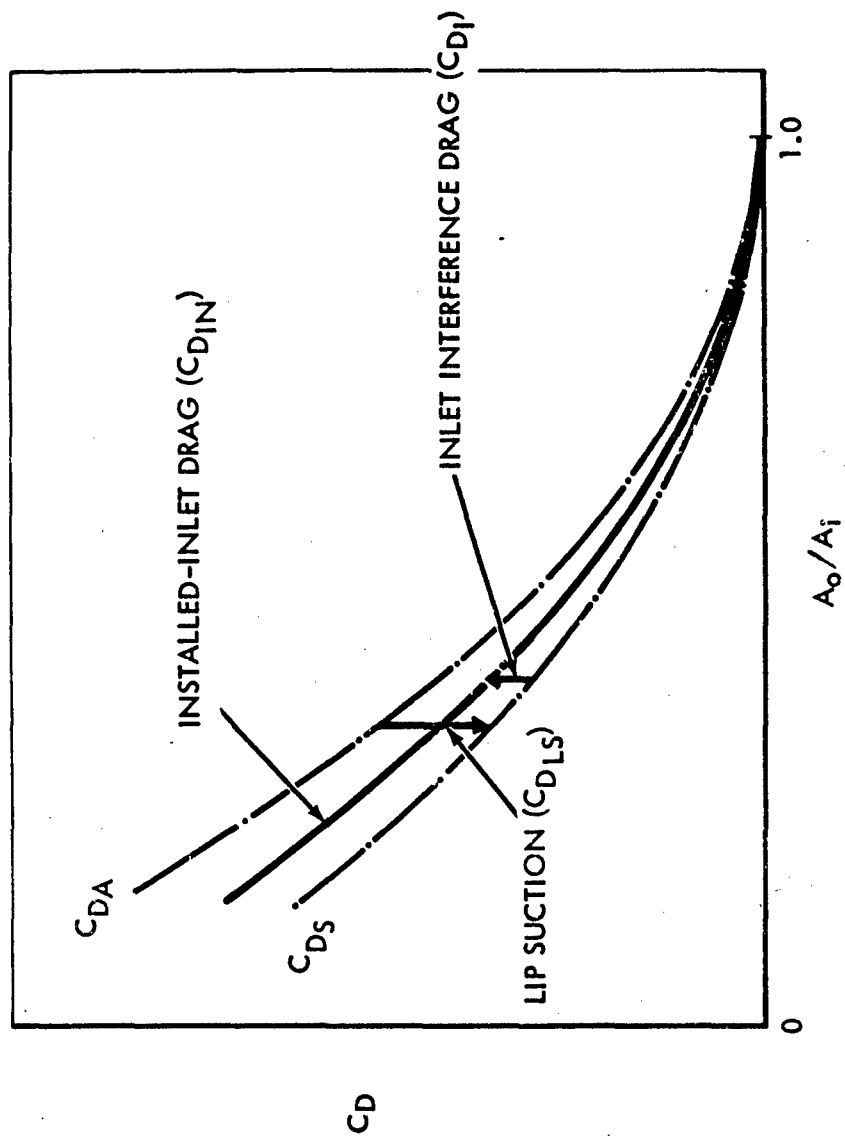


Figure 4 INSTALLED - INLET DRAG

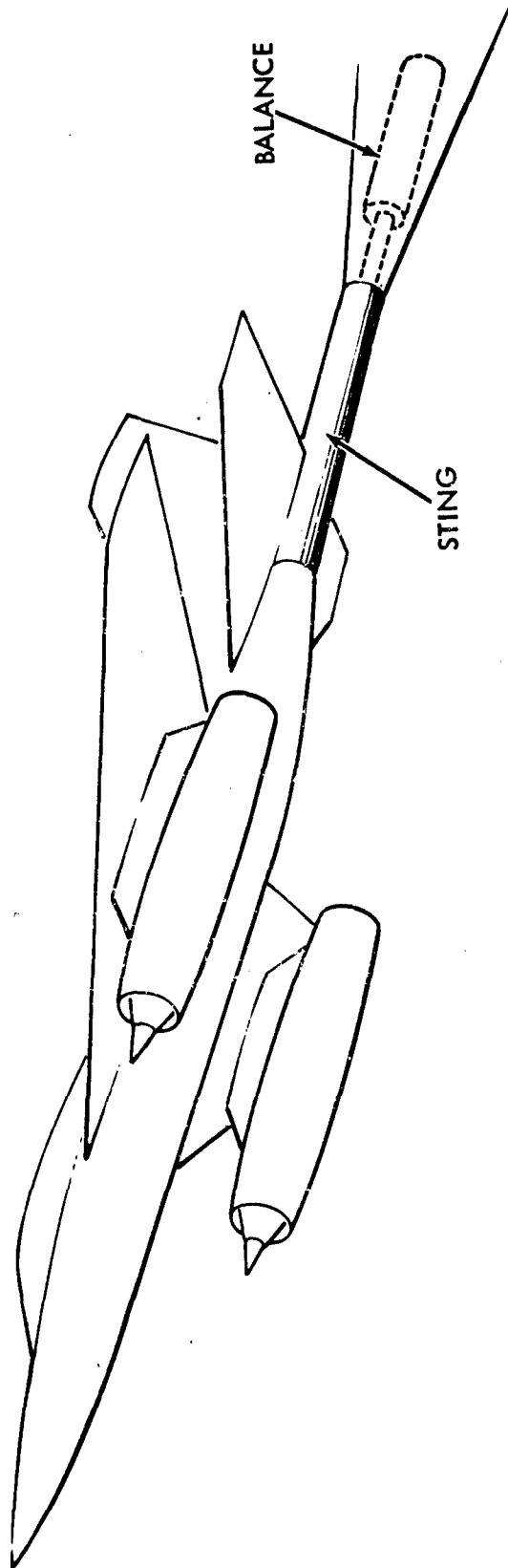
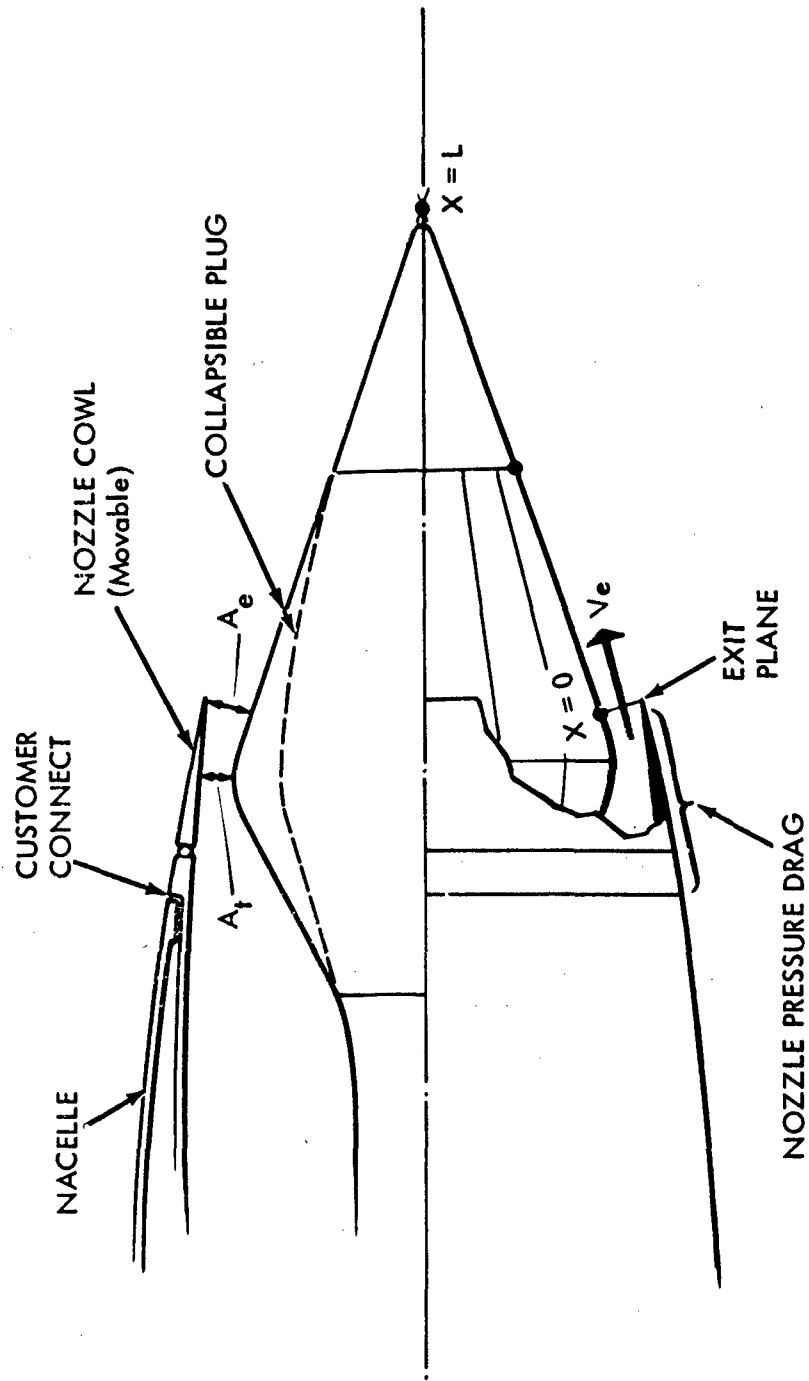


Figure 5 TYPICAL AIRPLANE FORCE MODEL



$$C_V = \frac{\text{ACTUAL GROSS THRUST}}{\text{IDEAL GROSS THRUST}} = \frac{m_e V_e + (P_e - P_o) A_e + \int_0^L (P_x - P_o) dA_p}{F_{GID}}$$

Figure 6 PLUG-TYPE EXHAUST NOZZLE

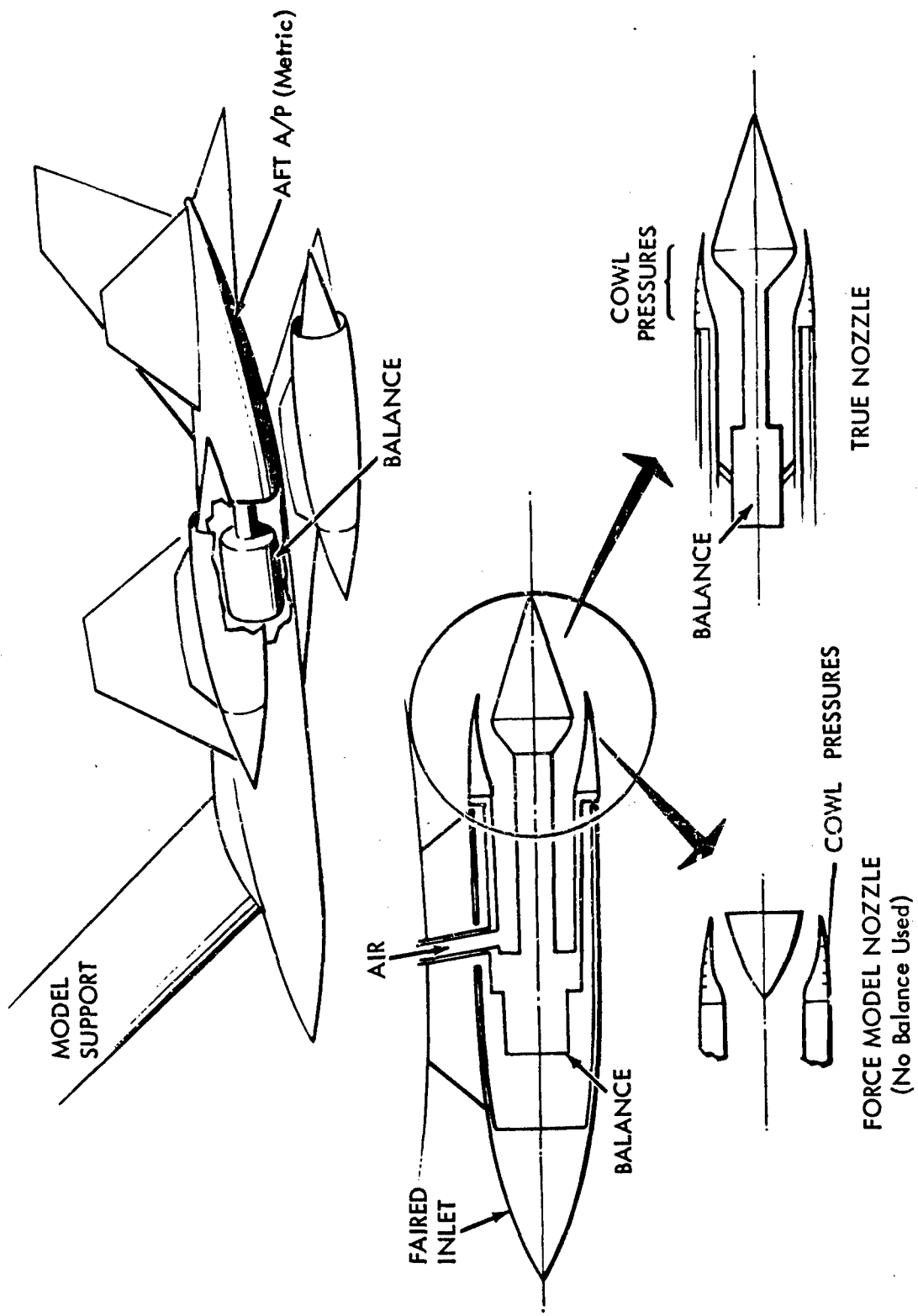
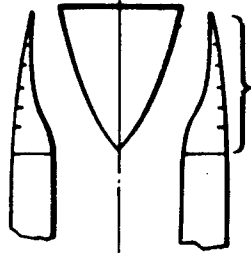


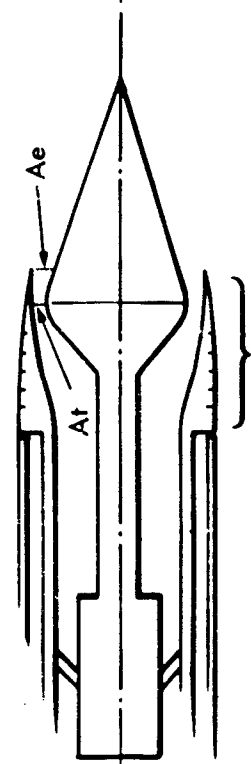
Figure 7 NOZZLE MODEL

FORCE MODEL NOZZLE
(No Balance Used)

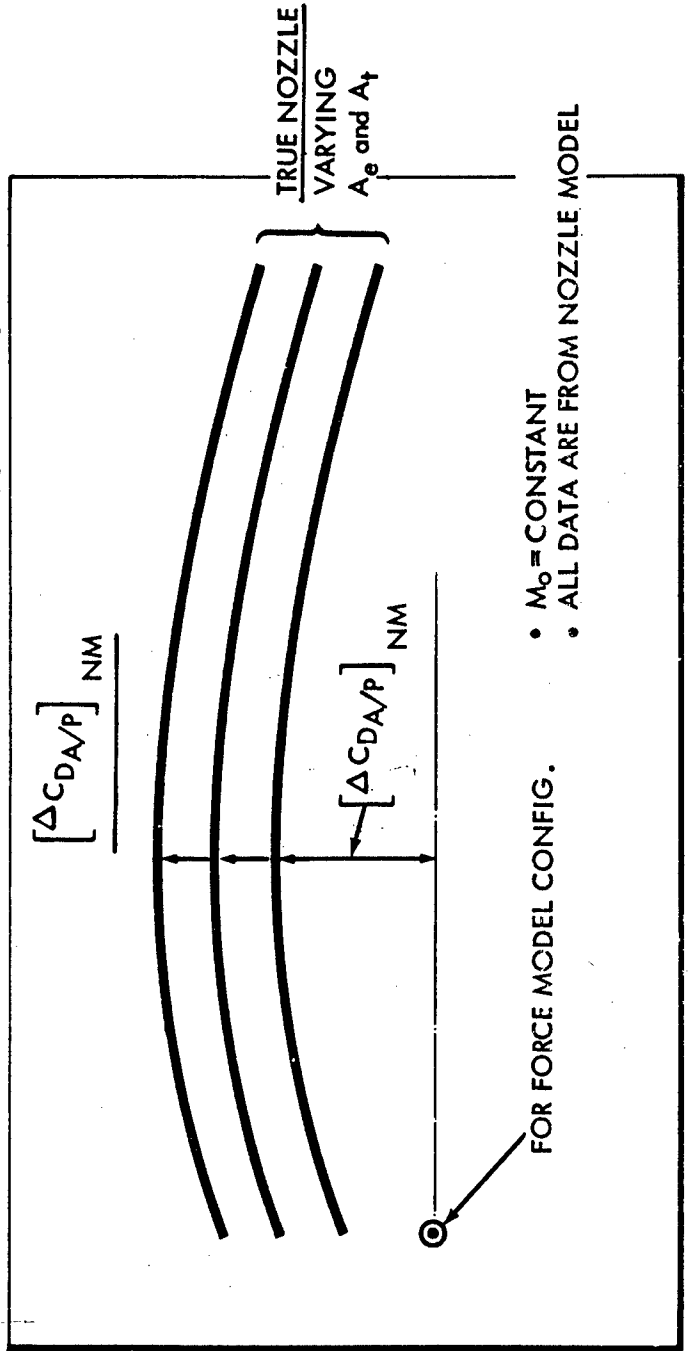


COWL PRESSURES

TRUE NOZZLE CONFIGURATIONS
(A_e and A_t Variable)



COWL PRESSURES

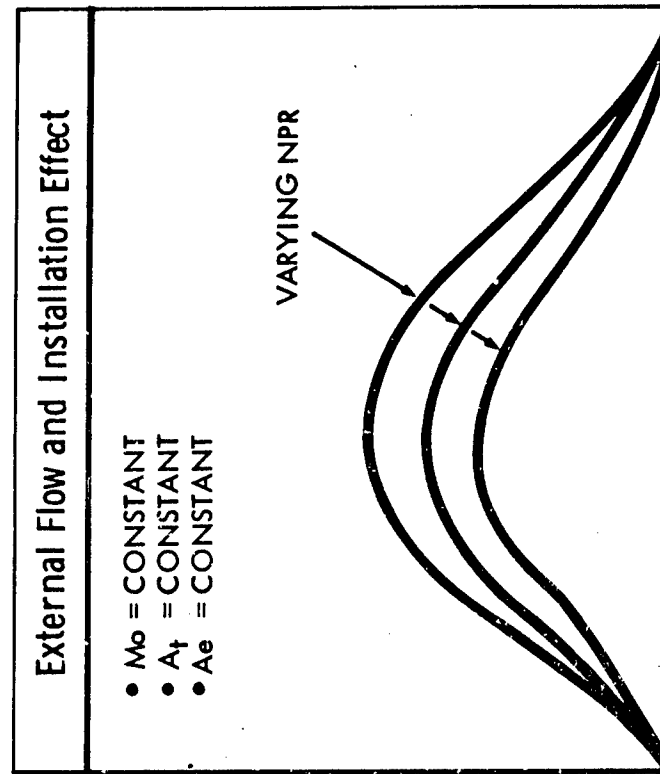
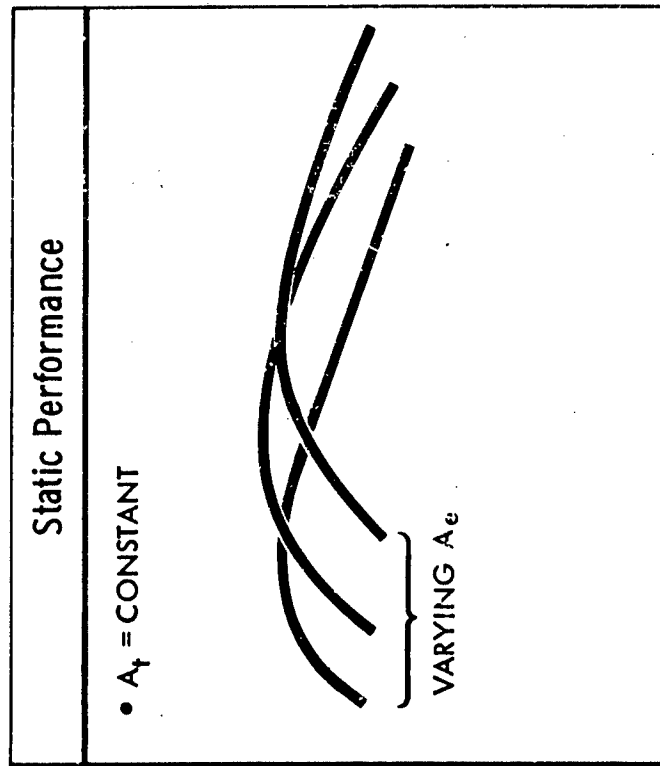


$C_D(\text{AFT A/P}) + \text{Nozzle}$

TRUE NOZZLE
VARYING
 A_e and A_t

- $M_0 = \text{CONSTANT}$
- ALL DATA ARE FROM NOZZLE MODEL

$$C_{VIN} = C_{VS} + \Delta C_V$$



C_{VS}

ΔC_V

NPR

M_0

Figure 9 INSTALLED NOZZLE PERFORMANCE COMPONENTS

DRAG COEFFICIENT

$$C_{D_{A/P}} = \left[C_{D_{FM}} \right]_{\frac{A_0}{A_i} = 1.0} + \left[C_{D_I} \right]_{\frac{A_0}{A_i}} + \left[\Delta C_{D_{A/P}} \right]_{NM}$$

$$\left[C_{D_{FM}} \right]_{\frac{A_0}{A_i} = 1.0} = f(M_0), \text{ for constant } \alpha, Re \text{ (from the Force Model)}$$

$$\left[C_{D_I} \right]_{\frac{A_0}{A_i}} = f\left(M_0, \frac{A_0}{A_i}\right), \text{ for constant } \alpha, Re \text{ (from the "small" and "large" scale Force Models)}$$

$$\left[\Delta C_{D_{A/P}} \right]_{NM} = f(M_0, NPR, Ae, At), \text{ for constant } \alpha, Re \text{ (from the nozzle model)}$$

GROSS THRUST COEFFICIENT

$$C_{V_{IN}} = \left[C_{V_s} \right] + \left[\Delta C_V \right]$$

$$\left[C_{V_s} \right] = f(NPR, Ae, At), \text{ for } M_0 = 0 \text{ (from the Nozzle Model)}$$

$$\left[\Delta C_V \right] = f(M_0, NPR, Ae, At), \text{ for constant } \alpha, Re \text{ (from the Nozzle Model)}$$

$$\text{DRAG} = \left(\left[C_{D_{FM}} \right]_{\frac{A_0}{A_1}=1.0} + \left[\Delta_1 C_{D_{A/P}} \right]_{NM} \right) \times \rho_0 \times A_{REF}$$

$$\left[C_{D_{FM}} \right]_{\frac{A_0}{A_1}=1.0} = f(M_0), \text{ for constant } \alpha, Re$$

$$\left[\Delta_1 C_{D_{A/P}} \right]_{NM} = f(M_0), \text{ for specified values of NPR, Ae, At} = f(M_0)$$

$$\text{Installed Net Thrust} = \left\{ \left(\left[C_{V_S} \right] + \left[\Delta C_V \right] - \left[\Delta'_2 C_{D_{A/P}} \right]_{NM} \right) \times F_{G_{id}} \right\} - \left\{ \left[C_{D_I} \right]_{\frac{A_0}{A_1}} \times \rho_0 \times A_{REF} \right\} - m_I V_0$$

$$C_{V_S} = f(\text{NPR, Ae, At}) = f(\text{engine power})$$

$$\Delta C_V = f(M_0, \text{NPR, Ae, At}) = f(M_0, \text{engine power})$$

$$\left[\Delta'_2 C_{D_{A/P}} \right]_{NM} = f(M_0, \text{NPR, Ae, At}) = f(M_0, \text{engine power})$$

$$F_{G_{id}} = f(M_0, \text{altitude, } T_0, \text{engine power})$$

$$C_{D_I} = f(M_0, A_0/A_1) = f(M_0, \text{engine power})$$

$$m_I = f(M_0, \text{altitude, } T_0, \text{engine power})$$

Figure 11 FINAL BOOKKEEPING SYSTEM

FIGHTER EXHAUST SYSTEM BLENDING*

D. Migdal

W. K. Greathouse

Grumman Aircraft Engineering Corporation

ABSTRACT

The scope of this presentation will be limited to exhaust nozzles for small compact twin-engine fighter installations powered with after-burning turbofan engines. Background information will be presented on F-111 type installations and previous exhaust nozzle choices to illustrate design features which may limit performance. Model test data will be used to display the merits of recently available nozzle designs and the effects of different fuselage installations. Interactions with the airframe, both external and internal, will be discussed. A compatible bookkeeping system used to account for these thrust and drag interactions will be outlined using an advanced fighter as an example. Tradeoffs of performance and mechanical aspects evolved from the selection of an exhaust system for this aircraft will be discussed.

*This paper not available for publication

**ANALYSIS AND DEMONSTRATION TECHNIQUES FOR INSTALLATION
AERODYNAMICS EFFECTS ON HIGH BYPASS TURBOFANS**

James L. Holdhusen

**FluidDyne Engineering Corporation
Minneapolis, Minnesota**

SUMMARY

The compressor performance of the fan stage largely determines the thrust delivered by a turbofan engine. The engine fuel consumption is determined by the efficiency of the gas generator, which must supply the energy for the turbine stage which drives the fan. The fan and gas generator are designed and developed as a unit and demonstrated in a direct-connect test stand by the engine manufacturer. The aircraft manufacturer then needs to determine the net thrust and specific fuel consumption at cruise. These may be predicted by using, first of all, the engine manufacturer's test data and introducing six additional aerodynamic factors:

1. Inlet internal recovery;
2. Inlet internal distortion;
3. Exhaust system thrust coefficient;
4. Inlet external drag;
5. Aft surface external drag;
6. Mutual interactions between the engine and aircraft flow fields.

Methods of conducting engine tests, wind tunnel tests, and flight tests are reviewed, and an analytical framework for combining the above six factors for predicting net cruise thrust is proposed. In this process, it is possible to identify and describe several minor aerodynamic phenomena which have not been modeled in the ground tests. A method for assessing the resulting uncertainty in predicting the net cruise thrust of the subsonic turbofan engine is presented.

LIST OF SYMBOLS

| | |
|-----------|--|
| A | Cross-sectional area (normal to x) |
| A'_s | Effective seal area from pressure calibration |
| C_T | Thrust coefficient |
| C_{T-D} | Thrust-minus-drag coefficient |
| D_a | Additive drag |
| D_I | Installation drag |
| H | Grounding force in balance or shear force in pylon |
| M | Mach number |
| m | Mass flow rate |
| P | Total pressure |
| p | Static pressure |
| S | Surface area (parallel to x) |
| T | Thrust force |
| t | Total temperature |
| τ | Shear stress |
| V | Velocity |
| x | Direction of flight |

SUBSCRIPTS

| | |
|----------|------------------------|
| c | Balance cavity |
| d | Demonstrator engine |
| f | Fan |
| g | Gross |
| I | Installed |
| i | Ideal |
| L | Inlet external lip |
| M | Powered nacelle model |
| s | Seal cavity |
| t | Turbine |
| u | Uninstalled |
| ∞ | Ambient or free stream |

I. INTRODUCTION

The high bypass ratio turbofan propulsion systems now being developed will power a new generation of transport aircraft whose cost effectiveness will be unparalleled in the history of commercial long-range transportation. The most important factors contributing to the reduction in cost per passenger-mile are the low specific fuel consumption (SFC of 0.6 pound of fuel per hour per pound of uninstalled cruise thrust) and the large size of the engines (40,000 pounds static thrust) which enables a single aircraft to carry 300 or more passengers. The low specific fuel consumption is a result of high thermodynamic efficiency of the engine cycle (pressure ratio of 25) combined with the high propulsive efficiency resulting from the low exhaust velocity of the fan (bypass ratio of 5).

When inlets, nozzles, and pylons are added to these relatively large engines there is a significant (perhaps ten percent) reduction in their cruise net thrust. This installation drag is probably still the least understood drag element of these new aircraft, as it was in 1965 (Ref. 1), although considerable progress has been made in techniques for analyzing, measuring, and reducing it.

It is the purpose of this paper to describe generally accepted definitions of the separate elements of installation drag and the tests which are used to determine their magnitude. Techniques for predicting the total installation drag, including interaction effects, will be described. Consideration will be limited to cruise performance, although installation drag analysis during take-off and climb can also be conducted with the methods described.

II. DETERMINATION OF UNINSTALLED CRUISE THRUST

The turbofan engine designer has traditionally been primarily concerned with "flange-to-flange" thermodynamic performance. An analysis of cruise thrust begins from his specification of the increase of total pressure and total temperature of the ingested air. Ideal thrust velocities for each of the two exit passages are calculated for an isentropic change of state from exhaust total pressure to ambient pressure. The ideal gross exhaust thrust is obtained by multiplying the mass flows in each passage by the ideal exhaust velocities:

$$T_{g_i} = m_f V_{i_f} + m_t V_{i_t} . \quad (1)$$

The ram drag is then subtracted to obtain a theoretically available net thrust for the turbofan engine called the ideal uninstalled cruise thrust, T_{u_i} :

$$T_{u_i} = m_f V_{i_f} + m_t V_{i_t} - m_\infty V_\infty . \quad (2)$$

The actual uninstalled cruise thrust, T_u , can be determined from ground tests of the engine and model tests of the exhaust nozzle system, as will be described. The difference between the actual uninstalled cruise thrust and the installed cruise thrust, T_I , is the installation drag:

$$D_I = T_u - T_I \quad (3)$$

and would be zero in inviscid subsonic flow.

Installation drag analysis is initially simplified by assuming that the propulsion system performance is not affected by the flow field of the aircraft. The aerodynamic interactions between the aircraft and the propulsion system are later applied as corrections to the isolated engine performance. If the portion of the pylon between the wing and the horizontal dashed line in Figure 1 is assumed to be lengthened sufficiently so that the flow field below the dashed line is not significantly changed by a further increase in

pylon length, the engine may be considered isolated. The portion of the pylon below the dashed line interface is considered to be part of the propulsion system.

In steady, level flight, the shear force in the pylon structure at this interface is the isolated engine installed cruise thrust. A cross-section of the isolated engine, which is assumed to operate with its axis parallel to the flight direction, is shown in Figures 2 and 3. The pylon shear force has not yet been measured in flight because of numerous practical difficulties. It is thus necessary to determine the installed cruise thrust by correcting the data obtained in ground tests of the engine, in which a corresponding pylon shear force can be measured, for the missing elements of installation drag.

Demonstration tests of the engine are conducted in test cells in which the static pressure can be maintained at cruise static pressure, p_∞ , (typically 0.25 atmosphere). Air with stagnation pressure and stagnation temperature corresponding to flight values (0.4 atmosphere and 0°F) is introduced at the upstream end of the engine (Figure 4). The engine is structurally isolated from the air supply ducting and the small gap is sealed with a flexible bellows, labyrinth seal, or fabric seal. The shear force in the pylon, H , is measured and transmitted to ground by a load cell.

In such a test, it is desirable to have the detailed internal flow processes in the engine simulate flight conditions as accurately as possible. Ideally, the supply ducting would have the shape of the captured streamtube and the inlet shape would match the flight inlet aft of the stagnation line. Such a configuration would create the transverse variations in static pressure and velocity near the inlet lip which occur in flight, if it were not for the boundary layer on the supply ducting. Even if the supply ducting terminates in a well-designed contraction, the boundary layer in the contraction would undoubtedly separate ahead of the simulated stagnation line and create an annular vortex before it reattaches. The practical alternative for ground testing is to introduce air at the inlet throat (Station 3, Figure 2) with as thin a boundary layer as possible so that the diffuser boundary layer has a maximum possibility of avoiding separation and reproducing flight performance.

This relatively minor detail brings to attention the first element of installation drag. In inviscid flow, every streamtube approaching the fan would have flight stagnation total pressure. Any loss of stagnation pressure in the diffuser will cause a reduction in the stagnation pressure leaving the engine, which will cause consequent reductions in V_{i_f} and V_{i_t} of Equation 1. The engine manufacturer specifies the derivative,

$$\frac{\partial T_u}{\partial P_5}$$

or its dimensionless equivalent, from analysis and tests, so that the first increment of installation drag (which is, in reality, a decrement of uninstalled thrust) is

$$\Delta D_1 = (P_\infty - P_5) \frac{\partial T_u}{\partial P_5} \quad (4)$$

This quantity is actually obtained from a set of performance curves (or a performance deck for a computer) at various values of corrected weight flow $\frac{m_\infty \sqrt{\theta}}{\delta}$ and corrected engine rotational speed $\frac{N}{\sqrt{\theta}}$.

Inlet studies for these engines reported to date generally show only a very small loss in cruise total pressure, and this loss probably is confined to the duct boundary layer. Current engine installation designs for commercial transports show a trend toward relatively long fan exhaust cowls, which raises the possibility that acceptable external aerodynamic performance for the cowl may be obtainable with the fan placed well forward of the cowl maximum external diameter. Overall engine length may then be significantly influenced by inlet diffuser length, and further studies to decrease this length may eventually lead to the conclusion that a shortened inlet diffuser resulting in some small inlet total pressure loss will optimize cruise performance.

The second factor which can reduce uninstalled thrust is total pressure or velocity distortion at the fan leading edge. The fan is normally able to tolerate some finite level of distortion without noticeable change in performance, but if the distortion index exceeds this threshold value, the fan output

average total pressure is reduced and a decrement in uninstalled thrust must be applied to the system performance. Again, symbolically, this increment in installation drag is

$$\Delta D_2 = \Delta P_5 \frac{\partial T_u}{\partial (\Delta P_5)} \quad (5)$$

where ΔP_5 is the total pressure variation across Station 5 in excess of the allowable threshold value. There is a current trend to analyze both total pressure and velocity variations as they affect fan performance, and a performance index for installation drag based on both of these factors may become industry practice in the future. The inlet flow at cruise is steady enough that fluctuations in velocity and total pressure are not a significant problem.

The third element of installation drag to be considered is the thrust loss resulting from inefficiencies in the fan and turbine exhaust systems. The "flange-to-flange" boundaries of the engine terminate at Stations 6 and 8 (Figure 3). These stations may be regarded as charging stations for the turbine and fan nozzles, and if the gross exhaust thrust is less than is theoretically available from an ideal nozzle system, a decrement in installed thrust will result. The most practical means of determining this increment of installation drag is by a model study as shown in Figures 5 and 6. Both the direct-connect test of the full-scale engine (Figure 4) and the models in Figures 5 and 6 involve similar flow phenomena on the aft pylon and turbine exhaust cowl. The drag on these components is automatically included in the measured force, H , which is obtained when air is fed to the fan and turbine exhaust charging stations of the model at cruise pressure ratio, so that these contributions to installation drag are properly accounted for. The model tests result in a thrust coefficient, C_T , which is the ratio of the actual gross exhaust thrust delivered minus the drag (under static conditions) on the turbine exhaust cowl and that part of the aft pylon inboard of the fan cowl trailing edge to the gross exhaust thrust an ideal nozzle would deliver at the same charging station conditions. The increment in installation drag is:

$$\Delta D_3 = (1 - C_T) T_{g_1} \quad (6)$$

In practice, the engine manufacturer guarantees the performance of the engine in the direct-connect tests of Figure 4. His demonstration tests are based on the measured pylon shear force, H , and include all of the elements of installation drag described to this point. The actual "flange-to-flange" performance (the actual uninstalled cruise thrust) may be calculated as follows. The cruise thrust of the demonstrator engine is:

$$T_d = m_\infty V_m - H + A'_s (p_m - p_\infty) - m_\infty V_\infty \quad (7)$$

where

V_m is the effective velocity which, when multiplied by m_∞ , gives the momentum flux in the airflow entering the demonstrator engine;

A'_s is the effective area of the seal between the air supply duct and the demonstrator engine;

p_m is the average static pressure over the entire cross-sectional area enclosed by the seal.

The uninstalled cruise thrust is larger than T_d by the amount of installation drag encountered by the demonstrator engine

$$T_u = T_d + \Delta D_1 + \Delta D_2 + \Delta D_3 \quad (8)$$

The model nozzle test and rakes in the inlet and charging stations of the demonstrator engine furnish the experimental data required to correct for these three increments of installation drag.

If the engine performance guarantees (SFC and thrust) are actually based on the uninstalled cruise thrust, it is necessary to determine these installation drag increments before the engine manufacturer can present demonstrator performance data. A more practical alternative, and one which is generally used at this time, is to guarantee the thrust performance, T_d , of the demonstrator engine with reference or demonstrator configurations for the inlet diffuser, pylon, fan exhaust nozzle, turbine exhaust cowl, and turbine exhaust

nozzle. Changes in flight performance resulting from changes in the final design of these components can then be initially assessed by model studies and later by direct-connect tests of the final flight version of the engine.

III. INCREMENTS OF INSTALLATION DRAG RESULTING FROM FLOW AROUND THE ENGINE

A. Inlet External Drag

The fan inlet cowl is defined as that part of the fan cowl and pylon surface which is forward of the maximum diameter and is not in contact with the captured streamtube (Station 1 to Station 4 in Figure 3). The goal of the inlet designer is to achieve a reduced pressure on this surface such that the axial component of the integrated relative surface pressure results in a thrust force equal to the additive drag. (Additive drag is the axial component of the integrated relative pressure on the captured streamtube up to the stagnation line.) Such complete additive drag cancellation would occur in inviscid flow (Ref. 2). Failure to achieve this level of lip suction is a consequence of viscous effects.

The high bypass turbofan inlet drag studies reported to date have in some cases depended on measurements of inlet pressure distribution to assess the degree of lip thrust achieved. Two practical difficulties occur in determining the difference between the lip suction force and additive drag:

1. The lip suction force is very strongly influenced by any errors in determining the location of the stagnation line.
2. An accurate solution for the compressible equations of motion of the flow ahead of the inlet must be calculated before the additive drag can be determined and compared with the measured lip suction force.

Both of these difficulties can be avoided if tests are carried out with an axial force measurement on inlet models. An arrangement which we are proposing to use in our transonic wind tunnel is shown in Figure 7.

After making the following definitions,

$$D_a = \int_{A_\infty}^{A_1} (p - p_\infty) dA$$

$$T_L = \int_{S_2}^{S_1} \tau dS + \int_{A_1}^{A_4} (p_\infty - p) dA - \int_{S_2}^{S_4} \tau dS$$

$$D'_L = D_a - T_L$$

it can be shown (see Appendix) that the lip drag, D'_L , can be calculated from measured quantities on such a test arrangement as:

$$D'_L = m_\infty (V_n - V_\infty) + A_n (p_n - p_s) + A_4 (p_c - p_\infty) + A'_s (p_s - p_c) - H \quad (9)$$

where V_n and A'_s have the same physical meaning as in Equation 7. After proper corrections have been made to D'_L to account for the change in skin friction, τ , for the higher Reynolds number of the aircraft installation, the fourth element of installation drag is simply

$$\Delta D_4 = D'_L \quad (10)$$

Such a test can also obviously incorporate studies of inlet total pressure loss and distortion without affecting the external drag.

B. Aft Surface External Drag

The effects of external flow on all of the components aft of the maximum fan cowl diameter can be determined from transonic wind tunnel tests of a model such as is shown in Figures 8 and 9. If this model is first tested with the wind tunnel shut off, the thrust coefficient, C_T , of Equation 6 will be measured. If the model is next tested with the wind tunnel operating at cruise Mach number, a lower thrust coefficient, commonly called the thrust-minus-drag coefficient, C_{T-D} , will be measured. (The appropriate definitions and equations for these coefficients are given in Ref. 3.) The difference between these coefficients when multiplied by the ideal gross exhaust thrust gives the aft surface external drag:

$$D'_{aft} = (C_T - C_{T-D}) T_{g1} \quad (11)$$

This drag is made up of the following elements:

1. the pressure drag and friction drag on the boattail and base of the fan exhaust cowl,
2. the pressure drag and friction drag on that part of the aft pylon which is outboard of the fan exhaust cowl trailing edge, and
3. any increase in turbine exhaust cowl drag and aft pylon drag resulting from interactions between the external flow and the fan exhaust flow.

When this drag is corrected by the skin friction on the outboard horizontal surface of the pylon (since this surface is never sheared by the external flow in flight) and for Reynolds number effects, the final increment of installation drag for the isolated nacelle is obtained:

$$\Delta D_5 = D_{aft} \quad (12)$$

In the test just described, the boundary layer growth on the support tube ahead of the model results in a boundary layer thickness at the fan cow maximum diameter which is somewhat thicker (relative to the cowl diameter) than would occur in flight. The support tube boundary layer and the absence of the flared portion of the captured streamtube also change the local pressure distribution at the inlet leading edge. We have conducted tests in which the effects of these factors have been studied as they might influence the fan cowl afterbody pressure distribution. The support tube was tested in its normal cylindrical (five inch diameter) shape and also with a shape which simulated a streamtube capture ratio of 0.75. The boundary layer thickness on the support tube was varied from 0.30 inch to 0.15 inch by blowing a layer of supersonic air along the support tube farther upstream (in the wind tunnel contraction, see Ref. 3). Neither of these factors caused an appreciable change in the pressure distribution on the fan exhaust cowl. This may be largely attributed to the fact that the fan exhaust cowls tested to date have been designed to have large radii and small boattail angles in the meridional plane. The resulting recompression on the boattail has been gradual

enough that separation was not encountered even with a boundary layer that was thicker than the corresponding flight value.

It will be noted that the grounded portion of the test configuration in Figures 7 and 8 begins or ends at the maximum diameter of the fan cowl. The total external aerodynamic drag ($D_L + D_{aft}$) should be independent of the longitudinal location of this gap as long as a consistent location is chosen for both models. It would perhaps be advantageous to locate the gap farther aft on both models, so that tests with the atypically thick boundary layer and with the simulated cylindrical captured streamtube (Figure 8) would have even less likelihood of affecting the measured installation drag.

IV. POWERED NACELLE MODELS

In 1965 there was developed a powered nacelle model of a high bypass ratio turbofan (Ref. 4). The primary purpose of the development was to find a better means of studying the effect of the combined flow fields of the engine and the aircraft than had previously been available using flow-through nacelle or blown nacelles (Ref. 5). Since that time, models have been designed and built for this purpose to simulate all three of the engines committed to production for the new generation of commercial transports (Pratt and Whitney JT9-Rolls-Royce RB.211, General Electric CF-6). Further data concerning engine-aircraft interaction from the original program have become available (Refs. 6 and 7) as well as a report describing the use of such models for studies of thrust reversers (Ref. 8). The advantages of using such a model for internal studies of inlets has also been mentioned (Ref. 9).

The fan blades and cowls for these powered nacelle models are designed to match full-scale performance as closely as possible. However, significant changes in the shape and number of the fan blades are required at the greatly reduced linear scale (1:25). Even so, these models (manufactured by Tech Development Corp., Dayton, Ohio) do develop the full fan total pressure ratio of the prototypes. The fan is driven by a high speed (80,000 r.p.m.) impulse turbine which is located in the volume occupied by the gas generator in the prototype engine (Figure 10). The turbine is driven by high pressure air (25 atmospheres) which is introduced through the pylon. Because of this the inlet mass flow is reduced by the reciprocal of the bypass ratio of the prototype if the fan exhaust nozzle is scaled.

A direct-connect test may obviously be made of the powered nacelle model (Figure 11) in the same manner that the full-scale engine is tested (Figure 4). The same wind tunnel tests to determine the external drag of the inlet (Figure 7) and the aft external drag of the pylon and exhaust system components (Figures 5 and 8) may also be made for the powered nacelle model as well as for the models of the full-scale engine. In fact, one single wind tunnel program would serve both for the powered nacelle model and the full-scale engine if the cowling and pylon shapes of the full-scale engine are

reproduced in the powered nacelle model. The only difference between the two sets of tests would be that the inlet model would have to be tested at both the cruise capture ratio of the full-scale engine and the somewhat lower capture ratio to which the powered nacelle model would be limited at cruise Mach number. The installed cruise thrust of the powered nacelle model can then be calculated.

$$T_I = T_u - \Delta D_1 - \Delta D_2 - \Delta D_3 - \Delta D_4 - \Delta D_5 \quad (13)$$

After this has been accomplished, the validity of all of the above procedures, tests, and definitions can be subjected to a critical test if the powered nacelle model is tested in a transonic wind tunnel at the cruise Mach number (Figures 11 and 12) and the pylon shear force, H , is measured. This measured pylon shear force should equal the installed cruise thrust for the powered nacelle model calculated from Equation 13. The same kind of test could be made for the full-scale engine except that the largest suitable wind tunnel for such a test has a test section area which is only a small fraction of the size that would be required for transonic tests of these large turbofans.

The point of the discussion above can be made in a different way. The cruise thrust of the powered nacelle model without external flow can be calculated from the tests of Figure 11 by

$$T_M = m_\infty V_m - H + A'_s (p_m - p_\infty) - m_\infty V_\infty \quad (14)$$

where the symbols have the same meaning as those following Equation 7. The cruise thrust with external flow is H in Figure 10. The difference between these forces should equal the sum of the increments of external drag resulting from flow around the powered nacelle model.

$$T_M - H \stackrel{?}{=} \Delta D_4 + \Delta D_5 \quad (15)$$

The amount by which this equation is not satisfied should, in principle, result only from the following two factors:

1. improper simulation of the flow properties upstream of Station 3 in the direct-connect test

and

2. excessive boundary layer thickness on the fan exhaust cowl and failure to simulate the flared shape of the captured streamtube in the tests of Figure 8.

A third factor which may also influence the comparison is the effect of uncertainties in the quantity m_{∞} in Equation 14. The cruise mass flow of the powered nacelle model must be measured in the wind tunnel test before the direct-connect test can be run. This can be accomplished if the transonic wind tunnel tests of the blown nacelle model or the direct-connect tests of the powered nacelle model are used to obtain a discharge coefficient for the exhaust nozzles. If the charging station total pressures for the nozzles are measured in the wind tunnel tests of the powered nacelle model, the captured mass flow can then be calculated.

A second alternative explanation of the same general conclusion is equally meaningful. If a powered nacelle model, an ejector-powered model, or a small turbofan engine can be tested both in a direct-connect test stand and in a transonic wind tunnel and if the external flow around any of these devices is the same as around a full-scale turbofan engine, the full-scale installation drag increments, ΔD_4 and ΔD_5 , can be determined by applying simple and well-known scaling factors for size and Reynolds number effects.

V. CONCLUDING REMARKS

The foregoing discussion has attempted to define by equations the principles and methods of analysis used in conducting tests to optimize and determine installation drag of high bypass turbofans. Several alternatives are possible in practice, such as using the inlet instead of the exhaust nozzles to measure the mass flow in flight and in the wind tunnel tests of the powered nacelle model. Practical means of analyzing, simulating, and testing the effects of nonuniform temperature, velocity, static pressure, and flow direction at the charging stations and at the nozzle exits have been developed in the past few years. Perhaps the most troublesome problem at this stage of development is coping with exhaust nozzles which become unchoked because of external flow effects. Even so, it is probably now possible to determine installation drag to within one percent of cruise thrust, although a completely integrated model program to demonstrate this has yet to be conducted. Incremental differences between alternative designs can be determined to one-half percent of cruise thrust, or one-sixth percent of gross exhaust thrust, at the 95 percent confidence level.

The basic difficulty encountered in optimizing and measuring installation drag is that the drag-producing flow fields occur in close proximity to flow fields of the propulsion system in which very large aerodynamic and thermodynamic gradients exist. Quite sophisticated techniques have been developed for measuring the exhaust system thrust coefficient (Item 3 in the Summary) and the aft surface external drag (Item 5). These two elements undoubtedly account for much more drag at cruise than the combination of all of the other four elements. The inlet external drag remains a somewhat elusive quantity for high bypass turbofans, perhaps because it is so small. The same status exists for Item 6, but this element may not remain small if the engines must be moved closer to the wing. An additional element of installation drag which has not been discussed here must also be included in the final assessment. This is the increase in inlet drag and exhaust system drag which results from leakage through auxiliary inlet doors and thrust reverser systems. Such leakage drags can be determined by the model studies described herein.

The engine cowlings and pylons are important components of the turbofan engine not only because of their influence on the installed thrust performance but also because of their large weight. In view of the fact that the primary design responsibility for these components now rests with the airframe manufacturer, and not the engine manufacturer, it would seem that a disproportionately large effort has been expended by the engine companies in developing test techniques and design information. This is a result of the intense competition involved in serving their customers. Because of this healthy and vigorous competition, essentially no specific performance information on installation drag has yet appeared in the literature.

A possible eventual goal for the engine companies, and one which the airframe companies would probably welcome, would be the complete responsibility for the installed thrust performance of the engines. A trend in this direction is evident in that in many cases the engine companies are building and guaranteeing the performance of the thrust reverser subsystems. This new definition of responsibilities will probably have to await the development of an in-flight thrust measurement system in the pylon, so that performance guarantees (at least of an isolated engine on a flying test bed) can be demonstrated. Such a division of responsibilities would also obviate the need for the complicated analyses of scrubbing drag on the aft pylon and turbine exhaust cowl which must now be made to correct the demonstrator engine direct-connect performance data to the contract guarantees.

REFERENCES

1. Swan, Walter C. A Discussion of Aerodynamic Problems on Integration of Propulsion Systems with Airframe on Transport Aircraft. Aerodynamics of Power Plant Installation. AGARDograph 103, Part 1, October 1965.
2. Klein, Harold The Calculation of the Scoop Drag for a General Configuration in a Supersonic Stream. McDonnell Douglas Company. Douglas Report No. SM-13744, April 1950.
3. Holdhusen, James S.
Lamb, Owen P. Scale Model Studies of Exhaust Nozzle Performance. AIAA Second Propulsion Joint Specialist Conference. AIAA Paper No. 66-641, June 1966.
4. Kutney, John T. Wind Tunnel Simulation of Inlet and Exhaust System Effects with the Powered Nacelle for Wing-Nacelle Combinations. General Electric Report No. R66FPD207, June 1966.
5. Lawrence, Robert L. Testing as an Aid to Locating Engines on Subsonic Transports. AIAA Second Propulsion Joint Specialist Conference. AIAA Paper No. 66-640, June 1966.
6. Patterson, James C., Jr. A Wind-Tunnel Investigation of Jet-Wake Effect of a High-Bypass Engine on Wing-Nacelle Interference Drag of a Subsonic Transport. NASA TN D-4693, August 1968.
7. Paterson, J. H. Aerodynamic Design Features of the C-5A. SAE Paper 670847, October 1967.
8. Poland, Dyckman T. The Aerodynamics of Thrust Reversers for High Bypass Turbofans. AIAA Third Propulsion Joint Specialist Conference. AIAA Paper No. 67-418, July 1967.
9. Cotter, H. N. Integration of Inlet and Engine - An Engine Man's Point of View. SAE Paper 680286, April 1968.

APPENDIX

If the internal surfaces of the shaded body of Figure 7 exert a force on the captured streamtube whose axial component, ϕ , is assumed to be directed downstream, the axial force on the captured streamtube between a station a of the model in undisturbed flow and the exit plane of the nozzle, n , is:

$$p_{\infty}A_{\infty} + \int_{A_{\infty}}^{A_1} p dA + \phi - p_n A_n$$

This force may be equated to the increase in the axial component of momentum flux of the captured streamtube between these two reference stations:

$$p_{\infty}A_{\infty} + \int_{A_{\infty}}^{A_1} p dA + \phi - p_n A_n = m_{\infty} V_n - m_{\infty} V_{\infty}$$

An equal but opposite force, $-\phi$, must be exerted by the streamtube on the body. Since the body is in static equilibrium, the total axial force acting on the surface of the body must be zero:

$$-\phi + \int_{A_1}^{A_4} p dA - \int_{S_2}^{S_1} \tau dS + \int_{S_2}^{S_4} \tau dS - p_c (A_4 - A'_s) - p_s (A'_s - A_n) + H$$

Simultaneous solution of the above two equations eliminates the force ϕ , giving

$$-m_{\infty} V_n + m_{\infty} V_{\infty} - p_n A_n + \int_{A_{\infty}}^{A_1} p dA + p_{\infty} A_{\infty} + \int_{A_1}^{A_4} p dA - \int_{S_2}^{S_1} \tau dS + \int_{S_2}^{S_4} \tau dS - p_c (A_4 - A'_s) - p_s (A'_s - A_n) + H = 0$$

Substitution of the definitions on pp. 8 and 9 into this equation gives Equation

In the derivation above, dA and dS are the normal and streamwise increments of the captured streamtube inlet surface area and τ and p are scalar quantities. The limits of integration for the axial shear loads are used in the sense that

$S_1 > S_2$ and $S_4 > S_2$. These awkward definitions could have been avoided if linear coordinates or vector notation had been used but at some sacrifice of clarity in displaying the forces involved.

It appears that the skin friction force between the stagnation line and the leading edge of the inlet contributes to the engine thrust. It is not recommended, however, that this surface be roughened to decrease the installation drag. The resulting increase in boundary layer displacement thickness would cause a net decrease in the actual lip force, T_L .

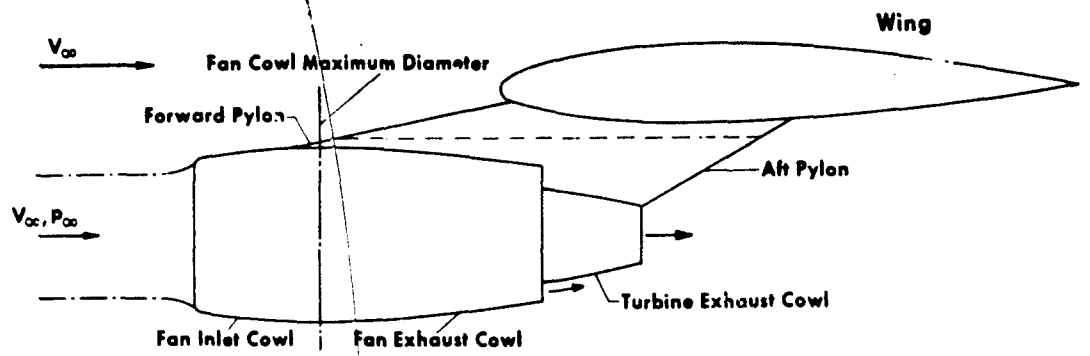


Figure 1. External Components of Turbofan Engine

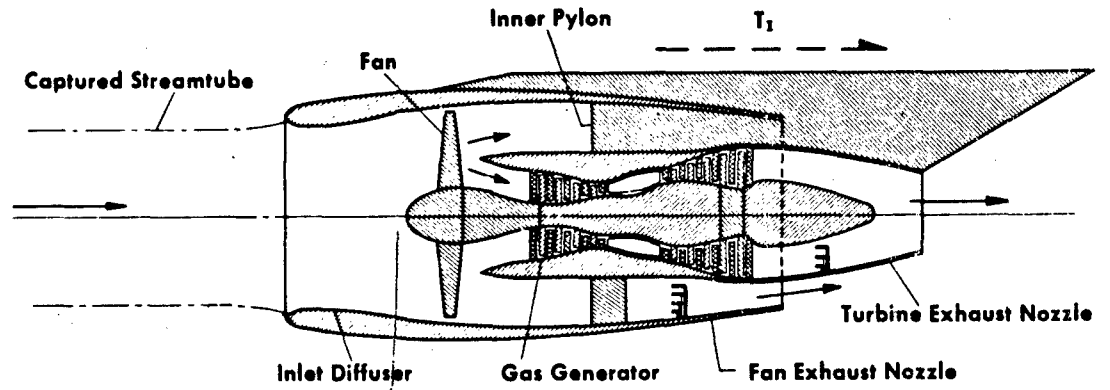


Figure 2. Internal Components of Turbofan Engine

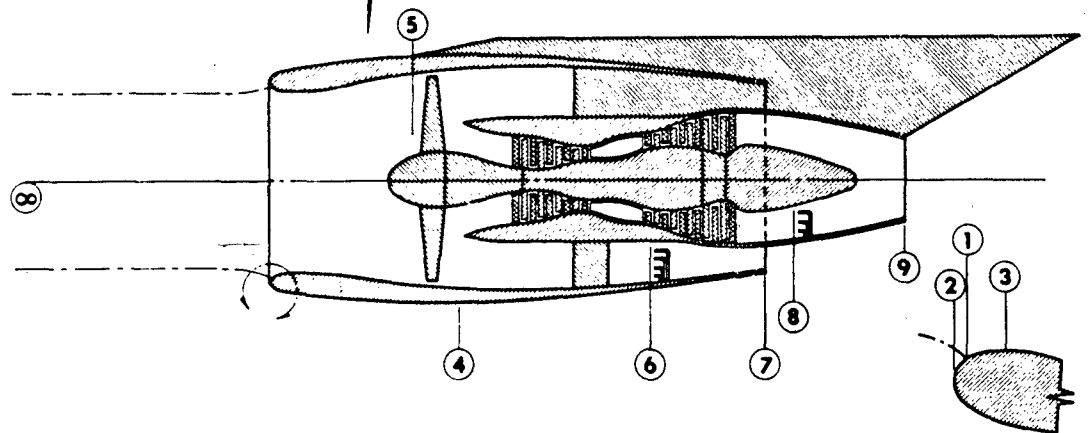


Figure 3. Station Designations for Turbofan Engine

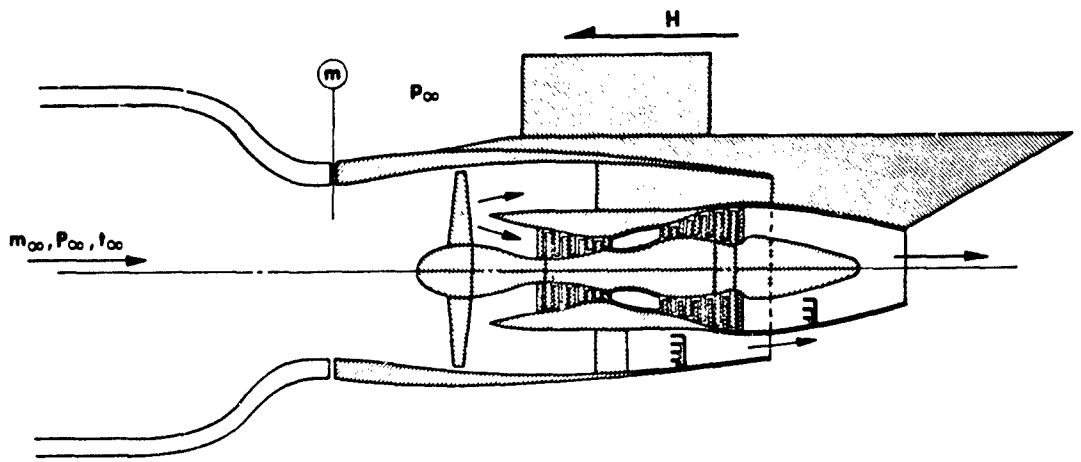


Figure 4. Direct-Connect Test of Demonstrator Engine

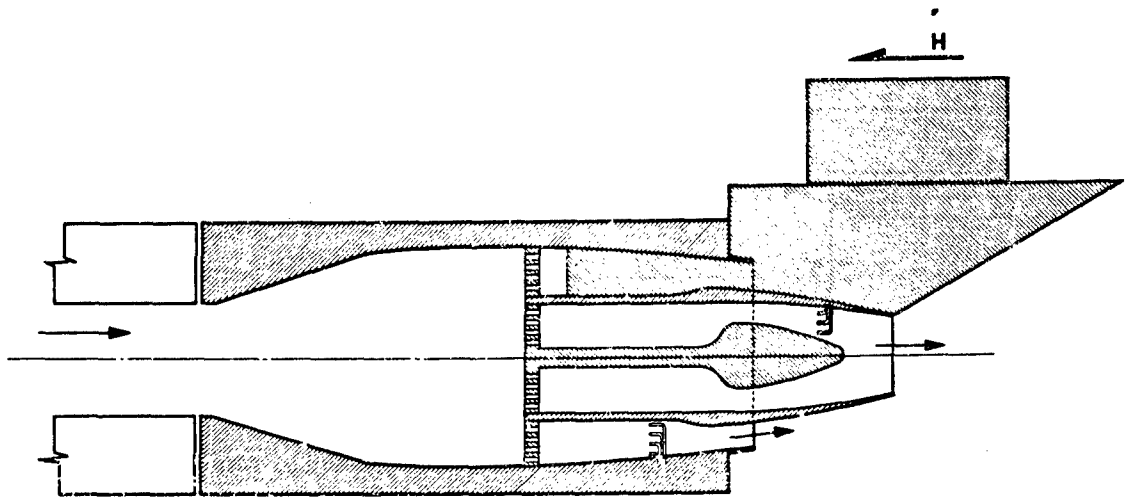


Figure 5. Static Test of Blown Nacelle Model

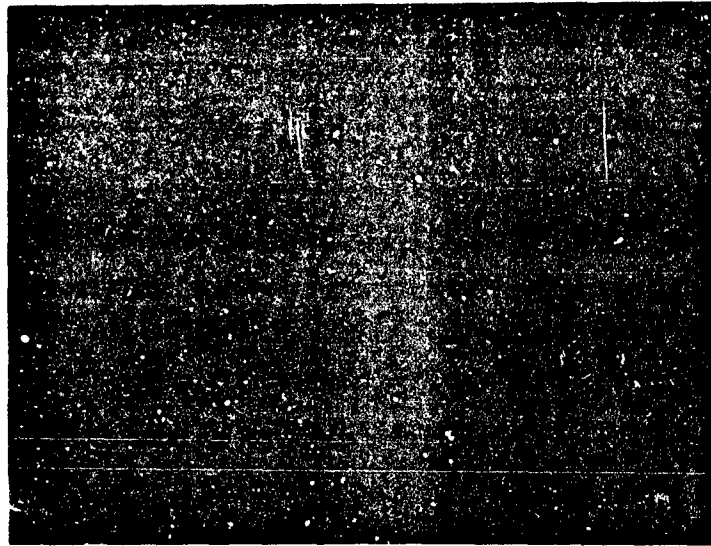


Figure 6. Turbofan Exhaust Nozzle Model in Static Test Stand

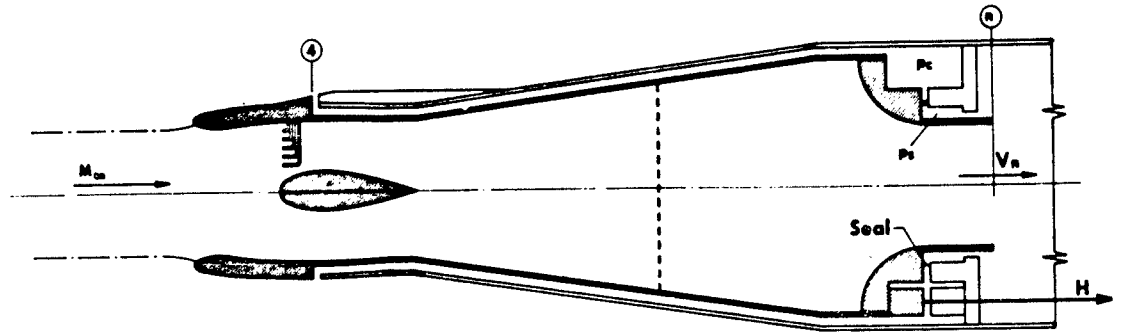


Figure 7. Wind Tunnel Test of Inlet Model

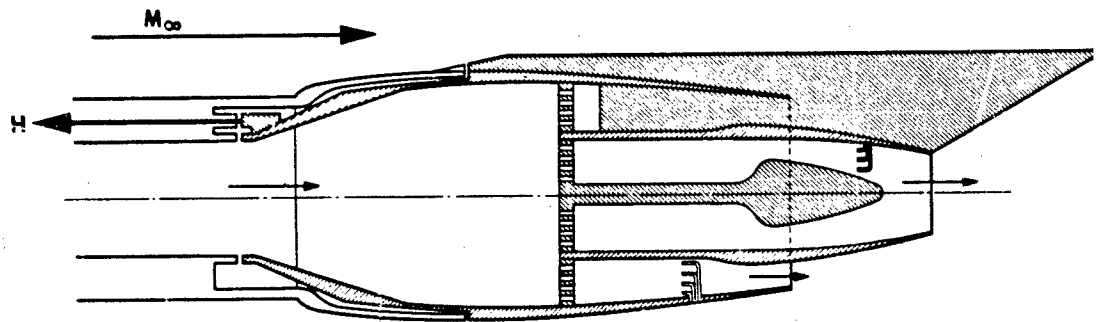


Figure 8. Wind Tunnel Test of Blown Nacelle Model

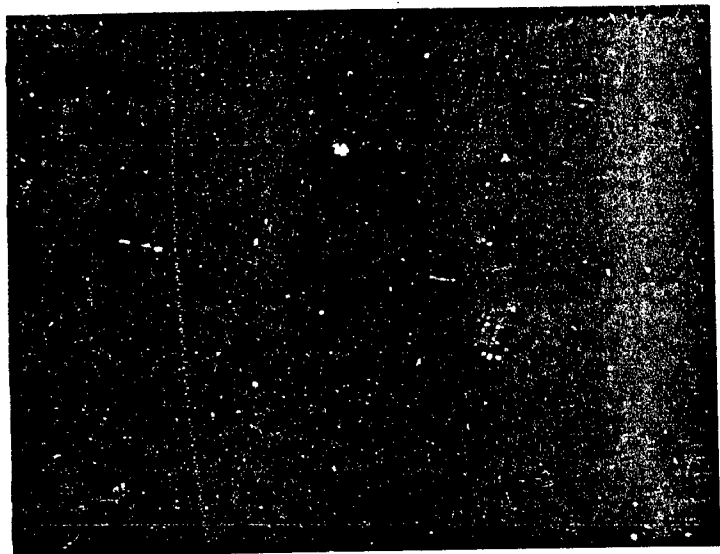


Figure 9. Turbofan Exhaust Nozzle Model in Transonic Wind Tunnel

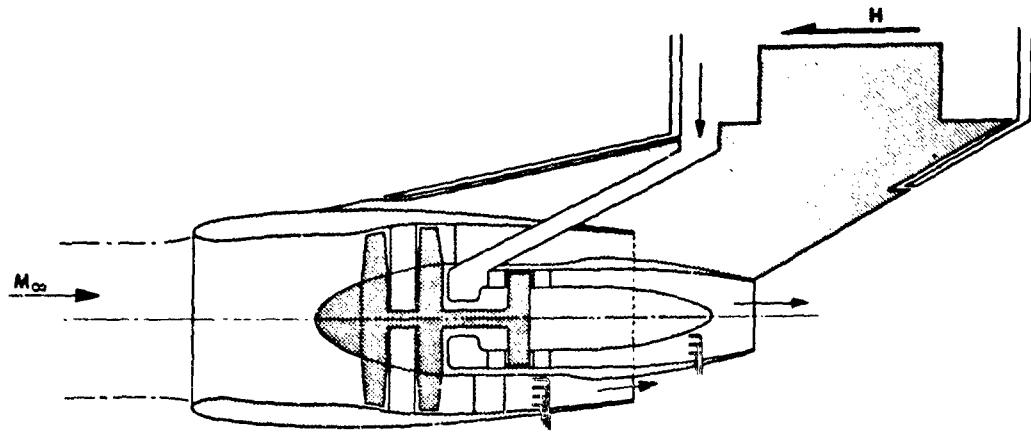


Figure 10. Wind Tunnel Test of Powered Nacelle Model

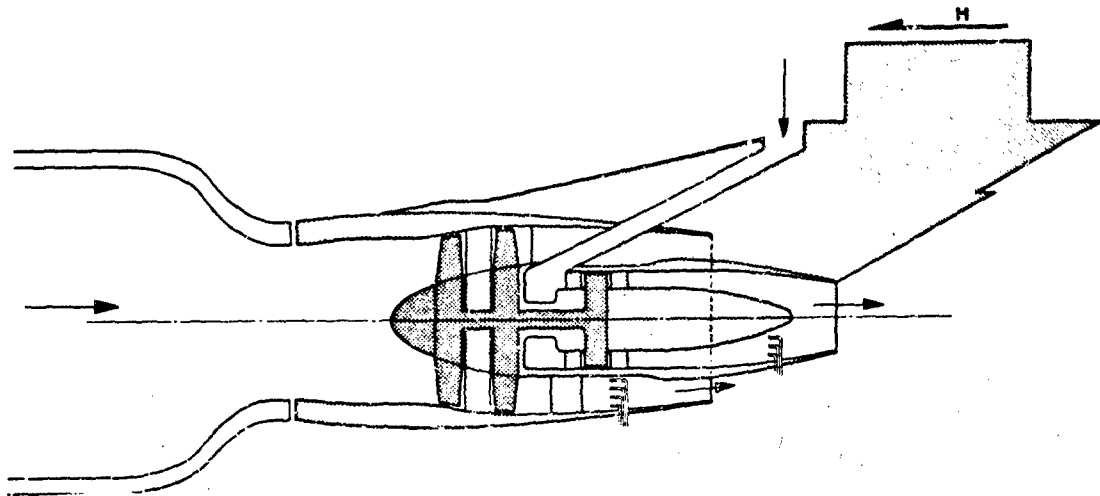


Figure 11. Direct-Connect Test of Powered Nacelle Model



Figure 12. Powered Nacelle Model in Transonic Wind Tunnel

PROPULSION SYSTEM INTEGRATED PERFORMANCE

(24 June 1969)

**H. I. Bush, Chairman
Air Force Aero Propulsion Laboratory**

SESSION II. EXHAUST SYSTEM CONSIDERATION

**Sqn Ldr Brian Brimelow, RAF, Cochairman
Air Force Aero Propulsion Laboratory**

FORCE MEASUREMENT OF AFTERBODY INTERACTION DRAG
AT TRANSONIC AND SUPERSONIC MACH NUMBERS
WITH PROPULSION EXIT PARAMETERS SIMULATED

P. L. Lemoine, Wind Tunnels Group

North American Rockwell Corporation Los Angeles Division

ABSTRACT

Wind tunnel tests were conducted to measure the drag arising from the interaction of the jet exhaust and external flow fields on an air vehicle afterbody. The model used was designed to simulate the complete air vehicle with various jet exit configurations and propulsion exit parameters. The model contained four exits to provide cold air simulation of the air vehicle propulsion units with a metric afterbody shell to measure the interaction drag of various nozzle shapes. The forces were measured by a six-component internal balance located in the forward fuselage section, and an additional normal force member at the afterbody. Pressure distributions over the model afterbody and nozzle shrouds and model internal chamber pressures and flow parameters were measured concurrently with the force data. The model was calibrated statically and tested in North American Rockwell's Trisonic Wind Tunnel statically and through the mach number range from $M = 0.60$ to 2.0 . The purpose of this paper is to present the model design and test techniques employed.

INTRODUCTION

The accurate estimation of air vehicle flight performance requires experimental data on all components of the vehicle. One of the major components is the vehicle afterbody configuration, including the installed propulsion unit exit nozzles throughout the jet exhaust exit area range.

A test program was recently undertaken at North American Rockwell Corporation to experimentally investigate the effects on the afterbody forces of the interacting external and jet exhaust plume flow fields generated by installed propulsion units through a range of vehicle operating flight conditions. The objective of this program was to obtain these forces with the jet exit flow simulated as an increment from a reference (no-flow) model.

This program required obtaining wind tunnel test data on the afterbody of a scaled representation of a typical air vehicle with exhaust nozzle exit conditions simulated. The entire vehicle must be simulated to duplicate the flow field approaching the afterbody and be tested throughout the mach number range from $M = 0.6$ to 2.0 and angle-of-attack range from $\alpha = 0^\circ$ to 12° . To obtain far-field and near-field effects, four nozzles were required to simulate exit propulsion units; one pair of plug nozzles and one pair of convergent-divergent (C-D) nozzles. Measurements of forces acting on the external surfaces of the afterbody were required to determine the force change with jet flow on and off. Pressure distributions over the afterbody were needed to diagnose and substantiate the measured force data. Because interaction drag is critical to the exit of the nozzle, the model was required to maintain scaled dimensions at the exit plane. To assist the analysis of the data, visualization of the jet plume flow was obtained at each test point.

MODEL TECHNIQUES

The model tested was a scaled representation of a variable sweep fighter type air vehicle design. The wing was simulated in the swept forward (30° LE) and swept aft (70° LE) to simulate real conditions of the approaching flow field. The model contained two pair of simulated propulsion system exit nozzles. One pair of ping nozzles, designed to obtain far field and near field effects, extended from the side of the lower fuselage just aft of the wing trailing edge. The other pair of nozzles, located at the base of the model, was designed to simulate convergent-divergent (C-D) nozzle exits.

The jet exit plume was simulated using ambient temperature air. Controlled air flow was conducted to two plenums, in tandem arrangement, through the model support strut. The strut entered the top of the fuselage so that it could be faired to simulate the vertical tail trailing edge, and thereby minimize the effect of its wake on the afterbody. The strut was swept forward to place the model such that it would not be struck by the shock emanating from the flowthrough sting at $M = 1.25$ (figure 1). The forward plenum supplied the two-plug nozzle exits and the aft plenum supplied the two C-D nozzle exits (figure 2). Pressure-drop plates were provided at the plenum exit to maintain a low mach number in the small size plenum.

The model afterbody, aft of the wing trailing edge, was built as a metric shell around the flow nozzle plumbing (figure 3), and included the C-D nozzle shrouds to the base of the model as well as a small segment of the C-D nozzle internal lines. The metric shell also included the horizontal tails. The presence of a vertical tail was simulated by a nonmetric fairing added to the model flowthrough strut, that extended from the strut maximum thickness to the tail trailing edge line (figure 4).

The purpose of the test was to determine the effect of the simulated jet exit flow on the air vehicle forces; therefore, the nozzle shrouds were built as a shell free of the nonmetric nozzles. A sharp trailing edge at the exit station of the nozzles was considered desirable to properly simulate the full scale geometry and produce corresponding model scale effects of the interacting internal jet and external flow fields. To maintain this trailing edge and measure the interaction forces, the C-D nozzles were constructed so that the separation between the nonmetric nozzle and the metric shroud was located internally in the aft section of the nozzle (figure 5). Inflatable seals were installed in the chamber between the metric shroud and nonmetric nozzle to prevent secondary flow from being induced through the vents in the

model shell by large pressure variations generated by both the internal and external flow fields. The resulting dead chamber corrections, to the data, are accurately determined. These seals were attached to each of the nonmetric nozzle flow tubes at an area of constant cross-section. The separation line between the metric and nonmetric plug nozzle shroud (figure 6) was located on the external shroud forward of the nozzle exit. A seal was not installed at this break because the split was not exposed to nozzle flow fields. Figure 7 illustrates the metric and nonmetric arrangement of these nozzles.

Interchangeable C-D nozzles and shrouds were constructed so that nozzle configurations having exit area (A_9) to nozzle cross-section area (A_m) of 0.15 to 1.0 (corresponding to variation of the aft boattail angle from 0° to 13.5°) could be tested. The reference configuration for these tests was a nonmetric conical extension of the boattail angle at $A_9/A_m = 0.50$. Figure 8 shows the nozzles tested and the conical fairings which were mounted to the nonmetric nozzle tube. One of these was used as a jet-off reference configuration.

FORCE INSTRUMENTATION

The model afterbody forces were measured by a six-component task corporation force balance, located in the forward fuselage ahead of the model flow plenums, and a normal force flexure N_3 at the afterbody (figure 3). A load carrying sting was required to extend from the balance to the afterbody, free of the nonmetric model parts, to transmit the afterbody forces to the balance. The additional normal force measuring support (N_3), flexured to free the body in chord force and side force, was provided to support the afterbody and was located at the approximate center of pressure of the afterbody. This support was required because the deflections under load would have been excessive and the accuracy of measurement would have suffered because of the large load transfer distance involved. The metric afterbody and load carrying sting arrangement is pictured in figure 9, with the nonmetric plumbing.

PRESSURE INSTRUMENTATION

The model was instrumented with 90 pressure taps to establish the nozzle flow parameters, determine the internal model chamber pressures, and the pressure distribution over the model afterbody. Each exit nozzle approach pipe contained a calibrated flow meter section to determine the weight flow split between the nozzles being fed by a common plenum. Exit total pressure was measured in each flow tube ahead of the nozzle throat. Static pressure taps were located internally as close to the exit of each nozzle as possible to determine nozzle exit static pressures.

Internal model cavities and model split areas were instrumented with pressure taps to determine corrections to the force data resulting from cavity and sting, area variations, and base area at the model split locations. The afterbody and nozzle shrouds were instrumented externally to permit determination of chord force by integration of the pressure distribution over the body shell. The 59 static pressure taps on the body shell were required to bridge the metric and nonmetric parts of the model with no restriction to the force measurements.

CALIBRATIONS

The model assembled on the strut was calibrated to determine the installed slopes of each force element and their interaction as well as the interference of the seal and pressure tube installation. The calibration also served as a model function checkout under load. The calibration was conducted by loading all force components with all pressure leads connected in the model. The model was first loaded in chord force with and without the 59 flexible pressure leads that bridge the metric and nonmetric model parts. The resulting slopes were compared with the balance-alone calibration, to ascertain that no interference was derived from the pressure tube installation. Comparison of calibrations revealed that without pressure tubes connected, chord force slopes obtained before and after installing the balance compared within 0.1 percent, thus proving that the third normal force member had no interference effect on chord force measurement. Secondly, the comparison with the pressure-tubes-installed-slope was within 1 percent, thereby proving that the pressure instrumentation caused essentially no significant interference with the force measurement.

Additional calibrations were required to determine the effect of the inflated seal and the effect of differential pressure across the seal on chord force and normal force.

The model was loaded along the axis of the balance chord force with various pressures applied to the seal. The chord force slope was determined at each seal pressure and the variation due to seal pressure determined. Figure 10 shows that the slope variation with seal pressure is less than 1 percent over the range from $P_{\text{seal}} = 8$ psig to 30 psig, although a slightly larger effect occurs when the seal is initially inflated.

The seal effect on normal force was investigated with constant normal loads applied at the third normal force location. The results (figure 11) show that once the seal is inflated, the seal pressure effect is negligible.

To determine the interaction on the metric body due to a pressure difference across the seal, the C-D nozzle shroud chamber was pressurized with the seal inflated at constant pressure (figure 12). With increasing seal pressure, a given ΔP across the seal transmits more force to the balance. Therefore, the test was conducted with the minimum seal pressure applied to adequately support the seal, minimizing the resulting restriction.

DATA REDUCTION

The measured afterbody forces C_N , C_m , and C_C were resolved at the air vehicle reference center located at the 25 percent wing MAC, swept forward, station at the intersection of the convergent-divergent nozzle centerline. These data were reduced from the balance chord force (C), and balance forces (N_1 and N_2), and the N_3 load gage using the complete model calibration slopes and interactions. These data were corrected for the pressure forces acting on the internal parts of the afterbody, balance cavity, and along the load-carrying sting. The data was also corrected for the pressure area force acting on the segment of the internal convergent-divergent nozzle aft of the split line. The force derived from pressure acting on the nonmetric external plug nozzle shroud was added to the force data so all external forces are accounted for.

Afterbody chord force, exclusive of the horizontal tail, was also derived from integration of the pressure data obtained from the external model pressures.

$$C_{C \text{ (pressure)}} = \sum_{x=1}^{x=56} \frac{P_x - P_o}{q} \frac{Ax}{S_w}$$

To use the same program, for tests or calibrations with and without external flow, the static data force was reduced to coefficient form using a q of 1,000 psf and a static pressure of P ambient

$$C_{C \text{ STATIC}} = \frac{C}{S_w \cdot 1,000}$$

TEST PROCEDURE

FACILITY DESCRIPTION

These tests were conducted in the North American Rockwell Corporation Trisonic Wind Tunnel (TWT). This facility is an atmospheric exhaust, blowdown tunnel capable of operating at mach numbers from 0.1 to 3.5, with 7 x 7-foot tandem test sections. The forward test section with solid walls was used for the supersonic test at mach numbers of 1.7 and 2.0. The transonic tests from mach numbers of 0.6 through 1.25 were conducted in the 19.7 percent perforated walls.

Two auxiliary systems at the TWT were developed to conduct these tests. One was the auxiliary air system which provides 350 psi, 13 pounds per second airflow, through three independently controlled flow streams to the model. The air system controller, built at the TWT, steps the airflow rate of each system as programmed at a preselected interval and controls the flow on system total pressure. Flow step and stabilized flow control is accomplished in 1-1/2 seconds. Two of the air streams were utilized by this test program and five test points per flow were obtained.

The other new system was a shadowgraph system of 14- x 18-inch format which provided pictures at the rate of one every 2 seconds. This system was used to provide visualization of the nozzle exit plumes at each test point in the transonic test section. This system is automatic and is integrated into the TWT tunnel control system so that the light source is fired concurrently with each data point.

TEST TECHNIQUE

The model was installed in the tunnel on a flow-through sting attached to the tunnel pitch sector (figures 1 and 13). The two independent air streams (plug nozzle and convergent-divergent), controlled by the auxiliary air system, were conducted to the model-sting assembly through two flexible hoses to allow for pitching the sector. Total pressure probes were installed in the flexible line at the connection to the sting. The total pressure measured here was used as the control point for the auxiliary air system nozzle flow.

The air system controllers were set up prior to each run to control each of the desired exit nozzle pressures for that run. The nozzle exit flow was established for the first data point prior to initiation of the

tunnel flow. The model pressures were allowed 3 seconds to stabilize between test points and the data from two data scans were selected at each test point for reduction. At this rate, five test points per 25-second blow were obtained whether angles of attack or nozzle pressure ratio were variable. The convergent-divergent nozzle simulation tests were run with the seal inflated with a preselected constant pressure. The pressure value (14.8 psig) was required to provide an adequate barrier against the pressures acting in the nozzle chamber during the test. This seal pressure was applied through a reservoir to insure stabilization.

Static runs were conducted in the tunnel with no tunnel flow to evaluate the effects of the simulated nozzle exit flow on the force measurement. These static tests were run for each exit nozzle configuration, over the range of pressure ratios limited by the air supply. This limitation prevented the pressure ratio range, encountered at mach numbers of $M = 1.25$ and above from being investigated statically.

RESULTS

From the static runs, the interference on the measured chord force caused by the exit nozzle flow was determined (figures 14 and 15). Since the force data is corrected for internal forces, and no resulting chord force from the afterbody pressure integration existed, the resulting data are forces acting on the metric parts which are not accounted for by the internal pressure instrumentation. From figure 14 it can be seen that practically no interference occurs when the (externally split) plug nozzle alone is run. However, the data from the internally split convergent-divergent (figures 14 and 15) show a large interference which varies with nozzle pressure ratio and different among the various configurations.

The quality of the test and the reliability of the data obtained is judged in part by the repeatability of that data. Figures 16 through 20 show good repeatability of data were obtained during the test for both balance measured forces and pressure integrated force. Normal force, pitching moment, and chord force repeatability are shown for one of the reference model configurations (no exit flow) through a range of angle of attack (figures 16 and 17). Figures 18 through 20 present chord force repeatability at three of the mach numbers tested with varying convergent-divergent nozzle pressure ratio. Repeatability of two comparable convergent-divergent nozzle runs are shown in figure 18. The plug nozzle flow for each run was different, but from other data it has been determined that the difference is negligible in data between the two plug nozzle pressure ratios.

Figure 20 illustrates the repeatability of the chord force obtained from the balance data. This data is corrected for the effects of the inflatable seal. The difference between the balance and the force data illustrates the magnitude of forces acting inside the metric shell. The variation of this difference with pressure ratio is caused by the forces acting internally in the convergent-divergent nozzle shroud.

The horizontal tail was not instrumented to obtain pressure integrated forces. Because of this and other differences, direct comparison of the measured force and pressure integrated force data could not be made. However, valid correlation of these data is possible when the jet-on data is viewed in relation to the jet-off data of the reference configuration. Figures 21 to 26 show these comparisons at mach numbers 0.85, 1.27, and 1.7 for two of the convergent-divergent nozzle configurations tested. The force data is shown with and without the corrections, resulting from the static tests, applied. The magnitude of this correction can be seen here. The differences in the variation of the jet-on data from the reference data between the corrected force and pressure data are observed greatest below a pressure ratio of 3 and 5 for the A_0/A_M of 0.3 to 0.5 respectively. Below these pressure ratios the internal nozzle flow is separated. Therefore, it is diagnosed that when the internal nozzle flow is separated, the data from these convergent-divergent nozzle configurations could not be adequately corrected. The normal force and pitching moment showed none of these effects.

The increment from the reference configuration to the jet-on configurations was determined from figures 21 through 26 and is presented in figures 27 and 28 for the fully expanded unseparated nozzle flow data. This data is presented as ΔC_C and was determined by

$$\Delta C_C = C_{C_{\text{FLOW CONFIG}}} - C_{C_{\text{REFERENCE CONFIG}}}$$

This data shows that the force data obtained (measured and pressure integrated) are in agreement for these conditions. Agreement was obtained from all the plug nozzle alone data (not shown). Therefore, with the exception of many of the internally split nozzle configurations, the model and test techniques used to measure the forces on the after-body resulting from the interaction of the nozzle internal and external flow fields were reliable.

CONCLUSION

Measurements of incremental afterbody interaction forces, resulting from the simulated propulsion exit nozzle parameters, were obtained by force and pressure instrumentation concurrently on a scaled model of the entire air vehicle. The force instrumentation measured lift, drag, and pitching moment throughout the angle-of-attack range tested, while the pressure data provided only body axis chord force. The incremental chord force derived during these tests from the two methods compared well for all plug nozzle alone tests but only for a few C-D nozzle configurations.

These forces were measured on a metric shell afterbody in the presence of exit flow simulation. Direct force measurement of the external afterbody forces was achieved by the unusual arrangement of a six-component force balance in the forebody, with the addition of a gaged normal force member supporting the afterbody normal force. An inflatable seal was used to separate the vented afterbody cavity and convergent-divergent nozzle shroud cavity. Successful calibrations of the assembled model were made and the interaction of the seal was determined and applied.

The internal break of the convergent-divergent nozzles resulted in undesirable interferences, that were caused by the internal nozzle flow field, and uncorrectable by standard methods. Static tests throughout the simulated pressure ratio range were required to determine these extraneous forces. However, because of the limitations of the air supply, the high pressure ratios attained in supersonic tests could not be calibrated statically. The resulting test data could not always be adequately corrected.

When the nozzle flow was separated internally, the force and pressure derived chord force did not correlate favorably. However, favorable agreement on some of the larger exit nozzles was obtained when the internal flow was fully expanded. In more recent tests, externally split convergent-divergent nozzles were tested and the results appear to be excellent.

The pressure data proved valuable to validating the force data and was useful in diagnosing problem areas.

Complete sealing of the afterbody split is recommended for future tests and the chambers vented to freestream static pressure. This, and externally split nozzle arrangements will alleviate these large corrections to the balance data.

NOMENCLATURE

| | |
|-----------------------|--|
| S_w | = Wing area |
| N_1 | = Forward balance normal force, lb |
| N_2 | = Aft balance normal force, lb |
| N_3 | = Normal force measured by the force member in the afterbody, lb |
| C | = Balance chord force |
| ΔP | = Differential pressure across seal between afterbody metric shell and nonmetric nozzle components, psid |
| P_t/P_o | = Ratio of nozzle total pressure to freestream static pressure |
| α | = Model angle of attack |
| C_N | = Normal force coefficient = normal force/ $q S_w$ |
| C_C | = Chord force coefficient = chord force/ $q S_w$ |
| C_M | = Pitching moment coefficient = pitching moment/ $q S_w c$ |
| q | = Freestream dynamic pressure, psf |
| c | = Mean aerodynamic chord of wing |
| MAC | = Mean aerodynamic chord of wing |
| A_g | = Nozzle exit area, ft^2 |
| A_M | = Nozzle cross-sectional area, ft^2 |
| M | = Freestream mach number |
| A_x | = Weighted area for each surface pressure orifice, ft^2 |
| P_o | = Tunnel freestream static pressure, psfa |
| P_x | = Individual model measured static pressure, psfa |
| P_t | = Nozzle total pressure, psfa |
| $\frac{P_x - P_o}{q}$ | = Pressure coefficient |

Subscripts

C-D Convergent-divergent nozzle

Plug Plug nozzle

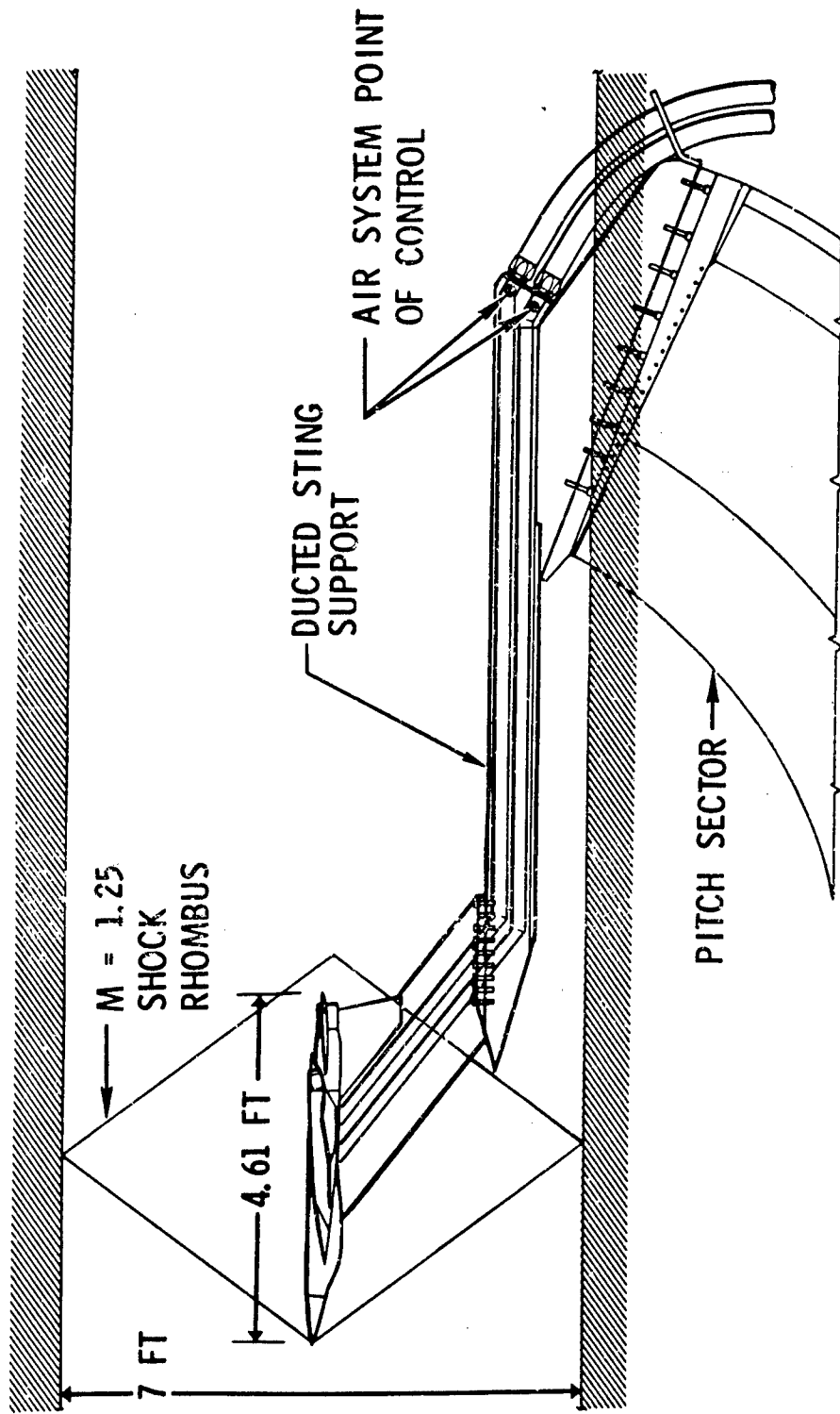


Figure 1. Model Installation

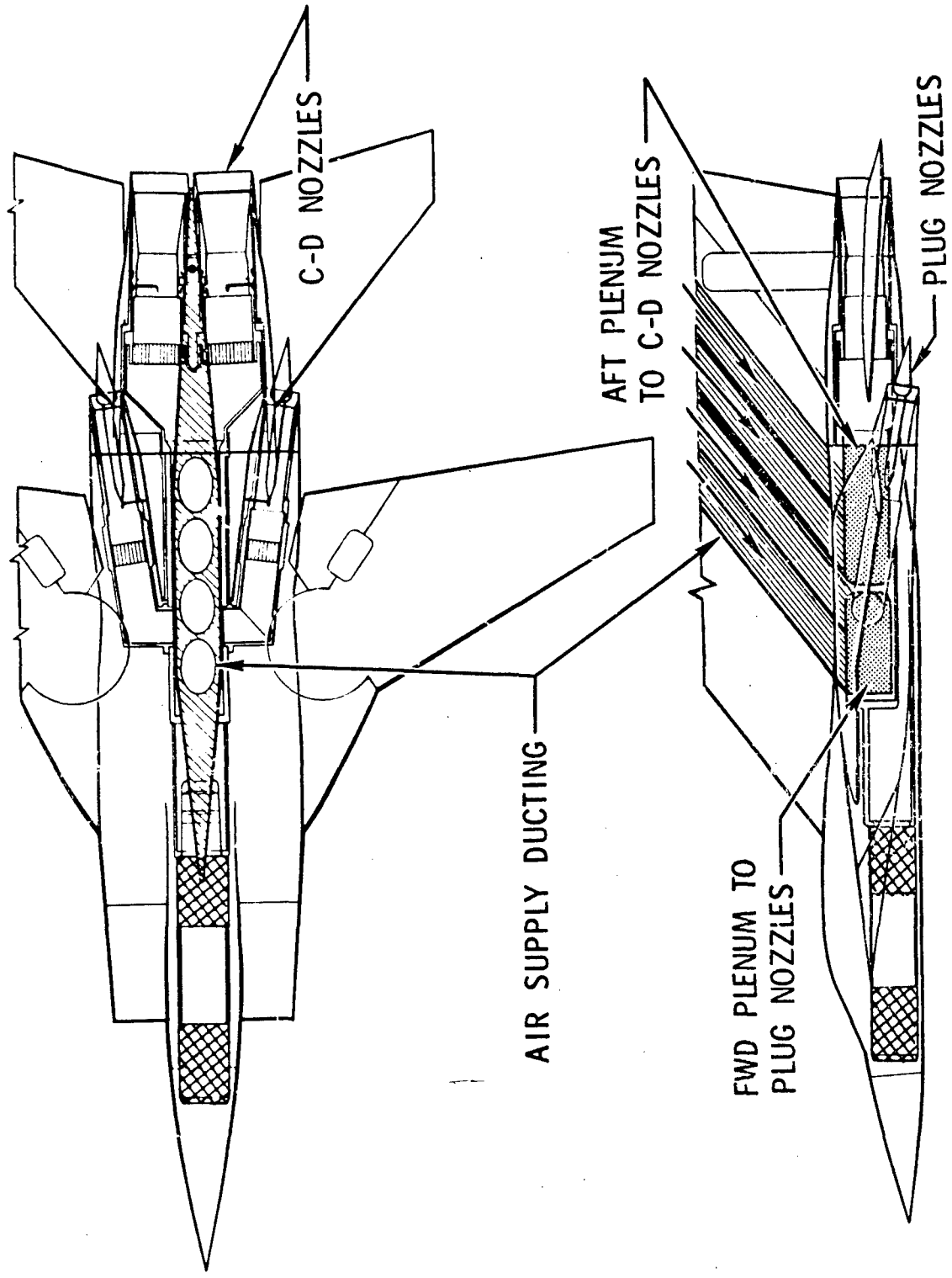


Figure 2. Mod I Flow Arrangement

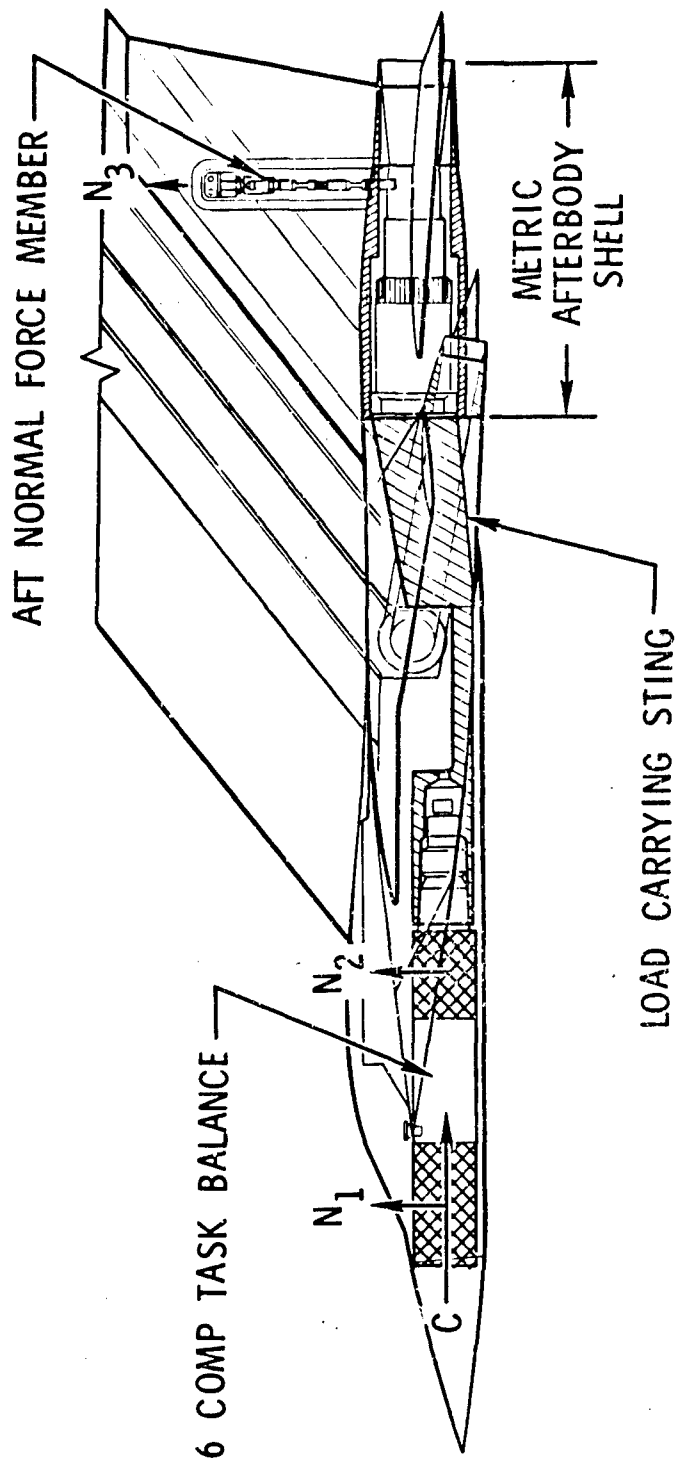


Figure 3. Force Measurement Arrangement

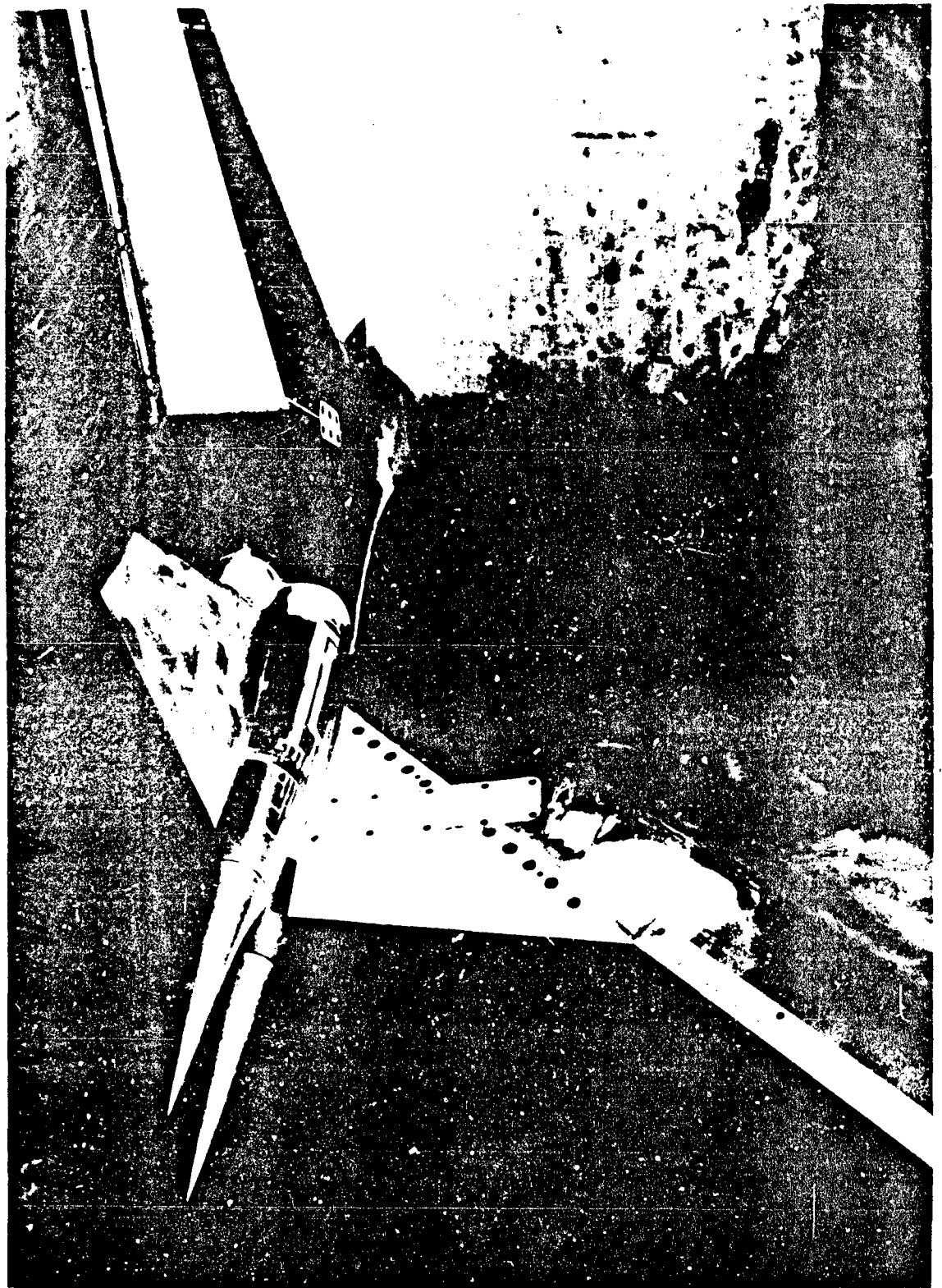


Figure 4. Three-Quarters Rear View of Model Showing Strut Mount and Vertical Tail Fairing

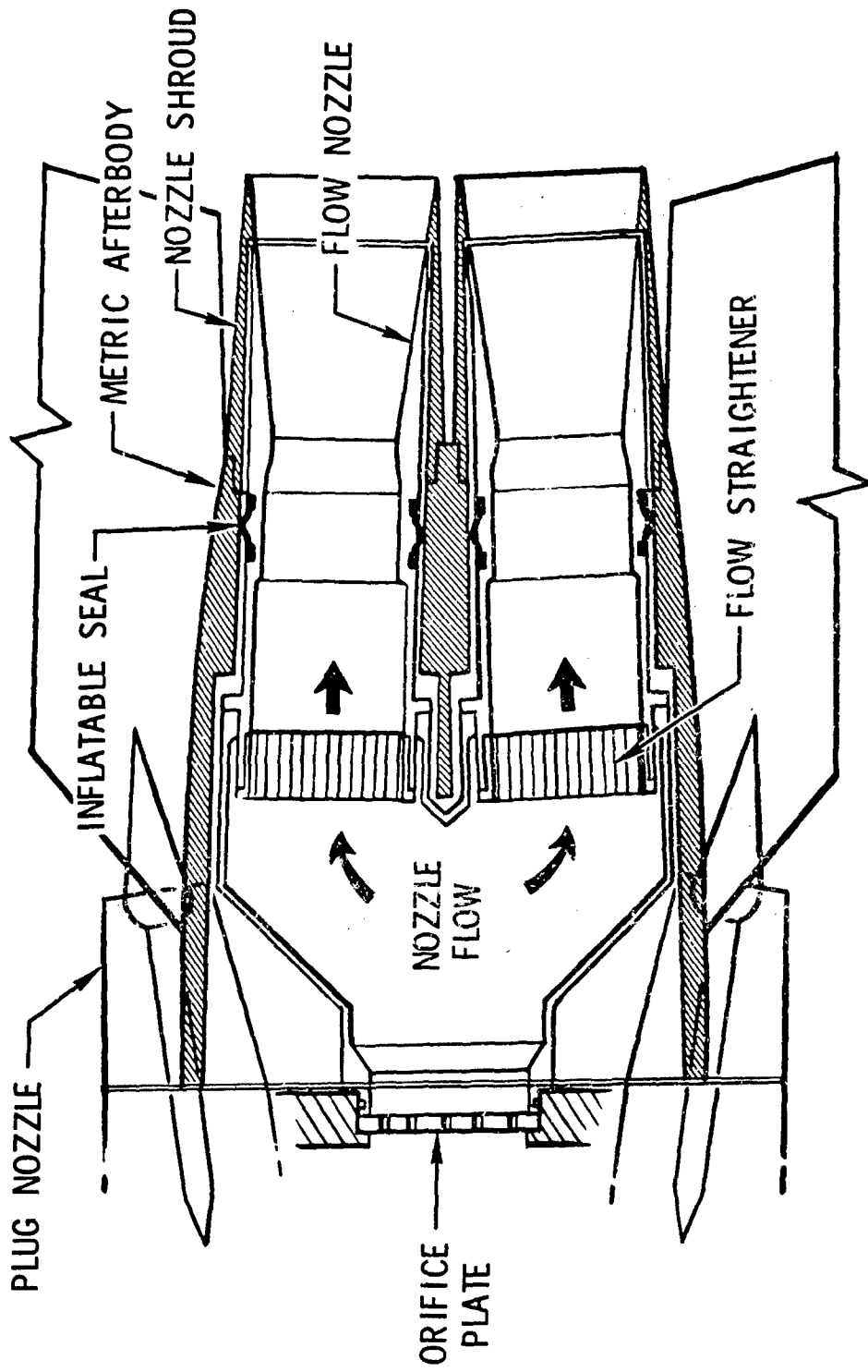


Figure 5. C-D Nozzle Shroud Arrangement

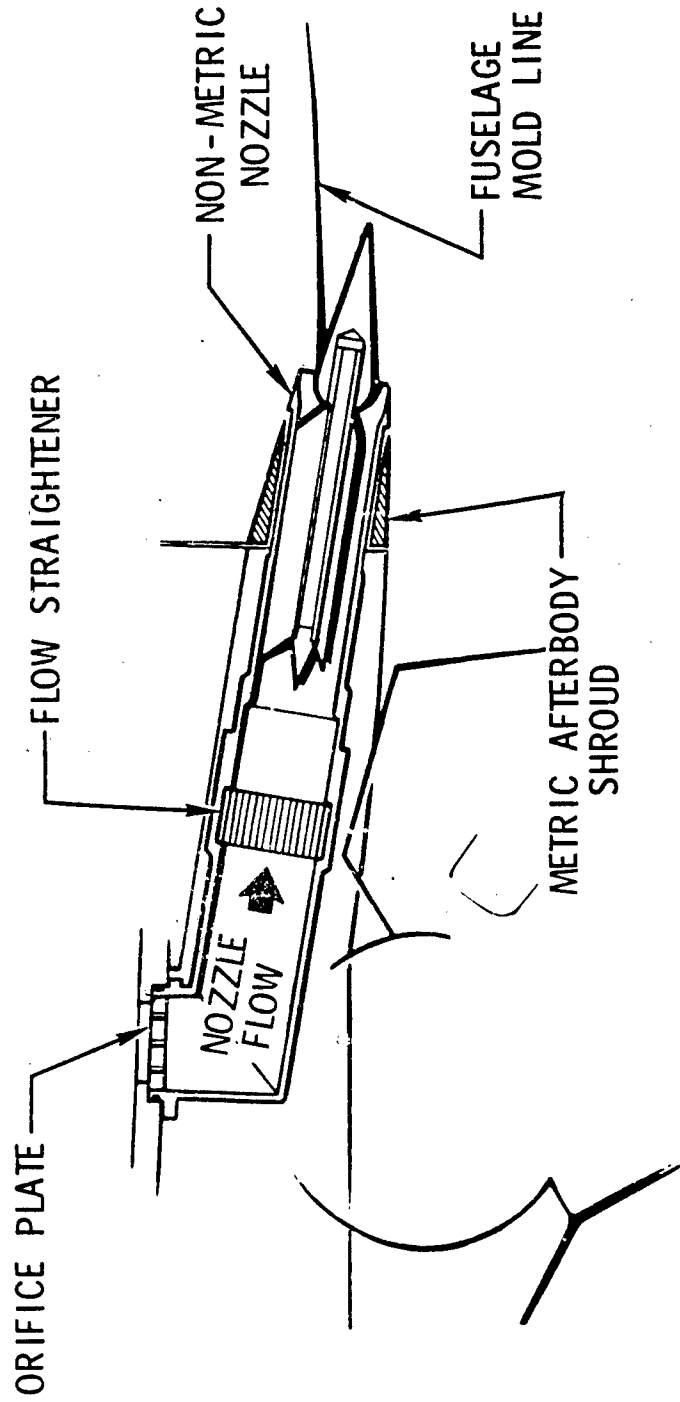


Figure 6. Plug Nozzle Shroud Arrangement



Figure 7. Closeup of Model Showing Metric Afterbody Split and Internal Nozzle Split

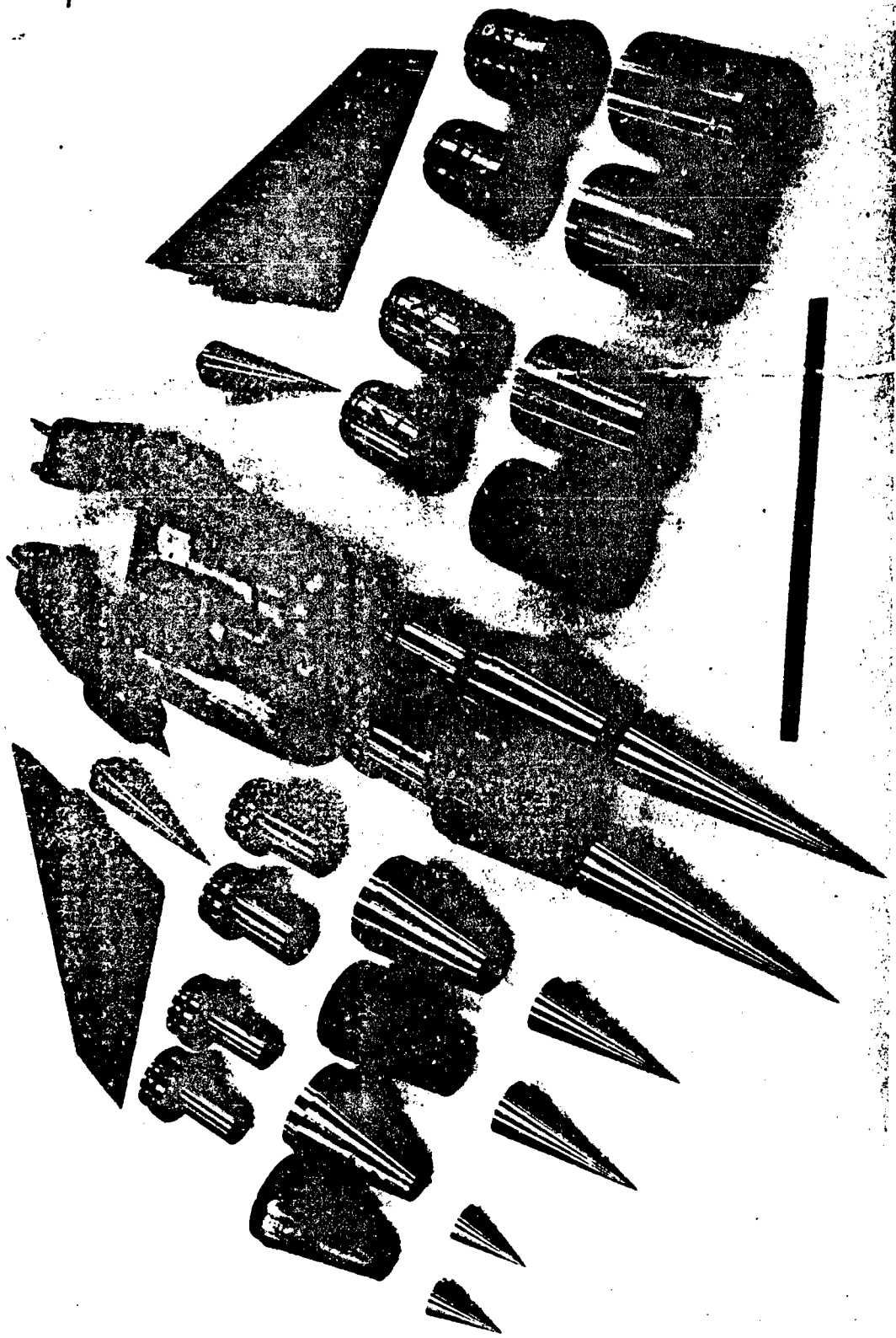


Figure 8. Metric Afterbody With Nozzels, Shrouds Tested

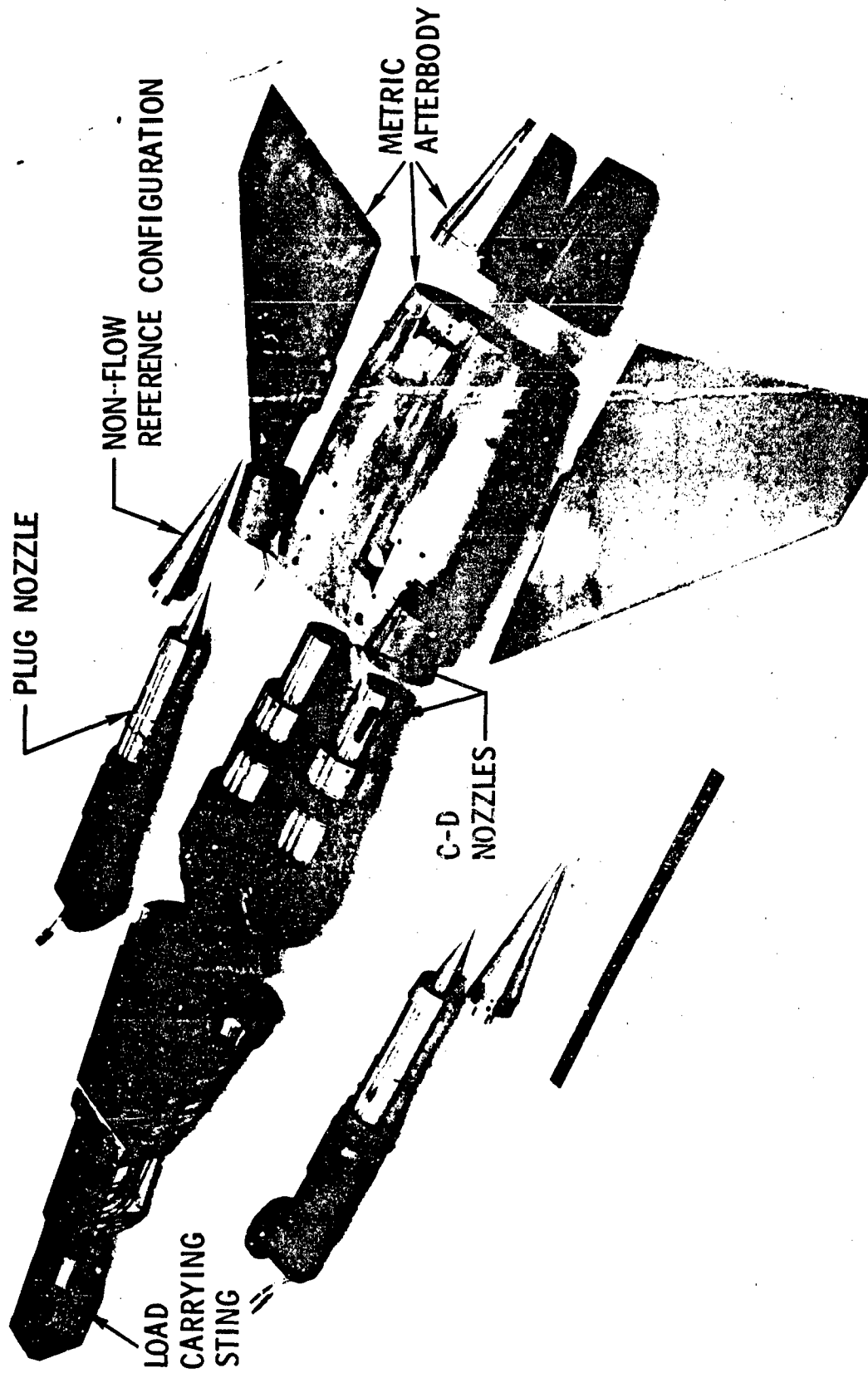


Figure 9. Metric Afterbody With Load Carrying Sting, C-D and Plug Nozzles

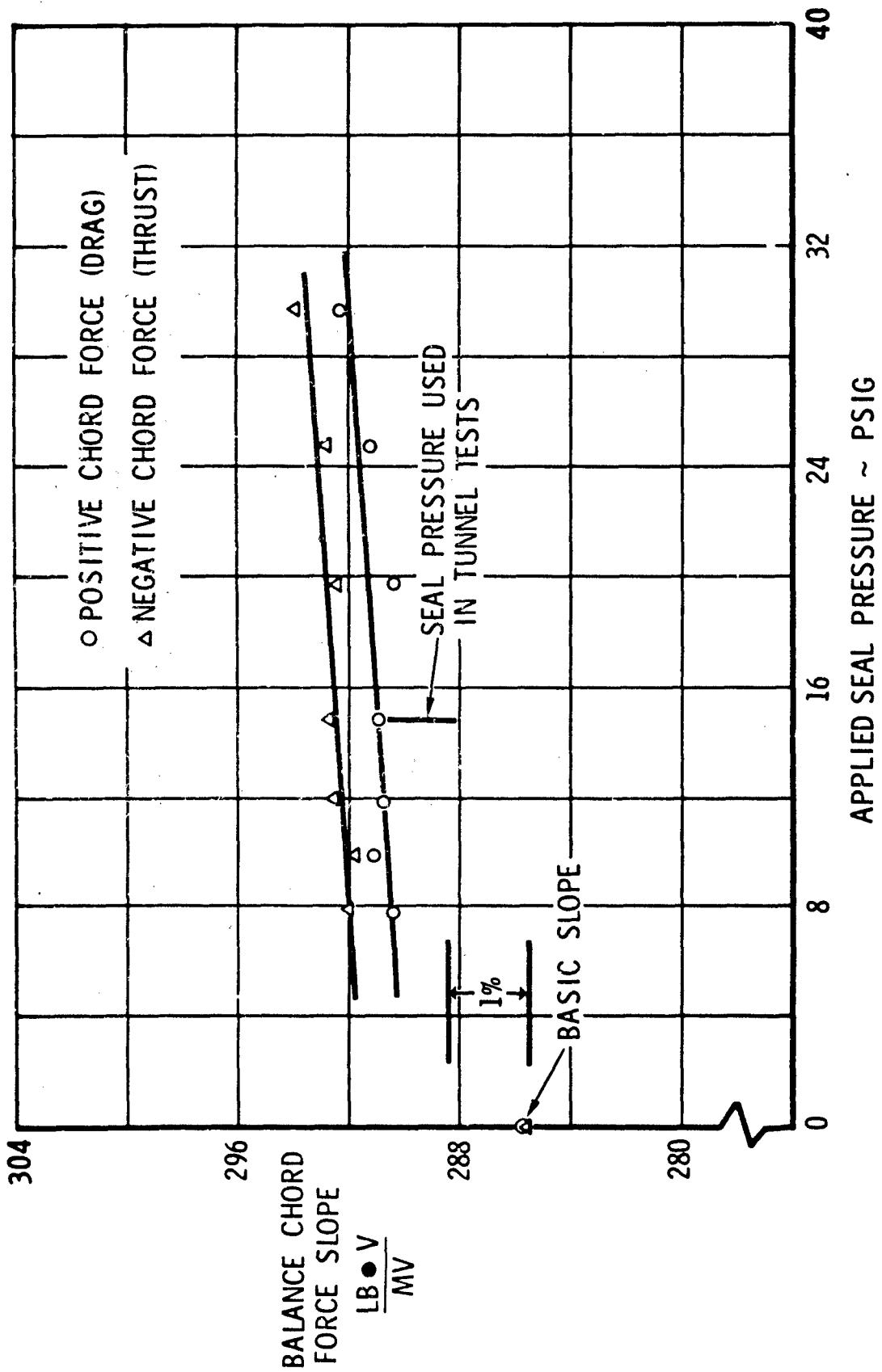


Figure 10. Calibration Results - Effect of Seal Pressure on Chord Force Calibration

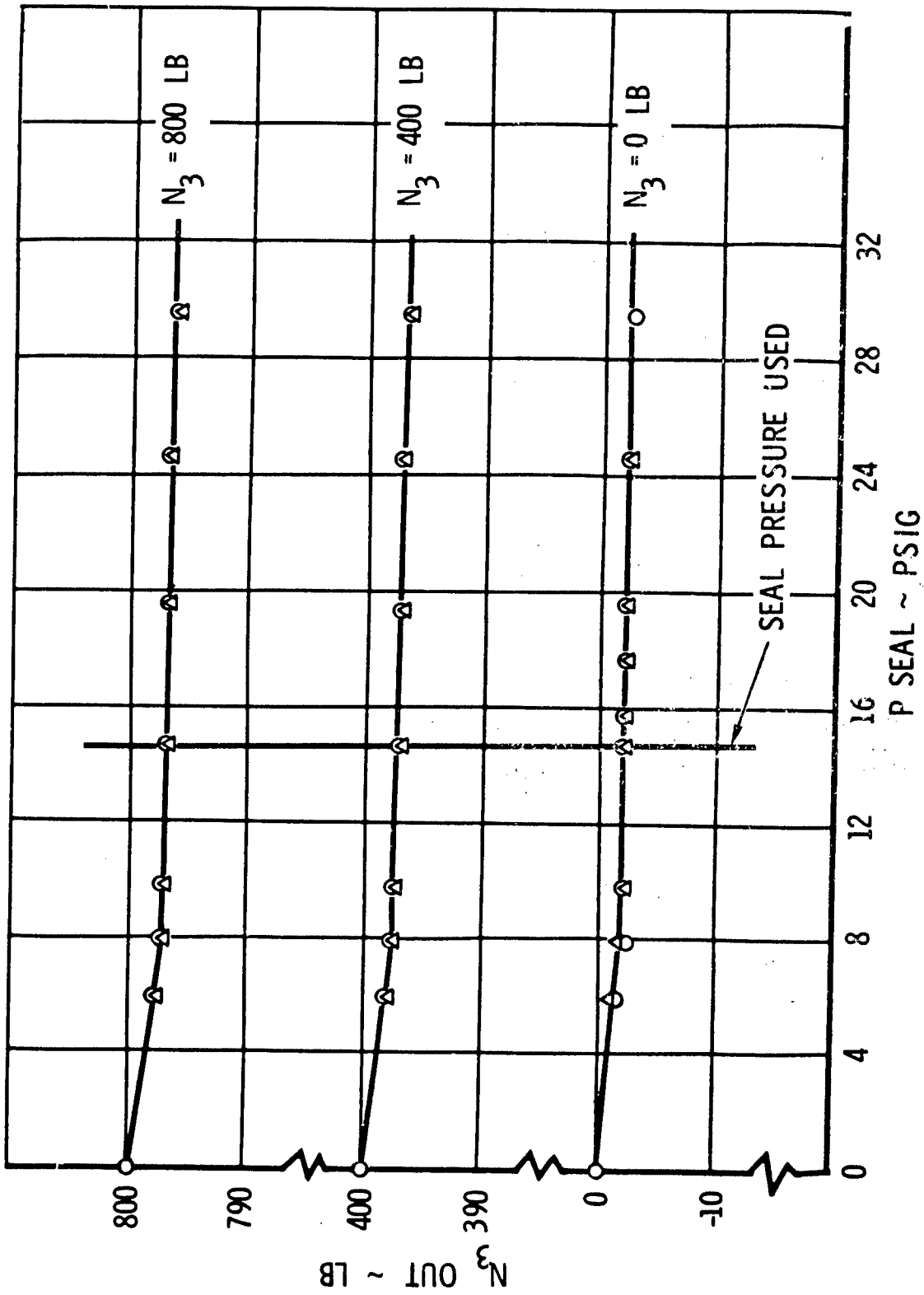


Figure 11. Calibration Results - Effect of Seal Pressure on Normal Force

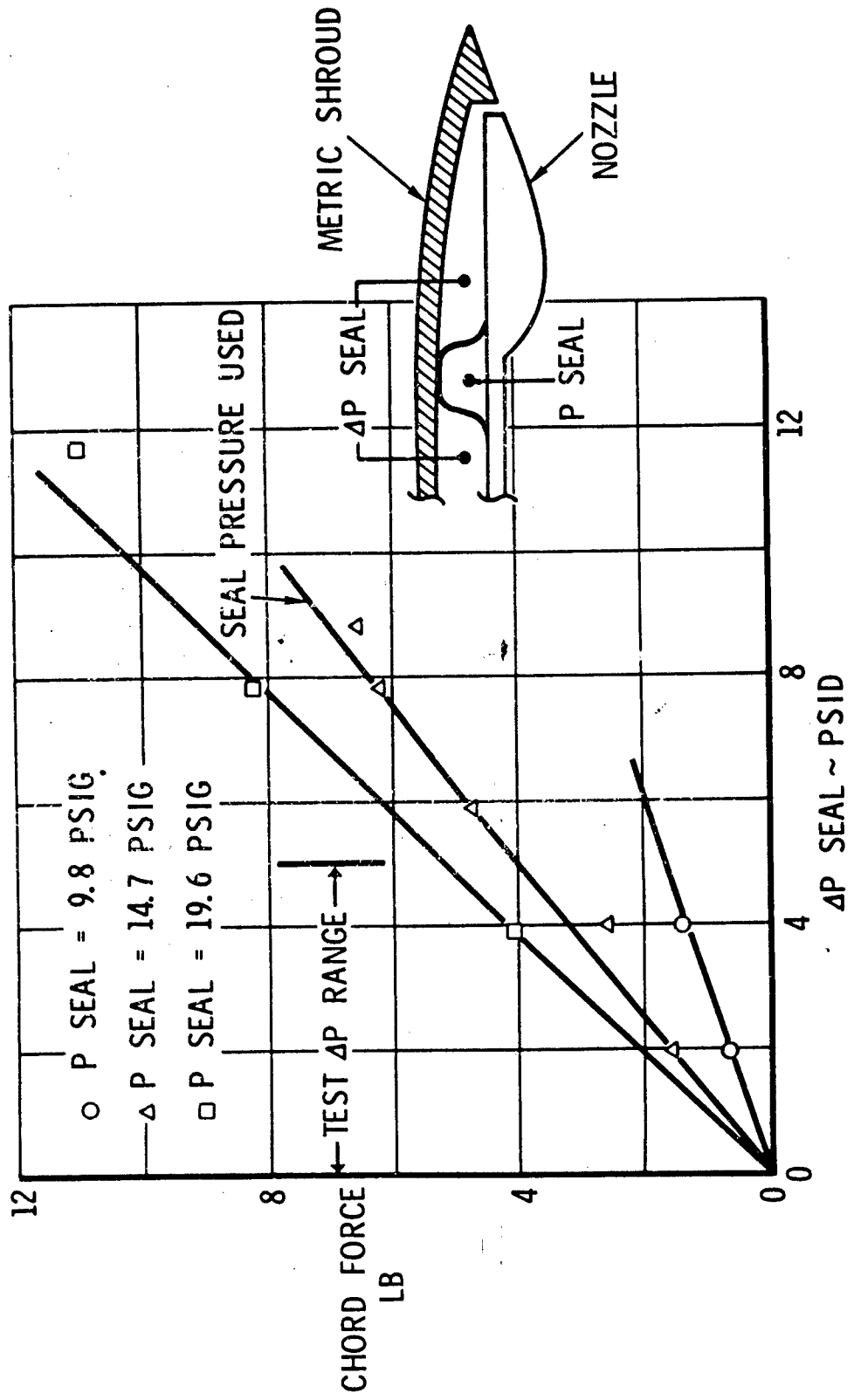


Figure 12. Calibration Results - Chord Force Correction for ΔP Across Seal

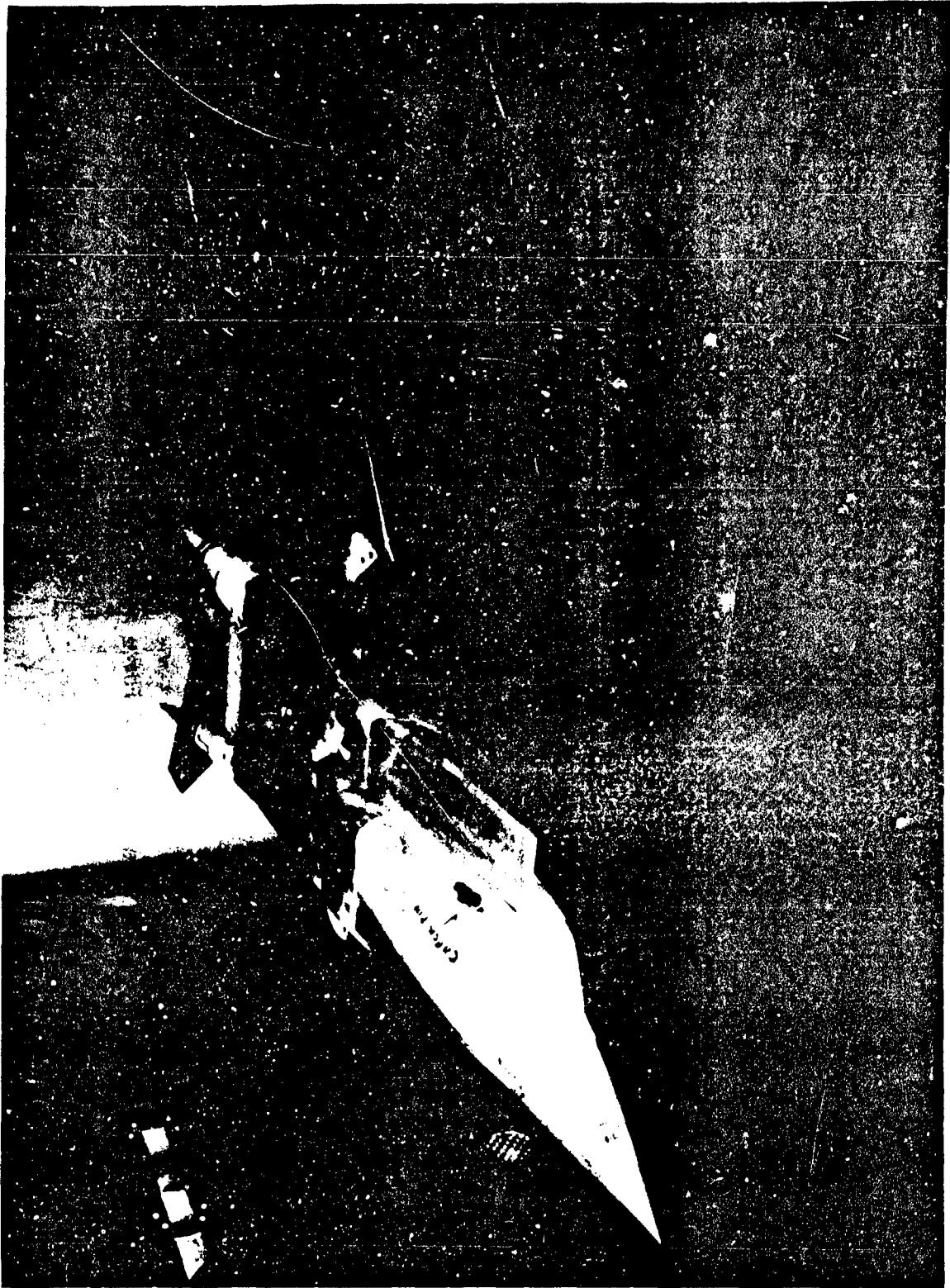


Figure 13. Installation. Reference Configuration

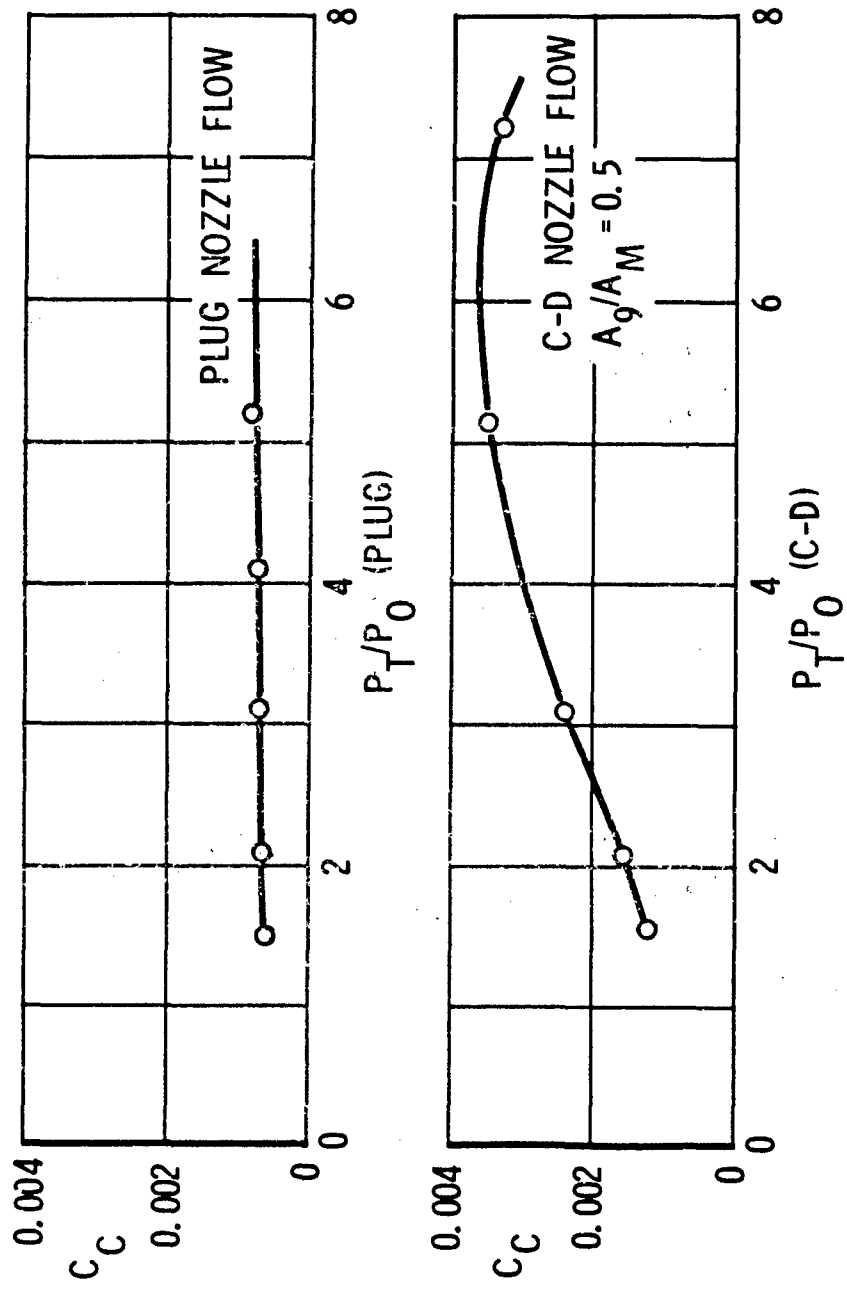


Figure 14 . Chord Force Induced by Nozzle Flow Only - $M = 0$

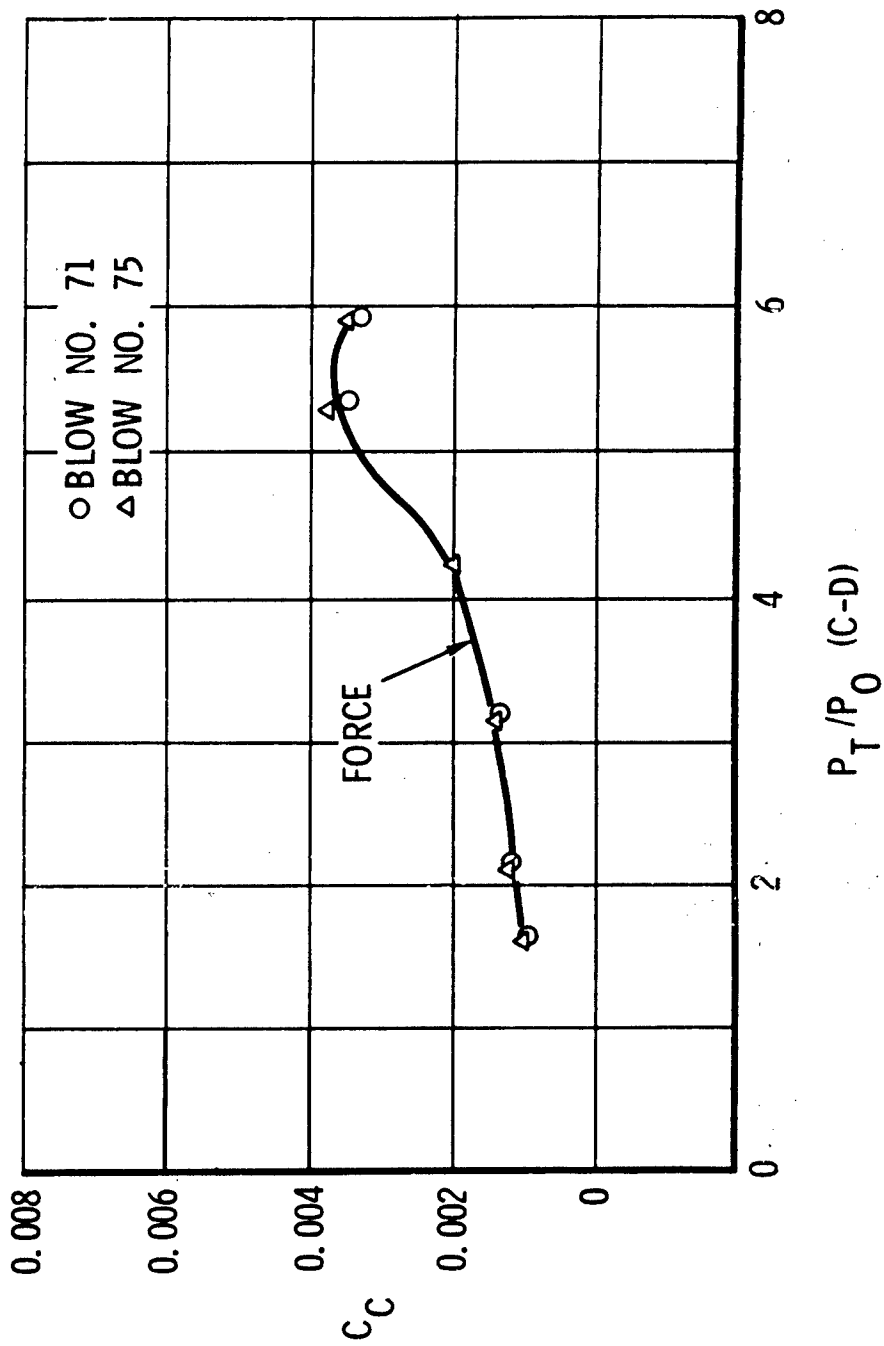


Figure 15. Chord Force Induced by Nozzle Flow Only - $M = 0$ -
 $A_9/A_M = 0.80$

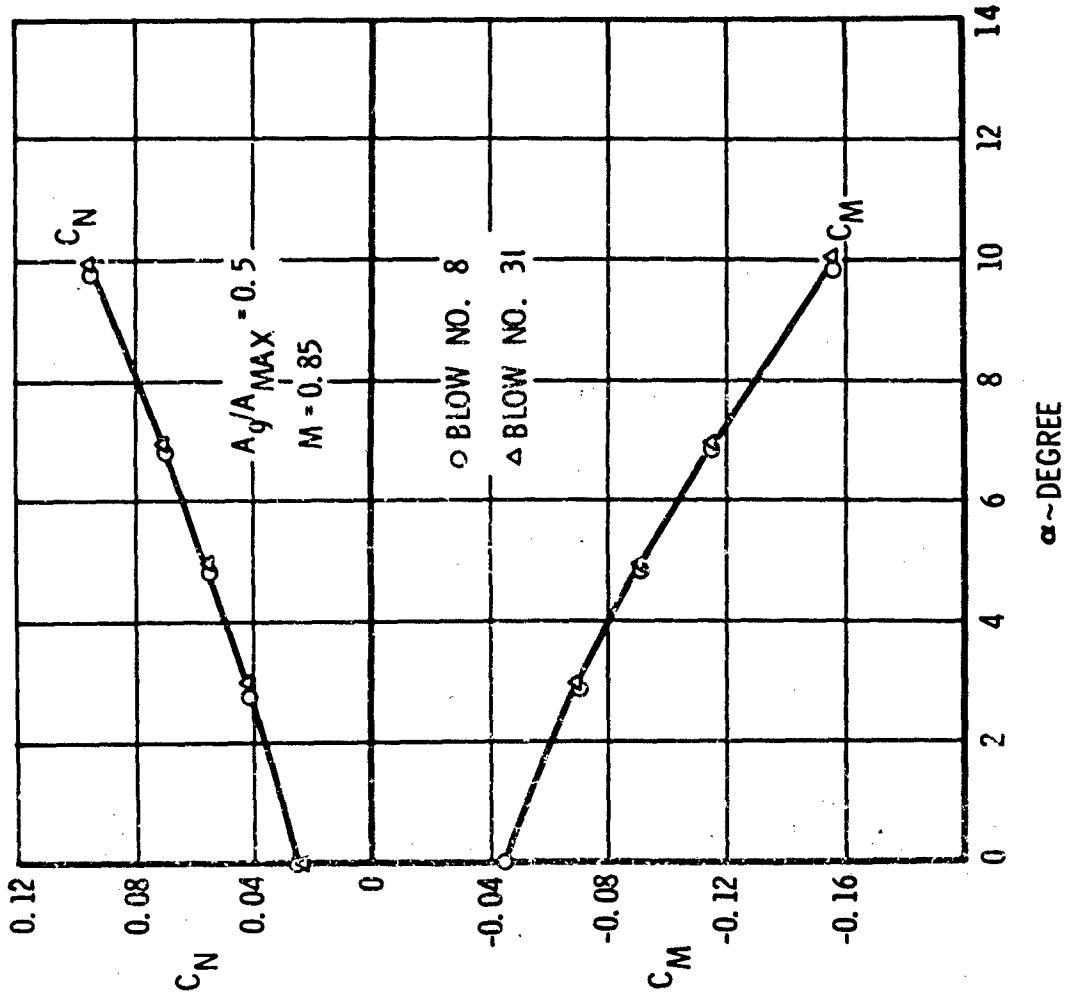


Figure 16 . Data Repeatability Reference Configuration
Normal Force and Pitching Moment

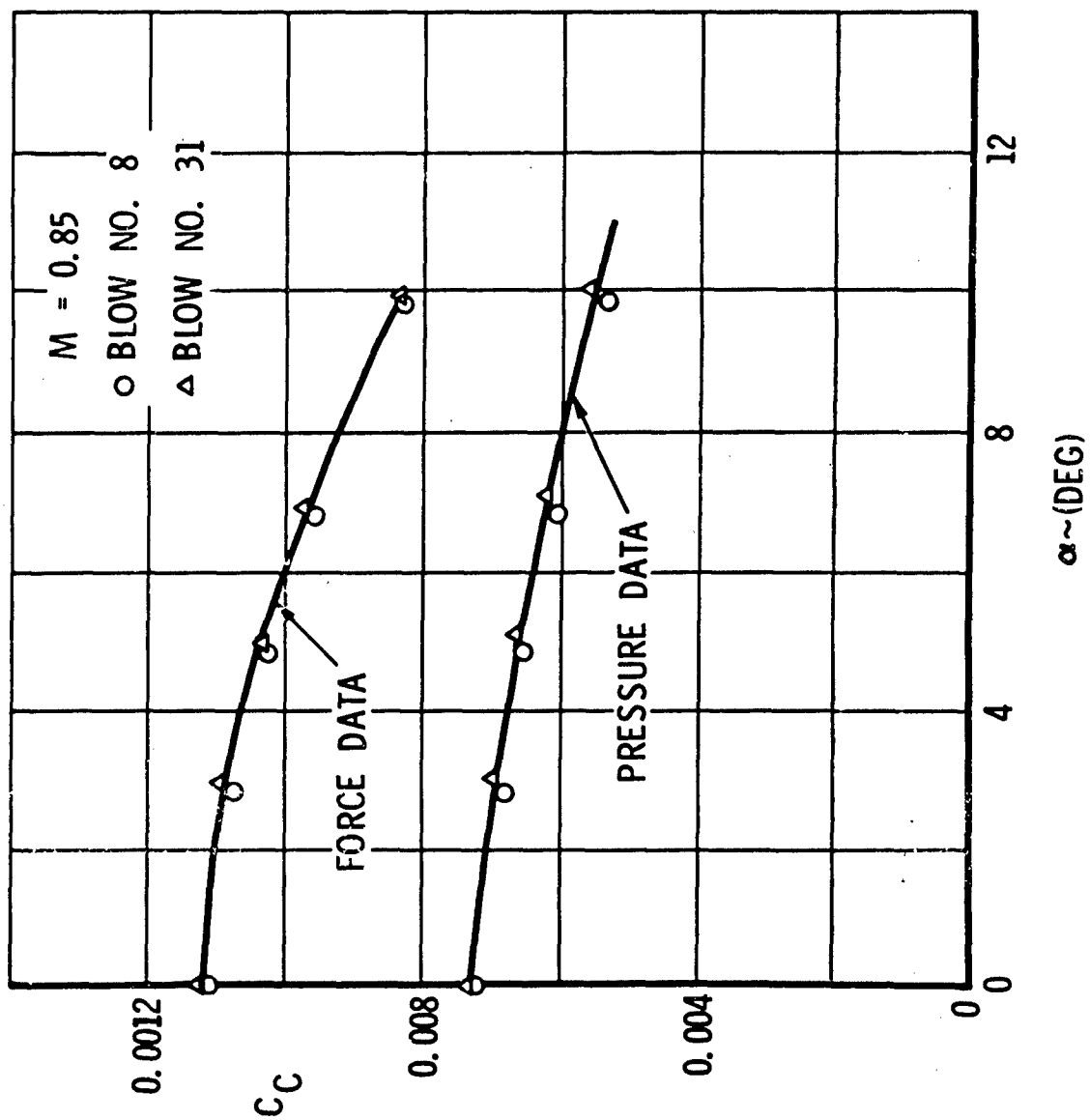
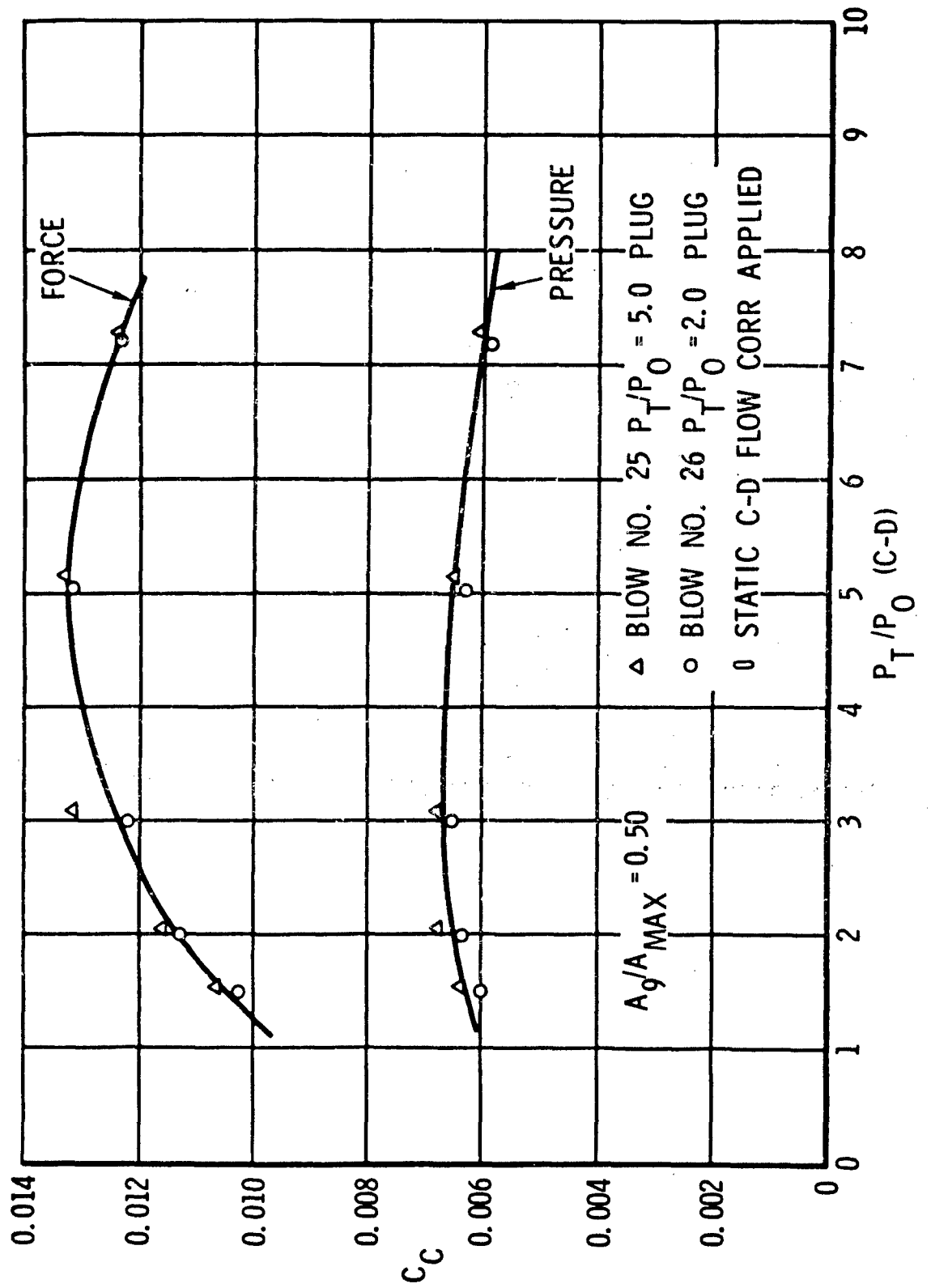


Figure 17. Chord Force Repeatability (Ref. Config)
 (No Model Flow)



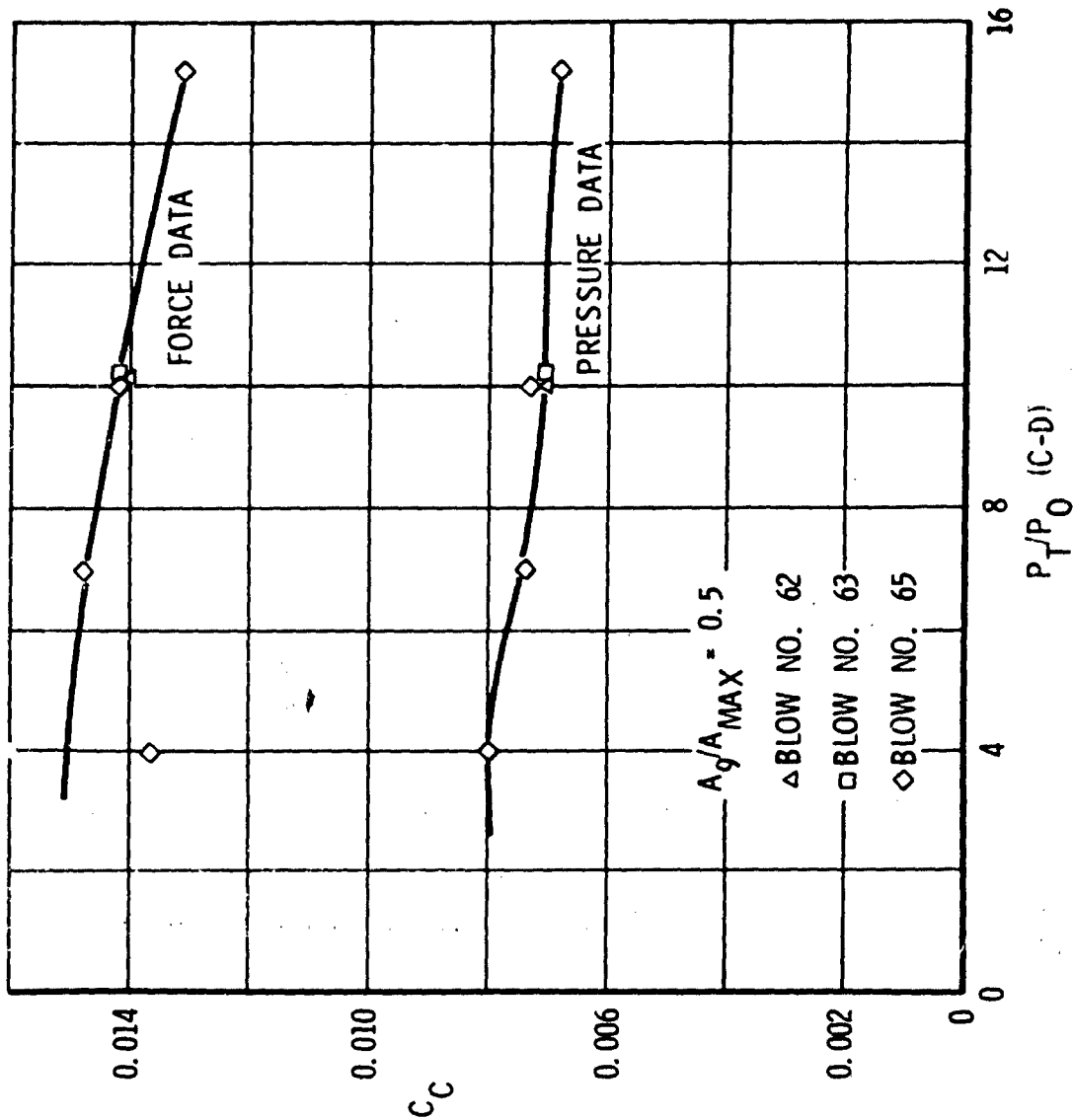


Figure 19. Chord Force Repeatability With C-D Nozzle Flow Variation $M = 1.7$

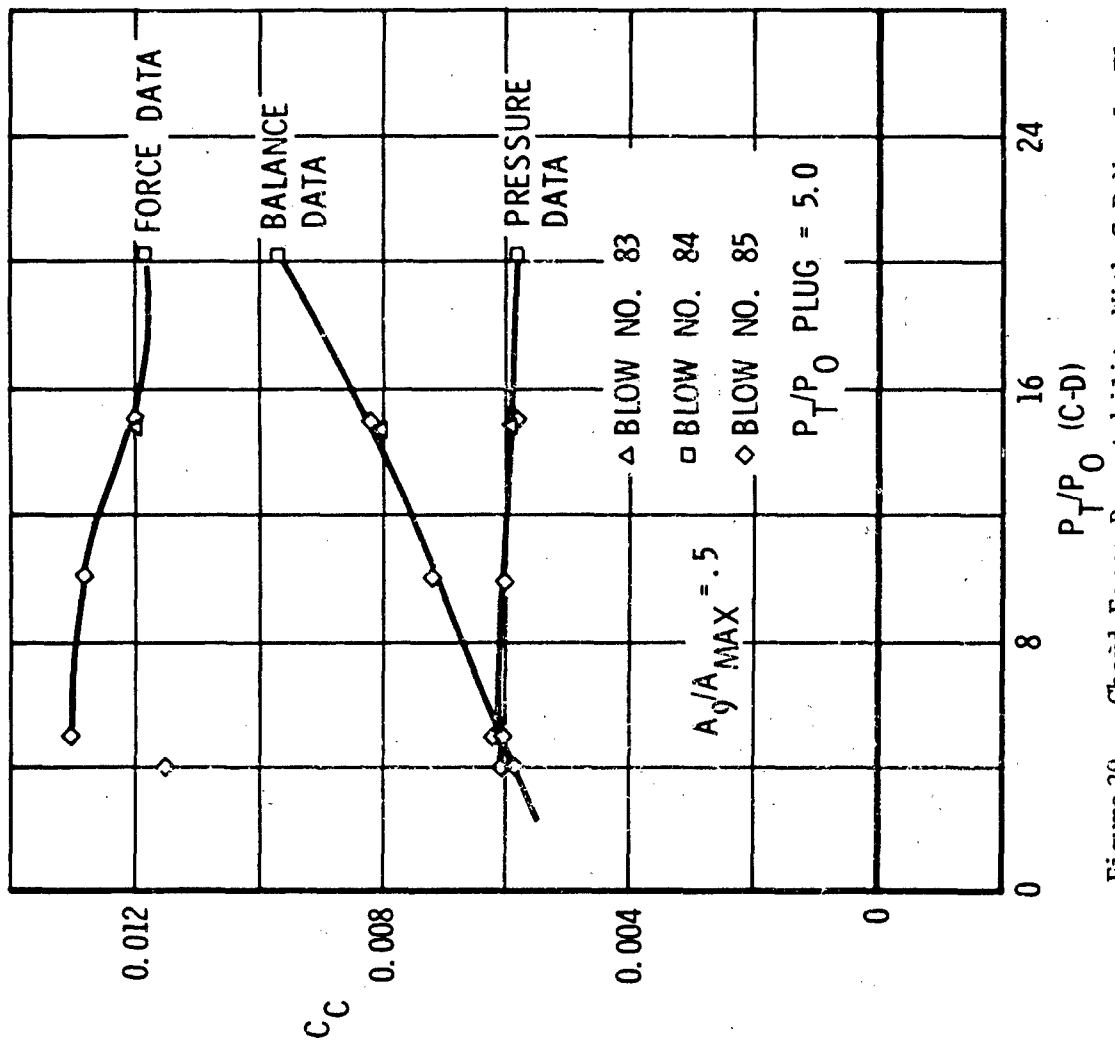


Figure 29. Chord Force Repeatability With C-D Nozzle Flow Variation $M = 2.0$

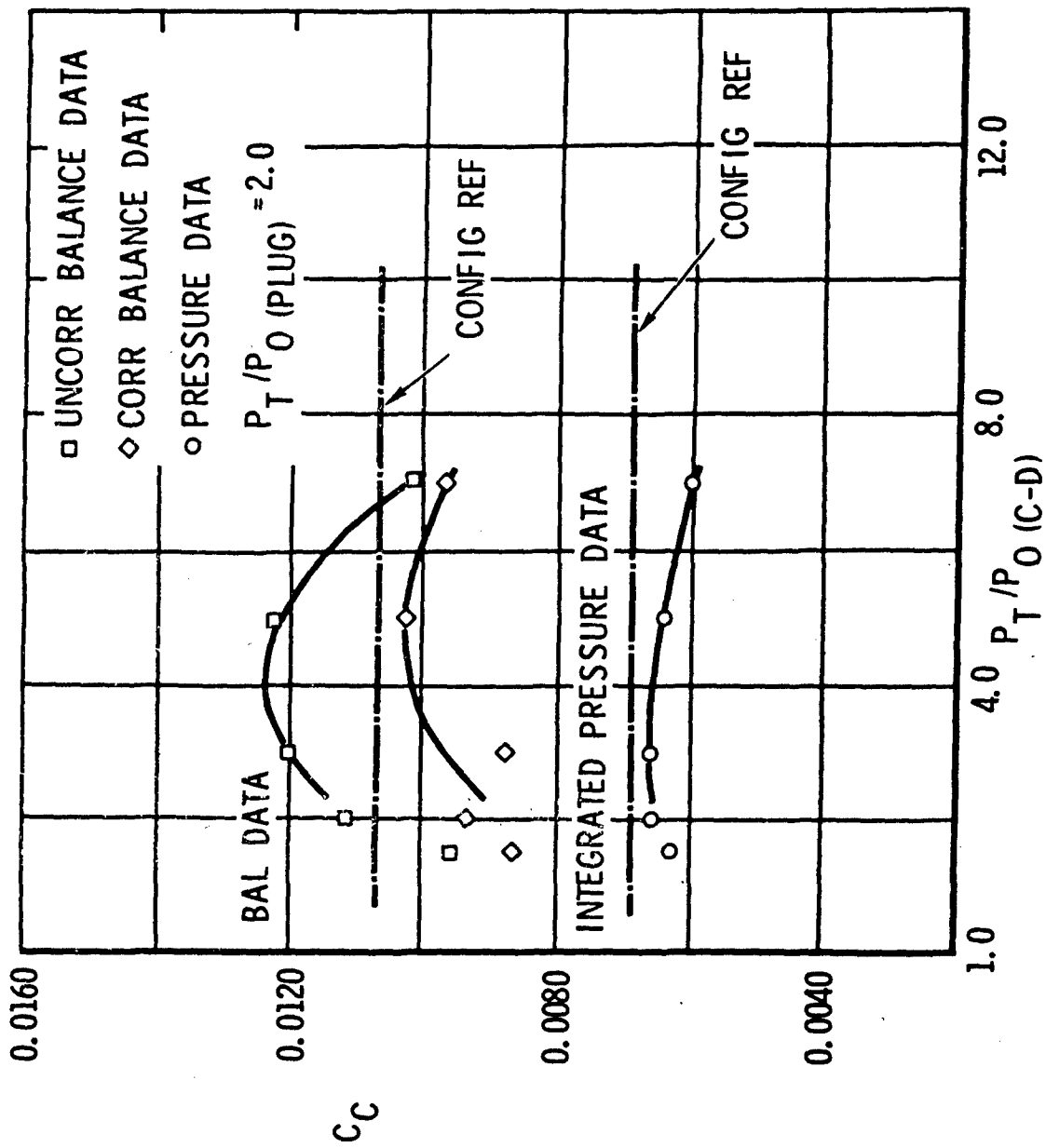


Figure 21. Chord Force Correlation - $M = 0.85$ - $A_0/A_M = 0.30$

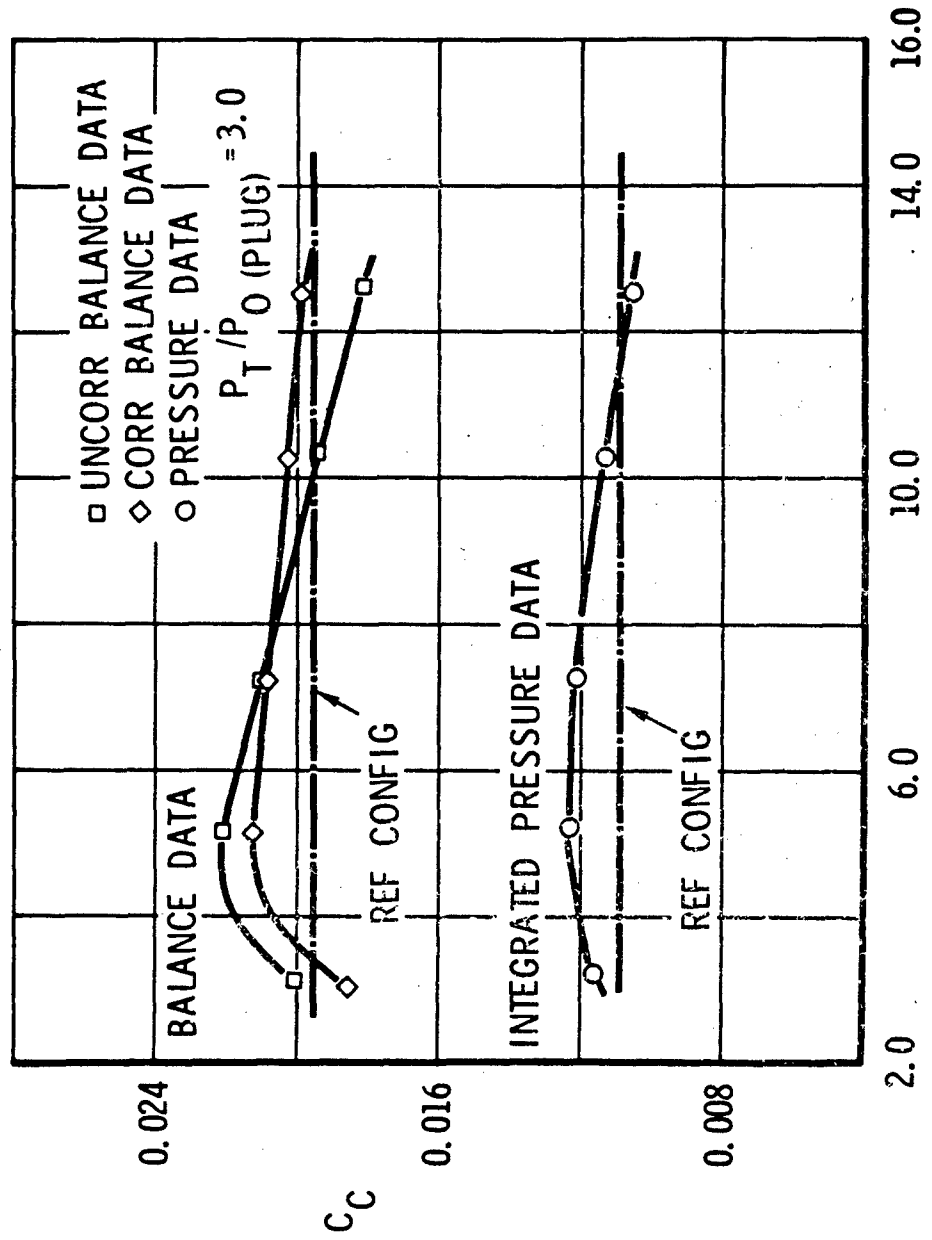


Figure 22. Chord Force Correlation - $M = 1.27$ - $A_9/A_M = 0.30$

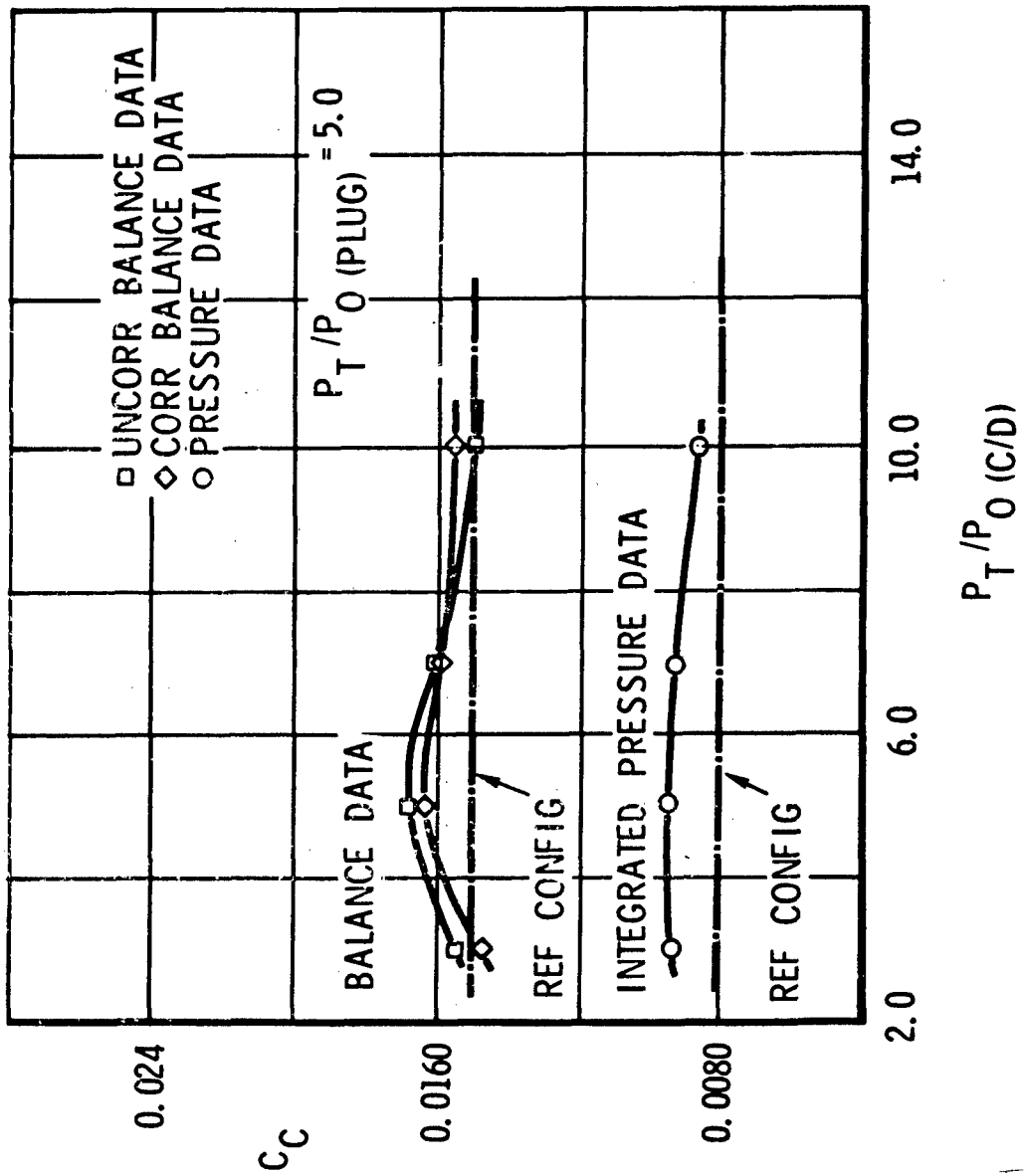


Figure 23. Chord Force Correlation - $M = 1.7$ - $A_g/A_M = 0.30$

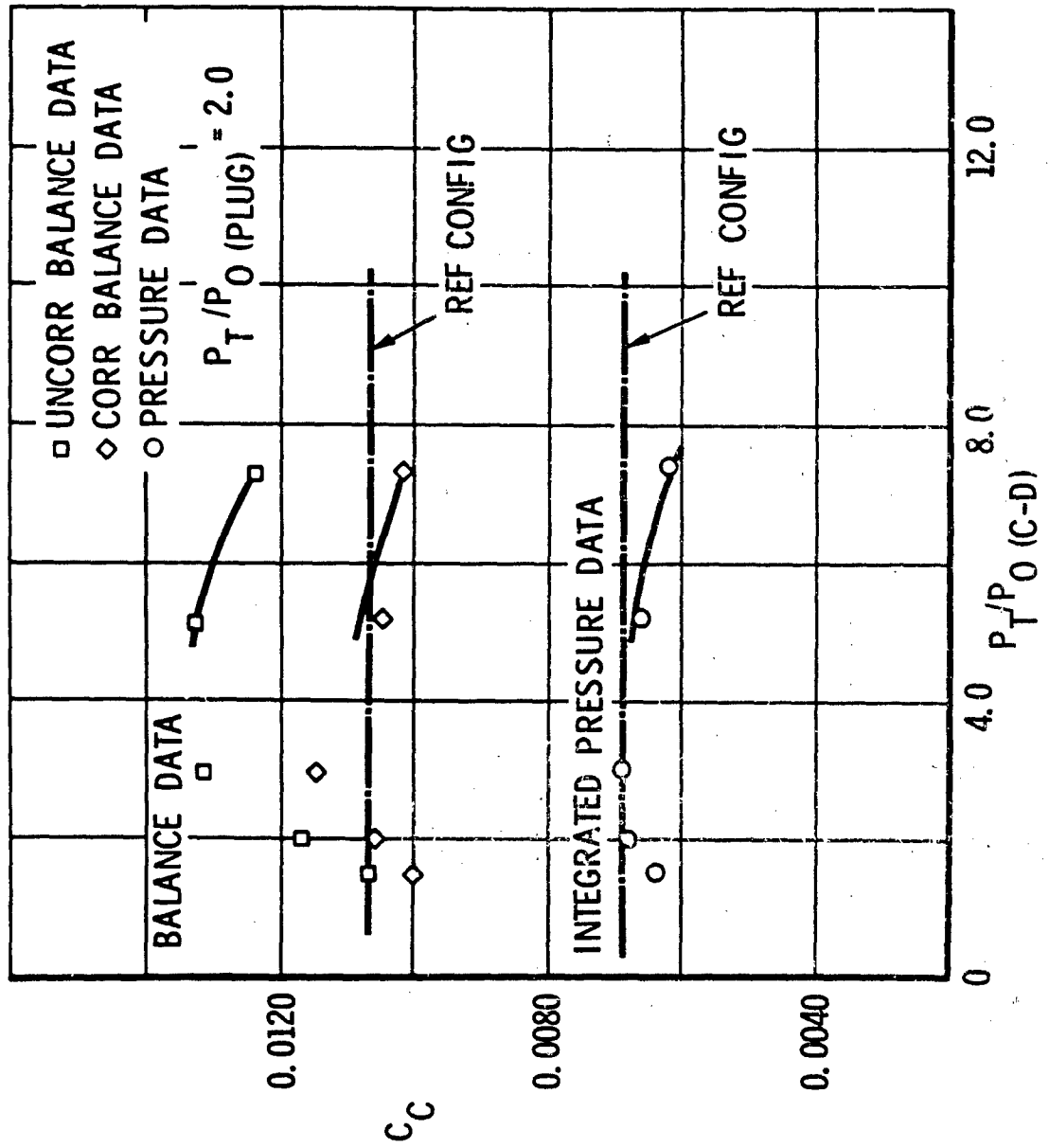


Figure 24. Chord Force Correlation - $M = 0.85$ - $A_9/A_M = 0.50$

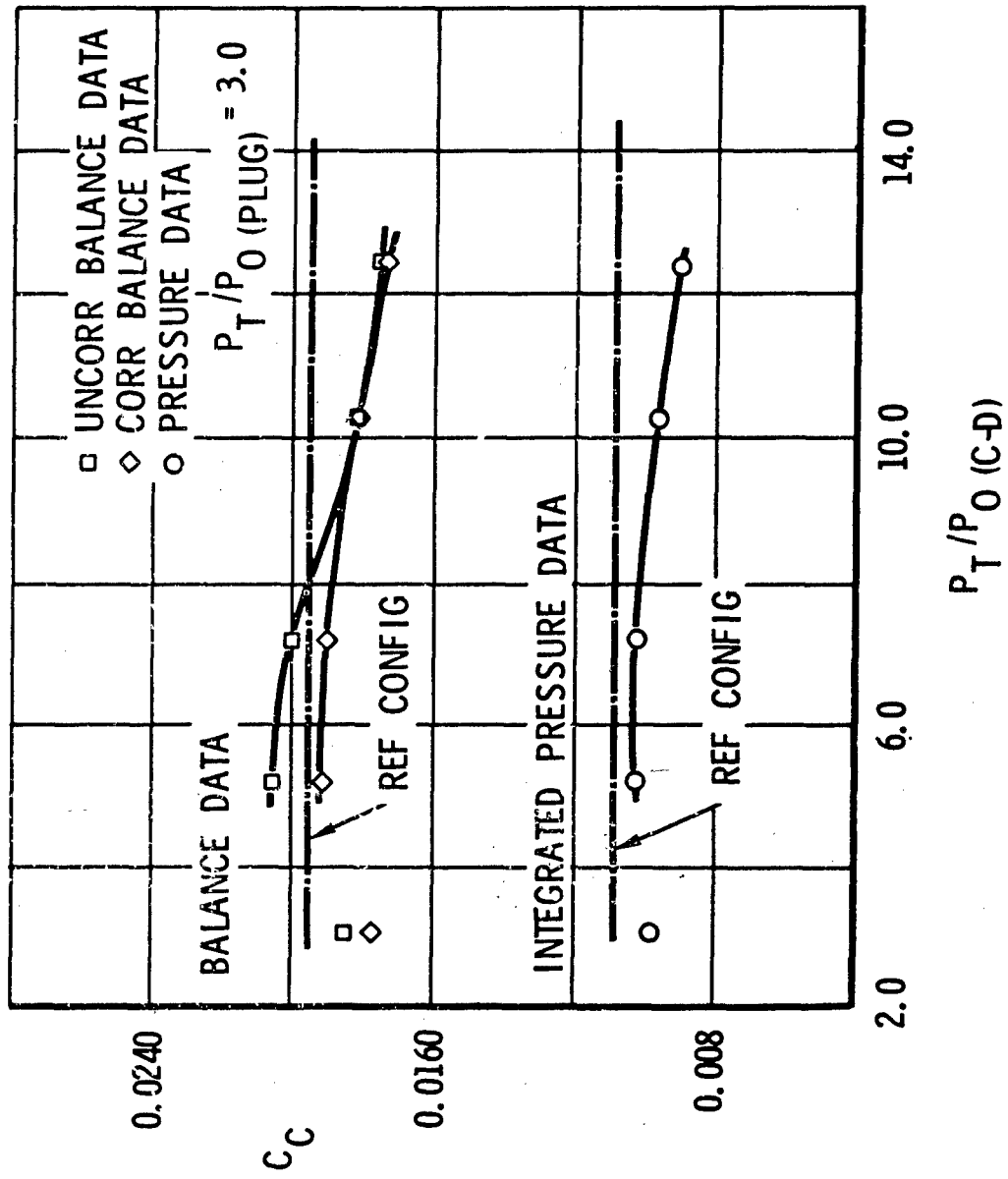


Figure 25. Chord Force Correlation - $M = 1.27$ - $A_9/A_M = 0.50$

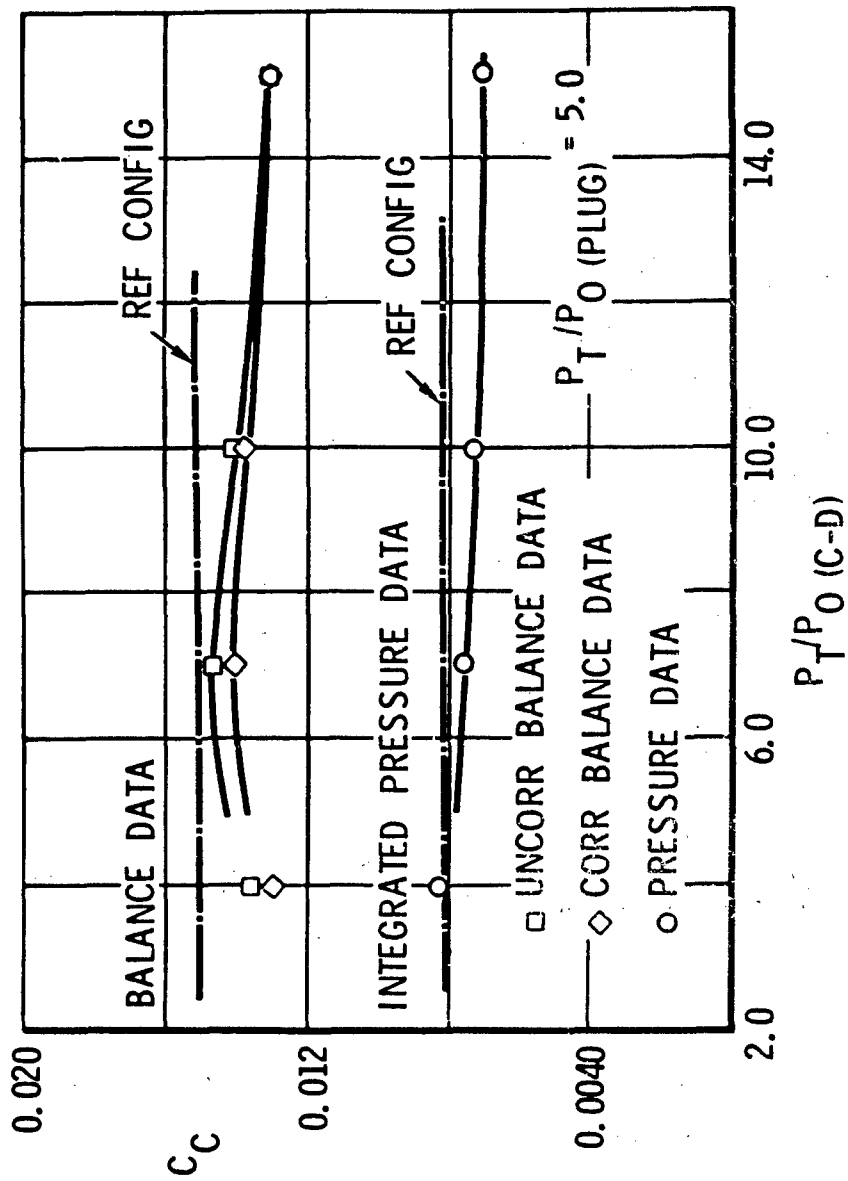


Figure 26. Chord Force Correlation - $M = 1.70$ - $A_g/A_M = 0.50$

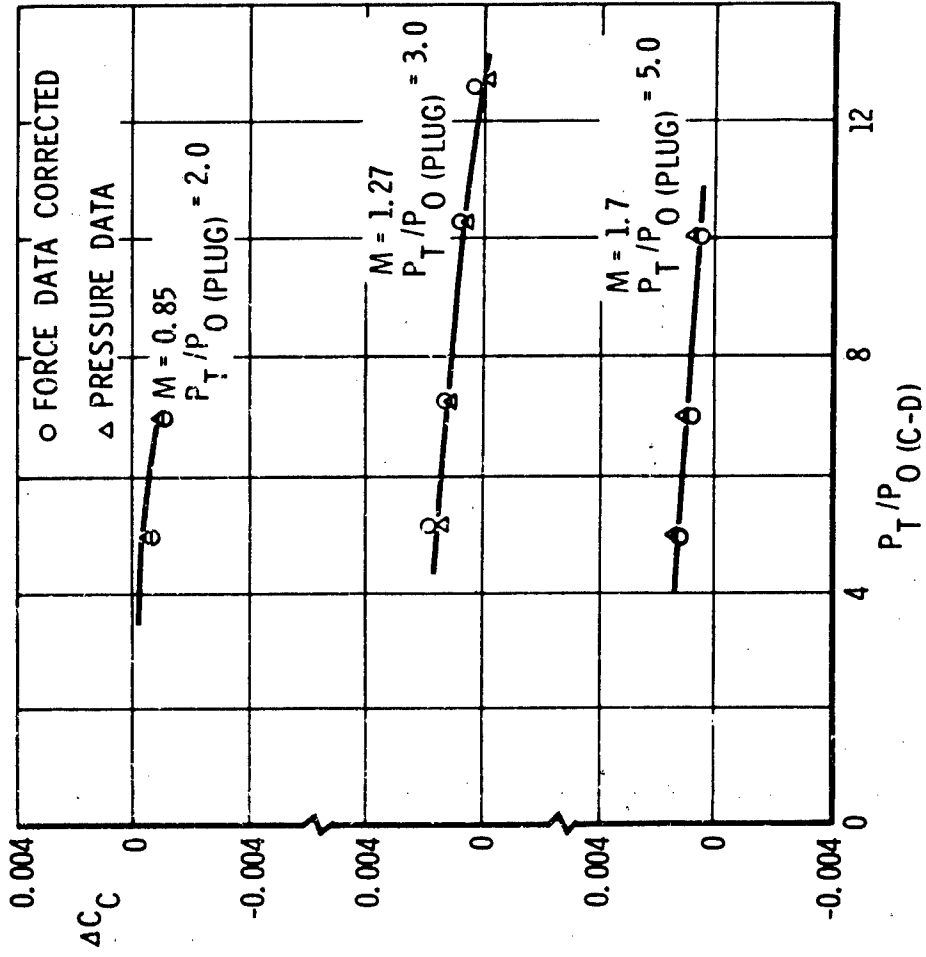


Figure 27. Incremental Chord Force From Reference Configuration Comparison of Force and Pressure Integration Data - $A_g/A_M = 0.3$

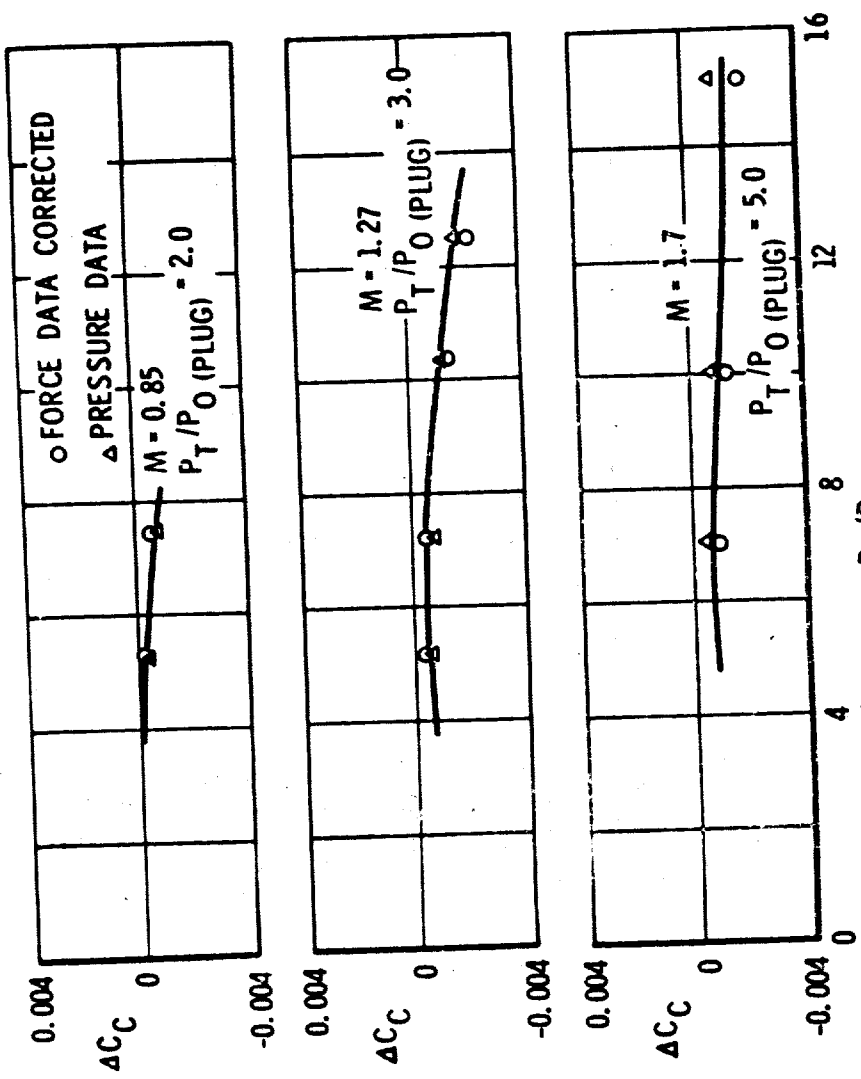
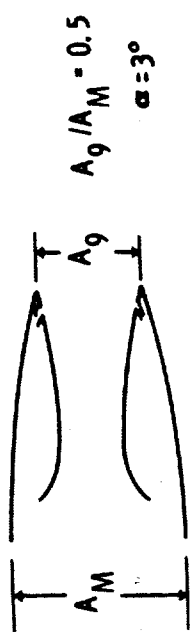


Figure 28 Incremental Chord Force From Reference Configuration -

TWIN-JET AIRCRAFT AFT-FUSELAGE PERFORMANCE PREDICTION

Craig E. Swavely

Pratt & Whitney Aircraft Florida Research and Development Center

ABSTRACT

Accurate determination of aircraft drag and performance is required to aid in the design and performance evaluation of mixed-mission aircraft. No generalized technique for the prediction of aft-end performance of fuselage-mounted twin-jet aircraft is available. Because of the large drag losses associated with the high subsonic-transonic flight regime, and the inadequacy of purely theoretical methods in this region, a test program was initiated to provide a matrix of experimental data for twin-jet installations. The important test variables affecting aft-end performance were selected to provide a parametric variation in the model program. The data obtained from the test program were reduced to model force coefficient and drag coefficient, and were correlated in several ways. Typical fuselage aft-end performance trends with the various geometric variables, as well as free-stream mach number and nozzle pressure ratio are presented and discussed in carpet plot form. An empirical correlation was made to permit extension of the data to a generalized performance prediction system for fuselage aft ends. A comparison of the results of this technique with data from several different sources is presented. A discussion of the limitations of the prediction method, and suggestions for additional work is also presented.

I. INTRODUCTION

A large portion (25 to 30%) of the twin-jet fighter aircraft drag in the transonic region can be attributed to the aircraft aft-end and exhaust nozzle. Unfavorable nozzle/aircraft interactions have been largely ignored in the past, with subsequent deficiencies in aircraft range and performance. Consequently, methods of accurately determining airframe aft-end performance are required to provide initial performance estimates and design information.

Full airplane/nozzle wind tunnel model tests can be conducted to determine the aft-end performance of a particular configuration. However, a wide range of configurations must initially be investigated to establish the preliminary design. Several analytical methods (such as linearized theory for bodies of revolution) are currently available to give insight into airframe aft-end performance. However, purely theoretical methods are limited, particularly in the high subsonic-transonic region, and no general performance prediction technique has been available.

A wind tunnel test program was conducted to fulfill the need for a performance prediction system, and to provide a matrix of experimental data for twin-jet installations. The important test variables affecting aft-end performance were selected to provide a parametric variation of test variables. The experimental program and correlation of the results is the subject of this paper. Comparison of the results of the prediction technique with data from several different sources is also presented, as well as a discussion of the limitations of the technique and suggestions for additional work.

II. TEST PROGRAM

The experimental program was set up to provide a parametric variation of the airframe aft-end geometric variables that appeared to significantly affect drag. Subsequent comparisons of the test results with other aft-end data indicate that the variables of prime importance were included in the test matrix. The geometric variables selected for investigation were nondimensionalized with the afterbody maximum cross sectional area (A_{max}) or the diameter of the circle of equivalent area (D_{eq}). The afterbody test variables, shown in figure 1, are: longitudinal spacing ratio = L/D_{eq} , lateral spacing ratio = S/D_{eq} , projected area ratio = A_e/A_{max} , area distribution = 1st, 2nd, and 4th degree.

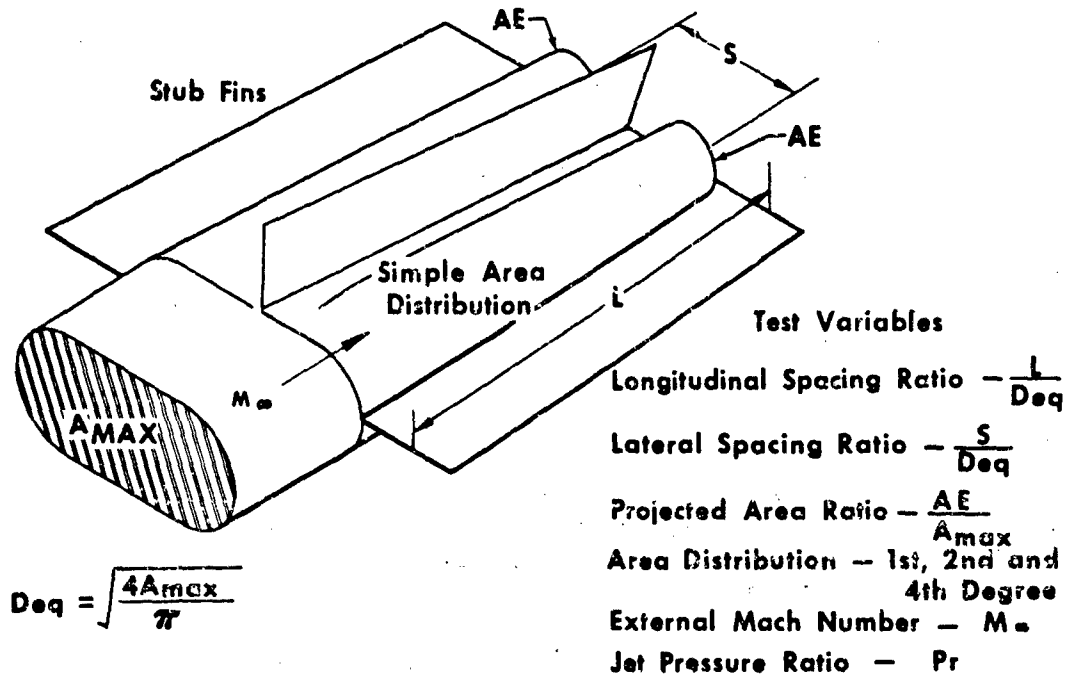


FIGURE 1. AIRFRAME AFT-END TEST VARIABLES. Important Test Variables that Affect Airframe Aft-End Performance Were Parametrically Varied.

GS 11298

The aerodynamic variables that were investigated are external Mach number (M) and jet pressure ratio (Pr). Only convergent nozzles were tested to reduce the number of test variables since it seemed that the afterbody/nozzle drag could be correlated as a function of the jet wake characteristics. All tests were run at zero angle of attack.

The range of variables tested is shown in table I, and includes most current airframe designs. The external Mach number variation was limited to the high subsonic-transonic range where drag losses are large. Also

current mixed-mission aircraft have subsonic cruise requirements and exhaust nozzle projected areas on which drag acts are large during subsonic cruise operation. Two afterbody lateral spacings corresponding to a narrow and wide configuration were tested as well as an equivalent body of revolution corresponding to each area distribution. First, second, and fourth degree area distributions from the fuselage maximum cross-sectional area to the nozzle exit were selected to provide a systematic variation in afterbody area progression. A symmetrical two-dimensional, or beavertail, fairing ending at the nozzle exit was designed for each afterbody, and was included in the area distribution. Figure 2 is a photograph of four typical models of the 32 configurations that were tested for length, spacing, projected area, and shape variations. A photograph of a twin-jet model and its equivalent body of revolution is shown in figure 3. A plot of typical 1st, 2nd and 4th degree area distributions that were investigated is given in figure 4. The test matrix with possible test combinations is shown in figure 5. The marked blocks indicate the configurations tested to provide a maximum of parametric data with minimum cost.

TABLE 1. TEST VARIABLE RANGE GS 11297

$$\frac{L}{D_{eq}} = 1.32, 1.98, 2.64$$

$$\frac{S}{D_{eq}} = 0.0, 0.67, 1.10$$

$$\frac{A_o}{A_{max}} = 0.102, 0.154, 0.206$$

$$M_{\infty} = 0.0, 0.7, 0.9, 1.2$$

$$Pr = 1.5 \text{ to } 8.0$$

The tests were conducted in the United Aircraft Research Laboratories 8-ft wind tunnel. The models were shaft mounted, as shown in figure 6, with the dual-jet flows fed from a divider in the single-flow shaft. A nonmetric transition section from the round shaft to the racetrack shape metric plane of the afterbody produces a windshield for the external flow. Stub vertical and horizontal fins of equal length (and ending at the nozzle exit plane) were tested for all configurations to include fin-afterbody interference effects. The pressure and friction drag of the stub fins was eliminated by using constant cross-section area tare models. The fin drags were not included since each airframe aft end will have fins of different sizes. The cross-sectional area of the fins is not included in the parametric area distributions.

The test data recorded includes afterbody/nozzle thrust minus drag forces, boundary layer characteristics at the metric plane, and static pressure distributions for the equivalent bodies of revolution. The

data reduction computer program calculated afterbody thrust minus drag coefficients, convergent nozzle discharge coefficients, wind tunnel Mach number, and nozzle pressure ratio. Integrated pressure drag coefficients were obtained for the bodies of revolution.

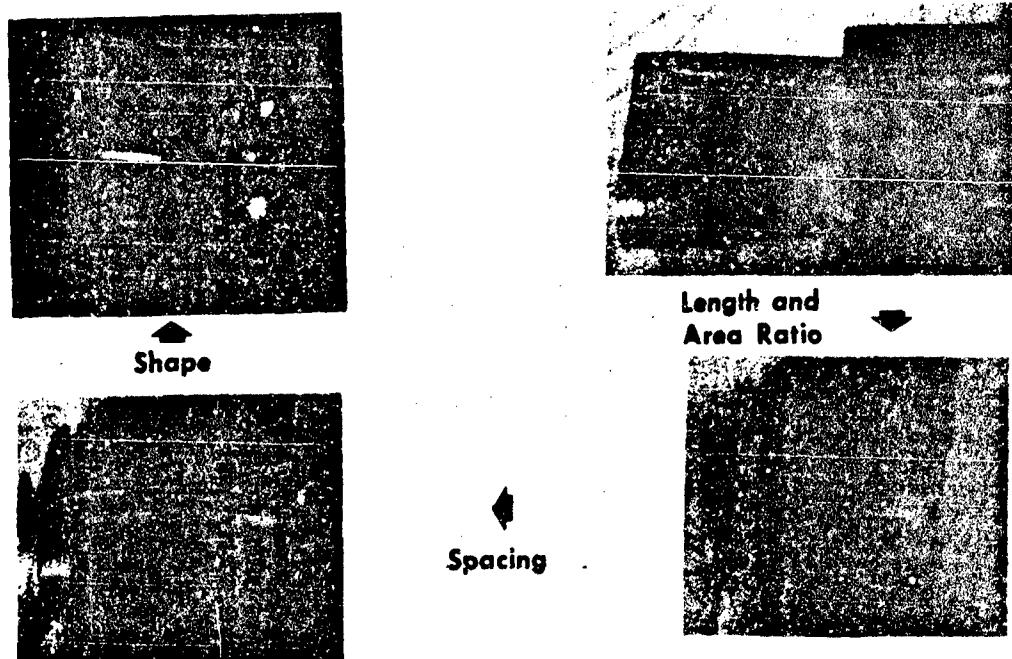


FIGURE 2. TWIN-JET INSTALLED TESTS. 32 Parametric Configurations Were Tested for Length, Spacing, Projected Area, and Shape Variations.

GS 9494A



FIGURE 3. EQUIVALENT BODY OF REVOLUTION. Equivalent Body of Revolution Models Were Tested for Each Twin-Jet Configuration.

GS 8647A

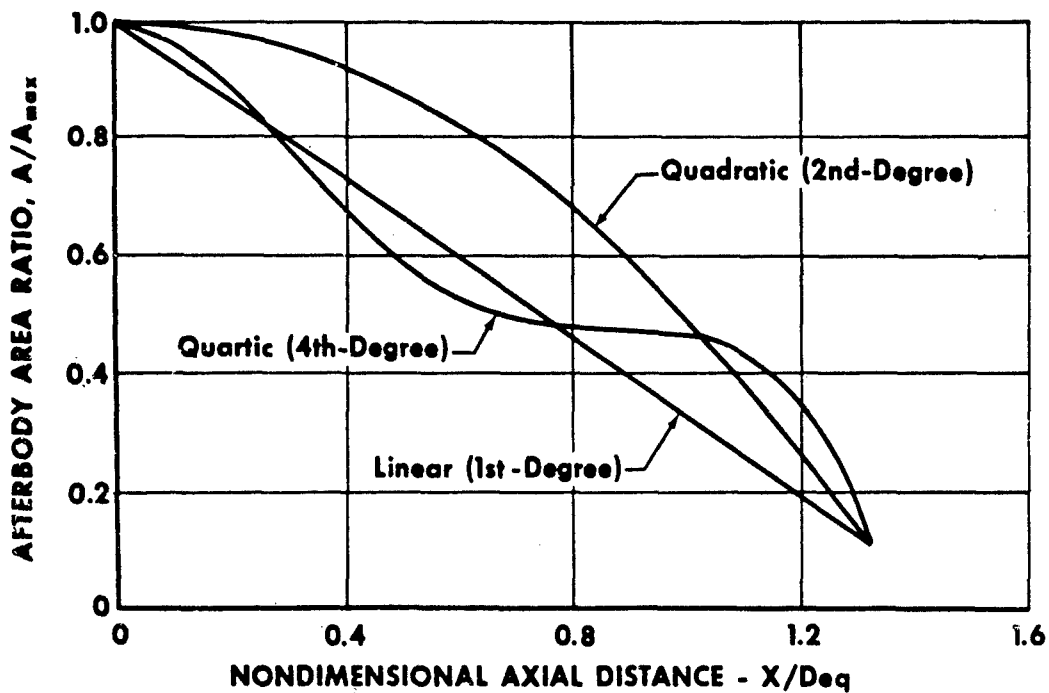


FIGURE 4. TYPICAL AFTERBODY AREA DISTRIBUTIONS. Three Afterbody Area Distributions Were Investigated.

GS 11299

| L/Deq | 1.3210 | | | | | | | | | | | | 1.9815 | | | | | | | | | | | | 2.6420 | | | | | | | | | | | | | | | | | | | | | | | |
|----------------------------------|----------|--|--|--|--------|--|--|--|--------|--|--|--|--------|--|--|--|--------|--|--|--|--------|--|--|--|--------|--|--|--|--------|--|--|--|--------|--|--|--|---|--|--|--|---|--|--|--|---|--|--|--|
| | 0 | | | | 0.6713 | | | | 1.1008 | | | | 0 | | | | 0.6713 | | | | 1.1008 | | | | 0 | | | | 0.6713 | | | | 1.1008 | | | | | | | | | | | | | | | |
| S/Deq | 1 | | | | 2 | | | | 4 | | | | 1 | | | | 2 | | | | 4 | | | | 1 | | | | 2 | | | | 4 | | | | 1 | | | | 2 | | | | 4 | | | |
| AREA DIST | X/Deq | | | | | | | | | | | | | | | | | | | | | | | | | | | | | | | | | | | | | | | | | | | | | | | |
| | 1.2 | | | | | | | | | | | | | | | | | | | | | | | | | | | | | | | | | | | | | | | | | | | | | | | |
| 0.9 | 0.9 | | | | | | | | | | | | | | | | | | | | | | | | | | | | | | | | | | | | | | | | | | | | | | | |
| | 0.7 | | | | | | | | | | | | | | | | | | | | | | | | | | | | | | | | | | | | | | | | | | | | | | | |
| 0 | 0 | | | | | | | | | | | | | | | | | | | | | | | | | | | | | | | | | | | | | | | | | | | | | | | |
| | MACH NO. | | | | | | | | | | | | | | | | | | | | | | | | | | | | | | | | | | | | | | | | | | | | | | | |
| A ₁ /A _{max} | | | | | | | | | | | | | | | | | | | | | | | | | | | | | | | | | | | | | | | | | | | | | | | | |

FIGURE 5. TWIN-JET TEST MATRIX. Systematic Tests of the Twin-Jet Configurations Provide a Maximum of Parametric Data with Minimum Cost.

GS 8805A

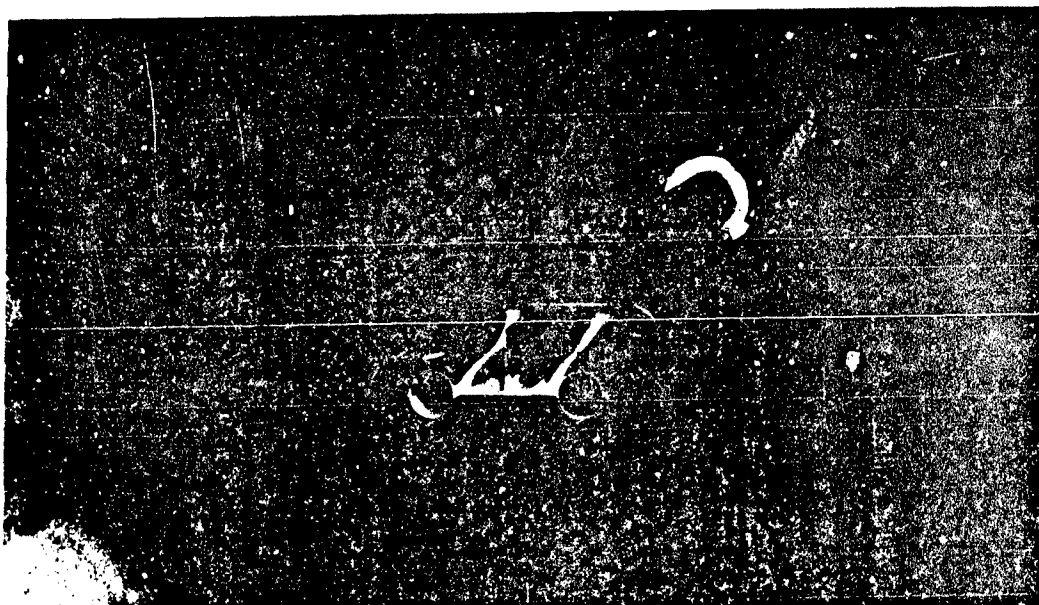


FIGURE 6. TYPICAL MODEL TEST SETUP. Parametric Aircraft Aft-End Configurations were Tested in the 8-ft Wind Tunnel.

GS 9493A

III. EXPERIMENTAL CORRELATIONS

Twin-jet afterbody pressure and skin friction drag was obtained for each configuration tested as a function of external Mach number and convergent nozzle pressure ratio. The drags were nondimensionalized by taking the difference between the measured aft end thrust minus drag coefficients, $(T-D)/F_{IP}$, at Mach number and at static conditions. A drag coefficient based on afterbody maximum area (A_{max}) was then obtained and plotted in carpet graph form, as shown in figure 7. These plots include the skin friction and pressure drag of the twin-jet afterbody only, but not the fin drag. The variation of afterbody drag coefficient with aft-end geometry for a particular Mach number and jet exit condition can be observed from the carpet plots. For example, increasing longitudinal spacing, L/D_{eq} reduces afterbody drag at Mach 0.9 for a given afterbody projected area ratio (A_e/A_{max}). The reverse trend is true at Mach 0.7, as shown in figure 8, because here friction drag is predominant and the longer spacing has a larger surface area than the short spacing.

Mach Number = 0.9
 Jet Pressure Ratio, $P_r = 2.5$
 Area Distribution - 4th Degree

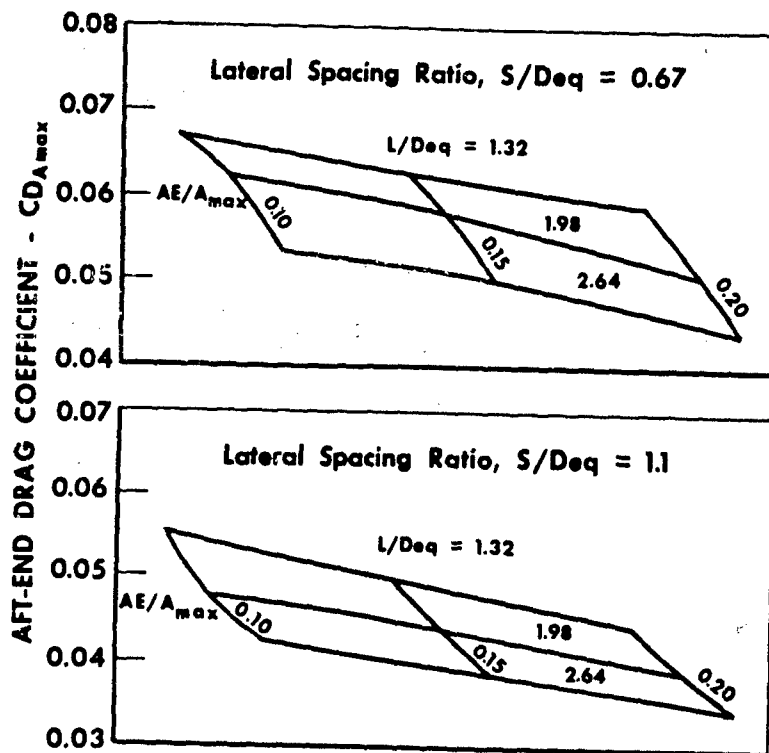


FIGURE 7. AFT-END DRAG COMPARISON. The Twin-Jet Data Have Been Correlated in Carpet Plot Form to Show the Variation of Drag Coefficient with Aft-End Geometry.

GS 11300

Mach Number = 0.7
 Jet Pressure Ratio, $P_r = 2.5$
 Area Distribution - 4th Degree

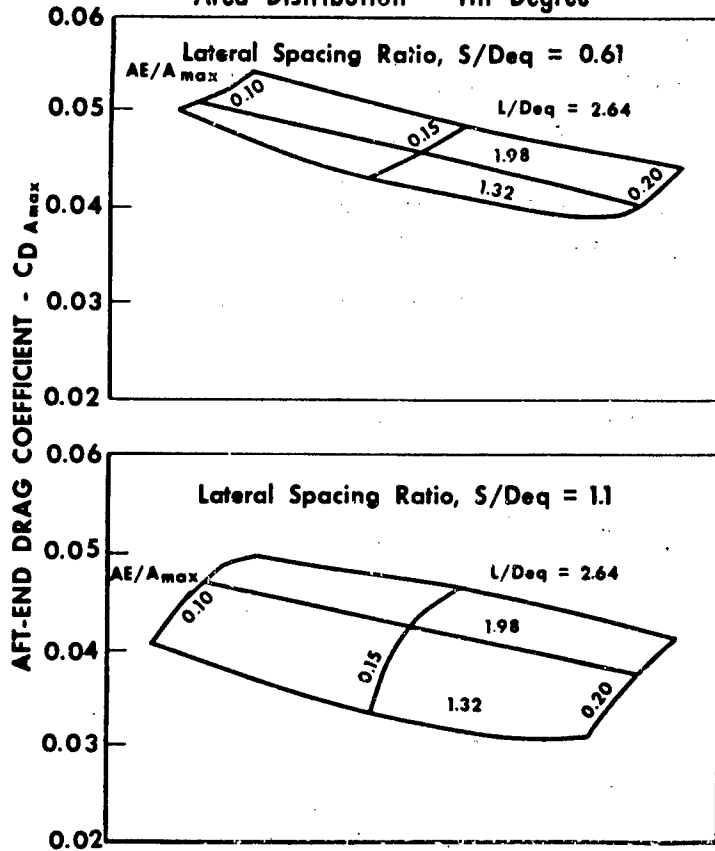


FIGURE 8. AFT-END DRAG COMPARISON. Increased Twin-Jet Aft-End Lateral Spacing Can Reduce Drag Coefficient. GS 11461

The carpet plots also show that an increase in lateral spacing reduced drag. This occurs because the interference effects between the twin jet boattails are reduced as spacing increases. However, the skin friction increases because of the larger surface areas and consequently the drag reduction is not as pronounced at Mach 0.7 as at Mach 0.9. The effect of jet pressure ratio can be observed by a comparison of figures 7, 9, and 10. An increasing jet pressure ratio will cause the wake to billow and pressurize the afterbody projected areas. This pressurization can significantly reduce the twin-jet afterbody drag coefficients.

Special attention must be paid to use of the data with varying pressure ratio. The tests were conducted with convergent nozzles, and afterbody configurations frequently include a convergent-divergent nozzle with a given area ratio. A close simulation of the jet pressurization effects can be obtained by approximating the jet wake billowing characteristics. Duplication of the initial jet boundary flow direction gives drag coefficients that show good agreement with coefficients obtained for con-

vergent-divergent nozzles. An even better simulation may be possible by use of a jet wake parameter that simulates the wake velocity as well as initial wake angle.

Mach Number = 0.9
 Jet Pressure Ratio, $P_r = 4.0$
 Area Distribution - 4th Degree

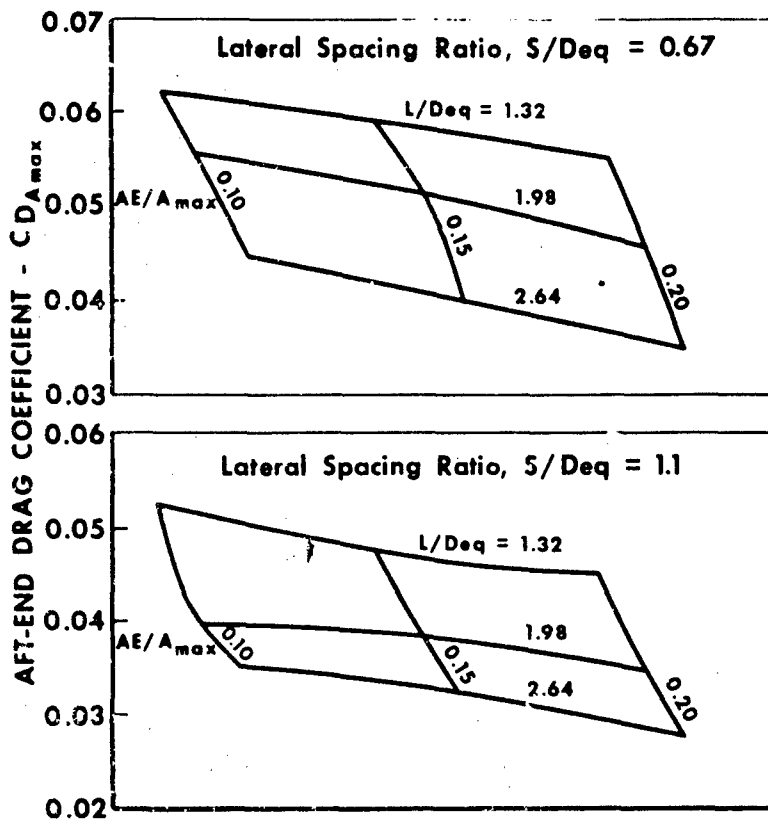


FIGURE 9. AFT-END DRAG COMPARISON. Increased Jet Pressure Ratio Reduces Aft-End Drag Coefficient. GS 11460

Mach Number = 0.9
 Jet Pressure Ratio, $P_r = 6.0$
 Area Distribution - 4th Degree

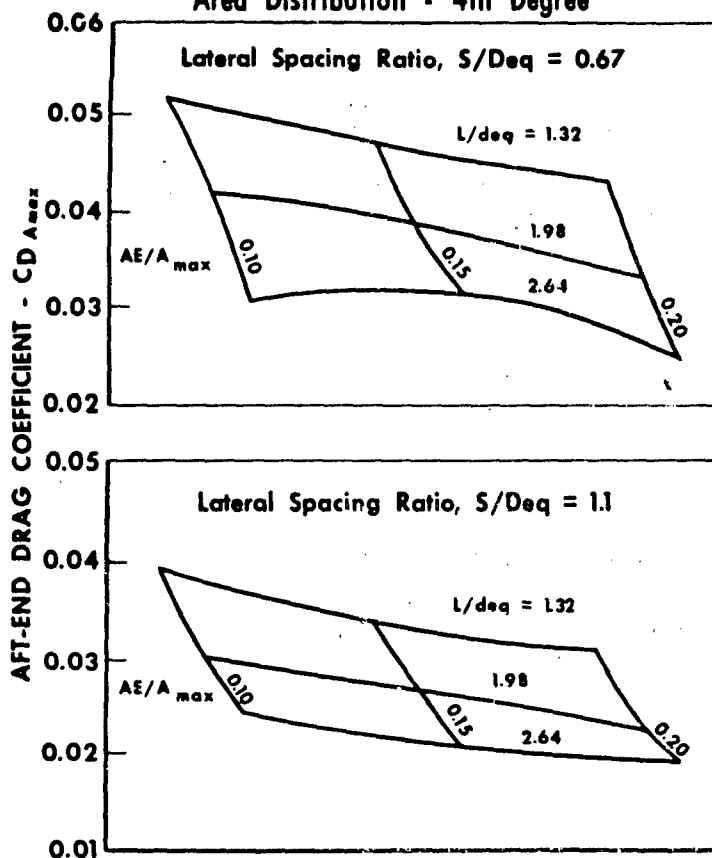


FIGURE 10. AFT-END DRAG COMPARISON. Increased Jet Pressure Ratio Reduces Aft-End Drag Coefficient. GS 11462

Equivalent bodies of revolution for each twin-jet configuration were tested with the hope of gaining a drag correlation between the two. If such a correlation could be obtained, twin-jet drag estimates could be easily accomplished because methods for analytical prediction of body of revolution pressure distributions are well known. Typical body of revolution pressure drags compared with twin-jet pressure drags are shown in figure 11. The pressure drags were obtained by integration of static pressures over the EBOR (equivalent body of revolution), while twin-jet pressure drags were obtained by subtracting the skin friction drag of an equal surface area tare model with no projected area. At subsonic speeds, the body of revolution drags are much lower than the twin-jet drag, indicating that a recompression is occurring on the EBOR. The larger twin-jet drags indicate that significant interference effects are present between the two nozzles. As previously noted, these drags are reduced as the spacing between the nozzles increases. At supersonic speeds the agreement between the twin-jet and EBOR is much better, indicating that the drag is primarily a function of the area distribution and the amount of turning the flow must undergo. No general correlation of EBOR and twin-jet drags has been developed from this study, but it merits continued investigation.

Mach Number = 0.9
 Jet Pressure Ratio, $P_r = 2.5$
 Pressure Drag Only

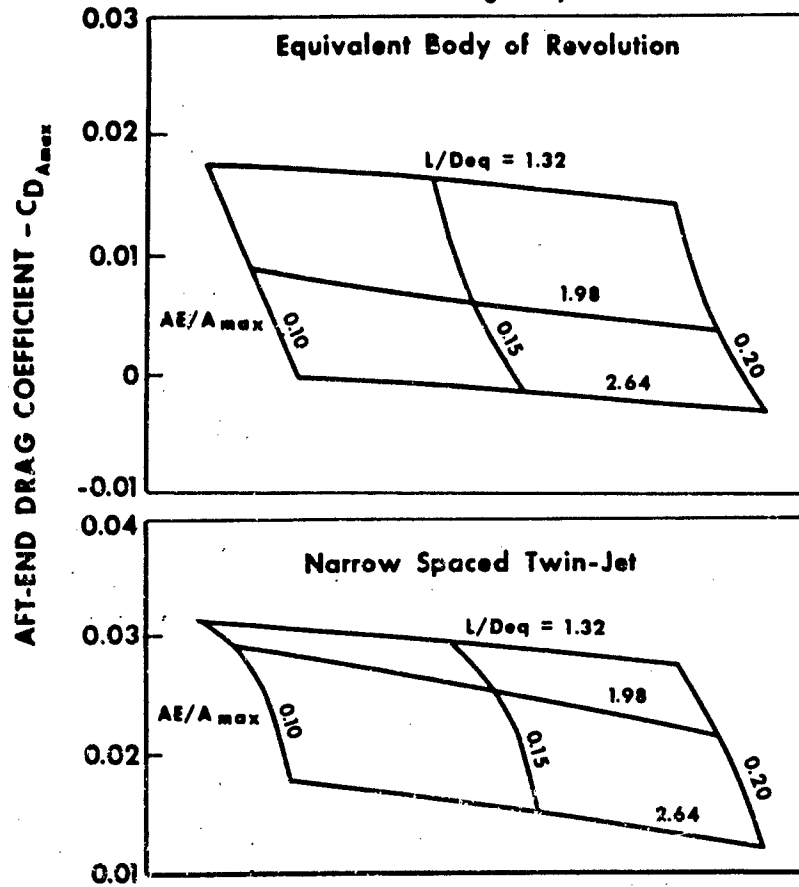


FIGURE 11. AFT-END DRAG COMPARISON. Twin-Jet Drags are Larger Than an Equivalent Body of Revolution Because of Interference Effects.

GS 11492

The body of revolution drags can also be used as indication of the drag limits obtainable for twin-jet bodies of very large spacings (isolated nacelles) by evaluating the drag of a body of one-half the projected area (figure 12). The comparison is made on the basis of pressure drag only to give insight into the magnitude of interference effects of two nacelles without the influence of skin friction forces, since the skin friction would increase as surface area increases.

Mach Number = 1.2
 Jet Pressure Ratio, $P_r = 4.0$
 Pressure Drag Only

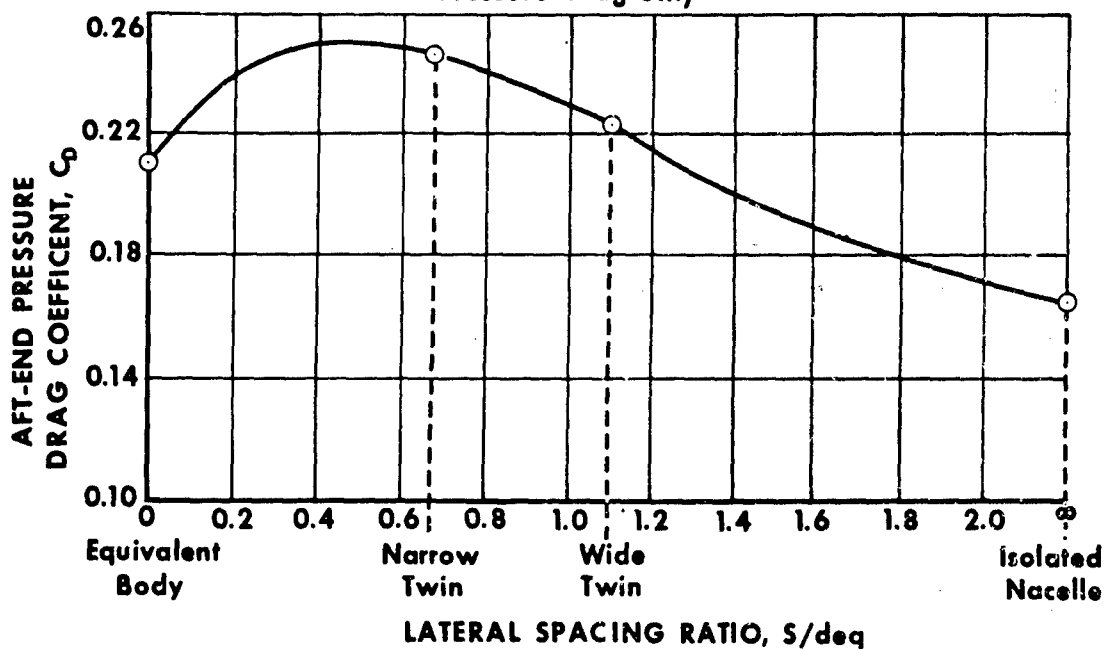


FIGURE 12. AFTERBODY DRAG COEFFICIENT VARIES WITH LATERAL SPACING RATIO. Equivalent Body Drags Give an Indication of Jet Interference Effects. GS 11463

Presentation of the data in carpet plot form illustrates many useful data trends, and interpolation between the geometric parameters can give close approximations to the drags of actual twin-jet bodies. However, it is very difficult to interpolate for one very important geometric parameter: aft-end area distribution. Pressure drag is significantly affected by area distribution, especially in the transonic range, as shown in figure 13 and actual airframe aft-end configurations, in general, will not match any of the three area distributions tested. Consequently, some sort of correlating parameter was needed to permit generalized predictions and interpolation of the data. From area rule considerations, this drag correlating parameter, or "shape factor," should be related to the rate of progression of afterbody area.

Mach Number = 0.9
 Jet Pressure Ratio, Pr = 2.5
 Narrow Spacing S/Deq = 0.65

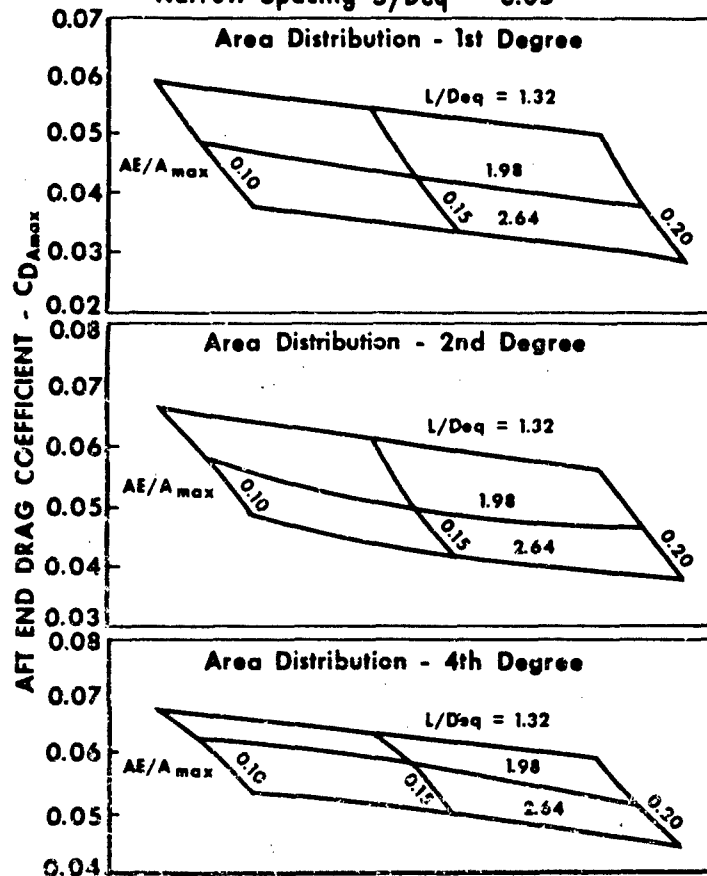


FIGURE 13. AFT-END DRAG COMPARISON. Twin-Jet Aft-End Area Distribution Significantly Affects Drag Coefficient. GS 11484

Calculation of a shape factor for each twin jet body, and its drag coefficient based on the projected area over which drag acts, showed good correlation (figure 14). Some scatter of the data about a mean line is evident, indicating that the shape factor accounts only for first order effects of geometry on drag. Some degree of theoretical basis for the shape factor can be found from linearized slender body theory, which also accounts only for first order effects. However, the correlation has proved accurate enough for initial drag estimates. Particularly, it is useful for investigation of incremental effects, as will be discussed later. A complete set of correlations with different curves for each Mach number, nozzle pressure ratio, and lateral spacing ratio was generated to provide a generalized prediction for afterbody drag coefficient.

All of the drag correlations for the various geometrics and flow conditions have the general shapes as shown in figure 14. The curves appear to become asymptotic to some value of drag coefficient as the shape factor

gets large. This indicates that a base region or separated flow condition is being approached at large values of shape factor. Comparisons of the data with theoretical base pressure calculations are currently being investigated. It should be remembered that the data correlations were generated for smoothly contoured twin-jet afterbodies with no sharp corners or vertical base areas, no side blockage due to tail booms or vertical control surfaces, and apply only to that type of configuration. Corrections for these effects are being investigated. However, the configurations tested are representative of the low drag installations required for today's high performance aircraft.

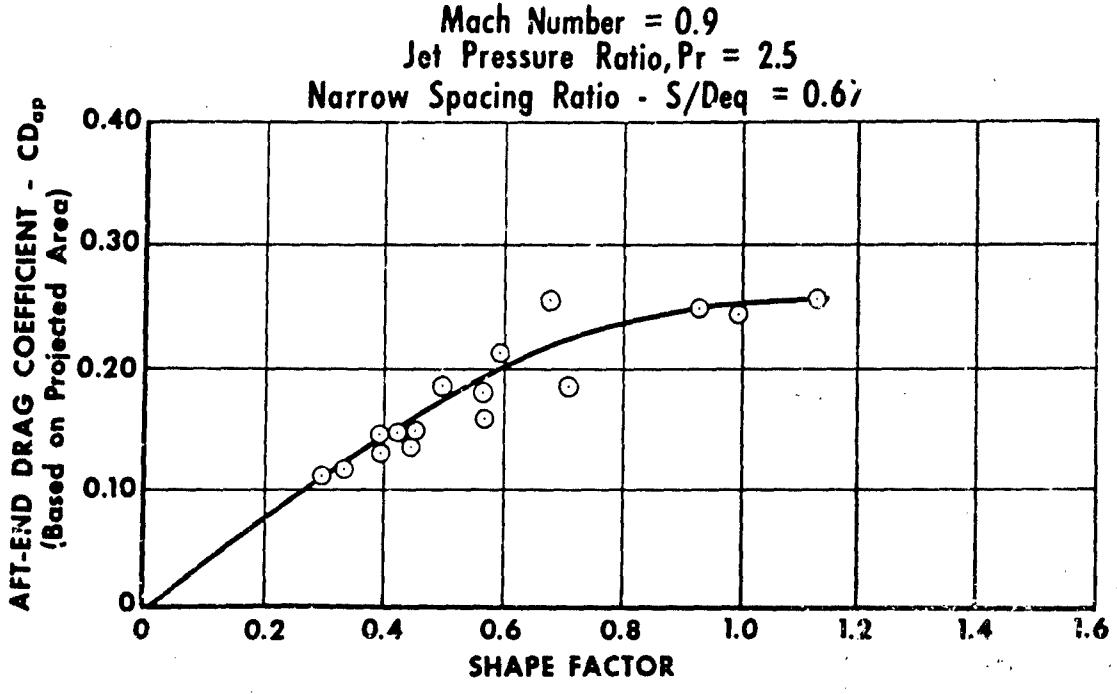


FIGURE 14. SHAPE FACTOR CORRELATION. Drag Coefficient Shows Correlation with Twin-Jet Afterbody Shape Factor. GS 9492B

IV. APPLICATION OF PREDICTION TECHNIQUE

The shape factor correlations were compared with wind tunnel model test data for several airframe aft-end configurations to verify the prediction technique. A shape factor was calculated for the area distribution of the metric section only, for each configuration investigated. This permitted determination of the aft-end drag coefficient exclusive of fin pressure and friction drag, but including fin interference effects on the afterbody. If fin drag is to be included in the comparison, theoretical calculations of the pressure and skin friction drags must be made. Since most control surfaces are symmetrical and of small thickness ratio, the pressure drag may be calculated using shock-expansion theory at supersonic Mach numbers, and ignored at subsonic Mach numbers. Skin friction drags may be obtained using the fin wetted area and standard calculations for the friction drag coefficient as a function of Reynolds number. When the measured data include the thrust of a convergent or convergent-divergent exhaust nozzle, the nozzle static thrust coefficient must be known or calculated to complete the comparison.

Figure 15, shows a typical comparison of predicted and measured aft-end thrust minus drag coefficients for a narrow-spaced configuration with a beavertail interfering and convergent nozzles. Agreement within 1 1/2% was obtained over the pressure ratio range of interest. Because of the proprietary nature of several of the configurations, a summary of the predicted versus measured thrust minus drag coefficients is presented in figure 16. These comparisons include checks for lateral spacing and convergent-divergent exhaust nozzles over a wide range of nozzle pressure ratio and external Mach numbers from 0.0 to 1.2.

The airframe aft-end performance predictions can be utilized to obtain overall airframe thrust minus drag performance in much the same way as the actual wind tunnel results are applied. That is, the aft-end performance may be referenced to an aero model aft-end drag or other convenient reference such as the drag of an equivalent body of revolution.

That is:

$$(T - D)_{\text{aircraft}} = T_{\text{static}} - D - \Delta D$$

where:

$$T_{\text{static}} = \text{static net thrust}$$

D = measured or predicted drag (including inlet drag) of the aircraft, but with a reference aft end.

$$\Delta D = D_{\text{predicted aft end}} - D_{\text{reference aft end}}$$

Application of the prediction technique using this type of thrust minus drag accounting system has pointed up a problem in the consistent comparison of aft-end performance. That is, unless all aft-end performance is predicted using a common set of ground rules such as length of the after-

body, all fins metric or non-metric etc, consistent comparisons cannot be made. A set of standards for back-end performance comparisons remains to be developed.

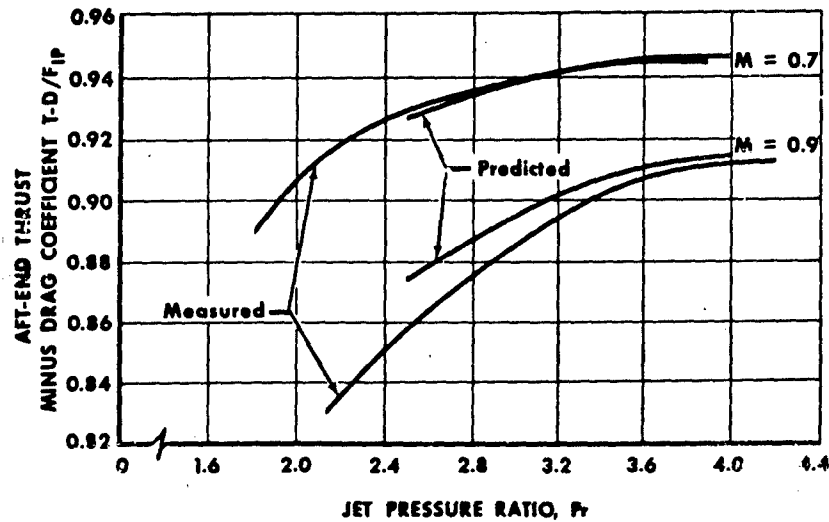
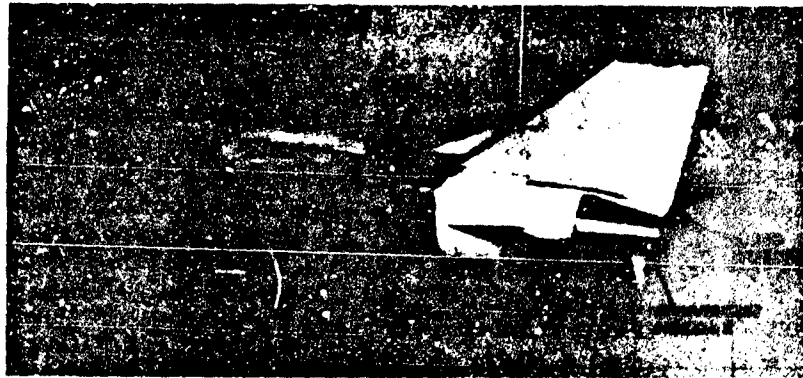


FIGURE 15. PREDICTION SYSTEM VERIFIED. Predicted Aft-End Thrust Minus Drag Coefficient Agrees with Test Data. GS 9491A

Note that all comparisons were made with configurations of similar design to the test models on which the prediction system was based. That is, the drag of configurations with large base areas, tail booms or other surfaces that block recompression on the afterbody could not be accurately predicted. The prediction system will be modified to account for these effects as data become available. Other limitations, such as boundary layer thickness, must also be considered and are discussed in the following section.

However, the prediction system has a more useful application where these limitations are not as restricting, that is, the prediction of incremental performance trends for various afterbody configuration changes. This capability can serve as a very useful preliminary design tool to narrow the selection of airframe/nozzle aft-end configurations

to be tested or studied. Thus, while the absolute performance levels may not always be accurate, the performance trends can be identified.

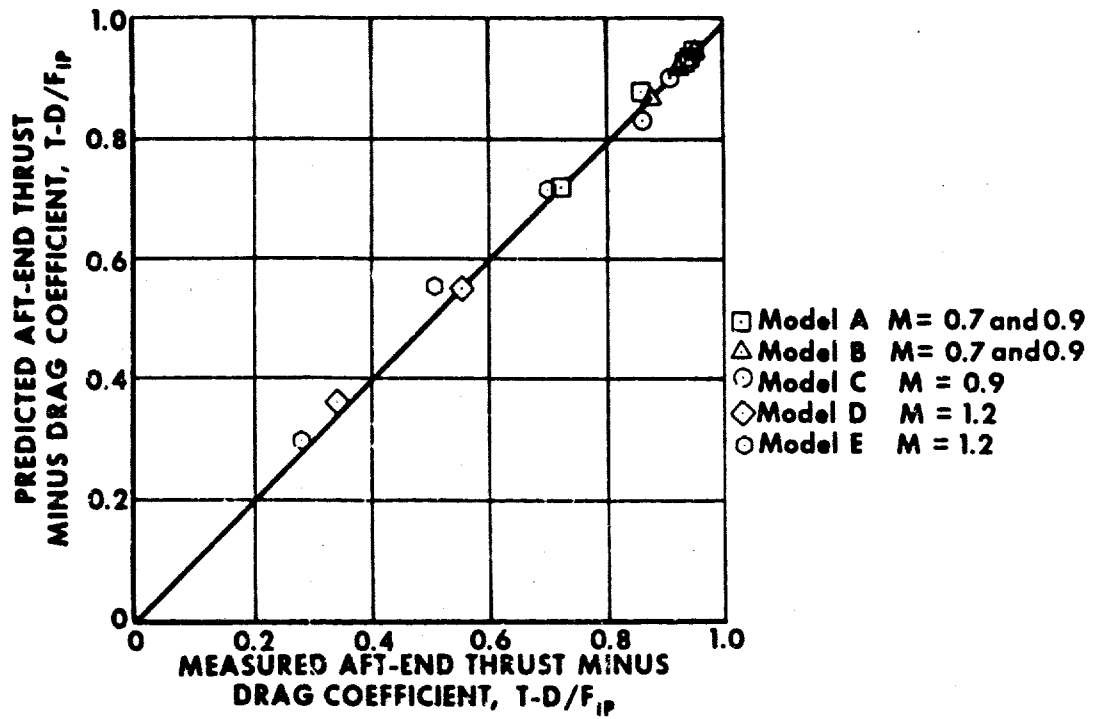


FIGURE 16. VERIFICATION OF PREDICTION SYSTEM. Comparison of Predicted and Measured Aft-End Thrust Minus Drag Shows Good Agreement.

GS 9499B

V. LIMITATIONS OF PREDICTION TECHNIQUE

Since the prediction technique described here is based upon experimental correlations, certain restrictions or limitations inherent in the test method must be considered. As previously mentioned, all tests were conducted with convergent nozzles only, and a method for extending the data to simple convergent-divergent nozzles was suggested. At present, the results appear valid only for these nozzle types, and are not applicable to plugs or blow-in door ejectors. This can be rationalized from the fact that the aft-end pressure distributions are a function of the jet wake characteristics, and the jet contours are significantly different for plug or blow-in door nozzles for the same jet pressure ratio.

Another important limitation to be considered is that no tail booms or vertical control surfaces that block flow recompression on the outboard sides of the aft-end, as shown in figure 17, were included in the test matrix. That is, the tests apply only to twin jet configurations where physical surfaces do not cross the streamline planes. However, the data correlations can be applied to certain aft-end configurations which do have tail booms or control surfaces. Consider the pressure distribution and flow recompression on the aft-end of a body of revolution. The recompression is caused by curvature of the streamlines to maintain a flow tube of approximately constant cross-sectional area as the axisymmetric boattail area is reduced. The streamlines are essentially displaced along radial lines from the center of the body and move in radial planes. Now, take a twin-jet configuration having the same area distribution as the body of revolution. Flow recompression between the twin-jets is locally blocked by the adjacent surfaces, and drag is significantly increased. This is an indication of the magnitude of twin-jet interference effects. If physical surfaces are now placed along the planes in which the streamlines normally move (figure 18) then blockage does not occur and the only additional drags to be accounted for are pressure and skin friction drags for the surfaces themselves. Corner flow effects due to the junction of the three stub fin surfaces and the afterbody are included in the test results, and are relatively small compared to drag caused by flow blockage.

Another factor previously mentioned is that the twin-jet configurations tested were all smoothly contoured bodies with no sharp corners or base areas. Methods to handle base areas are currently being investigated. For example, the asymptote of the shape factor correlation could be used to give a value of drag coefficient for the base area. This base drag coefficient could then be area-weighted with the drag coefficients obtained for the rest of the body by the usual method to give a final value. This technique requires further investigation.

Two limitations related to the particular test technique used should also be mentioned. Since the models were mounted on a shaft extending from the wind tunnel plenum chamber to the test section, a relatively large boundary layer exists at the metric station. The ratio of boundary layer displacement thickness divided by equivalent diameter at the metric section varies from 0.020 to 0.025 on the top to approximately 0.030 on the side of the shaft transition section. Consequently, the data and results presented in this paper are valid for these boundary

layers only. Other investigations have shown that a reduction of boundary layer thickness increased drag for bodies of revolution. However, boundary layer effect on twin-jet drag has yet to be determined.

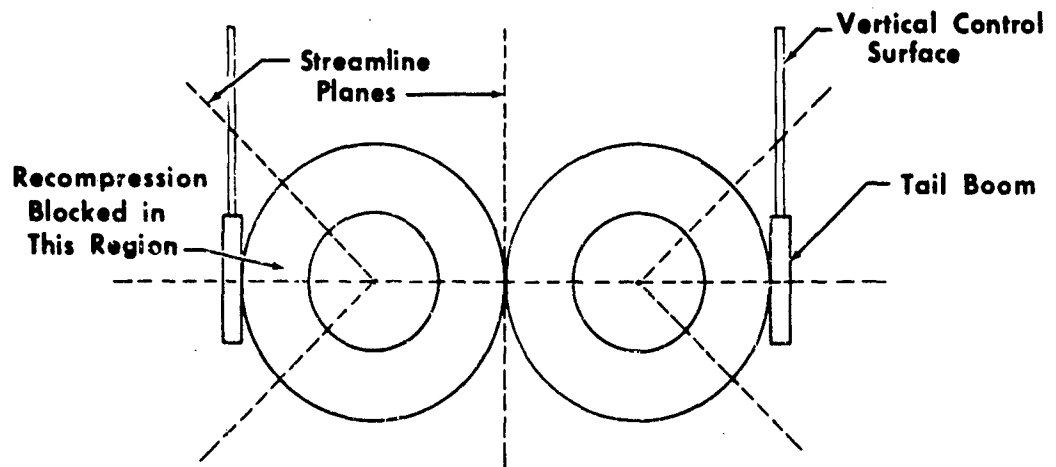


FIGURE 17. PHYSICAL SURFACES CROSSING STREAMLINE PLANES BLOCK RECOMPRESSION. Tail Booms or Control Surfaces that Cross the Streamline Planes Can Block Flow Recompression on Twin-Jet Bodies. GS 11485

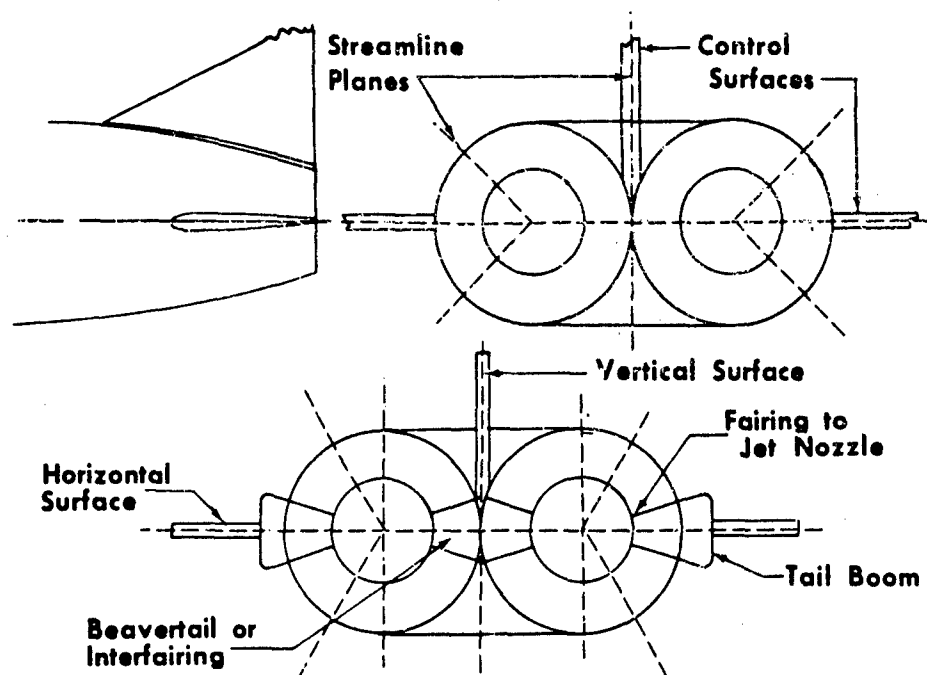


FIGURE 18. LOW DRAG AFT-END DESIGN. Physical Surfaces Located Along Streamline Planes Provide no Additional Blockage to Recompression. GS 11487

Finally, the effect of the forebody shape upstream of the metric section on aft-end performance has not been resolved. Analytical studies have indicated only small differences in boattail pressure distributions, and consequently boattail drag, for upstream geometry variations on bodies of revolution, as indicated in figure 19. Also, twin-jet tests of actual aircraft configurations with wings removed showed only small differences (1/2 to 1%) in aft-end drag coefficients. In general, drags increased when the wing sections were removed, indicating that the results presented in this paper would produce conservative drag predictions.

All of the restrictions and limitations indicated in this study suggest areas for additional work. Some investigations in these areas have been accomplished for particular installations, but no comprehensive parametric studies have been conducted that would permit systematic correlation of the results. To provide general data for wide application, future research programs should be as parametric as possible.

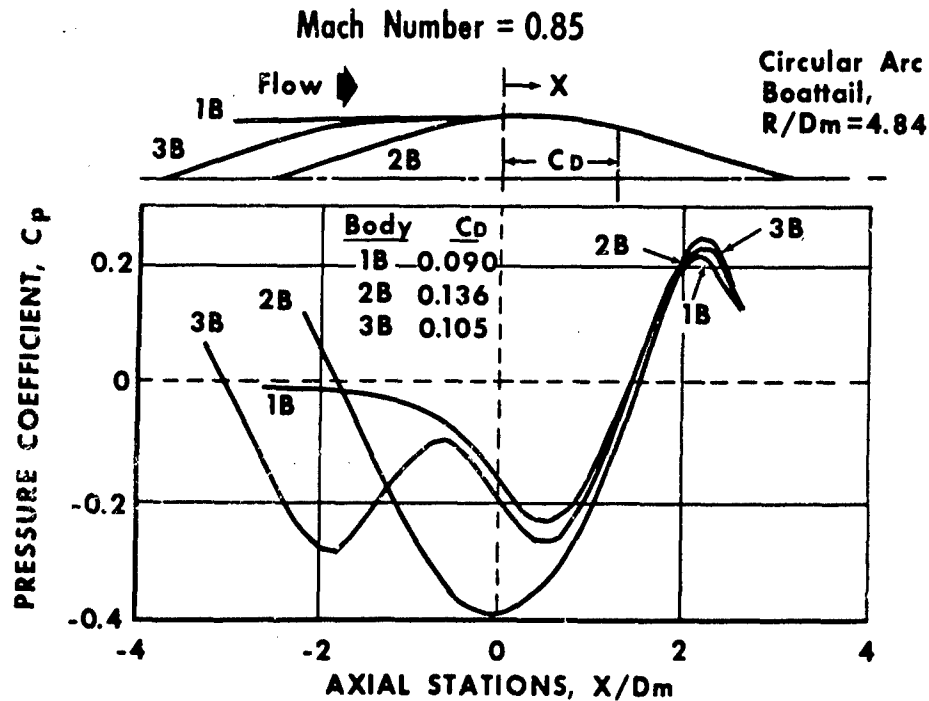


FIGURE 19. UPSTREAM GEOMETRY EFFECTS ON BOATTAIL DRAG. Large Forebody Geometry Variations can Have Only Small Effect on Afterbody Drag.

— GS 11488

VI. SUMMARY

A generalized technique for the prediction of airframe aft-end performance has been generated from a correlation of experimental twin-jet data. The correlations provide (1) an insight into performance trends due to the important aft-end geometric variables such as lateral and longitudinal spacing, projected area, and area distribution, and (2) performance estimates for specific aft-end configurations. However, certain limitations are inherent in the test methods, and the range of geometry investigated. These restrictions suggest additional areas of investigation where further work should be undertaken to aid in the design and performance evaluation of current and future mixed-mission aircraft.

EXHAUST NOZZLE-AFTBODY INTEGRATION ON TACTICAL FIGHTER TYPE AIRCRAFT

John L. Benson and Edsel R. Glasgow

Lockheed-California Company

ABSTRACT

An experimental research program is described which examined the effects of engine exhaust nozzle spacing and aftbody geometry on the installed nozzle performance of a twin engine tactical fighter type aircraft. The basic objectives of the study were (1) to determine whether there is an optimum nozzle spacing ratio, and (2) to examine the effect of aftbody geometric parameters on nozzle performance. Two types of nozzles were considered in this study: a conical plug nozzle type and a simple convergent-divergent nozzle. Scale models of the nozzle and aftbody were tested over a range of pressure ratios from Mach = .80 to Mach = 1.20. The nozzles were pylon-supported and could be separated to obtain nozzle centerline-to-centerline spacing ratios of 1.1 to 2.0.

INTRODUCTION

Tactical fighter aircraft are currently being designed for higher maneuverability and acceleration rates, over a wider range of flight operating conditions, than existing operational aircraft. These higher aircraft performance requirements, in turn, impose more severe operating conditions on the aircraft's propulsion system and make the problem of airframe propulsion system integration more difficult. Thus increased emphasis must be given to the design and development of the integrated airframe propulsion system configuration to ensure that the total system's performance and stability are adequate over the complete range of flight Mach numbers, angles of attack and yaw, altitudes and engine power settings. In recognition of this need for increased attention to airframe propulsion system integration on tactical fighter aircraft considerable research is being conducted at the present time by both the airframe industry and government agencies, on various aspects of this subject. This paper presents the results of one such industry sponsored study: an experimental investigation of the effects of nozzle spacing on the installed exhaust nozzle performance for a twin engine tactical fighter aircraft installation. The investigation was initiated in response to the need for such data on various FX and VFX fighter aircraft studies conducted during 1967 and 1968, at the Lockheed-California

Company. The test was conducted in LTV's 4 foot by 4 foot high speed wind tunnel. The following sections of this paper describe briefly the development of the preliminary aircraft designs, the objectives of the test programs and details of the models. Test results are presented and various aspects of these results discussed in detail.

CONFIGURATION SELECTION

The evolution of the tactical fighter aircraft configurations examined began with a definition of the aircraft's performance objectives in terms of climb and acceleration rates, mission radius, and other parameters such as vulnerability and reliability. These performance objectives led to the selection of the propulsion system configuration. This process is illustrated diagrammatically in Figure 1. The combination of performance requirements and wing loading lead to the requirement for a high total engine thrust to aircraft weight ratio, i.e. $T/W \geq 1.0$, and the need for an engine having a variable area exhaust nozzle and a good part power transonic thrust coefficient. The requirements for vulnerability and reliability lead to the selection of a twin engine arrangement. Examination of the thrust coefficient characteristics of several available potential exhaust nozzle configurations led to the decision to consider an engine incorporating a plug nozzle and one incorporating a C-D nozzle. The aircraft configurations evolved are shown in Figure 2 with the C-D engine exhaust nozzle arrangement. As can be seen the aircraft in the upper part of the figure incorporates two-dimensional horizontal ramp inlets located just ahead of the wing leading edge, at the wing root. The aircraft in the lower part of the figure incorporates two-dimensional vertical ramp inlets located considerably behind the leading edge. Because of the short inlet ducts of this configuration the engines were located almost directly behind the inlets to minimize the duct total pressure loss.

In conducting trade-off studies of these configurations the question arose as to what effect engine nozzle spacing ratio, defined as the centerline-to-centerline distance between the engines divided by the maximum nozzle diameter, had on the installed performance of the nozzle aftbody configuration. A review of the literature at the time of this study revealed that insufficient test data were available to aid in the selection of engine nozzle spacing ratio. A scale model test program was therefore initiated for the purpose of obtaining such data. Sketches of the exhaust nozzle aftbody configurations selected for testing are shown in Figure 3. The plug nozzle design shown was tested in its cruise power setting configuration, while the C-D nozzle design shown was tested at both cruise and maximum A/B power setting configurations. The model general arrangements were somewhat different in that the plug nozzle was tested with a symmetric interfairing, while the C-D nozzle arrangement was tested with an asymmetric interfairing. Also three different spacings were examined on the plug nozzle arrangement, while only two spacings were examined on the C-D nozzle arrangement. To determine interference effects the C-D test was conducted both with and without a vertical fin. Also aft fairing inserts were examined on the C-D nozzle arrangement. The matrix of test conditions examined are shown in Figure 4 for each of the three nozzles. Shown are the spacing ratios,

nozzle pressure ratios and test Mach numbers at which the three configurations were tested. As noted testing was conducted only at transonic Mach numbers since this was the region of maximum interest.

MODEL SUPPORT AND INSTRUMENTATION

Photographs of the nozzle test rig installed in the LTV 4 foot by 4 foot wind tunnel are shown in Figures 5 and 6. Figure 5 shows the plug nozzle arrangement while Figure 6 shows the C-D nozzle arrangement. The forebody of the test rig consists of two parallel 4-inch diameter tubes, 49 inches in length, separated by a spacer manifold. The flow tube assembly is rigidly held to the tunnel horizontal centerline by a forward sweeping strut, which is bolted to the tunnel ceiling. High pressure air is supplied through the strut and diverted into each of the flow tubes from the spacing manifold. The airflow to each flow tube is individually controlled and metered outside the tunnel. Single nacelle models were tested by sealing off one side of the spacer manifold with a fairing block. The 49 inch length of the test rig was established on the basis of providing a boundary layer thickness to fuselage diameter ratio approximately equivalent to that of the typical fighter type aircraft configurations shown earlier. The δ/D ratio of these configurations was approximately .145. In conducting the tests one nozzle flow tube contained a complete 3 component cylindrical force balance system while the other contained sufficient static pressure instrumentation to check the force measurements.

Details of the model instrumentation and force balance system are shown in Figure 7 for both the plug and C-D nozzle models. On the test of the plug nozzle arrangement a total of 197 static pressure taps, 8 total pressure rakes and 2 total temperature probes were used in addition to three force balances; one on the external cowling, one on the plug and one on the interfairing. Two six-probe rakes were located in each flow tube to measure the total pressure distribution of the air entering each nozzle and also to monitor the nozzle total pressure during each tunnel run. The average rake total pressure however was not used in calculating nozzle performance. For performance purposes, the jet total pressure was calculated from the orifice airflow and total temperature, and the nozzle internal diameter and static pressure. Four six-probe total pressure rakes were also used to survey the external boundary layer profile at the nozzle station.

On the test of the C-D nozzle arrangement a total of 116 static pressure taps, 2 total pressure probes and 2 total temperature probes were used in addition to a single force balance on the external cowling. The aft fairing between the two nozzles, which was connected to a force balance during the plug nozzle test was only pressure instrumented during the C-D nozzle test. Also the internal rakes used during the plug nozzle test were replaced by a single total pressure probe to monitor the nozzle total pressure in each flow tube in the C-D nozzle test.

The 3-component cylindrical balance was designed to accurately measure the small variations in boattail drag resulting from interference effects. This required that the balance error be small compared to the boattail

drag variation being measured. For the plug nozzle configuration the balance measured both the boattail drag and the internal forces on the nozzle shroud. Since the spike absorbed approximately 82 percent of the total internal plug nozzle forces, the magnitude and variation of the forces on the internal shroud were relatively low. For the C-D nozzle configuration the shroud was subjected to 100 percent of the total nozzle internal forces, as compared with 18 percent for the plug nozzle. In order to measure the boattail drag accurately in this case the cylindrical balance was connected to only the outer shell of the left hand nozzle. The inner shell was attached to the non-metric section just upstream of the balance. A bellows element was employed to seal the cylindrical balance. The static pressures on both sides of the bellows was measured during each run, and used (together with an experimentally determined effective bellows area) in calculating nozzle performance. The cylindrical balance calibration with the bellows installed was quite linear and accurate to within $\pm 1/2$ of 1 percent.

Pressure tubes on the plug nozzle spike were routed out through the center of the annulus pipe supporting the spike, while the pressure tubes on the plug and C-D nozzle shroud were routed along a groove in the flow tubes such that the external flow was not disturbed. Quick pressure tube disconnects were provided between the nozzle shroud and the flow tube. All pressure tubes were routed out of the tunnel through a channel provided in the support strut and connected to multi-headed scanivalve pressure transducers each capable of measuring 48 separate pressures. Electrical signals from the strain-gage balances and scanivalve transducers were transmitted to the tunnel control room, digitized, recorded on magnetic tape, and then transferred to punched cards.

DATA REDUCTION

Extensive use was made of digital computers to reduce the recorded pressure and force balance data to standard coefficient form. The primary terms used in the data reduction program are defined in Figure 7. The force terms shown as $SPxAx$ on this figure were computed by numerically integrating the pressures over the incremental areas.

The internal nozzle coefficient, C_T , was obtained by subtracting the measured pressure and the calculated friction forces on the nozzle internal surfaces from the upstream total momentum. The nozzle upstream Mach number, M_2 , which was used to calculate the upstream total momentum and nozzle pressure ratio, was obtained from the orifice airflow and total temperature, and the nozzle upstream static pressure and area, using one-dimensional compressible flow relationships. It was possible to use average flow field properties since the choke plates located in both flow tubes provided a fairly uniform velocity profile at the nozzle upstream station. The internal skin friction drag was calculated from Prandtl's universal law of friction for smooth pipes (Reference 1). The equations used for calculating C_T for the right and left hand plug and C-D nozzles are given below.

$$C_T \text{ (RH Plug)} = \left[TM1R - SP4A4 + SP5A5 - SP6A6 + SP8A8 - (f1R + f2R) - P_\infty (A_e + A_p) \right] / F_1 \quad (1a)$$

$$C_T \text{ (LH Plug)} = \left[TM2L + P_{b_1} A_g - SP3A3 - SP6A6 + SP8A8 - (f1L + f2L) + fpL - F2 - P_\infty A_e \right] / F_1 \quad (1b)$$

$$C_T \text{ (RH C-D)} = \left[TM2R - SP3A3 - SP4A4 + SP5A5 - f1R - P_\infty A_e \right] / F_1 \quad (2a)$$

$$C_T \text{ (LH C-D)} = \left[TM2L + (SP5A5 - SP3A3 - SP4A4) \frac{Pt2L}{Pt2R} - f1L - P_\infty A_e \right] / F_1 \quad (2b)$$

The boattail drag coefficient, $C_{D_{BT}}$, was calculated from pressure and force balance data on the right $C_{D_{BT}}$ and left hand nozzles respectively. Since the pressure drag coefficient does not include the external skin friction drag, it was necessary to subtract the friction drag from the force balance data. The external skin friction drag was calculated from the incompressible local skin friction coefficient developed by Sivells and Payne, Reference 2, which was adjusted for compressibility effects using the Sommer and Short T' method, Reference 3. The boattail drag coefficient for the right and left hand plug and C-D nozzles was calculated from the following equations:

$$C_{D_{BT}} \text{ (RH Plug)} = \left[P_\infty (A_{BT} + A_B) - SP7A7 \right] / q_\infty A_{max} \quad (3a)$$

$$C_{D_{BT}} \text{ (LH Plug)} = \left[F1 - SP6A6 + SP8A8 - (f1L + f_{ext}) + P_\infty (A_{BT} - S_b - S_{b_1}) \right] / q_\infty A_{max} \quad (3b)$$

$$C_{D_{BT}} \text{ (RH C-D)} = \left[P_\infty A_{BT} - SP7A7 - SP8A8 - DUNDF \right] / q_\infty A_{max} \quad (4a)$$

$$C_{D_{BT}} \text{ (LH C-D)} = \left[F1 - SP9A9 - f_{ext} + P_\infty A_9 - DUNDF \right] / q_\infty A_{max} \quad (4b)$$

The base drag coefficient, C_{D_B} , for the plug nozzle configuration was included in the boattail $C_{D_{BT}}$ drag coefficient. The base drag coefficient for the C-D nozzle configuration was calculated from pressure instrumentation. The aft fairing drag coefficient, $C_{D_{AF}}$, was obtained from force balance data and pressure data for the $C_{D_{AF}}$ plug and C-D nozzle configurations respectively.

$$C_{D_B} \text{ (RH C-D)} = \left[P_\infty A_B - SPA10 \right] / q_\infty A_{max} \quad (5a)$$

$$C_{D_B} \text{ (LB C-D)} = [P_{\infty} A_B - SP6A6] / q_{\infty} A_{\max} \quad (5b)$$

$$C_{D_{AF}} \text{ (Plug)} = [(F3 - r_{AF})] / q_{\infty} A_{\max} \quad (6)$$

$$C_{D_{AF}} \text{ (C-D)} = [P_{\infty} A_{AF} - SPAAF] / q_{\infty} A_{\max} \quad (7)$$

The total aftbody drag coefficient, C_{D_T} , nozzle thrust coefficient, C_F , and nozzle thrust minus drag coefficient, C_{T-D} , were derived from measured parameters using the equations shown below:

$$C_{D_T} = C_{D_{BT}} + C_{D_B} + 1/2 C_{D_{AF}} \quad (8)$$

$$C_F = (C_T - C_{D_{BT}} + C_{D_B}) q_{\infty} A_{\max} / F_1 \quad (9)$$

$$C_{T-D} = C_T - C_{D_T} (q_{\infty} A_{\max} / F_1) \quad (10)$$

TEST RESULTS

Plug Nozzle Configuration

A summary of the results obtained in the test of the plug nozzle configuration is presented in the bar chart shown in Figure 8. Presented is the nozzle thrust coefficient, C_F defined in the previous section, as a function of nozzle pressure ratio, $P_{t,1}/P_{\infty}$, test Mach number, M_{∞} , and spacing ratio, S/D . The most significant result to note is that the thrust coefficient decreased considerably as the nozzles were brought closer together, and that this effect was more predominant at the lower nozzle pressure ratios, than at the higher pressure ratios. Examination of the boattail drag coefficient, $C_{D_{BT}}$, reveals that it is the parameter largely responsible for the decrease in nozzle thrust coefficient with decreased spacing. This is shown by the data presented in Figure 9, which shows the boattail drag coefficient as a function of the same parameters used in Figure 8. The most significant point to note from Figure 9 is that the interference effects due to nozzle spacing are a maximum at Mach .9 and that this effect decreases somewhat with increasing nozzle pressure ratio. It was also determined that the magnitude of these boattail drags were quite high indicating that this boattail configuration was not necessarily the optimum.

Close inspection of the static pressure instrumentation on the nozzle boattail surface shows how nozzle spacing ratio effected the circumferential boattail flow. Figure 10 plots the measured static pressure ratio along the boattail at two circumferential stations, i.e. 90° and 270° , at Mach .90. The interesting thing to note is that the pressure distribution is most symmetrical when the nozzles are closely

spaced and, conversely, most unsymmetrical when the nozzles are furthest apart. It is rationalized that the large change in static pressure distribution in the wake of the interfairing is due to boundary layer effects. At the large spacings the boundary layer effectively masks the existence of the sharp shoulder and therefore the flow doesn't over expand as it normally does. At the close spacings there appears to be a jet pumping effect which acts to expand the flow to the minimum pressure level. Even so, the flow appears to separate midway along the boattail. Thus the boattail drag is maximum at the close nozzle spacing.

Examination of the total aftbody drag coefficient, and the configuration's thrust minus drag coefficient, reveals several important facts, as can be seen by the data presented in Figure 11. Consideration of the aftbody drag only shows that the minimum drag is obtained at a spacing ratio of approximately 1.25, however when the nozzle internal thrust coefficient is included in a thrust minus drag coefficient the optimum is obtained at a spacing ratio of approximately 1.40. This result is due to the interference effects on the nozzle plug, which reduced the nozzles internal thrust coefficient at close spacings. While the performance level of this arrangement could have been improved through configuration changes, this was not done since concurrent studies were at this time favoring a C-D nozzle arrangement.

C-D Nozzle Configuration

In designing the C-D nozzle arrangement use was made of the plug nozzle test results in an effort to improve its installed thrust minus drag. In particular, the nozzle interfairing was shaped differently and extended to the nozzle trailing edge. Also the sharp shoulder was eliminated from the boattail. Thus the results of the tests of the C-D nozzle arrangement are not directly comparable with the plug nozzle results.

A summary of the results obtained in the test of the C-D nozzle configuration is presented in the bar chart shown in Figure 12. Presented is the nozzle thrust coefficient as a function of nozzle pressure ratio, Mach number and spacing ratio for both the cruise and reheat nozzle geometries. The important thing to note from this data is that there is very little difference in performance between the two spacing ratios. The primary reason for this is that there was little if any effect of spacing on the nozzle boattail drag. This is shown by the bar chart presented in Figure 13. Shown is the variation of boattail drag coefficient with Mach number, pressure ratio and spacing ratio for both the cruise and reheat configurations. Probably the most interesting point to note is the large drag associated with the cruise nozzle at Mach 1.10.

Inspection of the static pressure distributions on the nozzle boattail surface revealed some variation with circumferential position. This is shown by the data presented in Figure 14 which plots the boattail static pressure ratio as a function of model axial station for the two spacing ratios tested. As can be seen the pressures are slightly

lower for the larger spacing ratio. Also, the pressures are greatest at the 270° station, which is in the channel region under the interfairing, similar the plug nozzle arrangement. The big difference between the plug and C-D configuration results is that the boattail pressures were not reduced when the nozzles were closely spaced in the C-D test, whereas they were in the test of the plug nozzle arrangement.

Figure 15 shows the C-D nozzle configuration total aftbody drag coefficient and the thrust minus drag coefficient as a function of nozzle spacing ratio. As can be seen both the minimum drag and maximum thrust are obtained at a spacing ratio of 1.25. While no tests were made of a smaller spacing, it would have been interesting to see if a further improvement in performance would be obtained by reducing the spacing ratio to 1.0.

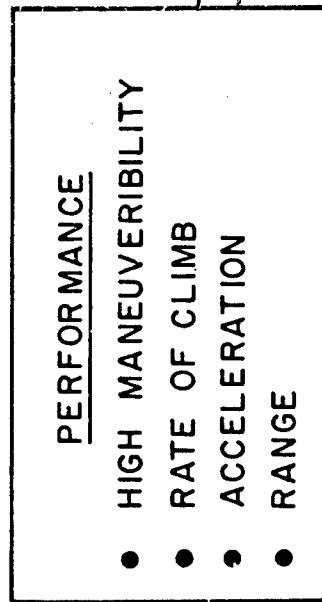
The effect of fairing inserts and a vertical fin on the total aftbody drag coefficient for both C-D nozzle configurations is presented in Figure 16. It can be seen that the effect of the vertical fin was to increase the drag on both the interfairing and boattail surfaces, however, the increase was still not as significant as the effect of nozzle spacing ratio. The effect of the inserts is not so clear. Actually a drag trade off is involved whereby the drag on the larger boattail surface with the inserts out is compared with the drag on the larger interfairing surface with the inserts in. It appears that an even trade results for the narrow configuration, while the larger spacing shows a higher aftbody drag coefficient with the inserts out. The same trend was observed for both cruise and reheat nozzles.

CONCLUSIONS

The major conclusions derived from the data obtained in the test program described herein are listed in Figure 17. The two most important conclusions were that for the plug nozzle arrangement the maximum aftbody thrust minus drag was achieved with a nozzle spacing ratio of approximately 1.4 whereas for the C-D nozzle arrangement the maximum performance was achieved with a spacing ratio less than 1.25. These tests also confirmed what has been recognized for some time, that is, when we are working with a closely integrated exhaust nozzle-airframe configuration the flow about the nozzle boattail is not symmetrical, or uniform, due to both boundary layer and mutual interference effects. Failure to consider these effects in the development of the aftbody-exhaust nozzle configuration can lead to a significant error in the prediction of aircraft performance.

In recognition of the above, considerable work is currently being done to improve the analytical techniques used to predict installed exhaust nozzle aftbody performance. Reference 4 describes one such effort conducted by the Lockheed-California Company using Air Force funds in 1966. Company sponsored efforts are continuing using potential flow techniques and transonic flow methods incorporating non uniform local flow conditions and the effects of the "real" boundary layer. It is expected that substantiated analytical techniques will be available within the next several years which will provide valuable aid in developing integrated exhaust nozzle configurations, hopefully reducing the need to conduct extensive and costly configuration development testing.

AIRCRAFT GOALS



AIRCRAFT
WING
LOADING

PROPULSION

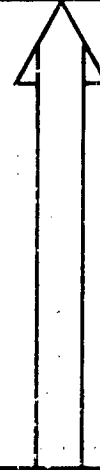
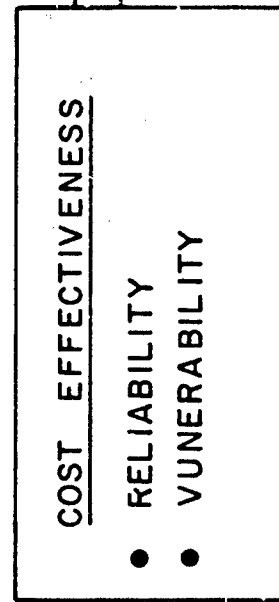
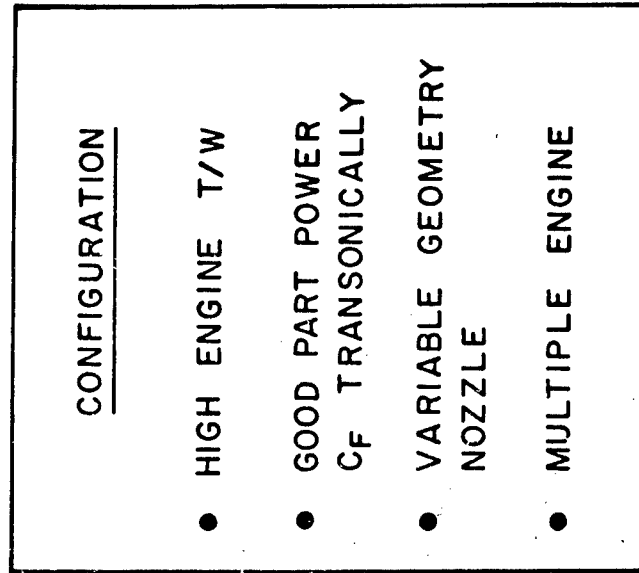


FIGURE 1 VEHICLE DESIGN REQUIREMENTS/CONSTRAINTS

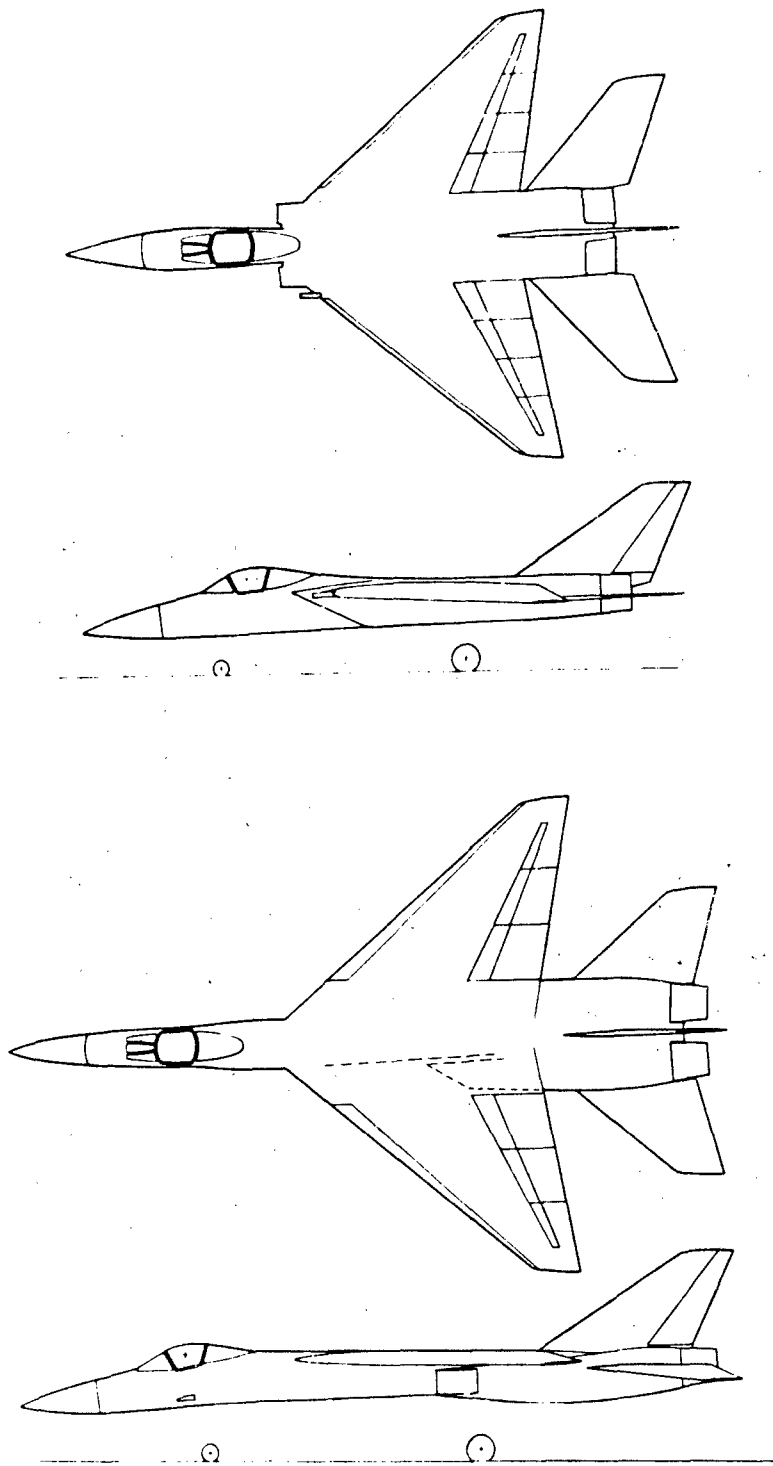


FIGURE 2. REPRESENTATIVE TACTICAL FIGHTER AIRCRAFT

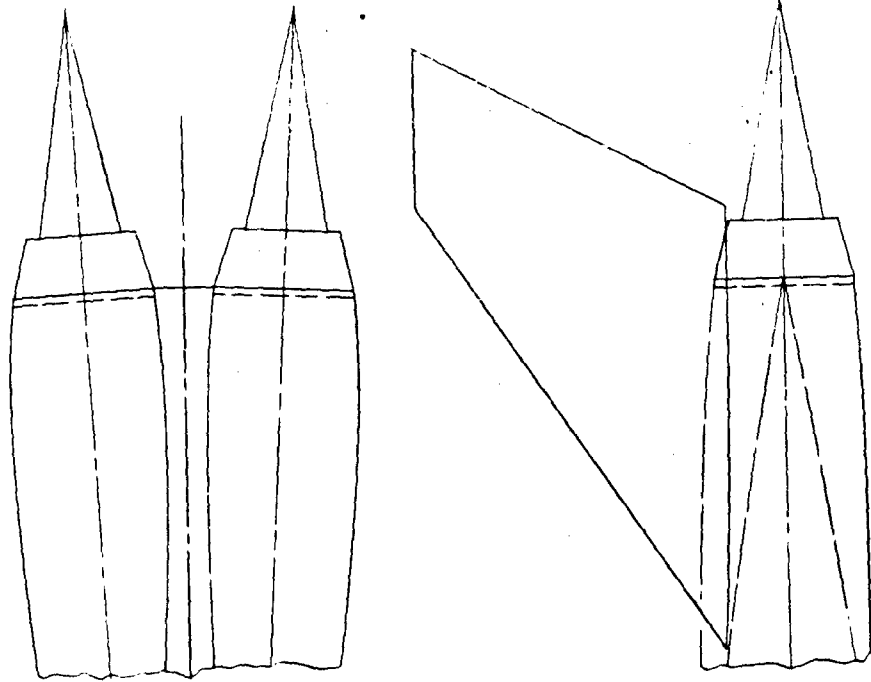
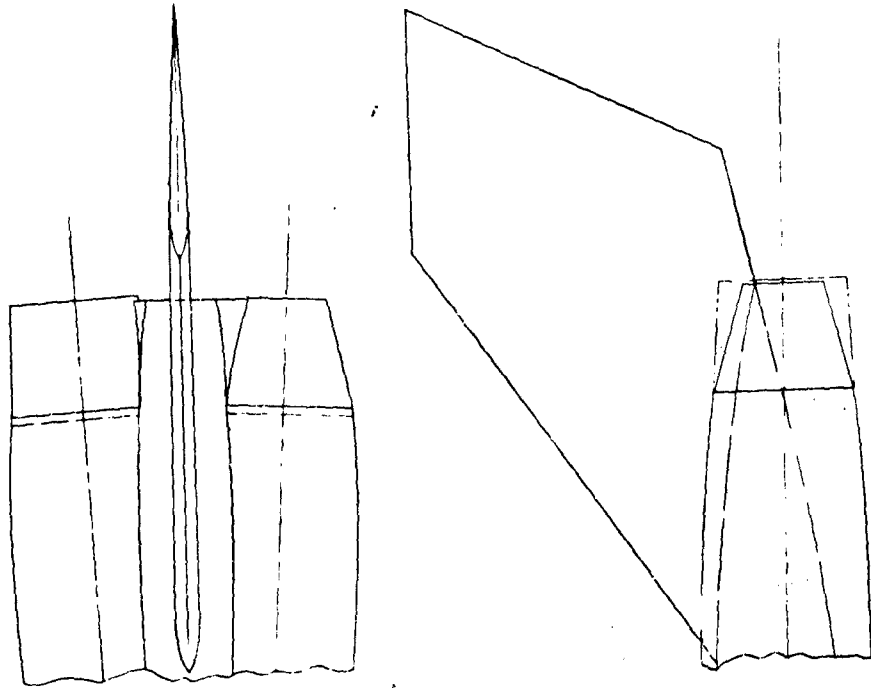


FIGURE 3. EXHAUST NOZZLE/AFTBODY CONFIGURATIONS

| CONFIGURATIONS | SPACING RATIO, S/D | NOZZLE PRESSURE RATIO, $\frac{P_{t,1}}{P_{CO}}$ | MACH NUMBER, M_{∞} |
|---|--------------------|---|---------------------------|
| 1. 10° CONICAL PLUG NOZZLE Nil Power Position Boattail Angle=12° | 1.1, 1.5, 2.0 | 1, 2, 3, 4, 5, 6 | 0.8, 0.9, 1.1, 1.2 |
| 2. CONVERGENT-DIVERGENT NOZZLE Max A/B Position Boattail Angle = 7° Fairing Inserts-In&Out Vertical Fin-On & Off | 1.25, 1.7 | 1, 3, 4, 5, 6 | 0.9, 1.1, 1.2 |
| 3. CONVERGENT-DIVERGENT NOZZLE Nil Power Position Boattail Angle = 15° Fairing Inserts-In & Out Vertical Fin-On & Off | 1.25, 1.7 | 1, 3, 4, 5, 6 | 0.8, 0.9, 1.1 |

FIGURE 4 MODEL TEST CONDITIONS

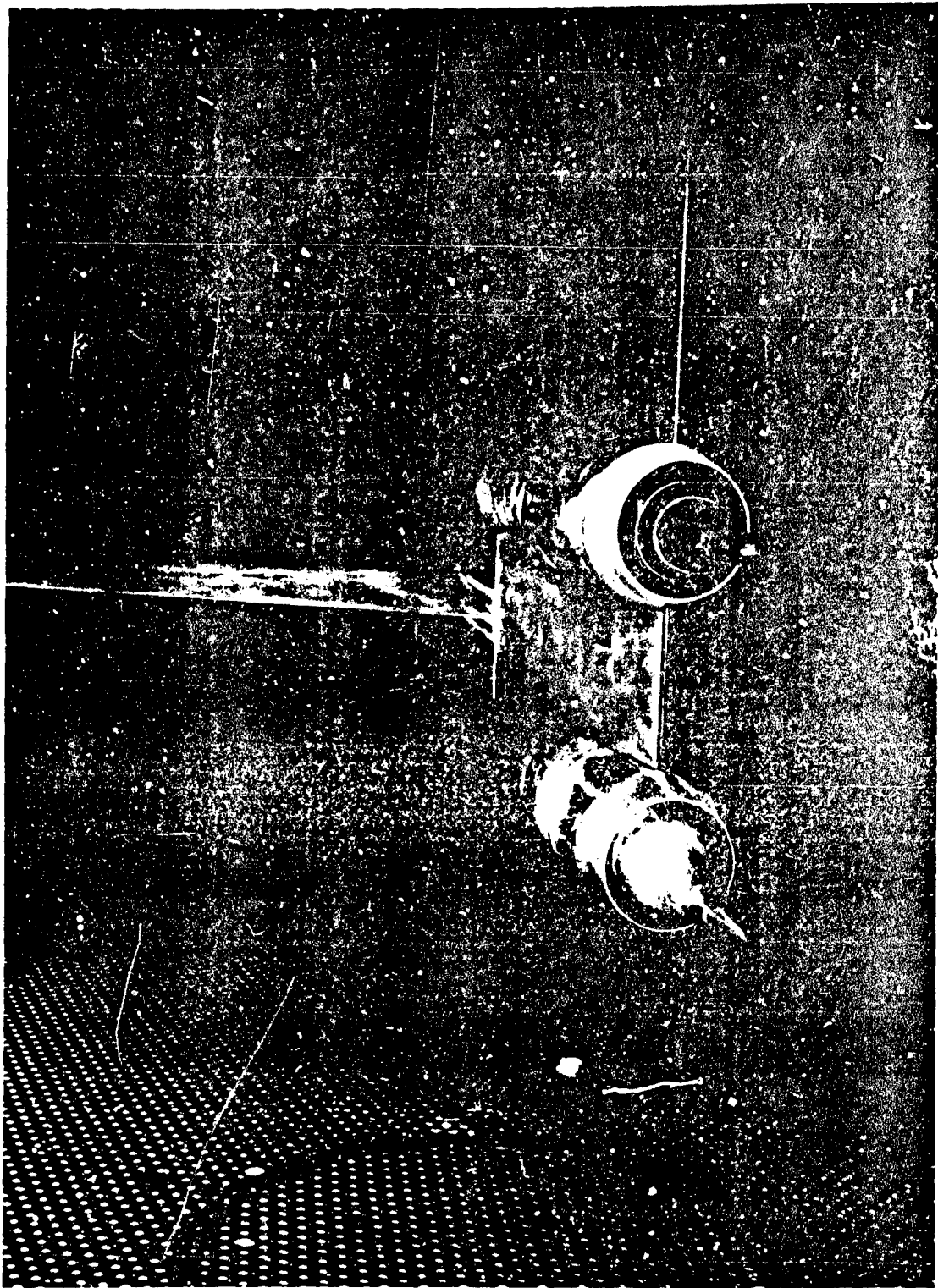


FIGURE 5. PHOTOGRAPH OF PLUG NOZZLE WIND TUNNEL MODEL

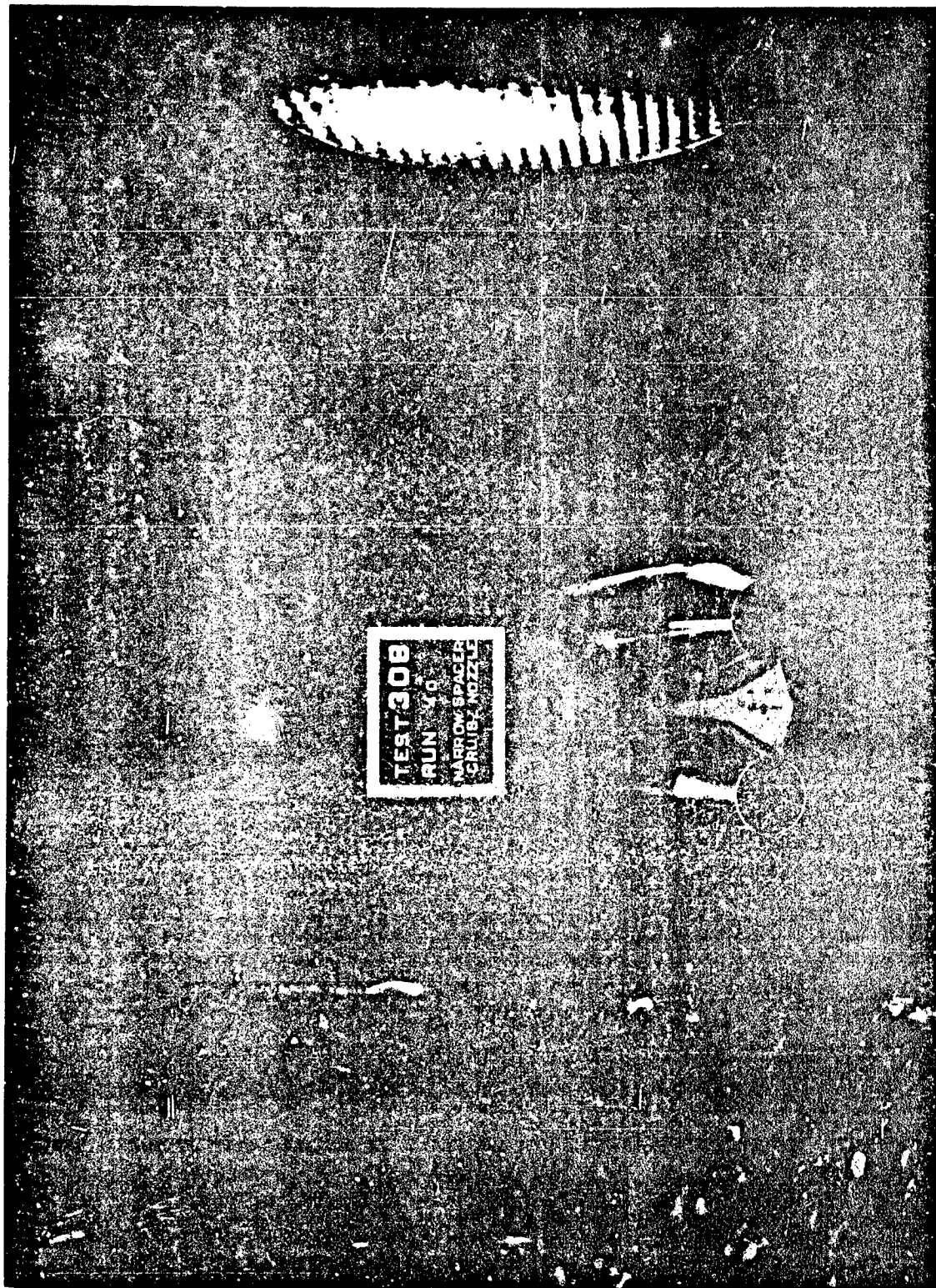


FIGURE 6. PHOTOGRAPH OF CONVERGENT-DIVERGENT NOZZLE WIND TUNNEL MODEL

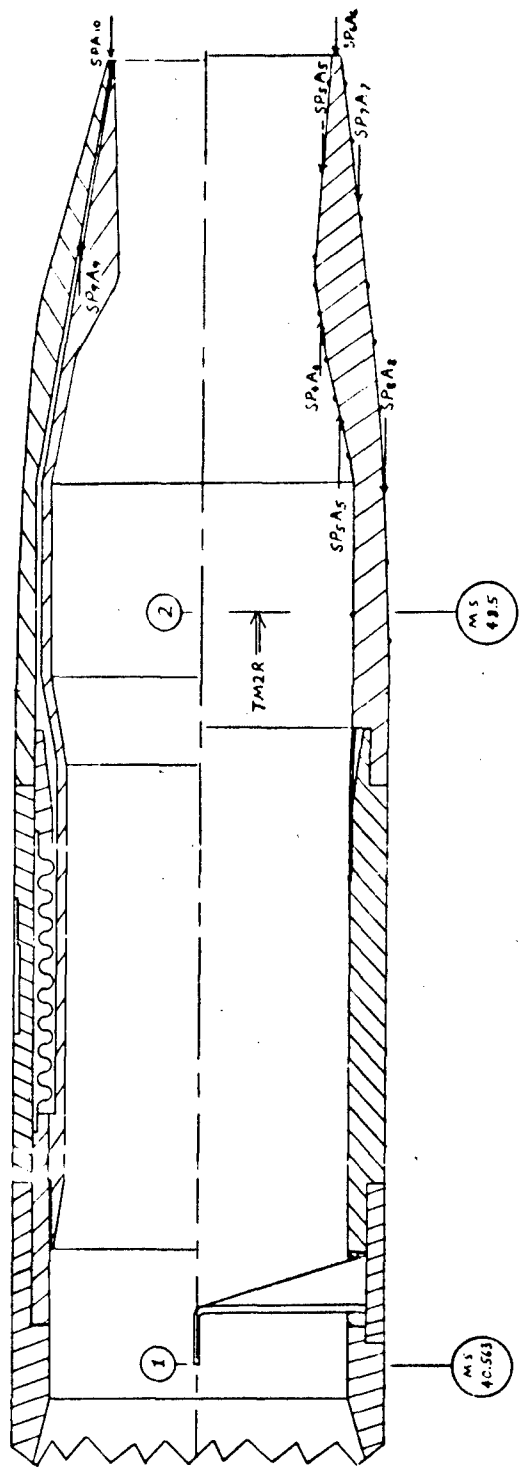
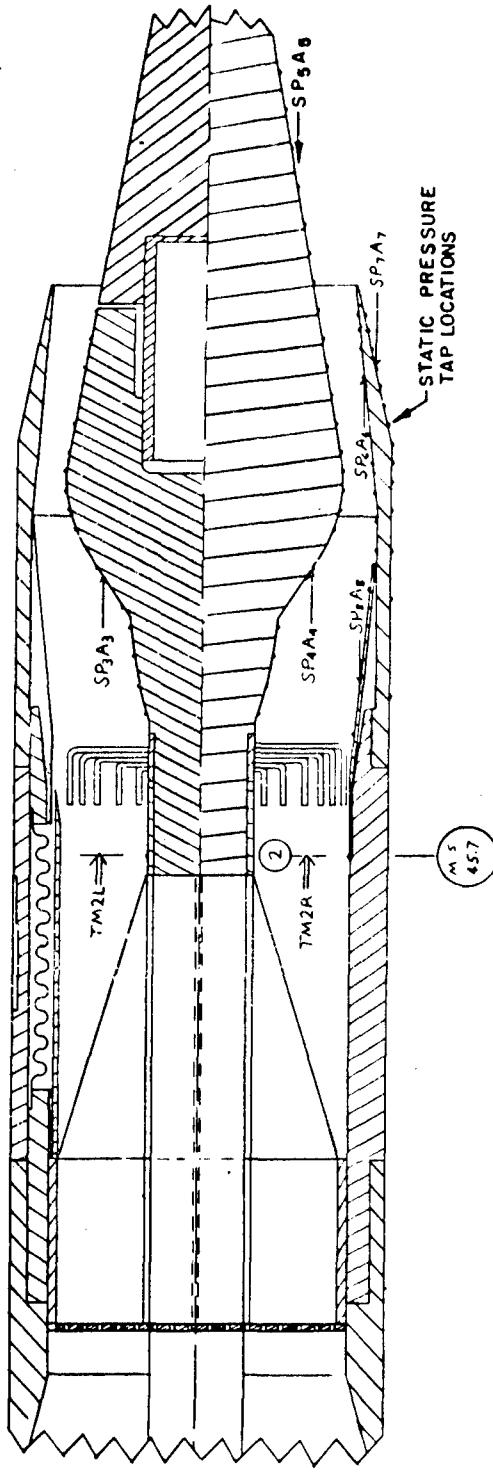


FIGURE 7. BALANCE AND AFTBODY SECTION ASSEMBLY

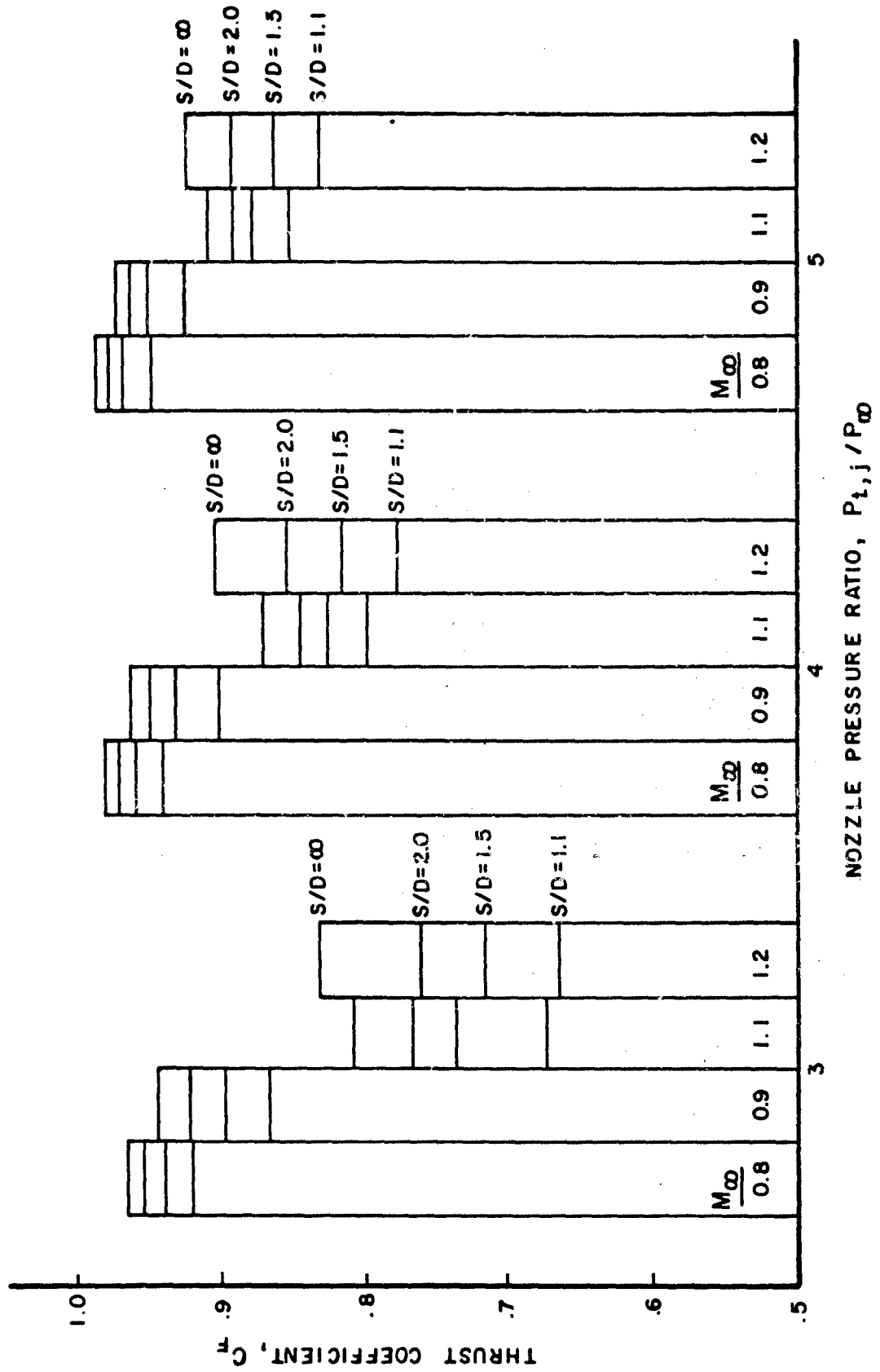


FIGURE 8 EFFECT OF PLUG NOZZLE SPACING RATIO ON C_F

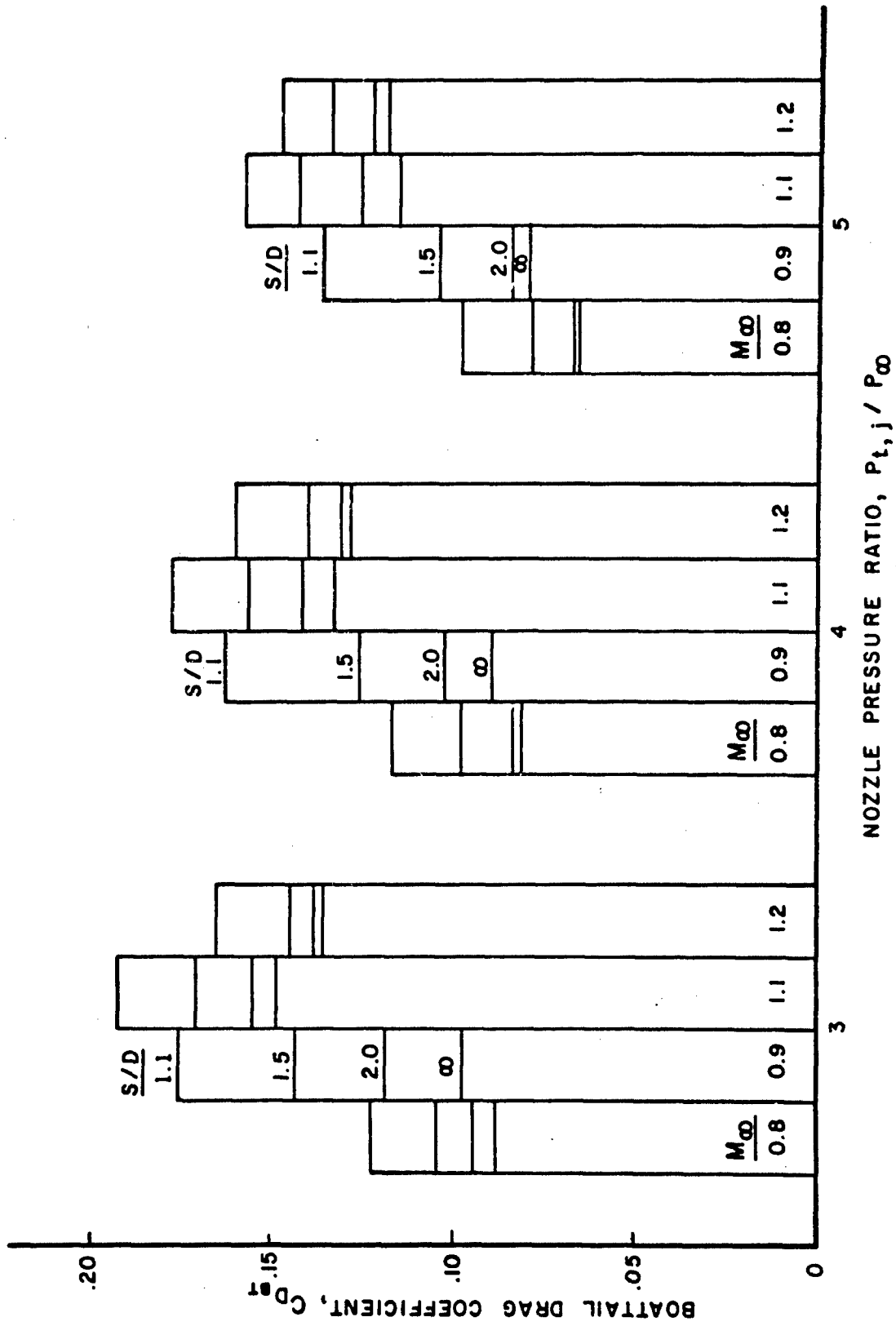


FIGURE 9 VARIATION OF PLUG NOZZLE BOATTAIL DRAG WITH SPACING

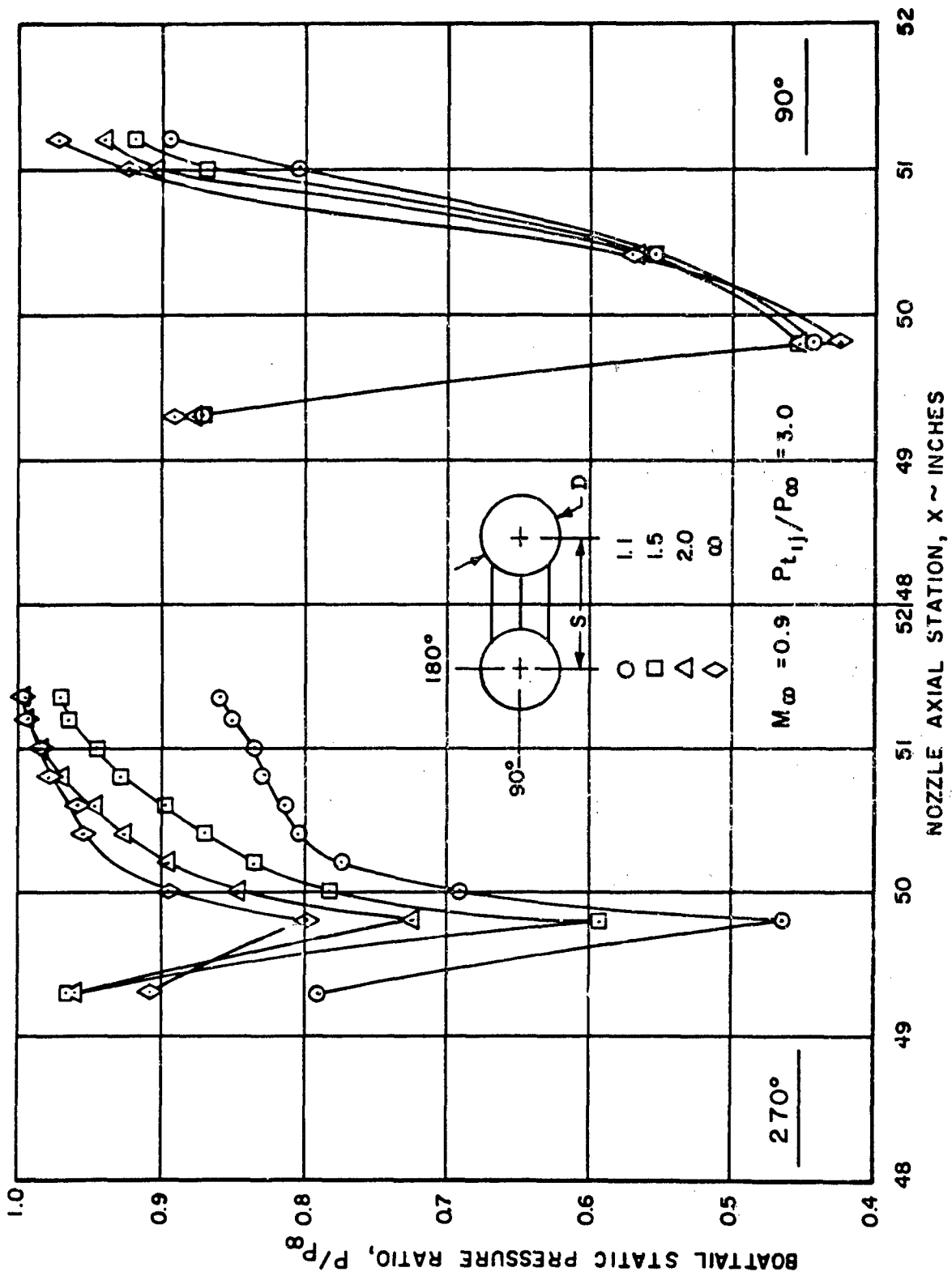


FIGURE 10 PLUG NOZZLE BOAT TAIL PRESSURE DISTRIBUTION



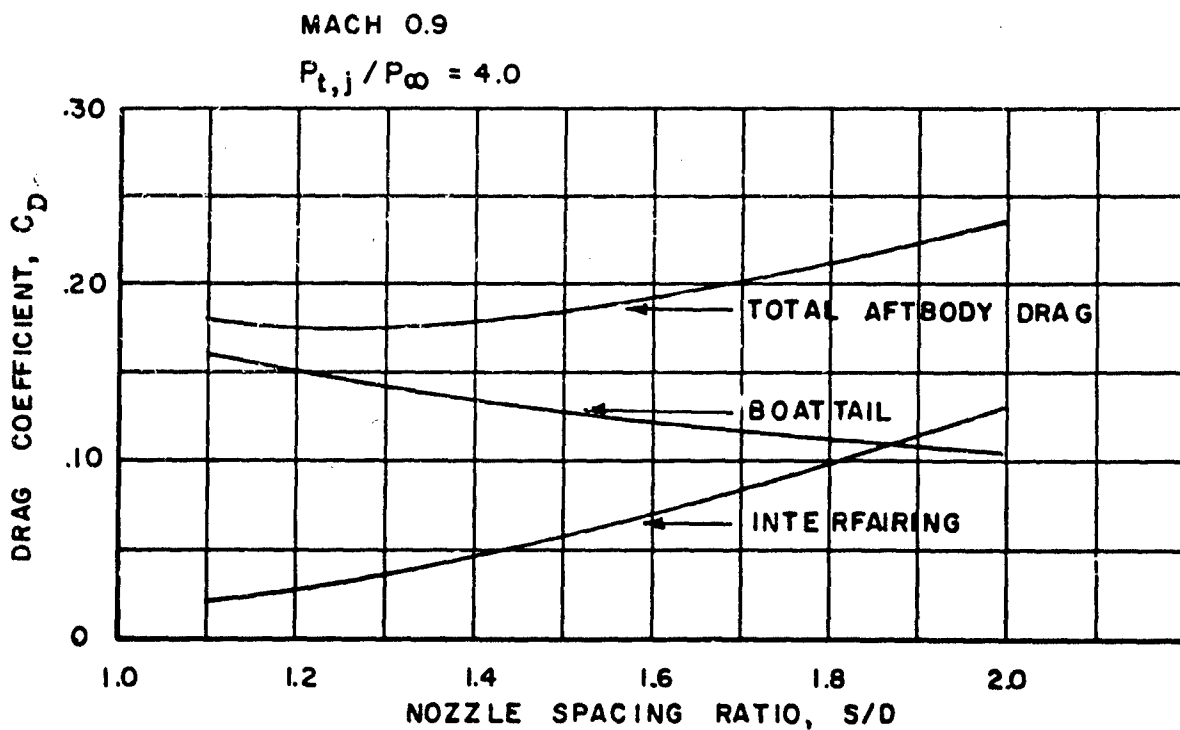
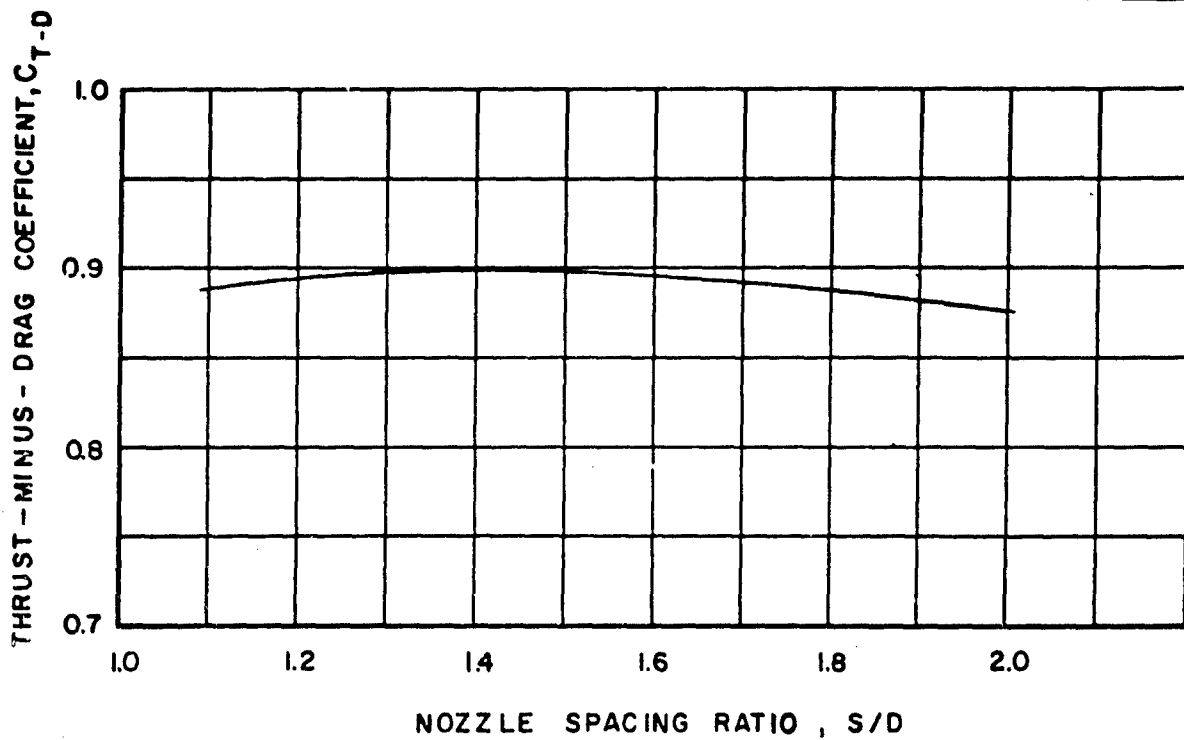


FIGURE 11 OPTIMUM SPACING RATIO FOR PLUG NOZZLES



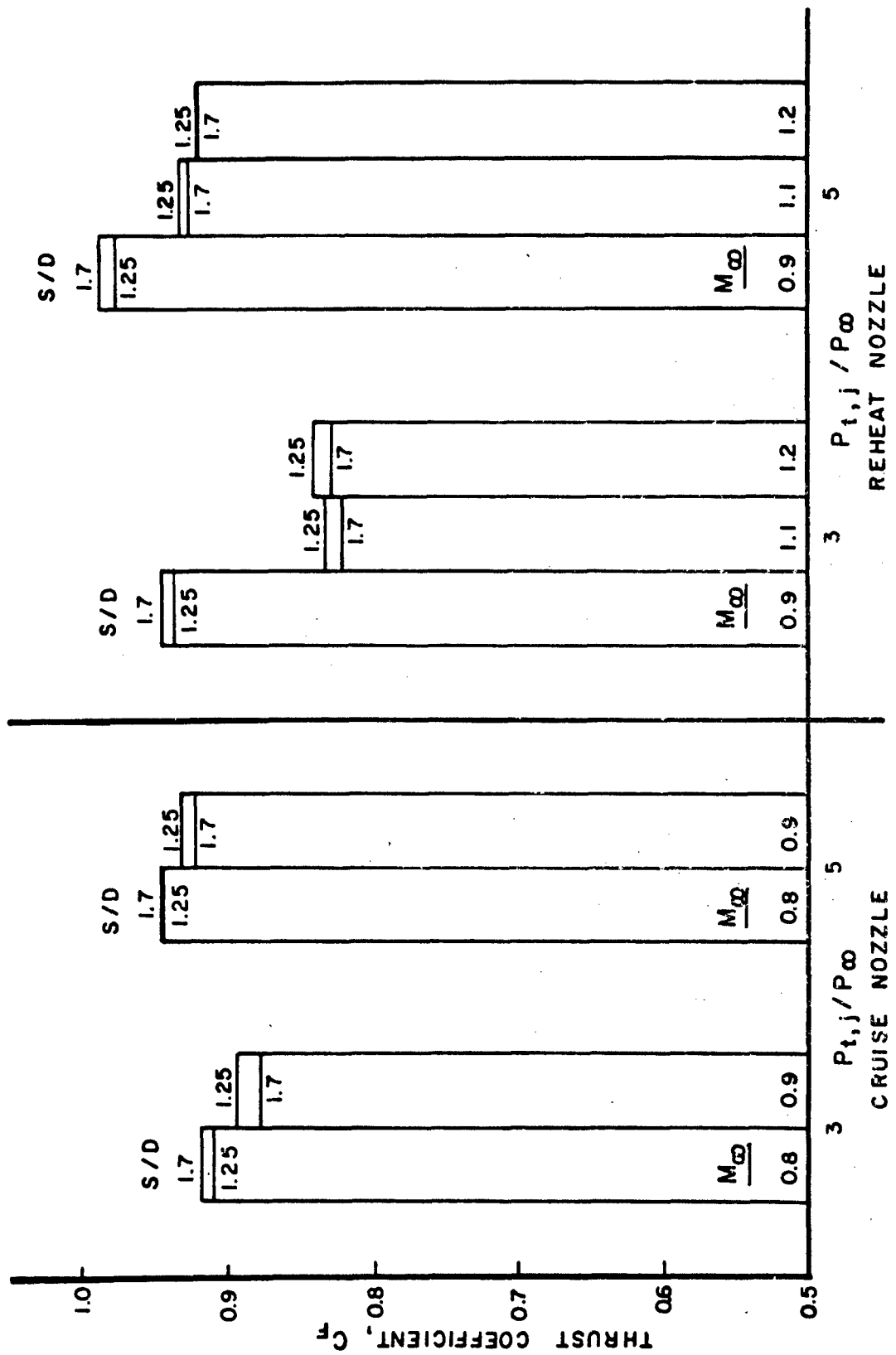


FIGURE 12 EFFECT OF C-D NOZZLE SPACING RATIO ON C_f

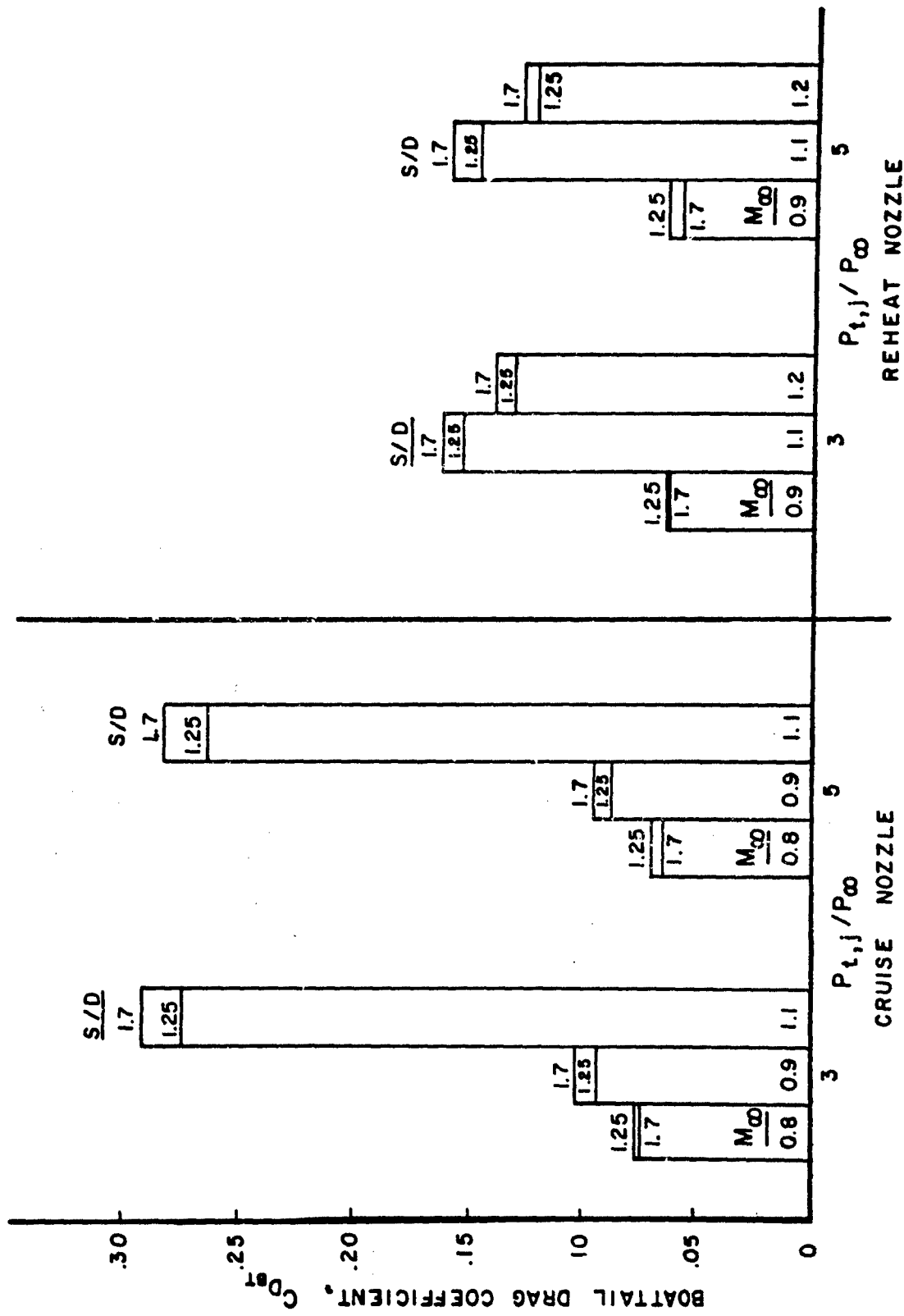


FIGURE 13 VARIATION OF C-D NOZZLE BOATTAIL DRAG WITH SPACING

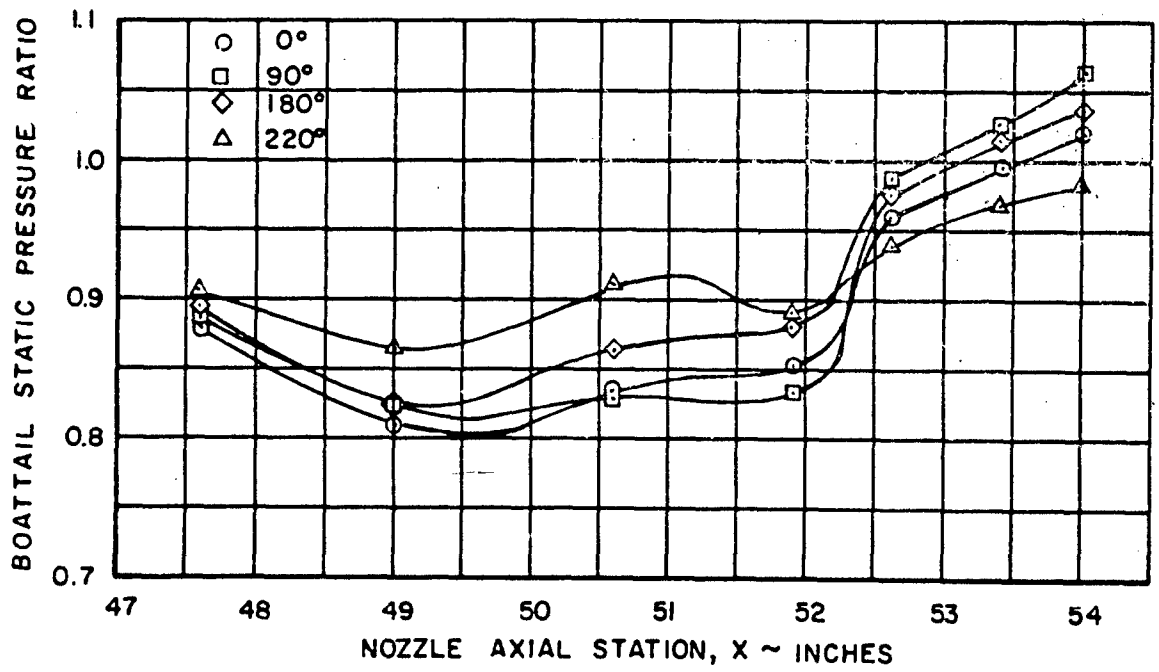
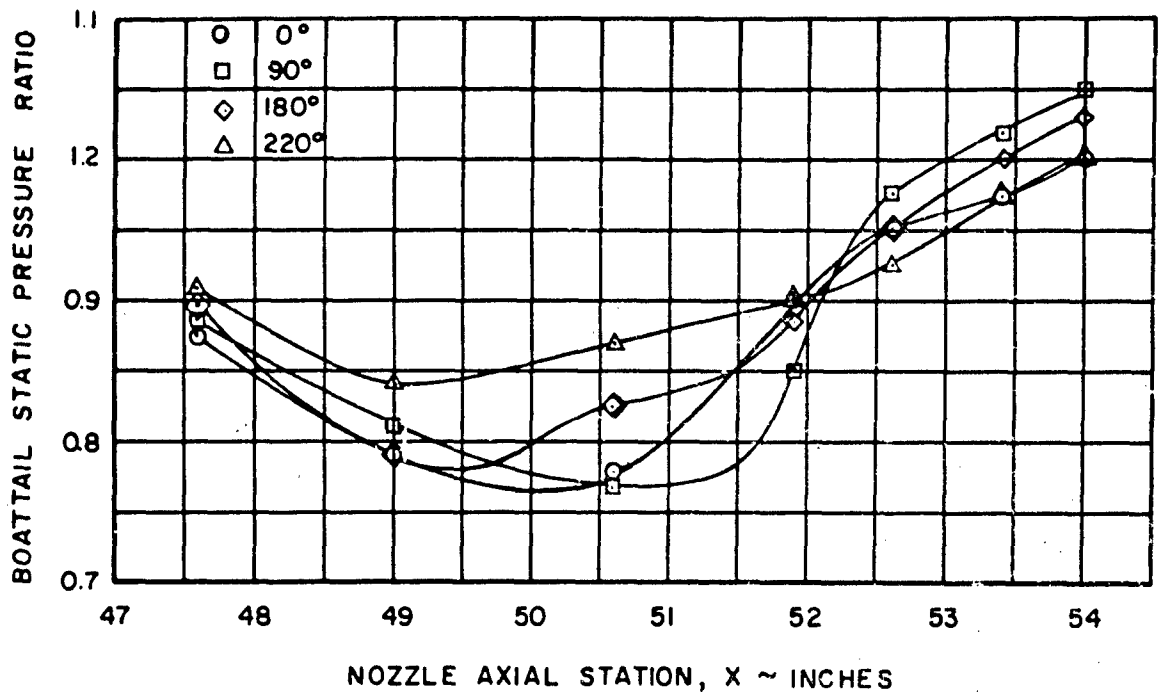


FIGURE 14 C-D NOZZLE BOATTAIL PRESSURE DISTRIBUTION



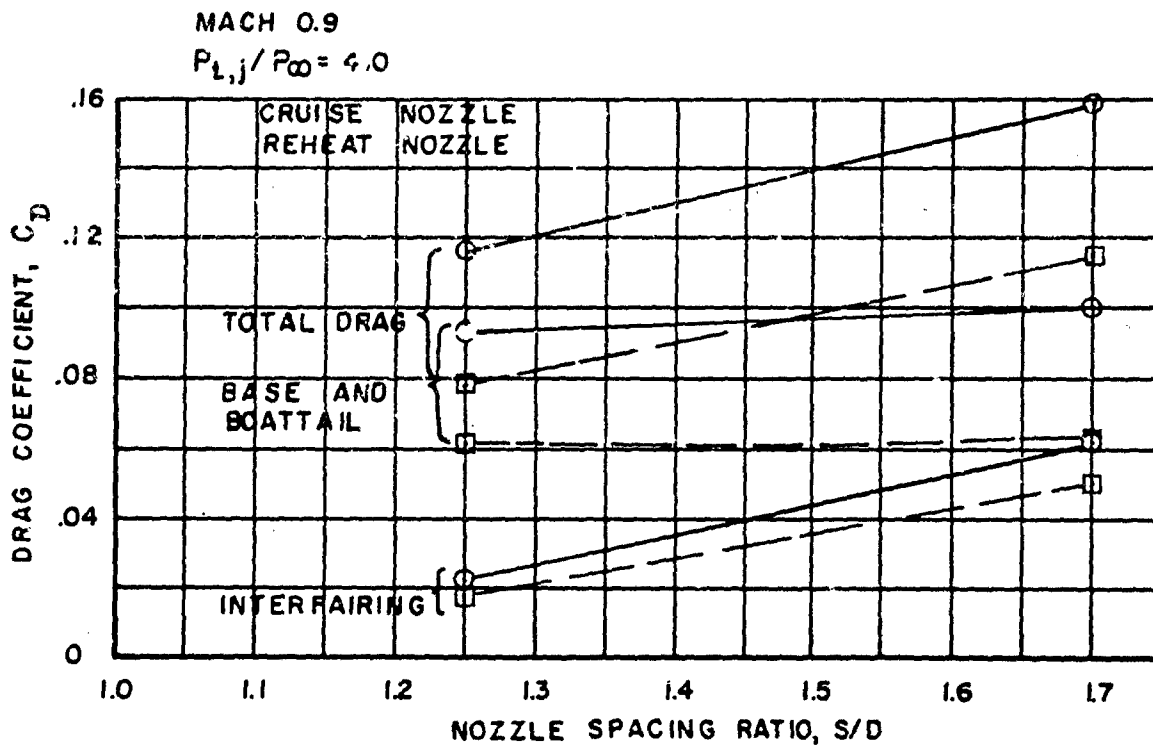
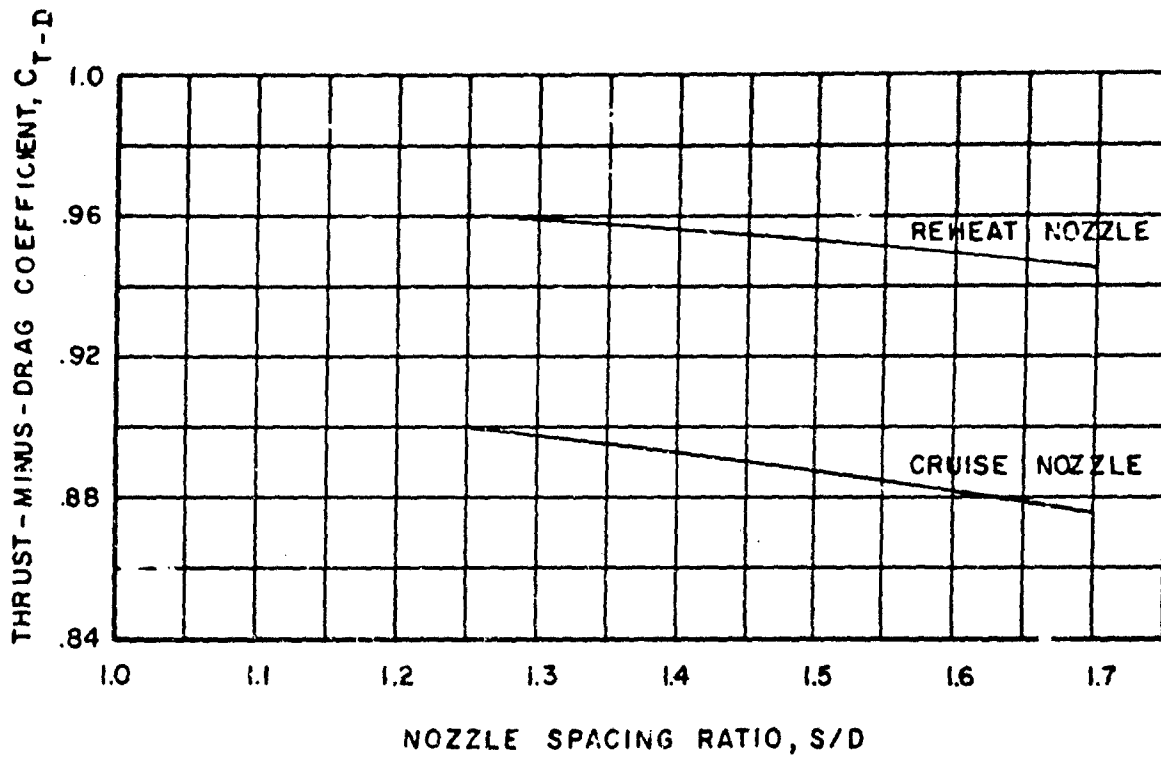


FIGURE 15 OPTIMUM SPACING RATIO FOR C-D NOZZLES

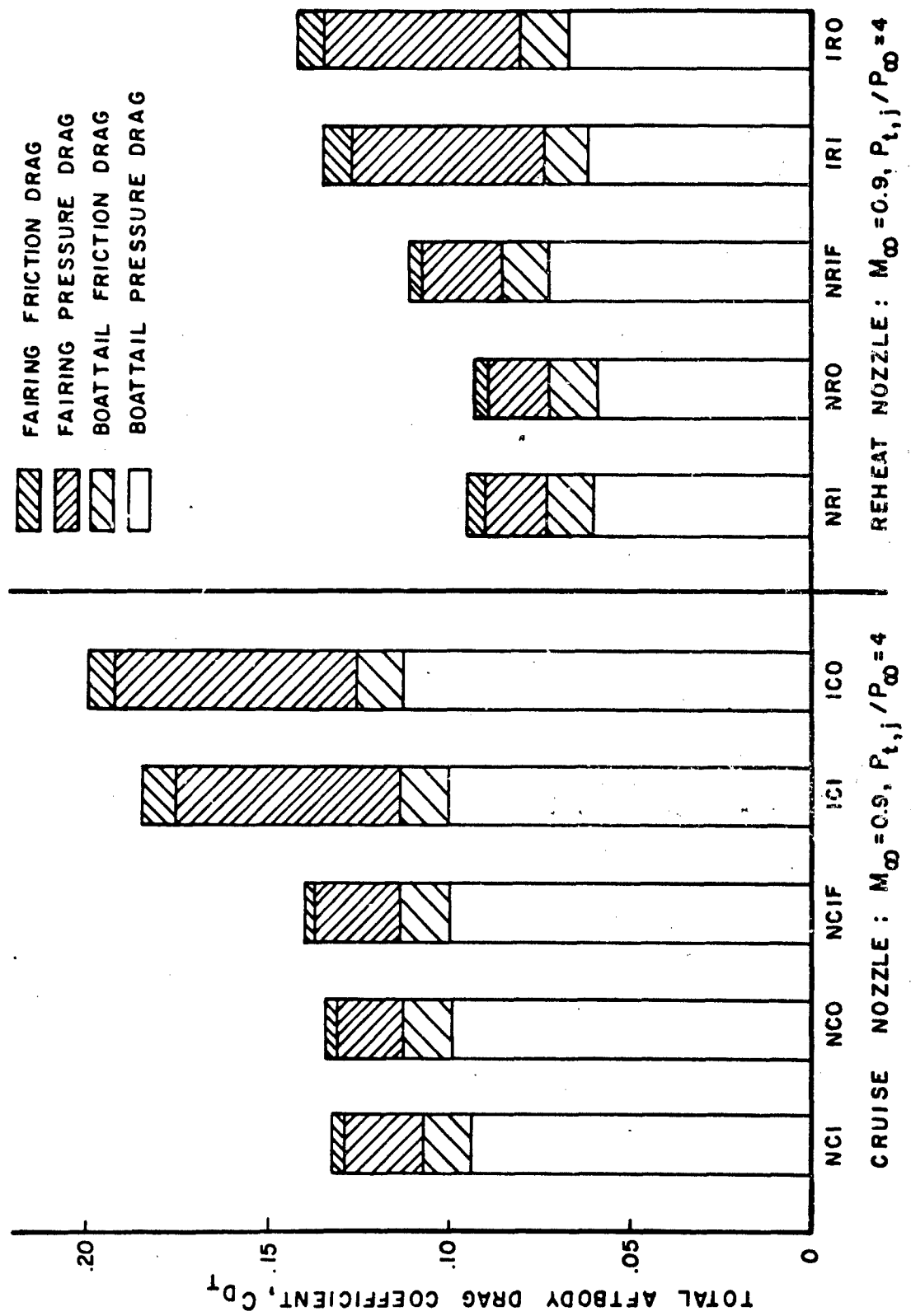


FIGURE 16 EFFECT OF AFTBODY MODIFICATIONS ON C-D NOZZLE AFTBODY DRAG

FIGURE 17 TEST PROGRAM CONCLUSIONS

- OPTIMUM SPACING RATIO FOR PLUG NOZZLE ≈ 1.40
- OPTIMUM SPACING RATIO FOR C-D NOZZLE ≤ 1.25
- VERTICAL FIN INCREASED AFT BODY DRAG
- INSERTS HAD MINIMAL EFFECTS

LIST OF SYMBOLS

| | |
|----------------------------------|---|
| A | projected area in square inches |
| A ₉ | equal to $A_{BT} - S_b - S_{b_1}$ |
| C-D | convergent-divergent nozzle |
| C _D | pressure drag coefficient, $\int (P_L - P_\infty) dA/q_\infty A_{max}$ |
| C _F | thrust coefficient |
| C _P | pressure coefficient, $(P_L - P_\infty)/q_\infty$ |
| C _T | internal thrust coefficient, $[mVe + (P_e - P_\infty)A_e]/F_i$ |
| C _{T-D} | thrust-minus-total aftbody drag coefficient |
| DUNDF | nozzle boattail drag on area under the interfairing |
| F1 | net drag, cylindrical boattail balance |
| F2 | net drag, external spike balance |
| F3 | net drag, aft fairing balance |
| F _i | ideal thrust for complete isentropic expansion of jet flow, $\frac{W}{g} \sqrt{2 Rg \frac{\gamma}{\gamma-1} (T_t) \left[1 - \left(\frac{P_\infty}{P_{t,j}} \right)^{(\gamma-1)/\gamma} \right]}$ |
| M | Mach number |
| M.S. | Model station |
| P | static pressure, psi |
| P _t | total pressure, psi |
| P _{t,j} /P _∞ | nozzle pressure ratio |
| R | gas constant, 53.35 ft-lb/lb ^o R |
| S | effective bellows area |
| SPxAx | pressure force in pounds, defined in Figure 7 |
| T _t | nozzle jet total temperature in degrees Rankine |
| TM | total upstream momentum, P.A $[1 + \gamma (M)^2]$ |
| W | orifice or nozzle weight flow in pounds per second |

f skin friction drag
 f1 friction drag on internal plug nozzle shroud surface
 f2 friction drag on internal plug nozzle spike surface
 g local acceleration of gravity, 32.174 feet per second square
 mV_e nozzle exit momentum, $P_e A_e \gamma M_e^2$
 q_∞ freestream dynamic head (incompressible)
 γ ratio of specific heats, = 1.4

Subscripts

AF aft fairing boattail surface
 B nozzle base surface
 BT nozzle boattail surface
 L local
 b external bellows base
 b_1 internal bellows base
 e nozzle exit station
 ext external metric surface of left hand nozzle
 g gap between plug nozzle cylindrical balance and shield
 max crosssection of flow tube, 4 inch diameter
 p external plug nozzle spike surface

Special Symbols

x1 internal flow tube properties at station 40.563, i.e. A1, M1, P2
 Pt2, TM1
 x2 internal nozzle properties at station 45.7 for plug nozzle and
 station 48.5 for C-D nozzles, i.e. A2, M2, P2, Pt2, TM2
 xR,xL "Right Hand" and "Left Hand" identification of model components
 and flow properties based on looking aft with strut on the top,
 i.e. TM2R, TM2L, f1R, f1L, f2R, f2L, Pt1L, Pt2R, fpl

Model Configuration Symbols

| | |
|------|--|
| NCI | Narrow C-D Cruise Nozzle, Inserts In, Fin Off |
| NRI | Narrow C-D Reheat Nozzle, Inserts In, Fin Off |
| NCØ | Narrow C-D Cruise Nozzle, Inserts Out, Fin Off |
| NRØ | Narrow C-D Reheat Nozzle, Inserts Out, Fin Off |
| NCIF | Narrow C-D Cruise Nozzle, Inserts In, Fin On |
| NRIF | Narrow C-D Reheat Nozzle, Inserts In, Fin On |
| ICI | Intermediate C-D Cruise Nozzle, Inserts In, Fin Off |
| IRI | Intermediate C-D Reheat Nozzle, Inserts In, Fin Off |
| ICØ | Intermediate C-D Cruise Nozzle, Inserts Out, Fin Off |
| IRØ | Intermediate C-D Reheat Nozzle, Inserts Out, Fin Off |

REFERENCES

1. Schlichting, Hermann: Boundary Layer Theory, McGraw-Hill, 1960.
2. Sivells, James C. and Payne, Robert G.: "A Method of Calculating Turbulent-Boundary-Layer Growth at Hypersonic Mach Numbers," AEDC-TR-59-3, March 1959.
3. Sommer, Simon C. and Short, Barbara J.: "Free-Flight Measurements of Turbulent-Boundary-Layer Skin Friction in the Presence of Severe Aerodynamic Heating at Mach Numbers from 2.8 to 7.0," NACA TN 3391, March 1955.
4. Benson, J. L.; Miller, L. D.; and Horie, G.: "Theoretical Study of Engine Exhaust Nozzle Airframe Integration," AEDC-TR-67-214, October 1967.

WIND TUNNEL INVESTIGATION OF INSTALLATION

EFFECTS ON UNDERWING SUPERSONIC CRUISE

EXHAUST NOZZLES AT TRANSONIC SPEEDS

Bernard J. Blaha, Daniel C. Mikkelson, and Douglas E. Harrington

Lewis Research Center
National Aeronautics and Space Administration
Cleveland, Ohio

ABSTRACT

To investigate airframe installation effects on engine nacelles and afterbodies at subsonic and transonic speeds a series of wind tunnel tests were conducted using a 1/20 scale model of the F-106 aircraft with simulated underwing engine nacelles. Boattail pressure drag, nacelle pressures, and wing pressures were obtained on a series of configurations including changes in nacelle and inlet geometry and nacelle position. Boattail drag was obtained by pressure integration with 15-degree conical boattail afterbodies and jet boundary simulators. Data were obtained over a Mach number range of 0.56 to 1.46 at angles of attack from 0° to 15°.

INTRODUCTION

One of the early phases in the development of an aircraft exhaust system is to determine the isolated nacelle performance of the nozzle in a wind tunnel without any adjacent airframe surfaces. Recent experience has shown that performance of an exhaust nozzle system can be appreciably affected by installation on an aircraft, especially at off-design conditions (Ref. 1). An engine nacelle for a typical supersonic cruise aircraft may be installed close to the lower surface of a large wing with the afterbody extending downstream of the wing trailing edge. This aft location of the nacelle provides shielding of the inlet by the wing surface and may also provide favorable interference between the nacelle and wing. This nacelle location has not been used in previous supersonic aircraft and little is known about the effects of such an installation on the exhaust systems required for this type of aircraft. To investigate installation effects on the exhaust system of a podded engine installation of this type, the Lewis Research Center is conducting a combined flight and wind tunnel test program utilizing an F-106 aircraft with underwing engine nacelles housing J-85 afterburning turbojet engines. The F-106 aircraft was selected because it has a wing planform which could be representative of present and future supersonic cruise aircraft. The flight program will obtain installa-

tion effects on complex exhaust nozzles in the high subsonic and transonic speed range where wind tunnel models are limited to very small size to avoid wall interference effects. In a concurrent effort, wind tunnel models are also being used to investigate configuration changes that would be too expensive, time consuming, and in some cases impossible to test on the F-106 aircraft. Such a series of tests were conducted in the Lewis 8- by 6-Foot Supersonic Wind Tunnel utilizing a 1/20 scale model of the F-106 aircraft with simulated underwing engine nacelles. Some of the early wind tunnel test results are presented in Ref. 2.

In the wind tunnel tests, nacelle and wing pressure distributions and boattail pressure drag were obtained on a series of nacelle configurations including changes in nacelle and inlet geometry and nacelle position. Although small in size, this model has been very useful in qualitatively explaining the installation effects observed both in flight and in the wind tunnel tests. Because of the small size of the test nacelle, only simple variable flap ejector nozzles could be studied. Boattail pressure drag was obtained by pressure integration with 15° conical afterbodies and jet-boundary simulators. These afterbodies simulated the geometry of a variable flap ejector when the exit area is closed for operation at subsonic and transonic speeds. Boattail pressure drag coefficients for these underwing nacelles are presented and compared with flight test results. Comparison is also made with wind tunnel data from isolated cold-flow nacelle tests and tests with a nacelle under a simulated wing. The simulated wing test included a larger nacelle, which was geometrically similar to the cylindrical nacelle on the 1/20 scale model, installed close to the lower surface of a rectangular wing. This test was a first attempt to investigate installation effects on larger-sized nacelles in the 8- by 6-Foot Supersonic Wind Tunnel with only portions of the wing and airframe present. If successful, this tunnel test technique offers the possibility of conducting installation effects tests with larger nacelles than can be used on complete airframe models without exceeding tunnel blockage limitations. In this paper, 1/20 scale model nacelle and wing pressure distributions are presented to qualitatively explain the observed installation effects.

MODEL DETAILS

In Fig. 1 the 1/20 scale model of the F-106 aircraft is shown installed in the transonic test section of the Lewis 8- by 6-Foot Supersonic Wind Tunnel. The model was sting mounted from the tunnel floor strut. The underwing nacelles shown are scaled versions of those which are being flight tested on the F-106 aircraft. Open inlets which allowed air to flow through the nacelles and jet-boundary simulators are shown. Tests were conducted over a range of Mach numbers from 0.56 to 1.46 at angles-of-attack from 0° to 15°. Reynolds number

varied from 3.6×10^6 per foot (11.8×10^6 per meter) at Mach number 0.56 to 4.96×10^6 per foot (16.28×10^6 per meter) at Mach number 1.46. Model blockage at 0° angle-of-attack was less than 0.3 percent. Although the model scale was relatively small, it was selected to avoid effects of tunnel wall interference at transonic Mach numbers.

A schematic drawing of the typical nacelle installation under the model wing is shown in Fig. 2. The nacelles were strut mounted to the lower surface of the wing on each side of the fuselage and the basic spanwise position was approximately 31 percent semi-span. The cylindrical nacelle diameter was 1.24 inches (3.15 cm). The nacelles were installed at -4.5° incidence angle with respect to the wing chord and extended 0.975 nacelle diameter aft of the wing trailing edge. The nacelles also extended below the lower surface of the fuselage which was fairly flat in the region of the nacelles. Each nacelle had a 15° conical boattail with zero radius of curvature at its juncture with the nacelle and was followed by a cylindrical jet-boundary simulator. The purpose of the simulator was to approximate the local flow field that would exist in the presence of a jet with an exit-to-local-static pressure ratio of 1.0. During the testing numerous changes were made to the nacelle geometry upstream of the boattail. Also for some configurations open inlets were used which allowed stream flow to pass through the nacelle body and exit aft of the jet-boundary simulator. All the nacelle afterbodies had a ratio of projected boattail area to nacelle cross-sectional area of 0.551.

All of the model instrumentation consisted of pressure orifices installed on the nacelles and the model wing. The solid nacelle configurations were instrumented over the entire length including the boattails. The open nacelle configurations were instrumented near the aft end only. Boattail drag data were therefore obtained by pressure integration and no force balance was used.

RESULTS

A comparison of flight and wind tunnel drag data for the 15° boattail nozzles is shown in Fig. 3 as a function of free-stream Mach number at nominally 0° angle-of-attack. Data from the 1/20 scale F-106 model are presented and compared to flight data; data from an 8-1/2-inch (21.59 cm) diameter isolated cold-jet model (Ref. 3); and data from a 4-inch (10.16 cm) diameter model under a rectangular flat-plate-simulated wing (similar to the model described in Ref. 4). The flight data presented were obtained with a J-85 engine at maximum afterburning which provided a nozzle pressure ratio and area ratio such that the cylindrical ejector nozzle was overexpanded below Mach 1.0 and underexpanded above Mach 1.0. The jet-boundary simulator used on the 1/20 scale F-106 model simulated a nozzle operating fully expanded over the entire speed range. Similar conditions existed for the cold-jet nozzle, and the model with the simulated wing also had a jet-

boundary simulator. It is apparent that installation of the nozzle on the airframe caused a significant decrease in drag compared to the isolated nozzle. This drag reduction was very large at high subsonic speeds and the transonic drag rise was delayed to Mach 0.98. The flight and wind tunnel installed drag data compare favorably except near Mach 1.0 where the flight values were considerably higher. It is also apparent that some of this drag reduction is obtained with just a flat plate wing simulation. The further decrease in afterbody drag seen at Mach 0.95 for the installed flight and 1/20 scale model data, as will be shown in the next few figures, is the result of the nacelle and wing transonic terminal shocks being near the boattail at these speeds. This terminal shock was also present on the cold-jet model and the model with the simulated wing but due to tunnel blockage the effect on afterbody drag was delayed to Mach 1.08 and 1.02, respectively.

These favorable installation effects on afterbody drag are the result of the effects of the combined wing and nacelle flow fields and are apparent in the wing and nacelle pressure distributions. In Figure 4 average wing lower surface pressure distributions without nacelles are shown for Mach numbers from 0.8 to 1.0 at 2.5 degrees angle-of-attack. These pressures are averages of those observed between 20 and 43 percent semispan and are presented as a function of wing station. The wing cross section at 31 percent semispan (basic nacelle spanwise location) is shown for reference. It is apparent that a region of low pressure exists on the lower surface of the wing in the region aft of the wing maximum thickness (which is approximately 50 percent chord) and is followed by a recompression near the wing trailing edge. An increase in Mach number results in lower pressure in this region and a much stronger recompression aft. Near Mach 0.95 this recompression has the characteristics of a terminal shock. At Mach 1.0 this shock has moved off the wing and the pressure remains low to the wing trailing edge. This result correlates with the sharp drag rise seen near Mach 0.98 in the preceding figure.

The effect of the nacelle installation on the wing lower surface pressure distribution is shown in Fig. 5 for Mach 0.85 at 2.5 degrees angle-of-attack. In this figure, pressures are shown for one row of orifices just outboard of the nacelle station; however, the observed effects extended over considerable regions of the wing lower surface. With the nacelle installed, a region of increased pressure occurs above the forward half of the cowl. The pressures above the center portion of the nacelle are lower than without the nacelle and are followed by a stronger recompression region near the wing trailing edge. The lower pressures above the center portion of the nacelle probably result from the expansion region generated by the cone-shoulder geometry of the cowl-nacelle juncture. As described in Ref. 5, this modification to the wing pressure distribution resulted in elevator trim changes for the flight aircraft especially at the high subsonic speeds.

The installation effect on the nacelle pressure distribution is shown in Fig. 6 for the cylindrical nacelle at Mach 0.95 and 0 degrees angle-of-attack. The isolated nacelle pressures show the typical cone-cylinder juncture flow overexpansion and recompression for this Mach number. With the nacelle installed the flow overexpansion is delayed to further aft positions on the cylinder. This is partly the result of the wing flow field in this region where low pressures were previously observed in Figs. 4 and 5. These low pressures are then amplified to some degree by a reflection of the flow expansion at the nacelle shoulder from the lower surface of the wing. The flow recompression, being further aft on the nacelle, is somewhat amplified because it then coincides with the strong recompression region seen at the wing trailing edge in Figs. 4 and 5. Therefore, at the high subsonic speeds the boattail is immersed in the recompression fields of both the nacelle and the wing, thereby resulting in higher boattail pressures and lower drag. As seen in Fig. 7 at Mach numbers 0.90 and 0.95, the low pressures forward on the nacelle recompress through a pressure discontinuity region, or terminal shock, which moves aft with increasing Mach number. At Mach 0.95 this pressure discontinuity coincides with the location of the terminal shock seen at the wing trailing edge without nacelles in Fig. 4. At Mach 1.00, the pressure discontinuity region moves aft of the boattail and the decreased pressures on the boattail result in the sharp drag rise observed previously at Mach 0.98.

As described in Ref. 5 these shocks evidently result in an undesirable installation effect that was observed in flight. At flight Mach numbers between 0.85 and 1.0 a vibration or buzz of the nacelles and the F-106 elevons was encountered with the peak amplitude occurring at Mach 0.95. The frequency of the buzz was found to be 47 hz. and the amplitude of oscillation was large enough to be perceived by the pilots. This vibration appeared to be caused by an unstable interaction between the terminal shocks and the boundary layer on the nacelle and wing surfaces. Unsteady flow interactions of this type could be of concern when floating type nozzle components are used. However, a change in the design of the nacelle strut tended to lower the amplitude of vibration.

The effect of angle-of-attack on installed boattail drag is shown in Fig. 8 for angles-of-attack from 2.5 degrees to 15 degrees. Over the Mach number range investigated, the effect of increasing angle-of-attack was small for angles less than 8.5 degrees, and near Mach 1.0 where increasing angle-of-attack resulted in reduced boattail drag. Similar results were seen for all configurations investigated.

Large variations in the shape of the nacelle also were found to generally have little effect on boattail drag. This is shown in Fig. 9 where boattail drag coefficient is presented as a function of free-stream Mach number at 2.5 degrees angle-of-attack for cylindrical, F-106 type, flared, and flared-bent type nacelle shapes. In

Fig. 9 these shapes are illustrated with schematic drawings. These nacelles had open inlets which allowed the stream flow to pass through the nacelle body and exit at the aft end of the jet simulators. The effect of nacelle shape is small except for the flared nacelle where the boattail drag is considerably increased with coefficients similar in magnitude to isolated nacelle results. This is probably the result of significant differences in the flow spillage around the forward portions of this nacelle in contrast to that of the others. With this configuration, the effect of the wing terminal shock is still seen to result in reduced boattail drag for Mach numbers near 0.95 when compared to isolated nozzle results. This flared nacelle is a rather unusual transonic case in that no flow is spilled at the inlet. Most supersonic inlets are oversized in the transonic speed range and the resulting flow spillage would provide a flow field similar to that of the other three nacelles.

The reduction in boattail drag that was observed was not altogether peculiar to the spanwise location of the nacelle. The data of Fig. 10 show that essentially the same installation effects were obtained at subsonic Mach numbers when the nacelle spanwise position was doubled. For transonic Mach numbers the installed boattail drag was further reduced from isolated nozzle values as the nacelle was moved outboard. The effect of an adjacent inboard nacelle on outboard nacelle boattail drag is shown in Fig. 11. At subsonic Mach numbers the presence of an inboard nacelle had little effect on the outboard nacelle boattail drags. However, for transonic Mach numbers boattail drag on the outboard nacelle increased when the adjacent nacelle was installed. These values are closer to the values observed on the inboard nacelle. This is probably the result of the inboard nacelle presenting a somewhat similar reflecting surface to the outboard nacelle as that seen by the inboard nacelle installed close to the fuselage. As described in Ref. 2 the effects of an adjacent outboard nacelle on inboard nacelle boattail drag were small except for Mach numbers greater than 1.3 where the drag was observed to increase.

During the flight and wind tunnel testing, another significant result was observed. It has been demonstrated that large reductions in boattail drag can be realized by increasing the radius ratio of the boattail juncture (e.g., Ref. 3). In Fig. 12 flight and isolated nozzle data are used to show the effect of afterbody shape on boattail drag. Data for boattail juncture radius to nacelle diameter ratios (radius ratio) of 0 and 2.5 are presented. With the isolated nozzle, a significant subsonic drag reduction was obtained when the radius ratio was increased from 0 to 2.5. The installation effect, however, produced a larger reduction in subsonic drag for the sharp-edge boattail, and rounding the juncture had very little additional effect. The drag reduction due to radius ratio is unaffected by installation in the supersonic region for both the isolated and installed nozzles.

CONCLUSIONS

To investigate airframe installation effects on engine nacelles and afterbodies at subsonic and transonic speeds a series of wind tunnel tests were conducted using a 1/20 scale model of the F-106 aircraft with simulated underwing engine nacelles. Pressures and boattail drag data were obtained on a series of nacelle configurations with 15-degree conical boattail afterbodies and jet-boundary simulators. Conclusions which can be made are:

1. Airframe installation of this type resulted in reduced boattail drag at all Mach numbers when compared with isolated nacelle results and the transonic drag rise was delayed to Mach 0.98.

2. Good agreement existed between flight and model results.

3. These installation effects were caused by the combination of the acceleration and recompression in the flow fields of the wing and nacelle creating high pressures on the boattail afterbody at high subsonic speeds.

4. Flight data indicate that the flow associated with the favorable interference can be unsteady and may cause floating nozzle stability problems.

5. The effects of increasing angle-of-attack were small for angles less than 8.5° .

6. The effects of changes in inlet and nacelle geometry were small except for a flared nacelle configuration where the installation effects were small. This configuration is unusual, however, in that it did not simulate inlet flow spillage which is normal at transonic speeds.

7. These installation effects were generally insensitive to changes in nacelle spanwise position except for Mach numbers greater than 1.0.

8. When installed near the wing, the boattail drag is much less sensitive to detailed changes of the afterbody juncture curvature than is an isolated boattail.

SYMBOLS

b wing span

$C_{D\beta}$ boattail pressure drag coefficient based on cross-sectional area at boattail juncture

C_p static pressure coefficient
D nacelle diameter
 M_0 free-stream Mach number
R nozzle boattail juncture radius
x axial distance
y spanwise distance
 α angle-of-attack

REFERENCES

1. Nichols, Mark R.: Aerodynamics of Airframe-Engine Integration of Supersonic Aircraft. NASA TN D-3390, 1966.
2. Blaha, Bernard J.; and Mikkelsen, Daniel C.: Wind Tunnel Investigation of Airframe Installation Effects on Underwing Engine Nacelles at Mach Numbers From 0.56 to 1.46. NASA TM X-1683, 1968.
3. Harrington, Douglas E.: Jet Effects on Boattail Pressure Drag of Isolated Ejector Nozzles at Mach Numbers From 0.60 to 1.47. NASA TM X-1785, 1969.
4. Shrewsbury, George D.: Effect of Simulated Wing on the Pressure-Drag Coefficients of Various 15° Boattails at Mach Numbers From 0.56 to 1.00. NASA TM X-1662, 1968.
5. Crabs, Clifford C.; Boyer, Earle O.; and Mikkelsen, Daniel C.: Engineering Aspects and First Flight Results of the NASA F-106 Transonic Propulsion Research Aircraft. Presented to the Society of Experimental Test Pilots, Ohio Group, Wright-Patterson Air Force Base, Dayton, Ohio, Dec. 2, 1968. NASA TMX-52559, 1968.

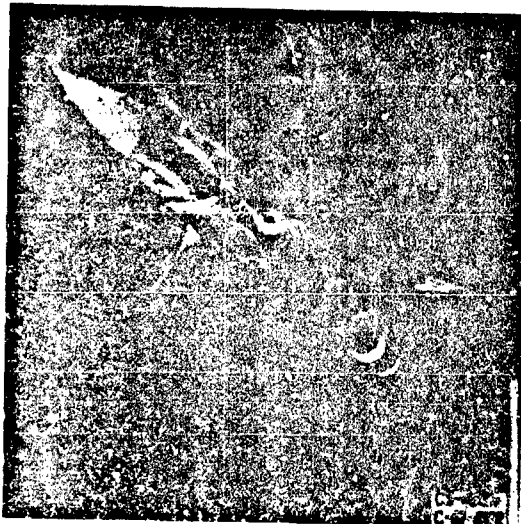


Figure 1. - 1/20th scale model of F-106 in 8- by 6-Foot Supersonic Wind Tunnel.

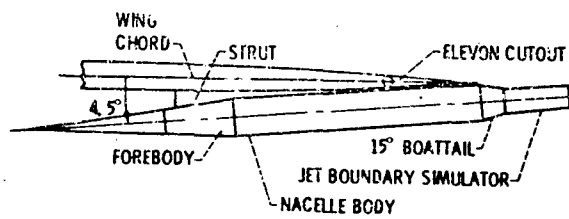


Figure 2. - Typical nacelle installation under model wing, solid cylindrical nacelle.

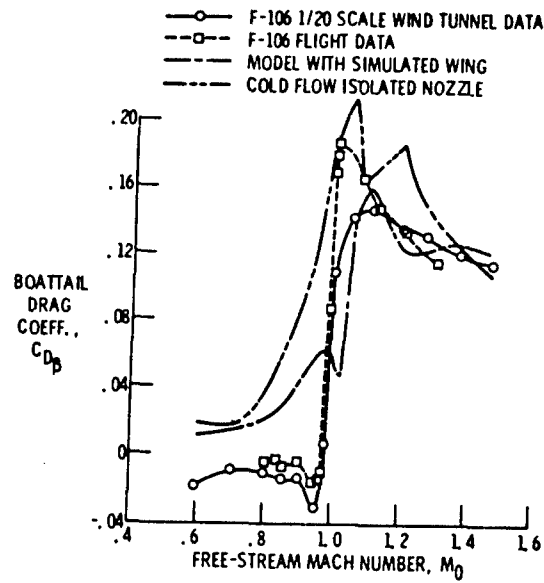


Figure 3. - Comparison of flight and wind tunnel data. 15° Conical boattail. $\alpha = 0^\circ$.

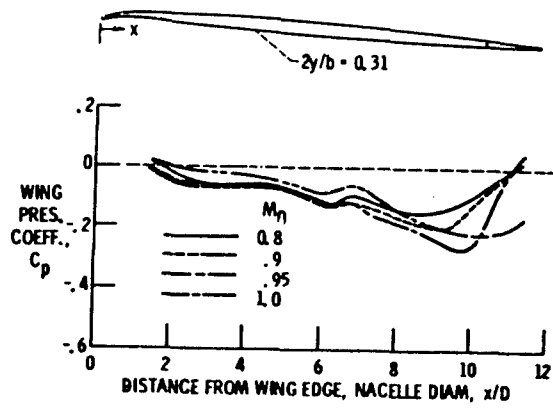


Figure 4. - Average wing lower surface pressure distribution without nacelle; $2y/b$ from 0.20 to 0.43. $\alpha = 2.5^\circ$.

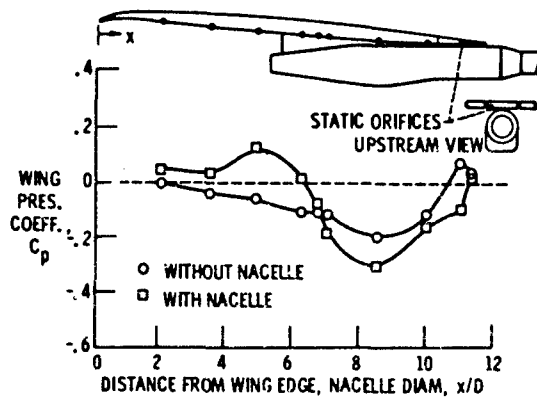


Figure 5. - Installation effect on wing pressure distribution. $M_0 = 0.85$; $\alpha = 2.5^\circ$.

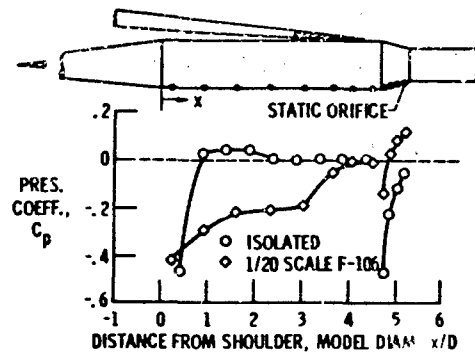


Figure 6. - Installation effect on nacelle pres
 $M_0 = 0.95$; $\alpha = 0^\circ$.

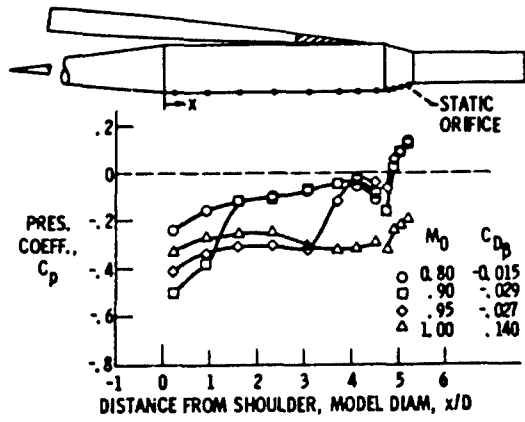


Figure 7. - Effect of Mach number on nacelle pressures. $\alpha = 0^\circ$.

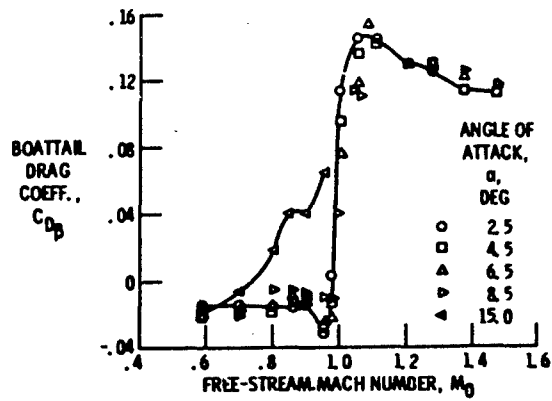


Figure 8. - Effect of angle of attack on boattail drag.

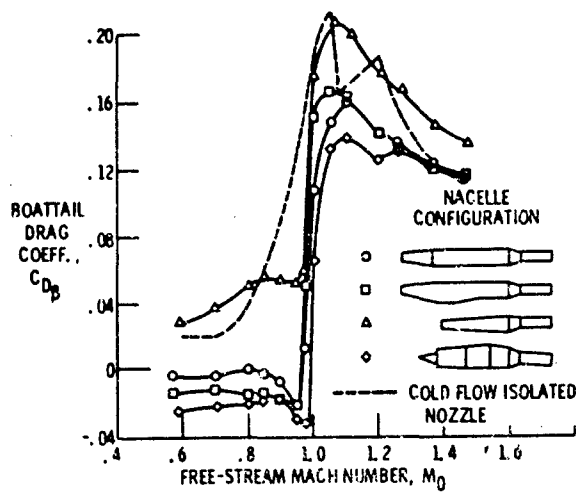


Figure 9. - Effect of nacelle shapes on boattail drag. $\alpha = 2.5^\circ$.

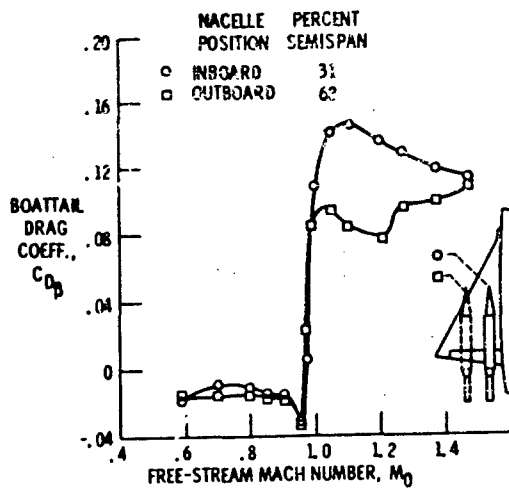


Figure 10. - Effect of nacelle spanwise position on boattail drag, solid cylindrical nacelle; no adjacent nacelle, $\alpha = 2.5^\circ$.

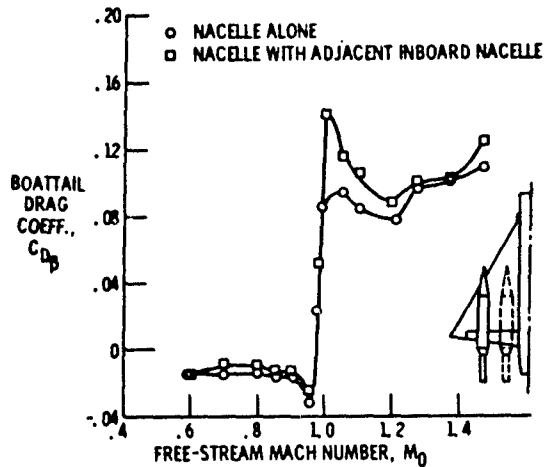


Figure 11. - Effect of inboard nacelle on outboard nacelle boattail drag, $\alpha = 2.5^\circ$.

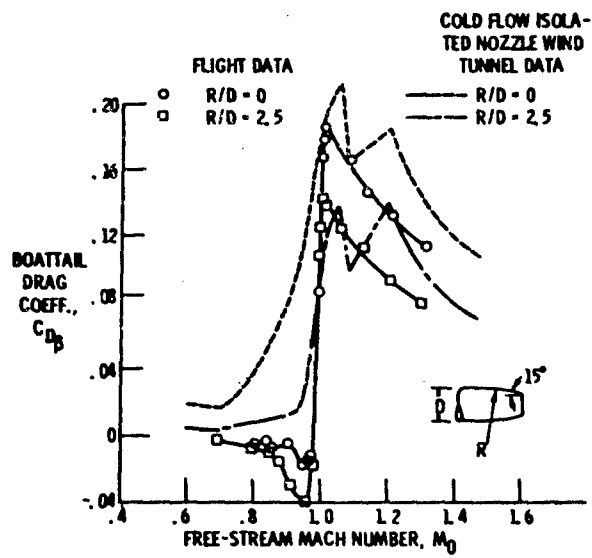


Figure 12. - Effect of afterbody shape on boattail drag, $\alpha = 0^\circ$.

CALCULATION OF SUBSONIC INLET DRAG

T. C. Rochow, B. M. Sharp, and E. D. Spong

McDonnell Aircraft Company

ABSTRACT

Calculation procedures for axisymmetric and two-dimensional fields have been developed to solve the compressible, potential flow problem in the subsonic regime.

The methods have been computerized and applied to the calculation of the flow field and drag of two-dimensional and axisymmetric inlets. Good agreement with experimental data has been shown and the calculations are considered superior to existing techniques for subsonic inlet drag determination.

INTRODUCTION

An analytic calculation of the drags associated with an inlet in the subsonic flow regime is a problem that has not been solved in a satisfactory manner in the past. The usual procedure has been to make a one-dimensional calculation of the additive drag and to apply an empirically determined estimate of the force on the inlet cowl. This force normally corresponds to a reduction in drag due to the fact that the pressure is below ambient. In addition, the empirical correction should account for cowl drag between maximum capture (air induction) and the capture at the operating point in question. In the opinion of the authors the uncertainty in these empirical corrections is so great that little credence can be put in inlet drags calculated by these techniques.

A more fundamental calculation of the inlet drags can be obtained by evaluating the flow field surrounding the inlet. For subsonic, compressible, potential flow in two-dimensional or axisymmetric coordinate systems, methods have been developed to facilitate this flow field determination. From numerical integrations of the flow field appropriate values of stream thrusts and forces can be used to directly calculate the values of additive and cowl drag.

In the following sections the analytical methods are thoroughly outlined, comparisons with experimental data presented, and a discussion of the limitations of the technique given.

ANALYTIC ANALYSES

The following subsections give a detailed presentation of the equations and techniques used to solve the subsonic, compressible, potential flow field in axisymmetric and two-dimensional coordinate systems. A closed form solution is not possible and numerical techniques are used. In each case the field to be solved is represented by a grid with nodal points defined by the intersections of two grid lines. The two approaches are slightly different, but in both cases the continuity equation is written for each node in a form using velocity potential, initially assuming a constant density field. The set of all such equations is then solved simultaneously to give a potential field, which in turn allows determination of the velocity, density, Mach number, and flow angle at the nodal points. Since the field is subsonic, a complete set of boundary conditions must be incorporated in the equations. Iterative techniques are used to converge on the compressible solution.

Axisymmetric Analysis

The nodal network shown in Figure 1 in the r - z coordinate system is considered. Conservation of momentum and energy with the assumptions of steady flow, negligible body force due to gravity, adiabatic flow, uniform entropy, inviscid fluid, and no electromagnetic effects gives the irrotational condition

$$\nabla \times \vec{V} = 0 \quad (1)$$

which implies that \bar{V} may be represented by the gradient of a scalar potential function ϕ as

$$\bar{V} = \nabla\phi \quad (2)$$

since

$$\nabla \times \nabla\phi = 0 \quad (3)$$

The mass flow may be represented by

$$\dot{m}_k = \rho A_{\text{trans}} V_k \quad (4)$$

and substituting for V_k from Equation (2) gives

$$\dot{m}_k = \rho A_{\text{trans}} \frac{\partial\phi}{\partial x_k} \quad (5)$$

Considering a node N in a grid with four orthogonal neighbors (Figure 1), the net mass flow at steady state must be zero. The next step in the development is to write an equation in the velocity potentials at the five points by integrating Equation (5) to get the mass flow from node N to its four neighbors, sum these mass flows, and set the sum equal to zero. Assumptions at this point are:

- Node N exchanges mass only with its four orthogonal neighbors.
- The strip width defining A_{trans} is set by the orthogonal bisectors of the nodal grid.

From the coordinate system we note

$$\begin{aligned} A_{\text{trans}} \text{ (right or left)} &= \pi(r_{\text{NA}}^2 - r_{\text{NB}}^2) \\ A_{\text{trans}} \text{ (radial)} &= 2\pi r(z_{\text{NL}} - z_{\text{NR}}) \end{aligned} \quad (6)$$

Substituting from (6) into (5) for the left-right direction gives

$$\dot{m}_R = \rho\pi(r_{\text{NA}}^2 - r_{\text{NB}}^2) \frac{\partial\phi}{\partial z} \quad (7)$$

and integrating from N to R

$$\dot{m}_R \int_N^R dz = \rho\pi(r_{\text{NA}}^2 - r_{\text{NB}}^2) \int_N^R d\phi \quad (8)$$

$$\dot{m}_R = \frac{\rho\pi(r_{\text{NA}}^2 - r_{\text{NB}}^2)(\phi_R - \phi_N)}{(z_R - z_N)} \quad (9)$$

Letting $C_R = \frac{\rho\pi(r_{NA}^2 - r_{NB}^2)}{(z_R - z_N)}$, we have

$$\dot{m}_R = C_R(\phi_R - \phi_N) \quad (10)$$

In the same manner by integration from N to L

$$\dot{m}_L = C_L(\phi_L - \phi_N) \quad (11)$$

For the radial direction by substitution of (6) into (5).

$$\dot{m}_A = \rho 2\pi r (z_{NL} - z_{NR}) \frac{\partial \phi}{\partial r} \quad (12)$$

Integrating from N to A yields

$$\dot{m}_A \int_N^A \frac{dr}{r} = 2\pi\rho(z_{NL} - z_{NR}) \int_N^A d\phi \quad (13)$$

$$\dot{m}_A = \frac{2\pi\rho(z_{NL} - z_{NR})}{\ln(r_A/r_N)} (\phi_A - \phi_N) \quad (14)$$

Letting $C_A = \frac{2\pi\rho(z_{NL} - z_{NR})}{\ln(r_A/r_N)}$, we have

$$\dot{m}_A = C_A(\phi_A - \phi_N) \quad (15)$$

In the same manner by integration from N to B

$$\dot{m}_B = C_B(\phi_B - \phi_N) \quad (16)$$

In the preceding development it should be noted that ρ has been assumed to be constant. Now a basic mass balance may be formulated by setting the sum of Equations (10), (11), (15), and (16) equal to zero.

$$C_L(\phi_L - \phi_N) + C_R(\phi_R - \phi_N) + C_A(\phi_A - \phi_N) + C_B(\phi_B - \phi_N) = 0 \quad (17)$$

Expanding and combining like terms yields

$$C_L\phi_L + C_R\phi_R + C_A\phi_A + C_B\phi_B - \sum_{j=1}^4 C_j\phi_N = 0 \quad (18)$$

Two common special cases of the basic Equation (18) of interest are

- ° Known mass flow or potential - specify term in the equation;

suppose \dot{m}_R is known for a certain mode

$$C_L \phi_L + C_A \phi_A + C_B \phi_B - \sum_{j=1}^3 C_j \phi_N = \text{Constant} \quad (19)$$

- ° Zero mass flow (impenetrable boundary) - remove term in equation; suppose \dot{m}_R is known to be zero for a certain node

$$C_L \phi_L + C_A \phi_A + C_B \phi_B - \sum_{j=1}^3 C_j \phi_N = 0 \quad (20)$$

A third special case of somewhat greater complexity is that occurring when the transfer area is partially bounded by a surface rather than the orthogonal bisectors of the nodal grid. In the computerized calculation each term has an input multiplier (B) to provide for this case. In the following paragraph the calculation of B for one of the several possible geometries will be outlined.

Figure 2 shows the geometry to be considered. The transfer area is shaded and is seen to be partially bounded by a solid surface. It is seen that the radial transfer area is given by

$$A_{\text{trans}} (\text{radial}) = 2\pi r(z_{NL} - z_s(r)) \quad (21)$$

and the mass flow may be written

$$\dot{m}_A = 2\pi r \rho (z_{NL} - z_s(r)) \frac{\partial \phi}{\partial r} \quad (22)$$

Integration yields

$$\dot{m}_A \int_N^A \frac{dr}{r(z_{NL} - z_s(r))} = 2\pi \rho \int_N^A d\phi \quad (23)$$

$$\dot{m}_A = \frac{2\pi \rho (\phi_A - \phi_N)}{\int_N^A \frac{dr}{r(z_{NL} - z_s(r))}} \quad (24)$$

In the computerized calculation \dot{m}_A is represented by

$$\dot{m}_A = \frac{2\pi \rho (z_{NL} - z_{NR})}{\ln(r_A/r_N)} (\phi_A - \phi_N) B \quad (25)$$

Equating Equations (24) and (25) and solving for B yields

$$B = \frac{\ln(r_A/r_N)}{(z_{NL} - z_{NR}) \int_N^A \frac{dr}{r(z_{NL} - z_B(r))}} \quad (26)$$

For straight line surfaces the calculations involved in solving for B are explicit, otherwise numerical procedures are employed.

Using the equations developed in the preceding part of this subsection, a solution for an incompressible field can be obtained by gridding the field into a nodal network, writing a mass balance for each node assuming $\rho = \text{constant}$, and solving the resulting set of simultaneous equations for the velocity potential. Since the problem is subsonic, a complete set of boundary conditions must be specified. These boundary conditions are some set of known potentials, known mass flow rates, and zero flow rates normal to the axis of symmetry and solid boundaries. Figure 3 is a schematic of a nodal grid of a field containing an axisymmetric inlet.

An automated iterative cycle is used to extend this technique to the solution of compressible fields. The steps are:

- (1) Set up the problem with $\rho = \text{constant}$ throughout the field as a first approximation.
- (2) Solve the set of simultaneous mass balances for the velocity potential field.
- (3) From the potential field calculate the density ratio, velocity magnitude, and flow angle at each nodal point using

$$\frac{\rho}{\rho_t} = \left[1 - \frac{(\gamma-1)}{2} \left\{ \frac{\left(\frac{\partial\phi}{\partial z}\right)^2 + \left(\frac{\partial\phi}{\partial r}\right)^2}{a_t^2} \right\} \right]^{\frac{1}{\gamma-1}}$$

$$v = |\bar{V}| = \left[\left(\frac{\partial\phi}{\partial z}\right)^2 + \left(\frac{\partial\phi}{\partial r}\right)^2 \right]^{0.5}$$

$$\theta = \tan^{-1} \left[\left(\frac{\partial\phi}{\partial r}\right) / \left(\frac{\partial\phi}{\partial z}\right) \right]$$

- (4) Read the values from Step (3) back into the calculation and reset the calculation to (2) generating new potential, velocity, density, flow angle fields.
- (5) Repeat the preceding loop until the calculation converges.

The potential function derivatives are obtained by standard numerical techniques. The calculation is programmed on an IBM Model 360 computer. The calculation of inlet pressure distributions and drags is carried out

in a separate program on a CDC 6400 computer.

Two-Dimensional (Plane) Analysis

This two-dimensional analysis is limited to irrotational, inviscid, adiabatic, compressible, steady flow. The approach is similar to that used for the axisymmetric case, however, the differential form of the continuity equation is used, leading to a second order differential equation in the velocity potential and a somewhat different form of the final finite difference equations. The basic differential equation, in terms of the velocity potential, obtained by combining the continuity equation with the restriction of zero vorticity takes the form (see Reference 1)

$$\phi_{xx} + \phi_{yy} + \phi_x \rho_x / \rho + \phi_y \rho_y / \rho = 0 \quad (27)$$

The density is related to the velocity potential ϕ by

$$\rho / \rho_t = \left[1 - \frac{(\gamma-1)(\phi_x^2 + \phi_y^2)}{2a_t^2} \right]^{\frac{1}{\gamma-1}} \quad (28)$$

The flow field to be analyzed is represented by an orthogonal grid and Equation (27) is applied in finite difference form at each node. As in the preceding subsection, a node is defined as the point of intersection of two grid net lines. Also, as before, a complete set of boundary conditions is incorporated in the basic equation set. In the computer program as written it is necessary that the nodes be equally spaced in the x direction. The total number of nodes used depends on the available computer core size.

Finite difference forms of Equation (27) have been derived for various types of grid spacing, body surfaces, and boundary conditions. The basic requirements, as seen from Equation (27), are finite difference approximations for the derivatives of velocity potential and density with respect to coordinate direction. The following presentation is limited to the development of two typical equations with the remainder of the necessary set presented without proof.

Derivation of the Finite Difference Equation for A Central Field Point - Referring to Figure 4, the first derivatives of the velocity potential in finite difference form are given by

$$\begin{aligned} \phi_x &= (\phi_{i+1} - \phi_{i-1}) / (\delta_{i+1} + \delta_{i-1}) \\ \phi_y &= (\phi_{i+n} - \phi_{i-n}) / (\delta_{i+n} + \delta_{i-n}) \end{aligned} \quad (29)$$

The second derivatives of the velocity potential are given by

$$\begin{aligned} \phi_{xx} &= 2 \left\{ (\phi_{i+1} - \phi_i) / \delta_{i+1} - (\phi_i - \phi_{i-1}) / \delta_{i-1} \right\} / (\delta_{i+1} + \delta_{i-1}) \\ \phi_{yy} &= 2 \left\{ (\phi_{i+n} - \phi_i) / \delta_{i+n} - (\phi_i - \phi_{i-n}) / \delta_{i-n} \right\} / (\delta_{i+n} + \delta_{i-n}) \end{aligned} \quad (30)$$

Similarly the first derivatives of the density are given by

$$\begin{aligned}\rho_x &= (\rho_{i+1} - \rho_{i-1}) / (\delta_{i+1} - \delta_{i-1}) \\ \rho_y &= (\rho_{i+n} - \rho_{i-n}) / (\delta_{i+n} - \delta_{i-n})\end{aligned}\quad (31)$$

Now substituting Equations (29), (30), and (31) into Equation (27) and using

$$\begin{aligned}R_x &= (\rho_{i+1} - \rho_{i-1}) / \{ (\delta_{i+1} + \delta_{i-1})^2 \rho_i \} \\ R_y &= (\rho_{i+n} - \rho_{i-n}) / \{ (\delta_{i+n} + \delta_{i-n})^2 \rho_i \}\end{aligned}\quad (32)$$

we obtain

$$\begin{aligned}\phi_{i+1} \{ 2/[\delta_{i+1} (\delta_{i+1} + \delta_{i-1})] + R_x \} &+ \phi_{i-1} \{ 2/[\delta_{i-1} (\delta_{i+1} + \delta_{i-1})] - R_x \} + \\ \phi_{i+n} \{ 2/[\delta_{i+n} (\delta_{i+n} + \delta_{i-n})] + R_y \} &+ \phi_{i-n} \{ 2/[\delta_{i-n} (\delta_{i+n} + \delta_{i-n})] - R_y \} + \\ \phi_i \{ -2/(\delta_{i+1} \cdot \delta_{i-1}) - 2/(\delta_{i+n} \cdot \delta_{i-n}) \} &= 0\end{aligned}\quad (33)$$

Derivation of the Finite Difference Equation for a Body Point with Positive Surface Slope, Surface Facing Top of Field - Referring to Figure 5, the flow direction at i is defined as θ , thus

$$\begin{aligned}\bar{v}_i &= (\nabla \phi)_i \\ u &= \bar{v}_i \cdot \bar{i} = |\bar{v}_i| \cos \theta = \phi_x \\ v &= \bar{v}_i \cdot \bar{j} = |\bar{v}_i| \sin \theta = \phi_y\end{aligned}\quad (34)$$

Therefore,

$$\begin{aligned}(\phi_x)_i &= (\phi_{i+1} - \phi_{i-1}) \cos^2 \theta / 2 \\ (\phi_y)_i &= (\phi_{i+1} - \phi_{i-1}) \sin \theta \cos \theta / 2\end{aligned}\quad (35)$$

To obtain the finite difference expressions for the second order derivatives of ϕ and the first order derivative of ρ , a value of ϕ and ρ is interpolated between nodes $i+n-1$ and $i-1$

$$\begin{aligned}\phi^* &= \phi_{i-1} \cdot \delta_{i+n} / \delta_{i+n-1} + \phi_{i+n-1} (1 - \delta_{i+n} / \delta_{i+n-1}) \\ \rho^* &= \rho_{i-1} \cdot \delta_{i+n} / \delta_{i+n-1} + \rho_{i+n-1} (1 - \delta_{i+n} / \delta_{i+n-1})\end{aligned}\quad (36)$$

and

$$\begin{aligned}\phi_{xx} &= 2 \left\{ (\phi_{i+1} - \phi_{i-1})/2 \cos^2 \theta - (\phi_i - \phi^*)/\delta_{i-1} \right\} / \delta_{i-1} \\ \phi_{yy} &= 2 \left\{ (\phi_{i+n} - \phi_i)/\delta_{i+n} - (\phi_{i+1} - \phi_{i-1})/2 \sin \theta \cos \theta \right\} / \delta_{i+n} \\ \rho_x &= (\rho_i - \rho^*) \\ \rho_y &= (\rho_{i+n} - \rho_i)/\delta_{i+n}\end{aligned}\quad (37)$$

Substituting Equations (35) and (37) into Equation (27), we obtain

$$\begin{aligned}\phi_{i+1} [K_1] + \phi_{i-1} [K_2/\delta_{i-1}^2 - K_1] + \phi_{i+n} [1/\delta_{i+n}^2] + \\ \phi_{i+n-1} [(1-K_2)/\delta_{i-1}^2] + \phi_i [-1/\delta_{i-1}^2 - 1/\delta_{i+n}^2] = 0\end{aligned}\quad (38)$$

where

$$\begin{aligned}K_1 &= [\cos^2 \theta \{1/\delta_{i-1} + R_x\} - \sin \theta \cos \theta \{1/\delta_{i+n} - R_y\}] / (\delta_{i-1} + \delta_i) \\ K_2 &= \delta_{i+n} / \delta_{i+n-1} \\ R_x &= [\rho_i - \rho_{i-1} \cdot K_2 - \rho_{i+n-1} (1-K_2)] / (\rho_i \cdot \delta_{i-1}) \\ R_y &= (\rho_{i+n} - \rho_i) / (\rho_i \cdot \delta_{i+n})\end{aligned}$$

Finite Difference Equation for a Body Point with Negative Surface Slope, Surface Facing Top of Field -

$$\begin{aligned}\phi_{i+1} [2K_2 - K_1] + \phi_{i-1} [K_1] + \phi_{i+n} [2/\delta_{i+n}^2] + \\ \phi_{i+n+1} [2(1-K_2)] + \phi_i [-2(\delta_{i+n}^{-2} + 1)] = 0\end{aligned}\quad (39)$$

with

$$\begin{aligned}K_1 &= \cos^2 \theta [1-R_x] + \sin \theta \cos \theta [\delta_{i+n}^{-1} - R_y] \\ K_2 &= \delta_{i+n} / \delta_{i+n+1} \\ R_x &= [\rho_{i+n+1} (1-K_2) + \rho_{i+1} K_2 - \rho_i] / 2\rho_i \\ R_y &= (\rho_{i+n} - \rho_i) / (2\delta_{i+n} \cdot \rho_i)\end{aligned}$$

Finite Difference Equation for a Body Point with Positive Surface Slope, Surface Facing Bottom of Field -

$$\begin{aligned} & \phi_{i+1}[2K_2 - K_1] + \phi_{i-1}[K_1] + \phi_{i-n}[2/\delta_i^2] + \\ & \phi_{i-n+1}[2(1-K_2)] + \phi_i[-2(1 + \delta_i^{-2})] = 0 \end{aligned} \quad (40)$$

with

$$\begin{aligned} K_1 &= \cos^2\theta(1-R_x) - \cos\theta\sin\theta(\delta_i^{-1} + R_y) \\ K_2 &= \delta_i/\delta_{i+1} \\ R_x &= [\rho_{i-n+1}(1-K_2) + \rho_{i+1}K_2 - \rho_i]/2\rho_i \\ R_y &= (\rho_i - \rho_{i-n})/2\delta_i \cdot \rho_i \end{aligned}$$

Finite Difference Equation for a Body Point with Negative Surface Slope, Surface Facing Bottom of Field -

$$\begin{aligned} & \phi_{i+1}[K_1] + \phi_{i-1}[2K_2 - K_1] + \phi_{i-n}[2/\delta_i^2] + \\ & \phi_{i-n-1}[2(1-K_2)] + \phi_i[-2(1 + \delta_i^{-2})] = 0 \end{aligned} \quad (41)$$

with

$$\begin{aligned} K_1 &= \cos^2\theta[1+R_x] + \sin\theta\cos\theta[\delta_i^{-1} + R_y] \\ K_2 &= \delta_i/\delta_{i-1} \\ R_x &= [\rho_i - \rho_{i-n-1}(1-K_2) - \rho_{i-1}K_2]/2\rho_i \\ R_y &= (\rho_i - \rho_{i-n})/2\delta_i \cdot \rho_i \end{aligned}$$

Finite Difference Equation for a "Stagnation" Body Point - Since the inclination of the body downstream of the "stagnation" point is arbitrary, provision is made for using interpolated and extrapolated values for the downstream value of velocity potential to be used in determining the x-direction derivatives. Referring to Figure 6, the "f" factor in the following equation reflects the selection of the appropriate downstream value.

$$\begin{aligned} & \phi_{i-1}[1-R_x] + \phi_{i+n}[K_6+R_y] + \phi_{i-n}[K_7-R_y] + \\ & \phi_{i-n+1}[f(1-K_1)K_8] + \phi_{i+1}[fK_1K_5] + \\ & \phi_{i+2n+1}[(1-f)(1-K_2)K_5] + \phi_{i+n+1}[(1-f)K_2K_5] + \\ & \phi_i[-2-K_6-K_7] = 0 \end{aligned} \quad (42)$$

with

$$K_1 = \delta_i / \delta_{i+1}$$

$$K_2 = (\delta_{i+n} + \delta_{i+2n}) / \delta_{i+2n+1}$$

$$R_x = [\rho_{i-n+1}(1-K_1) + \rho_{i+1} K_1 - \rho_{i-1}] / 4\rho_i$$

$$K_4 = 2 / (\delta_{i+n} + \delta_i)$$

$$K_5 = 1 + R_x$$

$$K_6 = K_4 / \delta_{i+n}$$

$$K_7 = K_4 / \delta_i$$

$$R_y = K_4^2 (\rho_{i+n} - \rho_{i-n}) / 4\rho_i$$

Finite Difference Equation for a Body Point Immediately Downstream of "Stagnation" Point on Surface Facing Top of Field -

$$\begin{aligned} & \phi_{i+n-1} [2(1-K_2)] + \phi_{i-1} [2K_2] + \phi_{i+n} [2/\delta_{i+n}^2] + \\ & \phi_{i-n-1} [-K_1] + \phi_{i+1} [K_1] + \phi_i [-2(1 + \delta_{i+n}^{-2})] = 0 \end{aligned} \quad (43)$$

with

$$K_1 = \cos^2 \theta (1+R_x) - \cos \theta \sin \theta (1-R_y)$$

$$K_2 = \delta_{i+n} / \delta_{i+n-1}$$

$$R_x = [\rho_i - \rho_{i+n-1}(1-K_2) - \rho_{i-1} K_2] / 2\rho_i$$

$$R_y = (\rho_{i+n} - \rho_i) / (2\rho_i \cdot \delta_{i+n})$$

Finite Difference Equation for a Body Point Immediately Downstream of "Stagnation" Point on Surface Facing Bottom of Field -

$$\begin{aligned} & \phi_{i+1} [K_1] + \phi_{i-1+n} [-K_1] + \phi_i [-2(1+\delta_i^{-1})] + \\ & \phi_{i-n} [2/\delta_i^2] + \phi_{i-n-1} [2(1-K_2)] + \phi_{i-1} [2K_2] = 0 \end{aligned} \quad (44)$$

with

$$K_1 = \cos^2 \theta (1+R_x) - \cos \theta \sin \theta (1+R_y)$$

$$K_2 = \delta_i / \delta_{i-1}$$

$$R_x = [\rho_i - \rho_{i-n-1}(1-K_2) - \rho_{i-1}K_2]/2\rho_i$$

$$R_y = (\rho_i - \rho_{i-n})/(2\rho_i \cdot \delta_i)$$

Finite Difference Equation for a Field Point with Node "Line" of Positive Slope (Figure 7) -

$$\begin{aligned} & \phi_{i+n}[K_6+R_y] + \phi_{i-n}[K_7-R_y] + \phi_{i-1}[K_{10}K_9] + \\ & \phi_{i+1-n}[K_{11}K_5] + \phi_{i+1}[K_2K_5] + \phi_{i-1+n}[K_1K_9] + \end{aligned} \quad (45)$$

$$\phi_i[-2-K_6-K_7] = 0$$

$$K_1 = (y_i - y_{i-1})/\delta_{i-1+n}$$

$$K_2 = (y_i - y_{i+1-n})/\delta_{i+1-n}$$

$$K_4 = 2/(\delta_{i+n} + \delta_i)$$

$$K_5 = 1 + R_x$$

$$K_6 = K_4/\delta_{i+n}$$

$$K_7 = K_4/\delta_i$$

$$K_9 = 1 - R_x$$

$$K_{10} = 1 - K_1$$

$$K_{11} = 1 - K_2$$

$$R_x = (\rho_{i+1-n}K_{11} + \rho_{i+1}K_2 - \rho_{i-1}K_{10} - \rho_{i-1+n}K_1)/4\rho_i$$

$$R_y = (\rho_{i+n} - \rho_{i-n})/(\delta_i + \delta_{i+n})^2/\rho_i$$

Finite Difference Equation for A field Point with Node "Line" of Negative Slope -

$$\begin{aligned} & \phi_{i+n+1}[K_2K_5] + \phi_{i+1}[K_{11}K_5] + \phi_{i-1}[K_1K_9] + \\ & \phi_{i-n-1}[K_{10}K_9] + \phi_{i+n}[K_6+R_y] + \phi_{i-n}[K_7-R_y] + \end{aligned} \quad (46)$$

$$\phi_i[-2-K_6-K_7] = 0$$

with

$$K_1 = (y_i - y_{i-n-1}) / \delta_{i-1}$$

$$K_2 = (y_i - y_{i+1}) / \delta_{i+n+1}$$

$$K_4 = 2 / (\delta_{i+n} + \delta_i)$$

$$K_5 = 1 + R_x$$

$$K_6 = K_4 / \delta_{i+n}$$

$$K_7 = K_4 / \delta_i$$

$$K_9 = 1 - R_x$$

$$K_{10} = 1 - K_1$$

$$K_{11} = 1 - K_2$$

$$R_x = (-\rho_{i+n+1} K_{10} - \rho_{i+n-1} K_1 + \rho_{i-n+1} K_{11} + \rho_{i+1} K_2) / 4\rho_i$$

$$R_y = (\rho_{i+n} - \rho_{i-n}) K_4^2 / 4\rho_i$$

Finite Difference Equation for Calibration Nodes (Figure 8) -

$$\phi_i(0.5) + \phi_{i-2}(-0.5) = v_1 [2 - (\rho_{i-1} / \rho_i)] \quad (47)$$

Finite Difference Equation for a Point on a Constant Velocity Potential Boundary (Figure 9) -

$$\phi_{i+1}[1+R_x] + \phi_{i+n}[1+R_y] + \phi_{i-n}[1-R_y] + \phi_i[-4] = \phi_i[-1+R_x] \quad (48)$$

with

$$R_x = (\rho_{i+1} - \rho_i) / 4\rho_i$$

$$R_y = (\rho_{i+n} - \rho_{i-n}) / 4\rho_i$$

Finite Difference Equation for a Point on a Constant Velocity Boundary (Figure 10) -

$$\begin{aligned} &\phi_{i+1}[1+R_x] + \phi_{i-1}[1-R_x] + \phi_{i-n}[1-R_y] + \phi_i[-4] = \\ & -[\phi_i + v_0 x][1+R_y] \end{aligned} \quad (49)$$

with

$$R_x = (\rho_{i+1} - \rho_{i-1})/4\rho_i$$

$$R_y = (\rho_o - \rho_{i-n})/4\rho_i$$

Application of Finite Difference Equations - The appropriate finite difference equation from the preceding listing is applied to each node of the flow field to be analyzed. Thus for a field with n nodes there will be n equations in ϕ_1 through ϕ_n and ρ_1 through ρ_n with ϕ and ρ related by Equation (28). Similarly to the axisymmetric analysis, the solution procedure takes the following steps:

- (1) The density field is assumed to be constant at the freestream value.
- (2) The n simultaneous equations are solved to determine the velocity potential at each node.
- (3) The density at each node is determined from Equation (28) using the velocity potential field.
- (4) The field is iterated, obtaining repeated solutions of the potential field with the current density field until the density field converges.
- (5) The surface pressures are obtained on the ramps and cowls and the inlet drag is calculated from (Figure 11)

$$D = \int_1^2 (P-P_o) dA_x + \int_1^3 (P-P_o) dA_x + \int_4^5 (P-P_o) dA_x + \int_3^4 (P-P_o) dA_x + \int_3^4 \rho v^2 dA_x - v_o \int_3^4 \rho v dA_x \quad (50)$$

A typical nodal network is shown in Figure 12. The analysis is presently programmed for the CDC 6400 computer with a case time of approximately 15 seconds.

DISCUSSION

Comparisons of the results of the axisymmetric analysis with inlet (additive plus cowl) drag and cowl pressure distribution data from Reference 2 are shown in Figures 13 through 15. As seen in Figure 13, the cowl pressure distribution is accurately predicted. In Figures 14 and 15 the shape of the theoretical drag curve is taken directly from results of the axisymmetric analysis, however the level has been adjusted at the maximum (choke) flow position. This adjustment was carried out by calculating the drag at the choke flow value using analytic pressure

distributions on the cowl and innerbody and one-dimensional stream thrusts at the leading edge of the innerbody and the inlet station rather than stream thrusts calculated by integrating the results of the analytic program. A complete discussion of the reasons for this agreement and more complete comparisons of theory and data are given in Reference 2.

Comparisons of the results of the two-dimensional analysis with additive drag data from Reference 3 are shown in Figures 16 and 17. Excellent agreement both in level and trend was achieved.

The calculation limit of the programs is set by the point at which the irrotational assumption breaks down, physically at the point at which shocks must appear in the field to satisfy the boundary conditions. Results to date indicate that supersonic "bubbles" may occur in the field and still permit convergence. The first appearance of shocks usually takes place on the exterior of the cowl, the Mach number depending on the mass flow ratio. Low mass flow ratios lead to strong expansions around the cowl lip and to flow breakdown at relatively low freestream Mach numbers. Each calculation is to some extent unique and no general statement of the limits of calculation can be given. For the cases run so far, valid results have been possible up to Mach numbers of approximately 0.85 at high mass flow ratios.

A feature of the two-dimensional program that has not been satisfactorily explained to date is a discrepancy between the mass flow at the cowl lip and duct stations further downstream. The mass flow at the downstream duct station is input as a boundary condition. Calculations are carried out in the program giving the mass flow at the cowl lip station. Obviously these mass flows should be the same, however, in practice they are somewhat different. It is thought that this discrepancy is a function of grid size and choice of node location. It is planned to investigate the effect of these variables in future work.

There is also an interesting question involved in determining how the flow angles at the leading edge of the cowl and innerbody should be calculated. For other body points the flow angle is taken as the body angle and for field points as the arctangent of the velocity components. Various methods have been applied to the body and cowl leading edge points. Fortunately the choice of method has little effect on the drag results although the perturbation of the local field properties may be severe.

CONCLUSIONS

- (1) For axisymmetric and two-dimensional subsonic potential flow, methods have been developed to calculate the flow field surrounding arbitrarily shaped bodies.
- (2) These methods have been programmed on high speed computers and applied to the calculation of inlet pressure distributions and drags.
- (3) Good agreement with experimental data has been achieved and the techniques are considered superior to existing methods for estimating inlet drag.

REFERENCES

1. Shapiro, Ascher H., "The Dynamics and Thermodynamics of Compressible Fluid Flow," Vol. I, Ronald Press Company, New York, N.Y., 1953.
2. McVey, Francis D., Rejeske, John V., Phillips, Edward J., "Experimental Evaluation of Inlet Drag Characteristics in the Transonic Mach Number Regime," Report AFAPL-TR-68-119, November 1968.
3. Muller, George L. and Gasko, William F., "Subsonic-Transonic Drag of Supersonic Inlets," Report TDM-1973, Pratt and Whitney Aircraft, May 1966.

SYMBOLS

| | |
|-----------|---|
| a | speed of sound |
| A | area |
| \dot{m} | mass flow rate |
| P | pressure |
| V | velocity |
| δ | coordinate distance of a node to its neighbor |
| γ | ratio of specific heats |
| ρ | gas density |
| θ | flow angle |
| ϕ | velocity potential |

Subscripts

| | |
|-------------------|---|
| t | total conditions |
| o | freestream conditions |
| k | general coordinate direction |
| trans | area available for mass transfer |
| L | left direction |
| R | right direction |
| A | above direction |
| B | below direction |
| x | first partial derivative with respect to x |
| xx | second partial derivative with respect to x |
| y | first partial derivative with respect to y |
| yy | second partial derivative with respect to y |
| i | i^{th} node |
| i+1, i+n, etc. | refers to node with number corresponding to subscript |

Figure 1 Typical Axisymmetric Nodal Network

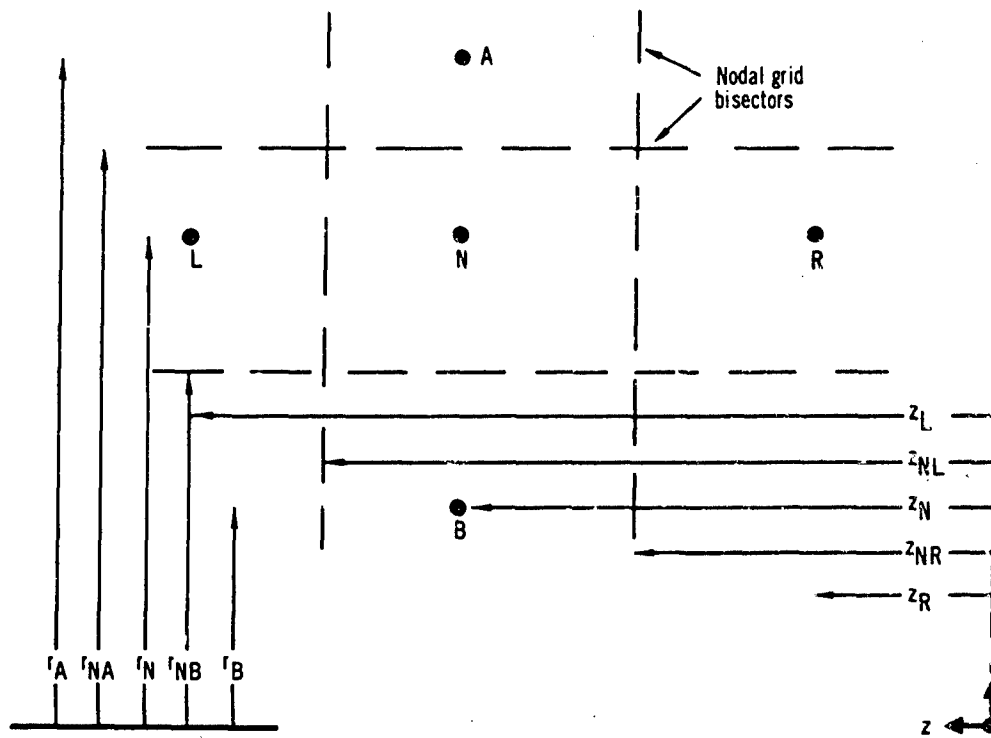


Figure 2 Geometry for B Factor Determination

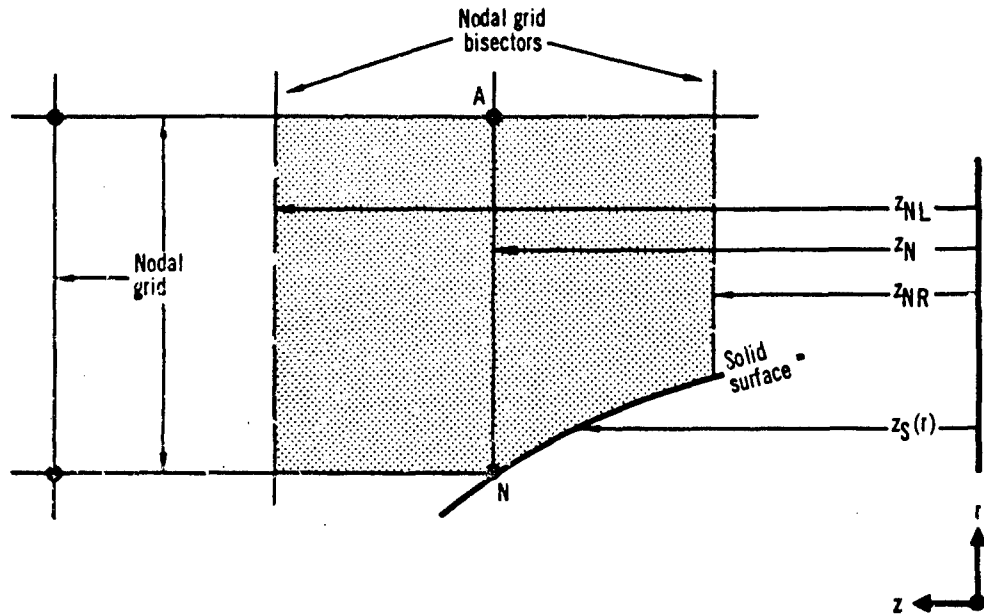


Figure 3 Schematic of Axisymmetric Nodal Network with Inlet

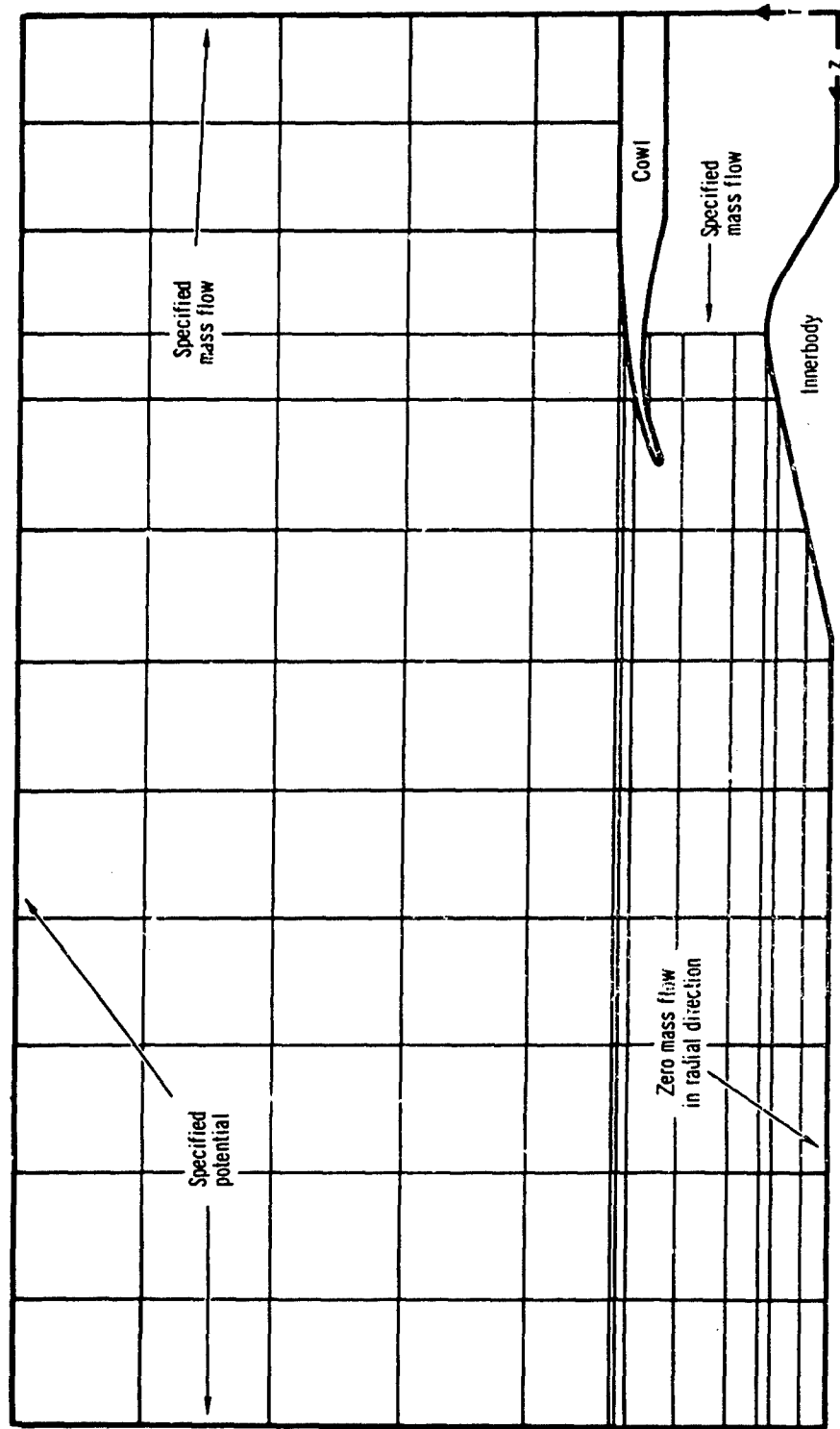


Figure 4 Central Field Point

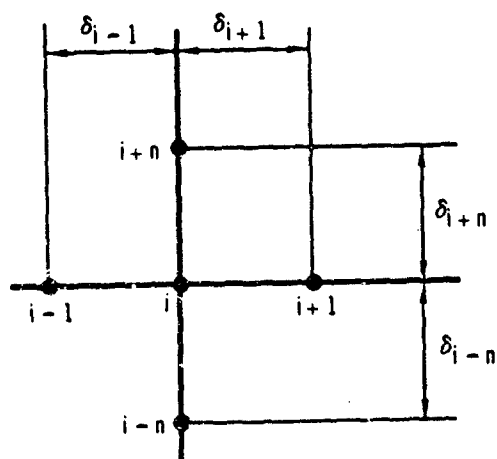


Figure 5 Body Point with Positive Slope

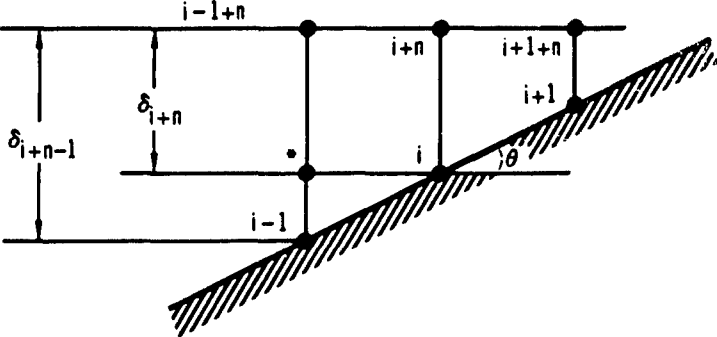


Figure 6. "Stagnation" or "Lip" Point

f is the fraction of the lower value of velocity potential in determining the value of ϕ_e i.e.
 $\phi_e = f(\phi_{e_{lower}}) + (1-f)\phi_{e_{upper}}$ where $\phi_{e_{upper}}$ and $\phi_{e_{lower}}$ represent values at e
 extrapolated from above or below e .

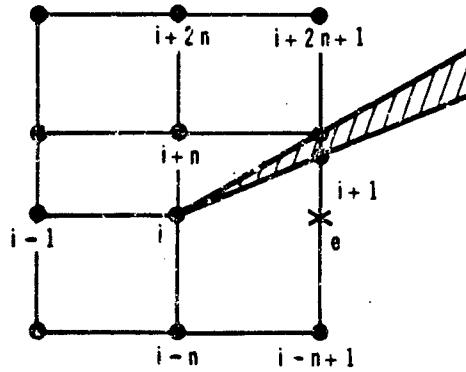


Figure 7 Field Point with Node "Line" of Positive Slope

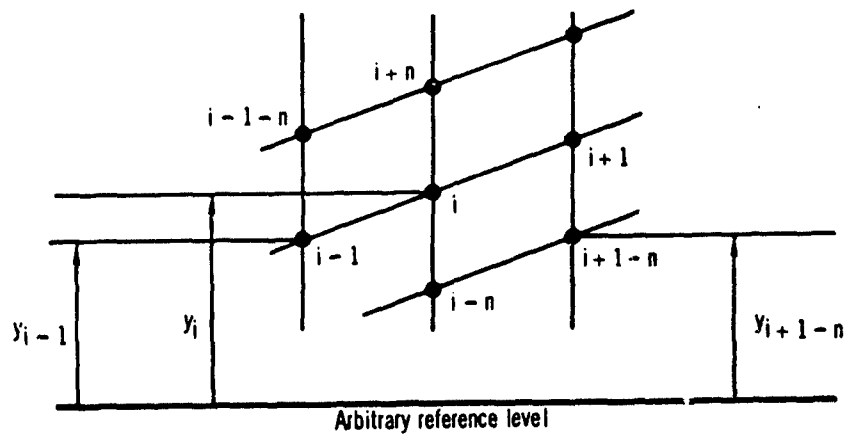


Figure 8 Calibration Nodes

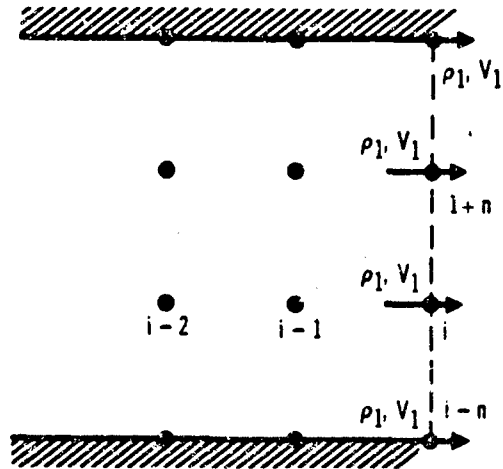


Figure 9 Constant Velocity Potential Boundary

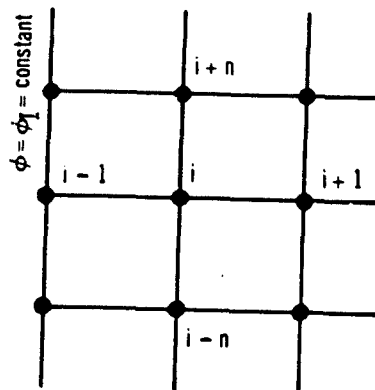


Figure 10 Constant Velocity Boundary

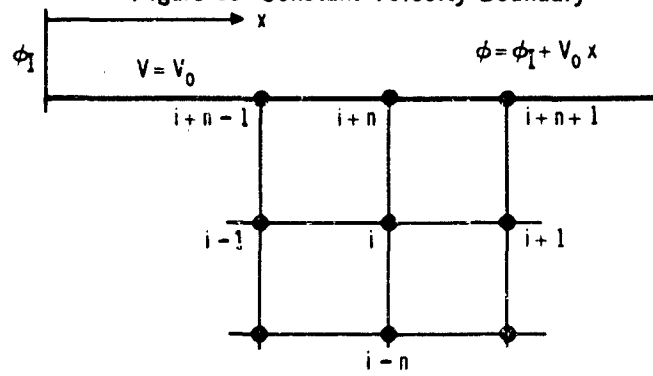


Figure 11 Control Volume Used to Determine Inlet Drag

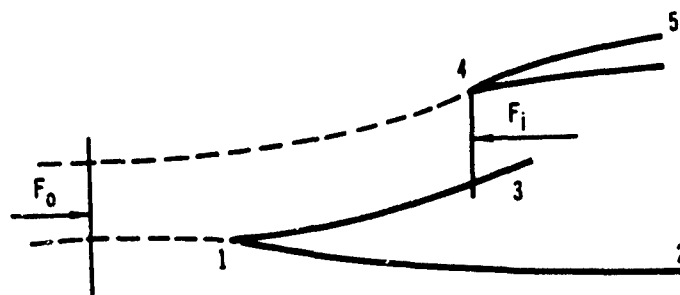


Figure 12 Example Nodal Network for Two-Dimensional Subsonic Inlet Drag Analysis

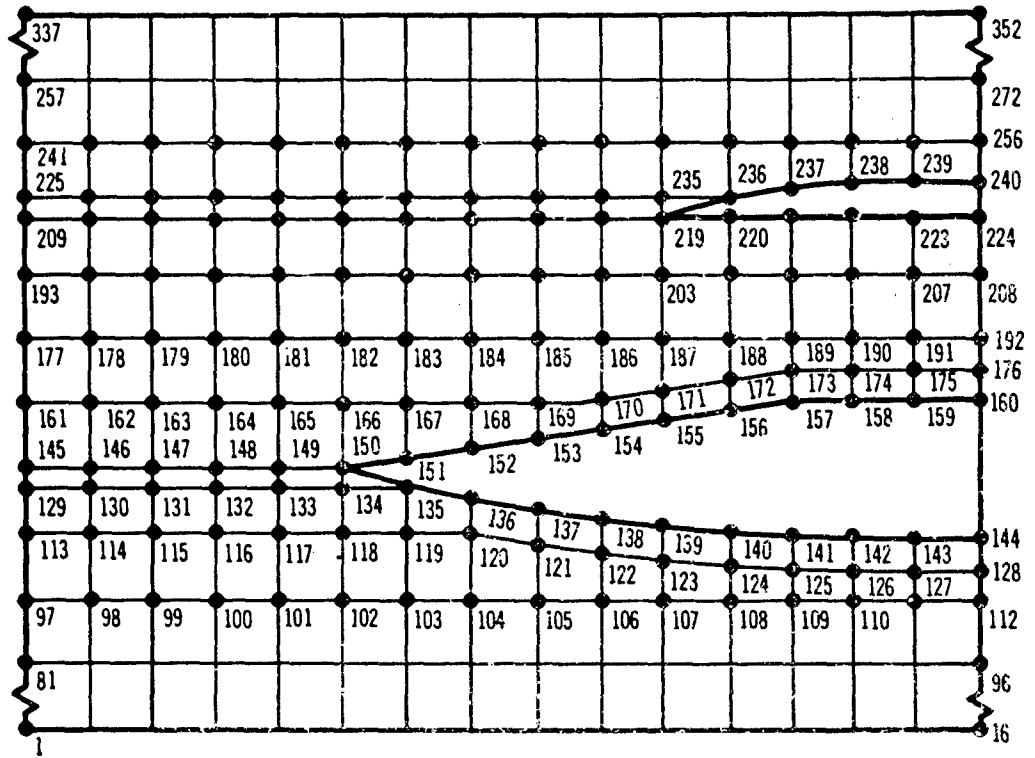


Figure 13 Comparison of Predicted and Measured Cowl Pressure Coefficient

Axisymmetric Single Cone Inlet Model

$A_0/A_c = 0.589$ $\alpha = 0^\circ$ $M_0 = 0.9$ $\theta_c = 20^\circ$

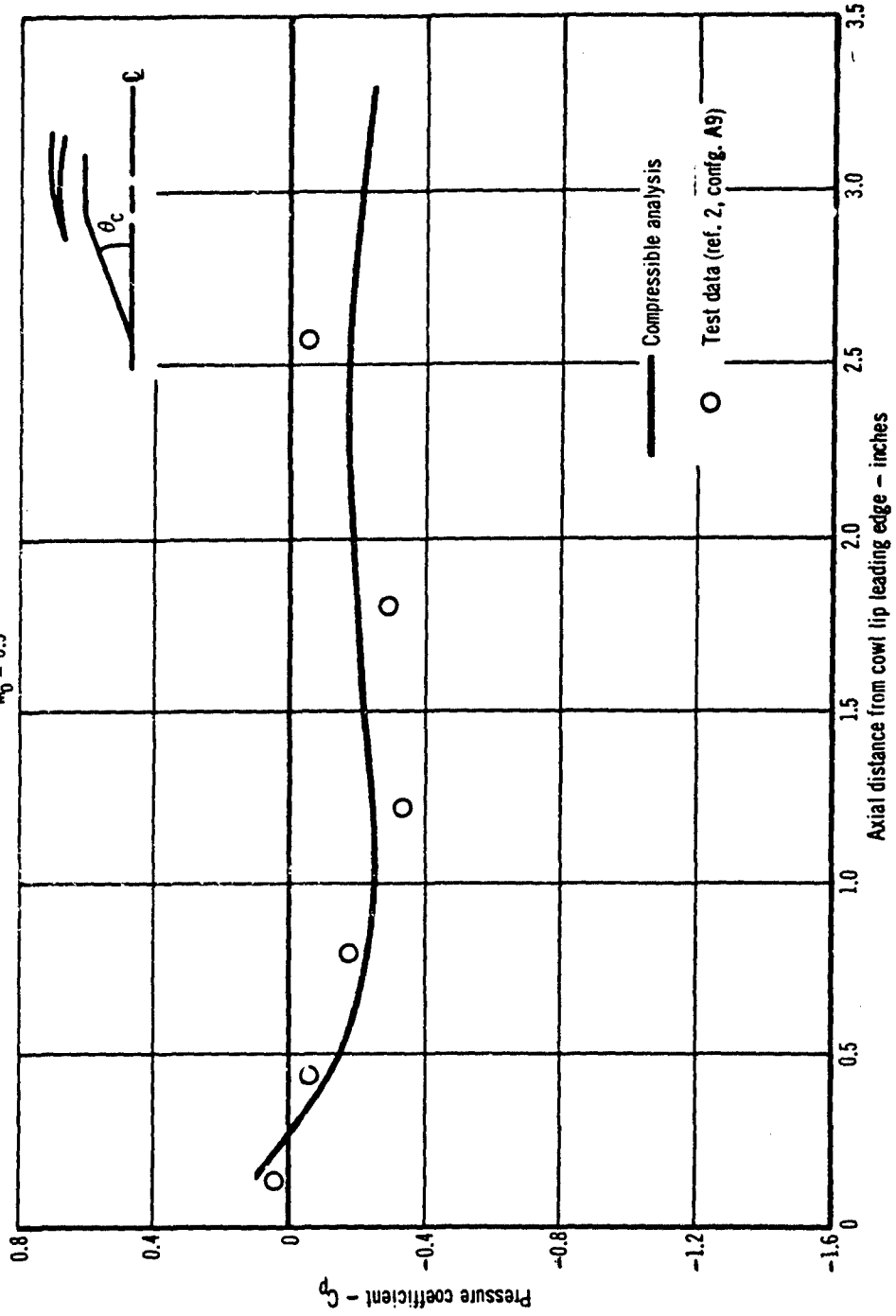


Figure 14 Comparison of Predicted and Measured Total Inlet Drag Coefficient
Axisymmetric Inlet

$M_0 = 0.7$ $\theta_c = 20^\circ$

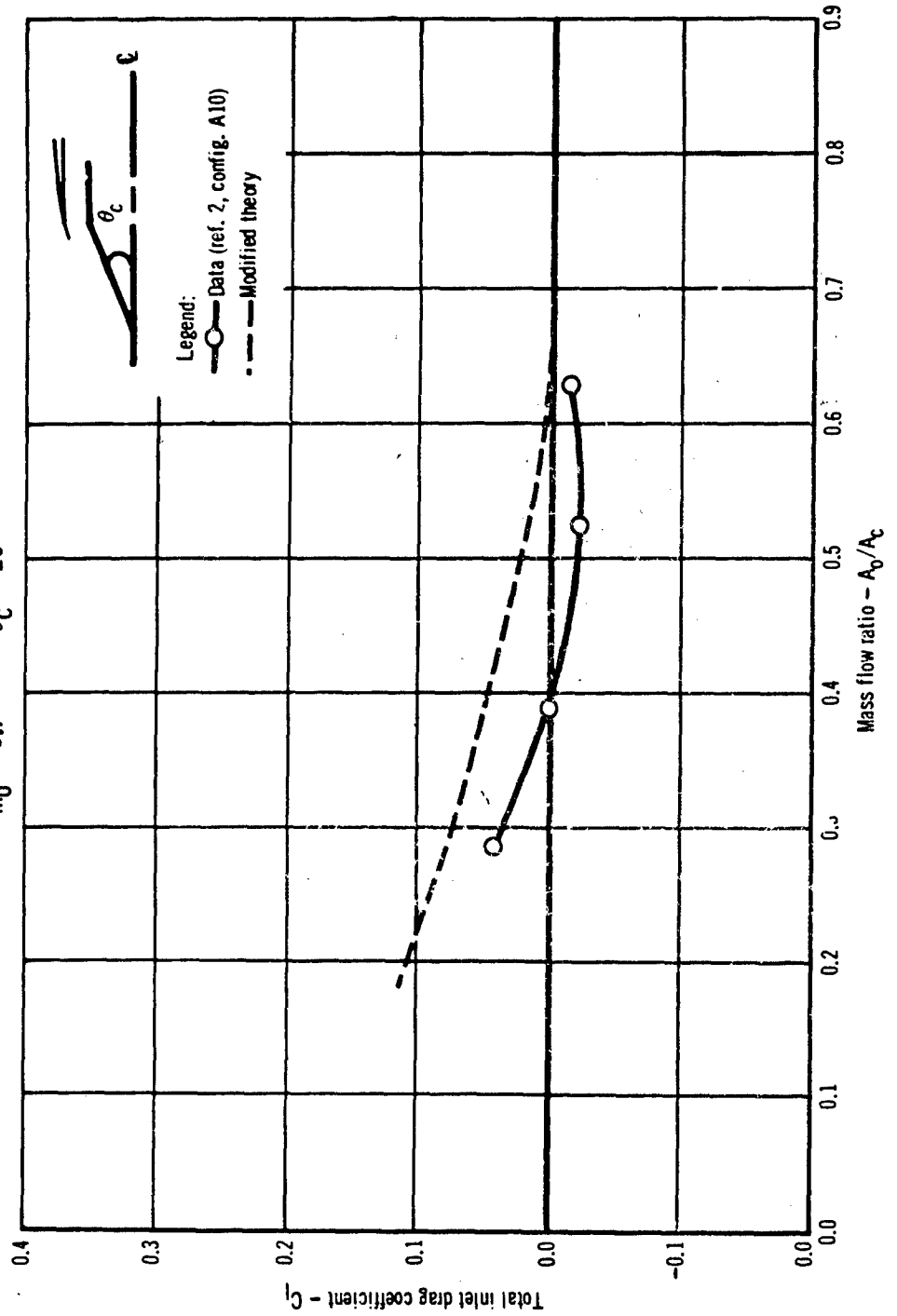


Figure 15 Comparison of Predicted and Measured Total Inlet Drag Coefficient
Axisymmetric Inlet

$M_0 = 0.9$ $\theta_c = 20^\circ$

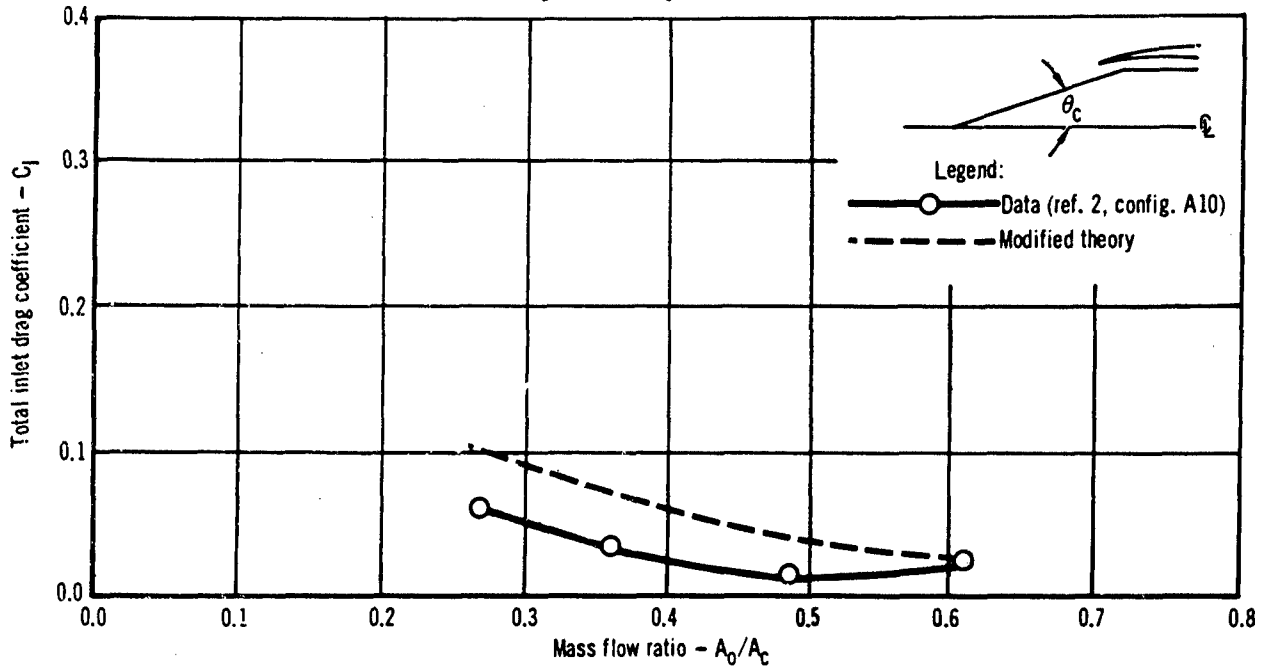


Figure 16 Comparison of Predicted and Measured Additive Drag Coefficient
Two-Dimensional Inlet $\delta = 90^\circ$

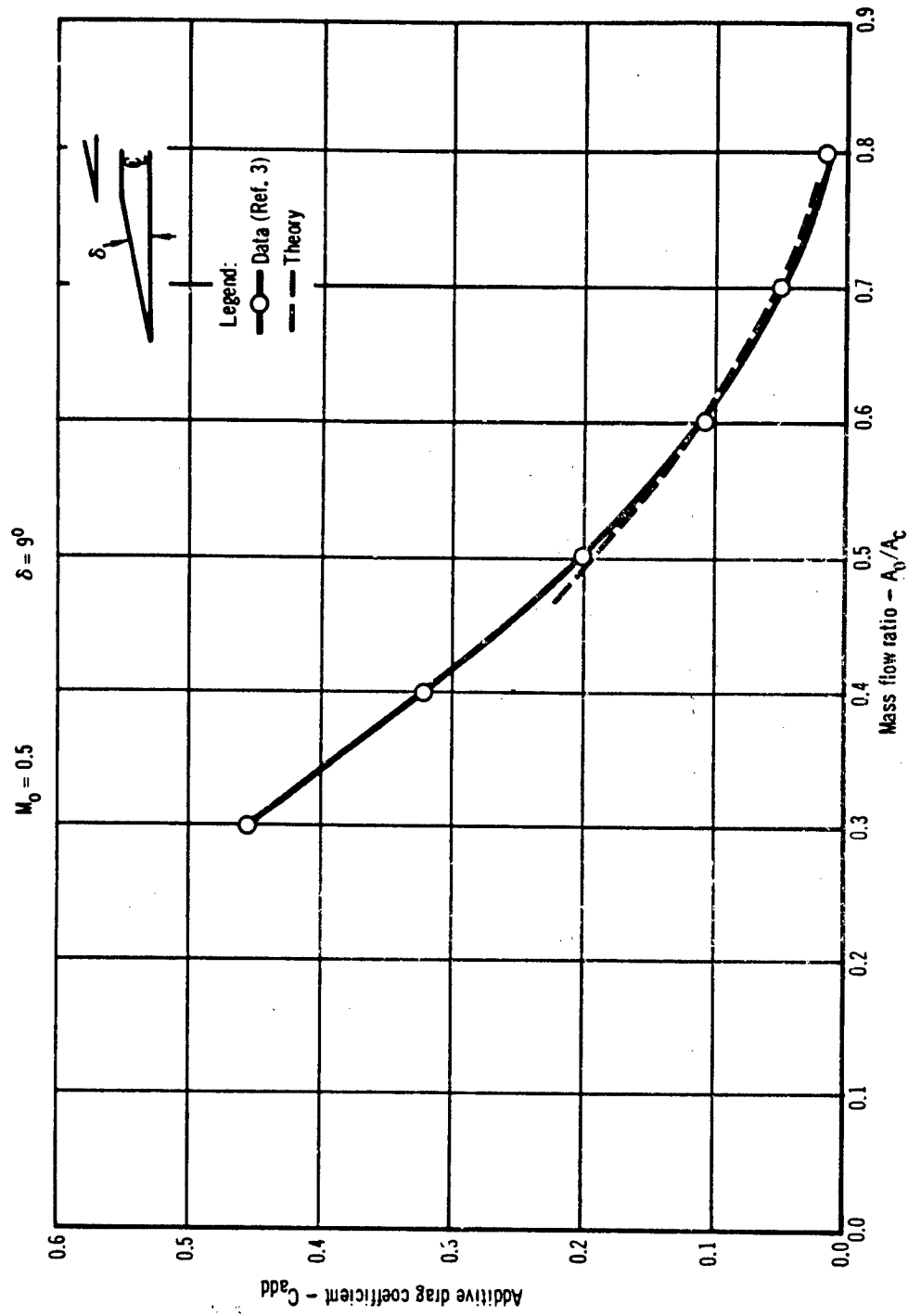
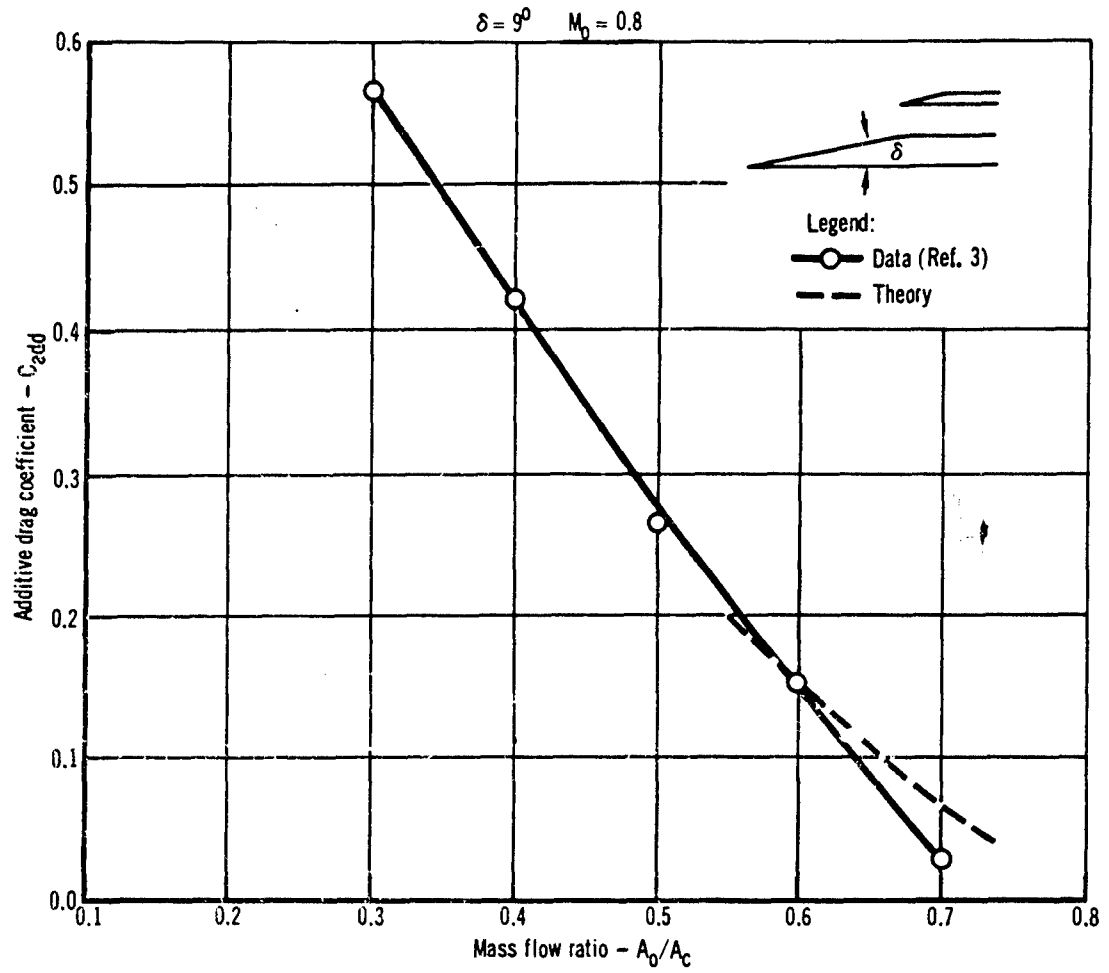


Figure 17 Comparison of Predicted and Measured Additive Drag Coefficient
Two-Dimensional Inlet



**INVESTIGATION OF INTEGRATED BOOSTER-SUSTAINER-AFTERBODY
DESIGN ON OVERALL VEHICLE PERFORMANCE**

H. H. Korst

J. S. Divita

**Rocketdyne Division
North American Rockwell Corporation**

ABSTRACT

Missile afterbody (boattail and base) drag has been investigated as related to overall missile performance. For a configuration with separate booster and sustainer rocket engines it is shown that the engine package design must be integrated with the afterbody design to achieve the minimum afterbody drag. An annular bell booster with a center mounted sustainer was found to allow the best overall integration of engine and missile for the minimum drag configuration.

SUMMARY

Missile afterbody drag has been investigated as related to installed booster-sustainer engine designs. For the particular configuration investigated (center engine sustainer engine with annular bell or bell cluster booster around the sustainer) it has been shown that engine package design must be integrated with the missile airframe (boattail) design to achieve minimum afterbody drag over the range of operating conditions for the missile. A large base diameter (needed for a cluster of booster engines) resulted in little or no boattailing and an overall high afterbody drag during sustain phase. On the other side an annular bell booster resulted in a smaller base diameter and a lower afterbody drag giving a considerably larger net thrust available for acceleration.

1. INTRODUCTION

Boost-sustain propulsion systems achieve their high performance characteristics through thrust level control to combine capabilities for a great variety of missions with favorable energy management conditions.

When the booster motor remains an integral part of the missile after termination of the boost phase, the operation of the sustainer motor in a large base area usually gives rise to high levels of jet-on base drag which can be of the order of 50% of the total missile drag. (Reference 1).

Design of a propulsive system must realistically be based on considerations which include both the propulsive forces generated by the jets and the drag experienced by the entire afterbody as a consequence of external and internal aerodynamics, as well as by jet-slipstream interference.

One expects that energy management will have to be cognizant of both the gross thrust (rocket motor and nozzle design) and the afterbody drag, combining them into the analysis of the net propulsive force of the engine(s) installed into the after-body and subjected to various internal and external operating conditions. (Reference 2).

In recognition of the need for providing design information for installed engine performance, extensive experimental programs have been carried out, (Reference 3) often as an afterthought to improve the capabilities of existing systems.

On the other side considerable progress has been made in developing comprehensive computer programs which permit a reasonably accurate evaluation of the net propulsive force of entire afterbodies under various operating conditions. (Reference 4).

2. UNIVERSITY OF ILLINOIS — AMC COMPUTER PROGRAM FOR INSTALLED PERFORMANCE OF PROPULSIVE JETS

A physically perceptive flow model, developed earlier by Korst, et al, (Reference 2) serves as the basis for the computer program. The overall flow model for the inviscid-viscid interaction of a propulsive jet and the external slipstream near the base region is delineated into its inviscid (method of characteristics, augmented by wave coalescence and shock routines) and viscous components (jet mixing). Satisfying the principles of conservation of mass and energy for the wake with special attention given to the pressure rise conditions near the end of the wake (semi-empirical modification through a "recompression coefficient") yields unique solutions for wake (base) pressure and temperature.

2.1 INVISCID SOLUTION

For any given initial condition at the exit of the nozzle, the program calculates the primary jet plume flow field for any selected (constant) jet surface pressure (wake pressure). Wave coalescence routines are included in the program. The external flow past the afterbody expands at the point of separation and forms a free jet boundary having a constant pressure (wake pressure) up to the impingement point with the jet plume. At the impingement point of the two free jet boundaries, a shock system is developed such that the flow is aligned along a slip line having continuous static pressures across it.

It shall be noted that the inviscid program does not produce the wake pressure but uses it parametrically.

2.2 VISCOUS MECHANISMS

The viscous mechanisms together with the "inviscid solution" determines the wake pressure and temperature. Of particular importance are details of the flow profiles developing in the mixing regions which extend from the points of flow separation toward the impingement point. Such information is available (Reference 5) in tabulated form, but for the sake of convenience is generated internally in the PROGRAM.

2.3 JET SLIPSTREAM INTERACTION

Conservation of mass and energy must be preserved in the wake. This is accomplished by accounting for the in-and-outflow of mass (and energy) between the respective "zero streamlines" (jet boundary streamlines) and stagnating (discriminating) streamlines of the impinging jets. The stagnation pressure for the discriminating streamlines is related to the terminal pressure rise resulting from the "inviscid solution" by a recompression coefficient. The latter, originally equated as unity, has been found to produce more accurate results when expressed as a function of the jet-to-base diameter ratio in the form:

$$\text{RECOMP} = 0.4867 + 1.1193 \frac{(Y_{2I})}{Y_{2E}} - 1.0708 \frac{(Y_{2I})^2}{Y_{2E}} + 0.4971 \frac{(Y_{2I})^3}{Y_{2E}} \quad (1)$$

In the wake, the conservation of mass can be expressed by:

$$G_B + G_I + G_E = 0 \quad (2)$$

Where G is the mass bleed into the wake and G_I , G_E are the mass rates carried within the mixing regions between the streamlines j and d , for flow I (primary jet) and E (slipstream) as the impingement point is reached.

Using the mass of the primary nozzle flow for a reference, one obtains:

$$\frac{G_B}{G_{N-I}} = - \left(\frac{1 + \cos \beta_I}{\sigma_I} \frac{Y_{imp}}{Y_{2I}} \frac{\Delta X_{mix_I}}{Y_{2I}} \frac{P_B}{P_{2I}} \sqrt{\frac{2 \gamma_I}{\gamma_I - 1}} \frac{1}{\sqrt{\frac{2 \gamma_I}{\gamma_I + 1} \left(\frac{M_{2I}^*}{1 - C_{a2I}^2} \right)}} \right)$$

$$\left[C_{a2I} \left(I_{1D_I} - I_{1J_I} \right) + \frac{\Delta X_{mix_E}}{\Delta X_{mix_I}} \frac{\sigma_I}{\sigma_E} \sqrt{\frac{T_{oI}}{T_{oE}} \frac{\gamma_E}{\gamma_I} \frac{R_I}{R_E} \left(\frac{\gamma_I - 1}{\gamma_E - 1} \right)} \right.$$

$$\left. C_{a2E} \left(I_{1D_E} - I_{1J_E} \right) \right] \quad (\text{BASED ON REFERENCE 2}) \quad (3)$$

In similar fashion, an energy balance gives

$$E_B + E_I + E_E = 0 \quad (4)$$

and again using the energy of the primary nozzle as a reference in the form

$$E_I = G_I C_{pI} T_{oI}$$

$$\frac{E_B}{E_{N-I}} = - \left(\frac{1 + \cos \beta_I}{\sigma_I} \frac{Y_{imp}}{Y_{2I}} \frac{\Delta X_{mix_I}}{Y_{2I}} \frac{P_B}{P_{2I}} \sqrt{\frac{2 \gamma_I}{\gamma_I - 1}} \frac{1}{\sqrt{\frac{2 \gamma_I}{\gamma_I + 1} \left(\frac{M_{2I}^*}{1 - C_{a2I}^2} \right)}} \right)$$

$$\left[C_{a2I} \left(I_{3D_I} - \frac{T_B}{T_{oI}} I_{1J_I} \right) + \frac{\sigma_I}{\sigma_E} \frac{\Delta X_{mix_E}}{\Delta X_{mix_I}} \sqrt{\frac{R_E}{R_I} \frac{T_{oE}}{T_{oI}}} \left(\frac{\gamma_E}{\gamma_I} \left(\frac{\gamma_I - 1}{\gamma_E - 1} \right) \right)^{1.5} \right.$$

$$\left. C_{a2E} \left(I_{3D_E} - \frac{T_B}{T_{oE}} I_{1J_E} \right) \right] \quad (\text{BASED ON REFERENCE 2}) \quad (5)$$

2.3.1 Zero Bleed Solution

In absence of mass bleed and energy addition to the wake, both

$$\frac{G_I + G_E}{G_{N-I}} \quad \text{and} \quad \frac{E_I + E_E}{E_{N-I}}$$

will be simultaneously equal to zero.

The Program finds this solution by iterative procedures, for base pressure ratio (P_B/P_{2E}) and the wake temperature ratio (T_B/T_{O_I}).

2.3.2 Mass and Energy Bleed into the Wake

Since the Program can be called on to produce the results of the iteration steps, one can evaluate the influence of mass and energy bleed on the base pressure and base temperature. Finally, the mass bleed ratio (G_B/G_{N-I}) and the energy bleed ratio (E_B/E_{N-I}) will be related to each other by

$$\frac{G_B}{G_{N-I}} = \frac{E_B}{E_{N-I}}$$

if the bleed is accomplished by a mass diversion from the primary jet combustion chamber.

2.4 BOATTAIL PROGRAM

The external flow past the afterbody is analyzed with the help of the Boattail Program. It utilizes the method of characteristics for supersonic flow (also accounting for vorticity due to viscous effects), including wave coalescence routines.

For a given initial flow condition the program calculates the entire flow field up to the end of the boattail (which it approaches accurately by an iterative process). The surface pressure distribution and the wave drag coefficient are determined together with information on the flow conditions at the end of the boattail. The latter becomes an input into the Base Pressure Program.

Presently the Boattail Program is specialized for conical, parabolic and ogive shaped boattails. It also can be utilized for corresponding flares.

2.4.1 Boattail Program Input-Output

Drag calculations on the missile boattail and base are performed with the aid of the computer programs. The first of these calculates the pressure distribution and pressure coefficients along the afterbody surface. Quantities needed as input to this program are (see Figure 1):

- 1) γ_E - ratio of specific heats for external stream
- 2) M_{1E} - approach Mach number to boattail
- 3) NSHAPE - factor which determines the boattail shape; ogive, parabolic, or conical
- 4) X_{1E} - boattail axial coordinate at station 1
- 5) Y_{1E} - boattail radial coordinate at station 1
- 6) β_E - initial boattail angle
- 7) X_{2E} - boattail axial coordinate at station 2
- 8) Y_{2E} - boattail radial coordinate at station 2 (not needed for conical case)

The program first calculates a left running characteristic line from X_{1E} , R_{1E} for uniform flow at Mach number M_{1E} and parallel to the missile axis. This flow is then expanded by a Prandtl-Meyer expansion fan through the angle β_E and a characteristic net is calculated to the boattail surface until station 2 is reached. Properties along the surface (X, Y, Mach number, P/P_{1E} and $C_{P(\text{local})}$) are determined. The surface pressure is integrated and an overall drag coefficient is calculated where:

$$C_{D_{BT}} = \frac{\text{Drag Force}}{\gamma_E P_{1E} M_{1E}^2 (Y_{1E}^2 \pi)}$$

Finally, the left running characteristic line from X_{2E} , R_{2E} is determined for use in the Two-Stream Base Pressure Program.

2.5 BASE PRESSURE PROGRAM

The Base Pressure Program takes the information generated by the Boattail Program to define the condition of the external flow as it reaches the afterbody base.

Initial conditions for the internal jet flow sustainer are chosen as either parallel outflow, or conical source flow or could be introduced from more general nozzle programs by specifying and matching flow conditions along characteristic or noncharacteristic lines at the nozzle exit.

Centered expansion fan subroutines for expansion around points 2E and 2I (see Figure 1) also capable of handling moderately strong shock compressions precede the calculation of constant pressure free jet boundaries, and the viscous mixing processes.

Location of the impingement point of the two jet boundaries is investigated from the viewpoint of geometrics and physical limitations imposed.

Recompression of the inviscid flows is presently restricted by the condition of regular shock intersection of the "weak" variety.

The use of semi-empirical recompression coefficient has been mentioned before but equation (1) has not been made part of the computer program so that the determination of RECOMP remains an input.

It is noteworthy that the iterative approach which bounds the zero bleed solution can be used to extract the influence of mass and energy addition to the wake (see also section 3.3.1).

2.5.1 Base Pressure Program Input-Output

A Two-Stream Base Pressure Program is used to calculate the pressure, P_B , at the base of the missile and, thus, the base drag. The external flow can be specified as either uniform flow parallel to the missile axis (no boattail) or as a previously calculated characteristic line.

Internal flow is specified as either uniform flow parallel to the axis or source flow at a given conic angle.* Specific inputs to the program are as follows: (see Figure 1)

- 1) X_{2I} - nozzle exit axial coordinate
- 2) R_{2I} - nozzle exit radial coordinate
- 3) β_I - nozzle conic angle (= 0 for uniform flow) in degrees

* Present program modifications will allow an arbitrary internal flow field specification.

- 4) R_I - nozzle flow gas constant, $\frac{lb_f - ft}{lb_m - ^\circ R}$
- 5) γ_I - nozzle flow ratio of specific heats
- 6) M_{2I} - nozzle flow exit Mach number
- 7) R_E - external stream gas constant, $\frac{lb_f - ft}{lb_m - ^\circ R}$
- 8) γ_E - external stream ratio of specific heats
- 9) T_{oE} / T_{oI} - ratio of external stream stagnation temperature to internal stream stagnation temperature
- 10) RECOMP - recompression factor
- 11) NSHAPE - = 0, no afterbody, program assumes uniform flow at M_{2I} parallel to axis; > 0 afterbody, program uses left running characteristic line input to program for external flow field.
- 12) NPRINT - = -1 prints out only final base pressure for 0 bleed case
- 13) X_{2E} - axial coordinate at station 2 (use only if NSHAPE = 0)
- 14) Y_{2E} - radial coordinate of external stream at station 2 (use only if NSHAPE = 0)
- 15) M_{2E} - approach Mach number to external stream (use only if NSHAPE = 0)
- 16) NPTSE - number of points along the input characteristic line (use only if NSHAPE > 0), 30 max.
- 17) X_1 - axial coordinate of first point on characteristic line
- 18) Y_1 - radial coordinate of first point on characteristic line
- 19) M_1^* - critical Mach number of first point on characteristic line
- 20) θ_1 - flow angle at first point on characteristic line - degrees

- 21) X_2
- 22) Y_2
- 23) M_2^* - second point on characteristic line
- 24) O_2

- 132) X_n
- 133) Y_n
- 134) M_n^* - last point on characteristic line
- 135) O_n

The program finds the zero mass and energy bleed (into the base region) condition by an iterative process. A value of P_B/P_{2I} is assumed and the internal and external jet boundaries are calculated. Temperature values in the base, T_B/T_{O_E} , are assumed and the base pressure calculations performed by the methods of Reference 2 until the mass bleed into the base is zero. The operation is continued judiciously choosing values of P_B/P_{2I} and T_B/T_{O_E} until both mass and energy bleed are zero. Thus, not only the zero bleed base pressure is available but also other values used in the iterations.

The output of the program consists essentially of the shape and intersection of the two jet boundaries, information concerning the shock system at the intersecting point and the current values of P_B/P_{2I} , T_B/T_{O_E} , mass bleed and energy bleed.

3. PERFORMANCE EVALUATION OF A TYPICAL NOZZLE-BOATTAIL ASSEMBLY

3.1 SUSTAINER NOZZLE FLOW

Design conditions are:

| | |
|-------------------------------------|---------------------------|
| P_{oI} | 1200 psia |
| Propellant | Compound A MHF_5 |
| Mixture Ratio | 2.6 |
| Ratio of Specific Heats, γ_I | 1.295 |
| Molecular Weight | 23.16 |
| Sea Level Thrust | 4000 lb_f |
| Area Ratio, ϵ_s | 3.5 |

3.1.1 Conical Nozzle, 15° Wall Angle

$$T_T = A_{2I\perp} P_{2I} \left[\left(1 - \frac{P_\infty}{P_{2I}} \right) + \gamma_I M_{2I}^2 \right] \quad (6)$$

and

$$\frac{T_T}{A_s^* P_{oI}} = \frac{A_{2I\perp}}{A_s^*} \frac{P_{2I}}{P_{oI}} \left[\left(1 - \frac{P_\infty / P_{oI}}{P_{2I} / P_{oI}} \right) + \gamma_I M_{2I}^2 \right] \quad (7)$$

where

$$\frac{A_{2I\perp}}{A_s^*} = \epsilon_s = 3.5 \quad (8)$$

but

$$\frac{A_{2I}}{A_s^*} \approx \epsilon_s \frac{2}{1 + \cos \beta_I} = 3.56 \quad (8)$$

so that

$$\frac{T_T}{A_s^* P_{oI}} = \frac{A_{2I}}{A_{2I}} \frac{A_{2I}}{A_s^*} \frac{P_{2I}}{P_{oI}} \left[\left(1 - \frac{P_\infty / P_{oI}}{P_{2I} / P_{oI}} \right) + \gamma_I M_{2I}^2 \right] \quad (9)$$

with

$$\frac{P_{2I}}{P_{oI}} \text{ and } M_{2I} \text{ evaluated at } \frac{A_{2I}}{A_s^*}$$

With the help of equation (8) one finds, for the present case

$$M_{2I} = 2.662$$

and, from equation (9)

$$A_s^* = 2.227 \text{ in.}^2$$

so that $A_{2I} = 7.794 \text{ in.}^2$ and the exit radius of the sustainer nozzle will be

$$r_{2I} = 1.575 \text{ inches}$$

3.1.2 Nozzle with Parallel Outflow

While principally unattractive due to length - weight consideration, the 100% bell nozzle serves as a (limiting) example for a tradeoff between optimum gross nozzle thrust and installed performance.

By letting $\cos \beta_w = 1$, one finds

$$Y_{2I} \left| \begin{array}{l} \text{parallel} \\ \text{flow} \end{array} \right. = 1.563 \text{ inches}$$

3.2 AFTERBODY CONFIGURATIONS

For a fixed position of the sustainer nozzle in the axis of the afterbody, the choice of different booster nozzle configurations will determine the base diameter of the afterbody. A given missile diameter and design features of actuating valves for the motors will give additional geometrical constraints on the afterbody configuration.

The predominance of the base drag in a sustainer-booster arrangement over other, only modifying influences, such as nozzle divergence losses and internal nozzle friction losses, makes it imperative to give prime attention to such measures as boattailing and base bleed as means to arrive at optimum design decisions. This will be clearly borne out by the following studies, utilizing the University of Illinois - AMC Programs after they have been adapted for the IEM-360 system at Rocketdyne.

For the present study, it was anticipated that a boattail length of 13 inches could be accommodated and that various design options for the booster arrangement produce base diameters of $10'' < Y_{2E} < 13''$ (the latter corresponding to

a cylindrical afterbody). It was, therefore, decided to select the following afterbody geometries.

| <u>Configurations</u> | <u>1</u> | <u>2</u> | <u>3</u> | <u>4</u> | <u>5</u> |
|-----------------------|----------|----------|----------|----------|----------|
| Y_{1E} | 6.5" | 6.5" | 6.5" | 6.5" | 6.5" |
| Y_{2E} | 6.5" | 5.75" | 5.0" | 5.0" | 5.75" |
| β_E | 0 | -3.3" | -6.58" | -8.25" | 0 |
| $\Delta X_{E_{1-2}}$ | -- | 13" | 13" | 10" | -- |
| Y_{2I} | 1.575" | 1.575" | 1.575" | 1.575" | 1.563" |
| β_I | 15° | 15° | 15° | 15° | 0 |

Configuration 4 serves as an illustration for the effects of shortening the boattail if future development of the motors should allow.

Configuration 5 was studied for the discussion of trade-off between nozzle divergence losses and installed performance gain for the 15° cone as compared to a 100% bell nozzle.

3.3 AFTERBODY DRAG CALCULATIONS

Afterbody drag will consist of two major components

- (a) the boattail drag
- (b) the base drag

The Boattail Program determines the former by calculating the boattail drag coefficient.

$$C_{D_{BT}} = \frac{\int_{Y_{2E}}^{Y_{1E}} (P_{\infty} - P) 2 Y \pi dY}{\frac{P_{\infty}}{2} V_{\infty} Y_{1E} \pi} = \frac{2 \int_{Y_{2E}/Y_{1E}}^1 (1 - P/P_{\infty}) \frac{Y}{Y_{1E}} d\left(\frac{Y}{Y_{1E}}\right)}{\frac{\gamma_E}{2} M_{\infty}^2} \quad (10)$$

so that the boattail drag can be found as

$$D_{BT} = C_{D_{BT}} Y_{1E}^2 \pi \frac{\gamma_E}{2} M_{\infty}^2 P_{\infty} \quad (11)$$

The value of P_B/P_{∞} can be found from the Base Pressure Program so that the drag force is:

$$D_B = A_B P_{\infty} \left(1 - \frac{P_B}{P_{\infty}}\right) \quad (12)$$

where

$$A_B = (Y_{2E}^2 - Y_{2I}^2) \pi$$

In case of base bleed, one also has to assess a penalty for the loss in propulsion force if the bleed mass is diverted from the combustion chamber of the sustainer nozzle.

If the mass bleed is accomplished such that no effect is felt on the afterbody drag, a net afterbody thrust gain coefficient can be defined

$$\Delta C_{T_{A_{1\infty}}} = \frac{F_{A_{BL}} - F_{A_{(BL=0)}}}{\dot{m}_{s_{total}} V_{id}} \quad (13)$$

where F_{ABL} is the jet thrust minus base drag force in the presence of bleed, while $F_{A(BL=0)}$ is the corresponding force without bleed.

F_{ABL} accounts for the loss in jet thrust as well as for the reduction in base drag, due to bleed.

\dot{m}_s is the mass rate of propellant generated in the sustainer combustion chamber

$$V_{id} \Big|_{P_\infty} = \sqrt{2g_c T_{oI} R_I \left(\frac{\gamma_I}{\gamma_I - 1} \right) \left(1 - \frac{P_\infty}{P_{oI}} \right) \left(\frac{\gamma_I - 1}{\gamma_I} \right)} \quad (14)$$

and

$$\dot{m}_{s_{total}} = A_s^* \sqrt{\frac{\gamma_I}{R_I g_c} \left(\frac{2}{\gamma_I + 1} \right) \frac{\gamma_I + 1}{\gamma_I - 1} \left(\frac{P_{oI}}{T_{oI}} \right)} \quad (15)$$

In terms of the operating parameters one arrives at

$$\Delta C_{T, A, P_\infty} = - \frac{\dot{m}_B}{\dot{m}_{s_{total}}} \left[\sqrt{1 - \left(\frac{P_{2I}}{P_{oI}} \right) \frac{\gamma_I - 1}{\gamma_I}} + \frac{A_{2I} P_{2I}}{A_s^* P_{oI}} \sqrt{\frac{\frac{\gamma_I - 1}{2 \gamma_I^2} \left(\frac{\gamma_I + 1}{2} \right) \frac{\gamma_I + 1}{\gamma_I - 1}}{\frac{\gamma_I - 1}{\gamma_I} \left(1 - \left(\frac{P_\infty}{P_{oI}} \right) \right)}} + \frac{A_B P_\infty}{A_s^* P_{oI}} \sqrt{\frac{\frac{\gamma_I - 1}{2 \gamma_I^2} \left(\frac{\gamma_I + 1}{2} \right) \frac{\gamma_I + 1}{\gamma_I - 1}}{\frac{\gamma_I - 1}{\gamma_I} \left(1 - \left(\frac{P}{P_{oI}} \right) \right)}} \right] \left(\frac{P_{B_{BL}}}{P_\infty} - \frac{P_{B(BL=0)}}{P_\infty} \right) \quad (16)$$

and by multiplication by $\dot{m}_{s_{total}} V_{id}$, one obtains the net increase (or decrease) in afterbody thrust due to primary jet chamber bleed.

The relationship between $(\dot{m}_B/\dot{m}_{s_{total}})$ (mass bleed ratio) and (P_B/P_∞) can be found from the bleed ratio - energy ratio relationship listed in the Base Pressure Program printout of the iteration process as it seeks the zero bleed solution. These values can then be plotted in a bleed-ratio vs energy-ratio diagram.

Intersection of individual $(P_B/P_\infty) = \text{constant}$ lines in this diagram with the

$$\frac{G_B}{G_{N-I}} = \frac{E_B}{E_{N-I}} \text{ line}$$

produces the derived (P_B/P_∞) vs $(G_B/G_{N-I}) = (\dot{m}_B/\dot{m}_{s_{total}})$ relation needed in Eq. 16.

It is of interest that experimental evidence is available to compare our computed results for mass bleed effects.

Shown in Fig. 2 are experimental data obtained for similar afterbody geometries Refs. 3 and 4 and the theoretical results for configuration 1 at an external Mach number of $M_\infty = 2.5$. Agreement is quite good.

We wish to stress, however, the need for viewing the net rather than the gross effect of bleed as expressed by Eq. 16, where the first term represents the decrease in available nozzle thrust while the second term shows the gain in installed thrust force due to base drag reduction.

3.3.1 The Cylindrical Afterbody - With and Without Base Bleed (Booster-Off)

Base drag calculations have been carried out for the following cases (all for sea level).

| Configuration (see 3.2) | M_∞ | | |
|-------------------------|------------|-----|-----|
| | 1* | 1.5 | 2.0 |
| 2 | 1.5 | 2.0 | 2.5 |

* including the effects of mass bleed into the base region.

The results of these calculations for configuration 1 are shown in Fig. 3 and clearly demonstrate the severity of the base drag.

It is also seen that the net effect of base bleed is rather small. As one converts the change in $C_{T_{A,\infty}}$ into drag force changes by multiplying it by $\dot{m}_{s_{total}} V_{id,\infty}$ (~ 4190 lbf) so that

$$- D_{A_{bleed}} = \Delta C_{T_{A,\infty}} \dot{m}_{s_{total}} V_{id,\infty} \quad (17)$$

one finds an optimum bleed ratio of $\sim 3\%$ corresponding to not more than 120 lbf gain. As shall be shown later, the base drag is indeed a major portion of the overall missile drag and its possible reduction by boattailing deserves prime attention while nozzle divergence and mass bleed remain rather secondary considerations.

Improvement in nozzle performance (100% bell, configuration 5) is offset by a slight increase of base drag as the beneficial influence of jet divergence on the jet-slipstream interaction is reduced.

It can be suggested that the choice of a nozzle contour which influences optimization of gross thrust may become a rather involved exercise of limited practical importance. Boattailing, on the other side, holds more promise.

3.3.2 Boattailing

Base drag and boattail drag calculation have been carried out for the following cases (all for sea level).

| Configuration (see 3.2) | 2 | 3 | 4 |
|-------------------------|-----|-----|-----|
| M_{∞} | 2.5 | 2.5 | 2.5 |

Results are shown in Fig. 4 where total afterbody drag, composed of boattail drag and base drag, is plotted against the boattail angle β (comparing configurations 1, 2 and 3). In addition, the shortened boattail of configuration 4 illustrates the effort of staying within the limit of design constraints while attempting to increase the boattail angle. There was, however, no improvement over the results of configuration 3.

Bleed effects were found to be of almost the same order as for cylindrical boattails (~ 40 lbf per 1%) although the optimum bleed rate was found to be less (1-2%).

Bleed, therefore, is only capable of improving the installed thrust performance in a rather limited way. Boattailing is a much more effective way of reducing afterbody drag and should be realized to the largest possible extent.

3.3.3 Sustainer Thrust and Missile Drag

A cursory appraisal of the overall missile drag will illustrate the importance of controlling the base drag contribution.

For the sake of simplicity the missile drag is here considered in 2 parts

- a) forebody drag (nose and friction drag)
- b) afterbody drag,

each of these contributions is evaluated for the zero angle of attack flight attitude, and for sea level flight.

3.3.3.1 Forebody Drag

For arriving at a rough estimate, we consider a cone-cylinder configuration

- a) nose cone drag, cone half angle

$$D_{FNose} = C_{DFNose}(M_\infty, \beta_w) M_\infty^2 \frac{Y_E}{2} Y_{1E}^2 \pi \quad (18)$$

where $C_{DFNose}(M_\infty, \beta_w)$ is readily available (e.g. Ref. 6).

The following drag situation is obtained.

| | | | |
|--------------|------|------|------|
| M_∞ | 1.5 | 2.0 | 2.5 |
| β_w | 15° | 15° | 15° |
| C_{DFNose} | 0.24 | 0.21 | 0.19 |
| D - lbf | 738 | 1147 | 1622 |

b) skin friction drag

One may estimate the skin friction drag by using boundary layer analysis for a smooth flat plate in compressible flow and assigning representative equivalent fineness ratios to the entire missile.

For sea level operation, one determines the Reynolds Number per foot as

$$\text{Re} \Big|_{\text{ft}} = 7.0609 \times 10^6 \cdot M_\infty$$

and computes the momentum thickness at the end of the missile approximately as (Ref. 7)

$$\frac{\theta}{2 d_0} = \left[\frac{N+1}{N} \alpha(N) \right]^{\frac{N}{N+1}} (Re_\infty, Y_{1E})^{-\frac{1}{N+1}} \quad (19)$$

$$\left(\frac{L}{2d} \right) \left(\frac{T}{T_0} \Big|_{M_\infty} \right)^{\frac{N-2}{N+2}}$$

selecting $N = 5$

$$\alpha(N) = .0085$$

as representative for the given Reynolds Number range one finds for $(L/D) = 10$ and since

$$D_{P_{\text{frict}}} = \gamma_E P_\infty M_\infty^2 \pi d_0 \theta \quad (20)$$

| | | | |
|---------------------|------|-------|-------|
| M_∞ | 1.5 | 2.0 | 2.5 |
| $\Theta'' \approx$ | .107 | .0919 | .0608 |
| $D_{F_{frict}}$ lbs | 200 | 308 | 416 |

3.3.3.2 Afterbody Drag has been evaluated in section 3.3.2 and

$$D_A = D_{A_{BT}} + D_{A_B} (+ D_{A_{bleed}})$$

3.3.3.3 The total missile drag, as exemplified for L representative (L/d) ratio of 10 and a nose cone of 15° half angle emerges as follows (sea level)

$$D_M = D_F + D_A = D_{F_{Nose}} + D_{F_{frict}} + D_{A_{BT}} + D_{A_B} (+ D_{A_{bleed}}) \quad (21)$$

and the missile drag summary (estimated) for configuration 1 at various Mach numbers is listed below.

| | | |
|-------------------------------|------|------|
| M_∞ | 1.5 | 2.5 |
| D_F | 937 | 2038 |
| D_A | 1065 | 1390 |
| $\Delta D_{A_{bleed}}$ (opt.) | -120 | -148 |

The drag situation for the zero boattail angle afterbody is critical as it reduces the available sustainer thrust margin for acceleration and every attempt has to be made to improve it, as suggested in the section on boat-tailing.

For comparison, the overall drag has been calculated for configuration 4. A comparison is made at Mach numbers 1.5 and 2.5 between configuration 1 ($\beta = 0$) and configuration 4 ($\beta = -8.25$). In each case the overall drag has been reduced on the order of 10 percent of the total sustainer thrust. This is even more startling when one evaluates the boattailing effect at $M_{1E} = 2.5$ on the thrust available for acceleration and maneuvering. Boattailing almost doubles the net thrust available. These conclusions are demonstrated graphically in Figs. 5 and 6.

for R. E. Schmitt
H. H. Korst
Basic Studies Unit
Advanced Systems

Jack S. Divita
J. S. Divita
Basic Studies Unit
Advanced Systems

HHK:JSD:nw

NOMENCLATURE

UPPER CASE

| | | |
|-----------|--|---|
| A | area | |
| A* | critical nozzle area | |
| C_{a_2} | Crocco number, V/V_{a_2} , at inviscid jet boundary Mach number | |
| C_D | drag coefficient, (see equation 10) | |
| C_P | constant pressure specific heat | |
| C_T | thrust coefficient (see equation 13) | |
| D | drag | |
| D_M | missile drag | |
| E | energy | |
| G | mass | |
| I_1 | auxiliary integral (Reference 2) | $= \int_{-\infty}^{\infty} \frac{\varphi^{(n)} \varphi}{1 - C_{a_2}^2 \varphi^2} d\eta$ |
| L | length | |
| M^* | critical Mach number | |
| N | exponent in equation (19) based on Reynolds number and data from Reference 7 | |
| P | static pressure | |
| R | gas constant | |
| R_e | Reynolds number | |
| T | static temperature | |
| T_0 | stagnation temperature | |
| T_T | theoretical thrust | |
| V | velocity | |

| | |
|----------|-------------------|
| V_{id} | ideal velocity |
| X | axial coordinate |
| Y | radial coordinate |

LOWER CASE

| | |
|--------------|----------------------|
| ϵ_c | dimensional constant |
| \dot{m} | mass flow rate |

GREEK

- α empirical factor in equation (19) based on Reynolds number and data from Reference 7.
- β boattail or nozzle wall angle
- γ ratio of specific heats
- ϵ_s sustainer nozzle area ratio
- θ momentum thickness
- σ similarity parameter for homogeneous coordinate (Reference 2)

SUBSCRIPTS

| | |
|----------|--|
| A | afterbody (includes boattail and base) |
| B | base |
| BL | base bleed |
| BT | boattail |
| D | discriminating streamline in mixing region (Reference 2) |
| E | external flow |
| F | friction |
| I | internal flow |
| J | jet boundary streamline (Reference 2) |
| N-I | nozzle-internal stream |
| w | nozzle wall |
| s | secondary flow |
| ∞ | free stream conditions |
| \perp | perpendicular to nozzle axis |
| 1 | start of boattail |
| 2 | end of boattail or base plane |

REFERENCES

1. Brazzel, Charles E., The Effects of Base Bleed and Sustainer Rocket Nozzle Diameter and Location on the Base Drag of a Body of Revolution with Concentric Boost and Sustainer Rocket Nozzles, U. S. Army Missile Command, Redstone Arsenal, Alabama, Report No. RF-TR-63, 23, July 1963.
2. Korst, H. H., W. L. Chow and G. W. Zumwalt, Research on Transonic and Supersonic Flow of a Real Fluid at Abrupt Increases in Cross Section, Final Report, University of Illinois, M.E. Tech. Report 392-5, December 1959.
3. White, Warren E., Effect of Base Bleed Exit Area on Base Drag with Simulated Rocket Exhaust at Mach Numbers 2.5, 3.0 and 3.5, Arnold Air Force Station, Tennessee, AFDC-TR-66-246, December 1966.
4. Computer Program Developed at the University of Illinois, Dept. of M.E. CIE in Cooperation with the U. S. Army Missile Command, Huntsville, Alabama, February 1968.
5. Korst, H. H. and W. L. Chow, Non-Isoenergetic Turbulent ($P_{rt} = 1$) Jet Mixing Between Two Compressible Streams at Constant Pressure, University of Illinois, M.E. Tech. Report 393-2, April 1965.
6. Shapiro, Oscher H., The Dynamics and Thermodynamics of Compressible Fluid Flow, Vol. II, Ronald Press Company, New York.
7. Culick, Fred E. C. and Jacques A. F. Hill, Journal of Aerospace Sciences, Vol. 25, 1958, pp. 259-262.

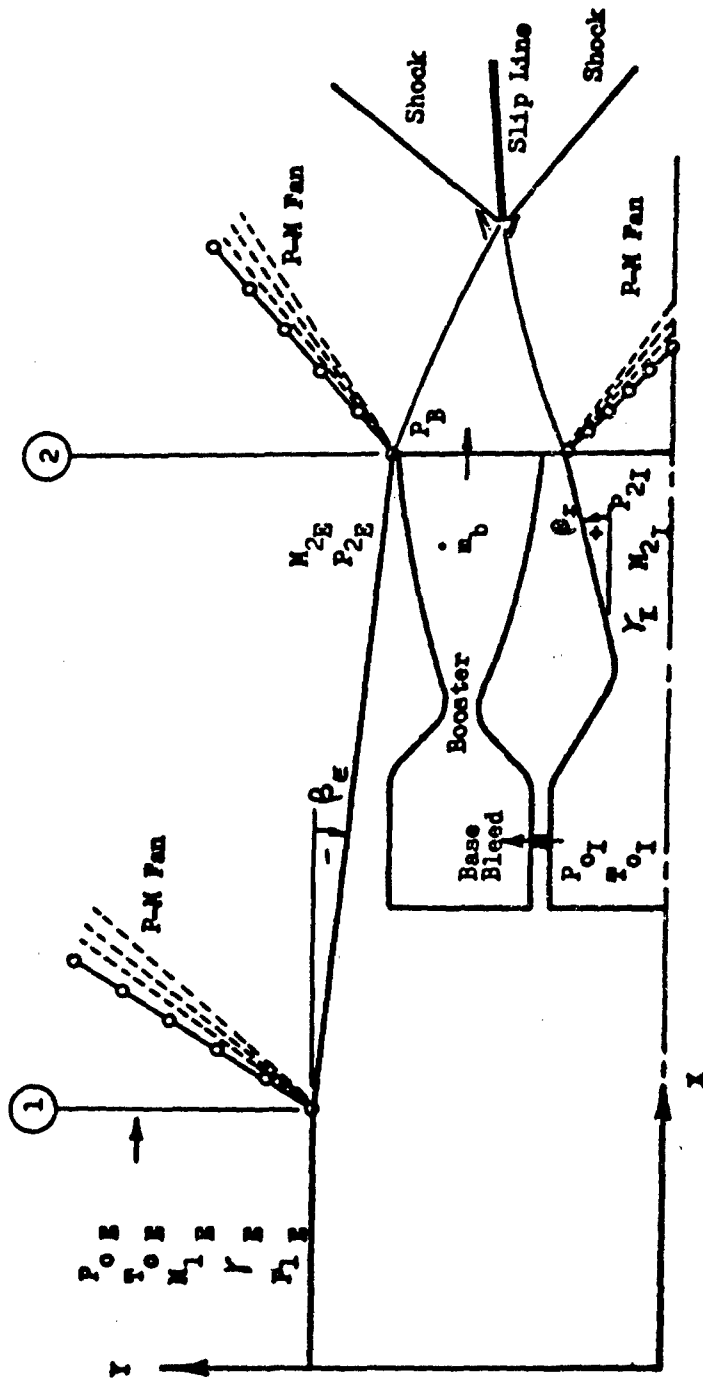


Figure 1. Missile Foattail and Base Nomenclature

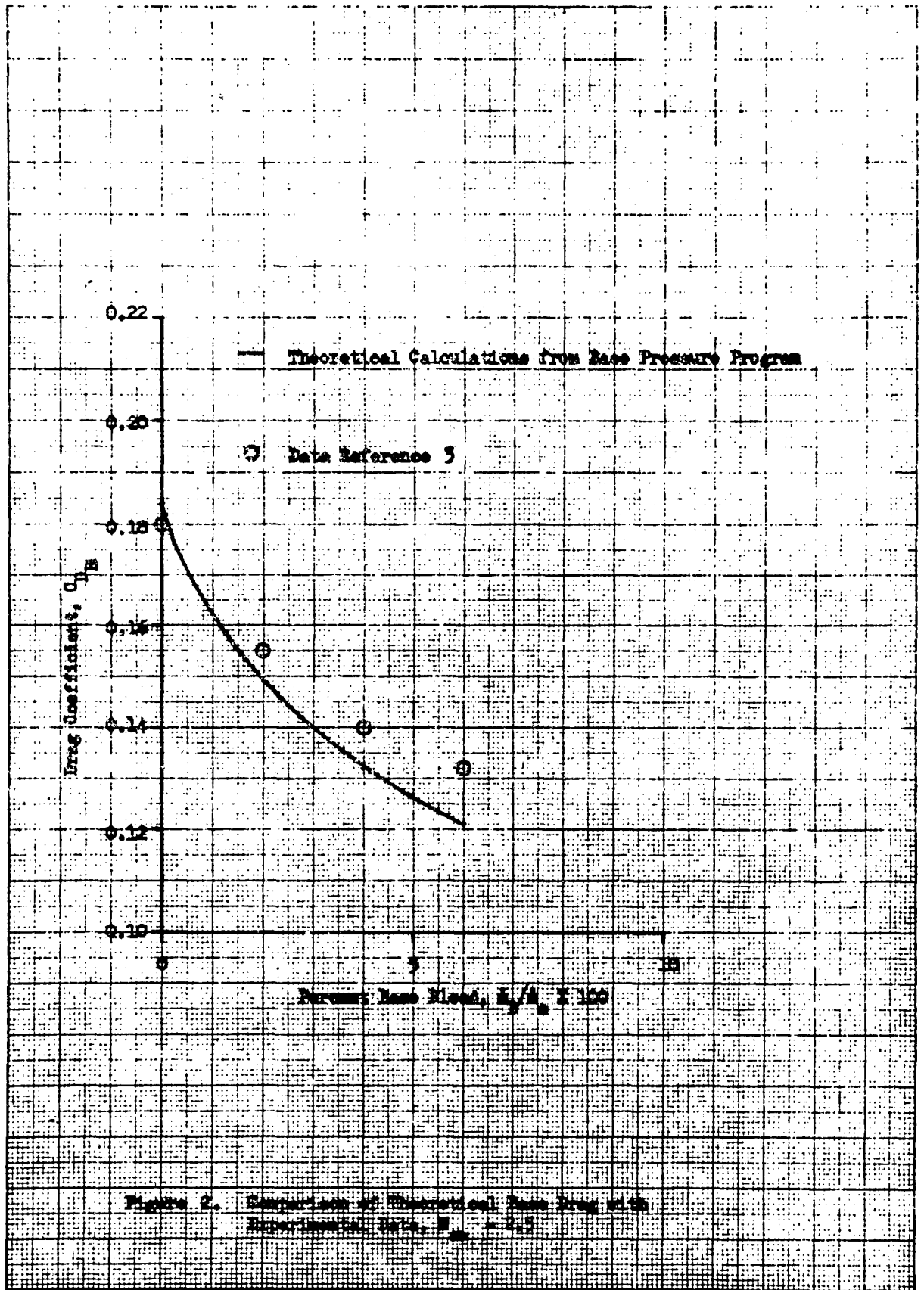


Figure 2. Comparison of Theoretical Drag Program with Experimental Data, $Re = 100$

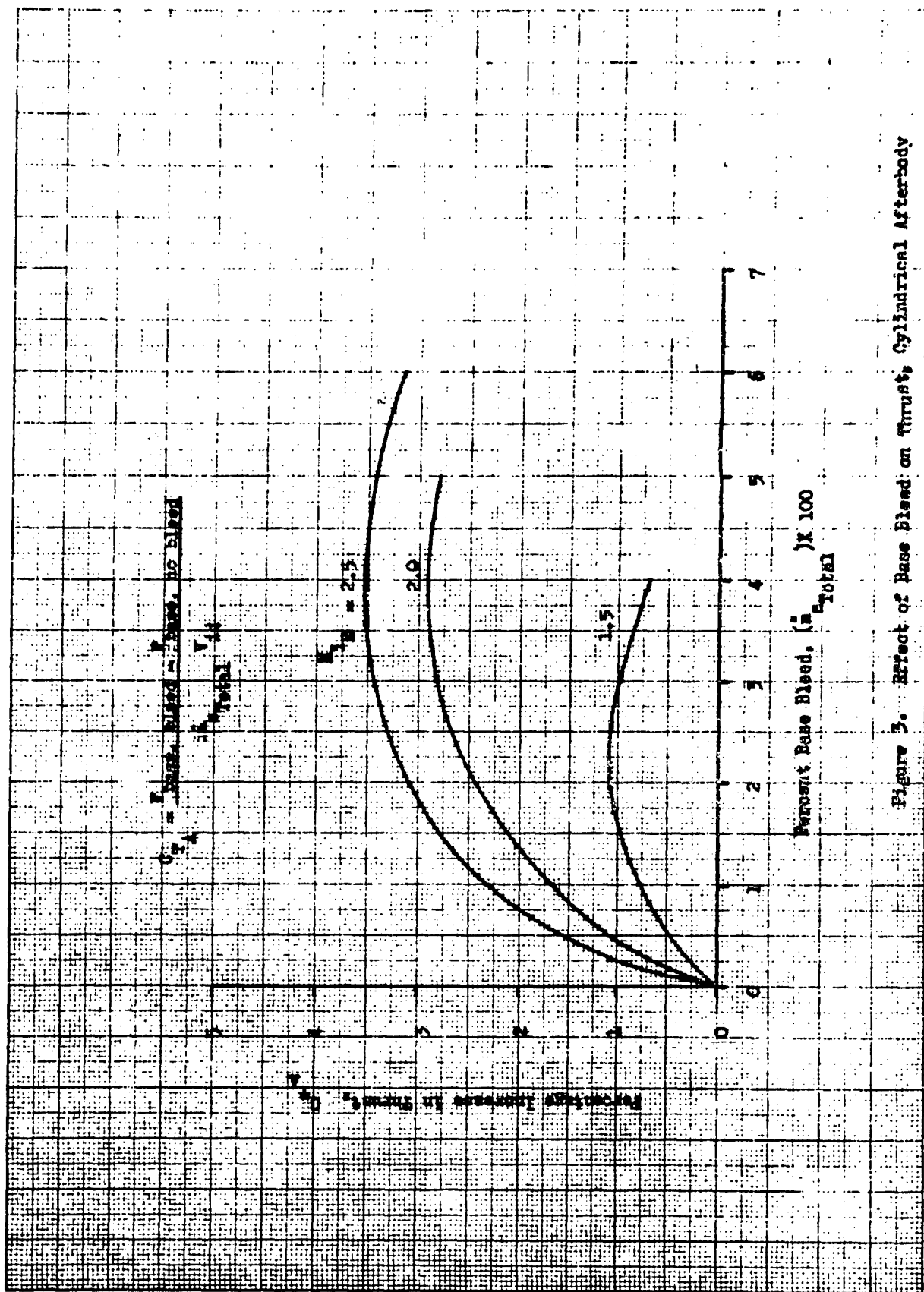


Figure 3. Effect of Base Bleed on Thrust, Cylindrical Afterbody

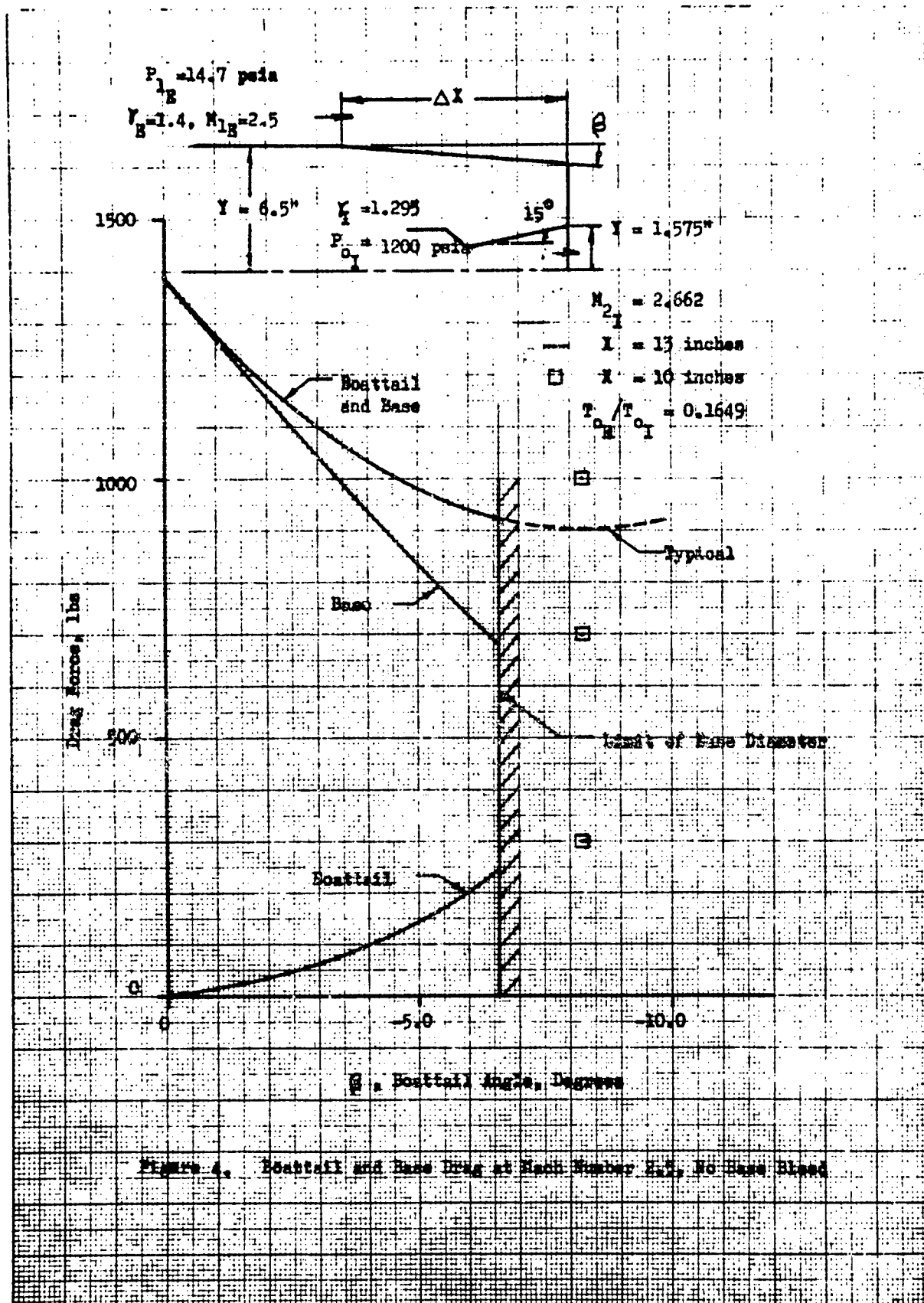


Figure 4. Boat Tail and Base Drag at Mach Number 2.5, No Base Bleed

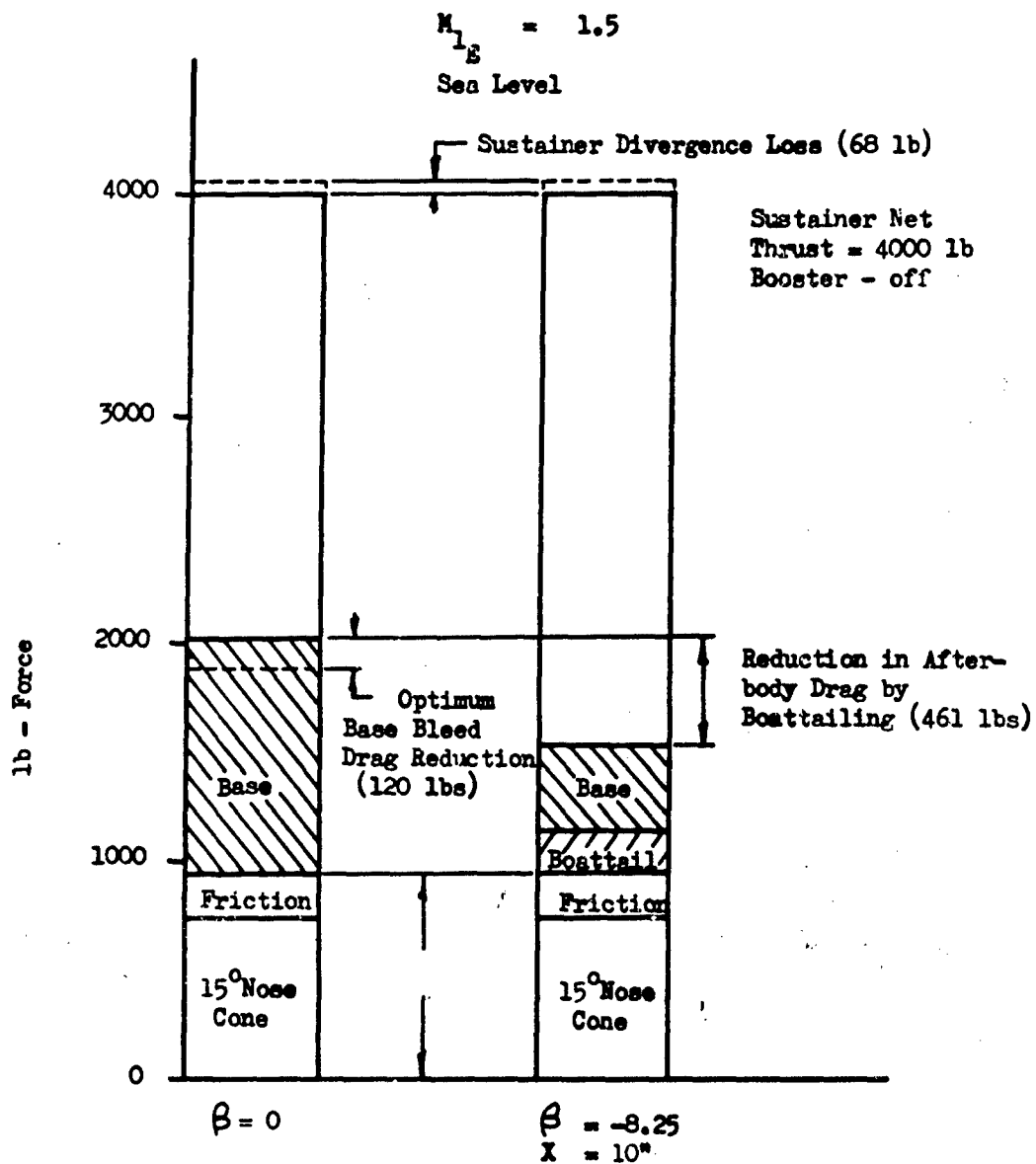


Figure 5. Influence of Boattailing on Overall Missile Drag, $M_{1E} = 1.5$

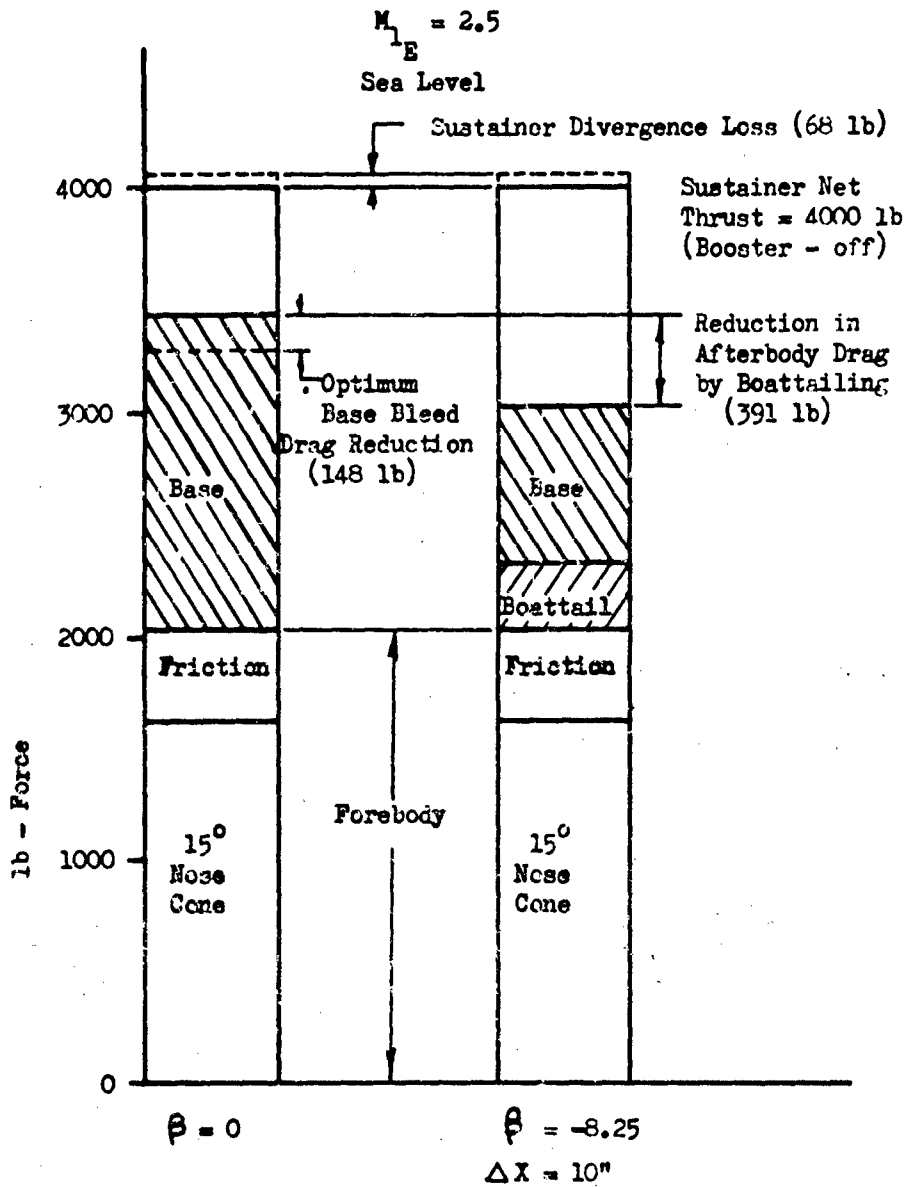


Figure 6. Influence of Boattailing on Overall Missile Drag, $M_{1E} = 2.5$

PROPULSION SYSTEM STABILITY
(25 June 1969)

Major G. E. Strand, USAF, Chairman
Air Force Aero Propulsion Laboratory

SESSION III
INLET DISTORTION INVESTIGATIONS

L. E. Surber, Cochairman
Air Force Flight Dynamics Laboratory

Paper 13 is classified. It is published as Supplement 1 to
AFAPL-TR-69-103.

PARADOX IN INTERPRETING INLET-ENGINE COMPATIBILITY
WITH HIGH RESPONSE INLET INSTRUMENTATION

C. E. Porcher

Propulsion Group Engineer
The Fort Worth Division of General Dynamics

ABSTRACT

High-response inlet pressure recovery and distortion data have been obtained at the Fort Worth Division of General Dynamics for an afterburning turbo-fan engine installation on a high-performance aircraft, the USAF strategic bomber FB-111A with the P&WA TF30-P-12 engine. The in-flight instrumentation and data recording system, designed at the Fort Worth Division, is a 60-channel, constant-bandwidth, multiplex airborne system that is capable of an 800-Hz frequency response and uses an IRIG B timing channel. Forty high-response pressure measurements are made at the compressor face, and the data reduction permits instantaneous time slices of pressure patterns to be observed over time intervals as small as 0.001 second. Thus a distortion pattern can be defined for a time interval during which the compressor blades rotate through a 60° arc. Compressor-face distortion values have been calculated as instantaneous values as well as averaged values. Unfortunately, the engine is a production-line model and as such is not equipped with instrumentation with response characteristics comparable to the inlet. Consequently, compressor discharge and turbine discharge pressures are recorded but cannot be correlated with the engine-face pressure changes to permit complete analysis of the total inlet/engine system.

The most interesting data at the compressor face show unusual pictures of large pressure dynamics in response to engine power changes for both cruise and maneuver conditions and for conditions of what may be clear-air turbulence at high supersonic Mach numbers. It is surprising that the engine can induce transients, through the inlet/engine

combination, which result in extremely high compressor-face distortions - some exceeding the estimated stall tolerance of the engine. The high distortion appears to precede the engine stall by a time increment equal to the estimated transport and dwell time required to carry the distortion pattern to the critical compressor stage (7th). However, the transient engine condition which produces the high inlet distortion must occur earlier, at a time when inlet distortions may be below surge limits. The inlet instrumentation is thus inadequate to positively tie down the "chicken-or-egg" question; hence, the paradox. Our thesis is that, after much analysis of the data, advanced propulsion systems requiring inlet/engine compatibility assurance must include appropriate high-response engine as well as inlet instrumentation to separate the inlet-vs.-engine-induced effects. Use of the afterburning turbo-fan engine makes this point critically important.

In this paper, we present typical flight test conditions for (1) power lever chops from maximum afterburning at Mach 2.0 and 2.2, (2) an engine downtrim condition at fixed power lever at Mach 2.2, (3) effects of weapons bay door operation at Mach 2.0, and (4) a high-g maneuver from 0° to 18° angle of attack at Mach 2.3. Dramatic patterns encountered at Mach 2.0 are attributed to clear-air turbulence which occurs at fixed power lever conditions. Such data as these clearly show through instantaneous pressure patterns, average and individual probe PRMS, power spectral densities, and cross correlation of compressor-face probes that both the inlet and the engine may induce stall-producing patterns. Differentiation of these events appears impossible in an effort to ascertain whether the engine or inlet is the primary cause.

Dynamic simulation of inlet/engine interactions is classically a powerful tool for analyzing the potential effects of transient conditions occurring with a coupled inlet, inlet control, engine, and engine control propulsion systems. However, unless adequate instrumentation is used to define the necessary input data early, such programs lose much of their value for potential problem solving.

NOMENCLATURE

| | |
|-------------|---|
| A/B | Afterburner |
| A_j | Jet Nozzle Area |
| $C_{xy}(t)$ | Cross-Covariance Factor |
| EPR | Engine Pressure Ratio - P_{T7}/H_2 |
| H_0 | Freestream Total Pressure |
| H_2 | Average Compressor Face Total Pressure |
| Hz | Hertz - cycles per second |
| K_D | Compressor Face Total Pressure Distortion Index defined by Pratt and Whitney Aircraft |
| K_{D1} | Compressor Face Distortion Index for 1/1000 Sec |
| K_{DAVG} | Compressor Face Distortion Index Calculated from Three Successive 1/1000 Sec Cuts |
| M_0 | Flight Mach Number |
| N_1 | Engine Low Speed Rotor Speed |
| N_2 | Engine High Speed Rate |
| P_{T2} | Compressor Face Total Pressure |
| $P_{s2.5}$ | Fan Discharge Static Pressure |
| P_{s3} | Low Compressor Static Pressure |
| P_{s4} | High Compressor Static Pressure |
| P_{T7} | Engine Tailpipe Total Pressure |
| P_{RMS} | Root-Mean-Square of Pressure Fluctuations |
| PSD | Power Spectral Density |
| R | Inlet Cowl Radius Reference |

NOMENCLATURE (CONCLUDED)

| | |
|-------|--|
| W_c | $W_{TV} \sqrt{\theta_{t_2}} / \delta_{t_2}$ Engine Corrected Airflow |
| WBD | Weapon Bay Doors |
| X | Spike Tip-to-Lip Dimension Along Spike Axis |
| X/R | Inlet Spike Translation Ratio Variable = 1.80 to 2.60 |

Subscripts

| | |
|----------------|---|
| α | Angle of Attack Degrees |
| θ_1 | Spike First Cone Angle |
| θ_2 | Spike Second Cone Angle, $8\frac{1}{2}^\circ$ to 26° |
| θ_{t_2} | Corrected Total Ram Air Temperature |
| δ_{t_2} | Corrected Total Pressure |

PURPOSE

During propulsion system development testing on the FB-111A, a USAF strategic bomber prototype airplane, high-response inlet data were obtained at subsonic and supersonic conditions for both transient and steady-state engine power settings and for both level and maneuvering flight attitudes. The purpose of this paper is to review some supersonic inlet/engine interactions that occurred during propulsion flight testing. These interactions of a sophisticated, external-compression, variable-geometry inlet and an afterburning turbo-fan engine provide interesting compressor-face data that show unusually large pressure dynamics in response to engine power changes and maneuvering flight.

Through the review of these data some lessons can be drawn relative to instrumentation, data recording, and data analysis in defining the stall-inducing event and identifying the engine or the inlet as the triggering mechanism. How and why these events occur and how to predict them have important implications on the inlet and engine development of future systems for both airframe and engine company engineers.

DISCUSSION ITEMS

The discussion items will cover a number of selected flight test events - some obtained by chance - which will clearly delineate several aspects of interpreting inlet-engine compatibility. The items to be discussed are:

1. Description of the FB-111A airplane inlet system and instrumentation system.
2. Selected flight condition for inlet/engine compatibility study:
 - o Interactions at supersonic speed.
 - o Effect of engine afterburner lights.
 - o Inlet stability.
 - o External inlet effects.

3. Implications for dynamic simulation.

4. Recommendations for future systems.

As a prelude to the discussion, some of the most important items that must be considered are:

- o The dynamic inlet stability limit must be known.
- o Engine airflow transients must be accurately determined (40- to 100-Hz response in measurements are indicated).
- o Inlet and engine instrumentation must be matched and be capable of high response, at least to 800-1000 Hz, to properly address inlet/engine interaction problems.

Reference 1 provides a comprehensive summary of the factors and aspects of propulsion system compatibility. Our data provides some good examples of events occurring in short time periods, pointing up the problems discussed in Reference 1.

We will describe briefly the FB-111A airplane, the inlet system, the objectives of the propulsion flight test program, the airborne instrumentation system, the data acquisition system, definition of terms, and data analysis procedures. Most of the data for review will be of the non-stationary total-pressure type and will be concerned with those events immediately preceding a stall-inducing event within about 500 milliseconds (1/2 second). Where statistical information can be obtained, data is checked for stationarity and samples of 3 to 5 seconds are analyzed. References 2 and 3 provide a good treatment of the necessity for obtaining stationarity of inlet data for understanding dynamic pressure measurements. As pointed out in Reference 3, unsteady flow data have not yet been reduced to meaningful parameters for understanding inlet/engine interactions. In References 3 and 4, discussions are presented on influence of the compressor flow on the upstream velocity and on static pressure conditions. Neither the compressor-face airflow angularity nor the velocity have proved useful so far in defining the distortion tolerance, although several researchers have indeed pointed to possible effects.

OBJECTIVES OF THE PROPULSION FLIGHT TEST PROGRAM

The objectives of the FB-111 propulsion flight test program were to

1. Establish the installed basic gas generator performance and characteristics for airplane performance confirmation.
2. Establish the installed rapid and slow transient and steady-state engine operational characteristics and continuity of thrust from windmilling to maximum augmented power for the airplane flight envelope.
3. Establish the inlet-engine compatibility with fixed and transient power lever conditions during maneuver and cruise flight conditions.
4. Determine any unusual effects of speed brake and weapon bay door and missile separation on inlet/engine compatibility.
5. Confirm satisfactory operation of the automatic air inlet control system.

AIRPLANE DESCRIPTION

The FB-111A (Figure 1) differs from the F-111A tactical model in that it has a nose stretch of 18 inches and modified wing tips. In other aspects the airplanes are aerodynamically similar except for the inlet, which is discussed below. The FB-111A also has a modified landing gear for higher gross weight, and a maneuver load limit of 3-g rather than 7.33 g. Avionics differ because of mission requirements. Variable wing sweep is the same, 16° to 72°, for both the bomber and tactical airplanes. The bomber has two Pratt and Whitney TF30-P-7 engines, which have greater thrust and about 6% more supersonic airflow than the TF30-P-3 engines for the TAC airplane. The P-7 and P-12 are the same basic engine but differ slightly in the fuel control configuration.

INLET DESCRIPTION

The inlet system (Figure 2) for all F-111D, E, and FB-111A airplanes is of the same configuration. It differs from the F-111A in that the inlet is approximately 11% larger in capture area, is moved 4 inches further outboard from the fuselage, and does not need a splitter plate for fuselage boundary-layer control. The inlet is an external compression type and uses a variable-diameter, double-cone spike that expands from $8\text{-}1/2^\circ$ to 26° for supersonic compression. The cone, or spike, translates independently of the second cone position for more efficient air spillage at low supersonic speeds. Porous spike bleed distributed over the spike shoulder is used for compression-surface boundary-layer control at high Mach numbers. An automatic air inlet control manufactured by Hamilton-Standard Division of United Aircraft Corporation controls spike and cone motions as functions of engine duct and under-wing glove Mach numbers.

ENGINE DESCRIPTION

The P&WA TF30-P-12 engine is an afterburning turbo-fan. Bypass ratio for the engine is 1 to 1, and the fan stream and core flow are confined in the afterburner and burned through five zones of thrust-modulated afterburning. Core and afterburner streams are not mechanically mixed. The engine incorporates a maximum airflow topping limit to down-trim the engine speed, and hence airflow, on a cold day to keep the inlet matched, as well as a minimum airflow limit to prevent inlet buzz during power lever retard to idle at high Mach number. A signal from the airframe air data computer controls these functions through a 'Mach lever' input on the engine fuel control. The automatic air inlet control has no control input to the engine fuel control.

COMPRESSOR-FACE AND ENGINE INSTRUMENTATION

Incorporated in the inlet duct 7 inches upstream of the engine face (Figure 3) are eight rakes of five probes each to measure the total pressure. No stream or wall statics are used; however, special streamline caps were designed to place over the total-pressure probes to measure static pressure in the event this becomes a necessary parameter in defining the distortion index of the engine. Since

the engine manufacturer only defines the distortion index in terms of total pressure, no static pressure or velocity surveys have been made. High-response transducers, Scientific Advances 1/4-inch diameter, are mounted directly in the rakes (Figure 4). No FOD protection is employed for the transducer diaphragm nor has this been indicated as necessary. Probes are placed on equal-area centers to provide inlet total pressure recovery and distortion calculation by numerical averaging. Since the engine is a production model, no high-response instrumentation is installed. Low-response measurements were made of low-compressor discharge P_{s3} , high-compressor discharge P_{s4} , and tailpipe pressure P_{T7} .

DATA ACQUISITION SYSTEM

The airborne high-response instrumentation system (Figure 5) is a constant-bandwidth, frequency-modulation multiplex system capable of recording 60 channels of data simultaneously on a single 1-inch-wide magnetic tape. The tape can record for approximately 55 minutes at a 15-in./sec speed. Time correlation is provided by IRIG B. This system can record transducer responses of up to 800 Hz with an amplitude roll-off of 3 db between 440 and 800 Hz. Only the compressor-face pressures are recorded on the high-response system.

A separate recording system records other airplane parameters such as flight conditions, airplane attitude and rates, and engine parameters such as engine speed, engine pressure, and inlet variable-geometry position. Time correlation is possible between the two systems; however, the response of the basic system is limited to 220 Hz by the electronics, and most of the other pressure data are limited to 25 Hz because of the line lengths between sensing port and the transducer.

DATA ANALYSIS TECHNIQUES

Data analysis includes a reduction of both steady-state and high-response parameters. Steady-state parameters are provided for all channels and are filtered to provide about a 25-Hz response. High-response data at the compressor face are sampled to provide pressure recovery and distortion up

to a maximum of 1000 cuts/sec at 800 Hz. A distortion pattern can thus be defined for a time interval during which the compressor blades rotate through a 60° arc.

Statistical data, PRMS, PSD, and cross correlation are developed on a Ubiquitous Analyzer and a Time/Data Corporation Analyzer from the stored tape data. Generally, 'quick-look' paper playout with a 25-Hz response of each channel is used to confirm data stationarity and to select the data for wave analysis.

A remark should be made about the calculation of engine (inlet) airflow. We use the engine manufacturers calibration of the fan for in-flight airflow measurement since under distorted flow conditions at the compressor face, it is not possible to calculate accurately by using total and static pressures. Airflow through the fan is a function of corrected speed and fan or engine pressure ratio (EPR) PT_7/PT_2 . Since we can measure PT_2 with high-response but PT_7 with slow response, we cannot really measure airflow during transients.

DISTORTION DEFINITION

In this paper we have reduced the inlet flight test data by using the P&WA definition of distortion index, K_D . This is an area-weighted index (Figure 6) empirically derived by the manufacturer from screen distortion testing of the TF30 compressor as well as from F-111 flight test inlet data to develop a correlation for engine distortion tolerance. The engine specification defines this index as a pattern lasting 1/150 second or longer. This corresponds to approximately 1 revolution of a compressor blade through the distortion pattern.

Based on studies of the USAF Aero Propulsion Laboratory, blade dwell time in a distorted region correlates relative to stall satisfactorily when distortion patterns last for 1/300 second, corresponding to 1/2 revolution of the low compressor. Very good agreement on a selected number of distortion patterns developed behind a turbulence generator was obtained by the Propulsion Lab engineers in their studies. In Reference 5 it is concluded that a compressor is sensitive to a minimum arc of distortion of approximately 60° to 90° . Since the Propulsion Lab used test stand data for a TF30 compressor, we chose to average the distortion indices for 1/2 revolution in most of the flight events.

Much useful work has been done (References 2, 6, and 7) on definition and use of statistical parameters for pressure and velocity measurements in unsteady flow. Some analyses of statistical parameters are reviewed here, but, generally, we are concerned with the stalls occurring during non-stationary events. As mentioned previously, no adequate published correlations are yet available to permit quantitative reliance on PRMS for engine stall. In References 7 and 8, however, it is shown that the PRMS is a contributing factor and is a useful tie for predicting propulsion system stability.

SPECIFIC INLET/ENGINE INTERACTION EVENTS

We began our flight investigations on the FB-111A with the spike bleed exit sealed off and a smooth spike (no porous bleed). This was done to permit a basic airplane performance (range) determination with minimum inlet drag. Bleed was added to the spike on Flight 5. Figure 7 provides a time history of the inlet pressure recovery and distortion sampling at a rate of 1000 cuts/sec. The event chosen (fixed power lever) shows two large pressure spikes occurring in which the total pressure drops in an interval of about 0.020 second. The engine stalled following the second total pressure drop. Two observations are noted: (1) the distortion K_D trend is to lag the inlet pressure recovery. At minimum pressure recovery, the K_D is still in an upward trend, reaching a maximum after the inlet pressure begins to recover; (2) the time-averaged distortion exceeds the engine stall tolerance in both cases, but an engine surge only occurred in the second case. Earlier, this event led us to believe that the engine may have partially stalled - prior to the P_{T2} drop - and the inlet responded by spilling the air subcritically as the normal shock moved forward. Another explanation, readily adopted by the engine company engineers, is that the inlet underwent a partial buzz cycle. We will explore this idea later. Obviously without high-response engine instrumentation, it could not be determined whether the inlet or the engine triggered the event. This event, needless to say, set into motion between the inlet and the engine designers "arguments that apparently derived self-contradictory conclusions by valid deductions from acceptable premises" - which according to Mr. Webster is the definition of a paradox. One obvious decision was to promptly install the bleed spike for further supersonic flying.

Figure 11 shows an example of an engine power lever chop at Mach 2.2 beginning at an airflow level of about 8% higher than the minimum airflow for the preceding event. Operation of the afterburner on the P-7 occurs at a reset engine airflow as the PLA is moved to or from the military detent. That is, military (dry) airflow is about 8% lower than augmented power airflow. Therefore a PLA chop to military power brings about a decrease in engine-corrected speed such that the airflow will be near the same level as the previous downtrim event. Since the airflow is changing rapidly during power lever changes (reset) and as the afterburner is cycling through the five zones of burning, airflow transients are occurring and being imposed on the inlet through the unchoked fan duct.

Figure 12 shows the evaluation of the compressor-face pattern as the stall is approached; a low-pressure area may be seen to grow at the compressor face on the lower side of the inlet. Whether this distortion caused the engine to stall is not known at this time, but it can be acknowledged to be greater than the engine stall tolerance.

Figure 13 depicts an engine stall at Mach 2.0. The engine was chopped to military power successfully and, after two seconds, the PLA was advanced into afterburner power. A stall occurred because of improper sequencing of the A/B Zone 1 ignition and nozzle unlatching and opening. The nozzle did not open, Zone 1 or Zone 2 lit, and the resulting oversuppression (high tailpipe pressure) caused the engine to surge. Notice the sudden increase in tailpipe pressure (P_{T_7}) trace shown in the insert of Figure 13.

Interestingly, a picture of the inlet distortion shows a rapid increase in the distortion level and a corresponding drop in inlet pressure recovery. In this case, although the averaged instantaneous distortion level approached the engine tolerance, it was finally decided that the stall was not caused by the inlet distortion but by the fuel control over suppressing the engine.

It became apparent from these data that separation of the contributor to the stalling event could not be ascertained by inlet instrumentation alone. Because of the difficulty of installing special high-response engine instrumentation, the investigation shifted to an examination of the inlet stability. Before this was done, however, the engine afterburner zone light sequence was modified by reversing the Zone 4 and 5 sequence (i.e., Zone 1-2-3-5-4). The Mach 2.2 engine airflow downtrim was repeated, this time

successfully to a lower airflow of about 159 pps with no stall. Figure 14 shows the airflow history for this event compared to the initial attempt, and Figure 15 shows the high-response data at minimum airflow. At this point, the inlet looked very stable and, after the afterburner zone sequence change, no further stalls occurred with power lever chops at high Mach number.

At Mach 2.2 the inlet cone angle was manually decreased to increase the strength of the normal shock which causes an increase in the normal-shock boundary-layer dynamics. The cone was decreased from 24.3° to 21.4° , corresponding to a normal-shock Mach number increase from 1.49 to 1.60. Instantaneous distortion increased to a maximum of about 1200 (Figure 16), and PRMS values increased from 2.0 to 2.5%. No engine stall occurred, although from past experience we know the engine is near stall at these conditions.

Distortion maps for the case of the decreased θ_2 (Figure 17) show that the distortion index, although increased and high, does not result from separated flow from the spike but from a lowering of the bottom pressures of the compressor face. This may be because the oblique shock tends to fall inside the lip and intersects the normal shock so that air enters the inlet at normal shock recovery instead of through the three-shock system. Obviously, the shock-intersection vortex must also enter the inlet, which classically has been thought to be the source of inlet buzz instability.

Power spectral density (PSD) and PRMS data shown in Figures 18 and 19 are compared for second-cone angles of 24.3° and 21.4° . More contribution in the lower frequencies of 0-200 Hz is apparent.

The above data show that the inlet is inherently stable; it is not easily triggered into buzz instability unless large airflow transients are imposed on the inlet.

A review of the specific events just covered shows that large changes in the inlet total pressure recovery and compressor-face distortion generally resemble the inlet instability near buzz. One may conclude, however, that these events of airflow transients should resemble buzz cycles since the inlet has no other way to respond but through a buzz cycle.

To examine this possibility more closely, we will look at a buzz cycle development at Mach 2.2 during a PLA retard

to idle power (Figure 20). Incidentally, this event is academic as far as engine/inlet operations are concerned because normally the engine fuel-control cam will provide a floor on the minimum airflow at supersonic speeds to prevent the inlet from getting to the buzz level. For this event it was necessary to take the floor out of the system by removing the Mach lever input, thus permitting the airflow to decrease to buzz levels.

Two significant items are noted here: (1) the inlet gradually enters buzz (is not triggered) at an "indicated" level of 158 pps (2) full buzz amplitude is not reached until the airflow falls to an "indicated" level of 130 pps. Note that the true airflows are not known since we have no valid way to measure airflow under these dynamic conditions.

High-response data for this event (Figure 20) show H_2/H_0 and K_D for the development of full buzz cycles. Despite the fact that the K_D 's are in excess of the engine distortion tolerance at that airflow condition, no stall occurred and power was readily re-established by advancing the power lever.

Similarity between the events of stall previously shown and the buzz cycles can be readily seen. The unknown fact is the mechanism by which the inlet is suddenly triggered into a single cycle of buzz with no apparent airflow change.

We can now draw some conclusions regarding the inlet stability. Basically, the instability (buzz) envelope of the inlet is derived by decreasing the airflow progressively until instability is observed. Usually there is some hysteresis, that is, buzz onset is not precise but tends to vary a few percent. As mentioned earlier, the buzz envelope for this inlet was determined from F-111A No. 14 with the P-3 engine. This matched closely with values determined from the wind tunnel. A very unique picture emerges here (Figure 21). There is an apparent instability appearing at a higher airflow than that with stabilized airflow. However, as mentioned previously, the airflow measurement is probably in error.

We do not yet believe valid conclusions can be drawn from the data of Figure 21 because the data are limited. It would appear that inlet stability is a function of how the stability limit is approached, i.e., the airflow at which instability occurs increases as the rate of airflow change increases. More work is necessary to prove this point since

it seems contrary to inlet test experience. Admittedly, the FB-111A inlet may have a lower stability margin than that of F-111A No. 14. There are, however, some conclusions to be drawn on the flight results:

1. Inlet changes show subtle effects on the high-response data when comparing bleed versus non-bleed spikes. The PRMS data is slightly improved and the instantaneous distortions are about the same level. However, it was clear, the interaction events leading to compressor stall were considerably reduced with the bleed spike.
2. The inlet, with bleed, appears to be inherently stable and is not easily triggered to buzz. The successful downtrim to a slightly lower airflow and the second cone angle decrease seem to confirm this.
3. The inlet/engine system stability improved with the afterburner fixes.

The advanced afterburning turbo-fan engine can be assumed to always have some airflow pulse with A/B ignition and zone changes. These transients, although difficult to measure accurately, must be determined both in amplitude and in rate of change (frequency). The inlet designer should therefore plan his wind tunnel test to include inlet dynamics that include pulsed duct flow as well as steady-state flow. Inlet stability margins with fixed-inlet geometry must be as large as possible, since no automatic inlet control will be able to keep up with these rapid changes. Inlet type is also expected to be an important parameter. For example, 2-D external compression inlets have relatively large movements of the normal shock to accomplish airflow spill as a result of the engine demand. This shock movement can use up the inlet stability margin. On the engine design side, transient airflows must always be identified and efforts made to keep all dynamics to a minimum.

DYNAMIC MODEL SIMULATOR

We now turn our attention to current dynamic model simulator programs, probably the most simple of which can closely

portray transients to about 20 Hz. References 1 and 9 presented the case for utilizing advanced mathematical models for solving more higher response problems. Methods of providing for an approximate mathematical model frequencies of up to 150 Hz are discussed in Reference 10. Such programs will be necessary to model inlet and engine dynamics adequately - as we shall see.

The engine manufacturer has a dynamic model simulator program with which the event of PLA chop at Mach 2.2 (Figure 11) was simulated. A comparison of the simulated event with the actual event is shown in Figure 22. The true airflow transients of the actual event are, of course, unknown. The representation of airflow given is based on the calculation of airflow from N_1 rotor speed, the high response P_{T2} and the low response P_{T7} . As mentioned earlier, EPR (P_{T7}/P_{T2}) appears in the airflow calculation of engine pressure ratio and has a strong effect on engine airflow. The simulator data do not show the airflow transients indicated by the test data. To be fair, the current program for either inlet or engine parameter does not contain the necessary inputs to explore such dynamic interactions. All of the model inlet data was run with steady-state instrumentation and no dynamic airflow pulses were applied. Further, dynamic engine airflow data are not available to permit valid engine response assessment. This comparison is shown to point up the problem of becoming aware of the necessary inputs required to really gain insight into the compatibility program. (See Reference 1 for further discussion.)

EXTERNAL INFLUENCE ON THE INLET

The cases investigated, then, constitute engine/inlet interactions in which it is not possible to identify the cause and effect paradox. There were some flight events, however, in which the disturbances could be positively traced to external influences. These events were (1) clear-air turbulence, in which the inlet pressure versus time represents considerable nonstationarity and instantaneous K_D 's were observed to increase; (2) weapon bay door openings, which cause disturbances to the fuselage boundary layer and interact with the inlet; and (3) a maximum maneuver in which the body vortex could be predicted to have an influence on the inlet performance.

The clear-air turbulence event, shown in Figure 23, affected the compressor-face parameters. Plots of pressure recovery and instantaneous K_D are shown along with a playout of a typical rake pressure versus time. Note that the rake pressures, shown in the insert of Figure 23, undergo rather sudden drops and become quite dynamic. The instantaneous distortion shows a four-fold increase, although it stays below the engine stall tolerance. None of the normal steady-state engine parameters showed any significant change during this condition, although the airplane accelerometers and angle-of-attack and sideslip indicators showed rather high oscillations.

PRMS data for this event were developed, although there could be some question concerning data stationarity. Compared to data from a previous flight, PRMS values increased from 2% to 2.2%. Cross correlation of the outer probes with the inner probes showed only weak correlation, indicating that the scale of the turbulent flow was probably somewhat less than the inlet size.

The second case of external effects on the compressor face is shown in Figure 24, in which high-response pressure recovery and distortion data are compared for the case of the weapon bay door open and closed. The weapon bay doors open along the lower fuselage side (Figure 1), and the open door apparently interacts with the fuselage boundary layer and creates turbulence along the fuselage which can enter the inlet or affect the inlet flow field. Both turbulence PRMS and instantaneous K_D are significantly increased. Figure 25 shows the development of the compressor face pattern, comparing closed and opened doors. The inboard side shows the greatest distortion with lowered total pressures.

The power spectral density is altered on opening the doors and shows much stronger contributions at the lower frequencies (0-200 Hz). PSD's are compared for the weapon bay doors open and closed in Figure 26. The cross power spectral density and cross correlation were examined for several pairs of probes at the compressor face for the doors open and closed. Figure 27A shows the cross PSD and cross correlation for two adjacent inboard probes; Figure 27B for an inboard probe and an outboard probe; and Figure 27C for two adjacent outboard probes.

The significance of these figures is that (1) a major increase in power at approximately 63 Hz occurs when the doors are opened on the lower inboard side (Figure 27A), as can be seen in both the cross-correlation data and the cross-PSD; and (2) correlation between the two adjacent outboard probes (Figure 27C) again shows a significant contribution at 63 Hz, but it is much weaker between inboard and outboard. Note that there is also a contribution showing up in all the data near 350 Hz.

These statistical data corroborate the compressor-face distortion patterns that show the major effect on the inboard side of the inlet. Reference 2 provides further explanation and use of statistical dynamic data.

Figure 28 shows a maximum capability wind-up turn at Mach 2.3. This maneuver is accomplished by rolling the airplane rapidly into a near vertical bank and pulling full stick and elevon deflection in less than one second. If executed properly the airplane can be made to overshoot slightly the maximum trim angle of attack condition. At these overshoot conditions, corresponding to angle of attack of about 17° , the fuselage vortex was predicted from model data to enter the inlet (Reference 11). Occasionally during the propulsion test program, we were able to verify this condition and sometimes an engine stall resulted. Figure 29 shows the time history of the last part of the angle-of-attack increase, which shows the evidence of breakdown in inlet flow. Pressure recovery and distortion are shown to smoothly drop and rise, respectively. Notice that the inlet pressure decrease occurs over 150 milliseconds which is about 3 times longer than the pressure spike observed with the PLA change of Figure 11. Again, it would appear that the inlet is not easily triggered into instability. Compressor face patterns (Figure 30) show the low pressure appearing at the bottom of the compressor face, thus resulting in severely distorted patterns.

SUMMARY

In summarizing the events covered in this paper, we would like to restate the lessons learned:

1. A paradox is created when insufficient instrumentation is applied to dynamic inlet/engine compatibility problems.

It is not sufficient to just know the compressor-face distortion at the point of engine stall, because distortion will probably always increase as the inlet is pushed to an off-design airflow match.

2. Engine and inlet dynamics both must be known from valid development tests.
3. Dynamic simulator programs must be as sophisticated as necessary to give insight into the particular inlet/engine propulsion system.
4. Future wind tunnel tests of the inlet not only must include dynamic turbulence scaling criteria but must also produce dynamic airflow pulses to simulate the dynamic effect of the engine.
5. The effect of airflow turbulence, swirl, and velocity at the compressor face must also be researched further to determine their full significance relative to engine stall and operation.
6. The afterburning turbo-fan propulsion system has a coupling between the engine and inlet which requires a more exacting management of the airframe/engine interface.

REFERENCES

1. Richey, G. K., et al., "Airframe-Propulsion Integration for Future Aircraft Systems", SAE Paper No. 680288, presented at the 1968 SAE Air Transportation Meeting in New York, 29 April-3 May 1968.
2. Steenken, W. G., Aerodynamic Inlet Noise - Statistics and Non-Dimensional Analysis, General Dynamics, Fort Worth Division Report ERR-FW-654, 31 December 1968.
3. Winslow, L. J., Wendland, D. W., Smith, B. D., and Welliner, A. P., Inlet Distortion Investigation, Upstream Engine Influence and Screen Simulation, Boeing Company Technical Report AFAPL-TR-68-140, January 1969.
4. Spring, A. H., Upstream Influence of Axial Compressor on Distorted Subsonic Duct Flows, General Dynamics, Fort Worth Division Report ERR-FW-755, 26 August 1968.
5. Reid, C., "The Response of Axial Flow Compressor to Intake Flow Distortion", ASME Paper 69-GT-29, presented at ASME Gas Turbine Conference and Products Show, Cleveland, Ohio, 9-13 March 1969.
6. Kostin, L. C., and Millstone, S. D., "Application of Statistical Parameters in Defining Airflow Dynamics", AIAA Paper 68-649, presented at the AIAA 4th Propulsion Joint Specialist Conference, Cleveland, Ohio 10-14 June 1968.
7. Goethert, B. H., and Kimzey, W. F., "Effect of High Frequency Fluctuations of Inlet Flow on Compressor Stall", paper presented at The University of Tennessee Space Institute, Tullahoma, Tennessee, 1968.
8. Cotter, H. N., "Integration of Inlet and Engine - An Engine Man's Point of View", SAE Paper 680286, presented at SAE Air Transportation Meeting, New York, New York.
9. Gardner, W. B., and Sampl, F., Jr., "Dynamic Simulation - A Tool for Engine Component Design", paper presented at SAE National Air Transportation Meeting, New York, New York, 21-27 April 1969.

REFERENCES (CONCLUDED)

10. Willah, R. G., A Mathematical Analysis of Supersonic Inlet Dynamics, NASA TN D-4969, Washington, December 1968.
11. Slaten, T. R., Investigation of Boundary Layer and Shock Structure on an Isolated Quarter-Circle, External-Compression Inlet, General Dynamics, Fort Worth Division Report ERR-FW-653, 31 December 1968.

BIBLIOGRAPHY

- Alford, J. S., Davies, D. P., and Young, L. C., "Inlet Duct-Engine Airflow Match and Compatibility for Supersonic Aircraft," paper presented at SAE National Aerospace Engineering and Manufacturing Meeting, Los Angeles, 8-12 October 1962.
- Alford, J. S., "Inlet Flow Distortion Index," paper presented at International Days of Aeronautical Sciences, Paris, France, 27-29 May 1959.
- Bauermeister, W. K., Roseburg, C. M., and Id, H. W., "727 Airplane Engine Inlet Development," AIAA paper presented at 4th Propulsion Joint Specialist Conference, Cleveland, Ohio, 10-14 June 1968.
- Bentz, C. E., "Propulsion System Controls Capabilities and Future Requirements," ASME Paper 68-GT-62, presented at the Gas Turbine Conference & Products Show, Washington, D. C., 17-21 March 1968.
- Gabriel, D. S., Wallner, L. E., and Lubid, R. J., "Some Effects of Transients in Inlet Pressure and Temperature on Turbojet Engines," IAS paper presented at 25th Annual Meeting, New York, 21-28 June 1957.
- Gratz, H. J., Procedures and Suggested Programming Emphasis to Obtain Criteria Essential to Attaining Propulsion System Flow Stability, Air Force Aero Propulsion Laboratory Report AFAPL-TR-68-30, May 1968.
- Gratz, H. J., "Propulsion System Flow Stability," paper presented at AIAA Meeting, Washington, D. C., 12 February 1968.
- House, J. T., Some Fluid Mechanical Problems Related to Subsonic and Supersonic Aircraft, NASA SP-183, Office of Technology Utilization, 1968.
- Randall, L. M., and Hand, W. H., "Integration of Inlet and Engine - An Airplane Man's Point of View," SAE Paper 680287, presented at SAE Air Transportation Meeting, New York, New York, 29 April-2 May 1968.

BIBLIOGRAPHY (CONCLUDED)

Roberts, F., Plourde, G. A., and Smakula, F., "Insights into Axial Compressor Response to Distortion," paper presented at AIAA 4th Propulsion Joint Specialist Conference, Cleveland, Ohio, 10-14 June 1968.

Smith, R. H., Bellman, D. R., and Hughes, D. L., "Preliminary Flight Investigation of Dynamic Phenomena Within Air Breathing Propulsion Systems of Supersonic Aircraft," AIAA Paper 68-593, presented at the AIAA 4th Propulsion Joint Specialists Conference, Cleveland, Ohio, 10-14 June 1968.

Tear, R. C., Propulsion System Stability Determination and Evaluation Approaches, Air Force Aero Propulsion Laboratory Report AFAPL-TR-67-75, January 1968.

Wasserbauer, J. F., and Whipple, D. C., Experimental Investigation of the Dynamic Response of a Supersonic Inlet to External and Internal Disturbances, NASA TMX-1648, Washington, D. C., September 1968.

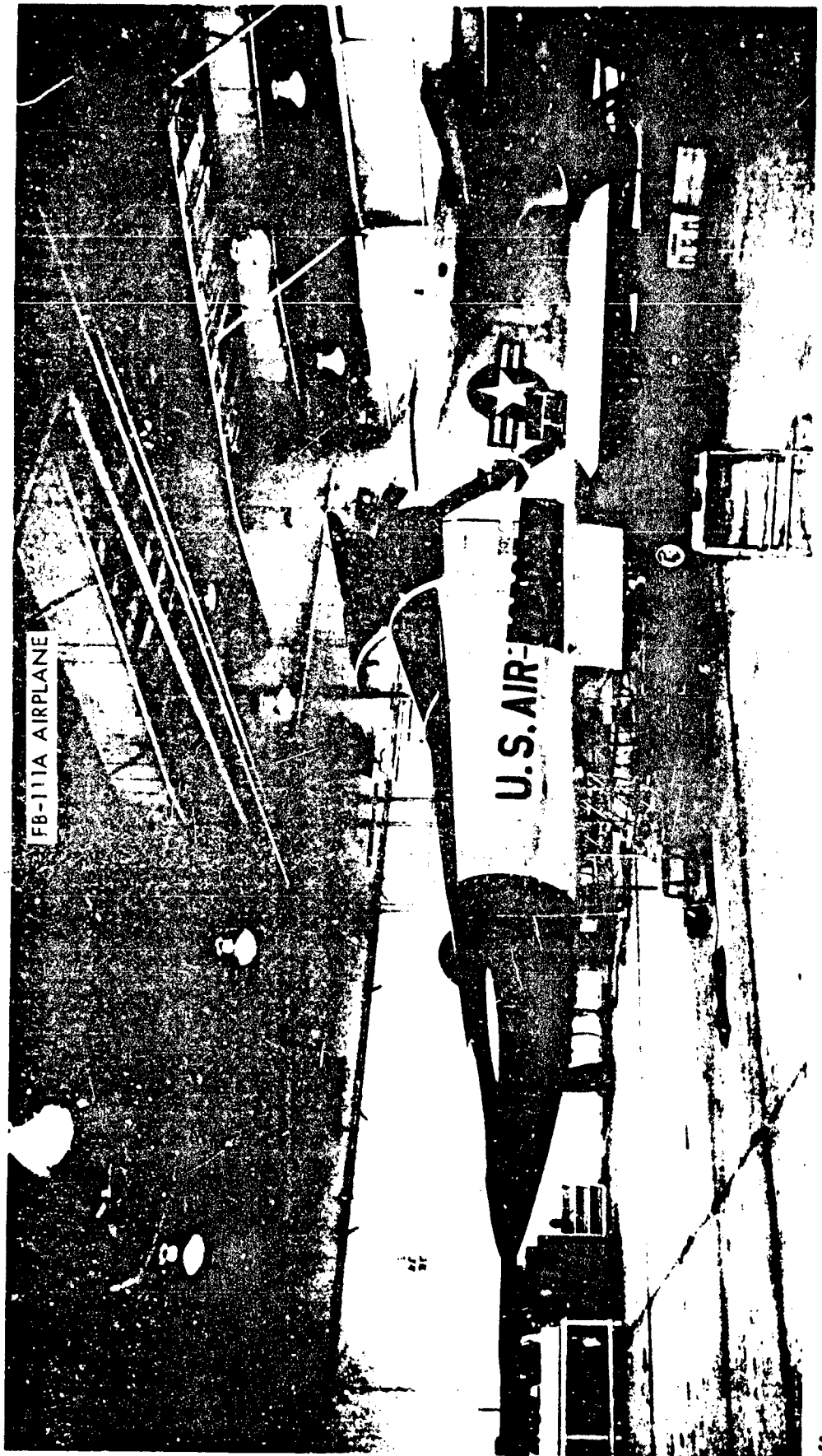
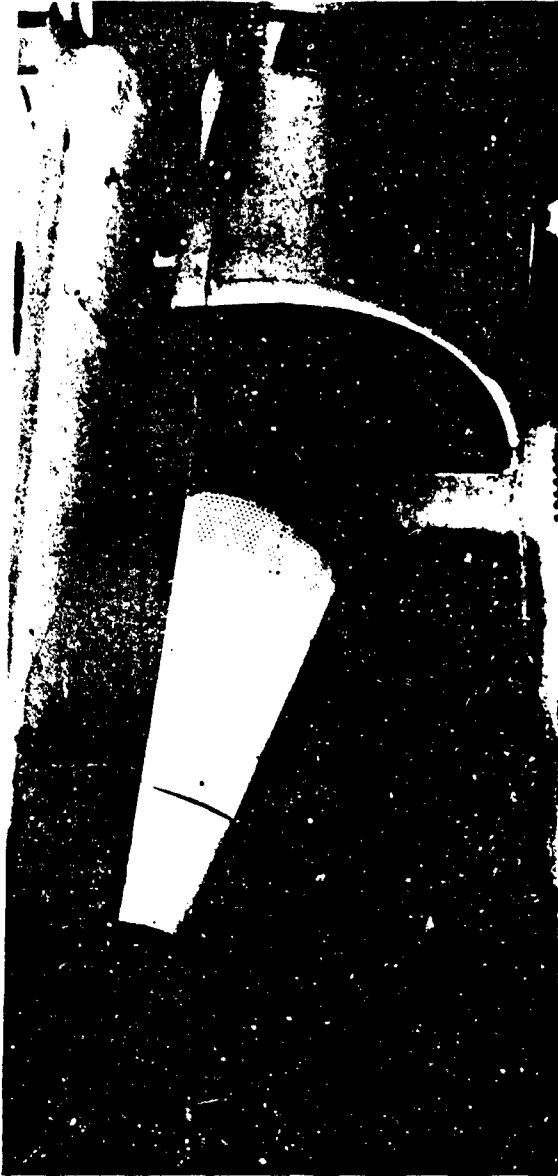
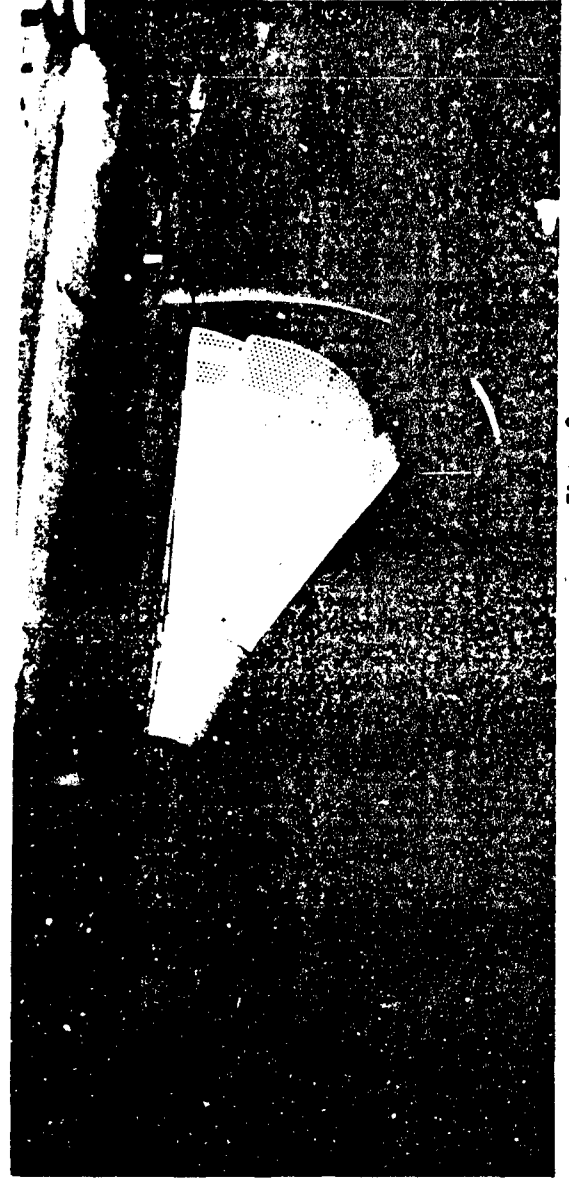


Figure 1

FB-111A INLET SYSTEM



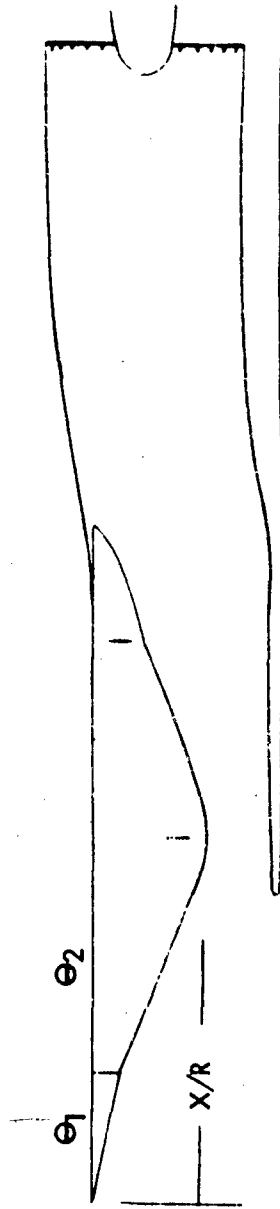
SUBSONIC



SUPERSONIC

Figure 2

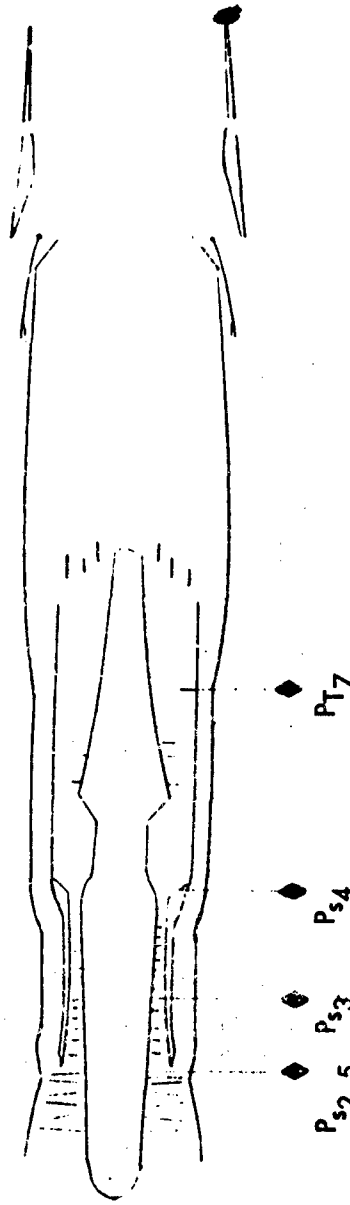
INLET AND ENGINE INSTRUMENTATION STATION



INLET INSTRUMENTATION

40-PT2

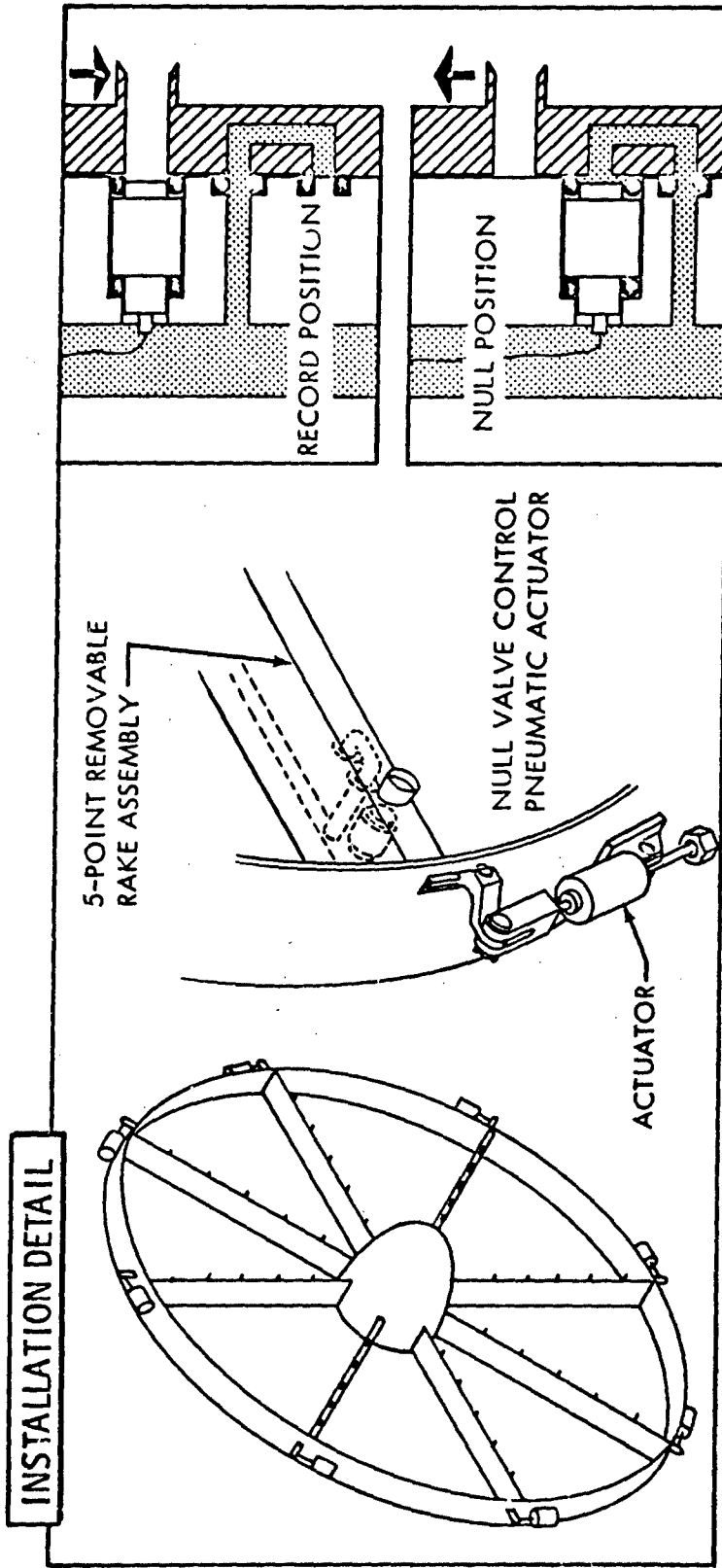
- N1
- N2
- PLA
- Aj
- A/B ZONE PRESS



ENGINE INSTRUMENTATION

Figure 3

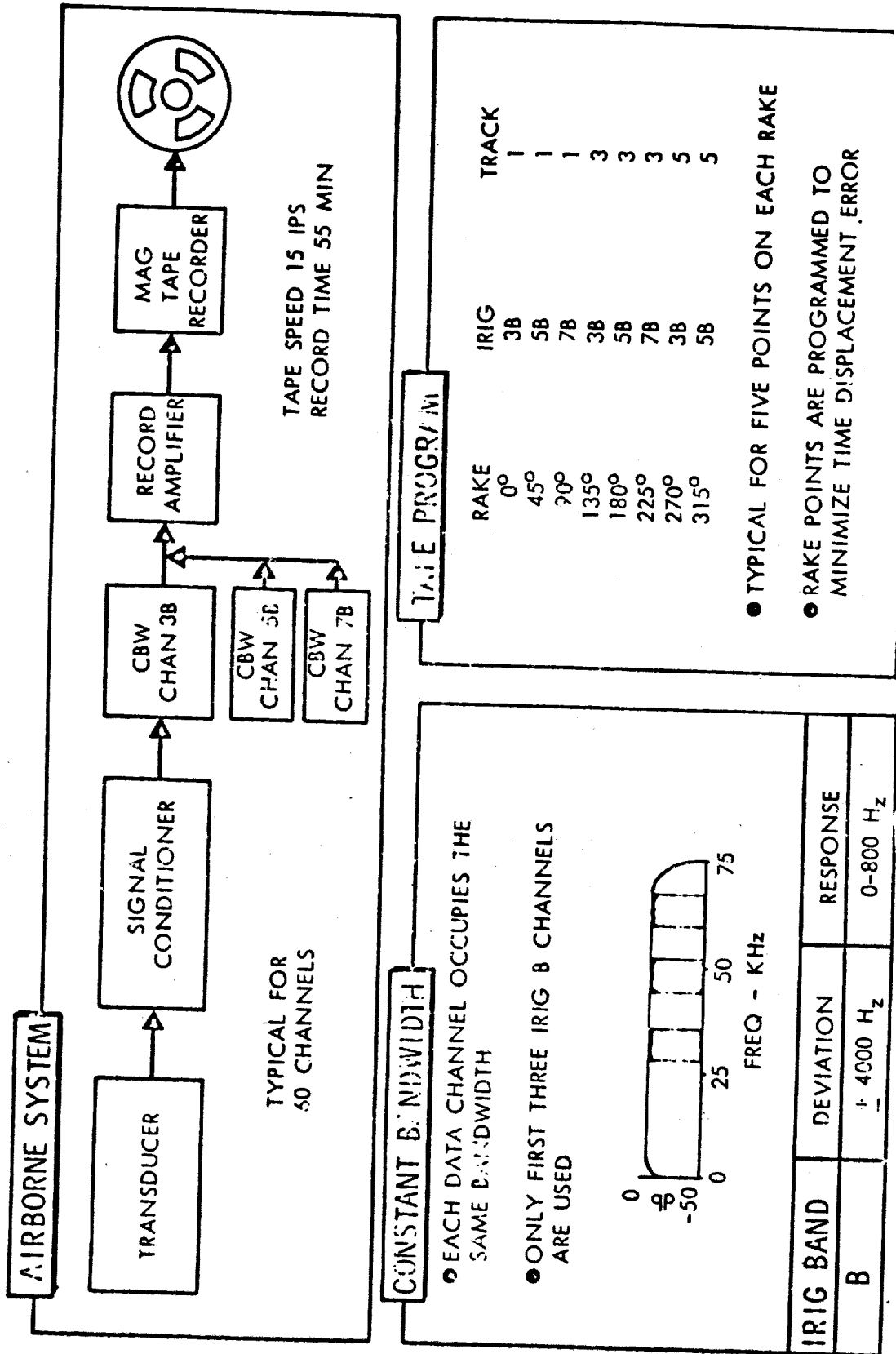
HIGH-RESPONSE PRESSURE MEASUREMENT



- TRANSDUCERS (SA-DS M-6H) MOUNTED IN RAKE ASSEMBLY
- REMOVABLE 5-POINT RAKE ASSEMBLY CAN BE INSTALLED OR REMOVED FROM WITHIN THE ENGINE INLET
- NULLING VALVE USED TO CORRECT TRANSDUCER "NULL SHIFT" DUE TO TEMPERATURE EFFECTS
- MICROELECTRONIC SIGNAL CONDITIONERS AND CONSTANT BANDWIDTH RECORDING USED TO PROVIDE 0-800 Hz RESPONSE

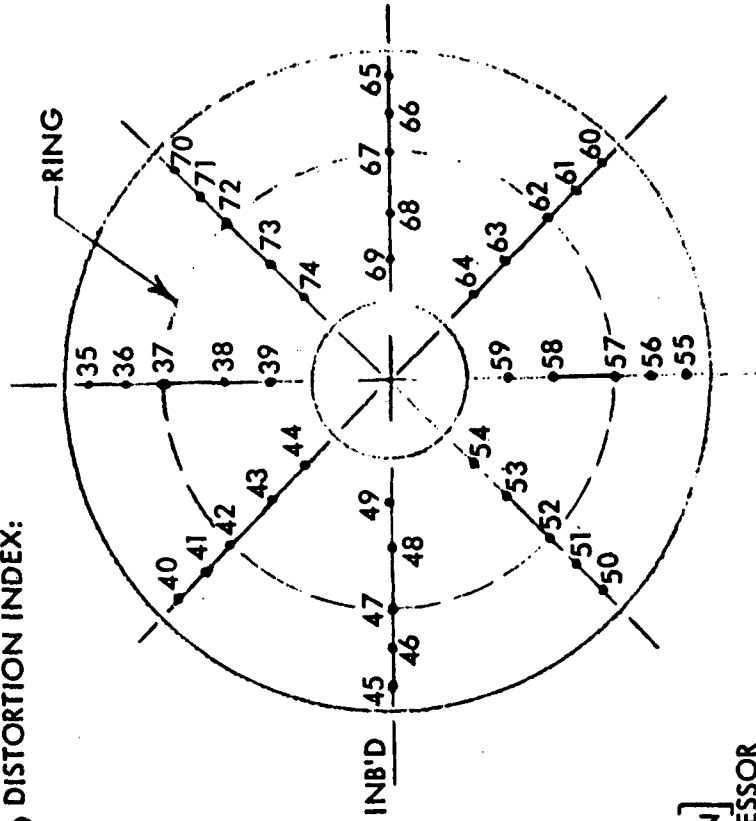
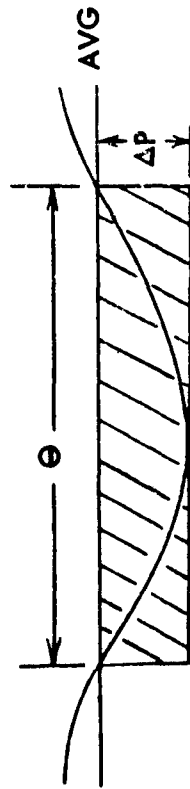
Figure 4

FB-111A HIGH RESPONSE INSTRUMENTATION SYSTEM



DEFINITION OF DISTORTION

o BASED ON PRATT AND WHITNEY'S DEFINITION OF K_D DISTORTION INDEX:



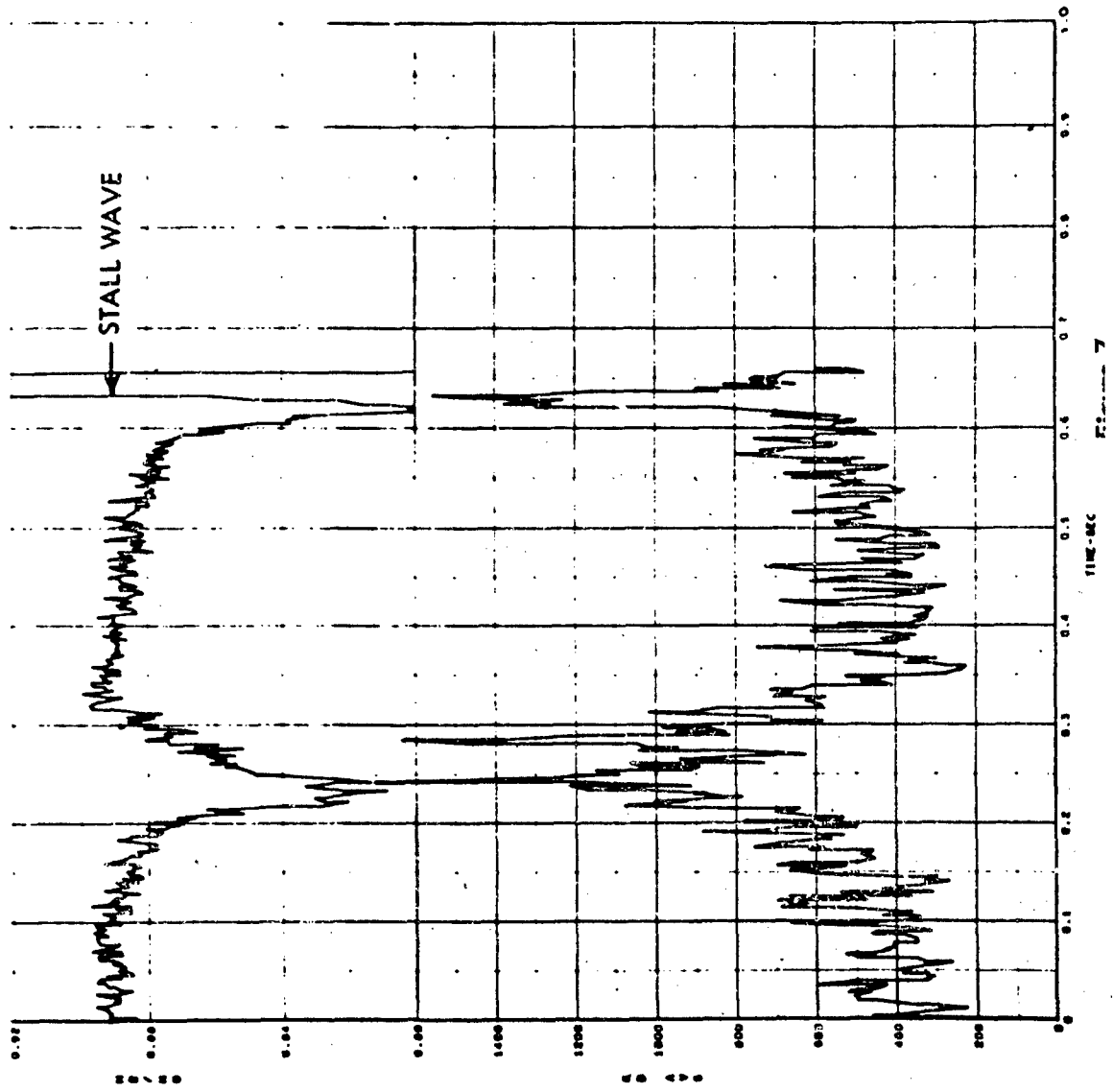
K_D = AVERAGE OF RINGS $\left[\frac{\theta_{LOW} \times \Delta P_A - MIN}{\theta_{HIGH} \times \Delta P_A - MIN} \right]$
INNER RINGS WEIGHTED FOR LOW COMPRESSOR

K_{D_i} = INSTANTANEOUS DISTORTION FOR 1000 CUTS/SEC

$K_{D_{AVG}}$ = K_D COMPUTED FROM AVERAGE PRESSURE OF THREE SUCCESSIVE 1/1000 SEC. CUTS

Figure 6

HIGH RESPONSE DATA FOR NO-BLEED, SMOOTH SPIKE - 2.2 M₀



PRMS SMOOTH SPIKE VS BLEED SPIKE

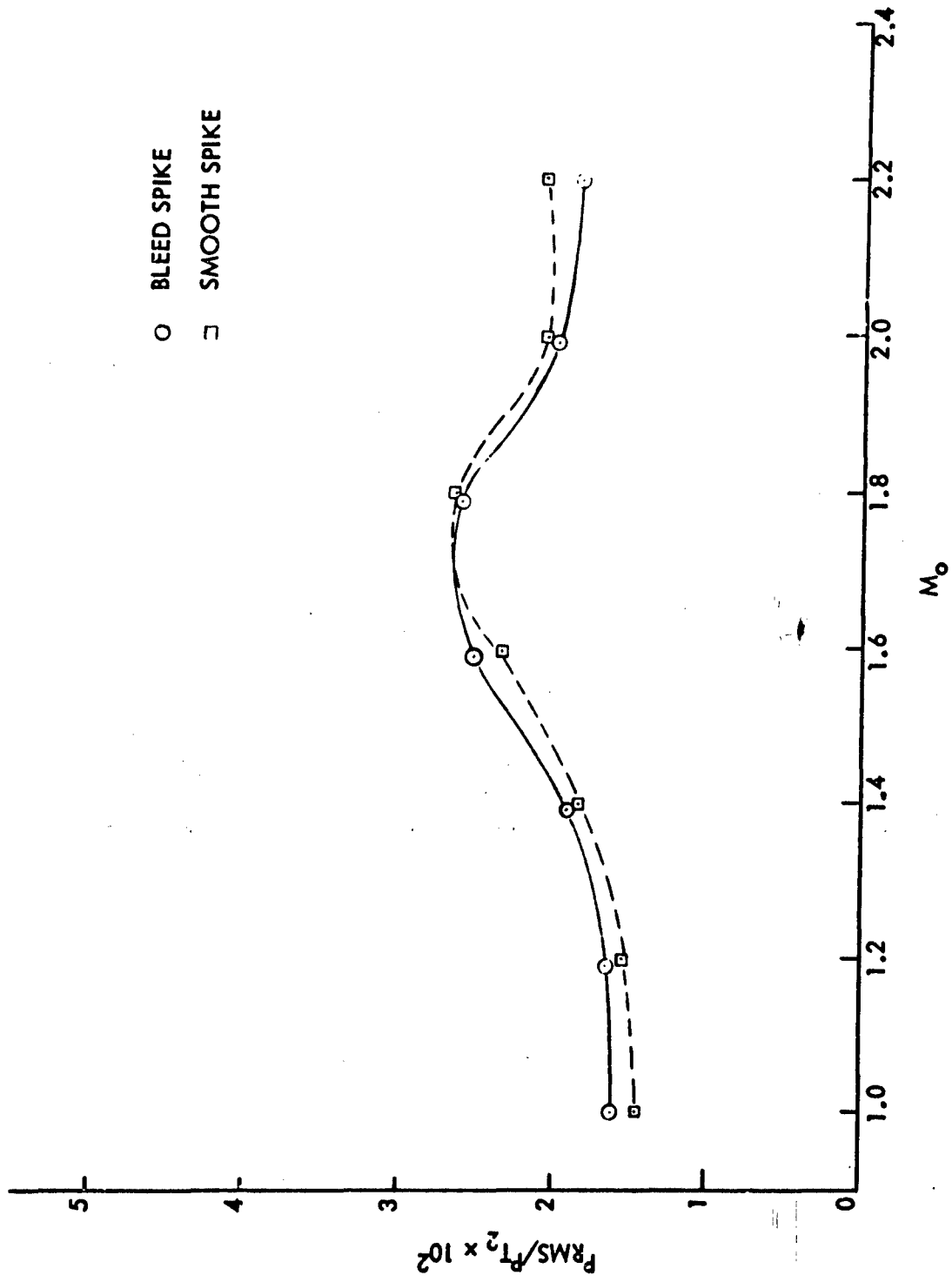


Figure 8

TIME HISTORY
MACH 2.2 ENGINE AIRFLOW DOWNTRIM
FLT 5

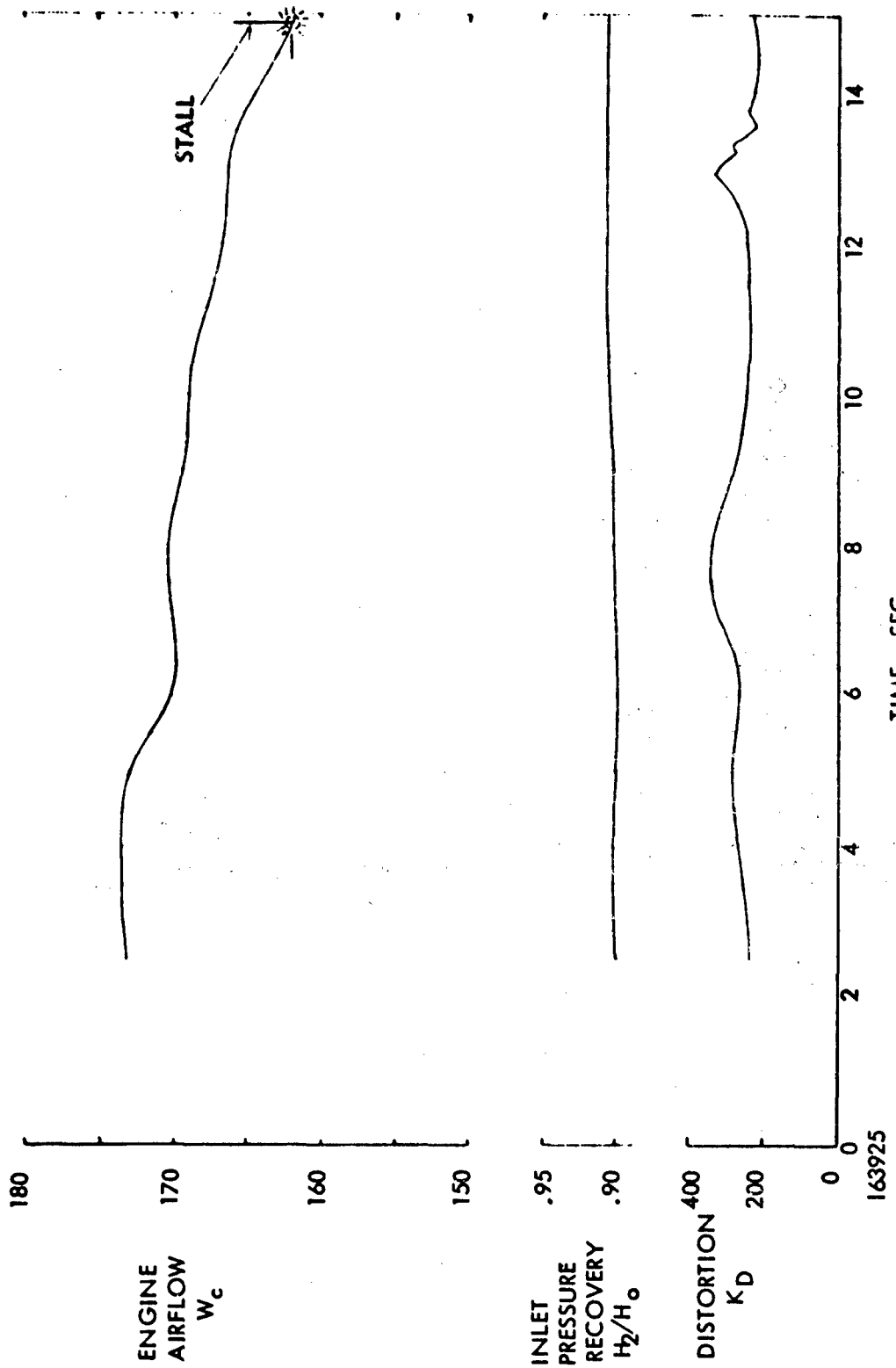


Figure 9

HIGH RESPONSE INLET DATA FOR ENGINE AIRFLOW DOWNTRIM AT 2.2 M₀

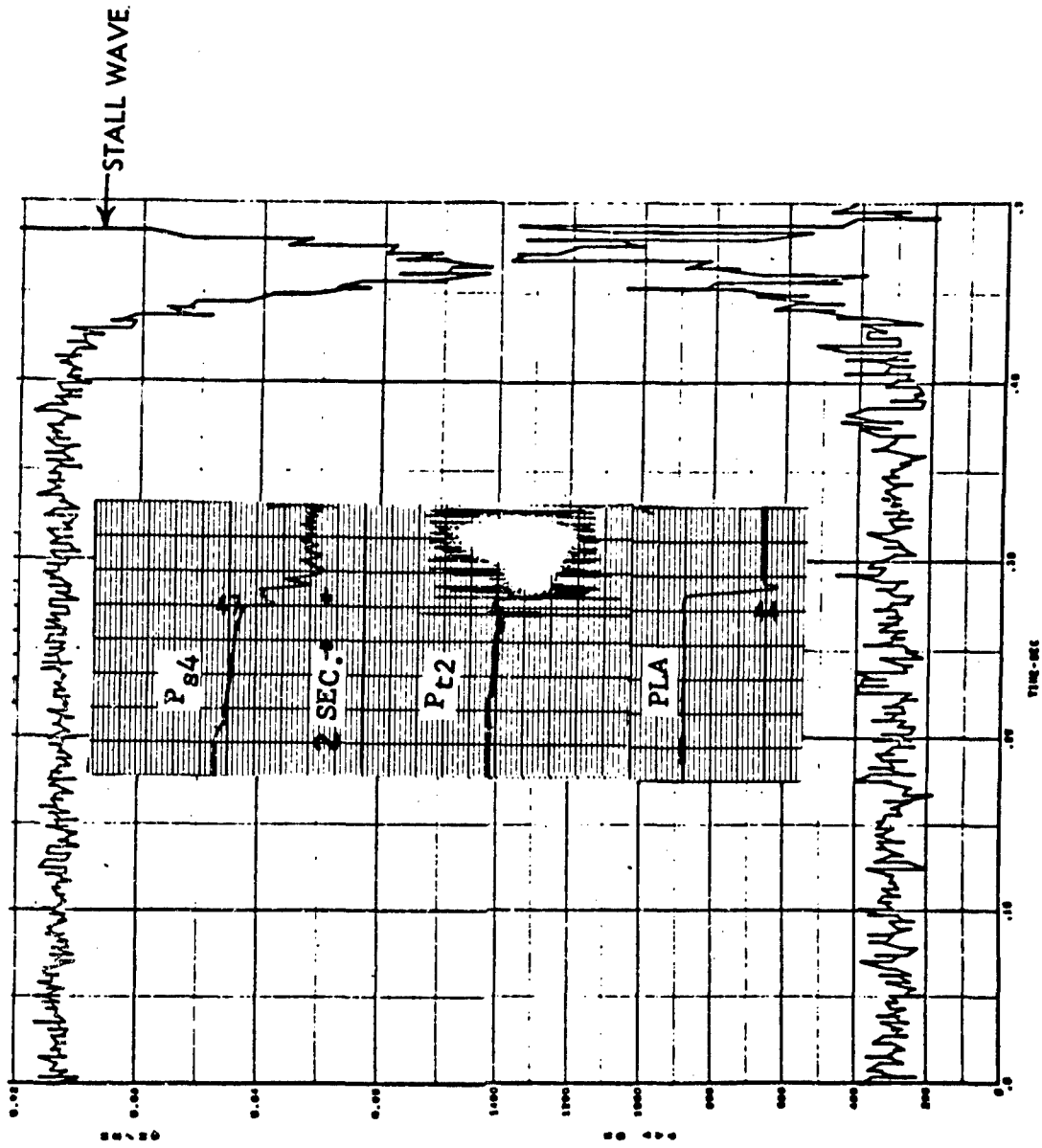


Figure 10

HIGH RESPONSE INLET DATA FOR POWER LEVER RETARD AT 2.2 M₀

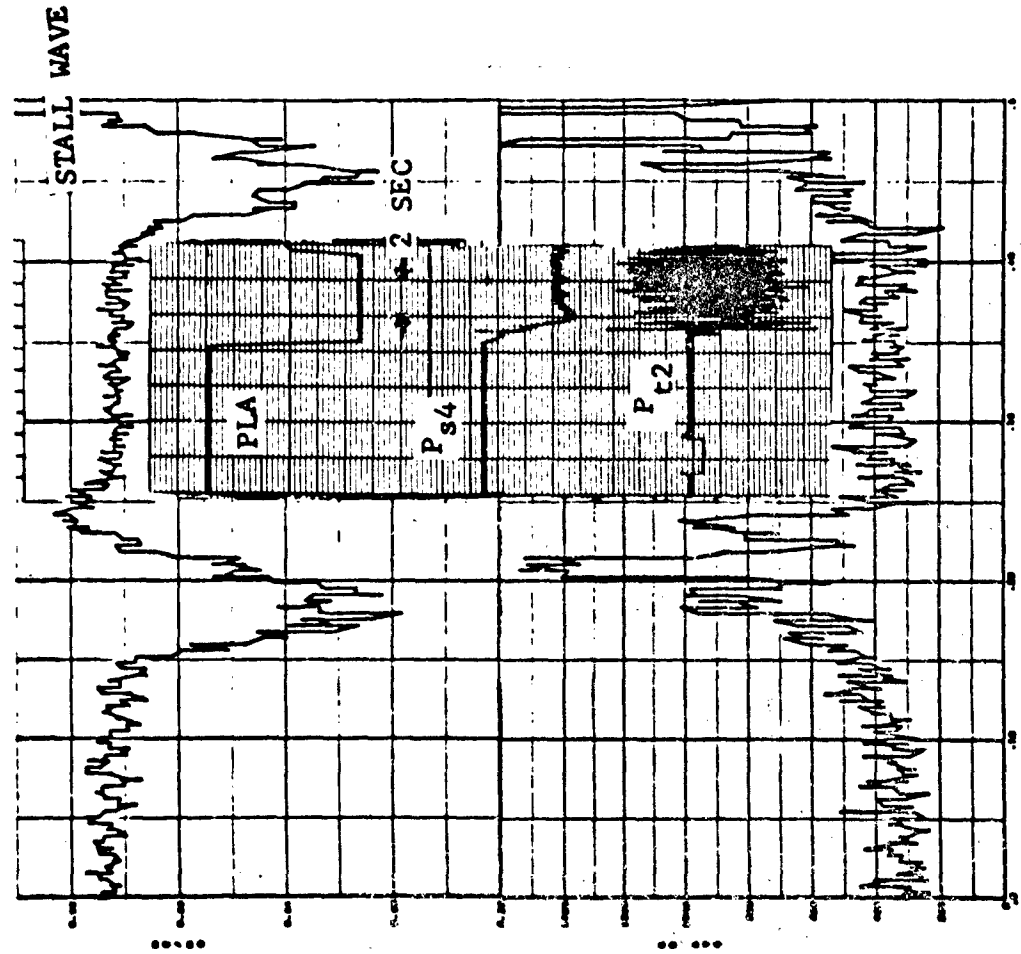


Figure 11

COMPRESSOR FACE PATTERNS AT STALL FOR POWER LEVER CHANGE - 2.2 M₀

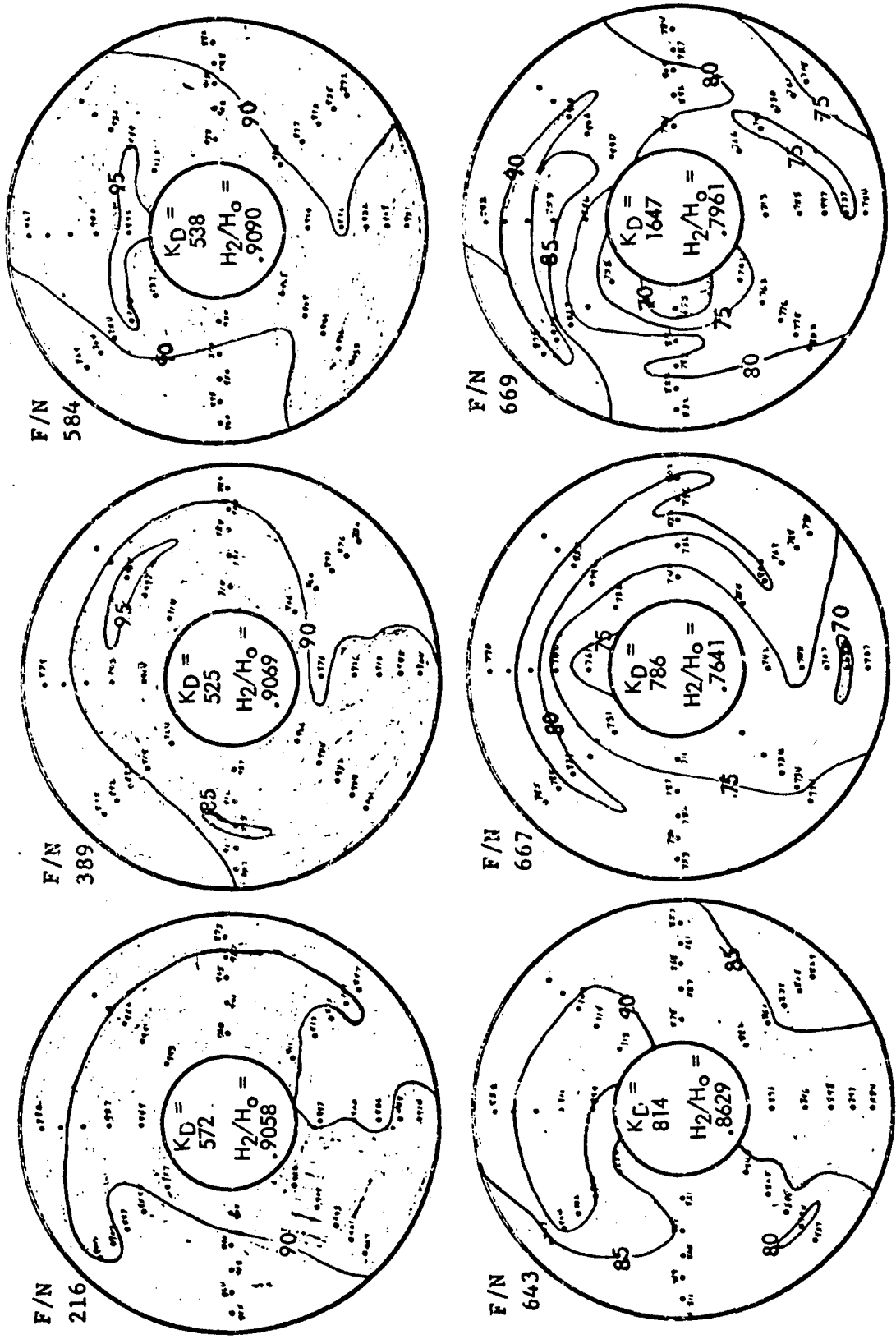
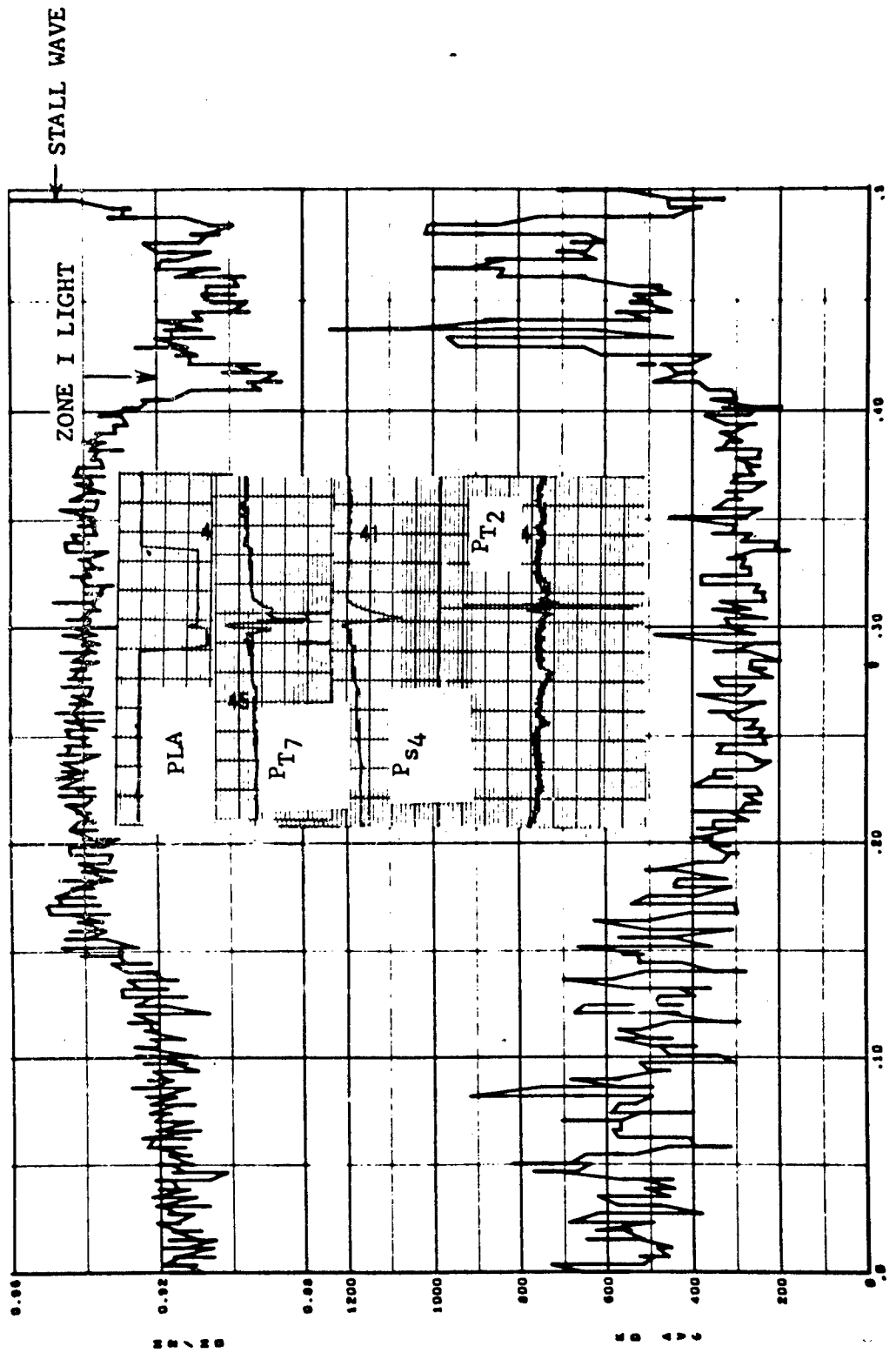


Figure 12

HIGH RESPONSE INLET DATA FOR ZONE 1 LIGHT STALL - 2.0 Mc



TIME-SEC

Figure 13

TIME HISTORY
MACH 2.2 ENGINE AIRFLOW DOWNTRIM
BEFORE & AFTER A/B FIX
FLT 5 VS. FLT 17

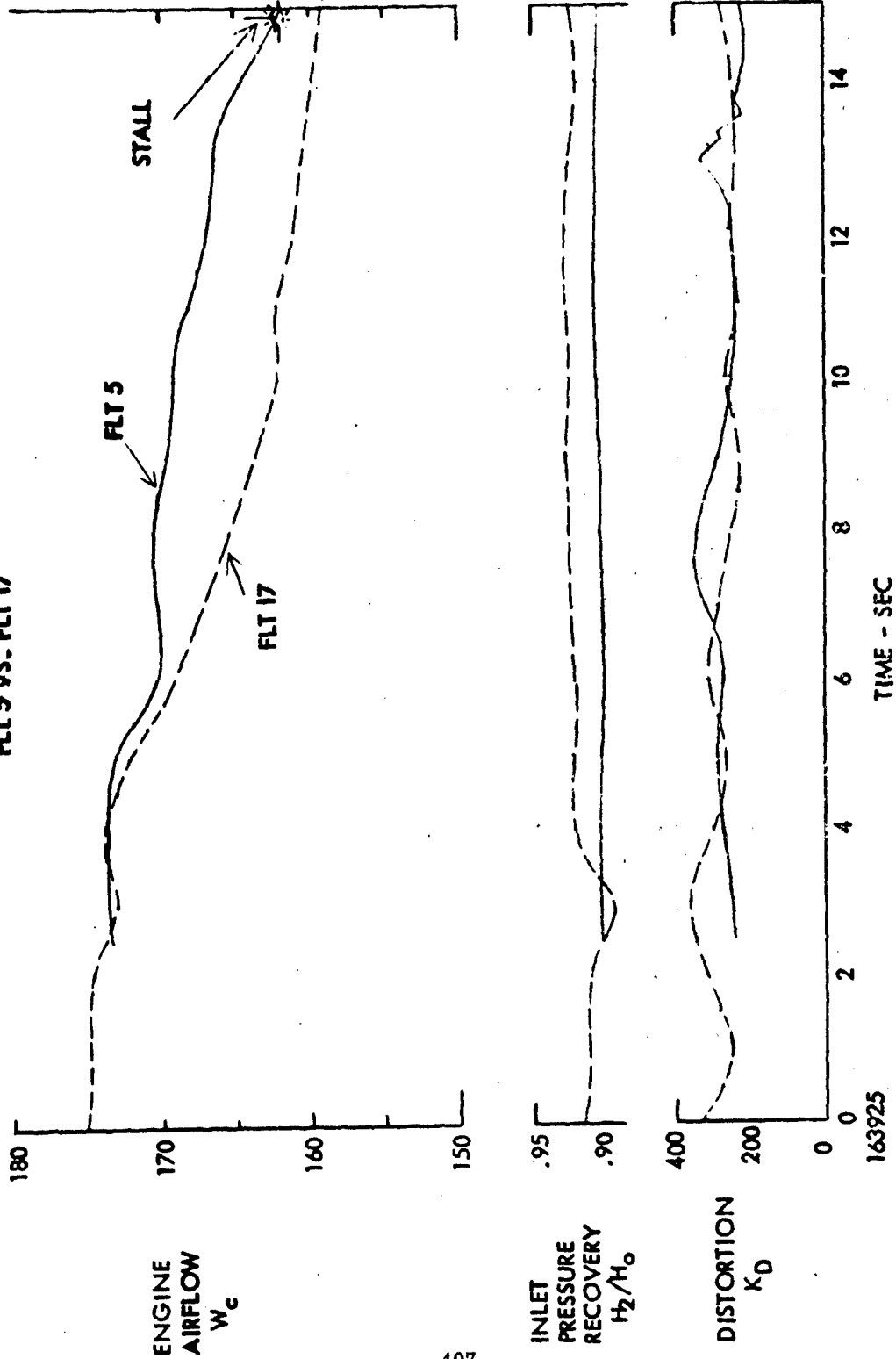


Figure 14

HIGH RESPONSE INLET DATA FOR ENGINE AIRFLOW DOWNTRIM WITH A/B FIX AT 2.2 M₀

WC MIN 158 PPS

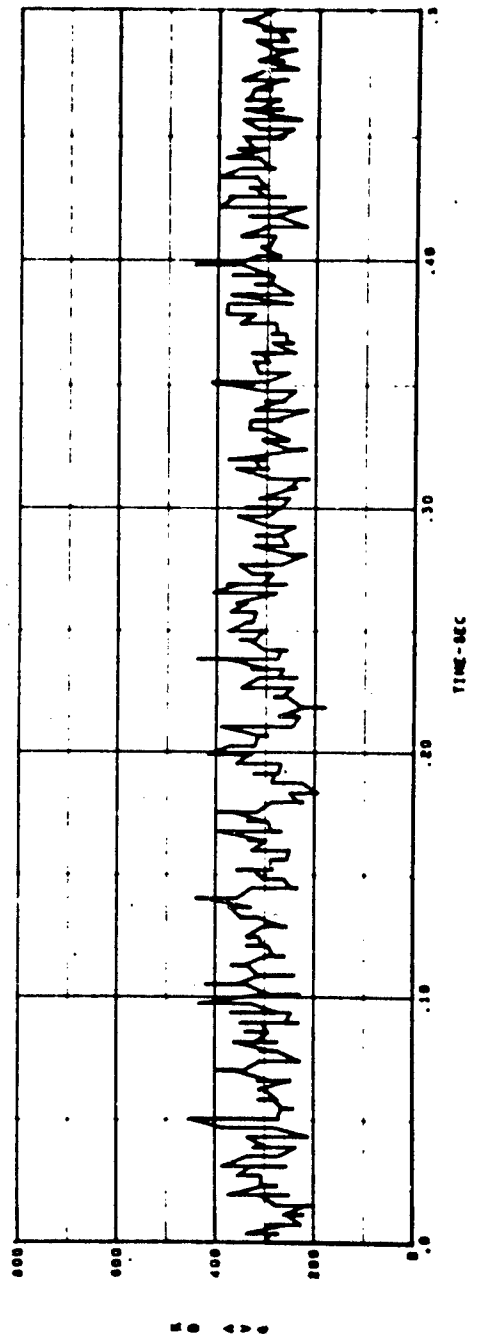
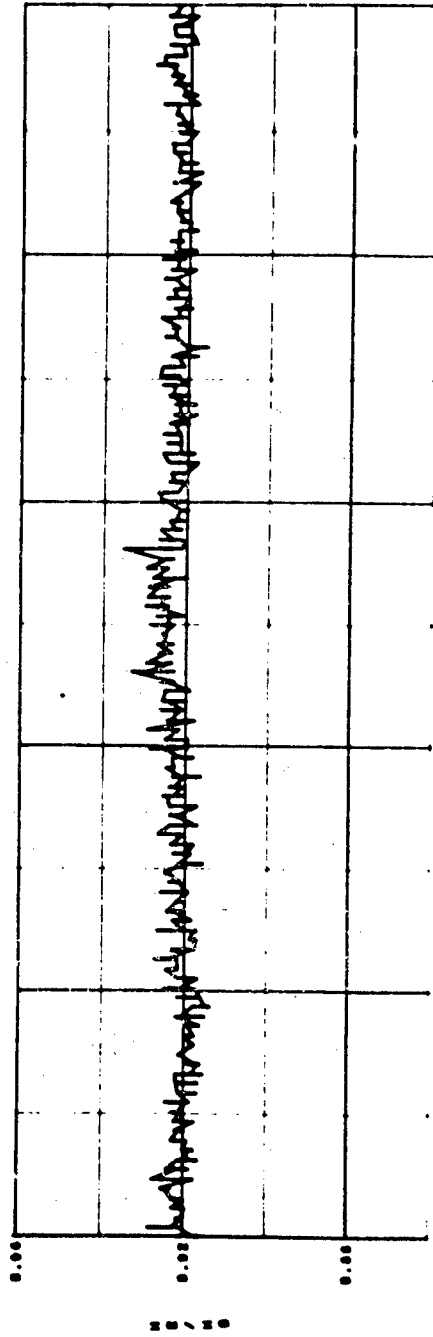


Figure 15

HIGH RESPONSE INLET DATA FOR SECOND CONE ANGLE DECREASE - 2.2 M₀

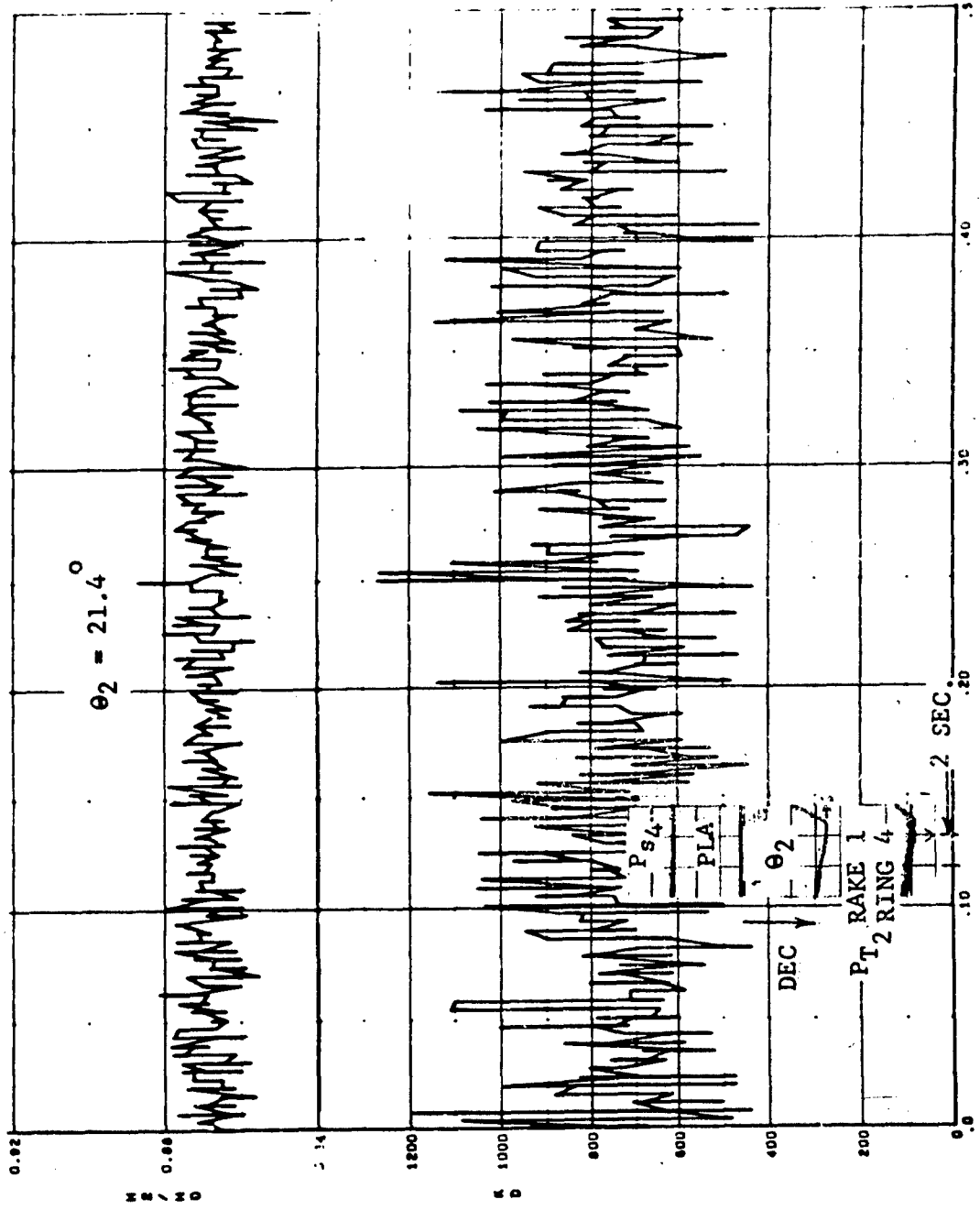


Figure 16

COMPRESSOR FACE PATTERN FOR SECOND CONE ANGLE DECREASE - 2.2 M₀

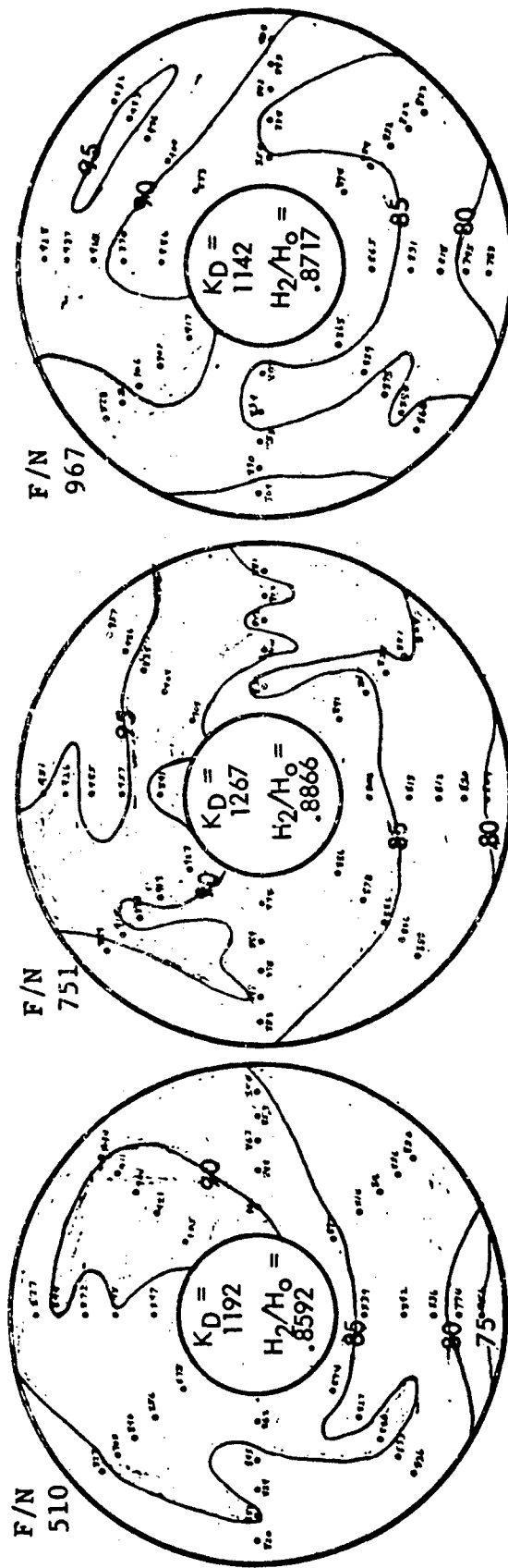


Figure 17

POWER SPECTRAL DENSITY CHANGE FOR SECOND CONE ANGLE DECREASE - 2.2M₀

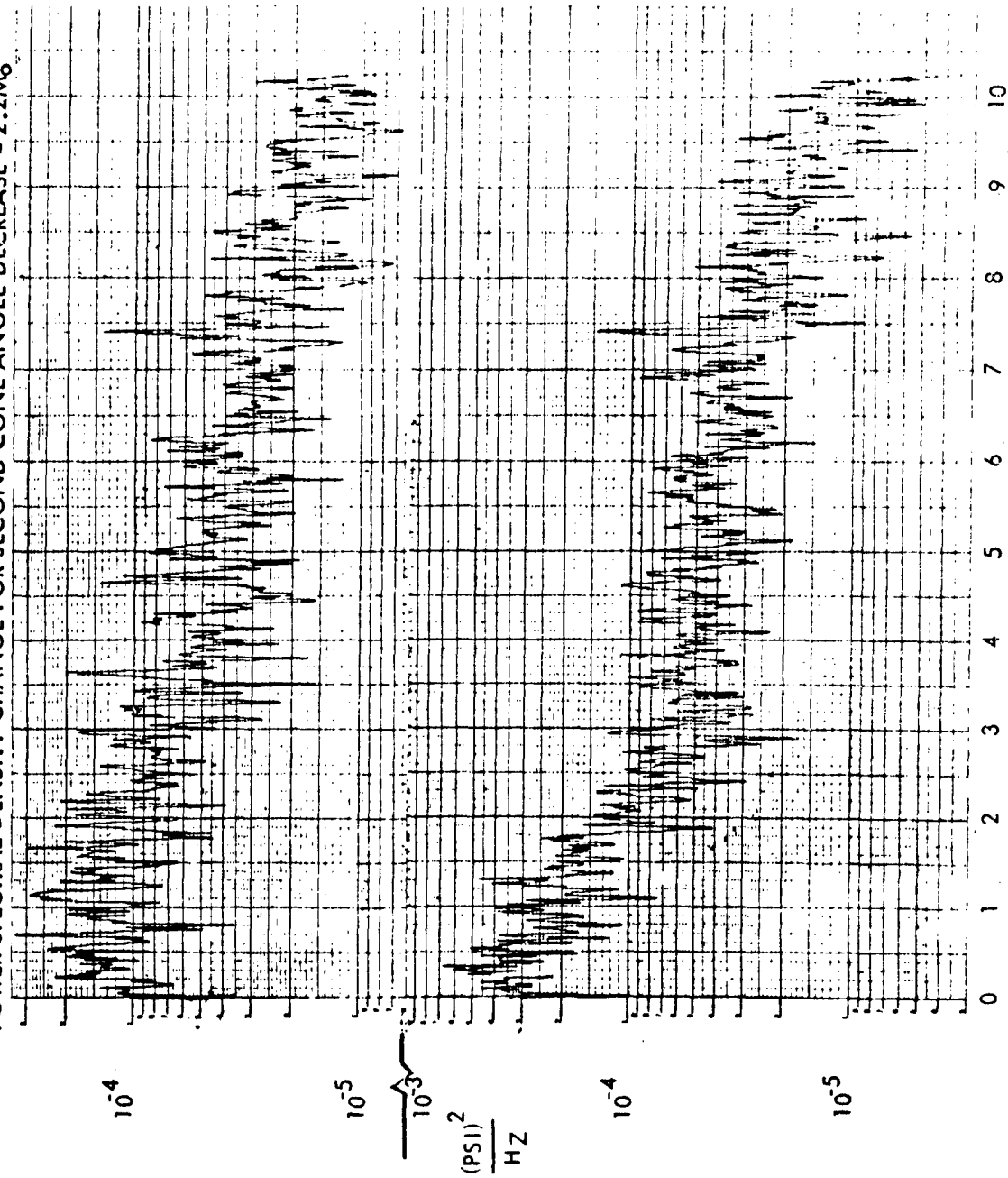


Figure 18 $HZ \times 10^{-2}$

PRMS CHANGE WITH SECOND CONE ANGLE DECREASE - 2.2 M₀

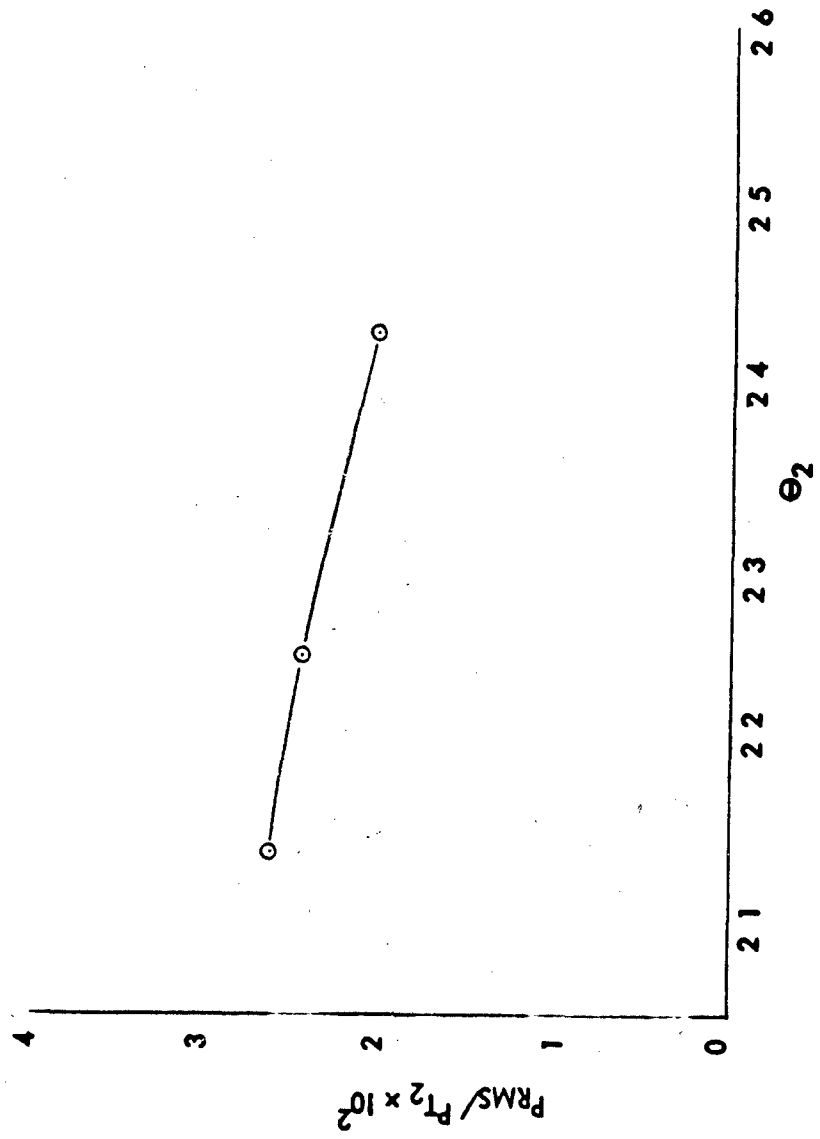
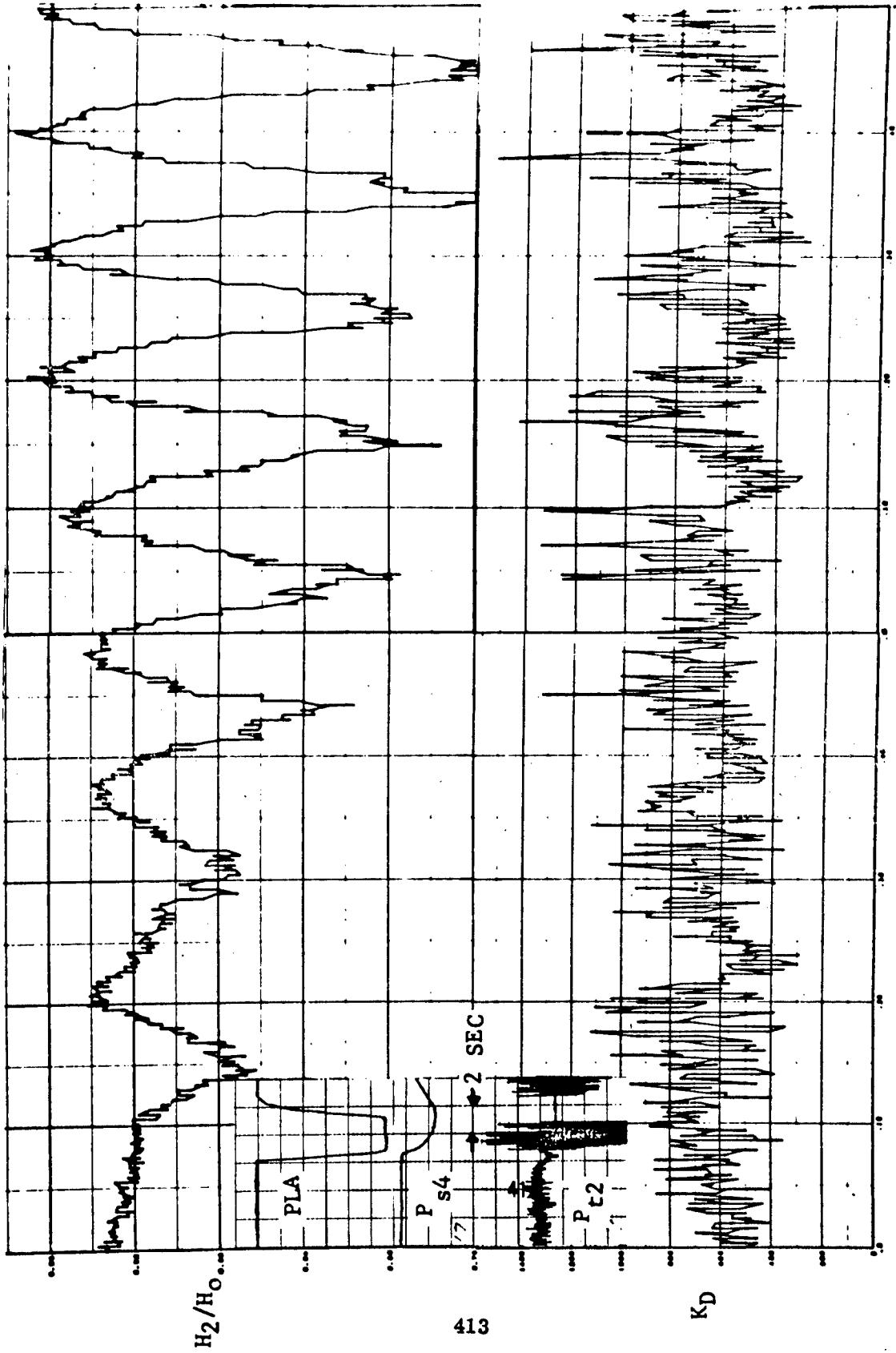


Figure 19

HIGH RESPONSE INLET DATA FOR POWER LEVER RETARD AT 2.2 M₀ AND 14.5° α



413

Figure 20

INLET STABILITY LIMIT

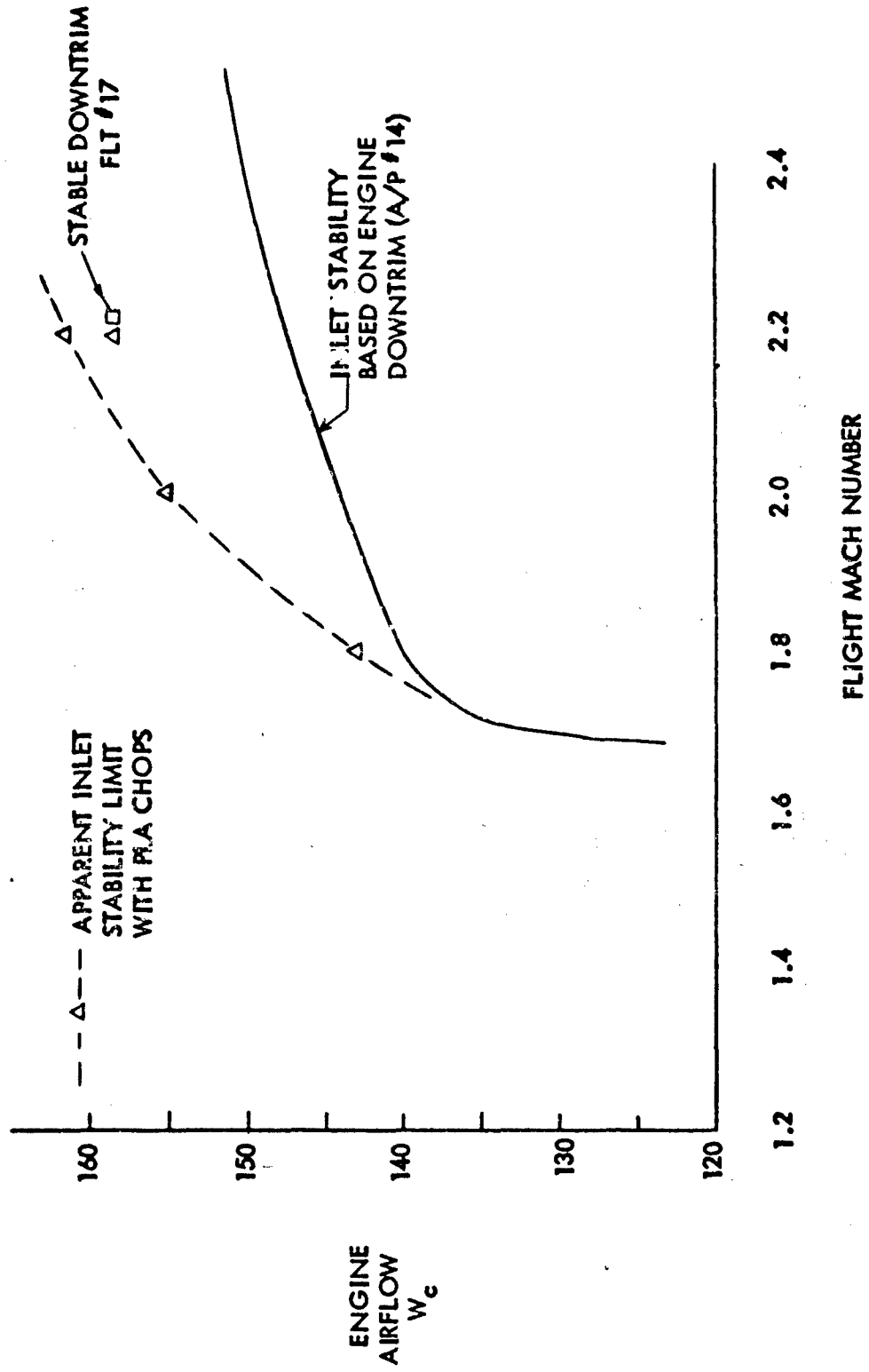


Figure 21

COMPARISON OF DYNAMIC SIMULATOR RUN WITH FLIGHT EVENT - 2.2 M₀

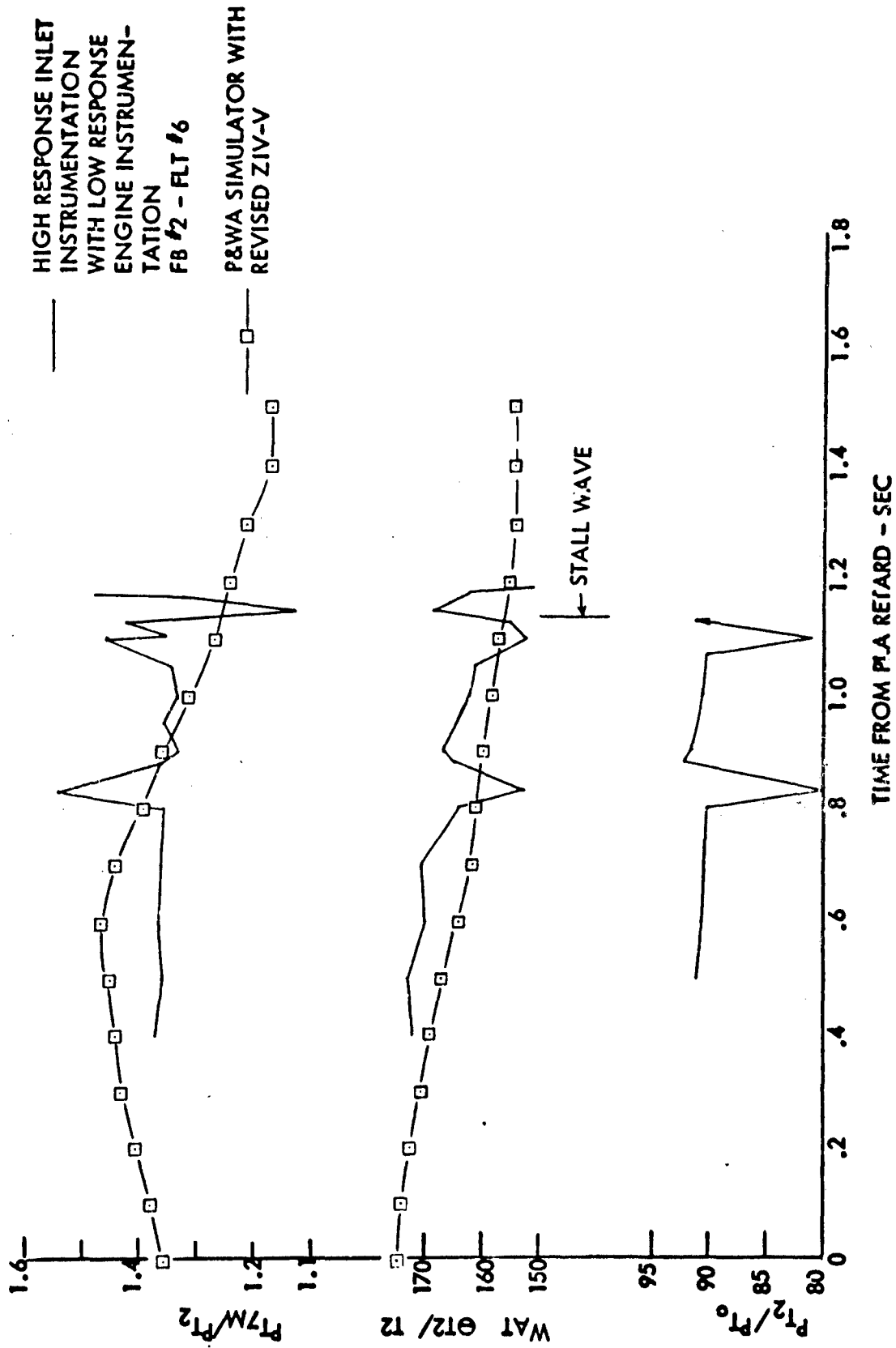
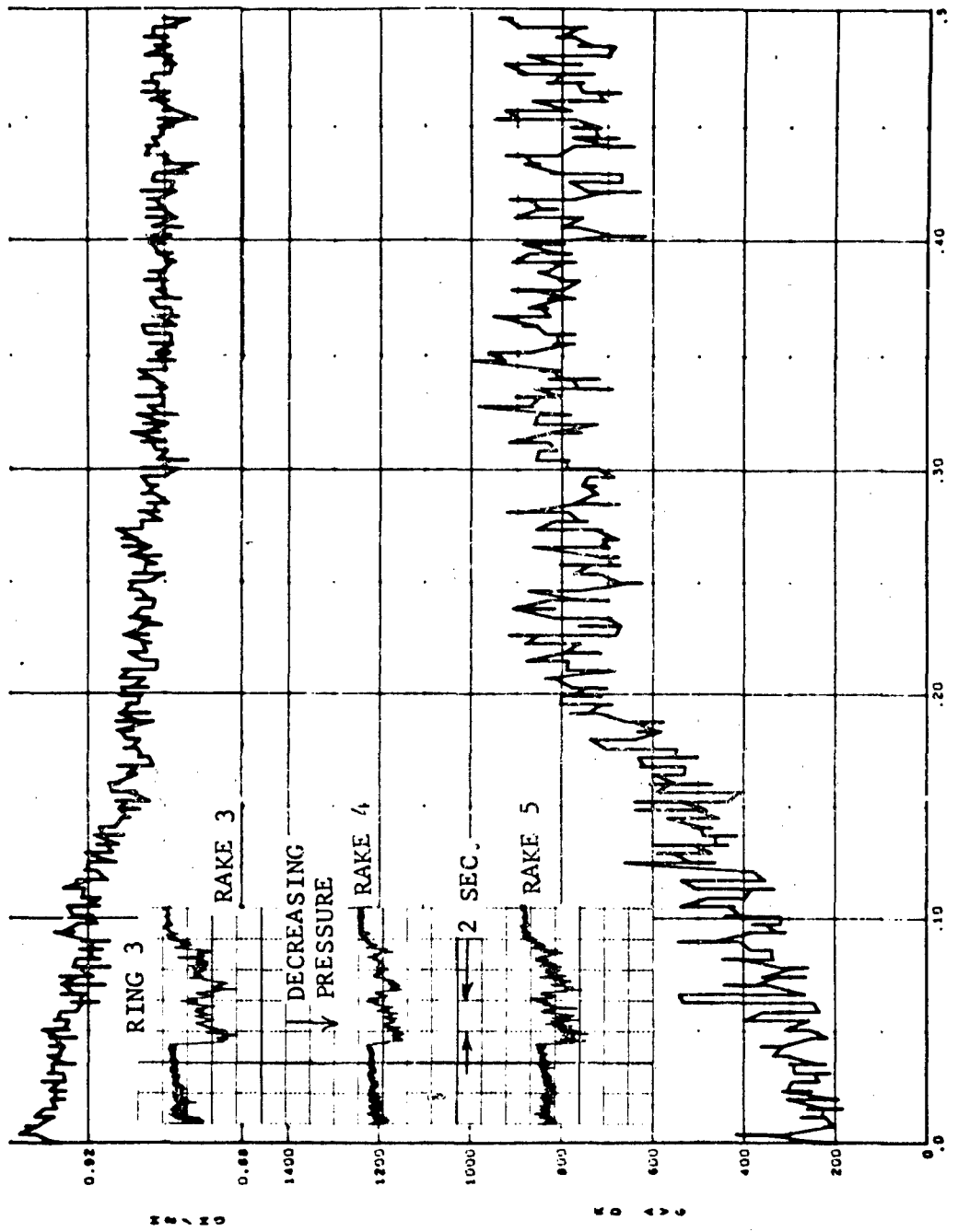


Figure 22

HIGH RESPONSE DATA FOR EFFECT OF CLEAR AIR TURBULENCE - 2.0 M₀



TIME-SEC

Figure 23

HIGH RESPONSE DATA FOR EFFECT OF WEAPONS BAY DOORS - 2.0 M₀

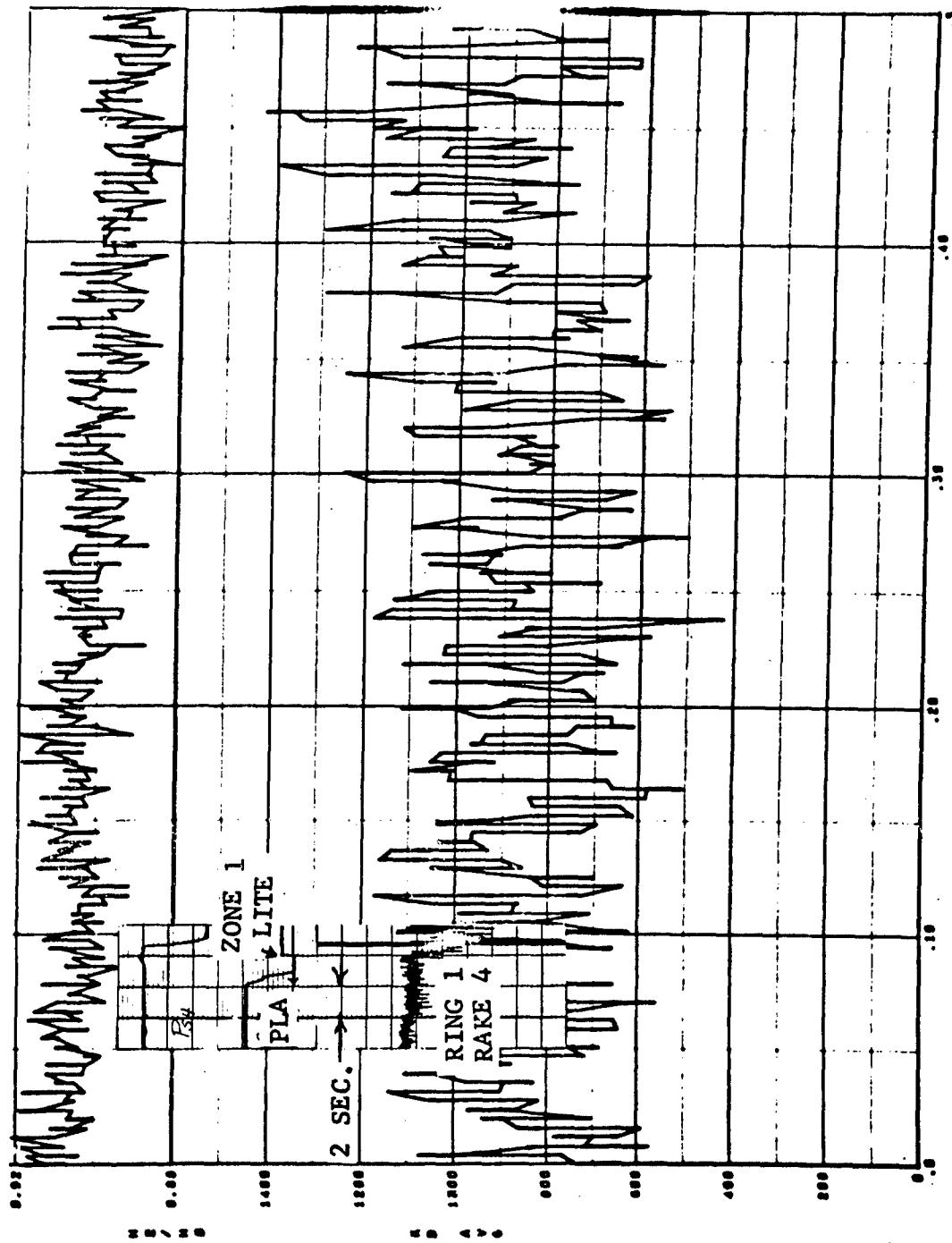


Figure 24

COMPRESSOR FACE PATTERNS FOR WEAPONS BAY DOOR OPENING - 2.0 M₀

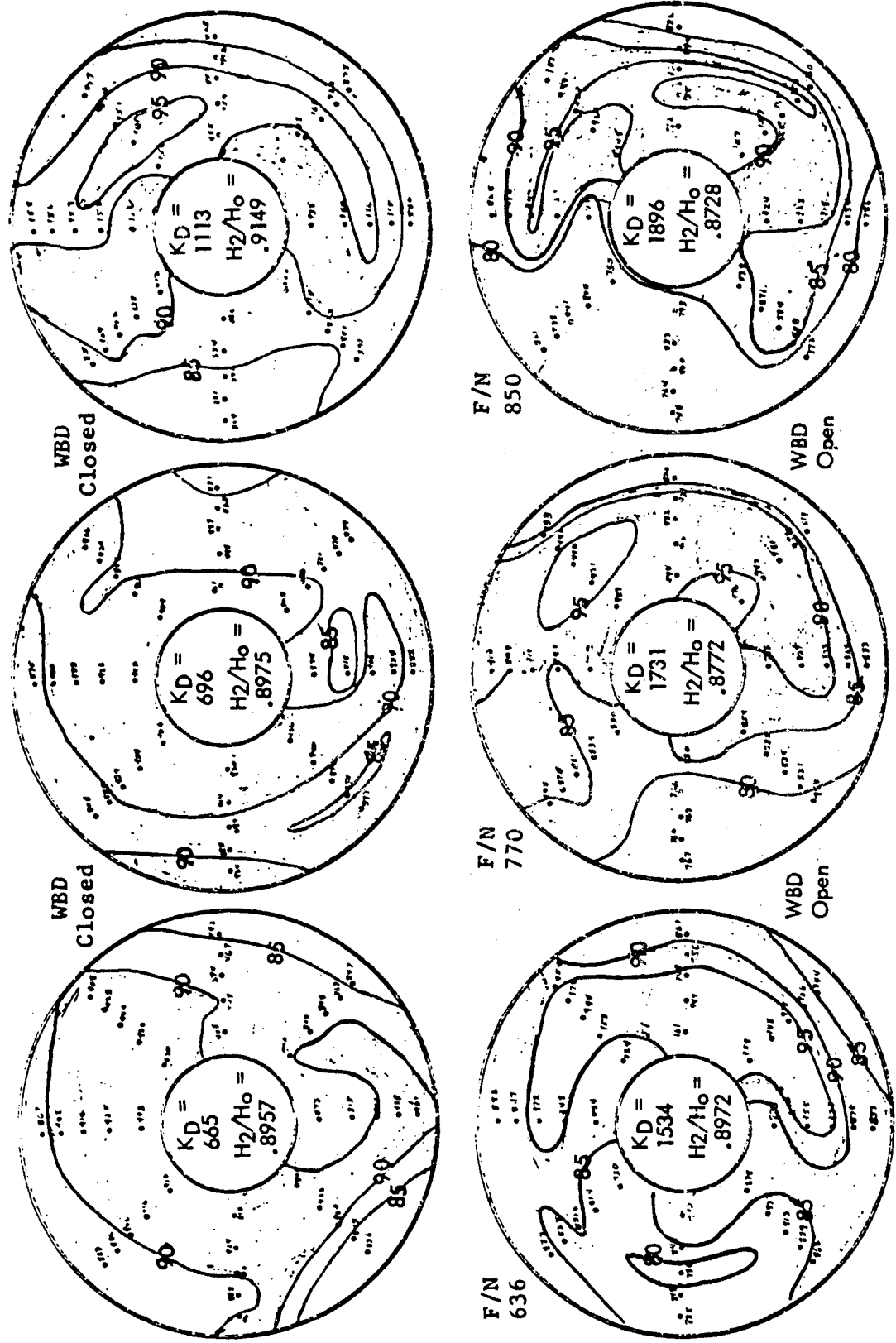


Figure 25

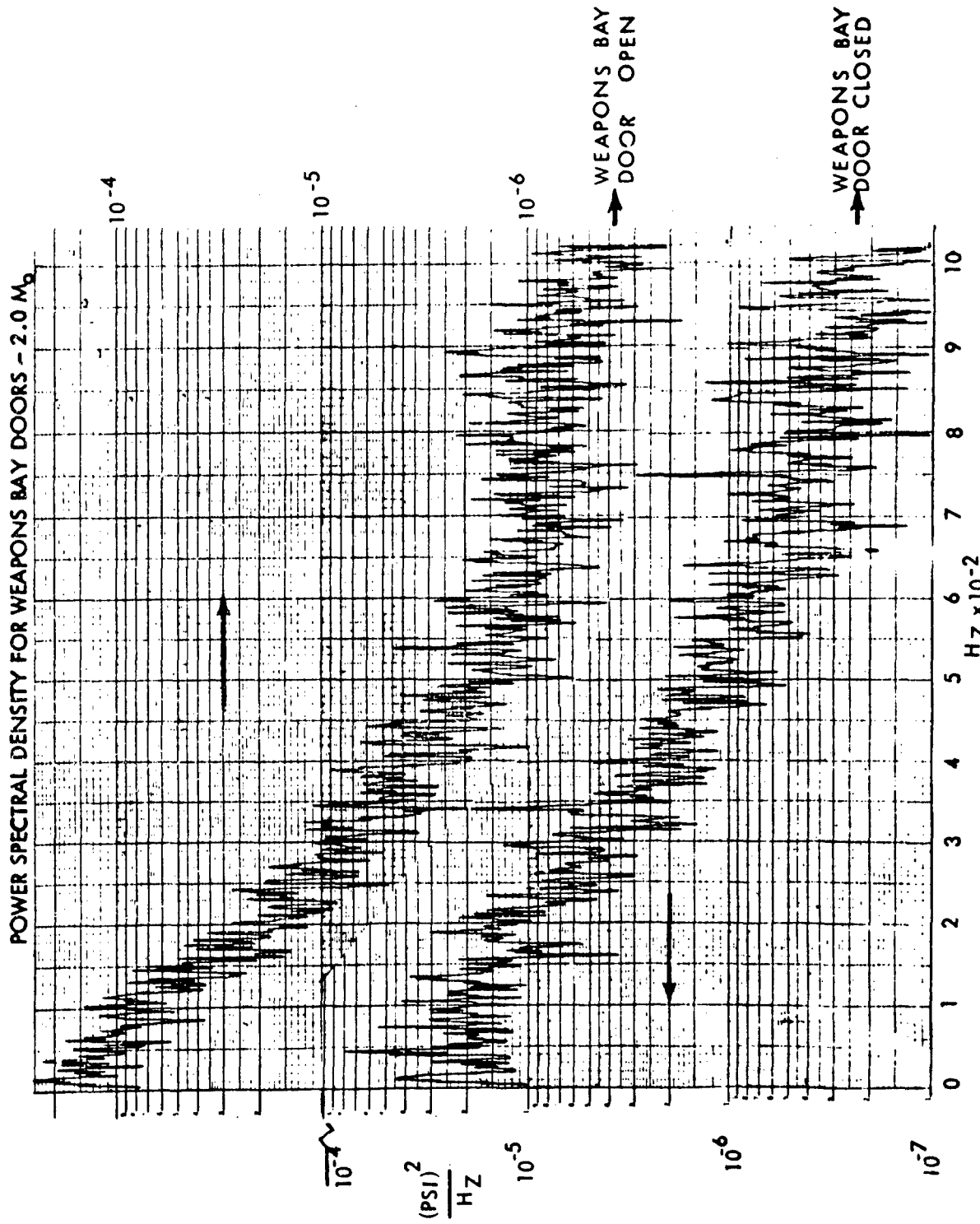
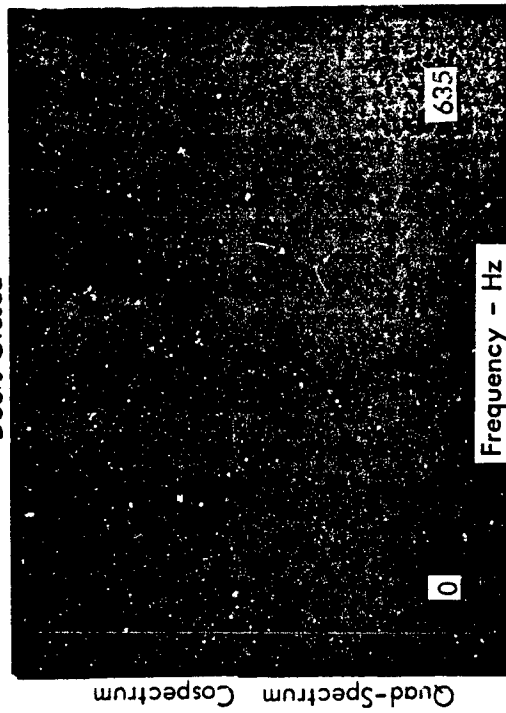
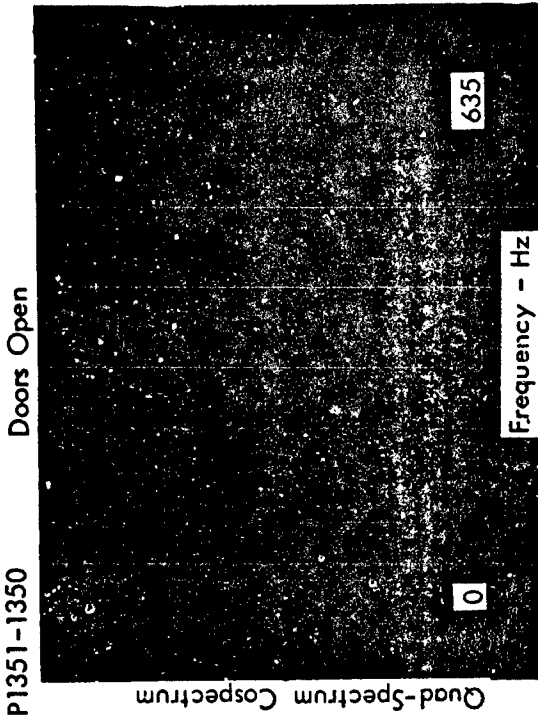


Figure 26

CROSS PSD & CROSS CORRELATION FOR WEAPONS BAY DOOR EFFECTS



420

Cross-Correlation for Probes 1351-1350

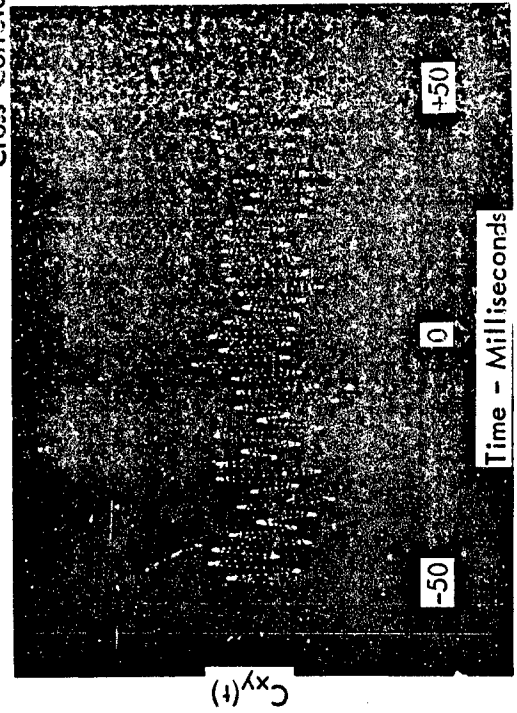
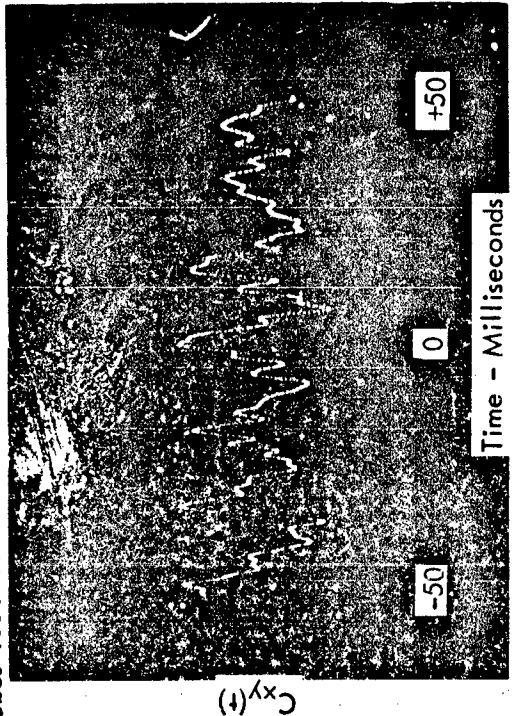
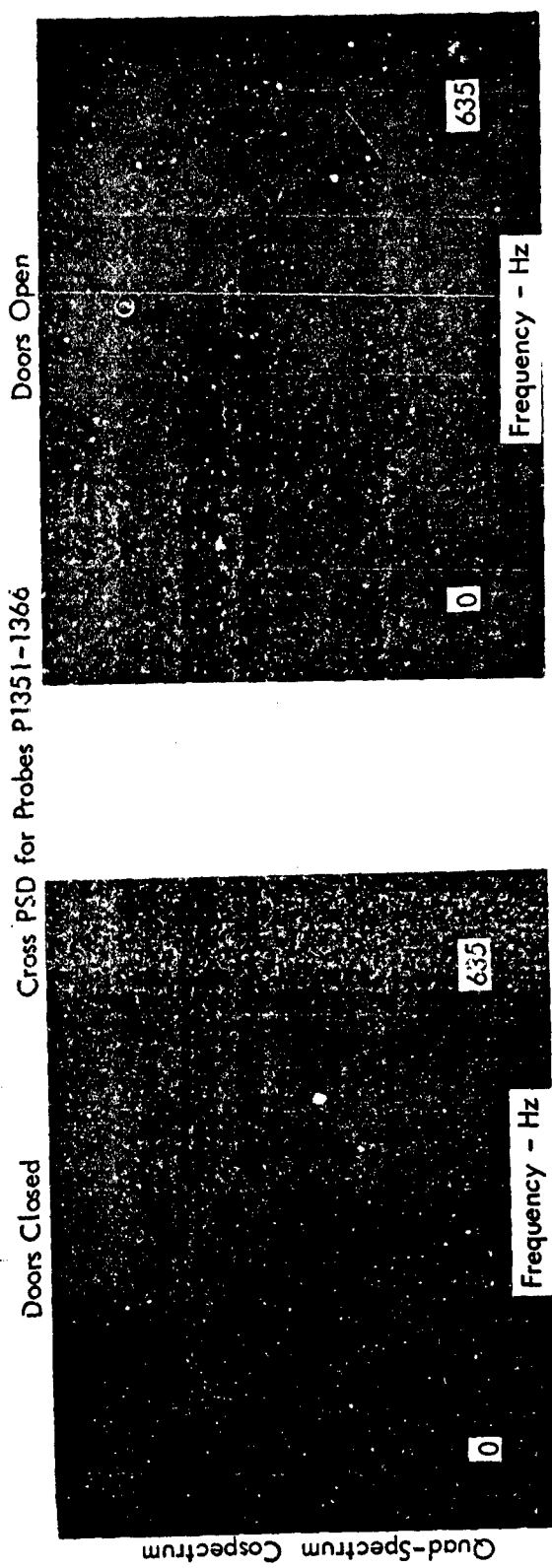


Figure 27 A

CROSS PSD & CROSS CORRELATION FOR WEAPONS BAY DOOR EFFECTS



421

Cross-Correlation for Probes P1351-1366

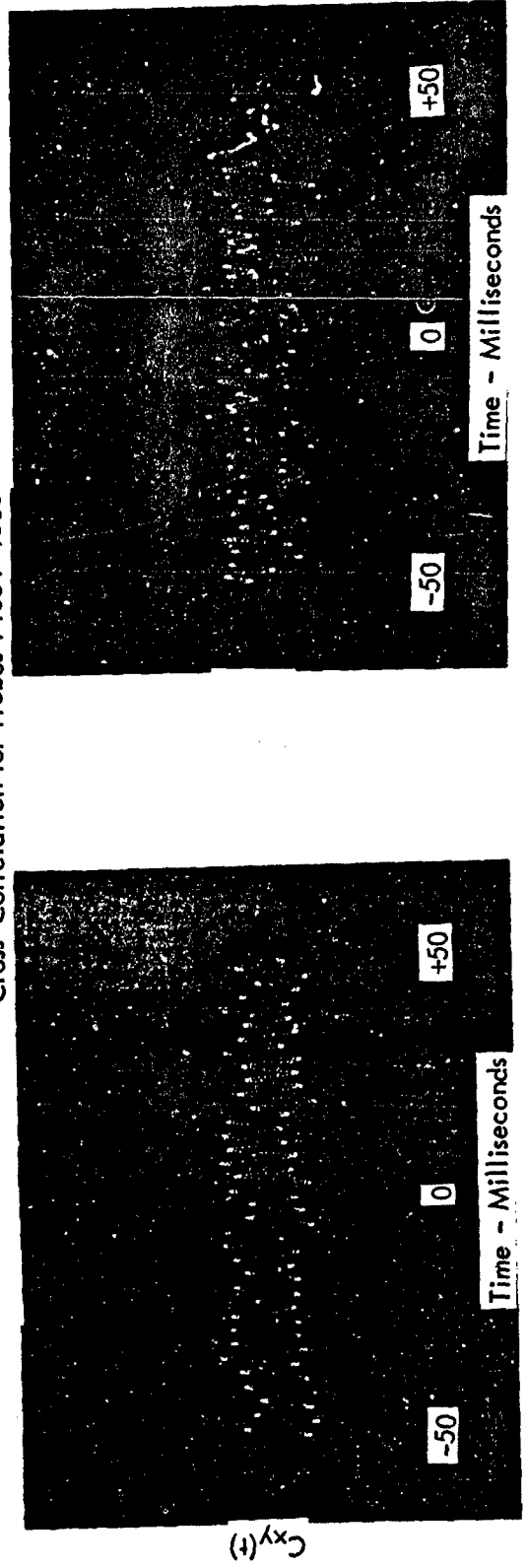
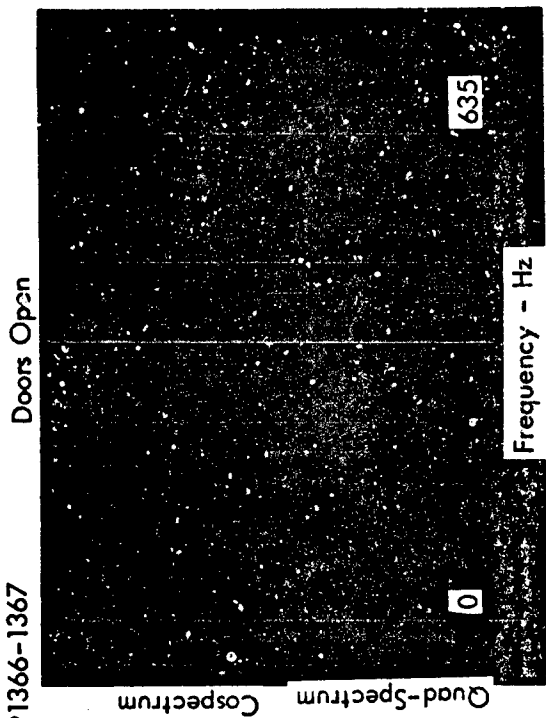
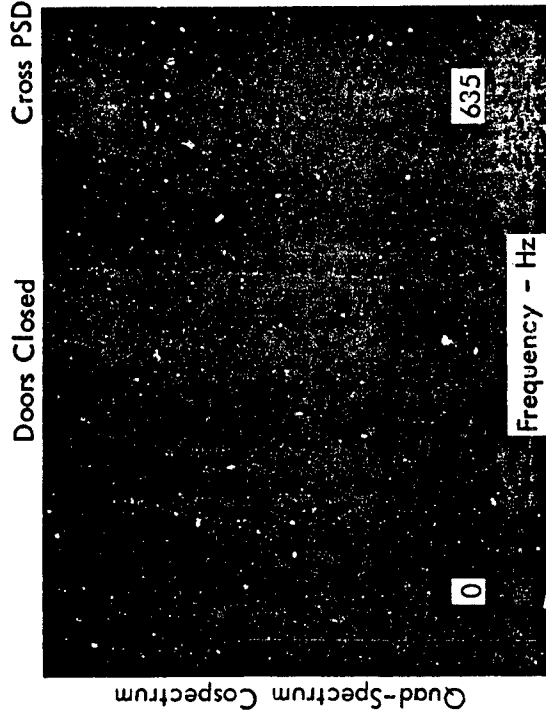


Figure 27 B

CROSS PSD & CROSS CORRELATION FOR WEAPONS BAY DOOR EFFECTS



422

Cross-Correlation for Probes P1366-1367

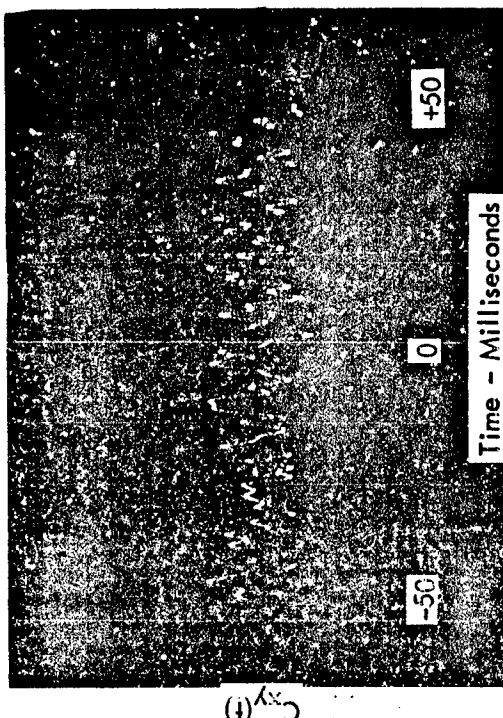
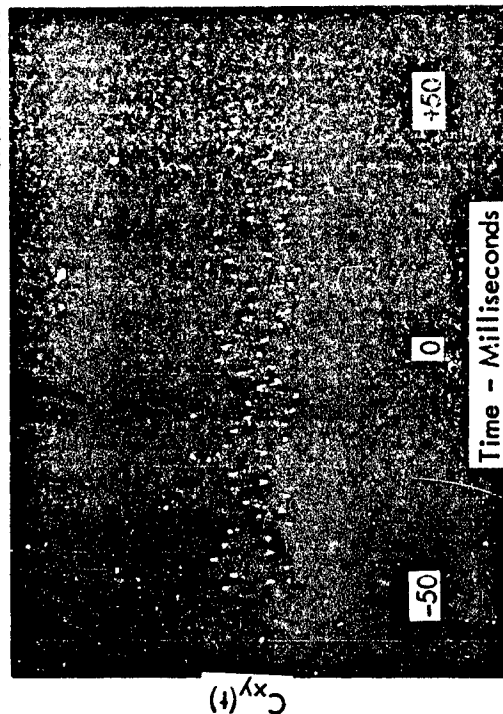


Figure 27C

STEADY STATE INLET DATA FOR MAXIMUM WIND-UP-TURN MANEUVER 2.3 M₀

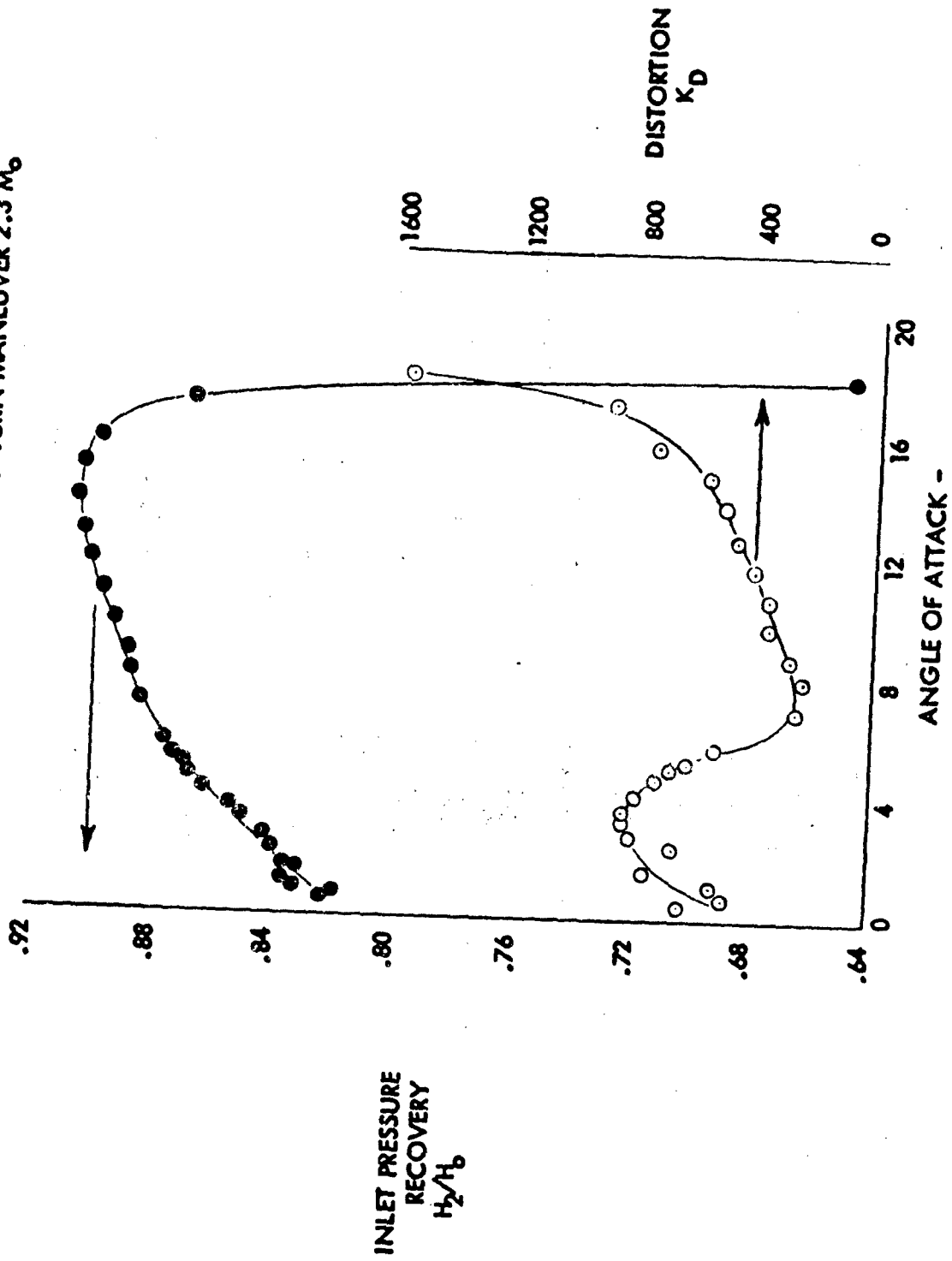


Figure 28

HIGH RESPONSE DATA FOR MAXIMUM WIND-UP-TURN MANEUVER - 2.3 M₀

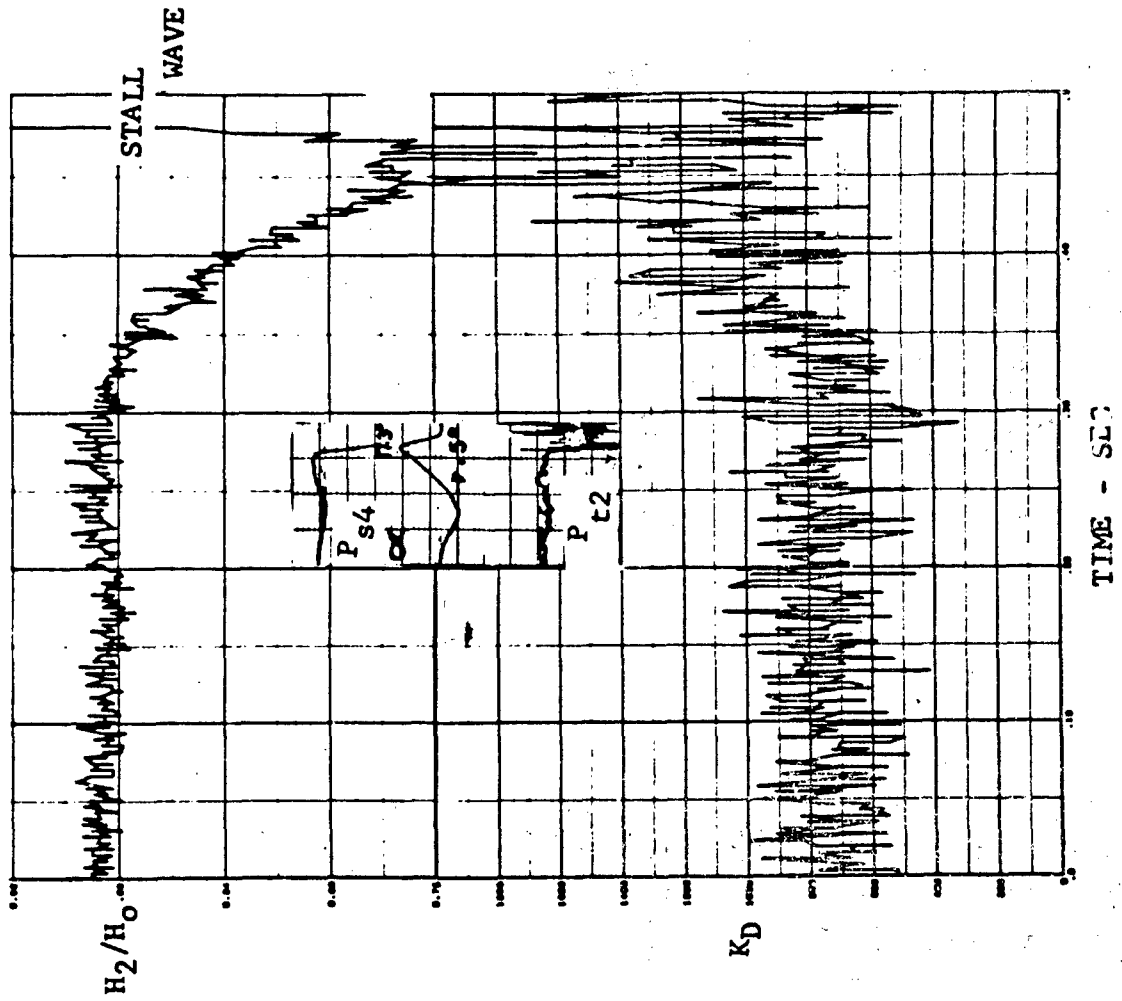


Figure 29

COMPRESSOR FACE PATTERNS FOR MAXIMUM WIND UP TURN - 2.3 M₀

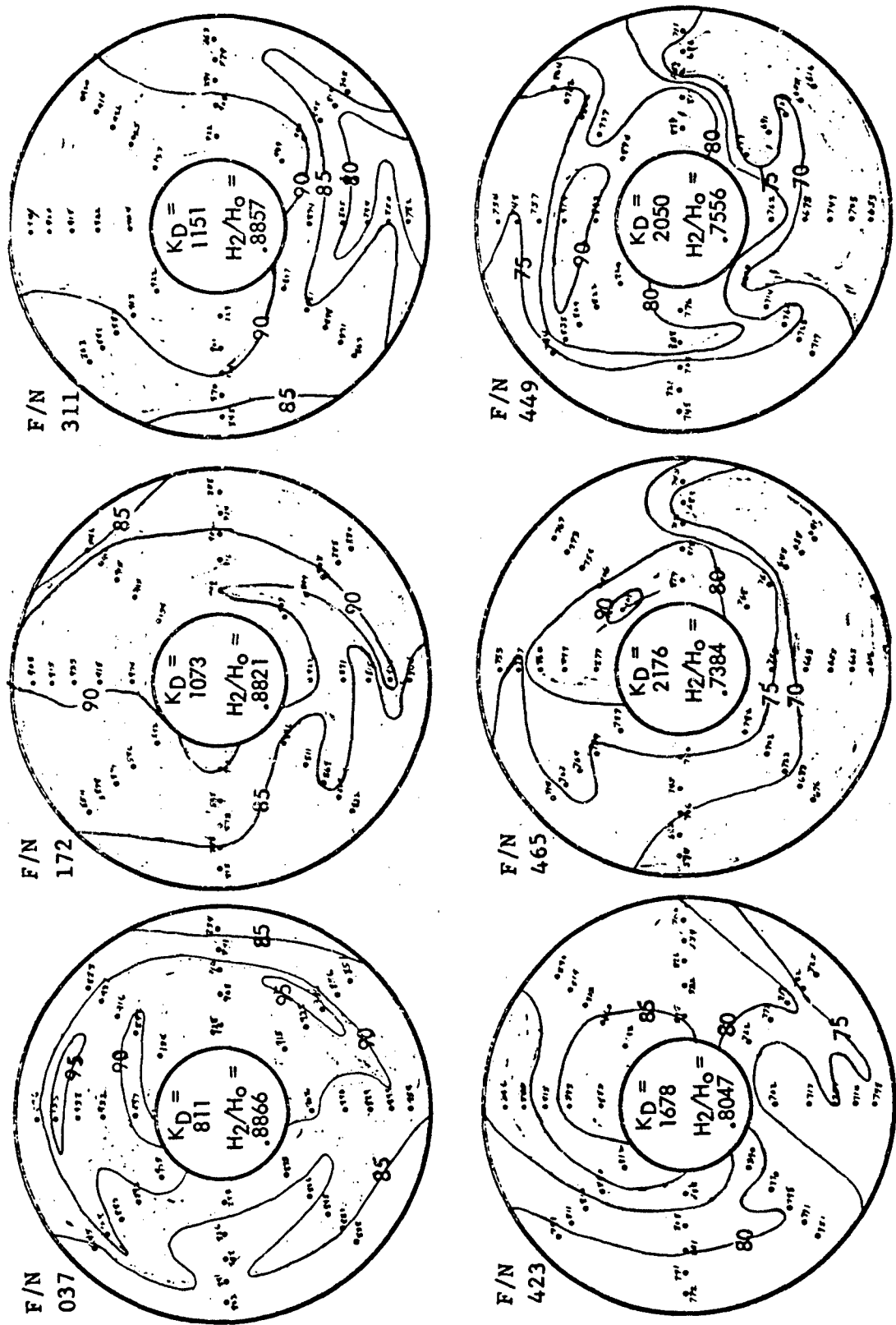


Figure 30

EXPERIMENTAL STUDY OF
INLET-GENERATED PRESSURE
FLUCTUATIONS

PWA-3682

Gordon C. Oates+
Dale A. Sherman*
David L. Motycka±
Pratt & Whitney Aircraft Division
United Aircraft Corporation

Abstract

The amplitude and frequency characteristics of the stagnation pressure fluctuations in a diffusing duct with a shock wave system were studied to assess the problem of turbulence in aircraft air intakes. The rate of decay of the pressure fluctuations generated in the full size duct was limited by dispersion and not by dissipation, which rendered the engine face turbulence intensity independent of Reynolds number. A simple procedure allows comparison of turbulence energy spectra between small scale models and full size intakes, providing the decay rate is dispersion-limited. This method is based on the premise that inlet turbulence is created almost exclusively very near the terminal shock wave, which allows estimation of the axial decay of turbulence within a diffuser. An equation was found to collapse decay measurements from a wide range of operating conditions to a single straight line. The results of a study to determine the minimum amount of instrumentation required at the engine face to describe instantaneous total pressure patterns are also presented.

+ Consultant. Assoc. Professor of Aeronautics and Astronautics, University of Washington, Seattle, Washington.

* Analytical Engineer.

± Project Engineer.

LIST OF SYMBOLS

| | |
|----------------|-------------------------|
| E | Energy |
| Hz | Hertz-unit of frequency |
| k | Wave-number |
| L | Length |
| M | Mach number |
| P | Pressure |
| P _t | Stagnation pressure |
| Pr | Prandtl number |
| R | Reynolds number |
| t | Time |
| u | Axial Velocity |

Greek Symbols

| | |
|----------|-----------------------------------|
| γ | Ratio of specific heats C_p/C_v |
| Δ | A change in value |
| ρ | Density |
| ω | Frequency |

Subscripts

| | |
|----------|--|
| 0 | Initial or reference value |
| u | Farthest upstream measuring station |
| i | Intermediate measuring station (at start of constant area section) |
| 2.0 | Compressor face station |
| ∞ | Conditions at infinity |
| ref. | Reference value |
| S | Static |

I. INTRODUCTION

Experience with aircraft operating in the Mach 2 to Mach 3 flight regime has revealed that fluctuations in inlet total pressure, which occur primarily due to shock wave-boundary layer interactions, effectively add to steady-state inlet total pressure distortion and can cause turbojet and turbofan engines to surge. It is therefore important that dynamic inlet total pressure patterns be measured and understood to ensure inlet-engine compatibility.

Some of the earliest experimental work on inlet turbulence was carried out at AEDC,^{1,2} Tullahoma, Tennessee. In these tests, a convergent-divergent duct produced turbulent inflow for a YJ93 turbojet engine operating at static conditions. The test results showed that ground-based simulation of some basic characteristics of the turbulence produced during flight was feasible. The engine was found to drift into surge at steady-state distortion levels considered acceptable for engine operation without turbulence. The primary conclusion was that compressor surge margin decreases with increasing turbulence level and that engine variations (closing forward stators, opening primary nozzle, etc.) which increase steady-state surge margin will increase the engine tolerance to turbulence.

Since the AEDC tests, many other similar experiments, both full scale and model scale, have been conducted^{3,4,5,6}, but many fundamental questions about turbulence remain unanswered, including "How do we scale turbulence from model to full size?", and, "How does turbulence decay within an inlet?"

The study described herein combines well-documented concepts from the theory of homogeneous turbulence with experimental results from inlet turbulence testing at Pratt & Whitney Aircraft in order to suggest answers to the above questions. Ultimately, it is the instantaneous distortion patterns which must be scaled; however, this is not within the scope of this paper.

Some of the important conclusions of the study are:

- The rate of decay of turbulence within both subscale models and full scale inlets is primarily limited by dispersion rather than by dissipation.
- As a consequence, the decay of inlet turbulence intensity will be independent of the inlet Reynolds number over a very broad range of Reynolds numbers. This simplifies the scaling of turbulence energy spectra.

- A simple procedure was developed which successfully correlated the decay behavior of turbulence within an inlet over a very wide range of operating conditions.
- An investigation into the minimum number of probes required to describe engine face distortion indicated that strongly circumferentially-distorted instantaneous total pressure patterns can be adequately described by steady-state and instantaneous total pressure measurements from 6 rakes containing 3 probes each.

II. DESCRIPTION OF TEST EQUIPMENT

The entire test program was conducted at the Andrew Willgoos Turbine Laboratory at Pratt & Whitney Aircraft in a compressor rig altitude test stand. The inlet air was supplied at pressures up to 44 inches HgA and as low as 10 inches HgA. The turbulence generator duct (Figure 1) was used to produce random pressure fluctuations at the compressor inlet. The turbulator (turbulence generator) comprised a converging-diverging section with a plug centerbody followed by a constant area section which fed the flow into the engine compressor. The centerbody could be moved axially (to control minimum flow area) and up or down (to adjust plug centering and to change the steady-state distortion pattern at the compressor face). The compressor used for these tests was a Pratt & Whitney Aircraft TF30-P-3 fan and low-pressure compressor, which consists of nine axial flow stages.

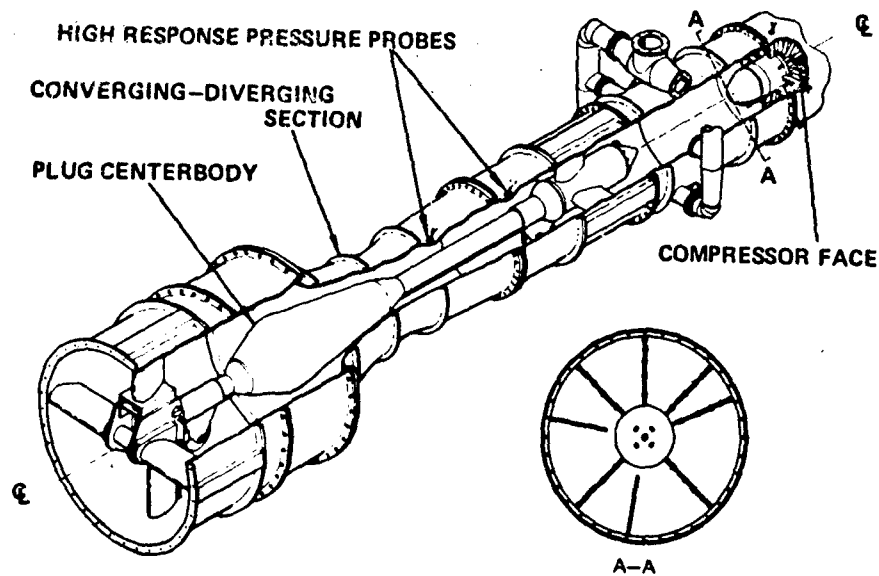


Figure 1 Turbulence Generator

The turbulator was instrumented with both low response (steady-state) probes and high response (dynamic) probes. The steady-state instrumentation included static pressure taps along the walls of the converging-diverging section for determining position and strength of the shock wave. Two rakes, each with five steady-state stagnation probes, were located just ahead of the compressor face at about 180° and 270° clockwise from top dead center, as shown in section A-A of Figure 1. The other six rakes were designed to contain both low response (0-40 Hz including pneumatic system) sense tubes for measurement of steady-state stagnation pressure and high-response Kistler miniature pressure transducers for measurement of fluctuations in stagnation pressure. These transducers maintain 1% linearity out to 25 KHz. Two of the high response probes were capped off during all testing in order that the contributions of probe vibration and electronic background noise to the overall signal could be evaluated. Figure 2 shows a photograph and a cut-away drawing of the specially-designed rakes. The signals from both the low response transducers and the high response transducers were recorded with a magnetic tape recorder operating in the FM multiplexed mode. The linear phase gain characteristic of the tape recorder was down 3 db at 1000 Hz.

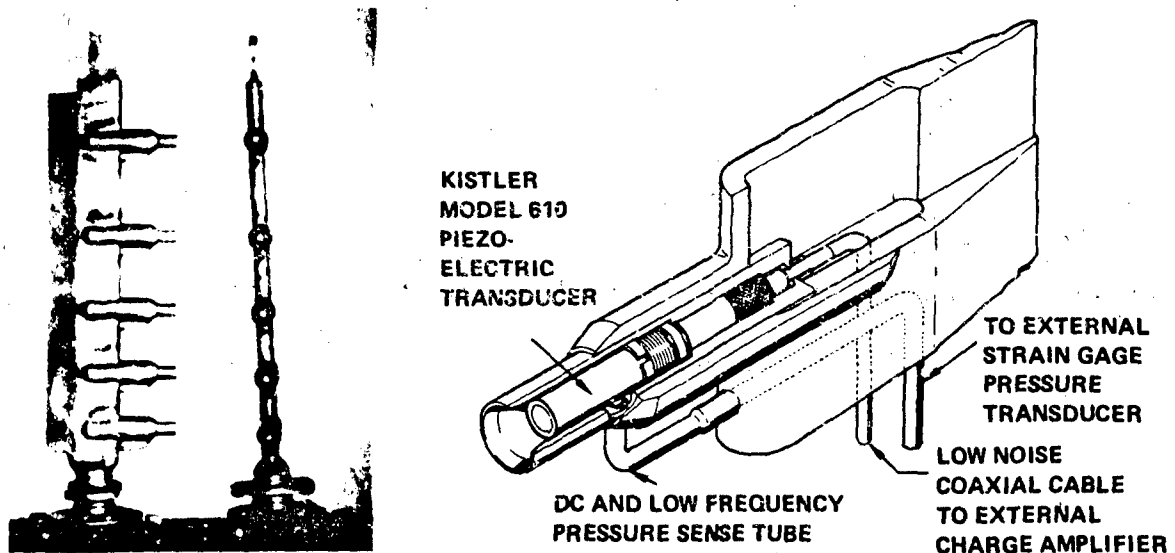


Figure 2 High Response Inlet Rake and High Response Total Pressure Probe

In order to study the decay behavior of turbulence, two high response Kistler miniature transducers were installed between the throat section and the compressor face. These probes, which measured fluctuating stagnation pressure, were located 1 foot 4 inches and 3 feet 6 inches downstream from the minimum

diameter of the converging-diverging section. The total distance between the minimum diameter and the compressor face was 13 feet 6 inches, and there were thus three stations for measurement of fluctuating pressure between the region of generation of turbulence and the compressor face.

III. DESCRIPTION OF TIME VARYING FLOWS

A. Statistical Terms

The description of flow at an engine face utilizing the concept of distortion has been long established. Until fairly recently, the distortion was considered as being time invariant and was generally represented by distortion maps wherein the stagnation pressure at the engine face was presented as a function of location. Recently, of course, the phenomenon of inlet-generated turbulence has been recognized, and with it the necessity of describing the engine face distortion as a function of both time and position. Conceptually, the easiest representation of such time variant flows is to consider the distortion as composed of the steady state component superimposed with a turbulent component. It is the turbulent component with which this paper is concerned, though it is clear that it would be difficult indeed to produce "pure turbulence" or "pure steady state distortion".

Like the steady state distortion, the turbulence can be mapped at the engine face to give lines of constant turbulence intensity. It is usual to represent such turbulence intensity in terms of the root mean square (r.m.s.) value of the fluctuating component of stagnation pressure measured at each point. As in Figure 3, the total distortion is then related to the sum of the steady state and turbulence distortion maps.

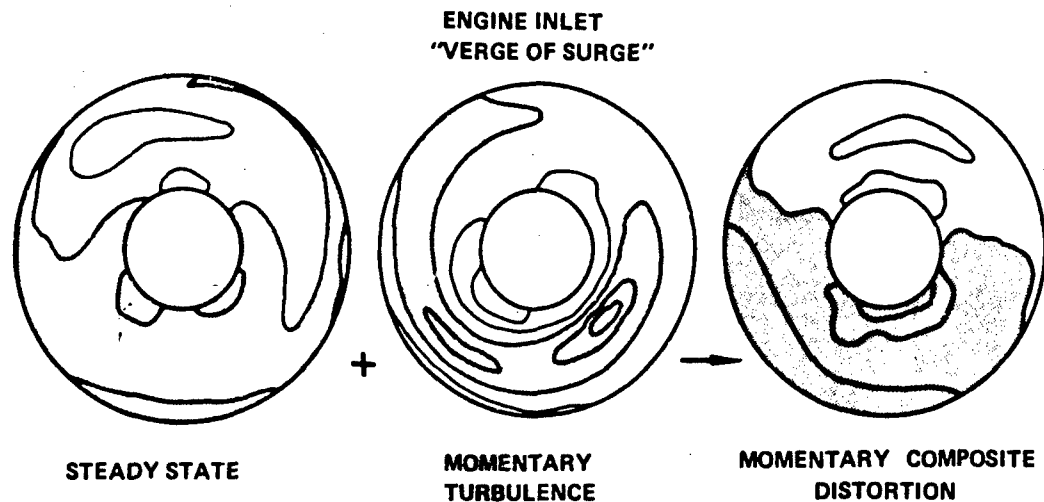


Figure 3 Construction of Momentary Distortion Map

It is evident, however, that we must be content with the distortion "to be expected" because the turbulent process is a random one. The most efficient representation of the turbulent component hence utilizes statistical concepts. The most frequently used statistical functions are the power spectral density (P.S.D.) and amplitude probability density function (A.P.D.) These two functions are defined in many references⁷ in both their normalized and un-normalized forms. It should be recalled that the P.S.D. represents the r.m.s. value, squared, per cycle per second of the variable being considered, so that the integral over all frequencies of the P.S.D. is equal to the total r.m.s. value squared, i.e.,

$$\int_0^{\infty} (\text{PSD}) \, d(\text{Hz}) = \int_0^{\infty} \frac{(\Delta P)^2}{\text{HZ}} \, d(\text{Hz}) = (\Delta P_{\text{rms}})^2$$

The great utility of the P.S.D. representation is that if "energy" is concentrated at or near particular frequencies, such concentrations appear as "spikes" on the P.S.D. graph, and the generating mechanism is hence often easily determined.

A possible P.S.D. is represented in Figure 4. In this case, the spike existing at ω_s would indicate the presence of an energy concentration at that frequency. Such spikes often result from energy being concentrated at natural resonances of the system, but great care must be taken to ensure that such spikes are not spuriously introduced because of resonances in the instrumentation system.

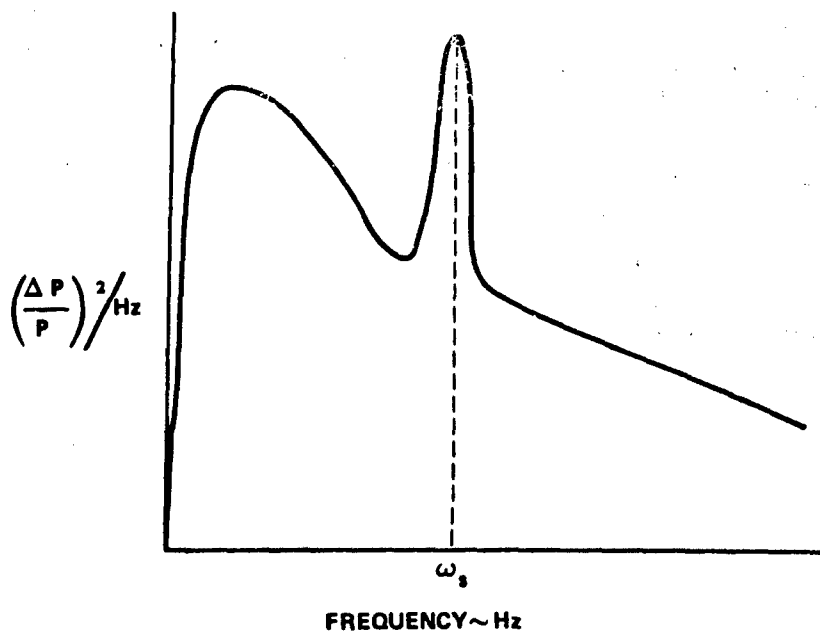


Figure 4 Example of Typical Power Spectral Density

The A. P. D. represents the probability of occurrence of a given amplitude at any given time. The Central Limit Theorem⁸ states that the A. P. D. for a variable that results from a succession of random events can be expected to approach a Gaussian distribution. Inlet turbulence occurs with many successive collisions of the turbulent "eddies", so, as expected, most A. P. D. 's observed for engine face turbulence do closely approach the Gaussian distribution (Figure 5).

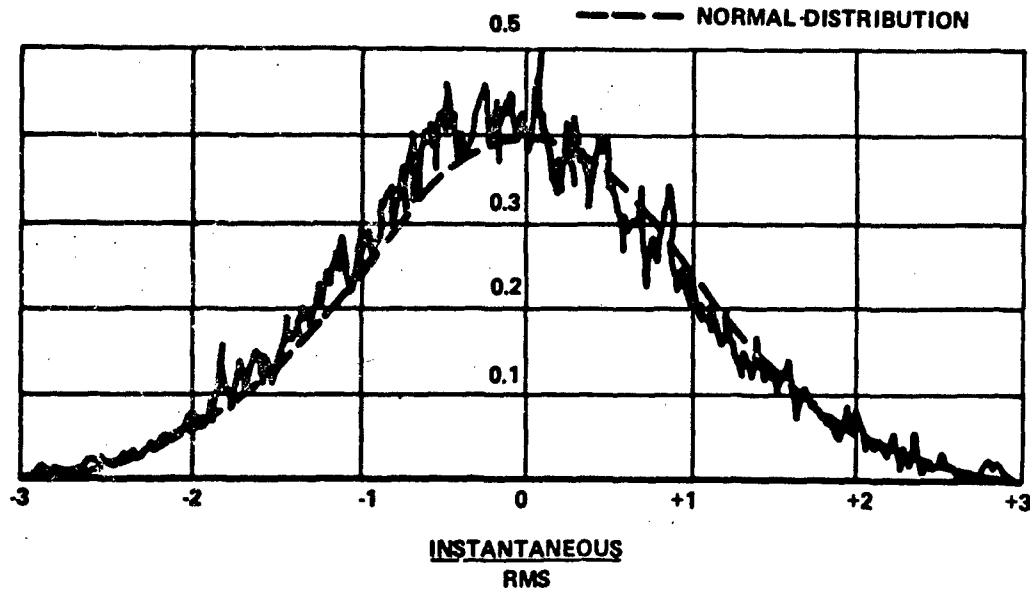


Figure 5 Amplitude Probability Density, Compressor Face

B. Some Aspects of Dynamic Similarity

The requirements for dynamic similarity have been developed in several books on fluid mechanics^{11, 12, 13}. The reasoning behind the various developments is that if the equations and boundary conditions describing the physical problem at hand can be written in terms of dimensionless variables, and the length, time, etc., scales of the model are so chosen that the equations and boundary conditions are exactly the same from model to model, the "solution" of the equations must be the same in the dimensionless variables. Usually, of course, the solution is not available analytically, but must be obtained experimentally.

For scaling purposes we first consider the full time-dependent Navier Stokes equations, postponing for the present any representation of the time-variant effects such as the introduction of turbulent transport coefficients, etc. For the case considered here, where the flow is adiabatic, gravity is unimportant,

and the walls of the duct are rigid, it follows that, in addition to geometrical similarity, four scaling parameters must be preserved between model and full scale device: the Reynolds number (R), the Mach number (M), the Prandtl number (Pr), and the ratio of specific heats (γ).

If these four parameters are maintained constant, the equations describing the flow will be preserved, but attention must be paid to the inlet and exit conditions in order to ensure that the boundary conditions can also be scaled. At the inlet, we must acknowledge the presence of turbulence by requesting that the root mean square of the time variant portion divided by the mean value of all quantities be preserved. Inlet turbulence intensity must also be preserved.

Finally, if the scaling is to be rigorously correct, the time-varying conditions at the exit must be scaled. It is the time variation (or frequency) which makes turbulent distortion unique, so it is instructive to consider what aspects of the time dependence might be of particular significance to the engine compressor. It is apparent that energy concentrations could occur at certain natural frequencies of the inlet duct^{9, 10}. In a recent experimental program¹¹, a scale model inlet with a simulated engine face and an empty volume in place of an engine was used to study inlet turbulence. Evidence of a standing wave was observed in the duct with a frequency corresponding to the distance between the inlet throat and the choke plane of the flow control plug at the downstream end of the engine volume. With an engine installed, the standing wave might have terminated at the engine face. A choke plate at the simulated engine face could also have been used to terminate the standing wave at the engine face station and thereby preserve the proper organ pipe frequency.

It is evident that for inlet model tests with air, the scaling requirements will be generally satisfied if the Mach and Reynolds numbers are conserved and, in addition, the inlet turbulence intensity and compressor face conditions are conserved. (Rigorously, simulation of compressor face conditions might require a scaled compressor; but unless a detailed analysis of the interaction between compressor and inlet natural frequencies is required, a choked screen simulation will suffice.) Unfortunately, it is rarely possible to conserve all these parameters, so an effort must be made to relate model results to full scale results by utilizing additional analytical or empirical information. In supersonic inlets, the majority of the turbulence intensity is created in the shock-boundary layer system, and as a consequence, description of the subsequent decay behavior is central to our understanding of the behavior of the scaling laws when the Reynolds number is not conserved. For this reason, the decay of turbulence will be discussed rather extensively in the next section.

IV. DECAY OF TURBULENCE

A. Dispersion vs. Dissipation

It is very important to be careful in the use of the terms decay, dispersion, and dissipation because considerable confusion can arise if the terms are used interchangeably.

- DECAY is the decline in magnitude of the turbulence kinetic energy
- DISPERSION is the spreading of the turbulence kinetic energy over the range of wave numbers by inertial interaction of the eddies
- DISSIPATION is the process by which the action of molecular viscosity actually converts the kinetic energy of the turbulence to heat.

In general, the minimal information required in order to describe a turbulent "eddy" would be some measure of the eddy size and some measure of its energy. (Here energy is measured relative to a frame moving with the average fluid velocity). A very useful description of the state of the fluid averaged over a suitable time would then consist of an "energy spectrum", where the average energy occurring for each characteristic size would be given. In practice, rather than giving the energy versus a characteristic "size", it is usual to use either the energy per frequency versus frequency (Power Spectral Density) or to use the energy per wave number versus wave number (Energy Spectrum Function vs. wave number). For a fluid in which turbulence is no longer being produced but is only decaying, the equation for the energy-spectrum function $E(k)$ is:^{14, 15}

$$\frac{\partial E(k)}{\partial t} = T(k) - 2 \frac{\mu}{\rho} k^2 E(k) \quad (1)$$

In this equation the term $T(k)$ represents the net increase in energy per wave number per time arising from the fact that energy at wave numbers other than $k \rightarrow k + dk$ is transferred into $k \rightarrow k + dk$ by collision, while at the same time energy is transferred out of $k \rightarrow k + dk$ by collision of eddies originally within $k \rightarrow k + dk$. This contribution to the change in energy-spectrum function is the dispersive contribution. It does not involve a net energy loss within the fluid, but only involves the transfer of energy from one wave number to another. As might be expected, it is an extraordinarily difficult task to actually compute the contribution $T(k)$ for any prescribed initial $E(k)$ because the $T(k)$ involves the non-linear interaction of all wave numbers from zero to infinity. Qualitatively one may note, however, that with time we usually expect a "spreading out" of energy amongst the wave numbers due to dispersion. From the equipartition principal, there is not an a priori reason for the energy to favor a particular energy spectrum; therefore, the energy will tend to become equally distributed amongst the wave numbers. It is important to note, also, that since the dispersive terms involve only the transfer of energy from one wave number to another,

the total change in energy due to $T(k)$ measured over all wave numbers will be zero. That is

$$\int_0^{\infty} T(k) dk = 0 \quad (2)$$

Integrating Equation 1, it then follows that

$$\frac{\partial}{\partial t} (\text{TOTAL ENERGY}) = \frac{\partial}{\partial t} \int_0^{\infty} E(k) dk = -2 \frac{\mu}{\rho} \int_0^{\infty} k^2 E(k) dk \quad (3)$$

Looking now at the term $-2 \frac{\mu}{\rho} k^2 E(k)$, we see that it represents the rate at which the molecular viscosity ρ changes the turbulent energy over to heat. This term, the dissipative term, gives the rate at which the mechanical energy per wave number actually leaves the fluid. Its integral, (Equation 3), gives the total rate of change of energy of the fluid.

Figure 6, reproduced from Reference 18, shows the inter-relationship of the various terms for an example turbulent flow. In this case, the energy is introduced at low wave numbers and is dispersed to higher wave numbers where it dissipates. In this particular example, the production of turbulence is shown as being equal in magnitude to the dissipation, so the decay would be zero.

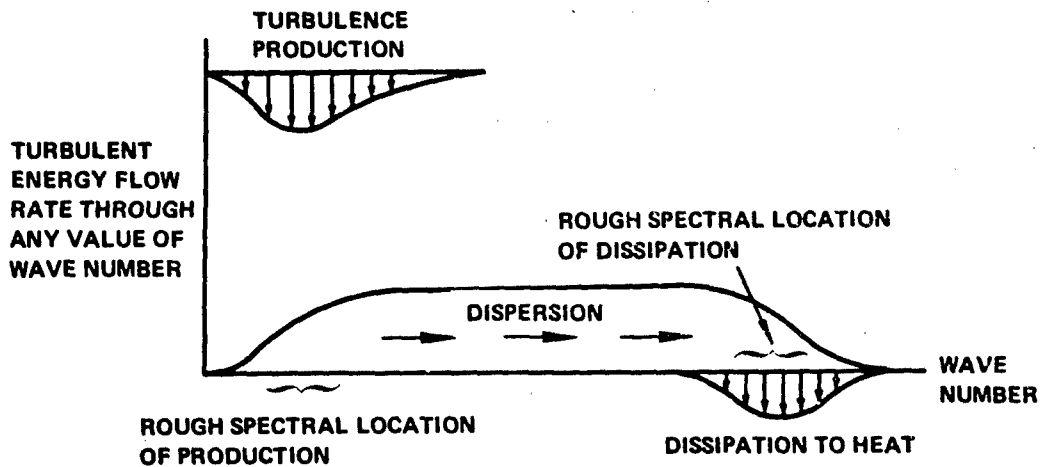
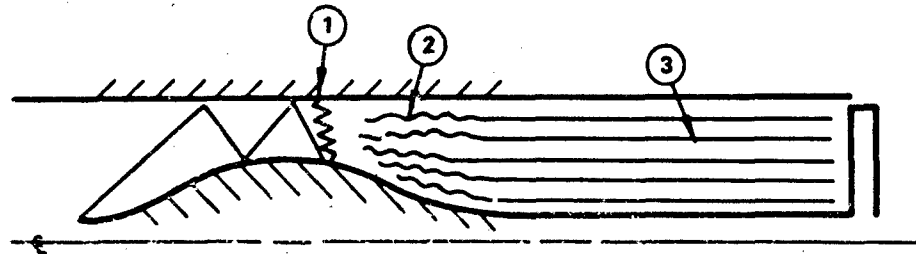


Figure 6 Production and Decay of Turbulence

Because of the relative simplicity of such flows, many studies^{16, 17} have been carried out to investigate the behavior of turbulence in a fluid in which there is no creation of turbulence, but only decay. The simplest of such flows

is that with "isotropic turbulence" (turbulence with properties that are independent of direction). The decay behavior of isotropic turbulence has been well documented with respect to its dependence on wave number (see Reference 15 pages 188 and 191), and it is useful to interpret the classical findings for conditions of interest to us. Wave number can be related to frequency through the "G. I. Taylor Criterion" $k = \frac{2 \pi \omega}{\bar{U}}$, where \bar{U} is the average convective velocity of the turbulent flow field and it is large compared to the turbulence velocity. For convenience, the term "frequency" will be used instead of "wave number".

In Figure 7, a typical inlet flow is divided into three flow regimes. In region (1), which consists of the normal shock system with the associated shock-boundary layer interactions, regions of very high shearing exist which lead to the vigorous production of turbulence. In region (2), some further turbulence production may occur, particularly if the diffuser is badly separated. In addition, the turbulence created will tend to become isotropic and to settle down to the high rate of decay characteristic of turbulence. (Reference 14, Page 136).



- ① SHOCK SYSTEM - REGION OF HIGH TURBULENCE PRODUCTION
- ② DIFFUSING PORTION - BEGINNING DECAY, TENDENCY TO ISOTROPY, SOME PRODUCTION
- ③ DECAY REGION - MOSTLY ISOTROPIC, DECAY ESTABLISHED, LITTLE PRODUCTION

Figure 7 Regimes of Flow

Finally, in region (3), the turbulence settles down to the process almost characteristic of isotropic turbulence. In this region, the turbulence production is very small compared to the rate of decay. The turbulence in this region, then, approximates that found in the classical grid-generated-turbulence experiments.

B. Dissipation Density

The very complex nature of the system leading to turbulence production in inlets renders the prediction of the turbulence produced (with respect to A. P. D.

and P.S.D.) impossible, so that we must be content with accepting experimental values for the turbulence produced in the inlet. The decay behavior, however, can be expected to approximate that found in the classical grid experiments. A relationship of vital importance involves the frequencies at which the maximum energy $\left(\frac{(\Delta P)^2}{\text{Hz}}\right)$ and the maximum dissipation density $\left(\frac{\omega^2 (\Delta P)^2}{\text{Hz}}\right)$ occur. If these two maxima occur at widely separated frequencies (that is, if the "energy containing eddies" are separate from the region of maximum dissipation), it follows that the decay process can be considered as composed of two separate steps:

- (1) The dispersion of the energy in the energy-containing eddies up to higher frequencies.
- (2) The dissipation of the energy after entry into the region of maximum dissipation density.

The "rate limiting step" then becomes the dispersion to higher wave numbers, because once the energy passes over to the region of high dissipation, it is very rapidly dissipated. This latter result may be inferred from the small amount of energy which usually exists in the region of maximum dissipation for flows with widely separated dissipation density and energy density maxima.

Figure 8 shows some P.S.D.'s and dissipation curves obtained at three axial positions within the test duct. (Note the use of the linear rather than logarithmic ordinate.) It can be seen that a complicated "camel back" P.S.D. has been generated within the shock system. The dissipation curve maximum at this station is not significantly separated from the (second) maximum energy point. At the second station, two feet further down the duct, slight separation of the maxima has begun. It is difficult to say, however, whether these curves represent dissipation and dispersion only, or whether some residual turbulence production exists within the duct. Finally, at the engine face station, twelve feet from the first measuring station, the effects of the dissipation have become very evident, as the maxima of the two curves are widely separated and the energy existing in the vicinity of the maximum dissipation points is very small.

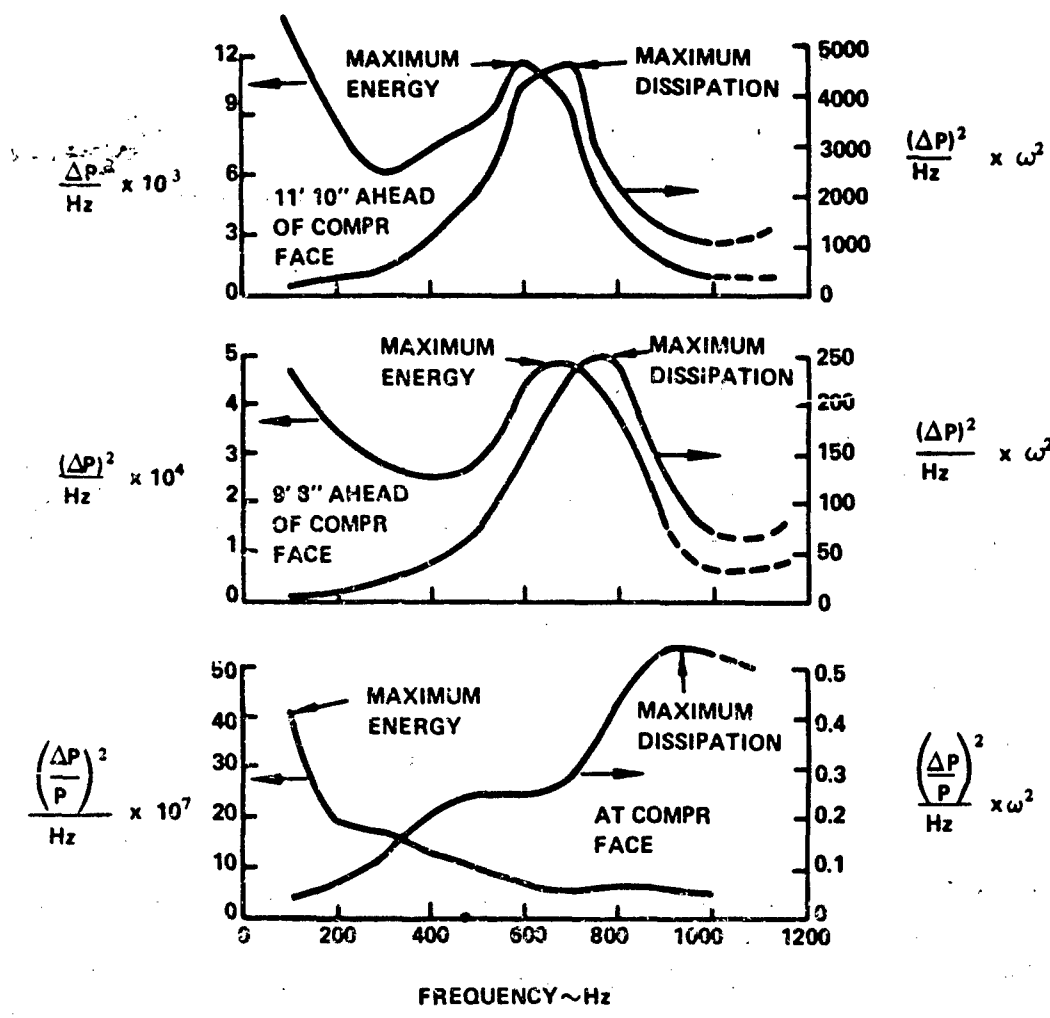


Figure 8 Axial Variation of Energy Density and Dissipation Density

V. IMPLICATIONS FOR SCALING

A. Reynolds Number Dependency

The description of turbulence outlined above has important implications with regard to the scaling of inlet decay data. In order to exemplify this, it is instructive to consider two limiting cases:

- (1) The case where the maximum $\frac{(\Delta P)^2}{\text{Hz}}$ in the P. S. D. is widely separated from the maximum $\left(\frac{\omega^2 (\Delta P)^2}{\text{Hz}}\right)$ in the dissipation density.

In case (1), the rate of decay in total turbulence energy will be limited by the rate of mutual interaction of the turbulent eddies. This rate of interaction will be proportional to the frequency of the eddies, ω , which will itself be inversely proportional to the length scale of the inlet, L . However, the flow time from shock system to engine face is directly proportional to the length, L , for the same Mach number flow. Thus, the number of encounters between eddies will be the same from model to full scale, and the percentage turbulent energy decay should be the same, even though the Reynolds numbers may be different. This situation leads to the often used rule for scaling power spectral densities where $\left(\frac{\Delta P_t}{P}\right)^2 \frac{1}{\Delta \omega} \frac{L_{ref}}{L}$ versus $\omega \frac{L}{L_{ref}}$ or an equivalent pair are used as coordinates.

Figure 9 shows the application of this simple rule to an example 1/12 scale model P.S.D. The predicted P.S.D. for the full scale inlet is obtained by contracting the frequency scale by the factor 12, while amplifying the ordinate values by the factor 12. The energy contained within the fluid is represented by the area under the curve which, of course, stays constant with this scaling procedure. The scaled 1/12 model P.S.D. is compared to an actual P.S.D. from a full size inlet. These inlets are both two-dimensional but are not geometrically similar. Note, however, that the slope of the scaled model P.S.D. curve is roughly the same as for the full size inlet and that the levels are comparable.

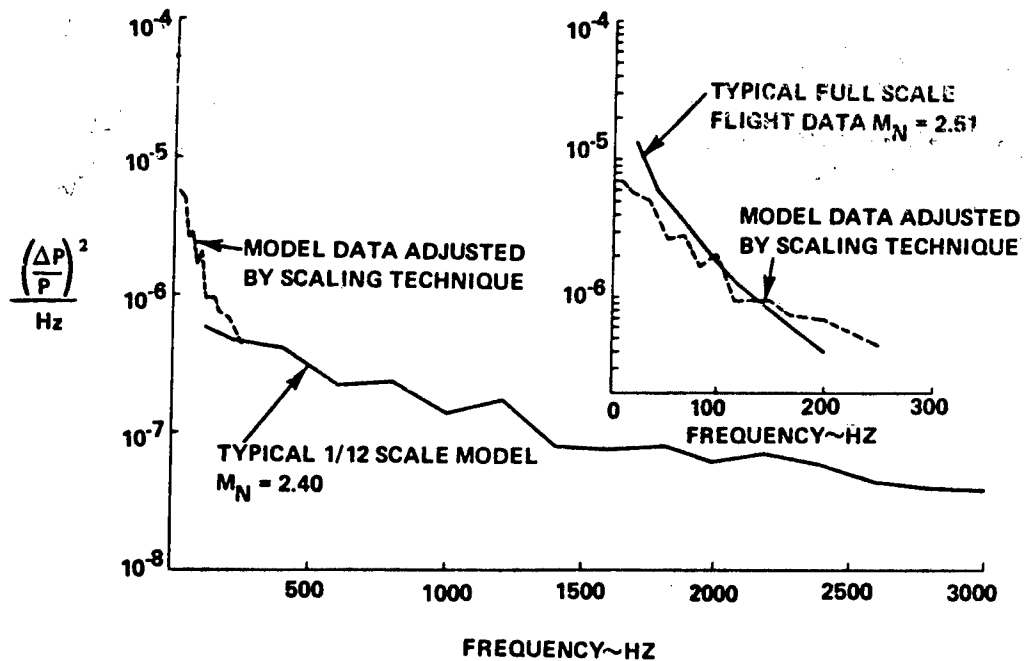


Figure 9 Application of Scaling Technique

- (2) The case where the maximum $\frac{(\Delta P)^2}{\text{Hz}}$ in the P. S. D. is close to the maximum $\frac{\omega^2 (\Delta P)^2}{\text{Hz}}$ in the dissipation density

In case (2), the decay is not limited by the spectral transfer of the turbulence but is instead limited entirely by the dissipation itself, which is, of course, Reynolds number dependent. From Equation 3 it is seen that the decay rate is proportional to the frequency of the eddies squared, with the result that the decay of energy from generation in the shock system to arrival at the engine face will be greater in a sub-scale model than in the full-scale inlet. This means, of course, that sub-scale turbulence tests would give an unduly conservative prediction of turbulence intensity at the engine face.

This result would seem quite ominous from the point of view of interpreting test data if it were not for the result that it appears that the rate of decay of most inlet turbulence seems to be dispersion limited. For example, consider the widely separated maxima at the bottom of Figure 8. Because the high dissipation rate has largely removed the energy density from the higher frequencies by the time the flow has reached the engine face, we know that the decay process is dispersion limited there. The residual effects of the dissipation limited portion of the decay would then be significant only because it had originally slowed the dispersion from the lower frequencies to the higher. We expect this effect to be small, however, because once the energy density begins to drop off with frequency, even slightly, dispersion of energy to higher frequencies becomes dominant. It is possible for turbulence production to favor certain frequencies, in which case the decay rate could be somewhat dissipation limited. Under these conditions, the decay rate would be dependent upon Reynolds number. For the case indicated in Figure 8, however, the dissipation rate corresponding to the peak near 500 cps. is sufficient to reduce the energy density only about 1/10 of that which actually occurs, as calculated from equation 3, indicating that even for this case of "overlapping peaks", the vast portion of the dissipation still occurs at even higher frequencies. Therefore, decay is dominantly dispersion limited throughout the duct, even in the full scale device, so it could be expected to be even more so in a sub-scale model where Reynolds number is lower and more energy is present at high frequencies.

An experiment to verify the turbulence insensitivity to Reynolds number was conducted by carefully adjusting the duct conditions to give equal shock Mach number and reduced engine speed settings at two substantially different Reynolds numbers. As is evident from Figure 10, a remarkable similarity of engine face P. S. D. 's resulted.

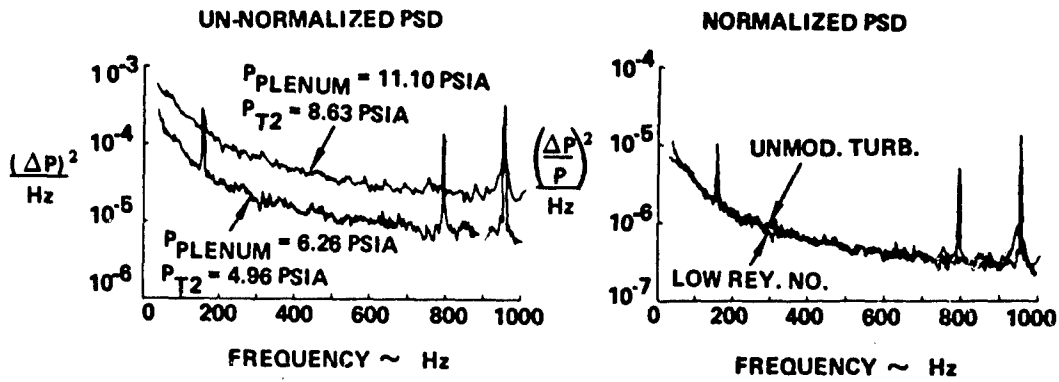


Figure 10 Change in Power Spectral Density with Reynolds Number

A further substantiation of the validity of assuming Reynolds number independence is given in Figure 11 where the results of many model tests are compared to full scale data. Only general trends can be expected here because geometric similarity has not been preserved. However, it is notable that the range of model results is similar to that of the full scale inlet, except for some points where the model data exceeds the full scale data. For at least some of these points, wind tunnel turbulence was high and might tend to account for these differences.

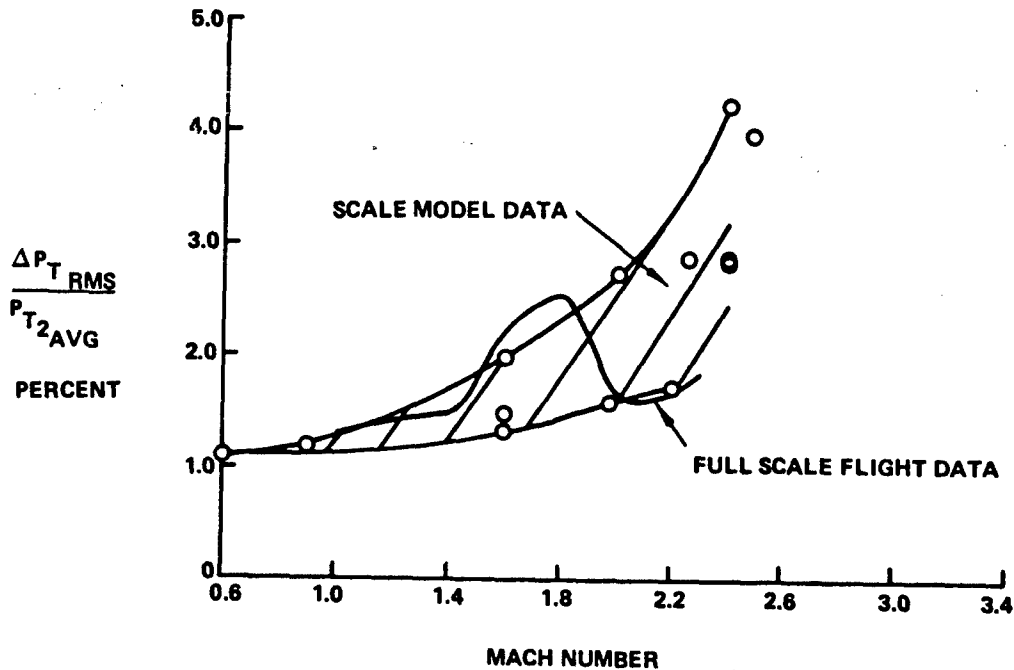


Figure 11 Comparison of Model Data to Full-Scale Data

B. Empirical Correlation of Energy Decay

It has been found^{16,19} from grid experiments that the turbulent energy decays approximately as $U'^2 \propto (t - t_0)^{-n}$ in the "initial period" of decay. The initial period is that period when the turbulence has almost achieved isotropy, but is still dispersion limited. The value of the coefficient n is variously determined as unity¹⁶ or $10/7$ ¹⁹.

The turbulence produced in our tests was certainly not isotropic throughout most of the duct. However, the data of several runs was fitted to a curve of the form

$$\left(\frac{\Delta P}{\Delta P_i}\right)^2 = \left(\frac{t - t_0}{t_j - t_0}\right)^{-n}$$

in the following manner.

From data obtained from the three axial measurement stations, the six curves shown in Figure 12 were plotted. These data led to six non-redundant sets of the empirical parameters P_i , t_0 , n . Selection of an average for the exponent n then led to the plotting of the six sets of data on the single curve of Figure 13. Table 1 lists the values of the parameters obtained for the six tests. In all cases the value of t_0 indicates that the virtual origin was downstream from the terminal shock system itself, which, together with the low value of n ($n_{av.} = 0.45$) indicates that there is probably considerable residual production of turbulence in the early portion of diffuser as well as a time lag before the motion settles down to the high rate of decay characteristic of turbulence.

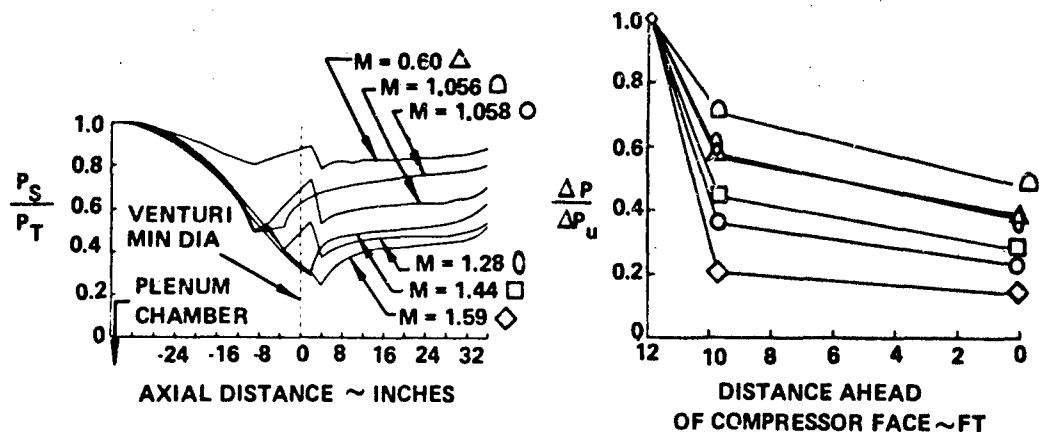


Figure 12 Turbulator Wall Static Pressure Distribution and Axial Decay of Turbulence with Length

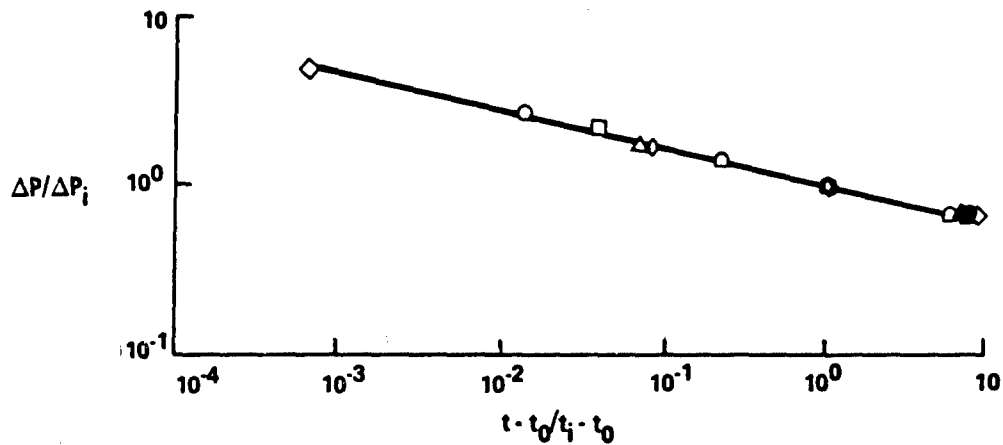


Figure 13 Axial Decay of Turbulence with Time

TABLE I

DECAY STUDY DATA

| RECORD | CONFIGURATION | TERMINAL MACH NUMBER | PRESSURE RECOVERY | $\frac{\Delta P_{T RMS}}{P_{T2}} _{AVG}$ | n | T_0 |
|--------|------------------------|-------------------------|----------------------|---|-------|------------|
| 1167 | BOUNDARY LAYER BLOW | 0.60 | 0.814 | 0.0164 | 0.42 | -0.00348 |
| 1173 | BOUNDARY LAYER BLOW | 1.056 | 0.804 | 0.0405 | 0.445 | -0.00073 |
| 1288 | UNMODIFIED | 1.058 | 0.861 | 0.0189 | 0.47 | -0.0000521 |
| 1174 | BOUNDARY LAYER BLOW | 1.28 | 0.844 | 0.0495 | 0.44 | -0.000217 |
| 1303 | UNMODIFIED | 1.44 | 0.727 | 0.0423 | 0.495 | -0.00010 |
| 1037 | UNMODIFIED | 1.59 | 0.832 | 0.0485 | 0.43 | -0.0000015 |

As is evident from Table I, the data of Figure 9 covers a very wide range of operating conditions, which illustrates the usefulness of this correlation procedure. The wall static pressure distribution corresponding to the various test runs is given in Figure 12.

The surprising constancy of the exponent n for the test diffuser, over a wide range of operating conditions, indicates that the decay rate of a given diffuser may be well characterized by such an empirical parameter. If this were the case, it would allow easy estimation of the effects of shortening a given

diffuser. It is apparent, however, the value of n will depend upon the performance level of the diffuser, so that we might expect a diffuser that permitted separation along its length to have a lower value of n than one which was designed to operate unseparated.

An illustration of downstream turbulence affecting the decay rate can be seen in the following example. Several 3 inch diameter vortex shedding pipes were inserted between the inlet shock wave system of the test duct and the compressor face. These pipes were selected so that vortices would be shed at a natural frequency of approximately 400 Hz at the high flow rates. That this occurs is evidenced by the large energy content in the P. S. D. in the region of 400 Hz. Figure 14 compares the corresponding P. S. D. at the furthest upstream measuring station to that at the engine face. Interestingly, this downstream turbulence production affected the upstream production of turbulence to a great extent, probably by amplifying the shock movement. A similar phenomenon occurred at lower flow rates when the pipes were present, but at proportionately lower frequencies.

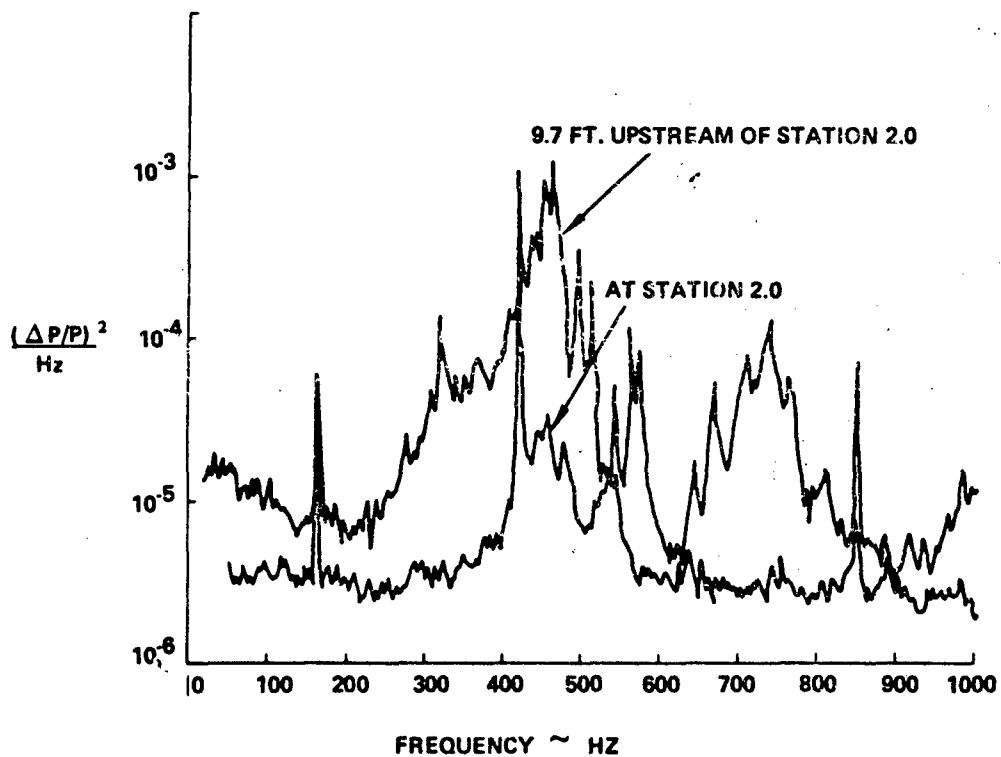


Figure 14 Effect of Vortex Shedding Pipes

VI. INVESTIGATION OF INSTRUMENTATION REQUIREMENTS

Because of the flow blockage which high response instrumentation can produce, a brief study of the number and distribution of total pressure probes required to accurately describe engine face turbulent distortion was conducted. A single composite (steady state plus turbulent) instantaneous distortion pattern, Figure 15, which had occurred just before a compressor surge was chosen for the study. The pattern is evidently highly distorted circumferentially, with relatively very little radial distortion. The combinations of probe-rake configurations used in the study are listed in Table II. Each probe-rake configuration was rotated through 360° in 20° increments and pressure readings were taken at each probe position for each incremental rotation. Circumferential and radial distortion factors, K_θ and K_{rad} (see Appendix), were computed from each set of data. The results are plotted in Figure 16 wherein ΔK_θ is the maximum K_θ minus the minimum K_θ realized for a given probe-rake combination. A similar explanation holds for ΔK_{rad} .

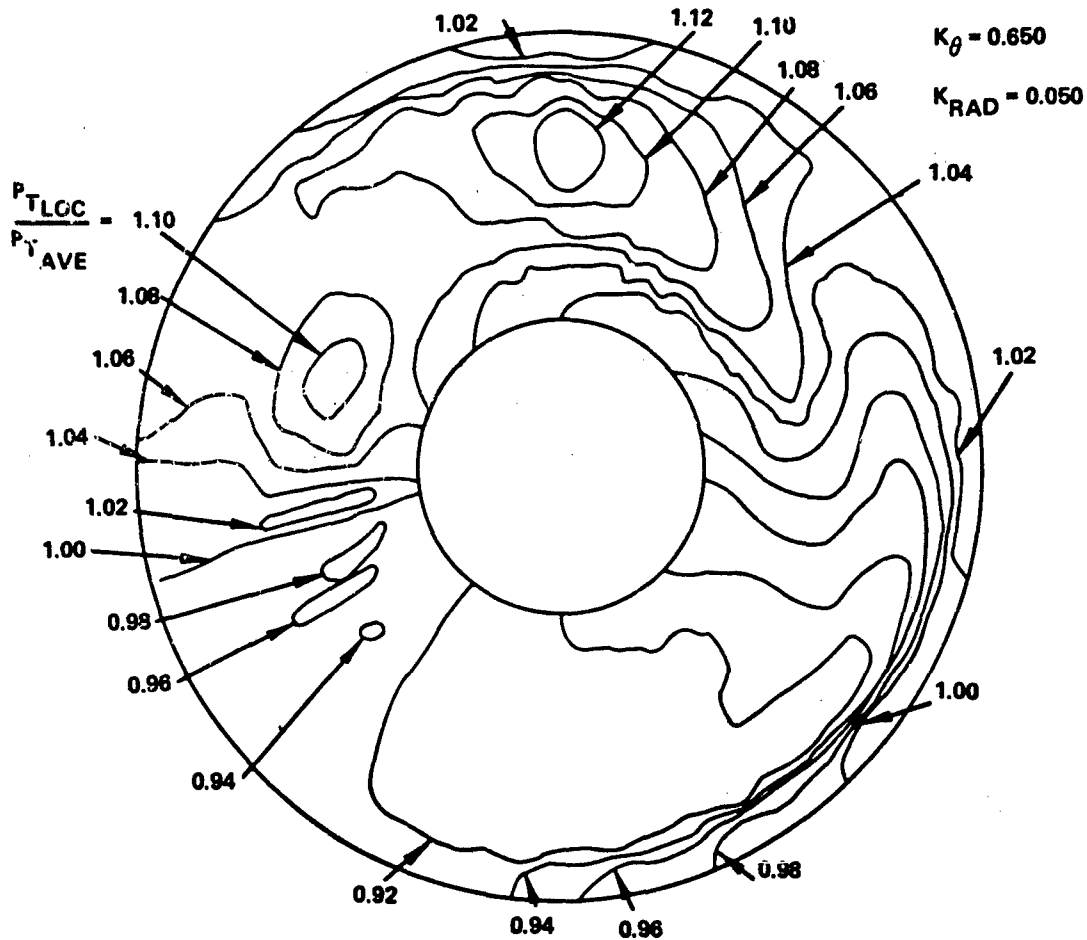


Figure 15 Distortion Pattern Studied

TABLE II

PROBE/RAKE COMBINATIONS USED FOR DISTORTION STUDIES

4 RAKES

3 PROBES PER RAKE
5 PROBES PER RAKE

5 RAKES

3 PROBES PER RAKE
5 PROBES PER RAKE

6 RAKES

3 PROBES PER RAKE
5 PROBES PER RAKE

8 RAKES

3 PROBES PER RAKE
5 PROBES PER RAKE

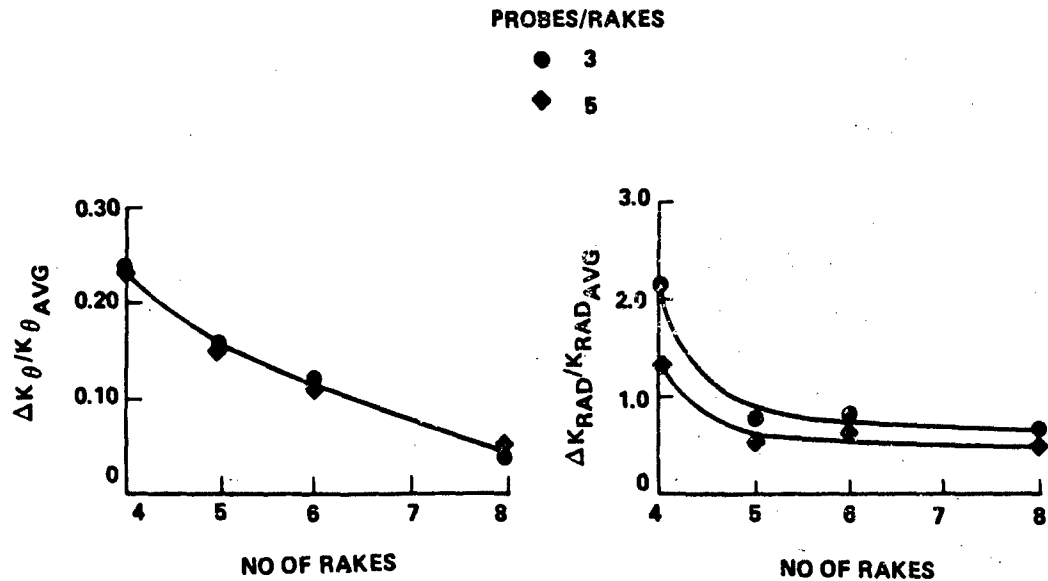


Figure 16 Distortion Factor Dependence on Probe/Rake Configuration

The conclusion is that, as expected, the more probes used the better the answer. However, it appears that for small scale model tests where the blockage of the rakes could limit the number of probes allowable, 6 rakes with 3 probes per rake are probably adequate to at least predict trends. When blockage is not a problem, 8 rakes or more of 5 probes each could provide much more precise distortion factors.

VII. SUMMARY AND CONCLUSIONS

The amplitude and frequency characteristics of the stagnation pressure fluctuations in a diffusing duct were studied. It was concluded that the turbulence Reynolds numbers were in a range where the decay of the turbulence intensity is limited by the dispersion, not by the dissipation. A consequence of the dispersion limited condition is that the decay data of small scale tests may be extended directly to large scale tests, without the requirement of preserving the Reynolds number. Also, P.S.D.'s from scale inlet tests can be scaled to full size inlets without difficulty, regardless of Reynolds number differences. Experimental data is presented which supports these hypotheses.

An empirical fitting procedure was exploited to correlate a wide range of decay results for the test duct. It was found that the empirically obtained exponent for the decay rate was very nearly constant for the entire range investigated, indicating that the technique should be useful in characterizing the behavior of a given inlet with regard to the axial decay of turbulence.

Investigation of the data indicated that there was significant turbulence production in the initial portion of the diffuser, following the shock system. It is believed that this production arises from the regions of high shearing identified with separation in the diffuser. It is recommended that the development of very short diffusers be accompanied by measurement of their turbulence characteristics because of the lack of length for decay ahead of the engine.

An investigation of the minimum number of probes required to adequately describe instantaneous engine face distortion indicated that in small scale tests where blockage is a problem, 6 rakes of 3 probes per rake are probably adequate to at least predict trends. Where blockage is not a problem, 8 rakes or more of 5 probes each could give much more precise information.

VIII. REFERENCES

1. Kimzey, W. F., An Investigation and Calibration of a Device for the Generation of Turbulent Flow at the Inlet of a Turbojet Engine, A. E. D. C. Technical Report 65-195, October, 1965.
2. Kimzey, W. F. and Lewis, R. J., An Experimental Investigation of the Effects of Shock-Induced Turbulent In-Flow on a Turbojet Engine, A. I. A. A. Second Propulsion Joint Specialist Conference, Air Force Academy, Colorado Springs, Colorado, June 13-17, 1966.
3. Martin, Arnold W. and Kostin, Leonard C., Propulsion System Dynamic Test Results, North American Aviation, Inc., Report No. NA-67-386, April 17, 1967.

4. Gray, William G., Analysis of TF30 Engine and Compressor Tests, Pratt & Whitney Aircraft, PWA-3497 (Contract No. F33615-67-C-1848), September 30, 1968.
5. Winslow, L.J. et. al., Inlet Distortion Investigation, Upstream Engine Influence and Screen Simulation, The Boeing Company, Technical Report AFAPL-TR-68-140, January, 1969.
6. Johnson, T.J. and Huff, J.F., Jr., Propulsion System Integration and Test Program Part IV, North American Rockwell Corp., NA-68-939 (F33615-67-C-1829), February, 1969.
7. Bendat, J.S. and Piersol, A.G., Measurement and Analysis of Random Data John Wiley & Sons, 1966.
8. Hoel, P.G., Introduction to Mathematical Statistics, John Wiley & Sons, 1954.
9. Wasserbauer, J.F. and Willoh, R.G., Experimental and Analytical Investigation of the Dynamic Response of a Supersonic Mixed-Compression Inlet. A.I.A.A. Paper No. 68-651, presented at A.I.A.A. 4th Propulsion Joint Specialist Conference, Cleveland, Ohio, June 10-14, 1968.
10. Crosby, N.J. and Neiner, G.H., High Performance Bypass Control for Mixed-Compression Inlets. A.I.A.A. Paper No. 68-652, Presented at A.I.A.A. 4th Propulsion Joint Specialist Conference, Cleveland, Ohio, June 10-14, 1968.
11. Martin, A. and Kostin, L., Dynamic Distortion at the Exit of a Subsonic Diffuser of a Mixed Compression Inlet, North American Rockwell, Los Angeles Division, Report TFD-69-588.
12. Schlichting, H., Boundary Layer Theory, McGraw Hill, 1960.
13. Howarth, L., Modern Developments in Fluid Dynamics, High Speed Flow, Oxford Press, 1953, pp. 1-7.
14. Von Doenhoff, A.E. "Principles of Model Testing" in High Speed Problems of Aircraft and Experimental Methods, Vol. VIII, High Speed Aerodynamics and Jet Propulsion, Princeton University Press.
15. Batchelor, G.K., The Theory of Homogenous Turbulence, Cambridge University Press, 1953.
16. Hinze, J.O., Turbulence, McGraw Hill, 1959.

17. Batchelor, G.K. and Townsend, A.A., Decay of Isotropic Turbulence in the Initial Period, Proc. Roy. Soc. A, 193, 539, (1948).
18. Stewart, R.W. and Townsend, A.A. Similarity and Self Preservation in Isotropic Turbulence, Philos. Trans. A, 243, 359 (1951).
19. Corrsin, S., Turbulent Flow, American Scientist, Vol. 49 No. 3, Sept. 61.
20. Comte-Bellot, G. and Corrsin, S., The Use of a Contraction to Improve the Isotropy of Grid Generated Turbulence, J. Fluid Mech. (1966), Vol. 25, Part 4, pp. 657-682.
21. Trilling, L., Oscillating Shock Boundary-Layer Interaction Journal of the Aeronautical Sciences, May 1958 pps. 301-304.

APPENDIX

DEFINITION AND CALCULATION OF CIRCUMFERENTIAL DISTORTION FACTOR (K_θ)

A typical turbofan engine inlet which has been instrumented to provide distortion measurements is shown in Figure A-1. An understanding of this figure is required to define the distortion factor. Eight radial instrumentation rakes are placed within the annular area. Each of these rakes contains five pressure probes at the center of five equal areas. Pressure variations can therefore be analyzed circumferentially as a function of the angle (θ). For instance, the dashed line in Figure A-1 would represent the circumferential variation of the third ring as it is formed by connecting the third probe on each rake.

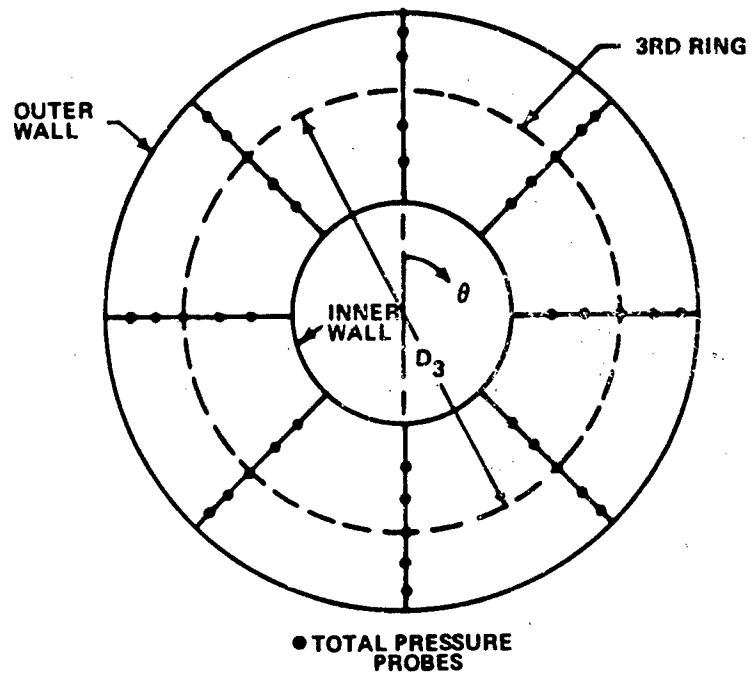


Figure A-1 Turbofan Engine Inlet Schematic Instrumented for Distortion Measurements

The formula for the circumferential distortion factor is

$$K_{\theta} = \frac{\sum_{\text{Ring} = 1}^J \left[\left(\frac{A_N}{N^2} \right)_{\text{max}} \right]_{\text{Ring}} \frac{P_{T2}}{Q_{av}} \frac{1}{D_{\text{Ring}}}}{\sum_{\text{Ring} = 1}^J \frac{1}{D_{\text{Ring}}}} \quad (\text{Eq. 1})$$

where

- J = number of total rings which is equal to number of probes per rake.
- D = diameter of the ring or radial probe.
- Q_{av} = average inlet absolute velocity head at the face of the engine ($1/2\rho Cx^2$).

To define the term $\left(\frac{A_N}{N^2} \right)_{\text{max}}$, more detailed explanation is required.

Figure A-2 gives a simple example of a pure 180-degree circumferential distortion in which the circumferential variation of local pressure (P_{T2}) to the average total pressure (\bar{P}_{T2}) is shown. The equation for this curve can be written in terms of Fourier series. In general,

$$\frac{P_{T2}}{\bar{P}_{T2}} = 1 + \sum_{N=1}^{\infty} a_1 \cos \theta + a_2 \cos 2\theta + \dots a_N \cos N\theta + b_1 \sin \theta + b_2 \sin 2\theta + \dots b_N \sin N\theta \quad (\text{Eq. 2})$$

where

$$a_N = \frac{1}{\pi} \int_{-\pi}^{\pi} \frac{P_{T2}}{\bar{P}_{T2}} (\theta) \cos N\theta \, d\theta$$

$$b_N = \frac{1}{\pi} \int_{-\pi}^{\pi} \frac{P_{T2}}{\bar{P}_{T2}} (\theta) \sin N\theta \, d\theta \quad (\text{Eq. 3})$$

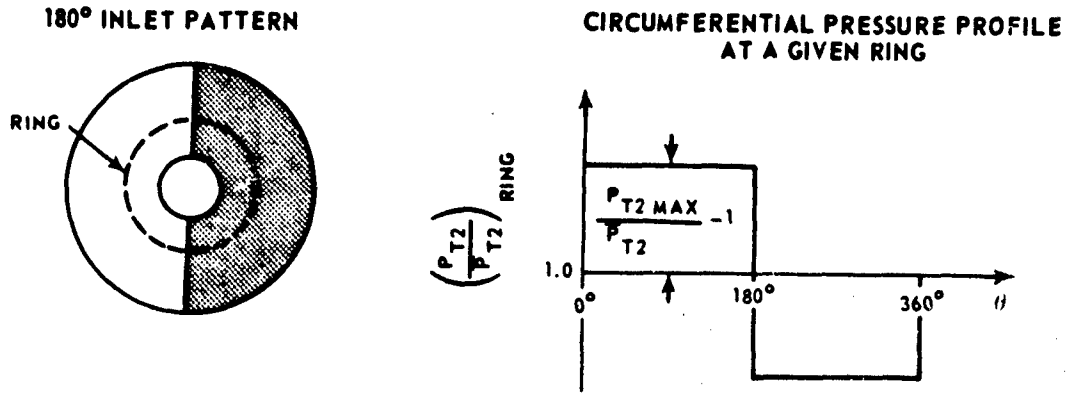


Figure A-2 Pure 180-Degree Circumferential Distortion Schematic

If we define $A_N = \sqrt{a_N^2 + b_N^2}$ then the series can be written as:

$$\frac{P_{T2}}{P_{T2}} = 1 + \sum_{N=1}^{\infty} A_N \sin(N\theta + \phi_N) \quad (\text{Eq. 4})$$

For this particular example, the series becomes after integration and simplification:

$$\begin{aligned} \frac{P_{T2}}{P_{T2}} = 1 + \frac{4}{\pi} \left[\frac{P_{T2 \max}}{P_{T2}} - 1 \right] \sin \theta + \frac{4}{3\pi} \left[\frac{P_{T2 \max}}{P_{T2}} - 1 \right] \sin 3\theta + \\ \frac{4}{5\pi} \left[\frac{P_{T2 \max}}{P_{T2}} - 1 \right] \sin 5\theta + \dots \end{aligned} \quad (\text{Eq. 5})$$

We now can look for the maximum $\frac{A_N}{N^2}$ term. Listing these terms they are:

$$\begin{aligned} \text{for } N=1 \quad \frac{A_1}{1^2} &= \frac{4}{\pi(1)^2} \left[\frac{P_{T2 \max}}{P_{T2}} - 1 \right] & N=4 \quad \frac{A_4}{4^2} &= 0 \\ N=2 \quad \frac{A_2}{2^2} &= 0 & N=5 \quad \frac{A_5}{5^2} &= \frac{4}{5\pi(5)^2} \left[\frac{P_{T2 \max}}{P_{T2}} - 1 \right] \\ N=3 \quad \frac{A_3}{3^2} &= \frac{4}{3\pi(3)^2} \left[\frac{P_{T2 \max}}{P_{T2}} - 1 \right] \end{aligned}$$

(Eq. 6)

For this case and for most cases, the first harmonic has the greatest influence. For this particular example then

$$\left(\frac{A_N}{N^2}\right)_{\max} = \frac{4}{\pi} \left[\frac{P_{T2 \max}}{\bar{P}_{T2}} - 1 \right] \quad (\text{Eq. 7})$$

which is then used to evaluate the distortion factor.

A formula for the radial component is

$$K_{RA} = \frac{\sum_{\text{Ring} = 1} \left(\frac{\Delta P_T}{\bar{P}_{T2}}\right)_{\text{Ring}} \frac{P_{T2}}{Q_{av}} \frac{1}{D^2_{\text{Ring}}}}{\sum_{\text{Ring} = 1} \frac{1}{D^2_{\text{Ring}}}}$$

where:

$$\left(\frac{\Delta P_T}{\bar{P}_{T2}}\right)_{\text{Ring}} = \frac{P_{T2} - (\bar{P}_{T2})_{\text{Ring}}}{\bar{P}_{T2}}$$

When this term becomes negative, it is set equal to zero, as given in Figure 3.

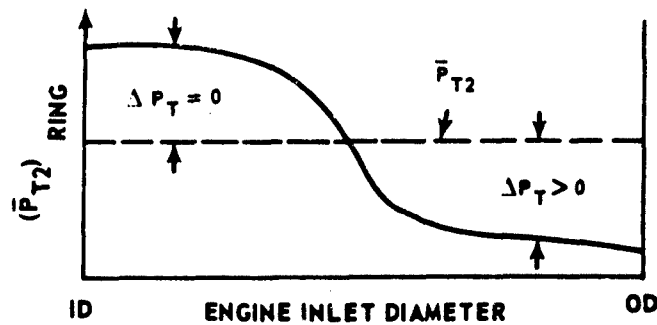


Figure A-3 Definition of the Term $(\Delta P_T)_{\text{ring}}$

A POSSIBLE MECHANISM FOR INLET/ENGINE INTERACTIONS DUE TO INLET FLOW FLUCTUATIONS

M. B. Sussman and G. W. N. Lampard
The Boeing Company
Commercial Airplane Division

SUMMARY

This paper presents several theories concerning compressor stall difficulties encountered in recent airplane development programs. Previously published material discussed all except one concerning the discrete frequency mechanism for inlet-engine instabilities. This theory is supported in this paper. Data concerning the proposed mechanism for injurious discrete frequency effects are drawn from varied sources and assembled. Some recent Boeing test data are included.

PROBLEM BACKGROUND

Compressor stalls encountered during ground and flight testing of two recent military supersonic aircraft systems have been discussed by F. T. Rall.¹ Numerous other references exist. The quality of air presented to the engine is recognized as the source of the stall difficulties. Studies of this problem have generated a great deal of test data concerning the condition of the air delivered by the inlet. The flow properties of the air are generally expressed in terms of distortion and turbulence characteristics.

The degree to which the engine will withstand poor quality air has also been the subject of investigation. Conclusions based on these diverse data have not always been unanimously accepted. This is due to a general lack of understanding of the precise manner in which the engine is affected by the quality of air entering it. Thus, today, several distinctly different theories are advanced by separate investigators concerning compressor stall problems. At least three are readily identifiable and are depicted schematically in Fig. 1. The major assertions of each are described below.

Theory 1

According to the first theory, the compressor is primarily sensitive to distortion patterns. This specifically includes those patterns that change rapidly with time. Thus, the current concept of turbulence is interpreted here simply as time-varying distortion. Moreover, the rapidity with which the pattern can change and still be "felt" by the compressor in a quasi-steady sense is believed to be scaled by the rpm of the rotor. Some flight test data recently analyzed to evaluate instantaneous distortion levels will be discussed later.

Theory 2

A second theory explaining the effect of nonsteady airflow on the operation of an engine has been suggested by Kimzey and Lewis.² A test was run at AEDC in which a J93 engine was operated behind a simulated inlet or "turbulator." From the results of this test, it was concluded that engine surge margin reduction can be correlated with the root-mean-square (rms) level of the time-varying

component of the total pressure at the compressor face. In this approach it is assumed that the significant parameters of the nonsteady flow must be interpreted in a statistical sense. Typically, data are analyzed in terms of its rms level, frequency spectra, and correlation properties.

Theory 3

The third theory considers that in a dynamic sense, the inlet flow field may not be what is predicted when based on a steady-state analytical model. Specifically envisioned are possible large-order pulsations of the flow. These may be partly, or perhaps completely, correlated over the compressor face. In any event, this line of reasoning associates particular discrete frequencies with a given inlet-engine configuration. It is believed that flow transients detrimental to system stability would occur at these rather low (and predictable) frequencies.

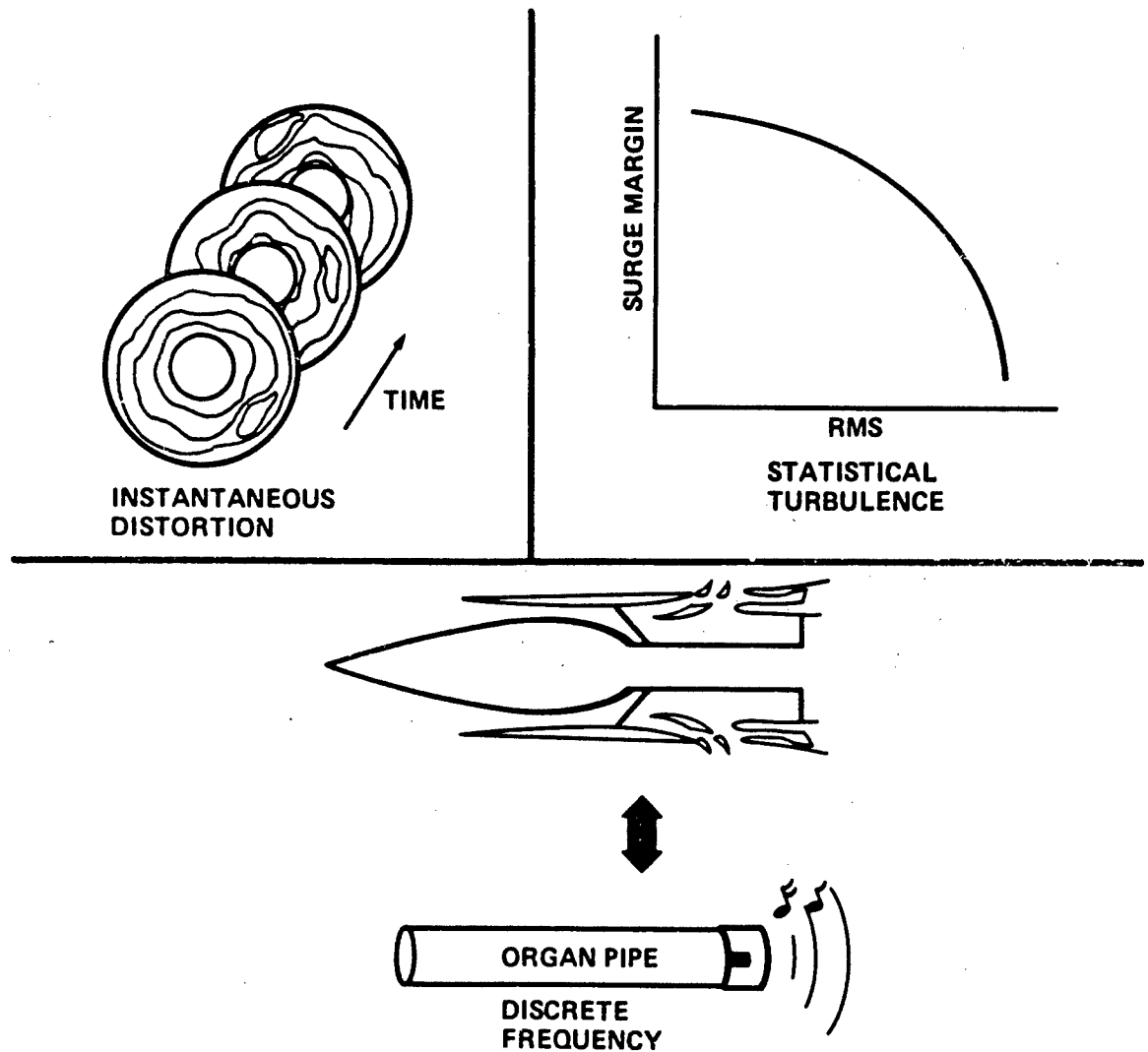


Figure 1. Current Inlet Dynamics Theories

The specific purpose of this paper is to show that substantial data exist to support this third (discrete frequency) theory. That is not to say that theories 1 and 2 are incorrect, but that in view of the importance of the problem, the discrete frequency argument should not be overlooked as a possible contributor. To understand the overall argument in concise, familiar terms, see Fig. 2. In this figure, we illustrate the amplitude frequency response of a typical high-response pressure transducer mounted in an "organ-pipe" configuration. The data is the transducer output for different frequency pneumatic input signals all of the same amplitude. The important point is that the mounting tube, while not interfering with the low-frequency (i.e., "steady state") characteristics of the system, drastically alters its dynamic properties. The three prominent amplification peaks are well recognized as the "natural" or "organ-pipe resonance" modes for the geometry employed. The amplification results, of course, from the more efficient conversion of the available input energy into pressure fluctuations at the resonant frequencies.

This paper intends to demonstrate that a supersonic inlet will often behave in a manner and exhibit dynamic properties very similar to the total pressure instrumentation of Fig. 2. A substantial amount of data related to current aircraft induction systems confirms this.

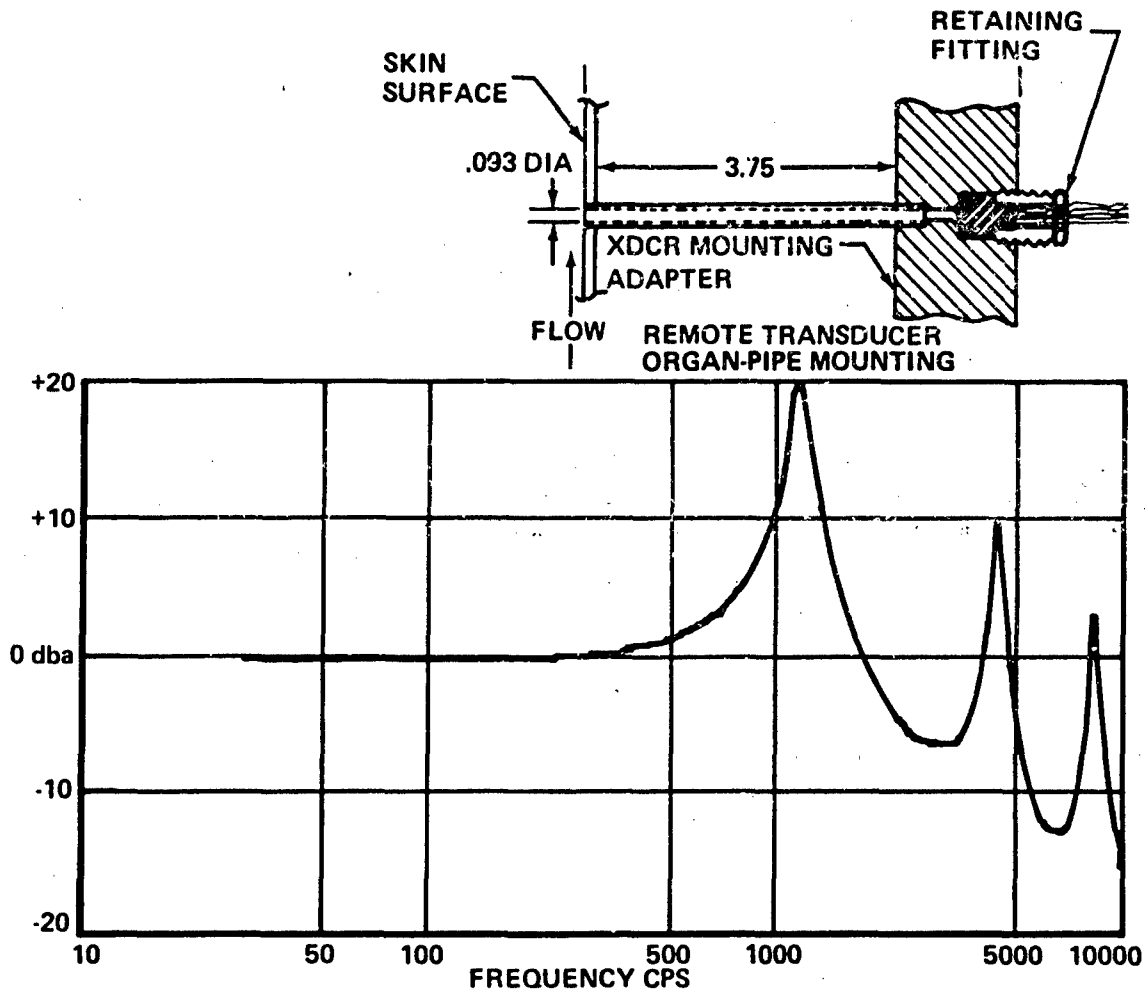


Figure 2. Common Example of Organ-Pipe Resonance

EVIDENCE OF INLET DISCRETE FREQUENCIES

A great deal of full-scale inlet-engine test data have been accumulated in connection with the B-70 and F-111 aircraft programs. These data have often been processed with either theory 1 or 2 in mind. That is, the data have been analyzed and displayed in terms of instantaneous distortion levels or in terms of rms averages. The fact that discrete frequency components apparently exist in the data has received only minor attention.

Figure 3 is a time-history trace of a compressor-face total pressure probe taken from Ref. 3. In this test, the properties of a choked-inlet turbulence generator were being cold-flow tested prior to running the device ahead of a YJ93 engine. The device was intended to simulate pressure fluctuations associated with compressor stalls experienced in previous B-70 inlet/YJ93 engine tests. This trace itself indicates a discrete frequency component at about 25 cps. These indications are confirmed in Fig. 4, an autocorrelation of other data from that test. Kimzey noted in his report that a large number of low-amplitude resonance spikes existed in the spectrum. This *in itself* is not exceptionally significant. It is, however, a point to keep in mind in connection with the following data.

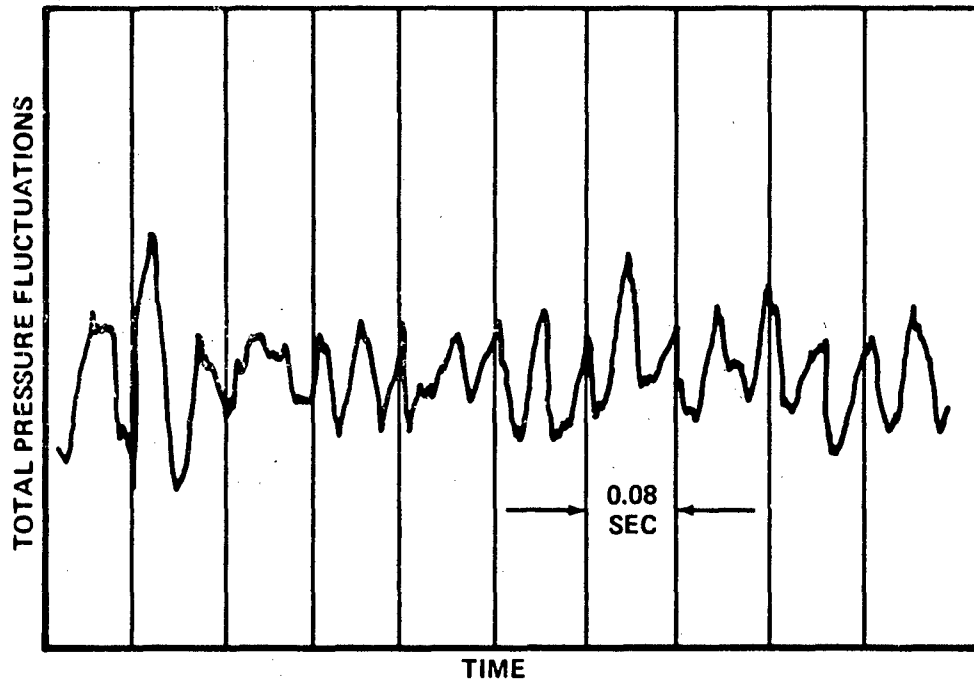


Figure 3. Total Pressure History, YJ93 Airflow Simulator and Turbulence Generator
(Kimzey, Ref. 3)

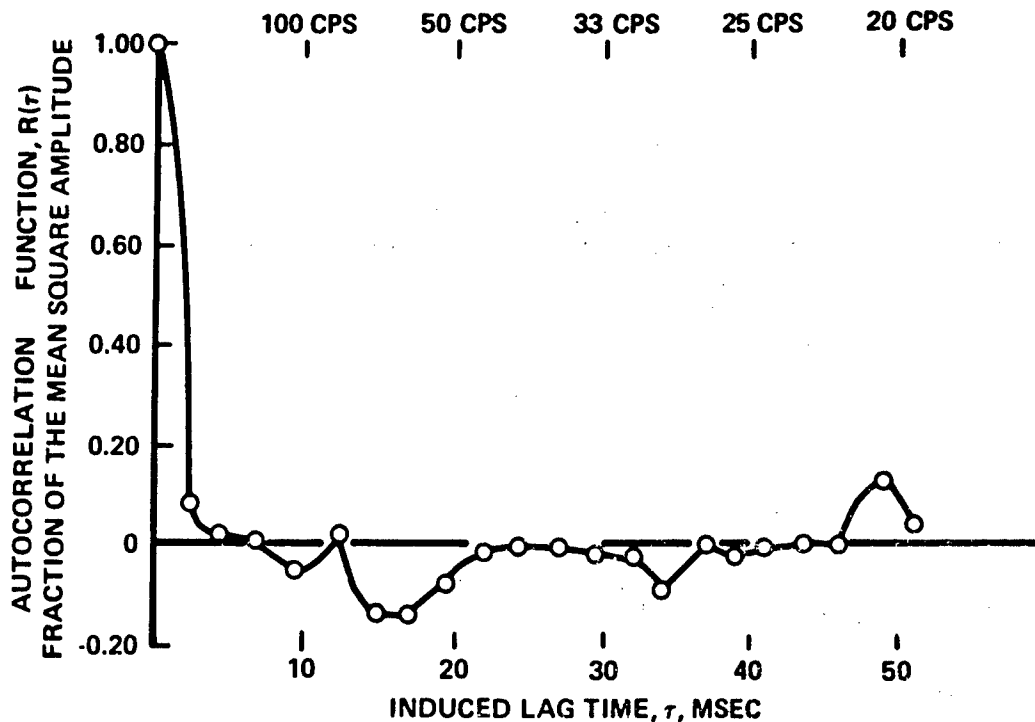


Figure 4. Autocorrelation of Total Pressure, YJ93 Airflow Simulator and Turbulence Generator (Kimzey, Ref. 3)

Figure 5 is data from an early phase of the F-111 flight test program. Distortion is plotted in terms of the engine manufacturer's index versus time. This plot is especially interesting because the data presented have been assembled to evaluate the instantaneous distortion argument. The distortion index shown is unquestionably undergoing rapid variations with time. However, a very interesting feature of this plot is the resemblance to a divergent oscillation building up just prior to stall. The last three large peaks can be visually estimated to have a frequency of about 25 cps. For an F-111 inlet duct, this frequency is of the order of the inlet "natural" frequency, computable by a simple formula. Perhaps the agreement is fortuitous. However, it is intuitively plausible that if the inlet were to be driven into resonance, this condition would build up in a manner very much like the figure depicts—as a kind of divergent oscillation.

Figure 6 represents some recently completed Boeing test data taken at Mach 2.6 from a 1/6-scale model of an early design concept for the SST inlet. Shown as a function of frequency are a third-octave analysis of a single compressor-face probe (thin solid line), and the joint correlation of two adjacent compressor-face probes (heavy solid line). Together, the two curves indicate activity around 130 cps, which at least in a limited area at the compressor face, is well correlated. The data shown are for an off-design inlet geometry (throat door open) condition and were partial results of an investigation of an unstart-restart sequence. By comparison, the broken lines indicate that the activity disappears when the throat door is closed. Because of limited instrumentation for this run, we have not pinpointed exactly where the resonance occurred; however, the frequency is of the right order to correspond with two or three inlet lengths determined by this inlet geometry.

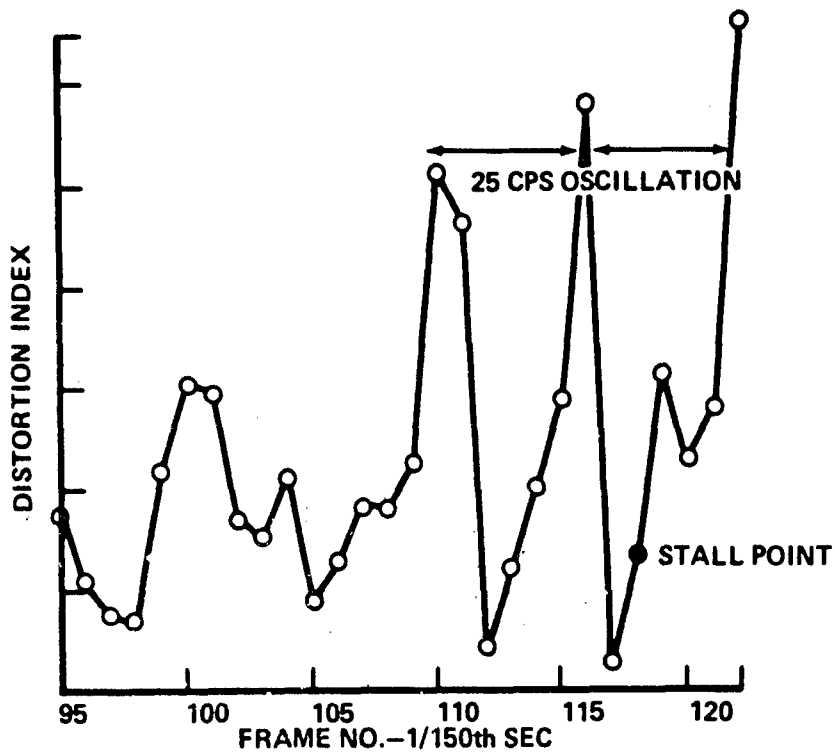


Figure 5. F-111 Distortion Prior to Stall, A/C 14, FLT 33
(Courtesy of AFAPL, WPAFB)

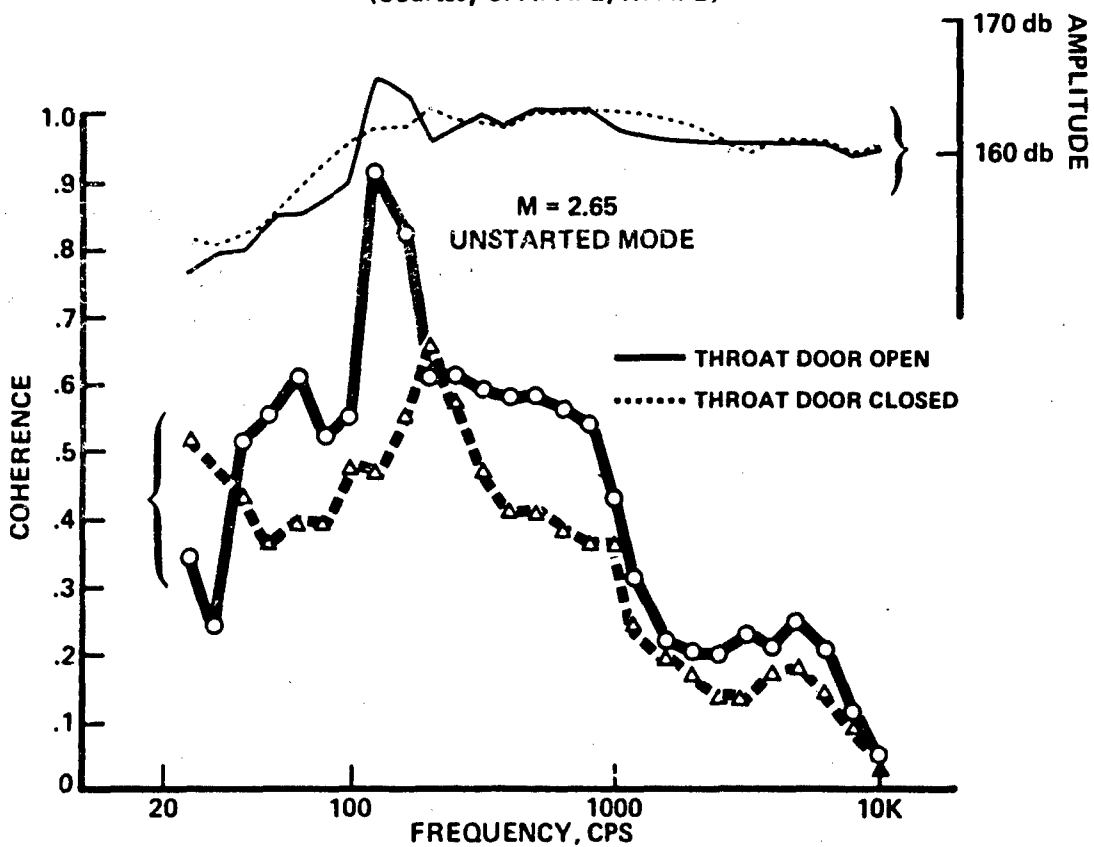


Figure 6. Individual and Correlated Total Pressure Spectra of an Axisymmetric Inlet

No dramatic conclusions can be drawn from the preceding figures. It is, however, important to observe that discrete frequencies have appeared in some of the test data associated with the aircraft programs noted. The tendency for these to appear is most evident at what would be termed off-design conditions.

INTERPRETATION OF DISCRETE FREQUENCIES

Figure 7 (taken from Ref. 4) is representative of a good deal of recent NASA Lewis testing concerning the frequency response characteristics of the subsonic diffuser portion of a supersonic inlet. The figure shows the amplitude response of the terminal shock wave normalized to its low-frequency (or quasi-steady) value. Two points are noteworthy.

- At higher frequencies, the shock motion becomes sluggish in trying to maintain the amplitude that it can achieve at low frequencies. It is only at the "natural" or resonant frequency that conditions are again conducive to large order amplitudes.
- The shock (inlet) resonant frequency is quite predictably determined from overall inlet geometry characteristics. In fact, the frequency is well predicted by the simple formula:

$$f = \frac{V}{nL} (1 - M^2)$$

Here, f is the resonant frequency in cps; V is the sound speed in ft/sec; M is the average subsonic duct Mach number; L is the inlet resonating length; and $n = 2$ or 4 depending on the boundary conditions.

It should be stressed that the above data are in response to an *imposed* sinusoidal disturbance. The device used to impart the disturbance and thus produce an inlet resonance is clearly contrived and not a part of the actual inlet. The data nevertheless clearly show how the inlet would be expected to behave dynamically and invite obvious comparison with Fig. 2.

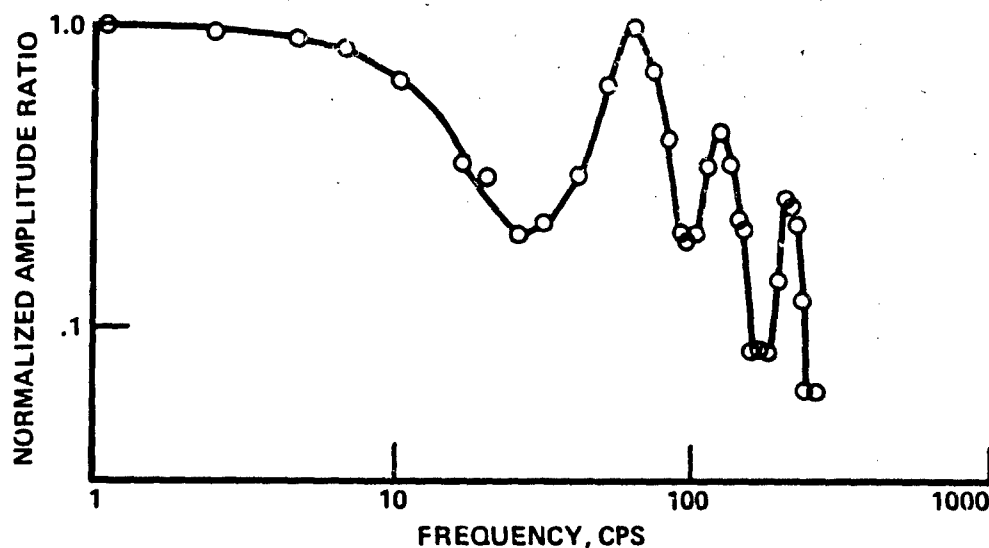


Figure 7. Dynamic Response of Terminal Shock Wave for NASA Lewis M2.5 Supersonic Inlet (Wasserbauer and Willloh, Ref. 4)

Figure 8 of Ref. 5 shows some recently published North American Rockwell data related to wind tunnel tests of a supersonic inlet operating in the started mode. The frequency spectra of a compressor-face total pressure probe for two different inlet recovery levels (i.e., different compressor-face corrected weight flows) are shown. Several important points should be noted.

- These data illustrate that inlet resonance can and does occur in a supersonic inlet operated in its intended fashion, i.e., without the use of a contrived device to produce inlet pulsations. The reference identifies the two prominent peaks which are brought out in the low recovery mode of operation with the Helmholtz and organ-pipe modes of the inlet geometry.
- The resonance peaks are tremendously exaggerated at the off-design inlet operating condition labeled "low recovery." Somehow, the energy which previously had been distributed in random fashion over the frequency range has been funneled up into the two discrete frequencies noted.

POWER SPECTRAL DENSITY

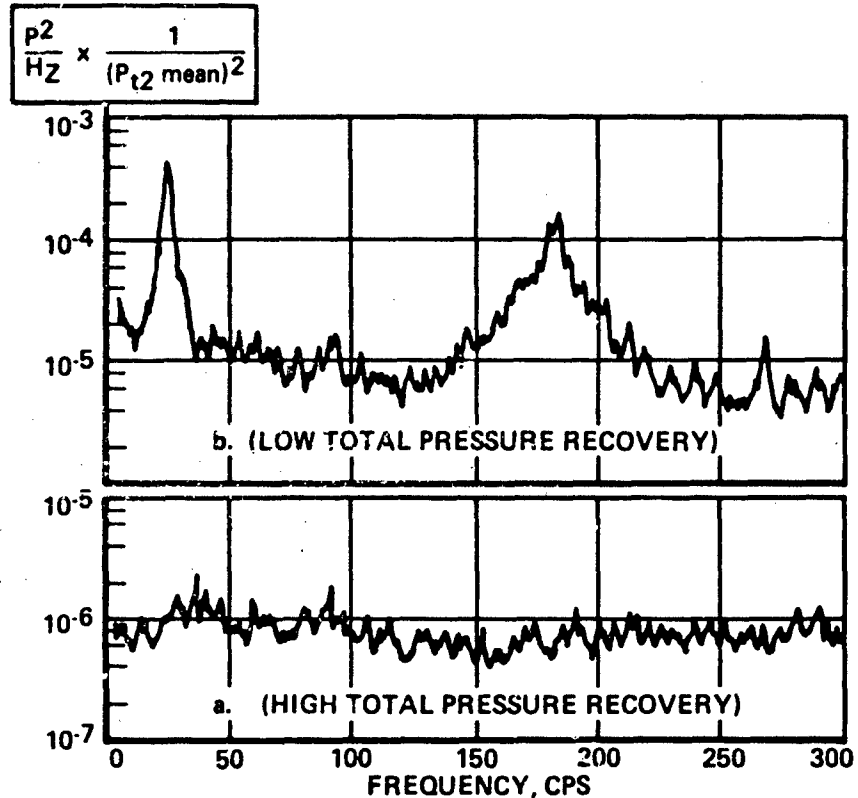
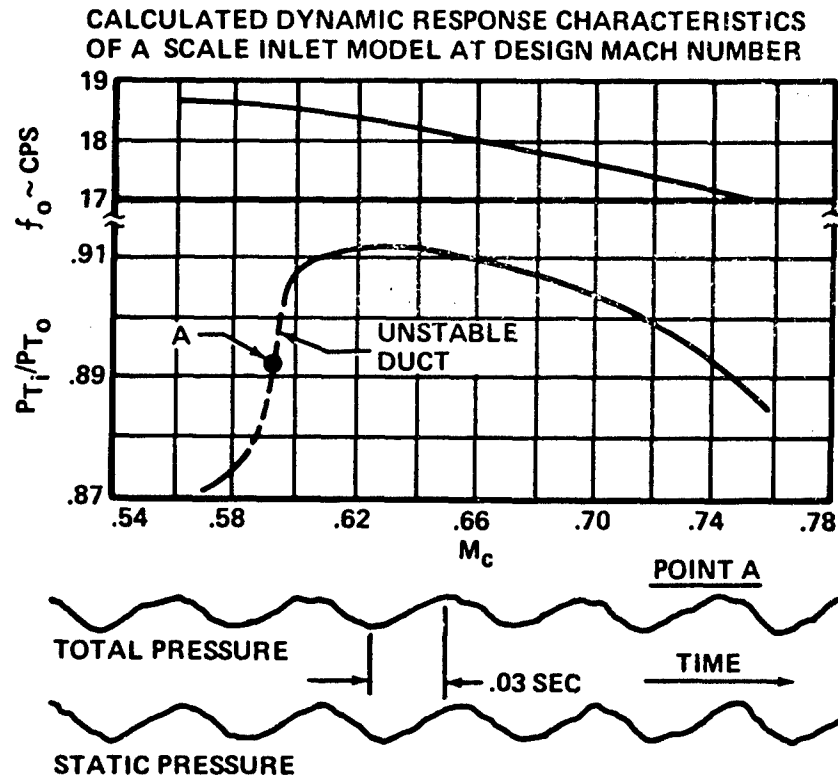


Figure 8. Inlet Total Pressure Spectra for Two Recovery Conditions
(Kostin and Millstone, Ref. 5)

Figure 9 of Ref. 6 helps clarify interpretation of inlet discrete frequency fluctuations. The data presented are related to the F8U-3 inlet which was tested at NASA Lewis in small scale some 10 years ago. Also shown are the measured inlet recovery and predicted frequency of instability. Both are plotted against duct Mach number. Fraiser termed the instability "flutter," and reported that agreement of measured data with predictions based on a Helmholtz resonator model of the induction system was quite satisfactory. Also included in Fig. 9 are two time-history traces recorded on an oscillograph for two separate inlet locations. Two interesting points were made by the investigator.

- The instability pictured was definitely not buzz. Fraiser made the useful distinction that "evidently, 'flutter' which is an instability caused by internal flow phenomena, occurs at the duct fundamental frequency while 'buzz' caused by external flow phenomena occurs on a harmonic of the fundamental frequency."
- Although the flutter was generally milder than buzzing for that inlet, the investigator points out that "at Mach numbers higher than design, the flutter amplitude increases rapidly."

Summarizing Figs. 7 through 9, we can say that inlet discrete frequencies can often be readily interpreted in terms of the inlet natural frequencies (either Helmholtz or organ-pipe) and that in fact, analytic treatment of these phenomena appears to hold quite good promise. Furthermore, it would appear that whereas the resonance is often quite weak or even indiscernible for *on-design* inlet operation, the situation changes quite rapidly for *off-design* conditions. It is interesting to note here that this was essentially the same state of affairs reported in the early J93 engine test series when the tendency for engine difficulty increased as the inlet was run *off-design*.



PRESSURE TRACE OF UNSTABLE DUCT AT POINT A

*Figure 9. Scale Model F8U-3 Inlet Duct Properties
(Fraiser, Ref. 6)*

CONSEQUENCES OF INLET RESONANCE

The thesis of the paper has been that engine surge problems have been encountered; that some of the data indicate the presence of discrete frequencies; and that these frequencies are entirely explainable and to some extent predictable. It would be nice to conclude here with data indicating the relationship between inlet resonance and engine surge. Unfortunately, these data do not yet exist, or at least the writers are unaware of them if they do. The closest data available are shown previously in Fig. 5 for the F-111 just prior to stall and this alone is not very satisfactory.

Although data relating resonance to engine surge are scarce, data illustrating the injurious effects of inlet resonance on air induction systems or engines are not.

Figure 10 is a schematic of The Boeing Company 737 ram-air inlet system which serves solely as a heat sink for a system of heat exchangers which reject heat generated by cabin air conditioning

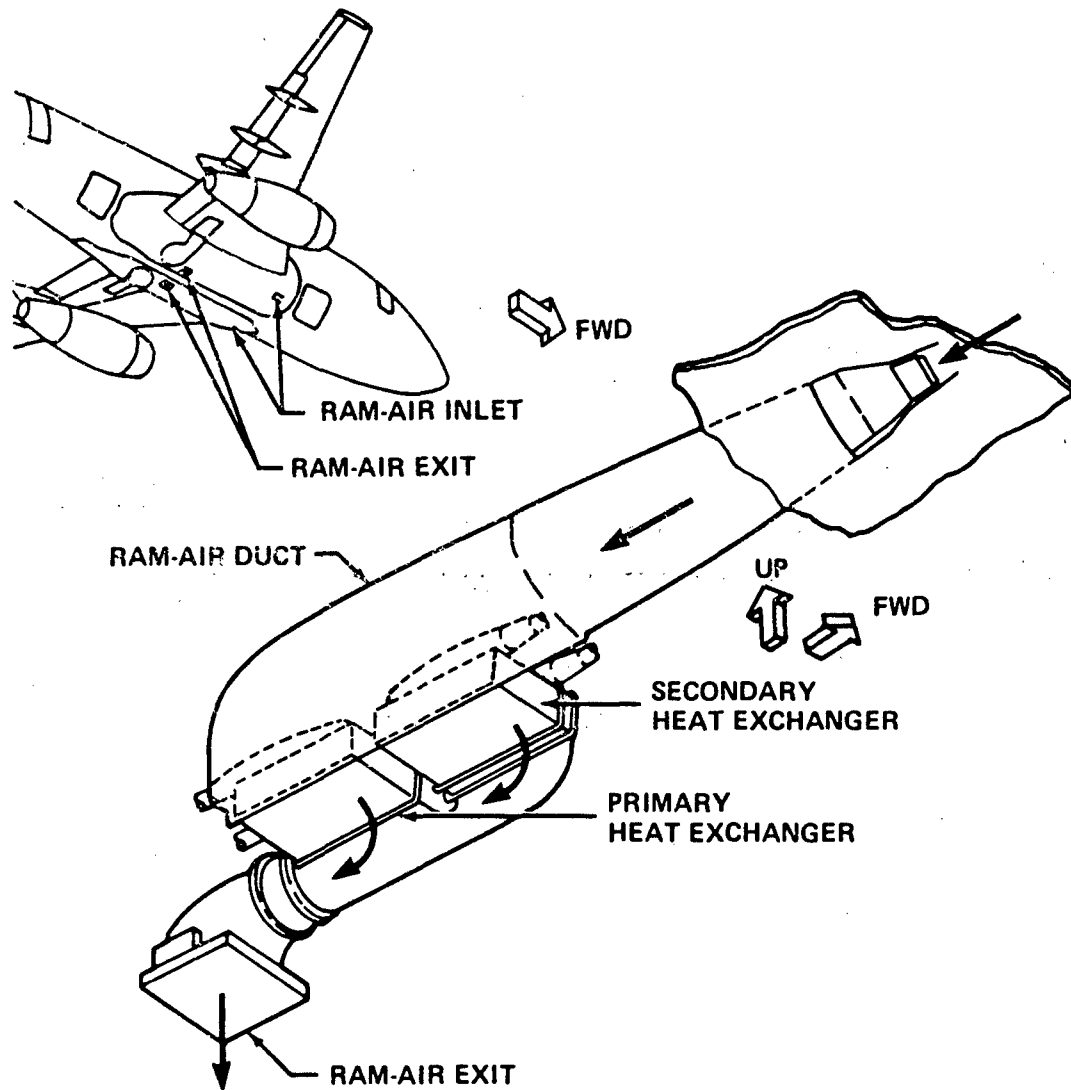


Figure 10. Ram-Air Induction System - 737 Airplane

systems. A recent investigation of a component failure problem associated with this duct work was linked to inlet pressure fluctuations of some magnitude. The data showed that peak-to-peak static pressure pulsations of up to 0.8 psi were occurring. Moreover, the oscillograph traces were shown to be either of a random nature or of a smooth sinusoidal form as shown in Fig. 11. The data indicated that the higher levels of fluctuation invariably occurred with the sinusoidal traces in association with resonance of the ducting system.

Figure 12 taken from Ref. 7 shows a problem which occurred during bellmouth inlet testing of a jet engine compressor. The figure shows the vibration levels as a function of rpm for the test configuration both with and without the bellmouth. The additional high level vibration with the bellmouth configuration at about 7,200 rpm was identified by November as resulting from an acoustic resonance within the bellmouth which was excited by a 1-per-rev excitation resulting from the compressor. November observed that the fluctuations associated with such resonance can generally be tolerated. However, on occasion, oscillation amplitudes of up to 15 psi peak-to-peak have been recorded. The results in these extreme cases have included damage to the test model.

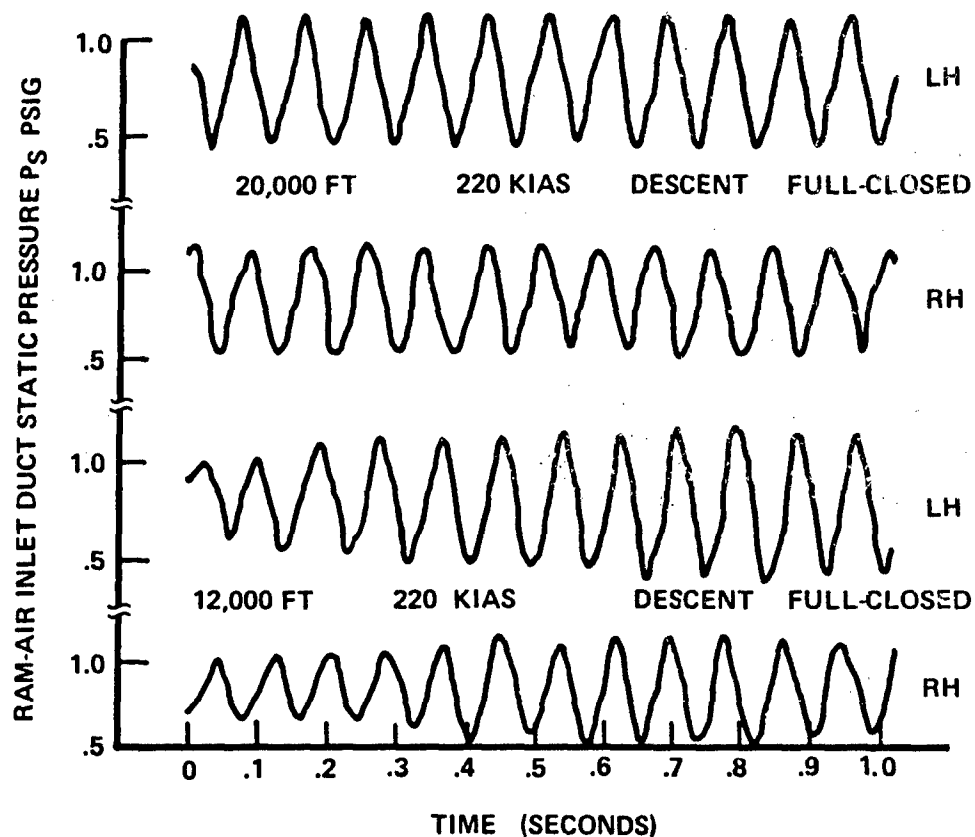


Figure 11. Ram-Air System Pressure Fluctuations

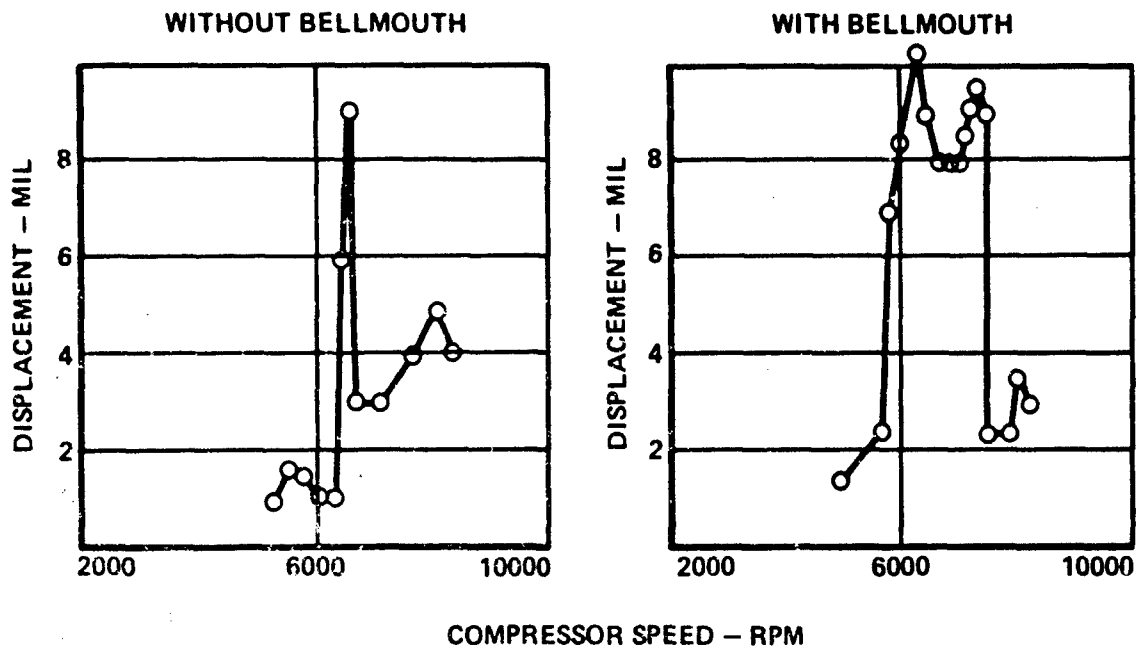


Figure 12. Compressor Rig Vibration With and Without Inlet
(November, Ref. 7)

SUMMARY OF DISCRETE FREQUENCY ARGUMENT

The arguments presented in this paper are summarized pictorially in Fig. 13. An analogy can be made with the simple mass-spring system and the schematic of the supersonic inlet. Imagine this system driven by a forcing function that has a random distribution of its spectral content. In such a case, we generally expect to observe the mass dancing around at the end of the spring in a similarly random fashion. Consider, however, that the driving force, over some particular interval of time, possesses slightly more energy than usual in the frequency range defined by the natural frequency of the mass-spring system. In this case, we would expect rather large order oscillations to occur in response.

If we extend the analogy to the inlet, the natural frequency becomes either the Helmholtz or organ-pipe type of acoustic modes. Furthermore, it appears that the driving force should be associated with the energy available from the flow fluctuations generated by the inlet shock-boundary layer interaction in the upstream flow. The role of shock-boundary layer interaction in this problem has been observed by a number of investigators. As the flow becomes increasingly disordered (i.e., as we proceed further off design), greater amounts of this white noise type energy are available to excite resonance.

The fact that observed engine stalls occur randomly, but more frequently at off-design conditions, is explained by the mechanism advocated here. On certain occasions, the energy associated with the shock-boundary layer interaction might tend to be concentrated near the inlet natural frequency. When this happens, a stall is likely to occur. Furthermore, as the inlet is run more and more off design, the strength of the driving force is increased, thus heightening the tendency of the engine to stall.

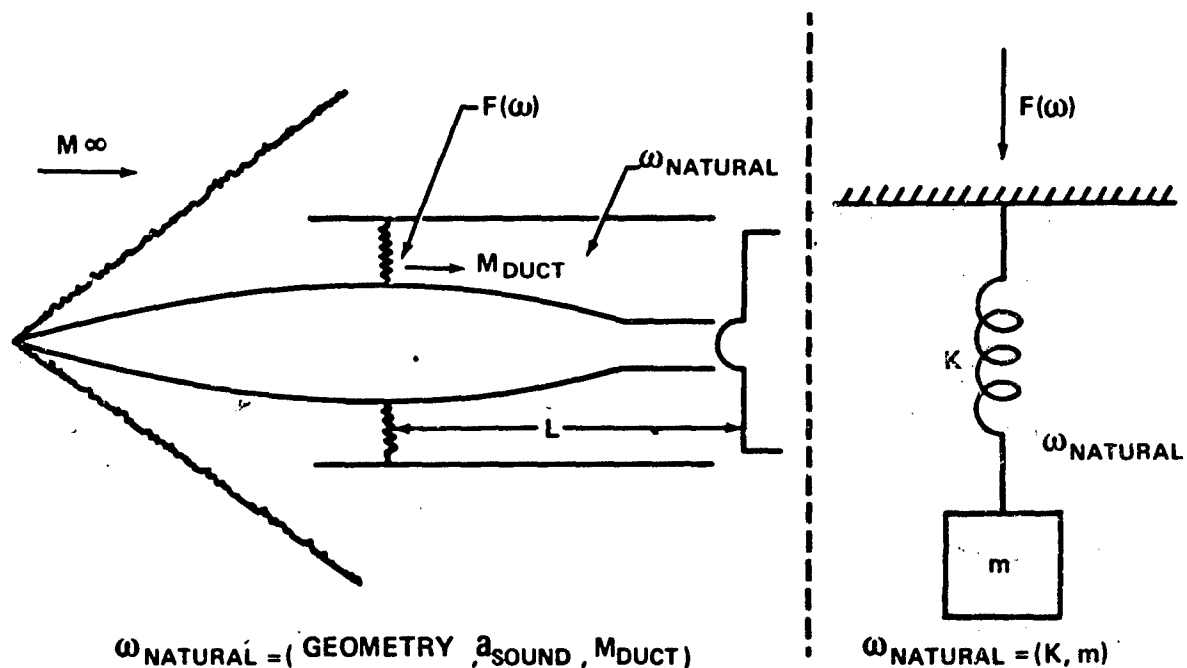


Figure 13. Proposed Mechanism for Inlet Dynamics – Mechanical Analogy

In conclusion, a mechanism has been proposed to help understand engine stall difficulties which occurred in two recent aircraft development programs. The ideas discussed here are summarized as follows:

- Data related to these specific aircraft programs (as well as to others) indicate the existence of discrete frequencies in the inlet system.
- These frequencies are readily interpreted and even analyzed in terms of inlet natural frequencies.
- While direct data linking resonance to engine stall do not exist, substantial evidence illustrates potentially injurious effects on both the inlet and engine systems.

CONCLUDING REMARKS

It should be stressed again that several currently existing theories explain the stall difficulties. While the arguments presented here suggest a discrete frequency mechanism as a cause, they do not rule out the correctness of other theories. However, in the interests of arriving at a satisfactory solution to this problem, the writers have attempted to give the resonance mechanism a fair hearing for general use in interpreting and correlating certain data of other test programs currently being run in this problem area.

The Boeing Company, under partial Air Force sponsorship, is currently engaged in such testing in conjunction with its own research and SST programs. This testing is to be conducted with a 1/4-scale SST-type inlet and a specially modified J85 engine in a transonic propulsion wind tunnel. A specific objective of the testing is detailed exploration of some of the ideas discussed here. Figure 14 is a photo of the test configuration.

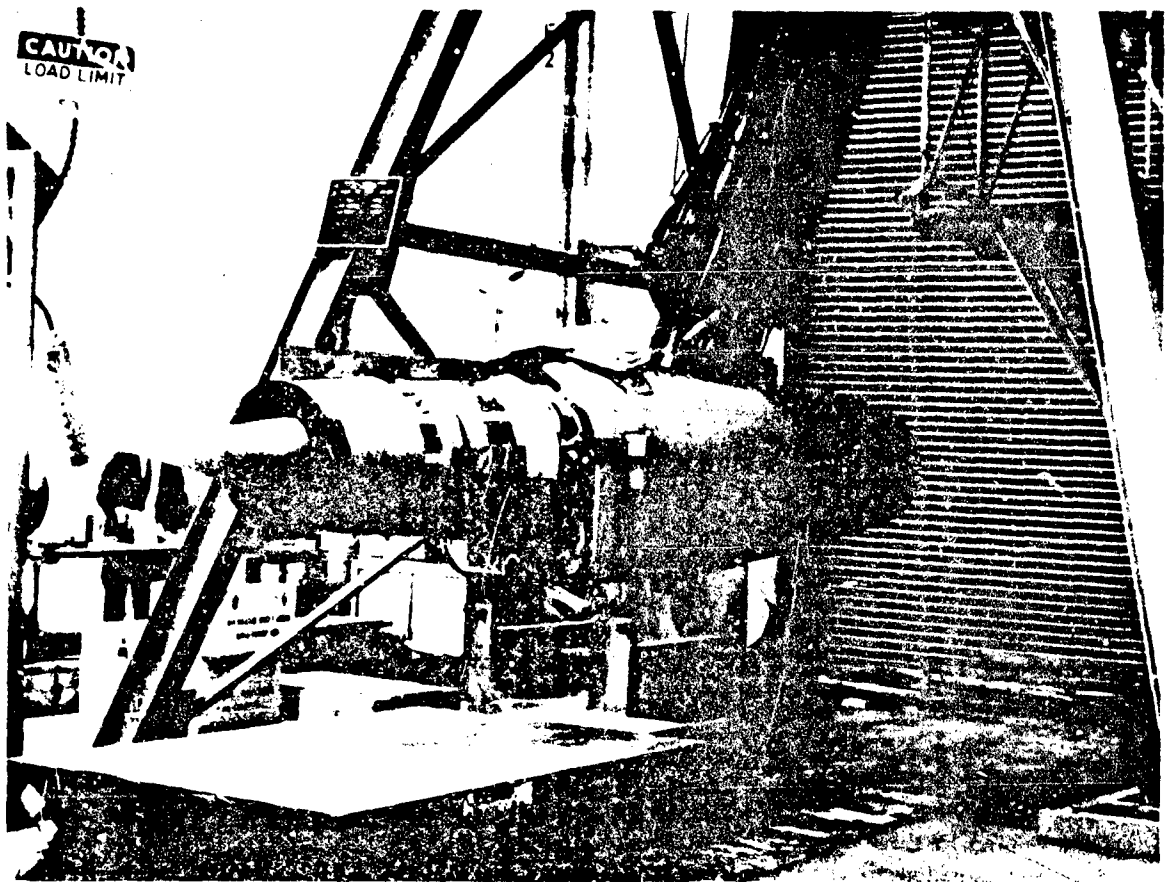


Figure 14. Boeing Transonic Test Arrangement

ACKNOWLEDGMENTS

While the writers must accept sole responsibility for any errors contained in the paper, we very gratefully acknowledge the useful discussions and contributions made by our many colleagues working in this field. In particular, thanks are due to: personnel of the Aero-Propulsion and Flight Dynamics Laboratories at Wright-Patterson AFB, the NASA Lewis Laboratory, and industry personnel from both airframe and engine manufacturing firms.

REFERENCES

1. Rall, F. T., "Aircraft and Propulsion Operational Considerations Related to Inlet Design," AGARD Flight Mechanics Panel, Gottingen, Germany, September 1967
2. Kimzey, W. F. and Lewis, R. J., "An Experimental Investigation of the Effects of Shock-Induced Turbulent In-Flow on a Turbojet Engine," (U) AIAA 2nd Propulsion Joint Specialist Conference, Colorado Springs, Colorado, June 1966 (C)
3. Kimzey, W. F., "An Investigation and Calibration of a Device for the Generation of Turbulent Flow at the Inlet of a Turbojet Engine," AEDC-TR-65-195, October 1965
4. Wasserbauer, J. F. and Willoh, R. G., "Experimental and Analytical Investigation of the Dynamic Response of a Supersonic Mixed-Compression Inlet," AIAA Paper No. 68-651, June 1968
5. Kostin, L. C. and Millstone, S. D., "Application of Statistical Parameters in Defining Inlet Airflow Dynamics," AIAA Paper No. 68-649, June 1968
6. Fraiser, H. R., "Supersonic Inlet Dynamics," J. Aerospace Sciences, June 1960
7. November, G., "Causes of Variable Acoustic Resonance During Tests of Jet Engine Compressors," ASME Technical Paper 67-VIBR-57, 1967

BIOGRAPHIES

Mark B. Sussman

Education: B.A.E. (1960) and M.A.E. (1962) from Rensselaer Polytechnic Institute; Ph.D in gas dynamics and fluid mechanics, Massachusetts Institute of Technology, 1966

At MIT, Dr. Sussman was a research investigator under U.S. Air Force contract to extend the method of characteristics of classical gas dynamics to three-dimensional unsteady flow fields. Later, as a research investigator under a U.S. Navy contract, he investigated the effects of thermodynamic nonequilibrium on the flow field about slender reentry vehicles.

Dr. Sussman's assignment at Boeing since 1966 has been research in the area of inlet distortion. These efforts contributed to the establishment of the current Boeing-Air Force inlet/engine test program. Recently he has been lead engineer in the inlet/engine compatibility group of the Propulsion Research unit. His responsibilities have included directing analytical and experimental programs and maintaining technical liaison in the compatibility field with representatives of other industrial and governmental agencies.

G. W. N. Lampard

Education: B.Sc. (Eng) first class honors, University College, London, 1952; aeronautical specialist, Royal Naval Engineering College, 1953; MSME, Seattle University, 1967

Before Mr. Lampard joined Boeing in 1961, he had served in the Royal Navy as an aircraft engineering officer and completed a graduate apprenticeship with Rolls-Royce Aero Division, Derby. He worked in Canada for Orenda Engines, for Canadian Pratt and Whitney, and as a representative for Rolls-Royce in North America.

With Boeing Mr. Lampard studied the problem of transonic transport engine noise, and analysis of engine weight. Work on the CX-6 V/STOL transport project continued about 2 years and included engine performance analysis, control systems, bleed effects, and lift-fan design. Lampard was propulsion engineer on the ADO-12 V/STOL fighter and was concerned with all propulsion aspects of the study, with emphasis on the integration of propulsion and control systems.

In 1965 he worked on an engine nacelle cooling problem and engine selection for the C-5A. He then became involved for 2 years in propulsion system integration analysis for AMSA, F-X, US/FRG, and VFAX. During the past year he has been responsible for Boeing's IR&D programs on engine technology and inlet/engine compatibility.

UPSTREAM INFLUENCE OF AN AXIAL COMPRESSOR ON CIRCUMFERENTIALLY DISTORTED FLOW

Alan H. Spring

Fort Worth Division of General Dynamics

For a more thorough understanding of subsonic duct flows and distortion phenomena, a particular analysis was applied which illustrates the upstream readjustment of the flow caused by the presence of a compressor. Several far upstream total pressure and velocity distortion patterns were assumed and results were computed which show that flow angularity and static pressure distortions are present at the compressor face where none were present far upstream. Conclusions are drawn with possible implications for engine-inlet compatibility and recommendations are made for experimental investigations to verify the theory and to determine possible methods for simple passive simulation of compressors for inlet testing.

INTRODUCTION

A thorough understanding of steady state distortion in a ducted flow is an essential element in resolution of the total engine-inlet compatibility problem. A distorted flow in the inlet of a typical highly integrated, high-performance propulsion system will be affected by duct bends and cross section changes as well as by the compressor itself. The upstream influence of the compressor has been predicted theoretically by a number of authors, but their attention has generally been confined to the flow within and downstream of the compressor.

As a first step toward understanding of the upstream effects of the compressor and the possible implications for engine-inlet compatibility, a linearized analysis (Ref. 1)

restricted to steady-state circumferential distortions in an incompressible flow was studied in detail and applied to obtain a variety of results for the region upstream of the compressor.

DISCUSSION

Several authors have addressed themselves to the problem of mathematically modeling the presence of rotating machinery in ducted flow. The most common approximation has been the so-called "actuator disc" approach in which a single row of rotor blades is described by discontinuities in certain flow properties. It is possible to analyze a number of situations depending on the combination of assumptions chosen. Hawthorne and Horlock (Ref. 2) presented theory which shows the radial re-adjustment of streamlines in a radial equilibrium flow. They also discuss representation of an axial compressor by means of a distribution of discs. On the other hand, Dunham (Ref. 3) considers the two-dimensional (small annular gap) flow in which circumferential distortions are modified by a series of actuator discs. Dunham also discusses the low hub-to-tip ratio situation and rotating stall. Extension of the "actuator disc" theory to include combined radial and circumferential distortion has been presented by Yeh (Ref. 4). Recently, Callahan and Stenning (Ref. 6) presented an analysis similar to that of Plourde and Stenning which included radial distortions and compressibility effects. Their theoretical predictions were confirmed by experimental data. Tests of a full scale engine-inlet combination which demonstrate the upstream influence of the compressor were reported by Winslow (Ref. 7). The above authors have provided a theoretical and experimental background to build further understanding of inlet distortion.

The impetus for this author's study of the upstream problem was provided by Sussman (Ref. 5) while the recent work of Plourde and Stenning (Ref. 1) has provided theory particularly adaptable to the illustration of the upstream effects. Plourde and Stenning have developed an analytical model of a multi-stage compressor which eliminates the complexities involved with the actuator disc analysis of a multi-stage machine. The compressor is modeled by a distributed axial body force and an empirical resistance to tangential flow. With the assumption of small circumferential distortions in an incompressible flow, the governing inviscid flow equations reduce to:

$$\frac{1}{r} \frac{\partial v'}{\partial \theta} + \frac{\partial u'}{\partial x} = 0 \quad (1)$$

$$\frac{\partial^2 u'}{\partial x \partial \theta} - Kr \frac{\partial^2 v'}{\partial x^2} = -\frac{B}{\rho \bar{u}} \frac{\partial u'}{\partial \theta} \quad (2)$$

The physical model implied by the assumptions of the analysis is shown in Figure 1 along with a definition of the nomenclature of equations (1) and (2). The quantities u' and v' are small perturbations to the axial and circumferential velocities, respectively. The factor K appearing in equation (2) represents an empirical description of the resistance of the compressor to tangential flow. The quantity B in equation (2) is interpreted as the compressor characteristic parameter and is proportional to the slope of the compressor pressure rise when plotted as function of mass flow per unit area. Closed form solutions to the set of equations (1) and (2) may be obtained such that for the region upstream of the compressor,

$$u(x, \theta) = \bar{u} + \sum_{n=1}^j \left[(\epsilon_n + A_n e^{nx/r}) \cos n\theta + (\delta_n + \hat{A}_n e^{nx/r}) \sin n\theta \right] \quad (3)$$

and

$$v(x, \theta) = v' = \sum_{n=1}^j \left(A_n e^{nx/r} \sin n\theta - \hat{A}_n e^{nx/r} \cos n\theta \right) \quad (4)$$

The details of the solution to equations (1) and (2) are quite involved and for the sake of brevity will not be repeated here. The complete details of the solution are given by Reference 8. The quantities A_n and \hat{A}_n are functions of K and B so that the characteristics of the compressor are seen to have a definite effect on the upstream re-adjustment.

In order to generate sample results which demonstrate the upstream influence of the compressor, the distortion patterns far upstream of the compressor face are assumed in the form

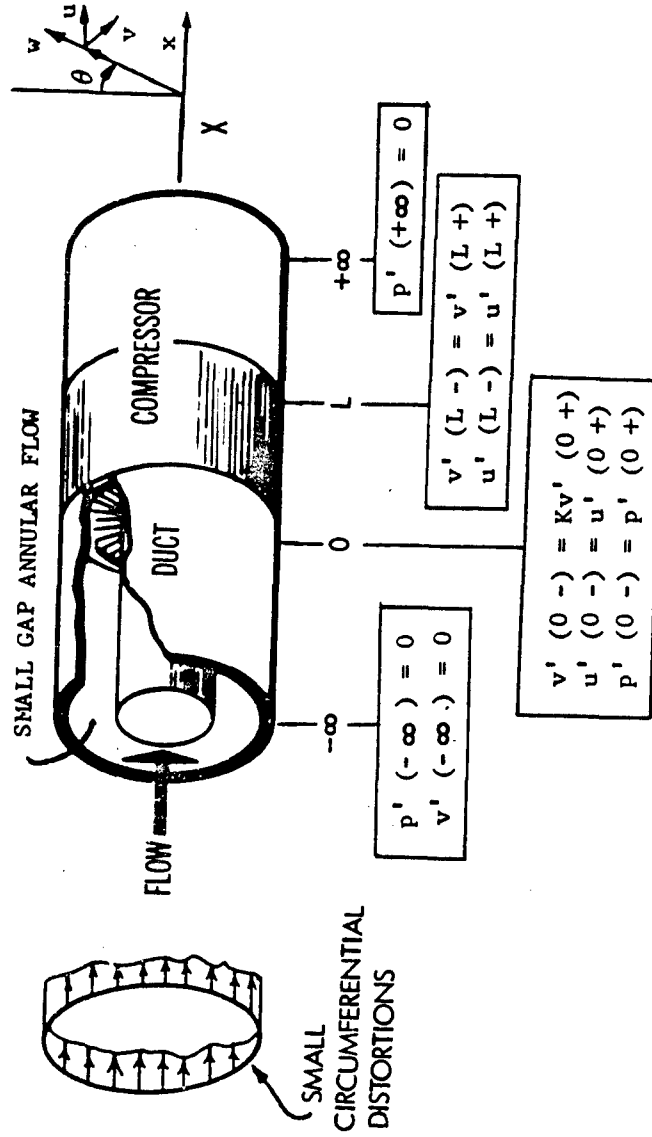


FIGURE 1 PHYSICAL MODEL IMPLIED BY ASSUMPTIONS OF ANALYSIS

$$p_t = \bar{p}_t + \sum_{n=1}^j \left[\gamma_n \cos n\theta + \xi_n \sin n\theta \right] \quad (5)$$

$$p = \bar{p} = \text{const.} \quad (6)$$

For small perturbations the upstream velocity coefficients ϵ_n and δ_n are written

$$\epsilon_n = \rho \bar{u} \gamma_n \quad (7)$$

$$\delta_n = \rho \bar{u} \xi_n \quad (8)$$

Equations (3) through (8) along with the expressions for A_n and \hat{A}_n provide a complete description of the upstream flow for a given set of the parameters K , $BL/\rho\bar{u}$, L/r , γ_n and ξ_n .

For the special case when $K = \infty$ the solutions for u and v reduce to the form

$$u = \bar{u} + \sum_{n=1}^j \left[\left[1 - \left(\frac{BL/\rho\bar{u}}{1 + BL/\rho\bar{u}} \right) e^{nx/r} \right] \left[\epsilon_n \cos n\theta + \delta_n \sin n\theta \right] \right] \quad (9)$$

$$v = v' = \sum_{n=1}^j \left[\left(\frac{BL/\rho\bar{u}}{1 + BL/\rho\bar{u}} \right) e^{nx/r} \left(\epsilon_n \sin n\theta - \delta_n \cos n\theta \right) \right] \quad (10)$$

The solutions for $K = \infty$ provide useful and simply obtained results. This solution is used for the sample results given in the discussion to follow. Figure 2 shows the variation of the induced velocity coefficient A_n/ϵ_n as a function of K with $BL/\rho\bar{u}$ as a parameter. Figure 2 shows that for values of K above five (5) that the results are essentially the same.

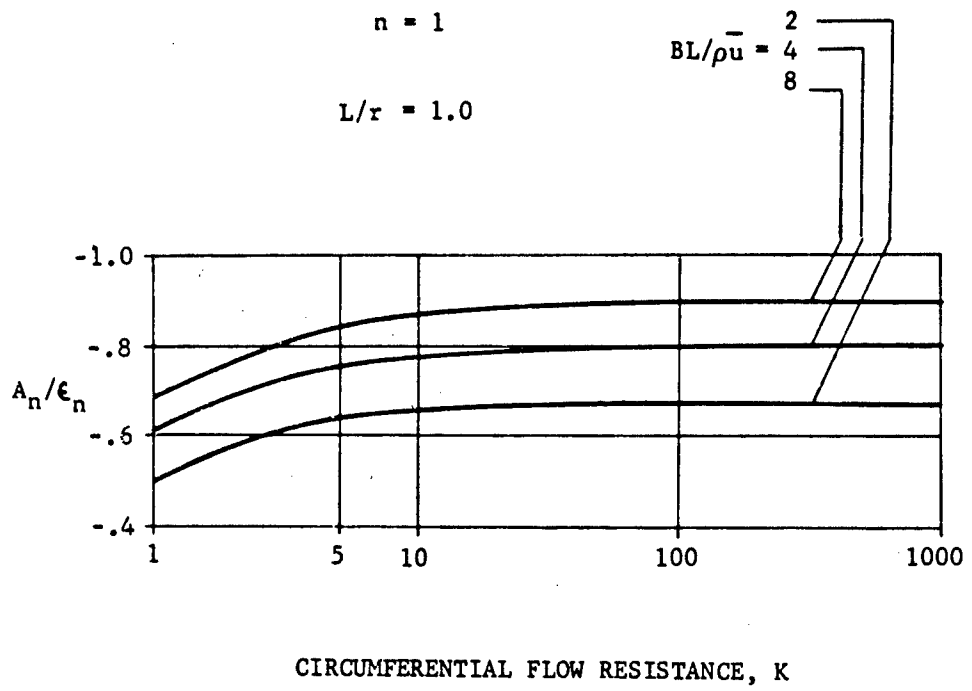


FIGURE 2 INDUCED VELOCITY COEFFICIENT AS A FUNCTION OF CIRCUMFERENTIAL FLOW RESISTANCE

SAMPLE RESULTS

For the studies reported in Reference 8, a variety of far upstream total pressure patterns were assumed and the resulting velocity and static pressure variations were computed. For example, the results shown in Figure 3 serve to illustrate the upstream influence of the compressor. In Figure 3, the simple sinusoidal total pressure pattern was assumed far upstream ($x = -\infty$). As was assumed in the analysis, the static pressure is uniform far upstream and the circumferential velocity is zero. The axial velocity variation shown is implied by the other far upstream conditions. At the compressor face ($x = 0$), the total pressure pattern is unchanged (by assumption), but significant changes occur in the static pressure and velocity distortion patterns. While the axial velocity and corrected flow distortions are attenuated, static pressure and circumferential velocity (flow angularity) distortions are generated. Additional results based on the simple sinusoidal case are shown in Figures 4, 5 and 6. Figure 4 shows the variation of the static pressure distortion amplitude with distance upstream of the compressor face. The variation of maximum flow angularity is shown in Figure 5. Figure 6 shows how the maximum flow angularity increases with the amplitude of the total pressure distortion.

The results shown in Figures 7 and 8 illustrate the pronounced effect of the shape of the initial total pressure pattern. The trend of re-adjustment is identical to that of the simple sinusoidal case except that the maximum flow angularity is much higher for the square wave case. A comparison of the sinusoidal and square wave cases is shown in Figure 9 where angularities and velocities are given relative to a compressor blade. Here again striking differences are noted between the sinusoid and square wave case even though the levels of total pressure distortion are the same.

CONCLUSIONS AND RECOMMENDATIONS

The analysis used to generate the sample results presented in the foregoing discussion is a useful and convenient tool for investigating the upstream influence of an axial compressor on a circumferentially distorted flow. Based on the theory some tentative conclusions may be drawn which have implications for engine-inlet compatibility. A basic

assumption of the analysis is that the total pressure distortion remains essentially unchanged, while flow angularity and static pressure distortions are induced. If this assumption is valid then the current use of the total pressure pattern as the basic parameter for distortion simulation by airframe and engine companies is valid. On the other hand, each company should recognize that upstream re-adjustment does occur and should plan their design and testing accordingly. Specifically, the airframe company should simulate the presence of the compressor in inlet testing to reduce the possibility of unrecognized effects. Likewise, the engine company should fully recognize in their design and testing the nature of the compressor induced re-adjustment (particularly circumferential flow angularity). Winslow (Ref. 7) has made similar conclusions and has pointed out experimentally the uncertainties involved in generalizing the upstream influence of the compressor.

Callahan and Stenning (Ref. 6) have made the obvious extensions to the presently applied theory. Hence, it is recommended that further theoretical work on the upstream problem be preceded by additional experimental efforts designed to place the upstream influence problem in proper perspective (i.e., Does it have a significant influence on engine-inlet compatibility?).

Theoretical and experimental investigations to determine possible techniques for simple passive simulation of compressor effects for inlet testing are recommended. While inflow distortion has been successfully simulated for engine testing (e.g., Ref. 7), little has been done to simulate the upstream influence of the compressor for inlet testing. Since a compressor tends to attenuate the axial velocity distortion, then a device such as a choked screen offers a distinct possibility for compressor simulation. Honeycomb sections are another possibility which do not exhibit the pressure rise characteristics of a compressor but nevertheless induce the upstream re-adjustment of the inlet flow.

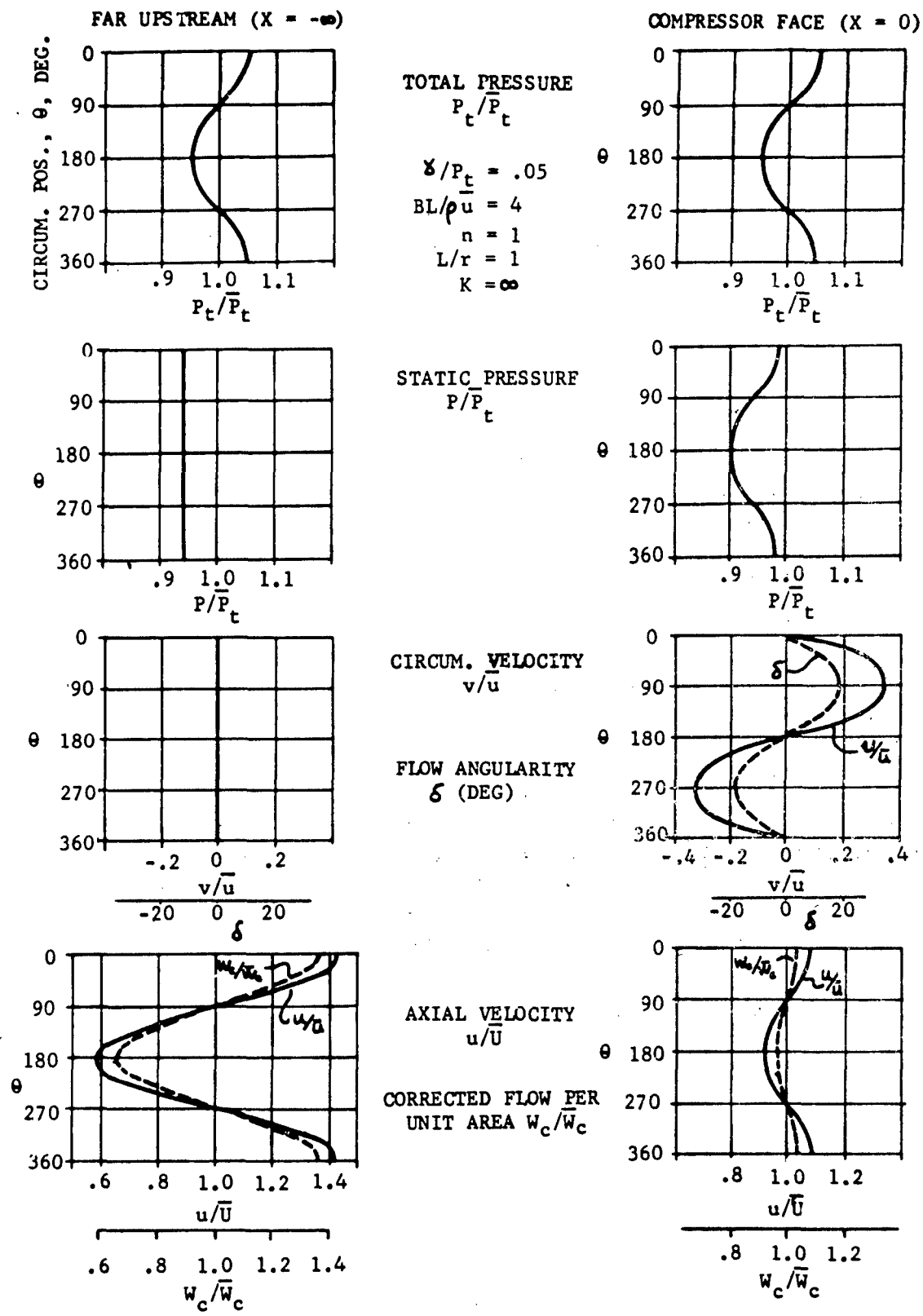
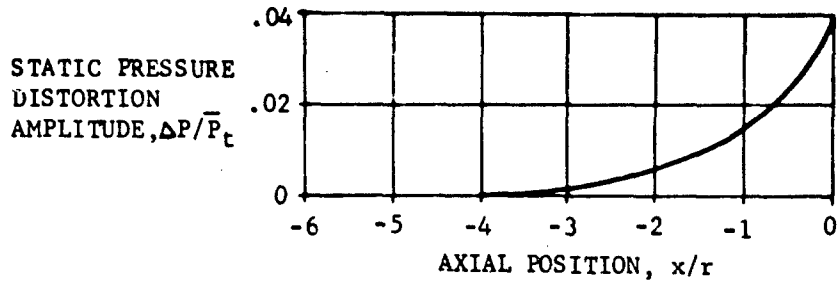


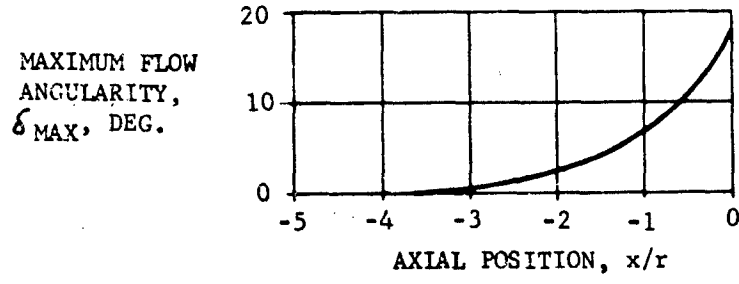
FIGURE 3 DISTORTION PROFILES FAR UPSTREAM AND AT THE COMPRESSOR FACE FOR SIMPLE SINUSOIDAL TOTAL PRESSURE DISTORTION



$$BL/\rho \bar{U} = 4$$

$$\gamma/\bar{P}_t = .05$$

FIGURE 4 STATIC PRESSURE DISTORTION AMPLITUDE UPSTREAM OF COMPRESSOR FACE



$$BL/\bar{U} = 4$$

$$\gamma/\bar{P}_t = .05$$

FIGURE 5 MAXIMUM FLOW ANGULARITY UPSTREAM OF COMPRESSOR FACE

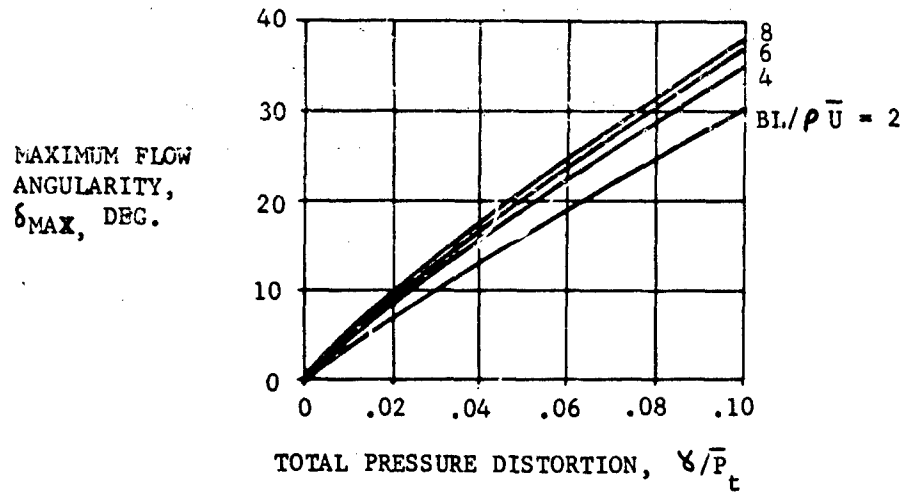
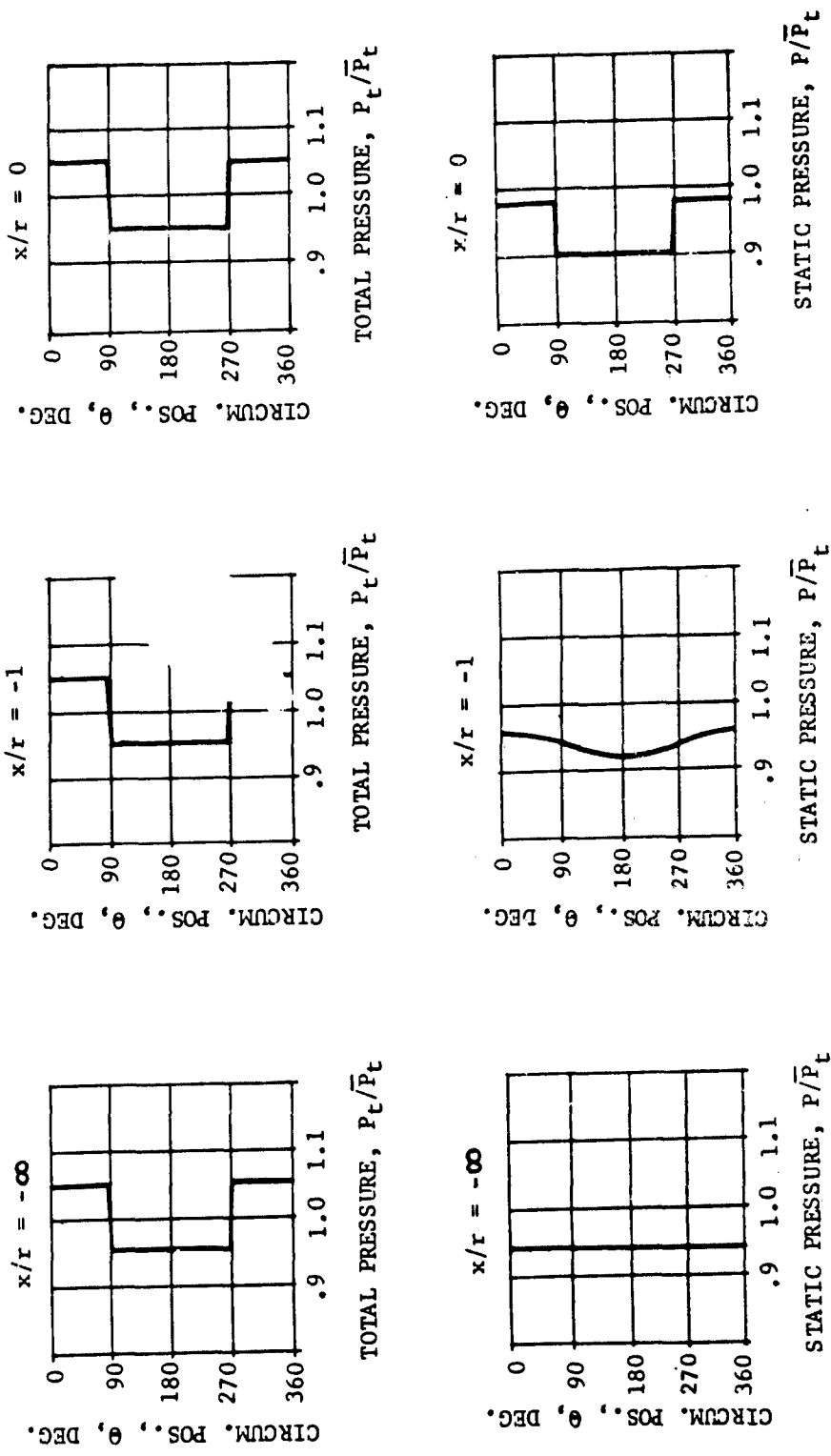


FIGURE 6 MAXIMUM FLOW ANGULARITY AS A FUNCTION OF TOTAL PRESSURE DISTORTION



$\lambda/\bar{P}_t =$ $BL/\bar{\rho}u = 4$ $n = 1$ $k = \infty$

FIGURE 7 TOTAL AND STATIC PRESSURE PATTERNS WITH AN INITIAL SQUARE WAVE TOTAL PRESSURE DISTORTION

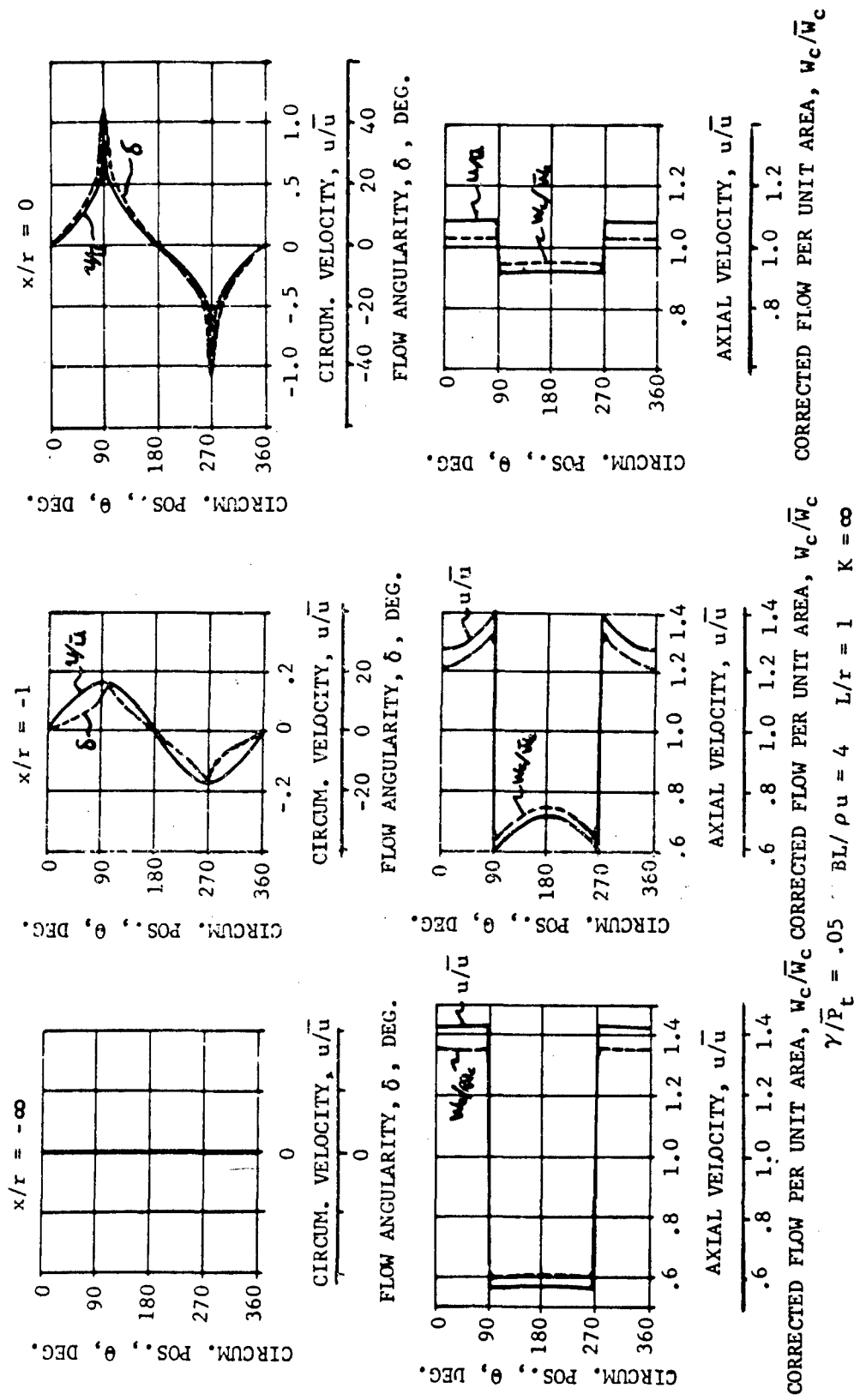


FIGURE 8 CIRCUMFERENTIAL VELOCITY, FLOW ANGULARITY, AXIAL VELOCITY AND CORRECTED FLOW PER UNIT AREA PATTERNS WITH AN INITIAL SQUARE TOTAL PRESSURE DISTORTION.

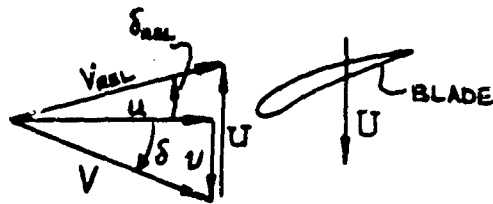
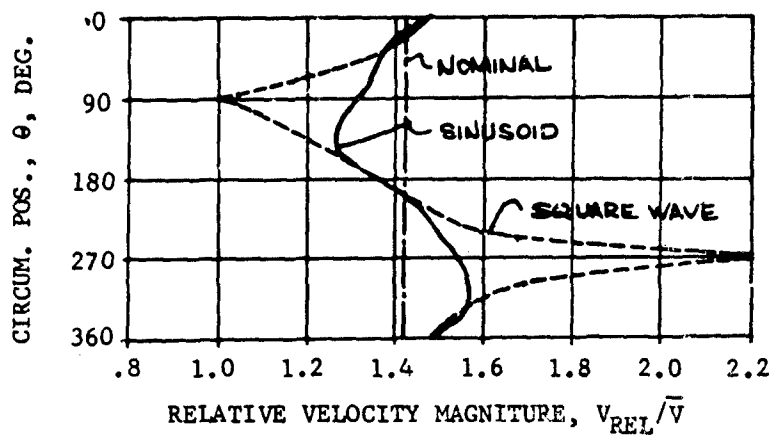
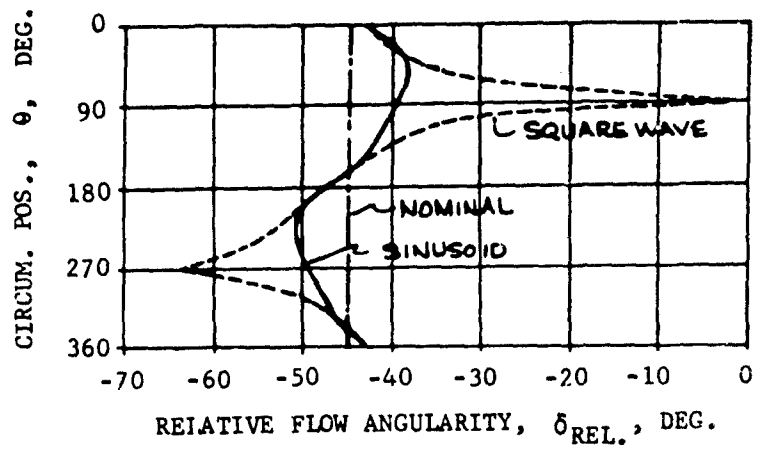


Figure 9 COMPARISON OF RELATIVE VELOCITY AND FLOW ANGULARITY FOR SIMPLE SINUSOID AND SQUARE WAVE WITH BLADE VELOCITY $U/u = 1.0$

REFERENCES

1. Flourde, G. A. and Stenning, A. H., "The Attenuation of Circumferential Inlet Distortion in Multi-Stage Axial Compressors", Journal of Aircraft, May-June, 1968 (Also AIAA Paper No. 67-415, July 1967).
2. Hawthorne, W. R. and Horlock, J. H., "Actuator Disc Theory at the Incompressible Flow in Axial Compressors", Proceedings of the Institution of Mechanical Engineers, Vol. 176, No. 30, (1962).
3. Dunham, J., Non-Axisymmetric Flows in Axial Compressors, Institution of Mechanical Engineers, Mechanical Engineering Science Monograph No. 3, October 1965.
4. Yeh, H., "An Actuator Disc Analysis of Inlet Distortion and Rotating Stall in Axial Flow Turbomachines", Journal of the Aeronautical Sciences, Vol. 26 (Nov. 1959), p. 739.
5. Sussman, M. B., "A Remark Concerning Engine-Inlet Distortion", J. Aircraft, Vol. 5, No. 1, Jan-Feb 1968, p. 95.
6. Callahan, G. M. and Stenning, A. H., Attenuation of Inlet Flow Distortion Upstream of Axial Flow Compressors, AIAA Paper No. 69-485, June, 1969.
7. Winslow, L. J., et al., Inlet Distortion Investigation - Upstream Influence and Screen Simulation, Air Force Aero Propulsion Laboratory Technical Report, AFAPL-TR-68-140, January 1969.
8. Spring, A. H., Upstream Influence of Axial Compressors on Distorted Subsonic Duct Flows, Fort Worth Division of General Dynamics, ERR-FW-755, 26 August 1968.

PROPULSION SYSTEM STABILITY

**Major G. E. Strand USAF, Chairman
Air Force Aero Propulsion Laboratory**

SESSION IV. ENGINE STABILITY INVESTIGATIONS

**L. D. McKenny, Cochairman
Air Force Aero Propulsion Laboratory**

PROPULSION SYSTEM FLOW STABILITY

Arnold W. Martin

North American Rockwell Corporation, Los Angeles Division

This presentation summarizes the objectives, status, and some of the highlights of the Propulsion System Flow Stability program. Of necessity, only a few parts of this Aero-Propulsion Laboratory-sponsored program will be discussed. Those desiring further information are referred to the Phase I final report, AFAPL-TR-68-142. The report consists of 20 volumes or parts; the first part being a summary of and a guide to the other parts.

The ultimate objective of the program is to develop a control system concept which will (1) provide optimum performance during steady-state operation and (2) maintain propulsion system stability by sensing and accommodating transients as they occur. Ideally, this concept would eliminate those steady-state performance penalties incurred when stability margin is obtained by scheduling steady-state operation of the various components below optimum.

The program is a team effort. Members of the team are the Allison Division of General Motors, the Autonetics Division of North American Rockwell, Honeywell, the Los Angeles Division of North American Rockwell, Northern Research and Engineering Corporation, and Pratt & Whitney Aircraft.

The program consists of two funded phases and a proposed third phase. The recently completed Phase I consisted of research on the fundamental causes of propulsion system instability and the development of analytic tools. Phase I is discussed later in more detail.

The primary objectives of Phase II, now in progress, are the definition and analysis of "accommodation control systems" for an RASC airplane with J-79 engines and an advanced tactical fighter. Additional portions of Phase II are (1) an analysis and test program to determine methods of scaling inlet-turbulence data, (2) programming the combustion instability model developed in Phase I and use of the resulting computer program in parametric studies, and (3) development of a computer program for predicting the performance and stability characteristics of arbitrary fan-compressor combinations operating over a range of bypass ratios. Phase II reports are scheduled for release in February 1970.

In the proposed Phase III, hardware for an accommodation control system would be fabricated, development tested, and installed in a flight test aircraft. As presently envisioned, it would be a completely integrated control

system for all elements of the propulsion system. The control system, centered on a digital computer, would control all the elements of the propulsion system as an integrated whole, rather than as subsystems such as engines, inlets, etc.

PHASE I TASKS

Phase I consisted of 7 tasks as shown in figure 1.

CATALOG OF TRANSIENTS- An industry survey was made and a catalog compiled listing those transients which have and/or which might, in the future, cause propulsion system instability. The catalog further listed those parameters which might be used to sense or anticipate the onset of instability by the accommodation control systems to be synthesized in Phase II.

INLET INSTABILITY RESEARCH- The inlet instability research was concerned primarily with inlet-induced turbulence. Existing model and flight test data were analyzed; and, various statistical analysis techniques were evaluated.

ENGINE INSTABILITY RESEARCH- A combination experimental and analytical investigation of engine response to both steady-state distortion and turbulence was conducted. A primary objective was to determine what characteristics of inlet-induced turbulence were critical from compressor surge considerations.

NUMERICAL DEFINITION OF DISTORTION- A format for defining the distortion (steady-state and dynamic) that an engine can tolerate, and conversely, the distortion that a specific inlet will generate, was derived.

PERFORMANCE POTENTIALS OF AN ACCOMMODATION CONTROL SYSTEM- The fifth task was an evaluation of the potential advantages (in aircraft performance terms) of an accommodation control system.

SURVEY OF SENSORS- A survey was made to determine both current capabilities and near future capabilities of those sensors which might be required in an accommodation control system.

PROPULSION SYSTEM SIMULATION DEVELOPMENT- The final task of Phase I consisted of the development of the digital computer simulation program to be used in the Phase II synthesis and analysis of accommodation control systems. The simulation program for the complete propulsion system is based on the IBM DSL/90 program modified as required. It includes the logic and routines necessary for self-initialization.

It might be noted that the development of a simulation program of the complete propulsion system provides good practice in integration of the

propulsion system of an actual aircraft. The same partners and methods of operation and cooperation are needed, as are the same types of data. In a similar vein, it was found that no amount of good intentions and managerial agreements was as effective in ensuring integration as the physical working together of the propulsion system simulation team members.

TYPICAL PHASE I RESULTS

INLET DYNAMIC DISTORTION -

Inlet Turbulence Characteristics - Three basic conclusions were reached from the inlet turbulence data analyses:

1. The most important turbulence-generating mechanism is boundary layer-shock interaction. This is true even at subsonic flight (or tunnel) Mach numbers where high turbulence levels are generally associated with supercritical inlet operation (regardless of the free stream Mach number, flow is supersonic downstream of the effective minimum-inlet area section during supercritical operation).
2. Turbulence contains both random and nonrandom components. As terminal shock strength increases (recovery decreases), discrete frequency energy peaks become more prominent; the peaks occurring at or near the acoustic frequencies of the duct configuration.
3. Engine face total pressure spatial distortion can vary appreciably in a millisecond; and, the maximum distortion values are much higher than would be measured by conventional "steady-state" instrumentation. Further, there can be an appreciable variation with time of the spatial average engine face total pressure.

Figure 2 shows the turbulence energy distribution with frequency at three different recovery levels. The power spectral density curves are for an engine face total pressure probe in a two-dimensional research inlet model.

As pressure recovery decreases (terminal shock strength increases), there is a marked increase in the turbulence energy level. Further, much of the increase is centered about two discrete frequencies. One corresponds to the calculated Helmholtz frequency of the test configuration; the other corresponds to the calculated organ pipe frequency. Other dynamic total pressure data have shown peaks in cross correlation and cross power spectral density curves at or near the inlet acoustic frequencies (even where no resonance peaks were discernable in the power spectral density plots).

These observations indicate that the probability of appreciable areas undergoing the same pressure transient is greatest at the inlet acoustic frequencies.

Both the variation of spatial average pressure with time and its tendency to vary with the inlet acoustic frequency are illustrated in figure 3. The data are from the NASA axisymmetric inlet tests conducted for the NASA/Ames Research Center, reference 1. The points on the curve were obtained by averaging the pressures of 20 engine face total pressure probes at intervals of 0.0005 second. An unrealistically low recovery condition was selected to emphasize the two points of significance. First, an engine is subjected to both varying spatial distortion and varying average total pressure during turbulent inlet operation. Second, the spatial average pressure oscillations tend to coincide with inlet acoustic frequencies. The "beat note" period of approximately 0.013 second that can be seen in portions of figure 3 is in close agreement with the calculated organ pipe frequencies of the inlet model.

Inlet Turbulence Scaling - A major question area is how can model test turbulence data best be scaled to full scale flight test conditions. From the foregoing discussion and figures, it is apparent that a portion of the data will frequency-scale in accordance with acoustic theory. To better resolve scaling questions, a special test program was run at AFDC wherein 3 models were tested at identical conditions. The tests were run and data analyses are being conducted as part of Phase II. However, a brief outline of the program may be in order.

The three inlet configurations tested were representative of a high performance aircraft and were identical except that:

1. One was a one-third scale model
2. One was a one-eighth scale model
3. One was a one-eighth scale model with a cylindrical extension such that the distance from the cowl lip to the sonic point flow control valve (just aft of the engine face rakes) was identical to that for the one-third scale model.

Hopefully, the combination of three models will provide the data necessary for scaling both the acoustic resonance and random frequency components of turbulence. Figure 4 is a preliminary plot of data from the tests wherein turbulence levels for the three configurations are compared at an extreme attitude condition. Obviously, the problem of scaling turbulence data is not a simple one.

Total Temperature Transients - It is customary to think of inlet-induced transients in terms of pressure only, just as engine face distortion and turbulence values are almost invariably based entirely on pressure measurements. The inlet simulation program developed and used on the XB-70 program indicated that pressure transients, such as inlet unstart and buzz, were accompanied by total temperature transients at the engine face which perhaps, equally as important, could determine whether the engine(s) would or would not stall. High-response thermocouples installed in one inlet of the XB-70 during the latter part of the flight test program have shown that such total temperature transients do indeed exist. Figure 5 shows both simulation and flight test engine face total temperature transients. Here the essential point is not the degree of agreement between simulation and test, but the fact that inlet-induced total temperature transients do indeed exist and must be considered.

ENGINE RESPONSE TO DISTORTION - Engine response to distortion, with emphasis on the basic mechanisms by which distortion results in compressor stall, was investigated in the 3-part program shown in figure 7. Details of these investigations are given in Parts IV, V, VIA, VIB, VII, VIII, IX, X, XI, and XII of AFAPL-TR-68-142, Propulsion System Flow Stability Program (Dynamic), Phase I Final Technical Report.

Compressor Characteristics with Steady-State Distortion - A 2-part mathematical model of compressor response to steady-state radial and circumferential engine face distortion was developed by Northern Research and Engineering Corporation.

The first part computes performance characteristics for any arbitrary compressor configuration and operating point. The engine face flow annulus is divided into an arbitrary number of streamtubes sufficient to define the engine face distortion (pressure and temperature). Iterative calculations are made to determine the path of each streamtube and the properties of the airflow at each station through the compressor. The resultant overall performance characteristics can be plotted as a conventional compressor map. Figure 7 illustrates two characteristic speed lines, as computed by the program, using as inputs the geometry of a NACA 5-stage compressor. Also shown are experimental data points.

The foregoing program does not implicitly indicate the stall or surge limit for the characteristic speed lines. The second portion of this effort was, therefore, directed towards determining the stability limits. The stability of the flow at each point in the computational grid of the above program is calculated using the local properties of the flow as computed in the original program. Limited checks with experimental data show that predicted stability limits are in good agreement with test data. Equally important, if the procedure is to be used as a design tool, it indicates the region where flow breakdown first occurs. Figure 7 shows

the agreement between calculated and experimental stability limits, and the region where the flow breakdown was predicted for each of two corrected speeds.

Compressor Response to Time-Variant Pressure - The mathematic models developed by Pratt & Whitney Aircraft were primarily concerned with compressor response to time-variant pressures or turbulence. The related experimental effort is discussed by Gary Plourde in a paper to be presented later in this session.

A key element in the several math models developed was a stage-by-stage model illustrated in figure 8. In this model, each stage (blade and vane) within the compressor is represented by a control volume (defined by the dashed line in figure 8), and the individual stage performance characteristics. The several "lumped-volume" stages are dynamically coupled using momentum-continuity relationships.

Preliminary use of the model has shown intriguing potentials both in predicting stability characteristics and in showing what configuration changes would improve stability.

Compressor-Induced Total Temperature Distortion - Compressor tests conducted by Allison and results from the Northern Research and Engineering Corporation computer program discussed previously show that appreciable total temperature distortions can be induced by a compressor. Such distortion could be of particular concern in multi-compressor engine configurations.

Total temperature distortions measured in Allison tests of a research compressor are presented in figure 9. The tests were run with screens just forward of the compressor to provide total pressure distortion.

As a highly simplified explanation of the cause of the measured total temperature distortion, consider two streamtubes passing through the compressor. Total pressure at the upstream face of one streamtube is less than that for the other. Both must empty into a common plenum area of essentially uniform total pressure. Consequently, different amounts of work must be added to the two streamtubes; and, exit total temperatures will therefore differ. That is, as total pressure distortion is eliminated by the compressor, total temperature distortion is introduced.

NUMERICAL DEFINITION OF DISTORTION - To define the distortion that an engine can tolerate and that an inlet will produce, a common language or definition is required. It must be measurable in inlet tests, meaningful relative to engine tolerance, and understandable to engineers and management. There are a number of distortion indices in existence. All on

occasion have shown two shortcomings. At distortion indices values where no stall should occur, stalls do occur. At distortion indices values where stall is predicted, engines operate normally.

Based on the investigations of this program, it has been concluded that existing distortion indices omit some of the factors tending to reduce compressor surge margin. Accordingly, an NDD (Numerical Definition of Distortion) has been proposed which is additive in format. This format is illustrated in figure 10. NDD is the summation of a series of functions, $f(a)$, $f(b)$, ..., each of which represents some factor such as circumferential total pressure distortion, radial total pressure distortion, total temperature rate of change, etc. Because a large value of one function may change the influence of another, the format includes influence coefficients for each term.

Those functions which have been found to reduce compressor surge margin, and which might be included in the NDD, are listed in figure 11.

The calculations for determining the various distortion functions are such that they represent the percentage loss in stall (surge) margin during fixed throttle operation. That is, stall is to be expected when the sum of the several factors exceeds 100 percent. There will be a further loss of stall margin during throttle transients. Test data and/or simulation data can be used to determine values of NDD that can be tolerated simultaneously with given throttle transients. Inasmuch as stability limits and tolerances differ with the engine operating condition, an additional parameter indicating the engine operating condition must be included, for example, corrected speed. Figure 12 is illustrative of an NDD engine limits map that might apply to a specific engine. (For simplicity, only one throttle transient line is shown.) It should be noted that while the NDD format is applicable to any engine, the constants and procedures used for computing the numerical value of the several functions would differ from engine to engine.

The counterpart to the engine limitation values of NDD are the inlet characteristics presented in NDD units. Because a given distortion function might reduce stall margin of each compressor unit by a different amount (and by an amount differing for each engine operating condition), an inlet operating at a given flight condition might have an NDD characteristics map such as shown in figure 13.

By superposition of the engine limits map and the inlet characteristics map, those areas of stall-free operation are apparent, and those areas of restricted operation are defined. Such a superposition is shown in figure 14.

PERFORMANCE ADVANTAGES OF AN ACCOMMODATION CONTROL SYSTEM - Two sets of calculations were made to determine the performance gains that might be obtained with an "accommodation control system". One was based on the RA-5C, the other on an advanced tactical fighter. Some of the results of the latter study are discussed here.

Performance increments were computed by comparing performance for 2 versions of the advanced tactical fighter. Conventional propulsion system steady-state stability margins were used for one. Propulsion system steady-state operating conditions for the other were established without regard to the stability margins that might be required for transient conditions. Identical propulsion system components and component performance characteristics were used for both. Airframe weight and lift and drag characteristics were also identical for each version.

Aircraft performance increments computed for each of two arbitrary missions are presented in figure 15. As can be seen, there were attractive performance gains in radius, cruise altitude, excess power at combat, and take-off distance for the supersonic reconnaissance mission. Startlingly, however, there was a decrease in the subsonic combat mission. Thrust levels were increased and SFC's were decreased, but the net result was a loss in range.

In the process of determining why the propulsion system performance improvements resulted in a range loss for the subsonic combat mission, the importance of the mission ground rules became most apparent. Some of the ground rules are listed in figure 16. Because thrust levels increased more rapidly than SFC decreased, increased quantities of fuel were required for the warm-up and take-off allowance. Similarly, the fuel required for X minutes of maximum power combat reflected the higher maximum thrust. The mission called for minimum-fuel-flow climb to the best cruise altitude. Because the best cruise altitude was considerably higher, more fuel was consumed in the climb. In combination, these factors resulted in a decreased radius.

To provide a more meaningful comparison, performance increments were computed using revised ground rules as shown in figure 16. When identical take-off fuel allowance, flight paths, and combat thrust levels were used, a radius increase of 11.2 percent was obtained with the accommodation control system. This contrasts with the 4.6 percent radius loss with the original set of ground rules. Obviously, great care must be used in establishing mission ground rules for performance comparisons.

Potential performance gains of an accommodation control system are large, larger for example than can be expected from advances in compressor design. Accordingly, increased research and development of the accommodation concept is strongly recommended.

FIGURE 1
PHASE I TASKS

- CATALOG OF TRANSIENTS
- INLET INSTABILITY RESEARCH
- ENGINE INSTABILITY RESEARCH
- NUMERICAL DEFINITION OF DISTORTION
- PERFORMANCE POTENTIALS OF AN ACCOMMODATION CONTROL SYSTEM
- SURVEY OF SENSORS
- PROPULSION SYSTEM SIMULATION DEVELOPMENT

FIGURE 2

ACOUSTIC RESONANCE

$$\left(\frac{\Delta P}{\bar{P}_{f2}}\right)^2 \cdot \frac{1}{\text{Hz}}$$

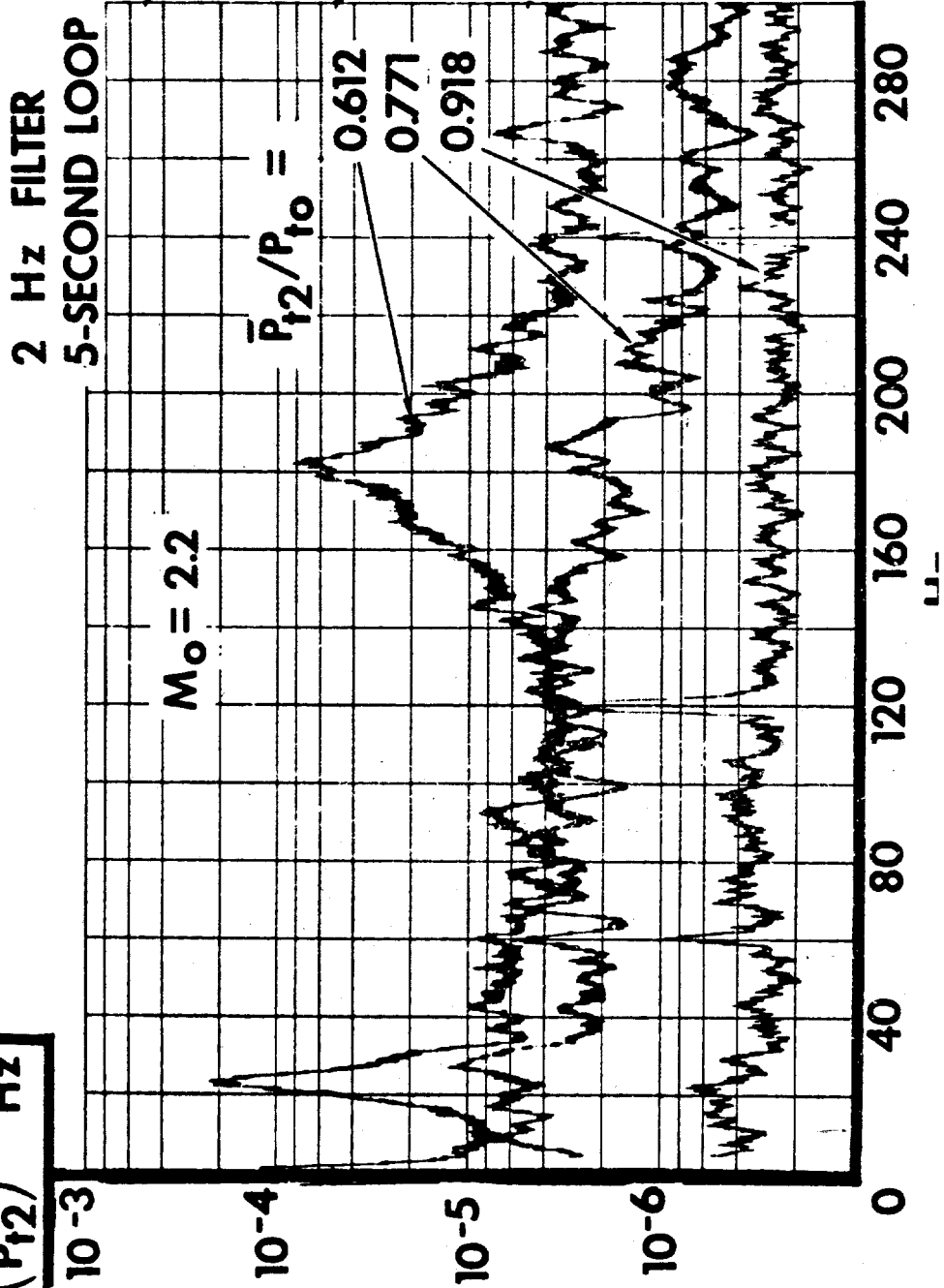
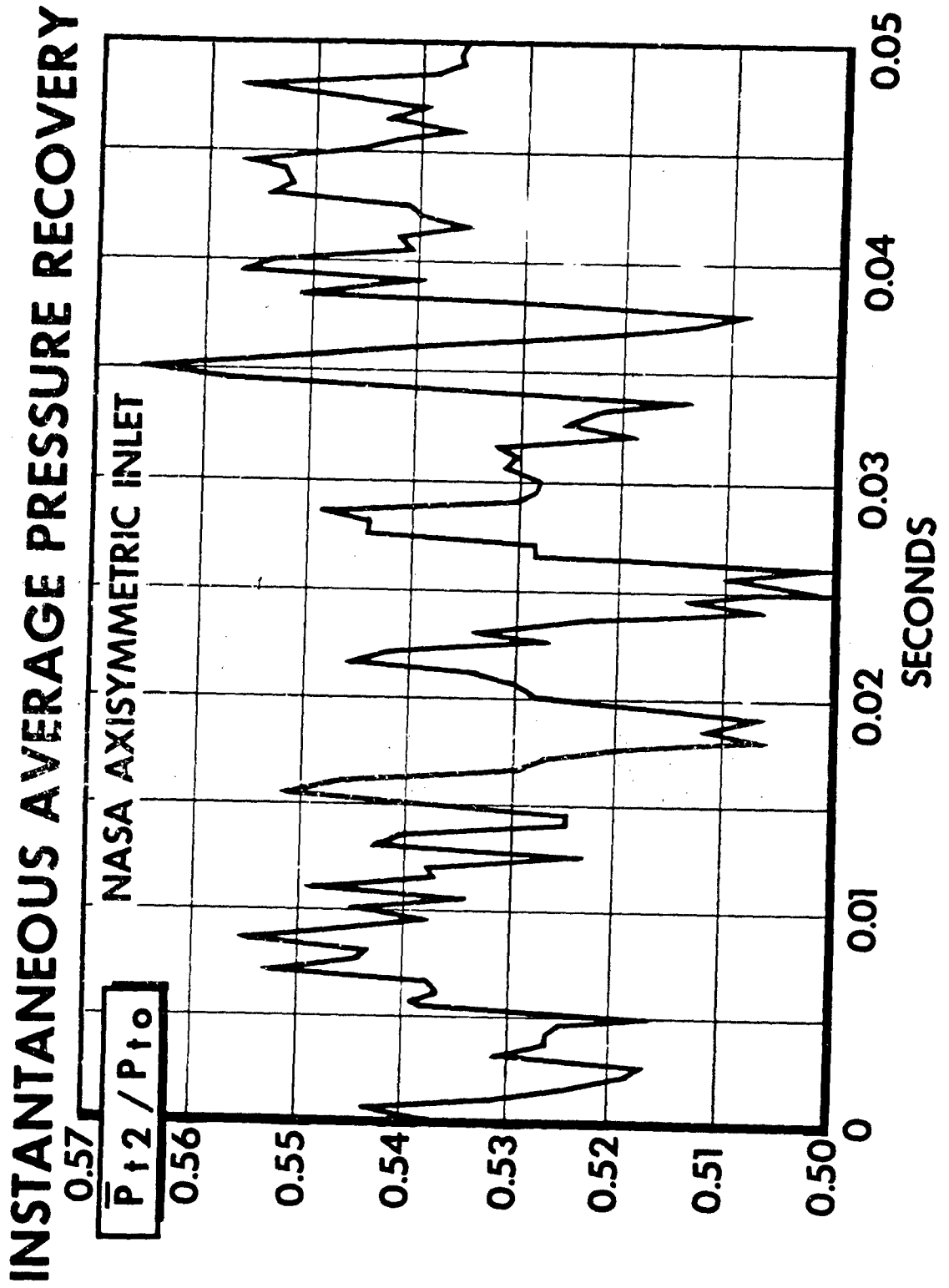


FIGURE 3



REFERENCE

1. Arnold W. Martin, Leonard C. Kostin, and Sidney D. Millstone, "Dynamic Distortion at the Exit of a Subsonic Diffuser of a Mixed Compression Inlet." (Submitted to NASA/Ames Research Center under North American Rockwell Report Number NA-69-218.)

FIGURE 4

TURBULENCE SCALING TEST RESULTS

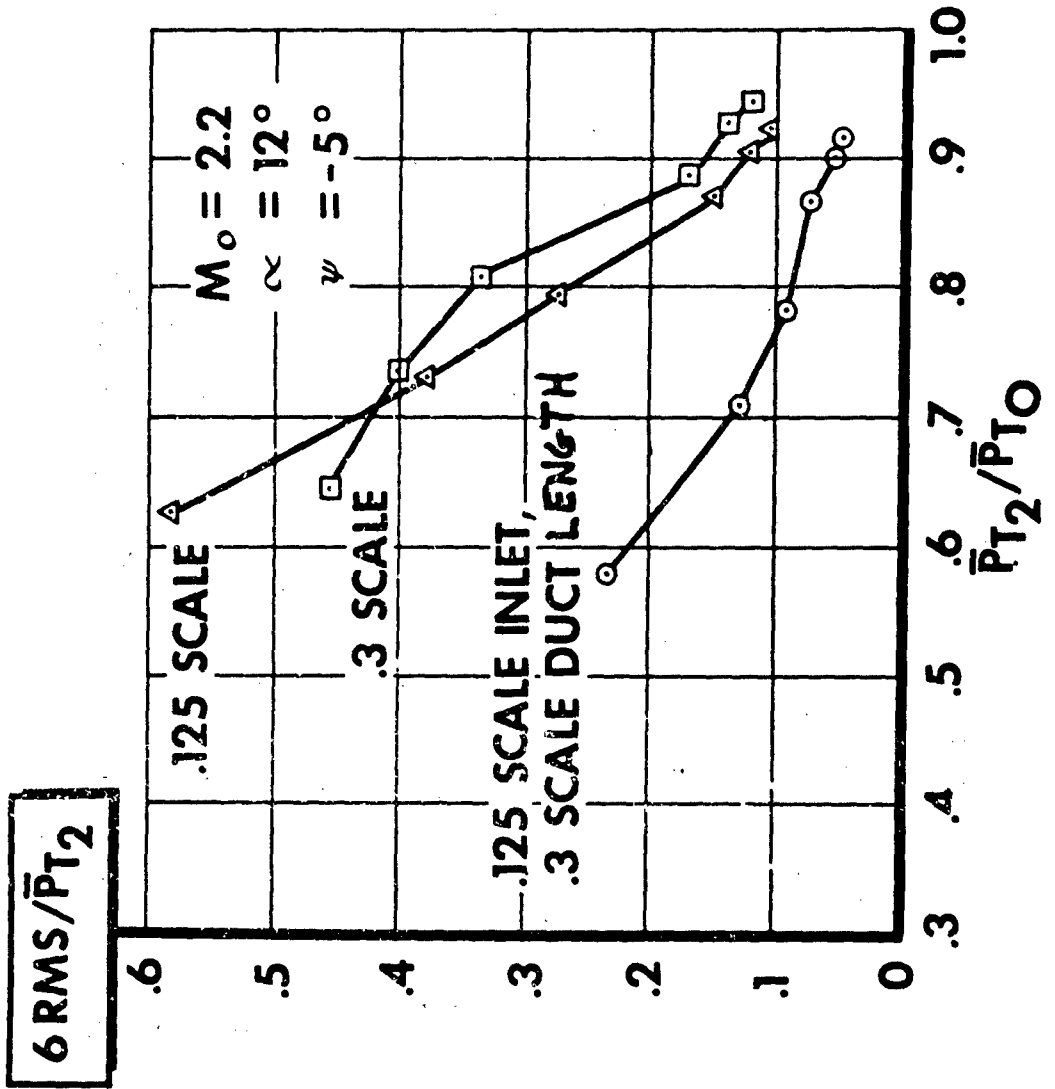


FIGURE 5
TOTAL TEMPERATURE TRANSIENT DURING
INLET UNSTART AND BUZZ

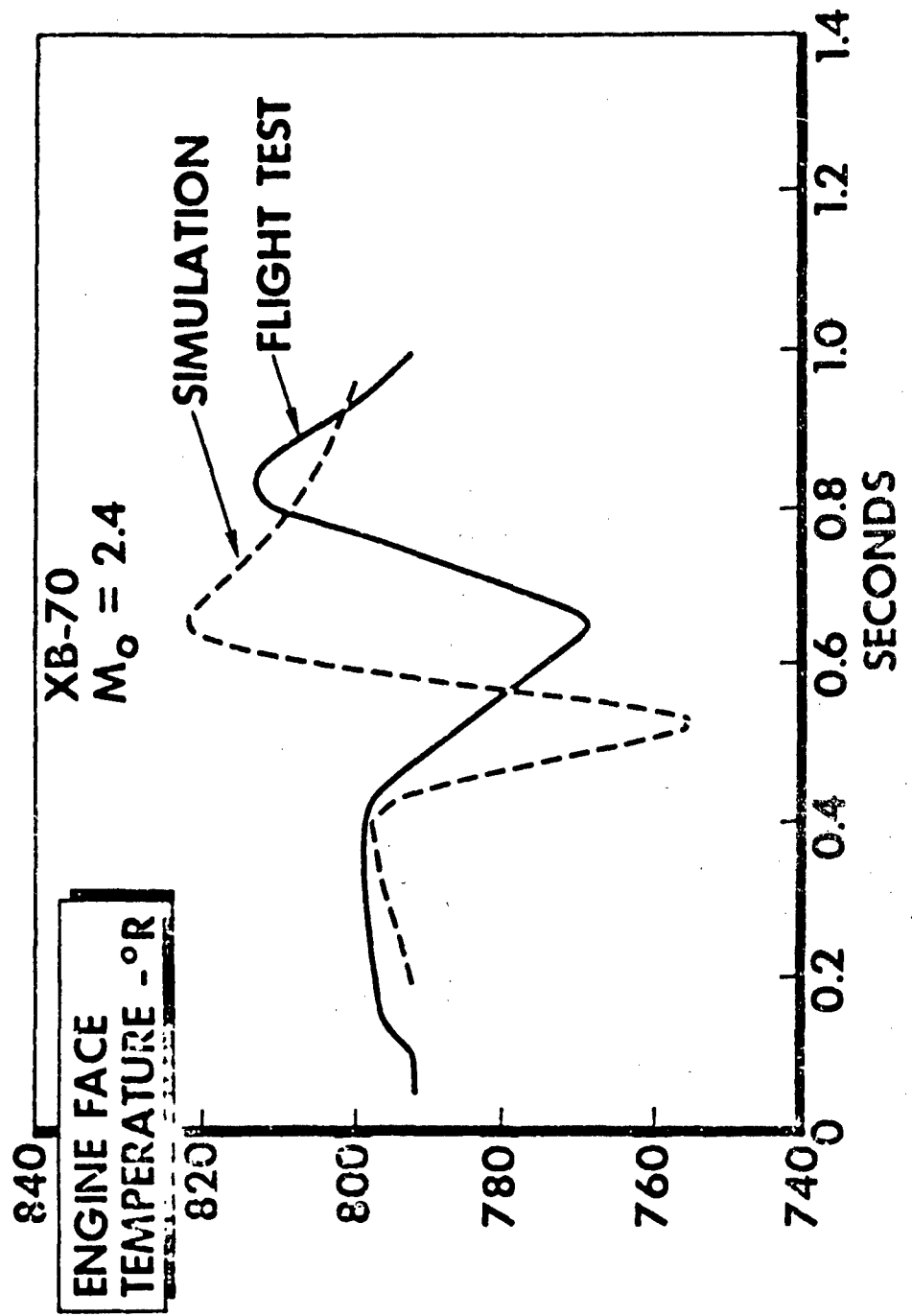


FIGURE 6

ENGINE RESPONSE TO DISTORTION

- **STEADY STATE DISTORTION**
 - **ALLISON COMPRESSOR TESTS**
 - **NREC COMPUTER PROGRAMS**
- **DYNAMIC DISTORTION**
 - **P & WA ENGINE & COMPRESSOR TESTS**
 - **P & WA MATH MODELS**
- **COMBUSTION INSTABILITY**
 - **NREC AFTERBURNER & DUCT BURNER**
 - **COMBUSTION INSTABILITY MODEL**

FIGURE 7
EXPLICIT SURGE PREDICTION FOR
NACA 5-STAGE COMPRESSOR

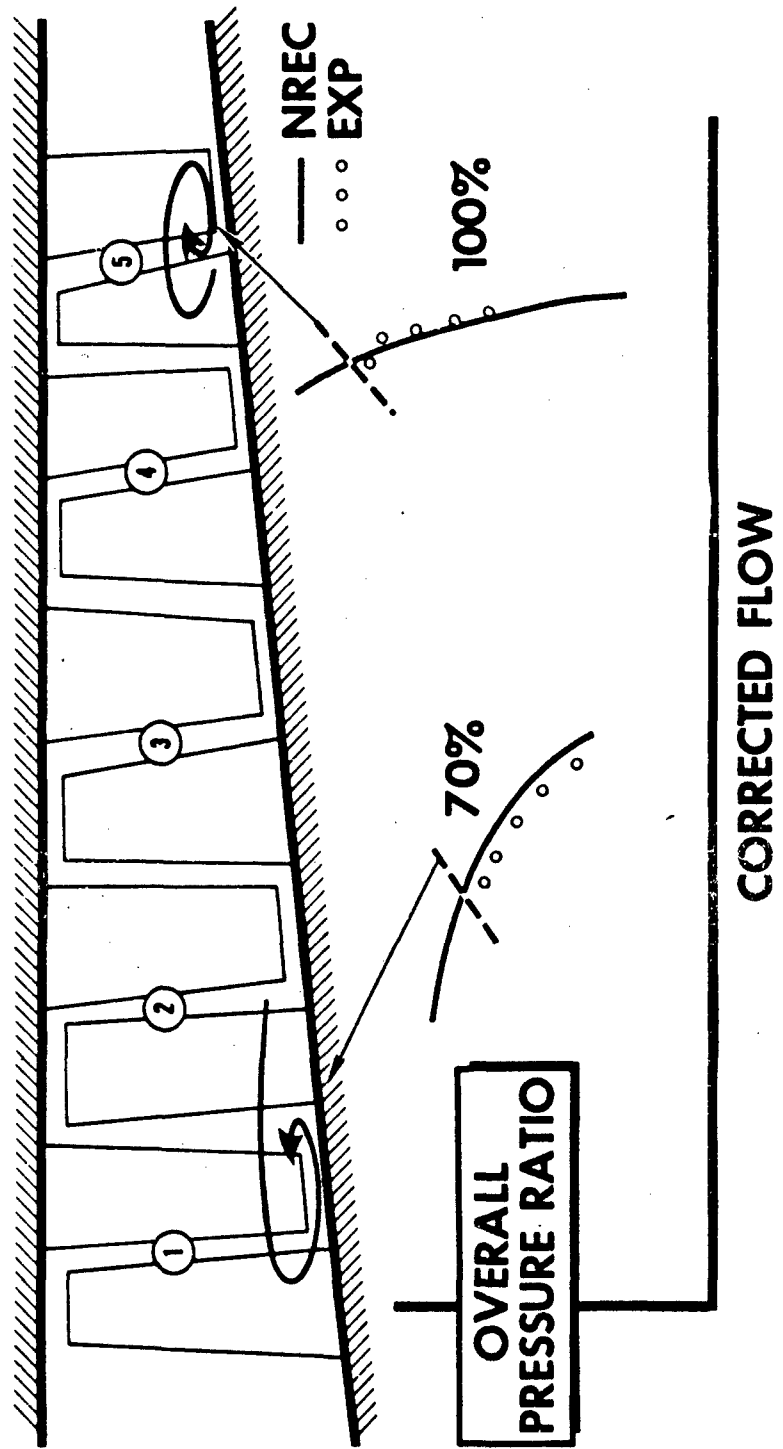


FIGURE 8
MATH MODEL FOR PREDICTING COMPRESSOR
RESPONSE TO TIME-VARIANT PRESSURE

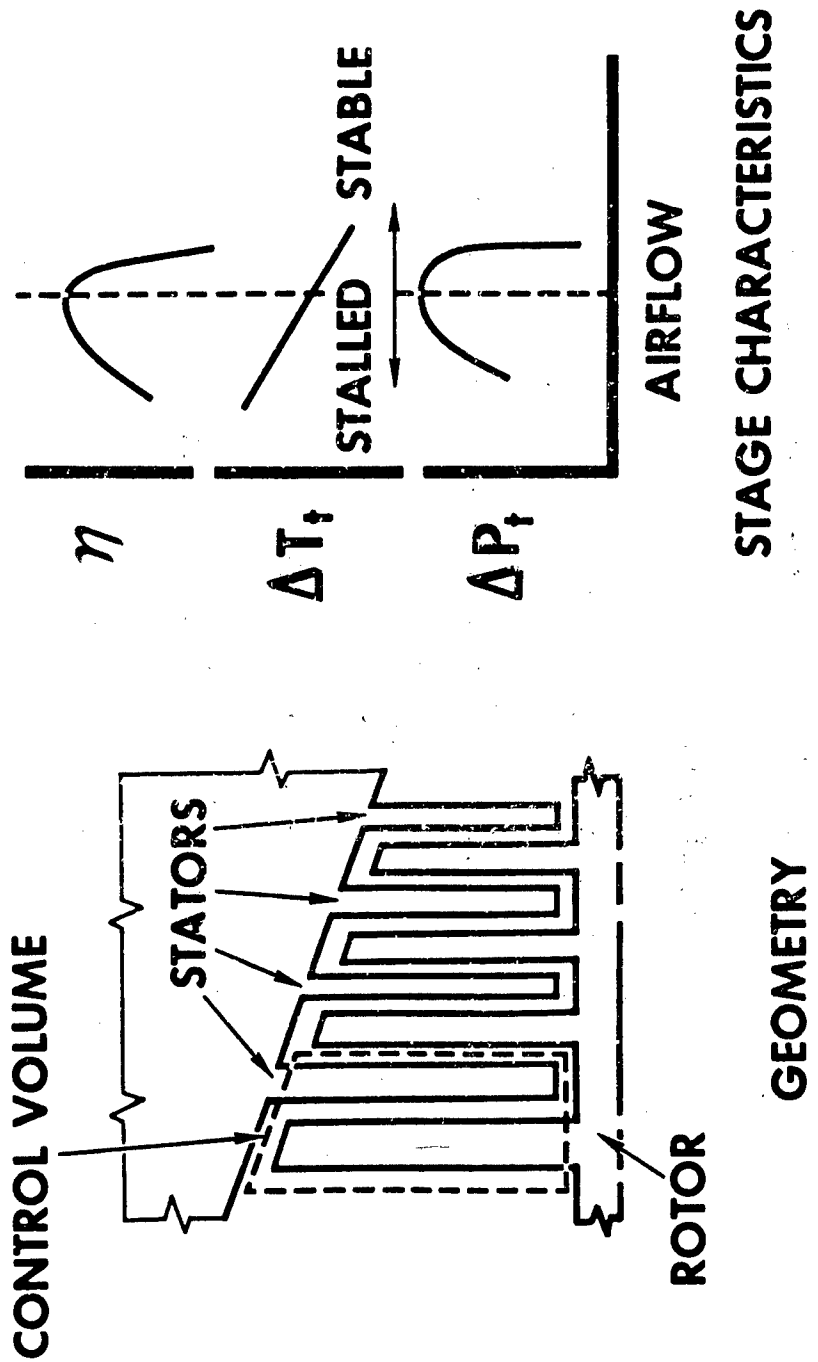


FIGURE 9
TOTAL TEMPERATURE DISTORTION

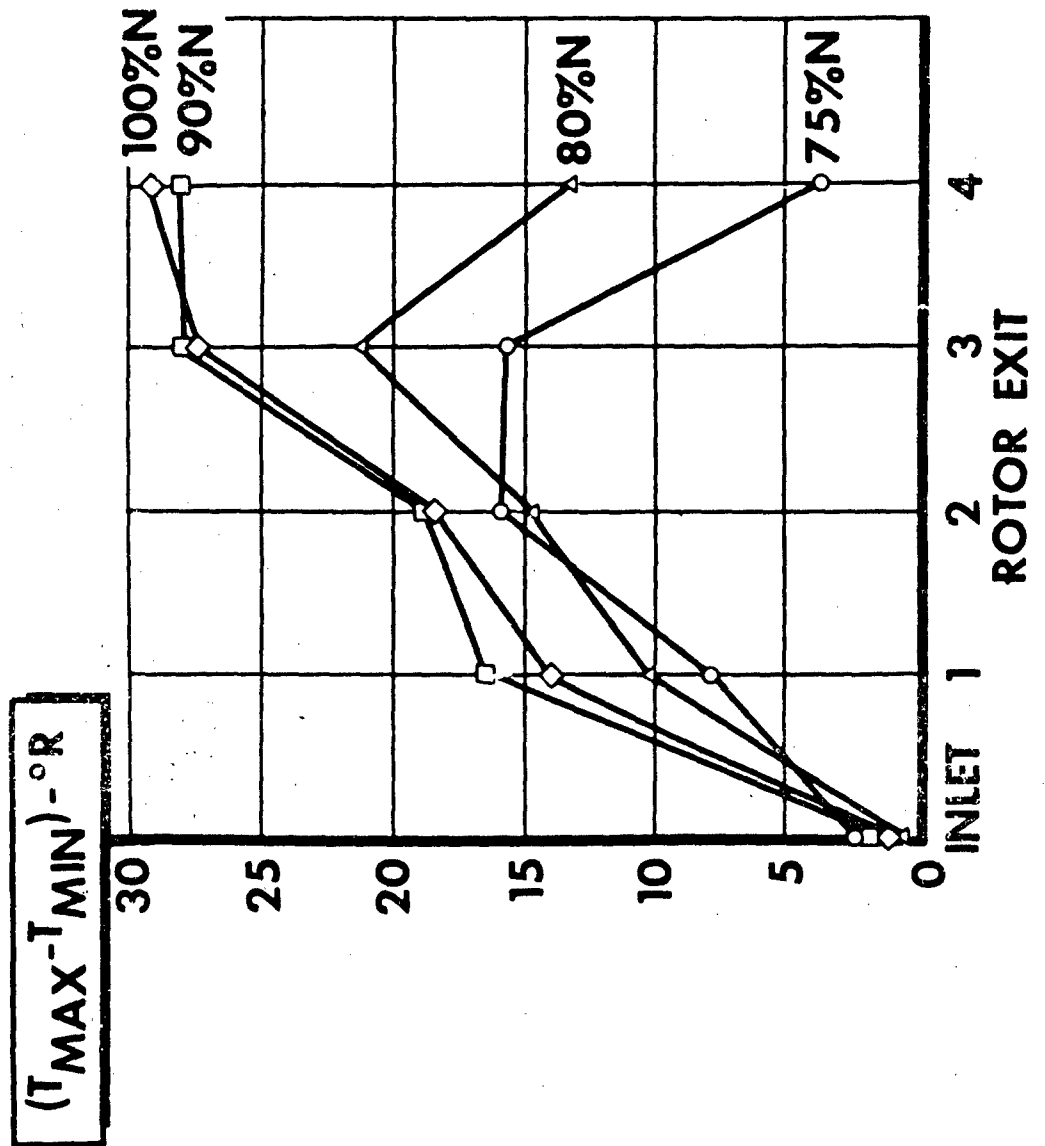


FIGURE 10

NUMERICAL DEFINITION OF DISTORTION

$$\text{NDD} = A f(a) + B f(b) + C f(c) + \dots$$

• "A" IS AN INFLUENCE COEFFICIENT.

• "f(a)" IS A QUANTITY COMPUTED FROM STEADY-STATE CIRCUMFERENTIAL DISTORTION MEASUREMENTS (OR ESTIMATES)

FIGURE 11

**NUMERICAL DEFINITION OF DISTORTION
FUNCTIONS**

- **CIRCUMFERENTIAL STEADY-STATE TOTAL PRESSURE DISTORTION**
- **RADIAL STEADY-STATE TOTAL PRESSURE DISTORTION**
- **DYNAMIC TOTAL PRESSURE SPATIAL DISTORTION**
- **ONE-DIMENSIONAL LOW-FREQUENCY DYNAMIC TOTAL PRESSURE DISTORTION**
- **ONE-DIMENSIONAL HIGH-FREQUENCY DYNAMIC TOTAL PRESSURE DISTORTION**
- **TOTAL TEMPERATURE SPATIAL DISTORTION**
- **ONE-DIMENSIONAL DYNAMIC TOTAL TEMPERATURE DISTORTION**
- **SWIRL**
- **COMPONENT MATCHING CHANGE WITH DISTORTION**

FIGURE 12

ENGINE LIMITS

NUMERICAL DEFINITION
OF DISTORTION - NDD

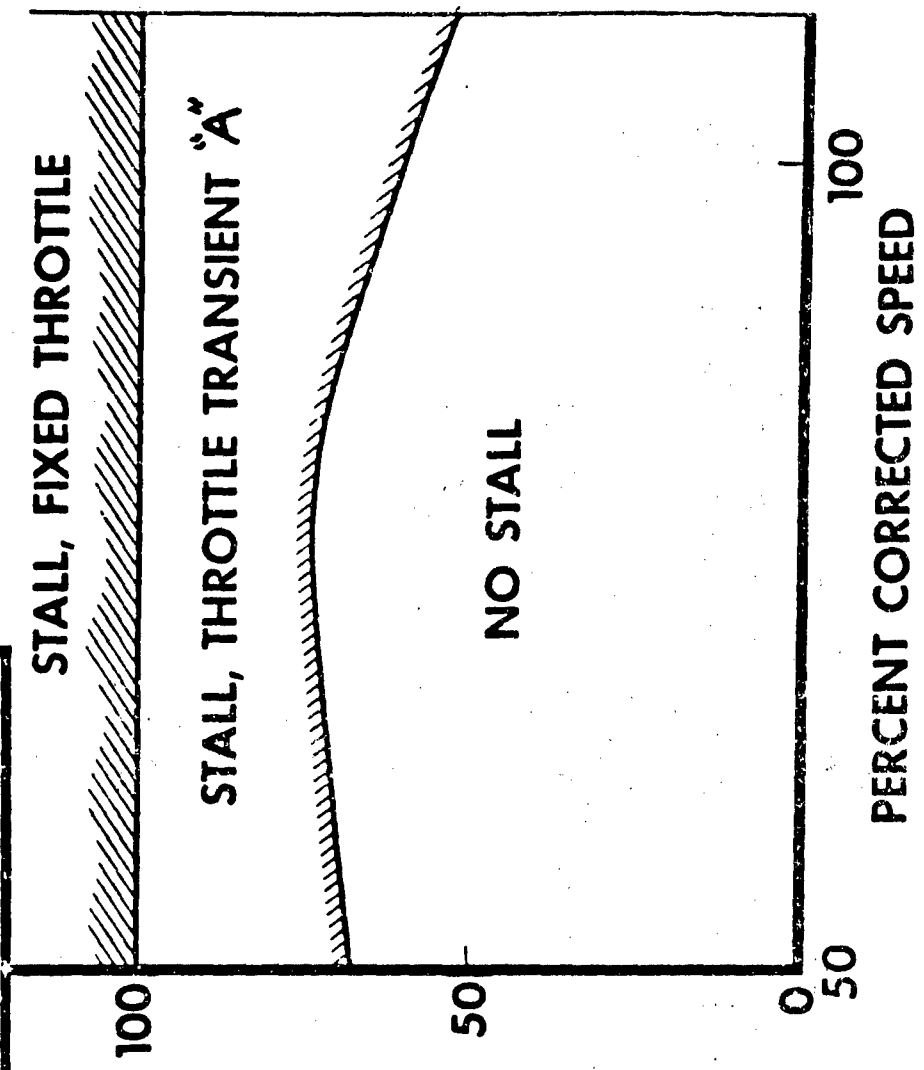


FIGURE 13
INLET CHARACTERISTICS

**NUMERICAL DEFINITION
OF DISTORTION - NDD**

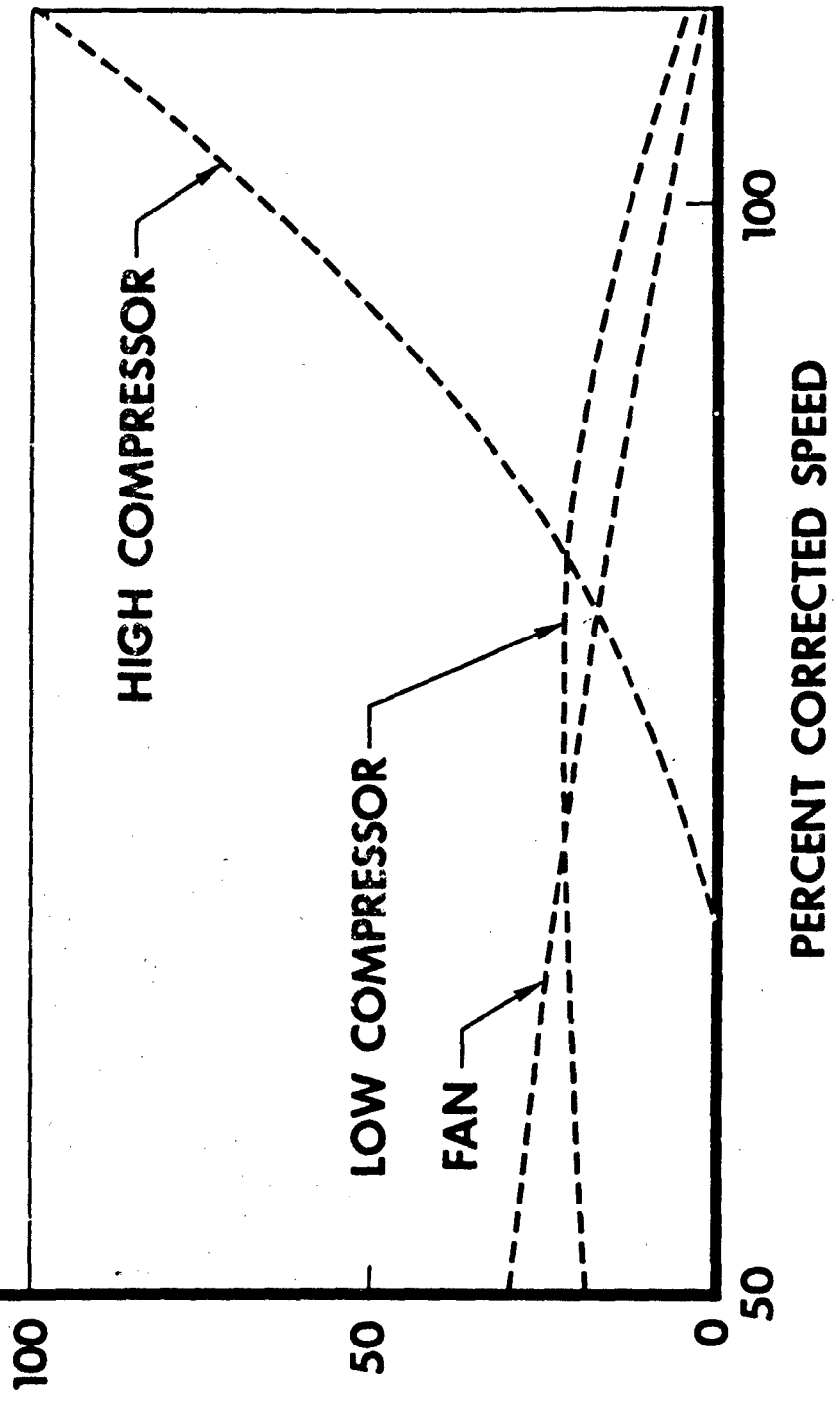


FIGURE 14

OPERATION LIMITS

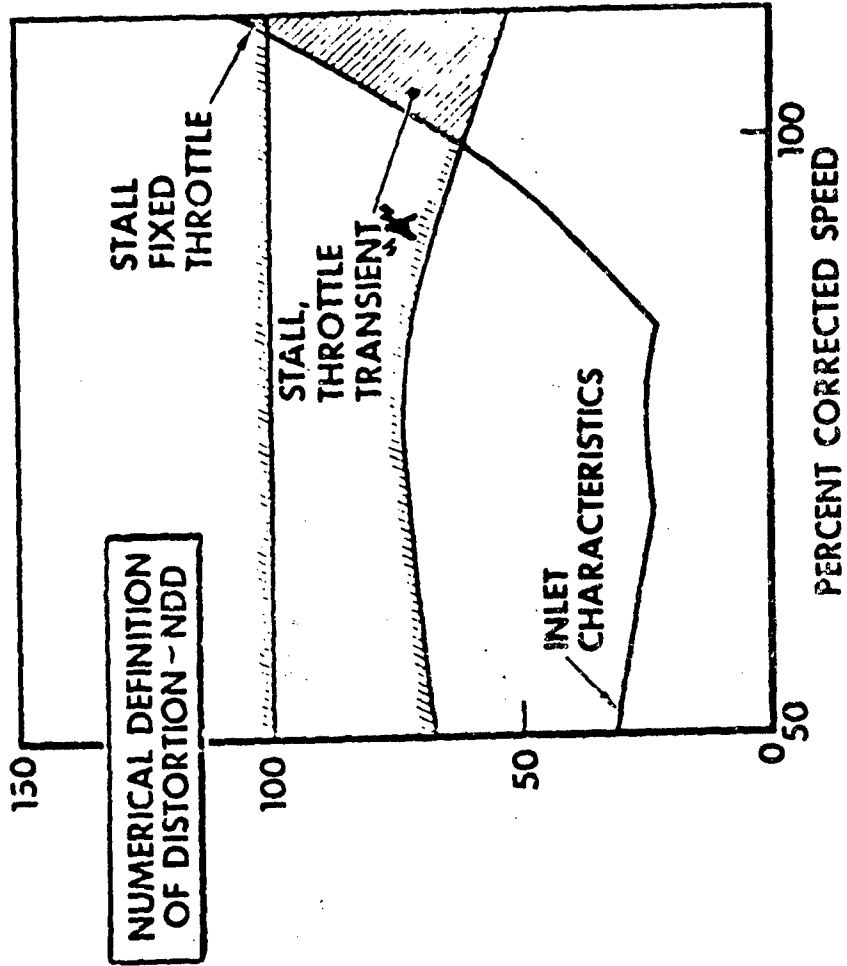


FIGURE 15

**ACCOMMODATION CONTROL PERFORMANCE -
ADVANTAGES, ADVANCED TACTICAL FIGHTER -
CONSTANT FUEL LOAD**

| CHANGES, % | SUBSONIC COMBAT MISSION | SUPERSONIC RECONNAISSANCE MISSION |
|-----------------------------------|------------------------------------|--|
| RADIUS | - 4.6 | + 5.2 |
| CRUISE ALTITUDE | + 27.2 | + 27.4 |
| EXCESS POWER AT COMBAT | + 4.0 | + 12.0 |
| TAKE-OFF DISTANCE | - 11.9 | - 11.9 |

DEVELOPMENT OF A PROTOTYPE
DISCRETE-FREQUENCY, TOTAL-PRESSURE
FLUCTUATION GENERATOR FOR
JET ENGINE-INLET COMPATIBILITY INVESTIGATIONS

G. R. Lazalier, Asst. Project Engineer

and

J. T. Tate, Supervisor

This document is subject
to special export controls and
each transmittal to foreign
governments or foreign nat-
ionals may be made only with
prior approval of
AEDC (AETS)

DEVELOPMENT OF A PROTOTYPE
DISCRETE-FREQUENCY, TOTAL-PRESSURE
FLUCTUATION GENERATOR FOR
JET ENGINE-INLET COMPATIBILITY INVESTIGATIONS¹

G. R. Lazalier, Asst. Project Engineer

J. T. Tate, Supervisor

Rocket Test Facility, ARO, INC., Arnold Engineering Development Center

ABSTRACT

An investigation of the design concepts and operational characteristics of a prototype generator to produce discrete frequency, total pressure fluctuations at the inlet of a jet engine was conducted in an altitude test cell. The generator was designed to provide the fluctuations by two total pressure loss mechanisms: diffuser induced and drag induced. The investigation was conducted over a range of compressor inlet station Mach numbers from 0.28 to 0.55 at imposed discrete frequency pressure fluctuations from 50 to 600 Hz. Spectral analyses of the data are presented along with conventional steady-state analyses. Total pressure fluctuations ranged from 1 to 7 percent of the mean (time-averaged) pressure. Local velocity variations from 5 to 25 percent were measured.

¹The research reported in this paper was sponsored by Arnold Engineering Development Center, Air Force Systems Command, Arnold Air Force Station, Tennessee, under Contract No. F40600-69-C-0001 with ARO, Inc. Further reproduction is authorized to satisfy the needs of the U.S. Government.

NOMENCLATURE

| | |
|------|--|
| A | Area, in. ² |
| B | Bandwidth of electrical filter, Hz |
| C | Amplitude of co-spectrum, constant |
| CPSD | Cross-power spectral density function |
| D | Total pressure distortion, $(P_{\max} - P_{\min}/P_{\text{avg}}) \times 100$, percent |
| f | Frequency, Hz; function |
| M | Mach number |
| P | Total pressure, psia |
| PSD | Power spectral density function, (amplitude/Hz) ² |
| Q | Amplitude of quadrature spectrum |
| T | Total temperature, °R |
| V | Velocity, ft/sec |
| Δ | Change |

SUBSCRIPTS

| | |
|--------------------|--------------------------|
| 00, 1n, 2, etc. | Instrumentation stations |
| avg | Average |
| orf | Orifice |
| max | Maximum |
| min | Minimum |

INTRODUCTION

The adverse effects of inlet flow distortion on turbofan/turbojet engine performance have long been recognized as important engine development considerations. Regions of flow separation and/or shock wave-boundary layer interactions can cause nonuniform distribution or distortion of the total pressure and velocity entering the compressor. Engine operational problems, including compressor stall and structural failure, can result when compressor inlet distortion exists. Screens, located forward of the compressor, have been an acceptable method to produce steady-flow distortion for simulated altitude testing of jet engines in ground test facilities. At subsonic and low transonic flight speeds, satisfactory simulation of flight performance has been obtained; however, the results of recent tests indicate that the unsteady or turbulent flow characteristics of supersonic aircraft inlet ducts are equally important engine design considerations. Based on the difficulties experienced with some current weapons systems, it is apparent that ground facility test techniques with controlled engine inlet flow conditions can be used to understand further engine-inlet matching problems and to shorten engine development cycle time requirements. As flight speed, maneuverability, and engine performance demands are increased, engine-inlet compatibility problems become more critical.

Recent investigations in ground test facilities have generally been limited to work with random frequency and amplitude flow disturbances, characteristic of the flow conditions in a high-speed aircraft inlet duct (Refs. 1 and 2). However, considerable effort is required to define the flow characteristics which cause unacceptable degradation of engine performance and stability. Statistical analysis methods are sometimes used to characterize inlet flow conditions at which engine performance degradation and/or engine stall occurs. Complete testing of a turbofan/turbojet engine requires that the sensitivity of the engine to specific inlet flow properties be determined. For analytical purposes, inlet turbulence may be described by the use of combined random frequency and discrete frequency waveforms.

The sensitivity of engine performance to random frequency pressure fluctuations has been investigated with some success by correlating time-dependent inlet pressure distortion (turbulent flow conditions) with steady-flow inlet pressure distortion. The results of these investigations indicate that the instantaneous inlet distortion of turbulent flow may be considered to be essentially the same as steady-state distortion when the instantaneous flow patterns exist for a finite length of time (on the order of the time period of one engine revolution) (Ref. 3). Total pressure distortions which exist over this length of time (averaged to remove extreme peaks) are correlated using standard steady-flow engine inlet distortion parameters.

Another analysis method considers the effects of the compressor frequency response to inlet pressure oscillations, or the phase shift of a discrete frequency pressure fluctuation through a compressor. The results reported in Ref. 4 indicate the probability of critical discrete frequencies which, as a result of the phase shift, may result in stage or stage group pressure ratios exceeding the stall limit.

The sensitivity of engine performance to discrete frequency pressure fluctuations has not been experimentally established over an extended frequency range. A discrete frequency pressure fluctuation generator, which produces a very low inlet pressure distortion, will provide a tool to determine if jet engines are sensitive to simple time-variant pressure fields or are sensitive only to "steady-state" total pressure distortion.

The purpose of this paper is to define the design concepts and operating characteristics of a prototype generator capable of producing discrete-frequency, total-pressure fluctuations uniformly over the inlet of a jet engine compressor. Details of the design and operating principles are presented, and measured performance of a prototype is included.

TEST ARTICLE

The design configuration of the generator consists of forward and aft stator assemblies, each containing 23 stators, with a 23-blade rotor located axially between the two stator assemblies (Fig. 1). The prototype generator was complete except that an aerodynamically isolated, quarter section, downstream stator assembly rather than the full-scale 23-stator assembly, was used for expediency in obtaining test results on the design concept. The rotor is driven by an externally-mounted air motor, through a 90-deg bevel gear assembly located in the generator hub. Rotational speed is controlled by using differential valving across the air motor which allowed the air motor to brake or drive the motor as required. The direction of rotor rotation was clockwise, looking upstream.

Details of the rotor and stator design are presented in Fig. 2. Ideally, the rotor-stator combination introduces total pressure losses by two separate processes. The first loss is caused by the action of the stators as subsonic diffusers with their attendant total pressure losses. The stators are designed to behave as 24-deg included angle, two-dimensional diffusers. As the rotor moves into the space between the stators the inlet Mach number of the diffuser increases, resulting in higher pressure losses. The second loss process is that associated with the drag produced by the presence of the rotor blade. Additionally, some loss is produced by mutual interference effects of the rotor blades in the diffuser passages.

INSTALLATION

The prototype discrete frequency turbulence generator was installed upstream of an engine simulator in an altitude test cell at the Arnold Engineering Development Center (Ref. 5), as shown schematically in Fig. 3. Airflow to the generator was supplied through a critical flow airflow measuring venturi located in the test cell inlet duct. An airflow straightening screen and an engine inlet bellmouth located in the engine inlet plenum chamber were used to obtain a smooth flow of air to the generator. An exhaust diffuser ducted the simulator exit air from the test cell. The internal volume of the ducting from the flow venturi throat to the generator front face was 3.5×10^6 cubic inches.

The jet engine simulator (Fig. 4) consisted of a 7-ft-length of 36.67-in. I.D. ducting with a conic discharge nozzle. The simulated compressor inlet station was 22 in. downstream of the rotor. A sonic flow orifice was located approximately 22 in. downstream of the compressor inlet station to provide a volume between the rotor and the orifice plate approximating the effective volume of a turbojet/turbofan compressor (Fig. 1b).

INSTRUMENTATION

Conventional steady-state instrumentation was used to determine time-averaged values of pressure and temperature at the simulator inlet. Time-averaged values of airflow were measured at the critical airflow venturi.

Dynamic instrumentation consisted of four piezoelectric total pressure transducers and one piezoelectric static pressure transducer located at the compressor inlet station in the quadrant behind the aft stators (Fig. 5a). The piezoelectric total pressure transducers were installed in a pressure rake as indicated in Fig. 5b. Steady-state total pressure measurements were obtained at each dynamic total pressure transducer location. The estimated uncertainty (2 sigma) of the dynamic pressure measurements was ± 10 percent of the peak-to-peak pressure variation in the frequency range from 10 to 1500 Hz. A hot-film anemometer probe (Fig. 5c) was located in the quadrant at a measuring depth of 2 in. from the outer wall. Data from the steady-state instrumentation were digitized and recorded on magnetic tape. Dynamic data were frequency modulation recorded on magnetic tape for later analysis.

Calibration data for the piezoelectric and hot film anemometer transducers were provided by the manufacturers and verified at AEDC. Calibrations of both steady-state and dynamic data conditioning and acquisition systems were made before and after each test period.

PROCEDURE

Conditioned air at a nominal steady-state total pressure of 7 psia and at a total temperature of 540°R was supplied to the compressor inlet station. Mach number at the compressor inlet station was set at nominal values of 0.28, 0.45, and 0.55 by the use of various sizes of the sonic orifice located aft of the compressor inlet station.

Generator rotor speed was varied from 130 to 1580 rpm to provide data at fluctuation frequencies from 50 to 600 Hz.

Standard statistical data analysis techniques utilizing an automatic wave analysis system (Fig. 6) were applied to the dynamic data to obtain amplitude, frequency, power-spectral density and cross power spectral density relations. In general, a bandpass filter width of 10 Hz was used to analyze the data. Data reduced with a bandpass filter width of 1 Hz yielded identical peak values and very similar noise background levels, indicating that the data peaks were very discrete. Waveform data were obtained by recording the magnetic tape data on a direct writing oscillograph through a low pass filter set at 1000 Hz.

RESULTS AND DISCUSSION

A theoretical and experimental investigation was undertaken to verify a rotor and stator concept for producing discrete-frequency, total-pressure fluctuations uniformly across the inlet of a jet engine compressor and to determine the performance of a prototype generator over a range of simulated compressor inlet Mach numbers from 0.28 to 0.55 at discrete data frequencies from 50 to 600 Hz. The results obtained in this investigation are discussed in terms of basic waveforms, spectral content, and steady-state radial distortion values. Comparisons with an analog computer model and a quasi-steady-state model are also presented.

THEORETICAL PERFORMANCE

Analog computer studies were conducted to determine frequency amplitude trends of a generator. The mathematical model (Fig. 7) assumed a constant mass flow into the system (a constant inlet pressure to the critical flow venturi), a constant volumetric flow out of the system (compressor rotor speed held constant), and a variable area orifice to replace the discrete frequency generator. The orifice area was assumed to vary both sinusoidally and trapezoidally. Results of these studies are shown in terms of amplitude ratios (Fig. 7d), which indicated a relative fall-off of approximately 3.5:1 of amplitude from 50 to 600 Hz. Typical output waveforms for the two types of area variation (sine and modified trapezoidal) are presented in Fig. 7e and f.

The choice of a constant volumetric flow boundary condition for the mathematical model was based on considerations of turbojet/turbofan characteristics. The use of a sonic orifice in the experimental investigation results in a constant Mach number for the compressor inlet station, rather than constant volume; however, for the Mach number range investigated, 0.28 to 0.55, the two systems are nearly identical. Therefore, the results of the experimental investigation are considered to be representative of those which would be obtained in an actual turbojet/turbofan installation.

The assumption of a variable area orifice in the mathematical model imposes certain restrictions on the data obtained. The variable area orifice implies complete total pressure head loss, which is not in agreement with the physical model. The total pressure losses of the physical model are strongly dependent on Mach number at the inlet to the aft stator assembly, as will be discussed in the next section. This Mach number, in turn, is a function of the solidity factors of both the rotor and stator blades. The design Mach number of the compressor inlet station may be set at any subsonic value by proper choice of rotor and stator solidities. For conditions near design, however, the mathematical model will predict total pressure losses accurately.

EXPERIMENTAL PERFORMANCE

WAVEFORM

Typical waveforms produced by the generator, along with waveforms predicted from the mathematical (analog) model, are presented in Fig. 9. A comparison of waveforms at 52 and 196 Hz at a compressor inlet Mach number of 0.45 is made in Fig. 9a. Good agreement with the mathematical model was obtained at both frequencies.

Static pressure variations were in phase with total pressure variations and had amplitudes of approximately one-half the total pressure excursions. Data shown in Fig. 9b are for a compressor inlet Mach number of 0.55 at a generator frequency of 58 Hz.

Velocity variations¹, compared to total pressure variations, were somewhat greater as shown in Fig. 9c for a compressor inlet Mach number of 0.45 at a generator frequency of 52 Hz.

All waveform definitions improved with increasing Mach number. Waveform definition (total pressure) improved with

¹The anemometer readout was the product of density and velocity. For the Mach number range investigated, the readout may be regarded as an indication of velocity only.

decreasing duct radial location (nearer hub) and with decreasing rotor rotation rates.

SPECTRAL ANALYSES

Amplitude frequency relations, power-spectral densities, and cross-power spectral densities of the data were obtained and analyzed. In general, amplitude and power content decreased with increasing frequencies.

Typical amplitude-frequency relations are presented in Fig. 10. The presence of a family of harmonics indicates a complex waveform at the prime frequency. Fourier series reconstruction of these frequency amplitudes yields a complex waveform like those in Fig. 7f. Background noise attributable to random turbulence ranged from 0.2 to 0.5 percent (peak-to-peak values) of mean pressure at simulator inlet Mach numbers from 0.28 to 0.55 (Fig. 10a and 10b). In general, signal to noise ratios (peak amplitude divided by background noise) were 10:1 or greater near the design Mach number.

A summary presentation of amplitude-frequency relations is made in Fig. 11. Results of the theoretical studies are presented for comparison. Values of discrete frequency pressure fluctuations (average peak-to-peak value) ranged from 7 to 1 percent over the frequency range from 50 to 600 Hz and the inlet Mach number range from 0.55 to 0.28.

The reduction in normalized total pressure losses compared to theoretical predictions with decreasing Mach number was expected from the steady-state analysis. The slope and level of the total pressure loss curve as a function of compressor inlet Mach number (Fig. 8) are dependent on the solidity factors of the rotor and stators. Any subsonic Mach number range may be obtained by proper selection of these solidity factors. The prototype was designed for optimum performance at a compressor inlet Mach number of 0.5.

Typical power-spectral density (PSD) functions for total pressure are shown in Fig. 12. The use of power-spectral density analyses for average peak-to-peak determination is best limited to broadband or white noise phenomena. However, the data in Fig. 12 are included to demonstrate the quality of the background noise of the test unit at the compressor inlet station. The power-spectral density in Fig. 12a ($M_2 = 0.55$) indicates that the noise is essentially random in its frequency distribution. At lower Mach numbers (Fig. 12b, $M_2 = 0.28$), nonrandom disturbances at frequencies between 200 and 400 Hz were noted. In both figures, the sharp peaks at 400 and 520 Hz, respectively, are the pressure disturbances produced by the generator. In general, the level of background noise declined with decreasing Mach number.

A typical cross-power spectral density (CPSD) function of total pressure is presented in Fig. 13. Absolute amplitudes of the cross-power spectral density were not obtained because only phase angle was desired. In general, phase shifts from -60 to +60 deg were noted between the sensor nearest the hub and the sensor nearest the wall. No clear dependence of phase shift on either frequency or Mach number at the imposed primary frequencies could be determined. A phase shift of ± 60 deg can result in the presence of a dynamic radial distortion which occurs at a rise time frequency at least six times the generator frequency. The amplitude of the distortion may be 40 percent of the peak-to-peak total pressure fluctuation measured between the radial locations. The net effect of phase shifts is to introduce a dynamic radial distortion at the generator frequency which approaches a square-wave time distribution.

STEADY-STATE DISTORTION

Values of radial steady-state total pressure distortion $(P_{\max} - P_{\min}/P_{\text{avg}}) \times 100$ are presented in Fig. 14a as a function of simulator inlet Mach number and frequency. The design level was 5 percent at a Mach number of 0.5. Distortions (excluding total pressure variations within 0.5 in. of either inner or outer wall) were less than 6 percent for all Mach numbers tested and were less than 4.5 percent at the design Mach number. The data formed a single curve below Mach number 0.45 and split into definite frequency distributions above this value. A typical radial total pressure profile is presented in Fig. 14b.

SUMMARY

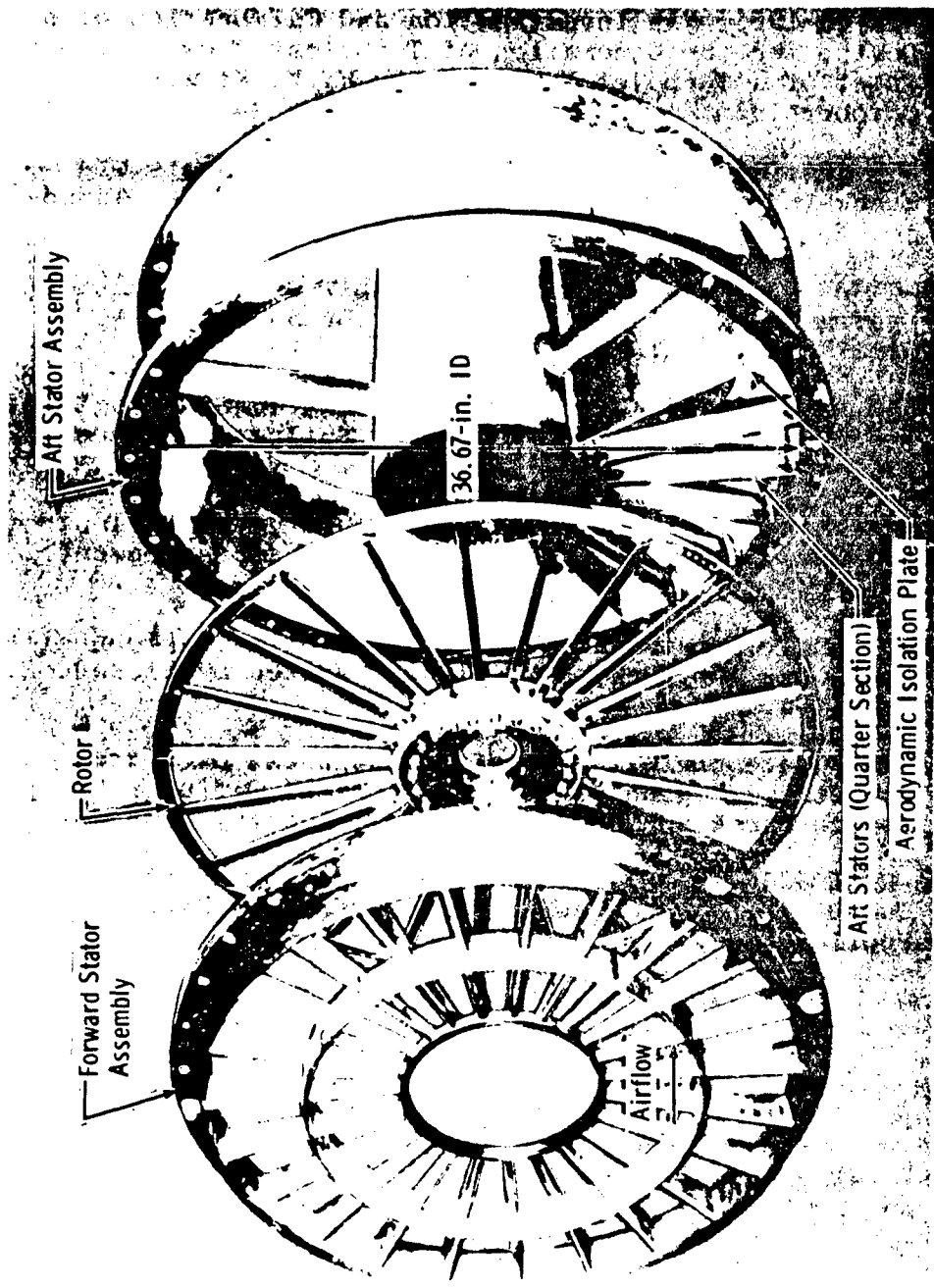
The results of a theoretical and experimental investigation to verify a rotor and stator concept for producing discrete frequency, total pressure fluctuations at the inlet of a jet engine, and to determine the performance of a prototype discrete frequency total pressure fluctuation generator over a range of compressor inlet Mach numbers from 0.28 to 0.55 and a range of data frequencies from 50 to 600 Hz are summarized as follows:

1. Amplitude variations of total pressure at discrete frequencies ranged from 7 to 1 percent of time-averaged total pressure over a frequency range from 50 to 600 Hz at a Mach number of 0.55. Amplitude variations generally decreased with increasing frequency. Rotor and stator solidity can be varied to vary the amplitude of total pressure losses and the design range of Mach numbers.
2. The background noise produced by the generator was at least an order of magnitude less than the discrete frequency peaks and was essentially random with regard to frequency distribution.

3. Phase shifts of total pressure from -60 to +60 deg between locations near the hub and near the wall were noted at the generator frequency with no clear dependence on either test Mach number or data frequency. The phase shifts can result in dynamic radial distortions with amplitudes of less than 40 percent of the total fluctuation.
4. Steady-state radial total pressure distortion was less than 6 percent at a Mach number of 0.55 and less than 4.5 percent at the design Mach number.
5. The prototype generator produced controlled frequency variations in total pressure fluctuations in the frequency range from 50 to 600 Hz.

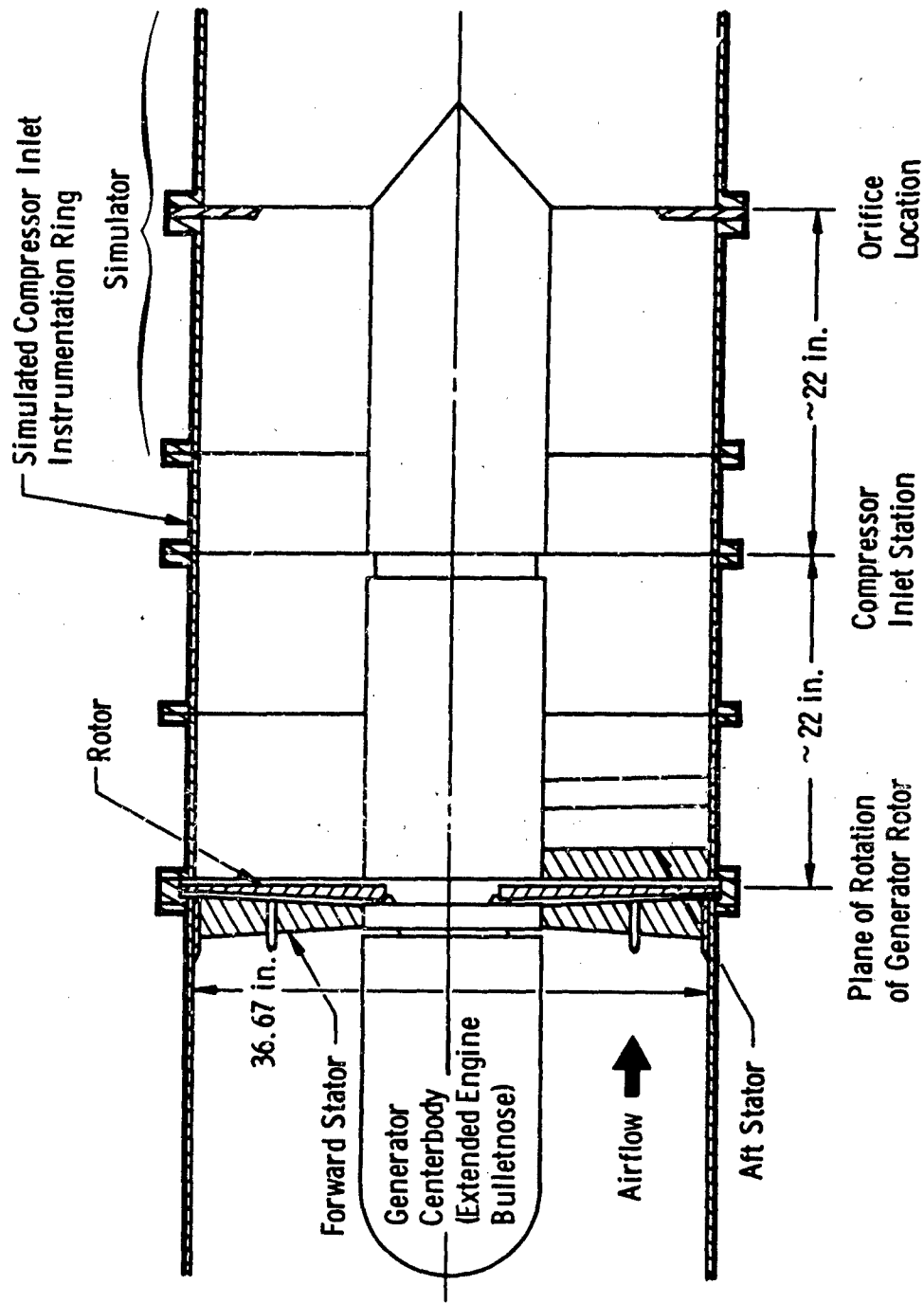
REFERENCES

1. AEDC-TR-65-195. "An Investigation and Calibration of a Device for the Generation of Turbulent Flow at the Inlet of a Turbojet Engine." by W. F. Kimzey, October 1965.
2. AEDC-TR-66-198. "An Investigation of the Effects of Shock-Induced Turbulent Inflow on a YJ93-GE-3 Turbojet Engine." by W. F. Kimzey, November 1966.
3. APTA-TM-69-12. "Techniques for Establishing Propulsion System Stability." by Sqn. Ldr. Brian Brimelow, April 1969.
4. ASME-58-A-133. "Stall Prediction in Gas Turbine Engines." by Robert J. Lubick and Lewis E. Wallner, December 1958.
5. Test Facilities Handbook, (7th Edition). "Rocket Test Facility, Vol. 2." Arnold Engineering Development Center, July 1968.
6. Design Data for Astronautics and Aeronautics." John Wiley and Sons, New York, N.Y., 1962. Edited by Richard B. Morrison.
7. NACA-TN-3066. "Effect of Surface Roughness Over the Downstream Region of a 23-deg Conical Diffuser." by Jerome Persh and Bruce M. Bailey, January 1964.
8. NACA-RM-E56C02. "Preliminary Investigation of Short Two-Dimensional Subsonic Diffusers." by Richard R. Woollett, May 1956.



a. Exploded View

Figure 1 Discrete Frequency Turbulence Generator Components



b. Schematic
 Figure 1 Concluded

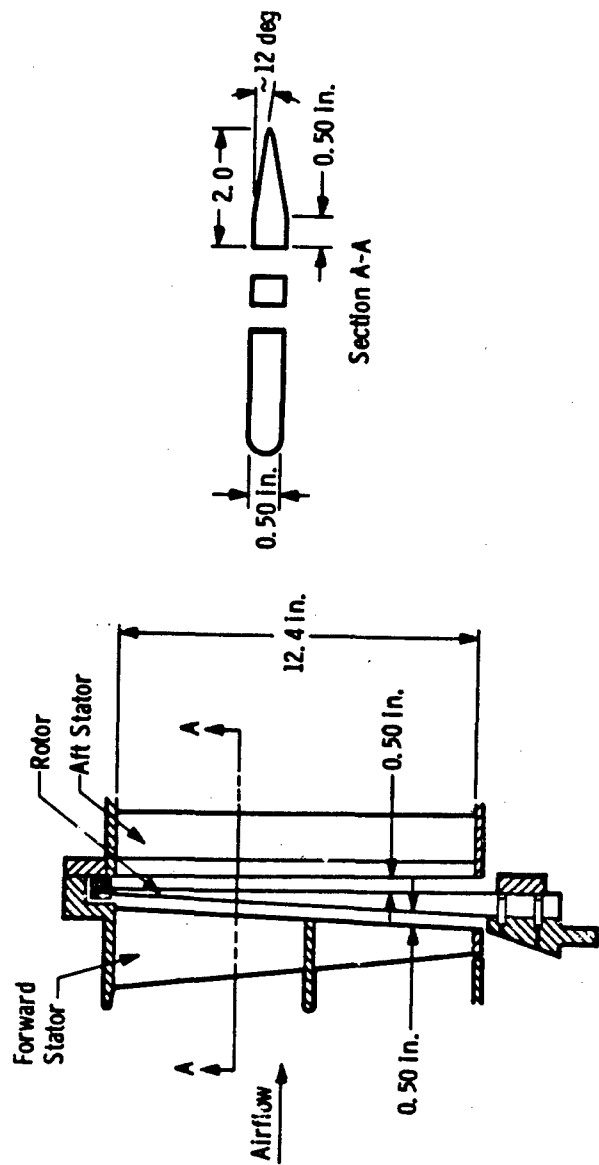


Figure 2 Rotor-Stator Design Schematic for Prototype Generator

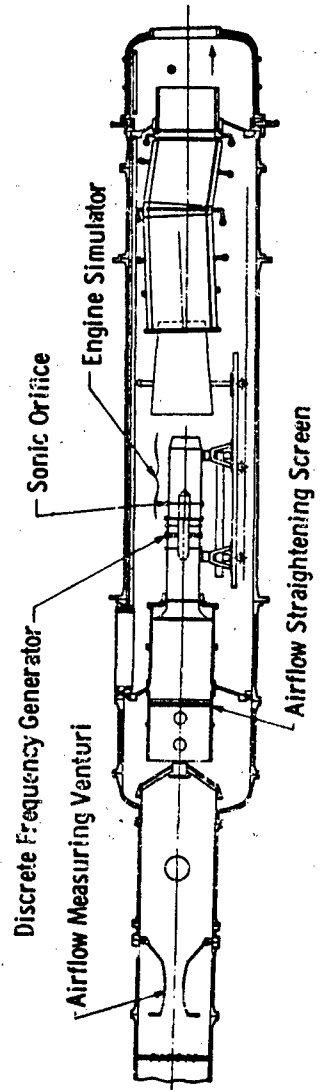


Figure 3 Prototype Generator Installed in Propulsion Engine Test Cell (T-1)

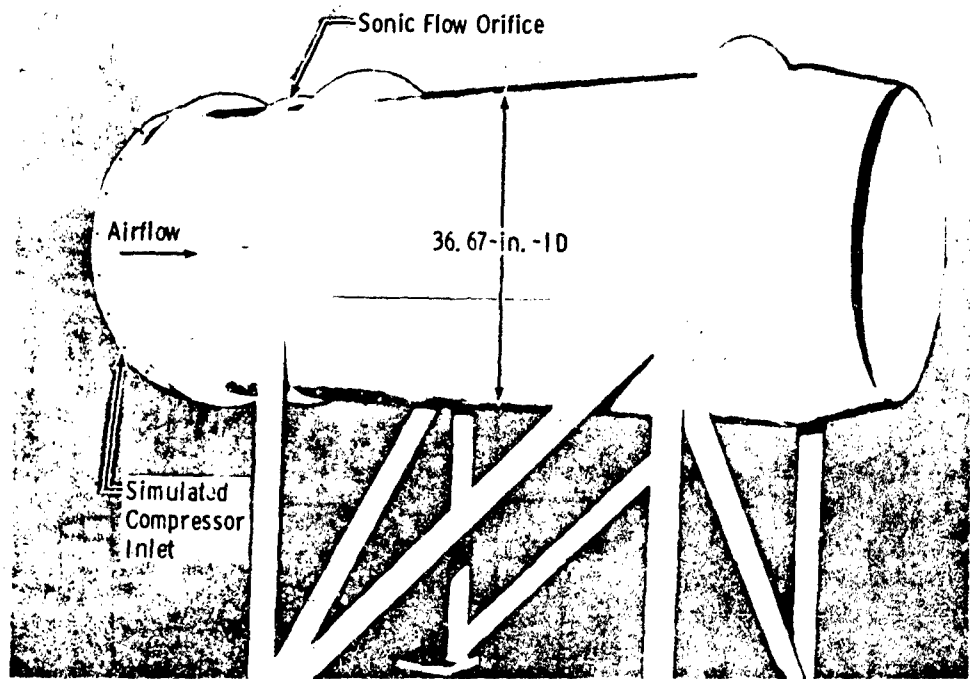
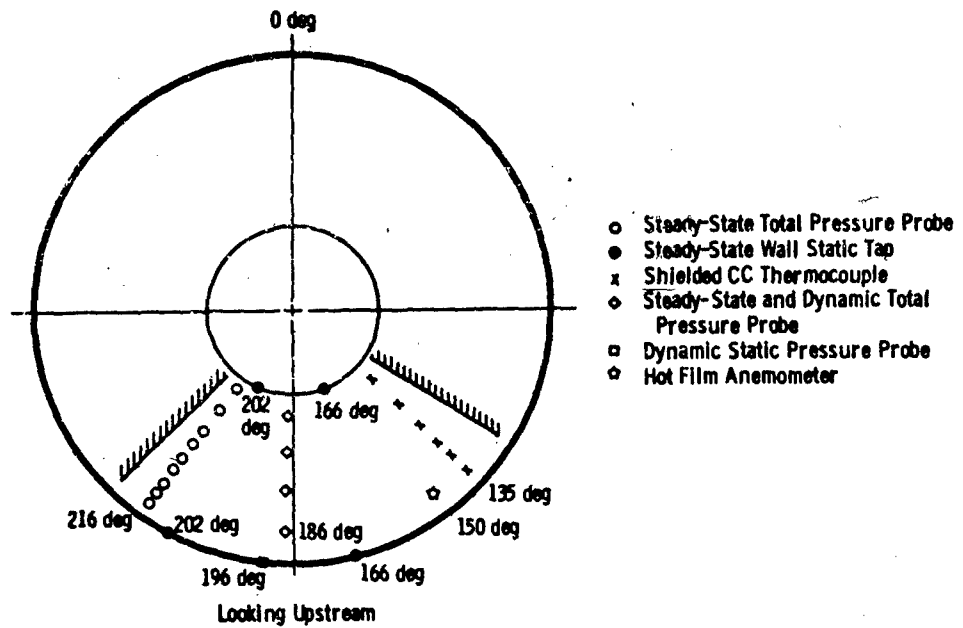
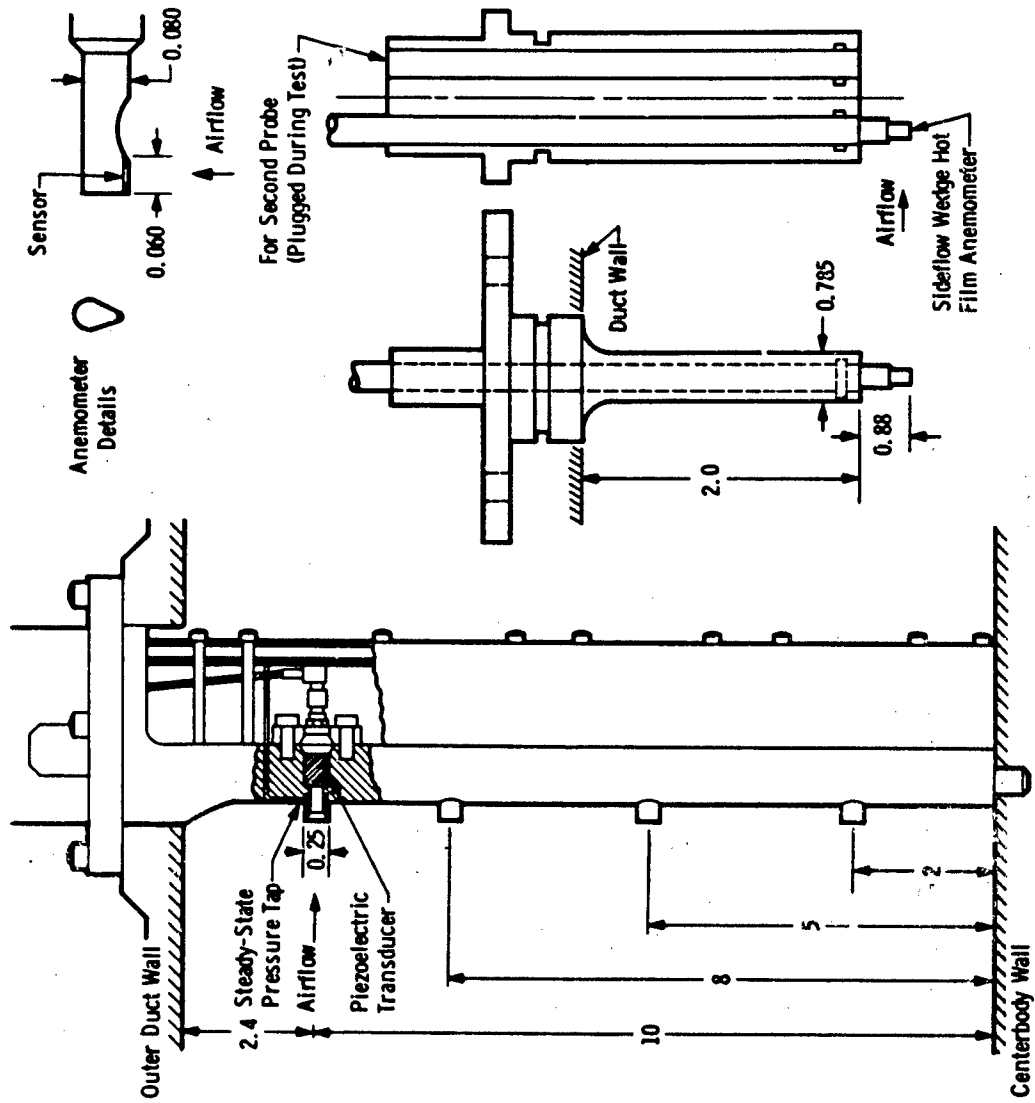


Figure 4 Jet Engine Simulator



a. Compressor Inlet Station (Located 22 in. Downstream of Discrete Frequency Generator Rotor)

Figure 5 Instrumentation



b. Steady-State and Dynamic Total Pressure Rake Schematic
 c. Schematic of Hot Film Anemometer Probe

Figure 5 Concluded

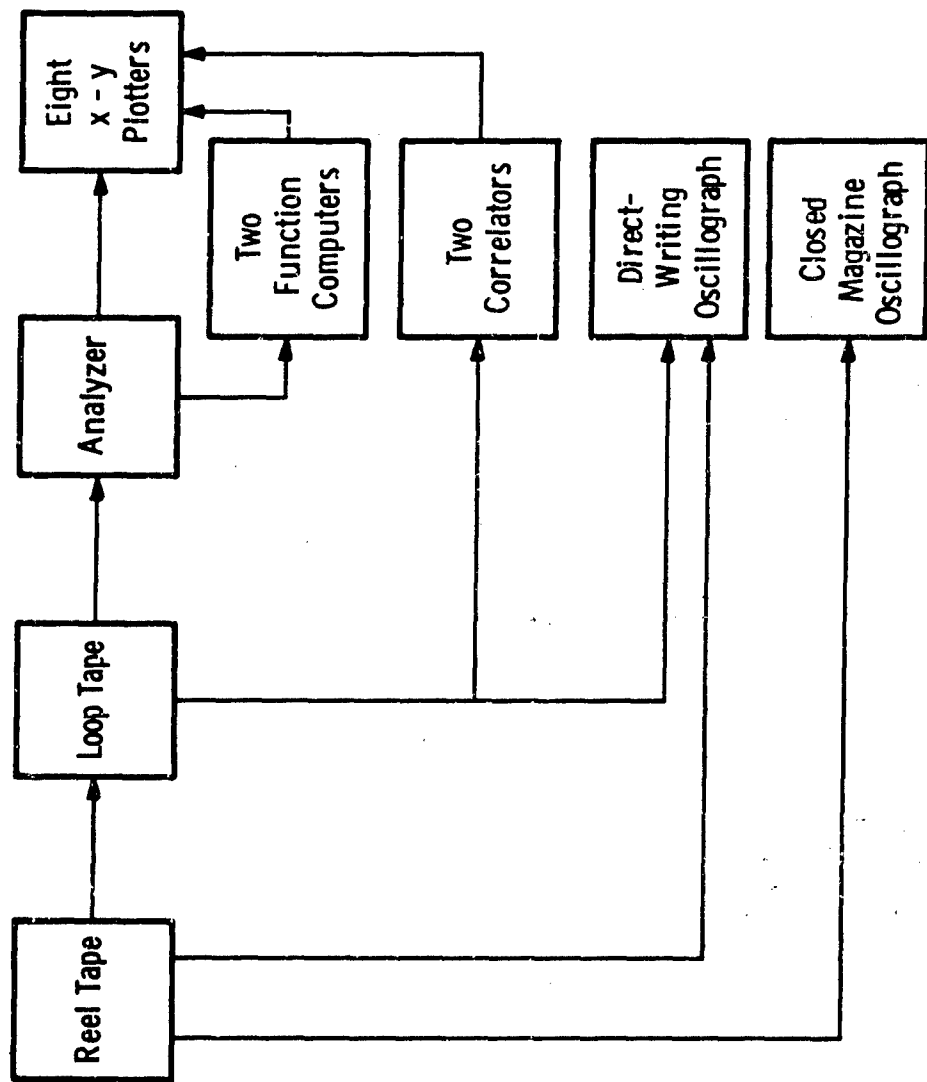
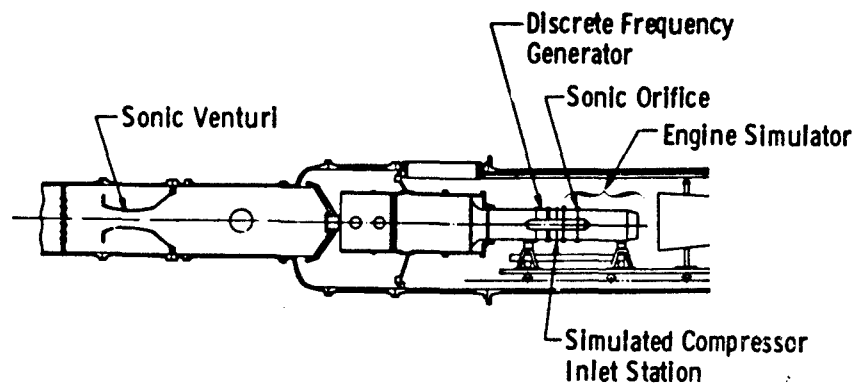
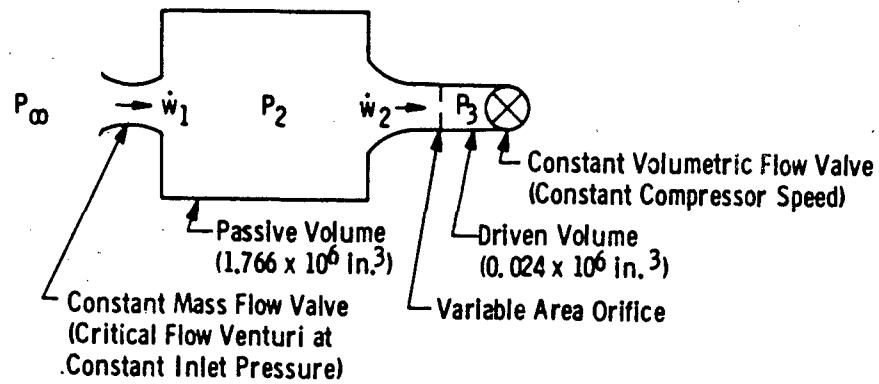


Figure 6 Automatic Wave Analysis System Schematic



a. Physical Test Configuration



b. Physical Model Assumed

$$\dot{w}_1 = k_1 P_\infty \quad k_1 = 8.26 \quad P_\infty = 10.0$$

$$\frac{dP_2}{dt} = \frac{1}{C_2} (\dot{w}_1 - \dot{w}_2) \quad C_2 = 3.789$$

$$\dot{w}_2 = \frac{k_2 P_2 A}{\sqrt{T}} f\left(\frac{P_3}{P_2}\right) \quad k_2 = 0.5318 \quad T = 520^\circ\text{R}$$

$f(P_3/P_2)$ = Standard Loss for Orifice (All Dynamic Head Lost)

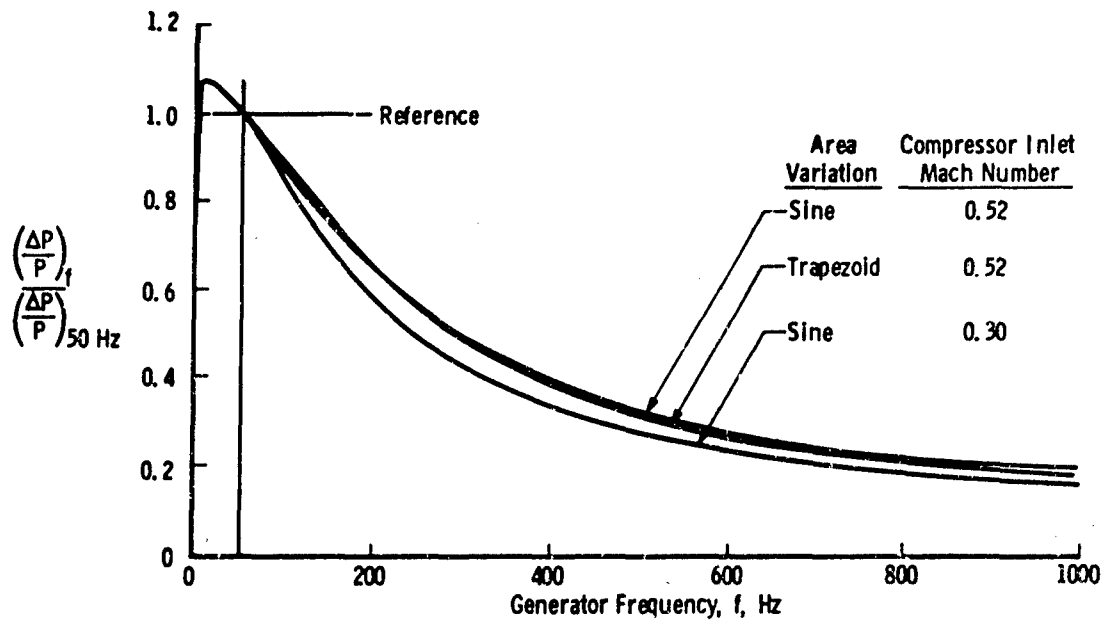
$$A = (724.2) + (70.1) \sin(\omega t) \quad \text{or Trapezoidal Wave between Same Limits}$$

$$\frac{dP_3}{dt} = \frac{1}{C_3} (\dot{w}_2 - \dot{w}_3) \quad C_3 = 0.0519$$

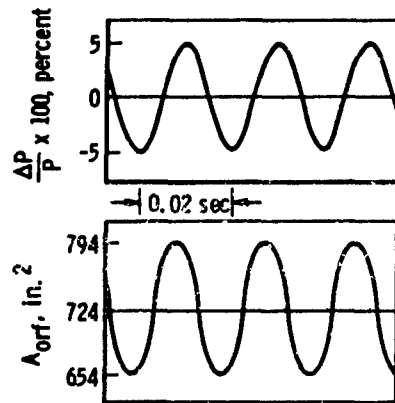
$$\frac{\dot{w}_3 \sqrt{T}}{P_3 A_3} = k_3 \quad k_3 = f(M_3), A_3 = 934.51$$

c. Mathematical Relations

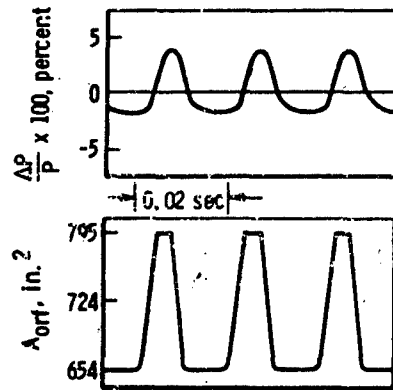
Figure 7 Mathematical Model



d. Pressure Amplitude Ratio Variation as a Function of Generator Frequency



e. Sinusoidal Area Variation with a Generator Frequency of 50 Hz at a Compressor Inlet Station Mach Number of 0.52



f. Trapezoidal Area Variation with a Generator Frequency of 50 Hz at a Compressor Inlet Station Mach Number of 0.52

Figure 7 Concluded

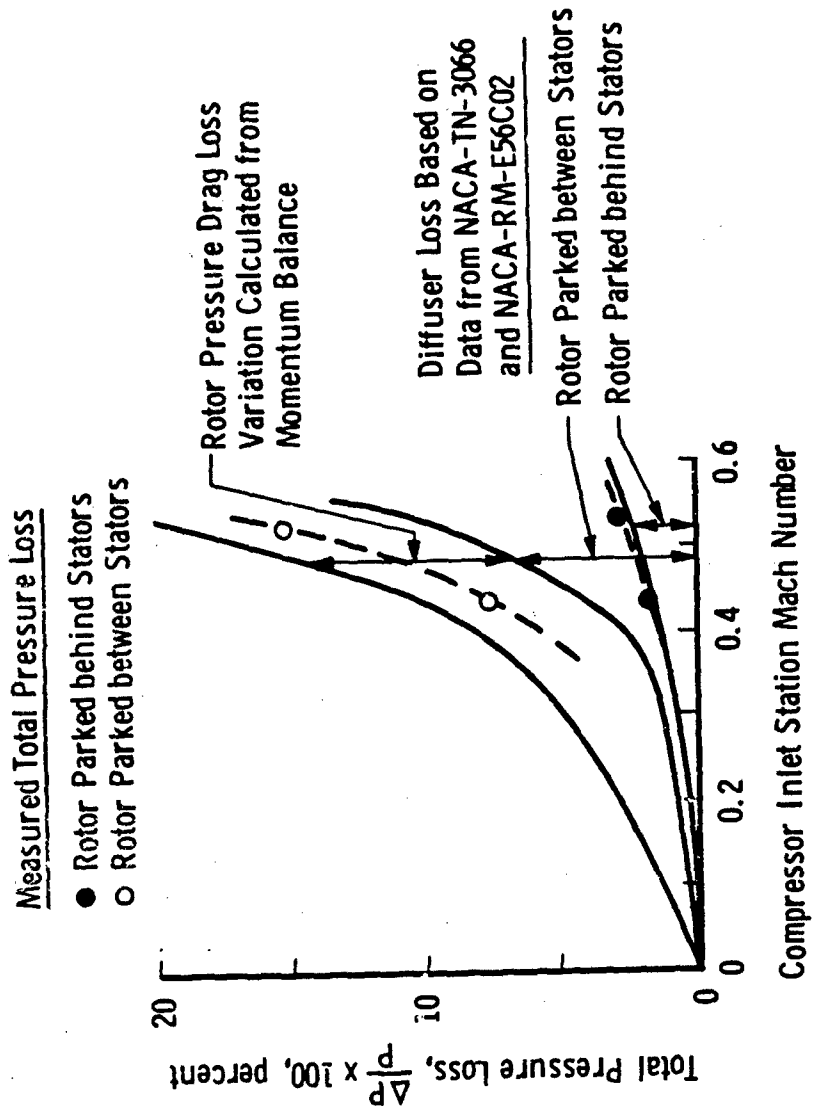
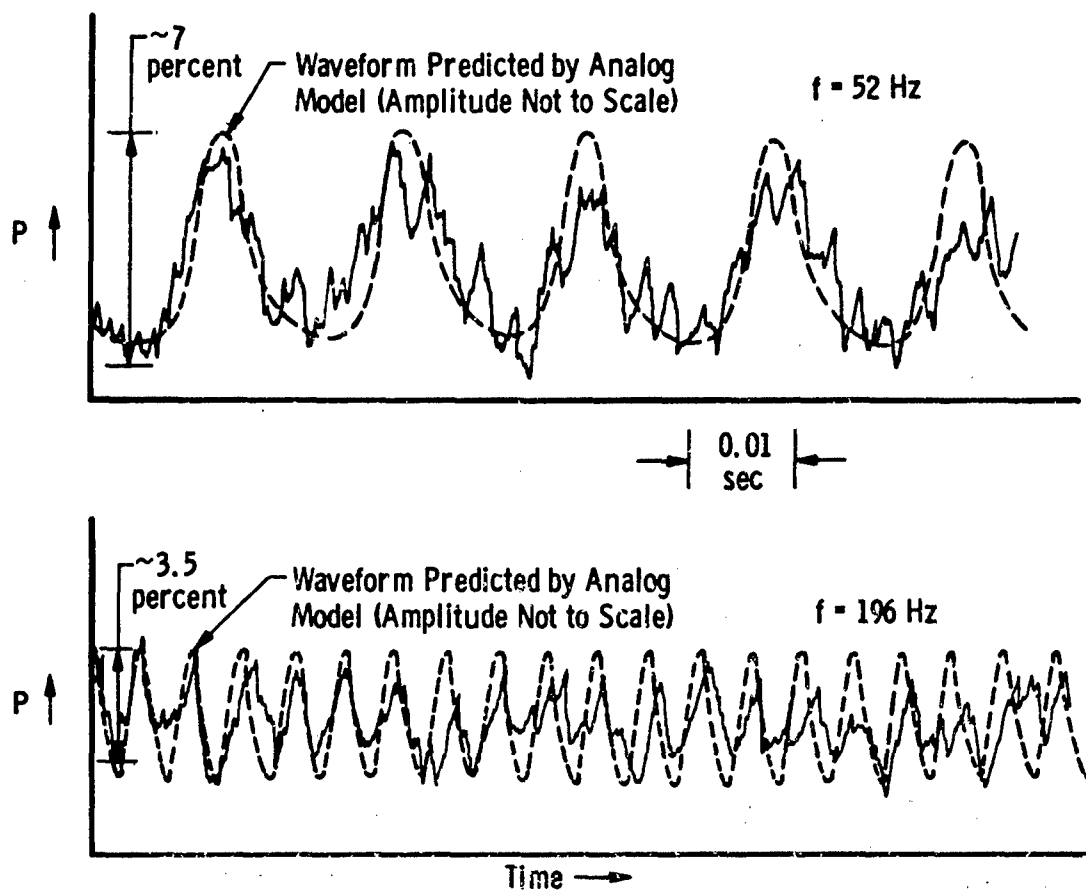


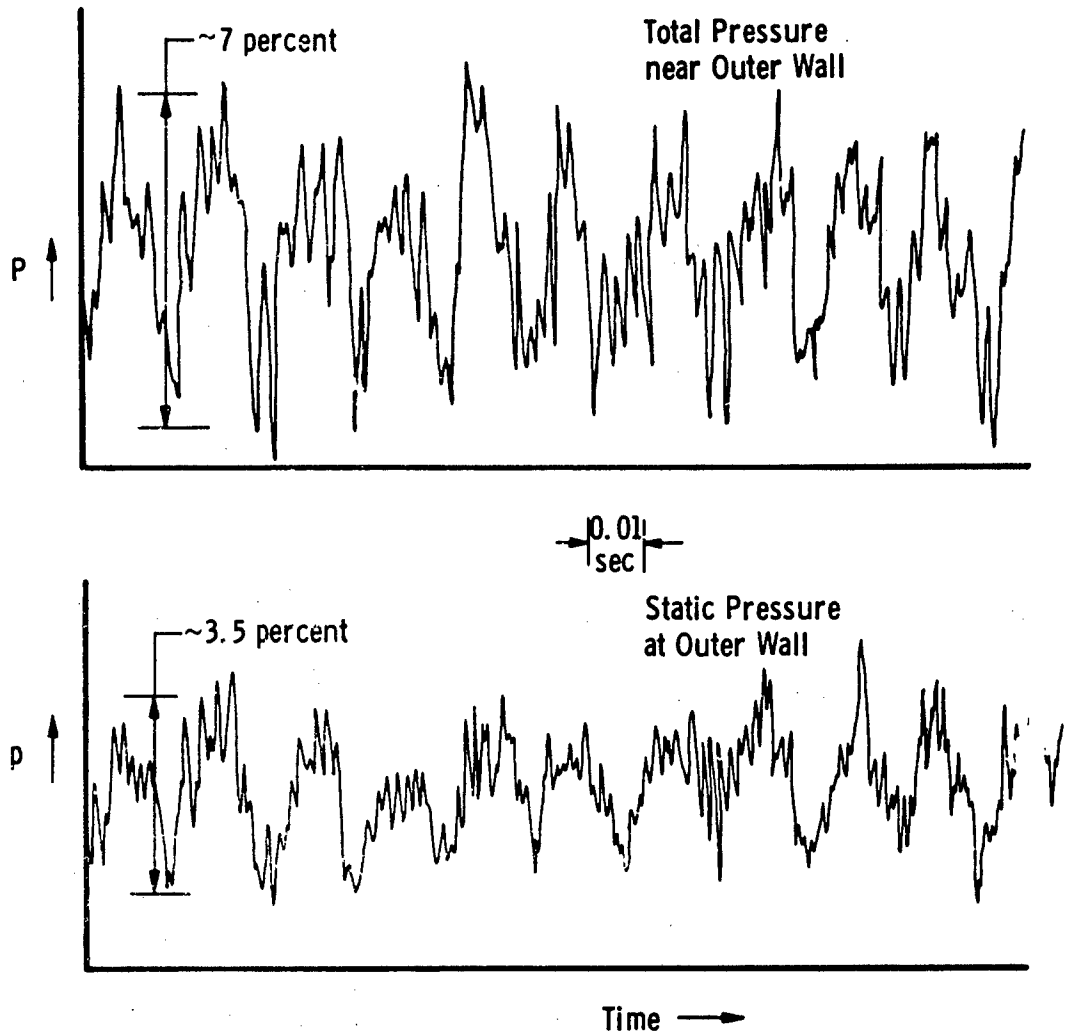
Figure 8 Steady-State Total Pressure Loss of the Prototype as a Function of Compressor Inlet Station Mach Number



Total Pressure (near Inner Wall)

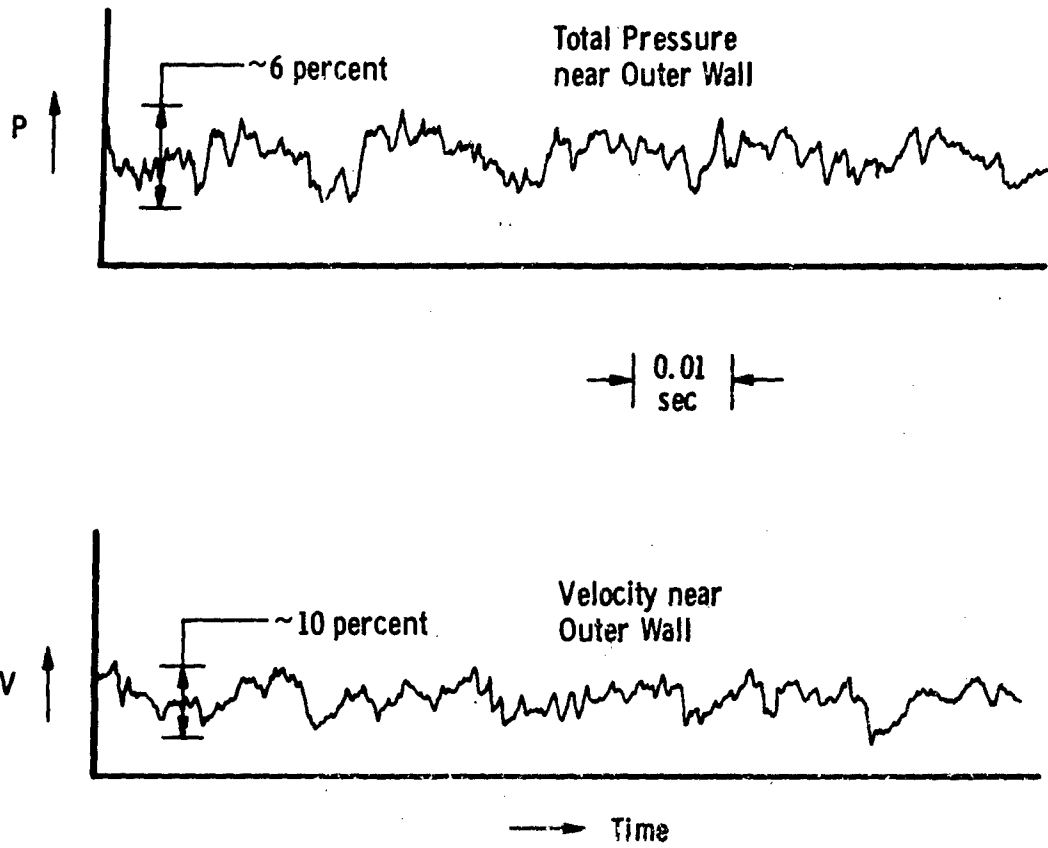
a. Compressor Inlet Total Pressure Waveforms at $M = 0.45$

Figure 9 Compressor Inlet Total Pressure, Static Pressure, and Velocity Waveforms



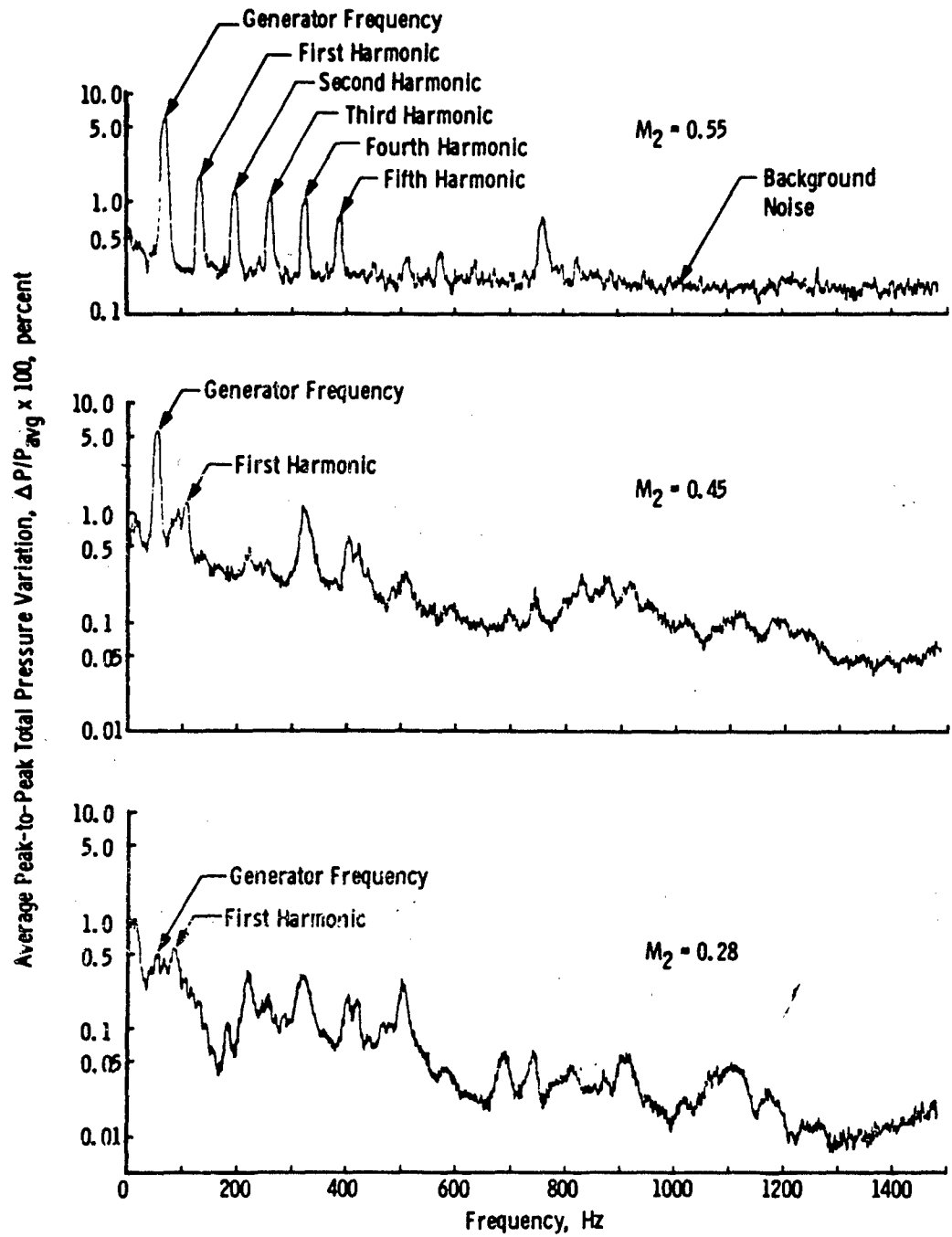
b. Compressor Inlet Total and Static Pressure Waveforms at $M = 0.55$ and $f = 58$ Hz

Figure 9 Continued



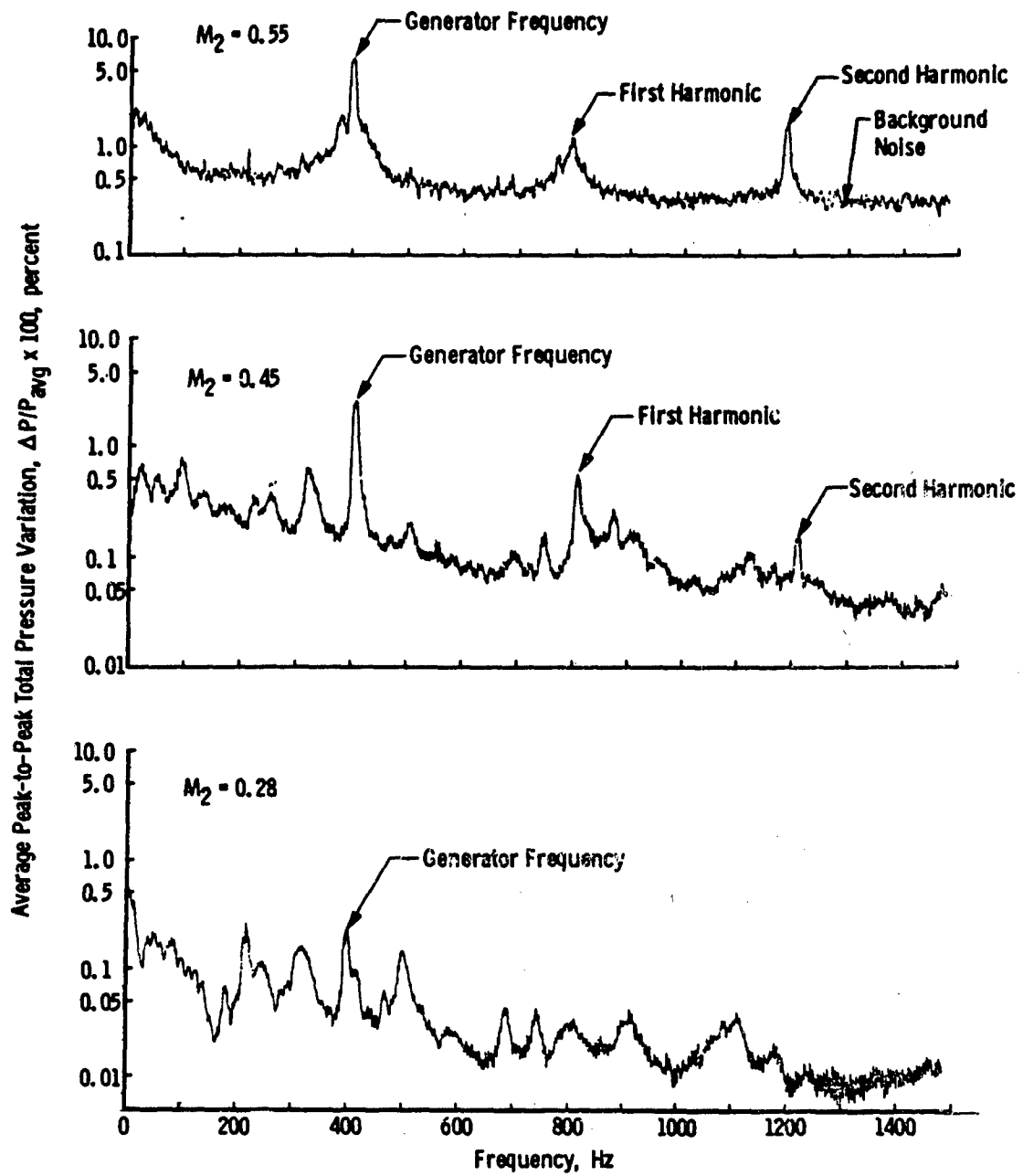
c. Compressor Inlet Total Pressure and Velocity Waveforms at $M = 0.45$ and $f = 52$ Hz

Figure 9 Concluded



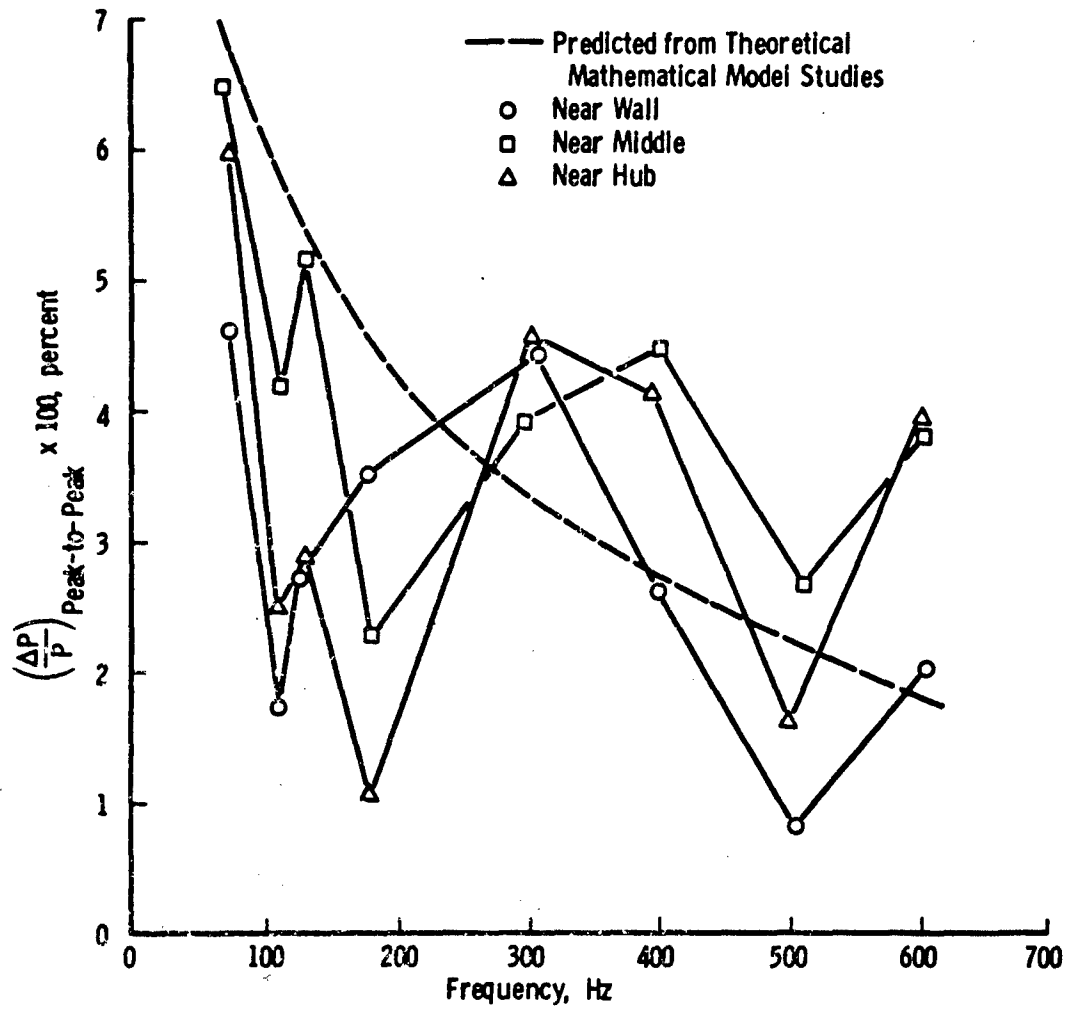
a. Total Pressure at a Generator Frequency of 50 Hz

Figure 10 Amplitude Frequency Distribution of Pressure and Velocity Variations



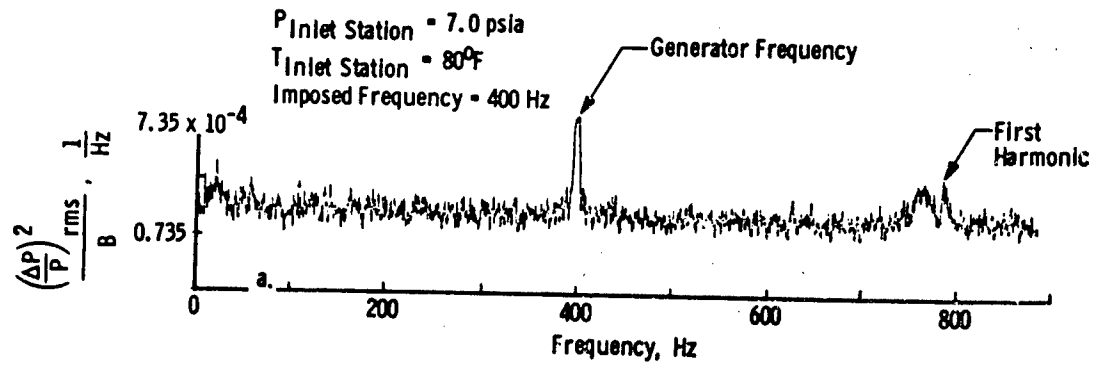
b. Total Pressure at a Generator Frequency of 400 Hz

Figure 10 Concluded

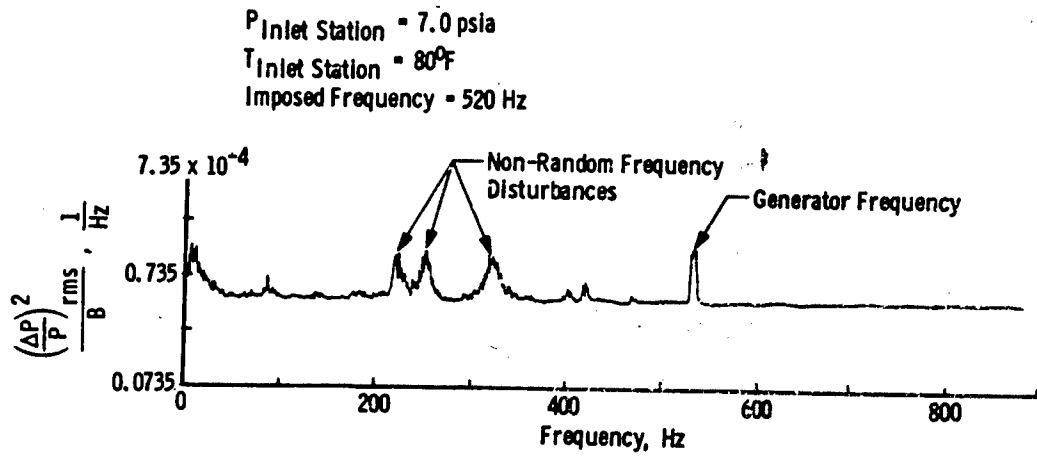


a. $M_2 = 0.55$

Figure 11 Amplitude Variation at Generator Frequency

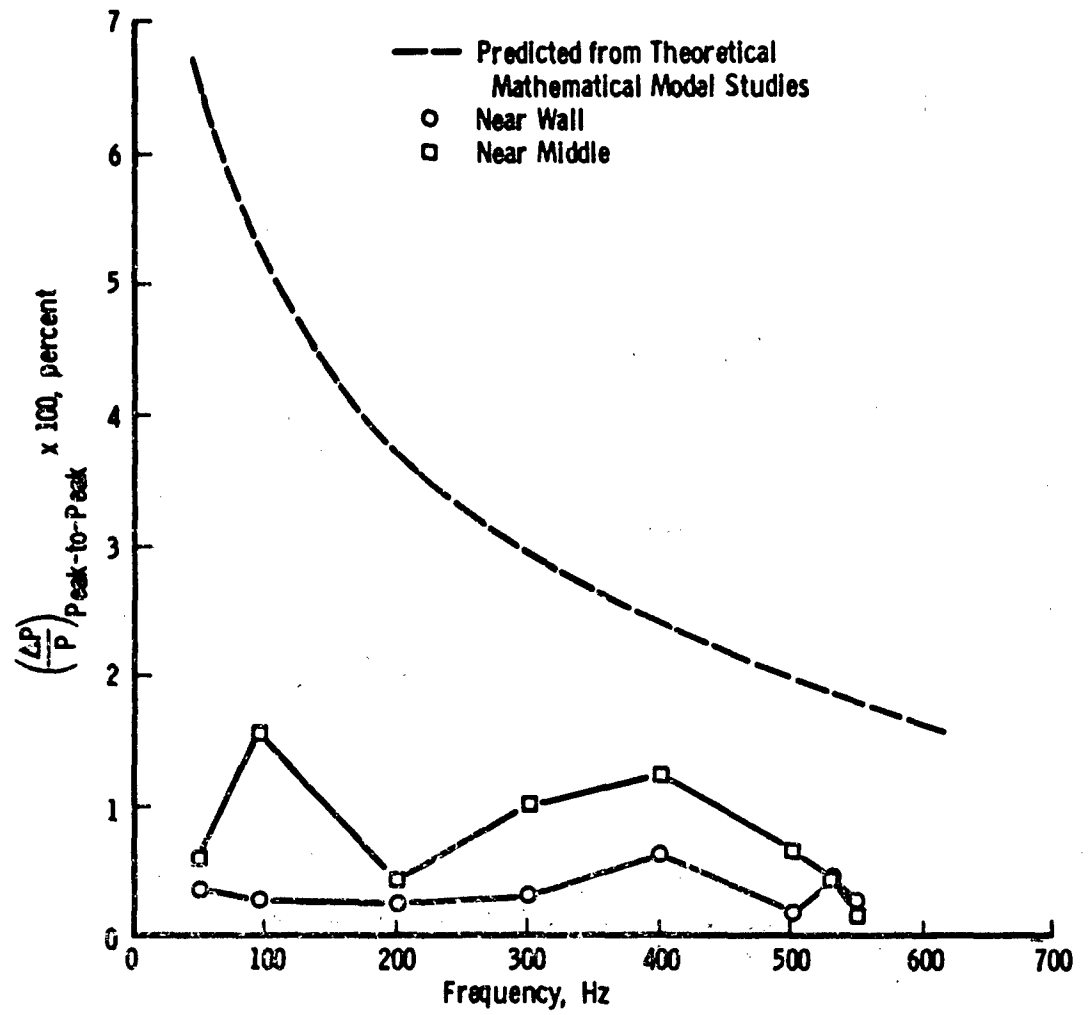


a. $M_2 = 0.55$, Sensor Near Wall



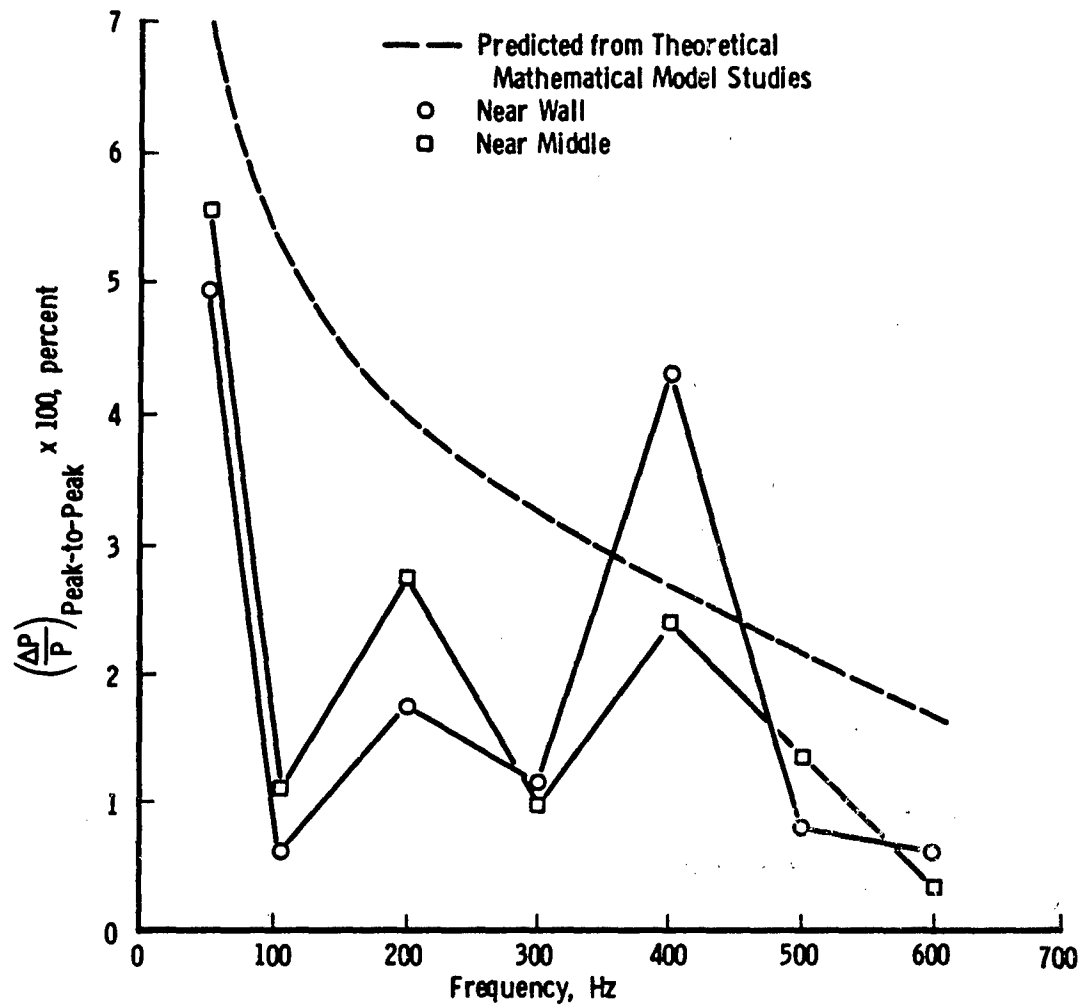
b. $M_2 = 0.28$, Sensor Near Wall

Figure 12 Typical, Normalized Power Spectral Densities of Total Pressure at the Compressor Inlet Station



c. $M_2 = 0.28$

Figure 11 Concluded



b. $M_2 = 0.45$

Figure 11 Continued

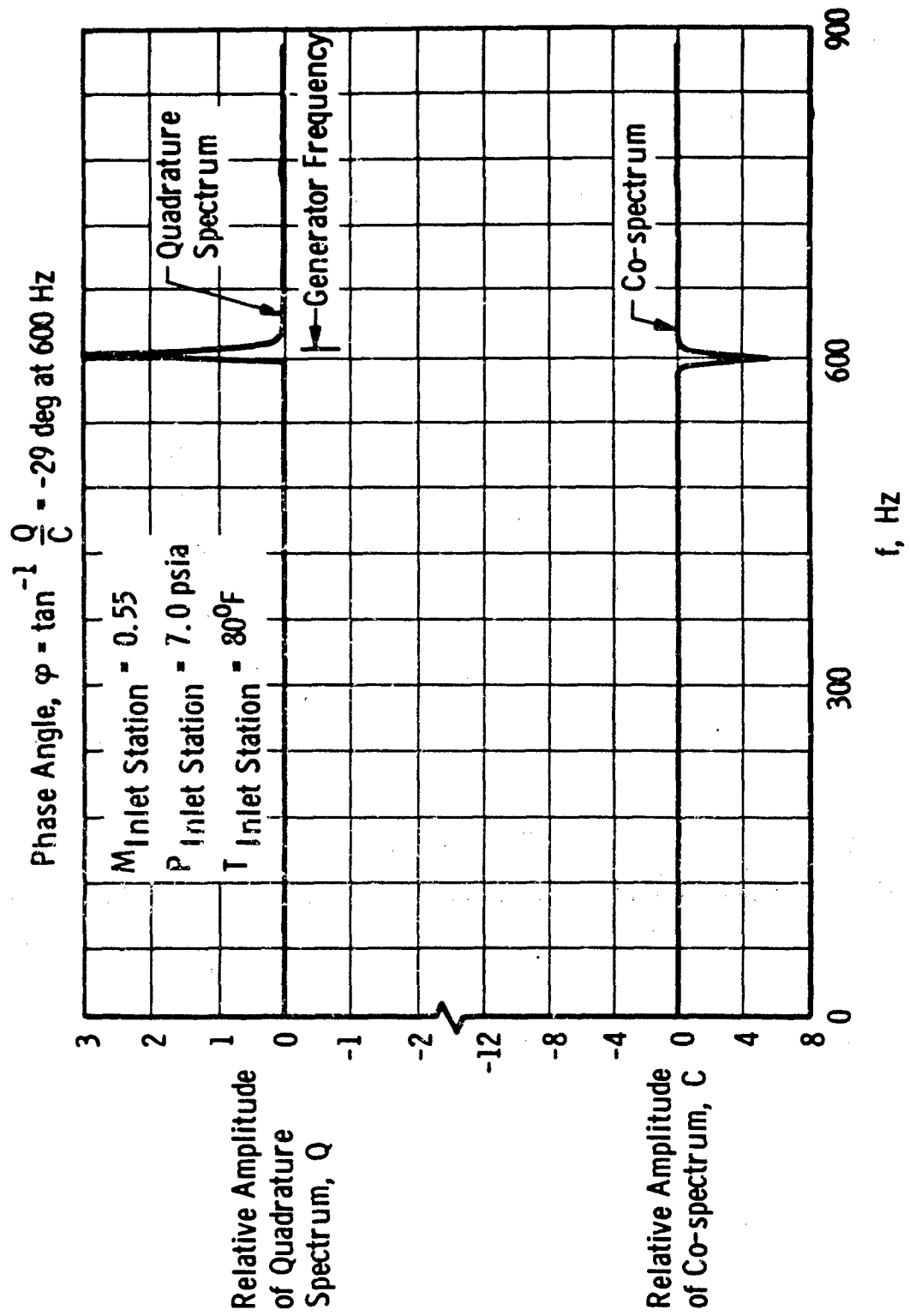
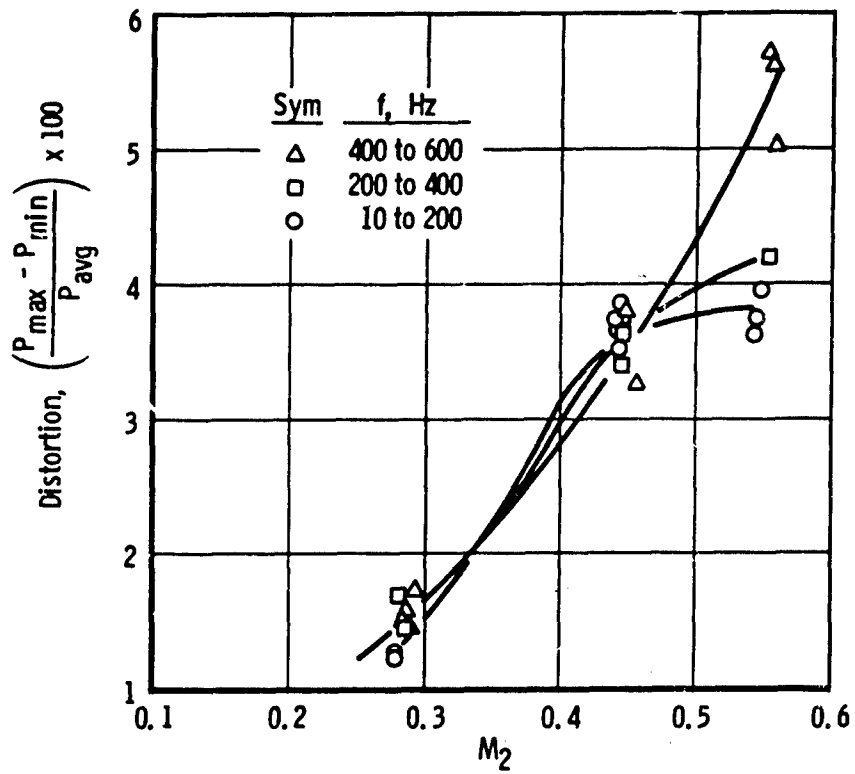
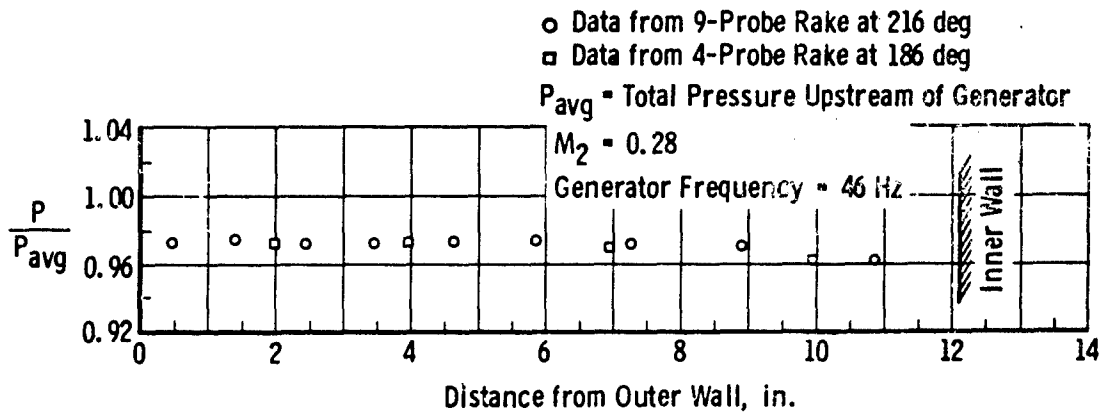


Figure 13 Cross Power Spectral Density of Total Pressure near the Wall and near the Hub

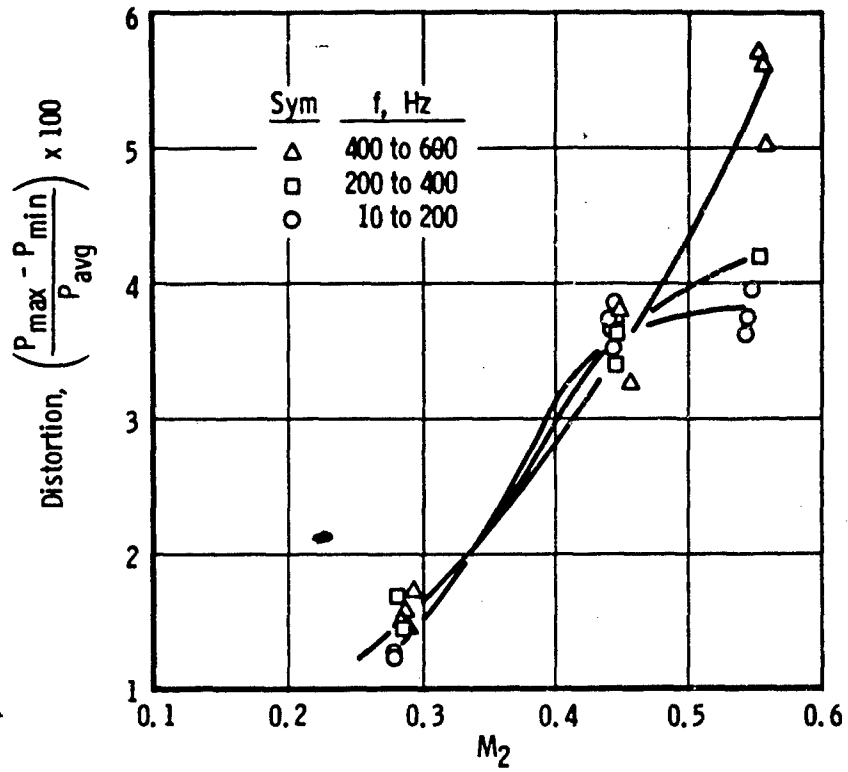


a. Distortion vs Compressor Inlet Mach Number and Generator Frequency

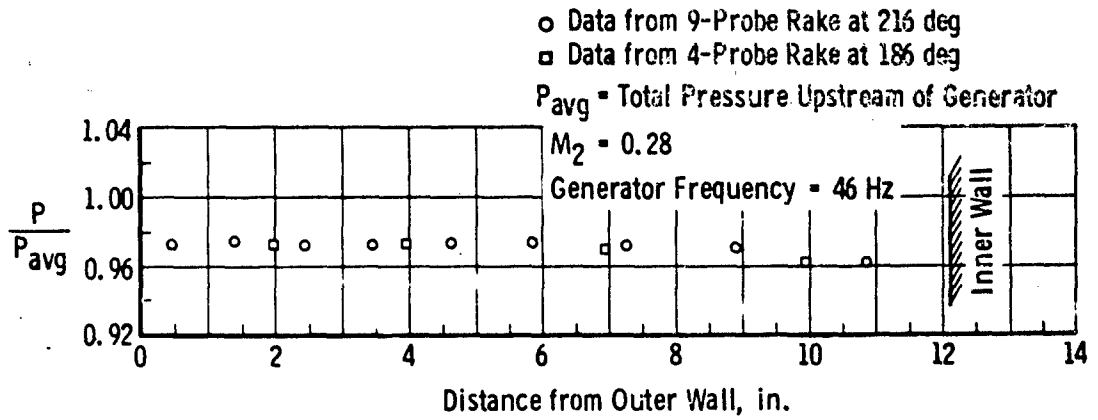


b. Typical Radial Total Pressure Profile

Figure 14 Steady-State Radial Total Pressure Distortion at the Compressor Inlet Station



a. Distortion vs Compressor Inlet Mach Number and Generator Frequency



b. Typical Radial Total Pressure Profile

Figure 14 Steady-State Radial Total Pressure Distortion at the Compressor Inlet Station

COMPUTER CONTROLLED PHOTOGRAPHY FOR REDUCTION OF
DYNAMIC DISTORTION DATA

W. J. Elliott

A. Medlock

R. C. Hood

Allison Division
General Motors Corporation

ABSTRACT

A procedure has been developed by which a computer creates a motion picture representing dynamic turbulent pressure distortion. The computer program reads pressure values at a given instant in time, interpolates the pressures over the annulus area, assigns a "grey code", generates the image on a cathode ray tube and operates a 16 mm movie camera to photograph the image.

I. INTRODUCTION

A technique has been developed by which dynamic distortion data may be reduced by a computer to the medium of motion picture film. The procedure provides an aerodynamicist with a data reduction mechanism to conveniently study radial and circumferential pressure distortion phenomena characterizing unsteady flow in turbo-machinery.

Several rakes of high response pressure probes may be distributed circumferentially in a plane normal to the axis of a gas turbine component. Typically the data are recorded on F-M multiplexed analog tape from which a digital tape may be generated. Ordinarily, only a small portion of the analog tape is digitized for further analysis, that portion representing the particular time domain of interest. Usually data representing some 100 ms. of real time during surge is sufficient for study.

This paper discusses an extension to the technique developed by Brimelow, Barrow, et.al¹ which, in effect, reduces multiple probe pressure data from digital tape to a series of light equivalent intensity patterns (each of which represents a particular time slice). Each of the intensity patterns is then photographed and a motion picture film is subsequently created. Brimelow utilized a computer print-out (Figure 1) in which a judicious choice of printed characters (including overstriking) is employed as a sort of grey code, thereby creating an image whose light-dark intensity is uniformly proportional to a pressure gradient.

Allison improved on this methodology through the exploitation of a computer augmented by a cathode ray tube type of graphics display device, on which the pressure intensity patterns were generated. The process was made further automatic through the design of an electro-mechanical system which permitted the computer to completely control the shutter mechanism on a modified 16 mm motion picture camera.

II. EXPERIMENTAL APPARATUS

A schematic of the specially developed electro-mechanical system to provide direct computer control over the camera is shown in Figure 2.

A. RECORDING SYSTEM

The function keyboard is an auxiliary unit to the graphics display terminal (IBM 2250) which is attached to an IBM 360/50 computer. There is a light source inside of each button which may be turned on or off by order of a computer program. One such button provides the stimulus for control over the camera.

¹ Squadron Leader Brian Brimelow, Exchange Officer, WPAFB/APL
Captain David Barrow, USAF, WPAFB/APL

A photocell is mounted above the appropriate button and the weak electrical signal is fed to an amplifier (Figure 3) whose output voltage is sufficient to operate a solenoid. The solenoid is coupled to a cable release which operates the shutter mechanism on a modified Bolex H 16 movie camera.

The computer generates an image on the CRT (Figure 4) and at the same time turns the light button on. The shutter is opened and the film is exposed for approximately 0.2 seconds after which the light button is turned off. Turning the light off causes the shutter to close and the film to be advanced one frame. Information is regenerated on the CRT automatically during this period and the number of regenerations per second is a function of the amount of information displayed. The camera shutter is held open for 0.2 second to minimize the effect on film exposure resulting from any partial regeneration cycles.

The entire cycle to complete the above sequence for one film frame is approximately 2.8 seconds. Therefore, a complete filming to study one particular surge requires about 45 minutes of computer time.

B. PROJECTION SYSTEM

Projection of the film is accomplished by using a Selecta-Frame 16 mm projector, model 16N manufactured by Traid Corporation which permits flickerless projection at continuously variable speeds from 1 - 24 frames per second.

III. COMPUTER HARDWARE

An IBM 360/50 computer was utilized in this project. Standard 360/OS MFT II software and the Graphics Subroutine Package (GSP) were used. Following is a detailed configuration of the 360 hardware and the organization of the machine is shown in Figure 5.

| <u>Unit</u> | <u>Model or Feature</u> | <u>Description</u> |
|-------------|-------------------------|------------------------------|
| 2050 | H | 262K Processor |
| | 6980 | Selector Channel |
| | 7920 | 1052 Adapter |
| 1052 | 8 | Console Typewriter Keyboard |
| 2821 | 1 | I/O Control |
| | 3615 | 1100 lpm Adapter |
| | 8637 | UCS Adapter |
| | 1990 | Reader Column Binary |
| 1403 | N1 | Printer 1100 lpm |
| | 8640 | UCS |
| 1416 | | Print Train (HN Arrangement) |
| 2540 | 1 | Card Reader - Punch |
| 2841 | 1 | Disk Control |
| 2311 | 1 | Disk Drives (6) |
| 2803 | 1 | Tape Control |
| | 3228 | Data Conversion |
| | 7125 | 7 Track Compatibility |
| 2401 | 2 | Tape Drives (3) |
| | 9557 | 7 Track R/W Heads |
| 2250 | 1 | Display and Control |
| | 1002 | Absolute Vectors and Control |
| | 1245 | Alphanumeric Keyboard |
| | 1499 | 8 K Buffer |
| | 1880 | Character Generator |
| | 4485 | Graphic Design Feature |
| | 5855 | Function Keyboard |
| 2501 | B1 | Card Reader |
| RPQ | F11902 | Data Channel Repeater 2944-1 |
| RPQ | 812322 | Data Channel Repeater 2944-2 |

IV. COMPUTER PROGRAMS

A. TIME INTERPOLATION

Motion pictures present a pleasing and intelligible image to the eye when the individual frames in a sequence differ from each other in only a minor way. Since turbulence data may contain pressure fluctuation with frequencies in any range, the pattern can change drastically in the smallest time interval causing the image to jerk. Since it was deemed important to view those frequencies in the lower end

of the spectrum and also to prepare a film which was not jerky, the digitized data were interpolated at finer time intervals. This interpolation reduces the change from film frame to film frame without alteration of the basic patterns. A linear interpolation was used to obtain the additional frames. The number of these frames which are generated by interpolation depends on the rate of change of the raw data frames. From one to nine interpolations have been tried with satisfactory results, however, it seems three to four should normally give good results without incurring unnecessary computer costs.

B. IMAGE GENERATION

1. THE (R - θ) SEARCH

Because approximately 4500 interpolated values are used to create each pattern, a procedure was sought to reduce the calculation time and hence the computer cost. It should be noted that neither the probe locations nor the location of CRT coordinates changes with time or film frame. It was decided that a linear interpolation scheme in both the radial and circumferential directions should be used since this would conserve computer time and not degrade the image content. This type of interpolation involves two operations. The first is a search to determine the proper table (or probe) values which are to be used in the computation. This is the portion of the program which does not change with the image and is not repeated. The second half of the interpolation is the actual evaluation of the interpolate polynomials.

It was noted that the search for the proper table values would be the most involved logically and computationally. This part of the procedure required some 90% of the computer time for one image. It seemed appropriate then to perform this operation only once for each data set. The calculation begins (see Figure 6) by changing the Cartesian coordinates of the addressable locations of the face of the CRT into cylindrical coordinates relative to the engine axis. Those points which fall within the annulus (only some 75%) are transferred from their matrix into a separate vector along with some information pertinent to that point. Specifically, the index of the appropriate probe radius and circumferential location are stored for future reference. For example, (Figure 7) if the i th point lay between the k th and $k + 1$ st radial probe positions then the FORTRAN statement used to remember where the point lies might be

$$IR(I) = K$$

A similar statement can be used to remember the circumferential index of the appropriate table. Certain steps in the evaluation of the equations such as calculating the inverse of the interval sizes are processed in the first half of the program to help meet the requirement of minimizing computer time. The difference between the radius of the image point and the radius of the appropriate probe value and the difference between the circumferential values may also be calculated and stored (Figure 6).

2. PRESSURE INTERPOLATION

The generation of each image is started by reading the probe values into the computer for the particular time increment. A check is made for probes which may have malfunctioned. An interpolation on the good probes is made at those locations where an "open" probe is detected, so that it appears to the remainder of the program that all of the measurements were in fact, successful. The interpolation is then performed at all of the pertinent CRT coordinates and character is assigned to each based on the interpolated value of pressure.

3. SHADING ALGORITHM

Considerations in determining the method to be used in representing the various light intensity levels (hence, pressure levels) on the 2250 display were the following:

- a. A relatively large amount of light must be generated in a small area of the screen with a minimum amount of 2250 buffer area being used. The 2250 character generator was the obvious choice to fulfill this requirement.
- b. An evenly distributed pattern allowing fairly high resolution and nearly complete light saturation for high pressure areas was desirable. It was found through experimentation that half row spacing with a half character offset of alternate rows yielded desirable results without exceeding available 2250 buffer space.
- c. At least ten different pressure ranges must be established with a significant, yet uniform, difference in light intensity between each level. Various characters arranged in offset rows as described above were displayed and photographed. These were then graded and one particular character applied to each pressure range. It was found that on the low intensity end it was desirable to decrease the density of period (.) characters (the lowest non-blank intensity character available) in order to provide two additional intensity levels. For the second lowest intensity, every other row and every other character were omitted, and for the third lowest intensity, only every other row was omitted.

The completion of the shading algorithm was established with very little difficulty in a very short period of time with quite satisfactory results. Figure 8 indicates the grey code employed.

The actual generation of the image on the 2250 screen is accomplished through a series of calling sequences to the Type I supported IBM GSP routines (reference Manual C27-6932-2). Three graphic data sets (GDS's) are used: one for the heading and the two circles representing the envelope of the engine inlet annulus, one for the average pressure versus time diagram, and the other for the alphanumeric characters representing the pressure distribution.

During the initialization phase, the three graphic data sets are established and the first GDS is loaded with the heading information defining the character pattern for each pressure range. Key 3l on the function keyboard is used to signal the computer to move into the calculation phase. The heading information is reset at this point and the non-variable part of the display is generated in the GDS.

The second GDS is used in the generation of the characters which produce the shading effect. One hundred lines of up to 69 characters are displayed for each frame. Immediately preceding the display of each frame, the previous shaded diagram is reset, thus the shaded picture is on the screen during the entire calculation of the following frame. At the completion of the generation of each frame, a test is made to see if function key 3l has been depressed. If this was the case, the calculation pauses until key 3l is again depressed. This allows time for rewinding the camera or other human action.

Also, at the completion of the generation of each frame, function key 1 is lit. This is the signal (through a photocell) to open the camera shutter. The signal to turn off the light (which closes the shutter) is inserted at a judicious point in the calculation of the next frame so that just the right exposure is given to each frame.

The average pressure versus time point plot is built up in the third GDS. The program is organized such that on every tenth frame a point is added to the diagram.

V. CONCLUSIONS AND RECOMMENDATIONS

The specialized hardware and computer software described in this paper were assembled in but a few days to reduce the data to pictorial form. The resulting film, after having been reviewed by many aerodynamicists, clearly indicates that simulated high speed photography of pressure patterns generated during a surge phenomenon is not only feasible but further represents a new aerodynamic design tool to better study flow instability.

Recommendations are set forth in two principal categories: 1) improvements to system described herein and 2) extensions to the general concept.

A. CURRENT SYSTEM IMPROVEMENTS

Provision for electric motor wind of the movie camera should be added.

An electronically operating shutter mechanism should also be adapted to the camera. This would obviate the need for an amplifier-solenoid-cable release system, the mechanical portion of which has a tendency to bind from time to time.

Cycle time may be reduced somewhat through the modification of the Graphic Subroutine Package to inhibit image regeneration. One image is sufficient to expose the film. Additional generations simply create a problem in tolerance to partial regeneration cycles. This problem is combatted by the generation of a sufficiently large number of images such that partial cycle effect is unnoticed by the camera.

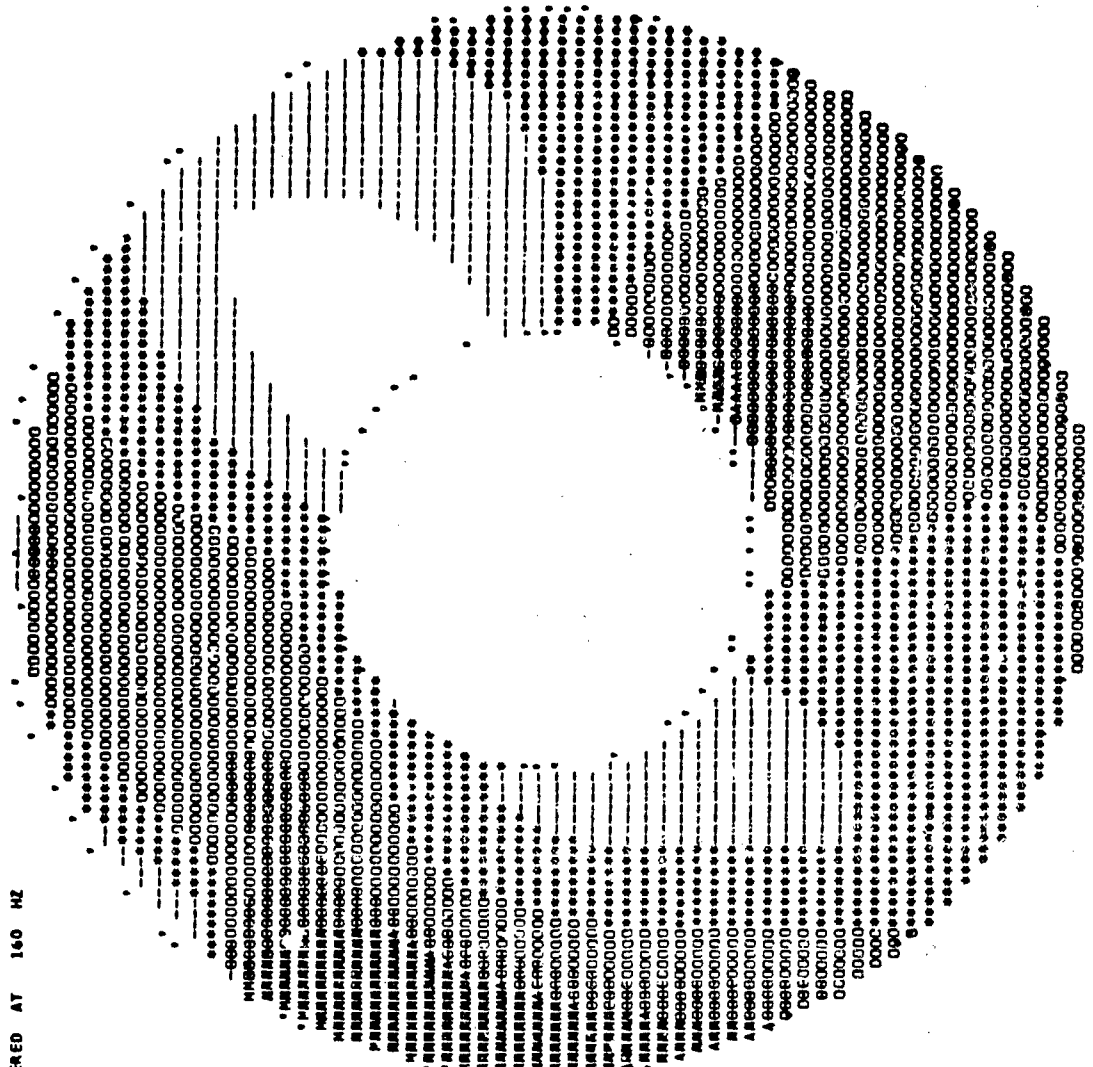
B. FUTURE CONSIDERATIONS TO THE CONCEPT

The system described herein permits recording and projection of distortion patterns in one axial plane of a turbo-machine. Of ultimate interest to the engineer would be a characterization of the distorted flow as it progresses through the machine.

Several independent film strips might be evolved, each portraying the dynamic conditions at a given axial station. Several projectors then may be ganged and controlled to operate synchronously, projecting several non-overlapped images concurrently. The images may then be studied on a time-space basis by exercising complete human control over the projection rate.

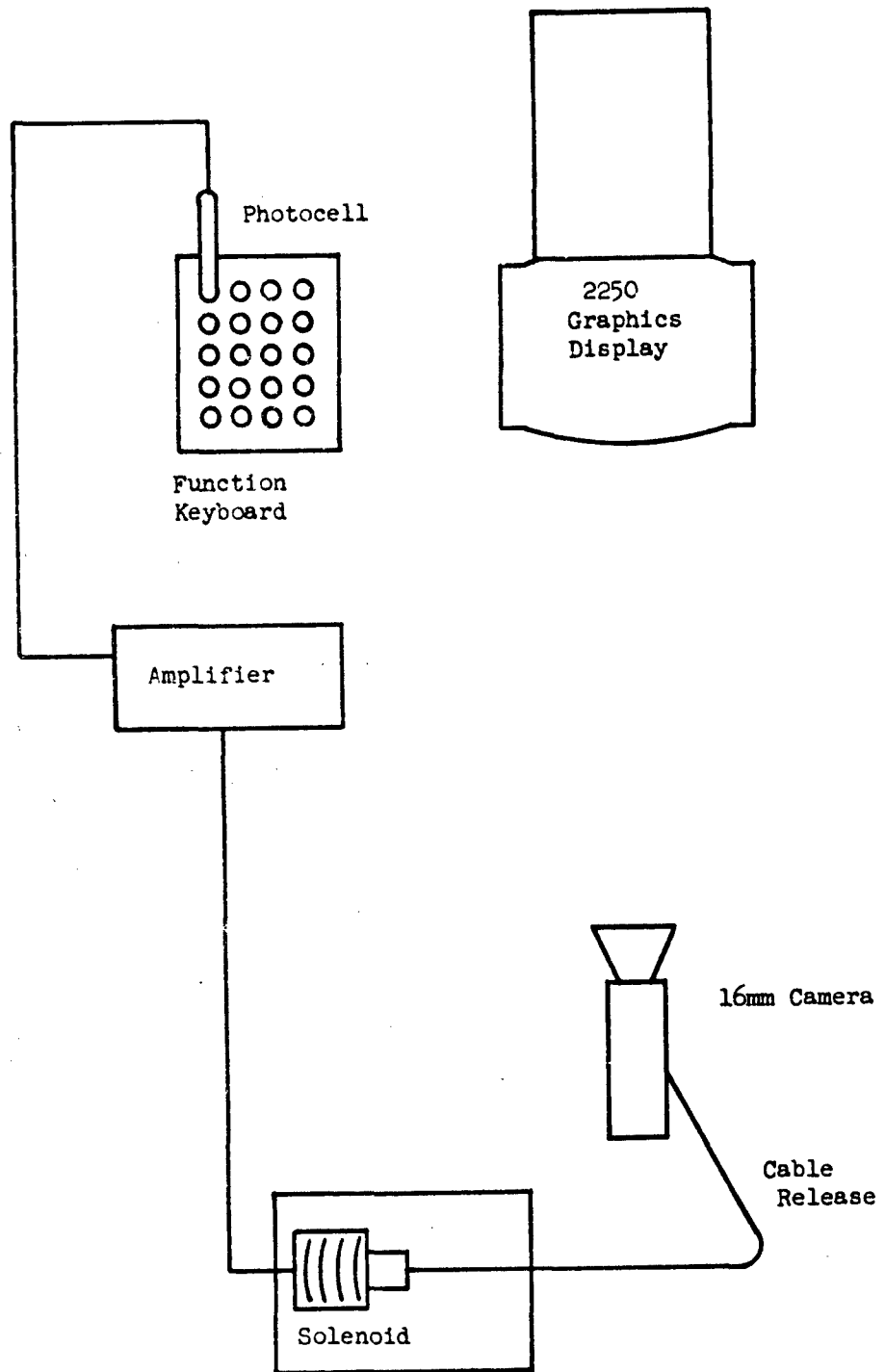
Holographic techniques hold considerable promise for studying propagation of distortion patterns in a 3-dimensional sense. Most current holographic research is restricted to static rather than dynamic holograms. Dynamic holography permitting an in-depth study of time variant 3-space phenomena will represent a scientific advancement providing a powerful tool for the study of flow instability.

FRAME FILTERED AT 160 HZ
BASE = 8.431E 00



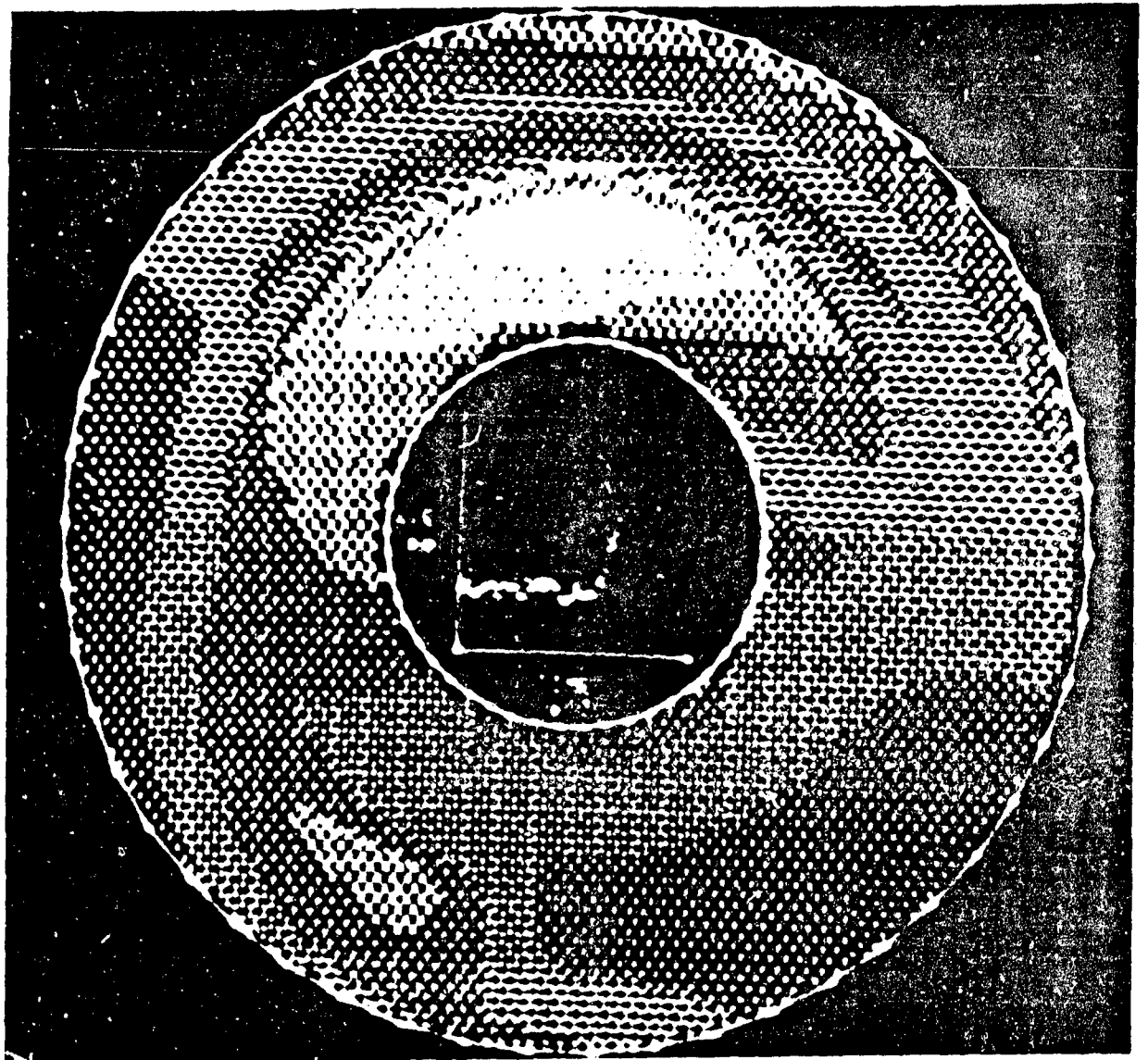
PRESSURE INTENSITY PATTERN - COMPUTER PRINTER SIMULATION

Figure 1



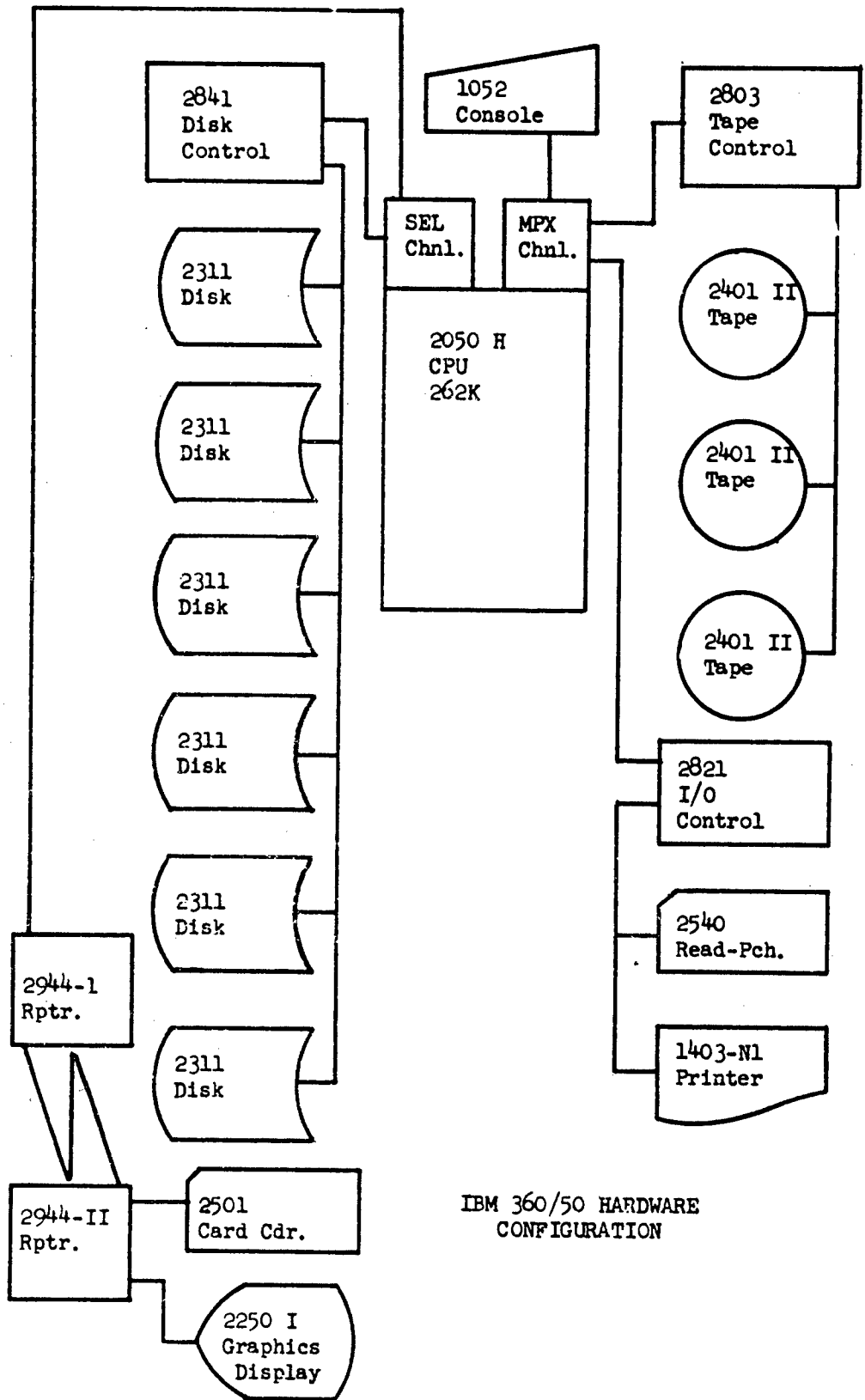
EXPERIMENTAL APPARATUS

Figure 2



PRESSURE INTENSITY PATTERN - CATHODE RAY TUBE SIMULATION

Figure 4



IBM 360/50 HARDWARE CONFIGURATION

Figure 5

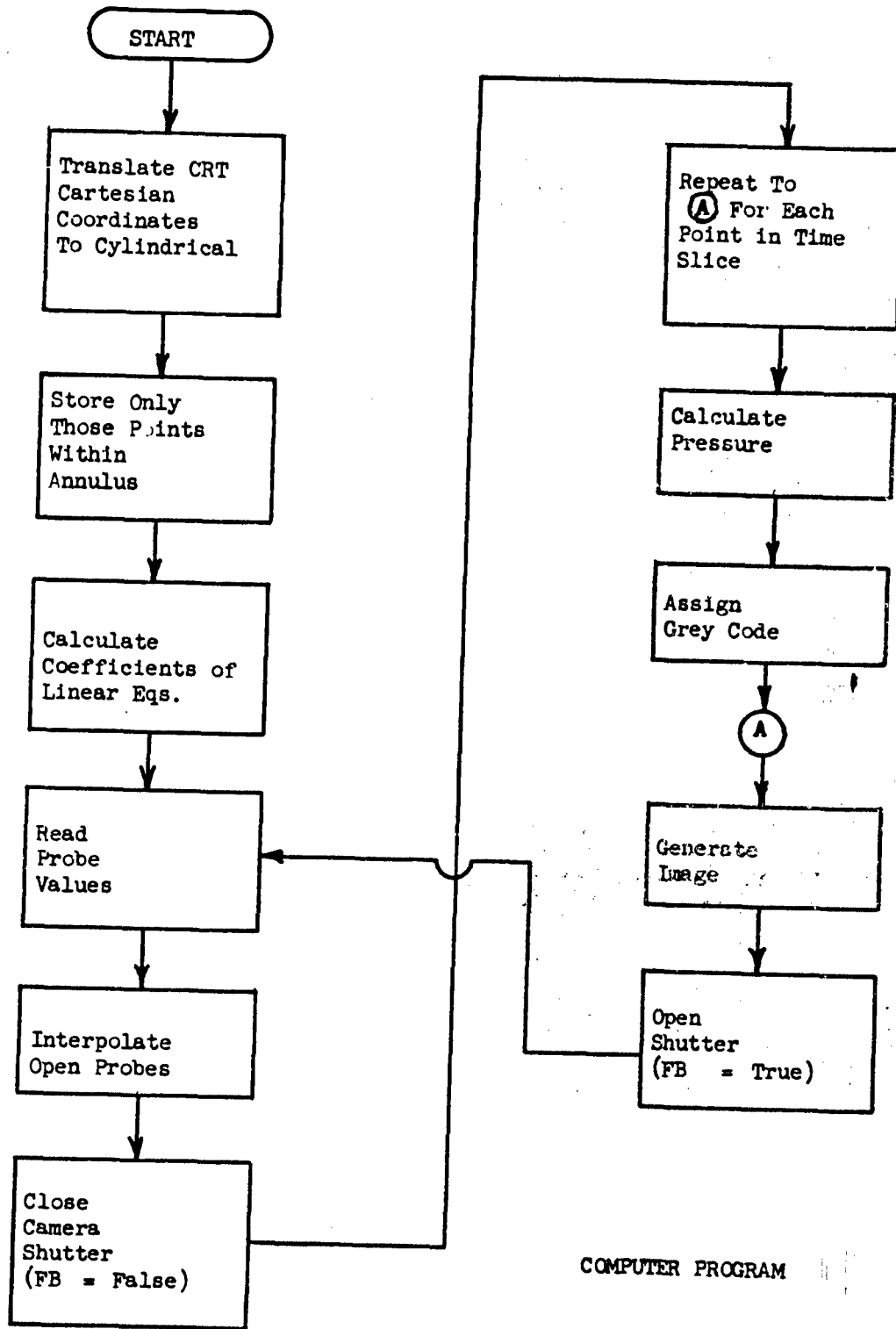
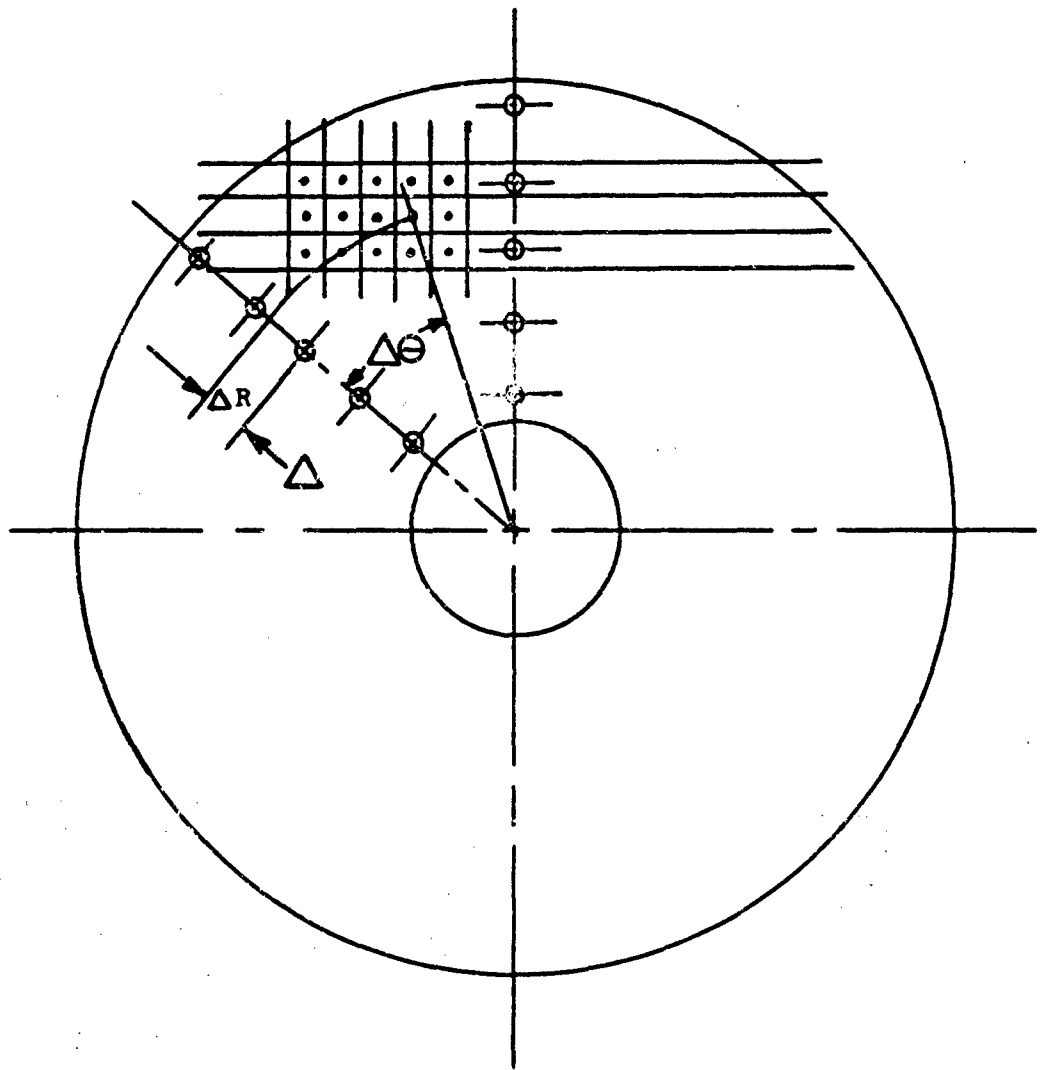



Figure 6




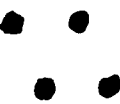
r, θ PRESSURE INTERPOLATION


Figure 7


$i_1 =$

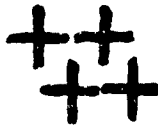
$i_2 =$ 


$i_3 =$ 


$i_4 =$ 


$i_5 =$ 

$i_6 =$ 

$i_7 =$ 

$i_8 =$ 

$i_9 =$ 

$i_{10} =$ 

$i_{11} =$ 

GREY CODE

Figure 8

PRESSURE FLUCTUATIONS CAUSE COMPRESSOR INSTABILITY

G. A. Flourde
Assistant Project Engineer
Pratt & Whitney Aircraft

B. Brimlow
Squadron Leader
Air Force Aero Propulsion Laboratory
Wright-Patterson AFB, Ohio

ABSTRACT

An experimental program was conducted to evaluate the effects of random inlet pressure fluctuations on the performance and stability of a fan/low pressure compressor. A device consisting of a converging-diverging section with a plug centerbody followed by a constant diameter duct created the random pressure fluctuations and fed them into the compressor. Additional devices were installed within the constant area duct to alter the properties of the random pressure fluctuations.

Both the root-mean-square (RMS) amplitude and the amplitude frequency spectra of the pressure fluctuations were varied. The gross effects of these inlet conditions were evaluated in terms of changes to the steady state performance maps. For all cases operation with random inlet pressure fluctuations resulted in a loss of steady state surge line and a reduction of corrected flow capacity, when compared to operation with a standard bellmouth. Correlations of the changes of surge line and airflow with RMS amplitude within various frequency ranges were attempted. Although "good" correlations were not achieved, the minimum loss in surge line of the fan/low pressure compressor correlated best with the RMS amplitude in the 0-100 Hertz range when the corrected speed was 9500 rpm. At a corrected speed of 7000 rpm the best correlation was obtained with the RMS amplitude in the 0-50 Hertz range. At both corrected speeds the flow capacity reduction correlated reasonably well with the RMS amplitude in both the 0-1200 Hertz and 500-1000 Hertz range.

Analysis of the time variation of the inlet pressure, for a compressor corrected speed of 9500 rpm, was conducted to determine the surge inducing events. This revealed that large amplitudes of spatial distortion immediately preceded each surge. By utilizing filtering techniques which reduced the amplitude of pressure fluctuations at frequencies greater than 100 Hertz the maximum spatial distortion produced by the random pressure fluctuations occurred immediately preceding surge. In addition, the magnitude of this spatial distortion correlated very well with the gross loss in surge line associated with each surge. The loss of stability produced by random inlet pressure fluctuations appears, for this compressor with these laboratory generated inlet conditions, to be spatial distortion produced by pressure fluctuations within the frequency sensitive range of the compressor.

INTRODUCTION

Propulsion system instabilities have been significant developmental and operational problems in advanced, gas turbine-powered aircraft. The primary sources of these instabilities have been traced to interactions between various related components of the airframe and propulsion systems. A particularly serious stability problem to be averted in future supersonic or high-speed tactical aircraft will be engine surge caused by total pressure fluctuations in the air induction system. These fluctuations, which are apparently created by shock/boundary layer interactions and flow separation, are random in time and space and generally described as "turbulence"

Turbulence similar to that generated in aircraft inlets was duplicated in early engine tests by W. Kimzey¹ at Tullahoma (USAF/AEDC) and by Pratt & Whitney Aircraft. These tests provided data to permit evaluation of the gross effects of turbulence characteristics on engine stability. For instance, it was shown that the amplitude of turbulence necessary to surge the engine was related to the compressor surge margin. However, the early tests did not provide a sufficient basis for determining the mechanism intrinsic in the turbulence/surge relationship.

In the spring of 1968 a developmental test program was conducted at Pratt & Whitney Aircraft, under a product support program sponsored by the Naval Air Systems Command, to investigate the effects of turbulence on the performance and stability of a fan/low pressure compressor of the high performance TF30 turbofan engine. This program produced sufficient data to support a comprehensive analysis of the turbulence/surge mechanism. The analytical effort was conducted by Pratt & Whitney Aircraft under contract to the North American Rockwell Corporation as part of the USAF/APL Propulsion System Flow Stability Program. The purpose of this paper is to discuss the test program and present the results and conclusions of the analysis.

- 1) Kimzey, W.F. "An Investigation and Calibration of a Device for the Generation of Turbulent Flow at the Inlet of a Turbojet Engine" Arnold Engineering Development Center, AEDC-TR-65-195.

CONCLUSIONS AND RECOMMENDATIONS

1. The surge line of the TF30 fan/low pressure compressor was reduced by laboratory-generated inlet turbulence.
2. The surge line reduction is due to instantaneous spatial distortion produced primarily by turbulence in the frequency range from zero Hertz to rotor revolution frequency.
3. The flow capacity at a given speed of the TF30 fan/low pressure compressor was reduced by laboratory-generated inlet turbulence.
4. The flow capacity reduction is due to either the turbulence in the total measured frequency range (0–1200 Hertz) or in the high frequency range (500–1000 Hertz).
5. It is recommended that additional experiments be conducted to investigate the effect of turbulence on other compressors so that the generality of these conclusions can be determined.

DESCRIPTION OF APPARATUS

FAN/LOW PRESSURE COMPRESSOR HARDWARE

Testing in this program was performed with a TF30 fan/low pressure compressor installed in an altitude test stand. The fan/low compressor assembly has nine axial flow stages, three fan stages followed by six low pressure compressor stages. A schematic of a TF30 fan/low pressure compressor is shown on Figure 1.

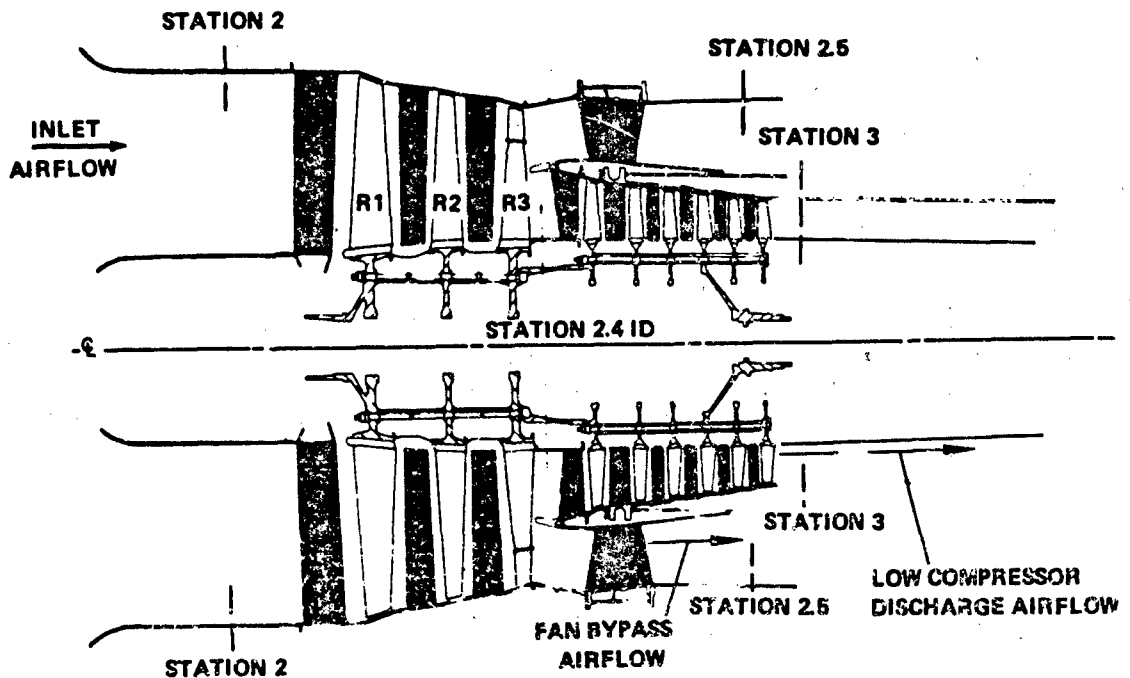


Figure 1 TF30 Fan/Low Pressure Compressor

TURBULENCE GENERATOR

The turbulence generator duct consisted of a converging-diverging section with a plug centerbody followed by a constant area pipe which fed the flow into the compressor. The centerbody plug could be moved axially to control the venturi throat area, and up or down to adjust plug centering and to change the steady state distortion pattern at the compressor face. The throat area could be adjusted from 188 square inches to 605 square inches. A flow bypass system was available for controlling normal shock strength independently of flow conditions at the engine compressor face. This bypass system, however, was not utilized during this test program.

A cutaway of the turbulence generator mounted to the TF30 compressor is presented on Figure 2, and a photograph of the rig installed in the test stand is presented on Figure 3. High response instrumentation can be seen downstream of the turbulence generator throat (left of center in the photograph). Tubing for compressor steady state instrumentation may be noted to the right of center in the picture. Large torus ducts at the fan and compressor exits collect discharge air and direct it into the exit duct work.

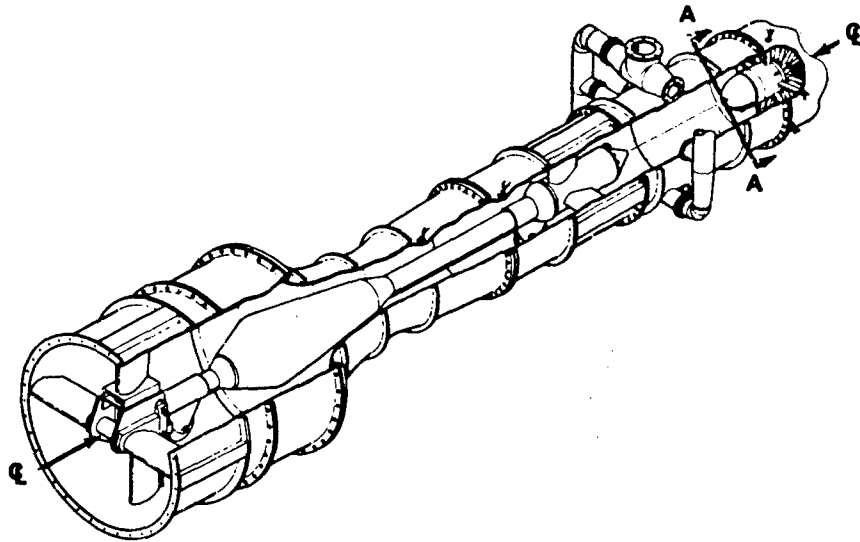


Figure 2 Turbulence Generator

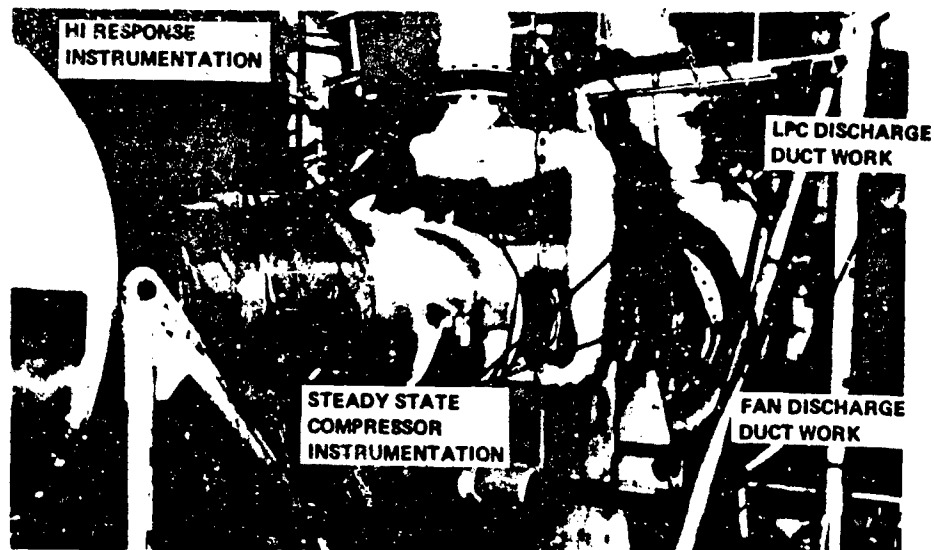


Figure 3 Rig with Turbulence Generator Installed in Test Stand - Looking Downstream

INLET MODIFICATIONS

The following modifications to the inlet system were evaluated as techniques to change the characteristics of the turbulence amplitude/frequency spectrum (the efficacy of these modifications and the corresponding effects on the fan compressor are discussed later):

- Two rows of 95 holes (1/4-inch diameter) drilled circumferentially in the venturi throat. The holes were open to atmospheric pressure allowing air to blow into the turbulence generator throat.
- Three rows of 95 holes (1/4-inch diameter) enclosed by a manifold positioned at the throat. The system was operated with the manifold pressurized (25-inches Hg gauge) and evacuated (14.5-inches Hg absolute at 7000 rpm and 6-inches Hg absolute at 9500 rpm.)
- An egg crate of one inch honeycomb 10-inches long, positioned about 14-inches upstream of the inlet guide vane (Figure 4).
- A 10 vane screen support with a 360 degree base screen (1.0 x 0.125-inches), as shown in Figure 5.
- A 24 vane screen support. The leading edge of the support was about 14.25-inches upstream of the compressor inlet vane. An extended nose cone was attached to the support to eliminate boundary layer separation (Figure 6).

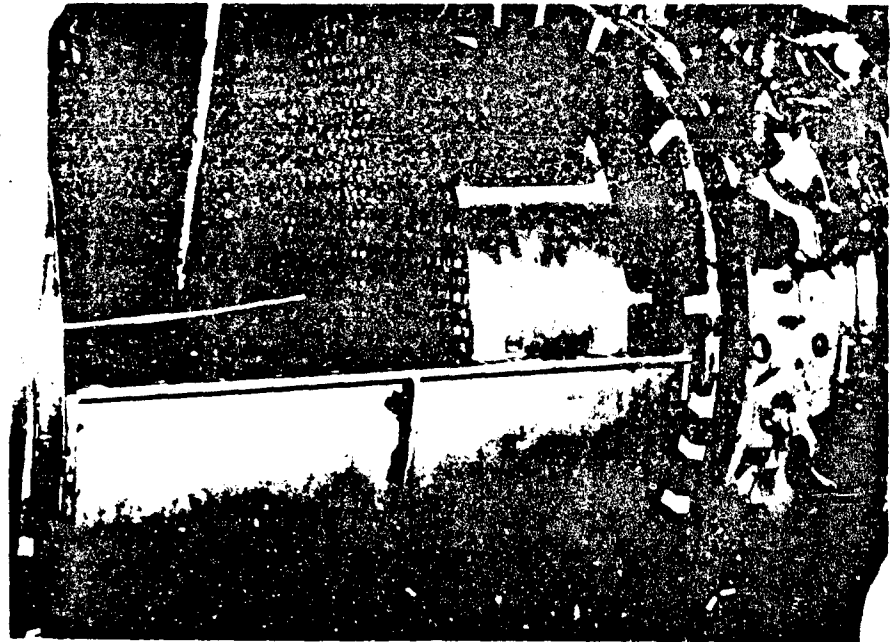


Figure 4 Honeycomb Air Straightener

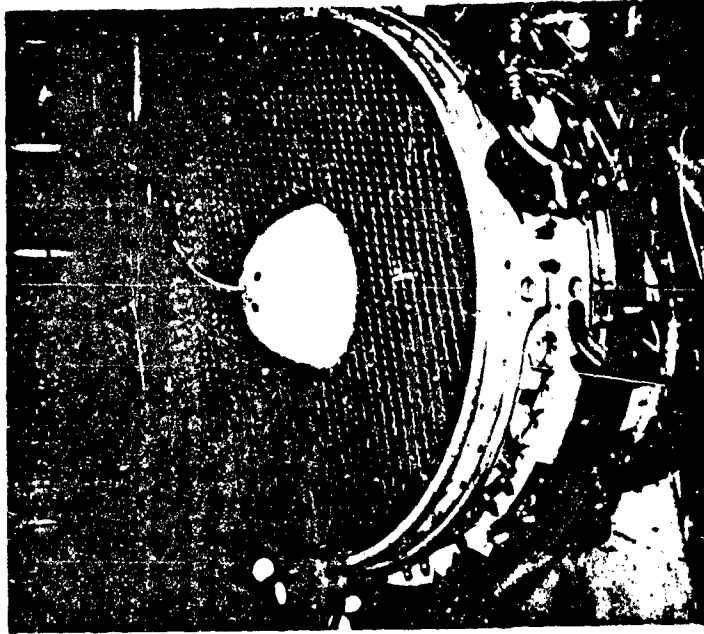


Figure 5 10 Spoke Distortion Spider

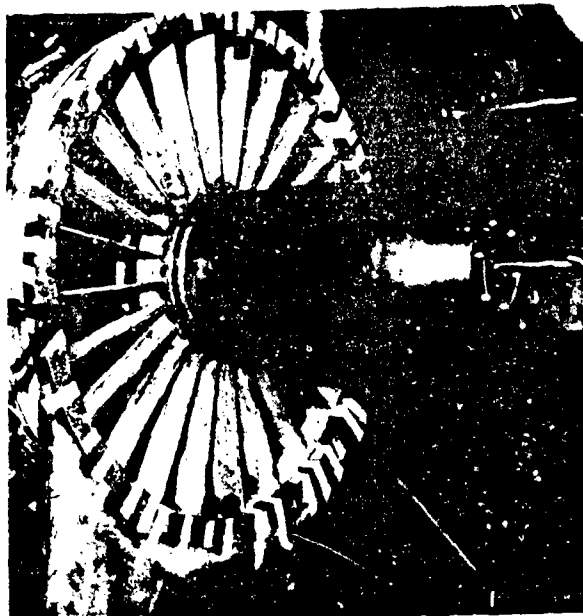


Figure 6 24 Spoke Distortion Spider with Nose Cone

- A 24 vane support and a 360 degree screen (1.0 x 0.125-inches).
- \ 24 vane support and a 180 degree distortion screen (1.0 x 0.125-inches).
- A grill with 1/2-inch square rods spaced every 5-inches vertically and horizontally and positioned 14-inches in front of the inlet guide vane (Figure 7).
- Two rows of 2.90-inch diameter pipe (three per row) installed in front of the compressor nose cone. The first row was vertical and was positioned about one foot upstream of the second row, which had the pipes positioned horizontally (Figure 8).

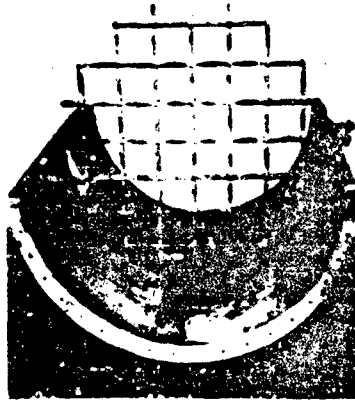


Figure 7 Grill of 1/2-Inch Square Rods



Figure 8 Two Rows of Three-Inch Diameter Pipe

INSTRUMENTATION

Both standard steady state and high response instrumentation were utilized in the test rig. The steady state instrumentation with a frequency response of less than one cycle per second (Hz) was used to determine the time average air flow characteristics and time average compressor performance. High response transducers (used with a data recording system designed for a frequency response from 1 to 1000 Hz) were used to measure the pressure variations associated with the turbulent flow and compressor transient conditions.

Steady State Instrumentation

Overall compressor performance was measured with standard steady state instrumentation connected to low frequency response transducers. Two rakes with five Kiel head pressure probes per rake were used to determine inlet total pressure. Inlet total temperature was measured by thermocouples in the plenum chamber upstream of the turbulence generator. Exit conditions were determined with Kiel head total pressure probes and total temperature probes in the discharge planes. Total flow was determined by the pressure drop through a calibrated orifice upstream of the plenum chamber. Core flow was determined with an orifice far downstream of the low pressure compressor exit valve.

High Response Instrumentation

Static and total pressures were measured with high frequency response pressure transducers mounted in/or connected to specially designed probes or rakes. Whenever practical the transducers were installed with their pressure sensitive axis aligned in the axial direction to minimize the influence of vibration. Kistler piezoelectric and MB strain gauge pressure transducers were utilized at the compressor inlet. At any other location, only Kistler transducers were used. The transducer's signals were recorded on magnetic tape and were monitored on a dual trace oscilloscope, a true RMS meter, and a digital voltmeter.

Total pressure probes with Kistler transducers were installed 11.8-feet and 9.7-feet upstream of the compressor inlet (Station 1), at the compressor inlet (Station 2), at the fan exit (Station 2.4 ID and OD), at the leading edge of the fourth-stage stator, and at the compressor exit (Station 3) in two axial locations. Kistler static pressure transducers were located at the compressor inlet (Station 2.0 OD), at the fan exit (flow splitter ID and OD, and fan duct OD), and at the compressor exit. The circumferential location of this instrumentation is shown schematically in Figure 9.

At the compressor inlet, total pressure rakes were positioned at 0° , 45° , 135° , 225° , 292.5° , and 315° (facing upstream). Most of these rakes can be seen in Figure 10. Each rake had Kistler transducers and low frequency response sensing tubes (connected to MB strain gauge transducers) at the centers of five equal flow areas. Electrical signals from both the low and the high frequency response systems were filtered and combined in a summing amplifier.

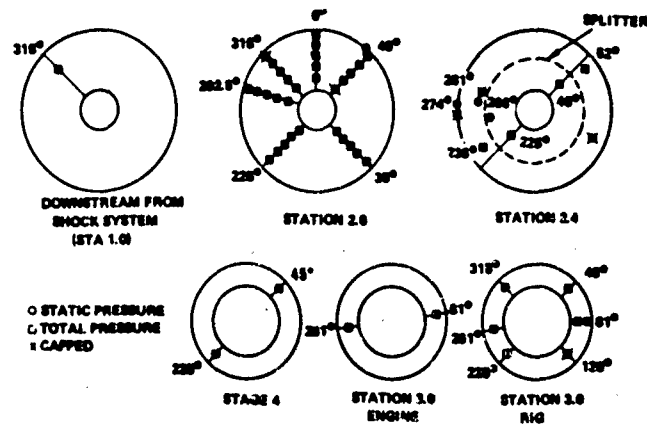


Figure 9 Circumferential Location of High Response Instrumentation Looking Upstream

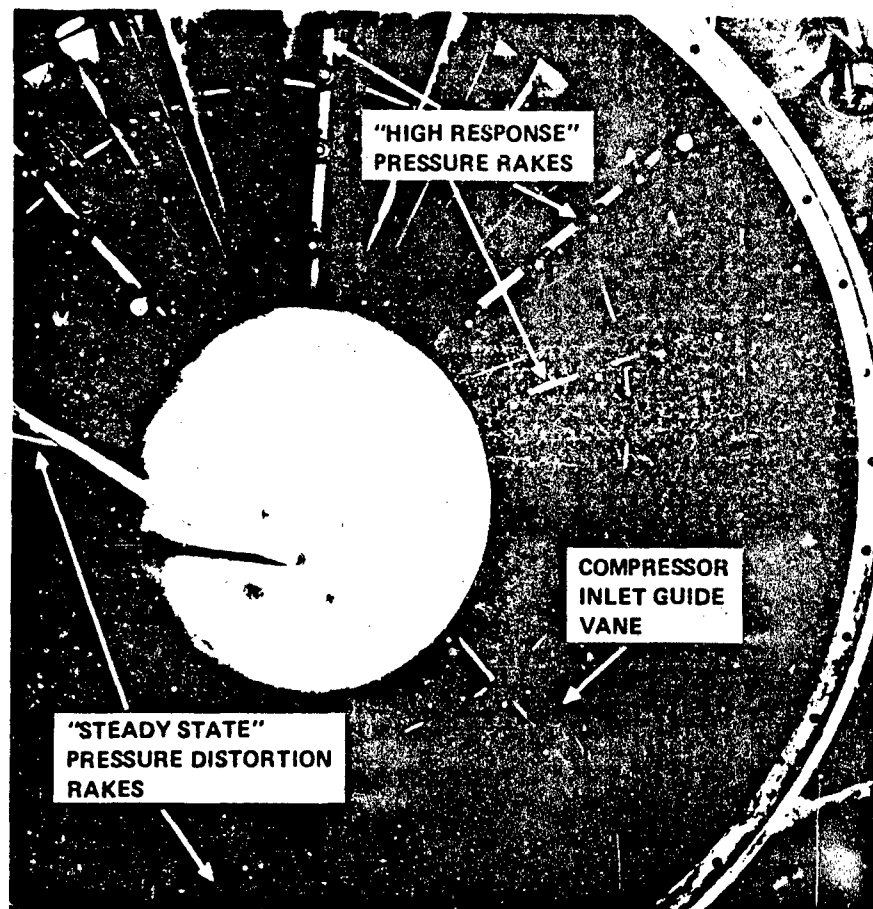


Figure 10 High Response Instrumentation at Rig Inlet

At the fan discharge (Station 2.4), four right-angle total pressure Kistler transducers were mounted at the end of removeable probes. Two probes were located in the fan stream (OD) and two in the engine stream (ID). All probes were mounted to the fan exit case with the two ID probes passing through and supported by the splitter assembly. Installation of these probes can be seen in Figure 11.

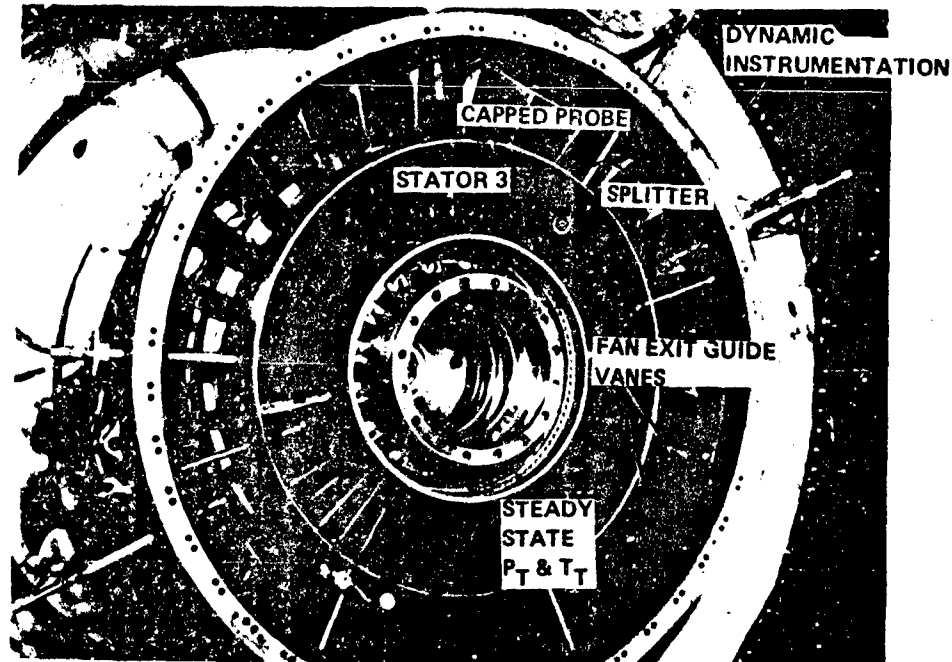


Figure 11 Instrumented Fan Exit

TEST PROGRAM AND PROCEDURE

The first phase of this experimental program was to establish baseline compressor performance with a minimal amount of turbulence imposed at the inlet. A standard bellmouth provided these inlet conditions to the fully instrumented compressor.

The second phase consisted of recalibrating the compressor with turbulence levels provided by the basic turbulence generator. This calibration was accomplished by:

- Setting the centerbody at a position at which a predetermined turbulence level would be produced
- Adjusting the compressor inlet total pressure level to the value desired (constant for each speed), and
- Closing the fan or low pressure compressor exit valve to produce the speed line

Each speed line was defined by several data points at which both steady state and high frequency data was recorded. The surge point was identified by visually monitoring the steady state instrumentation readout. Surge was generally repeated and high frequency data was usually obtained for at least one surge point per speed line.

In the third phase of the program the character of inlet conditions was modified. The various modifications to the basic turbulence generator described above were tested and compressor performance was obtained. In addition, steady state distortion and turbulence were imposed on the compressor. The procedure used to obtain compressor data in Phase III was identical to that used with the basic turbulence generator alone.

RESULTS AND DISCUSSION

OVERALL PERFORMANCE

An example of fan/low pressure compressor performance with and without turbulence is given in Figure 12. Each speed line was generated by closing the low pressure compressor exit valve while holding the fan on a nominal operating line. In addition to baseline (bell-mouth) performance, the data for three different turbulence spectra are shown. The turbulent inlet conditions were generated with the turbulence generator (unmodified and with 1/2-inch rods or 3-inch pipes in front of the compressor). The $\Delta P_{RMS}/P$ associated with each speed line contains energy in the frequency range of 0 to 1200 Hertz. In this figure, the slashed symbols denote surge points; straight line slashes indicate that the compressor surged while the exit valve was being closed; and curved slashes indicate surges which occurred while inlet and compressor conditions were apparently constant for 30 seconds or longer.

A significant effect of turbulence on a compressor is the reduction of the surge line, as illustrated by the data in Figure 12. It is evident that the parameter $\Delta P_{RMS}/P_{avg}$ (0 to 1200 Hertz) is not sufficient to determine even the maximum surge pressure ratio obtainable. The manner in which the turbulence was produced, such as with an unmodified turbulence generator or added rods and pipes, is also significant. These devices produced modifications of the amplitude/frequency spectra of the turbulence. The surge line reduction produced with the different spectra indicate that the compressor's sensitivity is a function of frequency. This frequency sensitivity was investigated by correlations of the minimum surge line loss and in the determination of the surge inducing event. These analyses revealed that the compressor surge line showed some correlation with pressure fluctuations in the frequency range from zero to about that of the rotor's revolution.

Another manifestation of the effect of turbulence on compressors, the reduction of flow capacity, is also illustrated in Figure 12. Good correlations of the change in flow capacity of the compressor were obtained with the RMS amplitude of the turbulence in both the frequency ranges of 0 to 1200 Hertz and 500 to 1000 Hertz. It is not clear whether the total frequency content or just the high frequencies are important.

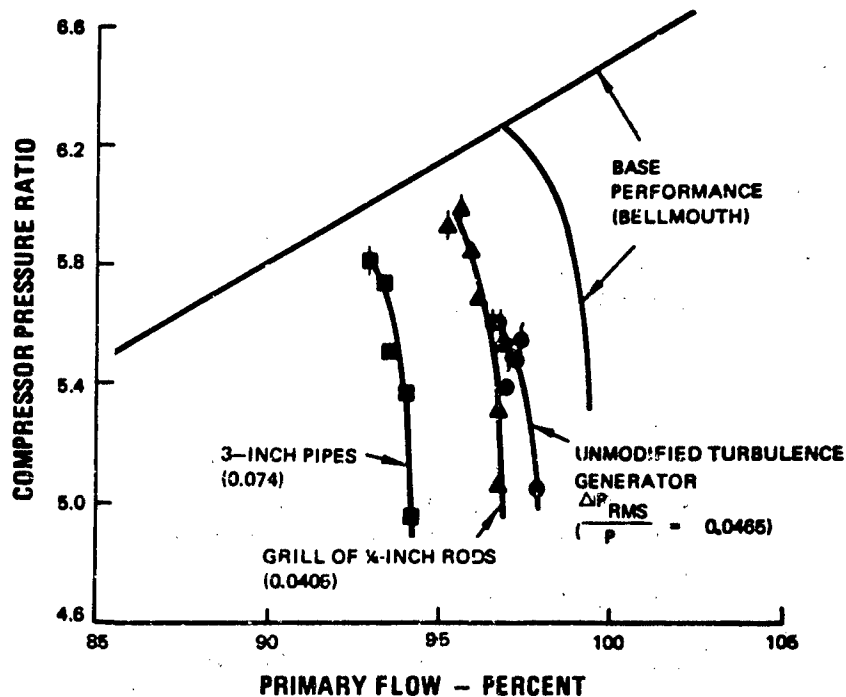


Figure 12 Fan/Low Pressure Compressor Performance

Surges were often encountered during this program while inlet and compressor conditions were constant, and, at times, up to thirty minutes had elapsed before a surge. This type of surge provides a clue to the surge-inducing phenomena. This propensity of the compressor to randomly be stable or to surge when the statistical properties of the inlet turbulence are constant is a significant facet of the effect of turbulence on the compressor. It suggests that the statistical properties of the turbulence determine the probability of producing an inlet condition which will induce surge. For example, consider that instantaneous spatial pressure distortion induces surge. The effect of a spatial pressure distortion on a compressor is a function of both the amplitude of the pressure variation and the geometric arrangement of the high and low pressure regions over the compressor face. Since turbulence creates randomly fluctuating pressure over the compressor face, the instantaneous spatial distortion pattern and amplitude is changing continuously. The pattern to which the compressor is most sensitive will appear for only a small percentage of the time. In addition, when this pattern does appear, its amplitude (maximum minus minimum pressure) will be different each time. The highest amplitudes will have the lowest probability of occurrence. For a low turbulence level, the probability of producing an extremely high amplitude for a given spatial distortion pattern is low. Suppose that at a given compressor setting it takes a 180° circumferential distortion of 12% maximum minus minimum amplitude to induce surge. If the RMS amplitude of the turbulence is 2%, the probability of producing this surge-inducing distortion is low but finite. Therefore, some stable running would be expected prior to surge.

In the previous discussion spatial pressure distortion was suggested to be the surge inducing event. Analysis of overall performance is, of course, not adequate to determine that this is the event. However, analysis of compressor face high frequency data, which is discussed below, does show that spatial distortion is in fact the surge inducing event.

INLET MODIFICATIONS

To determine the frequency sensitivity of the compressor, many devices were introduced into the turbulence generator to alter the amplitude/frequency spectra of the turbulence. Of all the devices tested, only two produced significant spectra changes. The grill of 1/2-inch rods produced a "flat" spectrum at the compressor face, and the 3-inch pipe configuration produced high amplitudes in the mid-frequency range. All other devices produced spectra which differed insignificantly from that produced by the unmodified turbulence generator. These other devices did alter the shock structure and/or the relationship between the shock Mach number and turbulence level, but were not useful to determine the frequency sensitivity of the compressor.

The spectra produced by the grill of 1/2-inch rods is compared in Figure 13 with that produced by the unmodified turbulence generator. Early in the test program flat spectra were observed to be produced immediately downstream of separated regions. The grill of rods utilized this phenomenon to generate a flat spectrum by producing separated flow over the whole compressor face. To a large degree this was achieved. The spatial variation in the turbulence spectra was small and is shown in Figure 13 as the difference between the turbulence measured between the rods and behind the rods.

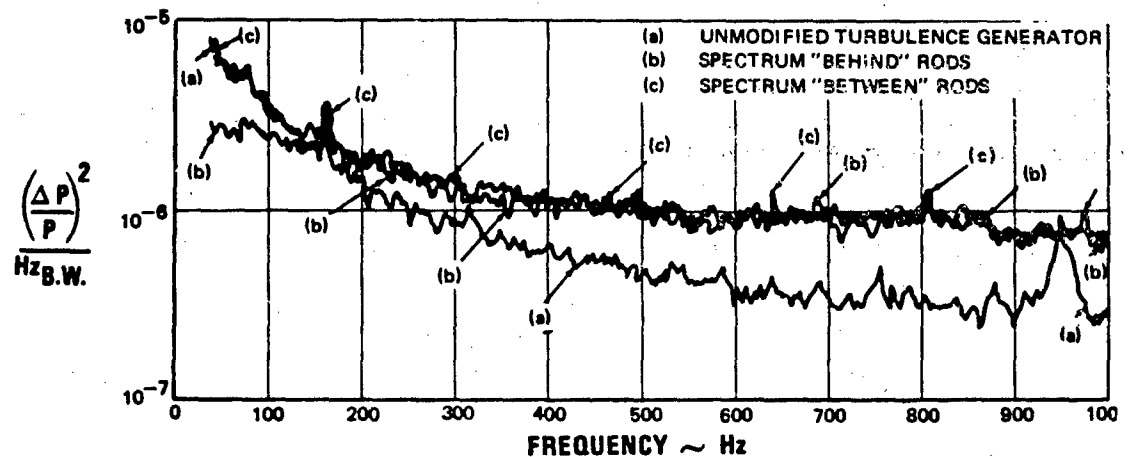


Figure 13 Power Spectral Density Comparison, Typical Levels at Compressor Inlet

The three-inch pipe configuration was designed to introduce a relatively high amplitude at a discrete frequency through the phenomenon of vortex-shedding. The resulting spectrum is compared to that of the unmodified generator in Figure 14. As expected, there is a high energy level in the frequency range surrounding the vortex-shedding frequency which was calculated to be 450 Hertz. Insignificant spatial variation in the spectra also was produced.

In Figure 14 and in the previous comparison of the spectra, high amplitudes are apparent at a discrete frequency of about 160 Hertz or rotor revolution frequency. This is caused by the voltage generated by the transducer due to mechanical vibration and not pressure fluctuations. Spectra obtained from capped probes, which measured no pressure signal and recorded the false signals produced by electronic noise in the system and vibration induced signals produced by the transducers, were used to determine this type of error in the data. Only the vibration induced signals as measured by the capped probes were of high enough amplitude to appear in the spectra generated by uncapped probes.

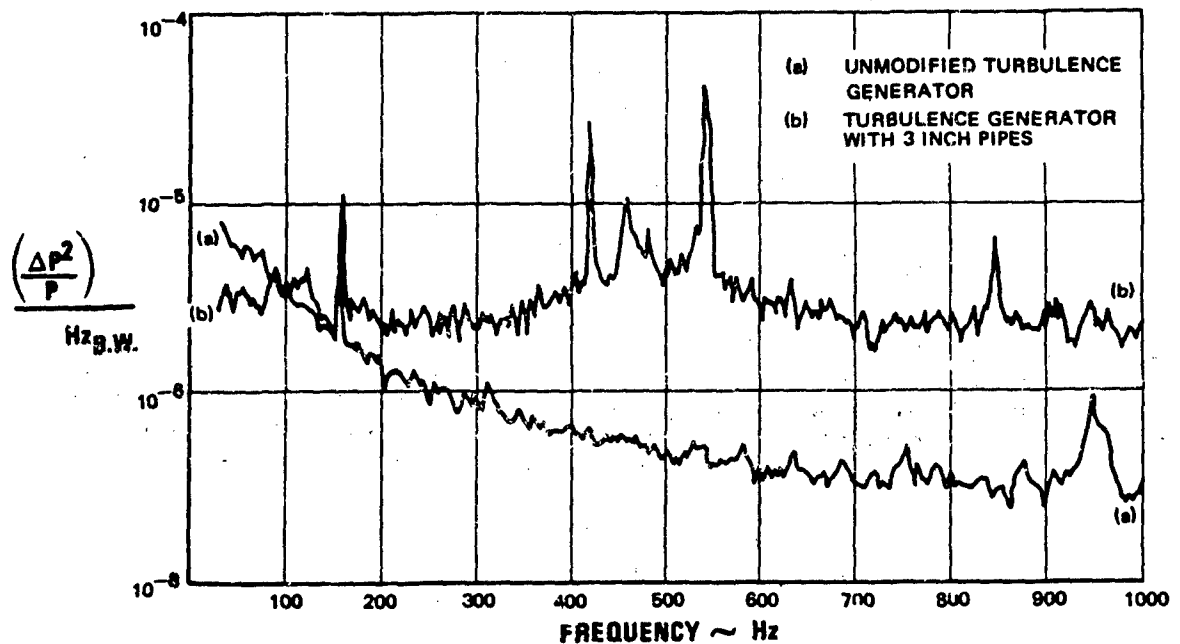


Figure 14 Power Spectral Density Comparison, Typical Levels at Compressor Inlet

Of the remaining inlet modifications used in an attempt to vary the frequency spectrum, the egg crate produced the greatest change. As shown in Figure 15, however, this change in spectrum is insignificant.

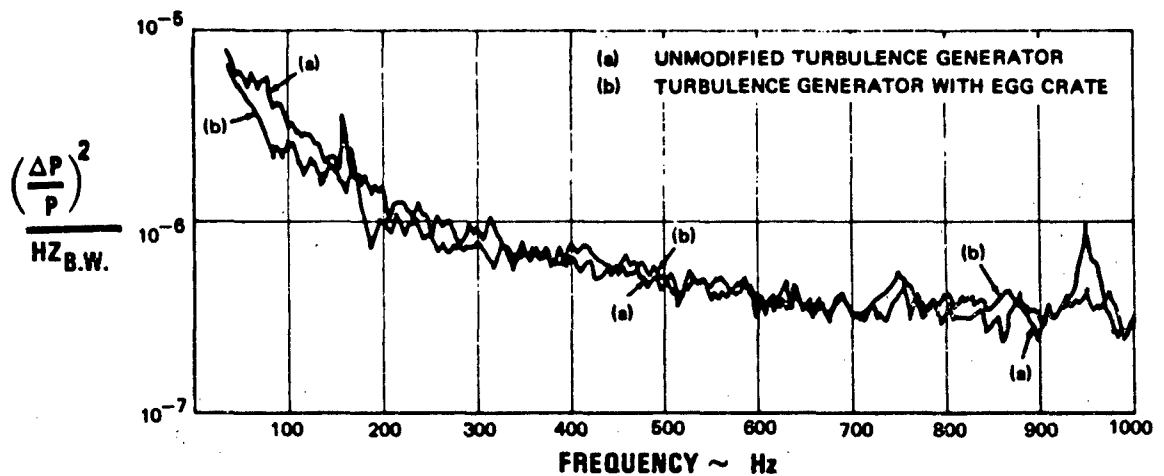


Figure 15 Power Spectral Density Comparison, Typical Levels at Compressor Inlet

CORRELATIONS

Data from all significant test conditions for the basic turbulence generator and modified inlet configurations were considered to determine possible correlations. Also, only driven stalls were included to reduce data scatter. These driven stalls represent the minimum loss in surge line and were obtained while closing the exit valve. Changes in fan root/low pressure compressor surge line and corrected fan airflow were investigated as a function of RMS pressure fluctuation amplitude in the following frequency ranges.

- Frequency Intervals: 0-50, 0-100, 0-500, 0-1000, 0-1200, 500-1000, and 750-1000 Hz.

The RMS amplitude used in the correlations was generally determined from the area under a power spectral density curve, as shown in Figures 13 through 15, produced by a midspan probe. The RMS amplitude in the 0 to 1200 Hertz range is the only exception. This amplitude was obtained from an on-stand true RMS meter reading from one probe. Spatial variations in RMS of $\pm 10\%$ were normal at the compressor face and errors of at least this magnitude can be expected in the relative amplitudes in frequency ranges less than 0 to 1200 Hertz.

The percent loss in surge line was calculated from steady state performance maps, as shown in Figure 12. The pressure ratio difference at surge (between the baseline data and the turbulence data) at constant flow was divided by the baseline surge pressure ratio at this same flow. Multiplication of this fraction by 100 gave the percent loss in surge line used for this analysis.

The percent of change in primary flow corrected to the fan inlet (Station 2) and the percent of change in total flow corrected to the same location was approximately equal for a given inlet condition. For this reason flow reduction correlations were attempted with total flow alone.

Representative "good" and "poor" correlations from this investigation are presented in Figures 16 through 23. Interpretations of this data and conclusions derived from the study are presented in the following paragraphs.

The loss in fan/low pressure compressor surge line at a corrected speed of 9500 rpm correlates reasonably well in the low frequency range with the best relationships obtained for the RMS amplitude in the 0 to 100 Hz range. This correlation is shown in Figure 16. The correlations are poorer in higher frequency ranges. There is a possible correlation in the 0 to 1200 Hz range (Figure 17); however, the inclusion of data from the three-inch pipe test invalidates this possible correlation. This data is not within the expected data scatter range.

The loss in surge line at a corrected speed of 7000 rpm also correlates better in the low frequency range than in the high. However, the upper limit of influence appears to be lower than that for 9500 rpm. The best correlation at 7000 rpm occurred in the 0 to 50 Hz range (0 to 100 Hz at 9500 rpm). The correlation in the 0 to 50 Hz range is shown on Figure 18.

In contrast to the best surge line correlations, the loss in airflow did not show a marked relationship to the RMS pressure amplitudes at the low frequencies or frequency ranges. Figure 19 shows that at corrected speed of 9500 rpm, a correlation does not exist in the frequency interval of 0 to 1000 Hz. Figures 20 through 23 show good correlation in the 0 to 1200 Hz and 500 to 1000 Hz range for both 9500 and 7000 rpm. Due to the relatively good correlations in both frequency ranges it is not possible to judge whether all the measured frequencies or just the higher frequencies are altering the flow capacity of the compressor.

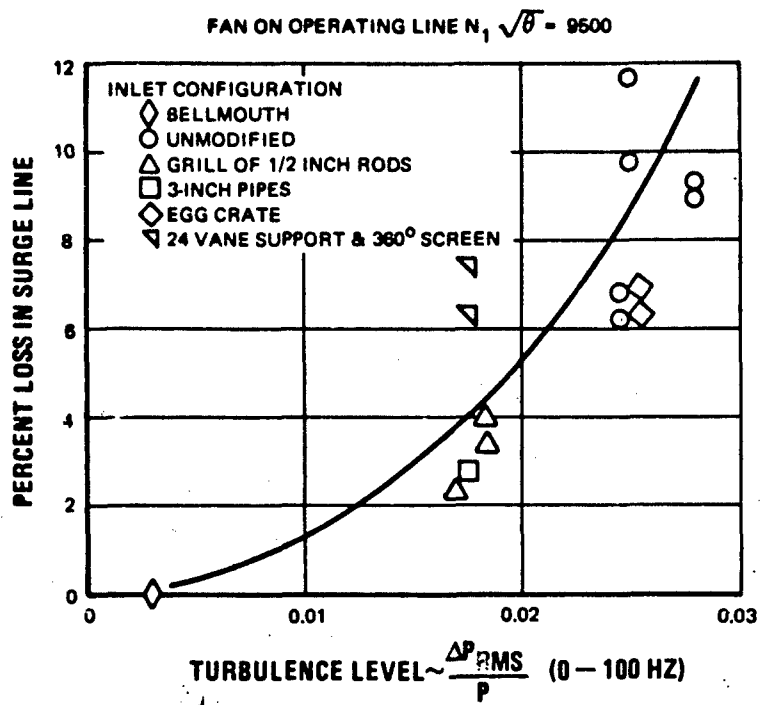


Figure 16 Surge Line Reduction vs Turbulence Level From 0 to 100 Hz

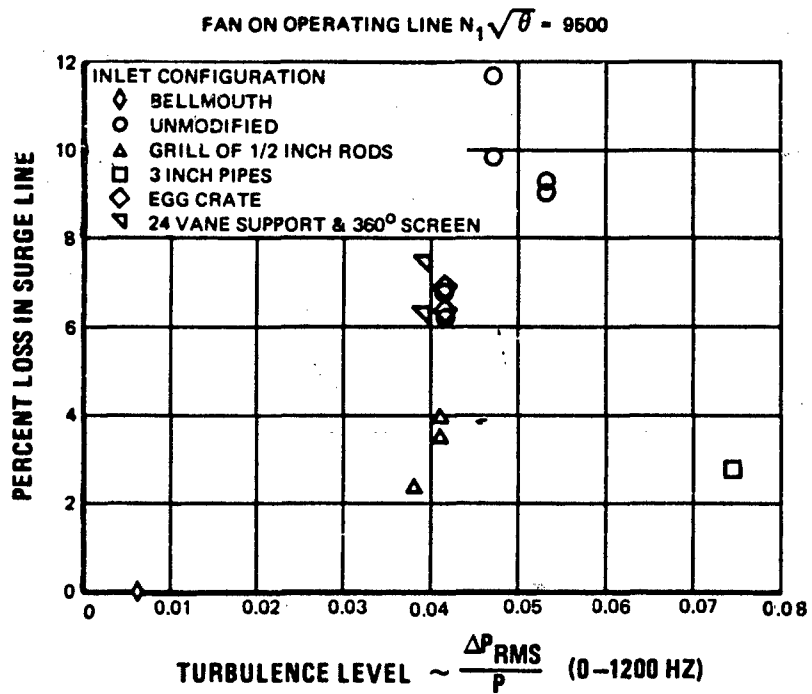


Figure 17 Surge Line Reduction vs Turbulence Level From 0 to 1200 Hz

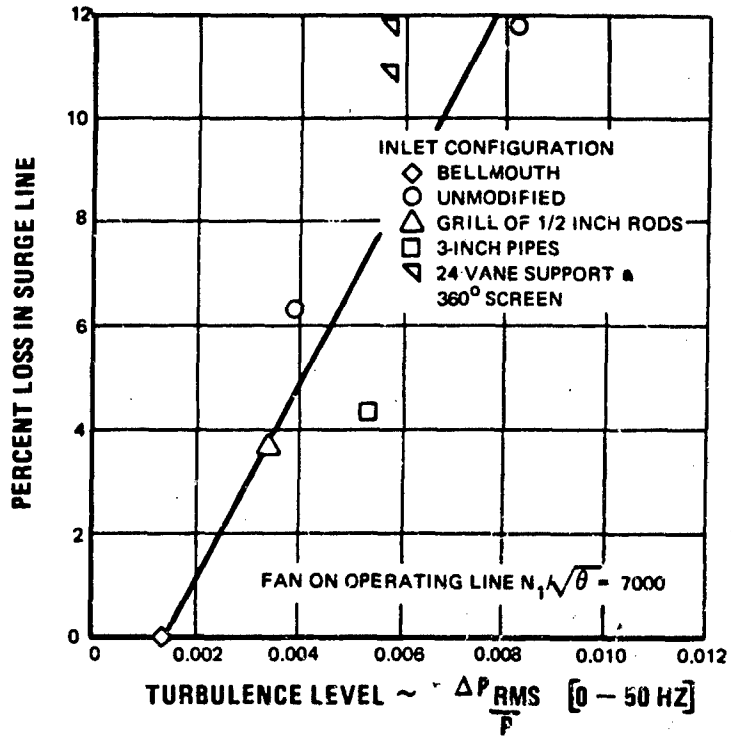


Figure 18 Surge Line Reduction vs Turbulence Level From 0 to 50 Hz

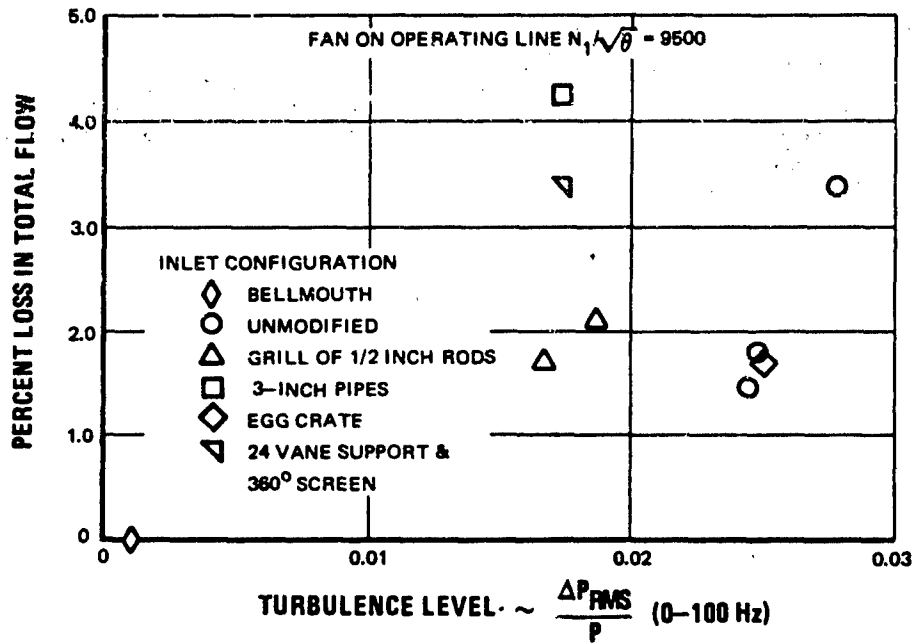


Figure 19 Loss in Flow vs Turbulence Level From 0 to 100 Hz

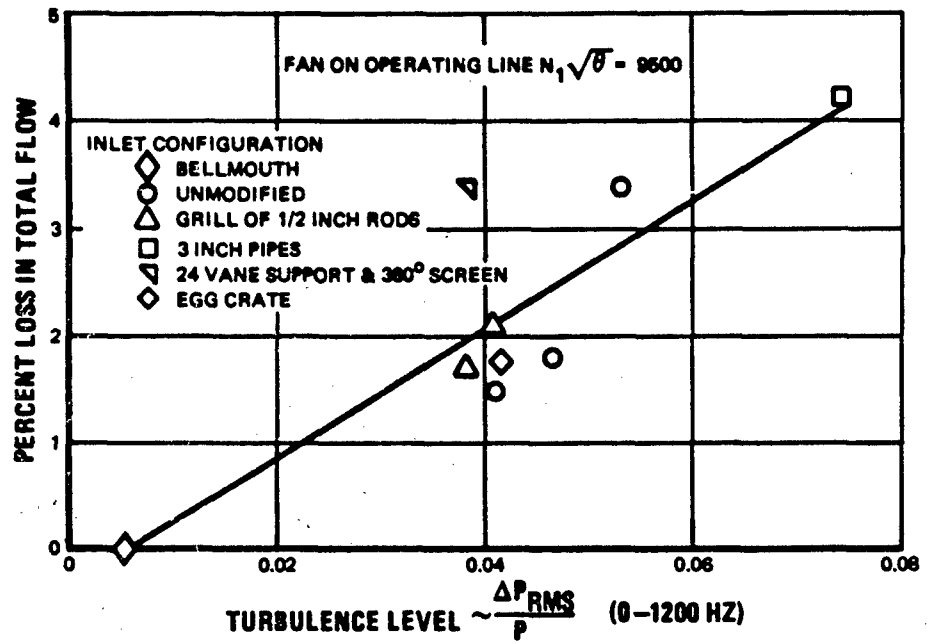


Figure 20 Loss in Flow vs Turbulence Level From 0 to 1200 Hz

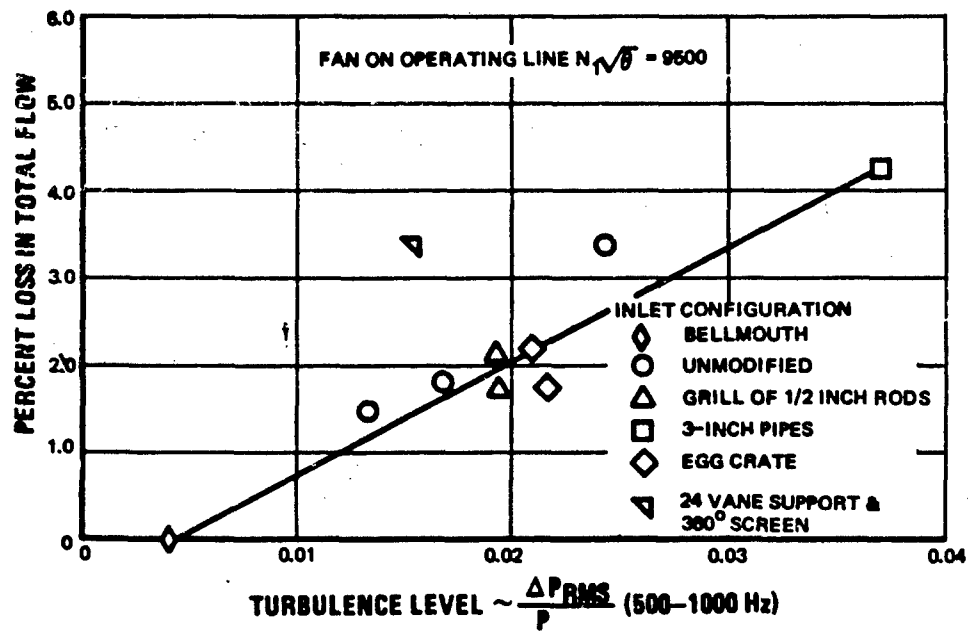


Figure 21 Loss in Flow vs Turbulence Level From 500 to 1000 Hz

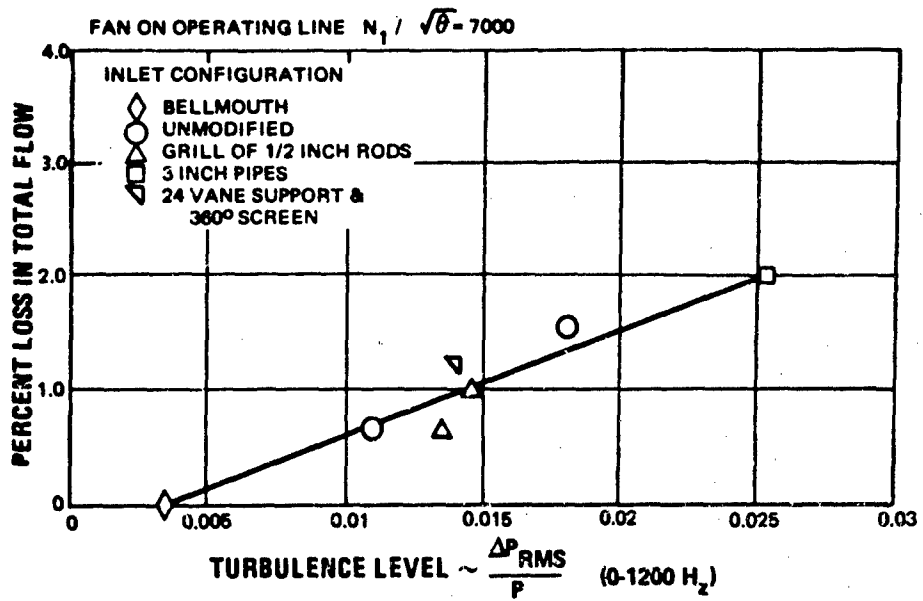


Figure 22 Loss in Flow vs Turbulence Level From 0 to 1200 Hz

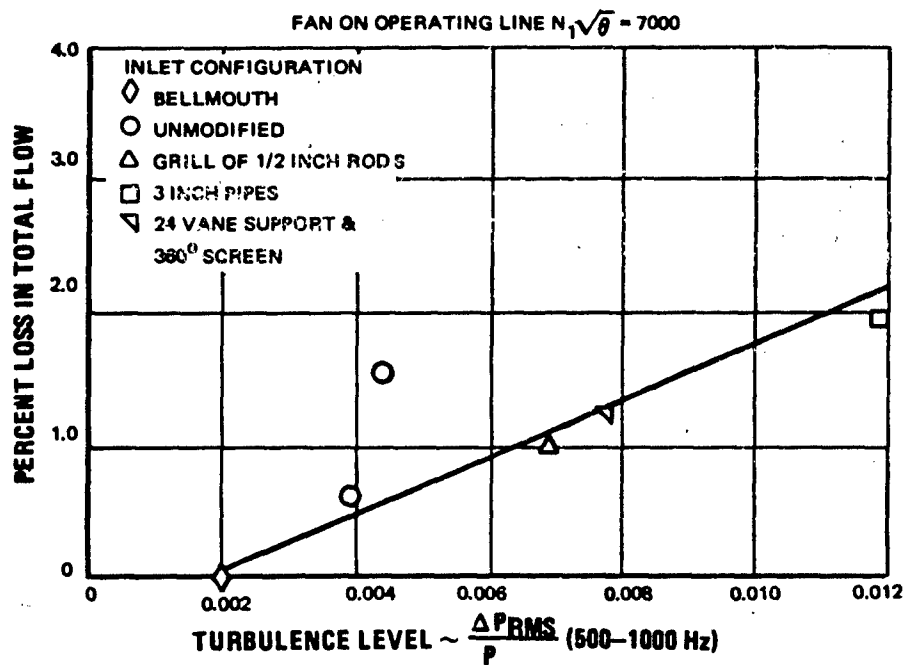


Figure 23 Loss in Flow vs Turbulence Level From 500 to 1000 Hz

SURGE INDUCING EVENTS

To establish surge inducing events, 34 surges at two compressor speeds were analyzed. These surges encompassed several levels of the many test variables. Included as variables were two compressor speeds and three inlet turbulence spectra at several levels, both alone and combined with steady state inlet distortion generated by distortion screens and centerbody plug offset. The surges were created by:

- Increasing the turbulence level by moving the centerbody plug,
- Increasing the back pressure by closing the low pressure compressor or fan discharge valve, or
- Operating with fixed conditions.

A study of inlet pressure contours was conducted to determine if instantaneous spatial distortion was the surge inducing event. Figure 24 illustrates a typical variation in spatial distortion produced by turbulence. These pressure patterns were measured within an interval of 0.1 seconds at the compressor face. The distortion factor (K_θ) associated with each pressure pattern is a measure of the relative severity in terms of the effect on the compressor, as determined by testing with steady state distortion. (The definition of K_θ is given in Appendix A). This study revealed that the surge inducing event was spatial distortion produced by turbulence in the frequency range from 0 to 80-160 Hertz. The uncertainty of the upper frequency is introduced by the response characteristic of the third order, constant amplitude, low pass filter applied to the data. This filter reduces the amplitude of the pressure fluctuations at the high frequencies. The gain characteristic (output amplitude divided by input amplitude) of this type of filter is given in Figure 25.

Figures 26 through 29 present the distortion factor for a stall that occurred at fixed operating conditions at 9500 rpm. The approximate time of surge, as determined by the time histories of the pressures within and at the compressor exit, is shown in Figure 26. The maximum K_θ (0.62) occurs 12 milliseconds prior to surge. The high levels of K_θ after surge are due to a rotating stall propagating upstream from the compressor. Figures 27 through 29 present K_θ versus time for various times preceding this surge. The distortion factor just prior to surge is greater than at any preceding time. Additional examples of distortion factor versus time for a fixed conditions stall are presented in Figures 30 and 31. This surge also shows that the distortion is greatest immediately preceding surge.

The time delay between the surge inducing distortion and the indicated surge is due to the time required for the distortion to propagate through the compressor and the time delay between the initial breakdown of the flow and the first clear indication of this breakdown on a probe. Actual time delays are on the order of 2 milliseconds greater than indicated due to the 160 break frequency low pass filter introducing a time shift in the K_θ history.

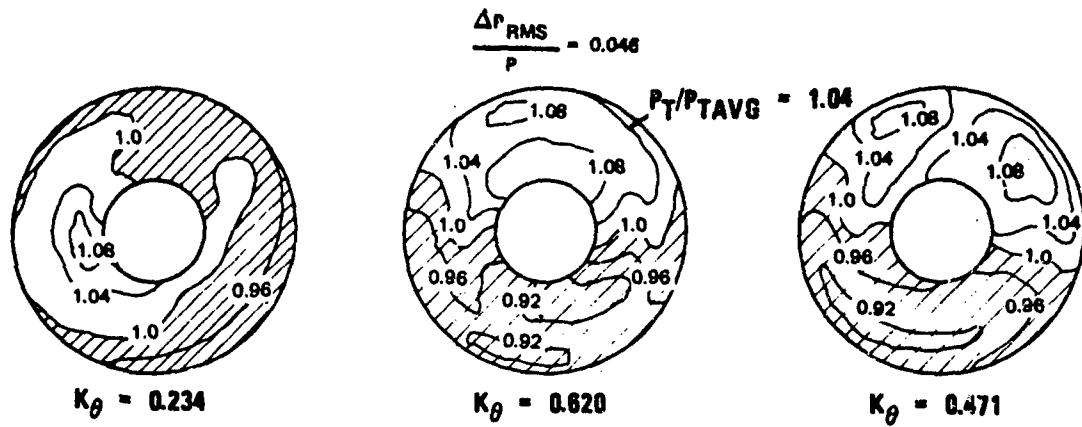


Figure 24 Instantaneous Inlet Pressure Contours

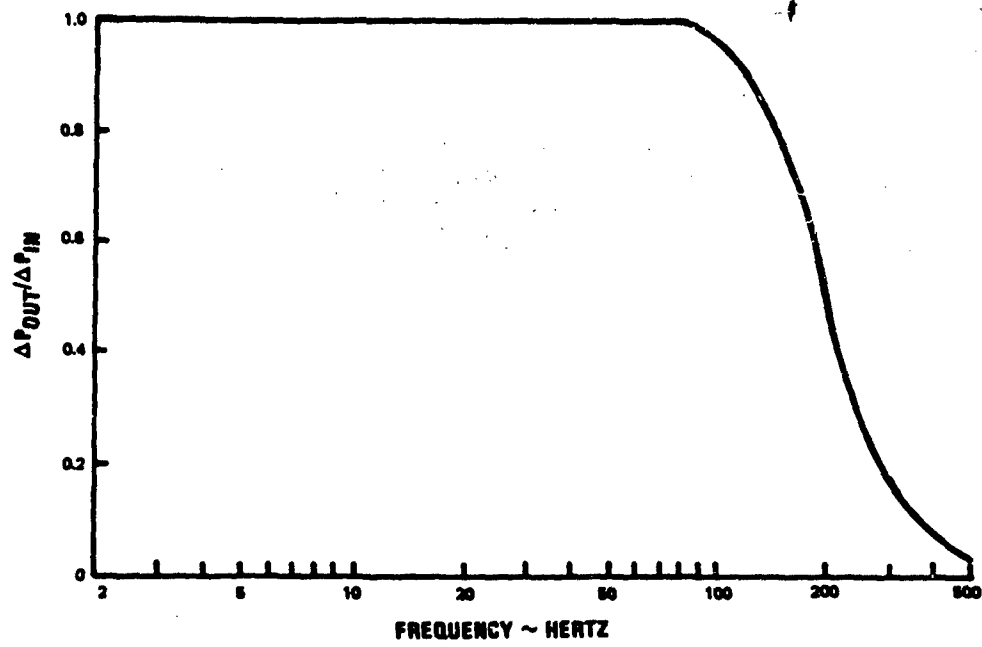


Figure 25 Gain Characteristic of 160 Hz Filter

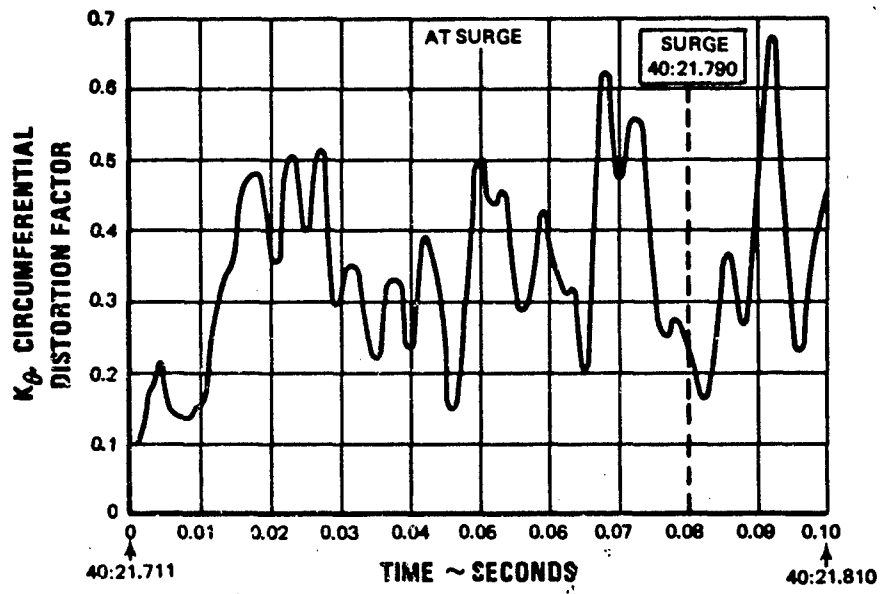


Figure 26 Instantaneous Distortion Factor, Record 281, 160 Hz Filter at Surge

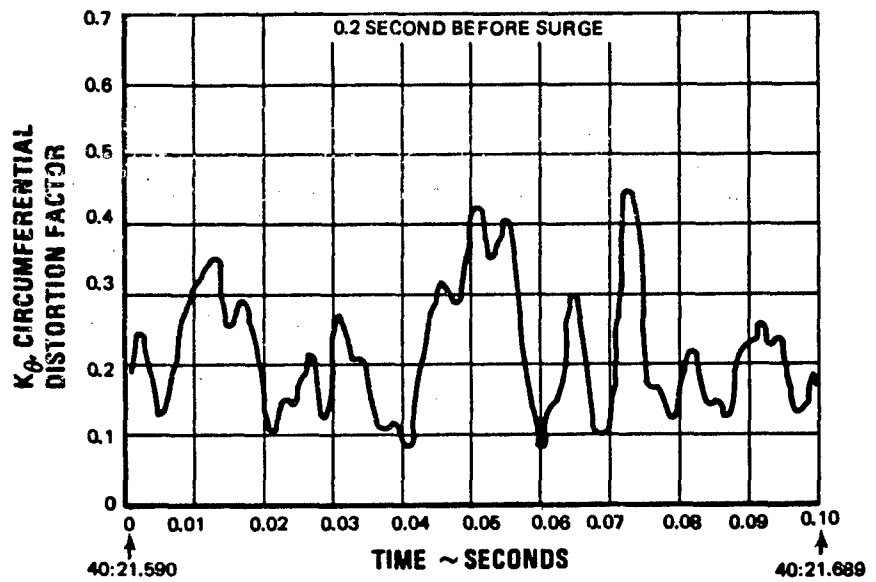


Figure 27 Instantaneous Distortion Factor, Record 281, 160 Hz Filter

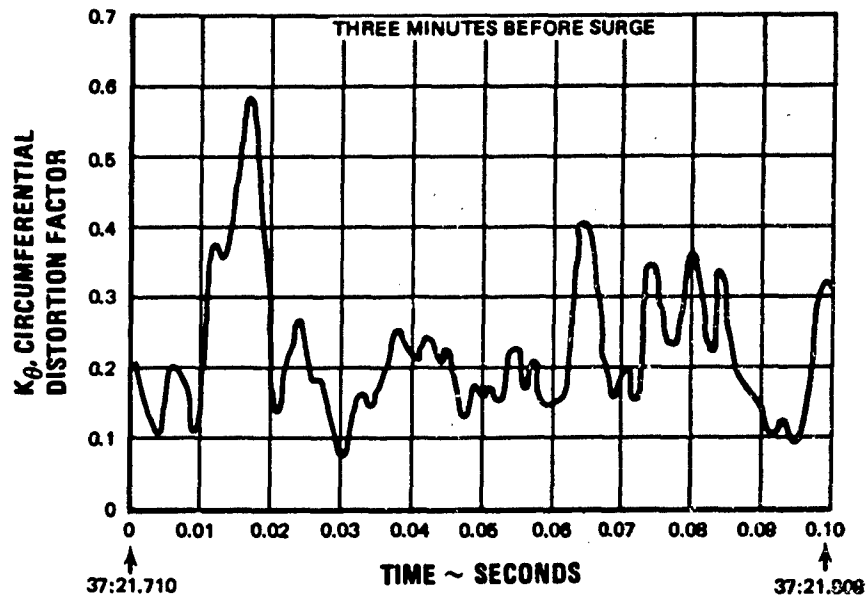


Figure 28 Instantaneous Distortion Factor, Record 281, 160 Hz Filter

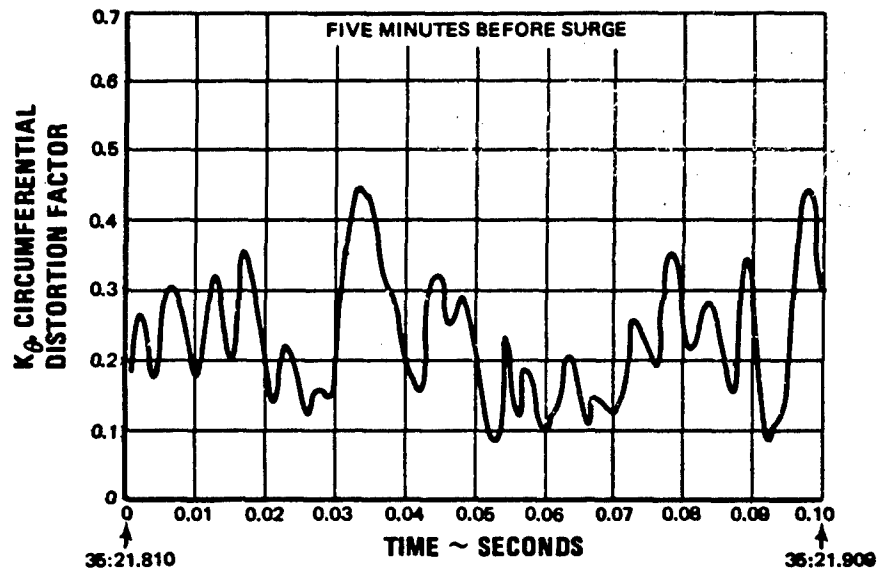


Figure 29 Instantaneous Distortion Factor, Record 281, 160 Hz Filter

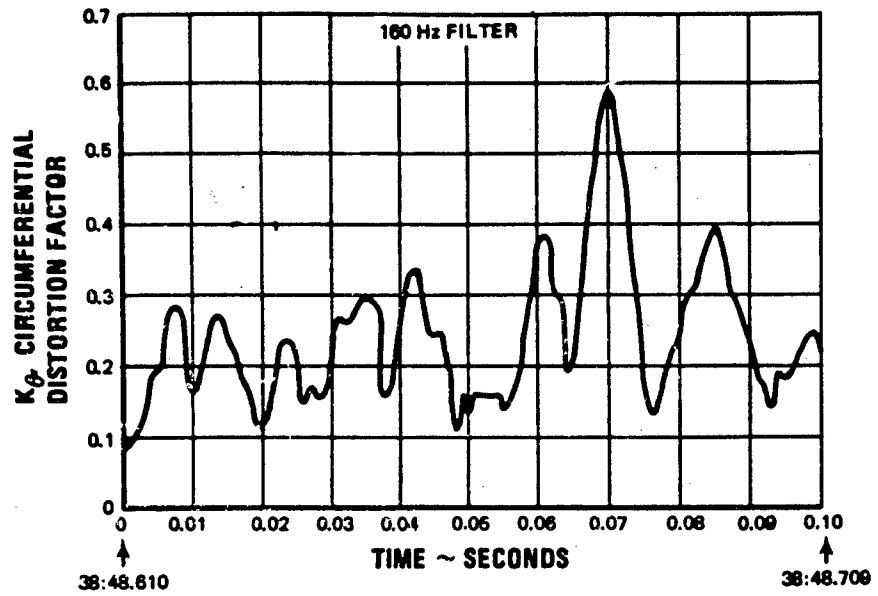


Figure 30 Instantaneous Distortion Factor, Record 1095 0.2 Second Before Surge

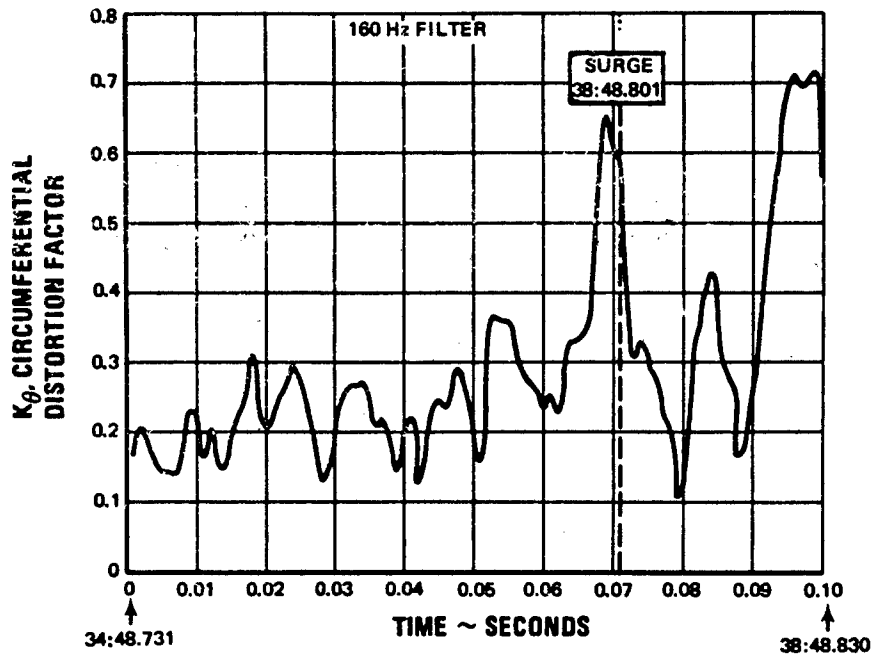


Figure 31 Instantaneous Distortion Factor, Record 1095 at Surge

Figures 32, 33 and 34 present distortion factor versus time for three records during which an exit valve was being closed. In Figures 32 and 33 the maximum K_θ again is immediately prior to surge. In Figure 34, K_θ is slightly higher (0.38) approximately 30 milliseconds prior to surge (0.36). Considering the possible rate of back pressure increase (estimated to reduce the distortion tolerance about 0.5 K_θ per second) and the accuracy to which the pressure can be measured, the fact that the compressor did not surge earlier is not inconsistent with the conclusion that spatial distortion was the surge inducing event.

Data presented in Figures 27 through 34 were obtained by filtering the recorded data, which was frequency limited at 1050 Hz, through a low pass filter having a break of 160 Hz. The results of such an analysis can be significantly different if different filters are used. Figures 35 through 38 present distortion factor versus time from one record using low pass filters with nominal break frequencies of 1050, 400, 160, and 45 Hz. The correct filter is one that produces a gain characteristic which reflects the sensitivity of the compressor to fluctuating pressure distortions at various frequencies. Since the results of the correlation of surge line loss indicate that compressor stability is controlled by turbulence in the frequency range from 0 to 80-100 Hz, a low pass filter (160 Hz) which passed this band but attenuated most of the signal above this range was selected.

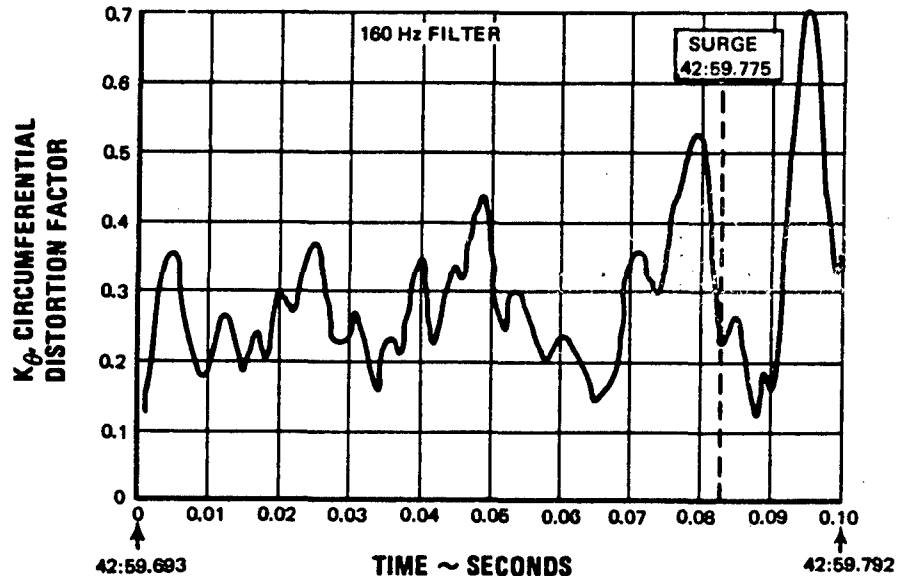


Figure 32 Instantaneous Distortion Factor, Record 1122 at Surge

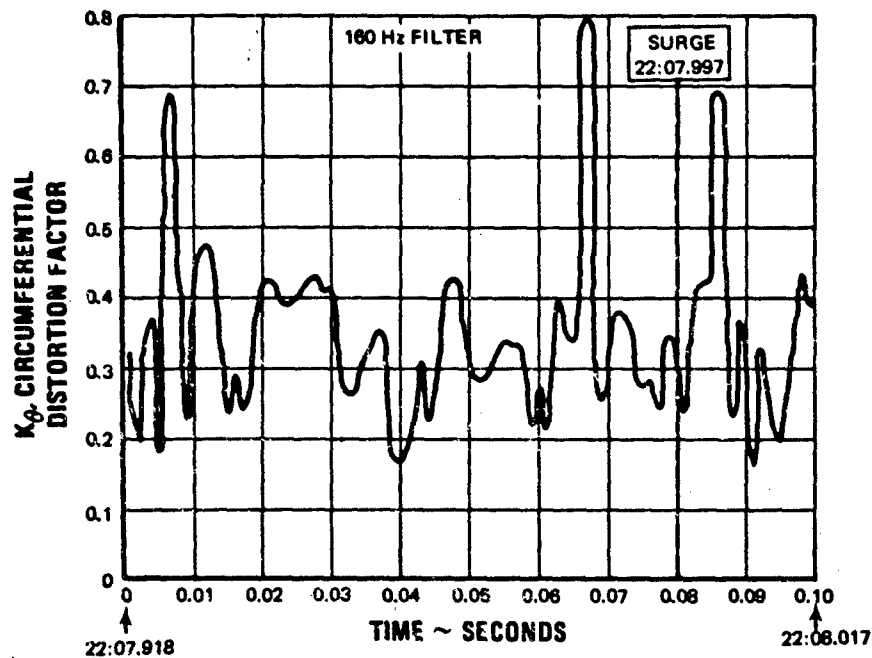


Figure 33 Instantaneous Distortion Factor, Record 1209 at Surge

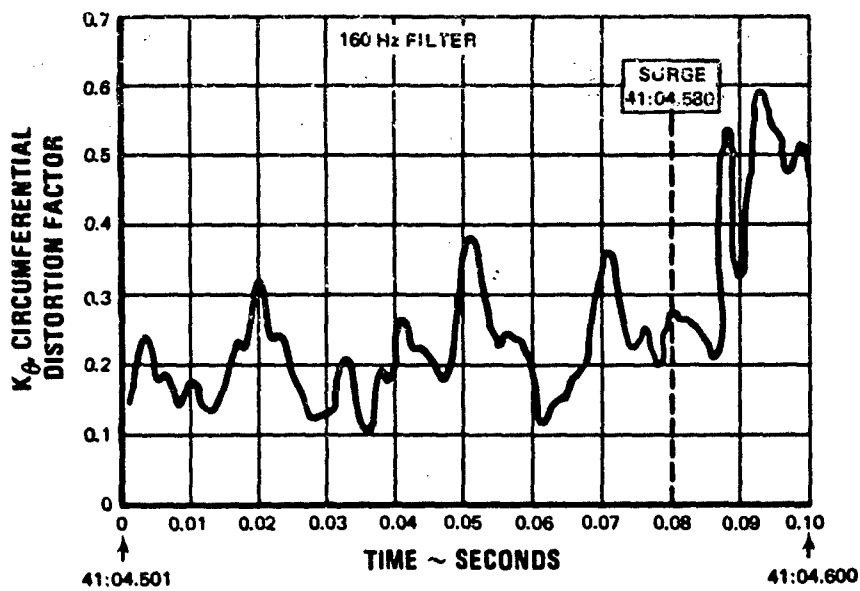


Figure 34 Instantaneous Distortion Factor, Record 1506 at Surge

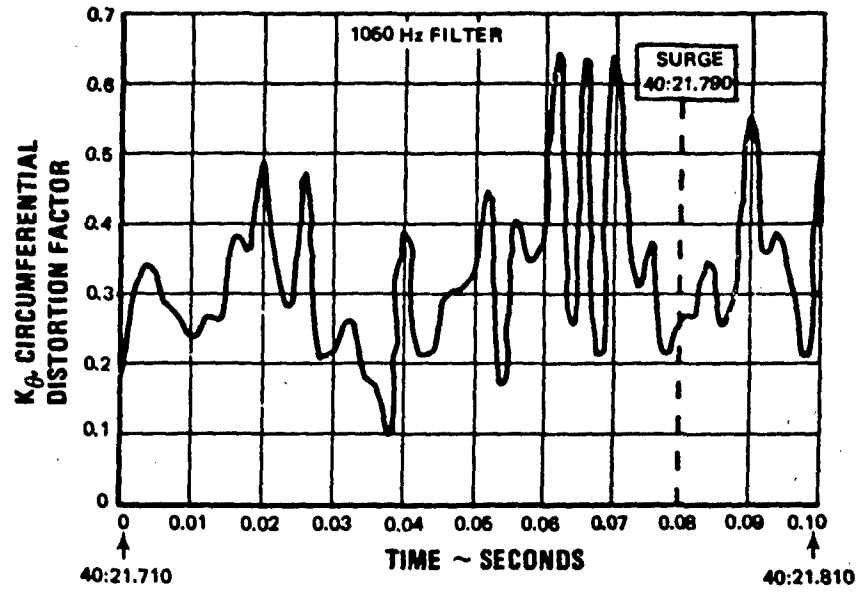


Figure 35 Instantaneous Distortion Factor, Record 281 at Surge

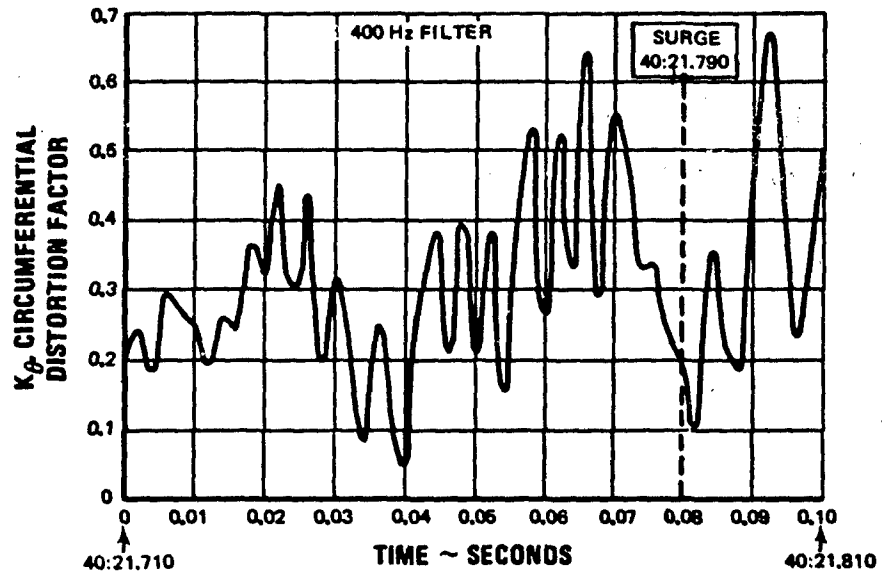


Figure 36 Instantaneous Distortion Factor, Record 281 at Surge

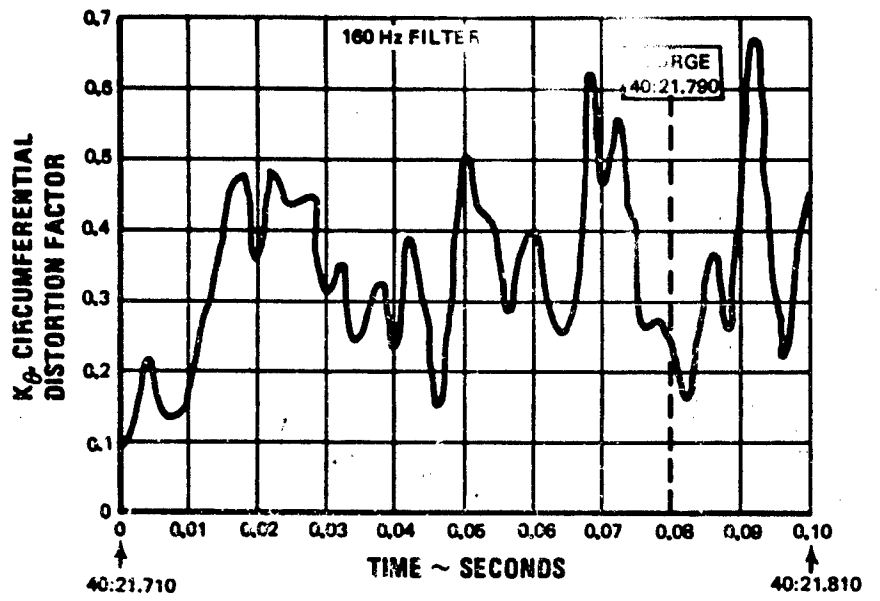


Figure 37 Instantaneous Distortion Factor, Record 281 at Surge

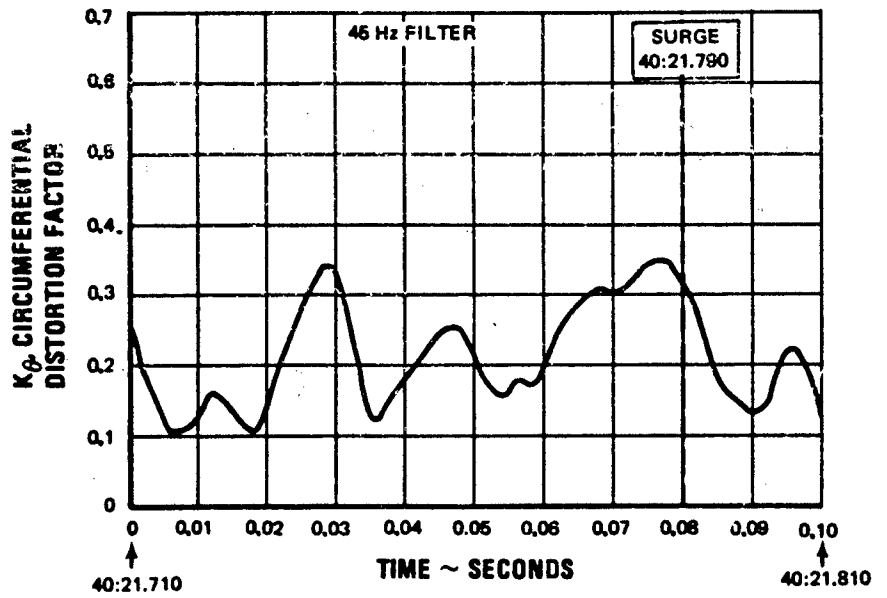


Figure 38 Instantaneous Distortion Factor, Record 281 at Surge

Analysis of the spatial distortion without a filter (maximum frequency 1050 Hz) revealed that there were very short duration distortions with higher magnitudes than the longer duration distortions which produced surge. An example of this is shown in Figure 39. The maximum K_{θ} (equal to 0.59) occurred approximately 30 milliseconds prior to surge and was significantly higher than that immediately preceding surge (0.53). However, utilizing the 160 Hz break frequency filter (Figure 40) the K_{θ} immediately preceding surge was in essentially every instance the largest value. This is further indication that compressor stability is most sensitive to the turbulence contained in the frequency range below 160 Hz.

The compressor setting at which surge occurred can be considered the compressor surge line with the spatial distortion produced by the turbulence. The turbulence induced surge line loss (measured at a constant flow and divided by the base surge pressure ratio) is plotted in Figure 41 against the magnitude of the spatial distortion factor as calculated using the 160 Hz low pass filter. The filled points represent the maximum K_{θ} immediately prior to surge and the open symbols are the highest K_{θ} which did not induce surge. The magnitude of the distortion which will cause the compressor to surge can be considered to lie between the open and filled symbols. This correlation is significant evidence that spatial distortion is the surge inducing event.

Four pairs of data points in Figure 41 indicate that steady-state distortion and turbulence were superimposed, which was accomplished either by introducing 180° distortion screens or by off-setting the centerbody of the generator. The highest point was obtained with the centerbody off-set and the steady-state distortion approximately 50 percent of the instantaneous surge-inducing distortion. For the other three similar points, the steady-state distortion was approximately 30 percent of the surge-inducing distortion. Two data points were obtained with the grill of 1/4-inch rods, and one was obtained with the 3-inch pipes in the inlet. The remaining eight points were obtained with turbulence as produced by the unmodified turbulence generator. The zero loss in surge-line intercept indicates that an instantaneous K_{θ} of approximately 0.16 would be measured for the baseline testing with a bell-mouth. Data obtained during baseline testing at 800 rpm indicate that this level is probable. Unfortunately, the high-frequency data, recorded on magnetic tape for the 9500 rpm baseline, was accidentally degaussed before this analysis was accomplished.

The results of these studies clearly indicate that instantaneous spatial distortion, with the attendant frequency considerations discussed previously, is the surge-inducing event. There is a phenomenon in the inlet which induces surge, as indicated by the occurrence of surges after many minutes of stable operation with constant operating conditions and constant statistical properties in the inlet flow field. The phenomenon is spatial distortion, evidenced by relatively large values of spatial distortion immediately preceding every surge, regardless of the manner in which the surge was approached or the amplitude/frequency spectrum of the turbulence. When the data were filtered with the 160 Hz break-frequency filter, it was evident that the magnitude of the spatial distortion was greater immediately preceding surge than at any prior time. The only exceptions occurred when the back-pressure of the compressor was being rapidly increased and consequently the magnitude of the distortion which would induce surge was being rapidly decreased. The greatest evidence, however, that instantaneous spatial distortion is the surge-inducing event is the correlation of surge-line loss with the instantaneous distortion factor. All the data correlate well for all inlet conditions, including different amplitude/frequency spectra, different RMS levels, and various amounts of steady-state distortion.

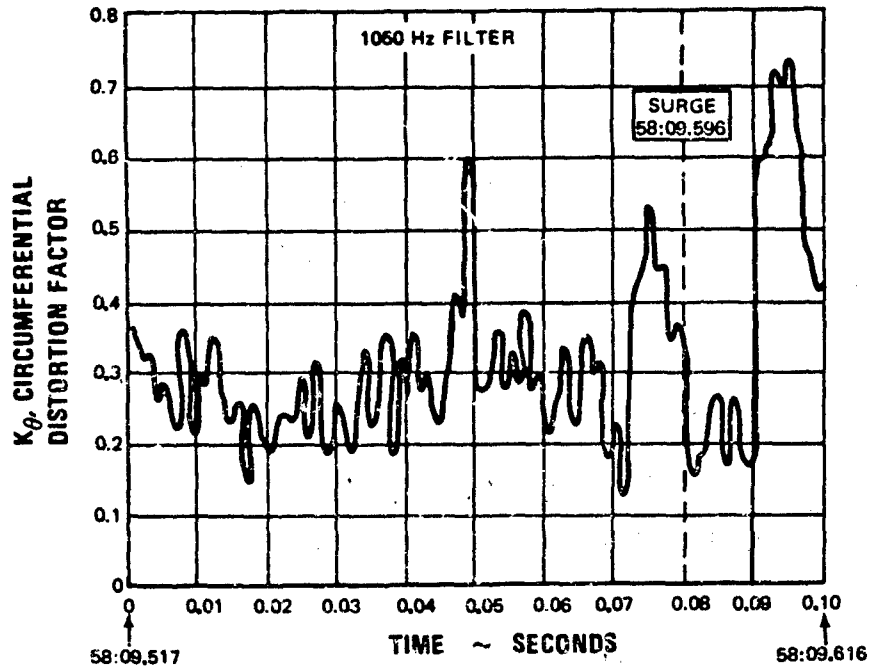


Figure 39 Instantaneous Distortion Factor, Record 1105 at Surge

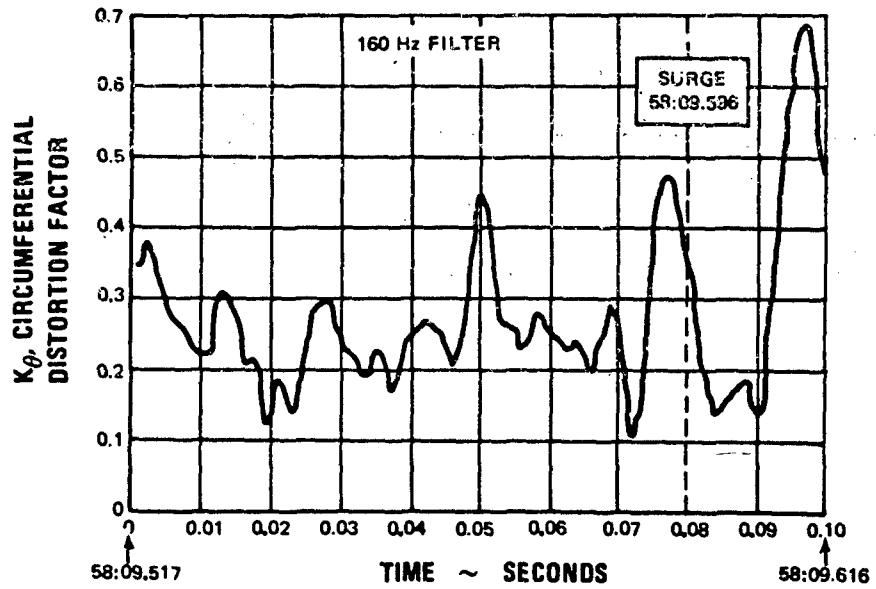


Figure 40 Instantaneous Distortion Factor, Record 1105 at Surge

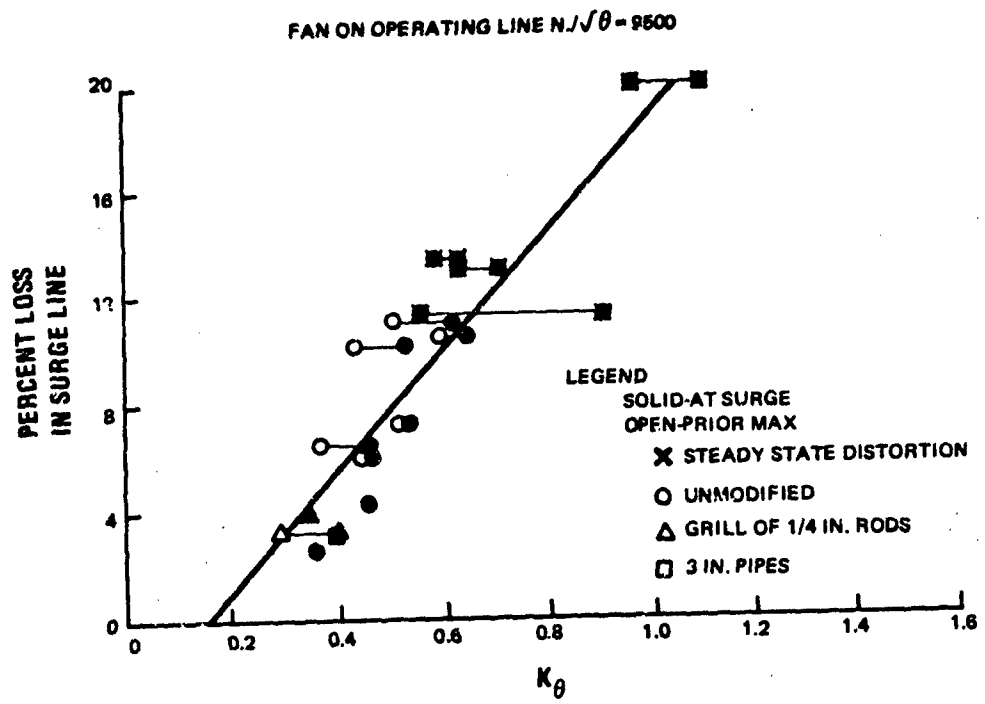


Figure 41 Surge Line Loss versus Instantaneous Spatial Distortion

APPENDIX A

DEFINITION AND CALCULATION OF CIRCUMFERENTIAL DISTORTION FACTOR (K_θ)

A typical turbofan engine inlet which has been instrumented to provide distortion measurements as shown in Figure 42. An understanding of this figure is required to define the distortion factor. Eight radial instrumentation rakes are placed within the annular area. Each of these rakes contains five pressure probes at the center of five equal areas. Pressure variations can therefore be analyzed circumferentially as a function of the angle (θ). For instance, the dashed line in Figure 42 would represent the circumferential variation of the third ring as it is formed by connecting the third probe on each rake.

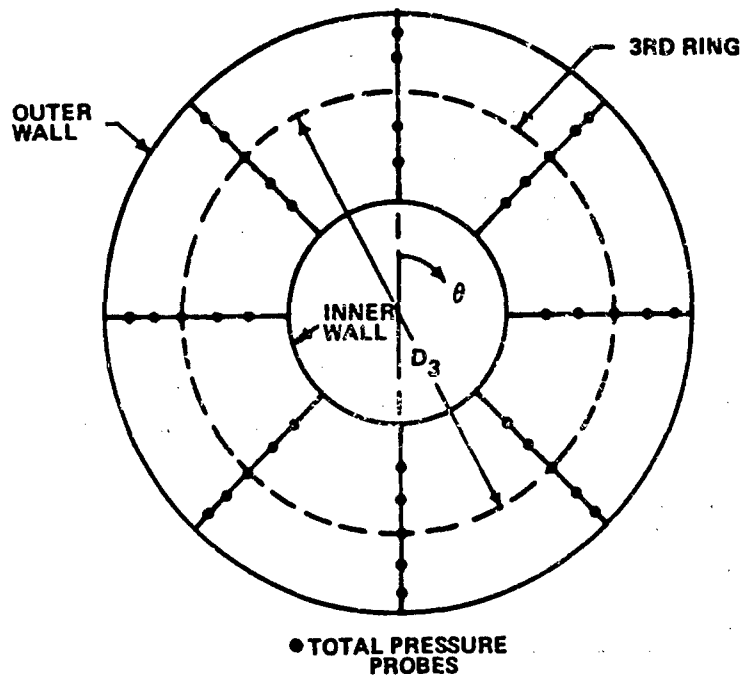


Figure 42 Turbofan Engine Inlet Schematic Instrumented for Distortion Measurements

The formula for the circumferential distortion factor is

$$K_{\theta} = \frac{\sum_{\text{Ring} = 1}^J \left[\left(\frac{A_N}{N^2} \right)_{\text{max}} \right]_{\text{Ring}} \frac{P_{T2}}{Q_{av}} \frac{1}{D_{\text{Ring}}}}{\sum_{\text{Ring} = 1}^J \frac{1}{D_{\text{Ring}}}} \quad (\text{Eq. 1})$$

where

J = number of total rings which is equal to number of probes per rake.

D = diameter of the ring or radial probe.

Q_{av} = average inlet absolute velocity head at the face of the engine ($1/2\rho Cx^2$).

To define the term $\left(\frac{A_N}{N^2} \right)_{\text{max}}$, more detailed explanation is required.

Figure 43 gives a simple example of a pure 180-degree circumferential distortion in which the circumferential variation of local pressure (P_{T2}) to the average total pressure (\bar{P}_{T2}) is shown. The equation for this curve can be written in terms of Fourier series. In general,

$$\frac{P_{T2}}{\bar{P}_{T2}} = 1 + \sum_{N=1}^{\infty} a_N \cos N\theta + a_2 \cos 2\theta + \dots a_N \cos N\theta + b_1 \sin \theta + b_2 \sin 2\theta + \dots b_N \sin N\theta \quad (\text{Eq. 2})$$

where

$$a_N = \frac{1}{\pi} \int_{-\pi}^{\pi} \frac{P_{T2}}{\bar{P}_{T2}}(\theta) \cos N\theta \, d\theta$$

$$b_N = \frac{1}{\pi} \int_{-\pi}^{\pi} \frac{P_{T2}}{\bar{P}_{T2}}(\theta) \sin N\theta \, d\theta \quad (\text{Eq. 3})$$

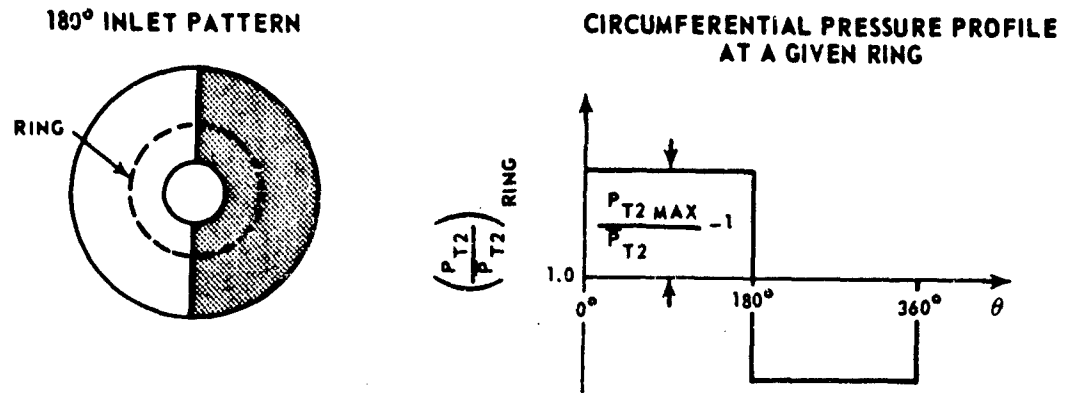


Figure 43 Pure 180 Degree Circumferential Distortion Schematic

If we define $A_N = \sqrt{a_N^2 + b_N^2}$ then the series can be written as:

$$\frac{P_{T2}}{\bar{P}_{T2}} = 1 + \sum_{N=1}^{\infty} A_N \sin(N\theta + \phi_N) \quad (\text{Eq. 4})$$

For this particular example, the series becomes after integration and simplification:

$$\begin{aligned} \frac{P_{T2}}{\bar{P}_{T2}} = 1 + \frac{4}{\pi} \left[\frac{P_{T2 \max}}{\bar{P}_{T2}} - 1 \right] \sin \theta + \frac{4}{3\pi} \left[\frac{P_{T2 \max}}{\bar{P}_{T2}} - 1 \right] \sin 3\theta + \\ \frac{4}{5\pi} \left[\frac{P_{T2 \max}}{\bar{P}_{T2}} - 1 \right] \sin 5\theta + \dots \end{aligned} \quad (\text{Eq. 5})$$

We now can look for the maximum $\frac{A_N}{N^2}$ term. Listing these terms they are:

$$\begin{aligned} \text{for } N=1 \quad \frac{A_1}{1^2} &= \frac{4}{\pi(1)^2} \left[\frac{P_{T2 \max}}{\bar{P}_{T2}} - 1 \right] & N=4 \quad \frac{A_4}{4^2} &= 0 \\ N=2 \quad \frac{A_2}{2^2} &= 0 & N=5 \quad \frac{A_5}{5^2} &= \frac{4}{5\pi(5)^2} \left[\frac{P_{T2 \max}}{\bar{P}_{T2}} - 1 \right] \\ N=3 \quad \frac{A_3}{3^2} &= \frac{4}{3\pi(3)^2} \left[\frac{P_{T2 \max}}{\bar{P}_{T2}} - 1 \right] \end{aligned} \quad (\text{Eq. 6})$$

For this case and for most cases, the first harmonic has the greatest influence. For this particular example then

$$\left(\frac{A_N}{N^2}\right)_{\max} = \frac{4}{\pi} \left[\frac{P_{T2 \max}}{P_{T2}} - 1 \right]$$

(Eq. 7)

which is then used to evaluate the distortion factor.

STALL AND DISTORTION INVESTIGATION OF A
YTF30-P-1 TURBOFAN ENGINE

John H. Povolny

Lewis Research Center
National Aeronautics and Space Administration
Cleveland, Ohio

Abstract

Preliminary results on a YTF30-P-1 engine are presented from a program that was instituted at the NASA-Lewis Research Center to evaluate and understand the effect of both steady state and dynamic distortions on the performance and stall characteristics of advanced turbine engines. The high response compressor inter-stage instrumentation and specialized testing techniques that were required for the conduct of this program are described herein, and some of the data so obtained are presented. The preliminary results indicate that the instrumentation and specialized techniques do provide invaluable information that will help immeasurably in formulating engine dynamic simulations.

I. Introduction

Operational limits of propulsion systems may restrict the capabilities of subsonic and supersonic aircraft. One such limit of gas turbine propulsion systems is compressor stall or surge. The performance and operating limits of the engine, especially the compressor, are influenced by the flow conditions at the compressor inlet. This leads to the necessity of adequately matching the inlet and engine so that the capabilities of the aircraft are not compromised by the flow condition supplied by the inlet and/or the susceptibility of the engine compressor to the inlet flow condition.

A program to evaluate and understand the influence of both steady state and dynamic inlet disturbances on the operating limits of advanced turbine engines has been initiated at the NASA-Lewis Research Center. The objectives of this program are presented in the first figure. The first engine to be investigated in this program was a YTF-30 P-1 afterburning turbofan engine which was selected as being typical of those used or proposed for supersonic military aircraft. To accomplish the desired evaluation and understanding it was necessary to develop a high response measurement capability for pressures within as well as at the inlet and exit of the compressors. Such capability is required in order to determine the location of the occurrence of stall and its progression through the compressor. It was also necessary to develop and evaluate some specialized testing techniques that would either provide the desired environment or would initiate the compressor stall in a desired location. In the interest of brevity, this paper will present a synopsis of this work to date, while hitting some of the high spots. An NASA report (ref. 1) has been issued on the first phase of this program; it covers a compressor stall evaluation of the YTF30-P-1 engine with no inlet distortions. A

second report covering the effects of steady state distortions on the performance of this engine is currently underway, and the data for a report on the effects of dynamic distortions is currently being analyzed. Some typical data from each phase of the program will be presented herein.

II. Engine Instrumentation

High response compressor pressure instrumentation was installed at the fan inlet (sta. 2.0), first stage stator (sta. 2.1) fan tip outlet (sta. 2.3f), fan hub outlet or low compressor inlet (sta. 2.3), sixth stage stator (sta. 2.6) low compressor outlet (ninth stage) or high compressor inlet (sta. 3.0), twelfth stage stator (sta. 3.12), and high compressor outlet (sixteenth stage and sta. 4.0). There were also high response pressure measurements in the combustor, fan duct and afterburner, as well as conventional steady state instrumentation throughout the engine. Capability was provided in the fan inlet rakes for a total of 40 high response total pressure measurements but this total was utilized only where required because of data acquisition limitations. All of the other compressor high response instrumentation consisted of two pairs of total and static pressures located approximately 180° apart installed at each of the stations indicated above. The response of these probes was linear within $\pm 5\%$ out to about 500 cps. A sketch of a typical interstage probe is shown in figure 2. Miniature transducers, 1/4 inch in diameter, were used and were located as close to the probe inlet as possible (≤ 2 inches). Inasmuch as the transducers were limited to an operating temperature of 170°F (the gas temperature was higher than this at many of the stations) and their calibrations were sensitive to temperature, it was decided to water cool all of them so that they would be at a low uniform temperature. The transducers were thus mounted in a water cooled jacket, the individual assemblies of which could be removed for repair without having to remove the rake or probe from the engine. In spite of the aforementioned precautions it was determined from preliminary calibration of these transducers that zero and sensitivity shifts occurred as a function of time. Therefore a system was devised to calibrate these transducers in their operating environment inside the engine just prior to recording data. Details of this calibration system and the instrumentation are presented in the reference 1. The high response data were recorded simultaneously on a high speed digitizer recorder and on magnetic tape. Inasmuch as the digitizer had a sampling rate of only 60 samples per second, the digitized information was used just prior to stall; the actual stall point and sequence of events during stall were obtained from the magnetic tape analog traces.

III. Engine Installation

The engine installation in the altitude chamber was a conventional direct connect type. The altitude chamber included a forward bulkhead which separated the inlet plenum from the test chamber. Conditioned air was supplied to the plenum at the desired pressure and temperature. The chamber aft of the bulkhead was evacuated to the desired altitude pressure. The conditioned air flowed from the plenum through a bellmouth and inlet duct to the engine. A high response bypass valve located in the bulkhead allowed some air to bypass the engine and was automatically controlled to maintain a constant inlet pressure and ram pressure ratio across the engine during both steady state and transient engine operation. The exhaust from the engine was captured by a collector extending through a rear bulkhead and discharged into the facility exhaust system wherein the exhaust pressure was maintained constant by automatically controlled valves.

IV. General Test Procedure

The investigation was conducted at a Reynolds number index of 0.5 with an inlet temperature of 60°F (16°C). This resulted in an inlet total pressure of 7.5 psia (5.2 N/cm²). Ram pressure ratio across the engine was held constant at 3:1 to assume a choked exhaust nozzle for all operating conditions. These test conditions were selected for several reasons. First, this Reynolds number index corresponds to a range of flight conditions representative of the flight regime of a supersonic aircraft, and second, the loss in performance due to Reynolds number effect was not expected to be significant at this level. Also, the pressure loadings on the instrumented compressor casing would be lower than at sea level pressure especially during stall and compressor surge.

In the initial stages of the program when operating the engine without inlet distortions two techniques were employed to induce stall in the three compressor units (fan, low compressor, and high compressor). The low pressure compressor operating line was raised toward the stall limit by increasing the exhaust nozzle area above rated; the engine was then very slowly accelerated (10 to 20 rpm per second) until the engine either stalled or reached one of its operating limits. In a similar manner the exhaust nozzle was closed to raise the operating lines of the high compressor and fan unit, and again a slow acceleration was made until stall occurred in one of these units or an engine operational limit was reached. The slow acceleration was used to keep the engine close to the steady state operating line for the particular exhaust nozzle area being employed. Data from the transient instrumentation were recorded during these slow accelerations until sometime after the engine had stalled. The second method of inducing stall (in the high compressor) was to inject an increment of fuel into the engine fuel system, which increment would cause a step increase in pressure at the high compressor exit. The size of the fuel step was then successively increased until stall was encountered in the high compressor. Stall data were obtained in the aforementioned manners over a range of rotor corrected speeds from idle to maximum. In addition to the foregoing there were some high response stall detection, overspeed and overtemperature systems that were employed to protect the engine during stall; these systems are also described in reference 1. There were also some newly developed techniques employed for stalling the engine and creating distortions which will be described in a subsequent section.

V. Clean Inlet Stall Data

Analysis of the transient data to obtain stall pressure ratios and rotor corrected speeds for each stage group and for each compressor component (fan, low, and high) was done in two steps: (1) identification of the stage group and component that stalled first; and (2) determination of the pressure ratio and corrected speed for that group and component immediately prior to stall. Identification of the unit stalling first was made from the analog total pressure time histories. A drop in the discharge and a corresponding rise in the inlet pressure of the group of stages or component identified it as stalling first. Pressures falling downstream and rising upstream of the stage group also aided in the identification. The pressure ratio and corrected speed of the stalling unit were taken from the computed output or the high speed digital system when stalls were

obtained with slow accelerations. For the fuel step transient data, the rate change of pressure was too great for the digital system and the engineering data were computed from the analog traces.

In some cases a method of analysis was used (ref. 2) for determining the stall pressure ratio of stages ahead of the stage that stalls initially. This method is based on the fact that as the first stage stalls its flow is reduced so rapidly that the pressure at the exit of the preceding stage will rise before the inlet pressure of that stage is affected. Thus, this stage in turn stalls and the process is repeated until the stall has progressed completely through the compressor to the inlet. The fuel step technique usually initiates stalls in the downstream stages of the high compressor, and thus with this technique the stall pressure ratio of stage group (or stage) can be determined from a single transient.

Typical time histories of pressures in the compressors for three types of observed stalls are presented in figures 3, 4, and 5. Figure 3 shows a slow acceleration to a low compressor stall with a large exhaust nozzle area (186% of rated); figure 4 shows a slow acceleration to a high compressor stall with a small exhaust nozzle area (78% of rated); and figure 5 shows a typical fan rotating stall pattern which often followed a hard stall in either of the other compressors. The vertical lines on each curve are for time correlation and each interval represents 0.01 sec. Figure 3 (low compressor stall) shows a rise in $P_{T,2.6}$ (sixth stage) and drop off in P_3 (ninth stage) occurring shortly before the abrupt changes in the other pressures indicating the initiation of stall in the group consisting of stages 6 through 9. The progression of stall forward from station 2.6 (sixth stage) to 2.3 (third stage), 2.1 (first stage), and finally 2.0 (inlet face of engine) is also shown. Figure 4 (high compressor stall) shows a simultaneous rise in $P_{T,3.12}$ (twelfth stage) and a drop in $P_{T,4}$ (sixteenth stage or compressor exit) indicating that the stall originated between those locations. The progression of the stall forward through the compressors can be seen in this case, also. Figure 5 (fan rotating stall) indicates that a single zone stall pattern rotated at 43 percent of low rotor (fan) speed was occurring. The 180° phase shift indicated by the two $P_{T,2.3}$ traces which were approximately 180° apart, confirms the one zone pattern. The pressure rise at station 2.1 (stage one) and the simultaneous drop off at station 2.3 (third stage) indicate that the stall was originating somewhere between the first and third stages. The drop off in pressure in all of the succeeding stages indicates that its effect was felt all the way through the low and high compressors.

The effect of the rotating stall on engine operation is presented in figure 6 which shows that the engine could not be accelerated above a high rotor speed of about 11,800 rpm while in rotating stall. This was due to a shift in the operating line of the engine which intersected the fuel control acceleration schedule at about 10,800 rpm thus preventing any further acceleration. In the interest of brevity none of the compressor and fan maps (with stall lines) that were obtained in this program will be presented (they are available in ref. 1). Suffice it to say, however, that in this program, as in other similar programs, there were determined to be discrepancies between compressor rig data and compressor data obtained on the engine. It appears that at least a part of this discrepancy

is a result of the different environment that the compressor is exposed to on the engine as compared to the rig and this difference may be classified as a distortion effect. For example, the low compressor discharge velocity, temperature, and pressure profiles which are fed into the high compressor may be completely different than those in the rig test and could have a very significant effect on its performance.

VI. Special Techniques and Results

Four special testing techniques that have been or are about to be employed in this program are indicated in figure 7. The pressure jet distortion system has been employed on the TF-30 engine to produce both steady state distortions and fluctuating pressures in the inlet duct ahead of the engine. The engine effects obtained when producing steady state distortions with the jets were practically identical to those obtained when using screens but were much easier to run off. Some of the preliminary results obtained when using the jets to produce fluctuating pressures will be discussed in succeeding paragraphs. The temperature distortion device has not been used to date but it has been built and is about to be checked out. It consists of a large (5½ ft. diameter) hydrogen burner mounted in front of the engine inlet bellmouth and has the capability of producing steady state circumferential and radial distortions, or providing temperature ramps as high as 5000°F per second. The choked inlet duct also has not been run on the TF-30 engine but will be shortly. It is similar to the device used by Kimzey (ref. 3) and has the possibility of simulating the environment provided by an aircraft inlet. This possibility is one of the items that will be checked out when the choked inlet is employed. The fourth technique involves reversing the flow in the compressor discharge ports and hence the name "compressor discharge in-flow bleed." It, of course, requires an external source of high pressure air but has the advantage of being able to "sneak up" on the stall limit of the high compressor at high corrected speeds without over-temperaturing the turbine.

A photograph showing the arrangement of the pressure jet system jet nozzles in the engine inlet duct is presented in figure 8, and a photo showing an external view of the engine installation with the pressure jet system installed is presented in figure 9. In this system secondary jets of air are injected counter to the primary air flow in the engine inlet duct forward of the compressor face. Through control of the secondary-air distribution and flow rate, variable amplitude steady state or dynamic pressure distortions or uniform dynamic pressure oscillations can be produced. As can be seen in figure 8 the secondary jet nozzles are uniformly distributed circumferentially and radially in a pattern that repeats every 60 degrees of circumferential extent. Six high response servo-operated valves, designed especially for this application, are employed to control secondary air flow to each 60-degree from each control valve to each jet nozzle in the segment with all lines having equal cross-sectional area and length. Momentum interchange between the secondary and primary streams occurring upstream of the jet nozzle array is primarily responsible for the total pressure loss that is generated. The amount of total pressure loss incurred is controlled by varying the secondary air flow. If it is varied in a pulsating manner then a pulsating pressure is generated at the engine face.

The performance of the pressure jet distortion system when operated in the pulsating mode (all jets operating) is summarized in figure 10 wherein the ratio of engine inlet total pressure amplitude to engine inlet steady state (average) pressure is plotted against the frequency of the pressure oscillation. It can be seen that the amplitude is relatively constant at a value slightly greater than 0.3 out to a frequency of about 20 HZ at which point it rapidly falls off to a value of slightly less than 0.10. It would be desirable to maintain the amplitude at the higher value out to as high a frequency as possible and some work is currently being performed toward that end. Preliminary results indicate that it should be possible to achieve an amplitude of about 0.20 at a frequency of 100 HZ. A plot of some of the individual pressure measurements at the engine inlet face as a function of time is presented in figure 11 for a pulsation frequency of 10 HZ. It can be seen that all of the individual pressure measurements are very well in phase and close together in amplitude and that a reasonable approximation to a sine wave was obtained.

Some of the preliminary engine performance data obtained when pulsating the inlet at a frequency of 10 HZ are presented in figures 12 and 13. Figure 12 presents the variation of a number of compressor interstage pressures as a function of time for an average steady state inlet total pressure of 7.4 psia and 87 percent corrected speed. The significant items to note on this curve are that the pressures measured at the high compressor discharge (sta. 4) and fan tip discharge (sta. 2.3F) appear to be more attenuated and seem to have more of a phase shift with respect to the preceding stage measurement than any of the other measurements. It is interesting to note that in each of these two cases there is a relatively large volume behind the station in question (combustor volume behind sta. 4 and fan duct volume behind sta. 2.3F). If the pressure ratios across the various stage groups are computed from the data in figure 12 and plotted in a similar manner against time the resulting curves presented in figure 13 are obtained. Here again the significant pressure ratio curves are for the stage groups immediately adjacent to a large volume (stage group 2.0 to 2.3F and stage group 3.12 to 4.0). It is to be noted that not only do these two stage groups go through a much greater pressure ratio variation but their swing above their steady state value of pressure (indicated by the short horizontal line on the right and measured just prior to the pulsation) is significantly greater than below it. The data presented in figures 12 and 13 were obtained at an amplitude just slightly less than that required to stall the compressor and is considered to be typical of conditions just prior to stall. Examination of the analog traces at the stall point indicated that the stall originated in the back end (stages 12-16) of the high compressor even though the pressure ratio excursion across the fan tip (stages 1-3F) was greater. Apparently the fan has more stall margin built into it than the high compressor.

If the ratio of peak pressure ratio to steady state pressure ratio for the various stage groups is plotted against frequency for some of the data obtained to date the resulting curves presented in figure 14 are obtained. Here again, the interesting curves are for the 2-2.3F and 3.12-4.0 stage groups. The data represented by the solid lines were obtained for an inlet amplitude of about 0.28

and are representative of performance just prior to stall. The data represented by the dashed curve are extrapolations of trends obtained at a lower inlet amplitude and are probably representative of the performance that might be obtained if the engine did not stall at the higher amplitude. (The higher amplitudes weren't obtainable at the higher frequencies.) In addition to analyses, similar to those described, that are currently under way the results of this investigation (in the form of generalized stage group performance) are also being utilized in formulating an engine dynamic simulation.

VII. Concluding Remarks

Preliminary results of a program to investigate the stall and distortion characteristics of a turbofan engine indicate that:

(1) Data from detailed high response compressor interstage instrumentation can provide an insight into the stall mechanism, its origin and progression through the compressor system, and the compressor interaction with other engine components.

(2) It is possible to evaluate in an engine the static and dynamic performance of each compressor component, stage group or even individual stages by the employment of specialized techniques, described herein.

(3) Results obtained on a component in an engine are not necessarily the same as those obtained in a component rig because of differences in inlet environment and component interactions.

(4) Information obtained from the type of program described herein will be invaluable in formulating and verifying the dynamic simulation of a turbofan engine both with and without inlet air distortions.

References

1. Braithwaite, Willis M., and Vollmar, William R., "Performance and Stall Limits of a YTF30-P-1 Turbofan Engine with Uniform Inlet Flow," TM X-1803, NASA, Cleveland, Ohio.
2. Lubick, Robert J., and Wallner, Lewis E., "Stall Prediction in Gas Turbine Engines." *Journal of Basic Engineering*, Trans. of A.S.M.E., Vol. 81, No. 3, September 1959, pp 401-408.
3. Kimzey, W. F., "An Investigation of the Effects of Shock-Induced Turbulent Inflow on a YJ93-GE-3 Turbojet Engine." A.E.D.C. - TR-66-198, November 1966.

FIGURE 1

CURRENT FULL SCALE ENGINE PROGRAM OBJECTIVES

1. EVALUATE STALL AND DISTORTION CAPABILITIES OF A HIGH MACH NO. AFTERBURNING TURBOFAN OVER THE RANGE OF FLIGHT MACH NO.
2. PINPOINT THE ORIGIN OF THE STALLS AND DEFINE THEIR PROGRESSION THROUGH THE MACHINE
3. DEFINE THE DYNAMIC INTERACTIONS OF THE VARIOUS COMPONENTS SUCH AS THE COMPRESSORS, AFTERBURNER, COMBUSTOR, AND INLET
4. FORMULATE AN ENGINE SIMULATION USING THE INFORMATION FROM ITEMS 1, 2, AND 3 THAT WILL ACCURATELY PREDICT ENGINE PERFORMANCE FOR ALL FLIGHT ENVIRONMENTAL CONDITIONS THAT COULD BE ENCOUNTERED
5. WORK OUT SOLUTIONS TO BASIC ENGINE PROBLEMS THROUGH UNDERSTANDING RATHER THAN TRIAL AND ERROR

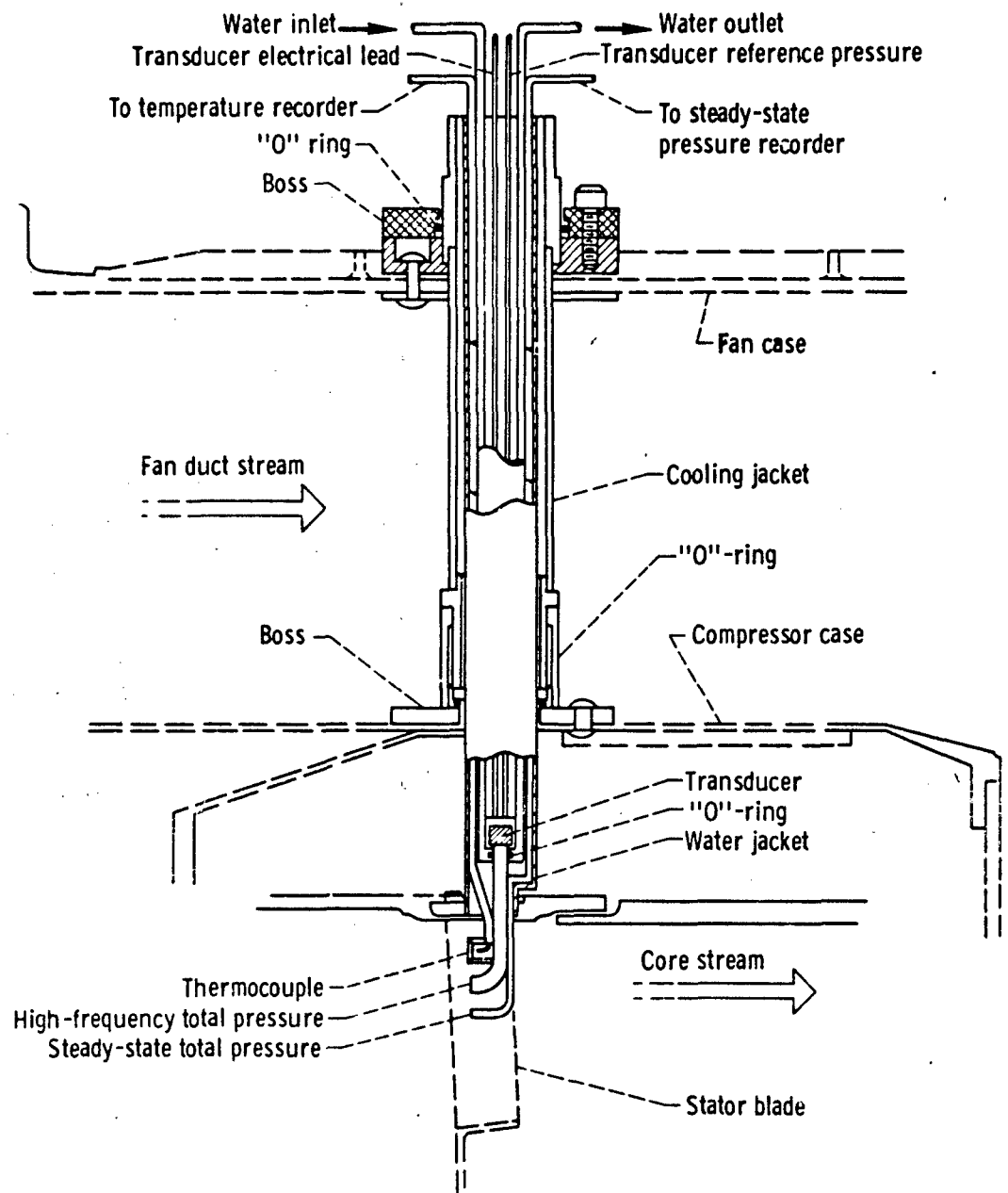
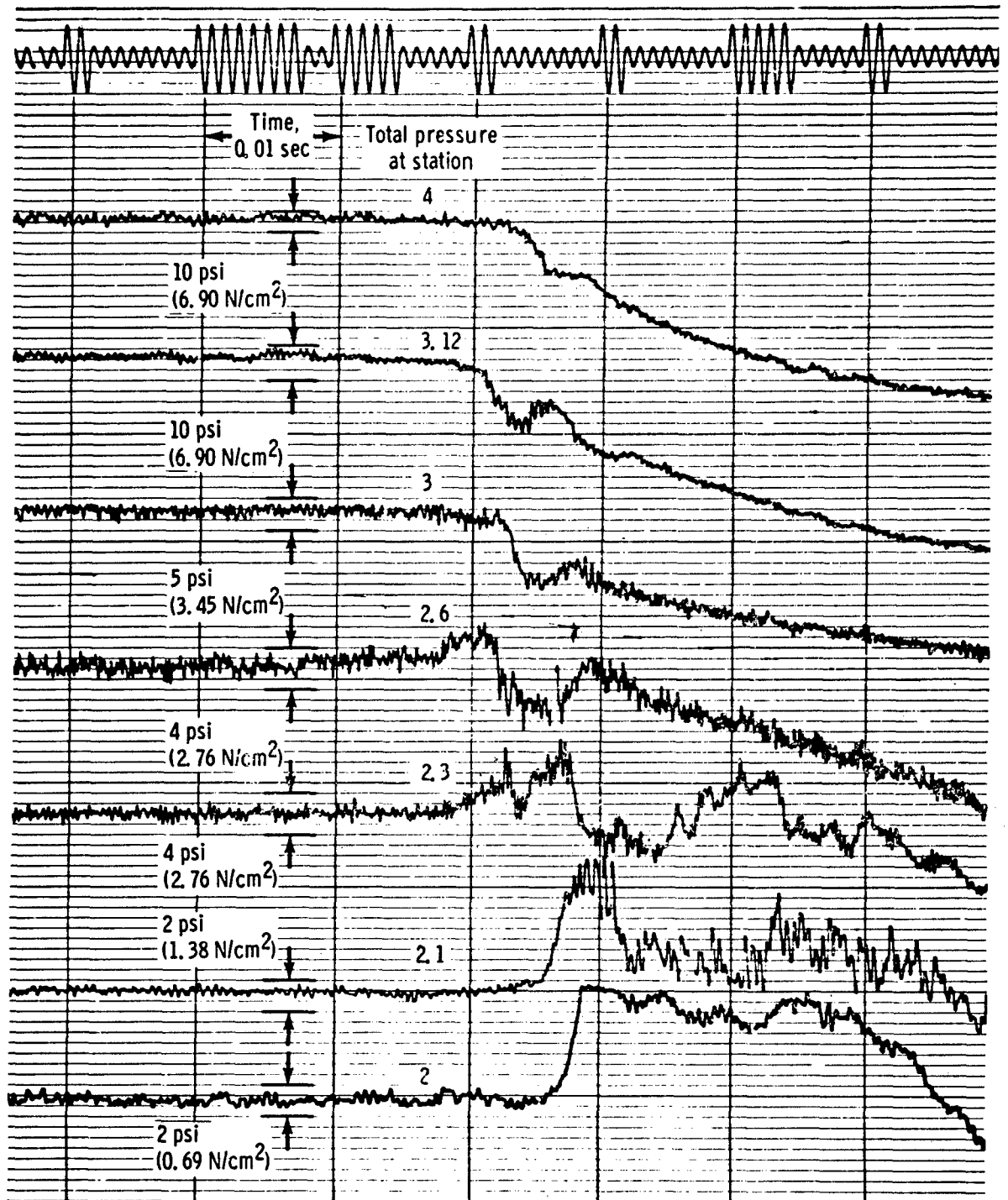
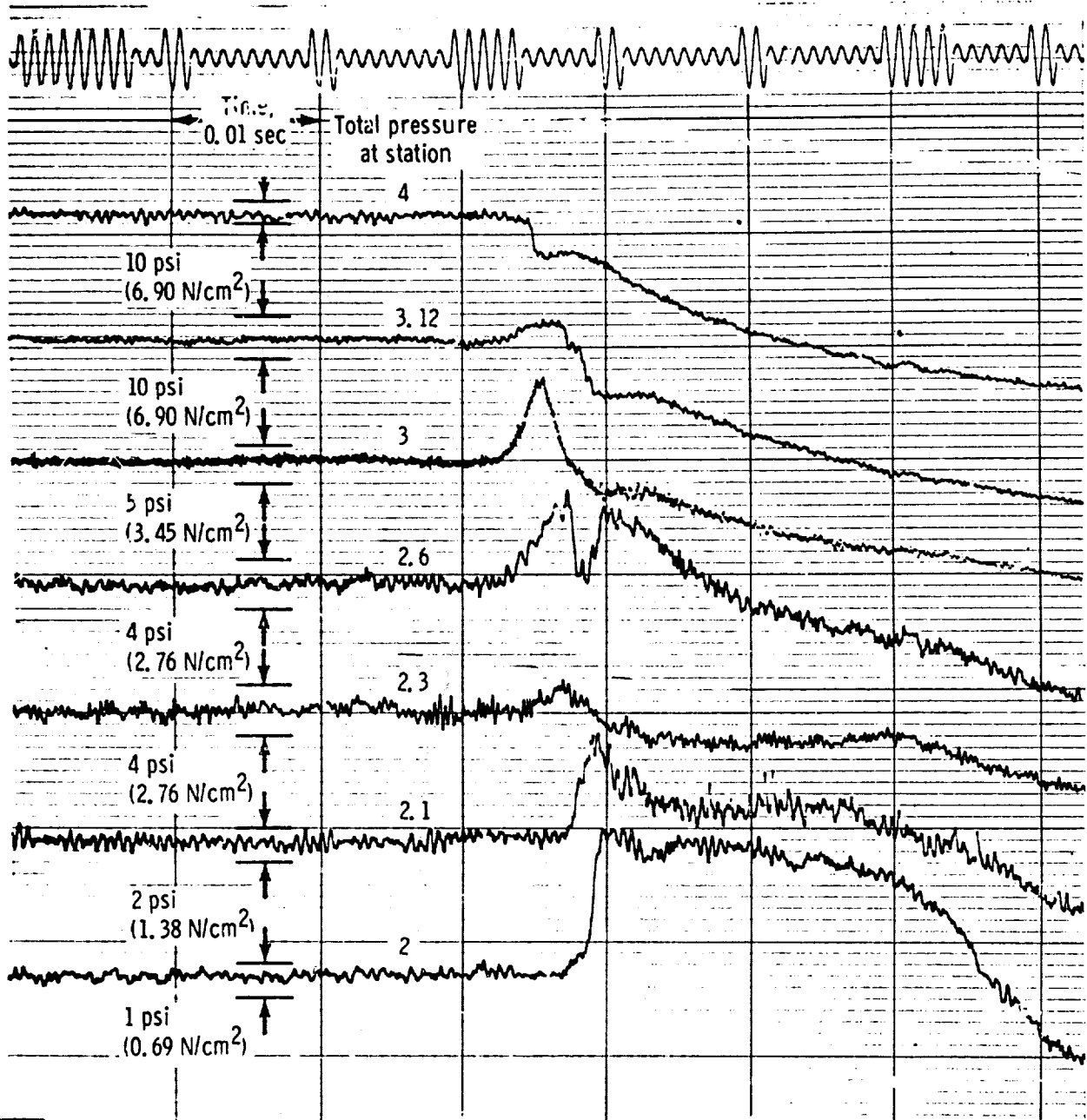


Figure 2. - Typical probe installation.



Low-pressure compressor stall. Low rotor speed, 73 percent; exhaust nozzle area, 186 percent rated.

Figure 3. - Typical time histories during stall transient of YTF30-P-1 turbofan engine at Reynolds number index of 0.5.



High-pressure compressor stall. High rotor speed, 97 percent; exhaust nozzle area, 78 percent rated.

FIGURE 4. - TYPICAL TIME HISTORIES DURING STALL TRANSIENT OF YTF30-P-1 TURBOFAN ENGINE AT REYNOLDS NUMBER INDEX OF 0.5.

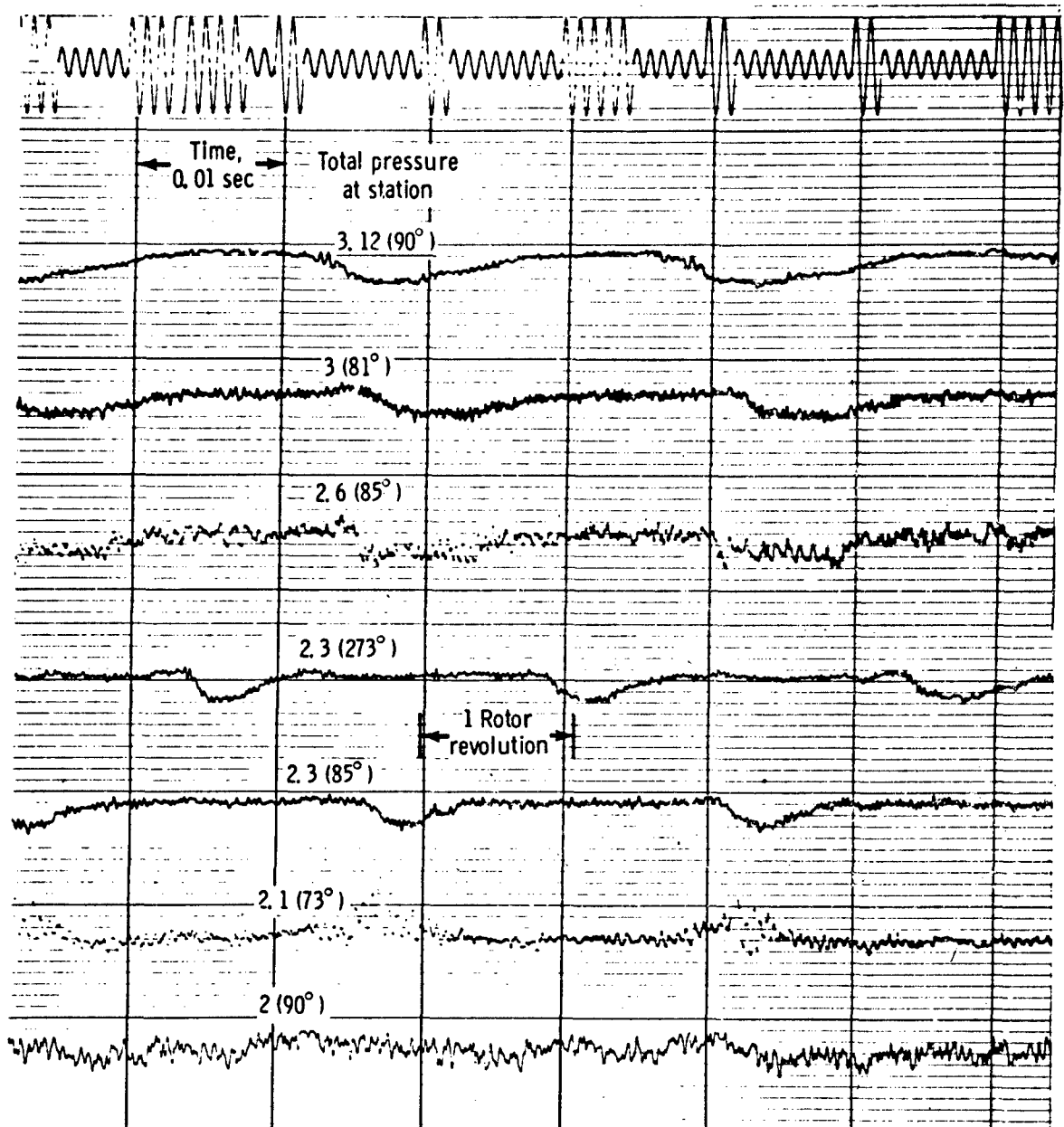


Figure 5. - Typical rotating stall pattern observed in YTF30-P-1 turbofan engine following compressor stall. Low rotor speed, 56 percent, high rotor speed, 77 percent; exhaust nozzle area, 186 percent rated. Reynolds number index, 0.5; stall frequency, 0.43 low rotor frequency.

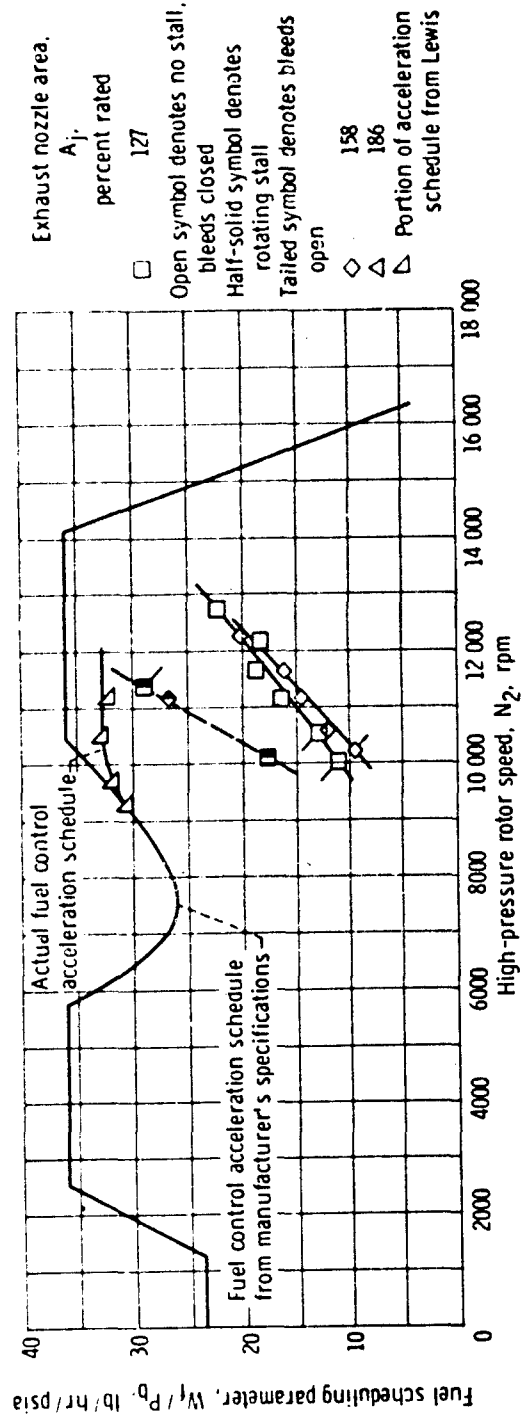


Figure 6 - Fuel schedule for YTF30-P-1 turbofan engine. Total temperature at station 2, 59° F (15° C).

**FIGURE 7 - FOUR SPECIAL TESTING TECHNIQUES USED TO DETERMINE
ENGINE TRANSIENT AND STALL CHARACTERISTICS**

- 1. PRESSURE DISTORTION JETS**
- 2. TEMPERATURE DISTORTION DEVICE**
- 3. CHOKED INLET DUCT**
- 4. COMPRESSOR DISCHARGE IN-FLOW BLEED**

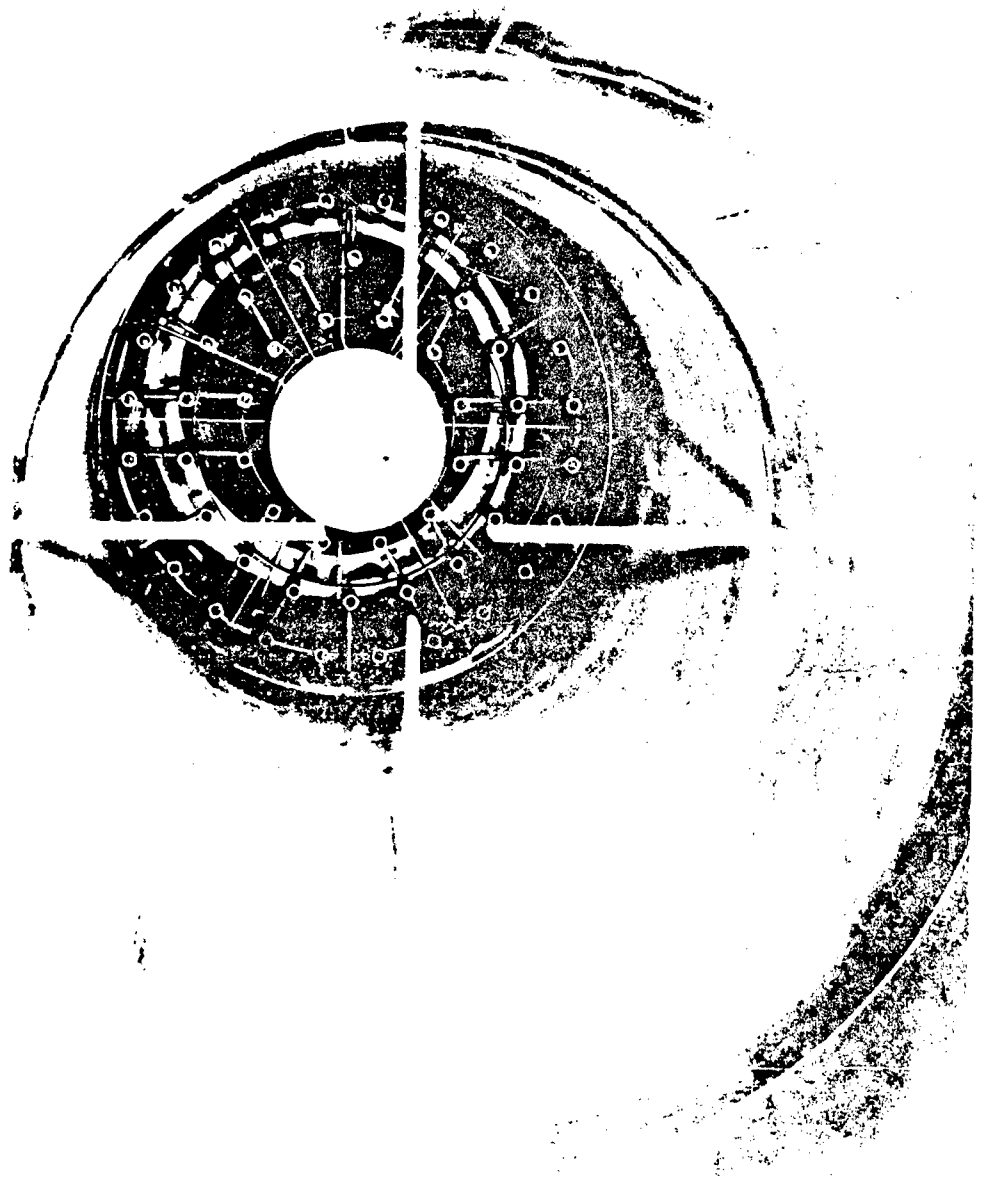


FIGURE 8. - PRESSURE JET SYSTEM INSTALLED IN ENGINE INLET DUCT
(View looking toward engine inlet)

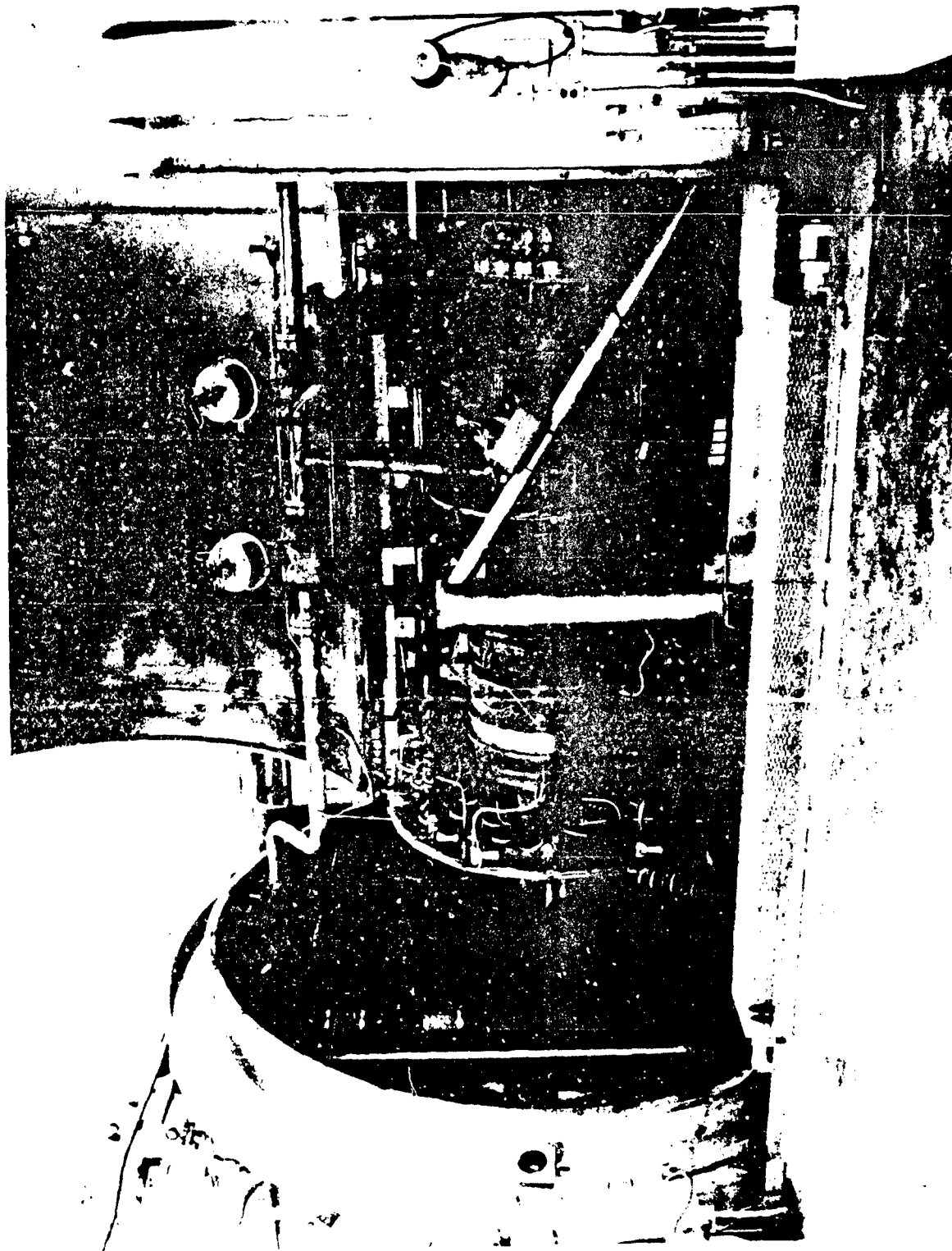


FIGURE 9. - PRESSURE JET SYSTEM INSTALLED (External View of Engine Inlet Duct)

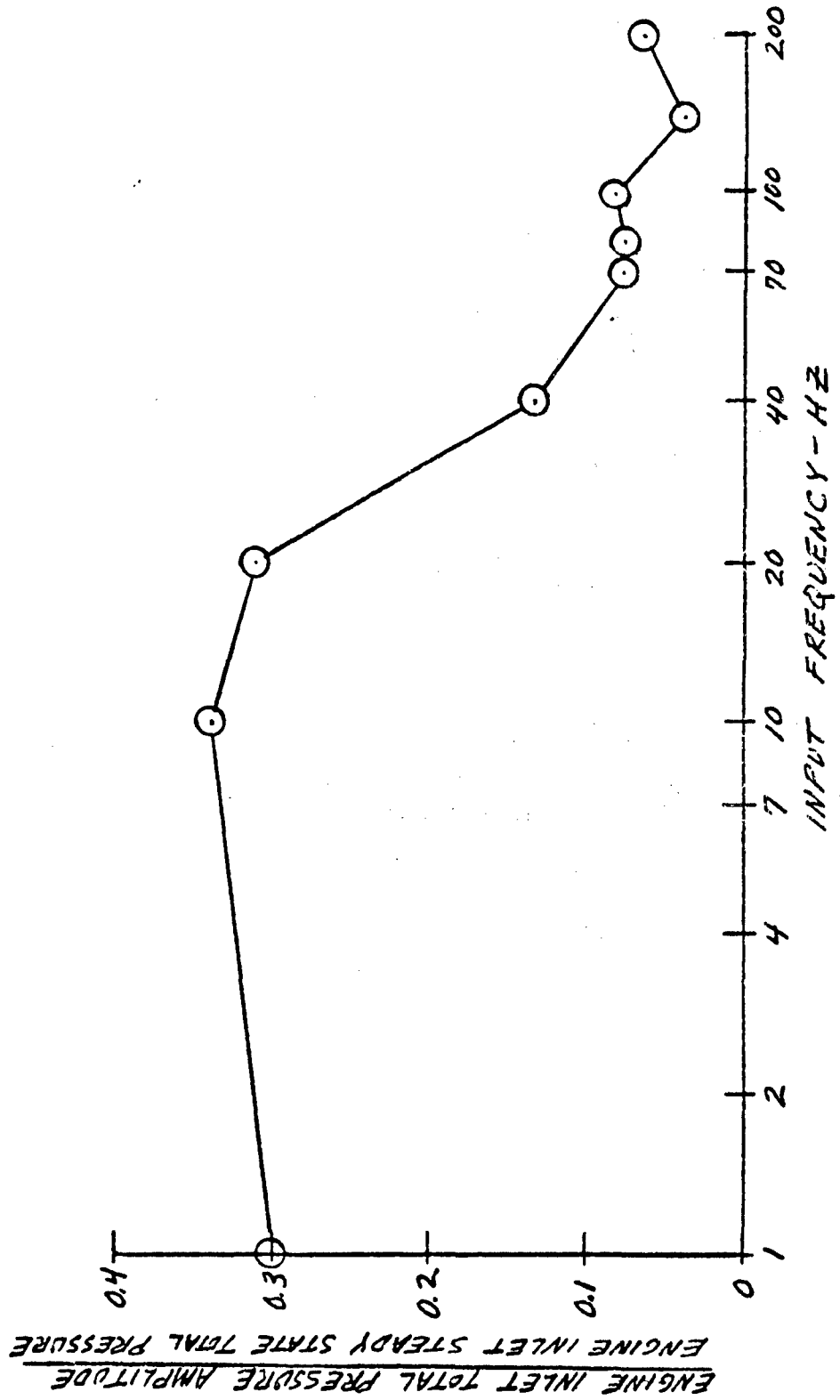


FIGURE 10.- MAXIMUM ENGINE INLET PRESSURE AMPLITUDE OVER A RANGE OF INPUT FREQUENCIES

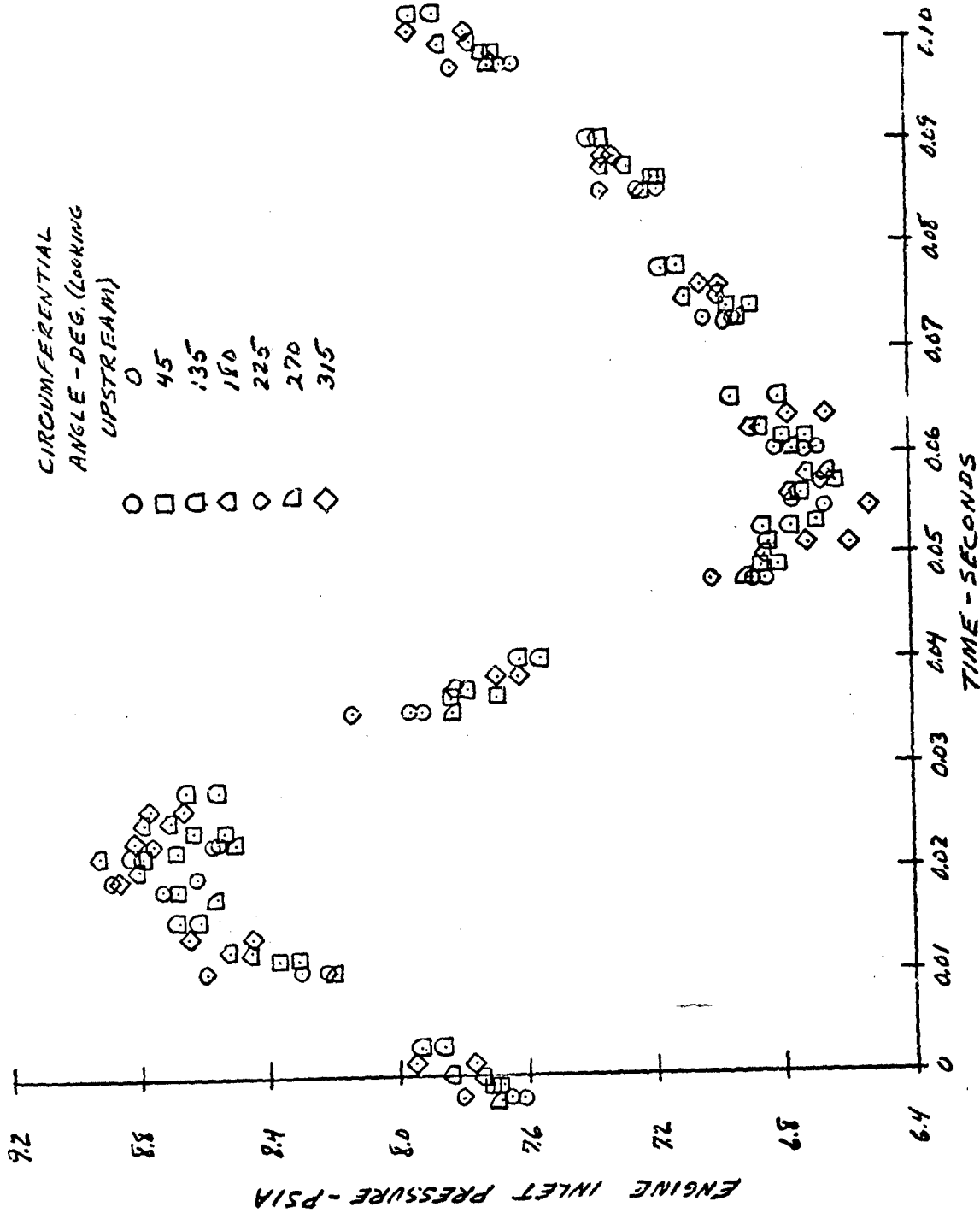


FIGURE 11.- TYPICAL VARIATION OF ENGINE INLET PRESSURE WITH TIME. INPUT FREQUENCY, 10 Hz

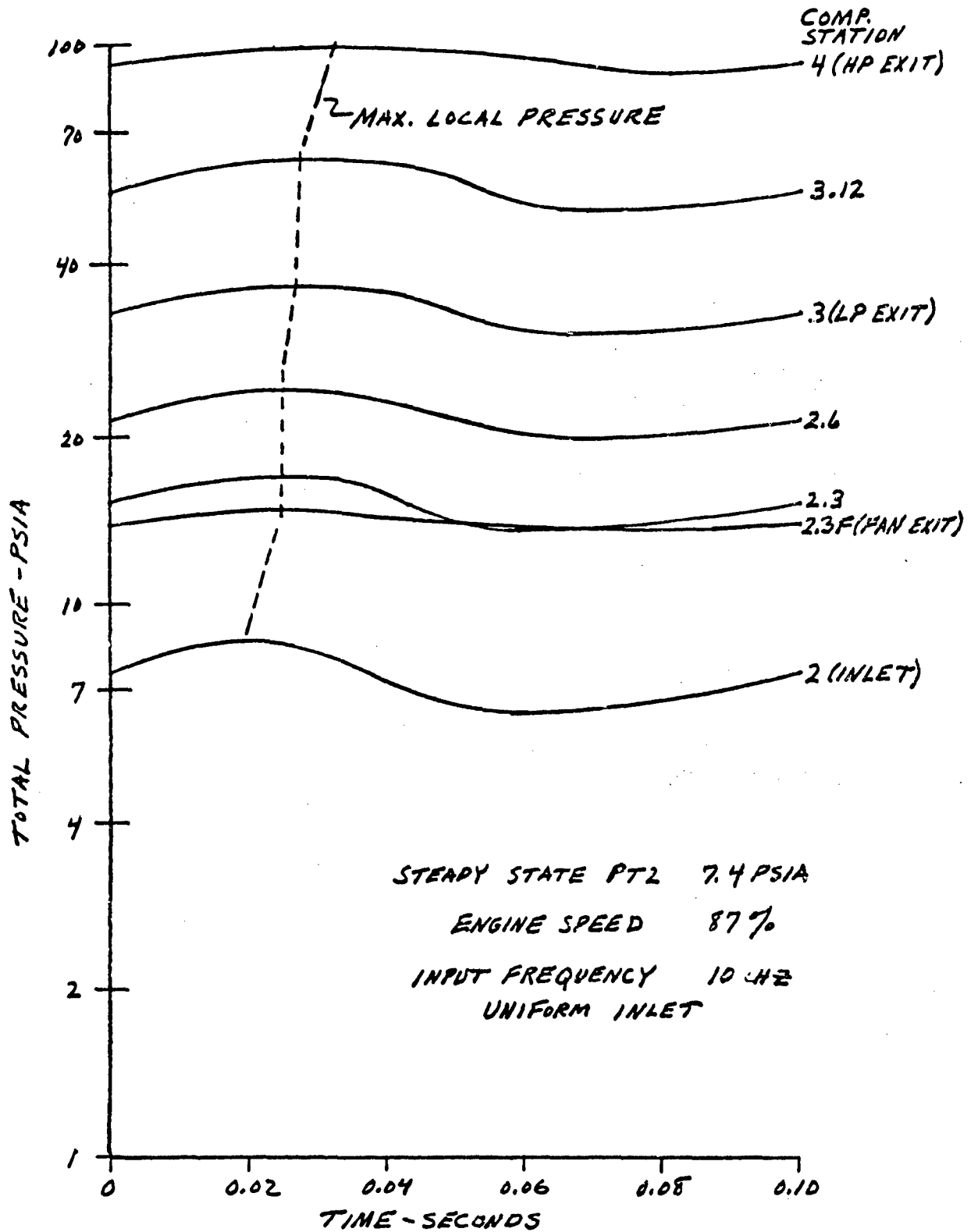


FIGURE 12.- TYPICAL VARIATION OF SEVERAL COMPRESSOR INTERSTAGE PRESSURES WITH TIME DURING UNIFORM ENGINE INLET PRESSURE VARIATIONS

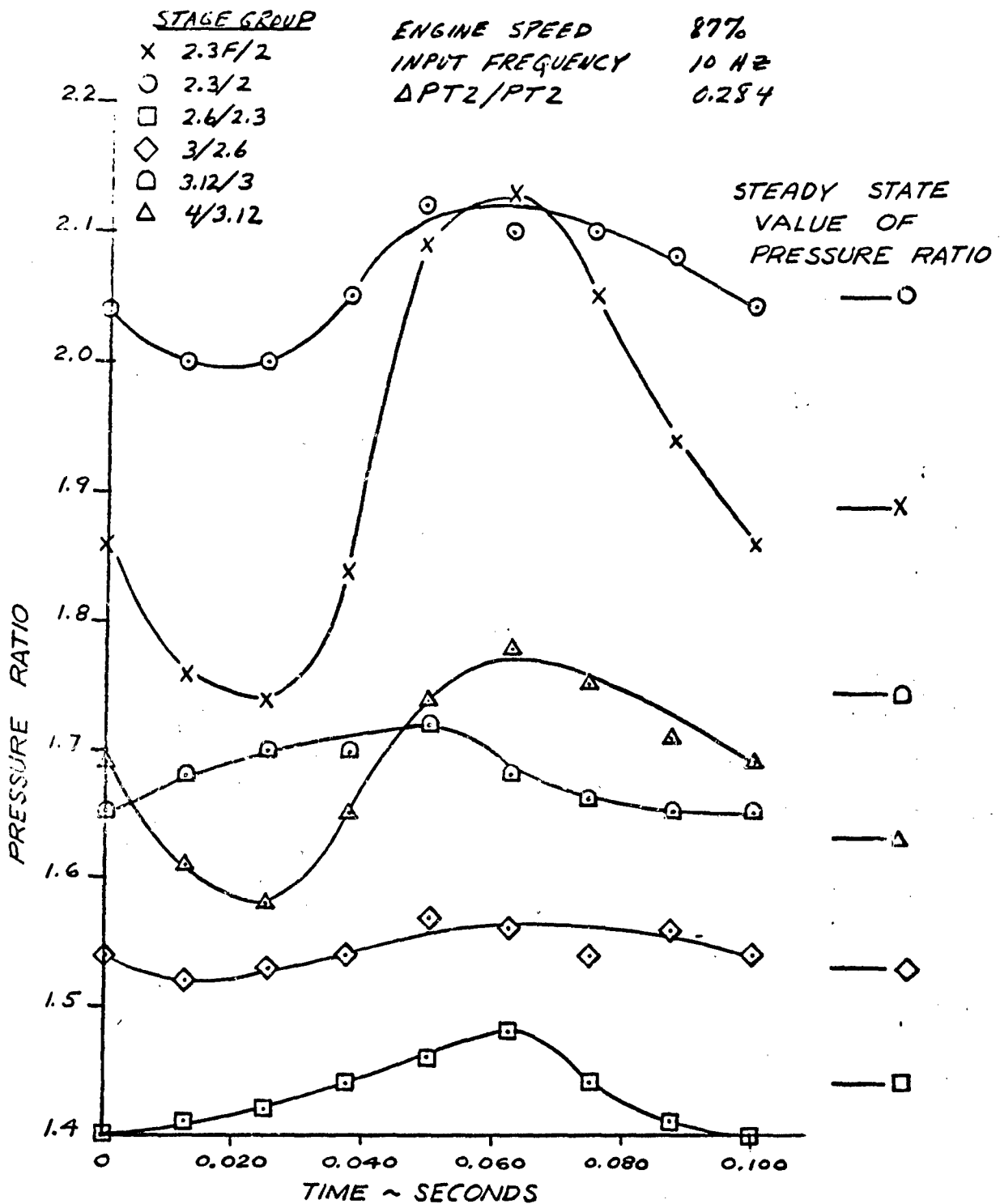


FIGURE 13.- TYPICAL VARIATION OF SEVERAL COMPRESSOR
COMPRESSOR STAGE GROUP PRESSURE RATIOS
WITH TIME DURING UNIFORM ENGINE INLET
PRESSURE VARIATIONS

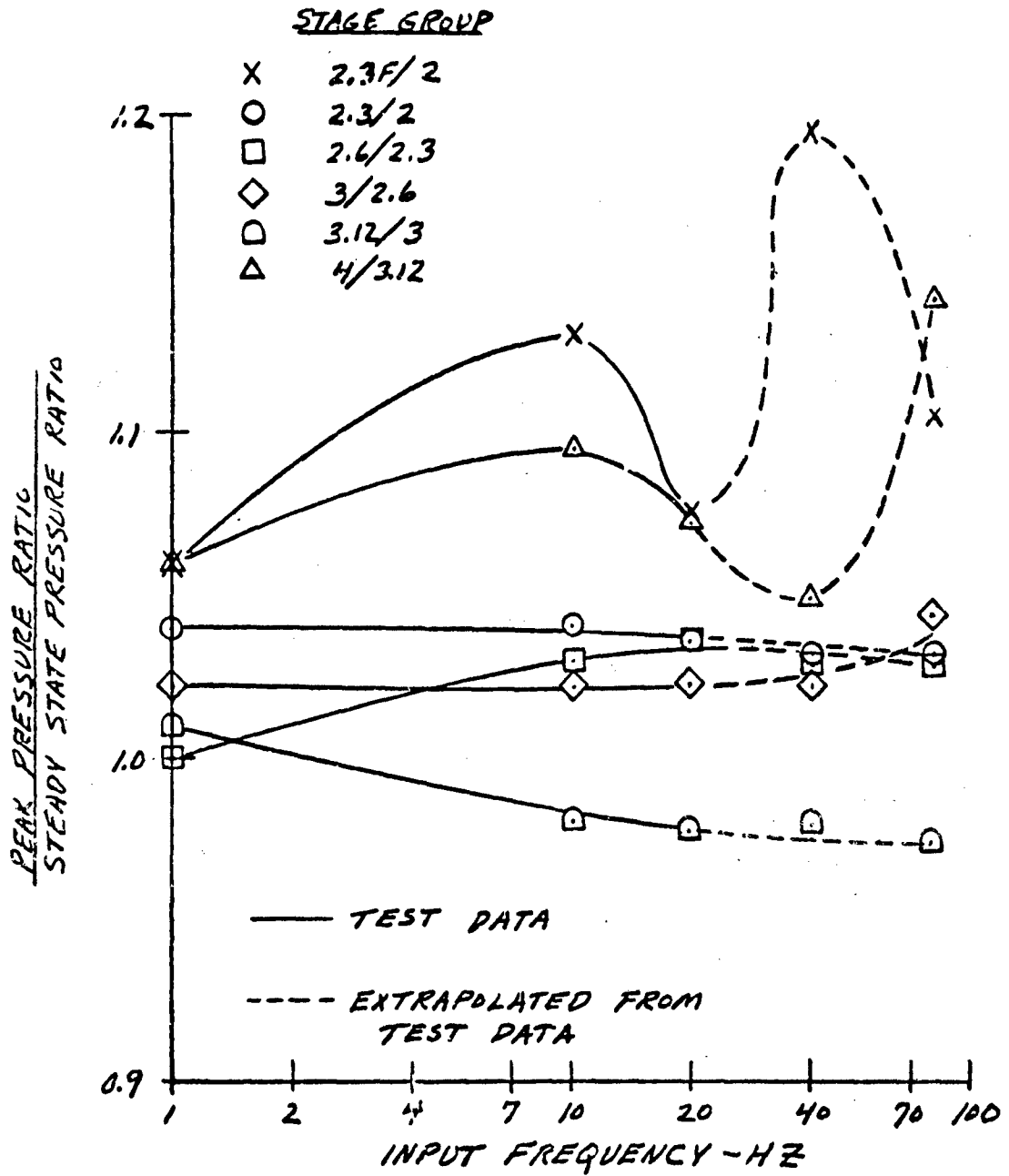


FIGURE 14.- VARIATION OF PEAK PRESSURE RATIO WITH INPUT FREQUENCY. $\Delta P T_2 / P T_2$, APPROXIMATELY 0.28

THE PERFORMANCE PREDICTION OF MULTISTAGE AXIAL
COMPRESSORS OF ARBITRARY GEOMETRY OPERATING
WITH COMBINED RADIAL AND CIRCUMFERENTIAL
DISTORTION

by R. A. Novak and R. M. Hearsey

Northern Research and Engineering Corp., Cambridge, Mass.

ABSTRACT

Method of predicting the performance of axial compressors operating with distorted inlet conditions is presented. A numerical procedure used to compute solutions is described, and some results are shown. It is concluded that the method is of practical value and could be usefully employed during the design stage of a compressor that is required to operate with non-uniform inlet conditions.

INTRODUCTION

This paper describes a method that was derived to predict the performance of axial compressors operating with non-uniform inlet conditions. The compressor may be of quite arbitrary design and the method predicts the performance of the compressor given a description of the geometry of the machine alone. The inlet non-uniformity may be in terms of total pressure, total temperature, or whirl angle, and of a radial, circumferential, or combined radial and circumferential nature.

A computer program was written for the method, and the development of the computer program has been reported in References 1, 2, and 3.

The model of the flow in the compressor that was assumed is simple, leading to a relatively simple analysis of the model, described below. The technique required to compute a solution is involved and is described in some detail. In particular, considerable effort was required to devise a numerical procedure that gives a convergent solution for the flowfield in the duct regions upstream and downstream of the compressor. Some results obtained from the computer program are shown, which both illustrate the general validity of the method, and give some insights into compressor operation with distorted inlet conditions.

ANALYSIS OF FLOW MODEL

General Description and Assumptions

The flowfield to be considered consists of an annular duct upstream of the compressor, the compressor proper, and an annular duct downstream of the compressor. The upstream boundary condition, imposed at the upstream face of the inlet duct, comprises of a specification of the distribution of total pressure, total temperature, and whirl angle at the boundary. The downstream boundary condition, imposed at the downstream end of the outlet duct, is the specification of a circumferentially uniform value for the static pressure. This choice of downstream boundary condition is not the only one possible, but it is one of practical interest. Experimental evidence from compressors on test both as components and installed in aero-engine gas turbines indicates a nearly uniform exit static pressure with varying circumferential inlet distortion.

Conditions along a number of streamlines in the flow are sought. Calculations are to be made at the points where the streamlines intersect axial computing stations. These are cones with their axes on the axis of the compressor, and will generally be placed at or near the edges of bladerows in the compressor. A number will also be placed in the ducts upstream and downstream of the compressor.

Actually, the location of the streamlines is the fundamental unknown. Given the streamline locations throughout the flowfield for a particular problem, determination of all other quantities would follow by relatively trivial calculation. A number of streamsurfaces called sector centerlines are defined. Each of these is described by a number of streamlines disposed radially in the flow at the inlet. As the streamsurfaces pass through the flowfield to the downstream boundary, they are displaced circumferentially by the static pressure field and the actions of the compressor blades. In general, the displacements will differ with radius, so that the sector centerlines will not be straight or radial. Sectors are associated with the sector centerlines. At any radius (and axial location) the circumferential extent of a sector is one half the arc included by the sector centerlines on each side of the centerline under consideration. Because the circumferential displacement of each sector centerline will, in general, be different, the sector widths will vary. For the purpose of applying the continuity condition, each sector is assumed to be a streamtube. (Whilst the streamtube shapes are not generally sectors in the strict geometric sense, it is convenient to refer to them as sectors.)

Two assumptions are made with respect to the flow.

Firstly, the working fluid is assumed to be an inviscid, perfect gas having constant properties. No particular comment is required here. Alternative assumptions could be employed at the cost of complicating the analysis.

Secondly, it is assumed that there is no transport of mass or energy across streamlines in the flow. For machines of few stages, this assumption is probably of little consequence. It may, however, introduce errors for machines of many stages in which appreciable mixing of the flowstream could occur.

In order to determine the changes in enthalpy and entropy that occur along each streamline as it passes through the bladerows of the compressor, the performance of the blade sections must be predicted. The approach used is described in Reference 4, and relies heavily upon experimental data. These data were obtained from two-dimensional cascade tests and from tests of compressors running under uniform inlet conditions. It is assumed that the data apply equally for the case of distorted flow conditions, when two new phenomena occur. There are circumferential gradients in the inlet and outlet conditions of the bladerows, and, in the case of the rotor rows, there is a periodic change in conditions. In fact, the difference between the non-distorted and distorted cases is to some extent paralleled by the difference between cascade and (non-distorted) compressor flows. Whereas in the former case the flow is steady and, presumably, uniform, in the latter case, all bladerows except the first are periodically swept by the wakes from the preceding bladerows. Generally, only small differences are seen between the performances of blades in cascade and compressor tests.

Experience in the prediction of the performance of axial compressors operating with uniform inlet conditions has shown that if realistic results are to be obtained, proper allowances need to be made for the effects of the annulus wall boundary layers. It is assumed that the method used, which is described in Reference 5, may be applied to the distorted-flow case, the annulus wall boundary layers being determined independently in each sector.

Derivation of Equations

The following nomenclature is used:

| | |
|-----------|---|
| \bar{A} | Direction cosine |
| \bar{B} | Direction cosine |
| \bar{C} | Direction cosine |
| C | Velocity |
| C_p | Specific heat at constant pressure |
| g | Acceleration due to force of gravity |
| H | Total enthalpy |
| J | Joules equivalent |
| ℓ | Sector centerline direction |
| m | Meridional projection of streamline direction |
| P | Total pressure |
| p | Static pressure |
| R | Gas constant |
| r | Radius |
| r_m | Radius of curvature |

| | |
|----------|--|
| S | Entropy |
| s | Streamline direction |
| T | Total temperature |
| U | Blade speed |
| W | Flow rate |
| z | Axial coordinate |
| α | Whirl angle, whose tangent is C_θ/C_m |
| γ | Station lean angle when viewed from side |
| γ | Ratio of specific heats |
| Σ | Sector circumferential extent |
| ϕ | Streamline slope angle as seen in meridional projection |
| θ | Circumferential coordinate |
| ω | Relative total pressure loss coefficient based upon inlet dynamic head |
| μ | Station lean angle when viewed parallel to axis |
| ρ | Static density |

Subscripts

| | |
|----------|-----------------|
| c | Casing |
| h | Hub |
| θ | Circumferential |
| r | Radial |
| m | Meridional |
| 1 | Inlet |
| 2 | Outlet |
| R | Relative |
| z | Axial |

A means of determining the velocity distribution along any sector centerline is required. Figure 1 illustrates the geometry of a typical sector centerline.

Using a straightforward directional derivative we may write

$$\frac{1}{\rho} \frac{dp}{ds} = \bar{A} \frac{\partial p}{\partial r} + \frac{\bar{B}}{r} \frac{\partial p}{\partial \theta} + \frac{\bar{C}}{\rho} \frac{\partial p}{\partial Z} \quad (1)$$

where \bar{A} , \bar{B} , and \bar{C} are direction cosines and may be related to the centerline geometry by

$$\bar{A} = 1/\sqrt{(1 + \tan^2 \mu + \tan^2 \gamma)}$$

$$\bar{B} = \tan \mu \bar{A}$$

$$\bar{C} = \tan \gamma \bar{A}$$

Substitution for terms in Equation 1 will give the desired result.

The radial and axial derivatives of static pressure may be written

$$-\frac{1}{\rho} \frac{\partial p}{\partial r} = c \frac{dCr}{ds} - \frac{C\theta^2}{r} \quad (2)$$

and
$$-\frac{1}{\rho} \frac{\partial p}{\partial Z} = c \frac{dCz}{ds} \quad (3)$$

Noting that

$$Cr = Cm \sin \phi$$

$$Cz = Cm \cos \phi$$

and

$$C \frac{d\phi}{ds} = C_m \frac{d\phi}{dm} + \frac{C\theta}{r} \frac{\partial\phi}{\partial\theta}$$

$$= \frac{C_m}{rm} + \frac{C\theta}{r} \frac{\partial\phi}{\partial\theta}$$

Equations 2 and 3 may be rewritten as

$$-\frac{1}{\rho} \frac{\partial p}{\partial r} = C \sin\phi \frac{dC_m}{ds} + \frac{Cm^2 \cos\phi}{rm} + \frac{Cm C\theta \cos\phi}{r} \frac{\partial\phi}{\partial\theta}$$

$$- \frac{C\theta^2}{r} \quad (4)$$

and

$$-\frac{1}{\rho} \frac{\partial p}{\partial z} = C \cos\phi \frac{dC_m}{ds} - \frac{Cm^2 \sin\phi}{rm} - \frac{Cm C\theta \sin\phi}{r} \frac{\partial\phi}{\partial\theta}$$

(5)

Attention is now turned to the lefthand side of Equation 1. For a perfect gas, we have

$$-\frac{1}{\rho} \frac{dp}{d\ell} = -\frac{dH}{d\ell} + \tau \frac{dS}{d\ell} - \frac{1}{2} \frac{dC^2}{d\ell} \quad (6)$$

By introducing Equations 4, 5, and 6 into Equation 1, along with the whirl angle defined by

$$\tan\alpha = C\theta/C_m$$

the final result may be obtained thus

$$\frac{1}{2} \frac{dC_m^2}{d\ell} = C_m^2 \cos^2\alpha \left\{ (\bar{A} \cos\phi - \bar{C} \sin\phi) \left(\frac{1}{rm} + \frac{\tan\alpha}{r} \frac{\partial\phi}{\partial\theta} \right) \right.$$

$$\left. - \frac{1}{2} \frac{d\tan^2\alpha}{d\ell} - \bar{A} \frac{\tan^2\alpha}{r} \right\} + C_m \cos\alpha (\bar{A} \sin\phi$$

$$+ \bar{C} \cos \phi) \frac{dC_m}{ds} + \cos^2 \alpha \left(\frac{dH}{d\ell} - t \frac{dS}{d\ell} - \frac{\bar{B}}{\rho r} \frac{\partial p}{\partial \theta} \right) \quad (7)$$

Equation 7 may be numerically integrated to give the meridional velocity profile along a computing station, given the distributions of the streamline characteristics, the enthalpy and entropy, the whirl angle, and the circumferential gradients of the static pressure and streamline slope angle. The arbitrary constant of integration is eliminated by applying the continuity condition for the streamtube, that is, sector.

In order to apply the continuity condition in any sector, conditions are assumed to be circumferentially constant at any radius. Then the continuity equation can be written

$$W = \int_{r_h}^{r_c} (C_z \rho \Sigma r) dr \quad (8)$$

Thus Equations 7 and 8 together define the meridional velocity profile along a sector centerline.

An integral form of the circumferential component of the momentum equation is now developed in order to be able to establish the changes in whirl angle along a streamline.

We may write the circumferential component of the momentum equation as

$$- \frac{1}{\rho} \frac{\partial p}{\partial \theta} = C \frac{d(r C \theta)}{ds}$$

In integral form this becomes

$$r_2 C\theta_2 - r_1 C\theta_1 = - \int_1^2 \frac{1}{C\rho} \frac{\partial p}{\partial \theta} ds$$

which may be rewritten as

$$r_2 C\theta_2 - r_1 C\theta_1 = - \int_1^2 \frac{1}{Cm\rho} \frac{\partial p}{\partial \theta} dm$$

Introducing the whirl angle we obtain

$$\tan\alpha_2 = \frac{r_1 C m_1 \tan\alpha_1 - \int_1^2 \frac{1}{Cm\rho} \frac{\partial p}{\partial \theta} dm}{r_2 C m_2} \quad (9)$$

Thus the change in whirl angle along a streamline may be determined from the circumferential gradient of static pressure. (Of course, Equation 9 applies across a blade-free space only.)

A geometric relation is now developed which allows the determination of the change in circumferential coordinate of a streamline from the variation of whirl angle along it. The definition of the whirl angle gives for any streamline

$$\frac{d\theta}{dm} = \frac{\tan\alpha}{r}$$

and hence

$$\theta_2 = \theta_1 + \int_1^2 \frac{\tan\alpha}{r} dm$$

In order to compute this equation across the interval between any two adjacent computing stations, linear variations of

$\tan\alpha$ and r with m are assumed. Then

$$\theta_2 = \theta_1 + \frac{m_2 - m_1}{r_2 - r_1} \left\{ \text{Log}_e \left(\frac{r_2}{r_1} \right) (\tan\alpha_1 - \frac{(\tan\alpha_2 - \tan\alpha_1)r_1}{r_2 - r_1}) + \tan\alpha_2 - \tan\alpha_1 \right\} \quad (10)$$

For the case when $r_2 = r_1$, the following result is obtained

$$\theta_2 = \theta_1 + (m_2 - m_1) \frac{(\tan\alpha_2 + \tan\alpha_1)}{2} \quad (10a)$$

Equation 10 (or 10a) can be applied along any streamline to determine the change in circumferential coordinate, both in a bladefree space and across a bladerow.

Between any two computing stations which encompass a bladefree space, the enthalpy and entropy (and hence total pressure and total temperature) are taken to be constant along any streamline, and Equation 9 expresses the angular momentum variation.

Between any two computing stations which encompass a bladerow, there are in general enthalpy and entropy changes along any streamline. The cascade prediction scheme incorporated into the method gives the relative outlet flow angle and total pressure loss coefficient for the blade section on the streamline. The usual velocity triangle relationships give the whirl velocity at the blade outlet, and then the

change in enthalpy is given by the Euler turbomachine equation thus

$$H_2 - H_1 = U_2 C_{\theta 2} - U_1 C_{\theta 1}$$

or, for our case of a constant property perfect gas,

$$T_2 - T_1 = \frac{U_2 C_{\theta 2} - U_1 C_{\theta 1}}{gJ C_p} \quad (11)$$

The total temperature change and loss coefficient are used to determine the total pressure (thus establishing the entropy change) from

$$\frac{P_2}{P_1} = \left(\frac{T_2}{T_1} \right)^{\frac{\gamma}{\gamma-1}} \left(1 - \left(\frac{P_1 R}{P_2 R} \right)_{\text{IDEAL}} \right) \omega \left(1 - \frac{P_1}{P_1 R} \right) \quad (12)$$

where

$$\left(\frac{P_1 R}{P_2 R} \right)_{\text{IDEAL}} = \left(1 + \frac{\gamma-1}{2} \frac{U_2^2}{\gamma g R T_1 R} \left(1 - \left(\frac{r_1}{r_2} \right)^2 \right) \right)^{\frac{\gamma}{\gamma-1}}$$

METHOD OF COMPUTING SOLUTION

Computational Sequence

As indicated in the general description of the flow model, the solution is obtained by considering the flow in a number of sectors which together comprise the complete compressor system of inlet, compressor proper, and outlet.

The circumferential extent of each sector is initially estimated to be invariant with axial location within the flowfield. Thus the sector centerlines are assumed to be radial (when viewed parallel to the axis) at each computing station. Conditions within each sector may then be evaluated on the basis of the above estimates for the specified downstream boundary condition, that is, static pressure. In order to obtain the solution for conditions in a sector for the specified exit static pressure it is necessary to estimate the sector flowrate, to examine the resulting exit static pressure, and then to reestimate the flow rate accordingly. Further details of the steps involved in this process are given below.

Equations 7 and 8 are solved to determine conditions at any computing station in a sector. Simultaneous solution of these gives the meridional velocity distribution along the sector centerline, and hence all other quantities. Inputs to these equations include the streamline characteristics, which are obtained from the meridional projection of the estimated streamline distribution within the sector. The total pressure and total temperature are specified at the sector inlet. Across any bladefree space they are constant along each streamline. Across any bladerow the changes along each streamline are obtained from Equations 11 and 12. The whirl angle distribution is specified at the sector inlet. Equation 9 gives the whirl angle after any bladefree space,

and requires knowledge of the circumferential gradient of static pressure. At this point in the calculation the circumferential gradients occurring both in Equations 7 and 9 are all assumed to be zero. At a computing station following a blade row, the whirl angle is given by the relative outlet flow angle from the blade row, and the usual velocity triangle relationships.

Thus at this point is obtained an estimate of conditions and flowrates within each sector consistent with the specified sector inlet conditions and exit static pressure, and the estimated circumferential extents of the sectors. Also, the flow in each sector was assumed to be axisymmetric. Comparison of conditions amongst the sectors now leads to new (non-zero) estimates of the various circumferential derivatives required for the solution of Equations 7 and 9, and also of the locii of the sector centerlines as they progress from the inlet to the exit.

These calculations are made on the same number of "mean streamsurfaces" as there were streamlines examined in the evaluation of conditions within each sector. The streamsurface radius at any computing station is the mean of the radii of the sector streamlines. Quantities which are considered from sector to sector are all interpolated from their distributions along the sector centerlines at at the mean streamsurface radius.

In order to produce a stable and rapidly convergent procedure, the static pressure distributions calculated to exist on each mean streamsurface in the inlet are modified using an approximate small perturbation solution for the flow in the inlet. Boundary conditions satisfied by this procedure are the total pressure and whirl angle distributions at the upstream boundary, and the static pressure distribution at the face of the compressor, as determined by the preceding sector analyses. Further details of this technique are given below.

Using the static pressures obtained by this means and the assumed circumferential locations of the sector centerlines, circumferential static pressure gradients are calculated for the inlet. Equation 9 is applied to obtain the flow angle distribution in the inlet, and Equation 10 (or 10a) then gives a new estimate of the sector centerline locations. As the locations of the sector centerlines at the compressor is a necessary input to the small perturbation procedure used to obtain the static pressure distribution, an iteration is performed between the determination of the static pressures and the determination of the sector centerline locations in order to maintain a consistent result.

Equation 10 (or 10a) is applied to obtain the loci of the sector centerlines as they pass from the compressor front face to rear face. The (absolute) whirl angles used are taken directly from the sector analyses.

The small perturbation solution is now applied to the region from the compressor rear face to the downstream boundary. In this case, the flowfield is solved for the total pressure and flow angle distributions determined (by the sector analyses) at the compressor rear face, and a zero circumferential static pressure gradient at the downstream boundary. The calculation is made so that flow angle rather than static pressure is obtained in the exit duct.

Equation 10 (or 10a) gives revised estimates of the locii of sector centerlines in the exit duct. Again, an iteration is required so that the derived angle distributions and sector centerline locii are consistent.

A revised set of data is now prepared to allow the entire procedure to be restarted. From the static pressure distribution, modified according to the small perturbation solution in the inlet, and the calculated centerline coordinates, the circumferential gradient of static pressure is everywhere obtained. The orientation of the sector centerlines at each computing station allows both the sector widths and the angle describing the inclination of the centerline from radial (when viewed parallel to the axis) to be evaluated throughout the flow field. Generally, the meridional projection of the streamline patterns derived for the flow in each sector will be different, and this is

reflected in the circumferential gradient of streamline slope angle, also calculated.

Using these new data, conditions in each sector are again evaluated for the specified downstream static pressure. By repeating the above process a number of times, a solution is obtained that has imposed upon it the influence of the approximate, small perturbation analysis of the flow in the inlet and exit ducts. An exact solution is obtained by progressively phasing out the results of the perturbation analysis over a number of cycles, so that finally the results correspond to the system of equations presented earlier.

Satisfaction of Downstream Boundary Condition

The determination of the flow in any sector that corresponds to the desired exit static pressure is an important part of the computing process, and the technique used is described here.

An estimate of the sector flow is supplied in the input data, and the sector analysis is commenced using this value of flow. The solution for the flowfield in a sector is iterative, even when the flowrate is specified, the streamline locations being unknown. Three passes through the computing process to determine streamline locations and hence conditions in the sector are made, and the resulting exit static pressure is noted. If it is too high, the flow is arbitrarily increased (by an amount dependent upon the estimated

flow range); if it is too low, the flow is decreased. Three further passes are performed, and the static pressure again noted. From this point onwards, the flow is reestimated after each third pass by linearly interpolating for the flow to give the desired static pressure, using the two previous results. After about six reestimates, the flow is essentially established, and the problem is reduced to the original "analysis for a given flow." Provision is made for the several possibilities that occur during the searching procedure. If the initial estimate of flow is such that the compressor is choked, the flow is reduced until a valid calculation is achieved. Alternatively, if the compressor is in surge (i.e., a velocity of less than 1.0 feet per sec is calculated to exist within the machine), the flow will be increased. Then, the first point will have been established. If the second point attempted is in choke (or surge), the flow will be reduced (or increased) towards the first value by "nesting." Nesting here means that the difference in flow between the first (valid) point and the failed point is halved repeatedly until a valid calculation is achieved. Thus, the first two points will be achieved. Should the two points achieved yield a positive slope characteristic, an arbitrary increase in flow is made to obtain two points defining a negative slope. Having obtained two points of negative slope, any lower (or intermediate) pressure can be solved for. A higher pressure may not always be possible. If surge is

subsequently encountered, or the slope of the characteristic becomes positive, the program notes that the specified static pressure is unobtainable.

Method Used to Produce a Convergent Procedure

Satisfaction of the equations presented earlier would constitute a precise solution to the problem posed, but this is not likely to occur using the computational sequence outlined without the incorporation of the small perturbation solution. This can be seen immediately by considering the results that would be obtained by excluding the small perturbation solution from the procedure during the first cycle of calculation. Because the initial estimate of the sector widths is that they are uniform throughout, the static pressure gradients determined at the compressor front face would apparently occur throughout the inlet duct. (A variation of area in the duct would modify the pressure distribution somewhat, but the argument still holds.) Application of Equation 9 and 10 would then result in a circumferential displacement of the sector centerlines essentially dependent only upon the length of the inlet duct considered.

It was to circumvent this problem that the small perturbation solution was introduced into the overall procedure.

The formulation employed is a two-dimensional, incompressible solution to the non-axisymmetric flow in a duct. It does recognize any variation in the mean velocity level in

the duct, and the finite distances between boundaries. In fact for many cases, the solution it gives will not differ significantly from an exact, compressible solution.

Slightly different boundary conditions are applied for the cases of the inlet and exit ducts. In the former case, the total pressure and whirl angle distributions at the upstream boundary together with the static pressure distribution at the downstream are employed. Static pressures throughout the flowfield are obtained. In the case of the outlet duct, the total pressure and whirl angle distributions are applied at the upstream boundary, and zero static pressure gradient is taken at the downstream boundary. Whirl angles throughout the flowfield are solved for.

As mentioned earlier, the small perturbation solution is used during the early cycles of calculation, and then progressively discarded. Finally, the calculation proceeds without resort to the perturbation solution at all.

Some Details of the Computer Program

The computer program that was written to compute the solution described above was based upon an existing axisymmetric analysis. This program had proved relatively successful in predicting the performance of various axial compressors (operating under axisymmetric conditions.) It was described in early form in Reference 4 and was subsequently considerably improved by the incorporation of the annulus wall boundary layer computation technique described in Reference 5.

The principal steps taken to create the program described here were

- (1) to rewrite the axisymmetric momentum equation for meridional velocity distribution in the form of Equation 7,
- (2) to modify the continuity equation to include the varying sector widths as in Equation 8,
- (3) to write a routine to determine the flowrate in any sector,
- (4) to write a routine to reestimate the circumferential gradients, the sector centerline orientations and sector widths, using Equations 9 and 10, and
- (5) to incorporate into this routine the small perturbation solution used to control the calculation during early iterations.

The program was written to handle up to 13 sectors, 15 streamlines, and 30 computing stations to describe the flow, that is 5,850 meshpoints. As it was required to run the program on an IBM 7094 Computer having only 32K of core storage, extensive use of magnetic tape and disk storage was required to store the data generated during computation. The program was also overlaid in two main segments plus two smaller ones. Both of the main segments were also further subdivided into segments. The principal problem as far as the generation, storage, and retrieval of data was concerned was that the data is generated for one sector at a time, station by station, in the station analyses, but is required for all sectors at a given station when the circumferential derivatives and so forth are subsequently reestimated. This

was handled by splitting the compressor system axially into five regions, each of up to six computing stations. Two storage units were assigned to each region, one to receive data generated by the sector analyses, and one to store the input data generated for the subsequent sector analyses by the circumferential consideration of the sector analysis results. Data relevant to all sectors in a region was stored on the designated unit. When the analyses had been completed for all sectors, the results were read back into core one region at a time. Thus results for all sectors and up to six computing stations were in core simultaneously, and could be readily processed. Upon completion of processing, the new input data sets were stored upon the designated unit sector by sector for use when the next cycle of sector analyses were made.

The prolonged nature of the calculation required running times on the IBM 7094 Computer of several hours for a multistage compressor analysis. These times would be reduced to fractions of an hour on a more modern and powerful computing system.

RESULTS OBTAINED FROM COMPUTER PROGRAM

Two-Dimensional Analysis of NASA/GE Rotor 1B

When the technique of incorporating the small perturbation solution into the overall procedure was being investigated, it was convenient to write a two-dimensional

meanline version of the program to limit computing expenditures. This involved the same procedure as has been described above, except that Equation 7 was not used, conditions at the R.M.S. radius being taken to be representative of conditions at all radii. The results described here were obtained from this meanline program.

Reference 6 describes a high-speed isolated rotor, Rotor 1B. An analysis of the flow through the rotor with inlet distortion was made using the meanline program. This type of problem is rather more difficult to handle than the usual compressor configuration consisting of both rotors and stators. With a final stator row, the flow angle in the exit duct is essentially uniform throughout, and the downstream uniform static pressure also pertains at the compressor face. In the isolated rotor case, the normal velocity triangle relationships will result in a large circumferential variation in the flow angle at the rotor exit. Continuity of course requires that the streamlines become parallel after some short distance. Hence a significant static pressure gradient exists in the exit duct.

One further minor difficulty occurred in the computation of the flow in this machine. It was found that the calculation broke down if the full distortion to be specified was imposed during the first cycle of calculation at the upstream boundary. Half the desired total pressure deficit of 12 per cent over a 90 degree sector was input for the

first three cycles of calculation, and this was then increased to the full 12 per cent over the next five cycles.

Figure 2 shows the axial velocity distributions computed at the rotor inlet and outlet. Little change in the profile occurs across the blade row.

Figure 3 shows the whirl angle distributions at the rotor inlet and outlet. Relative to the flow angles generated at the inlets to other machines operating with similar distortion levels, the upstream flow angles seen in Figure 3 are modest. The reason for this is that considerable re-alignment of the flow remains to be performed in the downstream duct, as evidenced by the 14 degree variation in whirl angle at the rotor discharge plane. Thus circumferential distorting testing of isolated rotors is probably of little relevance to their use with a closely-coupled stator bladerow.

Two-Dimensional Analysis of NACA Five-Stage Compressor

Reference 7 describes the testing of a five-stage compressor with circumferential distortion. Some results of a meanline analysis of this machine are given.

Figure 4 shows the variation of flow angle measured at the compressor face during distortion testing. This result is for design speed operation with a total pressure deficit of 15 per cent applied over a 120 degree sector. Also shown are two computed flow angle distributions, and below the two

input total pressure profiles that were defined for the two calculations. The different profiles were obtained by locating the sector centerlines differently at the upstream boundary. It can be seen that as the imposed pressure gradient is increased, the magnitudes of the maximum flow angles are increased, and then more nearly agree with the measured values. In both cases the general shape of the curve shows good agreement with the experimental curve.

The experimental total pressure deficit was imposed as a square wave at the upstream boundary, and must of course have changed somewhat before reaching the compressor due to turbulent mixing. The present analysis excludes this phenomenon, and this represents a limitation of the method.

Similar variations in the rotor face whirl angle distributions could have been produced by varying the whirl angle specified at the upstream boundary. It was assumed to be zero, but this was almost certainly not the case.

These two observations indicate that it would be wise to measure the flow angle and total pressure distributions at both the screen and compressor face in any future compressor distortion testing. As far as the computing process is concerned, this could be performed with the upstream boundary some distance upstream of the screen, where circumferentially uniform conditions might reasonably be assumed.

Three-Dimensional Analysis of NREC Single Stage Compressor

For the purpose of demonstrating the (three-dimensional) program, a single stage compressor of arbitrary design was created. The machine consisted of a rotor and a stator downstream of a flared inlet, as shown in Figure 5. This figure also shows the computed overall performance of the machine, both undistorted and with a radially uniform, circumferentially distorted inlet flow having a total pressure deficit of 10 per cent over 108 degrees. For the calculation 10 sectors, 9 streamlines in each sector, and 10 computing stations were used to describe the flow, making 900 meshpoints in all. Sixteen cycles of calculation were performed, the last four being virtually redundant. The perturbation solution restraint was imposed for the first five cycles, and was phased out over the following four cycles.

Figure 6 shows the total pressure distribution at the upstream boundary, radially uniform, and the resulting distributions for the hub, mean, and tip at the rotor and stator exits.

Figure 7 shows the whirl angle distributions for hub, mean, and tip at rotor inlet and exit. At the upstream boundary, and after the stator, the swirl angle was zero.

Figure 8 shows the total temperature distributions for hub, mean, and tip after the rotor. In the inlet, the temperature was uniform, and no changes occur along streamlines downstream of the rotor.

Figure 9 shows the meridional velocity distributions for hub, mean, and tip at the rotor inlet and outlet, and the stator outlet.

Figure 10 shows the incidence angle variations which occur at the hub, mean, and tip for both rotor and stator, and compare them with the values that exist for the same flowrate, undistorted.

These results illustrate well the way in which a total pressure distortion influences all conditions within a machine, and also the detailed description of conditions within the flowfield that is obtained from the computer program.

Distortion Decay Rates in Compressor Inlets

Earlier simplified formulations of small perturbation solutions for a two-dimensional (blade-free) space had clearly indicated that an exponential decay should be expected for quantities such as pressure gradient, velocity and angle, as one moved upstream from the compressor front-face toward the upstream boundary. It was early recognized in some of the cases investigated that the results being obtained with completely converged solutions did not conform, in this regard, to expectations. An investigation was made, and the results were sufficiently interesting so that explicit attention directed toward them seems warranted.

Figures 11, 12, and 13 display respectively the absolute flow angle, the tangential velocity, and the circumferential pressure gradient upstream of a contemporary, high Mach number, compressor. The two "sectors" which are shown lie on the edges of the stagnation pressure deficit region. The mean-line computer program has been used to analyze two cases:

1. A cylindrical inlet with a mean axial velocity of 662 ft per sec.
2. A flared inlet with a mean axial velocity of 273 ft per sec at the screen and 662 ft per sec at the face of the compressor.

In both cases the boundary conditions at the screen stipulate a uniform flow angle of zero and a 7 per cent stagnation pressure deficit over a 108 deg region; downstream of the compressor, both cases assume the same uniform value of static pressure.

Also displayed is the result of a mathematically explicit, small, perturbation analysis of an incompressible distorted flow in the flared inlet. The boundary conditions at the screen are the same as above, and at the downstream end of the inlet the boundary condition stipulates the circumferential static pressure gradient (at the face of the compressor). Thus, with the exception of a slight discrepancy in the static pressure distribution at the face of the compressor, this analytical solution is an idealized, incompressible analogue of the flared inlet case so long as attention is limited to the region upstream of the compressor.

The flow angle graphs for the cylindrical inlet case display the exponential decay which is expected. For the flared inlet, however, both the compressible and the incompressible solutions yield a counter-intuitive convex shape. An examination of the tangential velocity figure indicates that this convex shape is not explained simply by the variation of the mean axial velocity since the same counter-intuitive convex shape appears (to a lesser extent) for tangential velocity.

The pressure gradient (Figure 13) is more helpful. Specifically it shows that for a short, flared inlet the requirement of a uniform flow angle at the screen implies that the static pressure gradient does not decay uniformly upstream of the compressor. The correctness of the boundary condition may thus be questioned. On the other hand, the fact that the mathematically explicit incompressible solution requires a large static pressure gradient at the screen to satisfy the flow angle boundary condition does indicate a significant qualitative difference in the "decay length" between the cylindrical and the severely flared inlets.

In short, therefore, the investigation discussed above indicates clearly that the exponential decay which is characteristic of the cylindrical duct (especially one for which the upstream boundary is taken to be at upstream infinity) shifts to a considerably more complicated pattern for short, flared inlets. This conclusion is questionable only to the

extent that the assumed uniform angle upstream boundary condition affects the answer; its influence will not change anything but the precise quantitative pattern.

CONCLUSIONS

A method of predicting the performance of axial compressors operating under non-uniform inlet conditions has been presented, and shown to be sufficiently accurate to be of practical value. It does rely upon a knowledge of the characteristics of the blade sections of which the machine is composed, and is therefore limited in application to machines using conventional blade types for which data are available.

By using this tool, it should be possible to compare different compressor designs for use in projected distorted-flow situations, and hence select the most appropriate design for any application. Also, of course, an indication of the effect of distortion upon the machine's performance will be available from the design stage onwards.

Interest has been shown in deriving general distortion indices to permit simple overall predictions of the effects of distortion patterns on the performance of compressors to be made. By systematically investigating stages of various types with various distortion patterns, this end may be achieved. In any case, the sensitivity of various types of design to various distortion patterns could be established and catalogued.

ACKNOWLEDGMENT

The authors wish to acknowledge the participation of Mr. G. E. Smith, Senior Engineer, Northern Research and Engineering Corporation, in this project. Mr. Smith developed the small perturbation solution incorporated into the method, and assisted in the interpretation of various results obtained whilst the method was being developed.

REFERENCES

1. Novak, R. A., Hearsey, R. M., and Smith, G.E.: Model for Predicting Compressor Performance with Combined Circumferential and Radial Distortion - Basic Theory and Model Description. AFAPL-TR-68-142 Part VII. Air Force Aero Propulsion Laboratory, Wright-Patterson Air Force Base, Ohio.
2. Novak, R. A., Hearsey, R. M., et al: Model for Predicting Compressor Performance with Combined Circumferential and Radial Distortion - Computer Program. AFAPL-TR-68-142 Part VIII. Air Force Aero Propulsion Laboratory, Wright-Patterson Air Force Base, Ohio.
3. Novak, R. A., Hearsey, R. M., et al: Model for Predicting Compressor Performance with Combined Circumferential and Radial Distortion - Computed and Experimental Results. AFAPL-TR-68-142 Part IX. Air Force Aero Propulsion Laboratory, Wright-Patterson Air Force Base, Ohio.
4. Jansen, W. and Moffat, W. C.: The Off-Design Analysis of Axial-Flow Compressors. A.S.M.E. Paper No. 66-WA/GT-1. 1966.
5. Jansen, W.: The Application of End-Wall Boundary-Layer Effects in the Performance Analysis of Axial Compressors. A.S.M.E. Paper No. 67-WA/GT-11. 1967.
6. Seyler, D. R. and Smith, L. H. Jr.: Single Stage Evaluation of High Mach Number Compressor Rotor Blading. Part 1 - Design of Rotor Blading. NASA CR-54581. National Aeronautics and Space Administration. 1967.
7. Robbins, W. H. and Glaser, F.: Experimental Investigation of the Effect of Circumferential Inlet Flow Distortion on the Performance of a Five-Stage Axial-Flow Research Compressor with Transonic Flow in All Stages. NACA RM E57J17. National Advisory Committee for Aeronautics. 1958.

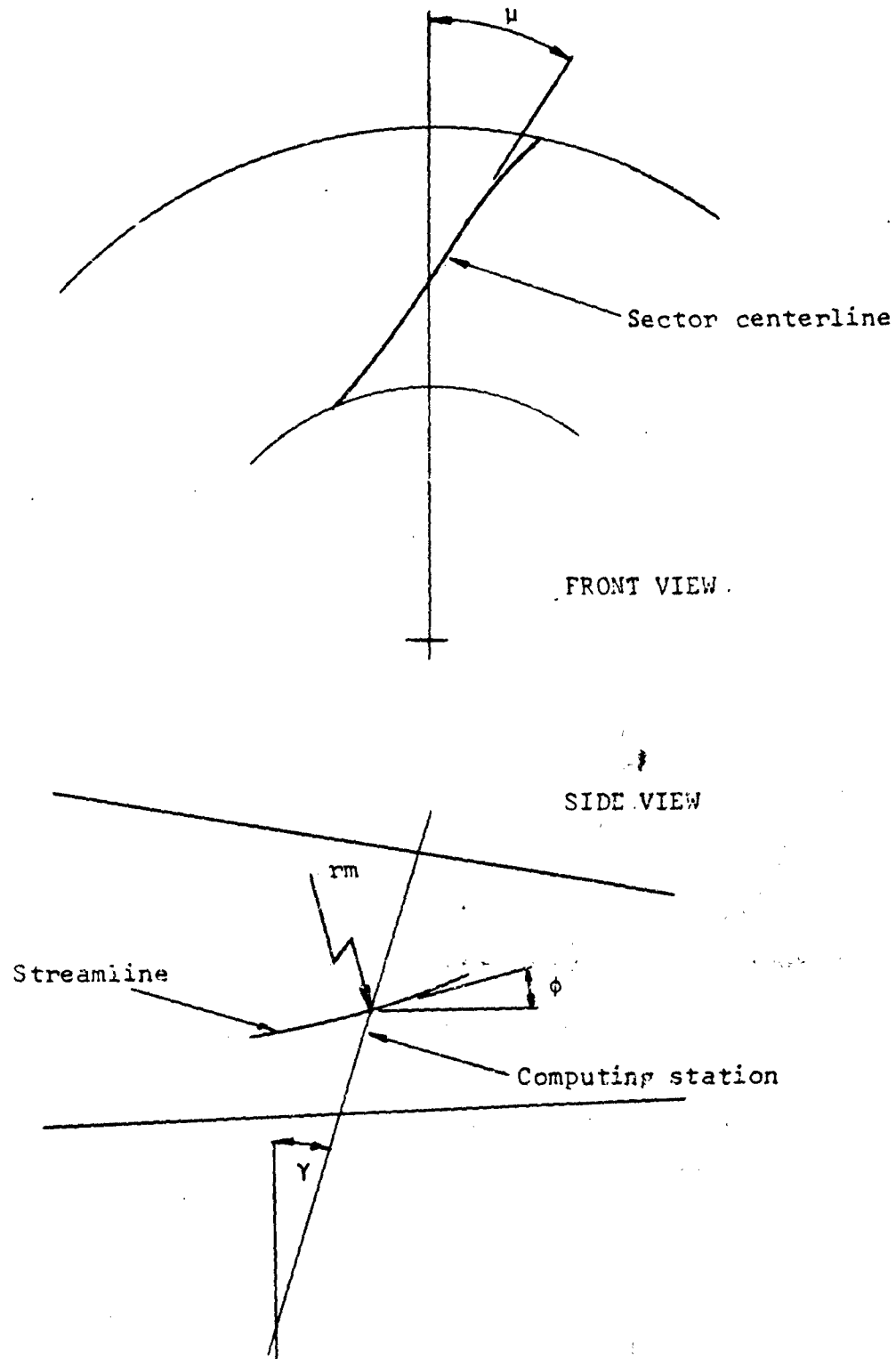


FIGURE 1. GEOMETRY OF TYPICAL COMPUTING STATION

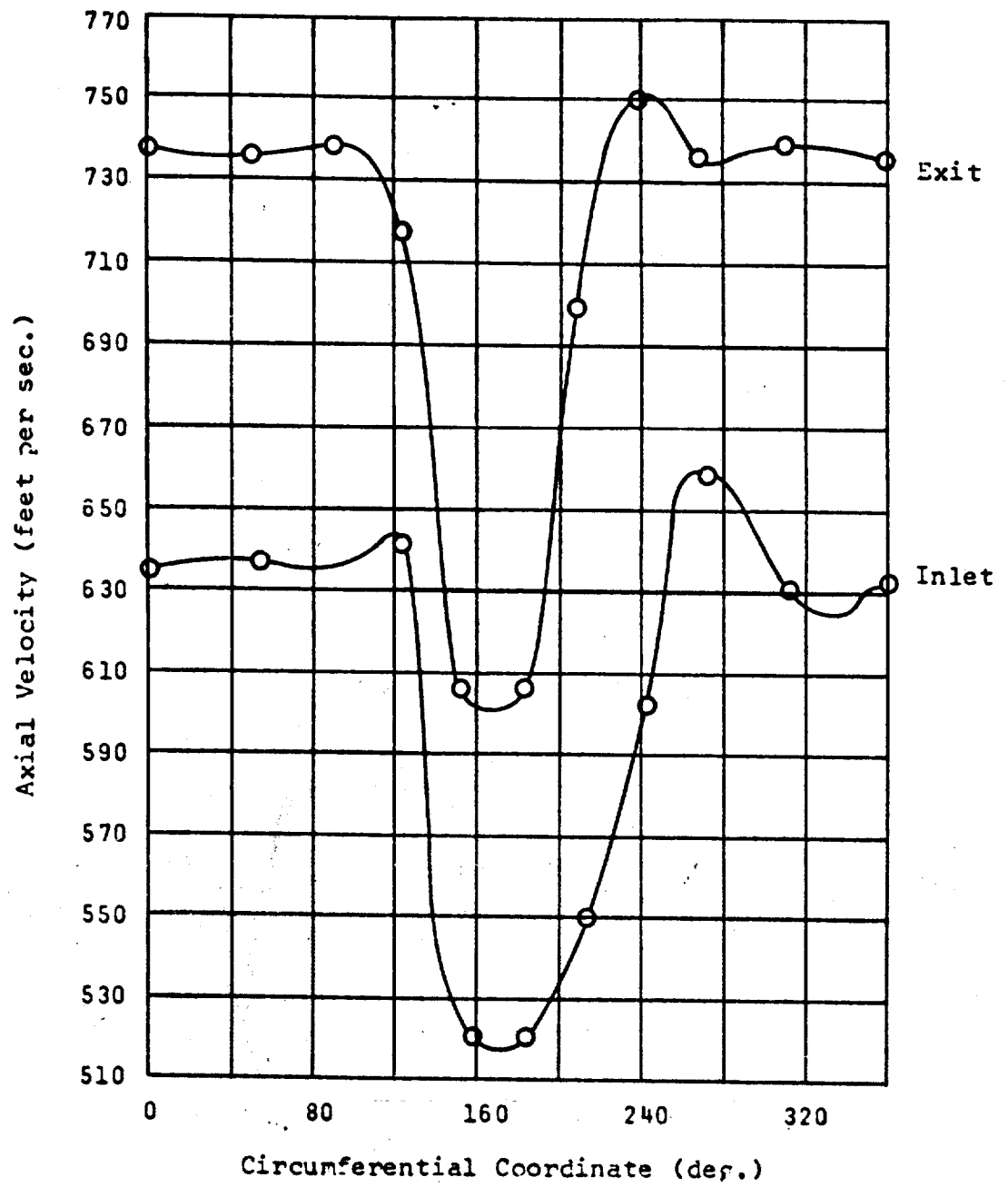


FIGURE 2. COMPUTED AXIAL VELOCITY DISTRIBUTIONS FOR NASA/CE Rotor 1B

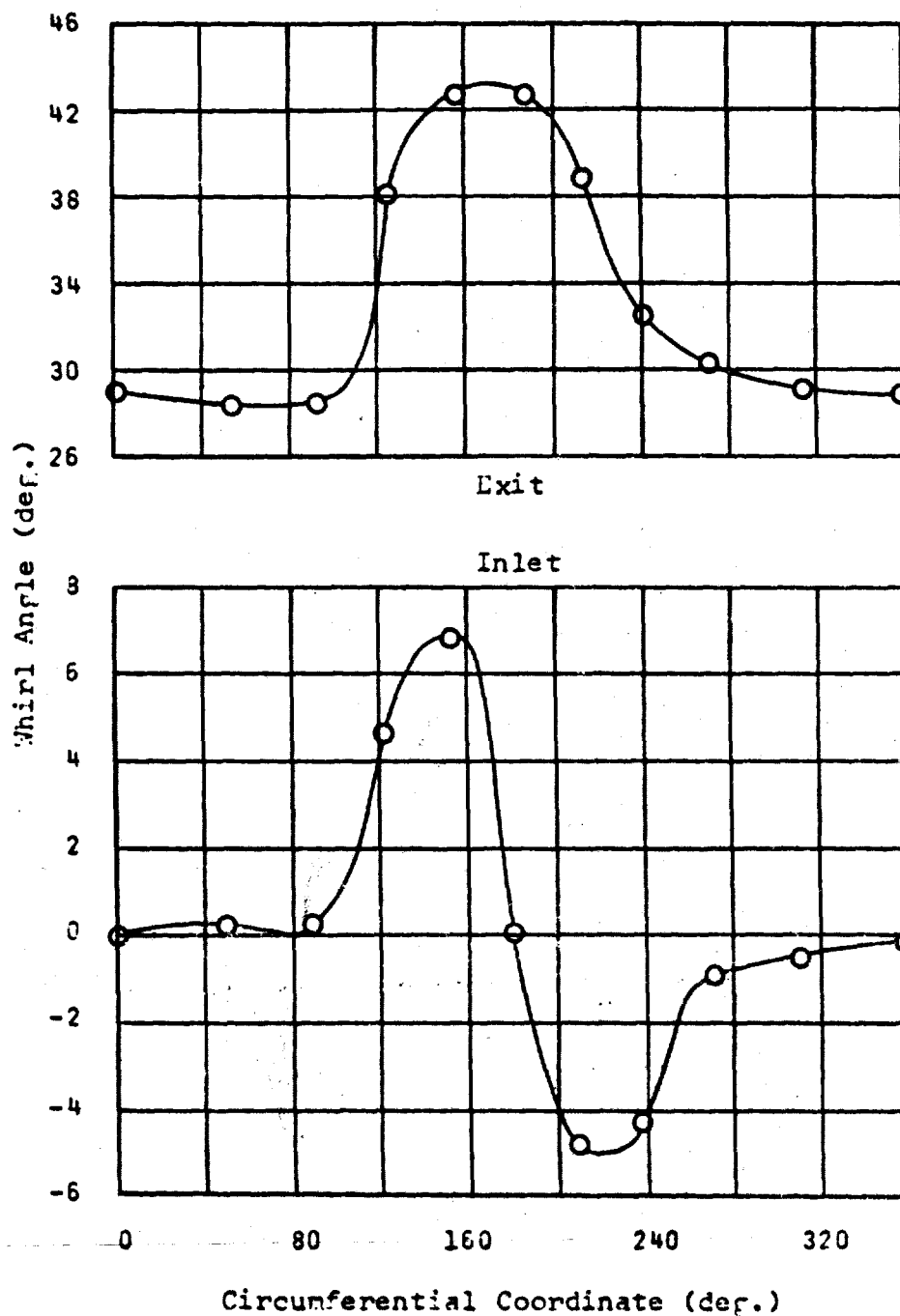


FIGURE 3. COMPUTED WHIRL ANGLE DISTRIBUTIONS FOR NASA/GE ROTOR 1B

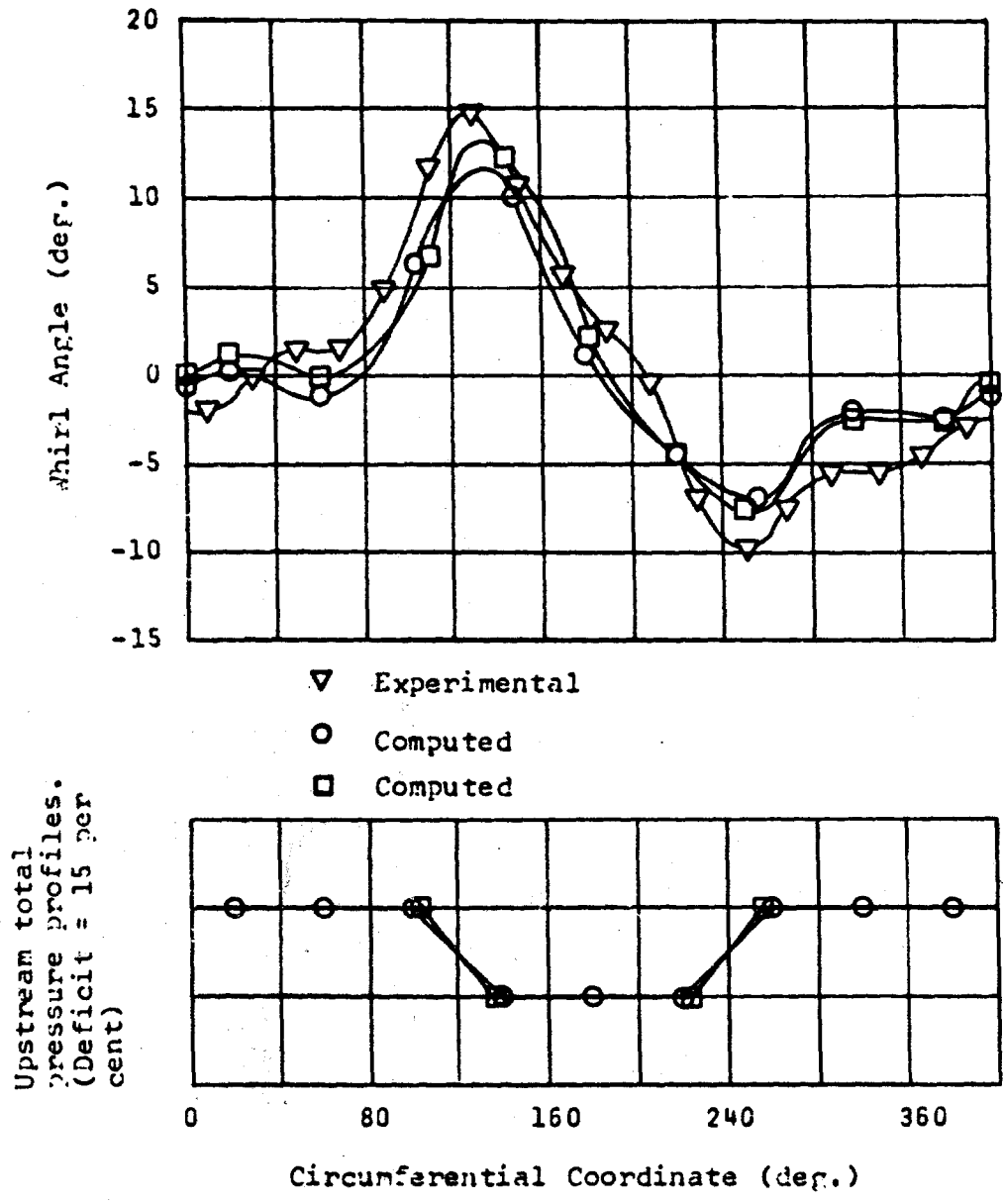
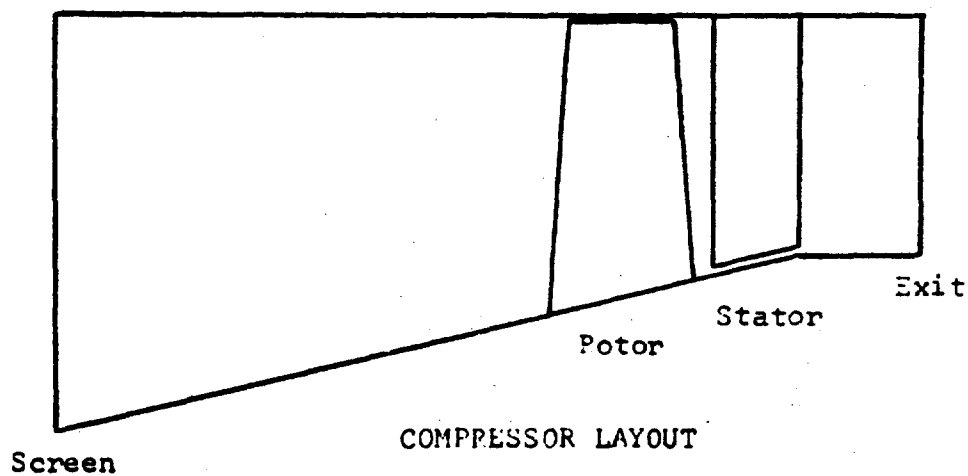


FIGURE 4. INLET WHIRL DISTRIBUTIONS FOR NACA FIVE-STAGE COMPRESSOR



COMPUTED OVERALL PERFORMANCE

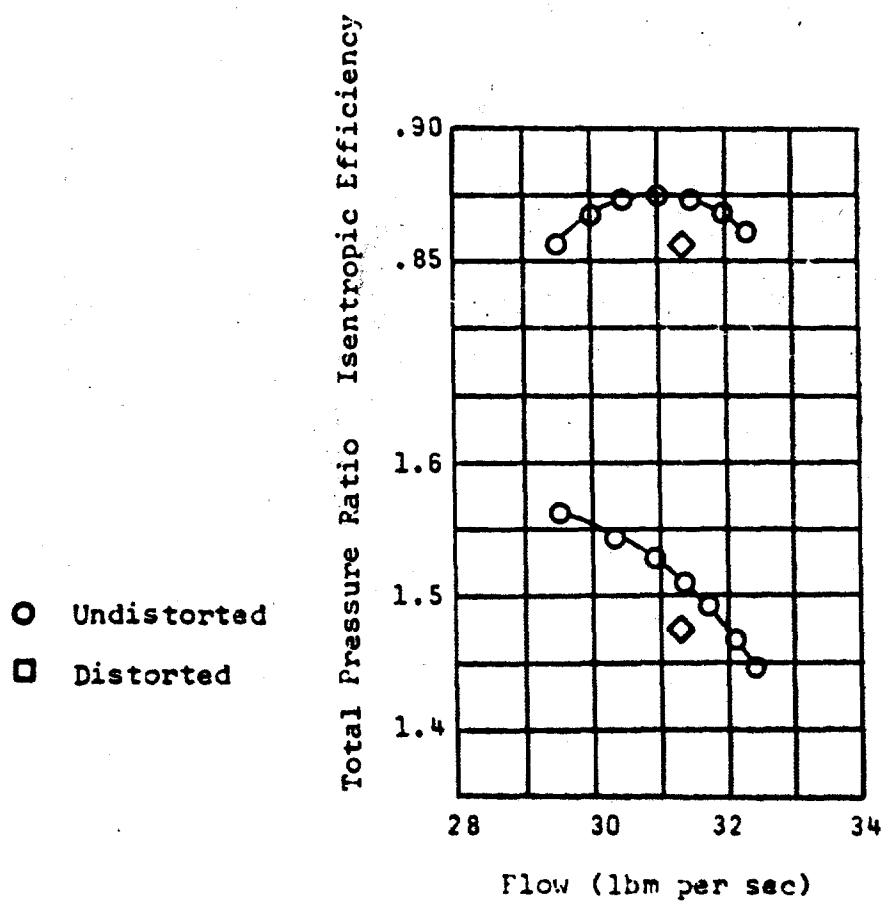


FIGURE 5. LAYOUT AND OVERALL PERFORMANCE OF NREC SINGLE STAGE

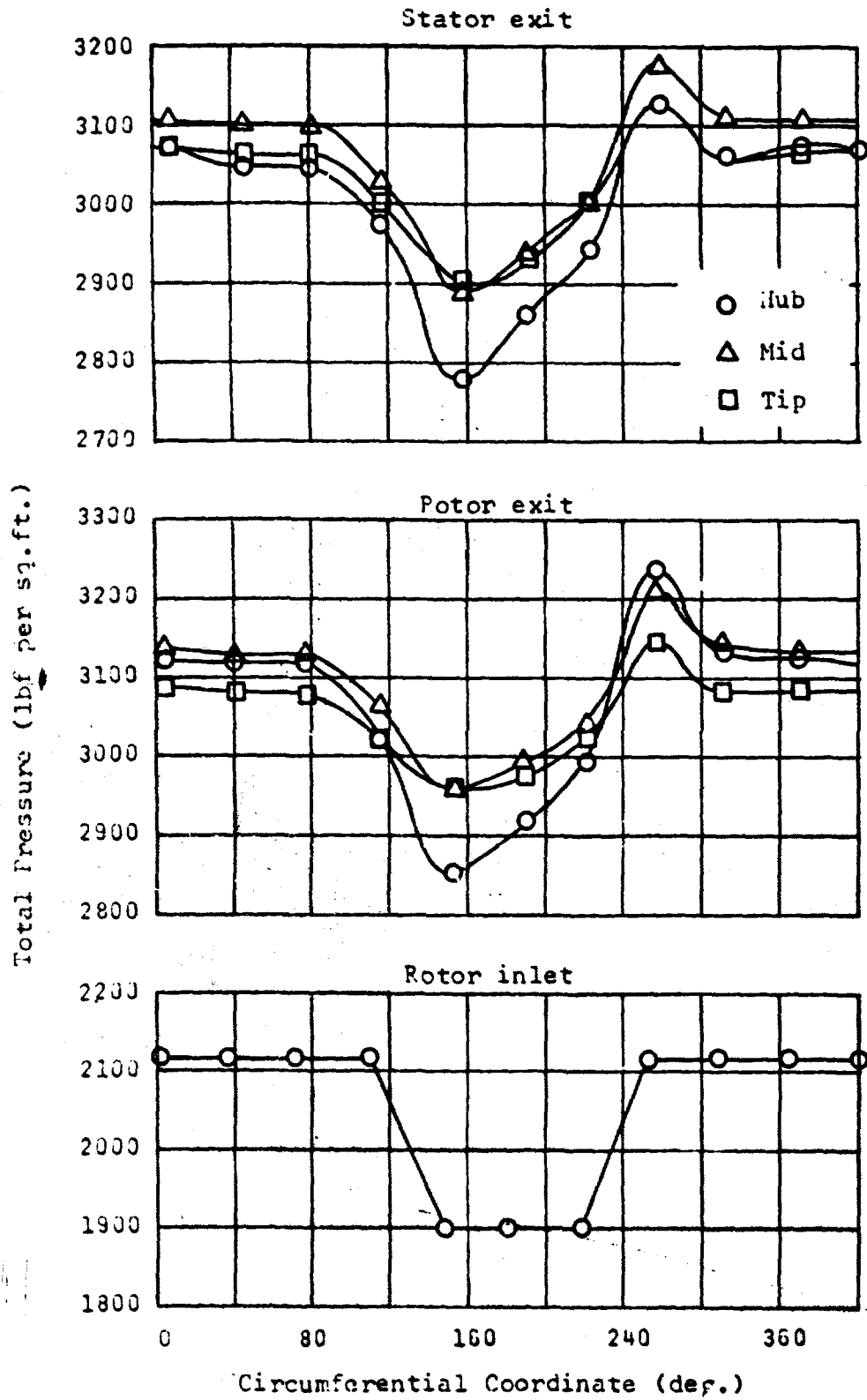


FIGURE 6. TOTAL PRESSURE DISTRIBUTIONS FOR NREC SINGLE STAGE

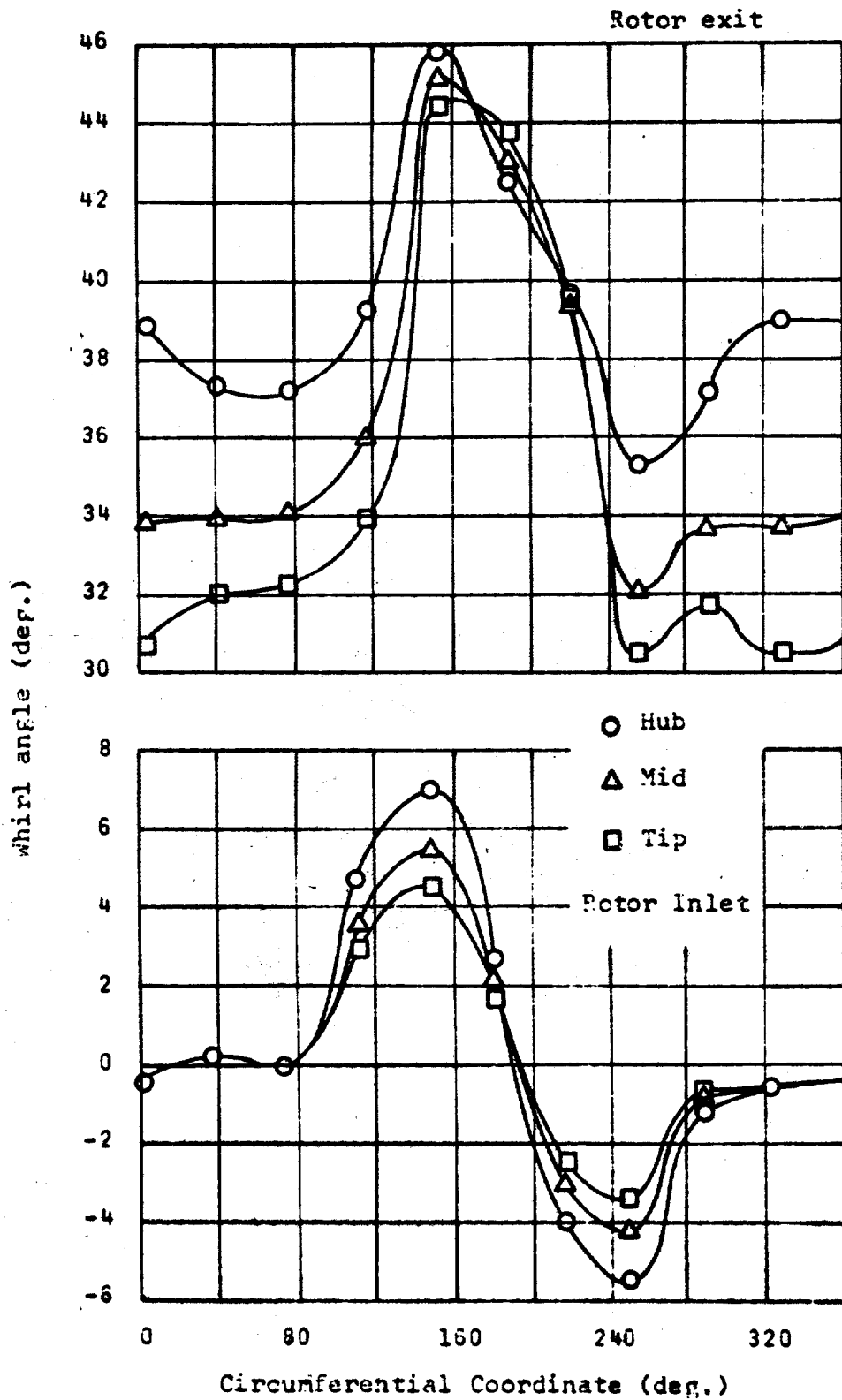


FIGURE 7. WHIRL ANGLE DISTRIBUTIONS FOR NREC SINGLE STAGE

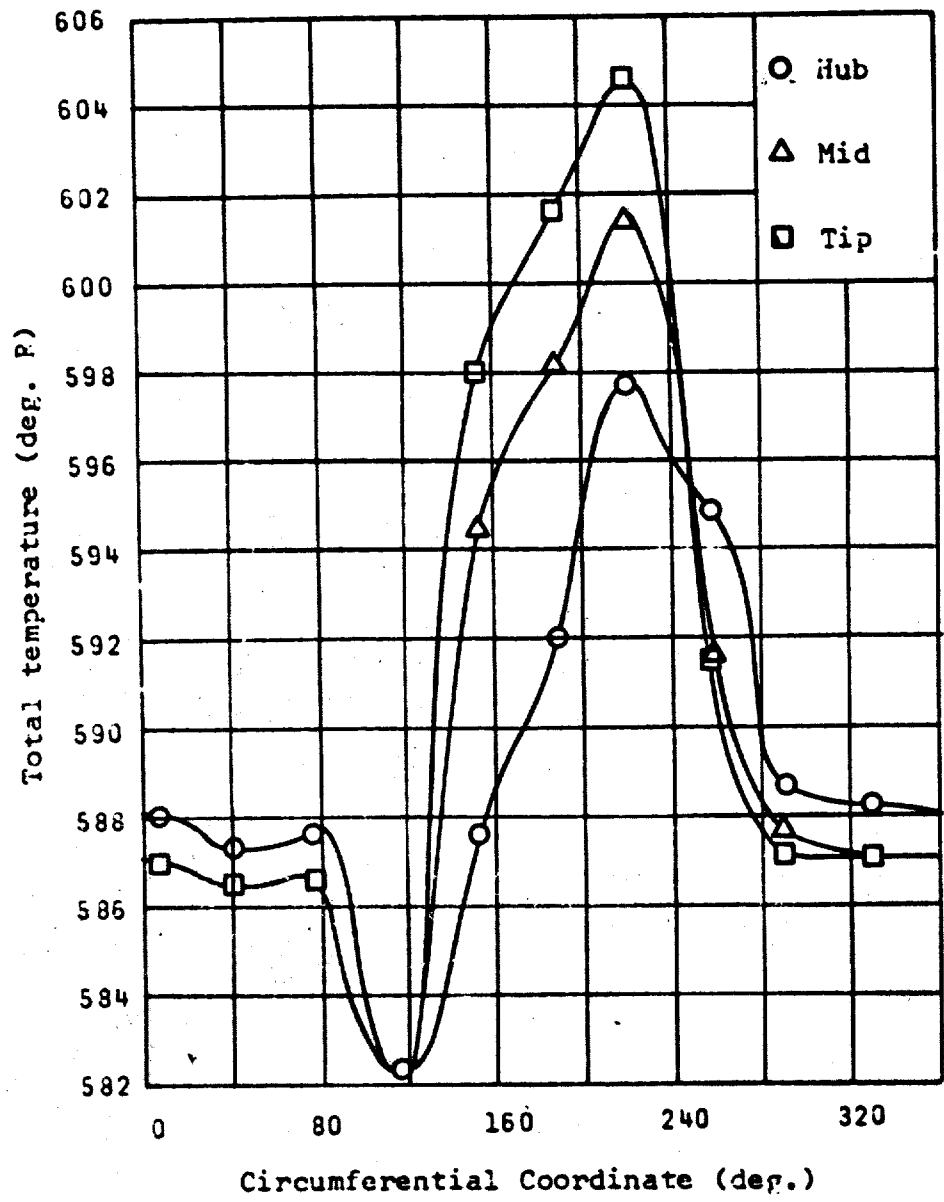


FIGURE 8. TOTAL TEMPERATURE DISTRIBUTIONS FOR NREC SINGLE STAGE

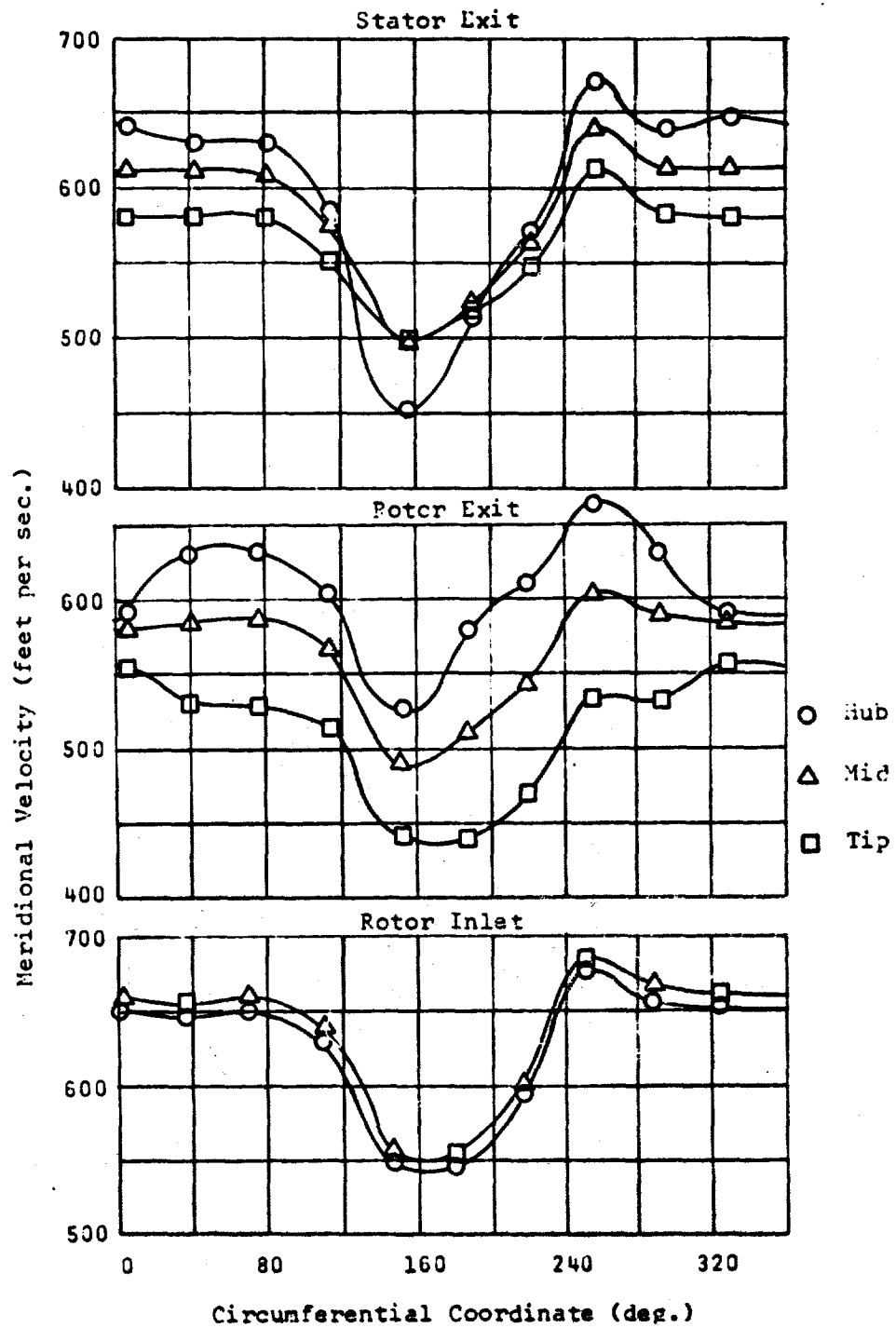


FIGURE 9. MERIDIONAL VELOCITY DISTRIBUTIONS FOR NREC SINGLE STAGE

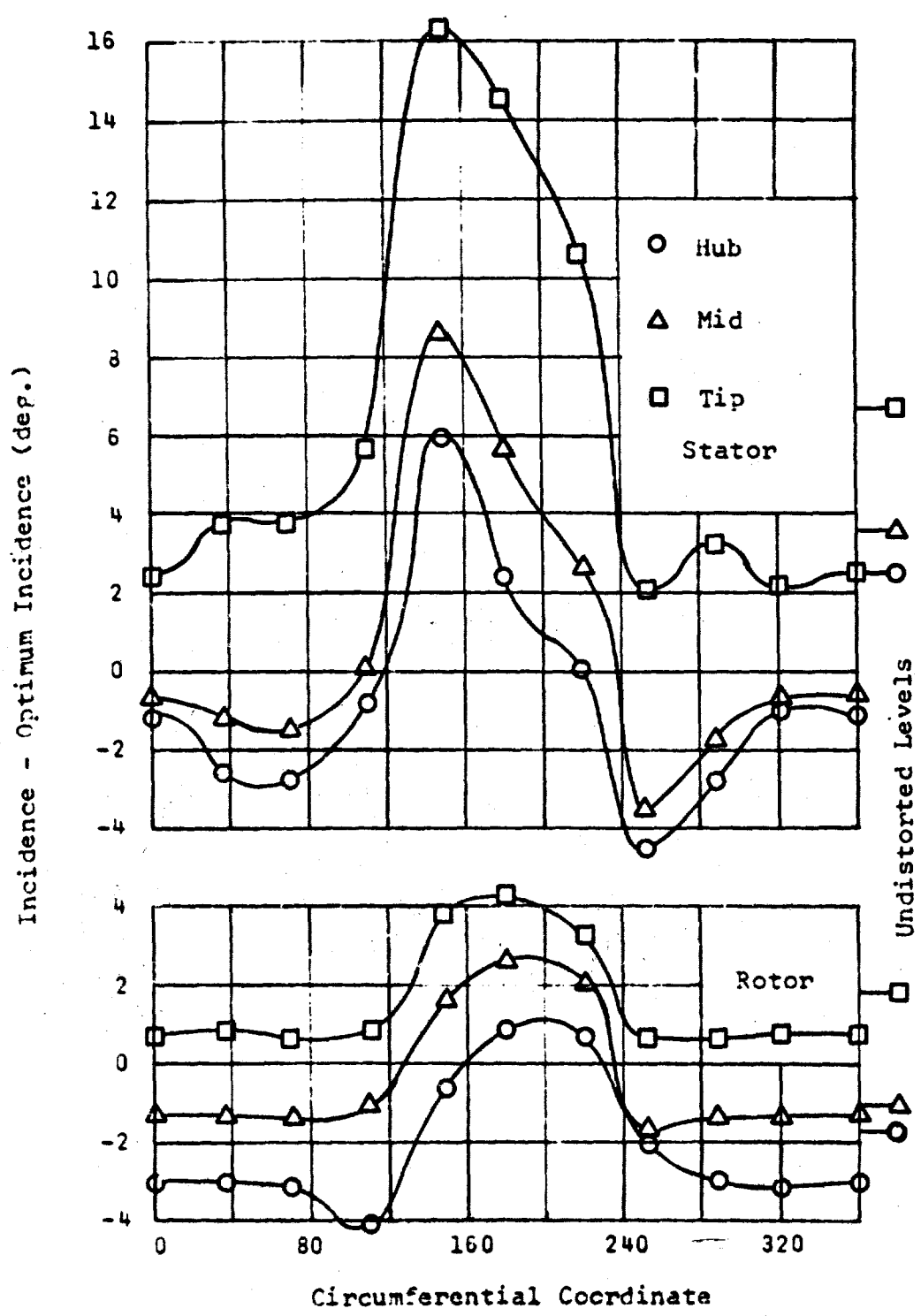


FIGURE 10. INCIDENCE ANGLE DISTRIBUTIONS FOR NREC SINGLE STAGE

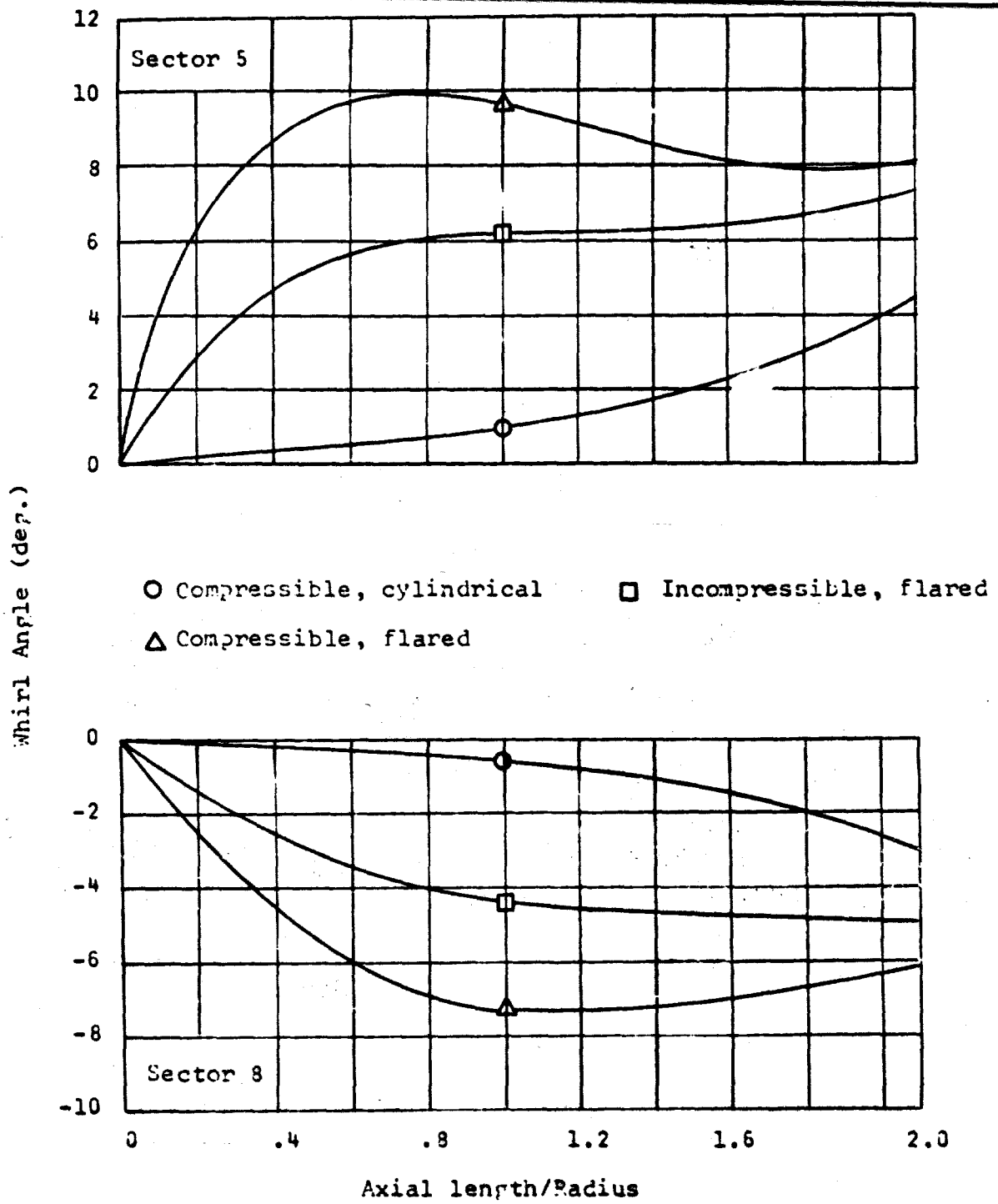


FIGURE 11. WHIRL ANGLES IN COMPRESSOR INLET DUCTS

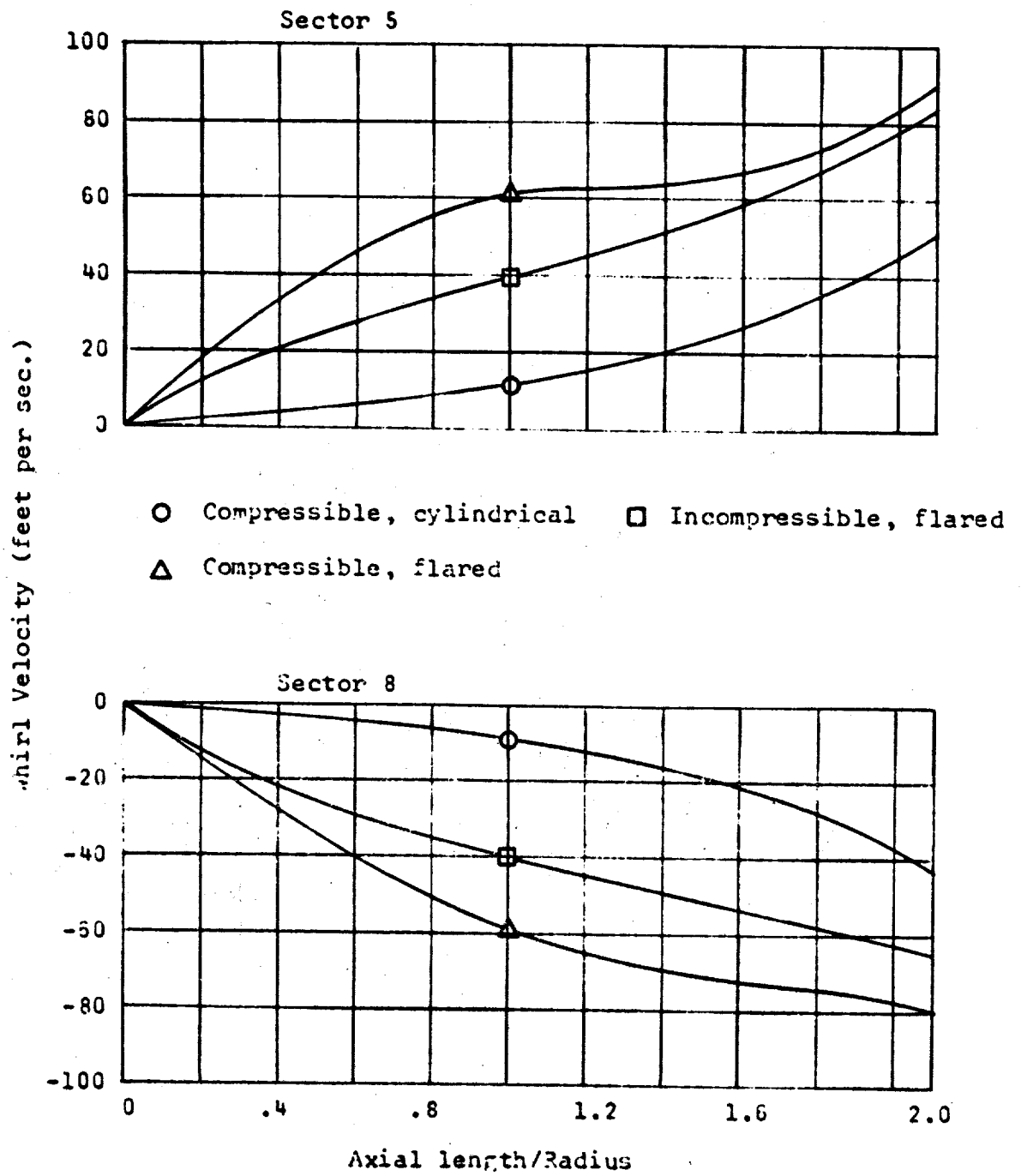


FIGURE 12. WHIRL VELOCITIES IN COMPRESSOR INLET DUCTS

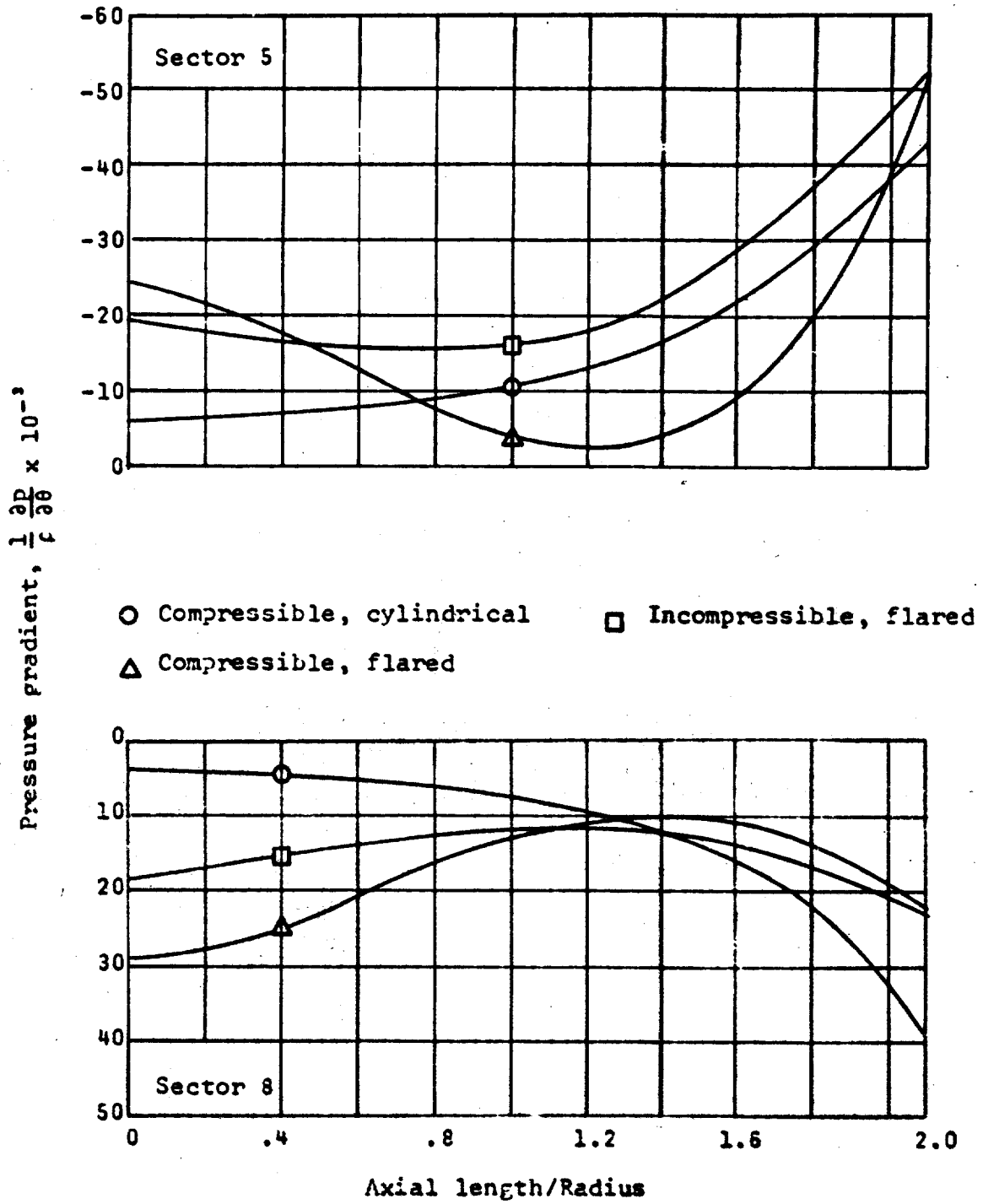


FIGURE 13. CIRCUMFERENTIAL STATIC PRESSURE GRADIENTS IN COMPRESSOR INLET DUCTS

**INLET-ENGINE CONTROLS AND AIRFRAME PROPULSION
COMPATIBILITY MANAGEMENT**

Major, J. R. Nelson, USAF, Chairman

Air Force Aero Propulsion Laboratory

SESSION V. CONTROL ASPECTS FOR PROPULSION INSTALLATION

C. E. Bentz, Cochairman

CRITERIA FOR A TURBINE ENGINE
CONTROL SYSTEM DEVELOPMENT MODEL

Stephen J. Przybylko

Air Force Aero Propulsion Laboratory
Turbine Engine Division
Performance Branch
WPAFB, Ohio

ABSTRACT

The utilization of solid state electronics and the achievement of inlet and engine compatibility are producing significant advancements in turbine engine control technology. This rapid evolution necessitates the establishment of specific goals and demonstration principles to minimize system development risk. This paper discusses various aspects of control systems and their development. Questions regarding hardware credibility and engine performance are raised along with the need to establish criteria to be applied to the concept of demonstration. The role of analog and digital computer dynamic analysis during the entire development cycle is discussed for a fully integrated inlet and engine control system. Considerations for timing and various milestones for system development from the exploratory stage through Preliminary Flight Rating Test are presented.

INTRODUCTION

The modern augmented turbofan engine is continuing to require more sophisticated control systems as has been the trend since the early development of the turbine engine. For the most part, these requirements were brought upon by the performance requirements of the engine in terms of thrust and fuel consumption over specific mission profiles. For the next generation of military aircraft, the requirements will be further expanded to provide stable inlet and engine operation during aircraft maneuvers and other adverse airflow transients. To accomplish this function an integrated inlet and engine control system will be required.

Since the trend is toward more computational sophistication it is very probable that controls designers will want to employ electronics to provide an integrated inlet and engine control system. Since we appear to be on the threshold of a new revolution in control hardware and performance, it is mandatory that a lesson learned from past experiences be employed. Over the years, certain attempts to introduce new control technology met with failure. Others experienced severe problems late in the development cycle. In many cases, ultimate success has proven that developmental procedures were more in error than the choice of basic technology. The procurement and development policies which have evolved since then are intended to prevent such mistakes and require the establishment of orderly system development procedures which filter down to the component level. To this end it is well to establish a development model specifically applicable to control systems.

THE PROBLEM

The challenge of inlet and engine compatibility is not new, but the application of augmented turbofan engines in highly maneuverable aircraft puts the achievement of inlet and engine stability at the top of the development list. A better understanding of the problems can be obtained by considering the effects of an aircraft maneuver on the operation of an inlet and engine system. Shown in Figure 1 is a plot of inlet operating lines in terms of pressure recovery and physical airflow for various angles of attack at constant aircraft Mach number. The two radial lines are lines of constant corrected airflow and represent the engine's airflow requirements at idle and military thrust settings. As shown, a throttle chop can be successfully performed during level flight with the inlet operating between its limits of high distortion and buzz. However, if simultaneously a pitch-up maneuver is performed, the higher angle of attack changes the inlet's operating line such that it is driven beyond its buzz limit as the engine tries to achieve its idle airflow. At extremely high angles of attack, the inlet will buzz regardless of power setting. One solution is to reschedule the engine's airflow with changes in aircraft angle of attack. Other parameters, such as aircraft Mach number, will also have to be considered. Thus is created the need for additional control system sophistication and a comprehensive well-coordinated development effort with inlet and engine designers.

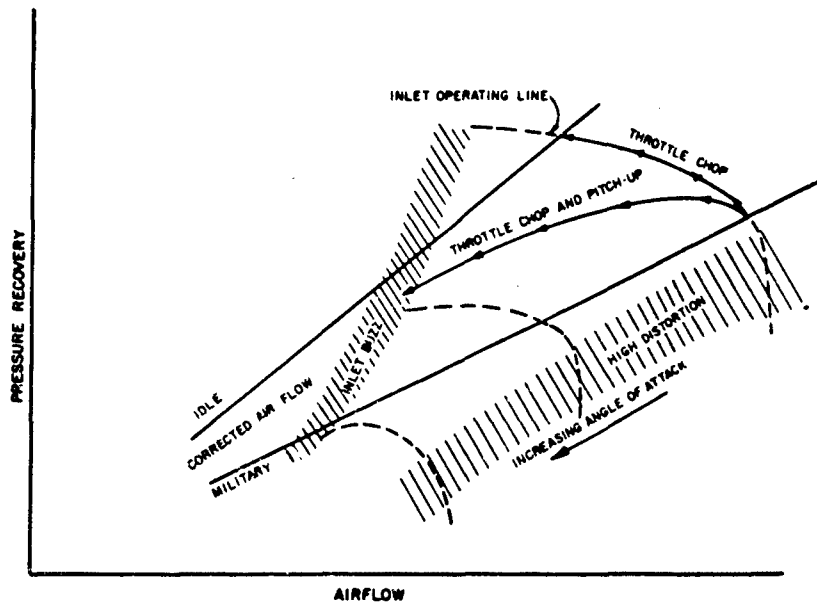


Figure 1 Effect of Aircraft and Engine Transients on Inlet Stability

The demand for greater sophistication coupled with major advances in solid state electronic technology is resulting in greater use of electronics on turbine engine fuel controls. The capability of electronics to provide a great deal of computation and accuracy was recognized years ago. In the early 1950's vacuum tube controls were used on the J47-17/33 and the J57-3/7 engines. Because of severe operational problems the J47 control became known as "the electronic nightmare" and the J57 electronic control was eventually replaced by a hydromechanical unit. The problems experienced during these early attempts to apply electronics created a controversy which still exists today. While no attempt will be made here to resolve this controversy, it is worthwhile to at least consider some of the charges made. It has been said that the basic hardware, vacuum tubes, were to blame. Others claim that they could have been made to work and, in the case of the J47, eventually were made to work. That the parallel development of hydromechanical controls surpassed electronics and became more attractive on their own merit is claimed by others. There are many such claims but one fact stands out. After the J47 and J57 electronic control experiences, the utilization of vacuum tube electronics almost ceased. This is illustrated in Figure 2 which compares the relative complexity of electronics on engine controls. A comeback supported in general by the use of magnetic amplifiers has occurred in the ensuing years. Advanced augmented turbofans today employ solid state electronics with at least as much authority as the electronic control on the J47. These controls are basically hydromechanical controls with the electronics performing a supervisory function.

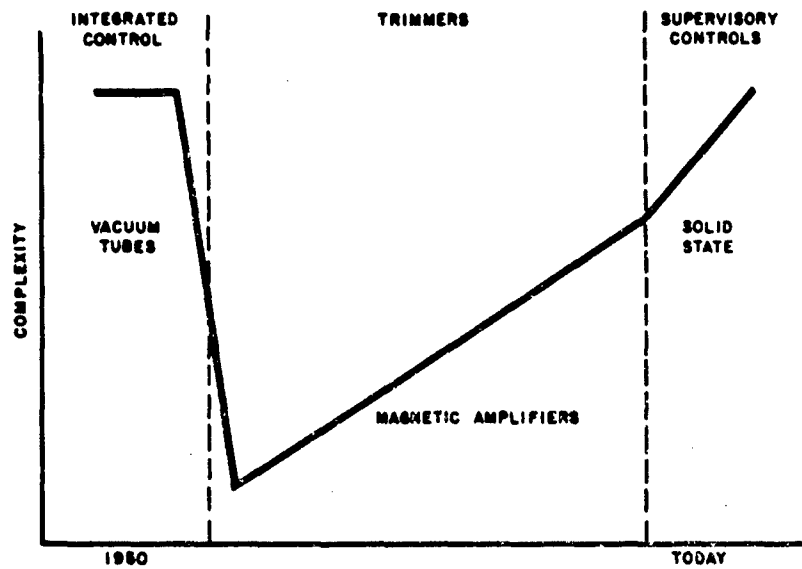


Figure 2 Electronic Controls

The problems experienced with the vacuum tube controls are cited here only as an example of severe problems due to novel control hardware. It is suggested that poor developmental planning was a significant contribution to the problems experienced. With the upcoming demand for inlet and engine compatibility and the utilization of new solid state hardware, it is extremely important to apply proper development principles to insure adequate demonstration before committing new controls to production.

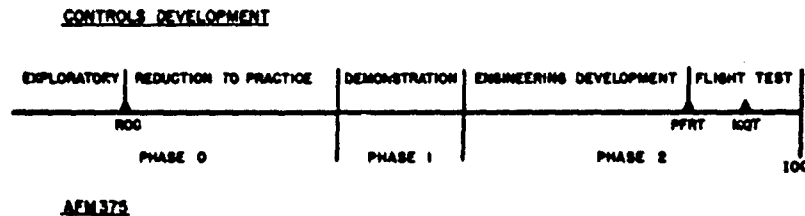


Figure 3 Ideal Development Cycle

THE DEVELOPMENT CYCLE

It is appropriate to relate any discussion of the orderly development of control technology to the basic procurement policy established in AFM 375. Shown in Figure 3 is a suggested relationship between the two. This relationship is idealized for the development of new technology. At various points along the development of control systems, there exists certain criteria which must be satisfied before any new aspect of control technology is allowed to undergo any further development. These criteria are quite nebulous at first but become better defined as development progresses until finally the control is qualified according to specific tests outlined in a Military Specification. The three phases of AFM 375 are as follows:

Phase 0 - This phase consists of basic technology development not yet specifically earmarked for a particular weapons system. At some point during this phase, a Required Operational Capability (ROC) is established. This becomes the first clue as to the ultimate configuration of a weapons system. This phase can be divided into two phases for control development as shown in Figure 3. Before the ROC is established, the control technology would be in the exploratory stage where basic invention and feasibility demonstrations occur. With the establishment of the ROC, the control components or techniques move into a period where their ultimate utility is established. During this period, controls are developed to meet the requirements of some sort of engine cycle or aircraft mission. Turbine inlet temperature sensors, stall sensors, and adaptive control techniques are particular examples of control components and techniques which are currently in this phase of development.

Phase 1 - Once the Air Force decides on the mission to be performed, the development enters Phase 1. For the purposes of this discussion, Phase 1 is considered to consist entirely of the technical effort. Control system development enters the demonstration phase. Here the basic configuration of the engine is defined and a demonstration engine is built. All aspects of the controls must be demonstrated before the end of Phase 1. Advanced solid state electronic controls and hybrid controls are current examples of this stage of development.

Phase 2 - This is the acquisition phase which ends in Initial Operational Capability (IOC). After the go-ahead the controls are fabricated and the engine undergoes the Preliminary Flight Rating Test (PFRT). During the flight test phase the engine passes its Model Qualification Test (MQT) and then goes into the Air Force inventory. Conventional hydromechanical controls with solid state and magnetic amplifier trimmers currently dominate this area.

DEMONSTRATIONS

Throughout the entire development cycle, there are various demonstrations performed to test a new control technology before further committing it to the next stage of development. DOD directives require all demonstrations to be completed prior to entry into the acquisition phase. The exact interpretation of what constitutes demonstration has been pursued by those involved in all aspects of systems development. A better understanding will be achieved by all if it is realized that various demonstrations occur during all phases and should be planned to provide technological advancement and the reduction of risk. The following is a discussion of the development cycle which attempts to outline the demonstrations accomplished at various stages. This discussion will focus on new technology being developed in an ideal programming environment.

a. Exploratory

As shown in Figure 3, the exploratory stage is the first part of AFM 375 Phase 0. The primary accomplishment during this stage is the invention of new control technology and the demonstration of its feasibility. This is accomplished when the validity of the basic principles are established. New hardware concepts are established using crude breadboards which may run existing engines. New control operating modes may be established solely on an analytical basis using dynamic computer simulations or they may run engines with some sort of flexible or programmable controller.

b. Reduction to Practice

To enter this phase of development, two basic requirements must be met. First there must be a need for whatever the new control technology has to offer, and secondly, the technology should show promise of being further developed and yielding fruitful results. Tied in closely with the former is an overall required operational capability which defines a certain military function to be performed. This provides rough guidelines and can at least define a basic engine configuration and operational extremes which

in turn provide a control designer with sufficient information to establish a development effort closely coordinated with other major component programs in support of the same operational capability.

This phase of development is invaluable in establishing the best operating mode using the most modern control hardware possible for the engine. It allows the results of the general development of the previous exploratory stage to be applied to the control design without necessarily jeopardizing the engine manufacturer's competitive position. Demonstrations are performed with sophisticated breadboards in conjunction with core engines, component rigs, and scale model inlets being simultaneously tested in support of the same overall objectives. Testing should include functional performance at ambient conditions, simulated environmental and inlet distortion testing and special tests for susceptibility to contamination, electromagnetic interference, and nuclear vulnerability.

c. Demonstrator Phase

During the time between the establishment of the ROC and the end of Phase 0, industry has been working on approaches to accomplish a certain military function. With the onset of Phase 1, the contractors narrow their considerations to arrive at a definition of a weapons system and proceed to demonstrate the level of technology required for the system. At the end of the technical effort all contractors submit a design to the Air Force for source selection.

At the start of this phase the engine should be defined specifically. Prior demonstration work should have established the control mode and defined all sensor and effector requirements as well as control schedules. The control must be based upon established design concepts and technological approaches. Basically, demonstrations should establish the ability of flight weight, packaged controls to successfully control an engine of the eventual configuration installed behind the inlet configurations being considered over the flight envelope of the weapons system. The control system should be demonstrated on the demonstrator engine. Hardware approaching prototype stage is a bare minimum requirement with flight weight controls being preferred.

d. Engineering Development

This phase begins with the selection of single sources to produce the various components of the weapons system. An engine manufacturer is selected who in turn selects a control vendor. Events occurring during this phase include modification of the control drawings to reflect production fabrication, production control design release, fabrication of production hardware, development testing of the experimentally fabricated controls, pre-qualification testing, official control qualification tests to MIL-E-5009C, and the Preliminary Flight Rating Test of the engine.

e. Flight Test

This phase begins with the first flight of the aircraft and ends with the release of the first squadron to an operational base. The most significant demonstration for the engine in this phase is its Model Qualification Test.

ANALYTIC DESIGN PROCEDURES

The primary objective of control system dynamic design is to establish an integrated engine-control system whose steady-state and transient performance satisfy the engine application throughout the required flight envelope. Various analytic techniques and tools are available to the systems analysts. One technique is the linear stability analysis conducted with the aid of an analog computer. Using standard servo analysis techniques, the desired transfer function for each control is developed considering the linear engine dynamics and the dynamic interaction of the other controls. This technique is utilized throughout the development of a control, finding its way to the detailed simulation of each and every moving part. As more data becomes available the linear engine model is updated and a non-linear analog model is used. This allows the designer to perform gross engine transients and study the effects of control schedules. Finally, using all the component data available, a comprehensive dynamic digital simulation is constructed. This model allows consideration of ambient conditions and airflow transients and serves as a definition of the stability characteristics of the propulsion system.

The digital computer simulation is the newest analytical tool available to the systems designer. Its major function is to verify the design results obtained from the linear and non-linear analog computer work. There are, however, other aspects of a more broadly applicable sense as far as overall systems development is concerned. The mere fact that the simulation is contained in a box of cards makes it readily transmittable. This greatly enhances an understanding of the dynamic characteristics of various components among the disciplines and companies involved in the propulsion system development. This particular aspect is considered so important that the Air Force requires that an engine manufacturer submit a dynamic simulation of his product. The requirements for this submission are established in an AFLC/AFSC Form 9, "Data Item," and is included in the appendix.

Another important feature of a dynamic computer simulation is that it can be used to establish at any point in time, the current dynamic characteristic of the engine. For example, the dynamic simulation requires component maps. At first these maps are estimated from known component performance trends. However, the ultimate performance estimate of the engine, the whole aircraft for that matter, is dependent upon these estimated maps. These maps also determine the transient and stability characteristics of the engine. As test data becomes available estimates of component performance and the performance and stability characteristics of the engine will change. The maps will be so updated and the validity of the computer model will be enhanced. By requiring that the model be kept updated it serves as a rallying point where all the component designers meet to insure the ultimate stability of the system. For this reason, it is considered important that as soon as an engine cycle is conceived, a dynamic digital computer model be constructed, no matter how crude the estimates of component performance may be.

The Air Force has expended considerable effort to promote the development of dynamic simulation techniques. To insure that the full benefit

of these efforts be realized, it is important to stress the proper utilization of this capability. The greatest benefits can be derived when the dynamic simulation efforts are tied in with the development of the system. Dynamic simulation can reduce development time and can contribute significantly to establish the credibility of an integrated inlet and engine control system design. Except for actual flight tests and full scale inlet wind tunnel tests it is extremely difficult to demonstrate the principles of an integrated inlet and engine control system. During the Phase 1 Demonstrator Program, there is generally no time available to release the demonstrator engine for full scale inlet wind tunnel tests. Nor is the inlet sufficiently defined at this stage. These are two disparities which some day may be rectified, but until then judicious use of dynamic simulation coupled with scale inlet data can help bridge the gap.

Shown in Figure 4 is a schematic of a computer simulation which takes into account the characteristics of the aircraft, inlet, engine, and their control systems. This simulation can be used to study the effects of angle of attack as presented in Figure 1. Just as a dynamic simulation of an engine requires the coordination of the component designers, so does a simulation of an entire system require the cooperation and exchange of data among the aircraft, inlet and engine designers. A system simulation should be constructed early in the development cycle, somewhere in AFM 375 Phase 0, and be continually updated as data becomes available. In Phase 0, inlet data would be provided by small scale inlet wind tunnel tests, large scale inlet tests in Phase 1, and full scale inlet and engine wind tunnel testing accomplished during Phase 2 approximately at PFRT. The simulation should continue to be updated during the flight test phase. After IOC the simulation, if no longer needed, should be kept on file for possible use in conjunction with operational problems associated with age, new weapons, overhaul procedures and aircraft or engine modifications.

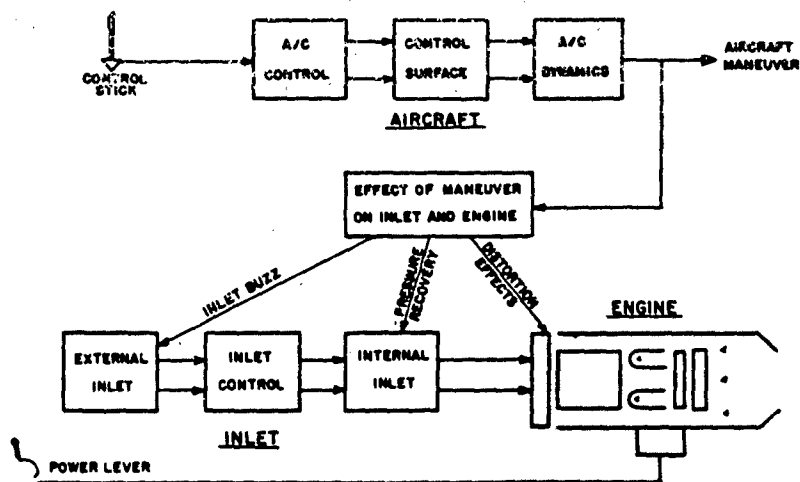


Figure 4 System Simulation

TIMING

Of critical importance to the establishment of a development model is the need to relate the various phases to time. It can be said, at least to a degree, that in the development cycle, time is an independent variable. Certain accomplishments just take time and nature can be very unforgiving if this time is not taken. The following is an attempt to apply a time scale to the development cycle.

AFM 375 - Phase 0

Exploratory - It is virtually impossible to apply a time scale to this portion of the development cycle. Generally a technology will stay in this stage until its feasibility is established or an application is found.

Reduction to Practice - A rough time estimate can be applied to this stage of development. In general, approximately three to five years are required before a contractor feels safe to commit a technology to a demonstrator program.

AFM 375 - Phase 1

Demonstration - This phase, as with the subsequent phase, is determined by contractual commitment. A typical demonstrator program is of one-and-a-half years duration.

AFM 375 - Phase 2

Engineering Development - A typical development program requires approximately two years to pass the Preliminary Flight Rating Test.

Flight Test - From Preliminary Flight Rating Test to Initial Operational Capability approximately two more years are required. During this time the engine passes its Model Qualification Test.

To attempt to place specific milestones within a phase of development is extremely difficult, especially for Phase 0. However, a reasonable approximation of several milestones for Phases 1 and 2 are presented in Figure 5.

According to the timing presented in this model of control system development, it takes anywhere from eight-and-one-half to ten-and-one-half years to proceed from the establishment of a ROC to IOC. This agrees quite well with the timing typically required to develop a new weapons system.

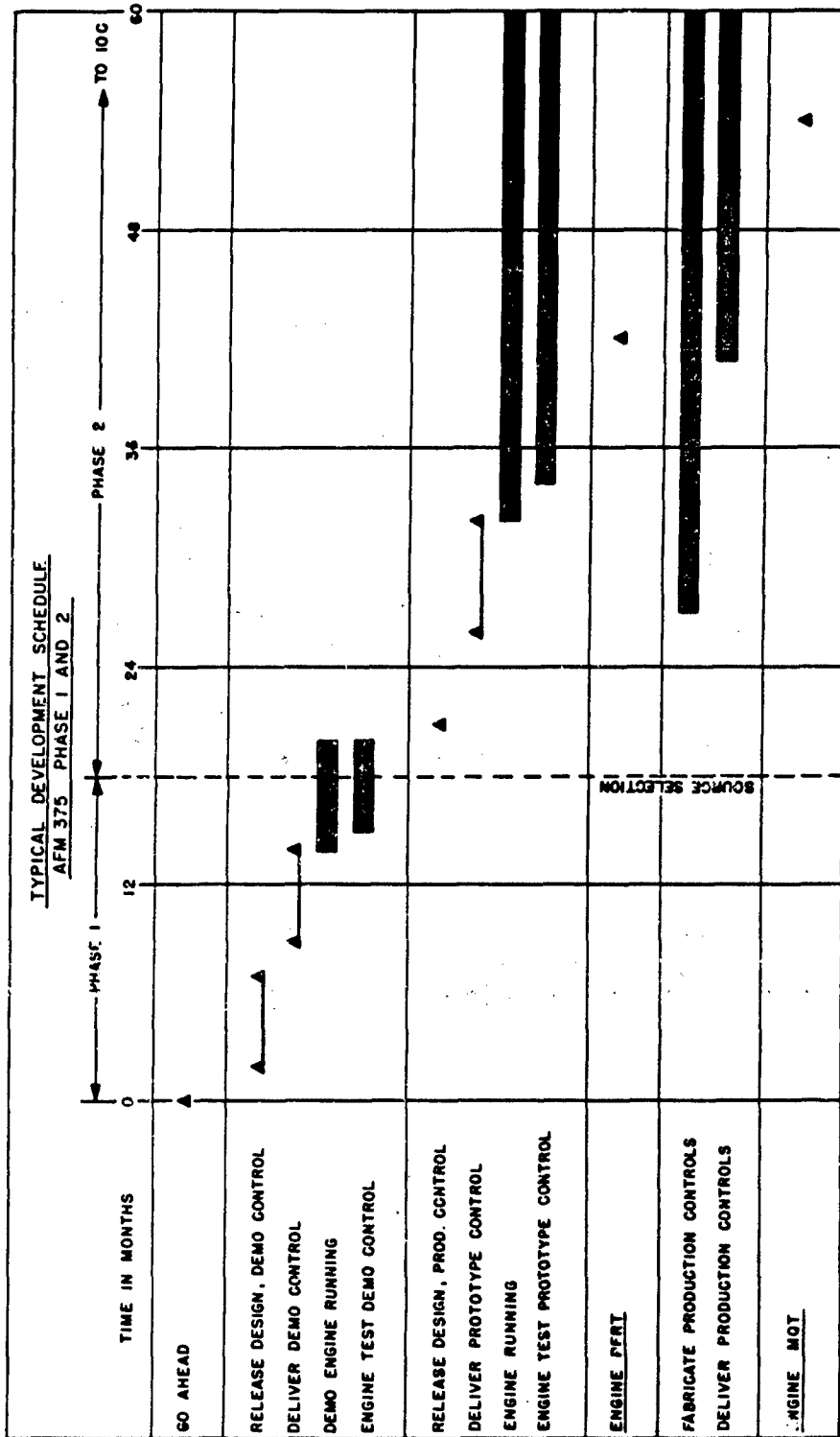


Figure 5 Typical Development Schedule, AFM 375 Phases 1 and 2

CONCLUSION

The development model presented in this paper is only an attempt at establishing the basic ground rules and demonstration principles necessary to insure proper controls development. The relationship between development activities with procurement policies has been suggested with an approximate time scale applied. The time estimates are based upon what experience has shown to be typical to achieve the level of demonstration and visibility required to advance to successive stages of development. An attempt has been made to help establish what these specific demonstration requirements are. This consisted of basically a discussion of at least the considerations which should be employed in laying down the specific requirements. Only with more experience in applying the development principles of AFM 375 will it be possible to be more specific in defining the required degree of demonstration.

APPENDIX

On the following pages is a typical AFLC/AFSC Form 9 which states the requirements for the delivery of a dynamic simulation of an engine.

| | |
|---|--|
| TITLE Electronic Automatic Machine Performance Presentation (Propulsion System Dynamic Performance) | NUMBER |
| PURPOSE This data item will be used to provide a detailed engine dynamic performance representation. | DATE |
| | RESPONSIBLE COMMAND |
| | DDC REQUIRED |
| | APPROVAL LIMITATIONS |
| APPLICATION | APPROVAL DATE |
| | REFERENCES (Non-contractual) |
| PREPARATION The following are the requirements for the dynamic computer simulations: <ol style="list-style-type: none"> 1. General Requirements <p>The model will be programmed and submitted in 'United States American Standards Institute' (USASI), X3.9-1966 FORTRAN. The model will be thoroughly checked-out at the contractor's facility and at least one point will be run at WPAFB to insure compatibility with the WPAFB computer system.</p> 2. Documentation Requirements <p>A user's manual must accompany the model and must include least the following:</p> <ol style="list-style-type: none"> a. A general description of the simulation technique b. A definition of all parameters, including limits c. Input/output instructions d. General operating instructions e. At least one sample case (both input and output) f. General overall model flow chart and detailed flow chart of each component g. Engine station designation diagram h. Graphic component performance maps as used in the program i. Approximate run time and number of lines of output per point | |

3. Model Requirements

a. The model must maintain component identity, i.e., the compressor or turbine or combustor must be identifiable as an entity within the overall model code.

b. The model must include as a minimum the following logic:

- (1) Fan/compressor stall/surge characteristics
- (2) Burner (main/augmentor) blow-out (rich and lean) and light-off characteristics
- (3) Distortion characteristics as they affect the engine components
- (4) Internal/external flow effects on the propulsion system
- (5) Reynolds' Number effects

4. Special Requirements

a. All cycle and control variables must be selectively available at output parameters.

b. The model must operate throughout the entire engine envelope.

c. Time will be the independent variable.

d. All model input parameters must be independently variable and the simulation must be capable of accepting multiple inputs simultaneously.

e. Input must be from data pack only, i.e., compilation will not be required for each different run.

f. The following flight mode options will be included:

- (1) Mach number, altitude and user specified ram recovery
- (2) Mach number, altitude and Mil Spec 5008B recovery selected automatically if not user specified
- (3) Delta temperature ambient combined with (1) or (2) above to provide hot or cold day conditions
- (4) Ambient temperature, pressure and engine face total temperature and pressure

g. In the event both dynamic and steady-state models are required, they should produce results which are within 5% of each other. Also, the input options and parameter definitions will be compatible, i.e., horsepower extraction, customer bleed, power setting, etc.

ANALYSIS FOR SPECIAL ENGINE CONTROLS
REQUIREMENTS FOR UNSTART/RESTART
OF MIXED COMPRESSION INLETS

I. E. Marvin and T. L. Schilling

General Electric Company

ABSTRACT

Test data and dynamic simulation results are presented which identify the special controls considerations for unstart and restart of a mixed compression inlet. Applicable test data is summarized from J93/XB70 tests: to indicate the probabilities for hung stalls, self-clearing stalls and burner blowout; to indicate the special engine "accommodation" requirements for inlet generated distortion and turbulence during inlet restart; and to indicate related requirements for a compatibility test program. Considerations in regard to scaling data are discussed. Digital mathematical models for stalled and unstalled engine are applied to the establishment of control requirements. A general description is provided for engine-in-stall math modeling techniques. Results are discussed for applying simulation to analysis of stall clearing techniques. Controls for an automated restart sequence will in general require the exchange of an interlock signal between engine and inlet controls.

INTRODUCTION

The unstart phenomenon is an important characteristic of inlets which obtain part or all of the supersonic compression internally. The inlet type which employs both internal and external supersonic compression (through an arrangement of oblique shocks) is termed a mixed compression inlet. This type of inlet is favored when overall propulsive efficiency is especially important at flight Mach numbers greater than 2. Unstarts involve an unstable collapse of the internal oblique shocks and this collapse results in a sudden decrease in the inlet compression ratio. Cycle efficiency drops and drag increases. The drop in inlet compression ratio also applies a momentary increase to the loading of the engine compressor (and fan where applicable). An increase in distortion and turbulence is also observed to result from increased shock strength. A buzz mode may develop from the unstart depending on the operating conditions and the design of the inlet. During unstart or an ensuing buzz the engine may stall due to rapid decrease in inlet pressure accompanied with increased levels of distortion and turbulence. A flameout is also a possible consequence of an unstart stall. Buzz suppression and inlet restart should be executed as soon as possible to:

1. Limit stress cycles on inlet and engine.
2. Minimize the possibility of a delayed stall.
3. Stabilize flight attitudes and minimize loss in flight speed and interruption of the mission.

The causes for unstarts and the approaches to minimizing the frequency of their occurrence are not within the scope set for this paper. Discussions of these subjects are readily available in the literature. At the present time the most practical designs for mixed compression inlets admit the possibility for unstarts due to engine transients, wind gusts, aircraft maneuvers, or wakes from other aircraft. The fact that best performance is achieved with small unstart margin is a factor which contributes to the probability that unstarts will not be eliminated.

Some examples presented in this paper were generated by using computer math models developed for the GE4 (SST) engine program; this paper must not, however, be construed to represent SST designs or design criteria. The design considerations are discussed for the recognized potential problems and design options which should be considered early in any development program involving a turbine engine and a mixed compression inlet. Design choices for controls will vary in particular cases depending on realized characteristics of engine and inlet and on the particular design criteria evolving from mission, airplane and controls state-of-the-art.

PROBLEM DEFINITION

Variable geometry requirements and inlet controls approaches to restart are discussed in a number of available publications. References 1, 2 and 3 are among the most recent of these. Relatively neglected in the known publications are engine considerations which affect the restart control requirements. These requirements must provide for the various possible engine states:

1. The engine may have a sustained stall resulting from the unstart.
2. The main burner may have flamed-out.
3. An engine transient may be impending, e.g. a relight of the augmentor or an RPM recovery.
4. Recurring stalls may be generated by an engine-inlet loop, e.g. stall recovery may cause another stall by way of the sudden flow increase (leading to highly supercritical inlet operation).

There is a rather respectable body of evidence that supports our concern for these possibilities. The J93 engine had a stall margin which ranged from 23 to 28 percent (military and A/B) over the Mach number range of 2.6 to 3.0 (Std. day T_0) yet testing provided the following experience:

1. Reference 4 summarized unstart-stall experience for XB70 flight testing. Of the 26 inlet unstarts which were obtained at flight Mach numbers of 2.7 or more, 8 encountered engine stalls.
2. Of the stall cases cited above, pilot action was required to clear 3 of the stalls. Reference 4 concluded that all three of the engines in a duct stalled at least once when any one of them stalled. This indicates that more than 24 stalls were logged and 1/8 or less of those were not self-clearing.
3. There were no mainburner flame-outs in the J93/XB70 flight program, but afterburner flameouts were observed twice during unstarts. A/B flameouts occurred only where the afterburner was operating at high augmentation ratio at the time of unstart. A/B relights occurred automatically.
4. AEDC windtunnel testing of the J93 and a .577 scale (1/3 airflow) model of the XB70 inlet produced mainburner flameouts at a frequency of about 1 in 10 for unstarts at Mach numbers above 2.6. Of the 6 flameouts noted, 5 were associated with buzz. Buzz increases the number of opportunities for stalls and blowouts. Abnormally high backpressure on the engine exhaust nozzle was required for the AEDC tests and this may have contributed to deeper stalls and increased flameout probability.

Unpublished results of NASA engine-inlet testing with the GE J85-13 show much higher probabilities for both stall and mainburner flameout during unstart at Mach 2.5. This inlet is described in References 3 and 5 as having: a design Mach number of 2.5, 60 percent of the supersonic flow contraction internal, a total length from cone tip to compressor face of 3.86 cowl lip diameters, and at design conditions a subsonic flow path length of about 2 cowl diameters to the engine face. The J85 has a stall margin of about 30 percent (according to data in Reference 1) at the 85 percent corrected speed associated with the unstart observations. Particular emphasis is attached to the relative length of the duct because of the influence this has on the transient loading of the compressor. A progression in degree of transient loading is hypothesized as the principal factor for the progressive increase in stall and flameout probabilities in the sequence: full scale XB70, .577 scale XB70 and the inlet for the referenced NASA investigations.

A discussion of this hypothesis and the evidence is believed valuable to the understanding of important considerations in the design of controls for new propulsion systems. The nature of the compressor loading and the effects of relative sizing (inlet and engine) are essential elements of the argument. Compressor loading is evaluated through the dynamic variation in P_3/P_2 . For unstarts this variation is due more to a direct P_2 loading than to the indirect P_2 effect through fuel-air ratio. The direct P_2 effect originates primarily from the stored air mass in the engine combustor which acts to restrain transiently the ability of P_3 to follow P_2 . The indirect effect derives from the increase in fuel-air ratio. This ratio increases due to the combined reduction of P_2 (airflow) and the lags or delays incident to correcting the fuel flow. These lags arise from the necessity (with existing control methods) that either RPM or P_{s3} must change enough to give the main fuel control a hard-over signal via the governor or the acceleration fuel schedule. For the GE4 and J93 turbojets the indirect effect is not the dominant factor for unstart stall margin variations. The high Mach characteristics of these engines are such that a 2:1 increase in mainburner temperature rise is not sufficient to cause stall providing that inlet distortion is low. These compressors could not tolerate more than a small fraction of a 2:1 increase in P_3/P_2 . It logically follows from these considerations that the ratio of effective time constants between inlet duct and combustor is an important factor in judging unstart stall probability (increase in distortion and turbulence is also an important factor). To judge the effects of scale size and geometry changes it is convenient to use the time constant approximations of equations 1 and 2.

$$\tau_B \approx \left[\frac{P_3 V_B}{\bar{T}_B W_4} \right]_{iv} \quad (1)$$

iv = initial value

$$\tau_D \approx \left[\frac{P_2 V_D}{\bar{T}_D W_2} \right]_{iv} \quad (2)$$

These are readily derived from the mass storage considerations and proportionality of flow to pressure. These equations assume that the distribution of temperatures and total-to-static ratios are sufficiently similar for the purpose and that inflow and outflow are largely determined by a bulk internal pressure and the conditions at the inlet and exit terminations.

Equations 1 and 2 tend to confirm the hypothesis stated earlier (pg. 3). Observe that τ_B is constant for the comparison of full scale and .577 scale, but τ_D for the scale model duct is .577 of that for the full size. For the J85 case τ_B is about .41 that for the J93; τ_D for the NASA inlet is however only .076 that for the .577 scale XB70. Observe also that if a dynamic disturbance is introduced at the entrance of an inlet duct that the proportion of that disturbance imposed on the compressor increases when the ratio of τ_B/τ_D increases.

Understanding is essential to good design but the limit for hand calculations is quickly reached. Understanding and design evaluations can be carried much farther using computer simulations. Computer simulations have been used extensively in the analysis of the engines (J93 and GE4) designed for applications with mixed compression inlets. An extension of the previous discussion on unstart-stall probabilities is possible through the introduction of some simulation results obtained from early GE4 studies.

Figure 1 shows the effect of a simulated unstart pressure transient on stall margin for a Mach 2.7 case. For this Mach 2.7 case it is evident that there is little chance that the estimated pressure transient will fail to stall the engine compressor. This simulation was made with the complete non-linear engine model (DYNASAR) subjected to a conservative estimate of the P_2 vs time driving function. The P_2 - time function estimate was based on the results of several correlations. Two of these are shown in Figure 2. One was obtained with a DYNASAR simulation of shock equations and volume dynamics (description of model type available from Reference 6). The other is a comparison with scale model XB70 test data (Reference 4) based on a "parametric" scaling of the time base. This scaling is based on the first order approximations of equation 2.

STALL SIMULATION

It would be presumptuous to assume that the state-of-the-art would permit the analytical development of an accurate stalled engine math model (comparable in prediction capability with the better unstalled math models). There is now, however, a recognized need for a stall model having the following uses:

1. To aid in the reduction and interpretation of stall test data and to calculate dynamic airflow from data on P_{s2} , P_{s3} and P_{s5} . Reference 7 shows the difficulties of getting representative total pressure measurements required for conventional airflow calculations.

2. To simulate hammerwave overpressures needed for calculating inlet duct stresses.
3. To aid in evaluating probabilities for mainburner and afterburner blowout under varying installation and flight conditions.
4. To evaluate the feasibility and capability for certain types of stall sensors which may be required for automatic inlet restarts.
5. To aid in evaluating the performance of stall-clearing procedures and extrapolating data to new conditions. Such procedures are of interest for missile firing consequences as well as those for those for unstart; GE has already applied this type of simulation analysis to the design of compressor test facilities, for the purpose of minimizing the duration of those deliberate stalls, incurred in stall test programs.

Our earliest application of a stall model was to estimate GE4 airflow transients for use in evaluating hammerwave overpressures. The development was based on the particular set of data for the J93 engine test data reported in part by Reference 7. This choice was determined by the criteria that:

1. The data must provide for two ways of computing airflow (for checking purposes): instrumented ducts at both ends of the compressor.
2. The pressure instrumentation must have a response suitable to the task.

An in-stall compressor map was formulated using dimensionless parameters; the first set of map values was considered to be the initial guess for an iterative solution. The rest of the engine was modeled as components similar with practice defined in Reference 6. Mainburner, augmentor and inlet ducting were dynamically modeled for conservation of mass, momentum and energy. Both burners account for the enthalpies of inflow, outflow and combustion. The inlet was represented by three lumps each for momentum and mass/energy and provided for simulation with flow in either direction (a short interval of reverse flow was expected). Approximate heat storage effects were included for compressor and turbine. The originally estimated in-stall compressor maps were trimmed through trial and error simulations to establish empirical characteristics which would give the observed pressure transients. Breakdown, recovery and normal modes are selected during the simulation based on P_3/P_2 and W_2/W_{Stall} criteria. Figure 3 gives the resultant empirical maps and Figure 4 gives the airflow transients for breakdown and recovery. Pressure data on which this analysis is based are given in References 7 and 8. Fuel-pulse stall (deliberate excess fuel from test facility for a fraction of a second) pressure data of equivalent or even better quality has recently been obtained for the GE4 coupled to a boiler plate inlet. Data is shown in Figure 5 for stalls at a corrected RPM which should give airflow results representative for SST cruise Mach number.

This data provides a broader base for improving the empirical factors of stall models and for evaluation of scaling techniques.

After developing the basic modeling techniques with available J93 data, a GE4 model was then developed assuming that the stall mapping features were scaleable. This model has been used subsequently by GE to study engine conditions during unstart stall. Figures 6 and 7 show the behavior of a few key variables during an unstart-stall simulation with a combined engine and inlet model (3-lump inlet model with hammerwave and reverse flow capability as discussed above). Unstart is the cause for stall in both cases and the only difference between the model configurations of Figures 6 and 7 is the timing of engine stall. The Figure 6 configuration set engine stall criteria at a map stall margin of 20 percent assuming that transiently a high distortion was absorbing this 20 percent. The Figure 7 configuration set the stall switching criteria at a map stall margin of 5 percent, assuming a low level of transient distortion. The major difference in second simulation was the virtual disappearance of stall hammerwave due to the reduced inlet Mach number and pressure. For both of these simulations a stall sensor (controls) criteria acted at approximately $t = .2$ seconds to chop main fuel flow to the deceleration fuel schedule. Stall recovery was completed at $t = .43$ seconds according to the simulation. A major portion of the interval between detection and clearing was involved with lags and rate limit in the main fuel control.

It is emphasized that this is all simulation; these simulations were performed for this paper; and there is no satisfactory stall sensor in hardware form. Simulations using estimated control performance are useful in studying the potentials for alternative controls schemes.

THE RESTART SEQUENCE

References 2 and 3 describe inlet controls means for restarting. These do not however, consider in sufficient detail all of engine factors affecting the restart procedure or sequencing. Both References 2 and 3 have considered the engine variables and others to the degree that a closed loop is proposed for bypass area control during restart. Earlier approaches usually involved scheduling of bypass area or position. Even if engine and T variations were neglected a varying bypass area should be scheduled during the throat area reset cycle to avoid an excessive degree of supercritical operation. For orientation or review purposes and with credit due to the inlet experts the basic closed loop inlet restart cycle is:

1. Sense unstart with the ratio of a throat total pressure (or subsonic diffuser pressure) to a far-forward internal static pressure.

2. Switch the bypass control to the unstart mode (revised control reference) and if necessary command the throat to open (spike to move forward, where applicable). The throat will open automatically without special command if the throat Mach number control of Reference 2 is used.
3. Control bypass area to a pressure ratio schedule which controls or limits supercritical range of a second normal shock which is formed during the throat opening mode. The reference pressure ratio (subsonic diffuser wall static to throat total in Reference 2) forces bypass area to open until a normal shock forms in the control region. A choked throat is normally desired for buzz suppression.
4. The throat continues to open until a restart is sensed with the signal of Step 1; with the unstart signal wiped out the throat slews closed. The Reference 2 control operates a little differently in that the throat Mach number alone indicates restart to the throat control; e.g. at the moment the shock is swallowed throat Mach number jumps to a much higher value, and this is in the direction to close the throat.
5. With restart signaled and throat closing, switch (if necessary) to a different schedule for the bypass control pressure ratio. Throat area continues to close.
6. The throat returns to the initial or design position and control returns to normal for started operation.

Throughout the restart a narrow channel must be navigated between excess supercritical and buzz (or renewed unstart). Even when channel limits are observed, distortion and turbulence levels are expected to be above those for normal started operation due to stronger shocks and off-design shock locations. Where these limits are far exceeded, intolerable levels of distortion and turbulence may be expected. This was first demonstrated during the J93/XB70 development program and Reference 9 provides a report of an extensive test investigation on the effects on engine operation. J93 program experience would indicate that restarts were generally stall-free where really excessive supercritical operation were avoided. Successful restarts were made at military, minimum A/B and maximum A/B over a range of Mach numbers to 3.0. A few stalls were encountered during restarts and even more might have occurred if it had not been common practice to restart with the engine at locked-up idle. Locked idle is a condition where RPM is maintained at 100 percent and A_8 is opened to the idle value which is 20 to 30 (depending on T_2) percent above the nominal military values. The stall margin was increased by one-third in the RPM lockup mode.

The message here is that restart can cause stalls and controls system design must take this into account. Consider the effect of a stall-clearing airflow transient (Figure 4 for $t > .05$ seconds) on an inlet which is being controlled slightly supercritical (assume that the stall persisted until the bypass control accommodated the airflow reduction; a sudden stall-clearing airflow increase would then catch the bypass valves far open).

Consider also the dynamic flow change due a normal RPM transient which could occur from throttle reset, mainburner relight, or automatic stall clearing procedure; see Figure 8 for a sample simulation which assumes a burst from unlocked idle. System design should plan to take any transient which may be expected at a pre-arranged most favorable situation. This could be implemented with an engine-generated interlock signal which would cause an automatic restart control to stop and hold at a prescheduled condition until certain engine criteria are met. Completed restart is not expected to be a "favored condition" because the terminal shock strength could be the highest for any given engine transient.

Increased distortion and turbulence during a properly controlled restart may for some engine-inlet combinations require that the engine take a reset mode such as the locked idle mode described above for the J93. Even for the restart which is well controlled there is the unavoidable supercritical state which exists between the time the shock is swallowed and the time that the bypass doors adjust to the sudden increase in throat recovery, P_T/P_{T0} (the time dependent characteristic of the turbulence-stall correlation T_0 is a factor in favor of fast bypass doors). Stall margin increases which could be obtained for steady state engine conditions (not fully realizable during restart) have been estimated for both the J93 and the GE4. Figure 9 illustrates the potential effects of possible controls resets. Figure 10 shows how these effects combine in terms of stall margin. The nozzle reset is preferred because it is readily available through the power lever without penalties for complexity and reliability. The stator reset should be avoided for complexity reasons and also because of the airflow transient associated with release of a stator reset. Figure 9 shows that the RPM reset has little value unless accompanied by a stator reset.

CONCLUSIONS

The mixed compression inlet provides some special challenges in the design of compatible inlet and engine control systems. Those that relate to inlet restart are discussed in this paper. The analysis concludes that with short-coupled ducts operating at Mach numbers on the order of 2.5 or more, unstarts will frequently cause engine stalls and the conjunction of unstart and stall will suffice in some cases to cause mainburner blowout and/or augmentor blowout. A fully automatic inlet restart control should make provision for assuring that the engine has cleared any stall and has reached a "ready state" appropriate for a restart with the given inlet characteristics; furthermore, the inlet control should probably establish a holding condition which minimizes distortion and turbulence which would be associated with an engine airflow transient. A holding condition could be terminated by either an engine-supplied interlock signal or a pilot command signal. Computer math models are essential to any well ordered development program and it is recommended that engine models for both stalled and normal states be applied in the development of a mixed compression system or in any other system where it might be necessary to treat stall as having a significant probability.

Off-design inlet test data should be obtained early in a development program to define distortion and turbulence characteristics as functions of throat settings and supercritical levels which may occur during the restart procedure. Engines should be tested with the simulated distortion and turbulence observed for restart as early as is practical; and, where possible, early tests of the combined engine and inlet should explore the unstart-restart possibilities.

NOMENCLATURE

| | | |
|--------------------|--|---|
| A | Area | |
| D | Total pressure distortion as measured by low response instrumentation $(P_T \text{ max} - P_T \text{ min})/P_T \text{ avg.}$ | |
| f | Fuel-air ratio | |
| N | Engine RPM | |
| P | Pressure (total pressure without subscript) | |
| T | Temperature (total temperature without subscript) | |
| \bar{P}, \bar{T} | Average pressure, average temperature | |
| Tu | Dynamic distortion and fluctuating total pressure as measured by high response total pressure instrumentation | |
| V | Volume | |
| W_{2k} | Corrected airflow - $\frac{W_2 \sqrt{\theta_2}}{\delta_2}$ | |
| %SM | Percent stall margin = 100 | $\left[\frac{\left[\frac{P_3/P_2}{W_{2k}} \right]_{\text{Stall}} - \left[\frac{P_3/P_2}{W_{2k}} \right]_{\text{Op.}}}{\left[\frac{P_3/P_2}{W_{2k}} \right]_{\text{Op.}}} \right]_{N_k = \text{Const.}}$ |

SUBSCRIPTS

| | |
|----|---|
| B | Mainburner station |
| D | Inlet duct station |
| iv | Initial value (for quantities which vary with time) |
| k | Corrected flow or corrected RPM |
| S | Static |
| T | Total |
| t | Inlet duct throat station |
| o | Free stream static |
| 2 | Engine inlet station |

- 3 Compressor discharge station
- 4 Turbine inlet throat station
- 8 Exhaust nozzle throat station

NOTE: The designation J93 has been used as a matter of habit; the technically correct designation is YJ93.

REFERENCES

1. Beheim, M.A. and Boksenbom, A.S., "Variable Geometry Requirements in Inlets and Exhaust Nozzles for High Mach Number Applications", NASA TM X-52447, September 1968.
2. Chun, K. S. and Burr, R.H., "A Control System Concept and Substantiation Test For An Axisymmetric Mixed Compression Supersonic Inlet", AIAA Paper 68-581, June 1968.
3. Crosby, M.J., Neiner, G.H. and Cole, G.L., "High Performance Bypass Control For Mixed-Compression Inlets", AIAA Paper 68-652, June 1968.
4. Martin, A.W. and Kostin, L.C., "Propulsion System Dynamic Test Results", North American Rockwell Report NA-67-386, April 1967.
5. Cubbison, R.W., Meleason, E.T. and Johnson, D.F., "Effect of Porous Bleed in a High Performance Axisymmetric, Mixed-Compression Inlet at Mach 2.50, NASA TM X-1692, November 1968.
6. Marvin, I.E. and Winkeljohann, A.A., "Propulsion System Modeling and Integrated Controls Optimization", AFAPL-TR-67-149, November 1967.
7. Alford, J.S. and Victor, I.W., "Dynamic Measurements of Forward Gas Expulsion During High Speed Stall of Jet Engines", SAE Paper 650840, October 1965.
8. Marvin, I.E., "Integrated Math Modeling for Turbofan and Supersonic Inlet", AIAA paper No. 68-648, June 1968.
9. Kimzey, W.F., "An Investigation of Shock-Induced Turbulent Inflow on a YJ-GE-3 Turbojet Engine", AEDC-TR-66-198, November 1966.

ENGINE SIMULATION DATA WITH P_{T2}
PRESSURE FOR NOMINAL ESTIMATED UNSTART

$M_o = 2.7$ - Undistorted inlet Flow
Stall Simulation Locked Out

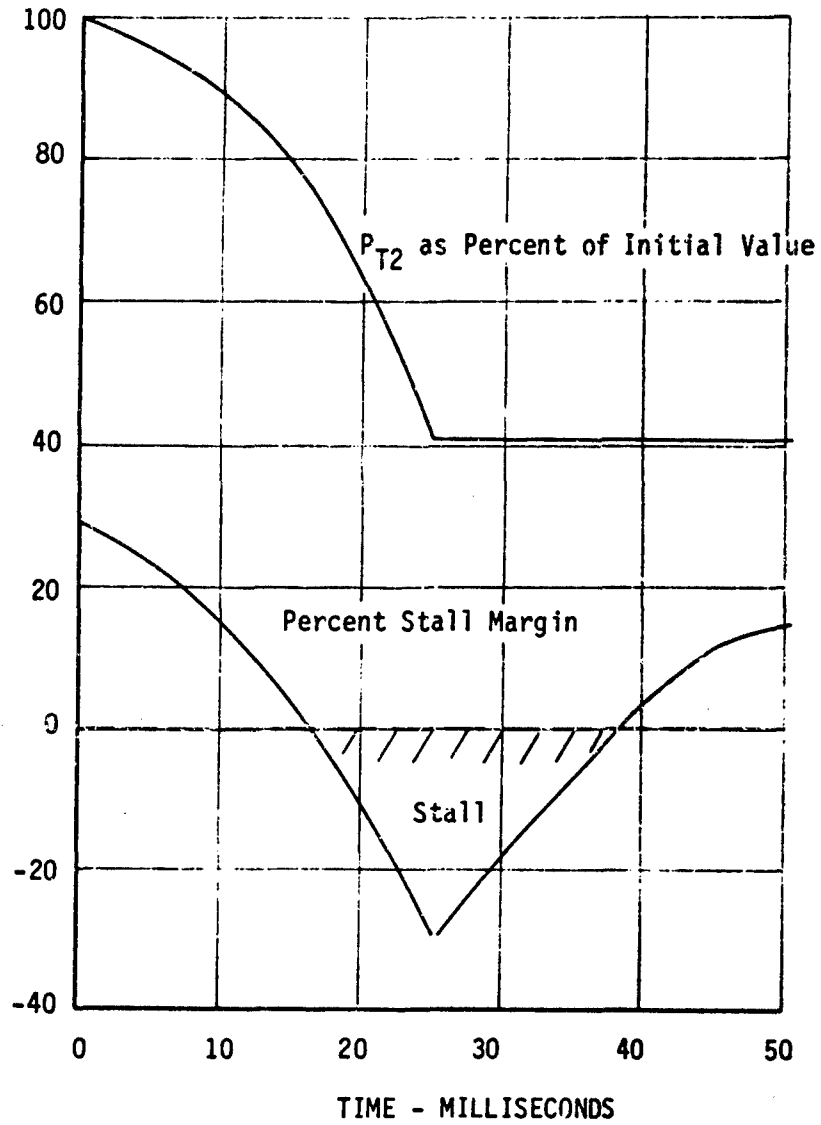


FIGURE 1

ESTIMATING SEVERITY OF UNSTART PRESSURE TRANSIENTS
(With No Stall Exhaust Flow Conditions)

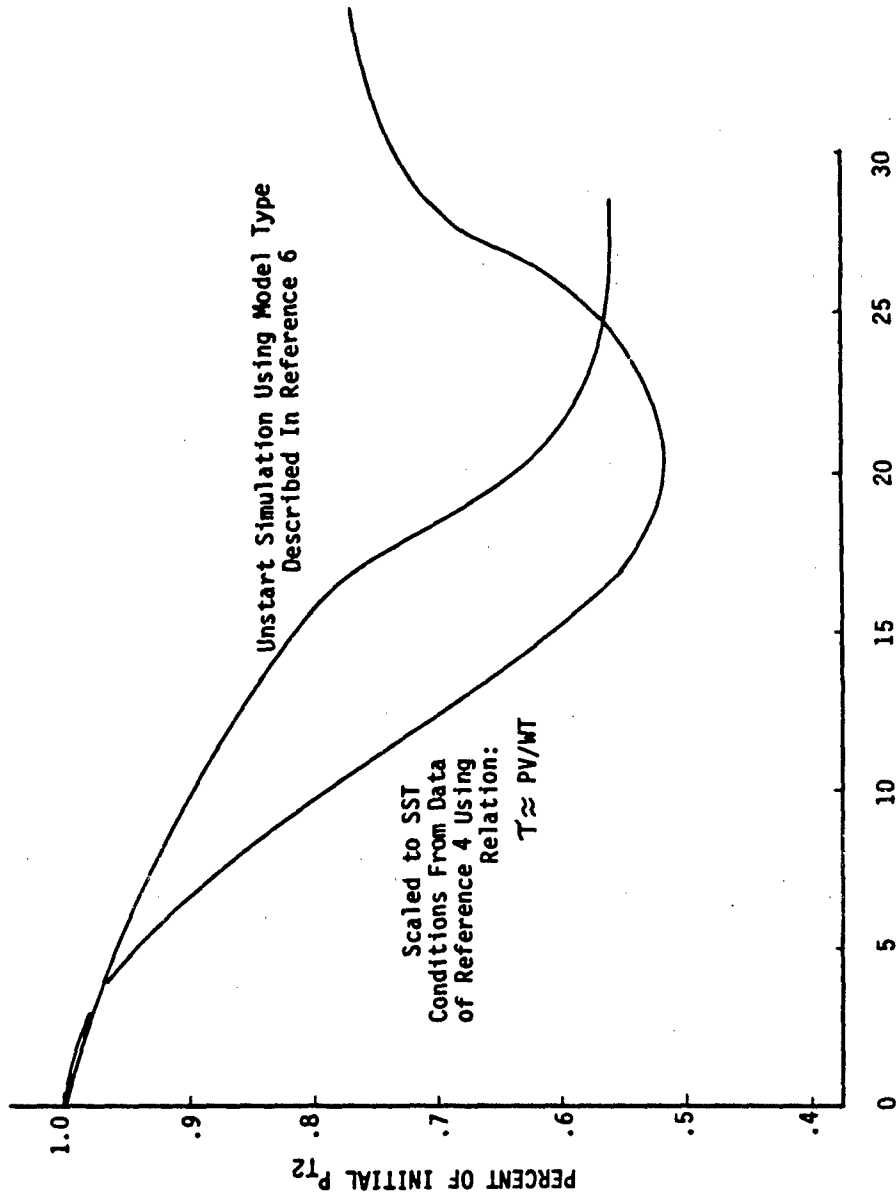
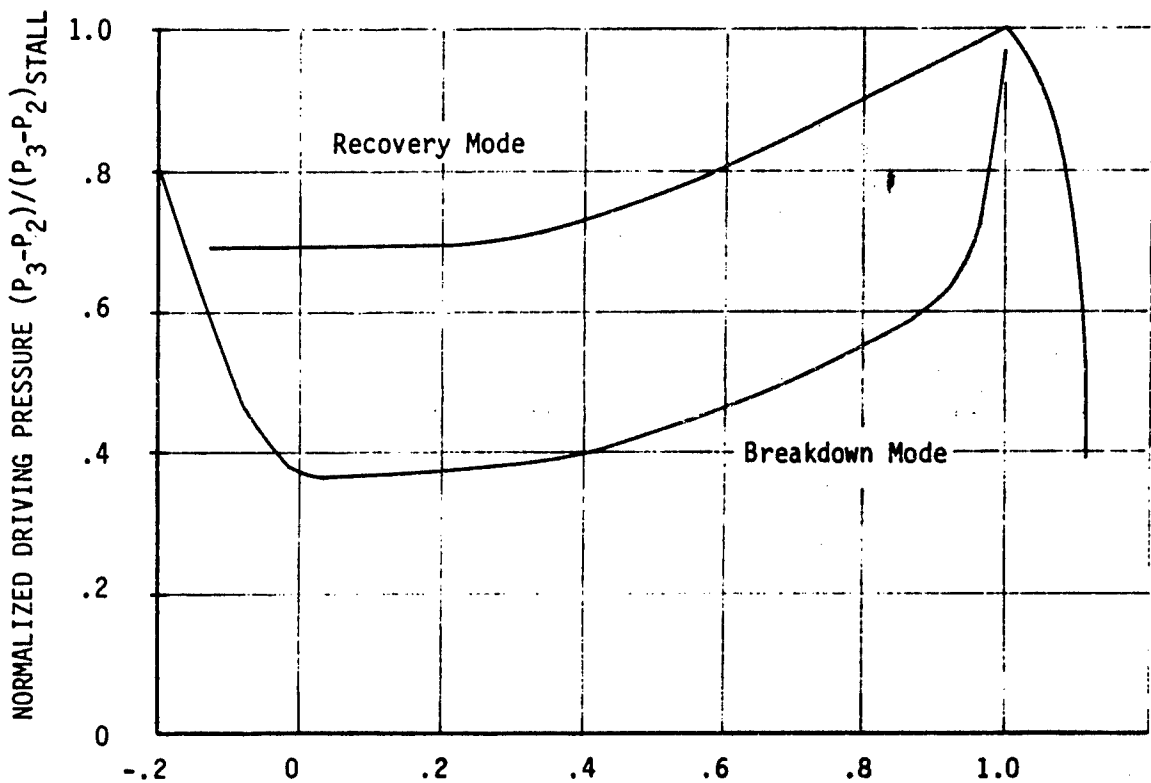
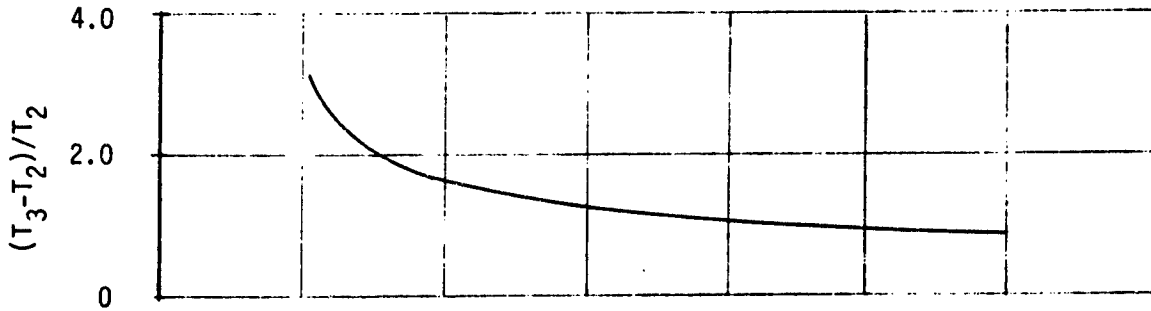


FIGURE 2

STALL MAP FUNCTIONS DERIVED FOR J93
 (HIGH CORRECTED SPEED RANGE)



W / W_{STALL}
 FIGURE 3

YJ93 STALL AIRFLOW TRANSIENT
SIMULATION TO MATCH PS2 AND PS3 DATA

SLS CONDITIONS WITH ATTACHED
SEVEN FOOT PIPE AND BELLMOUTH

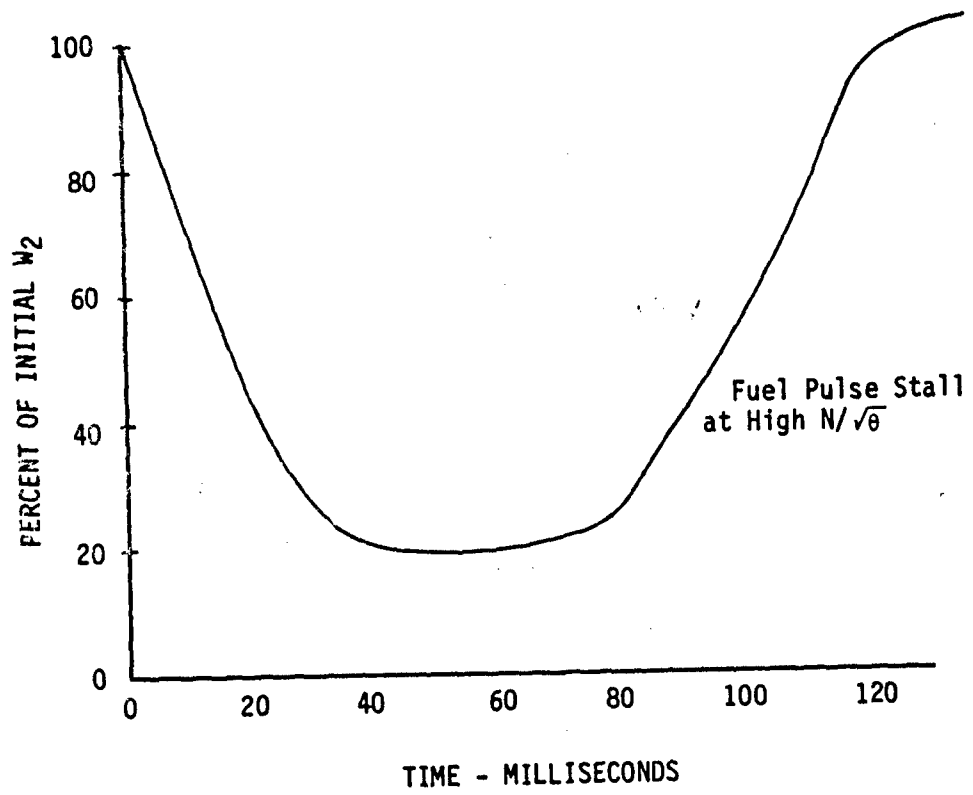


FIGURE 4

FUEL PULSED STALLS WITH THE GE4
(Sea Level Static Test With Attached Inlet)

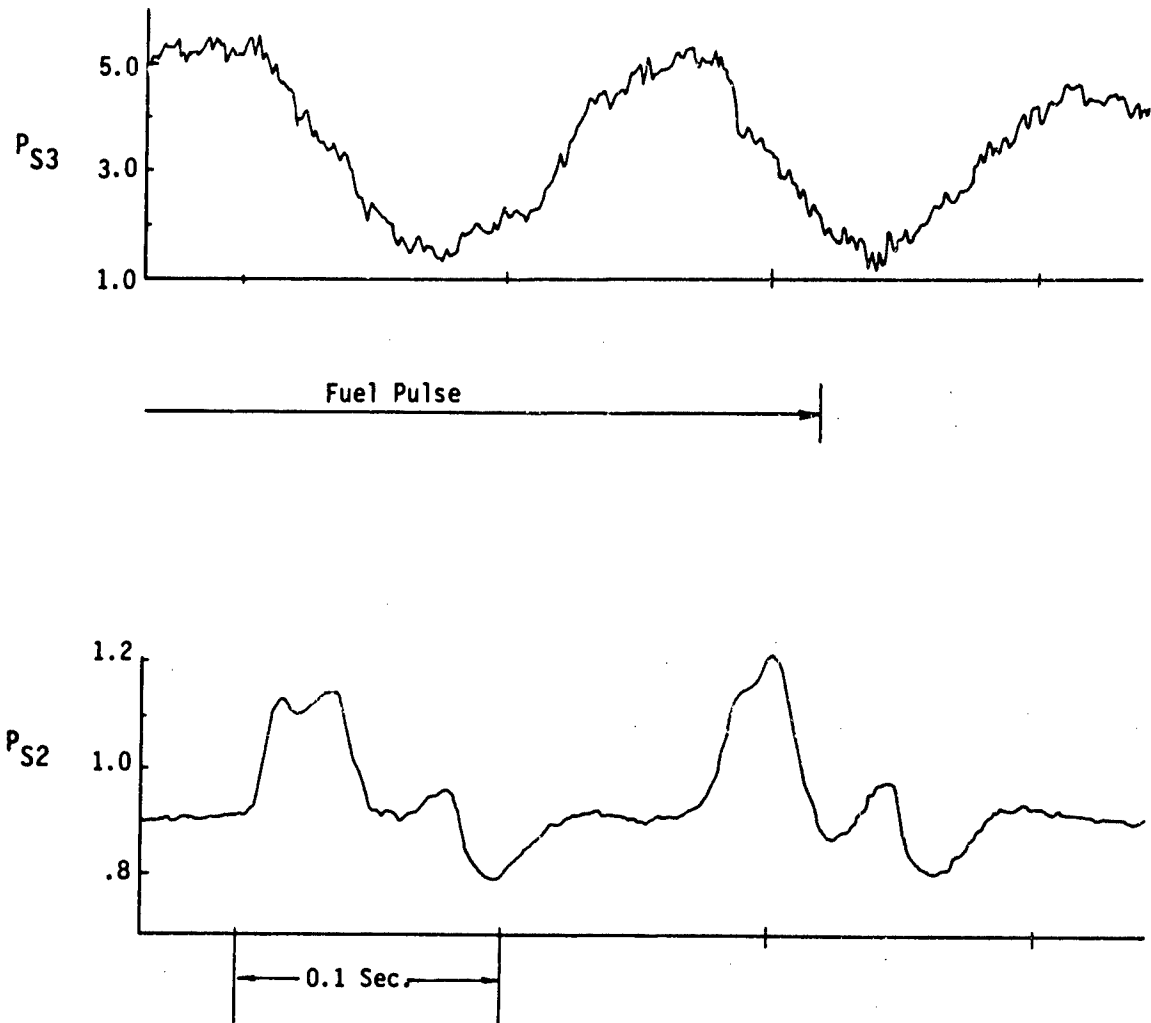


FIGURE 5

UNSTART STALL SIMULATION FOR GE4 MACH 2.7
 (Assuming High Distortion)

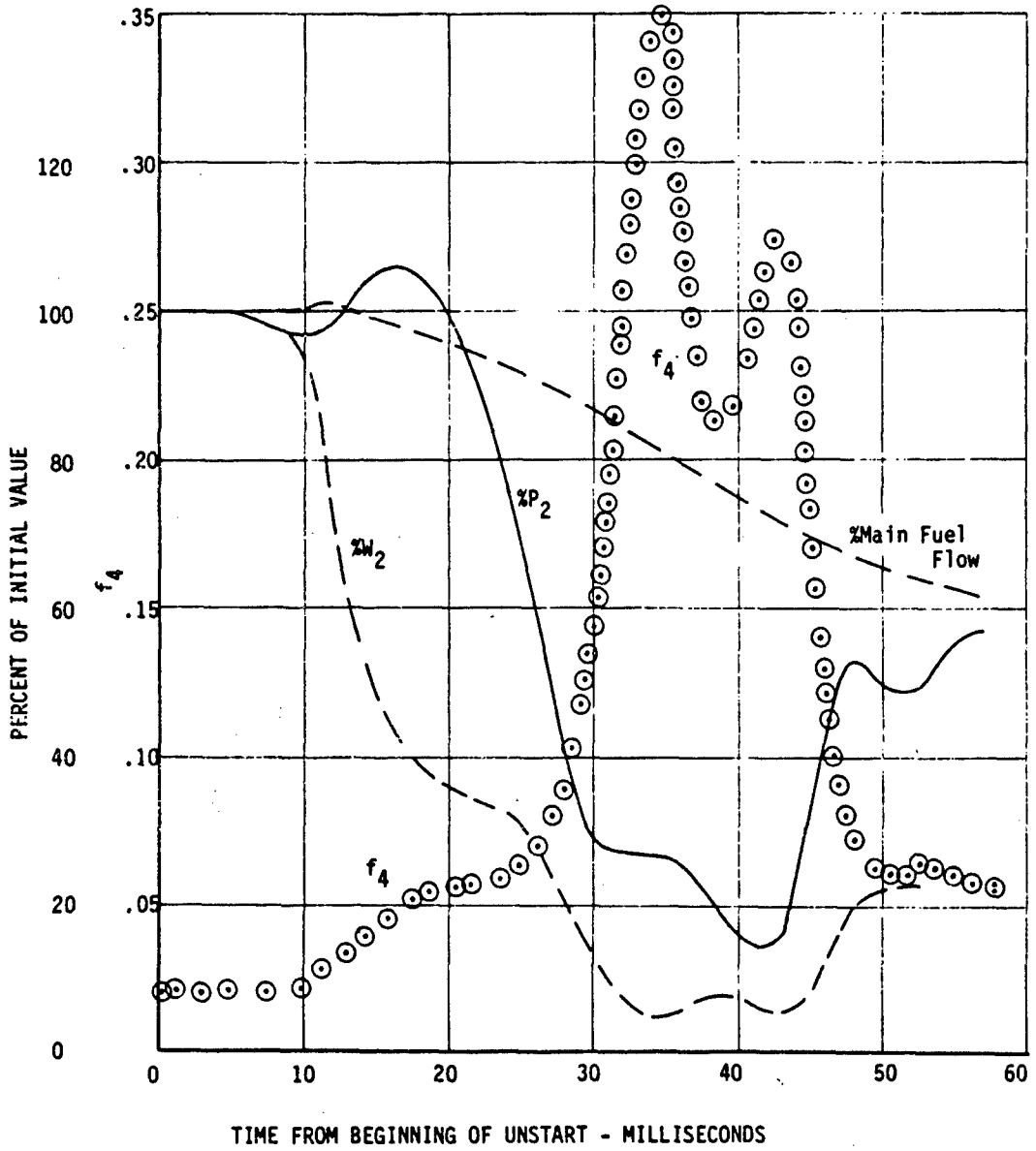


FIGURE 6

UNSTART STALL SIMULATION FOR GE4 MACH 2.7
(Assuming Low Distortion)

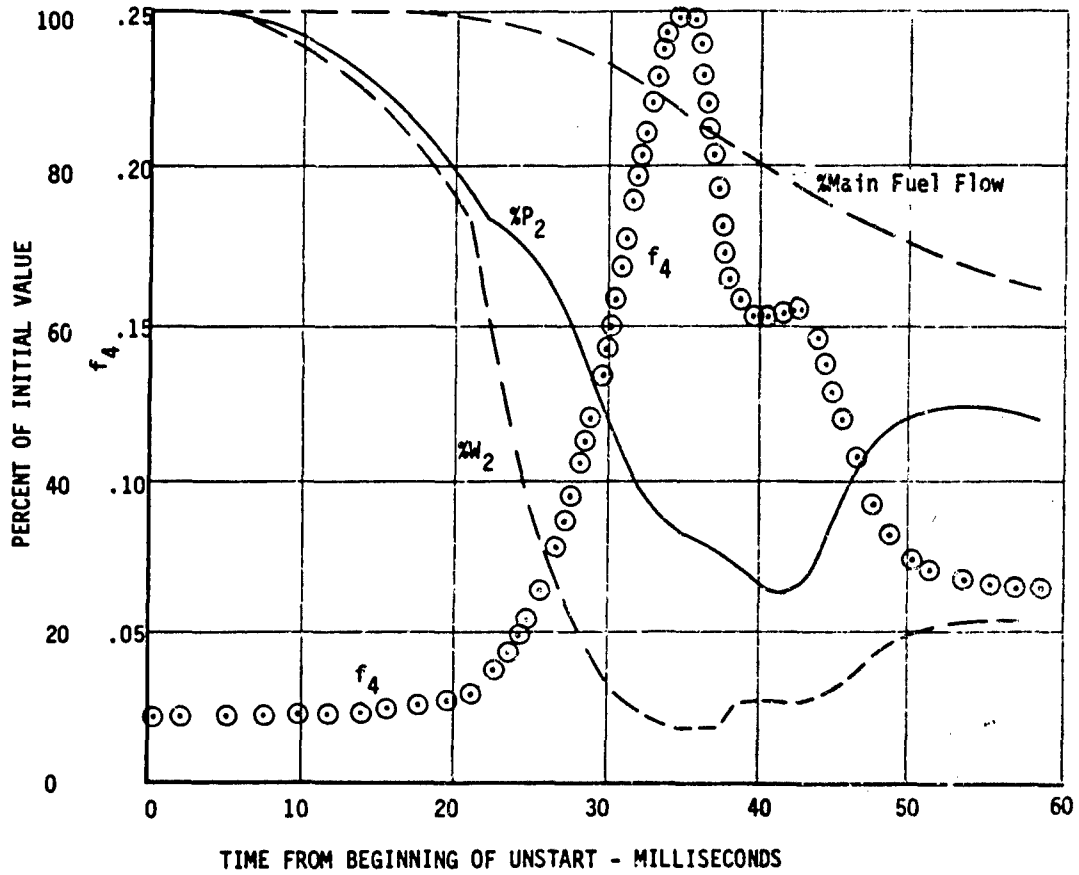


FIGURE 7

GE4 THROTTLE BURST FROM UNLOCKED IDLE
High Mach (Mo) Dynasair Simulation

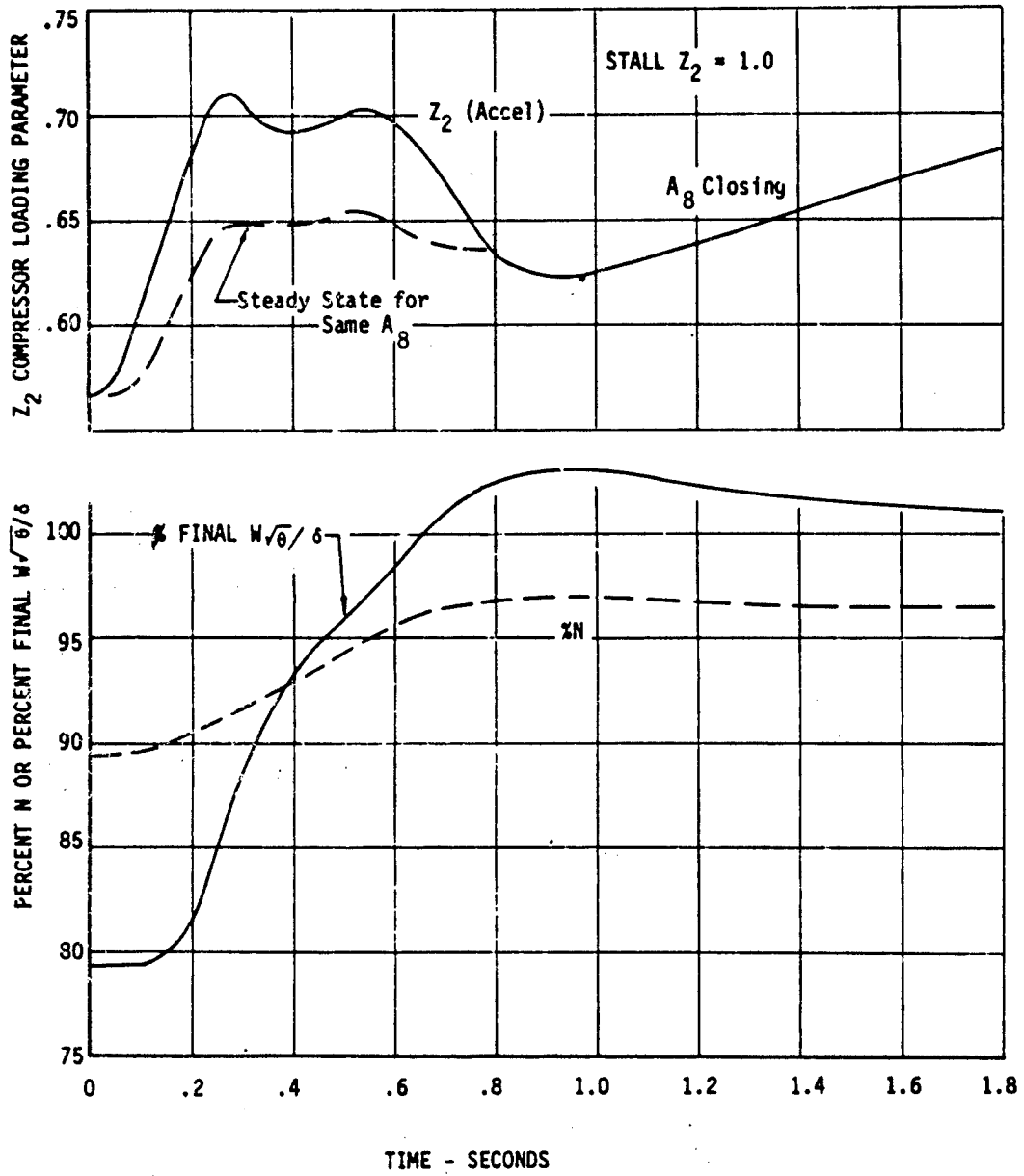


FIGURE 8

STALL MARGIN EFFECTS FOR CONTROLS RESETS
High Mach (M_0) Steady State Conditions
Undistorted P_{T2} -Computed Data

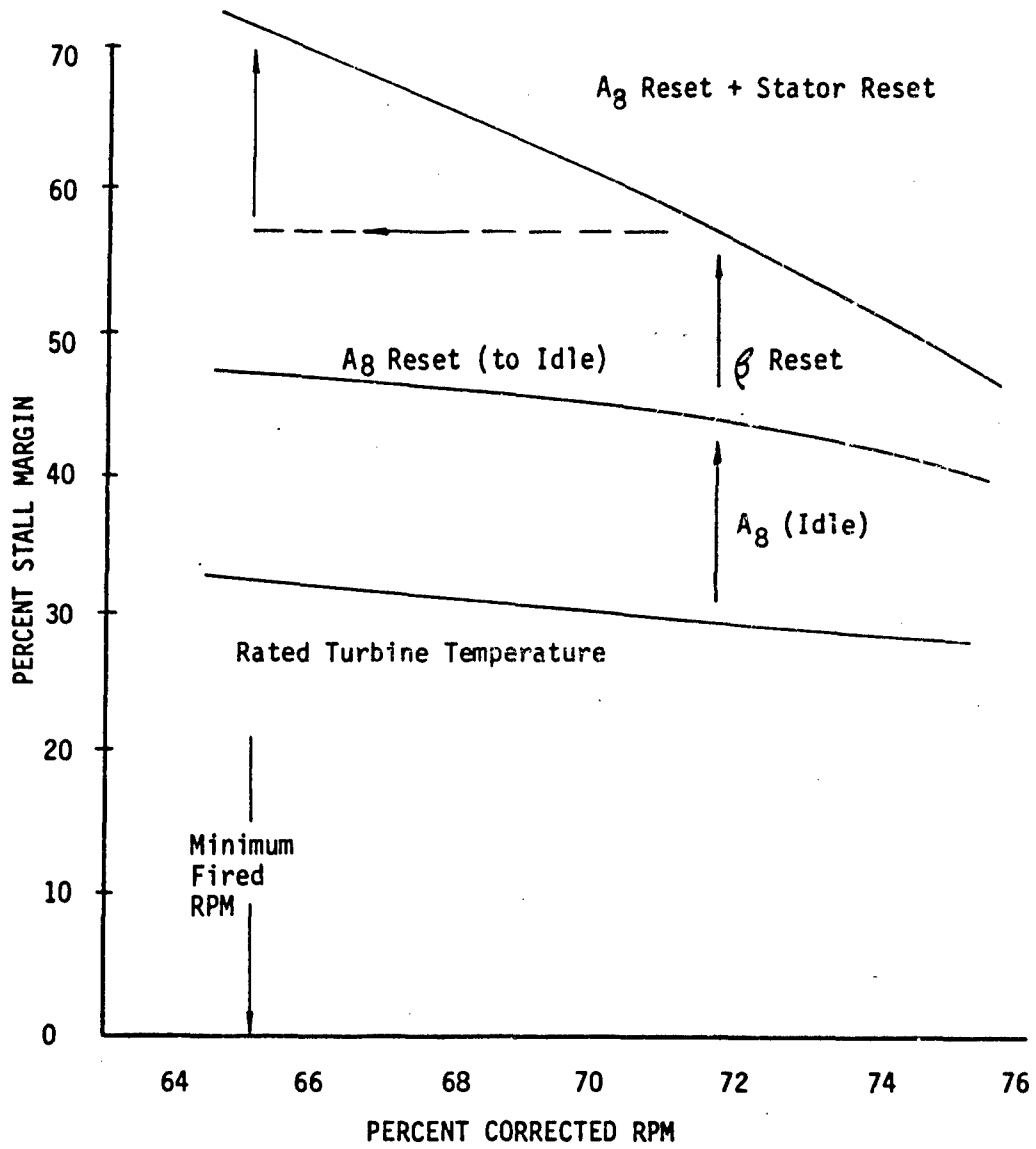


FIGURE 9

OPERATING EFFECTS FOR CONTROLS RESETS
 High Mach (M_0) - Undistorted P_{T2}
 (Computed Data for Steady State Conditions)

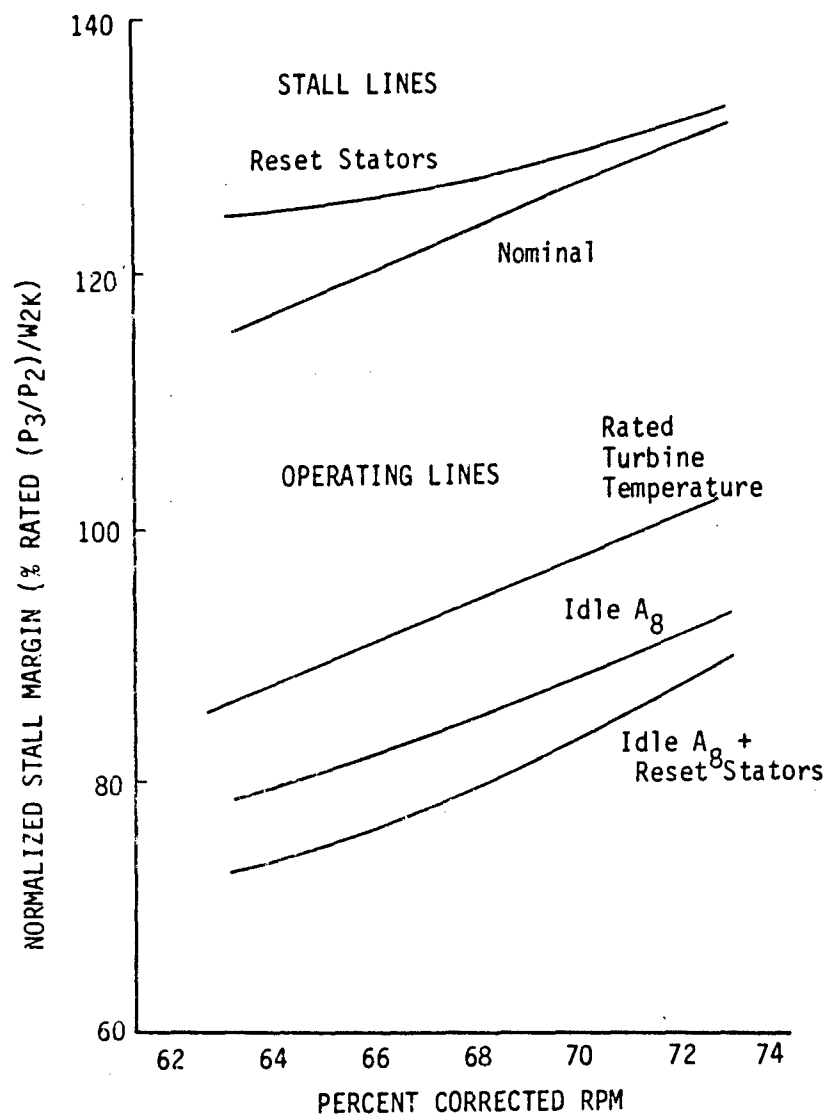


FIGURE 10

IMPACT OF MULTIPLEXING ENGINE/AIRCRAFT
INSTRUMENTATION AND CONTROL SIGNALS

Henry R. Ask

John Games

Daniel Stone

Hamilton Standard Division of United Aircraft Corporation

ABSTRACT

Advanced technology aircraft engines are interfaced by a maze of instrumentation and control wiring within the airframe. A vast majority of these signals terminate or originate in the forward section of the aircraft where the crew station and avionics bays are located.

These many long wiring runs present acute problems in EMI control, maintenance troubleshooting and are a significant weight factor in large airframe programs. In addition, the electrical interconnections between the basic engine and the airframe are complex, prone to malfunction, and require additional maintenance time during engine removals. The aforementioned problems can be alleviated by incorporating multiplexing techniques which can be implemented with state-of-the-art hardware.

This paper presents a multiplexing system configuration and discusses in qualitative and quantitative fashion the effect on the power plant/airframe interface. Weight, size, reliability, performance and maintainability are among the factors discussed. The impact on the power plant in terms of additional hardware and the effect on aircrew instrumentation and related subsystems is considered. The paper utilizes the results of some recent industry studies which examine the airborne multiplexing problem.

SECTION I

INTRODUCTION

OBJECTIVE

The objective of this paper is to present a multiplexing system configuration and discuss in qualitative and quantitative fashion the effect on the power plant airframe interface. Weight, size, reliability, performance and maintainability will be among the factors discussed. The impact on the power plant in terms of additional hardware and the effect on aircrew instrumentation and related subsystems will be considered. The paper utilizes the results of some recent industry studies which examine the airborne multiplexing problem.

PROBLEM

Advanced technology aircraft engines are interfaced by a maze of instrumentation and control wiring within the airframe. A vast majority of these signals terminate or originate in the forward section of the aircraft where the crew station and avionics bays are located.

These many long wiring runs present acute problems in EMI controls, maintenance troubleshooting and are a significant weight factor in large airframe programs. In addition, the electrical interconnections between the basic engine and the airframe are complex, prone to malfunction, and require additional maintenance time during engine removals. The aforementioned problems can be alleviated by incorporating multiplexing techniques which can be implemented with state-of-the-art hardware.

SUMMARY

The basic principle of multiplexing involves the sharing of a common transmission path (such as a wire) by separate and often different types of messages or signals which are to be simultaneously transmitted. By such methods as transmitting only samples of the several messages, or by assigning the various messages different transmission frequencies, the maze of hard wires, each carrying a single message, is replaced by multiplexer stations and a

few connecting cables.

Several advantages emerge as a result of the application of multiplexing.

In summary, some of the more important advantages are as follows:

- The engine to aircraft connections are simplified and therefore reduce the initial design and installation tasks as well as periodic maintenance requirements.
- Expansion of the electrical functions within the propulsion complex can be accomplished without additional wiring or rewiring between the engine cell and the airframe. The growth factor is vitally important to the sophisticated aircraft now being developed.
- On large airframes, the net reduction in weight resulting from replacing hard wiring with multiplexing equipment can be of major importance.
- Improved EMI control is realized because of simplicity in designing and routing a few wires versus hundreds of individual conductors.
- An increase in aircraft survivability is an extremely important advantage achieved by dispersion of redundant multiplexer elements.
- The task of standardization and integration of cockpit displays is aided by multiplexing since the multiplexer signals all arrive in a standard form. There is little need to reconstruct them to their original form and levels.

The following major conclusions can be drawn from the information presented in this paper and current industry developments:

- The accuracy and response needed for instrumentation and control can be maintained using multiplexing as a basic link between the engine and airframe.

- Techniques are available to allow the location of multiplexer stations near centers of many signal sources. A station can be mounted on the engine using techniques such as fuel cooling. The small net weight penalty (if any) paid to allow engine mounting in a high temperature and vibration environment is offset by the greater growth flexibility, higher aircraft availability, and survivability factors, among others.
- Recent developments in semi-conductor technology now allow multiplexing stations of reasonable size and weight for engine mounting.

SECTION II.
DETAILED DISCUSSION

1. COMPLETE PROBLEM STATEMENT

As aircraft become more complex so will the required electrical/electronic interface between the engine and airframe. More sophisticated engine mounted electronics in greater quantity are forthcoming. Control and/or monitoring of functions in areas of electronic fuel controls and inlet guide vanes, electric throttles, torque/thrust meters, engine pressure ratio transmitters and diagnostic sensors added to other existing engine instrumentation and control functions will demand a new solution to the ever increasing interface problem.

Multiplexing appears to offer a partial solution. It is being considered on many advanced aircraft for handling of communications, instrumentation and/or control functions. There is little doubt that engine signals will be handled as part of the signal complement in future multiplexing systems.

Past experience reveals that advanced aircraft require a large growth margin for handling electrical information. Adding or modifying equipment must be accomplished without extensive airframe rewiring. The weight and space factors and routing problems in hard wired configurations are significant in both large and small aircraft.

2. WHAT IS MULTIPLEXING?

Multiplexing has been used by the communications industry for many years. In principle, multiplexing is the art of sending and receiving many information bearing signals over a common communications media. The types of multiplexing fall into two basic categories: (See Figure 1)

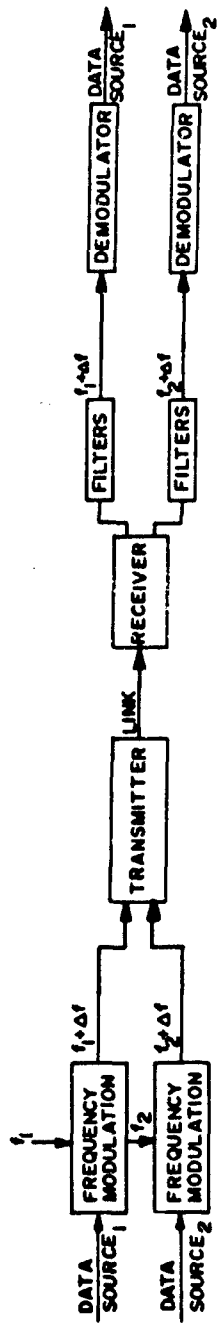
- Frequency Division Multiplexing (FDM)
- Time Division Multiplexing (TDM)

FD multiplexing has and is being used extensively in the communications and telemetry fields. FDM is the technique of sending information from individual sources on separate carrier frequencies over common links. Figure 1 shows in simplified form how two data sources each modulate separate carrier frequencies.

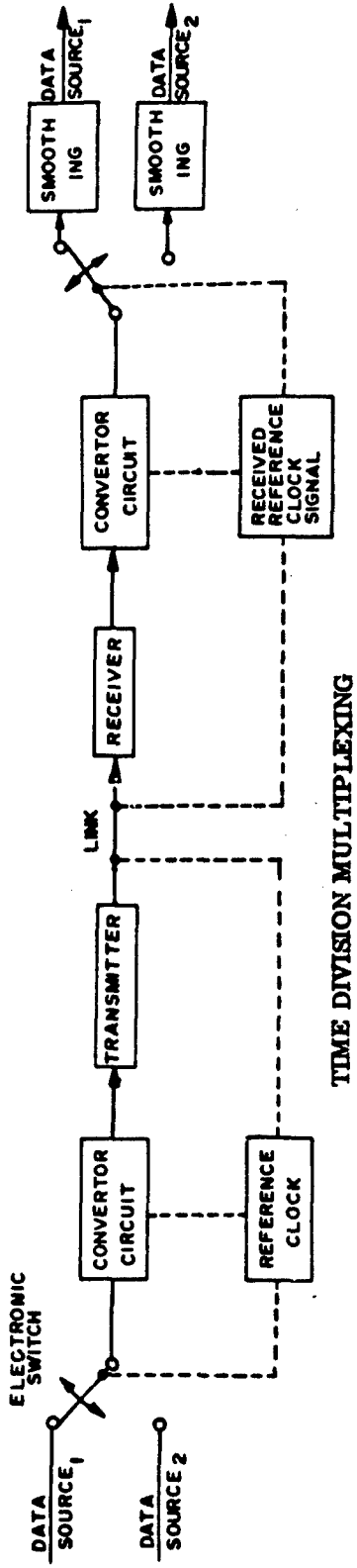
The frequency f_1 and f_2 plus the deviations of each due to modulation are combined and transmitted over a common link such as a single wire. The combined signals are received and the two frequencies are separated using filter circuits. Each frequency plus its deviation is then demodulated separately and the data sources are reconstructed. Each data source requires its own carrier, hence separate filters, modulators and demodulators must be provided for each signal. In addition, information can be sent both ways on the common link providing each signal, whether coming or going, has its own assigned frequency. Also, both sets of block functions shown must exist at each end.

FDM has its primary utility in systems where relatively few but high bandwidth signal sources are present.

TDM multiplexing differs fundamentally from FDM in that each data source is sampled in a fixed time sequence. A fixed time slot is allocated for sampling each respective data source, converting it, transmitting it, receiving, and reconstruction of the signal. This means that reconstruction data is made up of a series of samples and implies that information is lost if the sampling rate cannot keep up with changes in the signal. It should be noted that in a system of this type a common clock must provide the overall



FREQUENCY DIVISION MULTIPLEXING



TIME DIVISION MULTIPLEXING

FIGURE 1. BASIC TYPES OF MULTIPLEXING

system timing since a particular source is identified by its position in the data frame. The data frame is one complete cycle of sampling of all data sources. The signals can be converted into a number of common forms before transmission. One technique is to merely sample the amplitude of each incoming signal and transmit a pulse with its amplitude being a direct function of the signal level (Pulse Amplitude Modulation, PAM). The next level of sophistication involves taking the sampled PAM signal and converting each amplitude measurement into a digital signal represented by data bits. Each bit consists of one of two signal levels with each level representing a digital "one" or "zero". The digital group of bits (words) is reconverted and reconstructed at the receiving end. The technique is labeled Pulse Code Modulation (PCM). Transmitting digital bits in the form of two signal levels directly at the chosen bit rate is called "base band" transmission. A further possibility is to take the serial bit stream (the time sequential digital bits represented by either of two voltage levels) and modulate an FM carrier. Thus a system can be evolved using a combination of the basic multiplexing techniques. The system described in detail in this paper is a PCM/FM system.

3. FUNCTIONAL REQUIREMENTS OF A GENERAL PURPOSE MULTIPLEXER

The engine/aircraft interface, i. e., those electrical signals leading to and from the engine, impose certain requirements on a general purpose multiplexer. The multiplexer will, in all probability, be handling other signals derived from subsystems not directly associated with the engine. Hence, the total system requirements are formulated by all subsystems which are using the multiplexer as a communications link.

Fortunately the general types of signals, i. e., analog, AC and DC, discretely or digital and their desired transmission characteristics are fairly uniform no matter what the signal source. The primary factor which defines a particular multiplexer station is the signal mix (number of various signal types). For example, a mux station located adjacent to an electrical power distribution system would have a very high percentage of discretely indicating power status and control while an engine mux would have proportionally many more analog signals.

To allow the formulation of a representative engine mounted multiplexer certain functional requirements are presented. The signal mix assumed is believed typical of the engine/airframe interface. The actual signal count is representative of an advanced engine complex using a heavy concentration of electronics for control, measurement and status. The signal count assumed also allows for significant growth capability without affecting unit size.

SIGNAL DEFINITION

Analog Signals

Two classes of signals are defined under the analog category; these are referred to hereafter as high and low accuracy analog signals. Two categories are sufficient since some aircraft signal accuracies are very stringent (0.2% typical), requiring great care in multiplexing, while the majority of others are in the 2% class. Breaking the signals up into two classes results in lower overall hardware

complexity and cost. Included is a summary table of the requirements for these two classes of signals.

Discrete Signals

Discrete signals are assumed open circuited for the "zero" state, and either ground or +28 volts for the "one" state. A sampling rate of 10 cps is considered adequate for instrumentation and status reporting. An error rate of 1 error per 2 hours is typical as a requirement.

Digital Signals

Digital information is assumed available in shift registers at the source from which the multiplexer would receive information. It is assumed that this information is to be shifted into shift registers at the receivers to which the multiplexer feeds information. The clocking and enable pulses for these digital signals are to be provided by the mux station. A sampling rate of 10 samples/second is chosen with an error rate not to exceed one per 2 hours.

Synchro Signals

It is recognized that present aircraft systems utilize many synchros for angular data transmissions for servo-systems and instrumentation purposes. It is felt that future aircraft will tend to minimize the usage of synchros in favor of transmitters and readout devices with signal compositions more favorable to multiplexing techniques (such as digital shaft encodes, digital or analog readout devices). The assumption is made here that synchro sources of information are present in a limited number. Information is delivered on the output of the multiplexer either in digital or analog (high accuracy) form, rather than reconstructing and driving synchro receivers. The accuracy required is $\pm 1\%$ typical with a sampling rate

TABLE
ANALOG ACCURACY SUMMARY

| | <u>HIGH ACCURACY</u> | <u>LOW ACCURACY</u> |
|---|--|--|
| Signal Range | Input 0 → +5V or -5 → +5V Outputs 0 → +5V or -5 → +5V | Same as high accuracy. Same as high accuracy. |
| Input Signal Spectral Density | Flat to 5 cps, decaying at -40 db/decade to -60 db level, then remaining constant. | Same as high accuracy. |
| Signal Source Impedance | 5 KΩ maximum | Same as high accuracy. |
| Input Common Mode Voltage | DC to 900 Hz 2.1 peak volts, above 900 Hz decaying at rate of 10 db/decade to 90 K Hz level of 210 mv peak. | Same as high accuracy. |
| Signal Termination | 1 KΩDC resistance minimum with second order filter characteristic $G(s) = \frac{1}{\frac{s^2}{(12.5)^2} + 2 \times .7 S + 1}$ | Same as high accuracy. |
| Gain, set point and linearity specification | .2% RSS summation | 2% RSS summation. |
| Aliasing and reconstitution error | .1% | 1% |
| Analog response | + .5-1 db at 1 cps | Same as high accuracy. |

TABLE (CONTINUED)
 ANALOG ACCURACY SUMMARY

| | <u>HIGH ACCURACY</u> | <u>LOW ACCURACY</u> |
|---------------|--------------------------------|--------------------------------|
| Granularity | ±.025% full scale | ±.025% full scale |
| Sampling Rate | To meet accuracy requirements. | To meet accuracy requirements. |

of 10 sample/second minimum.

Signal Mixture

A typical signal mixture is chosen for a two way transmission to and from the engine multiplexer stations. This mixture was as follows:

| | | | |
|-------------------------|-----------|-------------|-----------|
| Each engine to airframe | 30 Analog | 40 Discrete | 4 Digital |
| Airframe to each engine | 15 Analog | 30 Discrete | |

NOTE: No synchros are specifically called out. Any two of the analog channels included above are required per synchro.

Cross Talk

A crosstalk specification of 60 db is imposed upon the analog signal transmission. This includes crosstalk with the discrete and digital information, and thereby imposed certain grounding requirements throughout the system.

Noise and EMI Susceptability

In general the design of the system should be inherently immune to noise and EMI sources typically present on aircraft.

Reliability

Single signal MTBF for digital and discrete functions is set at 1,000,000 hours. The MTBF number for an analog signal is 200,000 hours.

Maintenance

A faulty LRU is to be located with a high degree of confidence, and replaced within ten minutes. Any redundant circuit faults must be located with a confidence of greater than 99%.

First Failure Survivability

Any component failure can only cause, in the worst case, the loss of a single signal path. This implies that a fault in a circuit used in common by more than one signal thread cannot cause loss of any signal. This first failure survivability should be automatic. A second failure survivability either automatic or by manual initiation is a highly desirable feature.

Built-In-Test-Equipment (BITE)

BITE as required to meet the maintenance specifications is necessary. This includes BITE not only on redundant circuitry but also on a single signal thread basis to achieve a high confidence of isolating all failures of components.

4. OTHER FACTORS WHICH TEND TO FORMULATE SYSTEM REQUIREMENTS

Common Digital Readouts and Displays

Carrying the concept of multiplexing to the area of readout and display is a definite evolution of the use of multiplexing and holds promise in decreasing instrument panel clutter. The increase in complexity to the multiplexer is minimal in helping to reduce the panel clutter problem. The use of mux for aiding in display integration is possible since the information from a large number of sensors is available in digital form. This digital information can be selected individually under manual control to be read from a single digital display. Display panel integration is discussed further in the systems design section.

The type of equipments which interface with a mux system influence the system design. The synchro interface already has been mentioned. Also the mux itself provides some benefits to related functions.

Hardware Standardization

Since signals must be reconstructed at the outputs of a multiplexer, every attempt should be made to standardize the reconstruction circuitry and the instruments or elements that the signals drive. This has obvious benefits in terms of improved maintenance and reduced spares for both mux and instrumentation. This means rather than having synchro repeater indicators, DC and AC meters, all outputs would be standardized to the same DC voltage range driving similar elements. Actual signal differences would be handled by respective dial calibrations. For those instruments not requiring a pointer or a bar for human factor reasons, digital indicators of standard design should be used. This results in the highest possible accuracy on the output end since the information is retained in digital form all the way from the point of analog to digital conversion at the engine mux station through the cockpit mux station to the respective digital readouts.

5. SYSTEM DESIGN

A system based on the constraints and definitions given in the previous paragraphs is conceived below:

Gross System Organization

A logical mux system breakdown is on an engine basis see Figure 2. For example, a twin engine aircraft would have two main mux units near the power plants each carrying the signals associated with one engine, as well as other local non-engine related signals. These units would feed forward to the necessary complement of mux units in the air frame. A four engine aircraft would have four main engine mux units, again each carrying the signals associated with one engine plus approximately one quarter the signals obtained locally from such systems as hydraulics

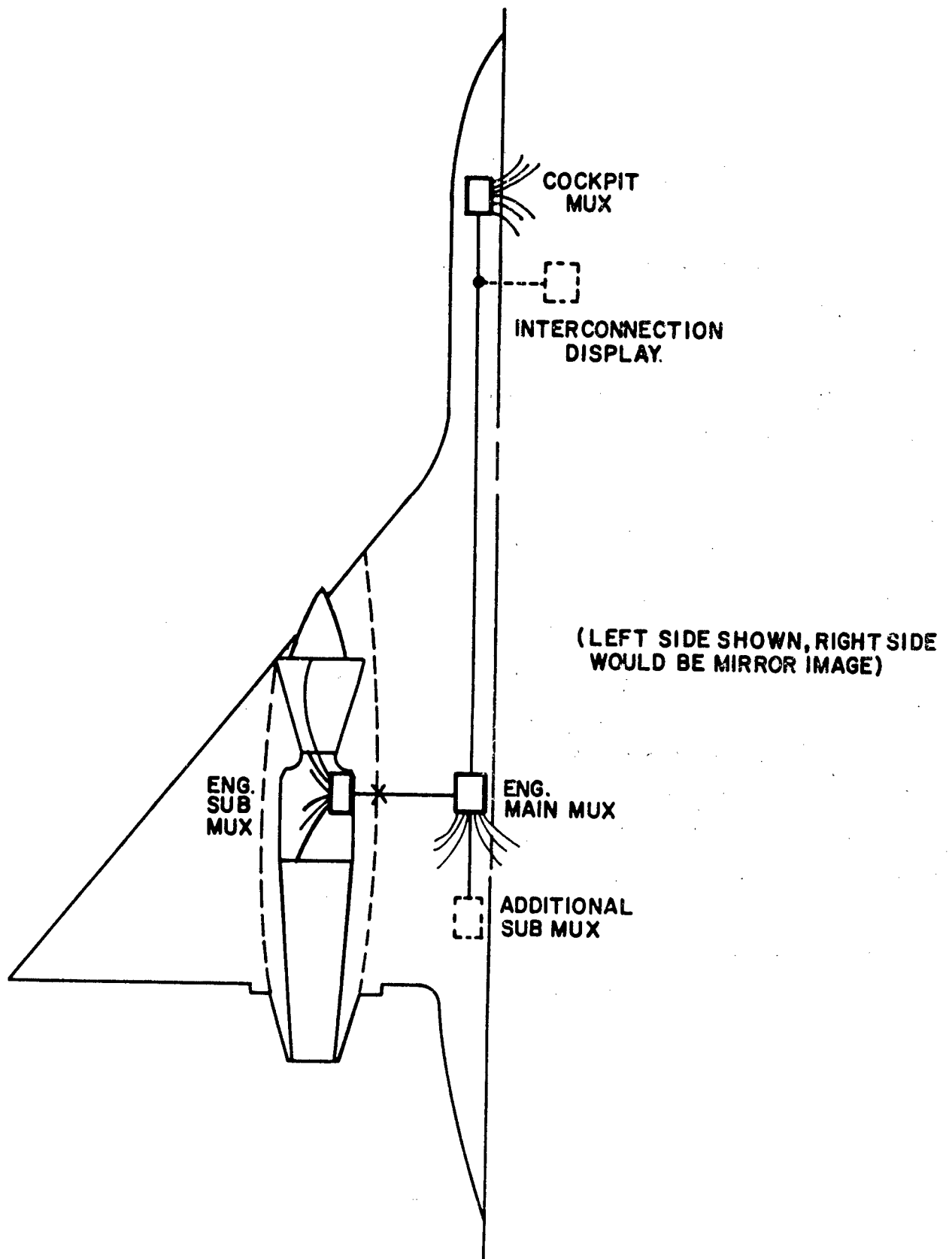


FIGURE 2. GROSS MUX ORGANIZATION

and power distribution. With such a multiplexer layout the destruction of a single engine main mux unit would prevent communication with one engine location only.

The next step would be to establish the total number of stations to be set up in the mux system.

The minimum number would of course be two, up to a maximum number that could be justified by considering all factors and the particular aircraft configuration.

In addition to main stations, submux stations can be set up. These would differ from the main multiplexer unit in some of the following ways:

1. Handle far fewer signals.
2. Have relatively short cable runs to the main multiplexer.
3. Rely on main multiplexers for power supplies, timing, A/D conversion, etc.
4. Environment may be more hostile.

An example of a submultiplexer would be a unit mounted directly on the engine. In a multi-engine aircraft the engine mounted multiplexers would communicate with a master multiplexer unit in the wing or fuselage area, which would also handle the multitude of discrete and analog signals from other equipments. The aft main multiplexer would be on a tie line connecting the pilot station with the aft electronic and electrical complex.

One of the significant advantages of the submultiplexer-multiplexer communication system is the fact that the system can be constant in spite of airframe subsystem design modifications. Growth capacity can be provided in the communication link between the various mux stations and substations to allow additional locations, without adding any physical wires.

There is an optimum configuration for each particular aircraft. To allow for further discussion here a particular organization is chosen because of availability of data. The choice was for a two engine aircraft with two main stations, one at the pilots compartment, and one at the aft electronics compartment. Each station had two submultiplexer stations, plus a power supply unit to excite the master multiplexers as well as the submultiplexers. A mirror image of this organization would exist on the opposite side of the aircraft to achieve physical equipment separation and enhance aircraft combat survivability. One of the submultiplexers is designed to handle discrete signals only. The other submux handles both analog and digital signals. Finally, a fault annunciator panel is provided in the crew area to indicate faults as determined by integral system test capability. Figure 3 illustrates in more detail the multiplexer, and its submultiplexers. Unit 1A is considered the master, 1B, and 1C the submultiplexers.

While the case presented here is specific, many factors make this study applicable at least to the extent of bringing to light the areas of consideration in concepting a mux system and its effect on the propulsion/airframe interface.

Basic System Approach

A triplicated system philosophy has evolved after studying in detail duplex and triplex approaches in the light of the system objectives stated. Among the important reasons for choice of the triplicated approach are the following:

1. It allows positive isolation of all faults without relying on coding or parity checks. (Coding and parity consist of putting test words into the

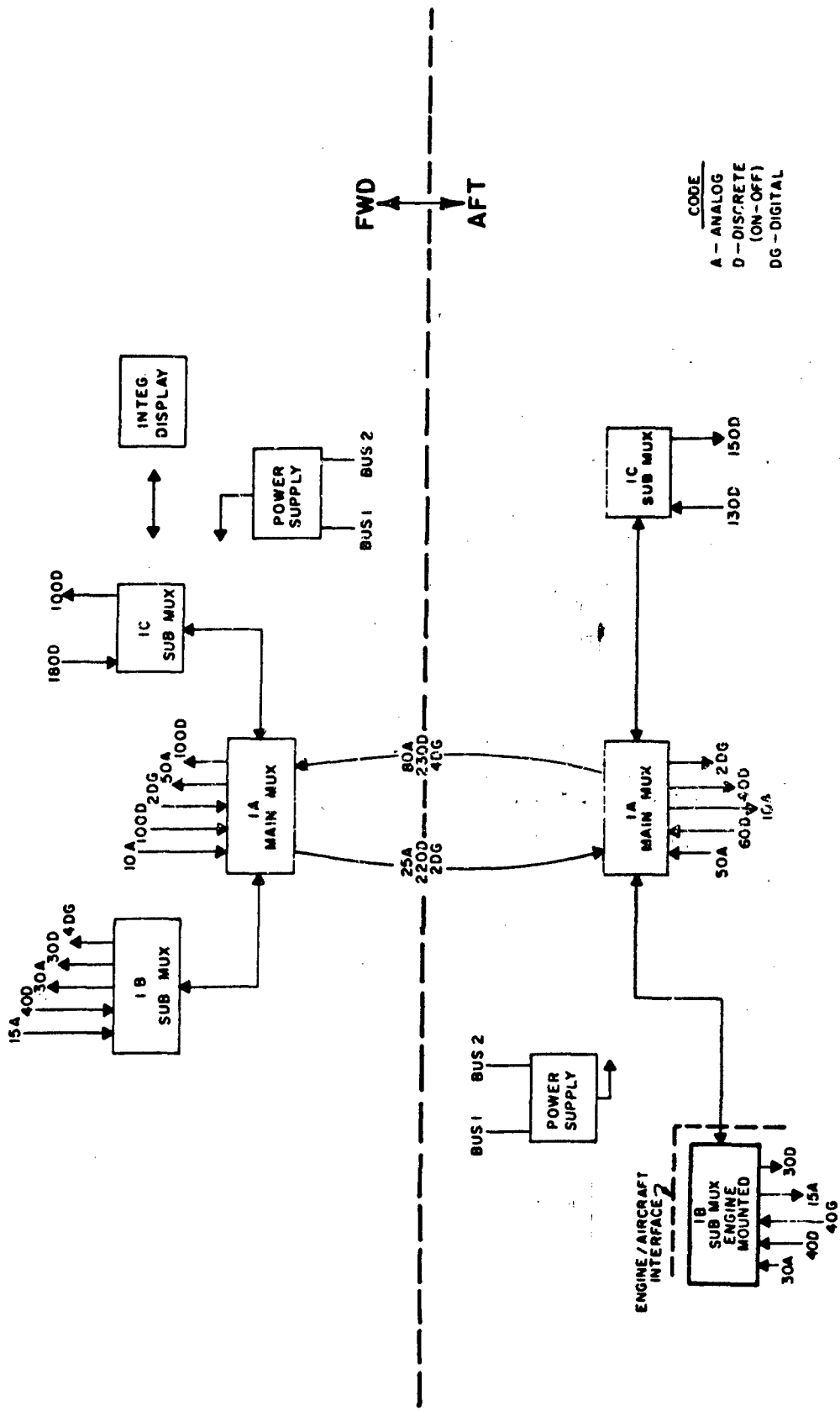


FIGURE 3. DETAILED MUX SYSTEM ORGANIZATION
 (ONE SIDE OF AIRCRAFT)

system and also checking to see if the right number of information bits have been received.)

2. Fault isolation philosophy is applicable to a large percentage of analog as well as digital circuits.
3. Higher reliability particularly for long mission times.
4. Capable of operation with a second fault using manual switch over.
5. No hardware disadvantage compared to a duplex system because of the techniques used in voting yield circuits simpler than the coding and decoding circuits required in the duplex approach.

DETAIL SYSTEM APPROACH

Transmission Mode

Studies have been made into various modes of main interstation communication. Many different transmission systems have been considered and traded off against each other in the areas of reliability, weight, susceptibility and flexibility. The results have indicated that the pulse code modulation/frequency modulation approach was superior for a large general purpose mux system. The capability of simultaneous two way transmission afforded by the FM technique effectively doubled the system bandwidth while the PCM time division multiplexing effectively handles the many limited bandwidth signals.

Figure 4 shows the basic transmission system between the main stations. This is repeated three times in the triplex approach. The NRZ (non return to zero) signal data is used to modulate an FM carrier in the 1 to 2 megahertz range. A $\pm 7.5\%$ frequency deviation provides the "ones and zeros" for digital transmission. The clock, (located at the aft station) is superimposed on the transmission line at its basic frequency (i. e. no carrier). The combined signal is passed through a low pass filter, down the transmission line, to be received at the forward main station through a low pass filter and discriminator, where the NRZ data is recovered. The clock is extracted as shown via a phase lock loop after the low pass filter. The data flow in the reverse direction is similar except that the carrier frequencies are separated by greater than 0.5 megahertz.

Figure 5 illustrates the concept of time diversity which is used to insure a continuous data flow from station to station even in the presence of massive electrical interference such as lightning strikes. It is important to note that a triplex transmission approach is required to implement this feature. The time diversity technique is the real time skewing of bit data prior to FM modulation, so that at any instant the data on the three transmission lines differs. Without diversity a lightning bolt could cause data on all three transmission lines to be lost for perhaps 50μ seconds. With time diversity, the data in real time would only be lost on one channel. As seen on Figure 4 the three channels are displaced from each other by the equivalent of 10 bits in time prior to encoding. The time diversity is removed after reception just prior to majority voting. Ten bits represent approximately 57μ seconds with longer delays being acceptable to a general purpose multiplexing system if necessary.

The number and type of signals going to and from the engine

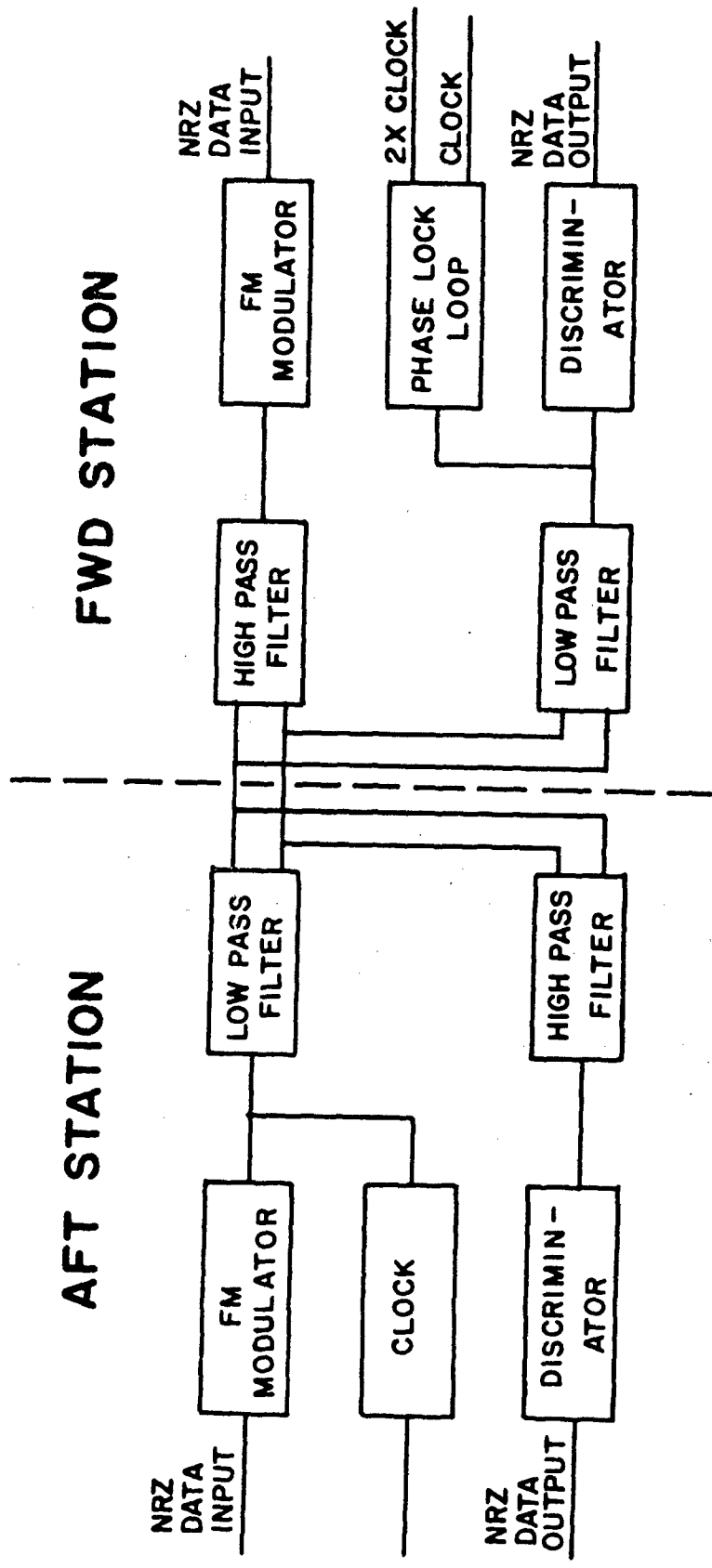


FIGURE 4. TRANSMISSION SYSTEM

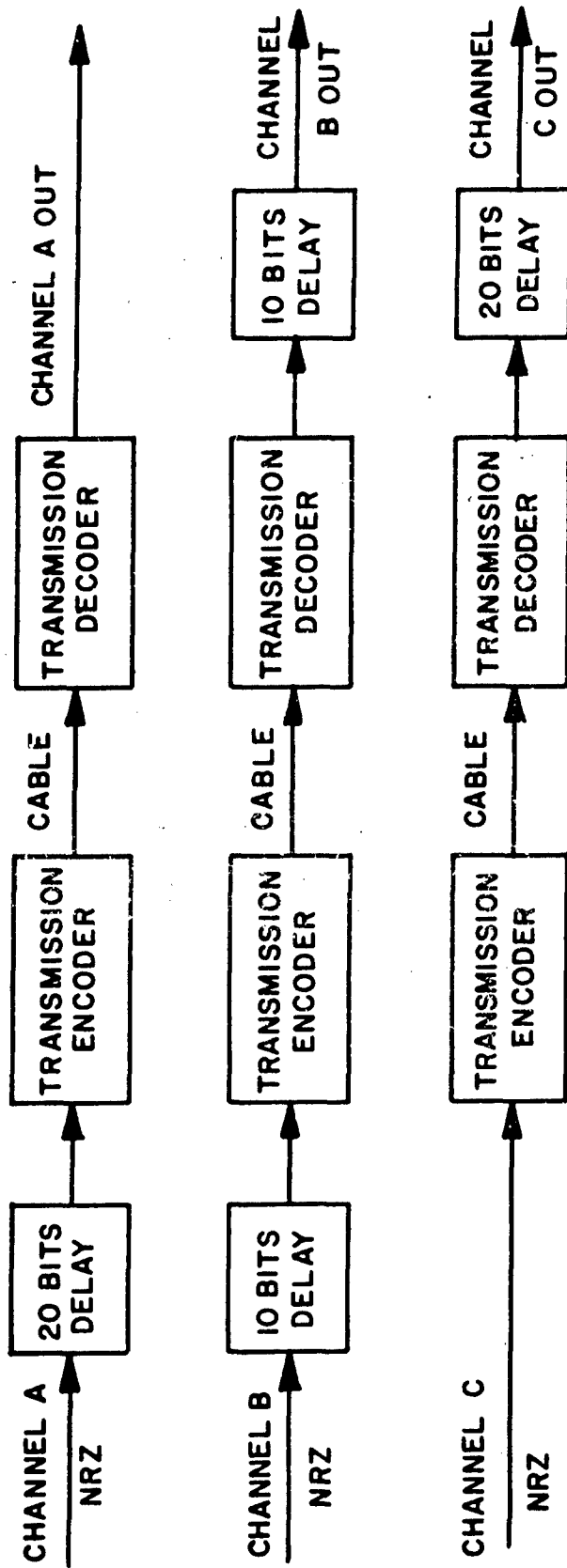


FIGURE 5. TIME DIVERSITY SYSTEM

mounted submux shown on Figure 3 is considered typical of the mix required in an advanced propulsion system.

Sampling Rate

One of the major factors in the design of a general purpose mux is the optimization of the sampling rate for the system. The high accuracy analog signals are those requiring the most frequent sampling based on the stated requirements.

Several constraints and/or factors must be considered to determine the sampling rate. Of course, a basic requirement that must be met is a sampling rate high enough to facilitate closed loop response when the mux is a series link in the loop of a particular control function. Sampling theory would require a sampling rate approximately 4 times the desired system bandpass frequency for basic stability reasons alone. However, the accuracy required to reconstruct a dynamically changing analog signal tends to require higher sampling rates than those chosen from closed loop stability considerations alone. In addition, lower sampling frequencies cause increased size of electrical filtering elements required to smooth the data. This increase in component size has a very adverse effect on total system utility by increasing system size and weight. This factor is shown graphically in Figure 6 . The figure shows how the system effectiveness¹ is low at the lower sampling rates and also drops off radically at higher sampling rates. The reason for the drop off at the high end is that certain basic electrical circuits have reached their limit in terms of operating speed. It is therefore necessary to parallel certain circuits such as analog to digital converters to handle the information rate. Metal oxide silicon (MOS)

¹System effectiveness was arrived at by summing a number of weighted factors on a common but arbitrary scale representing such things as reliability, size, weight, cost, etc.

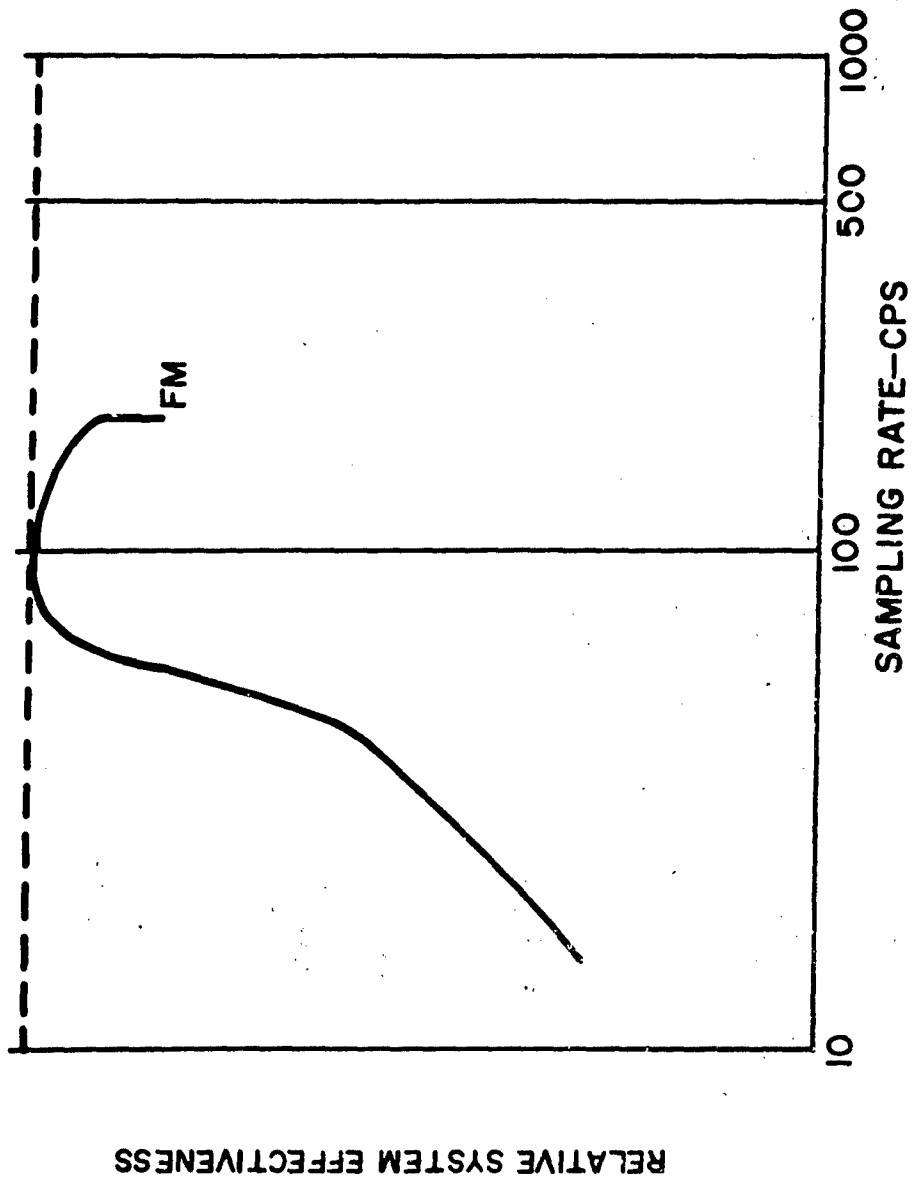


FIGURE 6. PCM/FM SAMPLING RATE TRADEOFF

circuit arrays were chosen for maximum circuit density and lowest cost per circuit function. The speed limitation of MOS was used as a basic constraint in determining the most practical sampling rate.

A general block diagram of a main multiplexer station is shown on Figure 7.

Analog input data is first signal conditioned by buffer amplifiers which provide the necessary impedance matching and proper voltage and setpoint scaling. Input signal overvoltage protection is also provided by the buffer amplifiers. The analog signal conditioners are non-redundant and feed into the three redundant channels of data multiplexing, as is illustrated. Triplicating analog input signal conditioners is expensive and results in high power consumption. Also, triplication of single signal carrying circuits is not a basic requirement as previously stated.

The discrete signal conditioners and digital signal conditioners provide impedance matching between the input devices and the input multiplexer circuitry, as well as providing voltage scaling. Transient overvoltage protection is included in the signal conditioning. The discrete signal conditioners are relatively simple, hence, are triplicated for the three redundant data handling channels. Triplication of single signal carrying elements does result in minimal built-in-test circuitry which can be a requirement for total system check-out and fault isolation. This is discussed further in subsequent paragraphs.

The conditioned signals are multiplexed into the triplex transmitters. Figure 8 shows this process in detail for one transmitter channel. The analog signals are multiplexed by FET switching and the resulting pulse amplitude modulated (PAM) signal is fed to an absolute amplifier. This converts plus or minus (bipolar) signals to full scale unipolar signals, and also generates a plus or minus sign bit. The voltage output is fed to an analog sample and hold

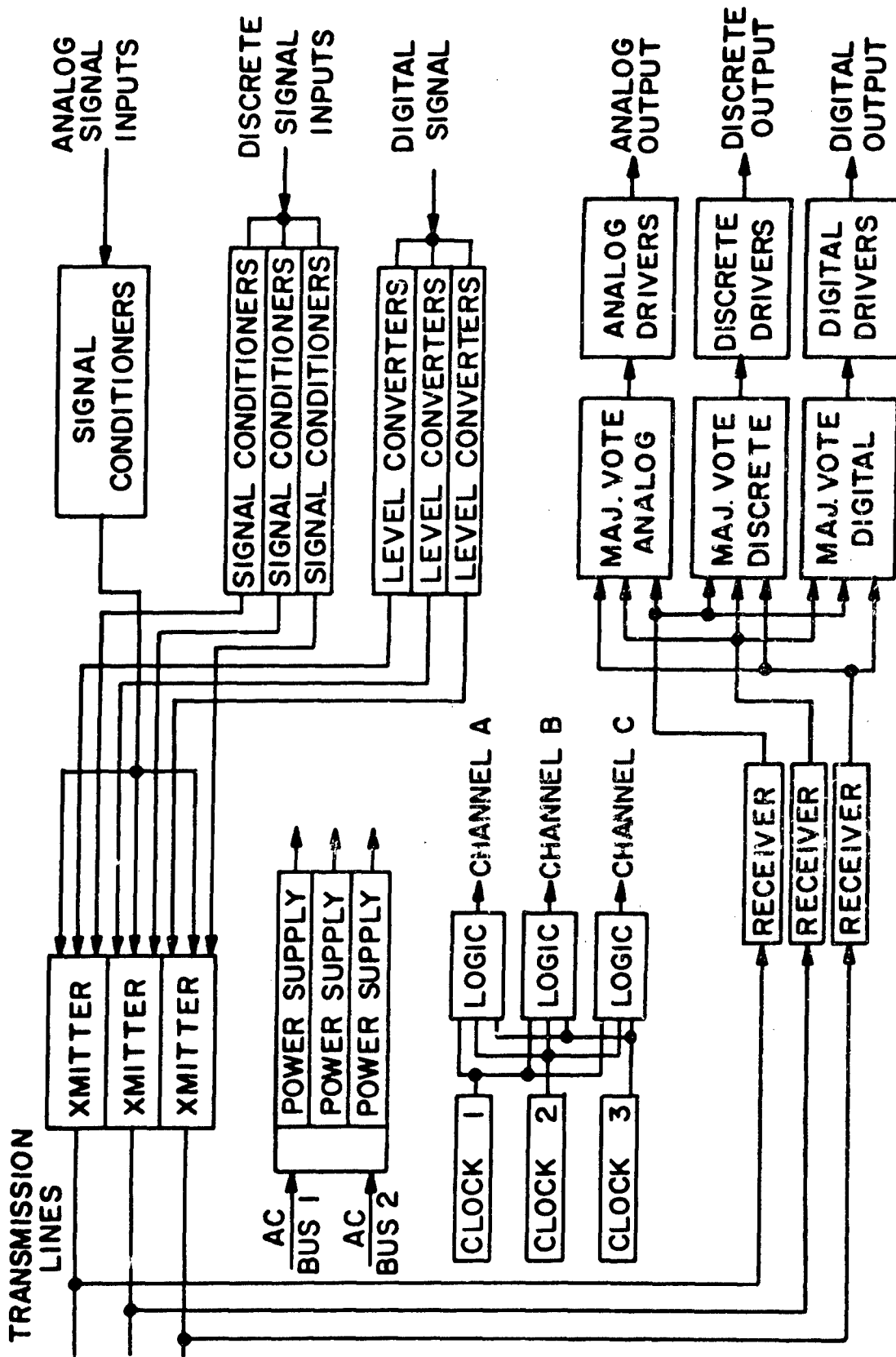
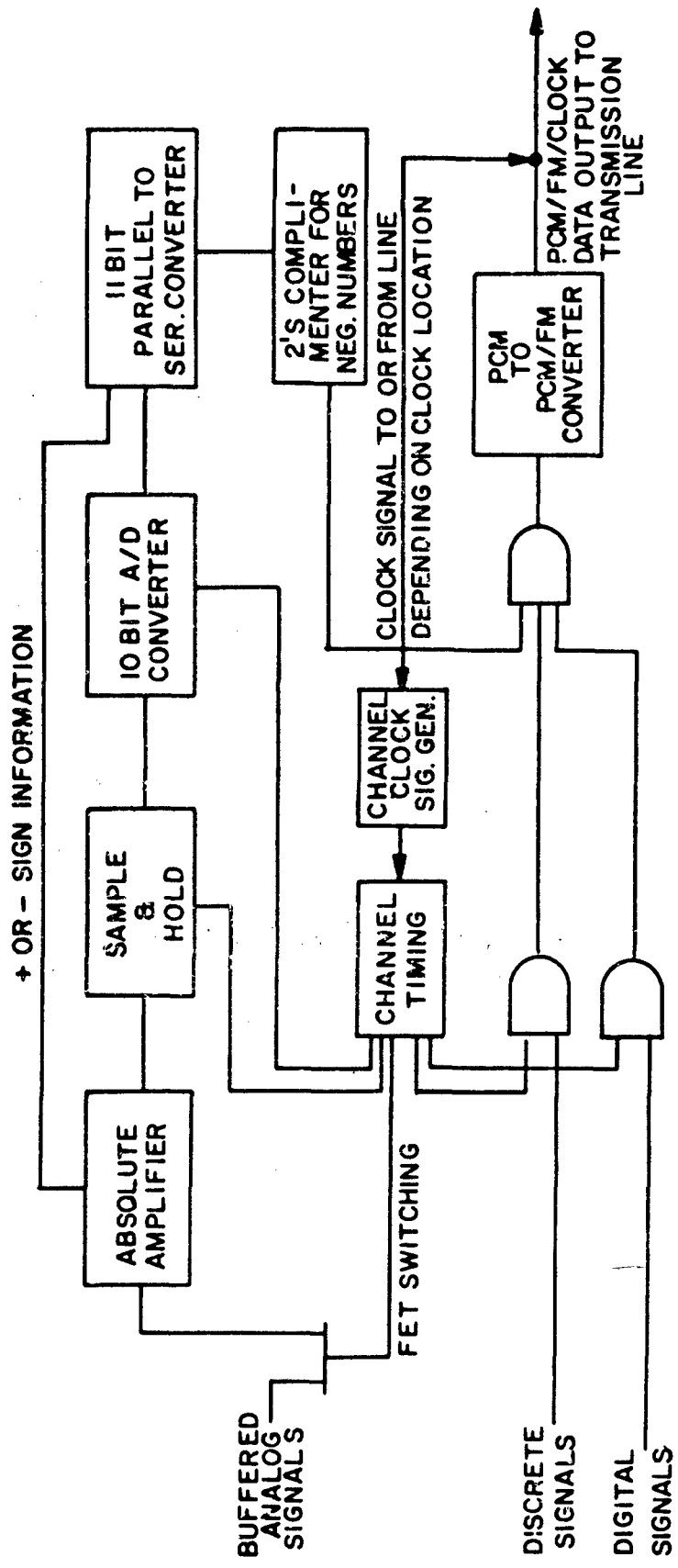


FIGURE 7. MAIN MULTIPLEXER



* APPEARS THREE TIMES AT EACH STATION

FIGURE 8. *TYPICAL CHANNEL TRANSMITTER

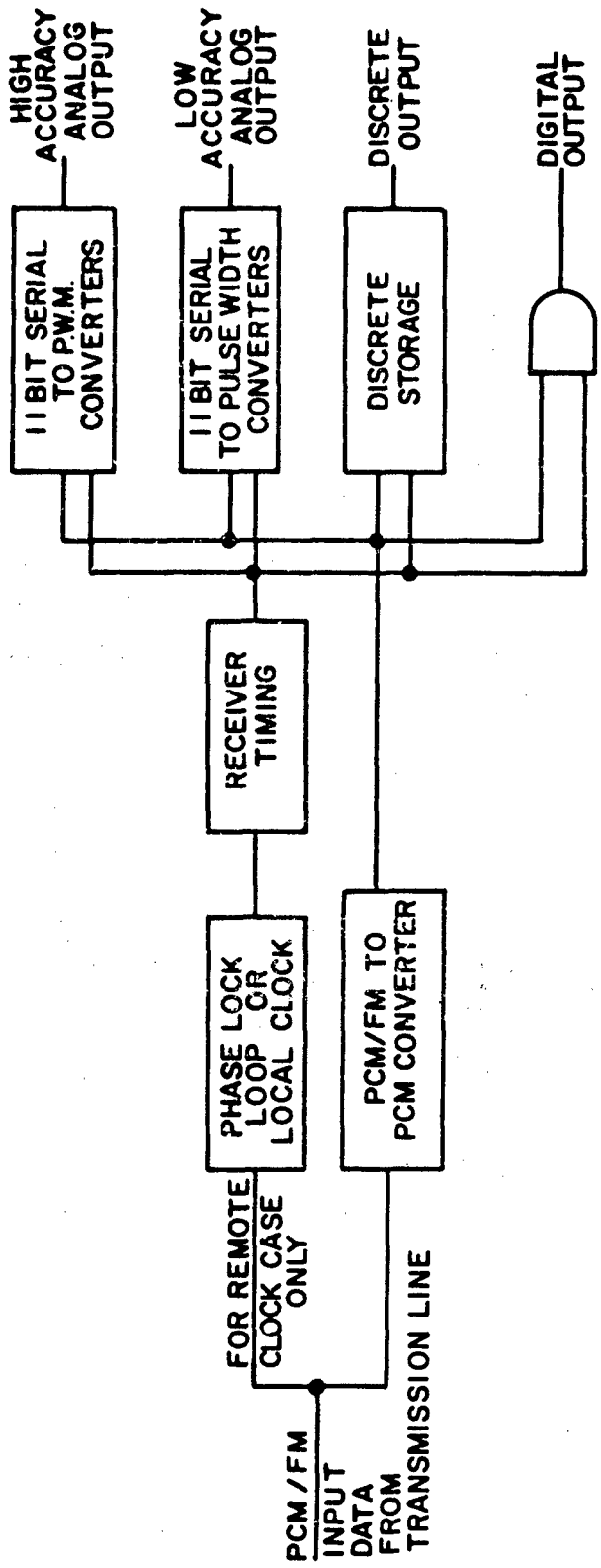
circuit, which in turn provides the input to a 10-bit A/D converter. Its output is combined at a serial to parallel converter with the absolute amplifier generated sign bit, to produce an 11 bit pulse code modulated (PCM) serial output word, representing the PAM input. The PCM output is applied to logic which passes the positive numbers unchanged or converts negative numbers to their 2's compliment form. This analog multiplexed PCM data stream is combined with multiplexed discrete and digital signals under control of the channel timing. The combined PCM data is then converted to PCM/FM via a FM modulator for transmission on the lines as previously described.

The channels are provided with separate power supplies, referring back to Figure 7. The power supplies are also majority voted. The clocks for the channels are provided via triple-redundant sequential switching logic from one of three system clocks. The clocks are located at one of the main stations and the clock signals added directly to the PCM/FM data on the transmission line as previously described.

The PCM data from any station is generated from the analog, discrete, and digital inputs in an identical manner to that described above. Only one main station would have clocks. At other stations the clock is received and fed to triplicated phase lock loops², which provide the triplex channel timing. Any other station would therefore be identical to that shown on Figure 7 except some would have triplex phase lock circuits in place of the clock shown.

Figure 9 shows the receiver block diagram for a single channel. The PCM/FM data is first converted to PCM data via

²A phase lock loop is a circuit which acquires a pulse train and locks on and reshapes the pulse for local clocking purposes.



*REPEATED THREE TIMES AT EACH STATION

FIGURE 9. *TYPICAL CHANNEL RECEIVER

a discriminator circuit. The PCM data is then fanned out to discrete storage gates, analog PCM to PWM (Pulse Width Modulated) converters, and digital gates. These units are addressed under the control of the receiver timing.

Triplex PCM to PWM converters for each analog signal are provided for analog detection and storage. The PCM data stream is constantly being supplied to shift registers contained within these converters. At the proper frame address, the word corresponding to the chosen analog signal is parallel transferred from the shift register, and used to simultaneously preset an up counter and set a flip-flop. The counter is then allowed to count to overflow. (A bit rate in the 150 to 200 kilohertz range is used for clocking the low accuracy signals, and a multiple of this bit rate (2 X typical) is used for high accuracy signals.) The difference is required in order that the high accuracy analog signals can be super-commutated.³ Counter overflow resets the flip-flop. The ratio of On to Off times of the flip-flop is an indication of the equivalent analog value.

The digital signals are demultiplexed via discrete gates enabled by appropriate receiver timing. During the proper frame time, therefore, serial digital data will be available.

The output of the discrete storage registers, the PWM waves proportional to analog signals, and the serial digital data are majority voted upon before feeding to the respective loads.

The submux stations such as the engine mounted unit would be similar in function to the main mux units. One major difference may be that digital encoding of the analog signal is done for the submux unit by the master mux unit. This requires the use

³Supercommutation is the technique of sampling certain signals at multiples of the basic sampling rate for purposes of increasing the accuracy and/or bandwidth of the particular signal.

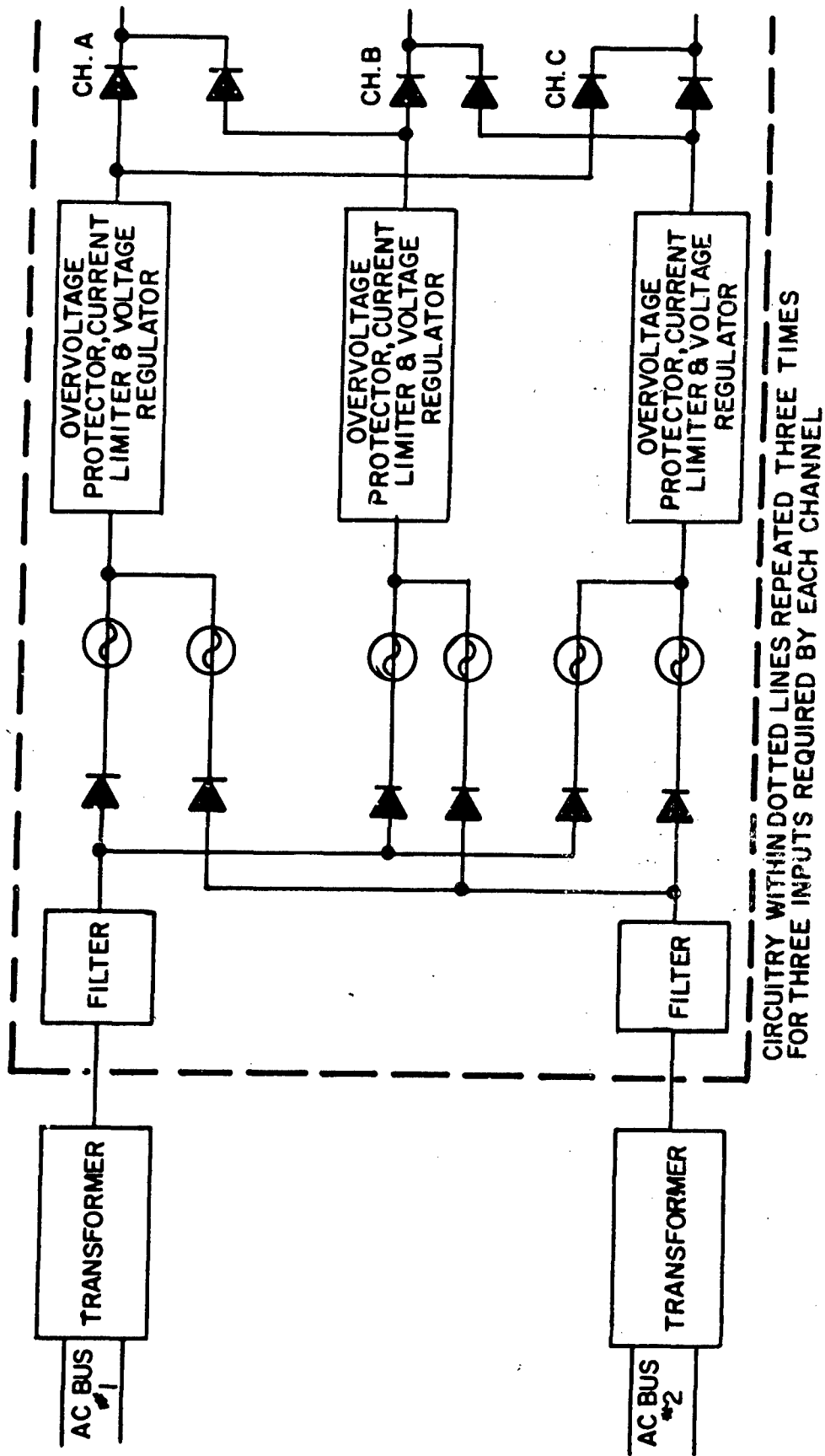
of PAM as a transmission mode from submux to main mux instead of the PCM/FM technique previously described. This is a trade off which must be made on an individual airframe basis. The PAM technique is somewhat more noise susceptible than PCM but results in a less complex system. Also, clock reconstruction and certain resynchronization logic functions would not be repeated in the submux unit. The clock and resynchronization logic may be directly wired to the submux unit.

System Power Supplies

Figure 10 illustrates the power supply concept utilized for the Multiplexer System. Separate transformers are provided for the two input AC busses. Shown within the dotted lines in block diagram form is the circuitry required for the generation of one DC supply voltage for each of three channels. This is repeated three times since three DC busses are required per channel. The rectified and filtered voltage from each of the two basic AC sources will feed all three triple-redundant circuits, i. e., the overvoltage protector, current limiter, and voltage regulator. The triple-redundant circuits are then combined by a two-of-three-most-gate sequence. The built-in redundancy and voting allows the following features to be achieved:

- a. No loss of a channel power supply due to loss of input transformer, filter series regulator, diode voter, or short on series regulator output.
- b. A short on the channel load or the input to the series regulator will cause loss of only one channel power supply.

The supply is shared by the master multiplexer and two sub-multiplexers available at each station.



CIRCUITRY WITHIN DOTTED LINES REPEATED THREE TIMES FOR THREE INPUTS REQUIRED BY EACH CHANNEL

FIGURE 10. POWER SUPPLY-GENERAL PURPOSE MULTIPLEXER

System Clocks

Figure 11 illustrates the triple redundant oscillator concept utilized to provide a reliable system clock. Three independent oscillators feed triple-redundant sequential switch logic circuits. The sequential logic picks one of the three oscillators at turn on, and by providing built-in-test indicates it is functioning properly.

The appropriate three clock gate is activated and provides the system clock excitation for the three channels. In the event that the BITE output indicates improper operation, the next clock will be sequentially chosen. If its BITE indicates proper operation, this clock will be chosen, if not, the third will be sequentially chosen. In the event that a fault should occur in an oscillator after it has been chosen, the next clock, per the sequential logic, will be chosen and retained if its BITE indicates proper operation. The features of the described concept include the following:

- a. Intermittent transient failure of one oscillator will cause switching to another oscillator, and switching back will not occur. Thus, intermittent oscillator faults will not continually falsify data.
- b. Two backup clocks are provided for ultimate reliability.

Built-In-Test-Equipment (BITE)

Two types of BITE are provided, one which tests for faults in the redundant circuitry, and another which can detect a fault in a single signal line. Triplicated circuit BITE detects faults in circuitry that is common to more than one signal path. This is the most important fault to annunciate since a second failure in this circuitry could cause many signals to be lost if second failure

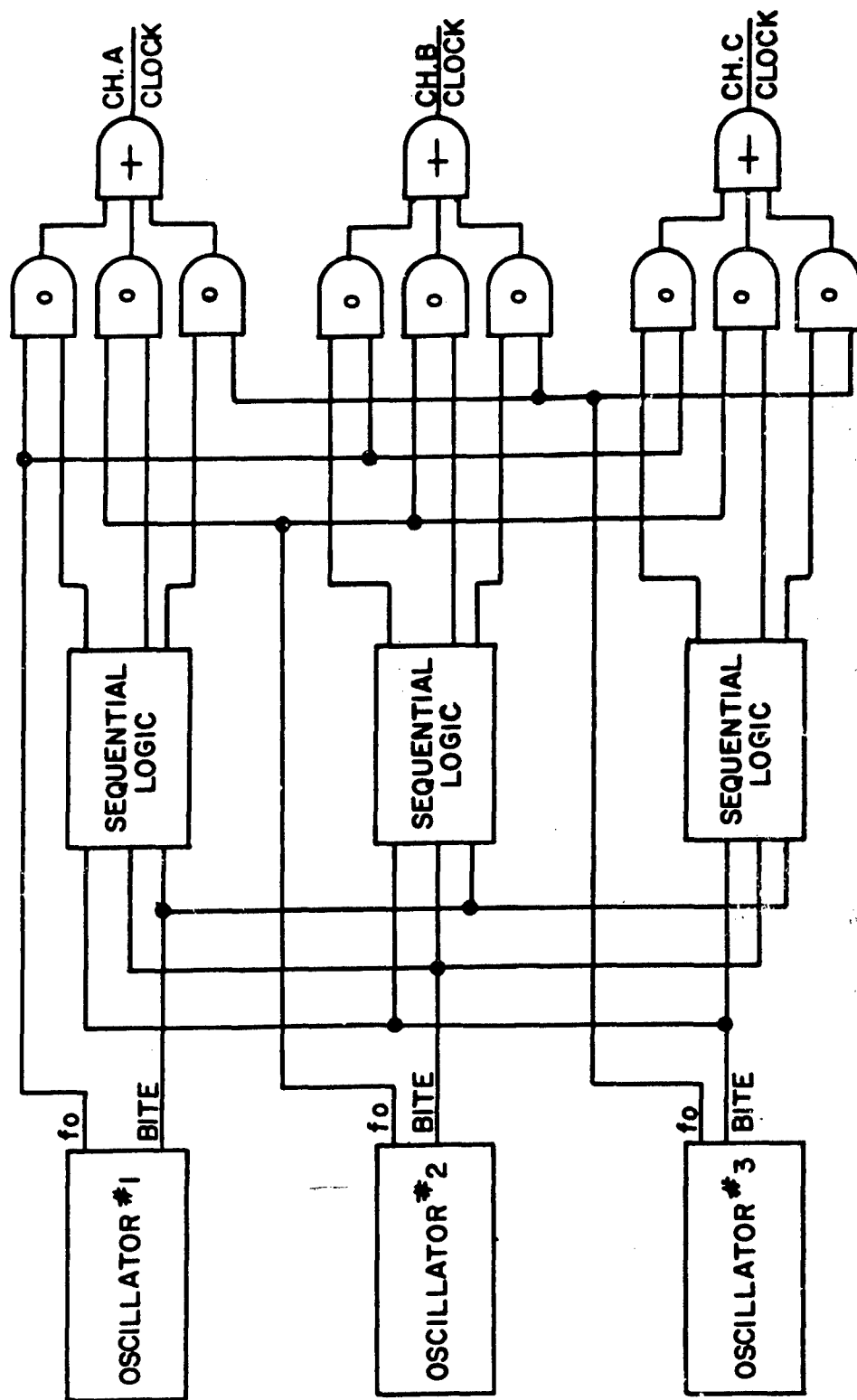


FIGURE 11. TRIPLE REDUNDANT CLOCKS

switching is not provided. Based on various priorities which have been established, the logic associated with the triplicated circuit BITE will locate the fault to a line replaceable unit (LRU). The integrity of the BITE circuitry itself is checked by test words which are purposely arranged to simulate certain types of faults.

The following circuits are checked by triplicated circuit BITE:

- a. Analog multiplexing and A/D conversion.
- b. Discrete, multiplexing and FM modulation.
- c. Transmission cables.
- d. Receiver timing.
- e. Power supplies.
- f. Master oscillator.

Analog signal single thread BITE will sample one analog input signal per frame, and hold this value for subsequent comparison. The analog signal is then transmitted in the normal manner, and received at the appropriate station. The PWM output of the signal in question is then fed to a reset integrator, where the pulse width is converted to an equivalent DC value in one frame interval. The output of the reset integrator is transmitted back to the original station in a similar manner as a normal analog input. At the originating station, it is converted to an analog value by a ladder D/A. The D/A output is then compared to the originally sampled analog signal. If the single thread plus BITE is properly functioning, the comparison will be favorable. If not, a fault bit is generated. The fault is isolated to the transmitter or receiver by an added comparison of the sampled analog word with its digital counterpart prior to transmission. Faults in BITE can be distinguished from single thread faults by the persistence of the

fault bit for many analog signals. Faults in a single thread discrete or digital path can be detected by a 4 input exclusive "or" of the three inputs to the majority voter and the discrete driver output. Lack of agreement will produce a fault bit. The 4 input exclusive "or" gates are multiplexed to minimize added hardware.

Second Failure Survivability

An important feature in a triplex Multiplexer System is the ability to be switched either automatically or manually to a simplex mode in the event of a second failure. The first failure would be tolerated automatically and enunciated. Once the first failure had occurred it would be normal procedure to manually select one of the two remaining operative channels. If in the extremely unlikely event that the channel then selected failed, manual switch over would take place in a timely manner without a decision making process involved. With the circuitry utilized in the majority voting implementation, if power is removed from two of the three channels the remaining channel is simply gated by the majority voter. Thus, it is possible to convert from a triplex system with majority voting to a simplex system by merely removing the power from two of the three channels.

Figure 12 illustrates the concept of second failure switching, where relays A, B and C (under control of a selector switch) are used to remove power from the appropriate channels to allow the desired simplex mode of operation.

DISPLAY PANEL INTEGRATION

Increased complexity of aircraft accompanied by reduced crew compliments and available space all are providing major reasons for more display integration. The general nature of multiplexing (i. e., having all signals available in digital

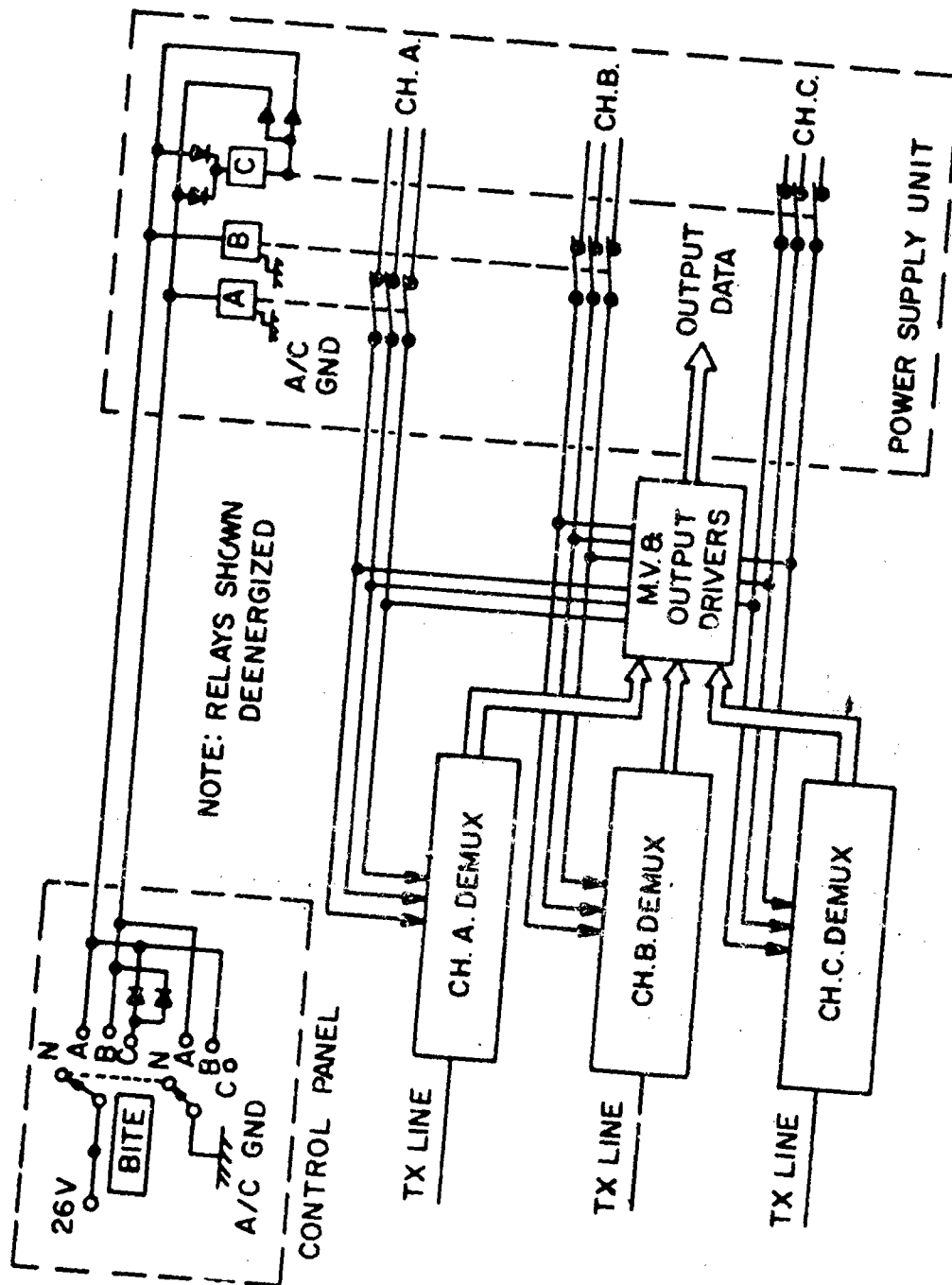


FIGURE 12. SECOND FAILURE SWITCHING MODE

form from two or three cables) allows the design of a single display which can on demand provide a readout of any multiplexed parameter. Many parameters, including some engine parameters, are secondary in importance but yet desirable enough to be displayed. In contemporary displays this results in massive instrumentation clutter. Multiplexing yields a technique whereby these secondary parameters can be displayed as desired. In addition, the integrated display can provide a backup for normal vital instrumentation. This in itself may eliminate one full complement of vital engine indications which might normally be provided on larger aircraft as backup. The following is a description of one possible method for utilizing multiplexing as a point source of data using minimum extra hardware to command and display information.

The levels of sophistication in the display area are many. The intent here is to show how meaningful data can be read out with a minimum of extra hardware. A minimum approach such as this requires more crew involvement in terms of identifying parameters by code numbers and applying the necessary scale factors to convert digitally displayed data into engineering units.

The multiplexer system would feed multiplexed data via a transmission line to a display panel where it would be decoded. The desired decoding could be accomplished by two sets of buttons yielding a combination of readings in decimal form. The desired readings would be displayed in % of full scale of any parameter to a three place accuracy. To convert percentages to numbers, a microfilm and reader are provided for a permanent cross reference table which would identify parameters by name, number and required scale factor conversion. A read only memory could also be provided to allow this conversion to be done automatically.

The operation is shown in block diagram form in Figure 13. The digital data (from analog signals which have been digitized) in the three channels is compared. Channel A is compared to B and C is compared to B. Based on this digital comparison it is determined if Channel A is good. If the channel is normal, the data is passed along with clock and frame synch signals to the display panel. If Channel A is determined to be faulty, Channel B is selected.

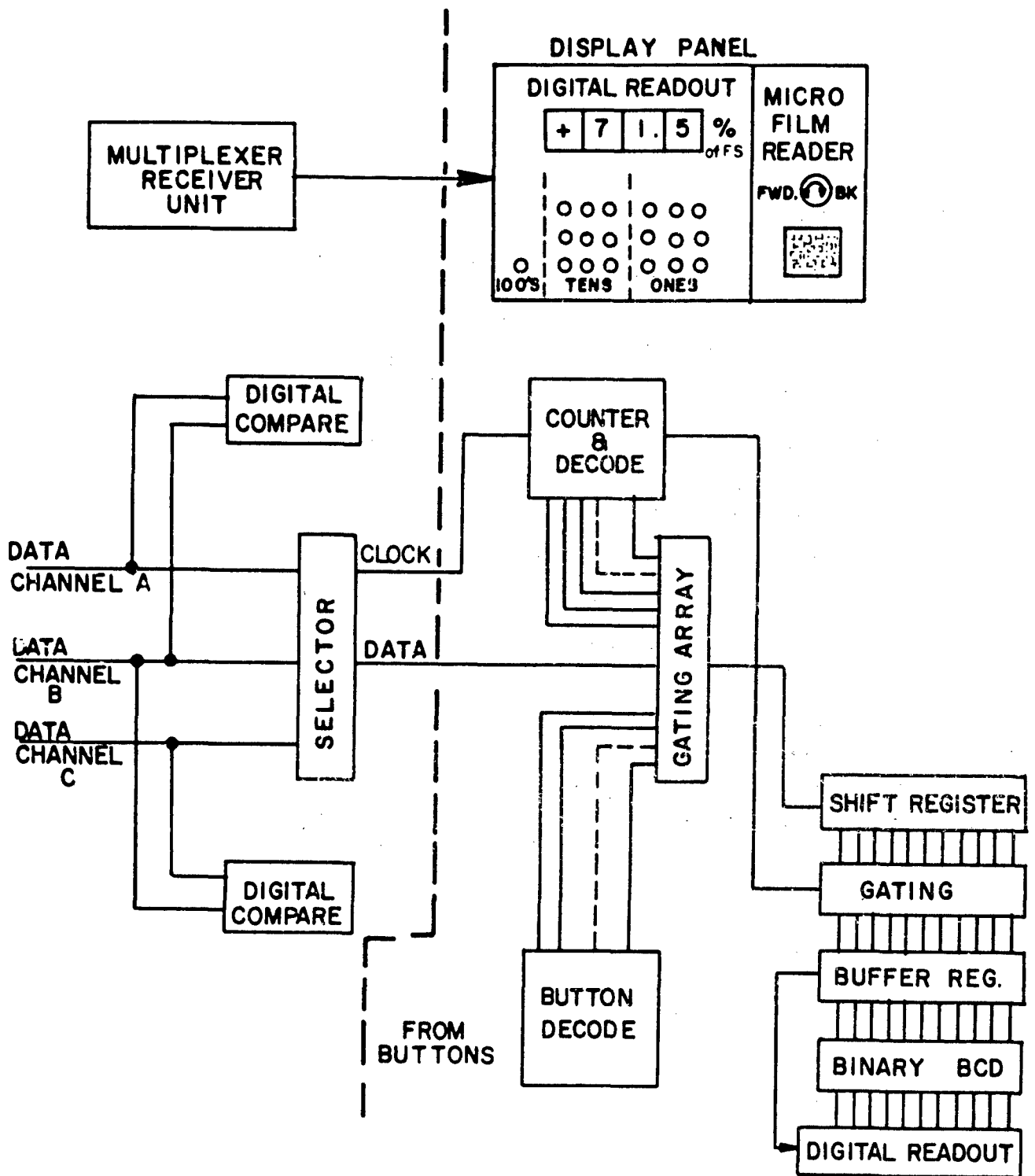


FIGURE 13. MULTIPLEXED PANEL DISPLAY

The digital data is fed to a gating array in the display panel. The gating array is also fed from counter and decode circuitry drivers from the multiplexer unit clock and frame synch, and a button decode which decodes the 18 buttons to 99 states. The last two sets of inputs are "anded" in pairs to provide the desired readout (based on position in frame and buttons pushed) to be shifted into the output shift register. From this register it is gated in parallel to a buffer register, where it is converted to a binary coded decimal form for display. The sign bit associated with the binary digital number is carried over directly.

6. HARDWARE CONSIDERATIONS

Semi-Conductor Technology

Major recent advances in semi-conductor technology have been one of the catalysts which have caused serious consideration of multiplexing in aircraft. Five years ago, the economics and sheer bulk associated with the use of (then) contemporary integrated circuits and discrete components prevented the practical application of multiplexing. Today, large scale integrated circuits (LSI), have allowed the design of reasonably sized electronic assemblies. This is accomplished by fabricating the equivalent of 500 to 1,000 discrete components as a single block. This is exemplified by the photographs in Figure 14, one showing a MOS digital array and for comparison an equivalent digital function made up of conventionally interconnected integrated circuits. The LSI arrays have not only caused a marked reduction in equipment size and weight but have reduced significantly the cost of implementing equivalent functions. Metal Oxide Silicon (MOS) LSI arrays have demonstrated successful operation at the lowest cost to date on an equivalent function basis. MOS field effect transistors (FET) in an LSI array now provide a viable solution to switching on and off analog signals using extremely high density solid state techniques. MOS logic circuits in large arrays are used extensively in major digital functions. MOS devices do have one major disadvantage over other basic LSI constructions in that they have a lower bandwidth (The logic takes more time to change its state).

THIS FIGURE SHOWS A SIZE COMPARISON BETWEEN A MOS DIGITAL ARRAY
IN TERMS OF EQUIVALENT CONVENTIONAL INTEGRATED CIRCUITS.

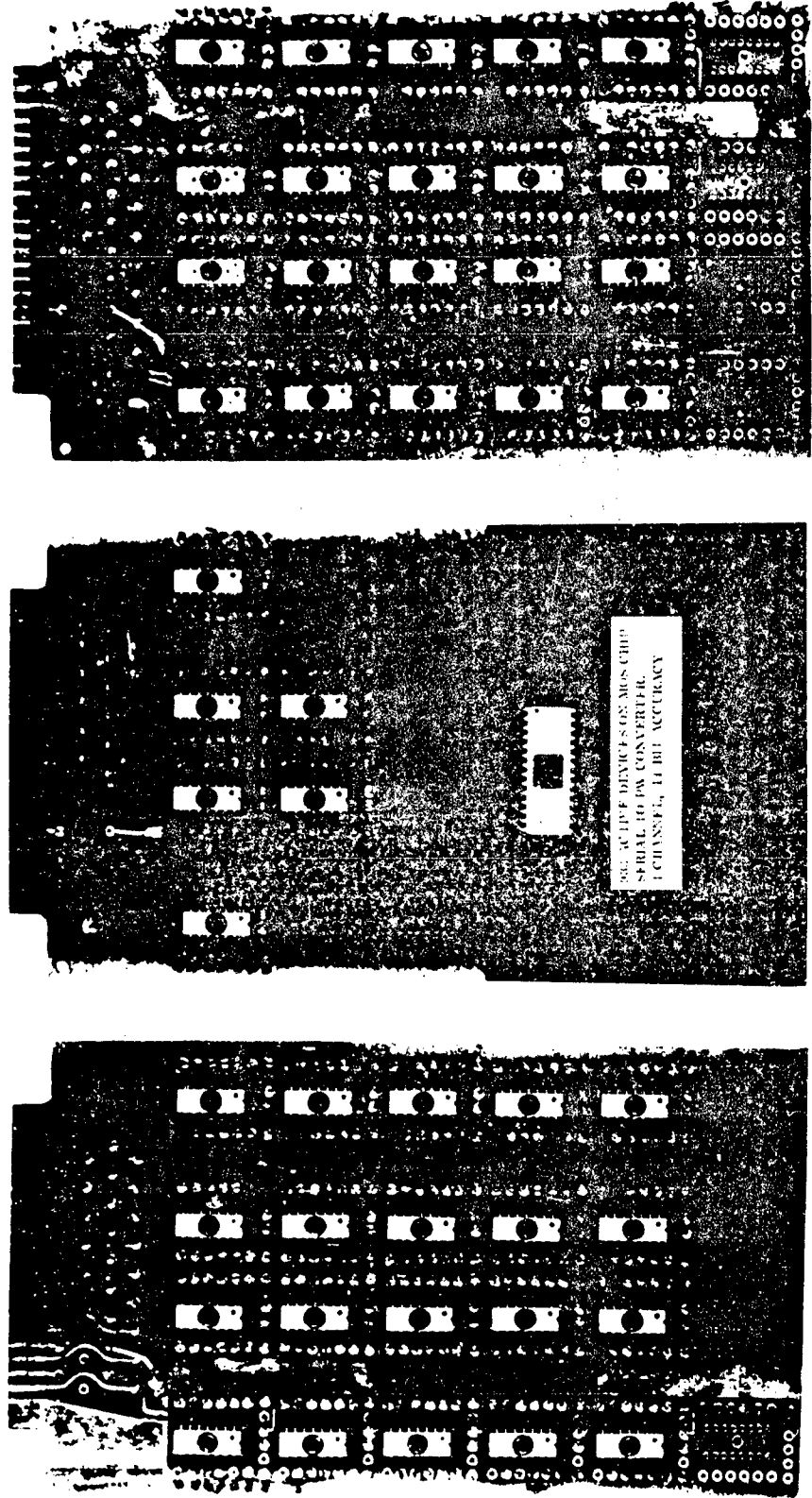


FIGURE 14

However, for general purpose multiplexing of control and instrumentation signals the speed limitation generally is not significant. Analog signal conditioning (at the input end) and analog signal reconstruction (at the output end) can be handled using hybrid packaging techniques where many individual chips are interconnected on miniature ceramic printed circuit boards. Signal conditioning circuit requirements are held to a minimum by time sharing of conditioning elements made possible by switching, using MOS FET arrays.

Environmental Factors

As has been pointed out previously, to take maximum advantage of multiplexing, the stations must be scattered strategically around the airframe. The units must therefore be capable of functioning in extreme environments. This is particularly true for a multiplexer station located adjacent to or on the engine. Electronic functions have been and are being used in an engine mounted configuration with satisfactory results. Current sophisticated engine development programs are utilizing electronics for engine propulsion management functions. The vibration environment associated with direct engine mounting can be met through proper structural design of the package with some increase in unit weight as a penalty. The temperature environment can be as high as 400°F with mounting base temperatures even higher depending on location. Silicon semiconductor devices are limited by practical design considerations to approximately 225°F. Applied research and early testing now underway in the industry promise semiconductor devices using materials such as gallium arsenide having a temperature tolerance up to 400°F. Interconnection process using welding instead of soldering must be used and a substantial amount of development will be required to approach the functional circuit density levels currently obtained when using silicon devices.

The alternate and more immediate solution to the high temperature problem is to provide a tolerable environment for existing electronic circuits using techniques for insulating and reducing internal temperature by heat transfer. Again relating to developments in the engine fuel control area, several programs are underway in the industry where engine mounted electronics use fuel as a coolant. An example of this is shown in Figure 15. This is an engine mounted special purpose digital computer used for supervisory control of an advanced turbojet engine. This particular engine mounted digital control utilizes many of the circuit elements used in a multiplexing station.

If the fuel temperature approaches the practical limit for contemporary electronics, other methods currently under study can be employed. They are as follows:

- a. Thermoelectrics
- b. Closed cycle liquid cooling
- c. Air cycle using engine bleed air

Thermoelectric techniques have recently improved to the point where the thermal elements can be assembled to function at the maximum ambient temperatures of interest in the presence of high vibrations. The thermoelectric process (essentially the reverse of the thermocouple effect) has an approximate 25% efficiency in terms of electrical power required to transfer a given amount of heat. To consider thermoelectrics therefore, the expenditure of relatively large amounts of electrical power must be permissible. Liquid or air cycle cooling technique involves miniaturizing systems already in a highly developed state. The disadvantage in these approaches is limited life of moving parts. It is not the intent of this paper to examine in detail the high temperature problem. However, it is necessary to note that solutions do exist providing the tradeoffs are acceptable. The use of fuel cooling involves an approximate 25 percent package weight penalty. Thermoelectrics also incurs a weight penalty of the same order in addition to the significant electrical power consumption factor.

The requirement for operation of electronics in high ambient temperature is not confined to the engine location. Supersonic aircraft will have requirements

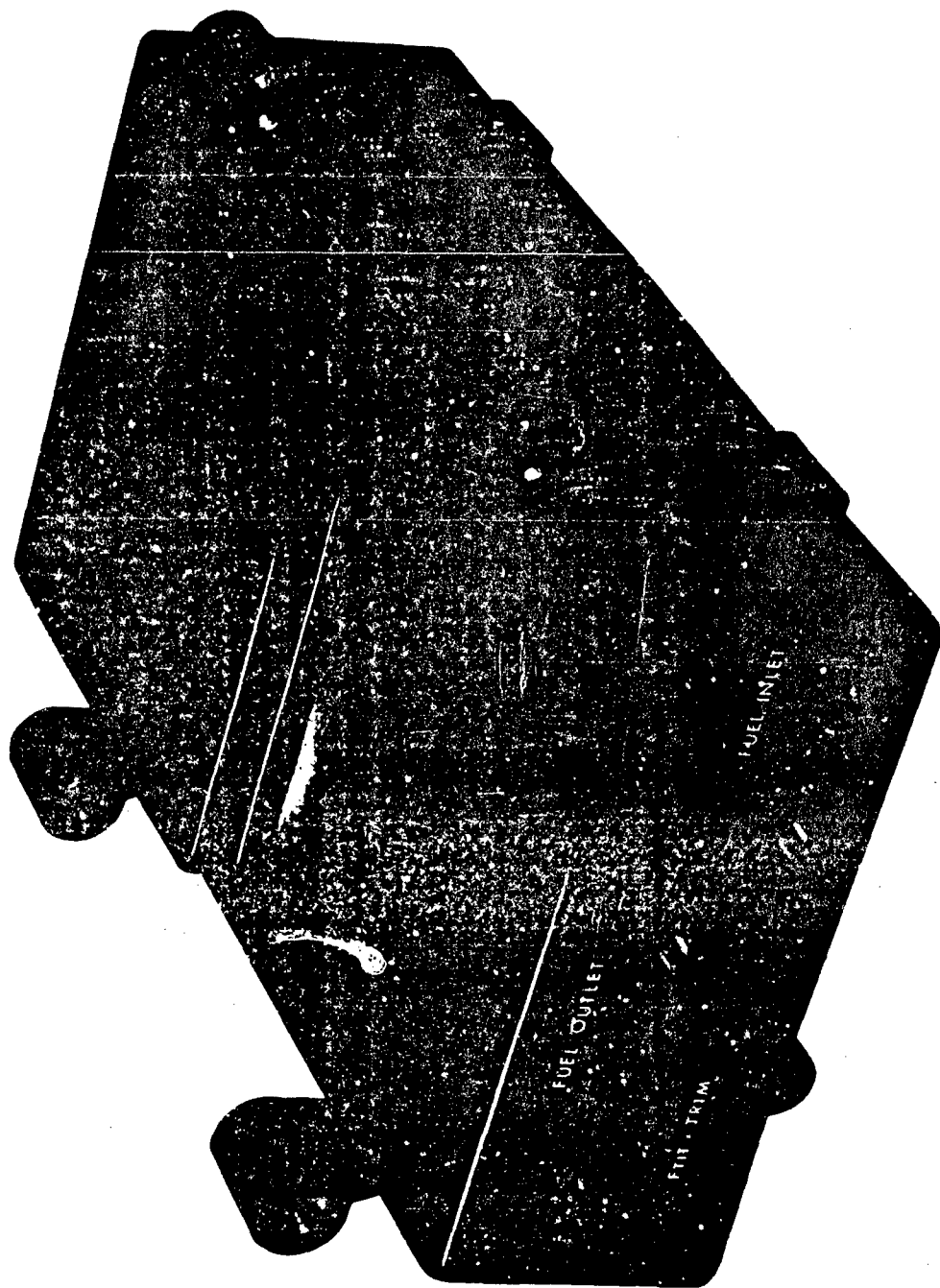


FIGURE 15. ENGINE MOUNTED SPECIAL PURPOSE DIGITAL COMPUTER

for electronic multiplexer stations in non-conditioned areas such as in the wing sections.

Typical Hardware Size and Weight

Hardware design and resulting physical characteristics are of course a function of each airframe application. However, to indicate gross magnitudes, some dimensions and weights are given based on the configuration discussed and shown schematically in Figure 3. Two engine mounted sub-multiplexers are assumed to be cooled by engine fuel. The balance of the system exists within the conditioned environment of the fuselage. The engine mounted units may be similar to the packaging arrangement shown on Figure 15. The estimated characteristics are as follows:

| <u>NO. OF UNITS</u> | | <u>SIZE</u> (in) | <u>WEIGHT</u> (lbs) |
|---------------------|------------------------------|------------------|---------------------|
| 4 | Main Mux Units | 5 X 8 X 18 | 12 |
| 6 | Sub Mux Units | 5 X 8 X 15 | 10 |
| 2 | Engine Mounted Sub Mux Units | 7 X 8 X 13 | 12 |
| 4 | Power Supply Units | 5 X 4 X 18 | 15 |
| *TOTAL WEIGHT | | | 192 pounds |

*It should be noted that this figure does not include any display functions. Also, of most importance is consideration of the net weight penalty to the particular aircraft. This is determined by subtracting the reduction in airframe wiring harness weight from the above system weight. For larger aircraft a significant net weight saving is realized. For fighter type aircraft the weight saving would be smaller.

SECTION III

THE FUTURE OF MULTIPLEXING

In view of the ever increasing complexity in aircraft subsystems, wiring and interface requirements are going to increase. In view of multiplexing advantages, it would seem multiplexing will be used extensively in the future. As the speed of required multiplexer circuits increases more signals may be handled within a given system. Communication signals, such as radar and video, audio and high bit rate digital transmission in addition to instrumentation and control signals may all be combined and handled by the same system. A few general purpose trunk lines routed throughout the aircraft may be responsible for handling all of the above electrical signals.

As multiplexing becomes more widely accepted and applied, interfacing functions such as input sensors and indicating devices will provide, or use, digital signals directly. This will reduce the need for massive use of analog signal conditioning circuits. Integration of displays and interface with Airborne Integrated Data Systems (AIDS) will be accomplished more readily.

Component technology advances will further reduce the size of multiplexing units and related equipment leading to further net airframe weight savings. Standardization of the basic multiplexing characteristics will allow electronic equipment to be added to the airframe or engine and possess within themselves a standard interface module which can communicate with other functions through the multiplexer.

SECTION IV

REFERENCES

1. Hamilton Standard Final Design Report for the SST Multiplexer HSER 5280 dated December 31, 1968.
2. Digital and Sampled Data Control Systems, J. T. Tot, McGraw Hill.
3. Practical Aspects of Information Theory, L. W. Gardenhire, Radiation Incorporated.
4. Error Problems in Sampling Representations, B. Liu and J. B. Thomas, 1964 IEEE National Convention Record.
5. Error Problems - The Reconstruction of Signals from Sampled Data, B. Liu and J. B. Thomas, Pro. National Electronics Conf., Vol. XXIII 1967.
6. Mean Square Reconstruction Error Automatic Control - July 1965, Vol. AC-10 Number 3, A. I. Lilt, IEEE Trans., Page 370.
7. Error Analysis in Sampling Theory, July 1966, Vol. 54 #7, A. Pysoukis, Proc. IEEE, Page 947.
8. Multiplexer Transmission Study for Boeing B-2707 Airplane, Preliminary Report, HSD Report, J. Saunders.
9. Transmission System Selection Criteria, Ref. PSDR HSD/Boeing, September 9, 1968, D68:54-S, J. Saunders.

RESPONSIVE THRUST CONTROL—ADAPTABILITY TO ADVANCED AIRCRAFT DESIGN

Sandro Westermayer

THE BOEING COMPANY
Commercial Airplane Division
Seattle, Washington

ABSTRACT

Thrust control in airplane systems design has changed little from what it has been subscribed to over the years. Innovations such as automatic power compensation, cruise/lift engine transition devices, and inflight thrust reverser controls have not been completely satisfactory, causing unacceptable weight penalties and complex airframe-engine interfaces with respect to interconnect points, cable routing, and system hysteresis.

Within this context, the evaluation and development of new control concepts were initiated. Of several concepts considered, the most promising was one using a force transducer installed within the primary thrust control loop. This unit transmits power requirement signals to the engine thrust control electronics. The solid-state electronics in turn shapes the signal and allows accurate and immediate response through electrically positioned power control units. Potential advantages include:

- Fully automatic thrust control
- No thrust control loss after any single failure within the system, i.e., fail-safe
- Elimination of resolution loss due to mechanical systems friction and hysteresis
- Manual overrides of the automatic system without operating a disengaging control
- No apparent change in manual control levers or "feel"
- Feasible retrofit to existing airplanes without the need to eliminate existing mechanical cable systems
- New design weight and cost reduction over conventional systems

A working model of this system was fabricated and tested. Even though the breadboard setup was assembled with low-quality hardware, it proved the feasibility of the system. The degrees of degraded mode operation were simulated, and logical straightforward remedies were devised to correct and/or aid during failed equipment operation.

Conclusions relate the impact of this type of thrust control on aircraft design.

INTRODUCTION

In 1966 The Boeing Company, Airplane Division, initiated an Automatic Flight Management research program designed to achieve fail-operative automatic flight path guidance and fail-operative automatic all-weather landing of subsonic and supersonic multiengine airplanes. These program goals generate the requirement for automatic fail-operative flight control systems.

Early in 1968, the AFM Controls and Laboratory organization initiated a study to add provisions for a fail-passive or fail-safe automatic control to the present Boeing engine thrust control systems as used on the 707, 727, 737, KC-135, and 747 airplanes.

It was assumed that the automatic command signals would be supplied by a flight path computer, engine pressure ratio computer, or Automatic Flight Management computer. This study did not concern itself with the control equations required to achieve optimum command signals; the study was confined to the control systems, including flight deck control, engine control units, and associated interface hardware.

THRUST CONTROL SYSTEMS REQUIREMENTS

For the purpose of this study, it was assumed that all requirements for the thrust control systems on current Boeing production airplanes would apply. Minor deviations between the various airplanes were ignored since the basic systems concept and requirements are the same for all Boeing production airplanes. The requirements, in addition to the foregoing, can be categorized as follows.

- 1) A thrust control system capable of full-time, automatic throttle operation shall be provided. The term "full time" means continuous automatic throttle operation in all flight regimes without severe authority limiting. Thus continuous automatic updating of true airspeed is provided, facilitating airplane position accuracy during automatic flight.
- 2) After any single failure of the control system, the pilot must be able to control thrust with the thrust levers without determining the source or cause of the failure or accomplishing any switching.
- 3) Manual overrides of the automatic system shall be accomplished with the same pilot's control used for manual operations and without the need for autothrottle disconnect. The manual override shall not result in an unusual feel behavior of the pilot's control.
- 4) Each engine has to be individually controllable in both manual and automatic mode to facilitate automatic engine pressure ratio (epr) trim and automatic airplane crab or decrab.
- 5) Improved resolution in both manual and automatic mode shall be obtained. Cable systems, especially on large airplanes, tend to provide something less than optimum control resolution, resulting in almost continuous throttle movement during autothrottle operation.
- 6) The pilot's control shall be a force/position control similar to existing throttle controls, with its position indicative of thrust setting.
- 7) The systems approach selected shall be suitable for retrofit to existing mechanical cable control systems, requiring a minimum of additional weight or hardware change.
- 8) The retrofit system shall provide the foundation for a lighter weight, less expensive new design.

EXAMINATION OF CURRENT THRUST CONTROL SYSTEMS AND AUTOThrottle PERFORMANCE

To provide a baseline for thrust systems improvements, it is necessary to examine the nature, capabilities, and limitations of our currently employed thrust control systems.

The 747 uses a mechanical throttle control system with push-pull cables between the various throttles and the engine control stand. The autothrottle for automatic speed control is part of the basic airplane. The current 747 autothrottle system operates the mechanical throttle control system through a clutch for manual override. A "bicycle" chain drive connects the single autothrottle servo motor to the control stand clutch, driving all four thrust levers together.

It is noteworthy that the thrust control systems on all current Boeing airplanes, except the 747, are rigged cable systems rather than the push-pull cable system used by the 747. The 747 design departed from the traditional rigged cable system because the space available for cable routing from the flight deck to the lower deck was not well suited for the installation of rigged cable systems.

The current autothrottle is primarily used for landing because fixed mechanical throttle travel limits are used in lieu of calculated epr, exhaust gas temperature (egt), and rpm limits. The autothrottle has a single airspeed-hold mode. (Mach hold is used to change altitude in climbout and descent; it is tied into the elevator control system and does not drive the throttle servo.) In operation, speed commands to the throttle are provided by indicated airspeed panel adjustments or by a self-contained unchangeable-bias "throttle retard" program when radar altitude is less than 500 feet.

The 747 autothrottle is typical of the type on many subsonic commercial airplanes. An exception, the 737, uses a more advanced engine thrust control system to reduce crew workload. The 737 system cannot be used in takeoff or go-around, but the airplane does have an epr analog computer that has a numeric display to show epr limits for current flight conditions. The epr computer is not currently tied into the autothrottle, but the computer does help reduce workload—pilots generally fly maximum epr during climbout and it is much easier to watch an instrument than to continuously look up book values. In practice, pilots ask for speed by setting epr's, and exceeding the epr limit can cause engine damage.

The current autothrottle is acceptable for Category II weather landings and current landing separation standards. It has not been shown that the current autothrottle is accurate enough for Category III landing or for possible decreased landing separations in tomorrow's traffic.

During cruise in today's air traffic, crew workload is light and autothrottle justification must be on the basis of improved speed control accuracy for reduced mission total operating costs. In tomorrow's air traffic, airplane cruise spacing may be reduced to increase capacity, and constant throttle readjustments and constant instrument attention may be necessary to maintain proper airplane spacing; therefore, a high workload, even during cruise, may result.

Currently, engines are "trimmed" by a fuel control adjustment to produce rated thrust at a fixed thrust lever position under standard operating conditions. The rpm will vary slightly from engine to engine due to manufacturing tolerances compensated for by changes in trim speed. Accounting for such small differences makes operation of current multiengine airplanes difficult. It therefore appears to be reasonable to provide for an automatic trim system on any future thrust control system.

I will first discuss the required improvements and changes to current thrust control systems and then describe a more advanced all-electric design that we have developed.

REQUIRED CHANGES TO MECHANICAL THRUST CONTROL SYSTEMS TO MEET ADDITIONAL AUTOMATIC CONTROL REQUIREMENTS

The requirement to provide for automatic engine trim inputs and the necessity of having a fail-safe system make it imperative that more than one power control unit be incorporated into the total thrust control system on any future airplane. Typical current airplane models have the single

throttle power control servo located remote from the engines; mechanical linkage and cables provide the driving link to the engine. This remote operation results in relatively high systems hysteresis, causing reduced control resolution. In addition, all mechanical linkage and cables between engine and power control unit add to the unreliability.

It is an obvious conclusion that locating the PCU's directly at the engines will remove many hardware components from the reliability loop during automatic operation. Locating the PCU's at the engine also will eliminate the loss of resolution due to control systems hysteresis. Furthermore, a single PCU at every engine provides for overall thrust system redundancy since a single PCU failure affects only one engine. It also appears possible to provide some limited interlock between all PCU's in the final design of such a system. This would greatly reduce the effect of a single PCU failure. Much applicable experience has been gained in the development of the current primary flight control PCU's; it appears logical to use this background to develop the PCU's and associated systems for thrust control. Engine manufacturers are now developing such PCU's. It is the writer's understanding that some units are commercially available.

The electrical loop of such a system is relatively straightforward, as shown in Fig. 1. Closer examination reveals that this basic system is practically identical to the aileron or elevator control system on the 737 airplane. To provide for manual inputs to this system, it is necessary to add only the control in the cab.

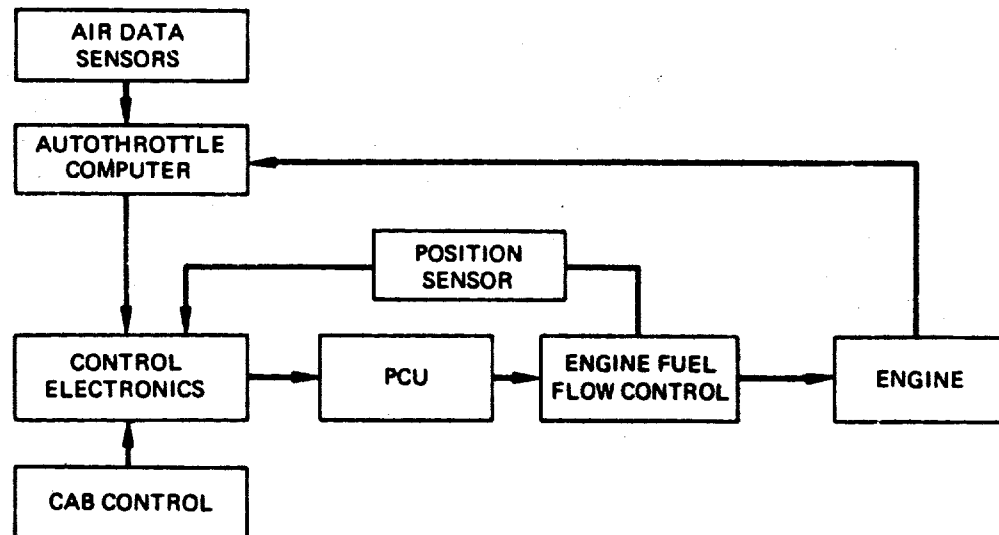


Figure 1. Basic Thrust Control System

Mechanization of such a system was accomplished with the development of the control wheel steering system for the 737 airplane. Rather than adding a separate controller, a force transducer is installed in the primary mechanical control loop. Figure 2 shows some of the mechanical details.

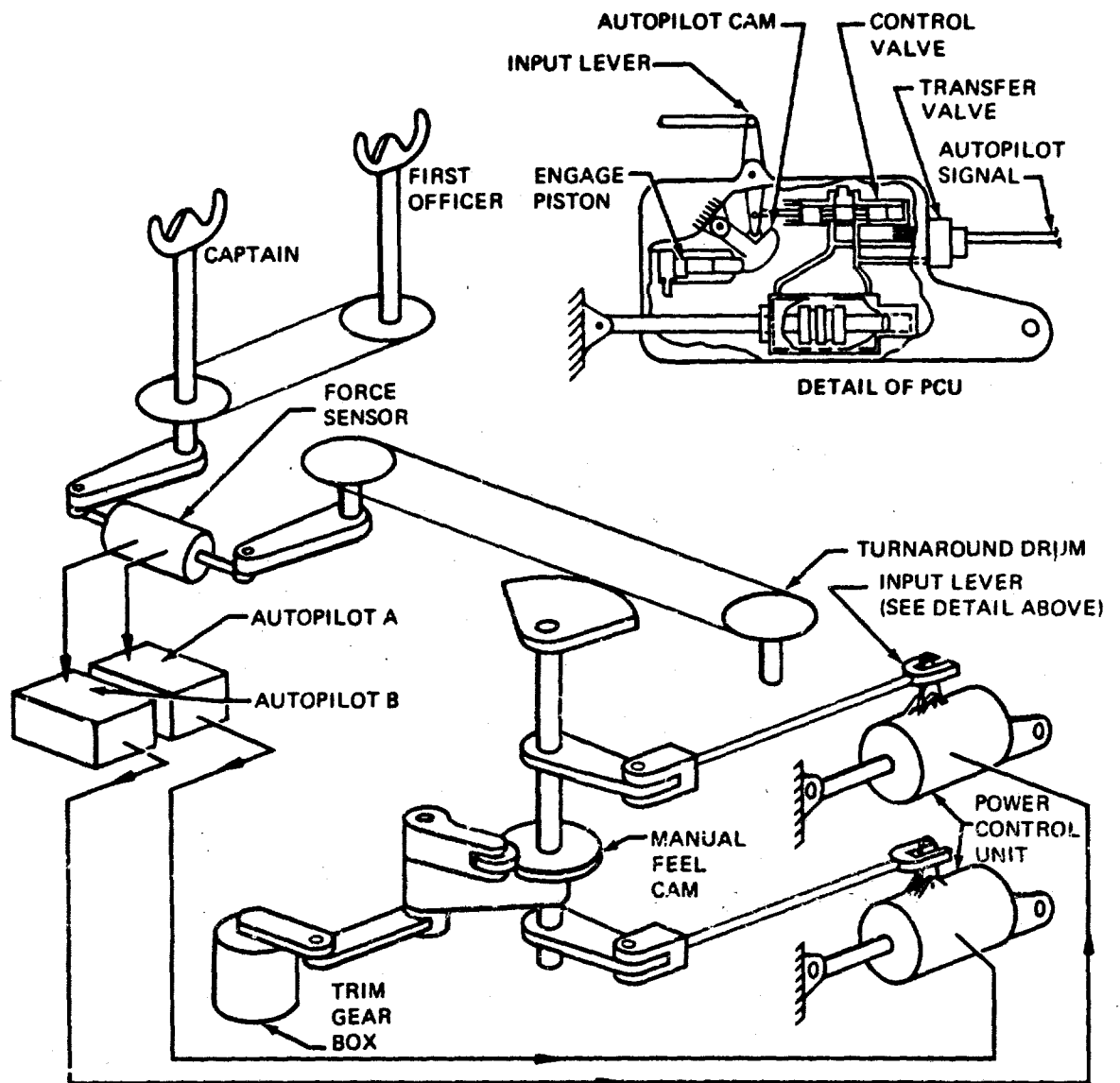


Figure 2. 737 Lateral Control System--Partial

Figure 3 indicates the implementation of this concept on the thrust controls. This now provides for automatic operation, manual operation from force transducers through controls electronics, and backup operation in case of electrical failure through a mechanical cable system. The PCU drives the engine controller, and backdrives the cable control system, through a clutch set at some required value that can be slipped via the mechanical system.

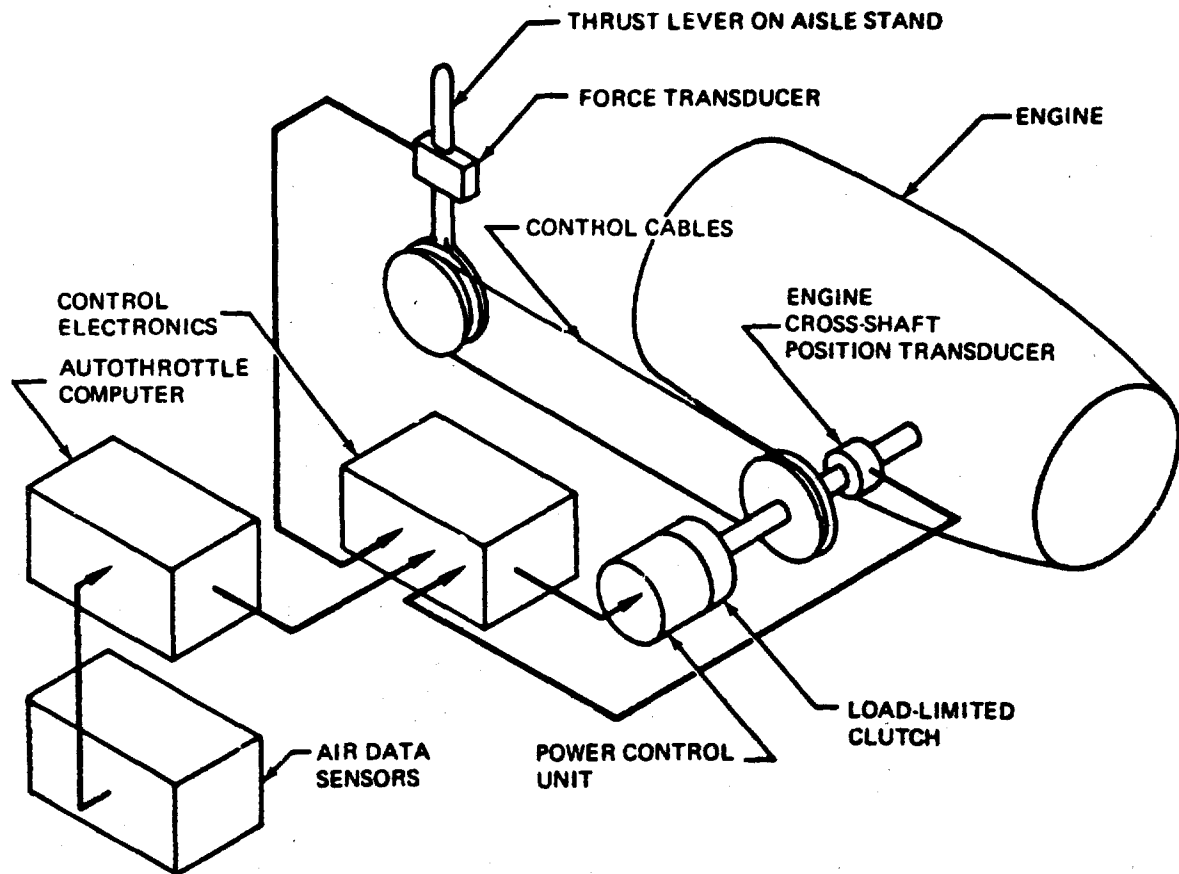


Figure 3. Electrical System Added to Mechanical Thrust Control System

This approach of superimposing an electrical system on the basic mechanical system has several advantages over both the straight electrical or mechanical system:

- Offers low technical risk at this time since the current mechanical system with its known reliability is retained
- Gives the fine resolution inherent to all electrical systems without being compromised by the presence of the mechanical control system
- Provides a true dual control system for each engine
- Provides for all required automatic modes
- Lends itself to changes in authority and override limits without major hardware redesign (these limits are a function of electrical signal levels). This point appears to be particularly important since it significantly reduces the risk of early production design decisions on this new system.

On the negative side is the systems increased weight and cost. Both weight and cost increases are mostly due to multi-PCU's replacing the single PCU currently used. Since the mechanical system remains relatively unchanged in its function, it does not appear probable that its weight can be reduced much even if the mechanical system serves in the primary mode (both automatic and manual) only to reposition the control levers in the cab. Because systems resolution and accuracy do not depend on the mechanical system, requirements can be relaxed over previous mechanical thrust control systems, perhaps resulting in a lighter weight and less costly mechanical system. If the system described in this section would be implemented on the 747, it is estimated that the approximate weight for the electronics PCU's and wiring is as follows:

| | |
|---|------------|
| 500 ft of electrical cabling (total length of wire required for four wires from the 747 cab to each engine is approximately 460 ft) | 10 lb |
| Electronic packages | 10 |
| Control handle sensor installation | 5 |
| 4 power control units | <u>20</u> |
| Total Weight of "Add-On" Electrical System | 45 |
| Approximate weight of existing 747 mechanical thrust control system | <u>240</u> |
| Total Weight of "New" Thrust Control System | 285 lb |

To make the relatively low weight of the PCU's plausible, it is noted that only about 50 in.-lb is required to operate the engine cross-shaft; additional force is required to backdrive the cables. The required time for total PCU travel need not be less than 2.5 seconds since all presently manufactured engines have a response time greater than 2.5 seconds. The above weight figures did not consider any potential weight reductions of the present mechanical system.

ELECTRICAL, FORCE-ACTIVATED CONTROL-THRUST SYSTEM (FACTS)

Since this system is seen as a next step in thrust control systems evolution, it is only logical that many components of the system described in the foregoing text are used in their basic form again. Flight experience gained on the electrical components of the system previously described should make the consideration of eliminating mechanical backup possible. As the weight figures on the previous page show, the major portion of the total systems weight of the "electrical add-on" approach is in the cables. The mechanical feedback loop to the control handle can be changed to an electric handle drive motor in the aisle stand. Figure 4 is an elementary schematic of this approach. It is most important to note that the handle drive motor and its associated position transducer are not included in the primary reliability loop in either the manual or automatic mode. Figure 5 is a functional diagram of the force-activated control-thrust system.

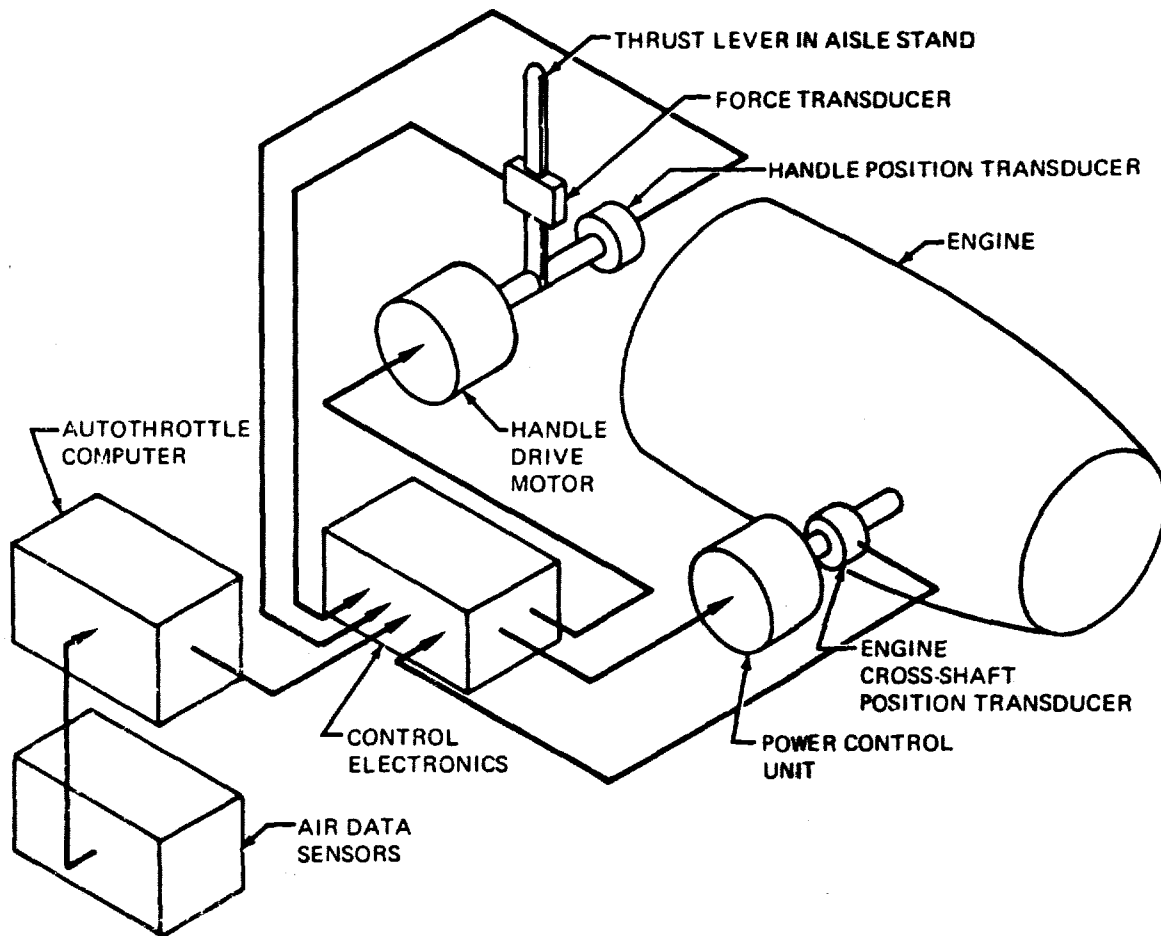


Figure 4. Force-Activated Control-Thrust System (FACTS)

The force transducer generating a rate signal can be operated without loss of authority with the handle drive motor disabled; quite naturally the handle will not be repositioned under this failure condition. To clarify the function of the system: A signal is supplied by either the control handle force transducer or the autothrottle computer to the control electronics. The control electronics supplies a signal to the PCU, which in turn repositions the engine cross-shaft position transducer. The signal from the cross-shaft position transducer is compared with the signal from the handle position transducer in the control electronics and, if there is a discrepancy, a command to the handle drive motor is initiated by the control electronics.

Since now there is no mechanical backup system, it is necessary to dualize the control systems components in the primary loop. These components are identified with a heavy outline in Fig. 5. To consider the desirability of this systems approach, let us examine the systems weight and its relative technical risk.

4 dual PCU's (It is estimated that the weight of the dual unit would not increase much over the single unit)

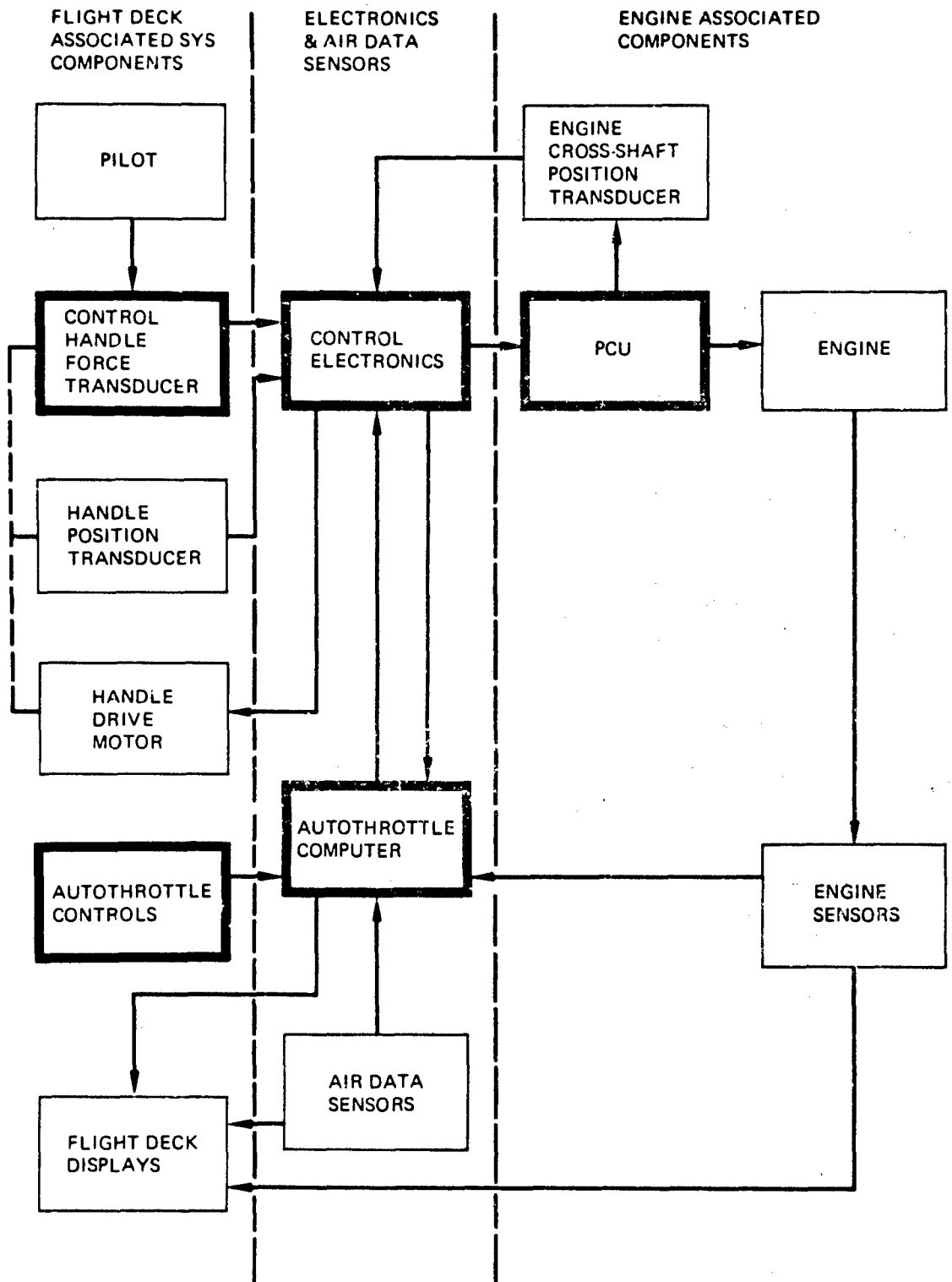


Figure 5. FACTS Functional Diagram

| | |
|--|-----------|
| proposed in the previous section because the clutch can be eliminated and the power requirement is reduced, i.e., no cables to backdrive.) | 24 lb |
| 500 ft of electrical cabling | 20 |
| Electronic packages | 20 |
| Control handle sensor installation | 5 |
| 4 control handle drive motors and associated electronics | <u>10</u> |
| Total Estimated FACTS Weight | 79 lb |

This represents a substantial potential weight decrease over the system outlined previously.

| | |
|--|-----------|
| Total weight of mechanical control system | 240 lb |
| Total weight of superimposed electrical system | <u>45</u> |
| Total Weight of System in Previous Section | 285 lb |

NOTE: All of these weight figures have been determined for the 747 airplane.

It is the writer's opinion that the greatest technical risk is in the dualization process of the critical systems components, such as the PCU's and the control electronics. The handle drive motors are a low-risk item, as was demonstrated by the laboratory tests conducted during 1968.

This system offers many advantages, some of which are summarized below.

- 1) A minimum of hardware is in the primary reliability loop.
- 2) Flight deck control sensor is a solid-state device, offering high reliability and low electrical noise.
- 3) The appearance, feel, and function of the flight deck control do not depart radically from the present control. In fact, the control can be designed to be identical.
- 4) Because the first single-thread version of this system, superimposed on a mechanical system, will provide flight-proven hardware, the risk of implementing this advanced dual system should be minimal.

- 5) This system lends itself ideally to modular packaging techniques, reducing installation and maintenance costs.
- 6) Because the system is electrical, the mechanical design constraints are minimal, e.g., aisle stand cable runs are eliminated.
- 7) A high degree of flexibility is provided for automatic inputs.
- 8) The possibilities of retrofitting should be good because hardware is mostly eliminated, therefore vacating space.
- 9) Engine change should be facilitated because of control cable elimination.
- 10) The adaptability to other control systems, such as variable inlet position, variable exhaust nozzle, speed brakes, and thrust vectoring, is inherent to this system.

During the last year, we also considered the design of a single propulsion lever for controlling all four (or three or two) engines. This would pay off in greater operating ease because four individual levers, all in various positions, would not have to be moved together in phase to advance or retard all engines the same amount. To provide manual control of each engine separately, we visualize one trim switch (similar to stabilizer trim switch) for each engine piggyback on the single control lever. Since we plan to trim the engines automatically, the need for individual engine control should be reduced. Much work remains to be done to show feasibility of this idea. However, the potential benefits of this single lever (such as a small package making possible two complete controls in the cab) cannot escape the reader.

LABORATORY EVALUATION STUDY

The piggyback electrical system described in the foregoing text requires no feasibility proof since a flight-proven systems model exists in the form of the 737 dual redundant control wheel steering system.

On examination of the material presented in the foregoing section on the force-activated control-throttle system, several questions become apparent:

- What is the "feel behavior" of this control handle, directly coupled to an electric motor (no clutch)?
- What is the "feel" of manual overrides of automatic command signals?
- Is there acceptable controllability of the system with the handle drive motor disabled when the control reverts to a pure "force control"?
- Can the stability of the total control servo loop be shown?

The hardware breadboard system shown in Fig. 6 and described below was designed, constructed, and tested to provide answers to the aforementioned four basic questions. Figure 7 shows the three basic packages of the FACTS breadboard.

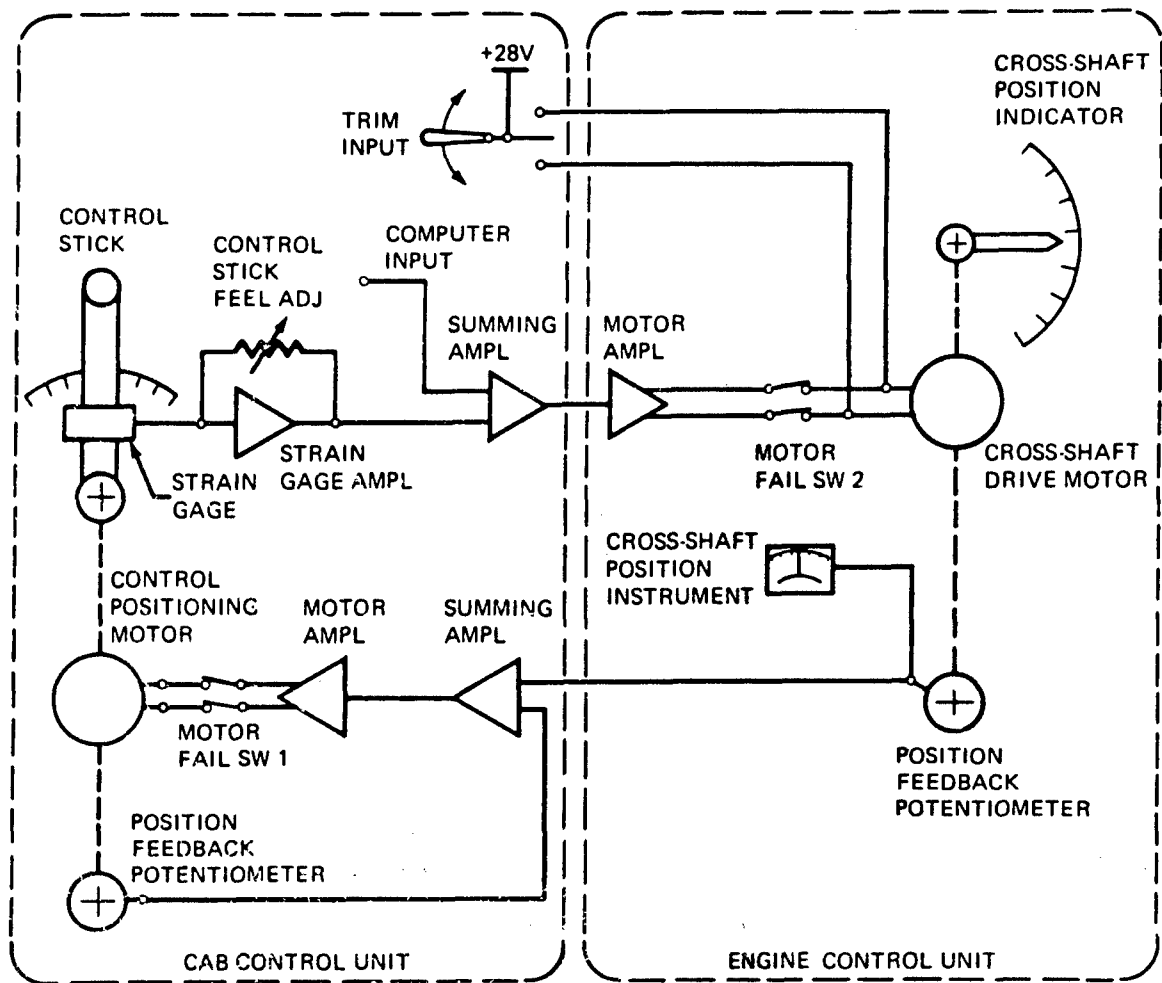


Figure 6. FACTS Breadboard (AFM Laboratory)

1. BREADBOARD HARDWARE DESCRIPTION

a. Cab Control Unit

The cab control unit contains the control handle assembly, the feel adjustment, computer input summing circuit, the handle drive motor amplifier, the feedback comparator circuit, and the handle position potentiometer. The following controls are provided:

- Control handle
- Trim switch
- Switch, simulating computer input

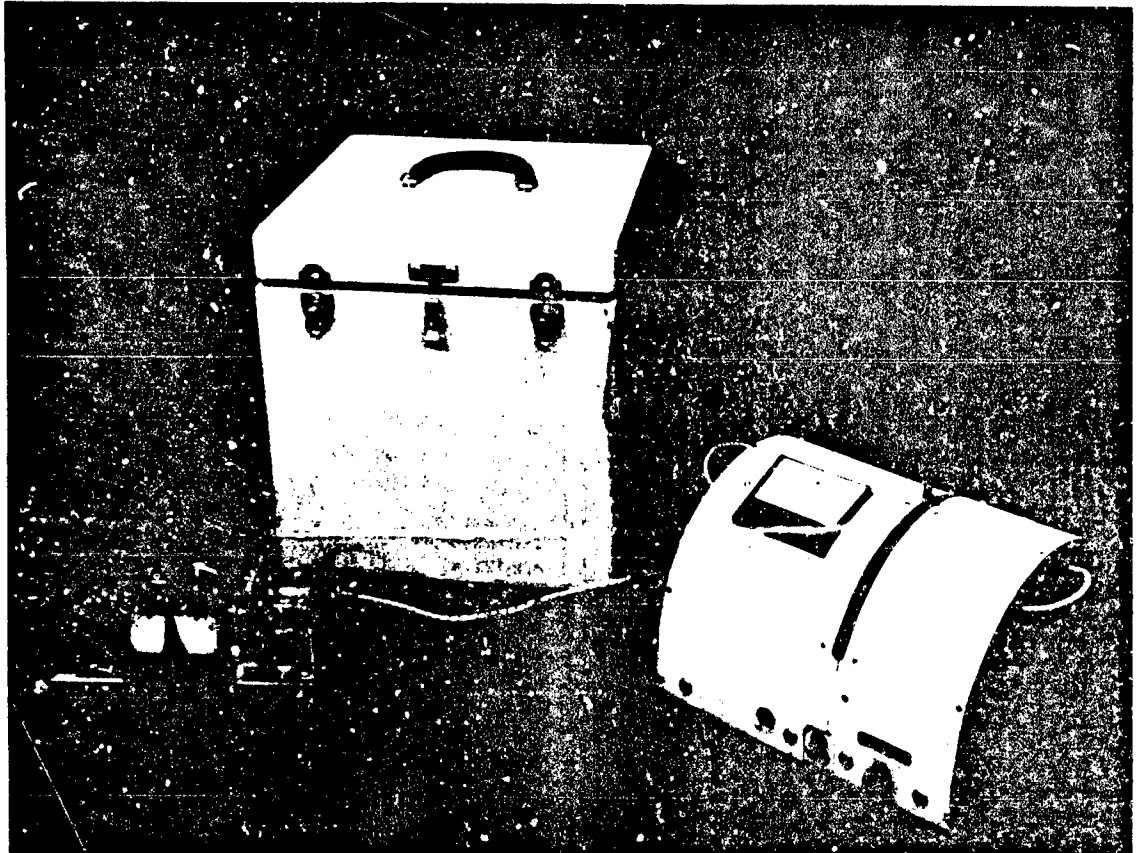


Figure 7. FACTS Breadboard

- Switch, simulating drive motor failure
- Feel control

Figure 8 shows the cab control unit with protective cover removed. The control handle assembly is made of a chrome-alloy steel, heat-treated to 55 Rockwell "C" scale to reduce hysteresis and therefore ensure repeatability of strain gage performance. The constantan alloy, 350-ohm, general-purpose, high-resistance strain gage is bonded to the handle near its base. The strain gage is not temperature compensated for the material used for the handle. The handle assembly is solidly attached to the output shaft of the rotary actuator. This actuator produces 64 rpm at full 24-vdc input and 1-1/3 rpm at 4-vdc input; minimum voltage required to break out is 4 vdc. It is powered by a 1/30-hp, 7,500-rpm, 3.2-amp, reversible dc electric motor equipped with an electrically operated friction brake.

The 5,000-ohm precision handle position potentiometer is also attached solidly to the output shaft of the actuator. The total handle travel is 100 degrees, protected against overtravel by limit switches actuated by cams mounted on the actuator output shaft.

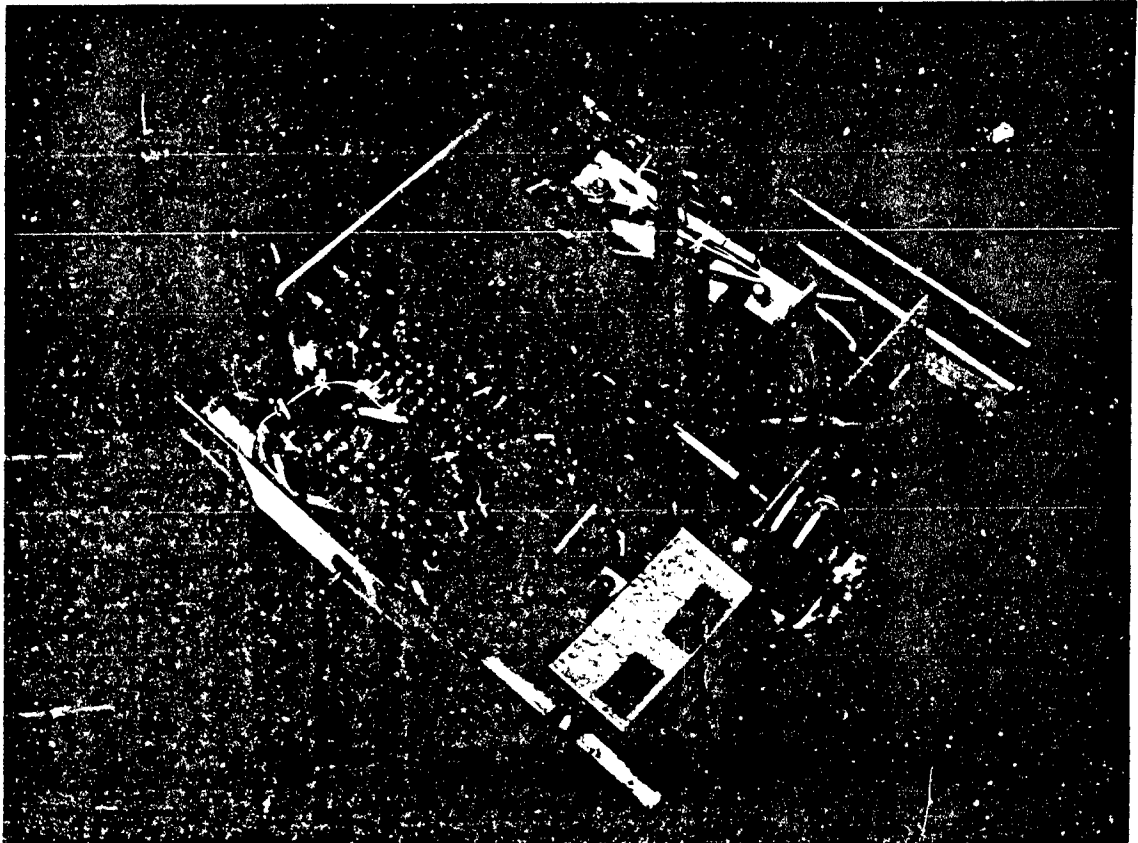


Figure 8. FACTS Cab Control Unit, Front View

The feel adjustment changes the gain of the strain gage amplifier by varying the feedback resistance value. The strain gage amplifier, feedback comparator amplifier, and the computer input amplifier use one each operational amplifiers. The motor amplifier is a low-gain, three-stage, linear dc solid-state amplifier.

A cross-shaft position instrument using a standard meter movement is mounted into the protective cover. This unit is provided to show cross-shaft position in case of handle drive motor failure. It is provided only for explanatory purposes in this breadboard. On a "real" system, this indication function would be served by the engine instruments in the cab.

b. Engine Cross-Shaft Controller

This unit shown in Fig. 9 contains the cross-shaft drive actuator, position potentiometer, cross-shaft angle indicator, and motor amplifier; the only control provided on this unit is a switch simulating drive motor failure. The motor amplifier is identical to the one used to drive the handle actuator except for a small change in gain to accommodate different motor characteristics. The rotary actuator is geared to provide 22-rpm output at 24 vdc

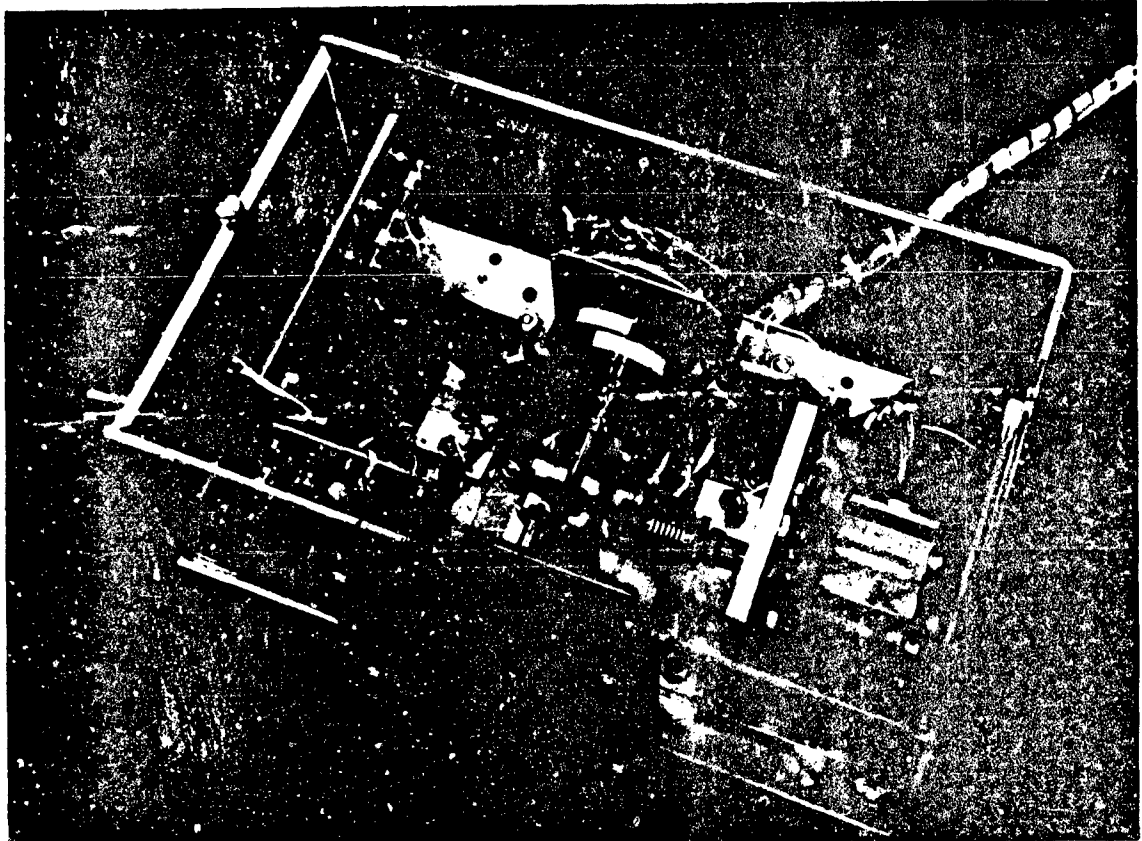


Figure 9. FACTS Engine Cross-Shaft Controller

and 0.5 rpm at 3.5 vdc; breakout is at 3.5 vdc. It is powered by a 1.8-amp, 0.015-hp, 7,500-rpm, reversible 24-vdc motor equipped with an electrically operated friction clutch. Attached to the actuator output shaft is a mechanical indicator and a 5,000-ohm precision position potentiometer. The total cross-shaft travel is 100 degrees, protected against overtravel by limit switches actuated by cams mounted on the actuator output shaft.

c. Power Supply

To make this breadboard portable, a power supply was constructed.

Input: 115 v, 60 cycles

Output: +12 v and -12 vdc regulated
+28 vdc not regulated

The power supply is built into the throttle breadboard transportation case.

Figure 6 also shows a control for trim input. This control is a momentary on-off switch that supplies current directly to the actuator, thereby providing for throttle operation when all the electronic components fail.

2. BREADBOARD FUNCTIONAL DESCRIPTION

Two failure modes can be simulated with the FACTS breadboard.

a. Failure Condition 1

Figure 10 shows failure switch 1 open; this simulates a failure by either or all of the components shown in the crosshatched area (handle positioning motor, position potentiometer, summing amplifier, and motor amplifier). This failure condition results in loss of position feedback to the control handle; the control now is a pure "force control"

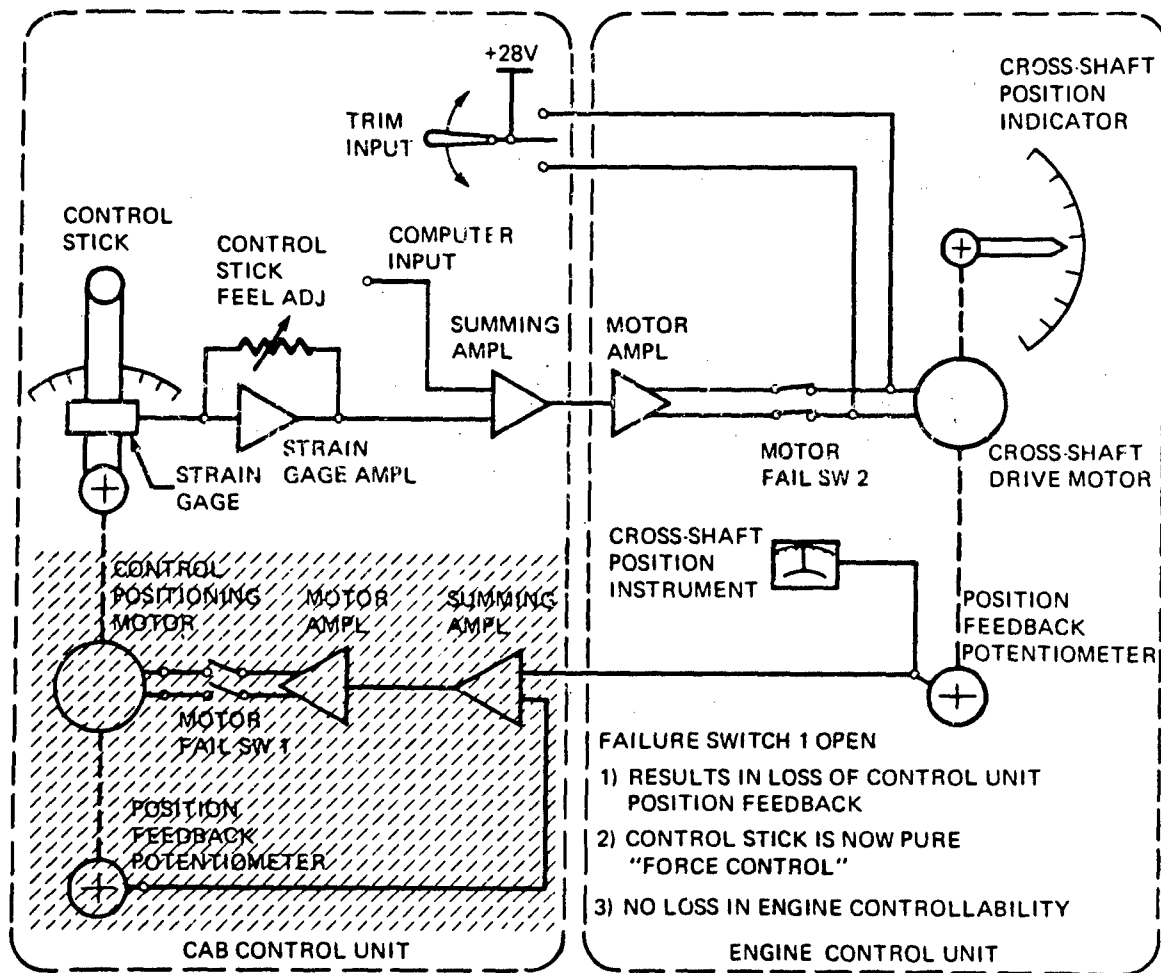


Figure 10. FACTS Breadboard, Switch 1 Open

with fixed lever. Engine data supplied to the pilot is provided by the engine instruments only. If failure of any one of the components in the crosshatched area of Fig. 10 manifests itself in a maximum drive signal to the motor (to either full thrust or throttle retard), no signal to the engine cross-shaft motor will result because a signal from the strain gages can be initiated only by applying force to the handle. The handle stops, and limit switches cannot induce such a force into the handle. Figure 8 gives a good view of this particular area. For the real system, it may be necessary to provide a handle drive motor-disabling switch similar to failure switch 1 to protect against the nuisance of possible failures causing handle oscillations.

b. Failure Condition 2

Figure 11 shows failure switch 2 open, simulating failure of either or all the components shown in the crosshatched area (strain gages, strain gage amplifier, computer input

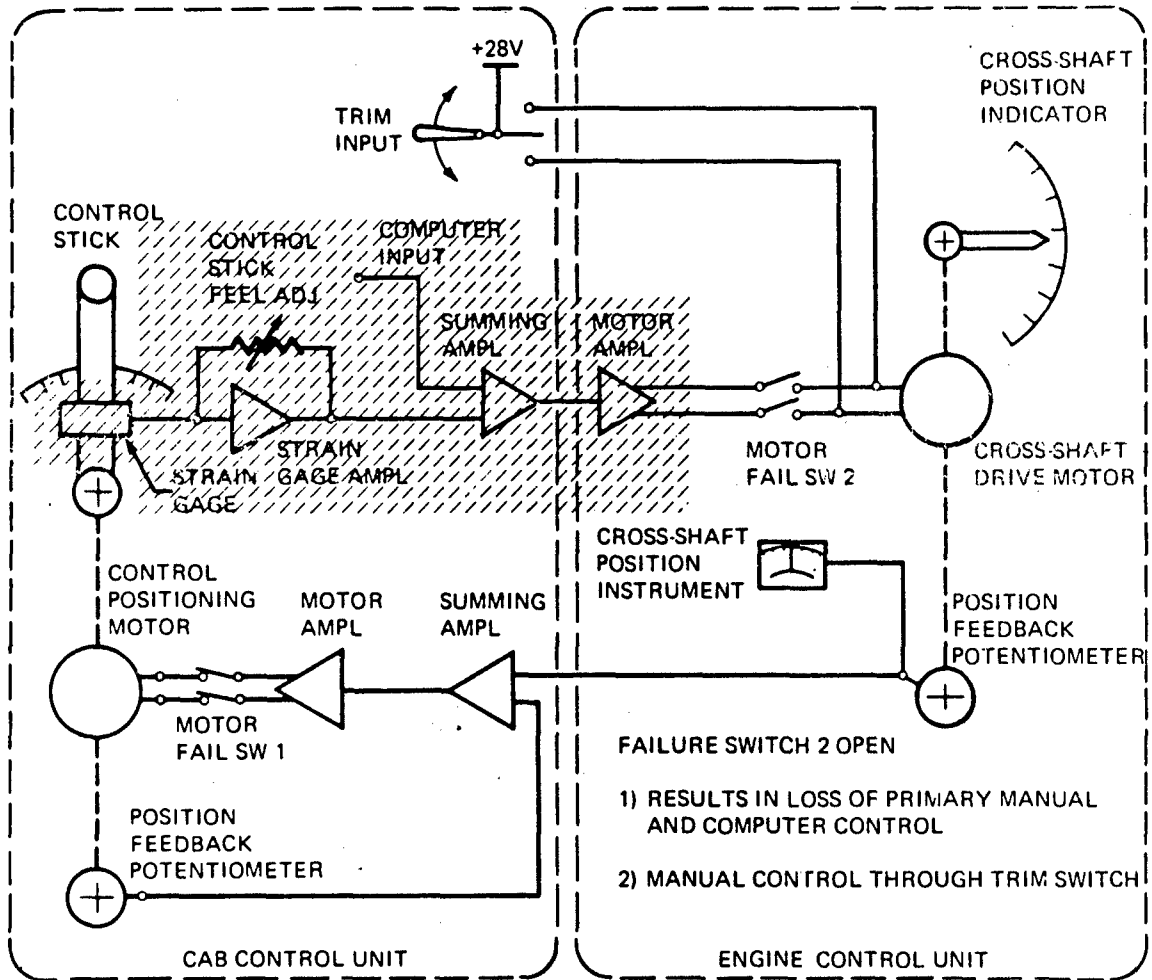


Figure 11. FACTS Breadboard, Switch 2 Open

summing amplifier, and engine cross-shaft amplifier). This failure results in loss of primary manual control mode and, in certain cases, loss of computer input; the only means of control is now through the trim input switch. The control handle position still is representative of cross-shaft angle. In a real system, it is imperative that redundancy be provided to protect against active failures. An active amplifier failure, for instance, could result in a maximum drive signal to the engine cross-shaft actuator, commanding either full thrust or throttle retard.

3. BREADBOARD PERFORMANCE

Construction of the FACTS breadboard was completed September 12, 1968. This breadboard has been operated continuously 8 hours per day, 5 days per week since its completion. Periodic cycling is accomplished daily.

There have been no failures to date; no recalibration or adjustments have been required. No degradation due to power supply drift has been observed. The total control servo loop appears to be extremely stable despite the relatively low-quality hardware. The drive motors are not servo units. Their gearing has a considerable amount of play due to wear and inexpensive construction.

The unit was cycled using a signal generator in an attempt to induce spontaneous oscillation. The motors did not respond beyond 10 cycles per second. Spontaneous oscillation, resulting in movement of the control, could not be induced. The systems stability is achieved by the relatively high breakout voltage (3.5 vdc) required by the motors, providing a generous amplifier and power supply drift tolerance.

The feel of this control is practically identical to that of a mechanical system. Following is a tabulation of actual measured travel time versus required control force with the feel adjustment in various positions.

| Feel Control Setting (deg) | Maximum Control Force Applied | | Minimum Force Applied to Just Exceed Breakaway | |
|----------------------------------|----------------------------------|---------------|---|---------------|
| | Time (sec) | Force (lb) | Time (sec) | Force (lb) |
| 0 (Most Sensitive) | 2 | 1.0 | 27 | 0.8 |
| 45 | 2 | 1.5 | 27 | 0.8 |
| 90 | 2 | 2.0 | 27 | 1.0 |
| 135 | 2 | 3.0 | 27 | 1.2 |
| 180 | 2 | 4.0 | 27 | 1.8 |
| 200 | 2 | 11.0 | 27 | 4.0 |
| 225 | 2 | 14.0 | 27 | 5.0 |

This electrical feel control behaves much like a mechanical friction control. No special effort was made to provide linearity in the adjustment.

This breadboard provided us with the capability of demonstrating manual overrides on automatic command inputs. The feel in this mode is quite satisfactory. The force levels required are low, yet high enough to provide the operator with an override indication. The override loads are approximately double the loads required in manual mode. Transition from automatic to manual mode is smooth—no hesitation or lag is experienced.

The controllability of the system with a failed drivemotor, in a pure "force control" condition, seems to be acceptable. We found control difficult with sensitive feel; the system reacted too fast with low handle input loads. However, this condition is easily corrected by adjusting the feel control to a less sensitive position. To either prove or disprove acceptability and safety of an instantaneous reversion from a conventional "feel-position" control to a pure "force-control" during flight, testing in a flight simulator is required. The Boeing Company has scheduled such a test program for its multimission simulator.

In conclusion, this breadboard has successfully answered the four basic questions stated at the beginning of this section and has proved beyond any reasonable doubt the feasibility and desirability of this force-activated control-thrust system.

CONCLUSIONS AND RECOMMENDATIONS

The foregoing text is a description of two thrust control systems, both providing for the automatic control of future airplanes:

System A: The piggyback electrical system superimposed on the present mechanical system and weighing approximately 285 pounds. (This weight figure is for the 747 airplane and includes 240 pounds for the existing mechanical system.)

System B: The electrical, force-activated control-thrust system weighing approximately 79 pounds. (This weight figure is for the 747 airplane.)

Taking all considerations (treated in the foregoing text to some detail) into account, it is recommended that the piggyback, system A, be adopted for any airplane project initiated during 1969. The primary reason for this recommendation is the low technical risk factor of system A. To implement this system in the near future, the major project tasks are as follows.

- 1) A detailed systems definition based on a specific airplane shall provide all requirements for detail components and controls (such as thrust reverser controls).
- 2) The selection, purchase, and/or development of the power control unit shall be made with consideration given to electric, fuel-powered, or hydraulic actuators.
- 3) The selection, purchase, and/or development of the force sensor installation in the control handles shall be made. Consideration should be given to strain gages and transducers. Strain gages appear to be most attractive because of their light weight, ease of installation, low cost,

and compact size. Most strain gage failures in the past have been caused by their bonding materials; considerable improvement has been made in this area during the last 2 years. Many types of transducers are available, among them the "E" core transducer used on the 737 and 747 control wheel steering system. The force sensor shall be located as close as possible to the operator's hand to minimize the mass ahead of the sensor. Excessive mass ahead of the sensor could cause erroneous signals in turbulent air.

- 4) Design of the control electronics shall consider both digital and analog techniques.

Any airplane project committed in 1970 or beyond should incorporate the advanced system B, the force-activated control-thrust system. To make this possible, the following tasks have to be completed during 1969 and early 1970:

- 1) Detail systems definition of at least a fail-passive or fail-safe redundant system, backed up by a failure and reliability analysis.
- 2) Development of a dual power control unit.
- 3) Development of lightweight, small dual control force sensors.
- 4) Development of dual position sensors.
- 5) Evaluation of impact on flight deck displays.
- 6) Ground simulation testing to verify systems safety.

The Boeing Company has committed this electrical system for flight test in the near future on its -80 test airplane.

PROPULSION CONTROL PROBLEMS
GENERATED BY ENERGY MANAGEMENT
CONTROL REQUIREMENTS

Ross D. Schmidt
Staff Engineer
Honeywell Inc.

ABSTRACT

The concept of multimission aircraft has resulted in numerous studies being conducted in the area of energy management of weapon systems. It is the function of energy management controllers to integrate the various aircraft subsystems and to provide improved performance over that obtainable with only the individual subsystem nominal controllers. With respect to the propulsion system, covetous eyes have been cast on regions of possible steady-state operation which lie outside the capability of the nominal engine control system. Mission studies made, assuming operation in such regions, show that, indeed, an energy management system could improve mission performance. Exploitation of this area, however, is going to affect the design and final configuration of the nominal propulsion control system. The propulsion system will be operating at reduced stability margins and closer to operating limits. Acceleration time will be affected. It is shown that sensor and actuator performance will probably have to be improved if useful energy management systems are to be attained. In addition, certain kinds of engine controllers, presently in use, will not be allowed since they will interfere with the energy management engine control functions. The basic assumption made in this paper is that the best operating point of the propulsion system cannot be determined from propulsion system measurements alone. Minimum fuel consumption is going to be a function of both propulsion and airframe settings and these interrelations are very complex. The proposed propulsion control configuration provides the flexibility needed to adopt present control concepts to energy management systems of the future.

INTRODUCTION

As the flight envelopes of modern aircraft become extended the corresponding propulsion system configurations have become necessarily more complex. This complexity has provided the capacity for propulsion system performance improvement as a function of mission.¹ Although this improvement could have been obtained on systems of the past, neither the operating envelopes of the aircraft or the resulting propulsion system configuration suggested a sufficient payoff for the effort involved. Further motivation for the use of energy management systems (EMS) has been the comparatively recent evolvement of suitable aircraft digital computers.

The purpose of this paper is to show the impact a superposed energy management system will have on the nominal propulsion system control, on the control components of the nominal engine control system, and some of the operational problems one might expect when using such a system.

There is no doubt that propulsion system manufacturers will be very uneasy about seemingly extraneous control system inputs introduced to their nominal control at points other than the throttle. It is hoped that their minds will be put at ease when it is shown that the control system configuration proposed here cannot violate engine boundaries as defined in their nominal control system. For in the final analysis, it is the propulsion system manufacturers' responsibility to ensure that strict observance of engine limits is maintained. This, however, will not relieve them of the responsibility of providing control system components and control configurations which are designed to cope with the increasingly severe operating conditions generated by an energy management system.

It is not the purpose of this paper to be concerned with the nature and control philosophy contained in the energy management system. Rather it is assumed that any energy management system will desire to operate the engine at some steady-state operating point -- some other point than that generated by the engine manufacturer's supplied control. Whether the energy management system is an on-line optimizing controller or contains some other philosophy, the duty of the nominal propulsion control will be to acquiesce to the energy management demands as long as a violation of engine operating limits is not required.

PROPULSION SYSTEM OPERATING ENVELOPE

A description of the relation between the engine variables is presented in Figure 1. The operating space is shown in two dimensions but is actually an n-dimensional problem n being a function of the complexity of the engine. The steady-state line shown is the combined result of the behavior of the engine under the influence of external variables such as compressor face total pressure and temperature and a designed relationship expressing the engine characteristics when driven by the implicit schedules of an engine controller. Without an

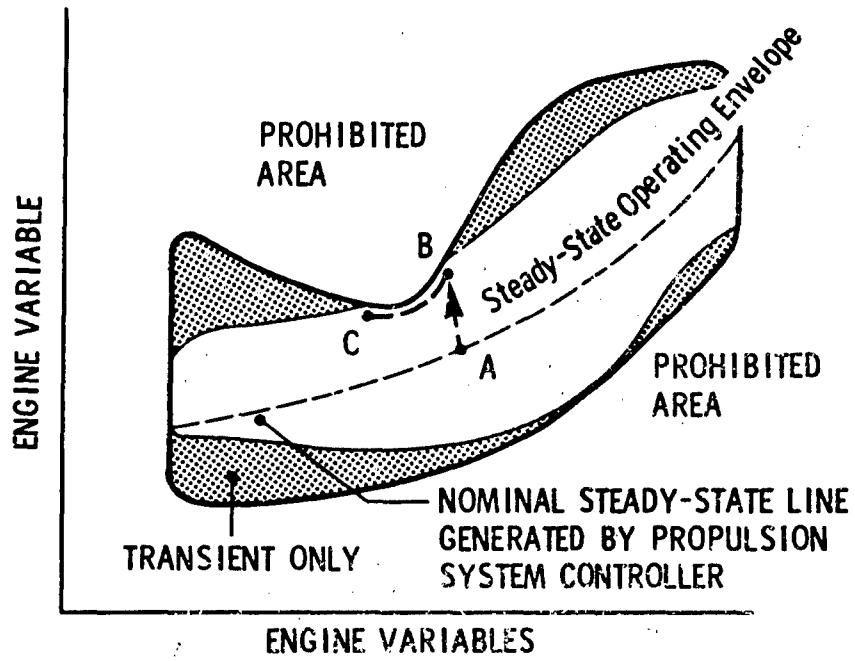


Figure 1. Characteristics of Engine Operating Envelope

energy management system the engine is in a "transient" state at all points other than the "steady"-state operating line. By "transient" is meant that a departure from that point will occur even though the engine input variables, fuel flow, exhaust nozzle area, compressor geometry, compressor face total pressure and temperature, distortion and others -- are held constant. This is usually associated with a variation in engine rotor speed but can be more generally considered to be points where derivatives with respect to time exist in the engine output variables.

The addition of an energy management system which can override and force the engine to depart from the implicit functions contained in the engine controller allows a large part of the available engine operating space to be used for performance improvement. Certain areas are still unobtainable due to limiting of input variables -- for example exhaust nozzle area encountering a limit before the limiting turbine temperature occurs. The function of the engine controller is to provide a linear thrust-power lever relationship, maintain under strict observance the limits of engine operation, provide sufficient acceleration-deceleration margin for reasonable acceleration time, and furnish stability of propulsion system operation. Addition or engagement of an energy management system should not violate these requirements.

If the propulsion system is initially at state A as shown in Figure 1 engagement of the energy management system could result in the system being driven to point B. It is obvious that at point B the propulsion system cannot successfully accelerate to higher thrust levels since the acceleration capacity of the system has been destroyed to provide better steady-state performance. The opposite could just as easily be true -- the deceleration capability of the system could have been destroyed instead. In order to regain acceleration capacity the inputs from the energy management system must be removed. Delay in this removal may increase or decrease the nominal engine acceleration time.

This large extension of the steady-state operating envelope which has been forced upon the propulsion control system by the energy management system has particular significance to the design of the propulsion controller. The steady-state behavior of the propulsion control system must be investigated not only along the nominal steady-state line but also throughout the complete steady-state operating envelope of the engine. This is a requirement not made in the past and indicates that the propulsion control system design has been complicated by probable extension of engine gain and dynamic terms as well as increasing the number of points which must be checked to ensure proper control behavior. Not only must the steady-state nominal engine control stability behavior be investigated over wider ranges of engine operating conditions but the acceleration behavior will also be affected. Since the initiation of acceleration can now occur from anywhere in the steady-state operating field it will be necessary to determine that the limits of engine operation are observed dynamically under a wider range of initial conditions.

ENERGY MANAGEMENT REQUIREMENTS

As previously stated the manner in which the energy management system operates or determines a desirable trajectory in the propulsion operating space is not the concern of this paper. However, with respect to its relationship to the propulsion control the following assumptions have been made:

1. A multimission aircraft will require a central computer to optimize airframe-propulsion performance.
2. This process should, at its option, be free to drive the propulsion system to any steady-state point within the operating envelope of the propulsion system.
3. Final authority as to the limits of the propulsion system operating envelope must lie with the propulsion control system.
4. Addition of an energy management system should not appreciably alter the ability of the propulsion control to perform its tasks:
 - a. acceleration-deceleration behavior
 - b. transient and steady-state stability
 - c. a linear thrust-power lever relationship along the nominal control line
5. Engagement of the energy management system should be at the pilot's option.
6. Disengagement of the energy management system shall be accomplished by either the pilot or the nominal engine control system.
7. The required energy management control system bandwidth is at least 10 times lower than the propulsion control bandwidth.
8. The energy management inputs to the nominal propulsion control system will be electrical in nature.

With these assumptions the required interfaces between the energy management system and the propulsion control may now be examined. A block diagram of a simple propulsion system having a variable exhaust nozzle and primary fuel flow as the only independent variables is shown in Figure 2. The nominal engine controller is straightforward in concept. The throttle commands speed and the exhaust nozzle is scheduled as a function of speed. For acceleration and deceleration purposes a maximum and minimum temperature are computed as a function of speed and compared to the instantaneous turbine temperature. It is the function of the logic to select the appropriate error

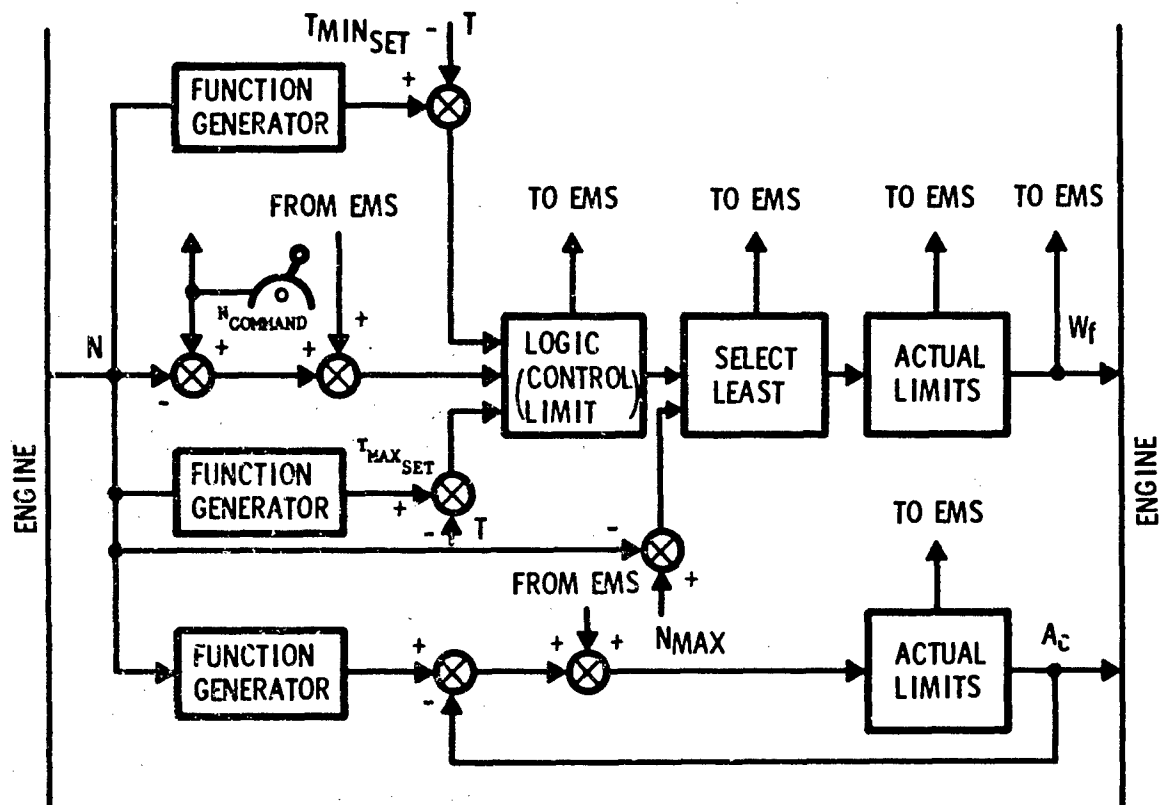


Figure 2. Block Diagram of a Control System Showing Required Energy Management Inputs and Outputs to Energy Management System

whenever these upper or lower limits are approached. With this control system an acceleration from idle to maximum rotor speed would be accomplished along the trajectory shown in Figure 3. Limits are observed along the upper boundary by the maximum turbine temperature set as a function of speed, along the right boundary by maximum speed and along the lower boundary again by temperature. It is interesting to note that the left boundary is not usually included into the limits designed in the forward control loop but is relegated to a detent on the power lever. Entrance to the operating envelope is then from the left through the minimum-speed set point.

Returning to Figure 2 the energy management system has inputs to the nominal controller somewhere before the nominal limiting system takes effect. Whether this input would be summed with the power lever output, the feedback or the error is dependent on the mechanization problems involved. If the energy management system inputs are before the nominal engine control limiters the engine will always be protected to the extent deemed desirable by the engine manufacturer. In some controllers it is possible to increase the stability margin prior to a pilot action. On such a control the EMS input must be either disconnected or be upstream of, and therefore controlled by, the stability margin extension. In order for the energy management system to know when limits are encountered it is necessary that a signal be sent back to the energy management system whenever a limiting condition occurs. Therefore in the fuel flow controller of Figure 2 it can be seen that the energy management system is made aware when a temperature limit is encountered, and when the hard limits of maximum and minimum fuel flow (a valve stop) and exhaust nozzle area are attained. It is necessary for the energy management system to have such information, for the signal from the energy management system comes from an integrating type system. The energy management system is driving in the direction to satisfy some type of control criteria and to reduce the error generated to zero. Therefore, unless the energy management system is aware that its controlling action has been disconnected or that a downstream limit has been reached, its integrator will drive to saturation. With proper control design this will not bother the nominal engine control at all but is a little hard on the energy management system's ego.

Also shown as an output is engine fuel flow for it is assumed that the energy management system requires this information in order to accomplish its task.

With the system of Figure 2 the energy management trajectory of Figure 1 can be generated. Starting at point A, the energy management system is engaged and proceeds to introduce errors into the nominal propulsion control system, forcing the area closed and reducing speed. It appears to like the result, for area continues to close, speed is reduced slightly, and fuel flow increases. Off the energy management system goes, hot on the trail of performance improvement. This continues to point B where the nominal engine control selects maximum temperature as a more suitable control variable, not allowing this point to be exceeded. The energy management system, aware that it has been rebuffed, but still eager, keeps driving

the exhaust nozzle closed. The fuel flow reduces in an effort to hold the maximum allowed temperature and the whole system goes off in a sudden transient from point B to C. The exact location of point C depends on the speed-area schedule of the nominal controller. Again the nominal engine control has kept its charge safe from harm but the combined energy management-nominal control combination has proved unstable at point B. It is expected that a pilot, expecting slow engine transients because he has engaged the energy management system, would be somewhat upset by a sudden large propulsion system transient with a corresponding change in flight conditions. The option could have been taken to disconnect all controllers whenever any limit is reached. This, however, denies the energy management system the right to move in a direction tangent to the limiting condition. In fact, the whole energy management system would have been made ineffective and if the weapons systems is in a climb-cruise mode the system would rapidly depart from an efficient operating point.

The nominal propulsion control system shown in Figure 2 is obviously not suited to be used with an energy management override. Whatever configuration is finally chosen by the engine manufacturer as suitable for use with an energy management controller, demonstration of this suitability is required. This means that the nominal propulsion control limits must be explored for stability during the design process by introducing errors as shown in Figure 2.

A system which is stable and would replace the system of Figure 2 is shown in Figure 4. The exhaust nozzle area, which was previously scheduled as a function of engine rotor speed, now controls engine speed. Engine temperature is controlled by fuel flow and engine over and under temperature is again protected by a median select logic. For nominal steady-state control this system controls to a commanded steady-state temperature and rotor speed. This system will require an exhaust nozzle actuator system with better frequency response and higher rate limits than the system of Figure 2.

Using the system of Figure 4, the trajectory of Figure 5 was obtained by introducing an extraneous input into the temperature -- fuel flow control system. When the maximum temperature was encountered at point B the energy management input to the fuel controller was assumed held constant.

An input to the speed-exhaust nozzle control than drove the system off at increasing speed along a trajectory parallel to the nominal schedule. If desired the trajectory could have gone toward decreasing speeds and tangent to the maximum temperature limit. It is important to note that once off the maximum temperature limit, the energy management system is again free to increase or decrease its bias into the fuel controller if it so desires. The control configuration of Figure 4 was used as an example of a system providing a stable nominal-energy management combination. Other stable nominal controllers exist and may have more desirable operating characteristics.

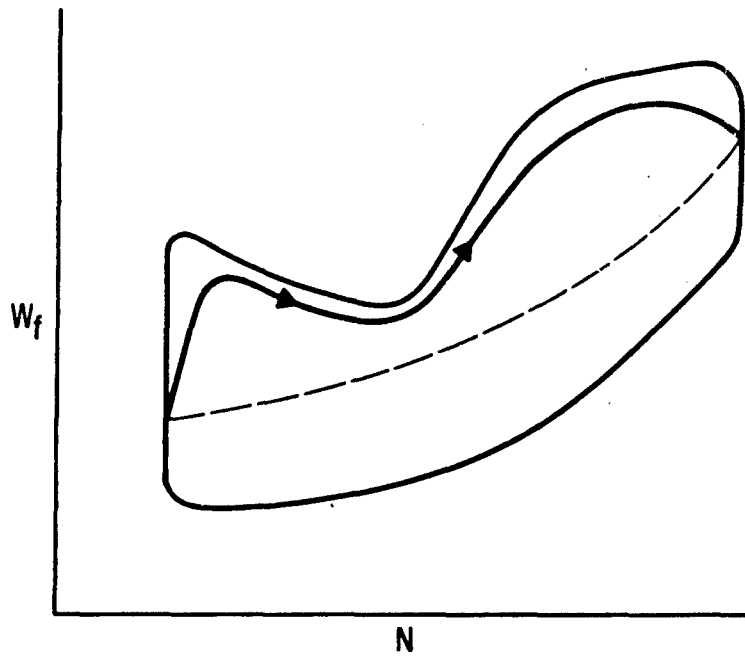


Figure 3. Characteristic Acceleration of Engine with Nominal Controller

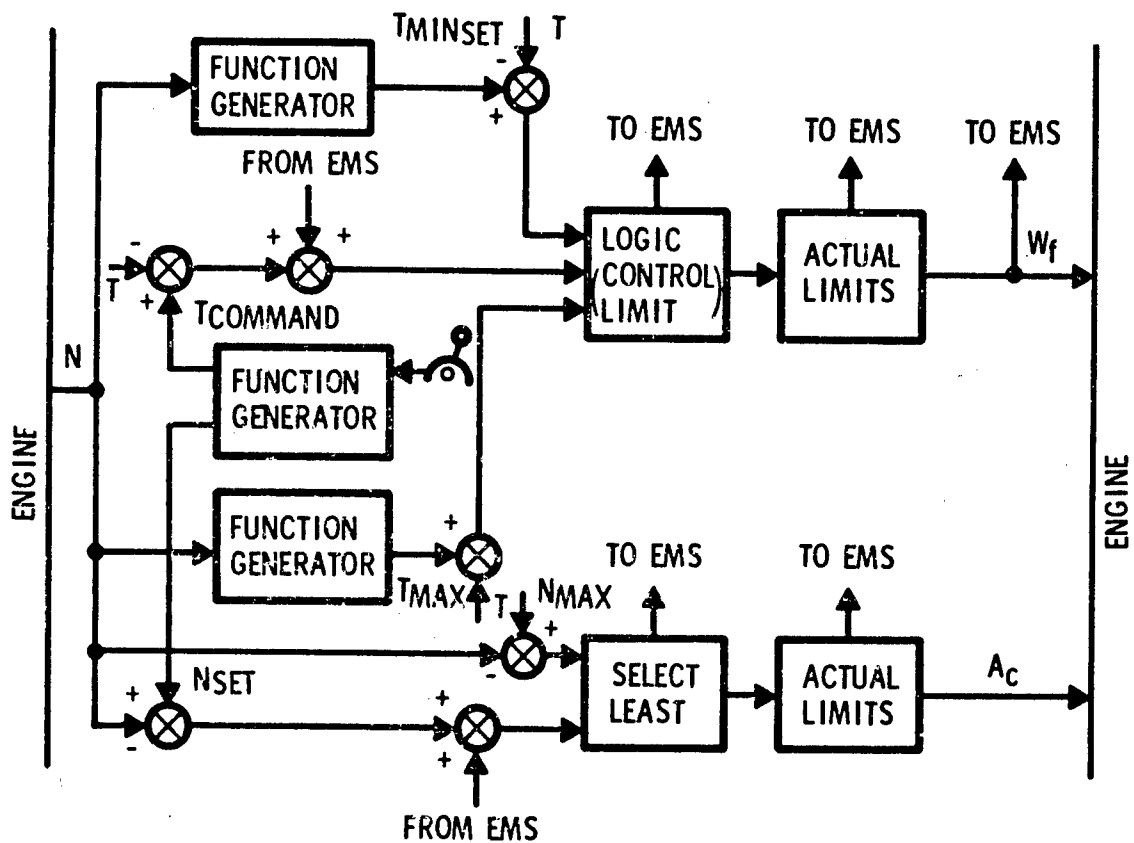


Figure 4. Nominal Propulsion Controller Designed for Stable Limit Intercepts Using Energy Management Override

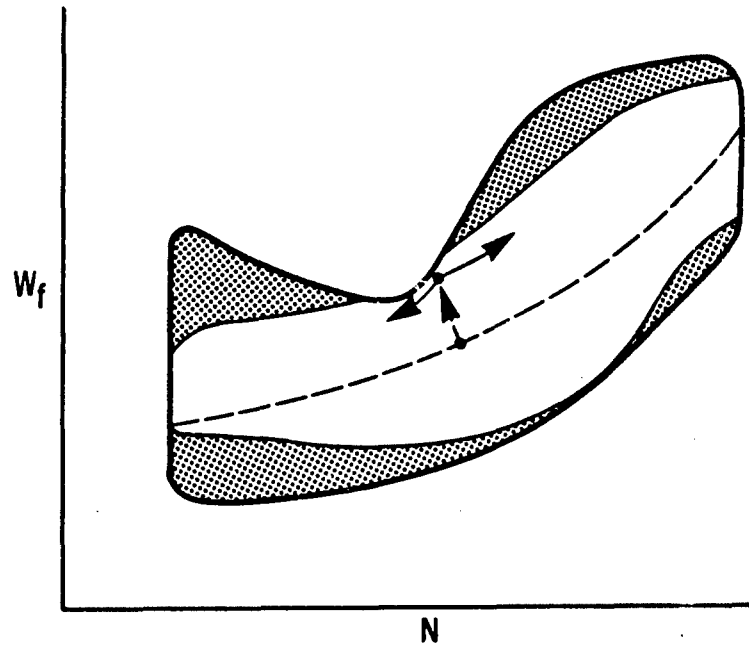


Figure 5. Characteristic Energy Management Trajectories
Obtained with Stable Nominal Propulsion
Control System

REQUIRED NOMINAL PROPULSION CONTROL CONFIGURATION

To this point it has been implied that the nominal propulsion control configuration had only to contain the input-output interfaces necessary to allow driving biases from the EMS and to inform the EMS of its state. This would not be satisfactory, for such a configuration gives authority for the removal of EMS input biases to the EMS itself. Responsibility for failure of the engine to accelerate must be with the propulsion system manufacturer. The circuitry necessary for giving the propulsion control this final authority is shown in Figure 6. This applies to a single-control loop only. Similar type circuits would be required in each of the control subloops where an energy management input is introduced. The energy management input to the nominal propulsion control may be disconnected by either motion of the pilot lever or by a manual disconnect from the pilot. The block diagram of Figure 6 is not intended to show the exact circuitry required. It may be desired to disconnect the EMS whenever the power lever moves and reset of the EMS would always require a manual pilot input. The characteristics of the electrical EMS input must be specified by the propulsion control manufacturer who will at the same time specify the EMS integrator output grounding characteristics. If a system is used wherein the EMS must always be manually reset there will be no requirement for a relatively fast discharge of the integrator output. A case could be made that the switch opening the input to the EMS integrator should be a part of the nominal propulsion control. This switch opens whenever a control limit (as shown) or a hard limit such as an exhaust nozzle area stop is encountered. It should also be grounded when the EMS is disengaged by pilot action either through the throttle or with a manual switch. If this switch does not open the integrator of the EMS may drive to saturation. This would only occur due to a failure in the EMS and could be bypassed by simply disengaging the EMS. Where many limits occur in the propulsion controller, incorporation of this switch in the propulsion control will reduce the number of required interfaces. With respect to disengagement of the EMS the block diagram of Figure 6 shows the EMS biases being removed immediately. This is desirable at very low Mach numbers but here the EMS is probably not being used anyway. At supersonic conditions it may not be desirable to generate these quick transients. The system of Figure 6 might then be revised to show the EMS bias being reduced to zero through a "fade out" circuit. This action would then be similar to a rate limited throttle input and the control of this transient should certainly lie with the propulsion system manufacturer.

One other problem not previously mentioned is whether the second assumption is warranted. There may be areas of possible steady-state operation where steady-state operation is not desired by the propulsion system manufacturer. Such areas may be associated with high compressor blade stress or other undesirable engine operating condition. A traverse through this area may be allowed in transient operation but disallowed in steady state. If there is such a requirement then the nominal control configuration would require the addition of a control element as shown in Figure 7. The EMS bias is introduced through a separate limiting logic which contains the restrictions necessary to

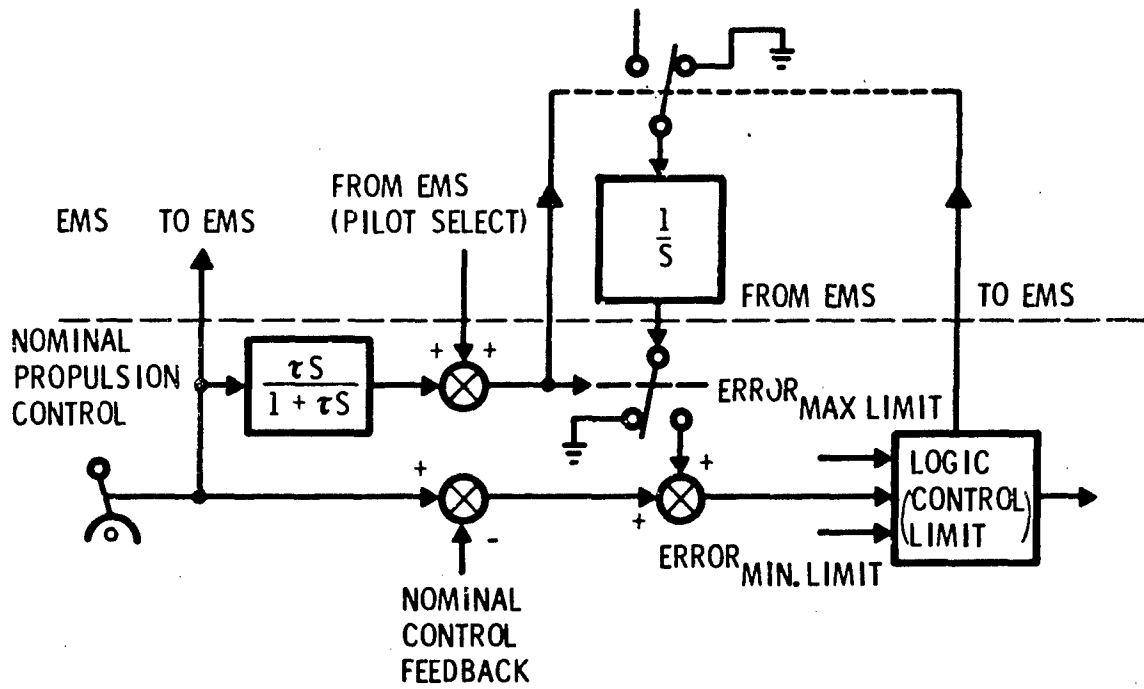


Figure 6. Required Addition to a Nominal Propulsion Control Designed For Use with an Energy Management System

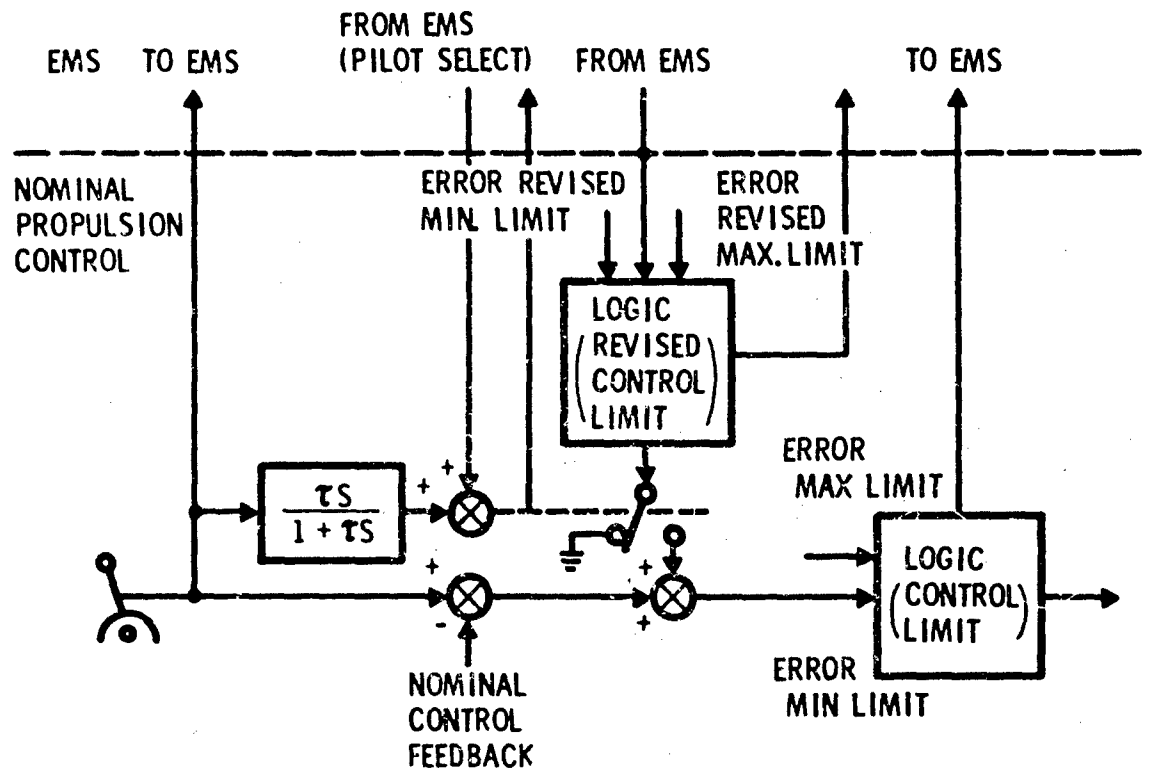


Figure 7. Nominal Propulsion Control Configuration for Denial to the EMS of Certain Steady-State Operating Regions

limit the steady-state operating space which is going to be made available to the EMS. The circuitry associated with computing the revised errors of the maximum and minimum set points is not shown.

Under influence of the energy management controller the propulsion system will be operating closer to its limits. The effect of external disturbances on violation of these limits will require sensors and actuators with better frequency response and rate limits than have been used in the past.² Also, closed loop control of these limiting boundaries will reduce the time spent in violation of the limit. In some systems wherein an outer loop (EMS) is in control of an inner loop (nominal propulsion control) stability problems sometimes result because of position and rate limiting taking place in the inner control system. This was the reason for the seventh assumption and it is felt that the assumption is reasonable since the required frequency response of the EMS can be related to the duration of a flight path segment. It must not be thought that the rate limits of the inner loop have to be improved to counter a possible stability problem resulting from the frequency response requirements of the EMS. There is an added benefit resulting from control system component improvement. The nominal propulsion control, under the influence of an EMS, will be operating over wider ranges of engine characteristics -- gain, time constants and rise ratios. Control component improvement will reduce and minimize the problem of control scheduling as a function of operating environment.

There are propulsion control subsystems where an input from the EMS will not be allowed. These subsystems include compressor bleed, compressor blade angle schedules and perhaps other engine variables where the engine manufacturer has strict relationships which may not be changed.

CONCLUSIONS

The addition of energy management system biases to the nominal propulsion control system will require further design and development effort by the propulsion control manufacturer. This effort will be in the following areas:

- Establish nominal propulsion control stability throughout the complete steady-state envelope allowed to the EMS.
- Probe nominal propulsion control limits for stable operation of the EMS -- propulsion control combination. Careful scrutiny must be given especially to open loop scheduled type controllers.
- Determine nominal propulsion control transient response characteristics when starting from the complete range of allowed initial conditions and for various EMS bias removal rates.

- Improve sensor and actuator response characteristics to the extent governed by the proximity of the limiting conditions. This would be a tradeoff against consideration of false limits. False limits means a separate limiting logic for the EMS based on nominal control capability compared to expected disturbances.
- Provide the necessary input-output electrical interfaces and corresponding components in the nominal control system. An output is required for fuel flows and wherever a control limit might be encountered.

It appears very possible that using the assumptions given in this paper a propulsion system control, suitable for use with an energy management system, can be developed with very little, if any, coordination with the supplier of the energy management system.

A number of present propulsion systems use trimming type signals to improve propulsion system performance on the basis that better cycle efficiency is obtained at higher operating temperatures. This narrow view of performance improvement has here been expanded to consider propulsion control configurations which will allow weapons system energy management controllers to use such trimming signals to provide multi-dimensional adjustment of propulsion system inputs.

REFERENCES

1. Bush, H. Ivan, Propulsion Flexibility Concepts Based on New Component Development, AFOSR Fifth Symposium on Advanced Propulsion Concepts, IIT Research Institute, April 1968.
2. Schmidt, Ross D., Effects of High-Frequency Disturbances on Turbojet Limit Controls, AIAA Fifth Propulsion Joint Specialist Conference, U.S. Air Force Academy, June 1969.

**INLET-ENGINE CONTROLS AND AIRFRAME PROPULSION
COMPATIBILITY MANAGEMENT**

**Major J. R. Nelson, USAF, Chairman
Air Force Aero Propulsion Laboratory**

**SESSION VI. MANAGEMENT AND SYSTEM DATA FOR ENGINE INLET
COMPATIBILITY**

**R. H. Klepinger, Cochairman
Aeronautical Systems Division**

**ENGINEERING MANAGEMENT PHILOSOPHY ON AIRFRAME
PROPULSION COMPATIBILITY**

K. L. Kanouse, ASD

G. K. Richey, AFFDL

G. E. Strand, AFAPL

D. A. Watne, ASD

**(Airframe Propulsion Compatibility APC Committee
Wright-Patterson AFB, Ohio)**

ABSTRACT

Dual mission aircraft requiring high performance at high/low altitude and sub/supersonic Mach numbers tend to exhibit closely integrated airframe/propulsion systems for reduced weight, volume and drag. Close integration of the propulsion system and airframe can lead to performance and stability trades which essentially compromise system effectiveness in particular regions of the design envelope. A proper design approach to insure maximum installed propulsion system performance and stability requires a logical time sequencing of testing and simulation of the engine, inlet-airframe, inlet-engine and propulsion system component assemblies. The purpose of this paper is to present an engineering/management philosophy on airframe-propulsion-compatibility. Suggested approaches are put forth on subsystem design, simulation, integration and testing covering the engine, inlet-airframe, inlet-engine and overall airframe propulsion interface to achieve the desired result. Examples of development programs are presented to clarify the design and testing philosophies.

I. Introduction

Ever since man's first flight he has sought to achieve higher performance from smaller, lighter, and less complex propulsion systems. Tremendous progress has been made, particularly with the advent of the jet engine. The jet engine itself has made impressive gains with a continuous series of new concepts, cycles, fuels, and designs improvements, always aimed at producing thrust more efficiently with less weight. Propulsion designers have increased engine cycle pressure ratios and temperatures to achieve high performance along with continued emphasis on lowering pressure losses and increasing component efficiencies. It has been necessary, in order to achieve the versatility required of modern engines, to make the "simple turbojet" much more complex by incorporating inlet and engine variable geometries, bypass cycles, and complex control systems. At the same time there is the ever present demand to reduce weight.

The requirement to reduce weight while increasing the performance and versatility of the gas turbine has created some propulsion system designs that operate too close to the stall boundary. The aircraft designers want inlets with higher rates of diffusion, engines with higher pressure ratios per stage in the compressor, shorter burners, higher work turbines, and shorter afterburners in order to keep weight down and maintain performance. Thus we have created an extremely complicated system, which is difficult to analyze and one whose design operates close to peak component performance where the upper operating limit is characterized by unstable conditions.

Although we continue to require engines that are more versatile and continue to emphasize higher thrust-to-weight ratios, we cannot tolerate instabilities within the required operating envelope. We must insure ourselves that everything has been investigated to minimize this possibility before the aircraft begins flight testing since changes at that time are very expensive.

The challenge confronting us is to design and develop a propulsion system having component operating points as close as necessary to the limiting conditions to provide high performance but always far enough from this limiting condition to prevent instability from occurring. The problem is complicated by the fact that neither the limiting condition nor the operating conditions are fixed in today's complex engines.

Past weapon system experience, as pointed out above, has clearly identified propulsion integration (inlet-engine-exhaust systems) as a major problem area encountered during the design and development of air breathing propulsion systems as shown on figure 1. Specifically poor integration may produce inlet flow distortion and subsequently reduce engine thrust and stability. Incomplete understanding of steady state and dynamic flow distortion phenomena (fluctuating pressure at the compressor face) and its effects on the propulsion installation have caused increases in development costs, delays in the weapon system development cycle, and, in certain instances, an ultimate derating of the air vehicle's performance objectives.

Flow distortion effects on the propulsion installation must be

determined early in the development cycle if the full performance benefit of the propulsion system is to be achieved. The system and engine contractors must devote their initial efforts toward specifically defining the propulsion system component stabilities both isolated and installed to assess their effects on total propulsion system performance. The derivation of stability margins (steady state and dynamic) and the performance matching characteristics of the inlet-engine nozzle configurations are essential ingredients toward achieving acceptable system integration characteristics.

This paper will not try to present a "cookbook" approach to air-frame propulsion compatibility, but it will attempt to discuss certain development tasks that must be addressed in the development of a typical weapon system. We have divided the problems into two groups for convenience of discussion. The first category discusses the requirements for continuing work in each component and subcomponent independent of a particular system application. The purpose of basic research effort is to perfect new designs and analysis techniques for the new technology base for the "next" unidentified Weapon System. The second problem area concerns the general approach to a system development and the need to spotlight stability as well as performance throughout the development cycle and into operational use.

II. Compatibility Problem Areas

If the acquisition of a new propulsion system for an operational system is to be "low risk", which is to say "high confidence" in achieving the predicted performance within the estimated cost and time, there must be a broad base of demonstrated technology available and waiting to be adapted to this particular mission requirement. The preparatory effort may represent several years or a very short amount of time starting with analysis and followed by sub-component testing, rig or scale model testing, and perhaps a demonstration of assembled components. This activity must be continuous and must contain all technical disciplines although those areas having the greatest potential payoff will receive the emphasis. This development effort not only includes improving the hardware items, but a continuing effort must be maintained to improve analytical performance and stability prediction techniques. Again, the emphasis must be applied in those areas where the prediction techniques are weakest. This technology base is expanded and specialized for application during the development of a weapon system. The weapon system developer - the "user" - takes a broad base of technology and channels it to a very specific requirement of meeting the weapon system mission, performance, and cost objectives. By this process, the research agencies see just how effective their work has been and where additional research effort is required. It is obvious that there must be an extremely close relationship between "research" and the "real world" of weapon system development.

A. Current Technology Levels and Preferred Prediction Techniques

(1) Inlet Integration and Origins of Distortion:

The maneuverability of advanced aircraft may dictate the airframe-propulsion system placement and integration of the inlet within the vehicle. Generally, this results in a close integration of the inlet with the fuselage/wing of the aircraft. It may be desirable to have the engines at least partially buried in the fuselage to minimize weight and drag as well as the yawing force which is produced in twin engine fighters when one engine is out. An inlet mounted on the top of the fuselage is in an expanding flow field with a higher local Mach number than free stream and, therefore, requires a larger capture area than an inlet operating in the free stream. Another disadvantage with this design is during operation, at high angle of attack, the vortex produced by the cross-flow separation around the fuselage can be ingested by the inlet. An advantage of this type of design is its inherently low radar cross-section characteristics.

As the inlet is integrated with the airframe, care must be taken to insure that installation effects are minimized. For instance, with an external compression inlet, the terminal shock location might interact with the fuselage boundary layer causing separation and increasing distortion at the compressor face. This flow separation could also disturb adjacent inlets, as with a twin engine nacelle, further complicating the problem. An example of this phenomena is shown in figure 2. The inlet must be located a sufficient distance from the body or wing

so that no fuselage boundary layer is ingested. The boundary layer thickness, of course, varies with its location on the aircraft. It will also be affected by a change in the pressure gradient caused by changes in the aircraft's speed and attitude. These conditions must be accounted for and should govern the diverter height which may significantly change the drag. Recently, a systematic investigation of airframe-inlet interactions using model components was conducted to define the flow field in the vicinity of various candidate inlet locations (see figure 3). An example of the test results is shown in figure 4.

For almost any inlet installation, the inlet is severely affected if the inlet ingests a significant amount of low energy airflow caused by unfavorable airframe-inlet interactions. The level of distortion at the engine face becomes quite high and can easily induce compressor stall. Distortion caused by viscous interaction or oblique shocks entering the inlet especially at high angles of attack during supercritical operation is highly dynamic and the flow at the compressor face may be pulsating at several hundred cycles per second. These oscillations are detrimental to the surge margin of the engine as discussed elsewhere in this report. At present, there is a lack of information on the frequency or amplitude characteristics of inlets under such dynamic conditions and the response of advanced engines to these pressure pulsations. However, test data has recently been generated on the fluctuating pressures in an inlet system. Further information may be found in reference 2 . Major contributors to dynamic distortion are zones of separated flow, ingestion of low energy

flow (viscous interaction), and oblique or normal shock interactions with the inlet boundary layer.

At supersonic conditions, the inlet performance is strongly dependent on the engine mass flow demand. If the engine demand is higher than the inlet is designed for, the inlet flow will compensate for this mismatching by lowering the pressure recovery to match the engine corrected airflow. The mechanism for achieving this is to move the normal shock downstream in the diverging part of the duct, which increases the local Mach number ahead of the normal shock and the total pressure loss across the normal shock system. For steady state operation, the inlet can be sized at the design point to match the expected airflow. However, the dynamic variations in airflow due to an afterburner ignition for highly augmented engines can also cause large changes in pressure recovery and distortion in the inlet. For example, if an airflow transient associated with afterburner-ignition drives the inlet supercritical, the pressure recovery drops rapidly; but, even more important, there is a rapid increase in steady state and dynamic distortion as the normal shock moves off the boundary layer bleed surface. The movement often causes flow separation. On the other hand, the airflow transient can temporarily lower the mass flow which may unstart or "buzz" the inlet. Therefore, compressor stall can occur if there is a large pressure pulse or a "hard light" of the afterburner. At the same time, the increased back pressure pushing on the fan and compressor stages will cause the engine to deviate

from the steady state operating condition reducing the ability of the engine to accept distortion. Thus, the lightoff can compound the problem by magnifying the distortion in the inlet and concurrently reducing the stability margin of the engine.

Another type of inlet-engine interaction which must be understood is that phenomena which occurs when the engine itself has an effect on the steady state and dynamic distortion characteristics of the inlet. Since the engine operates like a pumping device, it can change the pressure distortion pattern provided by the inlet. The biggest effect seems to be on the static pressure distribution at the compressor face. In an attempt to understand this inlet-engine interactions, a program has been recently initiated to test the inlet configuration shown in figure 5, both with and without a modified J85 afterburning engine. Instrumentation consisting of approximately 40 high response total pressure gages at the compressor face will measure inlet performance and distortion through a variety of inlet-engine operating points and transient conditions, including compressor stalls. Tests will be run to find the best method of simulating an engine in inlet-alone tests. Design criteria for properly simulating an engine in both steady and transient operating modes will be precipitated during this program.

(2) Flow Distortion Effects

The operating stability and performance of turbojet and turbofan engines are directly related to the characteristics of the airflow

delivered by the aircraft's inlet system. If the flow distortion is low with high total pressure recovery, the engine can be operated at maximum potential as determined by ground tests. If the steady state and dynamic flow distortion (fluctuating total pressure) produced by the inlet-engine combination is above a critical level, then the engine^{is} most sensitive to compressor stall or loss of thrust. This may require derating of the engine to accommodate the steady state and transient flow distortions. Certain operational maneuvers may be limited to insure that a positive stability margin is maintained. As a result, the overall performance of the aircraft is compromised to accommodate incompatibilities among the airframe-inlet and engine components.

Pressure distortion is currently recognized to consist of both steady state distortion and non-steady state distortion or pressure fluctuations. An enormous amount of data has been accumulated from inlet and engine testing for steady state distortions. Methods of simulating the distortion patterns generated as a result of steady state inlet testing during engine or compressor tests are well developed. This is not the case for dynamic distortion, and, although the major cause of compressor surge margin reduction for a well designed inlet is still steady state distortion, the effect of fluctuating flow conditions can no longer be ignored. These dynamic effects have required new methods of testing, the development and use of new high response instrumentation and data acquisition systems, and the development of new analysis techniques.

Fortunately, engine steady state experiences and methods can be used to evaluate several types of dynamic distortion. A distortion pattern that is seen by every compressor blade at the face of the engine is considered steady state by the engine, but, for an engine turning at 12,000 rpm, this requires that the pattern remain for only 5 thousandths of a second. If we assume that this compressor will react (surge) if only 120° or $1/3$ of the blades pass through the critical distortion condition, then the pattern has to remain for only a thousandth of a second for the steady state engine distortion criteria to be valid. Figure 6 is an example of how steady state distortion criteria has been used to evaluate dynamic distortion. The instantaneous data was generated by "freezing" the pressure contour's every few thousandth of a second and evaluating the isobasic patterns as for a stable condition. This analysis approach predicted not one but several conditions that should have surged the compressor before surge finally occurred. The dashed line on figure 5 indicates the result of averaging the patterns over a time period equal to one revolution of the compressor and giving a single maximum distortion level near the time surge was recorded. Using these data, a similar correlation was achieved by averaging for time periods equal to $1/2$ and $1/3$ of a compressor revolution but not at $1/6$ of a revolution.

Methods of identifying critical conditions and examining instantaneous pressure patterns are currently being pursued concurrently with statistical methods to improve the procedures for predicting when critical conditions may occur. The principal element lacking is an

understanding of the origin and control of distortion and its relationship to various types of engines and aircraft installations. There are, at present, no reliable design criteria to dictate the type of inlet-exit flow field required to insure inlet-engine compatibility. The effects of higher frequency pressure distortions and one dimensional uniform or in-phase pressure fluctuations may also contribute to the reduction in surge margin. More information is needed to evaluate the magnitude of these disturbances. Continued analytical and experimental work is required in order to improve the desired confidence level in predicting the engine response to nonsteady distorted flow.

(3) Engine Stability and Performance

a. Engine Analysis:

The introduction of complex engines in modern aircraft where both time variant and steady state engine operating conditions can have significant effects on engine stability characteristics has led to a requirement for establishing new techniques to determine the effective compressor stall margin. Traditionally, this stability margin has been defined in terms of the difference between the operating and surge lines of a compressor map (figure 7). For ^asimple turbojet, this form of presentation provides an adequate base for understanding engine stability characteristics; for a modern complex engine, it does not.

Consider, for example, a turbofan engine with a compressor layout as indicated in figure (8). There are effectively four compressor components to be considered: (a) fan inner, (b) fan outer, (c) low pressure compressor, and (d) high pressure compressor. Each compressor component

must be examined individually; the stability margin is not cumulative except that if the margin is driven to zero in any component the overall margin has dropped to zero. In addition to four compressor pressure ratio maps to be considered, the stall prediction is further complicated since neither the surge pressure ratio nor the operating pressure ratio are functions of mass flow and compressor RPM alone. For example, changes in pressure in the fan exit duct caused by either afterburner operation or a change in nozzle area can significantly affect both the surge and operating lines of the low pressure compressor. Furthermore, these fan duct pressure changes significantly affect the engine bypass ratio either supercharging or desupercharging the engine core flow. Since operating and surge lines are not affected equally, these changes have a significant effect on surge margin. Recent investigations have indicated that at a given corrected RPM there is a particular fan duct pressure which gives maximum steady state surge margin with relatively small increases in fan duct pressure. Deviations from this value can result in a very rapid fall-off in surge margin.

Transient operation of an engine is another major factor affecting surge margin since there is an automatic speed mismatch between the fan and compressor spools as the inner spool responds to fuel flow changes. Accelerations or decelerations of the outer spools are achieved, in general, through the aerodynamic coupling between spools. This mismatch is likely to drive one or the other components in the compressor towards surge. The degree of mismatching can be mitigated

by incorporating variable engine geometry or variable nozzle areas to match the outer spools flow & speed properties.

b. Engine Simulation:

The sheer volume of data which must be exchanged between engine and airframe companies is such that tabulated data or curves can only convey the general behavior of the system at steady state conditions. The specific behavior at all operating conditions across the complete flight spectrum including dynamic effects can only be documented effectively by the use of mathematical models which simulate and predict propulsion system operation.

Engine simulation using mathematical models is in an early stage of development but initial work has already proven their value and shows considerable promise for the future. There are basically three types of models currently in use -- engine steady state performance models, engine dynamic models, and component characteristic prediction models. The steady state model is based on empirical data from the engine manufacturers rig tests and control characteristics. It is then biased to match actual performance using engine test data. This biasing is achieved at the engine design point.

The dynamic model uses the steady state model as a starting point. Such factors as component inertia, heat absorption, volume dynamics, and engine controls feedbacks are incorporated into the steady state program. The transient behavior of any parameter of interest in the engine, such as airflow, fan duct pressure or spool

speed, can then be examined. Early results show considerable promise, but analysis efforts are hampered because of the lack of accurate test data on the transient behavior of internal engine parameters.

A considerable amount of research effort is going into the development of component characteristic prediction models. From this work on the compressor modeling will come the capability to predict the surge line and the flow characteristics which will indicate when stall is most likely to occur. Two approaches have been taken. There are methods being developed to analytically predict the three-dimensional flow field through the compressor, thereby determining exactly the flow conditions at and before stall. The alternate approach being examined is to determine the dynamic behavior of a multi-stage compressor using individual stage characteristics as building blocks. These methods will be used to study compressor behavior with uniform inlet flows, steady state and time variant distortions. Results of these research programs are then input as part of the stall logic in the complete engine models.

The engine simulation model will be updated or perhaps completely revised for system application as component data become available or design changes are made. The engine system is defined by the mathematical representations of its components and dynamic relationships between components. The key to dynamic propulsion system simulation is to accurately represent the inlet and engine control system and their interactions. Although the inlet and engine control

models used in the development of the controls are usually analogue simulations in order to transfer the models between companies, the dynamic propulsion system simulations are programmed in a compatible digital language. The dynamic model of the engine includes compressor/fan stall logic, burner blowout and light-off characteristics, inlet flow distortion effects, and Reynolds' number effects.

The value of propulsion system simulations in the tracking and managing of the system development cannot be overemphasized. But caution must be taken to first take the time and effort to make the simulation as accurate as possible; second, to insure the working model is updated continually to represent the current state of development of the engine and that the development test program will furnish the data required to validate the model; and, third, to know the limitation of the model so that decisions are not based on propulsion system simulation results that imply more than the model is capable of simulating. The following examples of how these models can be used and their advantages assume these types of precautions have been applied.

1. To predict answers to the "What if" questions. What if the turbine efficiency is X? What if the distortion level is X? What if the engine had to accelerate in X? What if the nozzle sticks open or the inlet throat will not open?

2. It can be used to identify weak areas in the propulsion system such as poor performance or low stability margin. It can identify areas where testing should be emphasized.

3. The model is an excellent tool for extrapolating test data. Often the test facility can only simulate flight conditions over a restricted range, and, after this data is used to validate the model, the model can extend the predictions of performance or stability trends over a wider range of conditions with some degree of confidence.

4. It can be used to interpolate between test data points. This technique reduces the amount of testing required and still provides continuous propulsion system performance and stability information over the entire flight envelope at a significant savings in testing time and cost. The interpolation technique requires a very careful selection of the points that will be tested, and, the more highly developed the system simulation, the fewer the test points required.

5. It can be used to reconstruct the propulsion system operating conditions prior to an unexpected and unexplained problem or failure so that each parameter can be studied in detail.

The models just discussed are, for all of their complexity, still only one dimensional representations of the propulsion system. Because of this basic limitation, two and three dimensional effects have to be interpreted separately and introduced into the program in some simplified manner.

(4) Exhaust Nozzle/Airframe Interactions

Current and future flight vehicles employing airbreathing propulsion systems have to accomplish various missions that dictate a need for different speed capabilities. Among the more important problems of aircraft propulsion systems integration are those

associated with the airframe nozzle interface. The interaction between the external airframe generated flow field and the exhaust nozzle stream frequently results in lower thrust levels than anticipated. Widely different nozzle area ratios are required for peak operating efficiencies at various flight conditions and these changes in nozzle dimensions must be accommodated within the fixed lines of the fuselage afterbody section. A nonuniform external flow field is usually produced by these fuselage contours due to the proximity of control surfaces and inter-fairings dictated by design considerations. The interaction of the exhaust plume and the external flow field can cause flow separation or can significantly alter the pressure distribution and drag of the fuselage afterbody.

The internal performance characteristics of nozzles are reasonably well understood for isolated nozzle systems. However, there is a severe limitation in the present capability for obtaining the proper integration of the exhaust nozzle with the aircraft to reduce installation penalties and minimize afterbody drag. Complete analytical procedures for predicting installation losses of exhaust systems integrated with an airframe do not exist, nor is there adequate empirical information available to develop definite airframe-exhaust nozzle integration design criteria. Preliminary experimental results indicate that the analytical methods do not properly account for those flow phenomena that influence the nozzle performance.

A nozzle design which is used on several recent aircraft is the blow-in-door ejector (BIDE) nozzle shown in Figure 9. This design

approach attempts to incorporate the performance of a variable geometry convergent-divergent (C-D) nozzle without the weight and mechanical complexity of the C-D configuration. The blow-in-doors allow external air to be induced to prevent the primary flow from over-expanding as the expansion area ratio required to produce maximum thrust decreases at decreasing nozzle pressure ratios. In some installations secondary airflow is used in addition to the passage of tertiary flow through the doors. The secondary flow can also be used to cool the inside surface of the nozzle shroud during afterburner operation when the blow-in-doors are closed. The doors open when the external pressure on the door surfaces is greater than the internal pressure. The pressure differential normally occurs at subsonic and transonic speeds. The divergent section of the nozzle shroud may also be hinged so that at higher speeds and high altitudes, where a large nozzle exit area is required for maximum thrust, the freely floating shroud section will open wider and the doors will close.

If a calculation of the isolated BID exhaust nozzle flow for various external boundary layers is computed by available procedures, an increase in the total pressure recovery through the doors is predicted when the boundary layer thickness is decreased. Likewise, the net thrust of the nozzle increases as boundary layer thickness is decreased for a range of freestream Mach numbers, as shown on Figure 10.

It is assumed in these types of calculations that the external flow properties are uniform around the circumference of the blow-in-

doors, and this flow is inducted with no separation with all secondary-tertiary airflow passing through the doors. The last assumption is necessary since available analyses are usually designed to handle only one stream in addition to the primary flow.

An indication that some of the assumptions made in the analysis may not be correct is given by the results obtained in a recent investigation of the variation of boundary layer thickness on the performance of a blow-in-door nozzle. The nozzle was installed so that the boundary layer thickness at the entrance to the doors could be varied by changing the length of the surface ahead of the nozzle.

A sample of the test results is presented in Figure 11 & Reference 1. The value of total pressure was obtained as an average of the values obtained from four rake positions located between the blow-in-doors and the internal surface of the shroud. Reference values of the average total pressure and the gross thrust coefficient correspond to those values obtained at a local boundary thickness to maximum diameter ratio ($\delta L/D_{MAX}$) of 0.04. The gross thrust coefficient was defined as measured thrust minus drag divided by the ideal gross thrust based on measured primary airflow and total pressure. As can be seen from the results, an improvement in performance is obtained as the total pressure of the tertiary flow increases. However, the change in both total pressure and thrust as the boundary layer thickness increases is opposite to that predicted by analytical methods. That is, for

the Mach numbers and nozzle pressure ratios investigated, increasing the boundary layer thickness definitely increases the nozzle performance.

From the comparison of theory and data, it is apparent that there are still several shortcomings in the analytical methods for calculating the relative increase or decrease in performance of a complex nozzle installation due to flow interaction phenomena. Some of the more pertinent problem areas that need further investigation are:

1. Asymmetrical and nonuniform flow fields
2. Shock wave-boundary layer interactions
3. Separation of the external and/or internal flows
4. Performance of inlets for blow-in-door nozzles
5. Influence of the primary jet on base and boattail pressures

More extensive model and flight test data should be obtained to improve both theoretical and empirical analyses techniques. Such data are required to better describe and understand the flow around and in the nozzle and to properly correlate the test results with the analytical methods. The most important information needed would be the thickness and shape of the boundary layer in the external flow field, the static pressure distribution along the exterior and interior surfaces of the nozzle, and, for blow-in-door nozzles, the total pressure recovery inside the entrance to the doors.

B. Testing Methods

(1) Inlets:

The proper simulation of inlet flow behavior in a wind tunnel is critical to the development of a compatible airframe-propulsion system combination.

Recognizing the limitations of ground test facilities, the best approach to preclude some of the problems of airframe-propulsion integration is to analyze and test inlets, inlet-airframe configurations, engines and inlet-engine combinations in available facilities in order to generate reliable compatibility design criteria based upon empirical and analytical methods.

Dynamic distortion of an inlet operating at various conditions in the aircraft envelope is becoming more important as the performance of modern engines is increased by higher pressure ratios per stage, operating the engine close to its surge margin, and the delicate interactions between engine components in a finely tuned machine. The dynamics of inlet flow have always been present, but recently the level of fluctuating total pressures delivered by the inlet to the engine has been recognized as a contributory cause of engine compressor stalls at critical aircraft operating points.

Recent experience on the effects of dynamic inlet distortion indicates that the engine may react to turbulence as instantaneous flow distortion in a manner similar to its reaction to steady state distortion. To the inlet designer, this hypothesis means that the turbulent distortion must be defined with equal resolution to that of steady state distortion. In other words, an inlet must have enough high response pressure probes at the diffuser exit (compressor face) to accurately map out an instantaneous distortion pattern or allow the calculation of an instantaneous distortion index. The density of instrumentation might vary between thirty to fifty probes

at the compressor face depending on the flow area. Figure 12 shows an installation in an inlet where 36 high response gages were installed. Recent advances in miniature pressure transducers have allowed this type of instrumentation density to be achieved.

Proper selection of instrumentation characteristics such as what kind of probe response is needed in an inlet test where the objective is to determine criteria for airframe-propulsion compatibility cannot easily be answered, since there is insufficient engine data to define what frequencies of pressure fluctuation are the most critical. In the meantime, we should try to obtain the highest frequency response that the probes are capable of delivering without affecting the transducer's life. It appears that by careful design we can achieve valid total pressure data on the order of 5000 cycles per second in an inlet flow field. It is relatively inexpensive to collect data at high frequency, once a decision is made to collect dynamic data. However, the processing of the data and its analysis is extremely expensive, requiring large amounts of time on modern high-speed computing machines. When better resolution on engine sensitivity is obtained, we will know how much of the high frequency data to discard.

The acquisition and analysis of high frequency inlet data must be based on considerations of not only the engine sensitivity but inlet flow sealing effects. The engine response will likely be based on full scale flow, but inlet data will be in model scale, ranging from approximately 1/8 scale in early testing to full scale

in final inlet-engine testing or ultimately, in flight testing. For example, if we pick 500 hertz as the upper limit (full scale) to which the engine will be sensitive to, and applying acoustic scaling relationships, then we should examine data to 4000 hertz in an 1/8 scale inlet model test. A simple analysis of dimensional groups will indicate that the RMS value of a fluctuating pressure should be identical between model and full scale, but the location of energy in the frequency spectrum will vary with this acoustic relationship. However, this analysis method assumes identical total Reynolds numbers, Mach number and geometry/flow duplication between model and full scale hardware. This is a poor assumption indeed in most wind tunnel test work. Since the dynamic phenomena in an inlet originates mostly in the viscous layers by such mechanisms as shock wave-boundary layer interactions and flow separation processes which are Reynolds number sensitive, it becomes clear that there is a great deal of uncertainty in the scaling relationships of inlet dynamic flows, and their extrapolations to meaningful airframe-propulsion compatibility criteria.

In order to provide some insight into the problem of scaling dynamic inlet data, the Air Force and Navy are jointly sponsoring a program called "Wind Tunnel/Flight Test Correlation Investigation". In this program, wind tunnel tests will be conducted on scale model inlets of the RA5C aircraft shown in Figure 13. Flight speeds up to Mach 2.0 will be generated over wide ranges of aircraft angles of attack and operating conditions. Both dynamic and steady state inlet

distortion data will be obtained using thirty high response pressure transducers at the compressor face. Model and flight test instrumentation will be located identically at the compressor face in order to allow direct comparison between wind tunnel and flight test data. Aircraft flight tests are scheduled to commence in late 1969. By the middle of 1970, we should have gained some valuable insight into the true scaling relationships of dynamic inlet phenomena which will help extrapolate new inlet data to flight conditions on a new aircraft reducing the possibility of flight test "surprises" which have plagued so many of our aircraft development programs of the past.

(2) Engine Testing

Only recently has high quality dynamic data been taken in propulsion system testing and many of the dynamic prediction techniques are still based on steady-state experience. Realizing that our prediction techniques are not completely accurate in defining the stability limits and the operating conditions, it is necessary to continually test propulsion system components to insure the required stability margin is achieved and to substantiate the reduction in this margin with internal and external disturbances. The development program for a new weapon system should approach stability in the same manner and at the same time it addresses performance. The first predictions are made in the early preliminary studies and the final substantiation is accomplished during the flight test program.

The stability of a propulsion system is defined when the stability margin for the system is known under all steady and unsteady conditions

that will be experienced in its operating envelope. Surge, buzz, or flame-out are the results of exceeding the stability limit of the compressor/fan, the inlet or the afterburner. It is usually the compressor surge criterion that is limiting for most of the propulsion system operating conditions, but other limiting conditions cannot be ignored, and must be thoroughly explored in engine and component testing.

This problem is complicated enough during steady operating conditions, but stability becomes even more complex to predict during transient operation. For instance, the example previously cited describing the behavior of the engine during an afterburner light-off. A brief ramp change in pressure and airflow results as the afterburner lights and the nozzle opens. This results in a brief but real change in the operating conditions of each component of the engine. The question, then, to be answered by test data is; has the net effect resulted in a decrease or increase in the stability margin for this brief interval of time and what was the change? Did the inlet buzz or the compressor surge? A complete testing program is required to obtain these answers on the stability characteristics of each component and the effects of one component on another. To achieve this goal, a definition and validation of stability must be a primary consideration from the very first phase of the engine's development.

The exact location of the thermodynamic interface between the engine and the inlet must be specified. At some axial location in the inlet within a compressor diameter or so, a plane must be

established that will be used by both contractors to define the interface flow conditions. This station is an instrumentation plane that will be used in both inlet and engine testing. There are arguments for having this plane closer to or farther from the compressor face, but for this discussion the most important point is that the two companies agree and use the same location.

The primary effect of distortion is on the surge margin of the compression section of the engine, but if the distortion is not attenuated in the fan or compressor the other components of the engine may also be effected, and inter-component or even inter-stage instrumentation is required to resolve the question. Various methods have been developed to analyze and predict the effects of distortion on engine stability margin. The experimental engine testing must be developed to measure the intensity or degree of nonuniformity of the distorted flow field and to correlate the reduction in compressor surge margin.

III. The Phases of System Development

The typical development of a propulsion system for a new weapon system can be divided into four phases, a study phase, a demonstration phase, a qualification phase, and an operational phase (See Fig 14). During these phases, the systems stability and performance must be predicted and the predictions substantiated to provide a degree of confidence in the propulsion installation.

The study phase includes all interested airframe and engine companies. There is usually little or no direct financial support from the Government. There will be some component testing during this time period, such as scale model inlet tests but most of the data base used to substantiate performance and stability predictions will come from related component tests. Therefore, some extrapolations of experimental data may be necessary.

The demonstration phase (which includes contract definition) is usually characterized by a reduction in the number of contenders with the Government making substantial resources available. In this phase the performance and stability margins of a demonstrator engine are validated by testing. The data accumulated in this phase forms the basis for substantiating the predicted stability margins and performance of the propulsion installation for the qualification and acquisition phase of development. Since the proposed technology should be closely related to the demonstrated performance, there should be little or no requirement to extrapolate the available data.

The purpose of the qualification phase is to develop the final flight hardware through qualification and flight testing. There is only one propulsion system being developed during this period and the identification of any major problem arising in this phase can be very expensive to fix in terms of time and money. A firm engineering definition of the proposed design based on the demonstrated performance and stability data generated during the demonstration phase is the best insurance for preventing problems during this critical final development phase.

A definition of the term "airframe propulsion system" integration is necessary before embarking on a discussion of the elements or tasks of the development and integration process. Integration in this sense means determining the best method to assemble all of the system components which will maximize mission performance of the total air vehicle system. Satisfactory integration can best be achieved by combining previous experiences, available design criteria and accurate test data to achieve an optimum combination of airframe and engine components (inlet-engine-nozzle, etc.). The best method for implementing integration is to develop an integration plan that will provide both the procedures and criteria for achieving satisfactory total air vehicle system performance. The purposes of the integration plan are:

1. To yield system design characteristics that satisfy the mission requirements.
2. To provide acceptable propulsion system performance.

3. To achieve adequate propulsion system stability.
4. To minimize both drag and weight penalties of the airframe.
5. To avoid high cost and high risk areas.

A. Study Phase:

We shall say that the study phase for a potential weapon system starts with a set of specified mission requirements, a date for initial operational capability (IOC) and perhaps some additional constraints on the systems such as maximum take-off weight.

(1) Technology Development:

The aircraft industry starts their preliminary design studies and may at least at the start, use their own engine cycle analyses for early mission studies. The engine companies are also doing cycle studies and perhaps they are also doing some mission studies with an assumed paper aircraft. Both contractors have made thorough technology reviews to determine, for the development time period of this system, exactly what levels of technology are required or will be available for incorporation into this weapon system. For instance, the engine companies will review their current demonstrator programs, and other systems (if any), their contributing engineering or IR&D programs, their technology development contracts, contracts with the other services, NASA, and any other recent or current efforts. If time allows they may initiate new programs to increase the technology levels of certain propulsion components. The contractors not only select technology levels on which to base the performance of the propulsion system, but also make assumptions as to the margins required for stability.

Advanced engine studies should include the examination of the various airframe manufacturers' predictions of inlet flow conditions to insure that engine stability predictions will at least define the extent and degree of stability for the propulsion system over the possible flight envelope. Both the predicted conditions and the predicted effect of the conditions in the engine should be substantiated early in the propulsion system development.

The effect of inlet distortion on the compressor surge margin depends upon the compressor type and the pattern or type of distortion encountered. An extensive amount of data has been taken from engine and compressor rigs to determine experimentally the quantitative effects of a limited number of types of distortion patterns. From these data there have been generalized techniques developed to evaluate distortions by combining several types of patterns tested to simulate the desired pattern and then calculating the effect of the composite distortions by combining the isolated results. These generalized techniques are used during the early phases of engine development and in the systems study phase while enough data is accumulated to either confirm or modify the prediction techniques.

Although it may only be possible to apply related engine compressor data on a similar configuration this early in the development, the behavior of the inlet can be given a first cut evaluation by testing small 1/10 scale models to indicate the steady and dynamic distortion levels (average turbulence).

Attitude limits for the aircraft, the inlet placement and configuration, the diffuser length, and the inlet controls will all have a

bearing on the engine performance and stability. Similarly, the engine airflow requirements and the effects of variable geometry on these requirements, the afterburner light-off characteristics, the acceleration characteristics and the sensitivity to distortion and unsteady flow will influence the inlet design. Sensitivity of cycle optimization to changes in mission and aircraft characteristics are investigated during the study phase and an engine cycle is tentatively selected. Although portions of these studies may be done independently, the engine and airframe contractors must work together to establish the effects of cycle or component changes on the aircraft and to determine the sensitivity of the propulsion system component performance and stability margin to aircraft changes.

During the study phase where it is necessary to select a particular inlet system design, its location on the aircraft must be determined by performing quantitatively trade-off studies on a variety of parameters to arrive at a satisfactory candidate. Bypass airflows, bleed flows, off design airflow matching and diverter losses will vary with the type of inlet selected and its placement on the aircraft. Flow field investigations on the aircraft should include determining the effects of vehicle attitude on the local flow parameters in areas where the inlet may modify upstream flow patterns. Methods for minimizing boundary layer ingestion accounting for airplane attitude effects and the effect of incorporating a B/L removal system on airplane drag should be investigated. Correlations

should also be made between freestream Mach No. and inlet Mach No. during supersonic flight to assess inlet performance (pressure recovery) and inlet sizing. The effect of one engine out or an inlet unstart moment on airplane stability and control should also be investigated. If the inlets are placed in close proximity, the effect of inlet spacing, or incorporation of splitter plate devices should be investigated in terms of an inlet engine transient influencing an adjacent inlet.

The engine designs at this stage of the program are mostly paper concepts using ideal inlet and nozzle performance values for predicting total propulsion system performance. The airframe designer usually assumes the engine characteristics to predict the approximate weight and volume of the propulsion system. He must determine the approximate location of the engine on the aircraft before aerodynamic performance predictions can be computed. Some gross engine characteristics must be available to the airframer before he can legitimately determine the best method of integrating the candidate engine hardware into the airframe. The engine companies are usually faced with a similar problem of having to generate airframe characteristics by performing mission analysis studies on a fictitious airframe design of their own. This design is used as a starting point to aid them in their initial sizing, cycle analysis, and bypass ratio selections depending upon the type of mission and payload objectives that must be satisfied. Therefore, the engine manufacturer initially embarks upon a series of studies exploring

the ramifications, advantages and problem areas of several candidate design offerings. The purpose of his design investigations is aimed at reducing the possible number of configurations to a single baseline for conducting a more detailed analysis with the eventual release of engineering drawings for fabricating a demonstrator engine. These efforts will be continued in the demonstration phase once the engine manufacturer is selected. Once the demonstrator design is released, the engine and airframe companies are in a position to jell the interface requirements since both performance and physical characteristics can be collated into a proposed integration plan. In the early design phases the propulsion simulation model discussed in Section II is used to assist the designer in the selection of control modes and control requirements. It is used to predict the effects of both internal and external transients on the system. Later in the test phases the model will be used to duplicate propulsion problems that occur during development to pinpoint the source of trouble so that a remedy can be proposed.

The two engine simulation programs (steady state and transient) become the fundamental source for predicting overall propulsion system performance and stability. But their accuracy in describing the performance and stability margins of the propulsion system is dependent upon the accuracy of the individual component performances and their relationships programmed into the model. It is essential that this model data be confirmed or revised as early in the development cycle as possible. These models will be of constant use throughout the program to predict

the influence of a design or an environmental change on the performance and stability of the system and it is important in the study phase that this procedure gets off to a good start.

(2) Compatibility Plan:

During the program study phase a compatibility plan will be formulated which basically will contain the proposed integration milestones and compatibility goals proposed for that particular propulsion installation. This collection of ideas will be generated by both airframe and engine contractors and will serve to provide these two contractors with the essential ingredients for controlling the interface, for identifying those critical performance and stability factors and for aiding in substantiating the level of compatibility between the engine and airframe subsystems. The compatibility plan should summarize the state-of-the-art that was used to define the stability goals pertaining to the particular type of airframe system.

The compatibility plan should describe the methods for testing and integrating the propulsion system components. The test program should be conducted in a manner that will result in developing a stable running propulsion unit having minimum performance losses due to the integration of these components into the airframe. An orderly development of the propulsion components must progress by testing each component over a wide range of environmental conditions to satisfy total propulsion system performance and stability requirements. The timing of these component development efforts and the

relating of these efforts to the engine test program must be an integral part of the compatibility plan.

A complete estimate of all thrust losses due to the installation of the engine and inlet into the airframe is necessary to properly predict the installed propulsion system performance (stability included) throughout its operating range. Since airplane performance must also be based on the installed performance predictions, the compatibility plan should clearly show what engine and inlet tests are required during the design and development phases to completely substantiate these propulsion system performance estimates. This initial planning by both engine and system contractors requires close cooperation and coordination to insure that engineering performance estimates and substantiating empirical data are generated to adequately define the performance interface.

Since the system contractor is responsible for conducting performance and stability trade analyses in his search for arriving at an optimized propulsion installation, the compatibility plan should also describe the contractor's methods and approaches (both analytical and empirical) which will be used to achieve an optimum design.

(3) Implementation of the Plan and Data Exchange:

Although part of the study phase efforts are done separately by the airframe and engine companies interested, these parties must work together in accomplishing the trade-off studies referred to above. The implementation of the study phase really begins when the aircraft industry recognizes the Air Force's needs. This

recognition may occur as much as 6-12 months before an RFP is conceived and disseminated. The engine and airframe companies recognizing these needs begin to confer with one another discussing what should the mission requirements of the new weapon system be and what sort of propulsion system design would be capable of complying with both performance and stability requirements as well as meeting the mission goals. The airframe contractor should then initiate trade studies in an attempt to determine such things as possible inlet and engine locations and compatible inlet types to blend with the aircraft's external contours. They should be examining the inlet location in particular, for the magnitude and extent of possible flow distortions steady state wise, investigating the need for bleed and bypass systems and sizing these subsystems for several candidate aircraft designs. The airframer should also be looking at ways to improve the efficiency of these systems in terms of both weight and performance. Similarly, the engine companies should be coordinating their activities with the airframe companies and government agencies always searching for new concepts and better design criteria, broadening their technology base and trying to apply and incorporate current technology levels into their propulsion concepts. The engine companies should be conducting trade studies on engine types (Turbojet or Turbofan), and engine cycle parameters such as bypass ratios if a turbofan fits, investigating possible nozzle configurations that will offer the desired performance with a minimum amount of weight increase if

variable geometry is required. The engine and airframes during this time period are continually consulting with each other and the government agencies such as NASA, Navy and the established Air Force system program office or cadre.

B. Demonstration Phase:

The end of what we have called the study phase and the start of the demonstration phase of the development of a propulsion system is identified by the Government's request for proposals to fabricate component hardware to demonstrate the predicted engine performance and stability. The purpose of this phase of development is to demonstrate that the technology levels predicted can be achieved with the new engine design and that this advanced design will live up to its estimated performance, stability and weight.

(1) Technology Development:

Although minor changes in design can be expected, the technology demonstrated in the demonstrator phase of the program is the level that will be available for the development engines for preliminary flight rating test (PFRT) and qualification test (QT) in the next phase of the development.

At this point in the propulsion system development cycle, the major trade-offs have been accomplished and the propulsion system design has been optimized for this particular weapon system and its mission. Results of the analysis leading to this final design and the reasoning behind each assumption is well documented.

The stability and performance predicted for each component is substantiated by the results of past and current development programs

in each component area. The similarities and differences between hardware previously tested and that proposed are identified. The predictions of total performance and stability margins are incorporated into the dynamic and steady-state propulsion system simulations and are made available to Government Agencies, and all competing airframe companies. The assumptions used in the prediction techniques, each individual component performance and stability map, and the dynamic relationships between components, are all well substantiated by analysis and/or data from test programs of related designs.

During the demonstration phase the contractors are expected to demonstrate the performance and stability limits at both the component (subsystem) level and (system) or engine demonstrator level. This testing must also establish quantitatively the influence of nonsteady and nonuniform flow conditions on the engine stability margin. During this time period the components and the engine must be subjected to the worst or most critical environmental conditions from the stability standpoint. These conditions must be jointly identified by the propulsion system partners by using the appropriate propulsion system simulations and confirming them with empirical data acquired from approximately 1/6 scale inlet tests and engine component tests.

The most critical environmental conditions simulated by the engine contractor are derived by inlet/airframe integration tests being conducted by the airframe manufacturers. These tests are done

with fairly large models (1/6 scale to 1/3 scale) of the complete inlet system and all fuselage or wing surfaces upstream of the inlet which could affect its performance or stability. The scale should be the largest which can be tested in available facilities and cover the complete attitude (angle of attack and yaw) and Mach number range of the aircraft.

The instrumentation in the inlet/airframe demonstration model is critical to establishing the proper interface between the airframe and engine contractors development work. Our present understanding of dynamic distortion influences indicate that the inlet model fluctuating pressure instrumentation at the compressor face must be sufficient in quantity and location to derive an instantaneous total pressure map of the flow at the engine face.

In addition to providing the interface data to the engine contractors, the inlet/airframe integration test is used by the airframer to develop inlet contours, variable geometry schedules and requirements, document installation drags (bypass, bleed, and spillage) and assure that the inlet configuration is the one best suited for the aircraft in its intended mission. There may be some tailoring of the integration of the inlet with the fuselage or wing flow field to eliminate undesirable upwash or downwash characteristics.

During the demonstration phase, inlet-engine airflow matching studies are used to substantiate the relative performance losses incurred by the installation when operating at optimum and mismatched flight conditions. Analyses for determining the degradation in

stability margin of the power plant and propulsion components during system transients such as off-schedule inlet operation, transient inlet airflow disturbances, engine power transients and vehicle attitude changes are outlined in sufficient detail to establish the credibility of the analysis approach. The exhaust nozzle airframe interface area should be studied with the objective of providing the best balance between internal thrust and external drag characteristics. This investigation should consider the type of external flow effects that the nozzle will be subjected to and the analysis approach to be used for determining the configuration that has minimum performance losses resulting from the interaction of the external flow field with the hot exhaust stream.

The system contractor must account for the flow losses produced by the secondary airflow system which provides air for cooling the engine and accessories, to properly predict the propulsion system's installed performance. Some degree of control must be provided for maintaining a reasonable margin of secondary total pressure to prevent sudden or unexpected total pressure drops from compromising the ability of the secondary airflow system to divert the required amount of air. Because boundary layer diverter drag and secondary airflow system drags do vary with flight Mach number, drag predictions must be developed across the operating flight spectrum instead of evaluating isolated operating points. These predictions must also be substantiated with empirical data to verify the performance capability of the secondary system.

(2) Integration Plan:

The idea of compatibility has first been recognized in the study phase and once the ideas have crystallized they can be converted into criteria in the demonstration phase and consolidated into a formal document of compatibility requirements for that system. This document can be called an Integration Working Plan. The engineering paper designs in each company participating have been reduced to the selection of one baseline airframe and one baseline engine or propulsion system. There are only a few companies competing in the demonstration phase of the program where in the study phase the competition was not restrictive. Actual performance has developed from the compatibility criteria that was derived in the study phase and attempts have been undertaken toward achieving the compatibility goals recognized in the study phase as being necessary for satisfying both mission and design requirements. Component designs are becoming more specific and the compatibility plan which originally contained a set of general criteria and goals has been transformed into a specific checklist for evaluating and monitoring progress and approaches for eliminating possible airframe propulsion system compatibility deficiencies.

The purpose of the Integration Working Plan is to identify work to be performed and the time-phasing required in order to be effective in (establishing) identifying and controlling the technical interfaces existing between propulsion system components to insure maximum system performance with adequate stability margin. This Integration

Working Plan should contain information covering both the technical and managerial aspects of the program. It not only addresses the interface areas requiring the attention of both engine and system contractor but also delineates the responsibilities of the contractors and where applicable, the Government.

The plan should indicate each component test and show how and when the data is made available to the propulsion system partner. It should reflect joint planning by the engine and airframe companies as to when data is needed, the instrumentation configuration and data format, data analysis techniques, instrumentation responses, and what parameters should be recorded. For example, such small details as the exact placement and number of probes can be very critical and should not be left to chance. These early instrumentation and data requirement decisions should be carried through the flight test program. Not that every piece of instrumentation on a large wind tunnel model or on an engine in the cell can be included in the flight test program, but if limited instrumentation can be used consistently throughout the program it will be easier to analyze sketchy flight test data.

The compatibility plan should also contain the airframe contractor's proposed nozzle test plan for substantiating installed nozzle performance during the development of the propulsion hardware. This plan should describe the methods to be used in simulating the external and internal flow fields and the procedures to be followed for analyzing flight interaction phenomena. This plan should

describe the temperature and pressure measurement techniques to be employed and the reasons for selecting these methods and sensor locations. The plan should also state the philosophy and reasoning used to select a particular model and model scale for investigating these flow interferences and their effects on nozzle internal performance and external drag.

(3) Implementation of Plan and Data Exchange:

During the demonstration phase many things "jell". More is known about the engine, the airframe is better defined and curves and preliminary plans and drawings now compliment the engine designs but there are fewer companies competing with one another. Although both the airframe and engine designers start out by examining a series of aircraft and engines, they soon narrow the candidates down to a small number. The more firm and definitive the mission requirements and IOC date, the more firm the aircraft and engine selection. There have been exchanges of information between the engine and airframe companies now that the design is becoming more firm and larger quantities of specific information are being exchanged. In order to handle this data effectively the engine has been mathematically simulated and transferred in the form of a computer deck. The performance of the inlet and the performance of the nozzle are also programmed and transferred so that the installed engine performance can be predicted by the airframe contractor for design or off-design conditions existing within the flight envelope. The engine simulation program has the capability to predict the

effects of inlet or engine bleed, horsepower extraction, jet nozzle area changes, distortion effects on surge margin and installed thrust.

During this phase the airframe and engine contractor should assign, on a full time basis, engineers to work at the other company's facility to accomplish the necessary coordination and exchange of technical information between the engine and system contractor.

The government engineer in the System Program Office must use the integration plan to monitor and evaluate such things as:

1. Plans for testing and integrating propulsion subsystems to maximize performance. This should include coordinating and defining the performance interface requirements.
2. Plans for defining and substantiating propulsion system stability characteristics.
3. Plans for conducting full scale integrated propulsion system integration.
4. Plans for developing, integrating, and using steady-state and dynamic computer performance modes of the inlet, engine, and controls.

The contractor must provide the customer with sufficient design details justifying his approach towards satisfying the interface requirements existing between the engine components and the airframe. The system and engine contractors must also exhibit an understanding of the stability tolerance of the propulsion system and its components and must provide the customer with a detailed definition of the

aircraft/propulsion interface and their method of achieving good integratin characteristics. Compatibility data can only be obtained through extensive testing and joint technical communication between the engine and airframe contractors. Results obtained from implementation of the compatibility/integration program shall provide the information and data needed to insure that the proposed engine design will satisfy the aircraft's system design and performance requirements. These results shall also provide data for certifying the stability characteristics of the propulsion package when installed in the aircraft.

The installed performance of the propulsion package should be presented in a format that identifies installation drag items and other flow losses in terms of thrust minus drag and SFC. An installed performance bookkeeping method should be able to handle all drag items related to the propulsion system. This method should have the versatility to account for variations in the inlet and nozzle geometries in terms of total system net thrust minus drag.

C. Qualification and Acquisition Phase:

The qualification phase of weapon system development is usually the most critical. The system and propulsion system are well defined by this point; in fact, there is often a great deal of pressure to "freeze" the propulsion system design and release drawings for production to meet a schedule set down by the government. However, some changes to the propulsion system and its installation may still be required and they will usually show up during final component testing or in the early stages of flight testing, which are included in the qualification phase of development.

(1) Technology Development:

During the qualification phase the basic inlet/airframe demonstration model is refined with all subsystems such as bypass, auxiliary inlets, etc., properly simulated and the expected aircraft environment simulated to provide the proper back pressure on these flow removal systems. In addition to performance documentation with the workhorse model, there should be some parametric testing done with various minor changes in geometry to provide a data base to draw from if early flight testing indicates problem areas.

The large scale inlet/airframe model forms the basis for the full scale inlet model which needs to be built in the qualification phase, and tested with the engine as described later. This full scale inlet must be an accurate representation of the aircraft hardware in all respects so that the wind tunnel data can be viewed with confidence and extrapolated to flight test conditions. Although the full scale model cannot be tested over the aircraft maneuvering envelope, some attempt should be made to simulate this flow environment which has been well defined from the previous inlet model. Boundary layer generators, flow angularity generators, etc., may be used to simulate the major features of the inlet/airframe flow field.

Identifying the pressure contours, both steady and unsteady, that represent the most critical conditions expected during operation is still only half the battle. These distortions need to be simulated

during compressor rig tests and during engine testing to measure the effect they will have on the undistorted stability margin. Screens and other spoiling devices have been used with great success in simulating the steady distortion patterns.

It is necessary to test several variations in intensity and shape in order to establish the amount of change in surge margin with changes in these particular patterns. Fortunately, much of the effect of nonsteady distortion can also be evaluated using the results of steady distortion testing. The compressor will react to distortions that persist for only a few thousandths of a second as though they were steady conditions. If the distortion exists just long enough for a sixth to a half of the compressor to "see" these flow conditions, the damage is done. Several methods have been used to simulate inlet dynamics for testing in the compressor rig and test cell, and others are currently being developed. These methods include both random and discrete frequency distortion generators and the techniques required to analyze these data.

(2) Propulsion Integration Plan:

Proceeding from the demonstration phase to the qualification phase, the propulsion integration plan has become an official portion of the ICD. It defines such things as the responsibilities of the two contractors and describes the level of participation by the government. The integration material in the plan should cover such things as physical, functional and performance interface requirements. The types of tests and procedures for qualifying the

propulsion assemblies such as endurance tests, failure tests, and flying test bed requirements are set forth.

The airframe contractor's (system) integration plan should contain plans for conducting inlet-engine compatibility tests such as determining the effect of inlet-engine coupling on propulsion system performance and stability during both steady state and transient operating conditions. A firm definition of the propulsion system component compatibilities should be determined during the qualification phase.

(3) Implementation of Plan and Data Exchange:

Implementation of the previous integration plan takes place during this phase and the time for paper airplanes and rubber engines is over. Only one propulsion system and one airframe is being developed now, and the identification of any major problem during this period can be expected to be very expensive to fix in terms of time, performance, and money.

During the qualification phase the propulsion system contractors should be able to predict the surge margin of the system under both steady and unsteady conditions with both internal and external disturbances. Critical points will have been tested to substantiate these predictions. The system development, acquisition phase, or as we have called it, the qualification phase, is characterized by adhering to an integration plan to build up the confidence to make the IOC date and to assure that there will be no major setbacks during the development, qualification or flight testing due to the

propulsion system. Full scale inlet-engine wind tunnel tests are considered essential for determining engine and inlet system responses, control functions and for adequately assessing if stability objectives are being satisfied. Compatibility testing should be performed in two phases. The first phase should be completed in time to assure acceptable performance for the first test flight using a PFRT engine. The second phase should investigate the characteristics of the production hardware prior to the design freeze, using QT engine hardware.

An important portion of the testing is the fallout of design criteria for establishing system characteristics that will offer good matching and stability throughout the engine's operating range in flight test. Some of the types of tests that should be conducted would be sea level and altitude full scale testing in a suitable wind tunnel facility. A calibrated convergent nozzle can be installed initially to obtain baseline operating characteristics than the actual version of the production nozzle hardware should be tested comparing these results to the baseline nozzle test data. If a flying test bed is used, consideration should be given to achieving the proper simulations between test and production type hardware. Does the inlet really simulate postulated flight conditions and will the engine installation losses match the performance degradations of the production flight hardware? These questions must be answered to determine if the system characteristics and performance capabilities of the hardware meet the design requirements and satisfy the mission objectives.

The engine contractors during the acquisition phase will be required to prepare an engine steady state and dynamic electronic automatic machine performance characteristics simulation model for predicting both design and off design operating conditions compatible with the end item specifications. The engine contractor will also be required to update these simulation models when changes to the configuration effects the performance characteristics and operating efficiencies of either the components or their assembly into the airframe. The airframe contractor will have a similar responsibility to substantiate the inlet-inlet control system simulation model in the qualification phase as a tool for substantiating the performance of the inlet system during transient operation. The airframe contractor will validate the authenticity of this model by demonstrating its ability to simulate the effects of the airplane environment on engine-airframe compatibility. The inlet/ICS and engine models should have the capability to predict the effects of input transients generated by either the engine or airframe separately or simultaneously. These data derived from both of these models when combined, should uniquely define the performance and stability characteristics of the propulsion installation. It is anticipated that these performance predictions used in these models will accurately represent those values proposed by the contractor for the production hardware.

D. Operational Phase:

(1) Operational Problems:

Past weapon system experience indicates that airframe-propulsion compatibility is a "cradle to the grave" phenomena, and just because an aircraft is being produced, meeting performance goals and flying stable throughout the required envelope doesn't mean that propulsion integration problems can be forgotten. This case is particularly true for an aircraft that made the mission with only a small amount of stability margin left in. Operational problems, and field maintenance procedures may reduce the remaining stability margin creating a stall problem requiring immediate attention.

Perhaps the most common operational problem is due to environmental conditions that were unexpected during development. This may be due to operation in a corrosive (salt spray) or erosive (sand) environment that accelerates wear in the engine. Stall margins may change simply with aging process of an engine or it may be due to changes to the fuselage forebody for some sort of avionics gadget, the relocation of weapons or the introduction of new weapons that either interfere with the flow to the inlet or allow weapon exhaust gas into the inlet. It may result from operating the aircraft outside of its defined envelope or at attitudes and conditions which were unexpected or originally prohibited. Operational problems also occur when a new or modified engine is introduced. In all of these cases the cure should depend on the cause and the most important first step should be to establish the cause. Although there is not too much propulsion system

technology development during the operational phase except for growth, the background of technology development accrued during the entire weapon system development should be used as the basis for making change decisions or for solving operational problems. Often the usual procedure followed for making changes to the engine, the inlet, the aircraft or the operating procedures are initiated at one time, then if the problem goes away, all of the changes are incorporated without having any idea which change or combination of changes actually resulted in the fix. This approach usually leads to a compromise in performance that is not necessary to the solution. Identifying the cause will usually cost more and take more time, but will probably result in a more effective weapon system.

(2) Flight Manual Guidelines:

Once the ICD requirements have been satisfied and substantiated through experimental testing and checked by analytical methods of analysis, the results of this compatibility analysis and test efforts should be compiled into a set of Flight Manual Guidelines for use in the operational phase. The flight manual should discuss the stability limitations of the propulsion system during high angles of attack and yaw and should cite what restrictions are imposed on the aircraft and propulsion system due to engine stall margin reduction caused by aging, dirt and dust effects, weapon system effects such as store release and gun gas ingestion. Off design stability reductions due to rapid throttle changes, thrust reverser initiations, blow-in-door effects,

inlet ramp, cone, or other variable geometry items that have a significant effect on propulsion system performance or stability should be defined in the flight manuals. The tie-in among the Math Model simulation, W/T test data and analytical methods is critical for identifying those possible A/C configurations where stability or compatibility is marginal or unacceptable, providing the aircraft user with a suitable road map for avoiding these problem areas.

During the entire operational phase the Flight Manual Guidelines should be updated regularly to incorporate field experiences on the effects of aging, maintenance procedures, control tolerances, etc.

Some of the compatibility problems that have been experienced in the field are shown in Fig. 15. The aircraft schematic represents a typical fighter having a closely integrated (buried) propulsion installation. The inlet is located at the wing root and it utilizes the fuselage as a boundary. An installation of this type requires some means for removing the boundary layer to minimize the effects of flow distortion. If miniguns or rapid fire cannon are installed in the forebody or nose of the aircraft, a gun gas port is required for handling the expelled hot gases. Care must be taken to properly locate the exhaust port to prevent possible temperature distortion in the inlet. The incorporation of a dive or speed brake may seriously affect performance if incorrectly located where it would generate high cross flows ahead of the inlet.

The nose boom and nose gear locations may also reduce the stability and performance of this type of propulsion installation. Other examples of problems arising in the field are shown in Figs. 16 & 17. Note the damage to the lower lip of the cowl shown in Fig. 16. This damage may be due to rain, hail, the elements, or maintenance procedures. Figure 17 shows another type of problem that has occurred. Note the physical mismatch between the engine and inlet at the adapter section. Also note the wide gap in the upper left hand quadrant. A pencil was placed in the opening to show the degree of mismatch occurring. This same installation also had a certain amount of duct eccentricity causing a sizable airgap at the interface. This particular installation did not provide any means for realigning the engine since the engine mounts are fixed. An improved adapter ring was incorporated to reduce the physical mismatching. These problems are only examples of the types of aircraft deficiencies that may cause compatibility problems which have occurred and will be expected to continue unless special measures are adopted to minimize these discrepancies. Other papers at this symposium address other operational problems such as new engine incorporation, operation near severe weather at high altitude, and operation of an aircraft in a somewhat different environment than it was originally intended for.

IV. Summary

A propulsion system must be designed with all components operating as close to limiting conditions as possible and still provide a sufficient operating margin to prevent instability from occurring. To achieve this difficult goal, the development program for the propulsion installation should approach stability with the same emphasis and at the same time it addresses performance. New designs and analysis techniques must either be perfected or old methods must be improved to make the new technology base applicable to the next unidentified weapon system. A continuous effort through basic research must be cultivated to improve the overall capabilities of each propulsion component and related subcomponents independent of a particular system application so that when a requirement for a weapon system exists, the technology will be available for its development. This technology base is expanded and specialized for application during the development of a weapon system. The weapon system developer takes a broad base of technology and channels it to a very specific requirement of meeting the system mission performance and cost objectives. By this process, the research agencies see just how effective their work has been and where additional work is required. It is obvious that there must be an extremely close relationship between "research" and the "real world" of weapon system development.

The typical development of a weapon system can be broken out into four phases: study phase, demonstration phase, qualification phase,

and an operational phase. During these phases the system stability and performance must be predicted and the predictions substantiated to provide the desired degree of confidence in the propulsion installation.

Airframe/Propulsion Compatibility cannot be legislated or quantized to put it in specification language which is meaningful. It must evolve through careful planning, testing, evaluating, and managing throughout the weapon system development cycle.

REFERENCES

1. James A. Laughrey, AFFDL, Calculation of the Performance of Installed Exhaust Nozzles on Supersonic Aircraft. AIAA Report No. 69-428, 5th Propulsion Joint Specialist Conference.
2. Paul H. Kutchenreuter, Jr., General Electric Co., Large Scale Inlet Compatibility Test Results. Airframe Propulsion Compatibility Symposium; Session III, Inlet Distortion Investigations, 25 June 1969.
3. S. A. Tremaine, An Orientation to Air Force Systems Management and the System Program Office. Management Operations Div., Deputy for Systems Management, ASD. December 1968.

INDUSTRY

COMPATIBILITY PROBLEMS

COMPATIBILITY PROBLEMS EXPERIENCED

- A. INLET ENGINE MATCHING
- B. SECONDARY COOLING SYSTEMS
- C. AFTERBODY/NOZZLE LOSSES
- D. INLET TEMPERATURE DISTORTION
- E. INLET FLOW DISTORTION
- F. INLET INSTABILITY
- G. INSTALLED PERFORMANCE DEFICIENCY
- H. F. O. D.
- I. AFTERBURNER INSTABILITIES

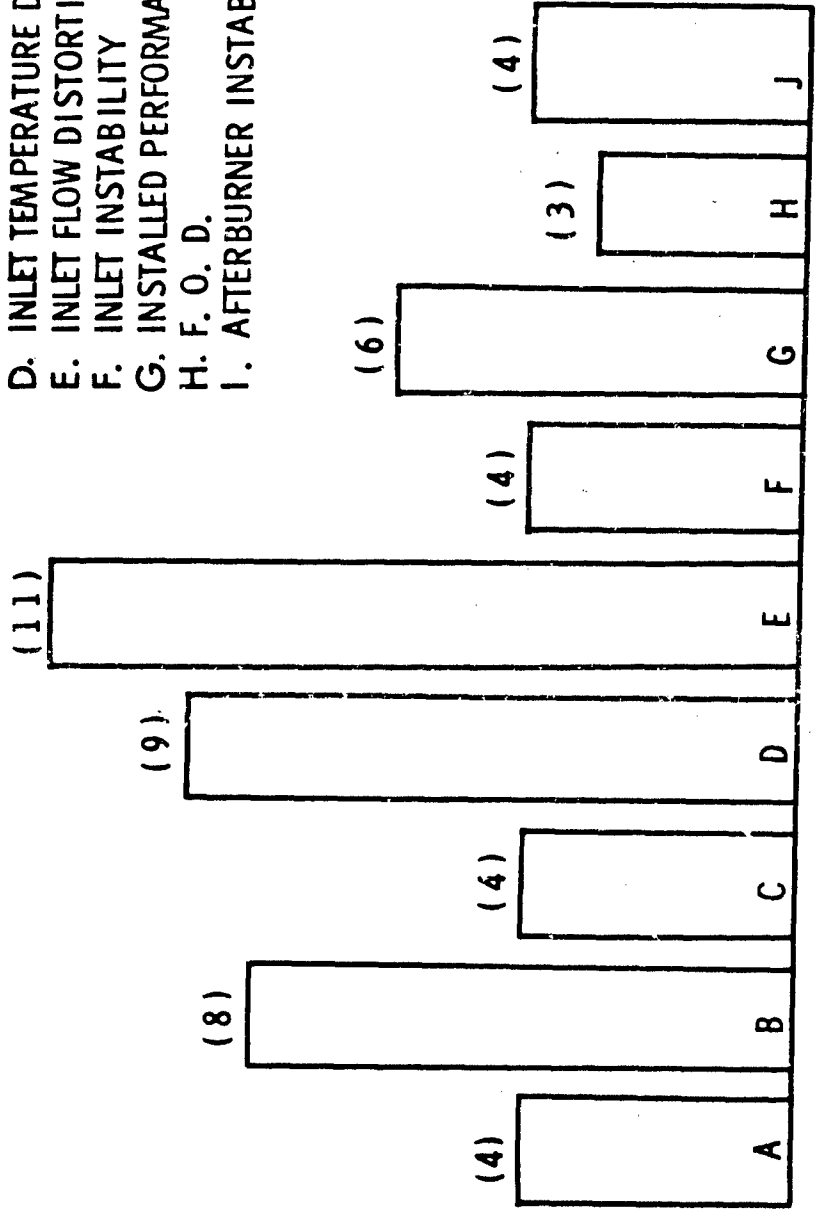


FIGURE 1

AIRFRAME-INLET INTERACTION

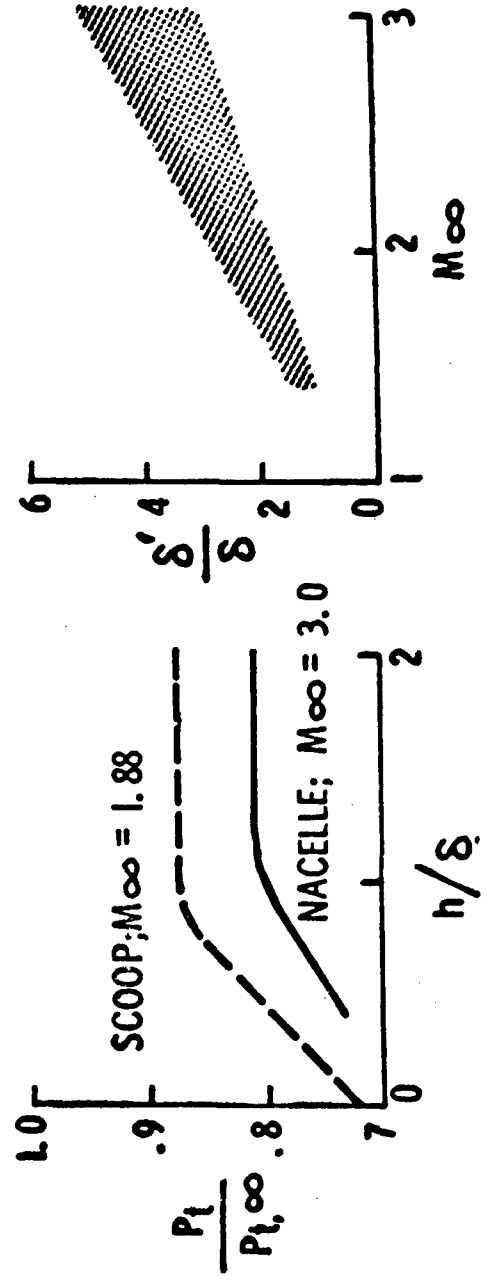
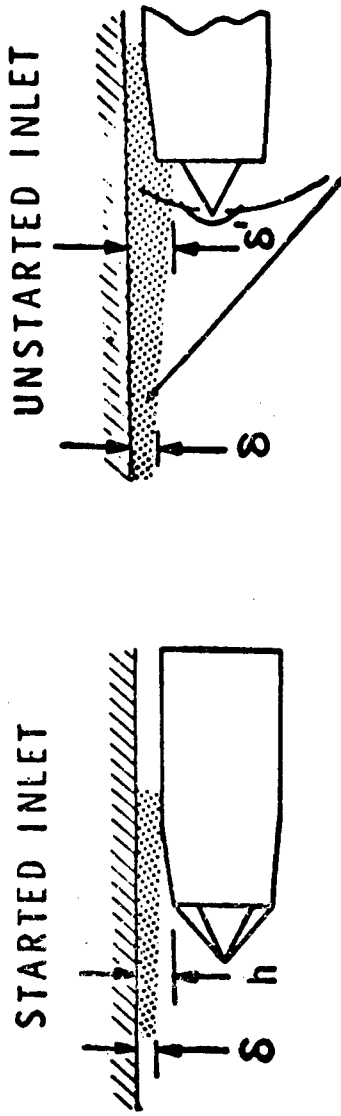


FIGURE 2. EFFECT OF INLET UNSTART ON FUSELAGE B. L. GROWTH

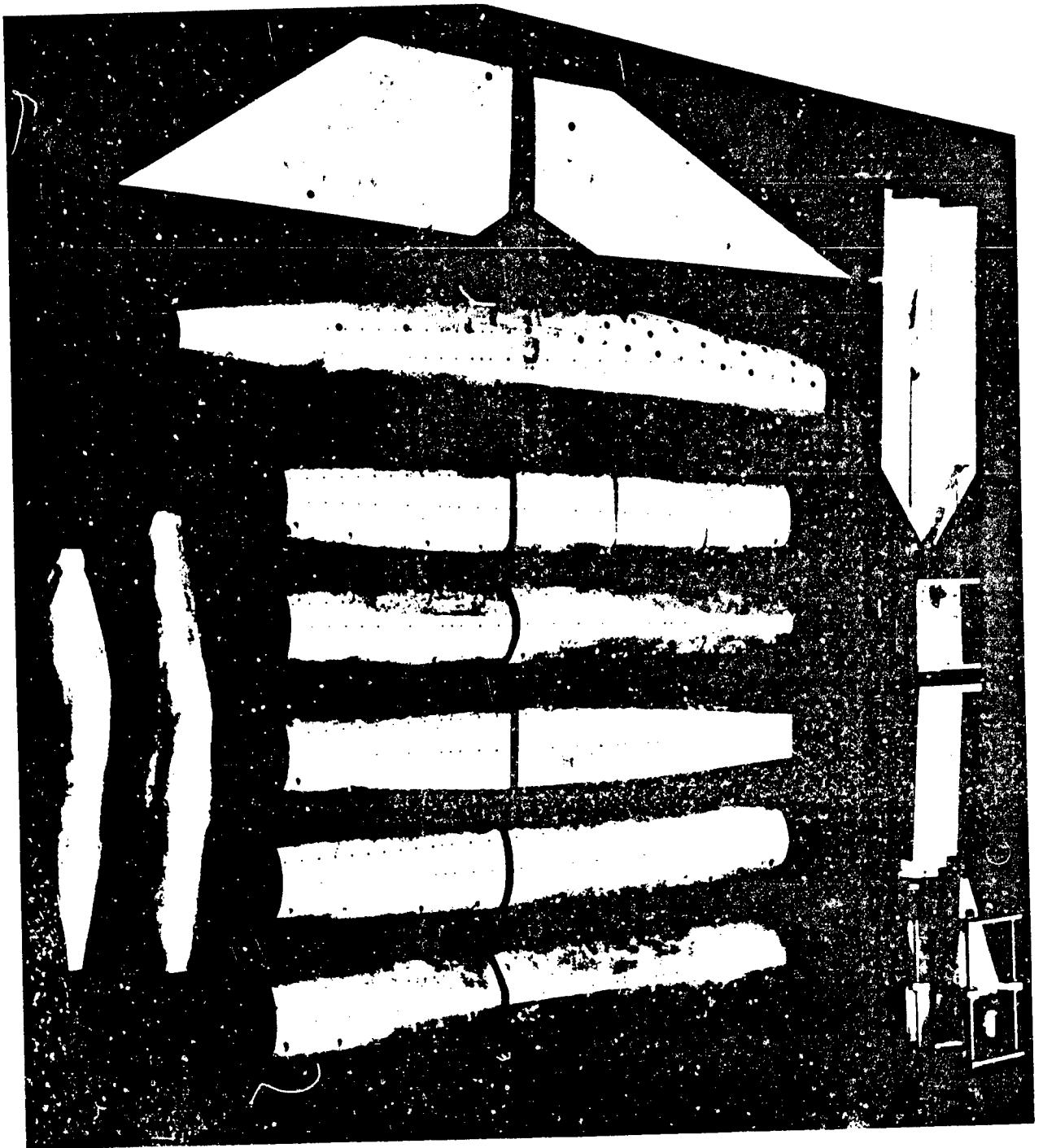


FIGURE 3. INLET-INTERACTION MODEL COMPONENTS SHOWING
VARIOUS FUSELAGE-WING-INLET COMBINATIONS

AIRFRAME / INLET INTERACTION

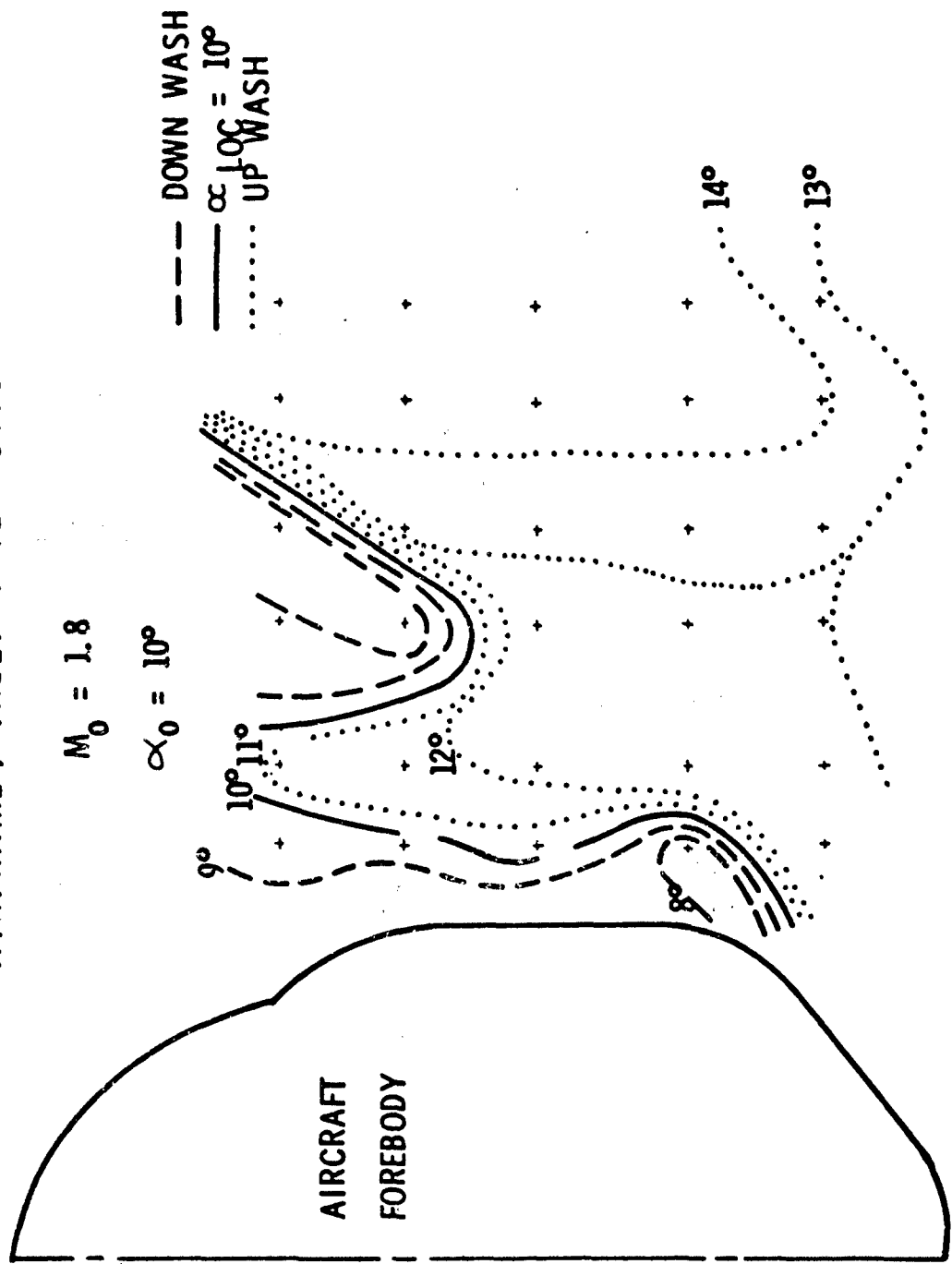


FIGURE 4. INLET FLOW FIELD TEST RESULTS

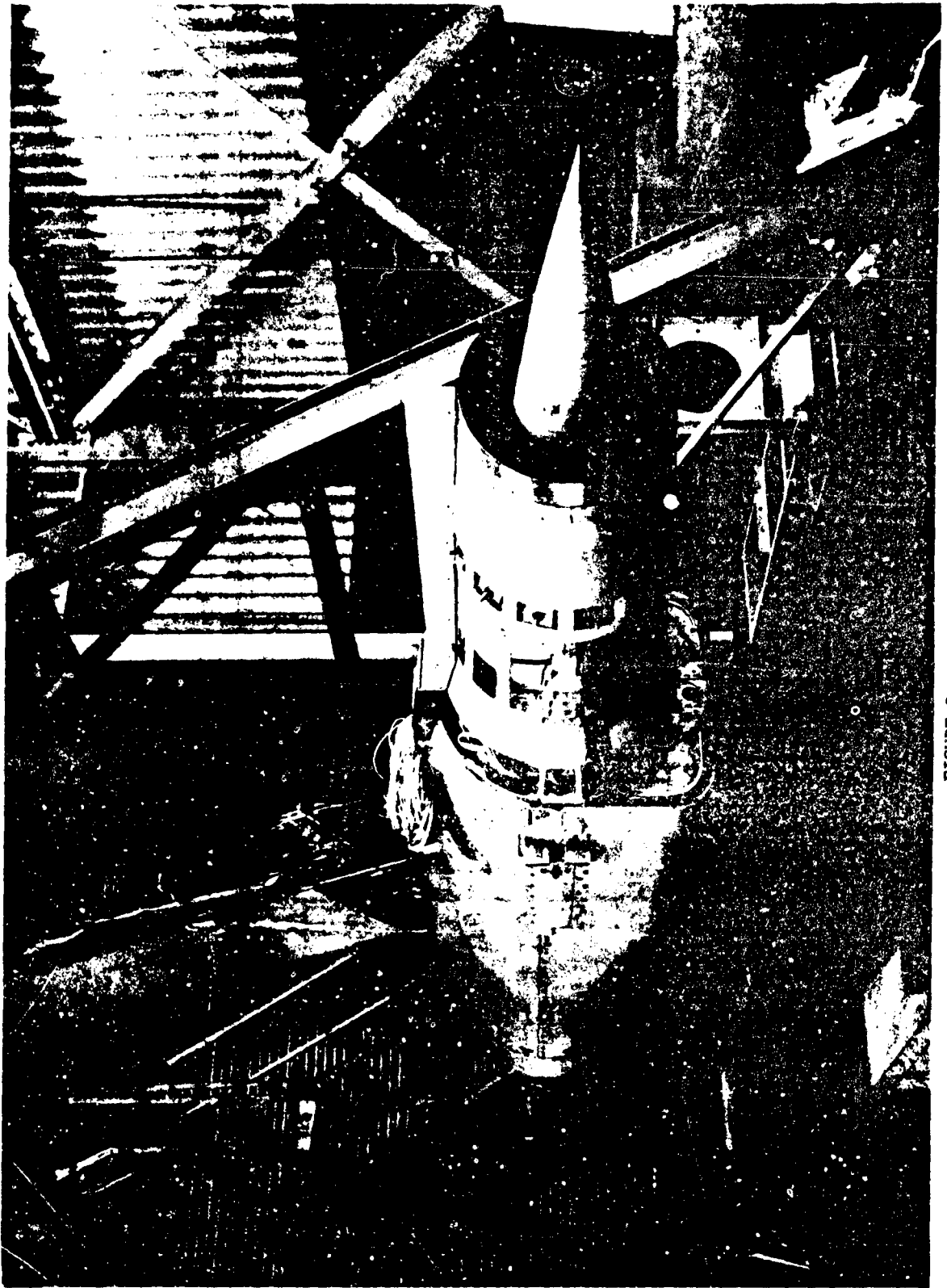


FIGURE 5. INLET ENGINE INTERACTION MODEL

ENGINE RESPONSE TO DYNAMIC DISTORTION

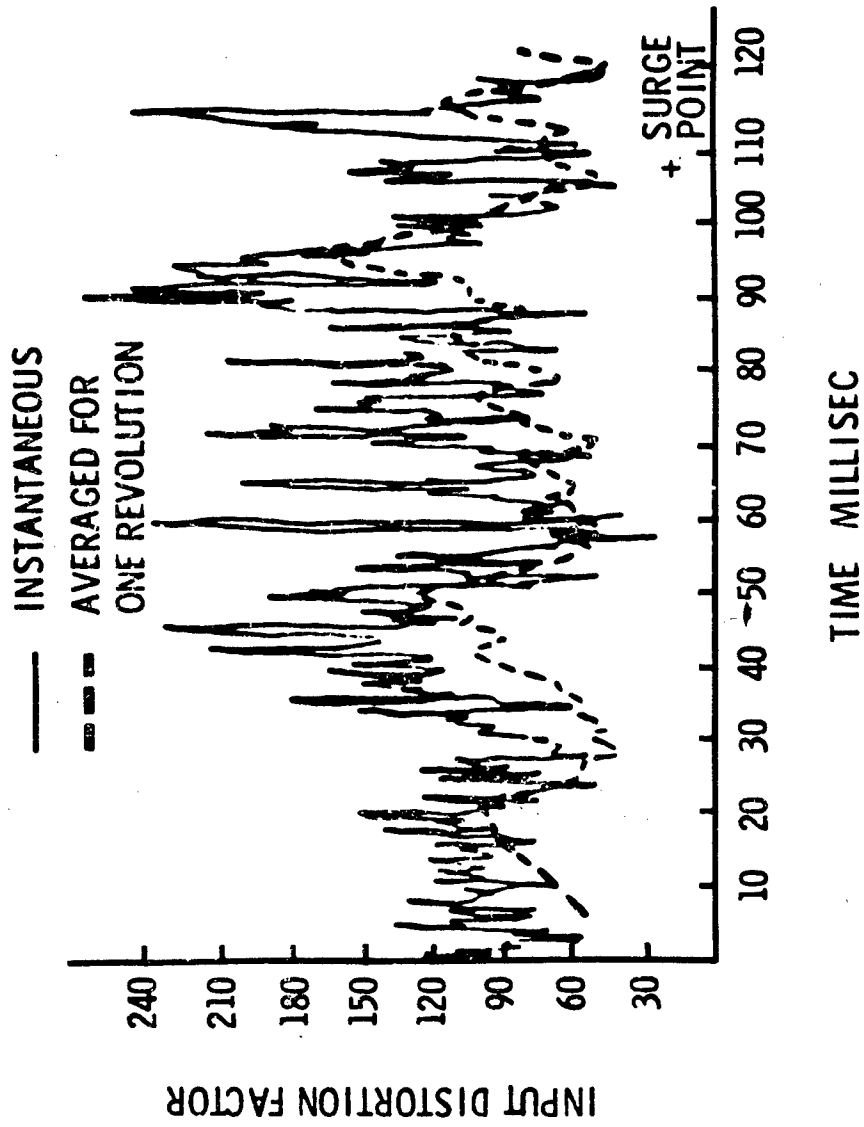


FIGURE 6

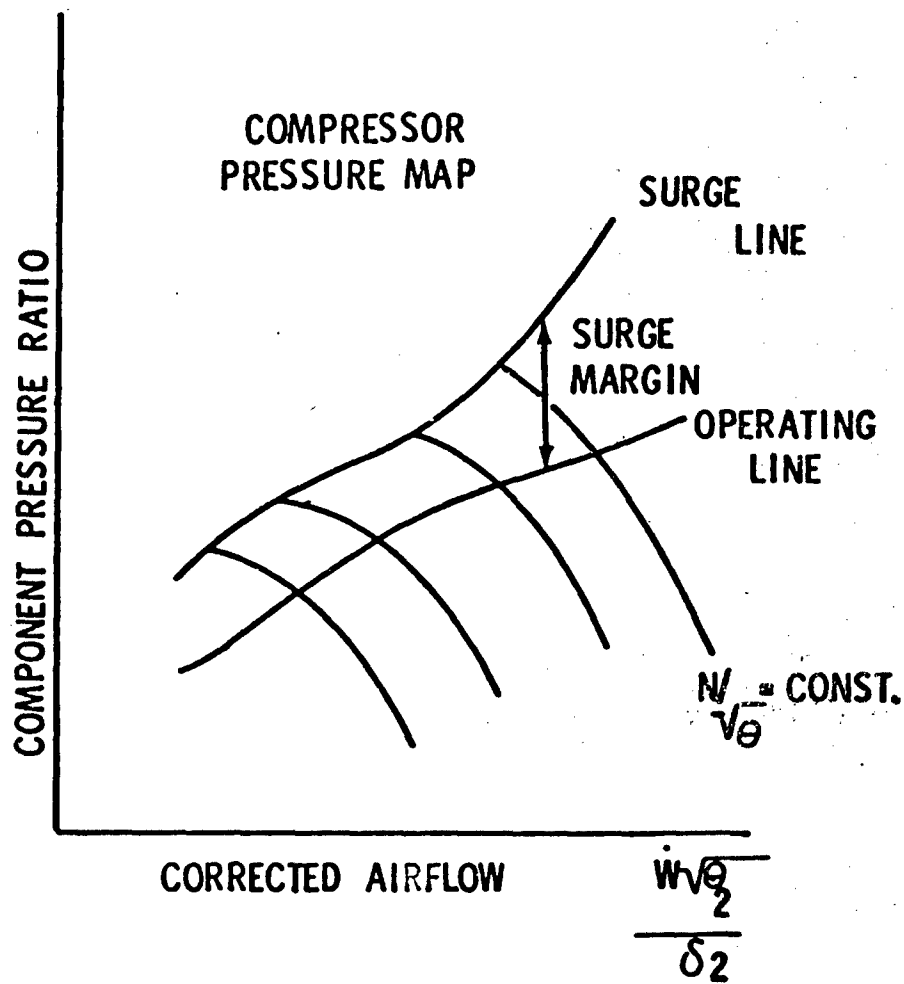


FIGURE 7

TURBOFAN ENGINE SCHEMATIC

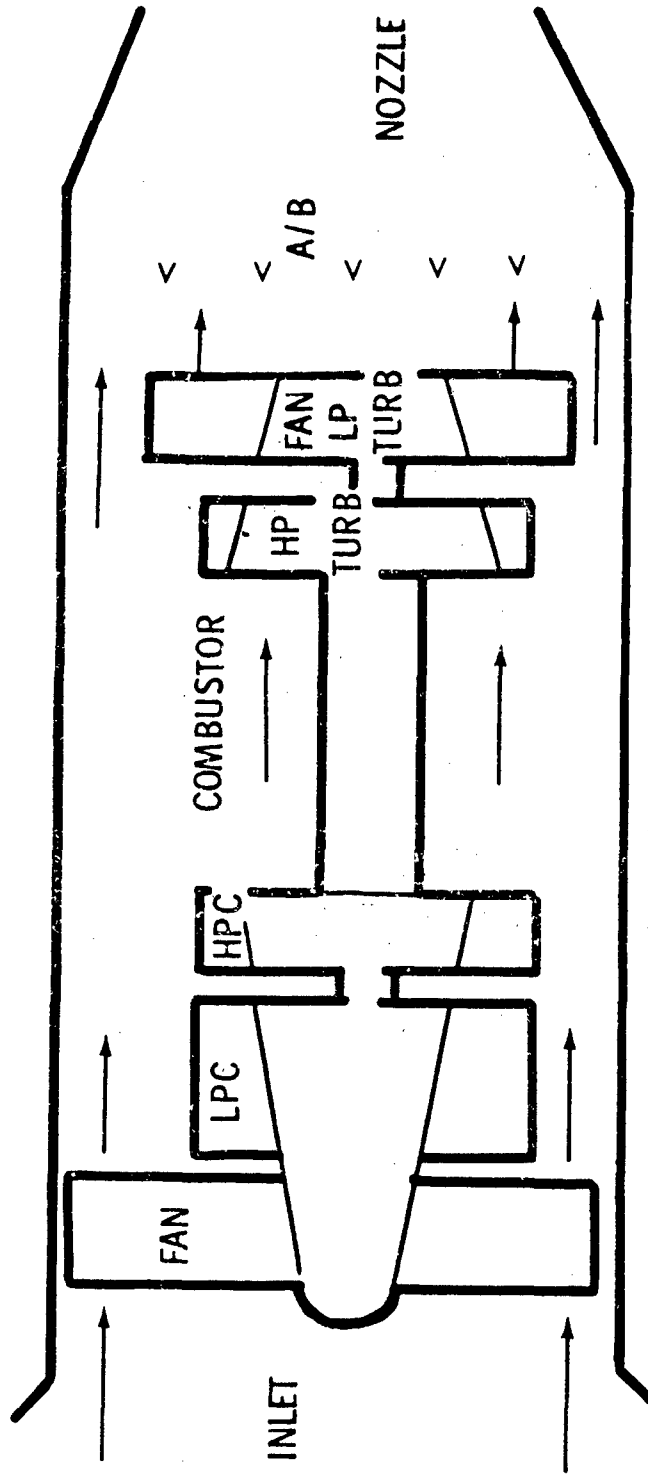


FIGURE 8. STEADY STATE AND DYNAMIC MODELING COMPONENTS

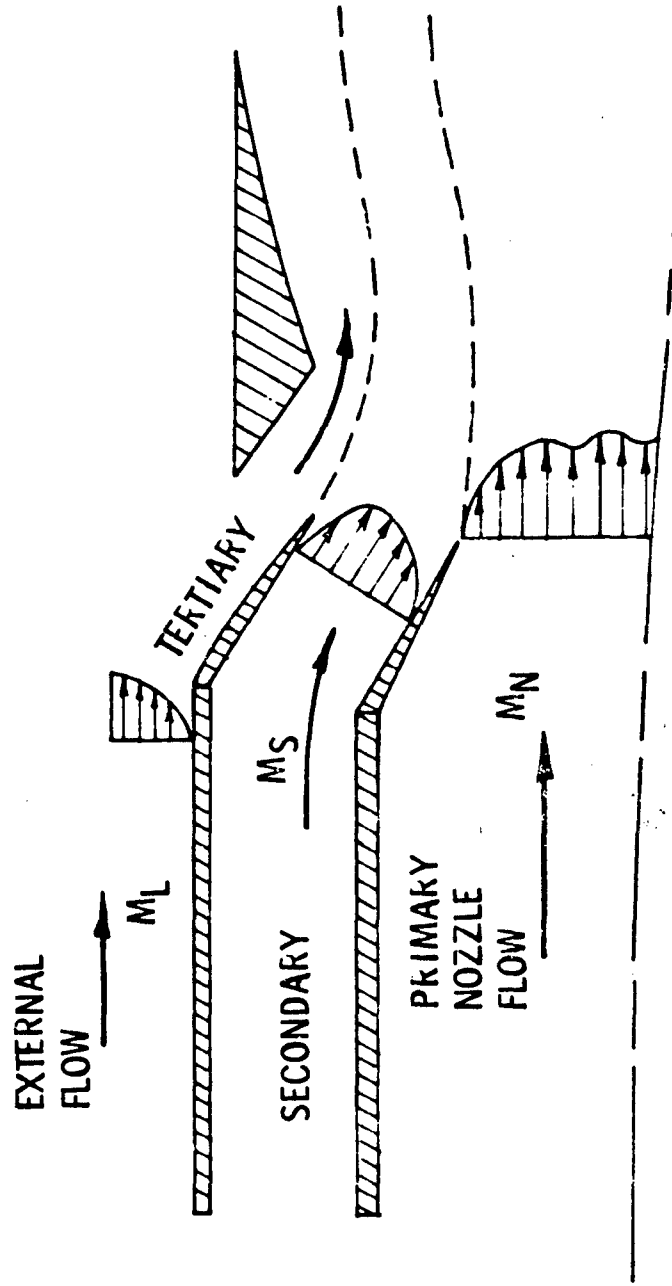


FIGURE 9. SECONDARY FLOW MIXING MODEL

PREDICTED EFFECT OF BOUNDARY LAYER THICKNESS
ON BLOW-IN-DOOR NET THRUST

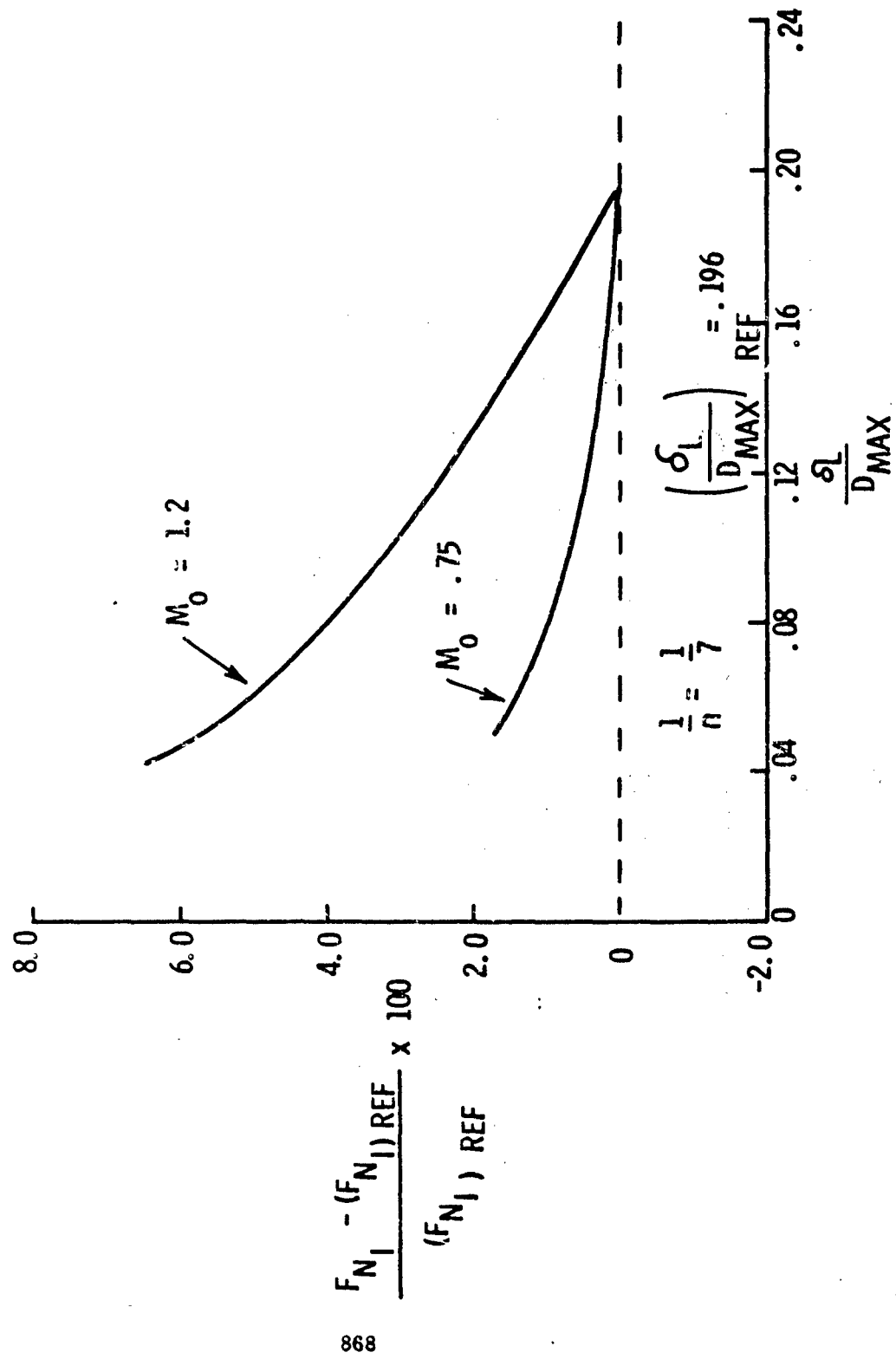


FIGURE 10

EFFECT OF BOUNDARY LAYER THICKNESS ON
 BLOW-IN-DOOR GROSS THRUST FROM EXPERIMENTS

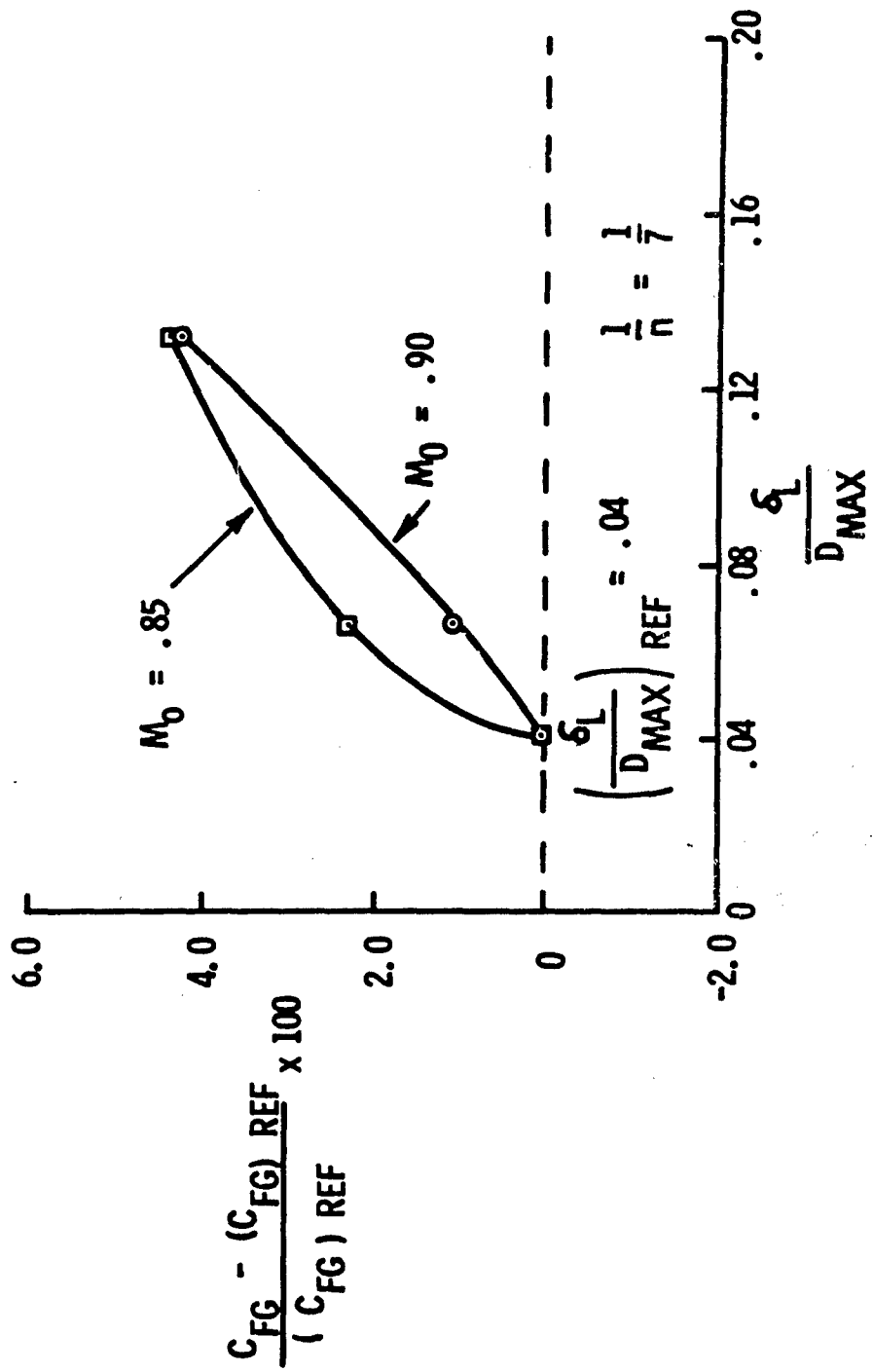


FIGURE 11

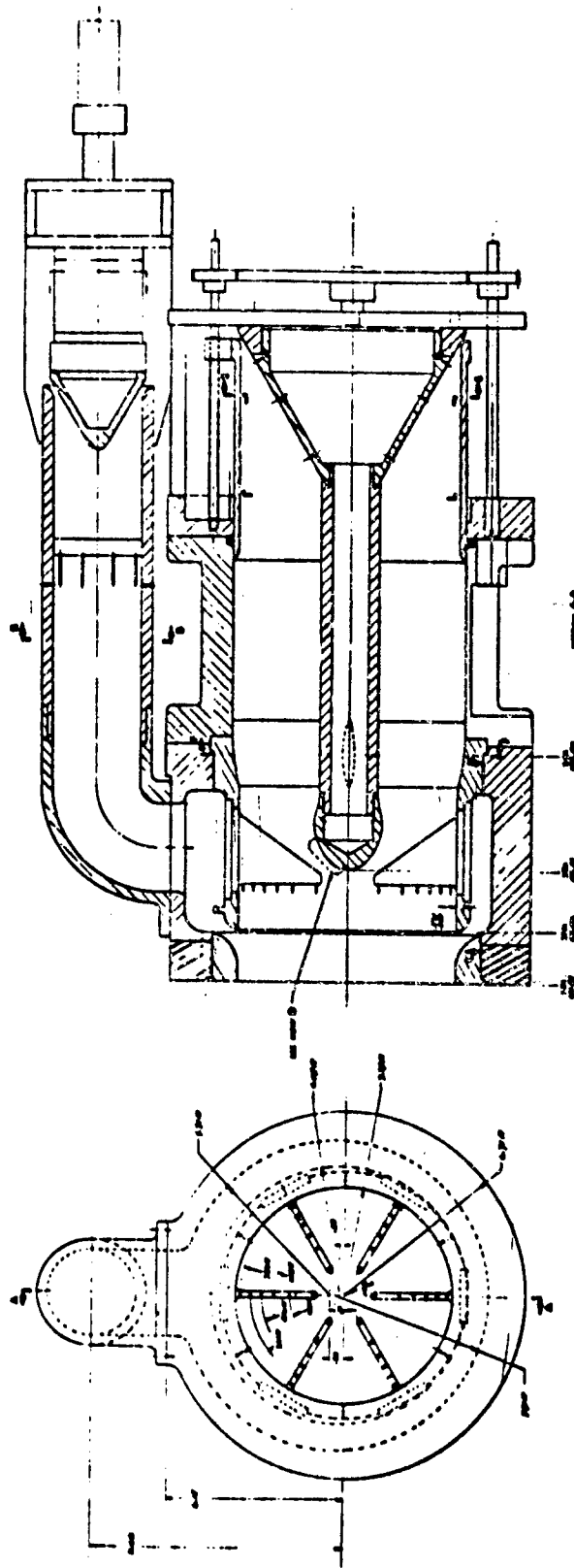


Figure 12. Inlet Model Flow Metering Section Assembly



FIGURE 13. RA5C AIRCRAFT

PROGRAM PHASES OF THE WEAPON SYSTEM LIFE CYCLE

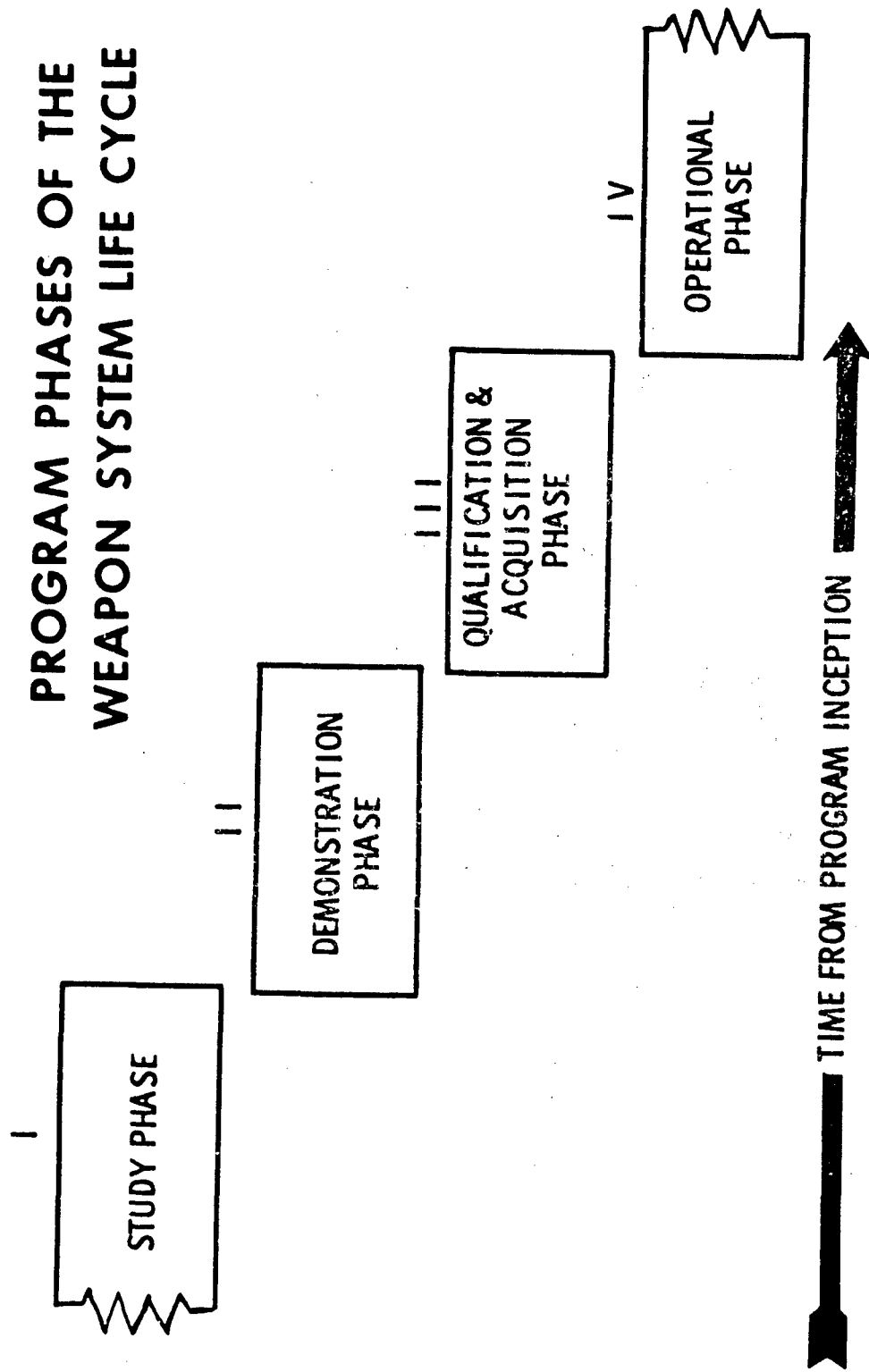


FIGURE 14

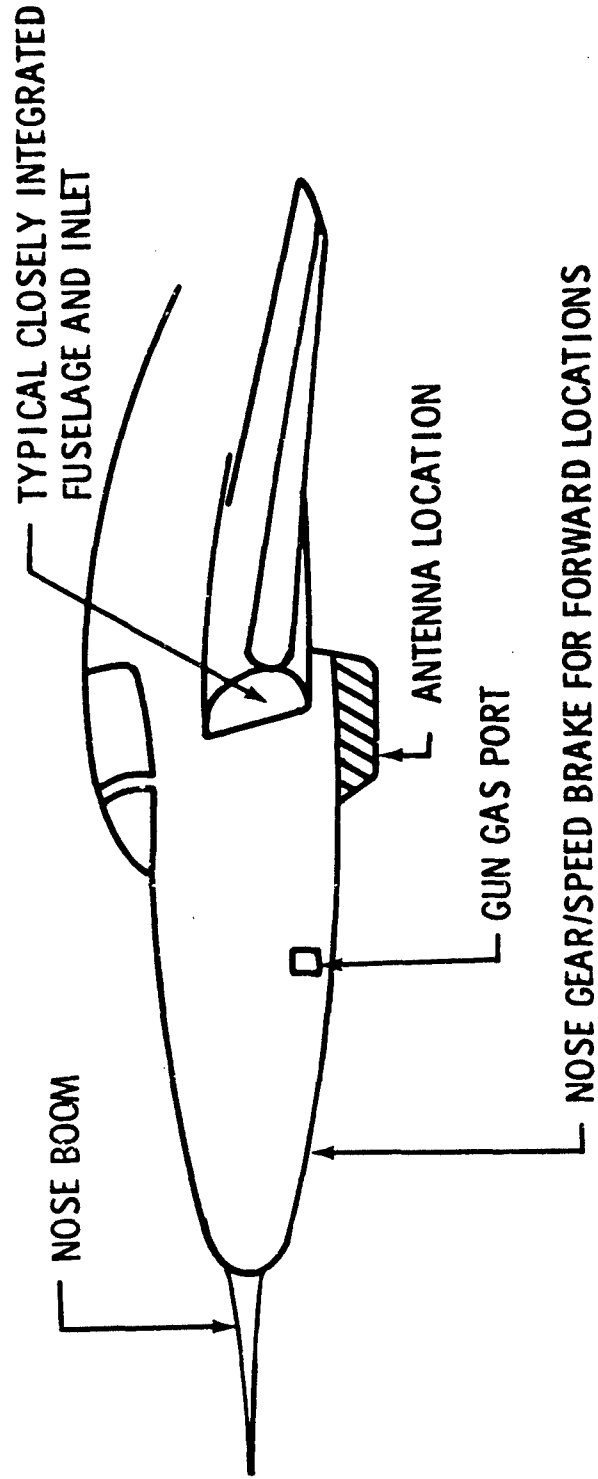
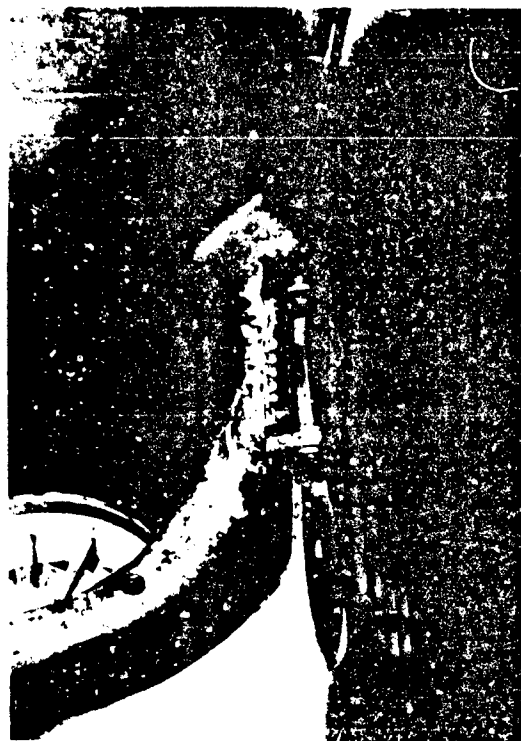
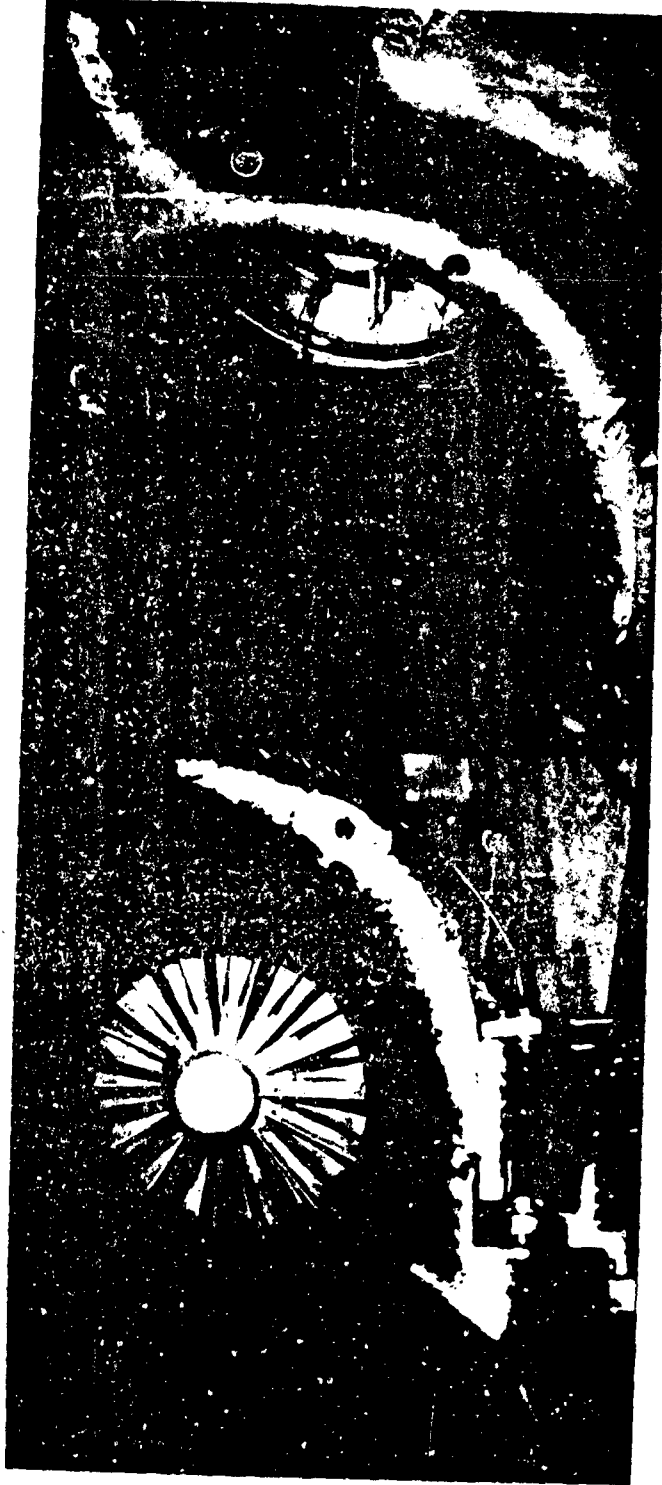


FIGURE 15. POSSIBLE FLOW DISTORTION SOURCES



DAMAGED INLET COWL IN OPERATIONAL USE

FIGURE 16



INLET-ENGINE INTERFACE MISALIGNMENTS

FIGURE 17

MANAGEMENT OF AIRFRAME-PROPULSION COMPATIBILITY

Leonard H. Schreiber

Manager of Propulsion
The Fort Worth Division of General Dynamics

A significant contributor to recent, severe, airframe/propulsion compatibility problems has been the existence of a management void in the associated compatibility programs. It is necessary that we recognize this void and take appropriate steps in the future if we are to capitalize on the technical advances which will become available. This paper presents some thoughts relative to the management aspects of airframe/propulsion compatibility. Past experience is reviewed to identify areas of management deficiency, and an integrated management plan is presented for future systems development. The desired goal is the development of a total product through definition of total system requirements from the customer's viewpoint, where the customer includes Development, Logistics, and User Commands. Management techniques which can be used to implement defined objectives and requirements are based on the following philosophy with regard to the participants: (1) they must communicate with each other, (2) they must be motivated, and (3) they must be realistic. Specific techniques for achieving this communication, motivation, and realism are discussed, centering upon a suggested organization of the interface documentation.

The very fact that the Air Force Aero Propulsion Laboratory is sponsoring this Airframe-Propulsion Compatibility Symposium is indicative of the problem that the Air Force and industry have experienced in integrating engines with airframes. These problems have not been encountered in every application, but unfortunately they have occurred too frequently. Further, if these integration problems had been solved quickly, with insignificant resources and with reasonable impact on their respective programs, there is a good chance that we would not be assembled here. But this has not been the case, and it has become clear that an adequate understanding of the concerned technology did not exist.

As most of us are aware, the R and D effort on these compatibility problems has been accelerated during the past few years, as is evident from a review of the papers being presented here. The technical advances that will result from this research are the key to the achievement of our mutual goals of airframe/propulsion compatibility. But I also believe that there are other fruitful areas for improvement; one of these is the management of our airframe/engine integration programs.

I believe that a significant contributor to our past problems has been the existence of voids in the management of the airframe/engine integration task. It is necessary that we recognize these voids and take appropriate action if we are to capitalize on the technical advancements which will become available.

Thus, the purpose of this paper is to present some thoughts relative to the management aspects of airframe/propulsion compatibility. The approach will be to (1) analyze past experiences in order to understand what factors have contributed to the results to-date, and (2) define the elements of an integrated management plan to support the technical effort.

It is appropriate to begin by considering the scope of the management task as it is interpreted herein. In this application, the objective of the management effort is to formulate the following elements to serve as a vehicle for applying the technical effort:

1. The characteristics that we want to embody in the system being developed.

2. The compatible design responsibilities for the Airframe and Engine Contractors.
3. The detailed tasks of the development and evaluation program.

Further, in the process of formulating these elements, we want to prepare the data in a form that will facilitate the subsequent technical effort by (1) promoting communication among the participants, (2) providing visibility of the technical effort, and (3) providing flexibility for handling the changes that we know will become evident as we learn more about the technical problems.

In summary, we want to document an orderly definition of our technical objectives and a methodic approach to the development program. Frequently, there is an adverse reaction to a documentation effort. However, if the objectives and plans are not documented, the technical program will probably not be thought through very well, some of the concerned people may not receive the required information, while others will "drop the ball" somewhere along the way. Although paperwork is no substitute for good thinking and good technical work, this documentation is needed to promote good communication, which will aid in capitalizing on the technical know-how.

In addition to the application of the management and technical elements, which will define the program goals and develop the capability for doing the job, respectively, it is also vital that the participants be motivated to do the job. This is the contractual element, since, when the contract is viewed from a very basic viewpoint, we may consider that one of its major purposes is to motivate the participant. However, I will try to limit discussion of contractual considerations because it is an extremely broad subject and outside the scope of this paper.

As I look back at many of the previous airplane development programs, I find that it is possible to generalize some of the factors that contributed to the difficulties which were experienced. The following summary of the most significant points includes some explanatory examples taken from past experience. We must consider them as we develop the management plans for future airframe/engine integration projects.

1. The requirements of the Total Propulsion System (the engine plus appropriate airframe components) were not defined adequately. For example,

a. The requirements for engine power transients in combination with airplane maneuvers were not stated.

b. The in-flight ram-air start characteristics of the bare engine were presented for limited conditions, but the effects of the installation were not defined. Thus, since the installation introduced conditions of lower ram pressure ratio and finite shaft power extraction, degraded air start capabilities resulted, as compared to advertised values.

As a result of the incomplete definition of the Total System requirements, they could not be properly translated into the appropriate component requirements.

2. The "separateness" of the airframe and engine development programs, emphasized during some previous programs, resulted in decisions which did not consider the total impact. For example, in one instance the engine RPM was rescheduled to include a cutback in the region of high dynamic pressure in order to save engine weight. While it appeared that the engine thrust was not degraded excessively, consideration was not given to the resulting inlet drag increase due to reduced engine airflow. Thus, the "separateness" of the development programs fostered an unintegrated approach.

3. The Contractors and the Air Force did not make an "all out" effort to ensure as complete and correct a definition of airframe/engine interfaces as the available technical knowledge would have permitted. This was encouraged by the separate engine and airframe development programs, since each party preferred to limit his commitments. The contractual approach was deficient since it did not motivate the participants to achieve a satisfactory Total System. In some cases, the engine and/or airframe requirements were defined in a manner that was not technically realistic, or the requirements were not defined at all. Thus, significant gaps and incompatibilities were introduced into the contracts of the Air Force/Airframe Contractor and the Air Force/Engine Contractor, resulting in a dissatisfied customer.

4. Engines were developed to meet the Qualification Test requirements, with considerably less attention given to the bulk of the engine characteristics quoted in the engine specification. Further, the Qualification Test requirements did not reflect that the engine is operated over an extremely wide range of conditions in the airframe and, as a result, there was insufficient testing to define the engine's real capabilities. For example,

a. Prior to flight tests in the using airframe, only an extremely limited test was conducted of the engine control system's ability to automatically control the engine within limits.

b. In some cases, the Qualification Test did not contain any requirements for the evaluation of engine distortion tolerance. In other cases, the extremely small number of test points and the very limited simulation of installed operating conditions (e.g., no power transients, no shaft power extraction) resulted in distortion tolerance tests which hardly "scratched the surface".

5. The interface design responsibilities were not clearly defined. At times, this resulted in a slow response by one or more of the participants to the need for additional development effort.

6. All of the participants did not mutually recognize that additional engine development would be required during flight test (after completion of the engine Qualification Test) to improve the engine performance and functional characteristics. (The need for additional development in the area of mechanical design/endurance was recognized.) Thus, some in-flight Propulsion System problems were attributed incorrectly to the airframe design, and there was a reluctance to fund additional engine development.

In summary, the separate airframe and engine development programs, the inadequate definition of the Total Propulsion System requirements, and the lack of extensive communication between the Airframe and Engine Contractors resulted, all too frequently, in incomplete development of the respective hardware before its integration in the airplane. Subsequent resolution of the resulting incompatibilities was often difficult.

An aggressive technical effort is needed on future projects if we are to preclude or minimize occurrences of airframe/engine incompatibilities, but, as stated previously, and as can be deduced from the above review, an improved management plan is vitally needed in order to act as a catalyst for the application of the technical know-how.

The logic of the plan may be summarized as follows:

1. One of the Contractors, i.e., Airframe or Engine, must "captain the team" and assume the responsibility for the Total Propulsion System, even though he does not furnish all of the system hardware. The logical recipient of this responsibility is the Airframe Contractor.
2. The Airframe Contractor and the Air Force must define the desired Total Propulsion System characteristics (inlet + inlet control + engine + nozzle + fuel system, etc.) in terms of the parameters of interest to the Air Force from the System viewpoint, as opposed to a consideration of the individual subsystems (i.e., inlet, inlet control, etc.).
3. The Airframe Contractor and the Air Force must agree on the test conditions and methods by which they can determine if the Total Propulsion System exhibits the characteristics defined in (2) above.
4. The Airframe and Engine Contractors must jointly define the characteristics that their respective hardware elements should exhibit by considering each of the interfaces that contributes to make up the Total System.
5. The Airframe and Engine Contractors must jointly define the specific tasks that each will pursue during their development programs in order to achieve the characteristics defined in (4) above. This should encompass analytical studies, development tests, and the required data exchange.

With the above framework in mind, let us discuss Items 2 through 5 and consider the salient features which could facilitate the application of the technical effort.

Total Propulsion System Characteristics (TPSC). The first element, as indicated in Item 2 above, is the definition of the objectives of the System in a "Total Propulsion System Characteristics" document. This should be approached by considering the needs and desires of the "total customer". In the case of a complete weapon system, this view of the "total customer" will require that we recognize (1) the Using Command (flight crew, maintenance, and operations personnel); (2) the Development Command (engineers, managers); (3) the Training Command (personnel managers); and (4) the Logistics Command (suppliers). This approach will produce a mechanism for communicating with the various segments of the Customer's organization so that both the Air Force and the Airframe Contractor have defined objectives. Further, the objectives will be visible, and there should be no surprises if certain "goodies" do not appear in the final hardware. Also, if this definition process is properly pursued, it will avoid a concentration of the design effort on the flyable hardware at the expense of the support items, which can represent a significant part of the total cost.

Inherent in the formulation of the TPSC document is a communications process between the Air Force and the Airframe Contractor that we want to encourage. As a result, the following are typical "System Characteristics" which would be defined:

- o Crew Station Controls
 - ✓ What Controls?
 - ✓ Manual vs. Automatic Features
- o Main Engine Ground Starting
 - ✓ Starting Time
 - ✓ Required AGE

- o In-Flight Ram Air Starting
 - ✓ Installed Conditions
 - ✓ Mach/Altitude Envelope
 - ✓ Starting Time
- o Propulsion System Stability
 - ✓ Airplane Maneuver
 - ✓ Throttle Transients
 - ✓ Mach/Altitude Envelope
 - ✓ Armament Firing
 - ✓ Inlet Air Contamination (water, steam)
- o Self-Test Features
- o Design Features
 - ✓ Applicable MIL Specs. and Deviations
- o Propulsion System Life and Reliability
 - ✓ Training Missions
 - ✓ Operational Missions
- o Component Removal and Installation
 - ✓ Which Components?
 - ✓ AGE
 - ✓ Removal and Installation Time

This type of System Characteristics definition highlights the features which the Air Force desires to have incorporated, features defined in terms that are meaningful to their operational situations.

Propulsion System Demonstration Plan. It follows that the resulting TPSC document will contain a broad definition of the System Characteristics, thus setting requirements and/or objectives that could imply a nearly "infinite" Evaluation Test task to prove complete compliance. But it is not practical to conduct such an extensive test program. Also, it is not practical for the industry Contractors to have a defined responsibility that is not adjudicated for an extended time period. Thus, the "infinite" design task must be interpreted into a finite test task. This is the function of the Propulsion System Demonstration Plan.

As an Airframe Contractor representative, I can anticipate the possibility of a negative reaction from Air Force personnel to this suggestion. They may consider that this interpretation process will, in reality, provide them with a lot of promises (TPSC) but insufficient tangible performance. This can be avoided by reasonable negotiations. For example, consider the definition of the Propulsion System Stability portion of the Demonstration Plan. The Airframe Contractor might propose anywhere from 20 to 40 specific combinations of airplane maneuver/engine throttle tests, depending upon the planned usage of the airplane, as a means of demonstrating the System Stability. Counter offers could be expected from the Air Force, and the process might be repeated several times. But ultimately, both parties would agree on a finite test program which, when completed satisfactorily, would be considered to be the equivalent of complying with the total TPSC requirement regarding System Stability.

The key to a successful negotiation will be the checks and balances that are involved. The Contractor has the incentive to do more than the minimum so that his customer is satisfied, but the Air Force must also recognize the increased resources and span time that will be incurred by an excessive test program. These incentives, plus reason, can lead to a realistic program definition.

Interface Control Document (ICD). This is a most important part of the proposed plan. Its purpose is to translate the Total Propulsion System Characteristics into side-by-side design requirements/objectives for the airframe and engine subsystems. This is the part of the process that defines the relative tasks of the Airframe and Engine Contractors; therefore, we can expect it to be somewhat difficult.

Since the Total Propulsion System includes at least the inlet, inlet control, engine, nozzle, accessory drive system, fuel system, and service bleed system, we can expect that the definition of the interfaces between the Airframe and Engine Contractors will be quite complex. If we are to have reasonable success in defining the requirements/objectives of the airframe and engine subsystems, we will need a proper definition and organization of the interfaces that comprise the Total System. This will be in consonance with the previously stated objectives of promoting communication and visibility and of providing the flexibility that facilitates the up-dating of these data as changes occur.

The following outline is suggested to provide the desired framework:

1. Physical interfaces: a description of the physical characteristics of the total engine and engine-supplied equipment (envelope, dimensions, weight), the dimensions of all mating connections, the location of all drains and service and inspection points, and the clear space required to remove and install each engine and airframe component that is engine-mounted or installed in the nacelle.
2. Functional interfaces: a definition of the conditions that will exist at an interface plane in terms of the parameters that characterize the physics on each Contractor's side of the interface plane. These data would be presented for each of the following:
 - a. Inlet/engine
 - b. Airframe/exhaust system
 - c. Airframe power accessories/engine power takeoff
 - d. Airframe bleed air system/engine service bleed
 - e. Airframe/engine fuel systems
 - f. Nacelle/engine temperature control

- g. Airframe/engine control
 - h. Electrical interfaces.
3. System interfaces: a definition of the total engine characteristics (i.e., characteristics that involve multiple functional interfaces):
- a. Airframe/engine performance
 - b. Acoustics and vibration
 - c. Reliability
 - d. Maintainability
 - e. Safety and vulnerability
 - f. Detectability.
4. Support interfaces: (a) a definition of the characteristics of the aerospace ground equipment (AGE) and the provisions within the Total Propulsion System for interfacing with this AGE, and (b) a definition of the characteristics of the training equipment.

The major point of presenting the above outline is to illustrate an organized approach to categorizing the total problem into meaningful elements. Only then is it feasible for the Contractors to define their respective design requirements and to check whether these appear to be compatible (or at least do not exhibit obvious incompatibilities).

Integration Plan. The final element is the Integration Plan. It is a schedule of planned studies, tests, milestones, and data exchange prepared jointly by the Airframe and Engine Contractors. It describes the development and evaluation tasks which are to be pursued to produce the desired characteristics for each ICD interface, as well as for the Total System as expressed in the TPSC documents. As currently envisioned, the Integration Plan would not attempt, initially, to describe each of the studies and tests in detail. Rather, it would present the significant information that is sufficient to scope the task. The details of each task would be coordinated as the development program progresses. Each interface integration plan would

also include a definition of the task(s) and scheduled time(s) for demonstrating whether the interface and system characteristics are achieved.

Since this Integration Plan addresses all of the design requirements/characteristics on the system and subsystem levels, it can serve as a prime management tool for monitoring the progress of the development program. Of course, this requires that a serious effort be made by each Contractor to prepare a meaningful Integration Plan.

Thus far, I have intentionally avoided the consideration of specifications since just the mention of them often tends to inhibit communication. It should be apparent, however, that the documents which have been described contain the data pertinent to specifications. The ICD can serve as an excellent source of specification requirements to augment the usual engine specification data. It can also serve a similar function for the airframe component specifications. And the Total Propulsion System Characteristics can lead to the definition of System requirements. The process of interpreting the data into specifications will naturally be a very important task that can "make or break" the entire effort. It can either stimulate the desired motivation through the proper definition of requirements, or it can provide the loophole(s) that convert requirements into estimates.

Joint agreement by the Airframe and Engine Contractors with the completed documentation should serve as the basis for initiating the airframe and engine development programs. And by requiring that changes be agreed to by both parties, we should be able to minimize the "separateness" of the respective development programs that was encountered during some of the previous integration programs. The documentation preparation and the subsequent employment of it to manage the development program should aid in achieving a significantly closer relationship between the Airframe and Engine Contractors.

The documentation plan can encourage us to do a complete job, and even "enforce" a degree of discipline by requiring the preparation of the data. However, in spite of determined efforts, we will not achieve perfection. It is almost certain that unexpected problems will be encountered that cannot rightfully be attributed to a deficiency on the part of either the Airframe or Engine Contractor. Also, some

problems probably will defy our attempts to isolate the causes to one side of an interface or the other. The assignment of Contractor responsibility for these "gray area" problems will be impossible, and special contractual provisions may be required in order to avoid any delay of their resolution.

In closing, I would like to add that, although the plan can provide the check list, we are going to have to be realistic as we define the development program and the evaluation tests. For example, the most extensive definition of desired engine characteristics is not going to produce satisfactory hardware. But, such things as a realistic engine Qualification Test, which evaluates the engine over its broad operating range, can stimulate the Contractor to produce the needed results. Realistic approaches will be required, not only from the Contractors but from the Air Force as well.

PROPULSION COMPATIBILITY CONSIDERATIONS FOR
ENGINE TRANSIENTS DURING EXTREME MANEUVERS

R. A. Herzmark
McDonnell Aircraft Company

I. W. Victor
General Electric Company

ABSTRACT

An example of the need for careful attention to the system aspects of aircraft/engine compatibility, particularly near limit operating conditions was recently encountered in the F-4 aircraft. Certain severe aircraft maneuvers combined with rapid throttle movements at low airspeeds at high altitude resulted in some engine compressor stalls. Satisfactory completion of the maneuver was established as a requirement and urgent resolution was necessary to meet deployment needs. This paper describes the means that were employed to improve the available stall margin with no sacrifice in performance using aircraft and engine control system modifications.

The combined cooperative effort between the engine and airframe companies illustrates the inherent requirement of a very closely integrated working arrangement as a mandatory part of the completed timely solution.

BACKGROUND

The F-4/J79 family has experienced several significant variations of the propulsion system configuration. This discussion will confine itself to the variations of the inlet, engine, and nozzle and their characteristics.

The F-4A design that first flew in mid-1958 with YJ79 engines had a supersonic double ramp inlet (with a near vertical hinge axis).

Figure 1 shows the major features of the current propulsion system arrangement including a double ramp inlet with a porous second ramp, a throat slot, a perforated variable bypass bellmouth, an auxiliary air door, and a secondary air system leading to the ejector nozzle.

An improved high speed inlet and an improved engine, the J79-8, were incorporated in the F-4B further enhancing the aircraft performance. The wide operational envelope which this combination has flown is shown in Figure 2. The compatibility which made this envelope possible was achieved by numerous detailed features of both the engine design and the inlet system. Several of these compatibility considerations, emphasized a decade ago, are worthy of special mention because of their current applicability:

1. Extensive engine distortion tolerance testing was performed with direct McDonnell representation at the altitude facility test site with access to the complete data. Inlet sizing and control selection was then made by simultaneous consideration of inlet pressure distortion and engine tolerance as well as recovery and drag characteristics.
2. The engine control was designed to satisfy a requirement to provide a high airflow idle setting to restrict the airflow transients with throttle chops at high flight speed.
3. The variable bypass system, within the limits of the inlet and nozzle sizing margins, was designed to automatically accommodate engine-to-engine airflow variations, reasonable engine airflow transients, moderate off-schedule operation of the inlet ramps, etc.

Successful operation throughout the wide flight regime was achieved because:

1. The engine tolerance to distortion in flight agreed with that obtained in the altitude facility tests and was sufficient to provide stall margin with combined inlet pressure distortion, low Reynolds Number, and engine transients.
2. The inlet and inlet control system limited the engine face distortion in flight to that determined by the inlet model wind tunnel testing.

As a result of the success of the F-4B/J79-8, additional aircraft models were developed for the Air Force and the Navy. The Air Force aircraft employed the J79-15 engine, having identical internal aerodynamic design to the -8 engine. Each succeeding model offered improved weapon system capability, but usually at the expense of some aircraft performance penalty due to the additional equipment, external stores, bumps, antennae, and weight. Consequently G.E. developed an improved model of the engine which could restore the excellent performance characteristics of the aircraft. This engine was later defined as the J79-17 (Air Force) and J79-10 (Navy) and its static S.L. performance is shown in Figure 3 along with the -2 and -8/-15 models.

The objectives of the -10/-17 engine were:

1. Increased Thrust - To be achieved by slightly increased and rescheduled TIT (Turbine-In-Temperature), revised control schedules to permit operation at higher compressor efficiency and slightly increased compressor pressure ratio, and use of a guided expansion nozzle.

Figures 4 and 5 show the comparison of the -8/-15 and the -10/-17 control schedules. Figure 4 shows the exhaust gas temperature scheduled by the controls. Figure 5 shows the revision to the speed schedule to limit the high corrected speeds to obtain higher compressor efficiencies.

The net result of this change (Figure 6) was an increase in thrust of several percent, along with an appreciable reduction in fuel consumption.

2. Improved Cruise Characteristics - To be obtained by use of a guided expansion nozzle having improved internal thrust coefficients, and a much lower boattail angle. (Boilerplate versions of this nozzle had been evaluated in F-4 flight tests by G.E. with MCAIR participation). Figure 7 compares the original aerodynamic ejector nozzle design and the guided expansion nozzle, whose internal surfaces prevent adverse over-expansion of the primary nozzle flow.
3. Improved Maintainability and Life - To be realized by detailed design changes, improved materials, improved cooling techniques, and corrosion preventive coatings.

The propulsion installation changes required for incorporating the -10/-17 engines into the two new F-4 models were modest:

1. A revised final fairing to blend with the new nozzle. The revised fairing and the lower boattail angle are apparent in Figure 8.
2. A change in the bypass schedule to hold the bypass open during subsonic cruise. This increased the secondary flow and pressure and allowed both improved nozzle thrust coefficient and reduced inlet spillage. This schedule is shown in Figure 9.

During 1966 and 1967 parallel flight test programs were conducted by MCAIR and G.E. to fully develop the performance advantages of the -10/-17 engines. Each participated in the other's flight testing, instrumentation, and data analysis. Analysis techniques and data were freely exchanged, and areas of further performance improvement were identified. Cruise improvements were explored and documented for a series of airframe modifications. Maximum power improvements achievable with engine control modifications were tested on both aircraft.

THE PROBLEM

Production deliveries of the new F-4 models began in mid-1966. In the late summer of 1967, F-4 flameout incident reports began to trickle in from squadrons. Incidents were occurring at high altitude, high angle of attack, and low airspeed, sometimes outside the minimum airspeed operation boundary. The particular conditions were a function of the skill and coordination of the pilot, but in each case the maneuver was extreme; the angles of attack were very high; the airspeed was low and the airplane in heavy buffet, at times on the verge of spin entry. Figure 10 shows the severity of the condition compared to the "limit" buffet condition employed in the aircraft specification. Our specification limit, unchanged from the F-4A days, is significantly less than the capability of the aircraft and the military pilots flying it today.

The frequency of stall/flameout incidents prompted the Navy to initiate a test program at NATC, Patuxent River, Maryland. Figure 11 shows the area in which stall/flameout tests were conducted in a single aircraft using both -8 and -10 engines. The qualitative results from these tests were that stalls and flameout could usually be induced with the -10 engine at low air speeds, high angle of attack by imposing a rapid throttle transient.

The -8 engine was not completely stall free in this adverse environment. The frequency of stall/flameout during this testing was 4% for the J79-8 and 85% for the J79-10.

Now, after 10 years of "wedded bliss" involving several thousand marriages, the engine-airframe honeymoon was apparently over. MCAIR and G.E. began the marriage counseling immediately with intensive examination of available data to see if further understanding could be reached. The two aircraft which MCAIR and G.E. had been using for performance testing were assigned, with Air Force concurrence, to this investigation. In addition, the Air Force began flying a Category II aircraft to add further information as rapidly as possible.

INITIAL TESTING

MCAIR flight data of engine accelerations showed that the -10/-17 engine acceleration from idle to maximum power was very fast at low compressor inlet temperatures. The acceleration fuel schedule at low ambient temperatures had been increased as a result of some early tests in which the -10/-17 fuel control, under certain conditions, exhibited a minor instability which sometimes resulted in a "lean shift". The addition of a small orifice in the control eliminated the instability. The net result was a rich fuel schedule when the instability did not occur. Figure 12 compares the fuel flow and RPM for -15 and -17 engine transients from idle to maximum power and back to idle under corresponding flight conditions. (The "lean shift" was not present in this -17 control). It was obvious that this much of an increase in acceleration fuel flow would have a significant effect on transient stall margin as well as engine acceleration.

The flight test program began evaluating the characteristics of other system contributions and the effectiveness of numerous modifications. The Air Force and Navy aircraft utilized cockpit instrumentation read by the pilot, supplemented in one case, by an "over the shoulder" camera record. The MCAIR and G.E. aircraft were already instrumented to varying degrees with both data recording systems and more importantly, data exchange channels between airframe and engine companies established and operating. Additional instrumentation in the form of an engine-mounted compressor face pressure and temperature rake, shown in Figure 13, was installed in the G.E. test airplane. The critical timing and the production nature of the test aircraft did not permit engine face (duct) dynamic pressures to be measured. To provide a relatively repeatable basis for comparison among the various proposed corrective measures, standardized flight test procedures employing severe, high-g, wind-up turns were used to consistently achieve speed, attitude, and power

conditions similar to those experienced in the rudder reversal maneuver. Flight procedures were:

1. Select altitudes of 35,000 feet and higher
2. Set Angle of Attack at 22 units
3. Set air speed at 200 KCAS or higher
4. Slow the aircraft to its lower air speed limit, using wind-up turn to maintain angle of attack
5. Make a series of power lever transients on one engine consisting of:
 - a) Burst from flight idle to military power
 - b) Burst from military to maximum afterburning
 - c) Burst from flight idle to maximum afterburning
6. Leave the second engine at a fixed power setting.

The results of the flight testing suggested several courses of action. The initial approach was to lower the acceleration fuel schedule in the low ambient temperature region to increase the transient stall margin during throttle jams. Concurrently, an alternate, more immediate approach was also pursued to provide a means for increasing the available stall margin during the periods of adverse environmental exposure, by lowering the operating line of the engine without an acceleration fuel schedule change. Two basic arrangements which could be readily implemented were:

1. A combination of overboard compressor discharge bleed and anti-icing bleed actuated by the pilot.
2. A combination of anti-icing bleed and a two percent increase in the first stage turbine nozzle area.

While these arrangements, particularly the first one, provided a significant improvement in the stall-free envelope of the weapons system, they did not comply with the objectives which the using services subsequently established. These were:

1. No engine performance degradation
2. No cockpit/pilot action required
3. No new flight restrictions

Other modifications tested were aimed at increasing stall margin by reducing the severity of the environment and focused on the inlet distortion characteristics. They included:

1. Adding vortex generators in the inlet duct in an effort to lower the distortion levels at the extreme angles of attack.
2. Positioning the variable ramp at a negative setting so as to increase the inlet throat area, reduce the initial duct Mach number, and obtain reduced distortion and possibly improved recovery.
3. Restricting and/or "closing" the variable bypass to reduce the inlet mass flow and lower distortion.
4. Revising the engine control scheduling of RPM cut-back so as to reduce engine airflow at this condition and obtain lower distortion.

The vortex generators shown in Figure 14 did not reduce the distortion, probably because the flow phenomenon involved was occurring too far forward on the duct lip to permit vortex generators to be effective. The negative ramp setting did not show any improvement. Closing the bypass bellmouth showed a small reduction in distortion and the reduced RPM schedule gave a smaller beneficial effect.

The flight testing was performed by incorporating the proposed change on whichever aircraft could best conduct the evaluation earliest. Reduced acceleration fuel flow schedules were achieved by using the fuel control specific gravity adjustment. Companion factory, altitude tank, and wind tunnel tests were performed to supplement and complement the flight testing.

The accumulating data from the various test activities permitted the following appraisals:

1. The depreciation of the compressor stall line with Reynolds number for these low speed, high altitude conditions was significant, but consistent with what could have been expected from previous experience.
2. The depreciation of the compressor stall line with simulation of the large one per revolution pressure distortion was appreciable, but also consistent with what could have been expected.
3. The compressor-to-compressor stall line variation was significantly greater than had been anticipated or understood. Figure 15 shows the spread obtained from static tests.
4. The measured engine face pressure distortion was large at the high angles of attack and increased with increasing inlet mass flow ratio. The strong-one-per rev pattern was clearly evident and flight and wind tunnel test results showed good agreement, as shown in Figure 16.

LATER TESTING

During the course of the flight testing, it was observed that the second engine, at a fixed power setting, would sometimes stall and flame out under the extreme maneuver conditions. This suggested that the problem included steady state as well as transient engine operation, and improvement of the transient stall margin alone would not result in a complete solution.

One of the puzzling early observations was that when the maneuver was performed with the secondary air bypass closed, the frequency of stall/flameout was reduced. (Depending upon the engine power setting, the bypass control would cause the bypass to close to the minimum area if the airspeed dropped to a low enough value). The influence of the bypass position on mass flow, and hence pressure distortion, had not been judged to be sufficient to explain the observations alone, but when viewed together with the engine face temperatures, which were above the estimated values, a connection between the two became evident.

Figure 17 shows the time history of a most interesting flight record that was obtained. Here, the engine face thermocouples were indicating local temperatures some 50°F above the compressor inlet temperatures (CIT) until the bypass bellmouth went to the closed position. The local temperatures then dropped rapidly to almost the nominal CIT values, and although the final airspeed was very low and the AOA very high, no stall occurred. This suggested the possibility that heated engine compartment air was circulating back through the open bypass. The nominal pressure gradient from the engine face to the nozzle would not cause such flow at these flight conditions, but close examination of the local static pressures at the engine face proved to be enlightening. Figure 18 shows the minimum static pressure (obtained from the 6 o'clock leg) compared with ambient static as a function of AOA. This clearly shows that compartment airflow was not being supplied from the lower quadrant of the duct, but to the contrary, flow was being induced into this quadrant from the rest of the engine face and from the compartment. Figure 19 schematically pictures this situation with flow into the compartment being heated and then recirculated and ingested by the engine.

The significance of the existence of a sector of elevated temperature air at the engine face may not be widely appreciated, but previous G.E. static test data on a high stage loading component compressor had established the potency of temperature distortion on stall margin loss. This is shown by Figure 20, based on measurements made with elevated temperature air being introduced in one 90° quadrant of the engine face. A calculated point for the J79 compressor showed a comparable degree of sensitivity. Because of the low total temperatures existing at the engine face at these flight conditions, the temperature distortion caused by a 90° quadrant averaging 32° above the freestream total temperature would result in a 6% loss in stall margin - a greater loss than that associated with all of the large pressure distortion.

Additional examination of the flight data revealed a further aggravation of the reingestion condition during engine transients which

included afterburner ignition. The afterburner light-off transient path is shown on Figure 21 where the momentary drastic reduction in secondary flow is apparent. The transient reenforcement of any recirculation into the engine would, of course, result.

THE SOLUTION

Sufficient understanding now existed to permit establishing and recommending a course of action, to restore the desired operational capability without sacrifice in performance or operational characteristics. The approach was:

1. Close the bypass bellmouth so as to eliminate or reduce the reingestion flow and the resulting temperature distortion and loss of stall margin.
 2. Reduce the transient engine operating line by reducing the acceleration fuel flow schedule.
 3. Exercise closer control over the acceleration fuel flow by tightening the tolerance at the low flow end where the stall problem was prevalent.
 4. Incorporate an exhaust nozzle area transient control mode modification to maintain the pilot desired engine acceleration time despite the reduction in acceleration fuel flow.
 5. Improve the inherent compressor stall pressure ratio by a reduction in clearances through the application of an abradable coating applied to the compressor rotor.
1. Close the bypass bellmouth to reduce secondary flow and reingestion and to restore the previous environmental conditions at the engine face.

The bypass bellmouth is positioned hydraulically by power from the aircraft utility hydraulic system. The position of the bypass is controlled by a hydro-pneumatic controller sensing a reference duct Mach number near the inlet throat. The controller compares the measured Mach no. (total to static pressure ratio) to the "built-in" reference value and moves the bypass to cause the measured value to approach the reference. Two reference values are available for use in different flight regimes and are selected by pre-set Mach switches in the CADC (Central Air Data Computer). Since the desired bypass scheduling at high angles of attack was now identical to the subsonic scheduling of the previous aircraft models, the addition of an angle of attack switch to the selector solenoid circuit of the controller was all that was required to hold the bypass closed under the desired conditions. Immediate implementation (without an angle of attack switch to allow the bypass to remain open for best cruise performance) was possible by resorting to the controller scheduling of the previous aircraft models, and this course of action was initially selected by both the Air Force and the Navy.

2. Reduction of the transient engine operating line by reducing the acceleration fuel flow schedule.

The engine utilizes a hydro-mechanical maximum fuel schedule based on a three-dimensional cam which limits the fuel during accelerations to provide protection against turbine over-temperature or compressor stall. The sensed parameters include engine speed and compressor inlet temperature. The operating region of interest was at very low inlet temperatures where the schedule had been enriched to provide rapid cold day wave-off accelerations with full bleed. Figure 22 shows the fuel flow reduction designed into a new three-dimensional cam which provided a significant lowering of the transient operating line, while still permitting the engine to accelerate at a reduced rate within model specification requirements.

3. Exercise closer control over the acceleration fuel flow by tightening the tolerance at the low flow end where the problem was prevalent.

The control vendor had demonstrated that in high production, control of the tolerances to tighter limits was attainable at no significant increase in cost.

4. Incorporate an exhaust nozzle area transient control mode modification to maintain the pilot desired engine acceleration time despite the reduction in acceleration fuel flow.

The engine exhaust nozzle is positioned hydraulically by power from the engine nozzle actuation system. The nozzle area is scheduled as a function of power lever angle at the lower power settings, but at the higher power settings the nozzle is controlled by signals from the temperature amplifier which vary the nozzle area to maintain a scheduled exhaust gas temperature limit. To retain engine acceleration characteristics to which the pilots had become accustomed, despite the reduced acceleration fuel flow, (which maintained engine acceleration time within model specification requirements) required reducing the engine back pressure. This was achieved by opening the exhaust nozzle sooner and holding it more open during the transient. Figure 23 is a schematic of the system developed to provide this transient control mode. A pressure switch, senses when the fuel control is operating on the acceleration schedule, and temporarily selects a reduced temperature schedule (T_5 reset) resulting in a more open nozzle position. Completion of the acceleration, or the presence of fuel pressure in the afterburner fuel annulus, restores the control to the normal T_5 schedule. The afterburner fuel pressure switch is employed to disarm the reset when the afterburner is ignited and the engine acceleration is essentially completed. The effectiveness of this system is shown by Figure 24. Acceleration times with and without the T_5 reset mode are compared for conditions in the flight regime of interest.

5. Improve the inherent compressor stall pressure ratio by a reduction in clearances through the application of an abradable coating applied to the compressor rotor.

To reduce the unit-to-unit spread in compressor stall character-

istics by providing more uniform and closer clearances, G.E. developed a unique abradable coating for the compressor rotor spacers which proved to be completely successful. Figure 26 shows the location and details of the buildup of the abradable coating. Satisfactory operation and retention has been demonstrated under all types of operating conditions, including very high rates of water ingestion in an altitude tank. The abradable coating's effectiveness is indicated in Figure 26 which shows the improvement in stall margin obtained on two production engines after they were returned from the field and the coating was applied. This was the only engine improvement aimed at the steady state (no throttle transients) stall margin, but it has not yet been approved by the government for incorporation.

CONCLUSIONS

The stall margin which resulted from the closed bypass schedule and the incorporation of the new fuel control (acceleration) cam is shown on Figure 27. The degradation of the sea level stall line with Reynolds Number and pressure distortion is shown along with spread in compressor characteristics which were found to exist. Air Force and Navy flight tests of these changes, along with the T5 reset feature, showed that the weapon system characteristics during the extreme maneuvering flight were equal to the previous models or better. The following quotation is an extract from Reference (a) evaluation report:

"The degree of effectiveness in eliminating the adverse transient and steady state engine stall/flameout characteristics shown by the proposed final fix configuration was impressive. The test results of the proposed final fix configuration were far superior to previous test results of the F-4J/J79-GE-10 and the F-4B/J79-GE-8 combinations. The proposed final fix configuration with a closed bellmouth could not be stalled or flamed-out within the engine operating envelope under the most adverse conditions. Test results indicate that the engine will perform satisfactorily at airspeeds well below the 150 KCAS minimum airspeed of the engine operating envelope".

Both using services consider the problem eliminated (References (a) and (b)).

The combined cooperative effort of the airframe company and the engine company was a mandatory part of the development of a complete timely solution. This is another illustration that a closely integrated working arrangement between the two manufacturers is inherently required to assure airframe/propulsion compatibility.

REFERENCES

- (a) Naval Air Test Center Report ST-06R-68, dated 9 July 1968
- (b) USAF Letter AFZMT to MCAIR, dated 6 January 1969

Figure 1

F-4 Propulsion System Schematic

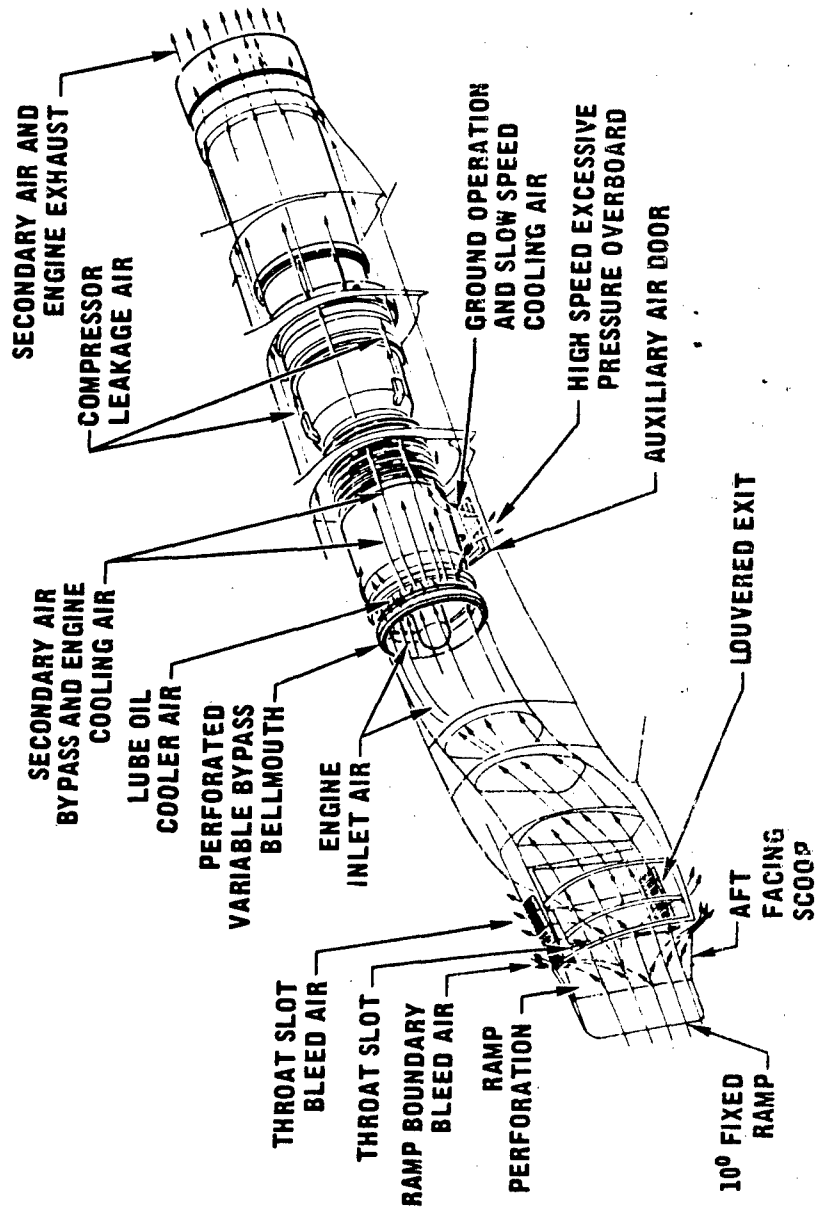


Figure 2
F-4/J79
Demonstrated Flight Region

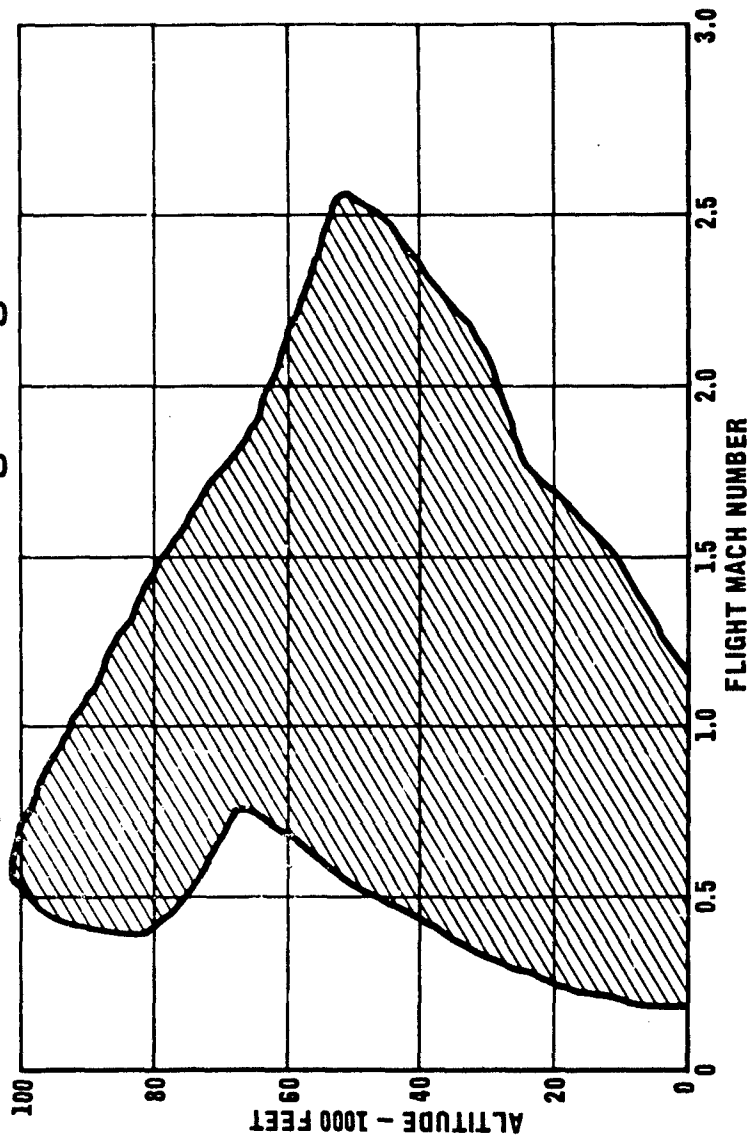


Figure 3

J79 Engine Models Used in F-4 Aircraft

| ENGINE MODEL | J79-2 | J79-8/-15 | J79-10/-17 |
|--|---------------|------------------|-------------------|
| RATING SEA LEVEL, STATIC STANDARD DAY | | | |
| MAXIMUM POWER THRUST (POUNDS) | 16,150 | 17,000 | 17,900 |
| MILITARY POWER THRUST, (POUNDS) | 10,350 | 10,900 | 11,870 |

Figure 4

EGT Control Schedule

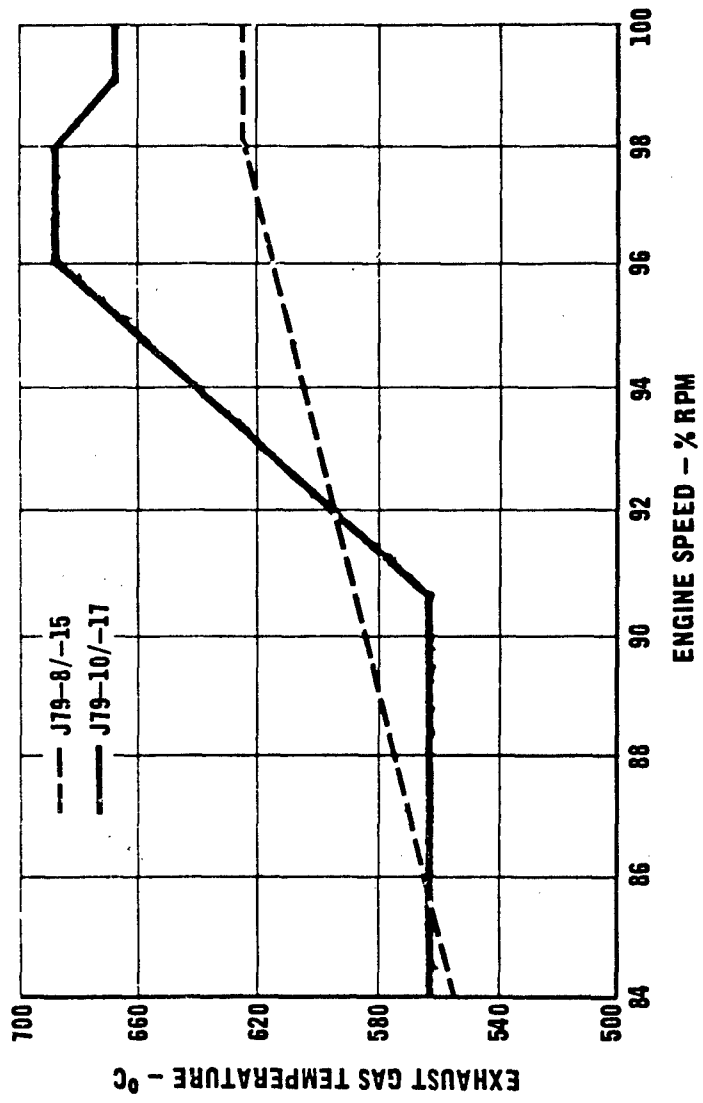


Figure 5

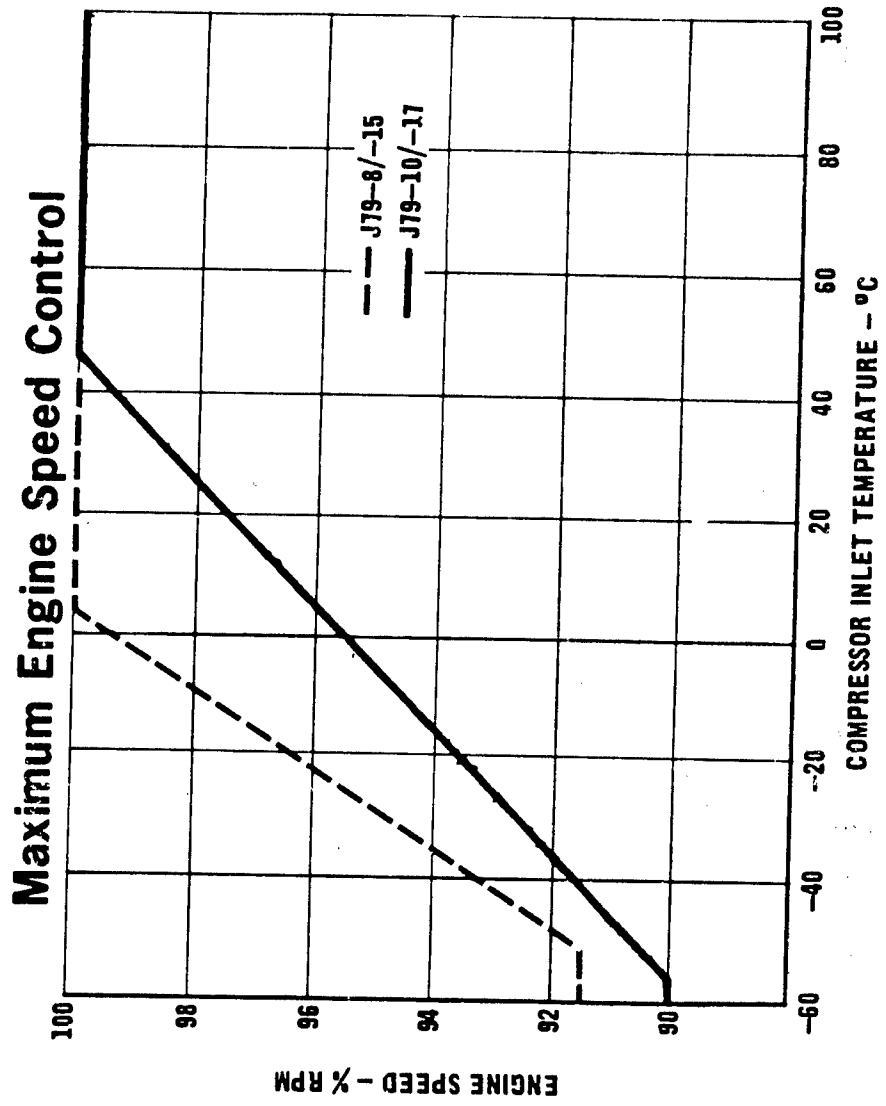


Figure 6
Effect of Speed Optimization
on J79 Compressor Performance

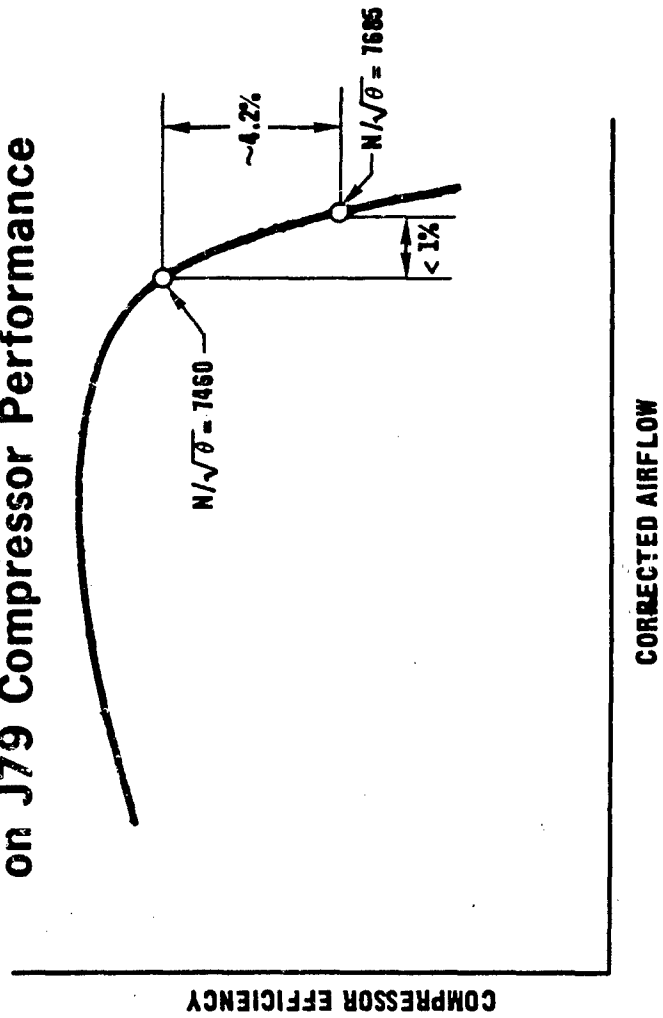
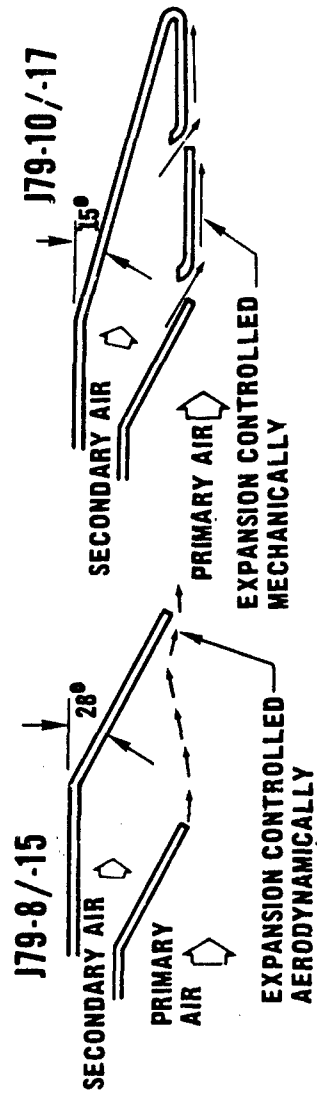


Figure 7

Nozzle Schematics
CRUISE POWER POSITIONS



MAXIMUM AFTERBURNING POSITIONS

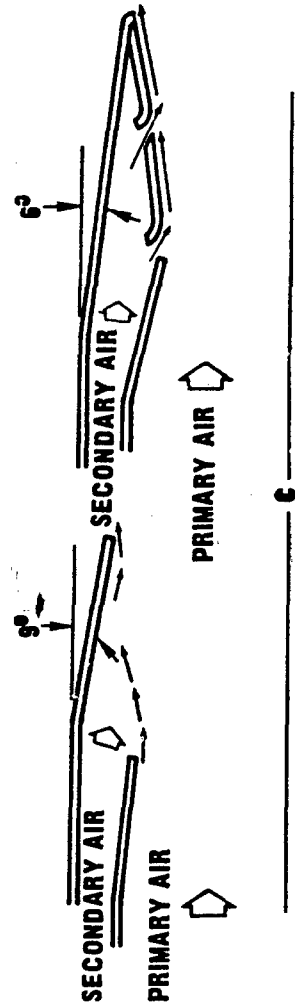
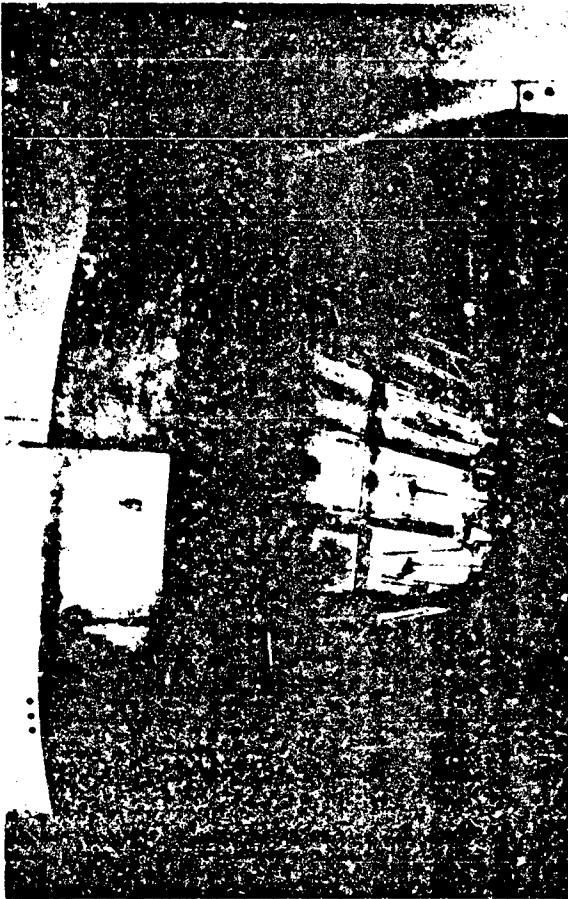


Figure 8

Nozzle Installations



J79-8/-15



J79-10/-17

Figure 9
Bypass Control Schedule

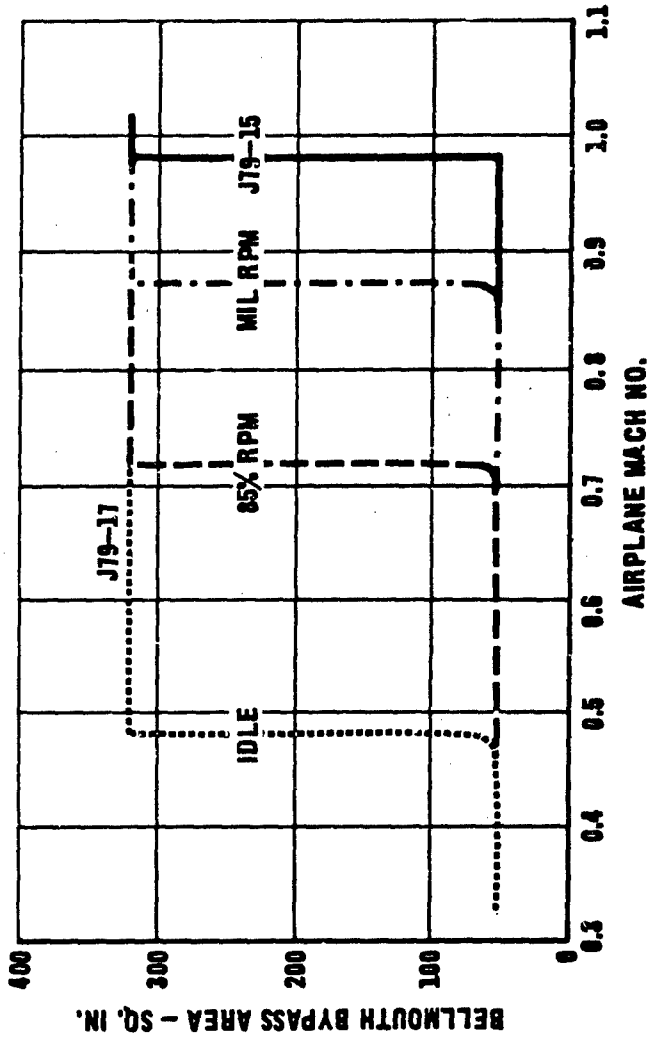


Figure 10
High Altitude Subsonic Maneuvering
Flight Investigation
NOMINAL ALTITUDE - 45,000 FT

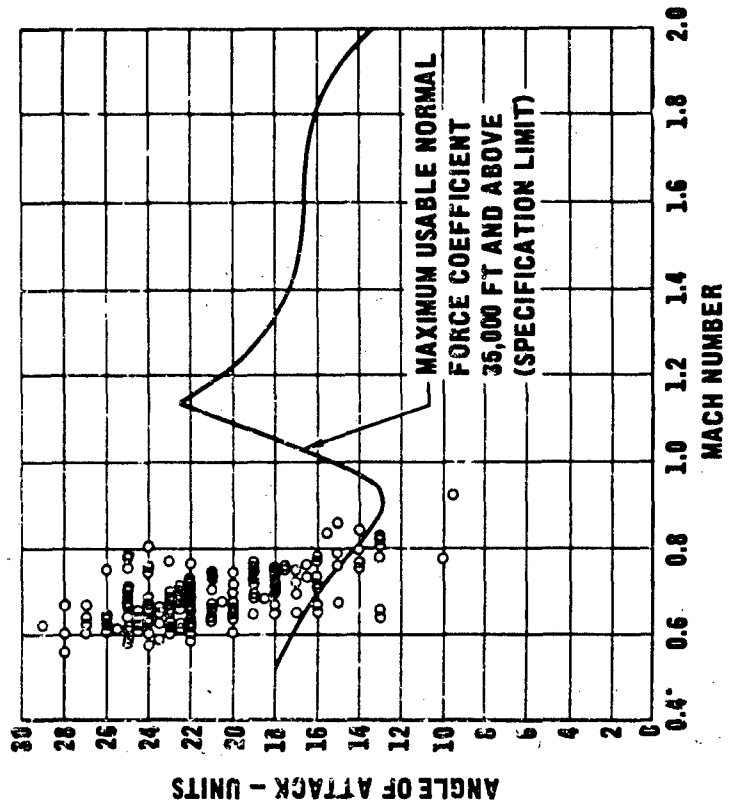


Figure 11

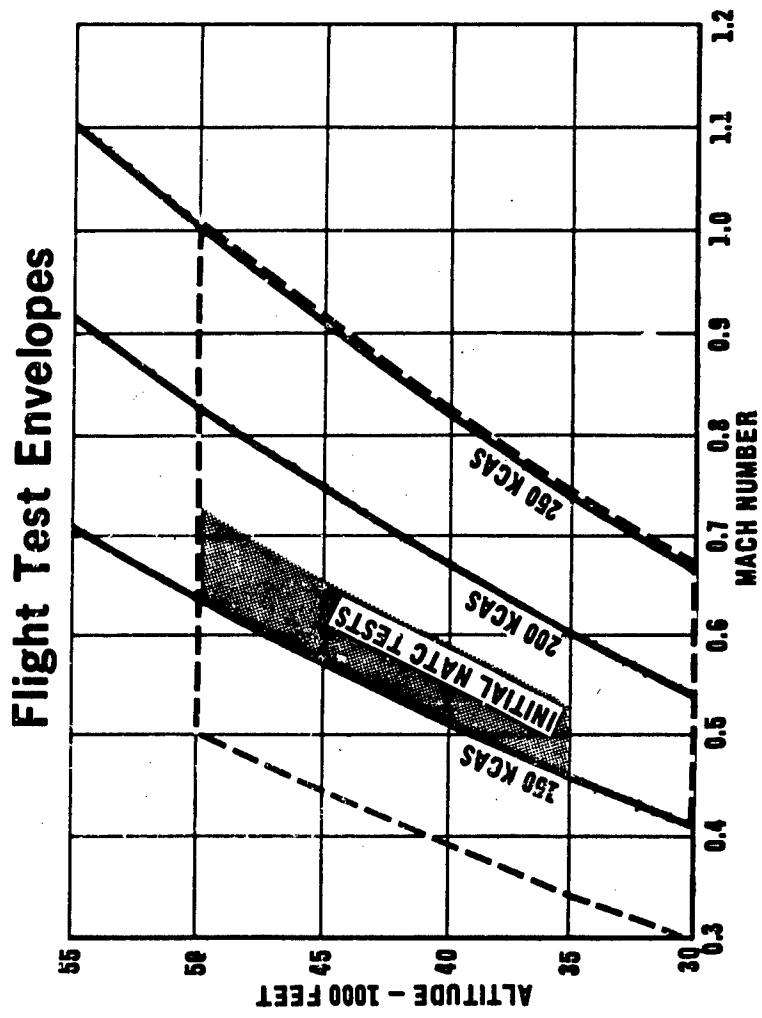
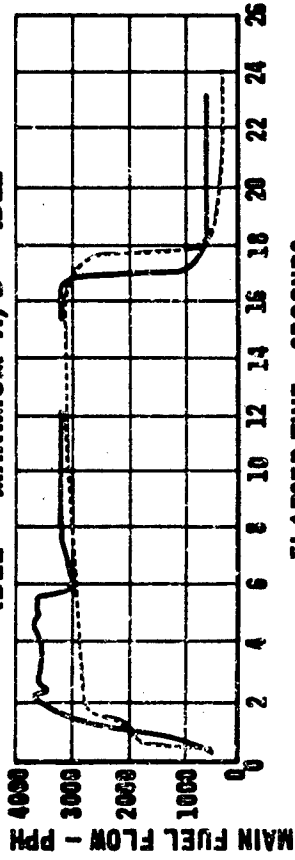


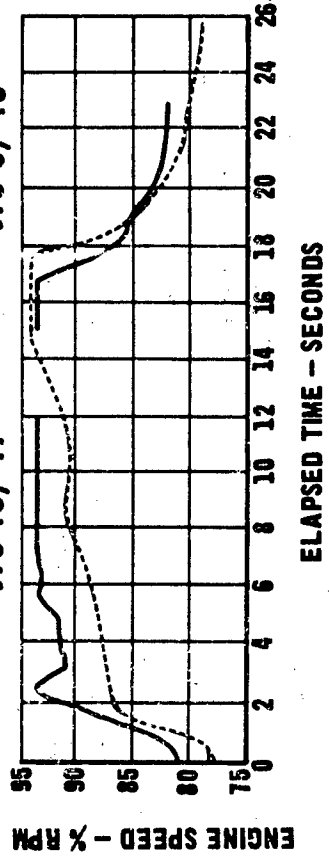
Figure 12

Engine Transient Comparison
41,500 FT (NOMINAL) .86 MO (NOMINAL)
IDLE - MAXIMUM A/B - IDLE



ELAPSED TIME - SECONDS

— J79-10/-17 - - - J79-8/-15



ELAPSED TIME - SECONDS

Figure 13

J79 Engine Face Instrumentation

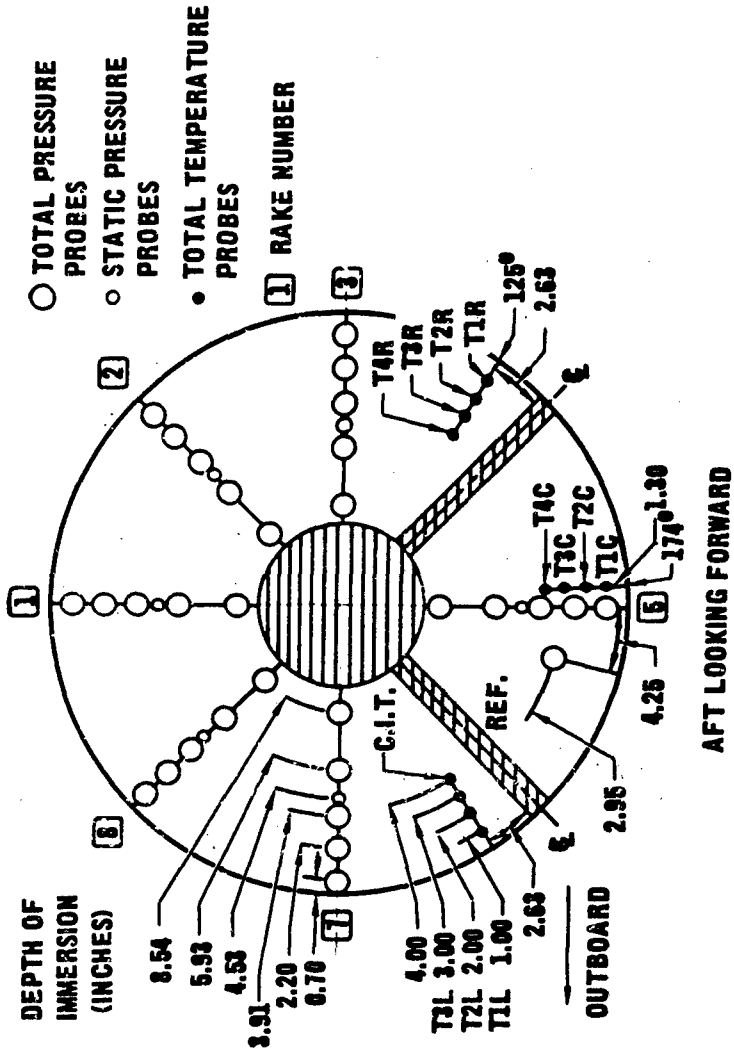


Figure 14

Inlet Vortex Generators

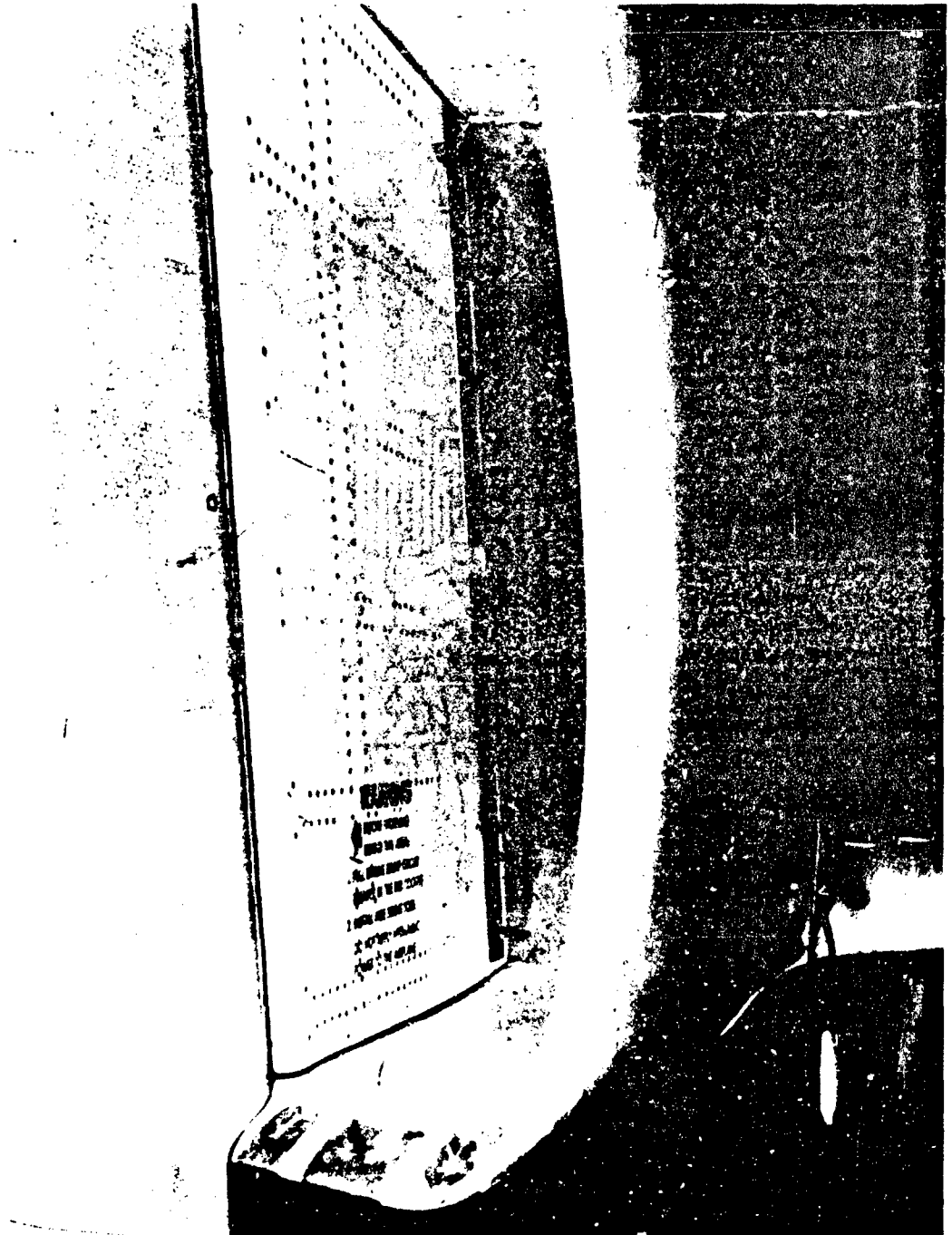


Figure 15

**Stall Margin Spread
J79-104-17 PRODUCTION ENGINES
CORRECTED SPEED = 100%**

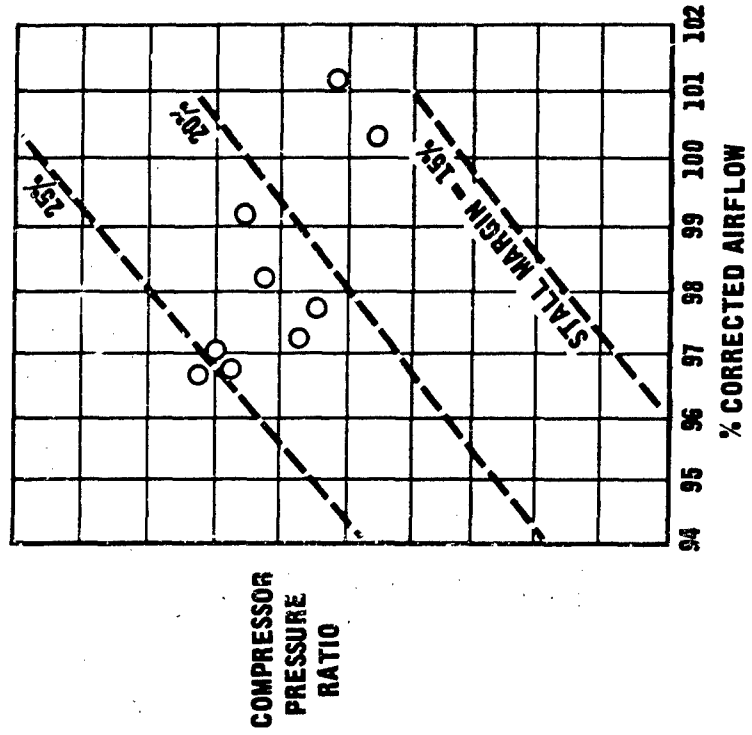


Figure 16

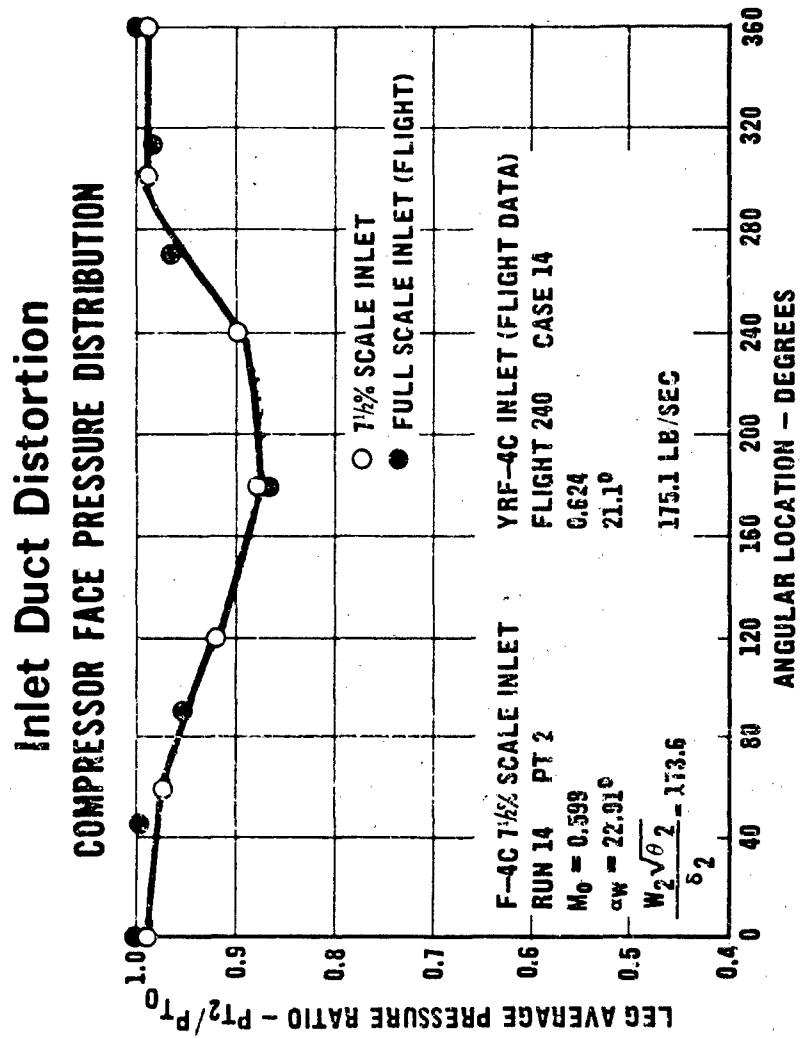


Figure 17

Flight Test Record

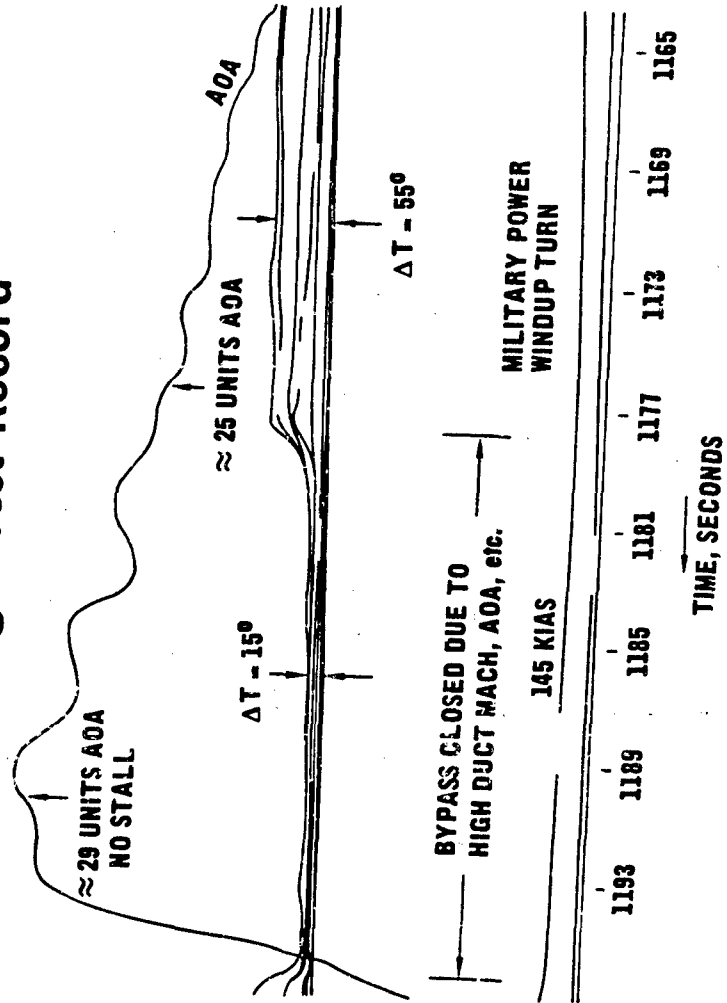


Figure 18

Minimum Compressor Face
Static Pressure Ratio

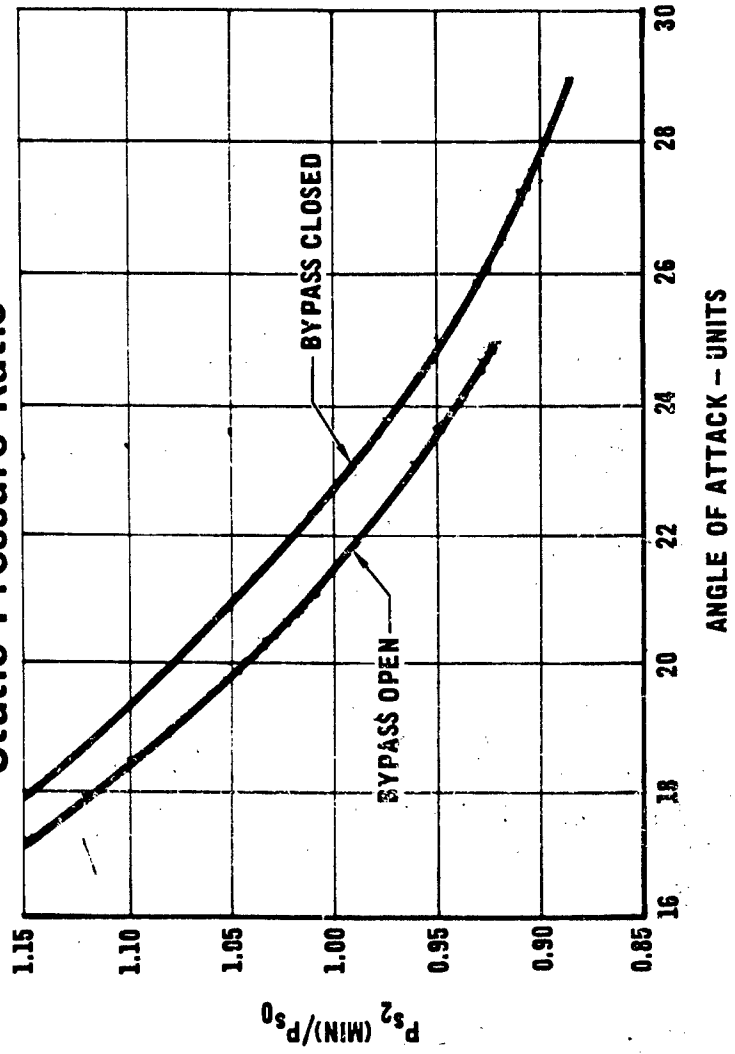


Figure 19
Recirculation Schematic

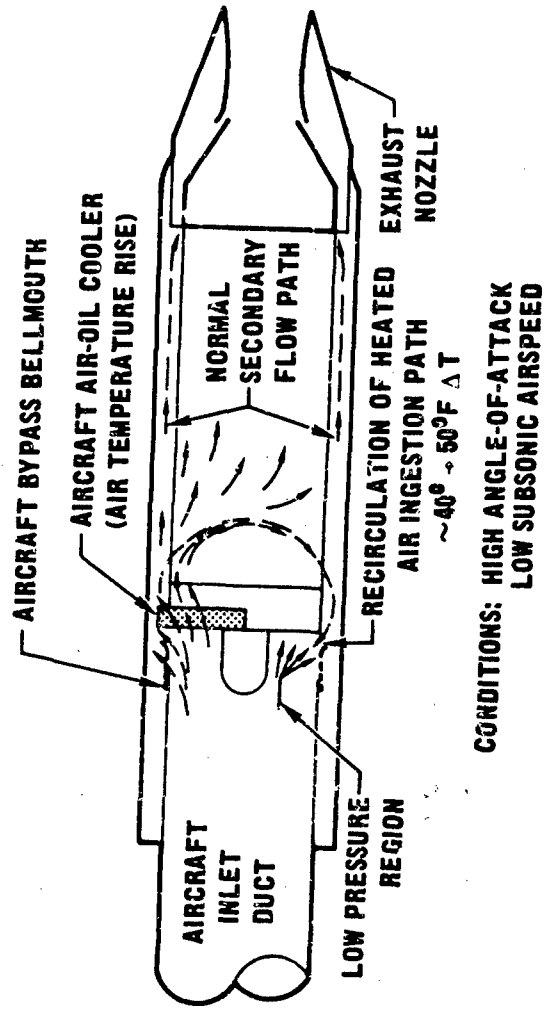


Figure 20

Inlet Temperature Distortion Effect on Stall Margin

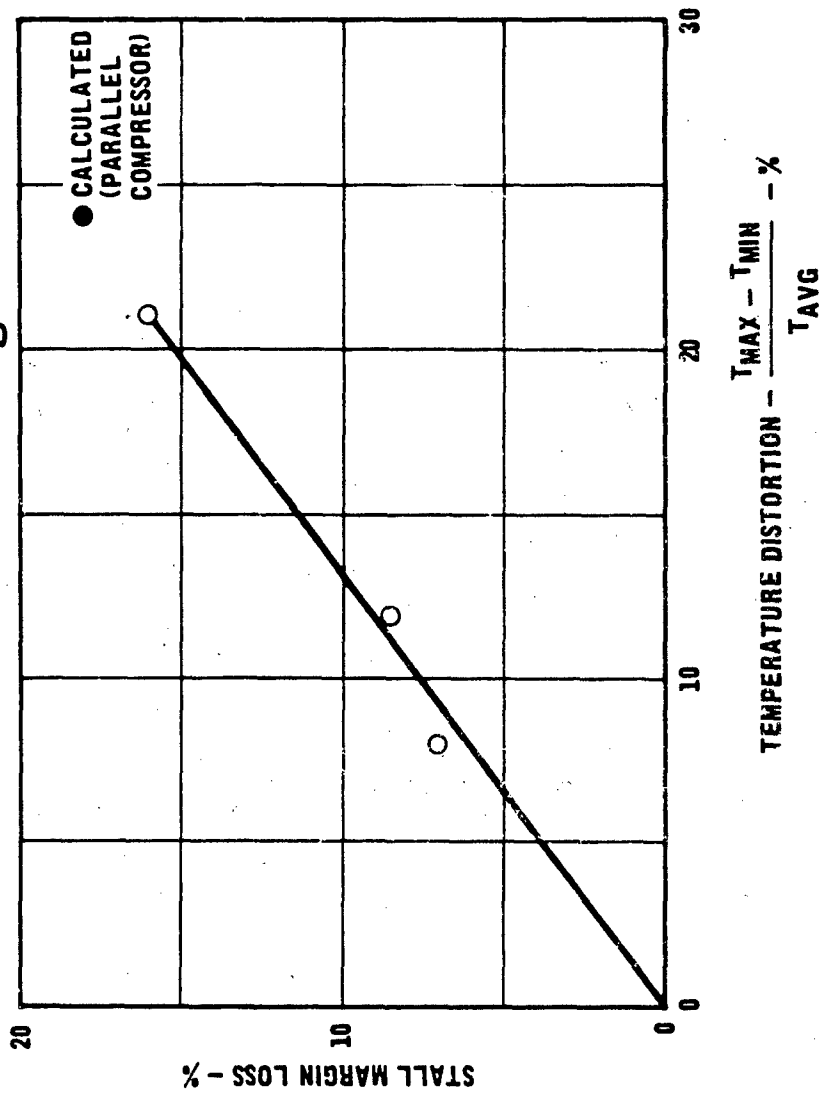


Figure 21
Effect of Afterburner Light-Off
on Secondary Flow

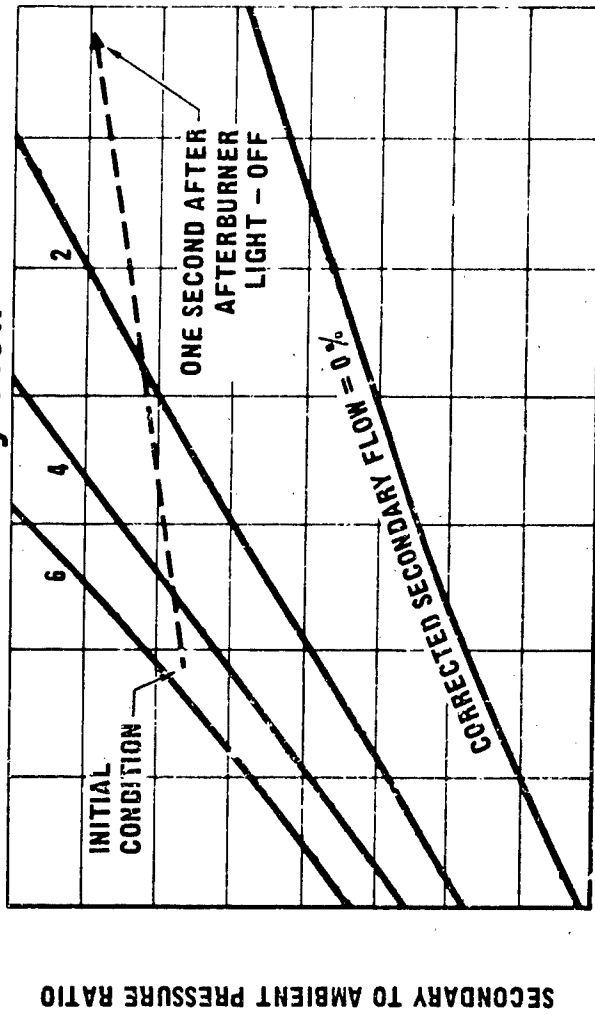


Figure 22
Reduction in Scheduled Acceleration Fuel Flow

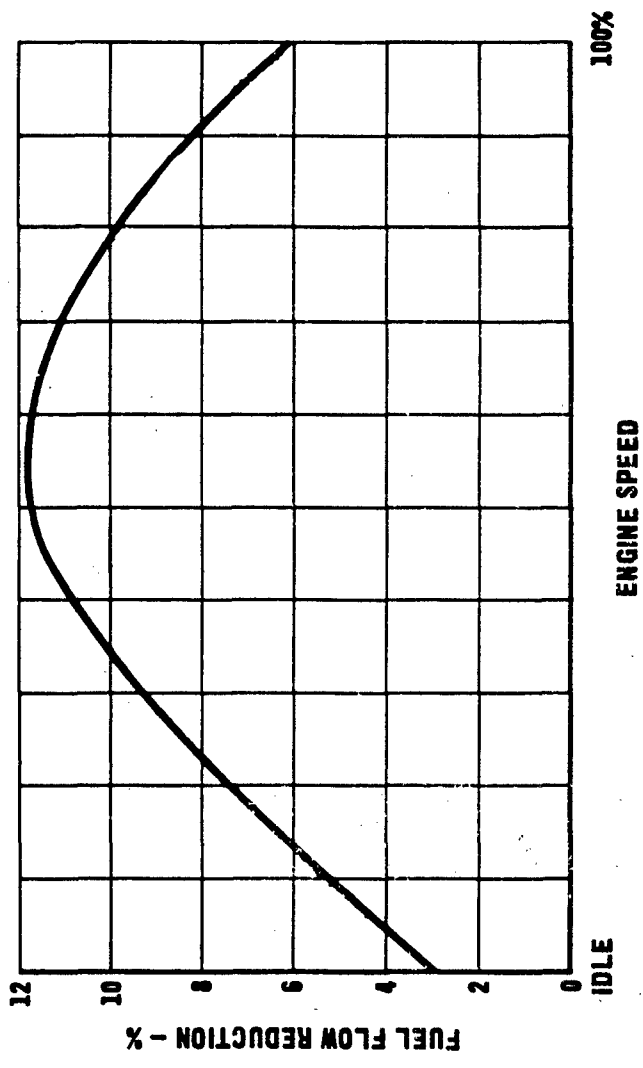


Figure 23
Acceleration T₅ Reset System

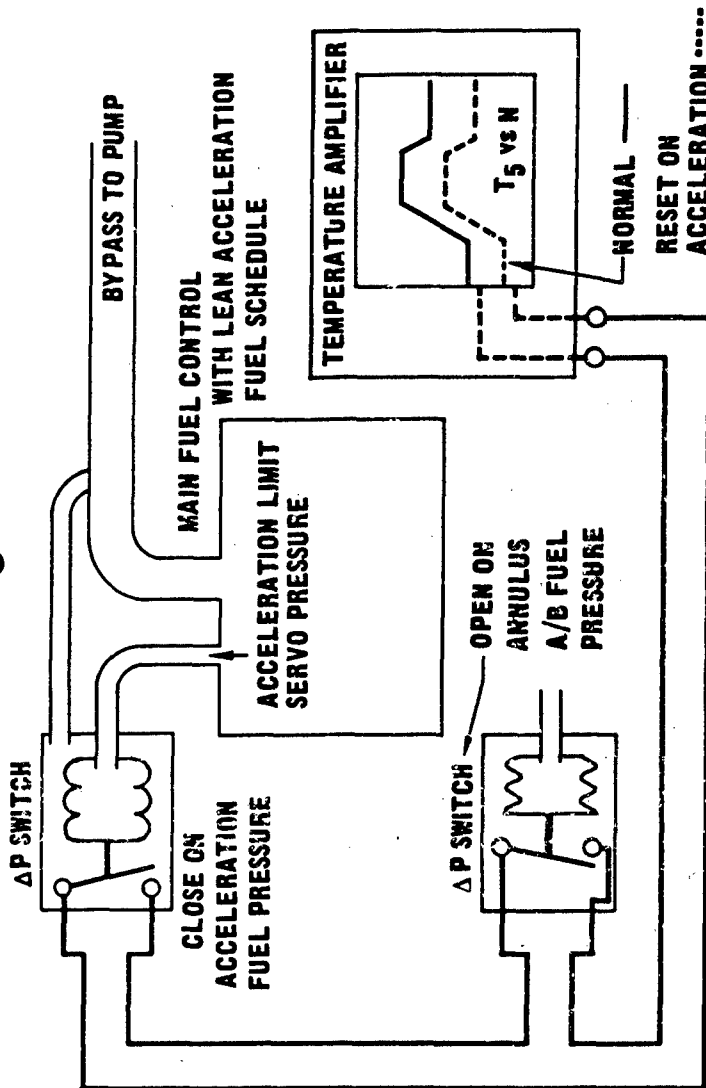


Figure 24
Acceleration Characteristics
- 186 Acceleration Cam

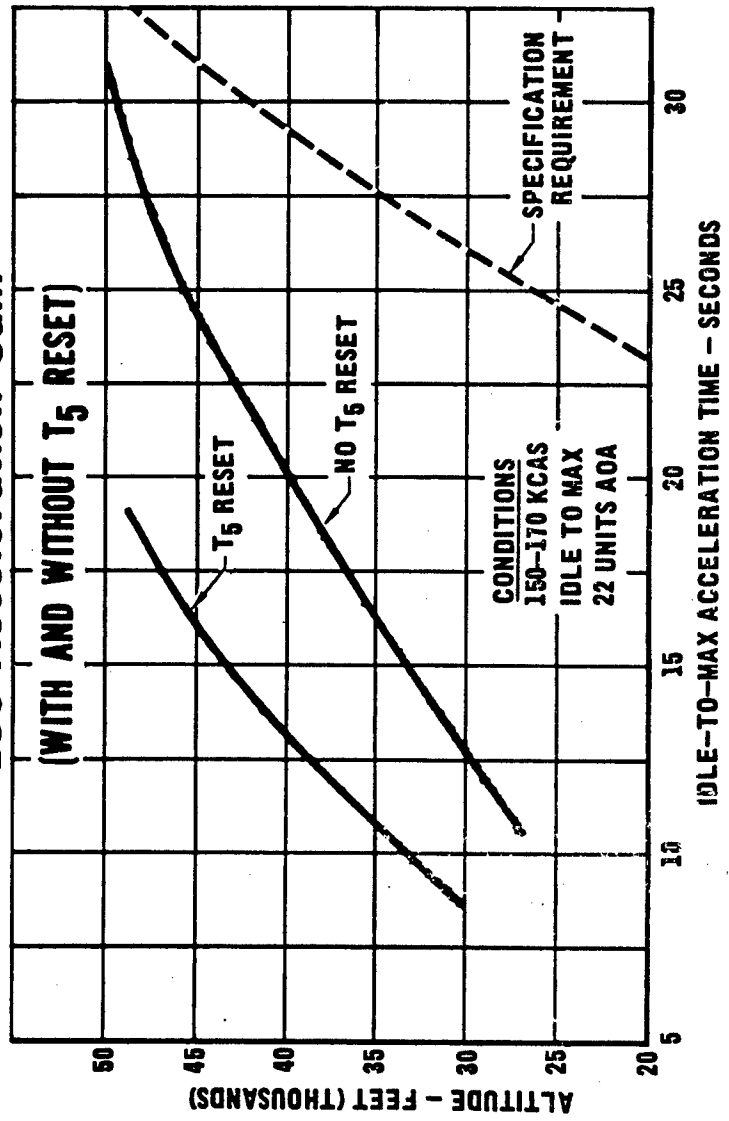
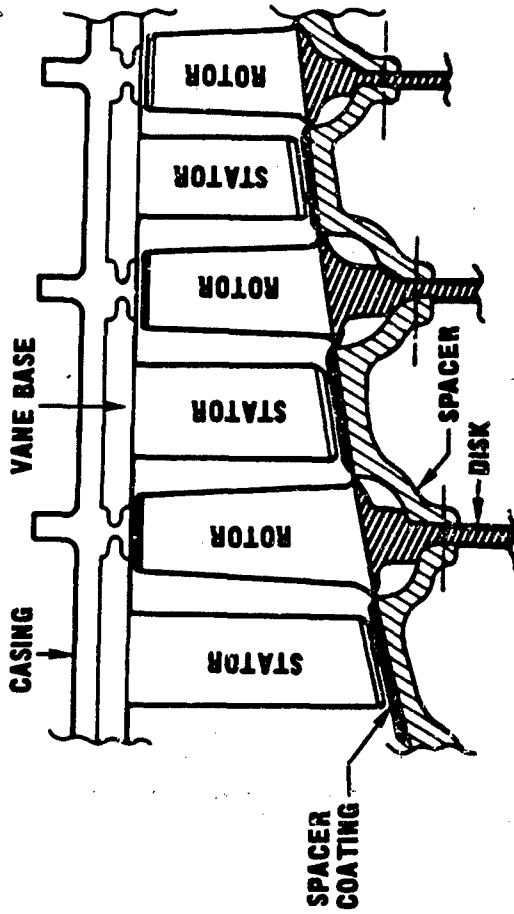


Figure 25

Nickel-Graphite Coating Schematic
J79-10 COMPRESSOR S/N 430-006 REAR STATOR CASING



- 1st COAT 0.0015-0.002 NICKEL PLATE
- 2nd COAT 0.001-0.002 METCO 404 BOND COAT
- 3rd COAT 0.015 SPRAY COAT
- 75/25 NICKEL-GRAPHITE

COATING MACHINED TO 0.012 INCH NOMINAL THICKNESS, 32 RMS FINISH.
"LEADING" AND "TRAILING" EDGES REVELED.

Figure 26

Stall Margin Improvement
with Coated Compressor Rotor

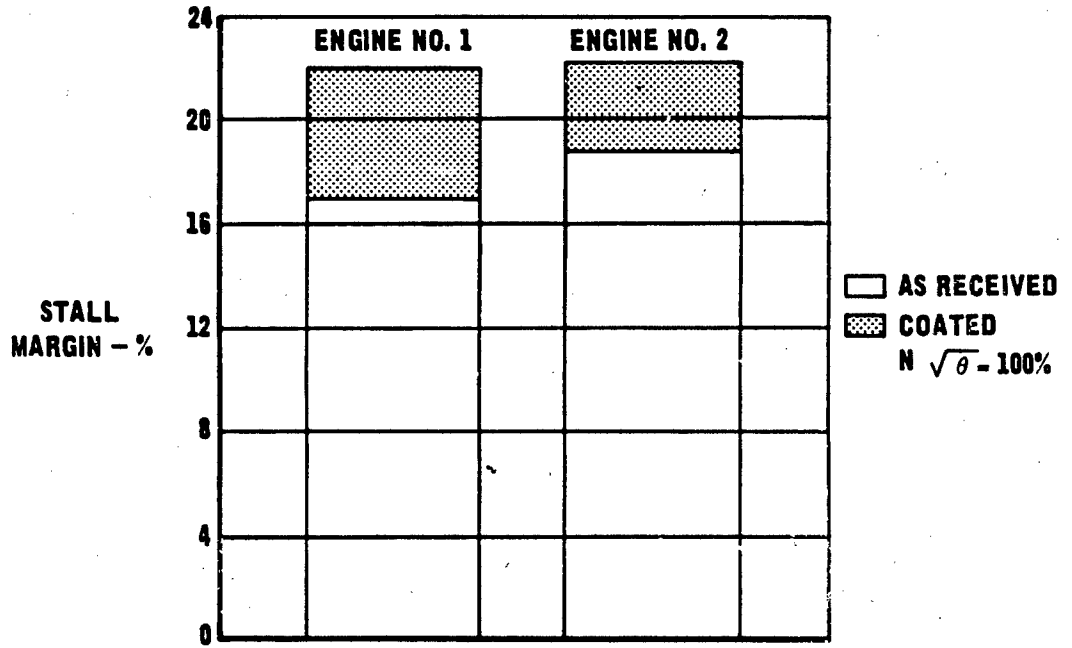
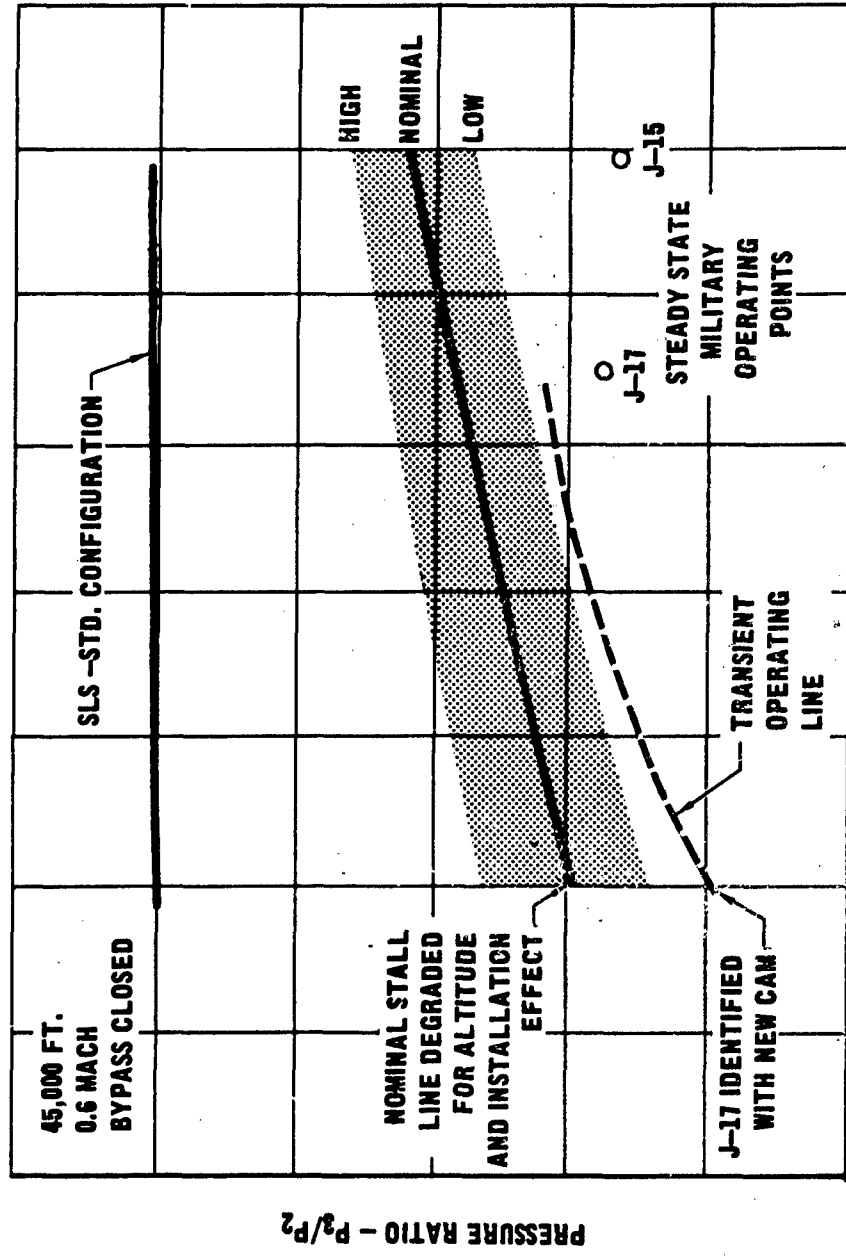


Figure 27
Demonstrated Stall Margin



CORRECTED SPEED $\sim N/\sqrt{\sigma}$

ICE CRYSTAL INDUCED COMPRESSOR STALL
IN F-102 AIRCRAFT

D. S. Oesterle
General Dynamics/Convair Division
San Diego, California

J. L. Tubbs
San Antonio Air Materiel Area (AFLC)
Service Engineering Division
Kelly Air Force Base, Texas

ABSTRACT

Flight test data reveals that the compressor stalls experienced by the F-102 in severe storm conditions are a unique phenomenon, not related to other occurrences of compressor stall. The cause of these stalls is thermal distortion. The thermal distortion is attributed to a high concentration of ice crystals in the air combined with a duct geometry that acts as a crude ice separator. The authors contend that both duct bending and flow rotation contribute to the separator action. The authors further contend that solution of this problem is imperative, not only for the F-102, but for future all weather aircraft as well.

SYMBOLS AND ABBREVIATIONS

SYMBOLS (Ref Fig. 1)

| | |
|----------|---|
| P_{S2} | Static Pressure at Engine Compressor Face |
| P_{T2} | Total Pressure at Engine Compressor Face |
| T_{T2} | Total Temperature at Engine Compressor Face |
| T_{T3} | Total Temperature at Exit of Engine Low Pressure Compressor |
| LWC | Liquid Water Content, usually specified as grams of water per cubic meter of air (gm/m^3) |

ABBREVIATIONS

| | |
|------------|--|
| USAF | United States Air Force |
| SAAMA | San Antonio Air Materiel Area Kelly AFB, Texas (Air Force Logistics Command) |
| GD/Convair | Convair Division of General Dynamics Corporation San Diego, California |
| ASD | Aeronautical Systems Division Air Force Systems Command Wright-Patterson AFB, Ohio |
| WADD | Wright Air Development Division Now ASD |
| AEDC | Arnold Engineering Development Center Arnold Air Force Station, Tennessee |
| APL | Aero Propulsion Laboratory Air Force Systems Command Wright-Patterson AFB, Ohio |

INTRODUCTION

The compressor stall problem in the F-102 dates from about 1958 at which time the problem was mostly confined to compressor stalls occurring in or near thunderstorm activity. Tests conducted by the Adverse Weather Section of ASD (then WADD) in 1959 and 1960 showed the F-102 to be more stall prone than the other aircraft tested (F-100, F-101, F-106, and KC-135).¹ These tests, which utilized limited minimal instrumentation, sought the storm conditions which induced compressor stalls, and comparisons between aircraft were reported on a qualitative basis. However, the causes of compressor stalls were not found, and instructions were issued to avoid thunderstorms in F-102 aircraft in order to avoid compressor stalls and the possibility of engine flame out. While the percentage of compressor stalls occurring in storms diminished, the total number of compressor stalls continued to increase taking a sharp upturn in 1966. A survey conducted by USAF agencies, which covered calendar years 1966 and 1967, showed a total of 143 compressor stall incidents in F-102 aircraft of which 36 occurred in or near thunderstorms.

A program was initiated under SAAMA direction to determine the cause of these compressor stalls. GD/Convair has conducted the program under contract to SAAMA. Initial analysis indicated that qualitative evaluation would not be satisfactory, so quantitative data were sought by means of a comprehensively instrumented airframe and propulsion system.

The purpose of this paper is to highlight one aspect of the F-102 compressor stall problem; ice crystal induced thermal distortion. The findings of this program are pertinent to airframe - propulsion system compatibility because the revealed phenomenon will very likely have some impact on future all weather aircraft design. Two basic considerations will be presented. The first is the cause of compressor stalls in the F-102 while flying in thunderstorms; the second is a postulation of the mechanism producing the compressor stalls.

CAUSE OF COMPRESSOR STALL IN A THUNDERSTORM

The first indication of the ice crystal phenomena was obtained from data collected during test flight 16 over Arizona in Oct 1968. A compressor stall was experienced during penetration of a cumulonimbus while the test aircraft was flying straight and level at 34,500 ft. altitude and Mach 0.76. The test engine had demonstrated greater than average stall margin during the normal weather testing that preceded flight 16. Immediately upon entering the cloud the aircraft encountered light turbulence and the total temperature at the exit of the low pressure rotor (T_{T3}) dropped (The location of this temperature sensor and other sensors is shown in Figure 1). The light turbulence was evident in flight parameters and in the total and static pressures in the inlet ducts. Figure 2 shows portions of the analog traces during cloud entry. As expected, very little attenuation of the turbulence occurred in the inlet as evidenced by static pressure data taken at intervals along the duct and at the engine compressor face. Since no perceptible change occurred in outside air temperature or compressor face total temperature,

the probable cause of the drop in T_{T3} is a change in enthalpy due to entrained ice crystals. There were eight rakes each with five total pressure probes (P_{T2}) at the engine compressor face. Shortly after entering the cloud, the signal became attenuated for most of these probes (static pressures were not affected) as shown in Figure 3.

The P_{T2} probes are 1/8 inch diameter tubes oriented to record dynamic pressure at the engine compressor face. The ice crystal collection efficiency was assumed to be high (few ice crystals will be diverted around the tubes). Regardless of the absolute value of the collection efficiency, it will be consistent for all of the similarly constructed probes at the compressor face. The attenuation of each pressure signal is caused by filling of the probe with ice crystals. Since all probes are the same length, a measure of the ice crystal concentration in the airstream is the time required to attenuate the pressure signal for each probe.

Figure 4 shows the probes that "filled" and attenuated. The probes in inlet rakes at 1:00, 3:00, 4:00, 9:00 and 10:30 o'clock positions were completely "filled" during the flight through the thunderstorm, while only one probe each of the 5:00, 6:00, and 7:00 o'clock rakes was filled. This indicates a change in ice crystal concentration from the inlet to the compressor face, since the ice crystals would be reasonably well distributed in the free stream. The concentration of ice crystals in the upper part of the duct means a greater specific heat in that region due to two-phase flow (ice/air). This will be termed enthalpic distortion for convenience in later discussion. Since there is almost no circumferential mixing in the compressor, the heat of compression acting upon enthalpic distortion will produce temperature distortion at the compressor stage where single phase flow is restored (ice crystals are vaporized).

A computer model of the J57-P23A engine was developed by the Air Force Aero Propulsion Laboratory (APL) in support of the F-102 compressor stall program. This simulation consisted of two basic computer programs; one a steady state model, and a dynamic model. By adjusting these models to match the flight characteristics of the test engine, it was possible to "fly" the models at the various test conditions to determine the effect on compressor stall margin. While it was not practical to introduce enthalpic distortion in this model, the temperature effects of a homogeneous air-ice mixture were simulated. The results of this simulation show that ice crystals in the air adversely affect the high pressure rotor stall margin, but not sufficiently to cause compressor stall with the ice crystal content calculated to have existed in flight 16. The difference, which is 5 to 10% of stall margin, is therefore attributed to thermal distortion. This establishes, with reasonable certainty, the cause of the compressor stall in storms since temperature distortion reduces compressor stall margin.²

The high concentration of ice crystals in the upper section of the duct at the compressor face was also observed by probe damping and water collection on subsequent thunderstorm penetrations. The ice concentration in the atmosphere for these flights was of a lesser magnitude and did not induce compressor stall, but the ice crystal separation and resulting enthalpic distortion were verified.

In order to verify that temperature distortion in the compressors follows the enthalpic distortion, additional temperature probes were installed at the exit of the low pressure rotor (station 3) and additional test flights were conducted. Since this testing was accomplished during the winter months, a time when thunderstorms are not prevalent, a KC-135 water spray tanker was used to produce a simulated ice crystal environment. This tanker sprays water droplets from an atomizing nozzle, which at high altitude freeze into ice crystals through which the test aircraft was flown.

There are limitations in using the water spray tanker to simulate the desired environment, since its primary design function is not thunderstorm simulation. The difference between simulated and natural environment definitely affects test results. The major differences noted were turbulence level and total pressure rake behavior in the secondary role of ice collection. Figure 5 shows the difference in level of turbulence between the natural environment and the tanker tests. Duct static pressures (P_{S2}) are used for this comparison because of the large deflection in total pressures due to turbulence. The inlet pressure probes reacted differently during the tanker tests, and the pressure signal did not attenuate as in the thunderstorm tests, although water was removed from the probes during the post-flight inspection. The lack of probe attenuation may have been caused by the pilot's inability to keep the test aircraft in the ice stream for an extended period of time due to turbulence and poor visibility. There is also a difference in ice crystal size and shape. The ice crystals produced by the water spray tanker are quasi-spherical in shape, and average about 25 microns (.0025 cm) in equivalent spherical diameter. Ice crystals in thunderstorms vary in shape from quasi-spherical to diverse crystalline shapes, and vary in size from a few microns to hailstones. A large percentage of the ice crystals encountered during thunderstorm penetrations during this test program would be several hundred microns in equivalent spherical diameter.^{3,4}

The primary purpose of verifying temperature distortion was accomplished. Figure 6 shows the depression in T_{T3} at the four stations for different test conditions. It should be noted that T_{T3} data did not exhibit the characteristic distortion when the test aircraft was flying very close to the tanker (150 foot separation). The turbulence was so severe that the ice/air mixture at the compressor face was homogeneous. Although there is little circumferential mixing in an axial flow turbojet engine, comparison of Figures 4 and 6 indicates that the flow does rotate slightly as it passes through the first stage compressor. The liquid water contents (LWC) shown on Figure 6 were calculated from a simple heat balance using the average of the four T_{T3} rakes. No allowance was made for the effects on compressor stage efficiency or possible fuselage effects on LWC near the duct inlet.

One water spray test flight was conducted below the altitude at which water freezes to assess the effects of water clouds. Temperature data from this flight (reference Fig. 6) show that the shape of the temperature depression curve is similar to the curves for ice crystals. Cooling effects would be nearly the same for water as for ice of the same volumetric concentration, but the mass of air to be cooled is different in

proportion to the ratio of density between 10,000 and 34,000-40,000 ft. altitude. The magnitude of distortion is therefore less for water clouds (low altitude) than for ice clouds at high altitude, and compressor stall is therefore less likely. Liquid water has, however, been reported by USAF pilots at high altitude and in ambient temperatures below the normal spontaneous freeze point of water droplets (-40° C). This phenomena, which has been reported by weather research teams,⁵ could also be a source of F-102 compressor stalls, especially since the LWC observed on occasions was very high.

CAUSE OF ICE CRYSTAL CONCENTRATION

Having established the probable cause of the compressor stall as thermal distortion, and the source of thermal distortion as a heavy concentration of ice at inlet rakes 1, 2, 3, 7, and 8, preliminary findings on the cause of ice concentration are now presented. In the prior cases of compressor stalls caused by thermal distortion, the distortion originated externally. Compressor stalls at takeoff from aircraft carriers were caused by steam from the catapult being ingested at the low point of the inlet lip.² F-4 Phantom compressor stalls were found to have been caused by ingesting hot compartment air at the outer annulus of the compressor face. J-57 compressor stalls in AEDC precompressor cooling tests were found to have originated from a single plugged nozzle in the spray nozzle array.⁶ In the case of the F-102 with the inlet close to the nose of the aircraft, it is presumed that the air-ice mixture was essentially homogeneous entering the duct. The duct, therefore, acts as a separator to concentrate the ice in the upper section of the engine compressor face.

The divided or bifurcated sections of the F-102 air inlet duct bends upward and inboard from the inlet to join eight feet ahead of the engine (reference Figure 1). While it is reasonable to expect that some ice separation is caused by this turn, it does not appear reasonable that this is the total cause. Preliminary particle trajectory calculations show some crystal migration away from the bottom center of the compressor face due to the inlet duct bends. However, this calculated migration or separation is not as severe as that indicated by the test data. It should be noted that the variations in ice crystal size, shape, and mass complicate theoretical analysis of particle trajectory, and little significance can be attributed to these findings other than gross comparisons. Nevertheless, the severe separation of ice crystals at the compressor face indicates to the authors the existence of strong secondary flows in the inlet ducts.

The previously mentioned flight testing conducted by WADD during 1959 and 1960 showed a substantial difference in tolerance to ice crystal ingestion between the F-102 and other J-57 powered aircraft (F-100, F-101, KC-135). Threshold of stall was reported as 2 gm/m^3 LWC for the F-102 and 7 gm/m^3 for the other aircraft. Since the F-100, F-101, and KC-135 stalled at the same ice crystal concentration with widely differing inlet duct shapes, the cause of these compressor stalls was total homogeneous ice concentration rather than a lesser concentration compounded by thermal

distortion. From this, it is apparent the various intake duct flow paths caused very little ice to separate from the airstream. Since both the F-100 and the F-101 have bends or protuberances which should be at least equal to the bend in the F-102 as ice separator, it is submitted that the existence of a contributing factor is verified. Note that of these four J-57 powered aircraft, the F-102 is the only one with a bifurcated section of the duct. Moreover, the assymetrical curves of the bifurcated section of the duct system shows the capability to form rotational flow in each leg of the system of opposite direction to the rotation in the other leg.⁷ This opposed rotation at the confluence could increase ice concentration in the upper part of the duct. It is postulated that this opposed flow rotation imparted in the bifurcated section of the duct does act as the contributory cause to ice separation.

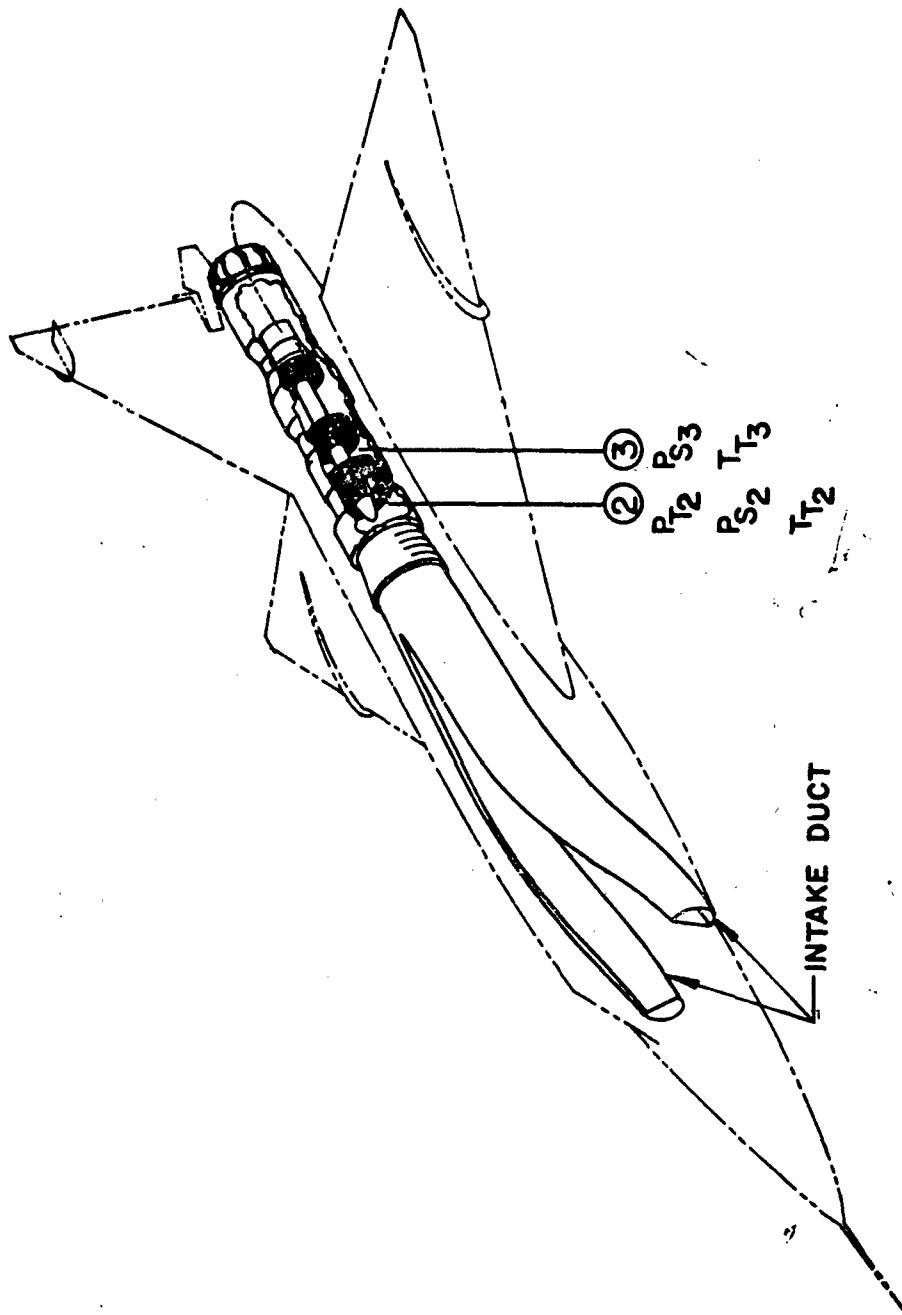
CONCLUSIONS

The authors conclude that F-102 compressor stalls during thunderstorm penetrations are caused by thermal distortion in the engine compressors. The thermal distortion is caused by a high concentration of ice crystals directed to the upper area of the engine compressor face by the air inlet ducts. A preliminary conclusion is that the ice crystal separator action is caused by: (1) inertia forces on the ice crystals due to duct bends, (2) aerodynamic forces on the ice crystals due to counter rotating secondary air flow originating in the divided sections of the intake duct.

The authors contend that the ice crystal separator action must be defined and solutions obtained. This is vital for F-102 flight safety, and could affect air inlet design for future all-weather aircraft.

REFERENCES

1. Paul, Philip J., 1st Lt, USAF, F-102 High Altitude Flame Outs In And Around Thunderstorms, WADD Technical Note 60-296, Jan 1961.
2. Tomasetti, Nicholas R., "Steam Ingestion by Aircraft Gas Turbine Engines," Proceedings of the Seventh Annual National Conference on Environmental Effects on Aircraft and Propulsion Systems, 25-27 Sep. 1967.
3. Koenig, Randall., Ice in the Summer Atmosphere: An Inquiry Into Its Structure, Genesis and Metamorphosis, The University of Chicago Cloud Physics Laboratory Technical Note Nr. 24, 1 Jun 1962.
4. Braham, Roscoe R., Jr., "The Aerial Observations of Snow and Rain Clouds," Proceedings of International Cloud Physics Conference, Tokyo, 24 May - 4 June 1965
5. Roys, G. P. and Kessler, E., Measurement by Aircraft of Condensed Water in Great Planes Thunderstorms, ESSA TN NO. 19 - NSSP, 19 July 1966.
6. King, Percy G. and Nygaard, Robert C., Mechanical Operating Experience with Three J57P11 Turbo-Jet Engines During a Pre-Compressor Spray Cooling Test in an Altitude Test Chamber, AEDC TN 57-70, Feb 1958.
7. Weske, John R., Experimental Investigation of Velocity Distribution Downstream of Single Duct Bends, NACA Tech Note 1471, Jan 1948.



F-102A ENGINE & AIR INTAKE DUCT CONFIGURATION
AND INSTRUMENTATION LOCATION

FIGURE 1

ANALOG DATA - ENTRY INTO ICE CRYSTALS

TEST FLIGHT 16

TEMPERATURE & PRESSURE -VS- TIME

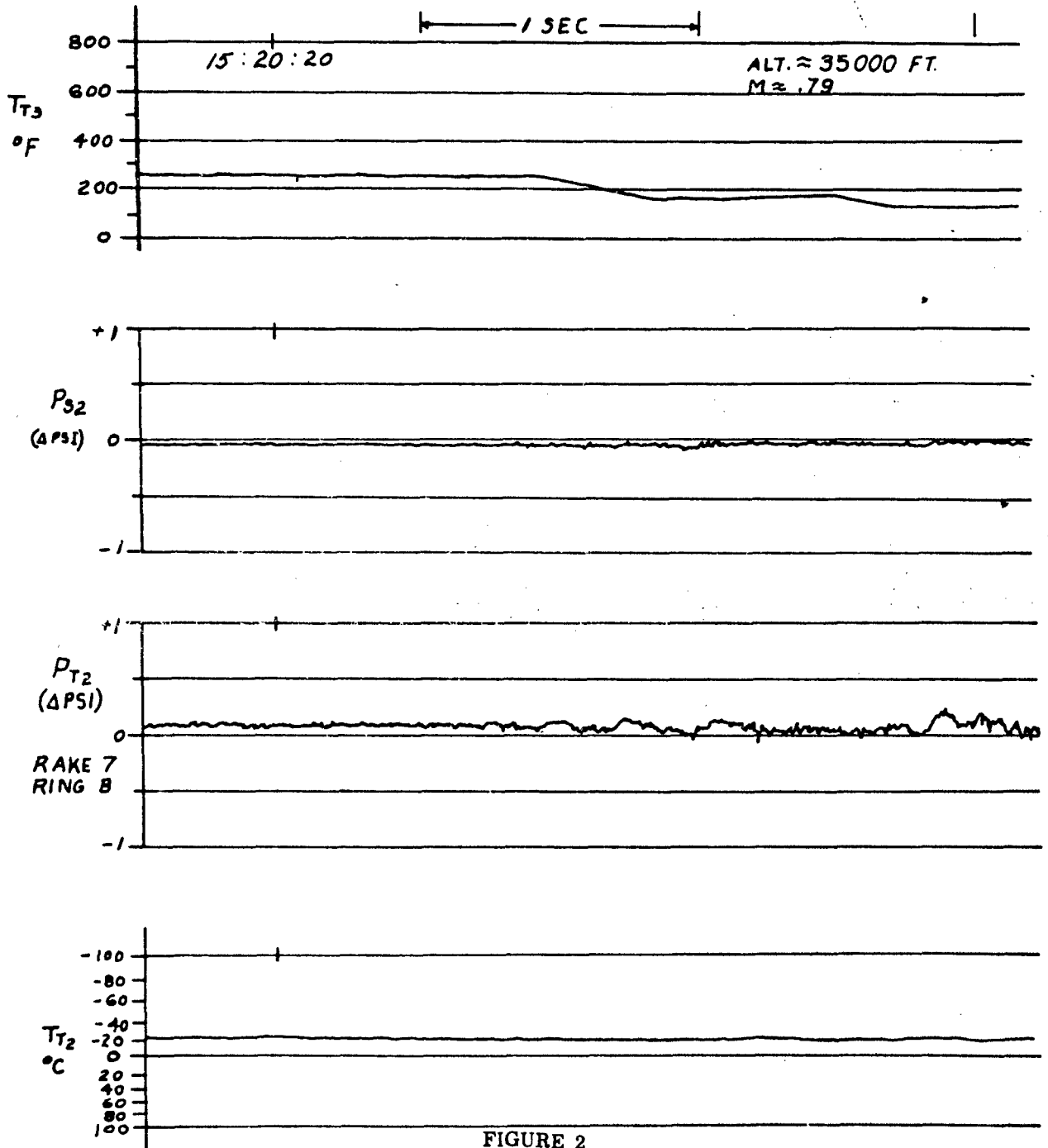


FIGURE 2

ANALOG DATA OF
ATTENUATION OF TOTAL PRESSURE PROBE DUE TO ICE

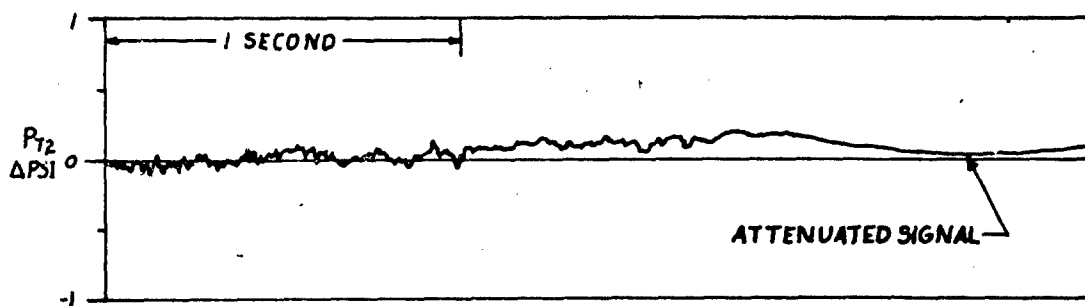
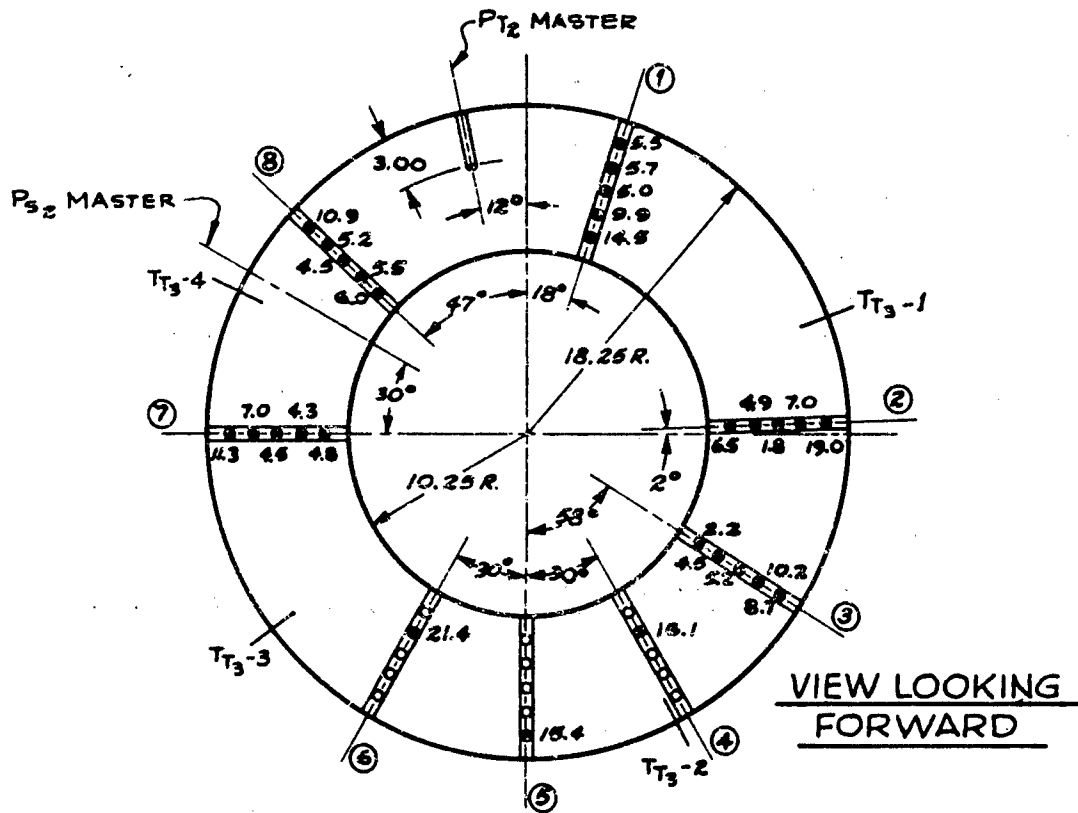
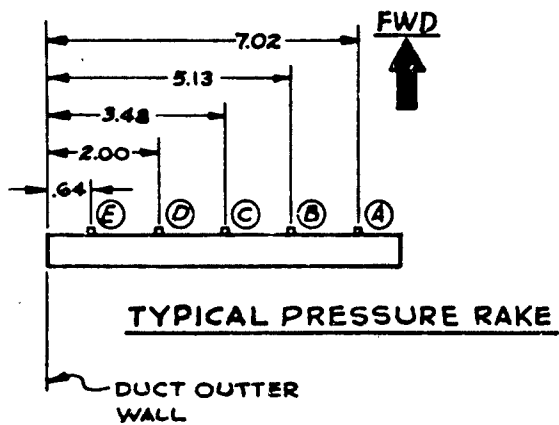


FIGURE 3



- - FILLED PROBE
- - CLEAR PROBE
- X.X - TIME TO FILL AFTER ENTERING CLOUD

**COMPRESSOR INLET
TOTAL PRESSURE (P_{T2})
PROBE LOCATIONS**

FIGURE 4

F-102A COMPRESSOR STALL PROGRAM

COMPRESSOR INLET STATIC PRESSURE (P_{S_2})
NATURAL AND SIMULATED ICE CRYSTALS

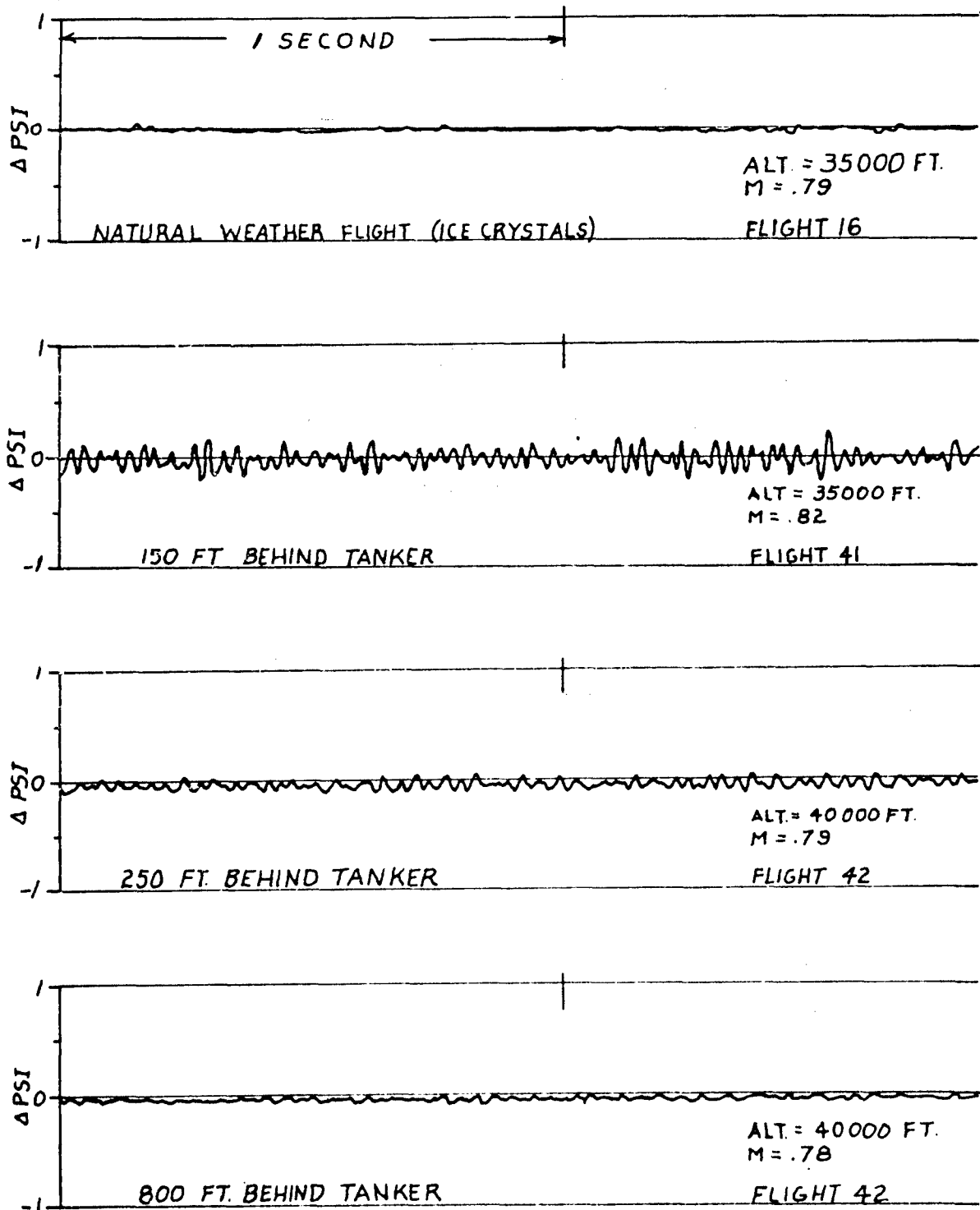
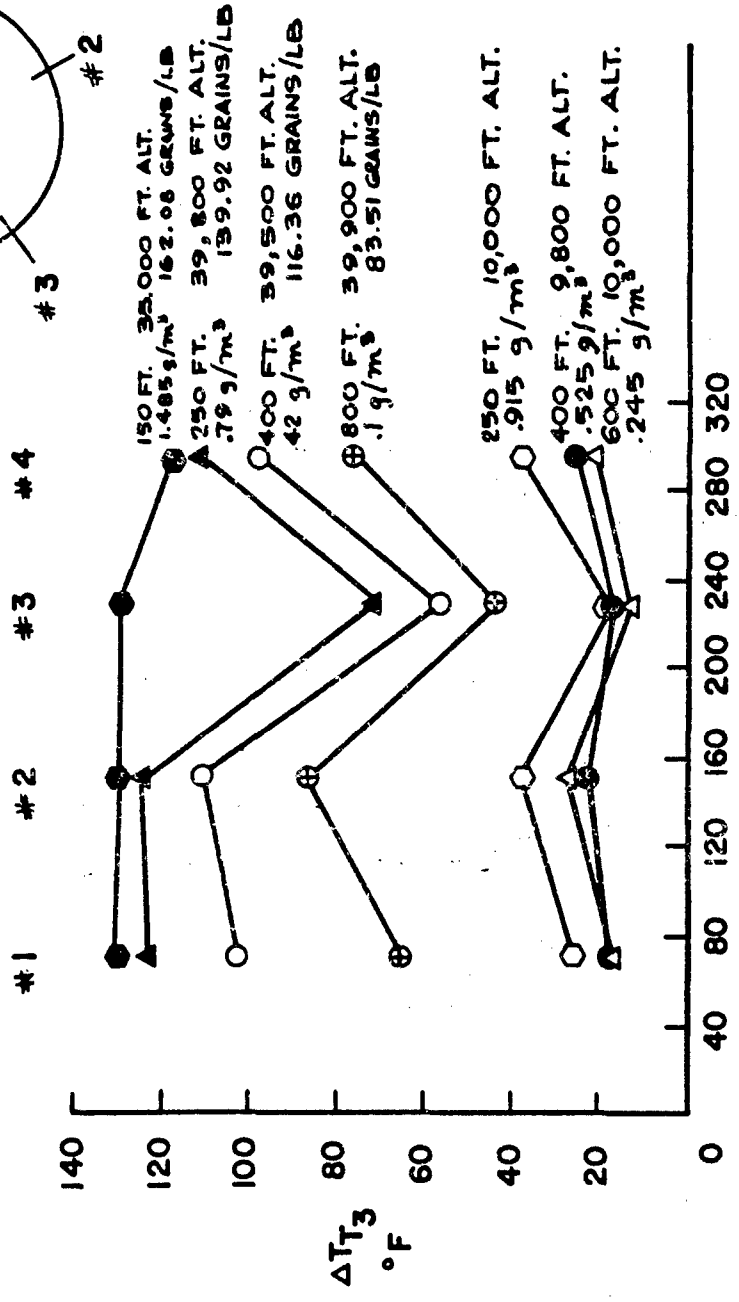
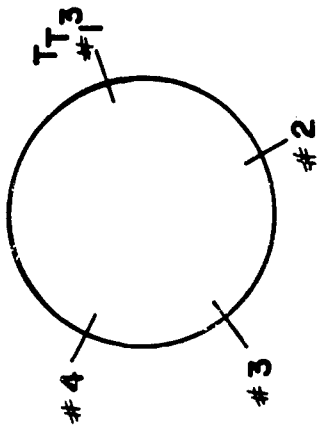


FIGURE 5

INTER-COMPRESSOR TEMPERATURE DISTORTION
(F-102A TEST FLIGHTS BEHIND KC-135 WATER
SPRAY TANKER)



CIRCUMFERENTIAL RAKE LOCATION - DEGREES
(LOOKING FORWARD - BETWEEN COMPRESSORS)

FIGURE 6

CLOSING REMARKS

Howard E. Schumacher, Technical Chairman
Air Force Aero Propulsion Laboratory

In closing this symposium, I would like to thank our audience. You have been most considerate and appreciative. Much of the success we will achieve here is due to you fine people.

I would also like to thank our exhibitors. These exhibits have lent much to the creation of the atmosphere surrounding this symposium. I am sure that the assembly of these fine displays has been the result of some very hard work for several individuals. My sincere thanks to all of you.

A very short review of the events and happenings at this conference to see what has been learned appears in order.

The first fact that becomes apparent is that we the Laboratory will be quite deeply involved in the systems business in the foreseeable future. Mr. Jones has made it quite clear that we must share in the responsibility of success or failure in systems development.

A second point is that the system of organizing installed propulsion system performance data and verification has not convinced the reviewers of such data that we know what we are talking about. Whether this system of accounting and proof test is called drag thrust resolution, bookkeeping, or whatever, we must develop a stronger rational and a more uniform procedure prior to general acceptance. The excuse that these factors are extremely configuration-oriented will not build the confidence level we must have for organized system development. This problem must be the Laboratories' first priority problem.

We have apparently built a strong skeleton for the determination of propulsion system stability definition. Here the Laboratory function must be to flesh out this skeleton by proper tests conducted at the required time in system development to allow orderly progress towards compatibility of inlet and engine at first flight dates.

We note the major contributions of control technology to the compatibility area. This is a favorable first occurrence in our eyes. We do note that the support to systems in process of definition has not materialized in hardware as necessary for achievement of stability by first flight. Thus, control technology is late as always. However the appearance at this time, prior to the occurrence of systems problems, is in itself a major step forward.

Finally, I believe we will need industry's help and support to get out of the shadow of too little too late in the propulsion compatibility area. In this vein, we from the Laboratory will be around to see each of you for your ideas, suggestions, and effort to dig out from under this shadow.

I would like to close this symposium with a vote of thanks to our hosts, the Carillon Hotel. This meeting is adjourned.

EXHIBITORS

Douglas Aircraft

Fluidyne Engineering

General Electric

Grumman Aircraft Engineering

Honeywell

Kistler Instrument

Kulite Semiconductor Products

McDonnell Aircraft

North American Rockwell

Pratt & Whitney Aircraft

UNCLASSIFIED

Security Classification

| DOCUMENT CONTROL DATA - R & D | | |
|---|---|---|
| <i>Security classification of title, body of abstract and indexing annotation must be entered when the overall report is classified)</i> | | |
| 1. ORIGINATING ACTIVITY (Corporate author) Air Force Aero Propulsion Laboratory Wright-Patterson Air Force Base, Ohio 45433 | | 2a. REPORT SECURITY CLASSIFICATION UNCLASSIFIED |
| | | 2b. GROUP |
| 3. REPORT TITLE PROCEEDINGS OF THE AIR FORCE AIRFRAME-PROPULSION COMPATIBILITY SYMPOSIUM | | |
| 4. DESCRIPTIVE NOTES (Type of report and inclusive dates) | | |
| 5. AUTHOR(S) (First name, middle initial, last name) | | |
| 6. REPORT DATE June 1970 | 7a. TOTAL NO. OF PAGES 929 | 7b. NO. OF REFS |
| 8a. CONTRACT OR GRANT NO | 9a. ORIGINATOR'S REPORT NUMBER(S) AFAPL-TR-69-103 | |
| b. PROJECT NO | 9b. OTHER REPORT NO(S) (Any other numbers that may be assigned this report) | |
| c. | | |
| d. | | |
| 10. DISTRIBUTION STATEMENT: This document is subject to special export controls and each transmittal to foreign governments or foreign nationals may be made only with prior approval of the Air Force Aero Propulsion Laboratory (APTA), Wright-Patterson Air Force Base, Ohio. | | |
| 11. SUPPLEMENTARY NOTES | 12. SPONSORING MILITARY ACTIVITY Air Force Aero Propulsion Laboratory Wright-Patterson Air Force Base, Ohio 45433 | |
| 13. ABSTRACT This report presents the proceedings of the Air Force Airframe-Propulsion Compatibility Symposium, held at the Carillon Hotel, Miami Beach, Florida, on 24-26 June 1969. Three topics were discussed during the symposium: (1) Propulsion System Integrated Performance, (2) Propulsion System Stability, and (3) Inlet-Engine Controls and Airframe Propulsion Compatibility Management. The first topic covered a session on Aircraft and Engine System Installations and another on Exhaust System Considerations. The two sessions under topic two concerned Inlet Distortion Investigations and Engine Stability Investigations. Last, the third topic also covered two sessions: one dealt with Control Aspects for Propulsion Installation and the other dealt with Management and Systems Data for Engine Inlet Compatibility. (The distribution of this abstract is unlimited.) | | |

DD FORM 1473
1 NOV 65

UNCLASSIFIED

Security Classification

UNCLASSIFIED

Security Classification

| 14. KEY WORDS | LINK A | | LINK B | | LINK C | |
|---|--------|----|--------|----|--------|----|
| | ROLE | WT | ROLE | WT | ROLE | WT |
| Turbine Engine Inlets Propulsion System Drag Inlet Control Engine Control Aircraft Performance Engine Stability | | | | | | |

UNCLASSIFIED

Security Classification